



K.A. Gschneidner, Jr.,
J.-C.G. Bünzli and V.K. Pecharsky
Editors



HANDBOOK ON THE
PHYSICS AND CHEMISTRY OF



RARE EARTHS

Volume 36

North-Holland



PREFACE

Karl A. GSCHNEIDNER Jr., Jean-Claude G. BÜNZLI and Vitalij K. PECHARSKY

These elements perplex us in our reaches [sic], baffle us in our speculations, and haunt us in our very dreams. They stretch like an unknown sea before us – mocking, mystifying, and murmuring strange revelations and possibilities.

Sir William Crookes (February 16, 1887)

This volume of the *Handbook on the Physics and Chemistry of Rare Earth* begins with a Dedication to late Professor LeRoy Eyring who had been a committed co-editor of the first 32 volumes of this series. The Dedication is written by Professor Karl Gschneidner Jr., Professor Emeritus Harry A. Eick, Dr. Zhenchuan Kang, Professor Emeritus Michael O’Keeffe, and Professor Emeritus Edgar E. Westrum, and contains a detailed vita of Professor LeRoy Eyring.

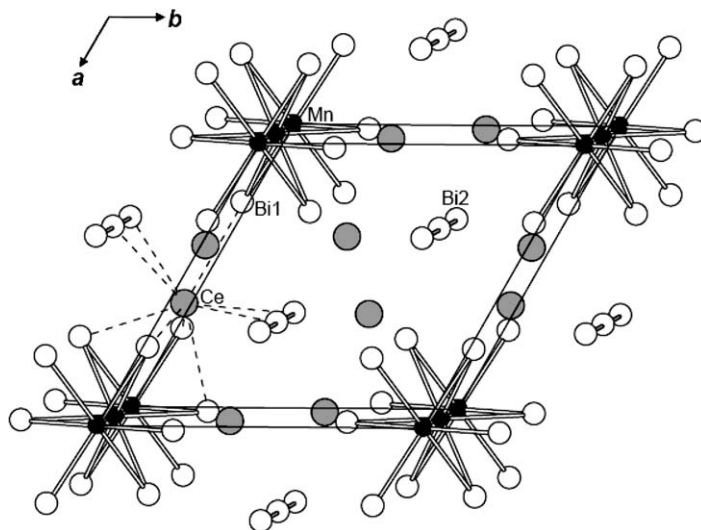
This volume of the Handbook covers four chapters, the first two pertaining to solid state physics and materials science, while the last two chapters describe organic (and inorganic) reactions mediated by tetravalent cerium-based oxidants and by divalent samarium-based reductants. [Chapter 227](#) is devoted to the description of the structural and physical properties of rare-earth bismuthides, a class of compounds showing large similarities with the rare-earth antimonides previously reviewed in [chapter 212](#) (vol. 33). The fascinating optical and electrical properties of rare-earth hydride films displaying *switchable mirror effect* are described in [chapter 228](#), along with their fabrication methods. Several chemical reactions take advantage of the tetravalent/trivalent Ce(IV)/Ce(III) redox couple and many of its potential applications are presented in [chapter 229](#), from analytical procedures, to electrosynthesis, and organic and industrial (polymerization) reactions. The last review ([chapter 230](#)) focuses on the synthesis and use of divalent samarium-based reductants in organic and inorganic reactions, mainly on those containing iodide and pentamethylcyclopentadienyl ligands, and is a valuable addition to an earlier review on divalent samarium derivatives in [chapter 50](#) (vol. 6).

Chapter 227. Bismuthides

by Arthur Mar

University of Alberta, Edmonton, Canada

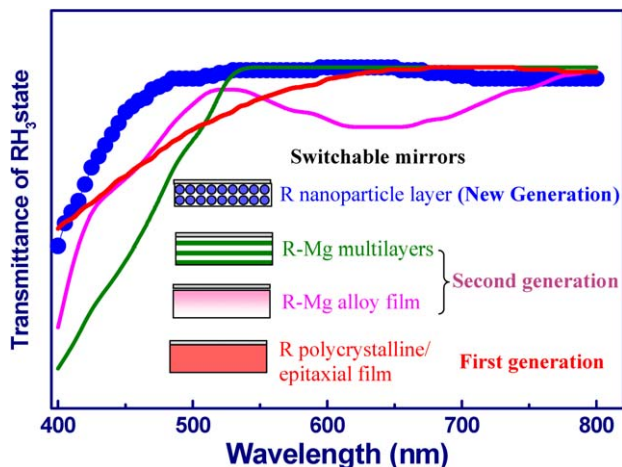
This lead chapter reviews known rare-earth-bismuth phases, focusing on the composition and structural data, but when available, physical properties are also given. The matter is organized



with respect to the order of the phases. First section describes the still incompletely investigated binary systems, while following four sections are devoted to the ternary systems, organized according to the third component M in R–M–Bi phases (M = s-, p-, d- or f-element). Ternary rare-earth bismuthides share many similarities with the corresponding antimonides, but their chemistry and physics remain less investigated. In metal-rich systems, many dense cluster-type structures are found because both R and Bi atoms have high coordination numbers, CN; the more metal-rich the compound, the higher the coordination number will be, e.g. from CN = 8 (tetragonal antiprismatic geometry) for R_5M_2Bi to CN = 12 (icosahedral) for $R_{12}Co_5Bi$. On the other hand, Bi-rich systems are more difficult to synthesize; they contain Bi–Bi one-dimensional or two-dimensional bonding networks, or finite Bi ribbons. The story of ternary rare-earth bismuthides is by far incomplete and numerous systems have yet to be investigated, particularly those containing early transition metals or post-transition metals. This review allows one to identify new opportunities in the field and to predict which compounds are expected to be isolated in the future.

Chapter 228. Switchable metal hydride films
by I. Aruna, L.K. Malhotra and B.R. Mehta
Indian Institute of Technology, Delhi, India

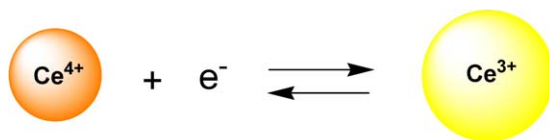
Rare-earth hydrides are stirring a large interest because of their relatively high hydrogen retention capacity given that they present the largest hydrogen-to-metal ratio (up to 3) among metals. Some hydrides containing rare earth metals are used in practical applications such as rechargeable batteries and they are also being tested for hydrogen-storage materials. In addition to being extremely hydrogen-rich, the hydrides possess interesting electrical, magnetic



and optical properties. For instance the existence of a metal to semiconductor transition has been reported for a number of rare-earth hydrides. In this review, the authors concentrate on a peculiar effect: the *switchable mirror effect* initially discovered in yttrium hydride. Films of this material a few hundred nanometers thick change from a shiny metallic state into a transparent yellow state upon applying high hydrogen pressure at 240 K (several thousands of atmospheres). The same transitions can be observed at room temperature and at much lower pressure, typically one bar, if the film is protected by a thin metallic layer (Pd for instance), and also with other rare earths. First generation (polycrystalline or epitaxial films), second generation (thin films of R–Mg alloys), and new generation (nanoparticles layers) of switchable mirrors are described in detail, from their fabrication to their optical and electric contrast, switching and recovery times, transparency, and color.

Chapter 229. Applications of tetravalent cerium compounds
by Koen Binnemans
Katholieke Universiteit Leuven, Leuven, Belgium

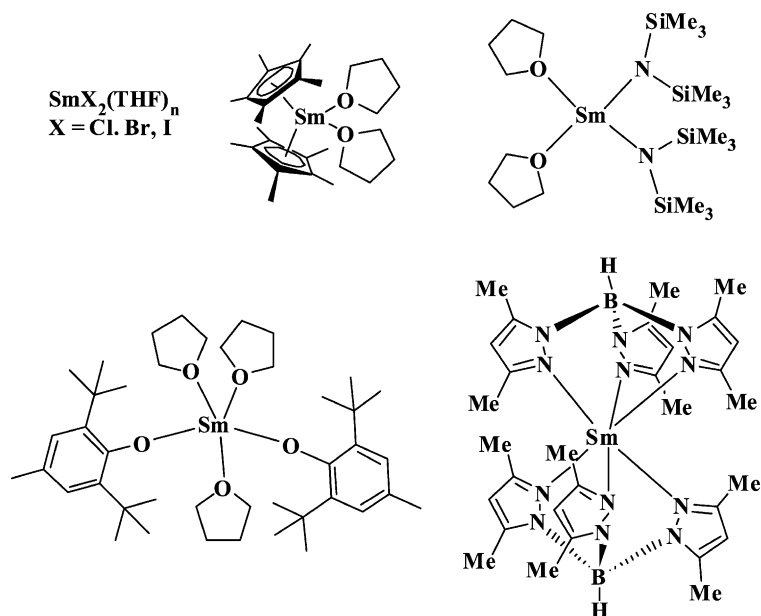
Cerium is the most abundant element of the rare earths and one of its special properties is a stable tetravalent state even in water. Therefore, many chemical applications of cerium take advantage of the Ce(IV)/Ce(III) redox couple. In this review, the author describes the applications of tetravalent cerium compounds in solution. Nearly all potential applications are



spanned; for instance their use as reagents in organic chemistry, as oxidizing agents for redox titrations, or their role in oscillating reactions and in biochemical transformations. The message is that cerium-containing reagents are not limited to ceric ammonium nitrate but that a wealth of other reactants are at hand, allowing a fine tuning of the sought for effects. After a general introduction on the properties of cerium(IV) and its role in oscillating reactions, the various reagents are described before detailing stoichiometric cerium(IV)-mediated reactions, indirect and catalytic reactions, cerium-mediated electrosynthesis, and radical-initiated polymerization reactions. The chapter ends by discussing several applications which emphasize the versatility of cerium(IV) salts and complexes in facilitating the course of a wide variety of organic reactions and the development of new materials and methods.

Chapter 230 Samarium (II) based reductants
by Robert A. Flowers II and Edamana Prasad
Lehigh University, Bethlehem, USA

Samarium (II) based reducing agents have been used extensively in synthetic chemistry for the last two decades. This review focuses on the synthesis and use of Sm(II) based reductants in organic and inorganic reactions. The authors describe the synthesis and utility of a variety of Sm(II) based reductants containing halides, cyclopentadienyl, amide, alkoxide and pyrazolylborate ligands. Since a great deal of scientific effort has been directed towards understanding the reactivity and behavior of Sm(II) reductants containing iodide and pentamethyl-



cyclopentadienyl ligands, the majority of this chapter concentrates on these two classes of Sm(II)-based reductants. In cases where sufficient mechanistic data are available, the role of solvent and additives including, proton sources and coordinating ligands in Sm(II) mediated reactions is described. The use of samarium (II)-based reagents as stoichiometric reductants is continuing to grow, particularly as integral part of multi-step syntheses or in the development of new methodologies and this timely review will be a source of inspiration for many synthetic chemists.

DEDICATION TO LEROY EYRING

Karl A. GSCHNEIDNER Jr.
*Ames Laboratory, and Department of Materials Science and Engineering,
Iowa State University, Ames, IA 50011-3020, USA*

Harry A. EICK, retired
Michigan State University, East Lansing, MI 48824, USA

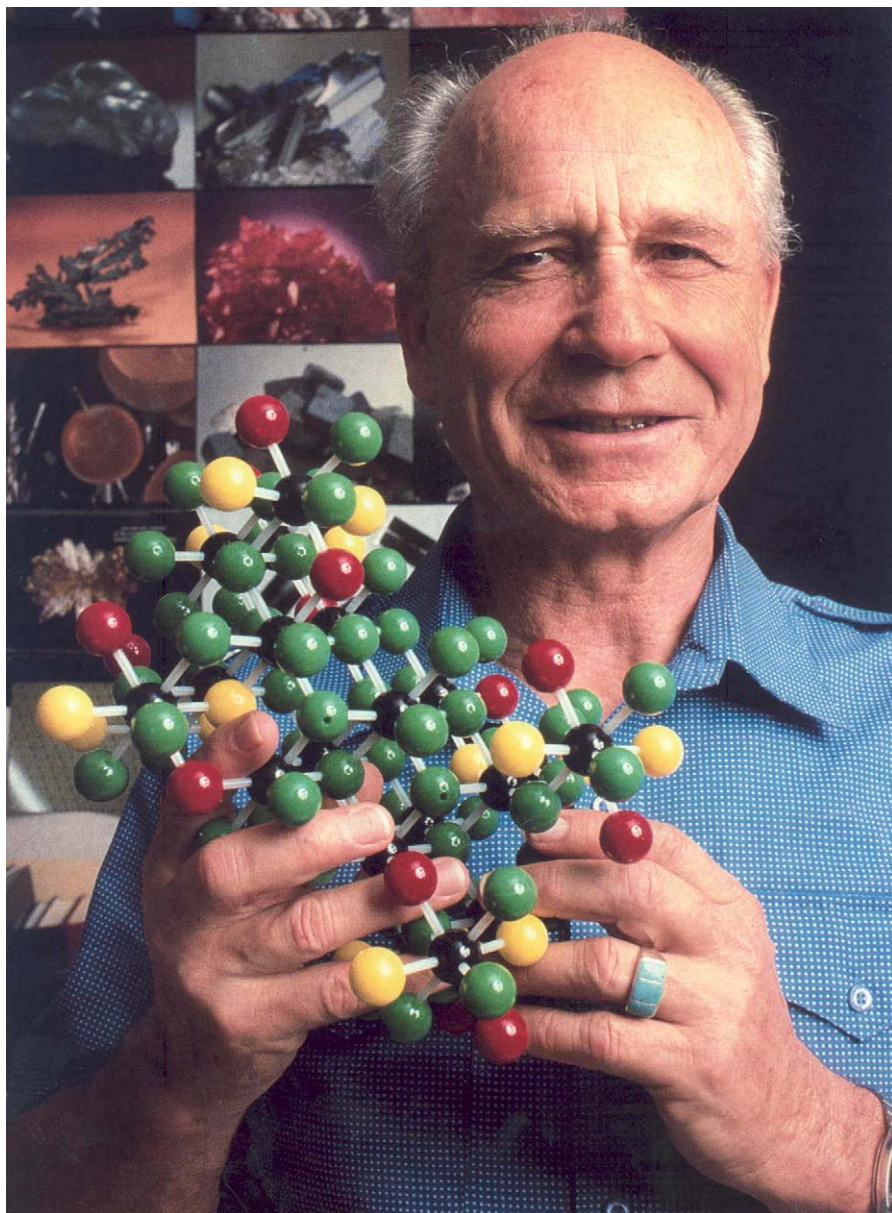
Zhenchuan KANG
REHOD (Rare Earth High Oxide Devices), P.O. Box 163, Stowe, MA 01775, USA

Michael O'KEEFFE
*Department of Chemistry and Biochemistry, Arizona State University, Tempe,
AZ 85069, USA*

Edgar F. WESTRUM Jr., retired
University of Michigan, Ann Arbor, MI 48109, USA

Contents

LeRoy Eyring (December 26, 1919–November 28, 2005)	
Karl A. Gschneidner Jr. and Michael O'Keeffe	xiii
Personal recollections	xvi
The Eyrings at home and on trails with the Westrums	
Edgar F. Westrum Jr.	xvi
Graduate days at State University of Iowa	
Harry A. Eick	xvii
Life at Arizona State	
Zhenchuan Kang	xix
Appendix	xxii
Vita	xxii
Publications	xxv
Books	xxxviii



Prof. LeRoy Eyring

LeRoy Eyring (December 26, 1919–November 28, 2005)

LeRoy Eyring was born on December 26, 1919 in Pima, a small farming town in southeast Arizona, the youngest of nine children born to Edward Christian and Emma (Romney) Eyring. He died peacefully at the age of nearly 86 on November 28, 2005. LeRoy married Ruth LaReal Patton, whom he met in West Virginia while serving as a missionary for the Church of the Latter Day Saints, on July 21, 1941. They had four children – Michelle, Patricia, Cynthia and Gregory.

He followed his oldest brother Henry's footsteps obtaining a B.S. degree in chemistry from the University of Arizona in 1943. Shortly after graduation from the University of Arizona he began his Ph.D. studies at the University of California, Berkeley but because of World War II he enlisted in the U.S. Navy in 1944 serving as a radar officer on the destroyer U.S.S. Schroeder until 1946. He returned to Berkeley and completed his Ph.D. studies in 1949. His Ph.D. thesis research was concerned with the chemistry, thermochemistry and metallurgy of the early actinide elements – thorium, neptunium, plutonium, and americium. During his Berkeley days a life-long friendship was cultivated with his research partner Edgar F. Westrum Jr. and their families (see below). LeRoy and Edgar jointly published six papers. LeRoy's lifetime passion for the higher oxidation states of the rare earth oxides was kindled during the latter days of his graduate studies at the University of California, Berkeley.

LeRoy joined the faculty of the Chemistry Department at the State University of Iowa as an assistant professor (1949–1955) and associate professor (1955–1961). While on the faculty of the State University of Iowa he had spent a year in Europe as a National Science Foundation Senior Postdoctoral Fellow (1958) and, a year in Australia as both a Fulbright-Hays Scholar and a John-Simon Guggenheim Foundation Fellow. LeRoy's research on the non-stoichiometric rare earth oxides started in full swing at the State University of Iowa, where he and his students studied the oxygen dissociation pressures, crystal structures and the thermochemistry of the higher oxides of Pr and Tb. They also investigated the chemistry of the $2^+/3^+$ aliovalent lanthanides, Sm, Eu and Yb. The nitrides of these three metals were found to be trivalent and isostructural with the normal trivalent rare earths having the cubic NaCl-type structure. In contrast to this behavior the Sm and Eu phases were reported to form the divalent SmO and EuO phases with the rock salt structure. Later research showed that the "SmO" phase was a ternary oxide–nitride, and confirmed that the EuO compound was a true binary oxide of divalent Eu (see below). About five years later physicists discovered that EuO was a semiconducting ferromagnet with a Curie temperature of 70 K, which confounded conventional theory of ferromagnetism because of the absence of conduction electrons which were thought to be required for ferromagnetism in lanthanide-based compounds. This dilemma was resolved when it was shown that superexchange via the oxygen atoms could account for this magnetic behavior. Furthermore, LeRoy's work opened the door to a new scientific and technical area of research and the eventual commercialization of magnetic semiconductors, primarily based on $3d$ elements.

In 1961 LeRoy Eyring returned to his home state to take over the Chemistry Department at Arizona State University and he remained there for the rest of his scientific and teaching career. When he came to Arizona State University that institution was just evolving from

Arizona State Teacher's College to a fully fledged university. He was a man with a mission and had the full support of the University president G. Homer Durham and enthusiastic backing from LeRoy's brother Henry. It is not at all fanciful to compare his impact on Arizona State University with that of G.N. Lewis on the University of California, Berkeley 50 years earlier. His idea was that the department should embrace non-traditional areas of chemistry such as solid state, materials and geochemistry, and immediately he recruited young scientists with a firm commitment to research and teaching: Peter Buseck, Sheng Lin, Michael O'Keeffe and Carleton Moore (who all ultimately became Regents' Professors at Arizona State University) were among those recruited in the early sixties. Scientists in LeRoy's own rare earth research group at that time included Bruce Hyde, D.J.M. "Judge" Bevan and Lars Khilborg (who all went on to become distinguished professors and lead important research groups). The famous, and still cited, paper on the Pr-O system (Hyde, Bevan and Eyring, *Phil. Trans. Roy. Soc. London*, 1966) appeared as a result of their collaborations. Stuart "J.S." Anderson, Professor of Inorganic Chemistry at Oxford University was a visitor for a memorable semester. Chemistry lead the way at Arizona State University (the first Ph.D. was in chemistry) and a significant fraction of all the funding for organized research at the University came to that department.

Another important early development, which again showed both LeRoy's vision and his personal charm, was his recruitment in 1970 of John Cowley to set up what is now the John M. Cowley Center for Electron Microscopy. This was coupled with a successful Area Development Grant application to National Science Foundation to establish what became the distinguished Center for Solid State Science at Arizona State University. Chemistry (i.e. Eyring!) hires at that time in connection with this development included Alex Navrotsky and Bob Von Dreele, names that may be familiar to many solid state chemists.

About the time LeRoy moved from Iowa City to Tempe, the Rare Earth Research Conferences (RERC) were initiated by Eugene V. Kleber in a format similar to the well know Gordon Conferences. LeRoy became fully involved serving as a session co-chairman at the RERC-1. In 1964 LeRoy Eyring organized the 4th RERC which was held at Camelback Inn in Phoenix, Arizona. It was a notable conference in that two of the early pioneers in the rare earth field gave invited addresses. J.H. Van Vleck (Harvard University) gave the keynote lecture on "The Magnetic History of the Rare Earths"; and Felix Trombe (who discovered that Gd was ferromagnetic at room temperature in 1935, and who was in 1964 the head of the Central Research Laboratory in Bellevue, France) spoke on "Séparations et Purifications Par Voie Sèche Dans le Groupe des Terres Rares," also many of the leading rare earth scientists of the time participated in the conference: S. Araj, D.J.M. Bevan, G. Brauer, F.L. Carter, A.F. Clifford, D.T. Cromer, A.H. Daane, H.A. Eick, P.W. Gillis, K.A. Gschneidner Jr., T.A. Henrie, J.M. Honig, B.G. Hyde, W.C. Koeller, S. Legvold, C.E. Lundin, T. Moeller, E. Parthé, J.E. Powell, A.E. Ray, Y.A. Rocher, R.A. Schmitt, K.S. Vorres, W.E. Wallace, and E.F. Westrum Jr. Not only representatives from academia but many industrial scientists, engineers, technical managers attended RERC-4 as was the case for the early RERC conferences. As LeRoy Eyring so succinctly stated in the Preface of the conference proceedings "... this family of substances, by the very nature of their broad similarity yet subtle differences, provides an avenue into the understanding of the physical world which is comprehensive yet deeply penetrating."

About five years later (1970) LeRoy organized another conference on the Chemistry of Extended Defects in Non-Metallic Crystals. “Everyone” came and it set the stage and the agenda for the immensely fruitful synergy of electron microscopy and solid state chemistry so beautifully exemplified by LeRoy’s own work over the next three decades.

Most of LeRoy’s research at Arizona State University was involved with the higher, predominantly non-stoichiometric lanthanide oxides, of Ce, Pr, and Tb (see below), but it also included non-rare earth oxides of Ti, Zr, Pb, Cm and Bk, mixed rare earth–non-rare earth oxides (especially with fluorite related structures) and rare earth carbonates. A complete list of his publications, awards and other notable achievements is given in the Appendix of the Dedication.

In 1974 Dr. Pieter S.H. Bolman of North-Holland Publishing Company approached Karl A. Gschneidner Jr. about editing a handbook on the rare earths. After considerable thought it appeared that about 40 topics (chapters) would cover the more important areas of the then current research being carried out in the fields of chemistry, ceramics, metallurgy, physics, and spectroscopy of the rare earth elements and their inorganic and organometallic compounds. Because of the magnitude of reviewing so many chapters, Pieter suggested that a second editor should be invited to help edit this four volume set of books. Without any hesitation LeRoy Eyring was invited to join Karl, and LeRoy wholeheartedly agreed. It was decided that Karl would be more concerned with the metals, metallic alloys and compounds, and the physics aspects, while LeRoy would oversee the inorganic and complex compounds and the chemistry aspects. Shortly after the first four volumes were published in 1978–1979, it became apparent to the editors that there were some topics not covered, and that there were new rapidly developing, areas of research which would justify continuing this initial set of four volumes. The fifth volume was published three years later in 1982. North-Holland Publishing Company, which in the early 1990s became a part of Elsevier, agreed with this assessment and continued to be the publisher. Subsequently, about a volume per year made its appearance, with this volume (36) being published in 2006. LeRoy Eyring was a co-editor through volume 32 after which he stepped down from active editing. He was replaced by Profs. Jean-Claude Bünzli (Swiss Federal Institute of Technology, Lausanne) and Vitalij K. Pecharsky (Iowa State University, Ames).

In addition to his numerous scientific contributions to the rare earth community, and to the life of the Arizona State University and the Chemistry Department, LeRoy was a humble person of total integrity and great humanity. He was a caring, upstanding, generous, lovable person and it was an honor and privilege to have known and worked with LeRoy Eyring over the years, and we are the better for it.

Karl A. Gschneidner Jr.
Editor

Ames Laboratory and Department of Materials Science and Engineering,
Iowa State University

Michael O’Keeffe
Department of Chemistry and Biochemistry, Arizona State University

Personal recollections

The Eyrings at home and on trails with the Westrums

by Edgar F. Westrum Jr., retired

University of Michigan (Ann Arbor)

From the days of our joint tenures as graduate students at the University of California, Berkeley, LeRoy and I and assorted family members often on weekends took in the cross-bay treats known to Berkeley's graduate students, e.g. McFarlane's Chocolates and the fisherman's wonderfully fresh wharf restaurants of San Francisco, by the Interurban Rail. The Berkeley hills also got their fair share too.

But we also hit the western wilderness. One of our first expeditions started from a park in Canada, we crossed to the US side of Glacier National Park (in Montana) and worked our way back to Berkeley.

LeRoy and his wife, LaReal were great travelers and the mix of kids provided no end of entertainment when together in the desert, on horseback, or on the highway, or in the mountains, or on the water. It was a natural congregation of kindred souls.

I visited two Mormon family homes and was privileged to read the wives' "Journals" at both, and on occasion visited most of his brothers' homes in the Salt Lake City area. One or another brother would house us and we could count on a passionate evening encompassed by a liberal education in Mormon discipline, theology, and faith.

Often at scientific meetings LeRoy and I rode horses all night and dismounted at the Conference door in time for the scientific session.

The LeRoy Eyring family over all of our adventures consisted of the two parents and four children – three daughters (Michelle, Patricia and Cynthia) and one son (Gregory). The Westrums were also six in number with Edgar, wife Florence, and four children, Ronald, James-Scott, Kris, and Michael. For many activities they paired by age and by he–she except at the youngest levels where the preference of the pairs was he–he or she–she.

One of our first explorations involved LeRoy, Edgar and Ronald. It was a joint expedition and was a scientifically motivated raft drift where the three of us explored a stretch of the Grand Canyon. We joined a party of about 24 geoscientists in running rafts to study the sand and sandstone in that portion of the Colorado River. We had three rafts for the expedition and the educational exploration was complimented by running rafts common to rapidly moving rivers.

For "expeditions" the families did most of their traveling in two cars. There were usually a dozen of us and our station wagon and the Eyring's sedan provided both luxury and reasonable comfort. Seating in the station wagon could be quickly converted to a "sleeping deck" if the clientele had an urge to nap or sleep. Another virtue of the station wagon was a varnished, large wooden box (about $4' \times 6' \times 3/4'$ [$1.2 \text{ m} \times 1.8 \text{ m} \times 0.23 \text{ m}$]) on the car roof that could be locked and was well tested on shorter excursions. It proved its worth in the Mexican country side and enabled us to carry sleeping bags, spare clothes, tents, a stove and food so we could convert into desert nomads when hotels and motels were not to be had. The two cars were necessary for seating and sleeping space and provided a measure of security in the event of an accident.

Mexico City with its endless attractions and museums was a favorite watering hole but the desert not far from the capital provided pyramids at Tenochtitlan (dedicated to the Sun and the Moon) to climb, and castles and archaeological wonders to explore. We enjoyed the motels too. We celebrated Christmas (Mormon-style) at one motel with high walls not far from Mexico City, with tree-slung piñatas. It was a delightful trip.

A side excursion took us into the “copper-country” and the coastal cities in the vicinity of the Gulf of California (Sea of Cortez). They too had their special charm. Then back to Mayan architecture in the areas north and east of Mexico City. But time was now limited. We crossed the border back into the States with Michael on the sleeping deck of the station wagon slyly entertaining the customs inspectors with contraband (oranges, etc., fresh fruit are not allowed to be brought in the US from Mexico). By the simple remedy of eating them before crossing the border we headed back to our respective Arizona and Michigan homes.

In 1966 the trip started in Maine near Bar Harbor and Frenchman’s Bay (diagonally across the US from the start of the Mexican expedition). Following a path roughly parallel to the Adirondack Trail to the Middle Atlantic States proved interesting, too. Washington D.C. provided a welter of art and museums.

Another time we crossed the Arizona Desert and went down the Bright Angel Trail and returned the same day. It was 104 F (40 °C) at the river level and below freezing when we emerged to the desert rim in the dark of evening.

Yet another year we explored the southwest corner of British Columbia then played in the Canadian and US national parks with their rich animal and plant life, and former railroads connected into down-hill bicycle roller coasters of mountain size proportions.

We built and navigated rafts on a number of lakes and rivers too. Space does not permit a more complete catalog of US and foreign spots we visited together.

Although the southeast Florida corner of the US did not get explored but none the less we look back with appreciation on the double-family travel that we did do and regret that these days are no more! The Eyrings provided wonderful traveling companions. Our walls still bear the art work from the artistic skill of the Eyring girls even on motorcycle helmets.

Graduate days at Iowa

by Harry A. Eick, retired

Michigan State University (East Lansing)

In the fall of '53, at the start of my second full year of graduate study at the State University of Iowa, I was appointed a research assistant and started to work in Professor Eyring’s laboratory. He assigned me to work with Cedric Stubblefield who was involved in a microcalorimetric study of lanthanide dichlorides and selected oxides. The adiabatic microcalorimeter, which was in a room immediately adjacent to LeRoy’s office, required two operators, and a ‘run’ could take many hours. Another graduate student, Gene Guth, working at that time was in a comparable-sized laboratory down the hall. Gene was working on praseodymium and terbium oxide systems determining equilibrium oxygen pressures; my interaction with him was minimal.

As lanthanide metals were expensive and were not of high purity, the reactant of choice was the sesquioxide and exceedingly small specimen sizes were the norm. The small calorimetric specimens were inserted into small (as I recall, about 6 mm diameter, 10 mm high) flask-like vials which Cedric or LeRoy blew from glass. The base was thin and flattened. After the sample was inserted into the specimen vial with a small funnel in a dry box, a small bead of 'black wax' was melted with resistance wire controlled by a variac to seal the vial. A before and after mass difference yielded specimen mass. (No 'automatic' balances – you counted swings.) The sealed vial was then mounted with black wax onto a rod inserted through the top of the calorimeter that could be plunged to crush the vial bottom, releasing the specimen into a precisely measured volume of a standardized acid solution.

There were no laboratory computers in the middle '50s. So as the specimen reacted with the acid, the evolved energy that increased the temperature of the calorimeter had to be matched by increasing the temperature of the external shield. The console operators monitored the temperature differential between the calorimeter and the shield, as detected by a thermopyle, and adjusted helipots to increment the temperature of the outer shield and maintain a (hopefully) zero temperature differential. As I recall, we could control bottom, sides, and top independently and monitored the calorimeter until the temperature drifted to background. Some of the oxide samples dissolved very slowly and 'run' times were long. When the time came for one of us to leave, LeRoy would willingly fill in.

LeRoy always seemed available to respond to questions and provide assistance. If something needed repair, he would tackle the project. I recall once when the fiber in the quartz fiber microbalance broke he assembled an oxygen-gas torch and repaired the fiber.

As Cedric's work progressed more to data reduction and wrestling with problems such as oxidation by dissolved oxygen instead of oxidation solely by protons, I moved onto a different project, the synthesis of samarium and europium monoxides. Again, we would be working with milligram-sized specimens and wanted products as pure as possible. We again chose to start with the sesquioxide. We knew $H_2(g)$ would not reduce the sesquioxide, so we decided to use atomic hydrogen which we planned to create with an arc in a bell jar-like assembly.

LeRoy took over additional space in which I constructed a vacuum rack, ran gas lines, and planned the construction of the atomic hydrogen apparatus. Although I had never soldered a pipe, LeRoy's confidence that I could do the job carried over to me. We wanted a metal 'tank' with a porthole so we could see the arc and I recall writing to many companies inquiring whether they could make such a device. One clever response was from a former Iowa chemical engineering graduate who pointed out that their business was manufacturing water tanks for small municipalities and he was confident they would be too large for our needs.

We ultimately found a metal tank design that could be evacuated and would allow a specimen to be 'irradiated' with atomic hydrogen. I do not remember how we determined that atomic hydrogen was present, but we did observe that when the arc was struck in a $N_2(g)$ atmosphere the 'straw color' reportedly associated with $N(g)$ was observed.

With the quartz fiber microbalance we could easily work with 10 mg samples and have sufficient precision to be confident of our results. Prepared specimens were analyzed by film X-ray powder diffractometry using equipment in Professor Norm Baenziger's laboratory and

interpreted with his help, and tested for nitride impurities by dissolution in a base under wet litmus paper. (I do not remember how we effected transfer of the product from the tank to the glove box where capillaries were filled.) We succeeded in preparing small amounts of EuO and we thought SmO, but the latter was shortly confirmed (by LeRoy and a subsequent grad student) to be actually Sm(O,N). It soon became clear that this synthesis procedure would never produce large enough samples for calorimetric measurements.

While the monoxide synthesis project was proceeding, LeRoy's emphasis moved more toward the PrO_x and TbO_x systems. No further microcalorimetric studies were undertaken after Cedric left.

I particularly remember an incident at the Miami American Chemical Society meeting which most group (and former group) members attended. We were going to lunch and LeRoy suggested a restaurant in a hotel when Cedric said that he, being black, would not be served there. LeRoy did not believe him and we proceeded to the dining room. As Cedric had predicted, he was refused a seat. LeRoy politely questioned the action and argued to no avail that we all be seated. When his request was denied, we all followed LeRoy out of the restaurant and went to a place that served blacks.

As I have indicated, LeRoy was always available to answer questions, even if he had a lecture in the next 10 minutes. And our discussions often covered topics far afield. After I submitted my dissertation, LeRoy allowed me to continue to work on a post-doc basis, paying me twice the grad student rate. LeRoy was more than a research advisor; he was simultaneously a colleague, a friend and a true confidant who through example led you to excel.

Life at Arizona State

by Zhenchuan Kang

REHOD (Rare Earth Higher Oxide Devices) (Stowe, MA)

In 1980 I came to Arizona State University to study high resolution electron microscopy with Professor J.M. Cowley and Dr. Somio Ijima. One day, I noticed a flyer on campus about a lecture on the non-stoichiometry of rare earth higher oxides by Professor L. Eyring. This was the first time I heard the word "non-stoichiometry." So I decided to attend the lecture to see what it was about. LeRoy's story on the mysterious phases of the homologous series of oxygen-deficient fluorite-related oxides of the rare earths fascinated me. After the lecture I went to his office to ask if I could study the rare earth higher oxides with him. He thought for a while and told me that the synthesis of the δ' phase of the terbium higher oxide would be an interesting project to take on. I immediately said I would like to do so. Little did I know that it was the beginning of a rewarding 20-year journey of learning and working with LeRoy.

I synthesized the δ' phase and obtained information on the unit cell of the δ' phase by electron microscopy. Professor Eyring told me the story of the δ' phase in the terbium higher oxides. At that time the formula of the oxygen-deficient fluorite-related homologous series of the rare earth higher oxides was $\text{R}_n\text{O}_{2n-2}$, and that there are two families: when n is odd the

phases are R_7O_{12} , R_9O_{16} , $R_{11}O_{20}$, when n is even the compositions are $R_{12}O_{22}$, $R_{10}O_{18}$, and $R_{24}O_{44}$. However, there were some exceptions: $RO_{1.808}$ (δ' phase) and $PrO_{1.818}$ ($n = 88$), and $CeO_{1.789}$ ($n = 19$). These three phases had a contradiction between the experimental oxygen content and the calculated oxygen content by using the formula R_nO_{2n-2} . When I asked the reason behind the exceptions, LeRoy said that nobody knew the mechanism yet and I should work on it.

At that time the structural principle of the homologous series of the rare earth higher oxides had been proposed by Professors B. Hyde, G. Bevan, R.L. Martin in Australia and LeRoy in the United States. But, the contradiction was not yet solved. However, it was eventually solved because LeRoy devoted most of his life to understanding the structural principles of the oxygen-deficient fluorite-related homologous series and the relationship between the non-stoichiometry and structures of the rare earth higher oxides.

As is well known, neutron diffraction is more sensitive than X-ray diffraction to the location of the oxygen atom in a solid containing heavy lanthanide atoms. When Professor R.B. Von Dreele told LeRoy that the high resolution neutron diffraction facility at Los Alamos National Laboratory (LANL) was available, LeRoy immediately sent Dr. Jie Zhang to collect neutron diffraction data of the most important five phases of the rare earth higher oxides. Dr. Zhang spent one year trying to determine the structures of $Tb_{11}O_{20}$, and $Tb_{24}O_{44}$ by the Rietveld refinements. But she did not succeed using a model with oxygen pair vacancies. However, when she used the hypothesis of a single oxygen atom vacancy, she solved and refined the structures of all five phases of the rare earth higher oxides in a few weeks. This was the trigger that made Professor Eyring to go back to the model with oxygen pair vacancies. He asked me to carefully analyze the five refined structures. When I compared the experimental electron diffraction data and the refined structures of the five homologous series phases, there was excellent agreement assuming that the fluorite-type blocks with the eight oxygens of a fluorite unit cell having an equally *a priori* possibility to be vacant. I immediately went to Professor Eyring's office to discuss this model with him. Since this concept was different from his ideas, he challenged me with thousands of questions and asked for more data to back up my idea. It took me a year, but I finally convinced him that all of the experiments could be rationalized without any exceptions by the general formula R_nO_{2n-2m} for the homologous series of phases.

When Professor L. Eyring and I wrote an article on the structural principles of fluorite-related rare earth higher oxides, I asked him where he wanted to publish it, and he said the *Australian Journal of Chemistry*. I asked why? He said that it was quite possible that one or more of the reviewers would be Professors Bevan or Martin or Hyde because they are experts on these structures, and we needed their comments on the new principles. After almost one year he received the comments of the reviewer of this paper. LeRoy carefully answered all of the questions. Finally the article was published in 1996. However, he was still concerned that the new principles had not gone under a rigorous scientific review. It was not until 2004 when I showed him the paper by S.V. Krivovichev, who extended our fluorite-type model to all of the known structures formed by a metal tetrahedron with an oxygen ion in the center as the building block. He smiled with confidence.

LeRoy also gave great attention to the mixed valence of the Ce, Pr, and Tb cations in the lanthanide higher oxides. Both PrO_2 and TbO_2 can only be prepared by a leaching process. If the R^{3+} and R^{4+} ions in the rare earth higher oxides are distributed statistically in the fluorite lattice, the result of leaching should allow one to obtain a solid of PrO_2 and TbO_2 having large micron size holes. Professor L. Eyring asked me to see if I could experimentally observe the tiny holes in the electron microscope. When I brought the results to him, he joked that this was “Swiss cheese.” He told me that this leaching process is a solvolytic disproportionation of the mixed valence oxides. These results demonstrate that the valence state of a cation in the rare earth higher oxides is flexible and it is hard to be sure which cation is trivalent and which is tetravalent. When the H^+ ion attacks the O^{2-} ion on the surface of the rare earth higher oxides an OH^- ion group is formed. This process promotes the electron hopping from R^{3+} to R^{4+} and creates more R^{3+} near the surface, and simultaneously produces more R^{4+} inside the solid. Because R^{3+} can be dissolved in an acid but R^{4+} cannot, the $\text{R}(\text{OH})_3$ is dissolved into the acid solution and leaves an emptied vacancy site. This process continues until a large number of the R^{4+} cations is formed in a region of the oxide because electrons are hard to supply. Therefore, a large void is created in this region. Defects, such as dislocations, stacking faults and grain boundaries may also be sites which react with the acid. The “Swiss cheese” structure shows the difference between the rare earth higher oxides and other mixed valent metal oxides, for example Pb_3O_4 . In the mixed valence Pb_3O_4 , Pb^{2+} is dissolved in a mineral acid but Pb^{4+} is not. When leaching the Pb^{2+} from the Pb_3O_4 no voids are formed in the solid crystal because Pb^{4+} is reduced by the acid and dissolved in the acid solution, while simultaneously some Pb^{2+} is oxidized and precipitated as PbO_2 . This indicates that electron hopping does not occur in Pb_3O_4 . As a result LeRoy told me that we now understand more about the mixed valence behavior of the Pr and Tb cations.

As LeRoy’s understanding of the mysterious behavior of the rare earth higher oxides evolved, he asked me if it is possible to design ternary oxides having a wide range of non-stoichiometry from MO_2 – $\text{MO}_{1.5}$. In 2003, he used a Cahn thermo-balance to make isobaric measurements on $\text{Ce}_{0.6}\text{Pr}_{0.2}\text{Zr}_{0.2}\text{O}_{2-\delta}$, and $\text{Ce}_{0.6}\text{Tb}_{0.2}\text{Zr}_{0.2}\text{O}_{2-\delta}$ and he obtained what he suspected to be a wide range non-stoichiometry in MO_2 – $\text{MO}_{1.5}$ systems. These data were collected by him, when he was 84 years old.

In the last six years of his life he was excited by the possible application of the rare earth higher oxides for the hydrogen production. When I found and proved that hydrogen could be produced by using $\text{Ce}_{0.8}\text{Zr}_{0.15}\text{Tb}_{0.05}\text{O}_{2-\delta}$ and other ternary or quaternary higher oxides with temperature swings between 700 and 300 °C and exchanging flows of methane and water vapor, he was very excited and even came to the laboratory to check my experimental data at midnight with his wife, LaReal. He was proud that we applied for a patent for this process. Before he passed away I checked his home page at the Arizona State University web site, and found he changed his interest into “oxygen and hydrogen sources for the hydrogen economy.”

He enjoyed the paradise of the solid state chemistry of the rare earth higher oxides for most of his life, especially the latter 50 years.

Appendix

Vita

Education:

University of Arizona (High Distinction)	1943 B.S.
United States Navy	1944–1946
University of California, Berkeley	1949 Ph.D.

Area of specialization

Physical, Solid State Chemistry

Professional experience:

State University of Iowa	
Assistant Professor	1949–1955
Associate Professor	1955–1961
Arizona State University	
Department Chairman	1961–1969
Professor of Chemistry	1961–1989
Regents' Professor of Chemistry	1988–1990
Regents' Professor Emeritus	1990–2005
Director, Area Development in Solid State Science supported by the National Science Foundation	1969–1972
Director, Center for Solid State Science	1974–1976

Research Activities

Solid State Chemistry (thermodynamic, kinetic, and structural properties of oxides, nonstoichiometry and extended defects in nonmetallic solids, application of high-resolution electron microscopy to solid state chemistry)

Visiting Professor, General Electric Co., Hanford Research Laboratories of the US Atomic Energy Commission (AEC), Summer of 1964

Visiting Professor, Battelle Northwest, Hanford Research Laboratories of the AEC, Summers of 1965 and 1967

Consultant, Battelle Northwest, Hanford Research Laboratories of AEC, Summers of 1969, 1970 and 1971

Professional organizations and honor societies:

American Chemical Society (ACS)	
Iowa Section, Chairman	1956
Executive Committee of the Physical Division	1970–1973
National Chairman Elect, then Chairman, Solid State Chemistry Subdivision of the Inorganic Division of the ACS	1978–1980

American Association for the Advancement of Science
 Arizona Academy of Science (Fellow)
 Sigma XI
 Phi Beta Kappa
 Phi Kappa Phi
 Phi Lambda Upsilon
 Pi Mu Epsilon

Miscellaneous:

National Science Foundation (Senior Postdoctoral Fellow Europe)	1958
Fulbright-Hays Award (Australia)	1959
John Simon Guggenheim Foundation Fellow (Australia)	1959
Division of Chemical Education (Visiting Scientist)	
Committee on Professional Training of the American Chemical Society (Associate)	
Robert A. Welch Foundation Lectureship in Chemistry	1964
Co-editor, "Handbook on the Physics and Chemistry of Rare Earths," a serial publication	1978–2001
Editorial Advisory Board, Journal of High Temperature Science	1971–1988
Editorial Advisory Board, Progress in Solid State Chemistry	1970–1992
Editorial Advisory Board, Journal of Solid State Chemistry	1970–2005
Advisory Panel to the Materials Research Laboratories, National Science Foundation	1976–1979
Panel on Small Programs in Materials Sciences, National Research Council	1977–1979
Executive Subcommittee, Materials Research Advisory Committee, National Science Foundation	1977–1979
CMS Advisory Panel, Materials Research Advisory Committee, National Science Foundation	1977–1979
Solid State Chemistry Oversight, Materials Research Advisory Committee, National Science Foundation	1977–1979
Participated in "Distinguished Lecture Series" (Five Lectures) at Texas A&M University	November 13–17, 1978
Workshop on "Synthesis and Characterization of Advanced Materials" Organized by the National Research Council	
Chairman of the Panel on Training and Orientation	December 1978

Member of the Solid State Sciences Panel of the National Research Council	1979–1983
Delegate to Indo – US Conference on Rare Earth Materials – Cochin, India	1980
Delegate to Franco – US Workshop on the Synthesis and Characterization of Advanced Materials – Bordeaux, France	1980
Member of the Program Committee, Intense Pulsed Neutron Source (IPNS), Argonne National Laboratory	1980–1982
Chairman of Symposium on “High-Resolution Electron Microscopy Applied to Chemical Problems”, Division of Inorganic Chemistry, American Chemical Society, National Meeting	August 1981
Lecture Tour sponsored by Chinese Academy of Science, People’s Republic of China, Beijing, Changchun, Hangzhou, Shanghai	June 1982
Delegate to US–UK Solid State Chemistry Workshop, Oxford, England	December 1982
Invited Lecturer, “Frontiers in Chemistry” Lecture Series, Case Western Reserve University	March 1984
Invited Lecturer, Universidad Complutense Summer School, Madrid, Spain	July 1984
Invited Lecturer, American Chemical Society “Intermountain States”, Utah, Idaho, Washington, Montana, Hawaii	1975
“Prairie Circuit”, Illinois, Iowa, Nebraska	1984
“Osage Circuit”, Arkansas, Missouri, Kansas	1985
Graduate College Distinguished Research Award for 1986–1987 Academic Year	May 1985
Visiting Fellow, Research School of Chemistry, Australia National University, Canberra, Australia	September 1987
Panel on “Education” in Materials Science and Engineering, National Research Council	1986–1987
Invited Lecturer Paris and Marseille, France Tübingen, Giessen and Karlsruhe, Germany	May, June 1988
Eyring Lectures in Chemistry at the Arizona State University established in honor of extraordinary instructional, research and professional accomplishments	1988

Invited Lecturer University of Cadiz University of Seville Complutense University, Madrid	June 1989
Invited Lecturer University of Pennsylvania Philadelphia, Pennsylvania	April 1990
Plenary Lecturer First International Conference on the <i>f</i> Elements, Katholieke Universiteit, Leuven, Belgium	September 1990
Invited Lecturer American Ceramic Society National Meeting, Cincinnati, Ohio	April 1991
Invited Speaker and Session Chairman The Metals Society/AIME joint meeting, San Diego, California	March 1992
Invited Speaker Texas Society for Electron Microscopy, Spring Meeting, San Marcos, Texas	March 1992
Keynote Speaker in the "Eyring Symposium" and an Organizer of Rare Earths '92, an International Con- ference in Kyoto, Japan	June 1992
Frank H. Spedding Award Recipient and Lecturer, Sponsored by Rhône-Poulenc. Presented at the 20th Rare Earth Research Conference, Monterey, Califor- nia	September 1993
Arizona State University Distinguished Achievement Award	May 1994
Invited Plenary Lecturer, Complutense University Summer School, Escorial, Spain	July 1995
Invited Plenary Lecturer and International Committee member, 3rd International Conference on Rare Earth Development and Applications, Baotou, Inner Mon- golia, China	August 1995
Invited Guest Lecturer, Institute of Atomic and Molec- ular Sciences, Academia Sinica, Taipei, Taiwan	September 1995

Publications

1. The Heat of Formation of Plutonium Trifluoride, L. Eyring and E.F. Westrum Jr. In: G.T. Seaborg, W.M. Manning and J.J. Katz (Eds.), *The Transuranium Elements*, McGraw-Hill, New York, 1949, Paper 6.52.

2. The Heat of Formation of Thorium Tetrachloride, L. Eyring and E.F. Westrum Jr., *J. Amer. Chem. Soc.*, **72**, 5555–5556 (1950).
3. The Preparation and Some Properties of Americium Metal, E.F. Westrum Jr. and L. Eyring, *J. Amer. Chem. Soc.*, **73**, 3396–3398 (1951).
4. The Melting Point and Density of Neptunium Metal. A Micro Melting Point Apparatus for Metals, E.F. Westrum Jr. and L. Eyring, *J. Amer. Chem. Soc.*, **73**, 3399–3400 (1951).
5. Heats of Reaction of Some Oxides of Americium and Praseodymium with Nitric Acid and an Estimate of the Potentials of the Am(III)–Am(IV) and Pr(III)–Pr(IV) Couples, L. Eyring, H.R. Lohr and B.B. Cunningham, *J. Amer. Chem. Soc.*, **74**, 1186–1190 (1952).
6. The Heat of Solution of Neptunium Metal and the Heats of Formation of Some Neptunium Chlorides. A Microcalorimeter for Heat of Solution Measurements, E.F. Westrum Jr. and L. Eyring, *J. Amer. Chem. Soc.*, **74**, 2045–2047 (1952).
7. The Heat of Formation of Thorium Sesquisulfide, L. Eyring and E.F. Westrum Jr., *J. Amer. Chem. Soc.*, **75**, 4802–4803 (1953).
8. Praseodymium Oxides. I. Phase Study by Dissociation Pressure Measurements, R.E. Ferguson, E.D. Guth and L. Eyring, *J. Amer. Chem. Soc.*, **76**, 3890–3894 (1954).
9. Praseodymium Oxides. II. X-Ray and Differential Thermal Analyses, E.D. Guth, J.R. Holden, N.C. Baenziger and L. Eyring, *J. Amer. Chem. Soc.*, **76**, 5239–5242 (1954).
10. The Terbium Oxides. I. Dissociation Pressure Measurements: X-Ray and Differential Thermal Analyses, E.D. Guth and L. Eyring, *J. Amer. Chem. Soc.*, **76**, 5242–5244 (1954).
11. Higher Oxides of Terbium and Praseodymium from High Pressure Molecular Oxygen Treatment, W. Simon and L. Eyring, *J. Amer. Chem. Soc.*, **76**, 5872–5874 (1954).
12. The Heats of Reaction of the Dichlorides of Samarium and Ytterbium with Hydrochloric Acid. A Microcalorimeter, G.R. Machlan, C.T. Stubblefield and L. Eyring, *J. Amer. Chem. Soc.*, **77**, 2975–2978 (1955).
13. On the Reaction of Europium Dichloride with Solutions of Hydrochloric Acid, C.T. Stubblefield and L. Eyring, *J. Amer. Chem. Soc.*, **77**, 3004–3005 (1955).
14. Praseodymium Oxides. III. The Heats of Formation of Several Oxides, C.T. Stubblefield, H. Eick and L. Eyring, *J. Amer. Chem. Soc.*, **78**, 3018–3020 (1956).
15. Terbium Oxides. II. The Heats of Formation of Several Oxides, C.T. Stubblefield, H. Eick and L. Eyring, *J. Amer. Chem. Soc.*, **78**, 3877–3879 (1956).
16. Lower Oxides of Samarium and Europium. The Preparation and Crystal Structure of $\text{SmO}_{0.4-0.6}$, SmO and EuO , H.A. Eick, N.C. Baenziger and L. Eyring, *J. Amer. Chem. Soc.*, **78**, 5147–5149 (1956).
17. The Preparation, Crystal Structure and Some Properties of SmN , EuN and YbN , H.A. Eick, N.C. Baenziger and L. Eyring, *J. Amer. Chem. Soc.*, **78**, 5987–5989 (1956).
18. Praseodymium Oxides. IV. A Study of the Region $\text{PrO}_{1.83}$ – $\text{PrO}_{2.00}$, C.L. Sieglaff and L. Eyring, *J. Amer. Chem. Soc.*, **79**, 3024–3026 (1957).
19. Diffusion of Oxygen in Rare Earth Oxides, U.E. Kuntz and L. Eyring. In: W.D. Kingery (Ed.), *Kinetics of High Temperature Processes*, John Wiley and Sons, New York, pp. 50–57, 1959.

20. Terbium Oxides. III. X-Ray Diffraction Studies of Several Stable Phases, N.C. Baenziger, H.A. Eick, H.S. Schuldt and L. Eyring, *J. Amer. Chem. Soc.*, **83**, 2219–2223 (1961).
21. High-Temperature Oxidation of Rare Earth Metals, K.S. Vorres and L. Eyring. In: E. Kleber (Ed.), *Rare Earth Research*, Macmillan Co., pp. 119–123, 1961.
22. On Rare-Earth Oxide Systems, L. Eyring. In: J.F. Nachman and C.E. Lundin (Eds.), *Rare Earth Research*, Gordon and Breach, New York, pp. 339–354, 1962.
23. On the Structure and Related Properties of the Oxides of Praseodymium, L. Eyring and N.C. Baenziger, *J. Appl. Phys., Suppl.*, **33**, 428–433 (1962).
24. Ordered Phases and Non-Stoichiometry in the Rare Earth Oxide Systems, L. Eyring and B. Holmberg. In: *Advances in Chemistry Series, No. 39*, American Chemical Society, Washington, DC, pp. 46–57, 1963.
25. Phase Relationships in the PrO_x System, B.G. Hyde, D.J.M. Bevan and L. Eyring. In: K.S. Vorres (Ed.), *Rare Earth Research II*, Gordon and Breach, New York, pp. 277–296, 1964.
26. Pressure and Polymorphism in the Rare Earth Sesquioxides, J.O. Sawyer, B.G. Hyde and L. Eyring, *Inorg. Chem.*, **4**, 426–427 (1965).
27. Kinetic Studies on Reactions of Praseodymium Oxides in an Oxygen Atmosphere: $\text{PrO}_{1.83} + \text{O}_2 \rightleftharpoons \text{PrO}_2$, B.G. Hyde, E.E. Garver, U.E. Kuntz and L. Eyring, *J. Phys. Chem.*, **69**, 1667–1675 (1965).
28. Fluorite-Related Homologous Series in the Rare Earth Oxides, J.O. Sawyer, B.G. Hyde and L. Eyring, *Bull. Soc. Chim. Fr.*, 1190–1199 (1965).
29. A Comment on the Paper ‘Higher Oxides of Titanium’, B.G. Hyde and L. Eyring, *Zh. Neorg. Khim.*, **10**, 2837–2839 (1965).
30. On Phase Equilibria and Phase Reactions in $\text{TbO}_x\text{--O}_2$ and Related Systems, B.G. Hyde and L. Eyring. In: L. Eyring (Ed.), *Rare Earth Research III*, Gordon and Breach, New York, pp. 623–664, 1965.
31. A Structural Model of the Rare-Earth Oxides RO_x ($\text{R} = \text{Ce, Pr, Tb}$; $1.5 < x < 2.0$), B.G. Hyde, D.J.M. Bevan and L. Eyring, *Int. Conf. on Electron Diffraction and Crystal Defects*, Melbourne, 1965.
32. On the Praseodymium–Oxygen System, B.G. Hyde, D.J.M. Bevan and L. Eyring, *Phil. Trans. Roy. Soc. London, Ser. A, No. 1106*, **259**, 583–614 (1966).
33. Dissociation Pressures and Partial Thermodynamic Quantities for Americium Oxides, T.D. Chikalla and L. Eyring, *J. Inorg. Nucl. Chem.*, **29**, 2281–2293 (1967).
34. Fluorite-Related Oxide Phases of the Rare Earth and Actinide Elements, L. Eyring. In: *Advances in Chemistry Series, No. 71*, American Chemical Society, Washington, DC, pp. 67–85, 1967.
35. Phase Relationships in the Americium–Oxygen System, T.D. Chikalla and L. Eyring, *J. Inorg. Nucl. Chem.*, **30**, 133–145 (1968).
36. On the Ternary System Samarium–Nitrogen–Oxygen and the Question of Lower Oxides of Samarium, T.L. Felmlee and L. Eyring, *Inorg. Chem.*, **7**, 660–666 (1968).
37. Some Tensimetric Studies in the Mixed Ceria–Terbia System, J. Kordis and L. Eyring, *J. Phys. Chem.*, **72**, 2030–2044 (1968).

38. A Tensimetric Study of the Terbium and Praseodymium Systems and the Mixed Praseodymium–Terbium System, J. Kordis and L. Eyring, *J. Phys. Chem.*, **72**, 2044–2054 (1968).
39. Praseodymium, L. Eyring. In: C.A. Hampel (Ed.), *Encyclopedia of the Chemical Elements*, Reinhold, New York, pp. 561–567, 1968.
40. Terbium, L. Eyring. In: C.A. Hampel (Ed.), *Encyclopedia of the Chemical Elements*, Reinhold, New York, pp. 701–706, 1968.
41. Self-Diffusion of Oxygen in Neodymium and Samarium Sesquioxide, G.D. Stone, G.R. Weber and L. Eyring, *Proceedings of a Conference on Mass Transport in Oxides*, pp. 179–186, 1968.
42. Phase Transformations in the Praseodymium Oxide–Oxygen System: High Temperature X-Ray Diffraction Studies, D.A. Burnham and L. Eyring, *J. Phys. Chem.*, **72**, 4415–4424 (1968).
43. High Temperature X-Ray Diffraction Studies of the Terbium Oxide–Oxygen and Mixed Cerium Terbium Oxide–Oxygen Systems, D.A. Burnham, L. Eyring and J. Kordis, *J. Phys. Chem.*, **72**, 4424–4431 (1968).
44. The Curium–Oxygen System, T.D. Chikalla and L. Eyring, *J. Inorg. Nucl. Chem.*, **31**, 85–93 (1969).
45. On the Rare Earth Dioxymonocarbonates and their Decomposition, R.P. Turcotte, J.O. Sawyer and L. Eyring, *Inorg. Chem.*, **8**, 238–246 (1969).
46. Optical Absorption Spectra of the Ordered Phases in the Praseodymium Oxide–Oxygen System, J.M. Warmkessel, S.H. Lin and L. Eyring, *Inorg. Chem.*, **8**, 875–882 (1969).
47. The Transport Properties of Rare Earth Oxides, G. Weber and L. Eyring. In: F. Trombe (Ed.), *Les Eléments des Terres Rares*, Colloques Internationaux du CNRS, Paris–Grenoble, May 5–10, 1969, Centre National de la Recherche Scientifique, Paris, pp. 179–188, 1970.
48. On the Thermodynamic and X-Ray Diffraction Behavior of a Widely Nonstoichiometric Region of the Praseodymium Oxide System, M.S. Jenkins, R.P. Turcotte and L. Eyring. In: L. Eyring and M. O’Keefe (Eds.), *The Chemistry of Extended Defects in Non-Metallic Solids*, North-Holland, Amsterdam, pp. 36–53, 1970.
49. The Tensimetric Reflection of Atomic Order, L. Eyring, *J. Solid State Chem.*, **1**, 376–385 (1970).
50. Refractory Oxides of the Lanthanide and Actinide Elements, L. Eyring. In: A.M. Alper (Ed.), *High Temperature Oxides*, Academic Press, New York, pp. 41–97, 1970.
51. Oxygen Transport Properties of Rare Earth Oxides, L. Eyring. In: *Heterogeneous Kinetics at Elevated Temperatures*, Plenum Press, New York, pp. 343–350, 1970.
52. A Structural and Thermogravimetric Investigation of the Rare Earth Formates, R. Turcotte, J.M. Haschke, M.S. Jenkins and L. Eyring, *J. Solid State Chem.*, **2**, 593–602 (1970).
53. On the Berkelium–Oxygen System, R.P. Turcotte, T.D. Chikalla and L. Eyring, *BNWL-B-108*, March 1971.
54. Thermochemical Measurements with a Capacitance Manometer, R.P. Turcotte, T.D. Chikalla and L. Eyring, *Anal. Chem.*, **43**, 958–960 (1971).

55. On the Phase Interval $\text{PrO}_{1.50}$ to $\text{PrO}_{1.71}$ in the Praseodymium Oxide–Oxygen Systems, R. Turcotte, J. Warmkessel, R.J.D. Tilley and L. Eyring, *J. Solid State Chem.*, **3**, 265–272 (1971).
56. Self-Diffusion of Oxygen in Iota Phase Praseodymium Oxide, G. Weber and L. Eyring. In: J. Hirschfelder and D. Henderson (Eds.), *Advances in Chemical Physics*, vol. 21, Chemical Dynamics, Wiley–Interscience, pp. 253–272, 1971.
57. Preparation, Analysis and X-Ray Identification of the Dioxy monocarbonates of Lanthanum and the Lanthanide Elements, J.O. Sawyer, P. Caro and L. Eyring, *Monatsh. Chem.*, **102**, 333–354 (1971).
58. Oxygen Decomposition Pressures and Thermodynamic Data for Nonstoichiometric Berkelium Oxide, R.P. Turcotte, T.D. Chikalla and L. Eyring, *J. Inorg. Nucl. Chem.*, **33**, 3749–3763 (1971).
59. Hydrothermal Equilibria and Crystal Growth of Rare Earth Oxides, J. Haschke and L. Eyring, *Inorg. Chem.*, **10**, 2267–2274 (1971).
60. The Infrared Spectra of Rare Earth Carbonates, P.E. Caro, J.O. Sawyer and L. Eyring, *Spectrochim. Acta, Part A*, **28**, 1167–1173 (1972).
61. Growth and X-Ray Studies of Single Crystals of Higher Oxides of Praseodymium and Terbium, M.Z. Lowenstein, L. Kihlberg, K.H. Lau, J.M. Haschke and L. Eyring, *Proc. NBS Inst. for Mat. Res. 5th Mat. Res. Symposium*, Gaithersburg, MD, October 18–21, 1971, NBS Spec. Publ., **364**, 343–351 (1972).
62. Phase Reactions Not Exhibited on the Usual Phase Diagram, L. Eyring, *Proc. NBS Inst. for Mat. Res. 5th Mat. Res. Symposium*, Gaithersburg, MD, October 18–21, 1971, NBS Spec. Publ., **364**, 761–763 (1972).
63. The ^{248}Cm –Oxide System, R.P. Turcotte, T.D. Chikalla and L. Eyring, *J. Inorg. Nucl. Chem.*, **35**, 809–816 (1973).
64. Pseudophase Behavior in the Epsilon and Iota Regions of the Praseodymium Oxide–Oxygen System, R.P. Turcotte, M.S. Jenkins and L. Eyring, *J. Solid State Chem.*, **7**, 454–460 (1973).
65. Hydroxy-Carbonates of the Lanthanide Elements, J.O. Sawyer, P.E. Caro and L. Eyring, *Rev. Chimie Minérale*, **10**, 93–104 (1973).
66. The Structural Chemistry of Extended Defects, L. Eyring and L.-T. Tai. In: L. Eyring (Ed.), *Ann. Rev. Phys. Chem.*, **24**, 189–206 (1973).
67. Lanthanide and Actinide Oxides, A Case Study in Solid State Chemistry, L. Eyring. In: C.N.R. Rao (Ed.), *Solid State Chemistry*, Marcell Dekker, New York, pp. 564–634, 1974.
68. On the Crystal Structures of the Fluorite-Related Intermediate Rare Earth Oxides, P. Kunzmann and L. Eyring, *J. Solid State Chem.*, **14**, 229–237 (1975).
69. Chemical Hysteresis in Phase Transitions in the Terbium Oxide–Oxygen System, A.T. Lowe and L. Eyring, *J. Solid State Chem.*, **14**, 383–394 (1975).
70. The Effect of Crystal Size on Chemical Hysteresis in Praseodymium and Terbium Oxides, A. Lowe, K.H. Lau and L. Eyring, *J. Solid State Chem.*, **15**, 9–17 (1975).

71. Refinement of the Crystal Structure of Pr_7O_{12} by Powder Neutron Diffraction, R.B. Von Dreele, L. Eyring, A.L. Bowman and J.L. Yarnell, *Acta Cryst. B*, **31**, 971–974 (1975).
72. The Structural Chemistry of Some Complex Oxides: Ordered and Disordered Extended Defects, L. Eyring and L.-T. Tai. In: B. Hannay (Ed.), *Treatise on Solid State Chemistry*, vol. 3, Plenum, New York, pp. 167–252, 1976.
73. Oxygen Transport in Polycrystals and Single Crystals of $\text{P}_7\text{O}_{12\pm\delta}$, K.H. Lau, D.L. Fox, S.H. Lin and L. Eyring, *High Temperature Science*, **8**, 129–139 (1976).
74. A Thermodynamic Model of Hysteresis in Phase Transitions and its Application to Rare Earth Oxide Systems, D.R. Knittel, S.P. Pack, S.H. Lin and L. Eyring, *J. Chem. Phys.*, **67**, 134 (1977).
75. Nonstoichiometry, Order and Disorder in Fluorite-Related Materials for Energy and Conversion, L. Eyring. In: J.B. Goodenough and M.S. Whittingham (Eds.), *Advances in Chemistry Series, No. 163*, American Chemical Society, pp. 240–270, 1977, Chapter 14.
76. On the Nature of Extended Defects and Their Ordering in Fluorite-Related Refractory Oxides, L. Eyring and R.T. Tuenge, from: *Conference on High Temperature Sciences Related to Open-Cycle Coal Fired MHD Systems*, Argonne, IL, April 4, 1977, ANL-77-21, pp. 170–179.
77. Calculated n-Beam Crystal Structure Images of Oxides Based on Fluorite and ReO_3 and the Interpretation of Observed Images, A. Skarnulis, E. Summerville and L. Eyring, *J. Solid State Chem.*, **23**, 59–71 (1978).
78. High Resolution Crystal Structure Image of Beta Phase ($\text{Pr}_{24}\text{O}_{44}$) in the Praseodymium Oxide System, E. Summerville, R.T. Tuenge and L. Eyring, *J. Solid State Chem.*, **24**, 21–31 (1978).
79. Electron Diffraction of Vanadium Fluoride Bronzes, R. Langley, D. Rieck, H. Eick, L. Eyring, R.F. Williamson and W.O.J. Boo, *Mat. Res. Bull.*, **13**, 1297–1303 (1978).
80. The Binary Rare Earth Oxides, L. Eyring. In: K. Gschneidner and L. Eyring (Eds.), *Handbook on the Physics and Chemistry of Rare Earths*, vol. III, North-Holland, Amsterdam, pp. 337–399, 1979, Chapter 27.
81. On the Structure of the Intermediate Phases in the Praseodymium Oxide System, R.T. Tuenge and L. Eyring, *J. Solid State Chem.*, **29**, 165–179 (1979).
82. Some Uses of High-Resolution Electron Microscopy in Solid State Chemistry, L. Eyring, *Advances in Chemistry Series*, Symposium volume 186, The American Chemical Society, Washington, DC, pp. 27–62, 1980.
83. A Kinetic Study of Oxidation of Praseodymium Oxides: $\text{PrO}_{1.714} + 0.032\text{O}_2 \rightarrow \text{PrO}_{1.778}$, H. Inaba, S.P. Pack, S.H. Lin and L. Eyring, *J. Solid State Chem.* **33**, 295–304 (1980).
84. The Application of High Resolution Electron Microscopy to Problems in Solid State Chemistry: The Exploits of a Peeping TEM, L. Eyring, *J. Chem. Educ.*, **57**, 565–568 (1980).

85. Phase Relationships, Reaction Mechanisms, and Defect Structures in Rare Earth Oxide-Oxygen Systems, L. Eyring. In: *Science and Technology of Rare Earth Materials*, Academic Press, pp. 99–118 (1980).
86. A Kinetic Study of the Oxidation and Reduction of Praseodymium Oxides: $\frac{1}{7}\text{Pr}_7\text{O}_{12} + (\frac{1}{7} - \frac{x}{2})\text{O}_2 \rightleftharpoons \text{PrO}_{2-x}$, H. Inaba, S.H. Lin and L. Eyring, *J. Solid State Chem.*, **37**, 58–66 (1981).
87. A Thermochemical Study of the Phase Reaction: $\frac{1}{7}\text{Pr}_7\text{O}_{12} + (\frac{1}{7} - \frac{x}{2})\text{O}_2 = \text{PrO}_{2-x}$, H. Inaba, A. Navrotsky and L. Eyring, *J. Solid State Chem.*, **37**, 67–76 (1981).
88. A Thermochemical Study of the Phase Reaction: $\text{TbO}_{1.5} + (\frac{3}{28} - \frac{x}{2})\text{O}_2 \rightarrow \frac{1}{7}\text{Tb}_7\text{O}_{12}$, H. Inaba, A. Navrotsky and L. Eyring, *J. Solid State Chem.*, **37**, 77–84 (1981).
89. Structure, Defects and Nonstoichiometry in Oxides: An Electron Microscopic View, L. Eyring. In: T. Sørensen (Ed.), *Nonstoichiometric Oxides*, Academic Press, pp. 337–398, 1981, Chapter 7.
90. An Electronic Microscopic Examination of VF_2 , H.A. Eick and L. Eyring, *J. Solid State Chem.*, **37**, 232–241 (1981).
91. The Kinetics of Oxidation of ϕ -Phase Terbium Oxide: $\frac{7}{2}\text{Tb}_2\text{O}_{3+\delta} + (\frac{3}{4} - \frac{7}{4}\delta)\text{O}_2 \rightarrow \text{Tb}_7\text{O}_{12}$, T. Sugihara, S.H. Lin and L. Eyring, *J. Solid State Chem.*, **40**, 189–196 (1981).
92. A Kinetic Study of the Oxidation of ζ Phase Praseodymium Oxide: $\frac{10}{9}\text{Pr}_9\text{O}_{16} + \frac{1}{9}\text{O}_2 \rightarrow \text{Pr}_{10}\text{O}_{18}$, T. Sugihara, S.H. Lin and L. Eyring, *J. Solid State Chem.*, **40**, 226–232 (1981).
93. Chemistry Viewed Through the Eyes of High-Resolution Microscopy, M. Beer, R.W. Carpenter, L. Eyring, C.E. Lyman and J.M. Thomas, *Chem. Eng. News*, **59**, 40–61 (1981).
94. The Role of High-Resolution Electron Microscopy in the Development of Solid State Chemistry, L. Eyring. In Symposium volume: L. Eyring (Ed.), *High Resolution Electron Microscopy Applied to Chemical Problems*, August 25–26, 1981, American Chemical Society, New York, *Ultramicroscopy*, **8**, 39–58 (1982).
95. Calculation, Display and Comparison of Electron Microscope Images Modeled and Observed, A.R. Smith and L. Eyring. In Symposium volume: L. Eyring (Ed.), *High Resolution Electron Microscopy Applied to Chemical Problems*, August 25–26, 1981, American Chemical Society, New York, *Ultramicroscopy*, **8**, 65–78 (1982).
96. On the Structures of the Intermediate Phases in the Terbium Oxide System, R.T. Tuenge and L. Eyring, *J. Solid State Chem.*, **41**, 75–89 (1982).
97. Electron Beam-Induced Reduction of Higher Oxides of the Rare Earths: A High-Resolution Electron Microscopic Study, H.A. Eick, L. Eyring, E. Summerville and R.T. Tuenge, *J. Solid State Chem.*, **42**, 47–74 (1982).
98. High-Resolution Electron Microscope Analysis of $\{100\}$ Twinning in β -Rhombohedral Boron, M.J. McKelvy, A.R. Rae Smith and L. Eyring, *J. Solid State Chem.*, **44**, 374–381 (1982).
99. Structures of Hexagonal Vanadium Fluoride Bronzes: A High Resolution Electron Microscopic Study, D. Rieck, R. Langley and L. Eyring, *J. Solid State Chem.*, **45**, 259–275 (1982).

100. A Theoretical Study of the Application of Time-Resolved X-Ray Scattering to Solid State Reaction Kinetics, T.L. Groy, S.K. Porter, R.B. Von Dreele and L. Eyring, *Comm. Int. J. Mol. Sci. (Wuhan, China)*, **2**, 93–105 (1982).
101. On Mixed Crystals of $\text{Pr}_{1-y}\text{Tb}_y\text{O}_x$ Grown Under High Oxygen Pressures, B. Chang, M.J. McKelvy and L. Eyring. In: G.J. McCarthy, H.B. Silber and J.I. Rhyne (Eds.), *The Rare Earths in Modern Science and Technology*, vol. 3, Plenum, New York, pp. 283–288, 1982.
102. Defect in Hexagonal Vanadium Fluoride Bronzes: A High Resolution Electron Microscopic Study, D. Rieck, R. Langley and L. Eyring, *J. Solid State Chem.*, **48**, 100–116 (1983).
103. Vacancy Ordering in Sc_{1-x}S , H.F. Franzen, R.T. Tuenge and L. Eyring, *J. Solid State Chem.*, **49**, 206–214 (1983).
104. Conditions Variation and Procedural Improvement for Hydrothermal Crystal Growth of Oxides Under Highly Oxidizing Conditions, M. McKelvy and L. Eyring, *J. Cryst. Growth*, **62**, 635–638 (1983).
105. Analytical and Structural Analysis of the Lanthanum Deficient Lanthanum Hexaboride, $\text{LaB}_{6+\delta}$, M.J. McKelvy, L. Eyring and E.K. Storms, *J. Phys. Chem.*, **88**, 1785–1790 (1984).
106. A Theoretical Model of Solid State Phase Reactions: Hysteresis and Kinetics, A. Maren, S.H. Lin, R.H. Langley and L. Eyring, *J. Solid State Chem.*, **53**, 329–343 (1984).
107. Order and Disorder in the Oxygen-Deficient Fluorite-Related Oxides, L. Eyring, *Mater. Res. Soc., Symp. Proc.*, **24**, 187–198 (1984).
108. Photoacoustic Spectroscopy of Rare Earth Oxides, J.R. Schoonover, Y.L. Lee, S.N. Su, S.H. Lin and L. Eyring, *Appl. Spectrosc.*, **38**, 154–158 (1984).
109. Raman and Resonance Raman Spectroscopy of Selected Rare-Earth Sesquioxides, L.A. Tucker, F.J. Carney Jr., P. McMillan, S.H. Lin and L. Eyring, *Appl. Spectrosc.*, **38**, 857–860 (1984).
110. Preparation and Electron Microscopy of Intermediate Phases in the Interval Ce_7O_{12} – $\text{Ce}_{11}\text{O}_{20}$, P. Knappe and L. Eyring, *J. Solid State Chem.*, **58**, 312–324 (1985).
111. The Reaction of Potassium Vapor with Tungsten Trioxide Crystals, D.A. Rieck and L. Eyring, *Inorg. Chem.*, **24**, 2461–2463 (1985).
112. Structure and Structural Defects in Anion-Deficient Fluorite-Related Materials: High-Resolution Electron Microscopy, L. Eyring, *High Temp. Sci.*, **20**, 183–201 (1985).
113. High-Resolution Electron Microscopic Studies of Chemical Reactions in Thin Films, L. Eyring, D.C. Dufner, J.P. Goral and A. Holladay, *Ultramicroscopy*, **18**, 253–274 (1985).
114. Time-Resolved Analysis of High-Resolution Electron Microscope Images, J.P. Goral, A. Holladay and L. Eyring, *Ultramicroscopy*, **18**, 275–280 (1985).
115. An HREM Investigation of Praseodymium Oxides Related to Pr_7O_{12} , L. Eyring, D.J. Smith and G.J. Wood, In: W.D. Corner and B.K. Tanner (Eds.), *Inst. Phys. Conf. Ser. No. 78: Electron Microscopy and Analysis*, Adam Hilger, Ltd., pp. 333–336, 1985, Chapter 9.

116. Ordered Phases, Nonstoichiometric and Solid State Reaction as Revealed by High-Resolution Electron Microscopy, L. Eyring, *Revista de la Real Academia de Ciencias Exactas, Fisicas y Naturales, de Madrid*, **80**, 333–345 (1986).
117. Some Applications of High-Resolution Electron Microscopy to the Study of Solid State Chemical Reaction Mechanisms, Z.C. Kang, L. Eyring and D.J. Smith, *Proc. XIth Int. Cong. on Electron Microscopy*, Kyoto, pp. 833–834, 1986.
118. High-Resolution Transmission Electron Microscopic Observations of Beta-Tin Thin Films, L. Eyring and D.C. Dufner, *Thin Solid Films*, **142**, 101–112 (1986).
119. High-Resolution Transmission Electron Microscopy and X-ray Microanalysis of Chemical Reactions in the Gold-Tin Thin Film System, D.C. Dufner and L. Eyring, *J. Solid State Chem.*, **61**, 112–132 (1986).
120. The Formation of Rare Earth Oxides Far From Equilibrium, M. Gasgnier, G. Schiffmacher, P. Caro and L. Eyring, *J. Less-Common Metals*, **116**, 29–40 (1986).
121. The Gold/Indium Thin Film System. A High-Resolution Electron Microscopic Study, J.P. Goral and L. Eyring, *J. Less-Common Metals*, **116**, 61–70 (1986).
122. Atomic Imaging of Oxide Surfaces. II. Terbium Oxide, Z.C. Kang, D.J. Smith and L. Eyring, *Surf. Sci.*, **175**, 684–692 (1986).
123. A High-Resolution Electron Microscopic Study of Some Members of the Vernier Structural Series $Ba_p(Fe_2S_4)_q$, A.C. Holladay and L. Eyring, *J. Solid State Chem.*, **64**, 113–118 (1986).
124. Domain Formation and Interfaces in Praseodymium and Terbium Oxides Obtained by Reduction of PrO_2 and TbO_2 : A Comparison with Group Theory Predictions, C. Boulesteix and L. Eyring, *J. Solid State Chem.*, **66**, 125–135 (1987).
125. Dynamic Edge and Surface Processes in Terbium Oxide, Z.C. Kang, D.J. Smith and L. Eyring, *Ultramicroscopy*, **22**, 71–80 (1987).
126. Rubidium Chromium Fluoride Structures of the Hexagonal Tungsten Bronze Type, R. Sharma and L. Eyring, *Ultramicroscopy*, **22**, 81–88 (1987).
127. *In-situ* Oxidation and Reduction of the Oxides of Cerium, Praseodymium and Terbium by High Voltage Electron Microscopy, E. Schweda, Z.C. Kang and L. Eyring, *J. Microscopy*, **145**, 45–54 (1987).
128. Electron Diffraction and Imaging Studies of Cerium Oxides Prepared in Far-From-Equilibrium Conditions, M. Gasgnier, G. Schiffmacher, L. Eyring and P. Caro, *J. Less-Common Met.*, **127**, 167–173 (1987).
129. Directional Decomposition of Some Ternary Rare Earth Sulfides in the Electron Beam, J.P. Goral, H.A. Eick, Y.-R. Du, J.C. Barry and L. Eyring, *J. Less-Common Met.*, **127**, 209–218 (1987).
130. X-ray Absorption Spectroscopy of Rare Earth Intermediate Oxides, M. Gasgnier, L. Eyring, R.C. Karnatak, H. Dexpert, J.M. Esteva, P. Caro and L. Albert, *J. Less-Common Met.*, **127**, 367–372 (1987).
131. Time-resolved X-ray Diffraction by Synchrotron Radiation: The Thermal Decomposition of $Cd(OH)_2$ Powders, Ö. Sävborg, J.R. Schoonover, S.H. Lin and L. Eyring, *J. Solid State Chem.*, **68**, 214–218 (1987).

132. Surface Processes Observed by High-Resolution Electron Microscopy: Transformation and Reduction in a Modified β -PbO₂ Crystal, Z.C. Kang and L. Eyring, *Ultramicroscopy*, **23**, 275–282 (1987).
133. Structural Transformation and Chemical Reduction of Pr₂₄O₄₄ Induced by the Electron Beam During Microscopical Examination, E. Schweda and L. Eyring, *Ultramicroscopy*, **23**, 443–452 (1987).
134. Electron Induced Decomposition of Rubidium Chromium Fluoride, R. Sharma, J. Barry and L. Eyring, *Ultramicroscopy*, **23**, 452–462 (1987).
135. Reduction of Praseodymium and Terbium Higher Oxides: A Chemical Reaction Similar to Diffusionless Phase Transitions, C. Boulesteix and L. Eyring, *J. Solid State Chem.*, **71**, 458–465 (1987).
136. The Solvolytic Disproportionation of Mixed-Valence Compounds. I. Pr₇O₁₂, Z.C. Kang and L. Eyring, *J. Solid State Chem.*, **75**, 52–59 (1988).
137. The Solvolytic Disproportionation of Mixed-Valence Compounds. II. Tb₁₁O₂₀, Z.C. Kang and L. Eyring, *J. Solid State Chem.*, **75**, 60–72 (1988).
138. The Solvolytic Disproportionation of Mixed-Valence Compounds. III. Pb₃O₄, Z.C. Kang, L. Machesky, H.A. Eick and L. Eyring, *J. Solid State Chem.*, **75**, 73–89 (1988).
139. A Disordered Intermediate Stage in the Reduction of Tb₁₁O₁₂ or Tb₇O₁₂ to C-type Tb₂O₃ in the Electron Microscope, C. Boulesteix and L. Eyring, *J. Solid State Chem.*, **75**, 291–295 (1988).
140. Solid State Chemistry, L. Eyring. In: P.R. Buseck, J.M. Cowley and L. Eyring (Eds.), *High-Resolution Transmission Electron Microscopy and Associated Techniques*, Oxford Univ. Press, New York, pp. 378–476, 1988.
141. Electron Interaction with Alkali Chromium Fluorides in the High-Resolution Electron Microscope, R. Sharma and L. Eyring, *Mater. Res. Soc., Symp. Proc.*, **125**, 285–290 (1988).
142. The Formation of a Gold/Silicon Alloy by Electron Beam Heating of Codeposited Thin Films, R. Sharma, W. Robison and L. Eyring, *Proc. Annu. Meet.: Electron Microsc. Soc. Am.*, **46**, 496–497 (1988).
143. Thickness of Interfaces Between Twins, Glide Domains, and Grain Boundaries in Oxides from HREM Studies, C. Boulesteix, M. Ben Salem, B. Yangui, Z. Kang and L. Eyring, *Phys. Status Solidi*, **107**, 469 (1988).
144. Twinning in Pr₂₄O₄₄: An Investigation by High Resolution Electron Microscopy, E. Schweda and L. Eyring, *J. Solid State Chem.*, **78**, 1–6 (1989).
145. The Polymorphic Transformation of Tb₂₄O₄₄ to Tb₄₈O₈₈ via a Partly Ordered Incommensurate Structure, Z.C. Kang, C. Boulesteix and L. Eyring, *J. Solid State Chem.*, **81**, 96–102 (1989).
146. Identification of an Electron-Beam-Induced Reaction Product in the Praseodymium Oxide System, H.A. Eick, L. Eyring and D.J. Smith, *J. Microscopy*, **153**, 31–37 (1989).
147. A Study of the Decomposition of Neodymium Hydroxy Carbonate and Neodymium Carbonate Hydrate, H. Hinode, R. Sharma and L. Eyring, *J. Solid State Chem.*, **84**, 102–117 (1990).

148. Domain Structures and Related Phenomena in the PrO_x and TbO_x Oxides, C. Boulesteix, E. Schweda, Z. Kang and L. Eyring, *Ferroelectrics*, **111**, 247–256 (1990).
149. Nanostructure Evolution During Chemical Processing of Gels: A High-Resolution Electron Microscope Study. 1. Rare Earth Oxide and Hydroxycarbonate Colloids, Z.C. Kang and L. Eyring, *J. Solid State Chem.*, **88**, 303–323 (1990).
150. Nanostructure Evolution During Processing of Thin-Film Gels: A High-Resolution Electron Microscopic Study. 2. The Thin-Film Gel Derived from $\text{Pb}(\text{Zr}_{0.45}\text{Ti}_{0.55})\text{O}_2\text{-(OR)}_2$, Z.C. Kang, S.K. Dey and L. Eyring, *Mater. Res. Soc., Symp. Proc.*, **183**, 291–296 (1990).
151. Processing Video Images of Chemical Reactions, L. Eyring and W.J. de Ruijter, *Proc. XIIIth International Cong. Electron Microscopy*, San Francisco Press, 1990.
152. On the $\text{Pr}_n\text{O}_{2n-2}$ Series of Oxides and the Structure of $\text{Pr}_{24}\text{O}_{44}$: An Investigation by High Resolution Electron Microscopy, E. Schweda, D.J.M. Bevan and L. Eyring, *J. Solid State Chem.*, **90**, 109–125 (1991).
153. The Binary Lanthanide Oxides: Synthesis and Identification, L. Eyring. In: G. Meyer and L.R. Morss (Eds.), *Synthesis of Lanthanide and Actinide Compounds*, Kluwer Academic Publishers, Dordrecht, The Netherlands, pp. 187–224, 1991.
154. Observation of Gold-Silicon Alloy Formation in Thin Films by High Resolution Electron Microscopy, W. Robison, R. Sharma and L. Eyring, *Acta Metall. Mater.*, **39**, 179–186 (1991).
155. Real-Time Atomic-Level Observations of *In Situ* Chemical Reactions and Transformations Utilizing High-Resolution Electron Microscopy, Z. Kang and L. Eyring, *Metall. Trans. A*, **22**, 1323–1329 (1991).
156. A Study of the Decomposition of Praseodymium Hydroxy Carbonate and Praseodymium Carbonate Hydrate, R. Sharma, H. Hinode and L. Eyring, *J. Solid State Chem.*, **92**, 401–419 (1991).
157. HREM Combined with Video Recording and Image Processing is Used to Reveal Atomic Level Mechanisms for the Decomposition of Lanthanide Compounds, L. Eyring and Z.C. Kang, *Eur. J. Solid State Inorg. Chem.*, **28**, 459–470 (1991).
158. Early Evolutionary Stages of Condensation and Crystallization in Acid and Base Catalyzed $\text{PbZrO}_3\text{--PbTiO}_3$ Gels: A High-Resolution Electron Microscopic Study, Z.C. Kang, S.K. Dey and L. Eyring. In: A.S. Bhalla and K.M. Nair (Eds.), *The Ceramic Transactions-Ferroelectric Films*, vol. 25, American Ceramic Society, Westerville, OH, p. 129, 1992.
159. Nanostructure Evolution During the Transition of TiO_2 , PbTiO_3 and PZT from Gels to Crystalline Thin Films, Z.C. Kang, A. Gupta, M.J. McKelvy, L. Eyring and S.K. Dey, *Mater. Res. Soc., Symp. Proc.*, **230**, 301–306 (1992).
160. The Preparation and Characterization of Hydroxycarbonate Colloidal Particles of Individual and Mixed Rare Earth Elements, Z.C. Kang, T.Z. Li and L. Eyring, *J. Alloys Compd.*, **181**, 477–482 (1992).
161. Surface Profiles and Substructures in CeO_2 and PrO_x , Z.C. Kang and L. Eyring, *J. Alloys Compd.*, **181**, 484–487 (1992).

162. Electron-Induced Decomposition of V_2MoO_8 and $(V_{0.7}Mo_{0.3})_2O_5$ During Imaging in the Electron Microscope, C. Kang and L. Eyring, *J. Solid State Chem.*, **99**, 343–354 (1992).
163. Non-equilibrium Reactions of α -phase PrO_x with O_2 , Z.C. Kang, J. Zhang and L. Eyring, *Austr. J. Chem.* (in honor of Bruce Hyde), **45**, 1499–1517 (1992).
164. The High-Resolution Electron Microscope as a Chemical Laboratory, L. Eyring and Z.C. Kang, Texas A&M University EM Views, No. 8, 29–32 (1992).
165. The Growth of Single Crystal-like and Polycrystal $VNbO_3$ Films via Sol-gel Process, C.H. Cheng, Y.H. Xu, J.D. Mackenzie, J. Zhang and L. Eyring, *Mater. Res. Soc., Symp. Proc.*, **271**, 383–388 (1992).
166. The Crystal Structures of Oxygen Deficient Rare Earth Oxides, (abstract) J. Zhang, L. Eyring and R. Von Dreele. In: Proceedings of the XVth Conference on Applied Crystallography, Cieszyn, Poland, August 8–10, 1992.
167. Nanostructures of the Product Sequence in the Decomposition of Mixed Rare Earth Hydroxycarbonate Colloidal Particles, Z.C. Kang, M.J. McKelvy and L. Eyring, *Mater. Res. Soc., Symp. Proc.*, **272**, pp. 59–64 (1992).
168. Study of the Decomposition of Colloidal Mixed Rare Earth Hydroxycarbonate Spheres by Conventional Thermal Treatment and by Electron-Beam Irradiation Within a High-Resolution Microscope, Z.C. Kang, M.J. McKelvy and L. Eyring, *Z. Anorg. Allgem. Chem.* (in honor of R. Hoppe), **616**, 125–132 (1992).
169. The Structures of Tb_7O_{12} and $Tb_{11}O_{20}$, J. Zhang, R.B. Von Dreele and L. Eyring, *J. Solid State Chem.* (in honor of J.S. Anderson), **104**, 21–32 (1993).
170. The Binary, Higher Oxides of the Rare Earths, J. Zhang, Z.C. Kang and L. Eyring, Rare Earths '92 in Kyoto, Japan, June 1–5, 1992, *J. Alloys Compd.*, **192**, 57–63 (1993).
171. A TEM Diffraction and Simulation Method for Early-Stage Studies of the Evolution of Gel-Derived Zirconia Precursors, J. Tong, J.M. Zuo and L. Eyring, *J. Amer. Ceram. Soc.*, **76**, 857–864 (1993).
172. The Effect of an Electric Field on the Crystallization of Gel-Derived Alumina Precursors Observed *In-situ* in the TEM, J. Tong, J.C. Wheatley and L. Eyring, *Ultramicroscopy* (dedicated to J.M. Cowley), **52**, 388–392 (1993).
173. Analysis of Time-resolved *In-situ* Change in High-resolution Electron Microscopy, Z.C. Kang and L. Eyring, *Ultramicroscopy* (dedicated to J.M. Cowley), **52**, 377–382 (1993).
174. Comparisons of the Binary Oxides, R. Haire and L. Eyring. In: K.A. Gschneidner Jr., G.R. Choppin and L. Eyring (Eds.), *Handbook on the Physics and Chemistry of Rare Earths*, vol. 18, North-Holland, Amsterdam, pp. 413–505 (1994).
175. Exploring the Black Oxide of Praseodymium, L. Eyring, *J. Alloys Compd.*, **207–208**, 1–13 (1994).
176. Nanoanalytical Characterization of $Pr_{0.5}Tb_{0.5}O_x$ Obtained from *In-situ* Video Observation in the High-Resolution Electron Microscope, J. Tong, J. Liu, Z.C. Kang and L. Eyring, 20th Rare Earth Research Conference, Monterey, September 1993, *J. Alloys Compd.*, **207–208**, 416–419 (1994).

177. Structures and Structural Defects in Colloidal Particles Altered *In-situ* in HREM, Z.C. Kang, J. Tong and L. Eyring, 20th Rare Earth Research Conference, Monterey, September 1993, *J. Alloys Compd.*, **207–208**, 420–423 (1994).
178. Structures, Structural Defects and Reactions in a Chevrel Phase Sulfide: a High-Resolution Electron Microscope Study, Z.C. Kang, L. Eyring, H. Hinode, T. Uchida and M. Wakihara, *J. Solid State Chem.*, **111**, 58–74 (1994).
179. Some Aspects of the Fluorite-Related Homologous Series of Rare Earth Oxides and Their Mixtures, L. Eyring and Z.C. Kang, *Eur. J. Solid State Inorg. Chem.* (in honor of Arne Magnéli), **31**, 717–726 (1994).
180. Structures in the Oxygen-Deficient Fluorite-Related R_nO_{2n-2} Homologous Series: Pr_9O_{16} , J. Zhang, R.B. Von Dreele and L. Eyring, *J. Solid State Chem.*, **118**, 133–140 (1995).
181. Structures in the Oxygen-Deficient Fluorite-Related R_nO_{2n-2} Homologous Series (II): $Pr_{10}O_{18}$, J. Zhang, R.B. Von Dreele and L. Eyring, *J. Solid State Chem.*, **118**, 141–147 (1995).
182. The Evolution of a Thin, Amorphous Neodymium Hydroxide Film to the C-type Oxide – An HREM Study, J. Tong and L. Eyring, 2nd International Conference on f-Elements, Helsinki, Finland, August 1–5, 1994, *J. Alloys Compd.*, **225**, 139–141 (1995).
183. Sintering in Colloidal Particles of Rare Earth Hydroxycarbonate and its Decomposition Products, Z.C. Kang and L. Eyring, 2nd International Conference on f-Elements, Helsinki, Finland, August 1–5, 1994, *J. Alloys Compd.*, **225**, 190–192 (1995).
184. Structures in the Oxygen-Deficient Fluorite-Related R_nO_{2n-2} Homologous Series (III): $Pr_{12}O_{22}$, J. Zhang, R.B. Von Dreele and L. Eyring, *J. Solid State Chem.*, **122**, 53–58 (1996).
185. The Structural Principles That Underlie the Higher Oxides of the Rare Earths, Z.C. Kang, J. Zhang and L. Eyring, *Z. Anorg. Allgem. Chem.*, **622**, 465–472 (1996).
186. The Structural Basis of the Fluorite-Related Rare Earth Higher Oxides, Z.C. Kang and L. Eyring, *Austr. J. Chem.*, **49**, 981–996 (1996).
187. A Compositional and Structural Rationalization of the Higher Oxides of Ce, Pr, and Tb, Z.C. Kang and L. Eyring, *J. Alloys Compd.*, **249**, 206–212 (1997).
188. The Prediction of the Structure of Members of the Homologous Series of the Higher Rare Earth Oxides, Z.C. Kang and L. Eyring, *J. Alloys Compd.*, **275–277**, 30–36 (1998).
189. Fluorite Structural Principles: Disordered α -Phase to Ordered Intermediate Phases in Praseodymia, Z.C. Kang and L. Eyring, *J. Alloys Compd.*, **275–277**, 721–724 (1998).
190. Binary Oxides with a Wide Composition Range: (3 sections) Transition Metal Lower Oxides, TiO, VO, MnO, FeO, CoO, NiO, NbO and Cu₂O; Oxygen-Deficient Fluorite Structures. Lanthanide Oxides (Ce, Pr and Tb Higher Oxides); Oxygen-Excess Fluorite Structures, $UO_2 + \delta$, L. Eyring. In: J.J. Zuckerman and A.D. Norman (Eds.), *Inorganic Reactions and Methods*, vol. 6, Wiley-VCH, New York, pp. 152–166, 1998, Part 2.
191. The Structural Principles and Their Consequences for the Anion-Deficient Fluorite-Related Oxides of the Higher Rare Earths, Z.C. Kang and L. Eyring, *Key Eng. Mater.*, **155–156**, 301–358 (1999).

192. Rare-Earth Oxides with Fluorite-Related Structures: Their Systematic Investigation Using HREM Images, Image Simulations and Electron Diffraction Pattern Simulations, C. Lopez-Cartes, J.A. Perez-Omil, J.M. Pintado, J.J. Calvino, Z.C. Kang and L. Eyring, *Ultramicroscopy*, **80**, 19–39 (1999).
193. A New Ceria–Zirconia Mixed Oxide Phase Based on Pyrochlore, T. Masui, T. Ozaki, G.-Y. Adachi, Z. Kang and L. Eyring, *Chem. Lett.*, **29**, 840–841 (2000).
194. Characterization of Ceria–Zirconia Mixed Oxide by High-Resolution Electron Microscopy, T. Masui, T. Ozaki, G.-Y. Adachi, Z. Kang and L. Eyring, *Kidorui*, **36**, 88–89 (2000).
195. Lattice Oxygen Transfer in Fluorite-Type Oxides Containing Ce, Pr, and/or Tb, Z.C. Kang and L. Eyring, *J. Solid State Chem.*, **155**, 129–137 (2000).
196. Redox Behavior of Ceria-Zirconia Solid Solutions Modified by the Chemical Filing Process, T. Masui, K. Nakano, T. Ozaki, G.-Y. Adachi, Z. Kang, L. Eyring, *Chem. Mater.*, **13**, 1834–1840 (2001).
197. Hydrogen Production from Methane and Water by Lattice Oxygen Transfer with $\text{Ce}_{0.70}\text{Zr}_{0.25}\text{Tb}_{0.05}\text{O}_{2-x}$, Z.C. Kang and L. Eyring, *J. Alloys Compd.*, **323–324**, 97–101 (2001).
198. Observation of Dynamic Nanostructural and Nanochemical Changes in Ceria-Based Catalysts During *In-situ* Reduction, R. Sharma, P.A. Crozier, Z.C. Kang and L. Eyring, *Philos. Mag.*, **84**, 2731–2747 (2004).
199. Proposal Structure of $\text{Pr}_{88}\text{O}_{160}$ Phase in Binary, Rare Earth Higher Oxides, Z.C. Kang and L. Eyring, *J. Alloys Compd.* **408–412**, 1123–1126 (2006).

Books

1. Progress in the Science and Technology of the Rare Earths, vol. 1, L. Eyring (Ed.), Pergamon, Oxford, 1964.
2. Rare Earth Research III, L. Eyring (Ed.), Gordon and Breach, New York, 1965.
3. Progress in the Science and Technology of the Rare Earths, vol. 2, L. Eyring (Ed.), Pergamon, Oxford, 1966.
4. Advances in High Temperature Chemistry, vol. I, L. Eyring (Ed.), Academic Press, New York, 1967.
5. Progress in the Science and Technology of the Rare Earths, vol. 3, L. Eyring (Ed.), Pergamon, Oxford, 1968.
6. Advances in High Temperature Chemistry, vol. II, L. Eyring (Ed.), Academic Press, New York, 1969.
7. Chemistry of Extended Defects in Non-Metallic Solids, L. Eyring and M. O’Keeffe (Eds.), North-Holland, Amsterdam, 1970.
8. Advances in High Temperature Chemistry, vol. III, L. Eyring (Ed.), Academic Press, New York, 1971.
9. Advances in High Temperature Chemistry, vol. IV, L. Eyring (Ed.), Academic Press, New York, 1971.
10. High Resolution Electron Microscopy and Associated Techniques, P.R. Buseck, J.M. Cowley and L. Eyring (Eds.), Oxford Univ. Press, New York, 1988.

11. Handbook on the Physics and Chemistry of Rare Earths, K.A. Gschneidner Jr. and L. Eyring (Eds.), North-Holland, Elsevier Science Publishers B.V., Amsterdam
 - Vol. 1: Metals, 894 + xxv pp. (1978).
 - Vol. 2: Alloys and Intermetallics, 620 + xiii pp., 1979.
 - Vol. 3: Non-Metallic Compounds – I, 664 + xiii pp., 1979.
 - Vol. 4: Non-Metallic Compounds – II, 602 + xiii pp., 1979.
 - Vol. 5: 701 + x pp., 1982.
 - Vol. 6: 574 + x pp., 1984.
 - Vol. 7: 579 + x pp., 1984.
 - Vol. 8: 382 + x pp., 1986.
 - Vol. 9: 434 + xi pp., 1987.
 - Vol. 10: High Energy Spectroscopy, 611 + xi pp., 1987 (also co-edited with S. Hüfner).
 - Vol. 11: Two-Hundred-Year Impact of Rare Earths on Science, 594 + xiii pp., 1988.
 - Vol. 12: 486 + xi pp., 1989.
 - Vol. 13: 473 + xii pp., 1990.
 - Vol. 14: 484 + xvi pp., 1991.
 - Vol. 15: 530 + xii pp., 1991.
 - Vol. 16: 589 + xiii pp., 1993.
 - Vol. 17: Lanthanides/Actinides: Physics I, 769 + xvii pp., 1993 (also co-edited with G.H. Lander and G.R. Choppin).
 - Vol. 18: Lanthanides/Actinides: Chemistry, 674 + xvii pp., 1994 (also co-edited with G.R. Choppin and G.H. Lander).
 - Vol. 19: Lanthanides/Actinides: Physics II, 700 + xvii pp., 1994 (also co-edited with G.H. Lander and G.R. Choppin).
 - Vol. 20: 464 + xiv pp., 1995.
 - Vol. 21: 420 + xiv pp., 1995.
 - Vol. 22: 802 + xiv pp., 1996.
 - Vol. 23: 648 + xiv pp., 1996.
 - Vol. 24: 583 + xv pp., 1997.
 - Vol. 25: 492 + xv pp., 1998.
 - Vol. 26: 413 + xv pp., 1999.
 - Vol. 27: 574 + xv pp., 1999.
 - Vol. 28: 413 + xv pp., 2000.
 - Vol. 29: The Role of Rare Earths in Catalysis, 419 + xvi pp., 2000.
 - Vol. 30: High-Temperature Superconductors – I, 637 + xvii pp., 2000 (also co-edited with M.B. Maple).
 - Vol. 31: High-Temperature Superconductors – II, 687 + xviii pp., 2001 (also co-edited with M.B. Maple).
 - Vol. 32: 751 + xix pp., 2001 (also co-edited with G.H. Lander).

CONTENTS

Preface v

Dedication to LeRoy Eyring xi

Contents xli

Contents of Volumes 1–35 xliii

Index of Contents of Volumes 1–36 liii

227. Arthur Mar

Bismuthides 1

228. I. Aruna, L.K. Malhotra and B.R. Mehta

Switchable metal hydride films 83

229. Koen Binnemans

Applications of tetravalent cerium compounds 281

230. Robert A. Flowers II and Edamana Prasad

Samarium (II) based reductants 393

Author index 475

Subject index 511

CONTENTS OF VOLUMES 1–35

VOLUME 1: Metals

1978, 1st repr. 1982, 2nd repr. 1991; ISBN 0-444-85020-1

1. Z.B. Goldschmidt, *Atomic properties (free atom)* 1
 2. B.J. Beaudry and K.A. Gschneidner Jr, *Preparation and basic properties of the rare earth metals* 173
 3. S.H. Liu, *Electronic structure of rare earth metals* 233
 4. D.C. Koskenmaki and K.A. Gschneidner Jr, *Cerium* 337
 5. L.J. Sundström, *Low temperature heat capacity of the rare earth metals* 379
 6. K.A. McEwen, *Magnetic and transport properties of the rare earths* 411
 7. S.K. Sinha, *Magnetic structures and inelastic neutron scattering: metals, alloys and compounds* 489
 8. T.E. Scott, *Elastic and mechanical properties* 591
 9. A. Jayaraman, *High pressure studies: metals, alloys and compounds* 707
 10. C. Probst and J. Wittig, *Superconductivity: metals, alloys and compounds* 749
 11. M.B. Maple, L.E. DeLong and B.C. Sales, *Kondo effect: alloys and compounds* 797
 12. M.P. Dariel, *Diffusion in rare earth metals* 847
- Subject index 877

VOLUME 2: Alloys and intermetallics

1979, 1st repr. 1982, 2nd repr. 1991; ISBN 0-444-85021-X

13. A. Iandelli and A. Palenzona, *Crystal chemistry of intermetallic compounds* 1
 14. H.R. Kirchmayr and C.A. Poldy, *Magnetic properties of intermetallic compounds of rare earth metals* 55
 15. A.E. Clark, *Magnetostrictive RFe_2 intermetallic compounds* 231
 16. J.J. Rhyne, *Amorphous magnetic rare earth alloys* 259
 17. P. Fulde, *Crystal fields* 295
 18. R.G. Barnes, *NMR, EPR and Mössbauer effect: metals, alloys and compounds* 387
 19. P. Wachter, *Europium chalcogenides: EuO , EuS , $EuSe$ and $EuTe$* 507
 20. A. Jayaraman, *Valence changes in compounds* 575
- Subject index 613

VOLUME 3: Non-metallic compounds – I

1979, 1st repr. 1984; ISBN 0-444-85215-8

21. L.A. Haskin and T.P. Paster, *Geochemistry and mineralogy of the rare earths* 1
 22. J.E. Powell, *Separation chemistry* 81
 23. C.K. Jørgensen, *Theoretical chemistry of rare earths* 111
 24. W.T. Carnall, *The absorption and fluorescence spectra of rare earth ions in solution* 171
 25. L.C. Thompson, *Complexes* 209
 26. G.G. Libowitz and A.J. Maeland, *Hydrides* 299
 27. L. Eyring, *The binary rare earth oxides* 337
 28. D.J.M. Sevan and E. Summerville, *Mixed rare earth oxides* 401
 29. C.P. Khattak and F.F.Y. Wang, *Perovskites and garnets* 525
 30. L.H. Brixner, J.R. Barkley and W. Jeitschko, *Rare earth molybdates (VI)* 609
- Subject index 655

VOLUME 4: Non-metallic compounds – II

1979, 1st repr. 1984; ISBN 0-444-85216-6

31. J. Flahaut, *Sulfides, selenides and tellurides* 1
 32. J.M. Haschke, *Halides* 89
 33. F. Hulliger, *Rare earth pnictides* 153
 34. G. Blasse, *Chemistry and physics of R-activated phosphors* 237
 35. M.J. Weber, *Rare earth lasers* 275
 36. F.K. Fong, *Nonradiative processes of rare-earth ions in crystals* 317
 37A. J.W. O’Laughlin, *Chemical spectrophotometric and polarographic methods* 341
 37B. S.R. Taylor, *Trace element analysis of rare earth elements by spark source mass spectroscopy* 359
 37C. R.J. Conzemius, *Analysis of rare earth matrices by spark source mass spectrometry* 377
 37D. E.L. DeKalb and V.A. Fassel, *Optical atomic emission and absorption methods* 405
 37E. A.P. D’Silva and V.A. Fassel, *X-ray excited optical luminescence of the rare earths* 441
 37F. F.W.V. Boynton, *Neutron activation analysis* 457
 37G. S. Schuhmann and J.A. Philpotts, *Mass-spectrometric stable-isotope dilution analysis for lanthanides in geochemical materials* 471
 38. J. Reuben and G.A. Elgavish, *Shift reagents and NMR of paramagnetic lanthanide complexes* 483
 39. J. Reuben, *Bioinorganic chemistry: lanthanides as probes in systems of biological interest* 515
 40. T.J. Haley, *Toxicity* 553
 Subject index 587

VOLUME 5

1982, 1st repr. 1984; ISBN 0-444-86375-3

41. M. Gasgnier, *Rare earth alloys and compounds as thin films* 1
 42. E. Gratz and M.J. Zuckermann, *Transport properties (electrical resistivity, thermoelectric power thermal conductivity) of rare earth intermetallic compounds* 117
 43. F.P. Netzer and E. Bertel, *Adsorption and catalysis on rare earth surfaces* 217
 44. C. Boulesteix, *Defects and phase transformation near room temperature in rare earth sesquioxides* 321
 45. O. Greis and J.M. Haschke, *Rare earth fluorides* 387
 46. C.A. Morrison and R.P. Leavitt, *Spectroscopic properties of triply ionized lanthanides in transparent host crystals* 461
 Subject index 693

VOLUME 6

1984; ISBN 0-444-86592-6

47. K.H.J. Buschow, *Hydrogen absorption in intermetallic compounds* 1
 48. E. Parthé and B. Chabot, *Crystal structures and crystal chemistry of ternary rare earth–transition metal borides, silicides and homologues* 113
 49. P. Rogl, *Phase equilibria in ternary and higher order systems with rare earth elements and boron* 335
 50. H.B. Kagan and J.L. Namy, *Preparation of divalent ytterbium and samarium derivatives and their use in organic chemistry* 525
 Subject index 567

VOLUME 7

1984; ISBN 0-444-86851-8

51. P. Rogl, *Phase equilibria in ternary and higher order systems with rare earth elements and silicon* 1
 52. K.H.J. Buschow, *Amorphous alloys* 265
 53. H. Schumann and W. Genthe, *Organometallic compounds of the rare earths* 446
 Subject index 573

VOLUME 8

1986; ISBN 0-444-86971-9

54. K.A. Gschneidner Jr and F.W. Calderwood, *Intra rare earth binary alloys: phase relationships, lattice parameters and systematics* 1
55. X. Gao, *Polarographic analysis of the rare earths* 163
56. M. Leskelä and L. Niinistö, *Inorganic complex compounds I* 203
57. J.R. Long, *Implications in organic synthesis* 335
- Errata 375
- Subject index 379

VOLUME 9

1987; ISBN 0-444-87045-8

58. R. Reisfeld and C.K. Jørgensen, *Excited state phenomena in vitreous materials* 1
59. L. Niinistö and M. Leskelä, *Inorganic complex compounds II* 91
60. J.-C.G. Bünzli, *Complexes with synthetic ionophores* 321
61. Zhiquan Shen and Jun Ouyang, *Rare earth coordination catalysis in stereospecific polymerization* 395
- Errata 429
- Subject index 431

VOLUME 10: High energy spectroscopy

1988; ISBN 0-444-87063-6

62. Y. Baer and W.-D. Schneider, *High-energy spectroscopy of lanthanide materials – An overview* 1
63. M. Campagna and F.U. Hillebrecht, *f-electron hybridization and dynamical screening of core holes in intermetallic compounds* 75
64. O. Gunnarsson and K. Schönhammer, *Many-body formulation of spectra of mixed valence systems* 103
65. A.J. Freeman, B.I. Min and M.R. Norman, *Local density supercell theory of photoemission and inverse photoemission spectra* 165
66. D.W. Lynch and J.H. Weaver, *Photoemission of Ce and its compounds* 231
67. S. Hüfner, *Photoemission in chalcogenides* 301
68. J.F. Herbst and J.W. Wilkins, *Calculation of 4f excitation energies in the metals and relevance to mixed valence systems* 321
69. B. Johansson and N. Mårtensson, *Thermodynamic aspects of 4f levels in metals and compounds* 361
70. F.U. Hillebrecht and M. Campagna, *Bremsstrahlung isochromat spectroscopy of alloys and mixed valent compounds* 425
71. J. Röhrler, *X-ray absorption and emission spectra* 453
72. F.P. Netzer and J.A.D. Matthew, *Inelastic electron scattering measurements* 547
- Subject index 601

VOLUME 11: Two-hundred-year impact of rare earths on science

1988; ISBN 0-444-87080-6

- H.J. Svec, *Prologue* 1
73. F. Szabadváry, *The history of the discovery and separation of the rare earths* 33
74. B.R. Judd, *Atomic theory and optical spectroscopy* 81
75. C.K. Jørgensen, *Influence of rare earths on chemical understanding and classification* 197
76. J.J. Rhyne, *Highlights from the exotic phenomena of lanthanide magnetism* 293
77. B. Bleaney, *Magnetic resonance spectroscopy and hyperfine interactions* 323
78. K.A. Gschneidner Jr and A.H. Daane, *Physical metallurgy* 409
79. S.R. Taylor and S.M. McLennan, *The significance of the rare earths in geochemistry and cosmochemistry* 485
- Errata 579
- Subject index 581

VOLUME 12

1989; ISBN 0-444-87105-5

80. J.S. Abell, *Preparation and crystal growth of rare earth elements and intermetallic compounds* 1
81. Z. Fisk and J.P. Remeika, *Growth of single crystals from molten metal fluxes* 53
82. E. Burzo and H.R. Kirchmayr, *Physical properties of $R_2Fe_{14}B$ -based alloys* 71
83. A. Szytuła and J. Leciejewicz, *Magnetic properties of ternary intermetallic compounds of the RT_2X_2 type* 133
84. H. Maletta and W. Zinn, *Spin glasses* 213
85. J. van Zytveld, *Liquid metals and alloys* 357
86. M.S. Chandrasekharaiah and K.A. Gingerich, *Thermodynamic properties of gaseous species* 409
87. W.M. Yen, *Laser spectroscopy* 433
Subject index 479

VOLUME 13

1990; ISBN 0-444-88547-1

88. E.I. Gladyshevsky, O.I. Bodak and V.K. Pecharsky, *Phase equilibria and crystal chemistry in ternary rare earth systems with metallic elements* 1
89. A.A. Eliseev and G.M. Kuzmichyeva, *Phase equilibrium and crystal chemistry in ternary rare earth systems with chalcogenide elements* 191
90. N. Kimizuka, E. Takayama-Muromachi and K. Siratori, *The systems R_2O_3 – M_2O_3 – $M'O$* 283
91. R.S. Houk, *Elemental analysis by atomic emission and mass spectrometry with inductively coupled plasmas* 385
92. P.H. Brown, A.H. Rathjen, R.D. Graham and D.E. Tribe, *Rare earth elements in biological systems* 423
Errata 453
Subject index 455

VOLUME 14

1991; ISBN 0-444-88743-1

93. R. Osborn, S.W. Lovesey, A.D. Taylor and E. Balcar, *Intermultiplet transitions using neutron spectroscopy* 1
94. E. Dormann, *NMR in intermetallic compounds* 63
95. E. Zirngiebl and G. Güntherodt, *Light scattering in intermetallic compounds* 163
96. P. Thalmeier and B. Lüthi, *The electron–phonon interaction in intermetallic compounds* 225
97. N. Grewe and F. Steglich, *Heavy fermions* 343
Subject index 475

VOLUME 15

1991; ISBN 0-444-88966-3

98. J.G. Sereni, *Low-temperature behaviour of cerium compounds* 1
99. G.-y. Adachi, N. Imanaka and Zhang Fuzhong, *Rare earth carbides* 61
100. A. Simon, Hj. Mattausch, G.J. Miller, W. Bauhofer and R.K. Kremer, *Metal-rich halides* 191
101. R.M. Almeida, *Fluoride glasses* 287
102. K.L. Nash and J.C. Sullivan, *Kinetics of complexation and redox reactions of the lanthanides in aqueous solutions* 347
103. E.N. Rizkalla and G.R. Choppin, *Hydration and hydrolysis of lanthanides* 393
104. L.M. Vallarino, *Macrocyclic complexes of the lanthanide(III) yttrium(III) and dioxouranium(VI) ions from metal-templated syntheses* 443
Errata 513
Subject index 515

MASTER INDEX, Vols. 1–15

1993; ISBN 0-444-89965-0

VOLUME 16

1993; ISBN 0-444-89782-8

105. M. Loewenhaupt and K.H. Fischer, *Valence-fluctuation and heavy-fermion 4f systems* 1
 106. I.A. Smirnov and V.S. Oskotski, *Thermal conductivity of rare earth compounds* 107
 107. M.A. Subramanian and A.W. Sleight, *Rare earths pyrochlores* 225
 108. R. Miyawaki and I. Nakai, *Crystal structures of rare earth minerals* 249
 109. D.R. Chopra, *Appearance potential spectroscopy of lanthanides and their intermetallics* 519
 Author index 547
 Subject index 579

VOLUME 17: Lanthanides/Actinides: Physics – I

1993; ISBN 0-444-81502-3

110. M.R. Norman and D.D. Koelling, *Electronic structure, Fermi surfaces, and superconductivity in f electron metals* 1
 111. S.H. Liu, *Phenomenological approach to heavy-fermion systems* 87
 112. B. Johansson and M.S.S. Brooks, *Theory of cohesion in rare earths and actinides* 149
 113. U. Benedict and W.B. Holzapfel, *High-pressure studies – Structural aspects* 245
 114. O. Vogt and K. Mattenberger, *Magnetic measurements on rare earth and actinide mononictides and monochalcogenides* 301
 115. J.M. Fournier and E. Gratz, *Transport properties of rare earth and actinide intermetallics* 409
 116. W. Potzel, G.M. Kalvius and J. Gal, *Mössbauer studies on electronic structure of intermetallic compounds* 539
 117. G.H. Lander, *Neutron elastic scattering from actinides and anomalous lanthanides* 635
 Author index 711
 Subject index 753

VOLUME 18: Lanthanides/Actinides: Chemistry

1994; ISBN 0-444-81724-7

118. G.T. Seaborg, *Origin of the actinide concept* 1
 119. K. Balasubramanian, *Relativistic effects and electronic structure of lanthanide and actinide molecules* 29
 120. J.V. Beitz, *Similarities and differences in trivalent lanthanide- and actinide-ion solution absorption spectra and luminescence studies* 159
 121. K.L. Nash, *Separation chemistry for lanthanides and trivalent actinides* 197
 122. L.R. Morss, *Comparative thermochemical and oxidation – reduction properties of lanthanides and actinides* 239
 123. J.W. Ward and J.M. Haschke, *Comparison of 4f and 5f element hydride properties* 293
 124. H.A. Eick, *Lanthanide and actinide halides* 365
 125. R.G. Haire and L. Eyring, *Comparisons of the binary oxides* 413
 126. S.A. Kinkad, K.D. Abney and T.A. O'Donnell, *f-element speciation in strongly acidic media: lanthanide and mid-actinide metals, oxides, fluorides and oxide fluorides in superacids* 507
 127. E.N. Rizkalla and G.R. Choppin, *Lanthanides and actinides hydration and hydrolysis* 529
 128. G.R. Choppin and E.N. Rizkalla, *Solution chemistry of actinides and lanthanides* 559
 129. J.R. Duffield, D.M. Taylor and D.R. Williams, *The biochemistry of the f-elements* 591
 Author index 623
 Subject index 659

VOLUME 19: Lanthanides/Actinides: Physics – II

1994; ISBN 0-444-82015-9

130. E. Holland-Moritz and G.H. Lander, *Neutron inelastic scattering from actinides and anomalous lanthanides* 1
131. G. Aeppli and C. Broholm, *Magnetic correlations in heavy-fermion systems: neutron scattering from single crystals* 123
132. P. Wachter, *Intermediate valence and heavy fermions* 177
133. J.D. Thompson and J.M. Lawrence, *High pressure studies – Physical properties of anomalous Ce, Yb and U compounds* 383
134. C. Colinet and A. Pasturel, *Thermodynamic properties of metallic systems* 479
Author index 649
Subject index 693

VOLUME 20

1995; ISBN 0-444-82014-0

135. Y. Ōnuki and A. Hasegawa, *Fermi surfaces of intermetallic compounds* 1
136. M. Gasgnier, *The intricate world of rare earth thin films: metals, alloys, intermetallics, chemical compounds, . . .* 105
137. P. Vajda, *Hydrogen in rare-earth metals, including RH_{2+x} phases* 207
138. D. Gignoux and D. Schmitt, *Magnetic properties of intermetallic compounds* 293
Author index 425
Subject index 457

VOLUME 21

1995; ISBN 0-444-82178-3

139. R.G. Bautista, *Separation chemistry* 1
140. B.W. Hinton, *Corrosion prevention and control* 29
141. N.E. Ryan, *High-temperature corrosion protection* 93
142. T. Sakai, M. Matsuoka and C. Iwakura, *Rare earth intermetallics for metal–hydrogen batteries* 133
143. G.-y. Adachi and N. Imanaka, *Chemical sensors* 179
144. D. Garcia and M. Faucher, *Crystal field in non-metallic (rare earth) compounds* 263
145. J.-C.G. Bünzli and A. Milicic-Tang, *Solvation and anion interaction in organic solvents* 305
146. V. Bhagavathy, T. Prasada Rao and A.D. Damodaran, *Trace determination of lanthanides in high-purity rare-earth oxides* 367
Author index 385
Subject index 411

VOLUME 22

1996; ISBN 0-444-82288-7

147. C.P. Flynn and M.B. Salamon, *Synthesis and properties of single-crystal nanostructures* 1
148. Z.S. Shan and D.J. Sellmyer, *Nanoscale rare earth–transition metal multilayers: magnetic structure and properties* 81
149. W. Suski, *The $ThMn_{12}$ -type compounds of rare earths and actinides: structure, magnetic and related properties* 143
150. L.K. Aminov, B.Z. Malkin and M.A. Teplov, *Magnetic properties of nonmetallic lanthanide compounds* 295
151. F. Auzel, *Coherent emission in rare-earth materials* 507
152. M. Dolg and H. Stoll, *Electronic structure calculations for molecules containing lanthanide atoms* 607
Author index 731
Subject index 777

VOLUME 23

1996; ISBN 0-444-82507-X

153. J.H. Forsberg, *NMR studies of paramagnetic lanthanide complexes and shift reagents* 1
 154. N. Sabbatini, M. Guardigli and I. Manet, *Antenna effect in encapsulation complexes of lanthanide ions* 69
 155. C. Görller-Walrand and K. Binnemans, *Rationalization of crystal-field parametrization* 121
 156. Yu. Kuz'ma and S. Chykhrij, *Phosphides* 285
 157. S. Boghosian and G.N. Papatheodorou, *Halide vapors and vapor complexes* 435
 158. R.H. Byrne and E.R. Sholkovitz, *Marine chemistry and geochemistry of the lanthanides* 497
 Author index 595
 Subject index 631

VOLUME 24

1997; ISBN 0-444-82607-6

159. P.A. Dowben, D.N. McIlroy and Dongqi Li, *Surface magnetism of the lanthanides* 1
 160. P.G. McCormick, *Mechanical alloying and mechanically induced chemical reactions* 47
 161. A. Inoue, *Amorphous, quasicrystalline and nanocrystalline alloys in Al- and Mg-based systems* 83
 162. B. Elschner and A. Loidl, *Electron-spin resonance on localized magnetic moments in metals* 221
 163. N.H. Duc, *Intersublattice exchange coupling in the lanthanide–transition metal intermetallics* 339
 164. R.V. Skolozdra, *Stannides of rare-earth and transition metals* 399
 Author index 519
 Subject index 559

VOLUME 25

1998; ISBN 0-444-82871-0

165. H. Nagai, *Rare earths in steels* 1
 166. R. Marchand, *Ternary and higher order nitride materials* 51
 167. C. Görller-Walrand and K. Binnemans, *Spectral intensities of f - f transitions* 101
 168. G. Bombieri and G. Paolucci, *Organometallic π complexes of the f -elements* 265
 Author index 415
 Subject index 459

VOLUME 26

1999; ISBN 0-444-50815-1

169. D.F. McMorro, D. Gibbs and J. Bohr, *X-ray scattering studies of lanthanide magnetism* 1
 170. A.M. Tishin, Yu.I. Spichkin and J. Bohr, *Static and dynamic stresses* 87
 171. N.H. Duc and T. Goto, *Itinerant electron metamagnetism of Co sublattice in the lanthanide–cobalt intermetallics* 177
 172. A.J. Arko, P.S. Riseborough, A.B. Andrews, J.J. Joyce, A.N. Tahvildar-Zadeh and M. Jarrell, *Photoelectron spectroscopy in heavy fermion systems: Emphasis on single crystals* 265
 Author index 383
 Subject index 405

VOLUME 27

1999; ISBN 0-444-50342-0

173. P.S. Salamakha, O.L. Sologub and O.I. Bodak, *Ternary rare-earth–germanium systems* 1
 174. P.S. Salamakha, *Crystal structures and crystal chemistry of ternary rare-earth germanides* 225
 175. B. Ya. Kotur and E. Gratz, *Scandium alloy systems and intermetallics* 339
 Author index 535
 Subject index 553

VOLUME 28

2000; ISBN 0-444-50346-3

176. J.-P. Connerade and R.C. Karnatak, *Electronic excitation in atomic species* 1
 177. G. Meyer and M.S. Wickleder, *Simple and complex halides* 53
 178. R.V. Kumar and H. Iwahara, *Solid electrolytes* 131
 179. A. Halperin, *Activated thermoluminescence (TL) dosimeters and related radiation detectors* 187
 180. K.L. Nash and M.P. Jensen, *Analytical separations of the lanthanides: basic chemistry and methods* 311
 Author index 373
 Subject index 401

VOLUME 29: The role of rare earths in catalysis

2000; ISBN 0-444-50472-9

- P. Maestro, *Foreword* 1
 181. V. Paul-Boncour, L. Hilaire and A. Percheron-Guégan, *The metals and alloys in catalysis* 5
 182. H. Imamura, *The metals and alloys (prepared utilizing liquid ammonia solutions) in catalysis II* 45
 183. M.A. Ulla and E.A. Lombardo, *The mixed oxides* 75
 184. J. Kašpar, M. Graziani and P. Fornasiero, *Ceria-containing three-way catalysts* 159
 185. A. Corma and J.M. López Nieto, *The use of rare-earth-containing zeolite catalysts* 269
 186. S. Kobayashi, *Triflates* 315
 Author index 377
 Subject index 409

VOLUME 30: High-Temperature Superconductors – I

2000; ISBN 0-444-50528-8

187. M.B. Maple, *High-temperature superconductivity in layered cuprates: overview* 1
 188. B. Raveau, C. Michel and M. Hervieu, *Crystal chemistry of superconducting rare-earth cuprates* 31
 189. Y. Shiohara and E.A. Goodilin, *Single-crystal growth for science and technology* 67
 190. P. Karen and A. Kjekshus, *Phase diagrams and thermodynamic properties* 229
 191. B. Elschner and A. Löidl, *Electron paramagnetic resonance in cuprate superconductors and in parent compounds* 375
 192. A.A. Manuel, *Positron annihilation in high-temperature superconductors* 417
 193. W.E. Pickett and I.I. Mazin, *$R\text{Ba}_2\text{Cu}_3\text{O}_7$ compounds: electronic theory and physical properties* 453
 194. U. Staub and L. Soderholm, *Electronic 4f state splittings in cuprates* 491
 Author index 547
 Subject index 621

VOLUME 31: High-Temperature Superconductors – II

2001; ISBN 0-444-50719-1

195. E. Kaldis, *Oxygen nonstoichiometry and lattice effects in $\text{YBa}_2\text{Cu}_3\text{O}_x$. Phase transitions, structural distortions and phase separation* 1
 196. H.W. Weber, *Flux pinning* 187
 197. C.C. Almasan and M.B. Maple, *Magnetoresistance and Hall effect* 251
 198. T.E. Mason, *Neutron scattering studies of spin fluctuations in high-temperature superconductors* 281
 199. J.W. Lynn and S. Skanthakumar, *Neutron scattering studies of lanthanide magnetic ordering* 315
 200. P.M. Allenspach and M.B. Maple, *Heat capacity* 351
 201. M. Schabel and Z.-X. Shen, *Angle-resolved photoemission studies of untwinned yttrium barium copper oxide* 391
 202. D.N. Basov and T. Timusk, *Infrared properties of high- T_c superconductors: an experimental overview* 437
 203. S.L. Cooper, *Electronic and magnetic Raman scattering studies of the high- T_c cuprates* 509

204. H. Sugawara, T. Hasegawa and K. Kitazawa, *Characterization of cuprate superconductors using tunneling spectra and scanning tunneling microscopy* 563
 Author index 609
 Subject index 677

VOLUME 32

2001; ISBN 0-444-50762-0

205. N.H. Duc, *Giant magnetostriction in lanthanide–transition metal thin films* 1
 206. G.M. Kalvius, D.R. Noakes and O. Hartmann, *μ SR studies of rare-earth and actinide magnetic materials* 55
 207. Rainer Pöttgen, Dirk Johrendt and Dirk Kußmann, *Structure–property relations of ternary equiatomic YbTX intermetallics* 453
 208. Kurima Kobayashi and Satoshi Hirosawa, *Permanent magnets* 515
 209. I.G. Vasilyeva, *Polysulfides* 567
 210. Dennis K.P. Ng, Jianzhuang Jiang, Kuninobu Kasuga and Kenichi Machida, *Half-sandwich tetrapyrrole complexes of rare earths and actinides* 611
 Author index 655
 Subject index 733

VOLUME 33

2003; ISBN 0-444-51323-X

211. Brian C. Sales, *Filled skutterudites* 1
 212. Oksana L. Sologub and Petro S. Salamakha, *Rare earth – antimony systems* 35
 213. R.J.M. Konings and A. Kovács, *Thermodynamic properties of the lanthanide(III) halides* 147
 214. John B. Goodenough, *Rare earth – manganese perovskites* 249
 215. Claude Piguët and Carlos F.G.C. Geraldes, *Paramagnetic NMR lanthanide induced shifts for extracting solution structures* 353
 216. Isabelle Billard, *Lanthanide and actinide solution chemistry as studied by time-resolved emission spectroscopy* 465
 217. Thomas Tröster, *Optical studies of non-metallic compounds under pressure* 515
 Author index 591
 Subject index 637

VOLUME 34

2004; ISBN 0-444-51587-9

218. Yaroslav M. Kalychak, Vasyl' I. Zaremba, Rainer Pöttgen, Mar'yana Lukachuk and Rolf-Dieter Hoffman, *Rare earth–transition metal–indides* 1
 219. P. Thalmeier and G. Zwicknagl, *Unconventional superconductivity and magnetism in lanthanide and actinide intermetallic compounds* 135
 220. James P. Riehl and Gilles Muller, *Circularly polarized luminescence spectroscopy from lanthanide systems* 289
 221. Oliver Guillou and Carole Daignebonne, *Lanthanide-containing coordination polymers* 359
 222. Makoto Komiyama, *Cutting DNA and RNA* 405
 Author index 455
 Subject index 493

VOLUME 35

2006; ISBN 0-444-52028-7

223. Natsuko Sakai, Katsuhiko Yamaji, Teruhisa Horita, Yue Ping Xiong and Harumi Yokokawa, *Rare-earth materials for Solid Oxide Fuel Cells (SOFC)* 1

224. Mathias S. Wickleder, *Oxo-selenates of rare earth elements* 45
225. Koen Binnemans, *Rare-earth beta-diketonates* 107
226. Satoshi Shinoda, Hiroyuki Miyake and Hiroshi Tsukube, *Molecular recognition and sensing via rare earth complexes* 273
- Author index 337
- Subject index 377

INDEX OF CONTENTS OF VOLUMES 1–36

- 4*f* levels, thermodynamic aspects **10**, ch. 69, p. 361
4*f* state splittings in cuprates **30**, ch. 194, p. 491
- absorption spectra of ions in solution **3**, ch. 24,
p. 171; **18**, ch. 120, p. 150
actinide concept, origin of **18**, ch. 118, p. 1
activated phosphors **4**, ch. 34, p. 237
activated thermoluminescence **28**, ch. 179, p. 187
amorphous alloys **7**, ch. 52, p. 265
– Al- and Mg-based **24**, ch. 161, p. 83
– magnetic **2**, ch. 16, p. 259
anion interaction in organic solvents **21**, ch. 145,
p. 305
antimony alloy systems **33**, ch. 212, p. 35
atomic properties (free atom) **1**, ch. 1, p. 1
atomic theory **11**, ch. 74, p. 81
- beta-diketonates **35**, ch. 225, p. 107
Belousov–Zhabotinsky reactions **36**, ch. 229, p. 281
biochemistry **18**, ch. 129, p. 591
bioinorganic chemistry **4**, ch. 39, p. 515
biological systems **13**, ch. 92, p. 423
bismuth alloy systems **36**, ch. 227, p. 1
- carbides **15**, ch. 99, p. 61
catalysis **29**, foreword, p. 1
– ceria-containing three-way **29**, ch. 184, p. 159
– metals and alloys **29**, ch. 181, p. 5
– metals and alloys in liquid ammonia solutions **29**,
ch. 182, p. 45
– mixed oxides **29**, ch. 183, p. 75
– zeolites **29**, ch. 185, p. 269
cerimetry **36**, ch. 229, p. 281
cerium **1**, ch. 4, p. 337
cerium compounds
– low-temperature behavior **15**, ch. 98, p. 1
– tetravalent **36**, ch. 229, p. 281
cerium(IV)
– catalysts **36**, ch. 229, p. 281
– mediated reactions **36**, ch. 229, p. 281
– redox properties **36**, ch. 229, p. 281
chalcogenides, magnetic measurements on mono-
17, ch. 114, p. 301
chemical analysis by
– atomic emission with inductively coupled plasmas
13, ch. 91, p. 385
– mass spectrometry, *see* spectroscopy, mass
– neutron activation **4**, ch. 37F, p. 457
– optical absorption **4**, ch. 37D, p. 405
– optical atomic emission **4**, ch. 37D, p. 405
– polarography **4**, ch. 37A, p. 341; **8**, ch. 55, p. 163
– spectrophotometry **4**, ch. 37A, p. 341
– trace determination in high-purity oxides **21**,
ch. 146, p. 367
– X-ray excited optical luminescence **4**, ch. 37E,
p. 441
chemical sensors **21**, ch. 143, p. 179
chemical understanding and classification **11**,
ch. 75, p. 197
chirality sensing **35**, ch. 226, p. 273
coherent emission **22**, ch. 151, p. 507
cohesion, theory of **17**, ch. 112, p. 149
complexes **3**, ch. 25, p. 209
– antenna effect **23**, ch. 154, p. 69
– beta-diketonates **35**, ch. 225, p. 107
– half-sandwich tetrapyrrole **32**, ch. 210, p. 611
– macrocycles **15**, ch. 104, p. 443
– molecular recognition in **35**, ch. 226, p. 273
– organometallic π type **25**, ch. 168, p. 265
– sensing in **35**, ch. 226, p. 273
– with synthetic ionophores **9**, ch. 60, p. 321
coordination catalysis in stereospecific
polymerization **9**, ch. 61, p. 395
coordination in organic solvents **21**, ch. 145, p. 305
coordination polymers **34**, ch. 221, p. 359
corrosion prevention and control **21**, ch. 140, p. 29
corrosion protection **21**, ch. 141, p. 93
cosmochemistry **11**, ch. 79, p. 485
crystal chemistry
– of intermetallic compounds **2**, ch. 13, p. 1
– of ternary germanides **27**, ch. 174, p. 225
– of ternary systems with chalcogenides **13**, ch. 89,
p. 191
– of ternary systems with metallic elements **13**,
ch. 88, p. 1

- of ternary transition metal borides **6**, ch. 48, p. 113
- of ternary transition metal silicides **6**, ch. 48, p. 113
- of ThMn₁₂-type compounds **22**, ch. 149, p. 143
- crystal field **2**, ch. 17, p. 295
- in non-metallic compounds **21**, ch. 144, p. 263
- crystal field parametrization, rationalization of **23**, ch. 155, p. 121
- crystal structures, *see* crystal chemistry

- dedications
 - F.H. Spedding **11**, p. 1
 - LeRoy Eyring **36**, p. xi
 - Friedrich Hund **14**, p. ix
- diketonates, *see* beta-diketonates
- diffusion in metals **1**, ch. 12, p. 847
- divalent samarium in organic chemistry **6**, ch. 50, p. 525; **36**, ch. 230, p. 393
- divalent ytterbium derivatives in organic chemistry **6**, ch. 50, p. 525
- DNA, cutting of **34**, ch. 222, p. 405
- dynamical screening of core holes in intermetallic compounds **10**, ch. 63, p. 75

- elastic and mechanical properties of metals **1**, ch. 8, p. 591
- electron paramagnetic resonance (EPR) **2**, ch. 18, p. 387; **24**, ch. 162, p. 221
- in cuprate superconductors **30**, ch. 191, p. 375
- electronic excitation in atomic species **28**, ch. 176, p. 1
- electronic structure
 - calculations for molecules **22**, ch. 152, p. 607
 - of metals **1**, ch. 3, p. 233; **17**, ch. 110, p. 1
- electronic theory of cuprates **30**, ch. 193, p. 453
- electron–phonon interaction in intermetallic compounds **14**, ch. 96, p. 225
- electron spin resonance, *see* electron paramagnetic resonance
- emission spectra **10**, ch. 71, p. 453
- europium chalcogenides **2**, ch. 19, p. 507
- exchange coupling in transition metal intermetallics **24**, ch. 163, p. 339
- excited state phenomena in vitreous materials **9**, ch. 58, p. 1
- Eyring, L. **36**, dedication, p. xi

- f*-electron hybridization in intermetallic compounds **10**, ch. 63, p. 75
- f*-element speciation in strongly acidic media (superacids) **18**, ch. 126, p. 507

- Fermi surfaces
 - of intermetallic compounds **20**, ch. 135, p. 1
 - of metals **17**, ch. 110, p. 1
- fluorescence spectra of ions in solution **3**, ch. 24, p. 171
- fluoride glasses **15**, ch. 101, p. 287
- fluorides **5**, ch. 45, p. 387
- flux pinning in cuprates **31**, ch. 196, p. 187

- garnets **3**, ch. 29, p. 525
- geochemistry **3**, ch. 21, p. 1; **11**, ch. 79, p. 485; **23**, ch. 158, p. 497
- germanium, ternary systems **27**, ch. 173, p. 1

- halides **4**, ch. 32, p. 89; **18**, ch. 124, p. 365
 - metal-rich **15**, ch. 100, p. 191
 - simple and complex **28**, ch. 177, p. 53
 - thermodynamic properties **33**, ch. 213 p. 147
 - vapors and vapor complexes **23**, ch. 157, p. 435
- Hall effect in cuprates **31**, ch. 197, p. 251
- heat capacity
 - of cuprates **31**, ch. 200, p. 351
 - of metals **1**, ch. 5, p. 379
- heavy fermions **14**, ch. 97, p. 343; **16**, ch. 105, p. 1; **19**, ch. 132, p. 177
 - phenomenological approach **17**, ch. 111, p. 87
 - photoelectron spectroscopy **26**, ch. 172, p. 265
- high pressure studies **1**, ch. 9, p. 707
 - anomalous Ce, Yb and U compounds **19**, ch. 133, p. 383
 - optical studies of non-metallic compounds **33**, ch. 217, p. 515
 - structural aspects **17**, ch. 113, p. 245
- high-temperature superconductors **30**; **31**
- history of the discovery and separation **11**, ch. 73, p. 33
- Hund, F. **14**, dedication, p. ix
- hydration **15**, ch. 103, p. 393; **18**, ch. 127, p. 529
- hydrides **3**, ch. 26, p. 299; **18**, ch. 123, p. 293
 - switchable films **36**, ch. 228, p. 83
- hydrogen absorption in intermetallic compounds **6**, ch. 47, p. 1
- hydrogen in metals, including RH_{2+x} phases **20**, ch. 137, p. 207
- hydrolysis **15**, ch. 103, p. 393; **18**, ch. 127, p. 529
- hyperfine interactions **11**, ch. 77, p. 323

- inelastic electron scattering **10**, ch. 72, p. 547
- infrared properties of cuprates **31**, ch. 202, p. 437
- inorganic complex compounds **8**, ch. 56 p. 203; **9**, ch. 59, p. 91

- intermediate valence **19**, ch. 132, p. 177
- itinerant electron metamagnetism in cobalt intermetallics **26**, ch. 171, p. 177
- kinetics of complexation in aqueous solutions **15**, ch. 102, p. 347
- Kondo effect **1**, ch. 11, p. 797
- lanthanide-induced shifts **4**, ch. 38, p. 483; **23**, ch. 153, p. 1; **33**, ch. 215, p. 353
- laser spectroscopy **12**, ch. 87, p. 433
- lasers **4**, ch. 35, p. 275
- light scattering in intermetallic compounds **14**, ch. 95, p. 163
- liquid metals and alloys **12**, ch. 85, p. 357
- LIS, *see* lanthanide-induced shifts
- luminescence studies of ions **18**, ch. 120, p. 150
- luminescence spectra of ions in solution **3**, ch. 24, p. 171
- μ SR studies of magnetic materials **32**, ch. 206, p. 55
- magnetic and transport properties of metals **1**, ch. 6, p. 411
- magnetic correlations in heavy-fermion systems **19**, ch. 131, p. 23
- magnetic properties
- of intermetallic compounds **2**, ch. 14, p. 55; **20**, ch. 138, p. 293
 - of nonmetallic compounds **22**, ch. 150, p. 295
 - of ternary RT₂X₂ type intermetallic compounds **12**, ch. 83, p. 133
 - of ThMn₁₂-type compounds **22**, ch. 149, p. 143
- magnetic structures **1**, ch. 7, p. 489
- magnetism **34**, ch. 219, p. 135
- exotic phenomena **11**, ch. 76, p. 293
 - surface **24**, ch. 159, p. 1
- magnetoresistance in cuprates **31**, ch. 197, p. 251
- magnetostriction
- RFe₂ **2**, ch. 15, p. 231
 - transition metal thin films **32**, ch. 205, p. 1
- marine chemistry **23**, ch. 158, p. 497
- mechanical alloying **24**, ch. 160, p. 47
- mechanically induced chemical reactions **24**, ch. 160, p. 47
- metal-hydrogen batteries **21**, ch. 142, p. 133
- mineralogy **3**, ch. 21, p. 1
- minerals, crystal structures **16**, ch. 108, p. 249
- mixed valence systems
- bremsstrahlung isochromat spectroscopy **10**, ch. 70, p. 425
 - calculation of 4*f* excitation energies **10**, ch. 68, p. 321
 - many-body formulation of spectra **10**, ch. 64, p. 103
- molecular recognition **35**, ch. 226, p. 273
- molybdates (VI) **3**, ch. 30, p. 609
- Mössbauer effect **2**, ch. 18, p. 387
- of intermetallic compounds **17**, ch. 116, p. 539
- nanostructures
- Al- and Mg-based systems **24**, ch. 161, p. 83
 - properties **22**, ch. 147, p. 1
 - synthesis **22**, ch. 147, p. 1
 - transition metal multilayers **22**, ch. 148, p. 81
- neutron scattering
- elastic **17**, ch. 117, p. 635
 - inelastic **1**, ch. 7, p. 489
 - intermultiple transitions **14**, ch. 93, p. 1
 - inelastic of anomalous lanthanides **19**, ch. 130, p. 1
 - in heavy-fermion systems **19**, ch. 131, p. 123
 - of magnetic ordering in cuprates **31**, ch. 199, p. 315
 - of spin fluctuations in cuprates **31**, ch. 198, p. 281
- nitride materials, ternary and higher order **24**, ch. 166, p. 51
- NMR **2**, ch. 18, p. 387
- in intermetallic compounds **14**, ch. 94, p. 63
 - lanthanide induced shifts for extracting solution structures **33**, ch. 215, p. 353
 - of complexes **23**, ch. 153, p. 1
 - of paramagnetic complexes **4**, ch. 38, p. 483
 - solution structure by paramagnetic NMR analysis **33**, ch. 215, p. 353
- nonradiative processes in crystals **4**, ch. 36, p. 317
- nuclear magnetic resonance, *see* NMR
- organic synthesis **8**, ch. 57, p. 335
- organometallic compounds **7**, ch. 53, p. 446
- oxidation–reduction properties **18**, ch. 122, p. 239
- oxides
- binary **3**, ch. 27, p. 337; **18**, ch. 125, p. 413
 - mixed **3**, ch. 28, p. 401
 - sesqui, defects in **5**, ch. 44, p. 321
 - sesqui, phase transformation in **5**, ch. 44, p. 321
 - ternary systems, R₂O₃–M₂O₃–M'O **13**, ch. 90, p. 283
- oxo-selenates **35**, ch. 224, p. 45
- oxygen nonstoichiometry and lattice effect in YBa₂Cu₃O_x **31**, ch. 195, p. 1

- permanent magnets **32**, ch. 208, p. 515
 perovskites **3**, ch. 29, p. 525
 – manganese **33**, ch. 214, p. 249
 phase equilibria
 – in cuprates **30**, ch. 190, p. 229
 – in ternary systems with boron **6**, ch. 49, p. 335
 – in ternary systems with chalcogenides **13**, ch. 89, p. 191
 – in ternary systems with metallic elements **13**, ch. 88, p. 1
 – in ternary systems with silicon **7**, ch. 51, p. 1
 – intra rare earth binary alloys **8**, ch. 54, p. 1
 phase transitions, structural distortions and phase separation in $\text{YBa}_2\text{Cu}_3\text{O}_x$ **31**, ch. 195, p. 1
 phosphides **23**, ch. 156, p. 285
 photoemission
 – angle-resolved studies of untwinned $\text{YBa}_2\text{Cu}_3\text{O}_x$ **31**, ch. 201, p. 391
 – in chalcogenides **10**, ch. 67, p. 301
 – inverse spectra, local density supercell theory **10**, ch. 65, p. 165
 – of Ce and its compounds **10**, ch. 66, p. 231
 – spectra, local density supercell theory **10**, ch. 65, p. 165
 physical metallurgy **11**, ch. 78, p. 409
 physical properties
 – of cuprates **30**, ch. 193, p. 453
 – of metals **1**, ch. 2, p. 173
 – of $\text{R}_2\text{Fe}_{14}\text{B}$ -based alloys **12**, ch. 82, p. 71
 pnictides **4**, ch. 33, p. 153
 – magnetic measurements on mono- **17**, ch. 114, p. 301
 positron annihilation in high-temperature superconductors **30**, ch. 192, p. 417
 preparation and purification of metals **1**, ch. 2, p. 173
 pyrochlores **16**, ch. 107, p. 225

 quasicrystalline, Al- and Mg-based systems **24**, ch. 161, p. 83

 Raman scattering of cuprates **31**, ch. 203, p. 509
 redox reactions
 – in aqueous solutions **15**, ch. 102, p. 347
 – Ce(IV)/Ce(III) **36**, ch. 229, p. 281
 relativistic effects and electronic structure **18**, ch. 119, p. 29
 RNA, cutting of **34**, ch. 222, p. 405; **36**, ch. 229, p. 392

 samarium (II) reductants **36**, ch. 230, p. 393

 scandium alloy systems and intermetallics **27**, ch. 175, p. 339
 scanning tunneling microscopy of cuprates **31**, ch. 204, p. 563
 selenates **35**, ch. 224, p. 45
 selenides **4**, ch. 31, p. 1
 selenites **35**, ch. 224, p. 45
 separation chemistry **3**, ch. 22, p. 81; **18**, ch. 121, p. 197; **21**, ch. 139, p. 1
 – analytical, basic chemistry and methods **28**, ch. 180, p. 311
 shift reagents **4**, ch. 38, p. 483; **23**, ch. 153, p. 1; **33**, ch. 215, p. 353; **35**, ch. 225, p. 107
 single crystals
 – growth from molten metal fluxes **12**, ch. 81, p. 53
 – growth of cuprates **30**, ch. 189, p. 67
 – growth of metals and intermetallic compounds **12**, ch. 80, p. 1
 skutterudites, filled **33**, ch. 211, p. 1
 solid electrolytes **28**, ch. 178, p. 131; **35**, ch. 223, p. 1
 solid oxide fuel cells (SOFC) **35**, ch. 223, p. 1
 solution chemistry **15**, ch. 103, p. 393; **18**, ch. 127, p. 529; **18**, ch. 128, p. 559; **21**, ch. 145, 305;
 solvation in organic solvents **21**, ch. 145, p. 305
 spectral intensities of $f-f$ transitions **24**, ch. 167, p. 101
 spectroscopic properties in transparent crystals **5**, ch. 46, p. 461
 spectroscopy
 – appearance potential **16**, ch. 109, p. 519
 – bremsstrahlung isochromat **10**, ch. 70, p. 425
 – circularly polarized luminescence **34**, ch. 220, p. 289
 – high-energy **10**, ch. 62, p. 1
 – magnetic resonance **11**, ch. 77, p. 323
 – mass
 – – spark source matrices **4**, ch. 37C, p. 377
 – – spark source trace element analysis **4**, ch. 37B, p. 359
 – – stable-isotope dilution analysis **4**, ch. 37G, p. 471
 – – with inductively coupled plasmas analysis **13**, ch. 91, p. 385
 – optical **11**, ch. 74, p. 81
 – photoelectron in heavy fermion systems **26**, ch. 172, p. 265
 – time-resolved emission in solution chemistry **33**, ch. 216, p. 465
 Spedding, F.H. **11**, prologue, p. 1
 spin glasses **12**, ch. 84, p. 213

- stannides, transition metal ternary systems **24**,
ch. 164, p. 399
- steels **25**, ch. 165, p. 1
- stresses, static and dynamic **26**, ch. 170, p. 87
- sulfides **4**, ch. 31, p. 1
- poly **32**, ch. 209, 567
- superconductivity **1**, ch. 10, p. 749; **30**; **31**; **34**,
ch. 219, p. 135
- crystal chemistry of cuprates **30**, ch. 188, p. 31
- in metals **17**, ch. 110, p. 1
- high-temperature layered cuprates: overview **30**,
ch. 187, p. 1
- surfaces
- adsorption on **5**, ch. 43, p. 217
- catalysis on **5**, ch. 43, p. 217
- switchable metal hydride films **36**, ch. 228, p. 83
- systematics, intra rare earth binary alloys **8**, ch. 54,
p. 1
- tellurides **4**, ch. 31, p. 1
- ternary equiatomic YbTX intermetallics **32**, ch. 207,
p. 453
- tetravalent cerium compounds **36**, ch. 229, p. 281
- theoretical chemistry **3**, ch. 23, p. 111
- thermal conductivity of compounds **16**, ch. 106,
p. 107
- thermochemical properties **18**, ch. 122, p. 239
- of cuprates **30**, ch. 190, p. 229
- of gaseous species **12**, ch. 86, p. 409
- of metallic systems **19**, ch. 134, p. 479
- thin films **5**, ch. 41, p. 1; **20**, ch. 136, p. 105
- switchable metal hydrides **36**, ch. 228, p. 83
- toxicity **4**, ch. 40, p. 553
- transition metal-indides **34**, ch. 218, p. 1
- transport properties of intermetallics **5**, ch. 42,
p. 117; **17**, ch. 115, p. 409
- triflates **29**, ch. 186, p. 315
- tunneling spectra of cuprates **31**, ch. 204, p. 563
- unconventional superconductivity and magnetism
34, ch. 219, p. 135
- valence fluctuations **2**, ch. 20, p. 575; **16**, ch. 105,
p. 1
- X-ray absorption spectra **10**, ch. 71, p. 453
- X-ray scattering **26**, ch. 169, p. 1

Chapter 227

BISMUTHIDES

Arthur MAR

Department of Chemistry, University of Alberta, Edmonton, Alberta, Canada T6G 2G2

E-mail: arthur.mar@ualberta.ca

Contents

Symbols and abbreviations	2	5.5.4. R_5Ni_2Bi	37
1. Introduction	3	5.5.5. Actinide compounds	38
2. Binary systems	3	5.5.6. Thin films	38
3. Ternary R -s-element-Bi systems	10	5.6. R -Pd-Bi	38
3.1. R -Bi-H	10	5.6.1. RPd_2Bi_2	40
3.2. R -Li-Bi	11	5.6.2. $RPdBi$	40
3.2.1. RLi_3Bi_2	11	5.6.3. RPd_2Bi	41
3.2.2. $RLiBi_2$	12	5.6.4. Properties of $RPdBi$ and RPd_2Bi	41
3.2.3. $RLiBi$	13	5.6.5. R_5Pd_2Bi	41
3.3. R -Mg-Bi	13	5.6.6. $R_8Pd_{24}Bi$	42
4. Ternary R -f-element-Bi systems	14	5.7. R -Pt-Bi	42
5. Ternary R -d-element-Bi systems	15	5.7.1. $R_3Pt_3Bi_4$	44
5.1. R -Mn-Bi	15	5.7.2. $RPtBi$	44
5.1.1. R_3MnBi_5	15	5.7.2.1. $YPtBi$	46
5.1.2. $R_{14}MnBi_{11}$	18	5.7.2.2. $LaPtBi$	46
5.1.3. R_6MnBi_2	19	5.7.2.3. $CePtBi$	46
5.1.4. Thin films	21	5.7.2.4. $PrPtBi$	46
5.2. R -Fe-Bi	21	5.7.2.5. $NdPtBi$	47
5.2.1. Phase diagrams	22	5.7.2.6. $SmPtBi$	47
5.2.2. R_6FeBi_2	22	5.7.2.7. $YbPtBi$	47
5.2.3. $R_6Fe_{13}Bi$	22	5.7.3. R_5Pt_2Bi	48
5.2.4. Thin films	23	5.8. R -Cu-Bi	48
5.3. R -Co-Bi	24	5.8.1. $RCu_{1-x}Bi_2$	48
5.3.1. R_5CoBi_2	24	5.8.2. $RCuBi$	50
5.3.2. R_6CoBi_2	25	5.8.3. R_5CuBi_3	51
5.3.3. $R_6Co_{13}Bi$	26	5.8.4. $R_5Cu_{1-x}Bi_{2+x}$	52
5.3.4. $R_{12}Co_5Bi$	26	5.8.5. Actinide compounds	52
5.3.5. Other data	28	5.9. R -Ag-Bi	52
5.4. R -Rh-Bi	28	5.10. R -Zn-Bi	53
5.5. R -Ni-Bi	30	5.10.1. R_6ZnBi_{14}	53
5.5.1. Phase diagrams	30	5.10.2. $R_9Zn_4Bi_9$	54
5.5.2. $RNi_{1+x}Bi_2 \dots RNi-$ $Bi_2 \dots RNi_{1-x}Bi_2$	34	6. Ternary R -p-element-Bi systems	56
5.5.3. $RNiBi$	36	6.1. R -triel-Bi	56
		6.1.1. R -Al-Bi	57

6.1.2. <i>R</i> -Ga-Bi	57	6.5.1. Phase diagrams	69
6.1.3. <i>R</i> -In-Bi	58	6.5.1.1. Ce-Bi-Se	69
6.2. <i>R</i> -tetrel-Bi	58	6.5.1.2. Sm-Bi-Se	70
6.2.1. <i>R</i> -Si-Bi	58	6.5.1.3. Tm-Bi-Se	70
6.2.2. <i>R</i> -Ge-Bi	59	6.5.2. Eu-Bi-Se	70
6.2.3. <i>R</i> -Sn-Bi and <i>R</i> -Pb-Bi	59	6.5.3. Gd-Bi-Se	71
6.3. <i>R</i> -Pn-Bi	60	6.6. <i>R</i> -Bi-Te	71
6.3.1. <i>R</i> -Sb-Bi	60	6.6.1. Phase diagrams	71
6.3.2. Actinide compounds	61	6.6.2. <i>RBi</i> ₂ Te ₄ and <i>RBi</i> ₄ Te ₇	73
6.3.2.1. Actinide-Sb-Bi	61	6.6.3. <i>RBi</i> Te ₃	73
6.3.2.2. Actinide-N-Bi	61	6.6.4. <i>R</i> ₄ Bi ₂ Te	73
6.4. <i>R</i> -Bi-S	62	6.6.5. Sc ₆ Bi _{1.68} Te _{0.80}	73
6.4.1. Phase diagrams	64	6.6.6. Other data	74
6.4.2. Ce _{1.25} Bi _{3.78} S ₈	64	6.6.6.1. CeBi _{1-x} Te _x	74
6.4.3. <i>RBi</i> ₂ S ₄ and related Eu-Bi-S phases	64	6.6.6.2. (<i>R</i> _x Bi _{1-x}) ₂ Te ₃	74
6.4.4. <i>RBi</i> S ₃	68	6.7. <i>R</i> -Bi-halogen	74
6.4.5. <i>R</i> ₄ Bi ₂ S ₉	68	7. Conclusion	75
6.4.6. Other phases	69	Acknowledgements	77
6.5. <i>R</i> -Bi-Se	69	References	77

Symbols and abbreviations

<i>a, b, c, α, β, γ</i>	unit cell parameters	XPS	X-ray photoelectron spectroscopy
CEF	crystalline electric field	<i>Z</i>	number of f.u. per unit cell
CN	coordination number	<i>ZT</i>	thermoelectric figure of merit
DFT	density functional theory	<i>χ</i>	magnetic susceptibility
EPR	electron paramagnetic resonance	<i>χ</i> ₀	temperature independent magnetic susceptibility
f.u.	formula unit	<i>γ</i>	electronic specific heat coefficient
LMTO	linear muffin-tin orbital	<i>μ</i> _B	Bohr magneton
<i>M</i>	transition metal, generally	<i>μ</i> _{eff}	effective magnetic moment
NQR	nuclear quadrupole resonance	<i>μ</i> _{RS}	magnetic moment calculated from Russell-Saunders coupling scheme
Pn	pnictogen (group 15 element)	<i>μ</i> _{SR}	muon spin resonance
<i>R</i>	rare earth metal	<i>θ</i> _p	paramagnetic Curie temperature
RKKY	Ruderman-Kittel-Kasuya-Yosida	<i>ρ</i> _{#K}	electrical resistivity at <i>T</i> = # K
SEM	scanning electron microscopy	<i>∞</i> ¹ []	one-dimensional chain
<i>T</i> _C	transition temperature (superconductor) or Curie temperature (ferromagnet)	<i>∞</i> ² []	two-dimensional layer
<i>T</i> _N	Néel temperature		
tetrel	group 14 element		
triel	group 13 element		
<i>X</i>	p-element, generally		

1. Introduction

Compared to other rare earth – pnictogen systems, which have been previously reviewed in other chapters of this *Handbook* [pnictides (Hulliger, 1979a); nitrides (Marchand, 1998); phosphides (Kuz'ma and Chykhrij, 1996); antimonides (Sologub and Salamakha, 2003)], understanding of rare earth – bismuth systems is still relatively limited. This chapter reviews known rare earth – bismuth phases and focuses on compositional and structural data, accompanied by brief descriptions of physical property data, where available. The presentation of crystallographic data (e.g., positional parameters) has been standardized according to rules formulated by Parthé and Gelato (1984) through use of the program STRUCTURE TIDY (Gelato and Parthé, 1987). Section 2 summarizes data on binary rare earth – bismuth phases. Sections 4–6 survey ternary rare earth – bismuth phases, organized according to the third component (M) in R – M –Bi systems, as differences in bonding character are more clearly emphasized in this manner. Where appropriate, ternary actinide – bismuth phases are also included.

For Bi-poor phases, the standard synthetic procedure of arc melting mixtures of the elements followed by annealing has been commonly applied, despite the ease of vaporization of Bi. For instance, R_6MBi_2 ($M = \text{Mn, Fe, Co}$), R_5M_2Bi ($M = \text{Ni, Pd, Pt}$), and $R_{12}Co_5Bi$ can be prepared through this route, with a moderate excess of Bi added to compensate for evaporative losses. For Bi-rich phases, this becomes less of a viable method, although compounds such as $RRhBi$ and $NdNi_{1-x}Bi_2$ have been prepared accordingly with the addition of as much as a 10 wt.% excess of Bi during arc melting. In the presence of highly active metals, reaction within a metal container (Nb, Ta) jacketed by silica tubing is prudent. Growth of crystals generally proceeds through solid-state reactions or through cooling of the melt, and only in rare cases has use of a Bi flux been successful (e.g., $RAgBi_2$, $R_3Pt_3Bi_4$). For congruently melting compounds, large crystals have been prepared via the Bridgman method (e.g., $CeRhBi$).

As expected from the trends on proceeding down the periodic table, the large majority of rare earth – bismuth phases can be considered true intermetallic compounds, given the smaller difference in electronegativity between rare earth elements (1.1–1.3) and bismuth (1.9), compared to rare earth phosphides, arsenides, or even antimonides. There are analogies with antimonides, as seen in compounds such as $R_{14}MnPn_{11}$ ($Ca_{14}AlSb_{11}$ -type) or $RNi_{1-x}Pn_2$ (defect $HfCuSi_2$ -type), but a greater number of these bismuthides adopt dense structures with efficient packing arrangements, characteristic of intermetallic compounds. Examples of bismuthides whose structure can be understood through a Zintl formalism are considerably rarer than in the antimonides. In a few Bi-rich phases, such as Ce_3MnBi_5 and $LaGaBi_2$, the Bi atoms are arranged in homoatomic bonding networks that are reminiscent of similar patterns found in antimonides.

2. Binary systems

Binary rare earth bismuth systems remain incompletely investigated. In two important reviews, the structures of individual phases were assessed (Yoshihara et al., 1975) and the

phase diagrams for most rare earth binary systems were surveyed (Abdusalyamova et al., 1996). References to the earlier literature, including the original phase diagrams, may be found in these relatively accessible reviews. Additional investigations of phase diagrams not cited in Abdusalyamova et al. (1996) include Gd–Bi (Abulkhaev, 1993a), Dy–Bi (Abulkhaev, 1992a), Ho–Bi (Abulkhaev, 1993b), Er–Bi (Abulkhaev, 1992b; Abdusalyamova and Rachmatov, 2002), Yb–Bi (Borzzone et al., 1995), and Lu–Bi (Abulkhaev and Ganiev, 1995). A recent report on the thermodynamic properties of Ho–Bi phases contains references to similar previous studies on other R –Bi systems (Parodi et al., 2003). Table 1 summarizes the extent of known phases and table 2 lists crystallographic data. Although two modifications of $R_5\text{Bi}_3$ apparently exist (a hexagonal Mn_5Si_3 -type for early R and an orthorhombic Y_5Bi_3 -type for later R , with Gd and Tb capable of adopting both forms), it has been speculated that the latter should really be designated as $R_{5+x}\text{Bi}_3$ with additional R atoms entering vacant sites in a host Y_5Bi_3 -type structure (Yoshihara et al., 1975; Wang et al., 1976).

The rare earth dibismuthides $R\text{Bi}_2$ ($R = \text{La, Ce, Pr, Nd, Sm}$) deserve special mention. Although they have been reported previously at various times, these Bi-rich phases tend to form soft plate-like crystals and their poor crystallinity has so far precluded structure determination (Yoshihara et al., 1975; Nomura et al., 1977; Sadigov et al., 1985; Petrovic et al., 2002). Attempts at indexing their X-ray diffraction patterns were initially based on a triclinic cell (Yoshihara et al., 1975) and later on an orthorhombic cell (Nomura et al., 1977). In the Gd–Bi phase diagram, GdBi_2 has been proposed to form via a peritectic reaction at 910°C (Abulkhaev, 1993a), but its existence has been questioned (Petrovic et al., 2002). Resistivity, magnetization, and heat capacity measurements have been made on $R\text{Bi}_2$ crystals, which were shown to display high anisotropy (Petrovic et al., 2002).

More recent structure determinations of binary rare earth bismuth compounds are scarce. Eu_4Bi_3 was prepared in quantitative yield in a Ta (but not Nb) container and its structure (anti- Th_3P_4 -type) was determined from single-crystal data (Wang et al., 1996). Physical property measurements were consistent with divalent Eu and revealed antiferromagnetic ordering at 18 K. From powder X-ray diffraction data, $\text{Eu}_{16}\text{Bi}_{11}$ and $\text{Yb}_{16}\text{Bi}_{11}$ were found to be isostructural to the Zintl phase $\text{Ca}_{16}\text{Sb}_{11}$, adopting a complex tetragonal structure built up of W_5Si_3 -type slabs (Leon-Escamilla et al., 1997).

Electrical and magnetic measurements were made on the series of orthorhombic (Y_5Bi_3 -type) $R_5\text{Bi}_3$ compounds ($R = \text{Gd, Tb, Dy, Ho, Er}$) and on Tb_4Bi_3 , which were prepared by induction melting (Drzyzga and Szade, 2001). Atomic positions were obtained from Rietveld refinement of powder X-ray diffraction data. These compounds show unusual magnetic properties suggestive of complex magnetic ordering. Photoelectron spectroscopy and band structure calculations were also performed on these compounds (Drzyzga et al., 2003). From SEM images, the presence of metallic Bi inclusions was observed in the intergrain boundaries in samples of these compounds, which may explain why X-ray powder patterns of binary rare earth bismuth compounds often show broad peaks attributable to Bi.

Table 1
Binary rare earth bismuthides

Compound	Structure type	Sc	Y	La	Ce	Pr	Nd	Sm	Eu	Gd	Tb	Dy	Ho	Er	Tm	Yb ^c	Lu
<i>R</i> Bi ₂	unknown			+	+	+	+	+									
<i>R</i> Bi	NaCl	+	+	+	+ ^a	+	+	+		+	+ ^b	+	+	+	+		+
<i>R</i> ₄ Bi ₃	anti-Th ₃ P ₄			+	+	+	+	+	+	+	+						
<i>R</i> ₁₆ Bi ₁₁	Ca ₁₆ Sb ₁₁								+							+	
<i>R</i> ₅ Bi ₃	Mn ₅ Si ₃			+	+	+	+	+		+	+						
<i>R</i> ₅ Bi ₃	Y ₅ Bi ₃		+							+	+	+	+	+	+		+
<i>R</i> ₂ Bi	La ₂ Sb			+	+	+	+	+									

^aUndergoes high-pressure transformations to CuTi-type and CsCl-type structures (Léger et al., 1985).

^bUndergoes a lattice distortion below 17 K to a HgIn-type modification (Hulliger and Stucki, 1978).

^cAlso YbBi₂ (ZrSi₂-type), Yb₅Bi₂ (unknown structure), and Yb₅Bi₄ (unknown structure) (Maksudova et al., 1985).

Table 2
Crystallographic data for binary rare earth bismuthides

Compound	Structure type	Pearson symbol	Space group	a (Å)	b (Å)	c (Å)	Reference
ScBi	NaCl	$cF8$	$Fm\bar{3}m$	5.954(6)			(Zhuravlev and Smirnova, 1962)
YBi	NaCl	$cF8$	$Fm\bar{3}m$	6.2597(3)			(Schmidt et al., 1969)
YBi	NaCl	$cF8$	$Fm\bar{3}m$	6.2609(2)			(Yoshihara et al., 1975)
Y ₅ Bi ₃	Y ₅ Bi ₃	$oP32$	$Pnma$	8.19	9.43	11.98	(Schmidt et al., 1969)
Y ₅ Bi ₃	Y ₅ Bi ₃	$oP32$	$Pnma$	8.1895(4)	9.4202(4)	11.9753(6)	(Yoshihara et al., 1975)
Y ₅ Bi ₃	Y ₅ Bi ₃	$oP32$	$Pnma$	8.179(1)	9.401(1)	11.957(1)	(Wang et al., 1976)
LaBi ₂	unknown	aP^*		6.575(2)	13.140(5)	11.976(5)	(Yoshihara et al., 1975)
LaBi ₂	unknown	$oP12$		4.737(2)	17.51(1)	4.564(2)	(Nomura et al., 1977)
LaBi	NaCl	$cF8$	$Fm\bar{3}m$	6.5797(4)			(Yoshihara et al., 1975)
LaBi	NaCl	$cF8$	$Fm\bar{3}m$	6.577(1)			(Nomura et al., 1977)
La ₄ Bi ₃	anti-Th ₃ P ₄	$cI28$	$I\bar{4}3d$	9.786(1)			(Hohnke and Parthé, 1966)
La ₄ Bi ₃	anti-Th ₃ P ₄	$cI28$	$I\bar{4}3d$	9.759			(Gambino, 1967)
La ₄ Bi ₃	anti-Th ₃ P ₄	$cI28$	$I\bar{4}3d$	9.7868(3)			(Yoshihara et al., 1975)
La ₄ Bi ₃	anti-Th ₃ P ₄	$cI28$	$I\bar{4}3d$	9.790(2)			(Hulliger and Ott, 1977)
La ₄ Bi ₃	anti-Th ₃ P ₄	$cI28$	$I\bar{4}3d$	9.774(1)			(Nomura et al., 1977)
La ₅ Bi ₃	Mn ₅ Si ₃	$hP16$	$P6_3/mcm$	9.6585(7)		6.6970(5)	(Yoshihara et al., 1975)
La ₅ Bi ₃	Mn ₅ Si ₃	$hP16$	$P6_3/mcm$	9.614(2)		6.694(3)	(Nomura et al., 1977)
La ₂ Bi	La ₂ Sb	$tI12$	$I4/mmm$	4.6737(4)		18.3952(4)	(Yoshihara et al., 1975)
La ₂ Bi	La ₂ Sb	$tI12$	$I4/mmm$	4.674(1)		18.390(4)	(Nomura et al., 1977)
CeBi ₂	unknown	aP^*		6.528(2)	13.056(5)	11.852(5)	(Yoshihara et al., 1975)
CeBi	NaCl	$cF8$	$Fm\bar{3}m$	6.5055(2)			(Yoshihara et al., 1975)
CeBi	NaCl	$cF8$	$Fm\bar{3}m$	6.500			(Rossat-Mignod et al., 1983)

continued on next page

Table 2, *continued*

Compound	Structure type	Pearson symbol	Space group	<i>a</i> (Å)	<i>b</i> (Å)	<i>c</i> (Å)	Reference
CeBi	CuTi	<i>tP2</i>	<i>P4/mmm</i>	3.993(3)		3.35(1)	(Léger et al., 1985)
CeBi	CsCl	<i>cP2</i>	<i>Pm$\bar{3}m$</i>	3.739(3)			(Léger et al., 1985)
Ce ₄ Bi ₃	anti-Th ₃ P ₄	<i>cI28</i>	<i>I$\bar{4}3d$</i>	9.672(1)			(Hohnke and Parthé, 1966)
Ce ₄ Bi ₃	anti-Th ₃ P ₄	<i>cI28</i>	<i>I$\bar{4}3d$</i>	9.64			(Gambino, 1967)
Ce ₄ Bi ₃	anti-Th ₃ P ₄	<i>cI28</i>	<i>I$\bar{4}3d$</i>	9.6736(2)			(Yoshihara et al., 1975)
Ce ₄ Bi ₃	anti-Th ₃ P ₄	<i>cI28</i>	<i>I$\bar{4}3d$</i>	9.672			(Alonso et al., 1992)
Ce ₅ Bi ₃	Mn ₅ Si ₃	<i>hP16</i>	<i>P6₃/mcm</i>	9.5313(4)		6.5871(3)	(Yoshihara et al., 1975)
Ce ₂ Bi	La ₂ Sb	<i>tI12</i>	<i>I4/mmm</i>	4.5911(2)		18.1539(7)	(Yoshihara et al., 1975)
PrBi ₂	unknown	<i>aP*</i>		6.510(2)	13.017(5)	11.822(5)	(Yoshihara et al., 1975)
				$\alpha = 91.48(1)$	$\beta = 102.92(2)$	$\gamma = 92.30(1)$	
PrBi	NaCl	<i>cF8</i>	<i>Fm$\bar{3}m$</i>	6.461			(Turberfield et al., 1971)
PrBi	NaCl	<i>cF8</i>	<i>Fm$\bar{3}m$</i>	6.4631(2)			(Yoshihara et al., 1975)
Pr ₄ Bi ₃	anti-Th ₃ P ₄	<i>cI28</i>	<i>I$\bar{4}3d$</i>	9.611(3)			(Hohnke and Parthé, 1966)
Pr ₄ Bi ₃	anti-Th ₃ P ₄	<i>cI28</i>	<i>I$\bar{4}3d$</i>	9.60			(Gambino, 1967)
Pr ₄ Bi ₃	anti-Th ₃ P ₄	<i>cI28</i>	<i>I$\bar{4}3d$</i>	9.6109(2)			(Yoshihara et al., 1975)
Pr ₅ Bi ₃	Mn ₅ Si ₃	<i>hP16</i>	<i>P6₃/mcm</i>	9.4494(4)		6.5553(3)	(Yoshihara et al., 1975)
Pr ₂ Bi	La ₂ Sb	<i>tI12</i>	<i>I4/mmm</i>	4.5872(6)		18.011(2)	(Yoshihara et al., 1975)
NdBi ₂	unknown	<i>aP*</i>		6.468(2)	12.980(5)	11.858(5)	(Yoshihara et al., 1975)
				$\alpha = 91.72(1)$	$\beta = 104.01(2)$	$\gamma = 92.36(1)$	
NdBi	NaCl	<i>cF8</i>	<i>Fm$\bar{3}m$</i>	6.4222(2)			(Yoshihara et al., 1975)
Nd ₄ Bi ₃	anti-Th ₃ P ₄	<i>cI28</i>	<i>I$\bar{4}3d$</i>	9.553(1)			(Hohnke and Parthé, 1966)
Nd ₄ Bi ₃	anti-Th ₃ P ₄	<i>cI28</i>	<i>I$\bar{4}3d$</i>	9.55			(Gambino, 1967)
Nd ₄ Bi ₃	anti-Th ₃ P ₄	<i>cI28</i>	<i>I$\bar{4}3d$</i>	9.5542(3)			(Yoshihara et al., 1975)
Nd ₅ Bi ₃	Mn ₅ Si ₃	<i>hP16</i>	<i>P6₃/mcm</i>	9.374(9)		6.535(5)	(Hohnke and Parthé, 1966)
Nd ₅ Bi ₃	Mn ₅ Si ₃	<i>hP16</i>	<i>P6₃/mcm</i>	9.3696(3)		6.5126(2)	(Yoshihara et al., 1975)

continued on next page

Table 2, *continued*

Compound	Structure type	Pearson symbol	Space group	<i>a</i> (Å)	<i>b</i> (Å)	<i>c</i> (Å)	Reference
Nd ₂ Bi	La ₂ Sb	<i>tI12</i>	<i>I4/mmm</i>	4.5619(3)		17.870(1)	(Yoshihara et al., 1975)
SmBi ₂	unknown	<i>o**</i>		6.42	12.80	11.64	(Sadigov et al., 1985)
SmBi	NaCl	<i>cF8</i>	<i>Fm$\bar{3}m$</i>	6.38			(Sadigov et al., 1985)
Sm ₄ Bi ₃	anti-Th ₃ P ₄	<i>cI28</i>	<i>I$\bar{4}3d$</i>	9.814			(Gambino, 1967)
Sm ₄ Bi ₃	anti-Th ₃ P ₄	<i>cI28</i>	<i>I$\bar{4}3d$</i>	9.8167(3)			(Yoshihara et al., 1975)
Sm ₄ Bi ₃	anti-Th ₃ P ₄	<i>cI28</i>	<i>I$\bar{4}3d$</i>	9.49			(Sadigov et al., 1985)
Sm ₅ Bi ₃	Mn ₅ Si ₃	<i>hP16</i>	<i>P6₃/mcm</i>	9.30		6.48	(Sadigov et al., 1985)
Sm ₂ Bi	La ₂ Sb	<i>tI12</i>	<i>I4/mmm</i>	4.52		17.60	(Sadigov et al., 1985)
Eu ₄ Bi ₃	anti-Th ₃ P ₄	<i>cI28</i>	<i>I$\bar{4}3d$</i>	10.00			(Gambino, 1967)
Eu ₄ Bi ₃	anti-Th ₃ P ₄	<i>cI28</i>	<i>I$\bar{4}3d$</i>	9.920(2)			(Wang et al., 1996)
Eu ₁₆ Bi ₁₁	Ca ₁₆ Sb ₁₁	<i>tP56</i>	<i>P$\bar{4}2_1m$</i>	12.906(3)		11.852(6)	(Leon-Escamilla et al., 1997)
GdBi	NaCl	<i>cF8</i>	<i>Fm$\bar{3}m$</i>	6.3108(2)			(Yoshihara et al., 1975)
Gd ₄ Bi ₃	anti-Th ₃ P ₄	<i>cI28</i>	<i>I$\bar{4}3d$</i>	9.385(2)			(Hohnke and Parthé, 1966)
Gd ₄ Bi ₃	anti-Th ₃ P ₄	<i>cI28</i>	<i>I$\bar{4}3d$</i>	9.383			(Gambino, 1967)
Gd ₄ Bi ₃	anti-Th ₃ P ₄	<i>cI28</i>	<i>I$\bar{4}3d$</i>	9.3858(3)			(Yoshihara et al., 1975)
Gd ₅ Bi ₃	Mn ₅ Si ₃	<i>hP16</i>	<i>P6₃/mcm</i>	9.182(8)		6.426(7)	(Hohnke and Parthé, 1966)
Gd ₅ Bi ₃	Mn ₅ Si ₃	<i>hP16</i>	<i>P6₃/mcm</i>	9.1580(9)		6.4186(6)	(Yoshihara et al., 1975)
Gd ₅ Bi ₃	Y ₅ Bi ₃	<i>oP32</i>	<i>Pnma</i>	8.2267(8)	9.531(1)	12.081(1)	(Yoshihara et al., 1975)
Gd ₅ Bi ₃	Y ₅ Bi ₃	<i>oP32</i>	<i>Pnma</i>	8.226(1)	9.540(1)	12.085(1)	(Drzyzga and Szade, 2001)
TbBi	NaCl	<i>cF8</i>	<i>Fm$\bar{3}m$</i>	6.2759(2)			(Yoshihara et al., 1975)
Tb ₄ Bi ₃	anti-Th ₃ P ₄	<i>cI28</i>	<i>I$\bar{4}3d$</i>	9.321(1)			(Hohnke and Parthé, 1966)
Tb ₄ Bi ₃	anti-Th ₃ P ₄	<i>cI28</i>	<i>I$\bar{4}3d$</i>	9.3215(4)			(Yoshihara et al., 1975)
Tb ₅ Bi ₃	Mn ₅ Si ₃	<i>hP16</i>	<i>P6₃/mcm</i>	9.101(2)		6.365(2)	(Yoshihara et al., 1975)

continued on next page

Table 2, *continued*

Compound	Structure type	Pearson symbol	Space group	<i>a</i> (Å)	<i>b</i> (Å)	<i>c</i> (Å)	Reference
Tb ₅ Bi ₃	Y ₅ Bi ₃	<i>oP32</i>	<i>Pnma</i>	8.1993(8)	9.4759(9)	11.999(1)	(Yoshihara et al., 1975)
Tb ₅ Bi ₃	Y ₅ Bi ₃	<i>oP32</i>	<i>Pnma</i>	8.170(1)	9.487(1)	11.968(1)	(Drzyzga and Szade, 2001)
DyBi	NaCl	<i>cF8</i>	<i>Fm$\bar{3}m$</i>	6.2491(4)			(Yoshihara et al., 1975)
DyBi	NaCl	<i>cF8</i>	<i>Fm$\bar{3}m$</i>	6.234			(Hulliger, 1980)
Dy ₅ Bi ₃	Y ₅ Bi ₃	<i>oP32</i>	<i>Pnma</i>	8.1603(4)	9.4214(4)	11.9341(6)	(Yoshihara et al., 1975)
Dy ₅ Bi ₃	Y ₅ Bi ₃	<i>oP32</i>	<i>Pnma</i>	8.155(1)	9.432(1)	11.934(1)	(Drzyzga and Szade, 2001)
HoBi	NaCl	<i>cF8</i>	<i>Fm$\bar{3}m$</i>	6.2291(3)			(Yoshihara et al., 1975)
HoBi	NaCl	<i>cF8</i>	<i>Fm$\bar{3}m$</i>	6.223(5)			(Fisher et al., 1985)
Ho ₅ Bi ₃	Y ₅ Bi ₃	<i>oP32</i>	<i>Pnma</i>	8.1328(4)	9.3820(6)	11.8744(7)	(Yoshihara et al., 1975)
Ho ₅ Bi ₃	Y ₅ Bi ₃	<i>oP32</i>	<i>Pnma</i>	8.128(1)	9.385(1)	11.874(1)	(Drzyzga and Szade, 2001)
ErBi	NaCl	<i>cF8</i>	<i>Fm$\bar{3}m$</i>	6.186			(Abulkhaev, 1992b)
ErBi	NaCl	<i>cF8</i>	<i>Fm$\bar{3}m$</i>	6.11			(Abdusalyamova and Rachmatov, 2002)
Er ₅ Bi ₃	Y ₅ Bi ₃	<i>oP32</i>	<i>Pnma</i>	8.0930(4)	9.3402(5)	11.8134(6)	(Yoshihara et al., 1975)
Er ₅ Bi ₃	Y ₅ Bi ₃	<i>oP32</i>	<i>Pnma</i>	8.090	9.340	11.813	(Abulkhaev, 1992b)
Er ₅ Bi ₃	Y ₅ Bi ₃	<i>oP32</i>	<i>Pnma</i>	8.090(1)	9.349(1)	11.806(1)	(Drzyzga and Szade, 2001)
Er ₅ Bi ₃	Y ₅ Bi ₃	<i>oP32</i>	<i>Pnma</i>	8.10	9.338	11.79	(Abdusalyamova and Rachmatov, 2002)
TmBi	NaCl	<i>cF8</i>	<i>Fm$\bar{3}m$</i>	6.1878(3)			(Yoshihara et al., 1975)
Tm ₅ Bi ₃	Y ₅ Bi ₃	<i>oP32</i>	<i>Pnma</i>	8.0645(7)	9.3055(8)	11.758(1)	(Yoshihara et al., 1975)
YbBi ₂	ZrSi ₂	<i>oC12</i>	<i>Cmcm</i>	4.56	16.68	4.28	(Maksudova et al., 1985)
Yb ₅ Bi ₄	unknown	<i>tI*</i>	<i>I4/mmm</i>	11.93		17.13	(Maksudova et al., 1985)
Yb ₄ Bi ₃	anti-Th ₃ P ₄	<i>cI28</i>	<i>I$\bar{4}3d$</i>	9.52			(Gambino, 1967)
Yb ₄ Bi ₃	anti-Th ₃ P ₄	<i>cI28</i>	<i>I$\bar{4}3d$</i>	9.5739(2)			(Yoshihara et al., 1975)

continued on next page

Table 2, *continued*

Compound	Structure type	Pearson symbol	Space group	a (Å)	b (Å)	c (Å)	Reference
Yb ₁₆ Bi ₁₁	Ca ₁₆ Sb ₁₁	<i>tP</i> 56	$P\bar{4}2_1m$	12.3694(7)		11.588(1)	(Leon-Escamilla et al., 1997)
Yb ₅ Bi ₂	unknown	<i>oP</i> *	$Pna2_1$	12.36	9.66	8.28	(Maksudova et al., 1985)
LuBi	NaCl	<i>cF</i> 8	$Fm\bar{3}m$	6.120			(Abdusalyamova et al., 1996)
Lu ₅ Bi ₃	Y ₅ Bi ₃	<i>oP</i> 32	$Pnma$	8.046(5)	9.768(5)	11.718(5)	(Abulkhaev and Ganiev, 1995)

Table 3
Crystallographic data for *R*-s-element-Bi compounds

Compound	Structure type	Pearson symbol	a (Å)	b (Å)	c (Å)	Reference
Sm ₅ Bi ₃ H	Ca ₅ Sb ₃ F (stuffed β -Yb ₅ Sb ₃)	<i>oP</i> 36	13.1252(8)	10.1418(6)	8.7613(5)	(Leon-Escamilla and Corbett, 1998)
Eu ₅ Bi ₃ H	Ca ₅ Sb ₃ F (stuffed β -Yb ₅ Sb ₃)	<i>oP</i> 36	13.158(2)	10.140(1)	8.752(1)	(Leon-Escamilla and Corbett, 1998)
Yb ₅ Bi ₃ H	Ca ₅ Sb ₃ F (stuffed β -Yb ₅ Sb ₃)	<i>oP</i> 36	12.560(1)	9.7369(6)	8.4104(4)	(Leon-Escamilla and Corbett, 1998)
YLi ₃ Bi ₂	Filled CaAl ₂ Si ₂	<i>hP</i> 6	4.6065(5)		6.922(4)	(Grund et al., 1984)
LaLi ₃ Bi ₂	Filled CaAl ₂ Si ₂	<i>hP</i> 6	4.704(2)		7.527(3)	(Grund et al., 1984)
LaLiBi ₂	HfCuSi ₂	<i>tP</i> 8	4.5206(4)		10.994(2)	(Pan et al., 2006)
EuLiBi	TiNiSi	<i>oP</i> 12	7.981(1)	4.848(1)	8.483(2)	(Prill et al., 2002)
YbLiBi	YLiSn	<i>hP</i> 24	9.595(2)		7.635(4)	(Grund et al., 1986)
La ₃ MgBi ₅	Hf ₅ Sn ₃ Cu	<i>hP</i> 18	9.7882(7)		6.5492(9)	(Pan et al., 2006)

3. Ternary *R*-s-element-Bi systems

Ternary rare earth bismuth systems with an s-element as the third component are limited to those containing H, Li, and Mg. Table 3 lists crystallographic data for known compounds. Investigation of additional systems containing heavier alkali or alkaline earth metals would seem worthwhile.

3.1. *R*-Bi-H

Three ternary rare earth bismuth hydrides are known for the divalent rare earths: Sm₅Bi₃H, Eu₅Bi₃H, and Yb₅Bi₃H. They were first identified after the hypothetical orthorhombic form of the parent binary rare earth bismuthides “*R*₅Bi₃” were understood to be stabilized by hydrogen impurities present in the starting rare earth metals or introduced through the evolution of water in heated silica tubes (Leon-Escamilla and Corbett, 1994, 1998). High yields of the ternary hydrides can be obtained through deliberate introduction of hydrogen via the rare earth dihydride, *RH*₂, with appropriate amounts of the other elements, and heat-

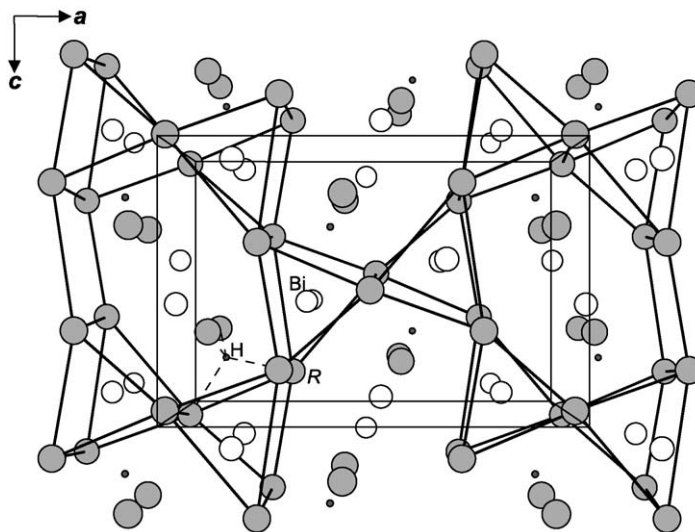


Fig. 1. Structure of $R_5\text{Bi}_3\text{H}$ ($R = \text{Sm}, \text{Eu}, \text{Yb}$) ($\text{Ca}_5\text{Sb}_3\text{F}$ -type).

ing within Ta tubes jacketed by silica tubes at 1100–1150 °C for 2 h and 850 °C for 14 d followed by quenching. Cell parameters have been refined from powder X-ray diffraction data (table 3), and the heavy atom structures of $\text{Sm}_5\text{Bi}_3\text{H}$ and $\text{Yb}_5\text{Bi}_3\text{H}$ have also been refined (Leon-Escamilla and Corbett, 1998). Although no positional parameters were reported, the bond distances were indicated to be consistent with divalent rare earth atoms; the magnetic susceptibility data also support the presence of divalent samarium in $\text{Sm}_5\text{Bi}_3\text{H}$. These compounds adopt the $\text{Ca}_5\text{Sb}_3\text{F}$ -type structure (Pearson symbol $oP36$, space group $Pnma$ (No. 62), $Z = 4$), in which the H atoms are assumed to enter small tetrahedral sites within a parent “ $R_5\text{Bi}_3$ ” host structure (fig. 1) (Corbett and Leon-Escamilla, 2003; Hurng and Corbett, 1989). As such, this can be regarded as a stuffed $\beta\text{-Yb}_5\text{Sb}_3$ structure. Moreover, these are formally closed-shell systems, $(R^{2+})_5(\text{Bi}^{3-})_3(\text{H}^-)$, and are expected to be semiconducting.

3.2. $R\text{-Li-Bi}$

3.2.1. RLi_3Bi_2

YLi_3Bi_2 and LaLi_3Bi_2 were prepared from stoichiometric mixtures of the elements placed within Ta tubes jacketed by silica tubes, pre-reacted at 580 °C, reground, and heated at 700 °C for 14–20 h (Grund et al., 1984). The products are air- and moisture-sensitive. Only powder X-ray diffraction data are available, but it is assumed that these compounds are isostructural to the corresponding antimonides, for which single-crystal X-ray and neutron diffraction data were collected (Grund et al., 1984). As shown in fig. 2, the structure (Pearson symbol $hP6$, space group $P\bar{3}m1$ (No. 164), $Z = 1$) is based on the CaAl_2Si_2 -type, in which the R atoms

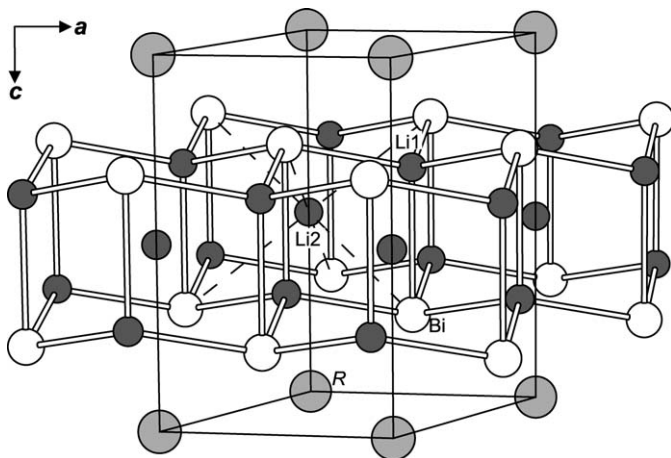


Fig. 2. Structure of RLi_3Bi_2 ($R = Y, La$) (filled $CaAl_2Si_2$ -type).

separate double layers of buckled hexagonal nets, built up of Li atoms tetrahedrally coordinated by Bi atoms. Additional Li atoms enter octahedral sites between the hexagonal nets. Since partial occupancy of the tetrahedral Li sites was indicated in “ $YLi_{2.6}Sb_2$ ”, the precise structures of YLi_3Bi_2 and $LaLi_3Bi_2$ will require confirmation from single-crystal methods. In principle, however, the idealized formulas are already electron-precise.

Earlier work had suggested the existence of RLi_2Bi_2 compounds for $R = Ce, Pr, Nd, Tb$, also adopting a structure based on the $CaAl_2Si_2$ -type (Zwiener et al., 1981). Cell parameters are not available, but magnetic susceptibility data indicate Curie–Weiss behaviour and give effective magnetic moments consistent with trivalent rare earth atoms. If this is correct, then the formula “ RLi_2Bi_2 ” clearly is not electron-precise. Further characterization would be helpful.

3.2.2. $RLiBi_2$

Single crystals of $LaLiBi_2$ were recently prepared by reaction of La, Li, and Bi in a 1 : 1 : 1.5 molar ratio in a Nb tube jacketed by a silica tube, heated at 980 °C for 2 d and 800 °C for 7 d, and then slowly cooled to room temperature at 0.1 °C/min (Pan et al., 2006). $LaLiBi_2$ has the common tetragonal $HfCuSi_2$ -type structure (Pearson symbol $tP8$, space group $P4/nmm$ (No. 129), $Z = 2$) also adopted by ternary rare earth transition-metal pnictides $RM_{1-x}Pn_2$, but with Li occupying the M site (section 5.5.2, fig. 10). Positional parameters are: La, $2c$ (1/4, 1/4, 0.2383(1)); Li, $2b$ (3/4, 1/4, 1/4); Bi1, $2c$ (1/4, 1/4, 0.6620(1)); Bi2, $2a$ (3/4, 1/4, 0). Although many ternary $RM_{1-x}Pn_2$ compounds often display deficiencies in the M site, $LaLiBi_2$ is reported to be completely stoichiometric, despite the rather high displacement parameter observed for Li. The presence of Li in the M site illustrates the importance of covalency in the Li–Bi bonds within the two-dimensional layers of edge-sharing $LiBi_4$ tetrahedra (Li–Bi, 2.878(1) Å). The Bi–Bi distances (3.1965(3) Å) within the square nets are consistent with weak “one-electron” covalent bonds. It is possible to arrive at a

valence-precise formulation “ $\text{La}^{3+}\text{Li}^+\text{Bi}1^{3-}\text{Bi}2^{1-}$ ”. The covalent character of these bonds is also supported by band structure calculations, which indicate that LaLiBi_2 should be metallic, although the Fermi level lies close to a pseudogap. Substitution of La with other R would seem feasible.

3.2.3. $RLiBi$

The equiatomic compounds EuLiBi and YbLiBi , containing divalent rare earths, are known. EuLiBi , which is extremely moisture-sensitive, was prepared from reaction of Eu, Li, and Bi in a 1 : 2 : 1 atomic ratio within Mo crucibles placed in steel ampoules jacketed by silica tubes at 1000 °C for 5–7 d (Prill et al., 2002). Powder X-ray diffraction indicates an orthorhombic TiNiSi -type structure (Pearson symbol $oP12$, space group $Pnma$ (No. 62), $Z = 4$), but atomic positions were not refined (section 5.4, fig. 9a). The presence of divalent europium is supported by ^{151}Eu Mössbauer spectroscopy (isomer shift of -11 mm/s) and magnetic susceptibility measurements (effective magnetic moment of $8.3 \mu_B$, close to that of the free-ion value of $7.94 \mu_B$ for Eu^{2+}). EuLiBi orders antiferromagnetically below 7.5 K.

Stoichiometric reaction of the elements Yb, Li, and Bi within Ta tubes at 700 °C leads to YbLiBi , but always accompanied by impurities of YbBi (Grund et al., 1986). Only cell parameters have been obtained from powder X-ray diffraction data, but YbLiBi is assumed to be isostructural with YLiSn , which is based on a filled wurtzite structure (Pearson symbol $hP24$, space group $P6_3mc$ (No. 186), $Z = 8$) (Steinberg and Schuster, 1979). Magnetic susceptibility measurements support the presence of divalent Yb.

3.3. $R\text{-Mg-Bi}$

The only known compound in this system is La_3MgBi_5 , which was recently prepared in the form of needle-shaped single crystals by the reaction of La, Mg, and Bi in a 2 : 1 : 3 molar ratio in a Nb tube jacketed by a silica tube, heated at 980 °C for 2 d and 800 °C for 7 d, and then slowly cooled to room temperature at 0.1 °C/min (Pan et al., 2006). La_3MgBi_5 has the hexagonal $\text{Hf}_5\text{Cu}_3\text{Sn}$ -type structure (Pearson symbol $hP18$, space group $P6_3/mcm$ (No. 193), $Z = 2$), which is also adopted by Ce_3MnBi_5 , discussed later (section 5.1.1, fig. 4). Standardized positional parameters are: La, 6g (0.6193(2), 0, 1/4); Mg, 2b (0, 0, 0); Bi1, 6g (0.2656(1), 0, 1/4); Bi2, 4d (1/3, 2/3, 0). Mg atoms are centred in Bi_6 octahedra (Mg–Bi, 3.0725(8) Å), which share faces to form chains aligned along the c direction. The analogy to Ce_3MnBi_5 again points out the importance of covalent character in the Mg–Bi bonds. The La atoms are ninefold coordinated by Bi atoms (La–Bi, 3.310(1)–3.4683(6) Å). A chain of Bi2 atoms (Bi–Bi, 3.2746(5) Å) also extends along the c direction. An extended Hückel band structure calculation indicates that metallic behaviour should be expected. The Bi–Bi overlap population (0.278) supports the presence of bonding interactions along the Bi2 chains. Properties have not been measured owing to the difficulty in obtaining phase-pure product.

A Ce–Mg–Bi alloy has been briefly examined in the context of pyrophoric materials in ignition devices (Reiswig and Mack, 1955). Both Ce–Mg–Bi and Sm–Mg–Bi liquid alloys have also been investigated in exchange reactions for extracting rare earth fission products from nuclear fuel reactors (Katz et al., 1960).

4. Ternary *R*-f-element–Bi systems

Single crystals of LaCeBi were prepared by heating stoichiometric mixtures of the elements in a Mo crucible at 1200 °C for 7 d (Oyamada et al., 1993). Although no crystallographic details and no cell parameters were provided, LaCeBi is assumed to adopt the tetragonal La₂Sb-type structure (Pearson symbol *tI12*, space group *I4/mmm* (No. 139), *Z* = 4) (fig. 3). It was speculated that La occupies mainly the larger *R2* site. The magnetic susceptibility follows the Curie–Weiss law with $\mu_{\text{eff}} = 2.05 \mu_{\text{B}}/\text{Ce}$.

Several members of the La_{*x*}Ce_{1-*x*}Bi solid solution have been prepared as well (Kasuya et al., 1993). They adopt the rocksalt structure of the end-members, and the cubic cell parameter for La_{0.2}Ce_{0.8}Bi (6.520 Å, assuming a typographical error in the original article) corresponds to the value interpolated between that for LaBi (6.579 Å) and CeBi (6.505 Å) (Kasuya et al., 1996). Electrical resistivity, transverse and longitudinal magnetoresistance, and Hall effect measurements have been carried out.

The ternary mixed rare earth bismuthides Sm₃GdBi₃, Eu₃GdBi₃, and Gd₃DyBi₃ have been prepared (Gambino, 1967). Sm₃GdBi₃ and Eu₃GdBi₃ melt congruently, whereas Gd₃DyBi₃ melts incongruently. They adopt the cubic anti-Th₃P₄-type structure, but characterization re-

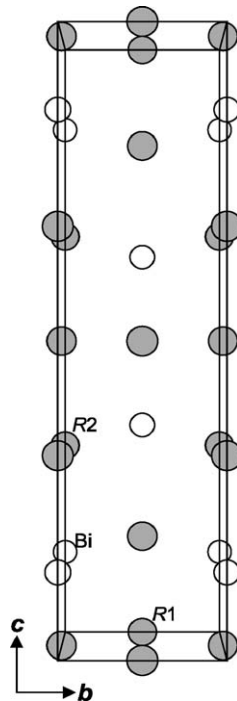


Fig. 3. Structure of LaCeBi (La₂Sb-type).

mains somewhat incomplete, with only the cell parameter for Gd_3DyBi_3 being determined ($a = 9.37 \text{ \AA}$). It was speculated that Sm_3GdBi_3 and Eu_3GdBi_3 are probably valence compounds, according to the formulation $(R^{2+})_3(R'^{3+})(\text{Bi}^{3-})_3$.

Procedures have been developed for the analysis of ternary bismuth-rich alloys containing up to 5–10% U and up to 5–10% Th, Nd, or Pr after separation of the ions dissolved in acidic solution (Milner and Nunn, 1957; Milner and Edwards, 1958).

5. Ternary *R*-d-element–Bi systems

The most well studied ternary rare earth bismuthides are those containing a d-element, but they are largely limited to either the first-row transition metals or the later triads (especially Ni, Pd, Pt). Table 4 summarizes the extent of known compounds in these systems. As expected, many of these bismuthides adopt structure types similar to those of the corresponding antimonides, such as the prevalent MgAgAs-type found among the equiatomic compounds RMPn ($M = \text{Ni, Pd, Pt}$). Pnictogen-rich phases tend to be less common among bismuthides than antimonides, although this paucity may reflect difficulties in synthesis rather than any inherent instability. Conspicuous in their absence are bismuth analogues of the rare earth filled antimonide skutterudites such as $\text{RFe}_4\text{Sb}_{12}$.

5.1. *R*–Mn–Bi

Known phases so far have been limited to those containing late *R*. Crystallographic data are listed in table 5.

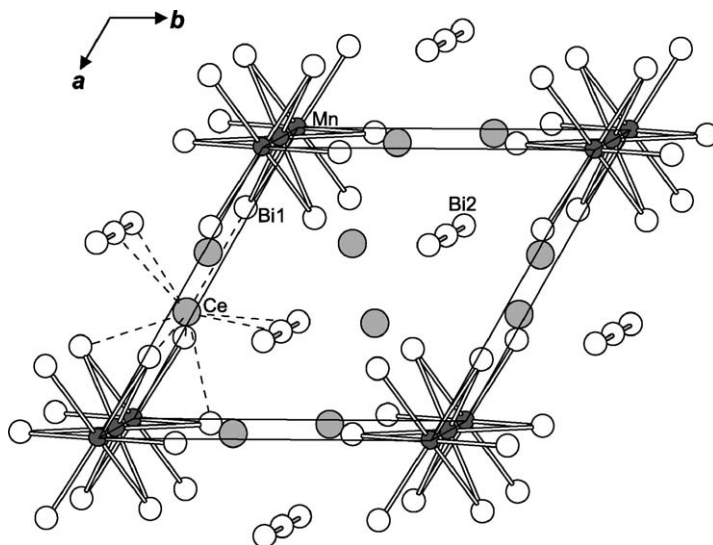
5.1.1. R_3MnBi_5

The compound Ce_3MnBi_5 was identified after analyzing nine alloys prepared in the Ce–Mn–Bi system (Pecharsky and Gschneidner, 1999). The alloys were prepared by reacting the elements, sealed under He in Ta crucibles, in an induction furnace followed by annealing in silica tubes at moderate temperatures (400–550 °C) for one week. Single crystals of Ce_3MnBi_5 were extracted from an alloy of composition “ $\text{Ce}_{26}\text{Mn}_{22}\text{Bi}_{52}$ ”. Ce_3MnBi_5 adopts a $\text{Hf}_5\text{Sn}_3\text{Cu}$ -type structure (Pearson symbol $hP18$, space group $P6_3/mcm$ (No. 193), $Z = 2$), an ordered variant of the Ti_5Ga_4 -type structure, which in turn is derived by stuffing octahedral sites within the Mn_5Si_3 -type structure (fig. 4). Standardized positional parameters are: Ce, $6g$ (0.6191(3), 0, 1/4); Mn, $2b$ (0, 0, 0); Bi1, $6g$ (0.2598(2), 0, 1/4); Bi2, $4d$ (1/3, 2/3, 0). There are chains of face-sharing Mn-centred octahedra, $\infty^1[\text{MnBi}_3]$, and linear skewers of Bi atoms, $\infty^1[\text{Bi}]$, extending along the *c* direction. The Ce atoms are ninefold coordinated by Bi atoms in approximately tricapped trigonal prismatic geometry. Magnetic susceptibility measurements were made on a single-phase sample that must be prepared slightly off composition at “ $\text{Ce}_{33}\text{Mn}_{15}\text{Bi}_{52}$ ”, with presumably a side reaction accounting for the consumption of excess Mn or perhaps with the existence of a homogeneity range. Ce_3MnBi_5 follows the Curie–Weiss law from 4 to 325 K, with $\theta_p = -53.4(8) \text{ K}$, suggesting an antiferromagnetic ground state. The isothermal magnetization at 5 K shows metamagnetic transitions at

Table 4
Ternary rare earth d-element bismuthides

Compound	Structure type	<i>M</i>	Sc	Y	La	Ce	Pr	Nd	Sm	Eu	Gd	Tb	Dy	Ho	Er	Tm	Yb	Lu
R_6MBi_{14}	Ce_6ZnBi_{14}	Zn				+												
$RMBi_2$	$HfCuSi_2$	Ni		+	+	+	+	+	+		+	+	+					
		Cu			+	+					+		+					
		Ag			+	+	+	+	+		+							
RM_2Bi_2	$CaBe_2Ge_2$	Pd								+								
R_3MBi_5	Hf_5Cu_3Sn	Mn				+												
$R_3M_3Bi_4$	$Y_3Au_3Sb_4$	Pt			+	+												
$RMBi$	$TiNiSi$	Rh			+	+	+	+	+									
$RMBi$	$ZrNiAl$	Rh									+	+	+	+	+			
$RMBi$	$MgAgAs$	Ni	+	+			+	+	+		+	+	+	+	+	+		+
		Pd	+	+	+	+	+	+	+		+	+	+	+	+	+		+
		Pt		+	+	+	+	+	+		+	+	+	+	+	+		+
$RMBi$	$ZrBeSi$	Cu								+								+
$RMBi$	$LiGaGe$	Cu																+
RM_2Bi	$MnCu_2Al$	Pd		+			+		+		+	+	+	+	+			+
$R_9M_4Bi_9$	$Ca_9Mn_4Bi_9$	Zn																+
$R_{14}MBi_{11}$	$Ca_{14}AlSb_{11}$	Mn									+							+
R_5MBi_3	Hf_5Sn_3Cu	Cu			+	+	+	+			+	+						
R_5MBi_2	unknown	Fe					+		+									
		Ni		+											+			
R_5MBi_2	$\beta\text{-Yb}_5Sb_3$?	Co									+	+	+	+	+			
		Cu												+				
R_6MBi_2	Zr_6CoAl_2	Mn		+									+	+	+	+		+
		Fe		+							+	+	+		+	+		+
		Co		+										+		+		
R_5M_2Bi	Mo_5B_2Si	Ni		+							+	+	+	+	+	+		+
		Pd		+							+	+	+	+	+	+		+
		Pt		+							+	+	+	+	+	+		+
$R_6M_{13}Bi$	$Nd_6Fe_{13}Si$	Fe					+	+	+									
		Co			+													
$R_8M_{24}Bi$	$Ce_8Pd_{24}Bi$	Pd				+												
$R_{12}M_5Bi$	$Ho_{12}Co_5Bi$	Co		+							+	+	+	+	+	+		

^aYbCuBi adopts the ZrBeSi-type above 375 K and the LiGaGe-type below 375 K (Tkachuk et al., 2006a).

Fig. 4. Structure of Ce_3MnBi_5 ($\text{Hf}_5\text{Cu}_3\text{Sn}$ -type).Table 5
Crystallographic data for $R\text{-Mn-Bi}$ compounds

Compound	Structure type	Pearson symbol	a (Å)	c (Å)	Reference
$\text{Ce}_3\text{MnBi}_5^{\text{a}}$	$\text{Hf}_5\text{Sn}_3\text{Cu}$	$hP18$	9.267(3)	6.456(1)	(Pecharsky and Gschneidner, 1999)
$\text{Eu}_{14}\text{MnBi}_{11}^{\text{a}}$	$\text{Ca}_{14}\text{AlSb}_{11}$	$tI208$	17.632(4)	23.047(6)	(Chan et al., 1997)
$\text{Yb}_{14}\text{MnBi}_{11}^{\text{a}}$	$\text{Ca}_{14}\text{AlSb}_{11}$	$tI208$	17.000(3)	22.259(6)	(Chan et al., 1998b)
Y_6MnBi_2	Zr_6CoAl_2	$hP9$	8.242(1)	4.292(1)	(Morozkin, 2003b)
Dy_6MnBi_2	Zr_6CoAl_2	$hP9$	8.211(1)	4.286(1)	(Morozkin, 2003b)
Ho_6MnBi_2	Zr_6CoAl_2	$hP9$	8.164(1)	4.250(1)	(Morozkin, 2003b)
Er_6MnBi_2	Zr_6CoAl_2	$hP9$	8.124(1)	4.235(1)	(Bolotaev et al., 2004)
Tm_6MnBi_2	Zr_6CoAl_2	$hP9$	8.062(4)	4.215(2)	(Bolotaev et al., 2004)
Lu_6MnBi_2	Zr_6CoAl_2	$hP9$	8.019(2)	4.185(1)	(Morozkin, 2003b)

^aSingle-crystal data.

1.3 and 5 T, but these are probably due to impurities. The effective magnetic moment of $\mu_{\text{eff}} = 5.85(6) \mu_{\text{B}}$ agrees well with the theoretical value of $5.86 \mu_{\text{B}}$ that results from an assignment of Ce^{3+} and Mn^{4+} , which is also supported by examination of Ce–Bi (3.245(4)–3.459(5) Å) and Mn–Bi (2.976(3) Å) bond lengths. This is consistent with the Zintl-type formulation $(\text{Ce}^{3+})_3(\text{Mn}^{4+})(\text{Bi}^{3-})_3(\text{Bi}^{2-})_2$ similar to what has been proposed for the corresponding antimonides $R_3\text{MSb}_5$ and U_3MSb_5 ($M = \text{Ti, Zr, Hf}$) (Ferguson et al., 1997; Tkachuk et al., 2006b). The analogy then implies that, in addition to the isolated $(\text{Bi}1)^{3-}$ ions, the Bi2 atoms participate in hypervalent Bi–Bi bonds (of approximately one-half bond order, or “one-electron bonds”) within the linear skewers. The Bi2–Bi2 bond length of 3.228(1) Å is certainly within the range of weak bonding found in other hypervalent Bi substructures. It would also seem feasible to prepare other R analogues of Ce_3MnBi_5 . Interestingly, a magnesium analogue, La_3MgBi_5 , has been prepared recently (Pan et al., 2006).

5.1.2. $R_{14}\text{MnBi}_{11}$

The compounds $R_{14}\text{MnBi}_{11}$ are known only for the divalent rare earths ($R = \text{Eu, Yb}$) (Chan et al., 1997; Chan et al., 1998b). They were prepared by reaction of the elements in a Ta tube jacketed by an outer silica tube, heated at 1000–1200 °C for up to 10 d. Both are isotypic with $\text{Ca}_{14}\text{AlSb}_{11}$ (Pearson symbol $tI208$, space group $I4_1/acd$ (No. 142), $Z = 8$), which is adopted by an extended family of $\text{A}_{14}\text{MPn}_{11}$ Zintl phases. Standardized positional parameters for $\text{Eu}_{14}\text{MnBi}_{11}$ are listed in table 6. The structure consists of fourteen R^{2+} ions, one MnBi_4^{9-} tetrahedron, one linear Bi_3^{7-} ion, and four Bi^{3-} ions per formula unit (fig. 5). Magnetic measurements reveal that $\text{Eu}_{14}\text{MnBi}_{11}$ undergoes an apparently antiferromagnetic transition at ~ 35 K, but with a positive value for θ_{p} of 45 K, indicating predominantly ferromagnetic exchange coupling (Chan et al., 1997). It exhibits colossal negative magnetoresistance, as large as 67% (at 20 K, 5 T) (Chan et al., 1998a). $\text{Yb}_{14}\text{MnBi}_{11}$ orders ferromagnetically at 56 K and a second transition of uncertain origin (possibly spin reorientation) occurs at 28 K (Chan et al., 1998b). The effective magnetic moments in $\text{Eu}_{14}\text{MnBi}_{11}$ (27.1(1) μ_{B} /f.u.) and $\text{Yb}_{14}\text{MnBi}_{11}$ (4.9(1) μ_{B} /f.u.) seem to be consistent with the assignment of R^{2+} and Mn^{3+} ions, but more recent X-ray magnetic circular dichroism (XMCD) measurements on the related $\text{Yb}_{14}\text{MnSb}_{11}$ compound supporting a Mn^{2+} configuration may require a reformulation of this assignment

Table 6
Standardized positional parameters for $\text{Eu}_{14}\text{MnBi}_{11}$ (Chan et al., 1997)

Atom	Wyckoff position	x	y	z
Eu1	32g	0.0220(1)	0.3762(1)	0.0004(1)
Eu2	32g	0.0418(1)	0.0736(1)	0.1722(1)
Eu3	32g	0.3404(1)	0.0710(1)	0.0928(1)
Eu4	16e	0.3553(1)	0	1/4
Mn	8a	0	1/4	3/8
Bi1	32g	0.1315(1)	0.0269(1)	0.0470(1)
Bi2	32g	0.3599(1)	0.2550(1)	0.0625(1)
Bi3	16f	0.1362(1)	0.3862(1)	1/8
Bi4	8b	0	1/4	1/8

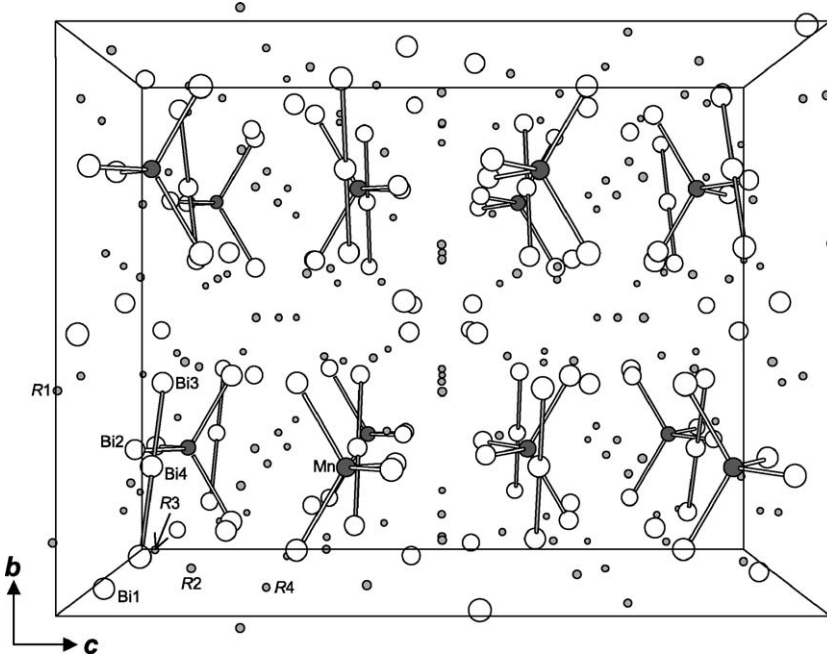


Fig. 5. Structure of $R_{14}MnBi_{11}$ ($R = \text{Eu, Yb}$) ($\text{Ca}_{14}\text{AlSb}_{11}$ -type).

for all $R_{14}M\text{Pn}_{11}$ compounds (Holm et al., 2002). Worthwhile targets for synthesis are the zinc analogues, $R_{14}\text{ZnBi}_{11}$.

5.1.3. R_6MnBi_2

Powder samples of R_6MnBi_2 ($R = \text{Y, Dy, Ho, Er, Tm, Lu}$) were prepared by arc melting of the elements followed by annealing under argon at 900°C for 170 h and quenching in water (Morozkin, 2003b; Bolotaev et al., 2004). The compounds were analyzed by powder X-ray diffraction and their structures were refined using the Rietveld technique. The R_6MnBi_2 compounds were described as adopting a Zr_6CoAs_2 -type structure (Kleinke, 1997), which is one of many examples of an ordered Fe_2P -type structure. This ordered variant is a common one found for many intermetallic compounds and has been more widely described as a Zr_6CoAl_2 -type structure (Pearson symbol $hP9$, space group $P\bar{6}2m$ (No. 189), $Z = 1$), which is the term we will use here (Krypyakevich et al., 1970; Kwon et al., 1990; Kleinke, 1998). Standardized positional parameters of six known compounds are listed in table 7. Here, the characteristic motifs are two types of R_6 trigonal prisms, each of whose quadrilateral faces is capped by the vertices of the other type (fig. 6). Columns of these tri-capped trigonal prisms extend along the c direction through sharing of the triangular faces. Ordering arises from the distribution of atoms at the centres of the trigonal prisms, with the smaller Mn atom located within the smaller trigonal prism and the larger Bi atom within the

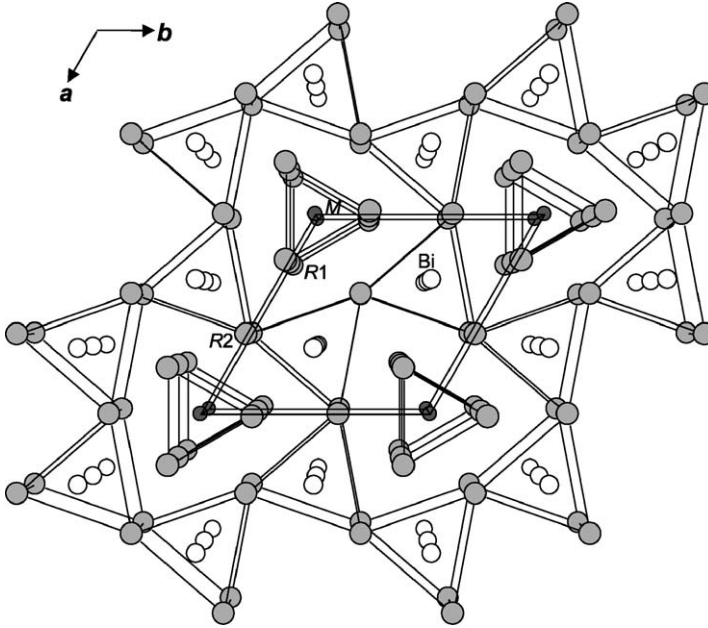


Fig. 6. Structure of $R_6M\text{Bi}_2$ ($M = \text{Mn, Fe, Co}$) (Zr₆CoAl₂-type).

Table 7

Standardized positional parameters for $R_6\text{MnBi}_2$ compounds (Morozkin, 2003b; Bolotaev et al., 2004)^a

Compound	x_1	x_2
Y ₆ MnBi ₂	0.238(2)	0.601(2)
Dy ₆ MnBi ₂	0.238(2)	0.605(2)
Ho ₆ MnBi ₂	0.238(1)	0.604(1)
Er ₆ MnBi ₂	0.233(2)	0.604(2)
Tm ₆ MnBi ₂	0.225(5)	0.610(4)
Lu ₆ MnBi ₂	0.234(3)	0.607(2)

^a R1 at 3g ($x_1, 0, 1/2$); R2 at 3f ($x_2, 0, 0$); Mn at 1a (0, 0, 0); Bi at 2d ($1/3, 2/3, 1/2$).

larger trigonal prism. With a valence electron count (VEC) of 35, the $R_6\text{MnBi}_2$ compounds are among the most electron poor among related compounds with the same stoichiometry (Chen and Corbett, 2004). It would be interesting to determine from band structure calculations the extent to which homoatomic bonding interactions contribute relative to heteroatomic ones. Er₆MnBi₂ apparently shows a magnetic transition at $T = 115$ K, of uncertain origin (Bolotaev et al., 2004).

5.1.4. *Thin films*

There is a series of reports claiming that thin films (as well as bulk powders) have been prepared in which various rare earths ($R = \text{Ce, Pr, Nd, Sm, Dy, Tb}$) are doped into MnBi (NiAs-type), in an effort to improve its magnetic properties for applications as permanent magnets (Dai et al., 1992; Fang et al., 1991, 1992, 1994, 1995, 1998, 1999; Saha et al., 2000). The authors proposed that R atoms substitute for Bi atoms, giving phases with composition $\text{MnBi}_{1-x}R_x$, at doping levels as high as $x = 0.25$. Powder X-ray diffraction revealed that the cell parameters for these samples are actually about 3–5% *smaller* than those of MnBi, and impurities of other phases are present. In a band structure calculation, the alternative scenario of R atoms entering vacant trigonal prismatic sites between layers of Mn atoms (yielding a partially filled NiAs-type or a defect Ni_2In -type structure) was also considered (Li et al., 1991). In either case, the resulting R –Bi bonds ($\sim 2.8 \text{ \AA}$) would be incredibly short without a significant distortion in the rest of the structure.

5.2. R –Fe–Bi

Crystallographic data for known phases, which are all metal-rich, are listed in table 8.

Table 8
Crystallographic data for R –Fe–Bi compounds

Compound	Structure type	Pearson symbol	a (Å)	c (Å)	Reference
“ Pr_5FeBi_2 ”	unknown				(Bodak et al., 2000)
“ Sm_5FeBi_2 ”	unknown				(Bodak et al., 2000)
Y_6FeBi_2	Zr_6CoAl_2	$hP9$	8.265(1)	4.214(1)	(Morozkin, 2003a)
Gd_6FeBi_2	Zr_6CoAl_2	$hP9$	8.343(2)	4.227(1)	(Morozkin, 2003a)
Tb_6FeBi_2	Zr_6CoAl_2	$hP9$	8.281(2)	4.194(1)	(Morozkin, 2003a)
Dy_6FeBi_2	Zr_6CoAl_2	$hP9$	8.229(3)	4.173(2)	(Morozkin, 2003a)
Er_6FeBi_2	Zr_6CoAl_2	$hP9$	8.161(2)	4.153(1)	(Morozkin, 2003a)
Tm_6FeBi_2	Zr_6CoAl_2	$hP9$	8.112(3)	4.135(2)	(Morozkin, 2003a)
Lu_6FeBi_2	Zr_6CoAl_2	$hP9$	8.059(2)	4.116(1)	(Morozkin, 2003a)
$\text{Pr}_6\text{Fe}_{13}\text{Bi}$	$\text{Nd}_6\text{Fe}_{13}\text{Si}$	$tI80$	8.116(1)	23.516(7)	(Weitzer et al., 1993)
$\text{Pr}_6\text{Fe}_{13}\text{Bi}$	$\text{Nd}_6\text{Fe}_{13}\text{Si}$	$tI80$	8.106(2)	23.481(8)	(Coey et al., 1994)
$\text{Pr}_6\text{Fe}_{13}\text{Bi}$	$\text{Nd}_6\text{Fe}_{13}\text{Si}$	$tI80$	8.117(1)	23.515(5)	(Bodak et al., 2000)

continued on next page

Table 8, *continued*

Compound	Structure type	Pearson symbol	a (Å)	c (Å)	Reference
Nd ₆ Fe ₁₃ Bi	Nd ₆ Fe ₁₃ Si	<i>tI</i> 80	8.103(1)	23.417(6)	(Weitzer et al., 1993)
Nd ₆ Fe ₁₃ Bi	Nd ₆ Fe ₁₃ Si	<i>tI</i> 80	8.094(3)	23.329(9)	(Coey et al., 1994)
Sm ₆ Fe ₁₃ Bi	Nd ₆ Fe ₁₃ Si	<i>tI</i> 80	8.057(1)	23.316(8)	(Weitzer et al., 1993)
Sm ₆ Fe ₁₃ Bi	Nd ₆ Fe ₁₃ Si	<i>tI</i> 80	8.060(2)	23.314(6)	(Bodak et al., 2000)
Pr ₆ Fe ₁₃ BiH _{13.8}	stuffed Nd ₆ Fe ₁₃ Si ?		8.185(2)	25.422(8)	(Coey et al., 1994)
Nd ₆ Fe ₁₃ BiH _{13.7}	stuffed Nd ₆ Fe ₁₃ Si ?		8.142(2)	25.267(7)	(Coey et al., 1994)

5.2.1. Phase diagrams

Isothermal sections of the Pr–Fe–Bi and Sm–Fe–Bi phase diagrams have been investigated, through analysis of 42 and 38 alloys, respectively, prepared by arc melting of the elements followed by annealing at 400 °C for 240 h (Bodak et al., 2000). Two apparently isostructural ternary compounds with the approximate compositions “Pr₅FeBi₂” and “Sm₅FeBi₂” were identified by microprobe analysis and powder X-ray diffraction, but no crystallographic information is available. The compounds Pr₆Fe₁₃Bi and Sm₆Fe₁₃Bi were confirmed to be present in the as-cast alloys, but they decompose at 400 °C to binary phases.

5.2.2. R_6FeBi_2

Similar to the R_6MnBi_2 and R_6CoBi_2 series, powder samples of R_6FeBi_2 ($R = Y, Gd, Tb, Dy, Er, Tm, Lu$) were prepared by arc melting of the elements followed by annealing under argon at 830 °C for 240 h and quenching in water (Morozkin, 2003a). Analysis by Rietveld refinement confirms a Zr_6CoAl_2 -type structure (Pearson symbol $hP9$, space group $P\bar{6}2m$ (No. 189), $Z = 1$), described earlier (section 5.1.3), containing Fe- and Bi-centred R_6 trigonal prisms that are tricapped and extend as confacial columns along the c direction (fig. 6). Standardized positional parameters of all known compounds are listed in table 9. An interesting observation is that although the c parameters are generally smaller in the R_6FeBi_2 series than in the R_6MnBi_2 series (for the same R), the a parameters are slightly larger. Perhaps the change in electron count affects the degree of metal-metal bonding in different directions.

5.2.3. $R_6Fe_{13}Bi$

The $R_6Fe_{13}Bi$ compounds, which are susceptible to rapid hydrolysis, were originally discovered for $R = Pr, Nd$ through arc melting of the elements followed by annealing at 800 °C for 4–7 d (Weitzer et al., 1993). The Sm analogue has been found during analysis of the Sm–Fe–Bi phase diagram (section 5.2.1). They belong to a large family of related compounds $R_6M_{13-x}X_{1+x}$ where M is Fe or Co and X can be a variety of p-block elements. Although the $R_6Fe_{13}Bi$ compounds are assumed to adopt the Nd₆Fe₁₃Si-type struc-

Table 9
Standardized positional parameters for $R_6\text{FeBi}_2$ compounds
(Morozkin, 2003a)^a

Compound	x_1	x_2
Y_6FeBi_2	0.237(2)	0.602(2)
Gd_6FeBi_2	0.243(2)	0.595(2)
Tb_6FeBi_2	0.243(2)	0.596(2)
Dy_6FeBi_2	0.244(3)	0.593(2)
Er_6FeBi_2	0.234(4)	0.601(3)
Tm_6FeBi_2	0.231(4)	0.595(3)
Lu_6FeBi_2	0.235(3)	0.608(2)

^a $R1$ at $3g$ ($x_1, 0, 1/2$); $R2$ at $3f$ ($x_2, 0, 0$); Fe at $1a$ ($0, 0, 0$); Bi at $2d$ ($1/3, 2/3, 1/2$).

ture (Pearson symbol $tI80$, space group $I4/mcm$ (No. 140), $Z = 4$) (Allemand et al., 1990) – an ordered variant of the $\text{La}_6\text{Co}_{11}\text{Ga}_3$ -type (Sichevich et al., 1985) – only powder X-ray diffraction data and no positional parameters are available. Under this assumption, the structure consists of two types of layers, one containing icosahedral iron clusters centred by an additional iron atom (FeFe_{12}) and another containing bicapped square antiprismatic rare earth clusters centred by a bismuth atom (BiR_{10}) (fig. 7). In analogy with other $R_6\text{Fe}_{13}X$ compounds, some type of ferrimagnetic ordering has been proposed ($T_C = 485$ K for $\text{Pr}_6\text{Fe}_{13}\text{Bi}$; 510 K for $\text{Nd}_6\text{Fe}_{13}\text{Bi}$), given the low observed magnetic moment of less than $\sim 1 \mu_B/\text{f.u.}$ The most remarkable property, however, is the ability of this family of compounds to absorb irreversibly an extraordinary amount of hydrogen at 120°C , typically up to about ~ 14 atoms per formula unit for the bismuthides (Coey et al., 1994). The tetragonal structure is retained, but the unit cell expands significantly along the c direction. The intercalation sites are proposed to lie within the layers containing the rare earth atoms, as inferred by analysis of the ^{57}Fe Mössbauer spectra. Upon hydrogen uptake, the magnetic moments of these compounds also increase dramatically ($31.7 \mu_B/\text{f.u.}$ for $\text{Pr}_6\text{Fe}_{13}\text{BiH}_{13.8}$; $33.1 \mu_B/\text{f.u.}$ for $\text{Nd}_6\text{Fe}_{13}\text{BiH}_{13.7}$), implying a fully ferromagnetic ordering of all magnetic sublattices.

5.2.4. Thin films

Amorphous ferrimagnetic thin films of a Gd–Fe–Bi alloy, with 80–100 nm thickness, have been prepared on glass substrates (Hansen and Urner-Wille, 1979; Urner-Wille et al., 1981; Hartmann and McGuire, 1983; Hartmann et al., 1985; McGuire and Hartmann, 1985). The composition of these films, determined by electron microprobe analysis, is $(\text{Gd}_{0.26}\text{Fe}_{0.74})_{1-x}\text{Bi}_x$, where x is between 0 and 0.2. The addition of Bi as a third component to these alloys of rare earth and transition metals improves their thermal stability and magneto-optical effects that may be useful in applications such as information storage media. A thermomagnetic switching device has been constructed using a $(\text{Gd}_{0.26}\text{Fe}_{0.74})_{0.95}\text{Bi}_{0.05}$ film in conjunction with a transparent electrode photoconductor sandwich (Heitmann et al., 1980).

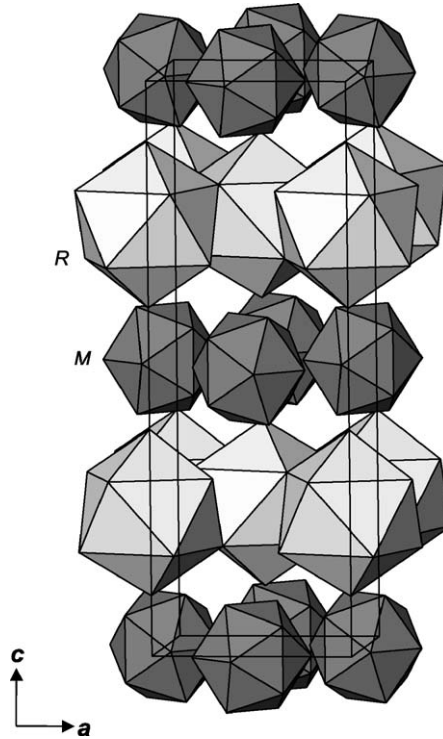


Fig. 7. Structure of $R_6\text{Fe}_{13}\text{Si}$ ($R = \text{Pr, Nd, Sm}$) and $\text{La}_6\text{Co}_{13}\text{Bi}$ ($\text{Nd}_6\text{Fe}_{13}\text{Si}$ -type).

5.3. $R\text{-Co-Bi}$

Similar to the Fe-containing systems, these Co-containing systems consist of metal-rich phases so far. Crystallographic data are listed in table 10.

5.3.1. $R_5\text{CoBi}_2$

In a recent report, Morozkin et al. (2005) claimed the existence of a series of $R_5\text{CoBi}_2$ ($R = \text{Gd, Tb, Dy, Ho, Er}$) compounds, prepared by arc melting of the elements under argon followed by annealing at 830°C for 240 h and quenching in water. These compounds were proposed to adopt a $\beta\text{-Yb}_5\text{Sb}_3$ -type structure (Pearson symbol $oP32$, space group $Pnma$ (No. 62), $Z = 4$), ostensibly by substitution of Co atoms in one of the Bi sites in the parent binaries $R_5\text{Bi}_3$. However, the rare earth bismuthides $R_5\text{Bi}_3$ adopt not the $\beta\text{-Yb}_5\text{Sb}_3$ -type, but rather the Mn_5Si_3 - or Y_5Bi_3 -type structures, the latter being similar but not identical to $\beta\text{-Yb}_5\text{Sb}_3$ -type (Wang et al., 1976). Magnetic measurements revealed ferromagnetic ordering for Dy_5CoBi_2 , Ho_5CoBi_2 , and Er_5CoBi_2 at $T_C = 34, 25$ and 20 K, respectively.

Table 10
Crystallographic data for R -Co-Bi compounds

Compound	Structure type	Pearson symbol	a (Å)	b (Å)	c (Å)	Reference
Gd ₅ CoBi ₂	β -Yb ₅ Sb ₃ ?	$oP32$	12.242(3)	9.099(2)	8.017(2)	(Morozkin et al., 2005)
Tb ₅ CoBi ₂	β -Yb ₅ Sb ₃ ?	$oP32$	12.160(3)	9.070(2)	7.975(2)	(Morozkin et al., 2005)
Dy ₅ CoBi ₂	β -Yb ₅ Sb ₃ ?	$oP32$	12.113(3)	8.983(2)	7.922(3)	(Morozkin et al., 2005)
Ho ₅ Co _{0.9} Bi _{2.1}	β -Yb ₅ Sb ₃ ?	$oP32$	12.114(2)	8.882(2)	7.893(2)	(Morozkin et al., 2005)
Er ₅ CoBi ₂	β -Yb ₅ Sb ₃ ?	$oP32$	11.968(4)	8.980(3)	7.906(2)	(Morozkin et al., 2005)
Y ₆ CoBi ₂	Zr ₆ CoAl ₂	$hP9$	8.312(1)		4.144(1)	(Morozkin, 2003c)
Ho ₆ CoBi ₂	Zr ₆ CoAl ₂	$hP9$	8.246(2)		4.095(1)	(Morozkin, 2003c)
Tm ₆ CoBi ₂	Zr ₆ CoAl ₂	$hP9$	8.155(2)		4.066(1)	(Morozkin, 2003c)
La ₆ Co ₁₃ Bi	Nd ₆ Fe ₁₃ Si	$tI80$	8.114(2)		23.477(9)	(Weitzer et al., 1993)
Y ₁₂ Co ₅ Bi	Ho ₁₂ Co ₅ Bi	$oI36$	9.524(3)	9.533(3)	9.952(2)	(Tkachuk and Mar, 2005)
Gd ₁₂ Co ₅ Bi	Ho ₁₂ Co ₅ Bi	$oI36$	9.602(4)	9.623(4)	10.054(3)	(Tkachuk and Mar, 2005)
Tb ₁₂ Co ₅ Bi	Ho ₁₂ Co ₅ Bi	$oI36$	9.502(3)	9.519(3)	9.989(2)	(Tkachuk and Mar, 2005)
Dy ₁₂ Co ₅ Bi	Ho ₁₂ Co ₅ Bi	$oI36$	9.459(3)	9.471(3)	9.949(2)	(Tkachuk and Mar, 2005)
Ho ₁₂ Co ₅ Bi	Ho ₁₂ Co ₅ Bi	$oI36$	9.387(1)	9.393(1)	9.884(1)	(Tkachuk and Mar, 2005)
Er ₁₂ Co ₅ Bi	Ho ₁₂ Co ₅ Bi	$oI36$	9.327(1)	9.328(1)	9.836(1)	(Tkachuk and Mar, 2005)
Tm ₁₂ Co ₅ Bi	Ho ₁₂ Co ₅ Bi	$oI36$	9.272(2)	9.276(2)	9.791(2)	(Tkachuk and Mar, 2005)

5.3.2. R_6CoBi_2

Only three R_6CoBi_2 ($R = Y, Ho, Tm$) compounds have been reported so far (Morozkin, 2003c), but presumably it should be possible to prepare other rare earth analogues to form a series as equally extensive as R_6MnBi_2 (section 5.1.3) and R_6FeBi_2 (section 5.2.2). As before, these were synthesized by arc melting of the elements followed by annealing under argon at 900 °C for 170 h and quenching in water. A Zr₆CoAl₂-type structure (Pearson symbol $hP9$, space group $P62m$ (No. 189), $Z = 1$) is adopted, which has been described earlier (section 5.1.3, fig. 6).

5.3.3. $R_6Co_{13}Bi$

Only $La_6Co_{13}Bi$ has been prepared, through arc melting of the elements followed by annealing at 800 °C for 7 d (Weitzer et al., 1993). Powder X-ray diffraction analysis suggests that it adopts the $Nd_6Fe_{13}Si$ -type (ordered $La_6Co_{11}Ga_3$ -type) structure, like the $R_6Fe_{13}Bi$ ($R = Pr, Nd, Sm$) compounds described previously (section 5.2.3). The absence of other rare earth analogues besides $La_6Co_{13}Bi$ has been attributed to size effects, decreasing the stability of $R_6M_{13}X$ ($X = p$ -block elements) as M is changed from Fe to Co. Although no magnetic data are available, $La_6Co_{13}Bi$ is expected to be ferromagnetic like other $La_6Co_{13}X$ compounds.

5.3.4. $R_{12}Co_5Bi$

A new series of $R_{12}Co_5Bi$ ($R = Y, Gd, Tb, Dy, Ho, Er, Tm$) compounds was recently prepared by arc melting of the elements (with a 5 wt.% excess of bismuth added to compensate for evaporative losses) followed by annealing at 600 °C for 720 h (Tkachuk and Mar, 2005). The crystal structure of one member, $Ho_{12}Co_5Bi$, was determined from high-resolution powder X-ray diffraction data obtained using synchrotron radiation and refined by the Rietveld technique. Standardized positional parameters for $Ho_{12}Co_5Bi$ are listed in table 11. The structure (Pearson symbol $oI36$, space group $Immm$ (No. 71), $Z = 2$) is related to the Ho_6Co_2Ga -type, adopted by compounds $R_6M_{2+x}X_{1-x}$ (where M is a transition metal (Co, Ni) and X is a p -block element (Ga, In, Sn, Pb)), but the distribution of atoms is different. In particular, the $2a$ site is exclusively occupied by Co atoms in $Ho_{12}Co_5Bi$, whereas it accommodates a mixture of M and X atoms in $R_6M_{2+x}X_{1-x}$, progressing to the other extreme of being occupied by all X atoms in Ho_6Co_2Ga itself. The structure can be built up of space-filling polyhedra with Ho atoms at the vertices (fig. 8a). The Co atoms are at the centres of compressed octahedra and distorted tetragonal antiprisms, whereas the Bi atoms are at the centres of icosahedra. If Schläfli symbols are used to denote the connectivity within nets (Wells, 1977), an alternative description involves the stacking of 3^2434 and 4^4 nets of Ho atoms, with Co and Bi atoms positioned within voids in the plane of the 4^4 nets (fig. 8b).

Complex electrical and magnetic properties are displayed by the $R_{12}Co_5Bi$ compounds (table 12). Although all these compounds are metallic, the electrical resistivity of polycrystalline samples does not follow a simple temperature dependence and in some instances shows kinks at temperatures that correspond to transitions seen also in the magnetic susceptibility. $Y_{12}Co_5Bi$ does not exhibit Curie–Weiss behaviour, showing instead a cusplike maximum at

Table 11
Standardized positional parameters for $Ho_{12}Co_5Bi$ (Tkachuk and Mar, 2005)

Atom	Wyckoff position	x	y	z
Ho1	$8n$	0.1843(2)	0.2834(2)	0
Ho2	$8m$	0.1977(2)	0	0.2155(2)
Ho3	$8l$	0	0.3044(2)	0.3132(2)
Co1	$4j$	1/2	0	0.3874(6)
Co2	$4e$	0.3767(6)	0	0
Co3	$2a$	0	0	0
Bi	$2c$	1/2	1/2	0

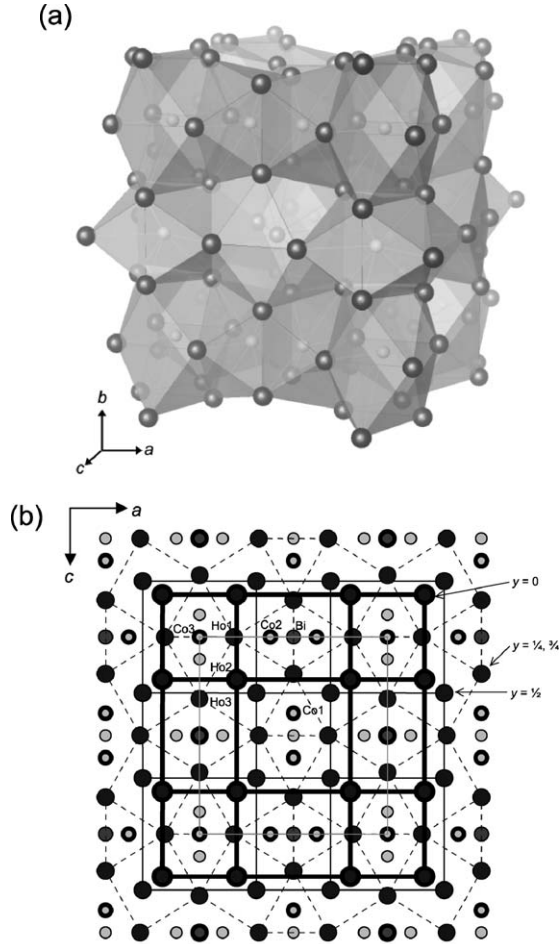


Fig. 8. Structure of $\text{Ho}_{12}\text{Co}_5\text{Bi}$ shown as (a) a polyhedral representation and (b) a stacking of interleaved $3^2 4^3 4$ (dashed lines) and 4^4 (solid lines) nets.

2.6 K in the dc magnetic susceptibility and frequency-dependent maxima in the ac magnetic susceptibility. All other compounds follow the Curie–Weiss law at high temperatures, and the effective magnetic moments are close to the free-ion moments for trivalent R ions, implying that there is probably little contribution from the Co atoms. $\text{Gd}_{12}\text{Co}_5\text{Bi}$ appears to undergo possible ferrimagnetic ordering at 120 K. There are at least three transitions in the temperature dependence of the magnetic susceptibility for $\text{Tb}_{12}\text{Co}_5\text{Bi}$, $\text{Dy}_{12}\text{Co}_5\text{Bi}$, or $\text{Ho}_{12}\text{Co}_5\text{Bi}$ and one for $\text{Er}_{12}\text{Co}_5\text{Bi}$ or $\text{Tm}_{12}\text{Co}_5\text{Bi}$, associated with antiferromagnetic ordering. These latter compounds also show metamagnetic transitions as revealed by the isothermal magnetization

Table 12
Electrical and magnetic properties of $R_{12}\text{Co}_5\text{Bi}$ compounds (Tkachuk and Mar, 2005)

Compound	$\rho_{300\text{ K}}$ ($\mu\Omega\text{ cm}$)	$\rho_{2\text{ K}}$ ($\mu\Omega\text{ cm}$)	μ^{eff} (μ_{B}/R^{3+})	μ_{RS} (μ_{B}/R^{3+})	θ_{p} (K)	T_{N} (K)
$\text{Y}_{12}\text{Co}_5\text{Bi}$	550	320	non-Curie–Weiss			
$\text{Gd}_{12}\text{Co}_5\text{Bi}$	650	500	7.72	7.94	111.9	118.2
$\text{Tb}_{12}\text{Co}_5\text{Bi}$	650	440	10.34	9.72	43.2	74.7
$\text{Dy}_{12}\text{Co}_5\text{Bi}$	640	480	11.71	10.65	14.4	39.8
$\text{Ho}_{12}\text{Co}_5\text{Bi}$	530	320	10.95	10.61	5.6	15.9
$\text{Er}_{12}\text{Co}_5\text{Bi}$	1280	870	9.36	9.58	0.4	6.9
$\text{Tm}_{12}\text{Co}_5\text{Bi}$	770	440	7.68	7.56	-4.0	2.7

curves at 2 K. RKKY interactions are implied by the proportionality of T_{N} values to the de Gennes factor.

The bonding in these $R_{12}\text{Co}_5\text{Bi}$ compounds was analyzed by extended Hückel band structure calculations using $\text{Y}_{12}\text{Co}_5\text{Bi}$ as a model compound. Y and Co d-states overlap significantly, giving rise to strong Y–Y and Y–Co bonding. Y–Co and Y–Bi, but not Y–Y bonding is optimized in this compound. An anomalously short Co–Co distance ($\sim 2.3\text{ \AA}$) probably arises from matrix effects.

5.3.5. Other data

As rare earth cobalt alloys serve as important magnetic materials, attempts have been made to dope the rare earth element with Bi. A bulk sample of global composition “ $\text{Sm}_{0.9}\text{Bi}_{0.1}\text{Co}_5$ ” was prepared by arc melting, but this led to a mixture of hexagonal (CaCu₅-type) and rhombohedral (presumably $\text{Th}_2\text{Zn}_{17}$ -type) phases (Washko et al., 1976). Amorphous thin films of $\text{Gd}(\text{Fe}_{1-x}\text{Co}_x)$ on glass substrates have been doped with Bi using an rf-magnetron sputtering system, but these are probably microstructurally inhomogenous owing to the formation of some Gd–Bi binary phase (Saiki et al., 1985). Through electrodeposition of Lu, Co, and Bi salts in dimethylsulfoxide (DMSO), amorphous thin films of Lu–Co–Bi on copper electrode substrates were prepared (Li et al., 2004a).

5.4. R–Rh–Bi

The only known compounds in R–Rh–Bi systems are the equiatomic phases RRhBi . Crystallographic data are listed in table 13. LaRhBi and CeRhBi were first prepared by reaction of the R element with a RhBi alloy (Yoshii et al., 1996, 1997), and the remaining members were subsequently prepared by arc melting of the elements, with a 10 wt.% excess of Bi added to compensate for evaporative losses, followed by annealing in evacuated silica tubes at 900 °C for 7 d (Haase et al., 2002). The compounds are stable in air. Only cell parameters determined from powder X-ray diffraction data were originally available for LaRhBi and CeRhBi , and the presence of impurities in a CeRhBi sample prevented its structure from being refined (Salamakha et al., 2000). Crystal structures were later refined from single-crystal X-ray diffraction data for SmRhBi and DyRhBi (Haase et al., 2002). Standardized positional parameters for SmRhBi and DyRhBi are listed in table 14. SmRhBi is strictly stoichiometric,

Table 13
Crystallographic data for R–Rh–Bi compounds

Compound	Structure type	Pearson symbol	<i>a</i> (Å)	<i>b</i> (Å)	<i>c</i> (Å)	Reference
LaRhBi	TiNiSi	<i>oP</i> 12	7.588	4.772	8.087	(Yoshii et al., 1997)
CeRhBi	TiNiSi	<i>oP</i> 12	7.438	4.740	7.985	(Yoshii et al., 1997)
CeRhBi	TiNiSi	<i>oP</i> 12	7.4648(5)	4.7173(4)	7.9715(6)	(Salamakha et al., 2000)
PrRhBi	TiNiSi	<i>oP</i> 12	7.417(2)	4.728(1)	8.009(2)	(Haase et al., 2002)
NdRhBi	TiNiSi	<i>oP</i> 12	7.377(2)	4.710(1)	8.008(2)	(Haase et al., 2002)
SmRhBi	TiNiSi	<i>oP</i> 12	7.291(2)	4.691(1)	7.971(2)	(Haase et al., 2002)
SmRhBi ^a	TiNiSi	<i>oP</i> 12	7.280(2)	4.679(1)	7.957(2)	(Haase et al., 2002)
GdRhBi	ZrNiAl	<i>hP</i> 9	7.616(1)		3.969(1)	(Haase et al., 2002)
TbRhBi	ZrNiAl	<i>hP</i> 9	7.596(2)		3.938(1)	(Haase et al., 2002)
DyRhBi	ZrNiAl	<i>hP</i> 9	7.583(2)		3.919(1)	(Haase et al., 2002)
DyRhBi ^a	ZrNiAl	<i>hP</i> 9	7.579(2)		3.926(1)	(Haase et al., 2002)
HoRhBi	ZrNiAl	<i>hP</i> 9	7.576(1)		3.912(1)	(Haase et al., 2002)
ErRhBi	ZrNiAl	<i>hP</i> 9	7.565(2)		3.892(1)	(Haase et al., 2002)

^aSingle-crystal data.

Table 14
Standardized positional parameters for SmRhBi (TiNiSi-type) and DyRhBi (ZrNiAl-type) (Haase et al., 2002)

Atom	Wyckoff position	<i>x</i>	<i>y</i>	<i>z</i>
SmRhBi				
Sm	4 <i>c</i>	0.01016(9)	1/4	0.70116(9)
Rh	4 <i>c</i>	0.2933(1)	1/4	0.4201(1)
Bi	4 <i>c</i>	0.19029(6)	1/4	0.09053(7)
DyRhBi				
Dy	3 <i>f</i>	0.60163(7)	0	0
Rh1	2 <i>d</i>	1/3	2/3	1/2
Rh2 ^a	1 <i>a</i>	0	0	0
Bi	3 <i>g</i>	0.26746(5)	0	1/2

^aOccupancy of 0.951(6).

but in DyRhBi, there is a perceptible deficiency in the Rh2 site, which has an occupancy of 0.951(6). These two compounds adopt different structure types, with SmRhBi being representative for the early *R* members and DyRhBi being representative of the later *R* members in the *RRhBi* series. Both structures are based on the motif of filled trigonal prisms, a common theme in the structural chemistry of many compounds with a metal-to-nonmetal ratio close to 2 : 1. SmRhBi adopts the orthorhombic TiNiSi-type structure (or anti-PbCl₂) (Pearson symbol *oP*12, space group *Pnma* (No. 62), *Z* = 4), which contains Bi-centred trigonal prisms whose vertices are four *R* and two Rh atoms. These trigonal prisms are connected to form layers parallel to the *ab* plane, and these layers are alternately displaced by $1/2b$ as they are stacked along the *c* direction (fig. 9a). (The use of the term “layers” is only meant to be descriptive and not to imply anything about bond strengths). DyRhBi adopts the hexagonal ZrNiAl-type structure (Pearson symbol *hP*9, space group $P\bar{6}2m$ (No. 189), *Z* = 3), with two types of Rh-centred trigonal prisms, whose vertices are either all *R* atoms or all Bi atoms (fig. 9b). This structure, an ordered variant of the Fe₂P-type structure, is similar to that of the *R*₆*M*Bi₂ (*M* = Mn, Fe, Co) compounds described earlier (fig. 6), but with a different ordering of the atom sites. Haase et al. (2002) have drawn attention to the relative sizes of atoms, which dictate the preferential occupation of sites, differing in coordination numbers, in these structures.

The physical properties of LaRhBi and CeRhBi have been studied carefully (Yoshii et al., 1996, 1997). The first measurements of the electrical resistivity were made on polycrystalline samples of CeRhBi, showing a double-peaked profile. A single crystal of CeRhBi was subsequently grown by the Bridgman method in a molybdenum crucible, and the double-peaked profile was retained in the electrical resistivity, which is lower along the *b* axis than along the *c* axis. A maximum at 70 K was attributed to a reduction of spin-dependent Kondo scattering caused by the crystal field, and a maximum at 6 K to the onset of coherent Kondo scattering. The magnetic susceptibility follows the Curie–Weiss law above 200 K, with a paramagnetic Curie temperature of –77.6 K and an effective magnetic moment of 2.68 μ_B/f.u. From its large electronic specific heat coefficient (500 mJ/mol K² at 2 K), CeRhBi was identified to be a non-magnetic heavy-fermion material. LaRhBi, a superconductor at 2.4 K, was used as a reference compound from which the magnetic contribution of the 4f electrons to the specific heat in CeRhBi could be determined. Further investigation of CeRhBi by ²⁰⁸Bi NQR measurements confirmed that no magnetic ordering occurs down to 0.15 K (Kawasaki et al., 2004).

5.5. *R*–Ni–Bi

The Ni-containing systems have been extensively studied and form a wide range of phases. Crystallographic data are listed in table 15.

5.5.1. Phase diagrams

Mozharivskii et al. (1998) have investigated the 450 °C sections of the Y–Ni–Bi and Ho–Ni–Bi phase diagrams, focusing on the metal-rich regions and avoiding the Bi-rich regions because of the low melting point of Bi (271 °C). In the Y–Ni–Bi system, YNiBi (MgAgAs-type) was

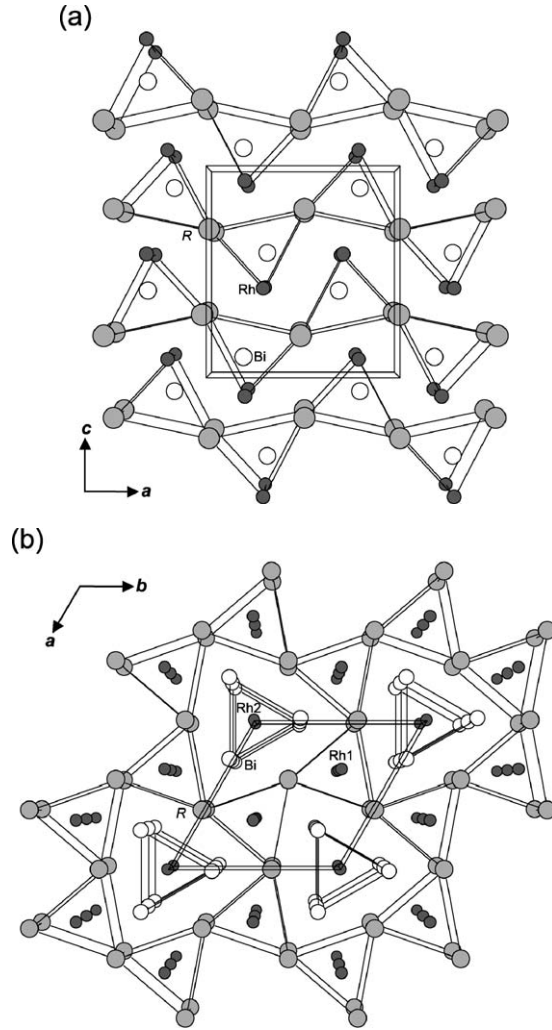


Fig. 9. Structures of $RRhBi$: (a) $TiNiSi$ -type for $R = La, Ce, Pr, Nd, Sm$, and (b) $ZrNiAl$ -type for $R = Gd, Tb, Dy, Ho, Er$.

reconfirmed, and three other compounds, Y_5Ni_2Bi , “ Y_5NiBi_2 ”, and “ $Y_{67}Ni_{38}Bi_5$ ” were identified from powder X-ray diffraction analysis. In the $Ho-Ni-Bi$ system, there exist $HoNiBi$ ($MgAgAs$ -type), Ho_5Ni_2Bi , and “ Ho_5NiBi_2 ”. The structures of “ Y_5NiBi_2 ”, “ $Y_{67}Ni_{38}Bi_5$ ”, and “ Ho_5NiBi_2 ” remain unknown, but listings of the unindexed powder patterns were provided. On the other hand, the structure of Ho_5Ni_2Bi was refined from the powder diffraction data, and the series has been subsequently expanded to include many other rare earths, R_5Ni_2Bi (Mozharivskiy and Franzen, 2000).

Table 15
 Crystallographic data for R–Ni–Bi compounds^{a,b,c,d}

Compound	Structure type	Pearson symbol	<i>a</i> (Å)	<i>c</i> (Å)	Reference
YNi _{0.82} Bi ₂	HfCuSi ₂	<i>tP8</i>	4.48350(4)	9.30026(2)	(Lu et al., 2005)
LaNi _{1+x} Bi ₂	HfCuSi ₂	<i>tP8</i>	4.565(1)	9.814(4)	(Hofmann and Jeitschko, 1988)
CeNi _{1.5} Bi ₂	HfCuSi ₂	<i>tP8</i>	4.546(1)	9.656(3)	(Hofmann and Jeitschko, 1988)
CeNiBi ₂	HfCuSi ₂	<i>tP8</i>	4.5419(9)	9.638(3)	(Flandorfer et al., 1996)
CeNiBi ₂	HfCuSi ₂	<i>tP8</i>	4.54(2)	9.63(8)	(Jung et al., 2002)
PrNi _{1+x} Bi ₂	HfCuSi ₂	<i>tP8</i>	4.5349(6)	9.604(1)	(Hofmann and Jeitschko, 1988)
NdNi _{1+x} Bi ₂	HfCuSi ₂	<i>tP8</i>	4.521(1)	9.556(3)	(Hofmann and Jeitschko, 1988)
NdNi _{0.64} Bi ₂ ^c	HfCuSi ₂	<i>tP8</i>	4.525(2)	9.546(4)	(Zeng and Franzen, 1998)
SmNi _{1+x} Bi ₂	HfCuSi ₂	<i>tP8</i>	4.5049(9)	9.438(3)	(Hofmann and Jeitschko, 1988)
GdNi _{1+x} Bi ₂	HfCuSi ₂	<i>tP8</i>	4.496(1)	9.370(2)	(Hofmann and Jeitschko, 1988)
GdNi _{0.86} Bi ₂	HfCuSi ₂	<i>tP8</i>	4.48882(5)	9.3658(2)	(Lu et al., 2005)
TbNi _{1+x} Bi ₂	HfCuSi ₂	<i>tP8</i>	4.4899(7)	9.309(2)	(Hofmann and Jeitschko, 1988)
TbNi _{0.78} Bi ₂	HfCuSi ₂	<i>tP8</i>	4.48486(3)	9.3062(2)	(Lu et al., 2005)
DyNi _{1+x} Bi ₂	HfCuSi ₂	<i>tP8</i>	4.481(3)	9.271(8)	(Hofmann and Jeitschko, 1988)
DyNi _{0.77} Bi ₂	HfCuSi ₂	<i>tP8</i>	4.47493(4)	9.25852(1)	(Lu et al., 2005)
ThNiBi ₂	unknown				(Smith and Ferris, 1970)
UNiBi ₂	HfCuSi ₂	<i>tP8</i>	4.470	9.073	(Kaczorowski, 1992)
ScNiBi	MgAgAs	<i>cF12</i>	6.191		(Dwight, 1974)
YNiBi	MgAgAs	<i>cF12</i>	6.411		(Dwight, 1974)
PrNiBi	MgAgAs	<i>cF12</i>	6.512(2)		(Haase et al., 2002)
NdNiBi	MgAgAs	<i>cF12</i>	6.479(2)		(Haase et al., 2002)
SmNiBi	MgAgAs	<i>cF12</i>	6.433(2)		(Haase et al., 2002)
GdNiBi	MgAgAs	<i>cF12</i>	6.435		(Dwight, 1974)
TbNiBi	MgAgAs	<i>cF12</i>	6.419(1)		(Haase et al., 2002)
DyNiBi	MgAgAs	<i>cF12</i>	6.415		(Dwight, 1974)
HoNiBi	MgAgAs	<i>cF12</i>	6.392(2)		(Marazza et al., 1980)
HoNiBi	MgAgAs	<i>cF12</i>	6.391(1)		(Mozharivskii et al., 1998)
HoNiBi	MgAgAs	<i>cF12</i>	6.391(1)		(Haase et al., 2002)
ErNiBi	MgAgAs	<i>cF12</i>	6.375(1)		(Haase et al., 2002)
TmNiBi	MgAgAs	<i>cF12</i>	6.368		(Dwight, 1974)
LuNiBi	MgAgAs	<i>cF12</i>	6.340		(Dwight, 1974)

continued on next page

Table 15, *continued*

Compound	Structure type	Pearson symbol	<i>a</i> (Å)	<i>c</i> (Å)	Reference
Y ₅ Ni ₂ Bi	Mo ₅ B ₂ Si	<i>tI</i> 32	7.673(2)	13.566(5)	(Mozharivskii et al., 1998; Mozharivsky and Kuz'ma, 1999)
Gd ₅ Ni ₂ Bi	Mo ₅ B ₂ Si	<i>tI</i> 32	7.756(2)	13.537(6)	(Mozharivskii et al., 1998; Mozharivsky and Kuz'ma, 1999)
Tb ₅ Ni ₂ Bi	Mo ₅ B ₂ Si	<i>tI</i> 32	7.693(2)	13.445(6)	(Mozharivskii et al., 1998; Mozharivsky and Kuz'ma, 1999)
Dy ₅ Ni ₂ Bi	Mo ₅ B ₂ Si	<i>tI</i> 32	7.651(4)	13.450(9)	(Mozharivskii et al., 1998; Mozharivsky and Kuz'ma, 1999)
Ho ₅ Ni ₂ Bi	Mo ₅ B ₂ Si	<i>tI</i> 32	7.6107(6)	13.397(1)	(Mozharivskii et al., 1998)
Ho ₅ Ni ₂ Bi	Mo ₅ B ₂ Si	<i>tI</i> 32	7.624(4)	13.420(6)	(Mozharivsky and Kuz'ma, 1999)
Ho ₅ Ni ₂ Bi	Mo ₅ B ₂ Si	<i>tI</i> 32	7.6140(3)	13.4435(6)	(Mozharivskyj and Franzen, 2000)
Er ₅ Ni _{1.72(4)} Bi	Mo ₅ B ₂ Si	<i>tI</i> 32	7.5813(9)	13.395(2)	(Mozharivsky and Kuz'ma, 1999)
Tm ₅ Ni ₂ Bi	Mo ₅ B ₂ Si	<i>tI</i> 32	7.522(4)	13.411(8)	(Mozharivsky and Kuz'ma, 1999)
Lu ₅ Ni ₂ Bi	Mo ₅ B ₂ Si	<i>tI</i> 32	7.429(2)	13.415(9)	(Mozharivsky and Kuz'ma, 1999)
"Y ₅ NiBi ₂ "	unknown				(Mozharivskii et al., 1998)
"Ho ₅ NiBi ₂ "	unknown				(Mozharivskii et al., 1998)
"Y ₆₇ Ni ₃₈ Bi ₅ "	unknown				(Mozharivskii et al., 1998)

^aRNi_{1-x}Bi₂: Defect HfCuSi₂-type, space group *P4/nmm* (No. 129), *Z* = 2; *R* in 2*c* (1/4, 1/4, ~0.27), Ni in 2*b* (3/4, 1/4, 1/2), Bi1 in 2*c* (1/4, 1/4, ~0.64), Bi2 in 2*a* (3/4, 1/4, 0).

^bRNi_{1+x}Bi₂: Stuffed HfCuSi₂-type or defect CaBe₂Ge₂-type. Same as above but with an additional Ni site at 2*c* (1/4, 1/4, ~0.88).

^cRNiBi: MgAgAs-type, space group *F* $\bar{4}3m$ (No. 216), *Z* = 4; *R* in 4*b* (1/2, 1/2, 1/2), Ni in 4*c* (1/4, 1/4, 1/4), Bi in 4*a* (0, 0, 0).

^dR₅Ni₂Bi: Mo₅B₂Si-type, space group *I4/mcm* (No. 140), *Z* = 4. Atomic parameters for Ho₅Ni₂Bi: Ho1 in 4*c* (0, 0, 0), Ho2 in 16*l* (0.1555(2), *x* + 1/2, 0.1372(1)), Ni in 8*h* (0.3706(6), *x* + 1/2, 0), Bi in 4*a* (0, 0, 1/4) (Mozharivskyj and Franzen, 2000).

^eSingle-crystal data.

5.5.2. $RNi_{1+x}Bi_2 \dots RNiBi_2 \dots RNi_{1-x}Bi_2$

The first in a series of layered compounds in this system was originally identified as $RNi_{2-x}Bi_2$ (Hofmann and Jeitschko, 1988), but in view of more recent results, perhaps these are better formulated as $RNi_{1+x}Bi_2$. They were prepared for $R = La, Ce, Pr, Nd, Sm, Gd, Tb, Dy$ from the reaction of R filings, Ni powder, and Bi powder in a 1 : 2 : 2 ratio in evacuated silica tubes between 750 and 800 °C, resulting in presumably multiple-phase samples. No single-crystal structure refinements were performed at the time, but x was assumed to be close to 0.5, in analogy to corresponding antimonides such as $LaNi_{1.51}Sb_2$, and a wide homogeneity range was expected. A listing of intensities from the Guinier powder pattern for $CeNi_{1.5}Bi_2$ was reported and compared with a hypothetical pattern calculated assuming atomic positions and occupations based on $LaNi_{1.51}Sb_2$.

Later, other groups carried out reactions in which the atomic ratio of $R : Ni : Bi$ is closer to 1 : 1 : 2. Flandorfer et al. (1996) reacted ingots of Ce, Ni, and Bi by arc melting, followed by annealing at 600 °C for 170 h, resulting in “ $CeNiBi_2$ ”. $CeNiBi_2$ was also prepared by Jung et al. (2002), who give no synthesis details, and by Thamizhavel et al. (2003), who prepared crystals using excess Bi as a self-flux. The elements were reacted in “an appropriate ratio” within an alumina crucible placed in a silica tube under argon, which was heated at 1000 °C for 2 d, cooled to 650 °C over 4 weeks, and then rapidly cooled to room temperature. The Bi flux was removed by centrifugation, resulting in large plate-shaped single crystals ($4 \times 3 \times 3$ mm). “ $NdNi_{1-x}Bi_2$ ” was prepared by Zeng and Franzen (1998), who reacted Nd foil with a cold-pressed mixture of $NiBi_2$, with an 8 wt.% excess of Bi added, by arc melting, followed by annealing encased in Ta foil within a silica tube at 700 °C for 20 d. Recently, Lu et al. (2005) prepared $RNi_{1-x}Bi_2$ for $R = Y, Gd, Tb, Dy$ by arc melting of samples with nominal composition “ $RNi_{0.8}Bi_2$ ” with a 6 wt.% excess of Bi, followed by annealing at 600 °C for 8 d.

It is fairly certain that the structures of these compounds must be based on the $HfCuSi_2$ -type structure, or some variant thereof, shown in fig. 10. (The $HfCuSi_2$ -type structure is also known by other names, such as $ZrCuSi_2$ -type or $CaMnBi_2$ -type.) The idealized structure consists of R atoms separating anionic ${}^2_\infty[NiBi]$ layers (built up from edge-sharing $NiBi_4$ tetrahedra) and square nets of Bi atoms (fig. 10b). The only single-crystal investigation performed so far, on a Nd member of this series, revealed a significant deficiency on the nickel site, with the refined formula being $NdNi_{0.64}Bi_2$ (Zeng and Franzen, 1998). This type of defect $HfCuSi_2$ -type structure (fig. 10a) is quite common among the corresponding rare earth transition-metal antimonides, $RM_{1-x}Sb_2$. Rietveld refinements of powder X-ray diffraction data confirmed that this deficiency also exists for other members: $YNi_{0.82}Bi_2$, $GdNi_{0.86}Bi_2$, $TbNi_{0.78}Bi_2$, and $DyNi_{0.77}Bi_2$ (Lu et al., 2005). Standardized positional parameters are listed in table 16. The compounds first prepared by Hofmann and Jeitschko (1988) were proposed to adopt defect $CaBe_2Ge_2$ -type structures, where the R atoms separate two types of layers, in which the Ni and Bi atoms are interchanged, so that half the Ni atoms are coordinated in a tetrahedral fashion by the Bi atoms and the other half in a square pyramidal fashion (fig. 10c). If the deficiency in the square pyramidal sites is significant ($RNi_{2-x}Bi_2$ with large x), then an alternative description is that this corresponds to a stuffed $HfCuSi_2$ -type structure ($RNi_{1+x}Bi_2$ with small x). A similar situation arises in the $RCu_{1+x}As_2$ series (Wang et al., 1999;

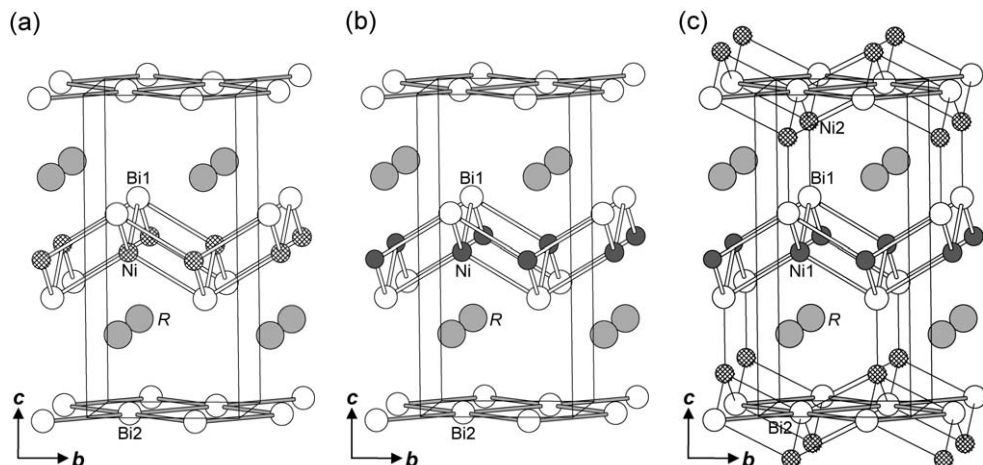


Fig. 10. Structures of (a) $RNi_{1-x}Bi_2$ (defect HfCuSi₂-type), (b) $RNiBi_2$ (HfCuSi₂-type), and (c) $RNi_{1+x}Bi_2$ (stuffed HfCuSi₂-type or defect CaBe₂Ge₂-type). Hatched spheres represent partially occupied Ni sites.

Table 16
Standardized positional parameters for $RNi_{1-x}Bi_2$ compounds (Lu et al., 2005; Zeng and Franzen, 1998)^a

Compound	z_1	z_2
$YNi_{0.82}Bi_2$	0.2691(4)	0.6444(9)
$NdNi_{0.64}Bi_2$ ^b	0.2687(5)	0.6424(4)
$GdNi_{0.86}Bi_2$	0.2699(3)	0.6400(2)
$TbNi_{0.78}Bi_2$	0.2604(4)	0.6465(2)
$DyNi_{0.77}Bi_2$	0.2697(3)	0.6434(2)

^aDefect HfCuSi₂-type, space group $P4/nmm$ (No. 129), $Z = 2$; R in $2c$ ($1/4, 1/4, z_1$), Ni in $2b$ ($3/4, 1/4, 1/2$), Bi1 in $2c$ ($1/4, 1/4, z_2$), Bi2 in $2a$ ($3/4, 1/4, 0$).

^bSingle-crystal data.

Jemetio et al., 2002). Since most of the crystallographic work on these compounds has been limited to powder X-ray diffraction data, the degree of nonstoichiometry arising from the Ni partial occupancy in either $RNi_{1+x}Bi_2$ or $RNi_{1-x}Bi_2$ remains somewhat ambiguous and requires further investigation. An interesting observation is that on going from an antimonide to the corresponding bismuthide, the a parameter is larger, as expected, but the c parameter is smaller (e.g., $LaNi_{1.51}Sb_2$, $a = 4.466(1) \text{ \AA}$, $c = 9.918(2) \text{ \AA}$; $LaNi_{2-x}Bi_2$, $a = 4.565(1) \text{ \AA}$, $c = 9.814(4) \text{ \AA}$).

Physical properties have been measured only for $CeNiBi_2$ so far. In view of the nonstoichiometry problems discussed above, it will be important in future investigations to establish the composition of these compounds more firmly, as this will most certainly affect the

physical properties. From measurements on a powder sample, CeNiBi_2 was identified as an antiferromagnetic Kondo-lattice compound (Jung et al., 2002) with $T_N = 6$ K. The high-temperature (50–300 K) magnetic susceptibility was fit to the modified Curie–Weiss law, yielding $\chi_0 = 0.00791$ emu/mol, $\mu_{\text{eff}} = 2.83 \mu_B/\text{Ce}$, and $\theta_p = -27.7$ K. The isothermal magnetization at 1.5 K reveals a metamagnetic transition at 5 T. The electrical resistivity shows a broad shoulder at 100 K, attributed to Kondo and crystal-field effects, and a sharp decrease at $T_N = 6$ K. With increasing applied field, this sharp transition at T_N in the electrical resistivity is suppressed, and the slope of the magnetoresistance changes from positive to negative. Large single crystals of CeNiBi_2 grown from Bi flux were examined by Thamizhavel et al. (2003). There are some differences from the data measured on the powder sample above, which are attributed to the presence of trace amounts of Bi. The antiferromagnetic ordering ($T_N = 4.7$ K) was confirmed, with the easy axis being parallel to the c direction, and a magnetic phase diagram was determined. Specific heat measurements indicate a large value of $\gamma = 470$ mJ/K² mol, implying heavy-fermion behaviour.

5.5.3. $R\text{NiBi}$

The earliest report of a study of the R –Ni–Bi system was by Dwight (1974), who prepared equiatomic $R\text{NiBi}$ compounds by arc melting for some of the smaller R elements ($R = \text{Sc}, \text{Y}, \text{Gd}, \text{Dy}, \text{Tm}, \text{Lu}$), in analogy to $R\text{NiSb}$. From Debye-Scherrer powder X-ray diffraction patterns, he identified these compounds to have the MgAgAs-type structure (having no free positional parameters) and obtained their cell parameters. HoNiBi was identified by Marazza et al. (1980) and reconfirmed by Mozharivskii et al. (1998), who refined the structure from powder diffraction data. Recently, the $R\text{NiBi}$ series has been considerably extended by Haase et al. (2002), who prepared well-crystallized, air-stable, black samples by arc melting of the elements (R chips or ingots, Ni powder, and Bi shot, all with >99.9% purity) in the strict atomic ratio 1 : 1 : 1, annealing at 800 °C for 7 d, and quenching in air. Cell parameters were refined from Guinier powder patterns on these samples, and the atomic distribution in PrNiBi was determined by comparison of experimental and calculated intensities from different models. The structure of $R\text{NiBi}$ (MgAgAs-type) is also adopted by RPdBi and RPtBi (sections 5.6.2, 5.7.2, figs. 12a, 14). As first described by Dwight (1974), the R and Bi atoms are arranged as in the NaCl-type structure of the binary rare earth bismuthides $R\text{Bi}$. The Ni atoms are then inserted in half of the octants within the cubic unit cell, being coordinated tetrahedrally by R atoms and tetrahedrally by Bi atoms. This relationship led Dwight to demonstrate that Ni atoms could gradually enter a parent binary antimonide DySb , to form a solid solution up to $\text{DyNi}_{0.26}\text{Sb}$. The solubility of Ni in the corresponding binary bismuthides $R\text{Bi}$ has not yet been investigated. The structure of $R\text{NiBi}$ is, of course, also the same as that of the so-called half-Heusler alloys such as $M\text{NiSn}$ ($M = \text{Ti}, \text{Zr}, \text{Hf}$) which have attracted attention given their potential as thermoelectric materials. Although no physical property measurements are available for $R\text{NiBi}$, a LAPW (linearized augmented plane-wave) band structure calculation was carried out on YNiBi , which was predicted to be a narrow band-gap semiconductor with an indirect gap of 0.13 eV (Larson et al., 1999).

5.5.4. R_5Ni_2Bi

The R_5Ni_2Bi compounds ($R = Y, Gd, Tb, Dy, Ho, Er, Tm, Lu$) were prepared by arc melting of 1 g stoichiometric mixtures of R , Ni, and Bi, followed by annealing in evacuated silica tubes at 800 °C for 10 d (Mozharivskyj and Franzen, 2000). An earlier Rietveld refinement suggested a significant Ni deficiency for $Er_5Ni_{1.72(4)}Bi$ (Mozharivsky and Kuz'ma, 1999), but a subsequent, more reliable refinement for Ho_5Ni_2Bi (and the corresponding antimonide Ho_5Ni_2Sb) did not reveal any deficiencies (Mozharivskyj and Franzen, 2000). The R_5Ni_2Bi series most likely is strictly stoichiometric for all existing members (Mozharivskyj, 2005). The structure, shown in fig. 11, corresponds to the Mo_5B_2Si -type, an ordered variant of the Cr_5B_3 -type. It can be considered to be built up from 3^2434 nets of $R2$ atoms stacked in an ABBA sequence along the c direction, in which the A and B nets are rotated by 45° relative to each other. Between nets in the same orientation (AA or BB) are trigonal prismatic and tetragonal prismatic voids, and between nets in different orientation (AB) are tetrahedral and tetragonal antiprismatic voids. Ni atoms occupy the trigonal prismatic, Bi atoms the tetragonal antiprismatic, and $R1$ atoms the tetragonal prismatic sites. In Ho_5Ni_2Bi , there is a rather short Ho2–Ho2 distance of 3.348(2) Å that arises because of the need to maintain reasonable Ho2–Bi distances within the tetragonal antiprisms. Physical properties have not been reported for any members of this series, but they are expected to be good metallic conductors and their magnetic properties should be quite interesting in light of what has been found in the related $R_{12}Co_5Bi$ series (Tkachuk and Mar, 2005).

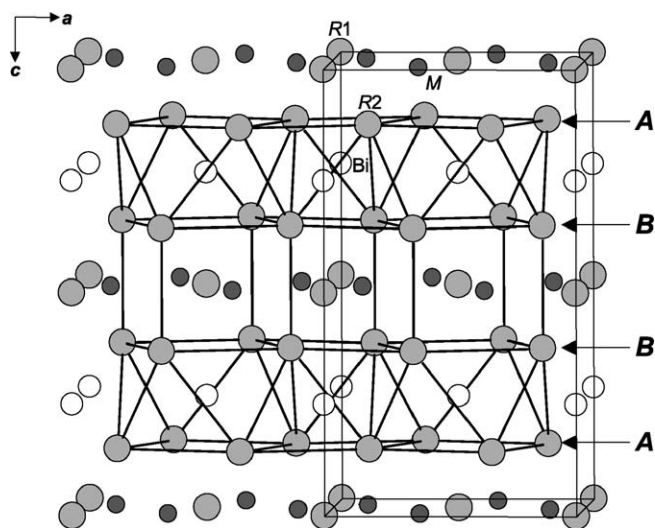


Fig. 11. Structure of R_5M_2Bi ($R = Y, Gd, Tb, Dy, Ho, Er, Tm, Lu$; $M = Ni, Pd, Pt$) (Mo_5B_2Si -type).

5.5.5. Actinide compounds

Interestingly, ThNiBi₂ was identified well before any of the RNiBi₂ compounds mentioned above through an investigation of the effect of adding nickel on the solubility of thorium in liquid bismuth in the temperature range of 550–700 °C (Smith and Ferris, 1970). An unindexed powder X-ray diffraction pattern was provided. At 650 °C, the standard free energy of formation of ThNiBi₂ was found to be –51 kcal/mol. Powder samples of UNiBi₂ were prepared by reaction of UBi₂ and Ni in silica tubes at 700 °C for 2 weeks (Kaczorowski, 1992). The structure is assumed to be the HfCuSi₂-type, as determined from powder X-ray diffraction data. Magnetic susceptibility measurements indicate antiferromagnetic ordering below 166 K.

5.5.6. Thin films

Amorphous Lu–Ni–Bi thin films on copper electrode substrates have been grown by electrodeposition of Lu, Ni, and Bi salts in DMSO (Li et al., 2004b).

5.6. R–Pd–Bi

The Pd-containing phases have relatively simple crystal structures but they display interesting physical properties. Crystallographic data are listed in table 17.

Table 17
Crystallographic data for R–Pd–Bi compounds^{a,b,c,d,e}

Compound	Structure type	Pearson symbol	<i>a</i> (Å)	<i>c</i> (Å)	Reference
EuPd ₂ Bi ₂	CaBe ₂ Ge ₂	<i>tP</i> 10	4.735(2)	10.297(6)	(Hofmann and Jeitschko, 1985)
ScPdBi	MgAgAs	<i>cF</i> 12	6.435(1)		(Haase et al., 2002)
YPdBi	MgAgAs	<i>cF</i> 12	6.640		(Marazza et al., 1980)
LaPdBi	MgAgAs	<i>cF</i> 12	6.825(1)		(Haase et al., 2002)
CePdBi	MgAgAs	<i>cF</i> 12	6.830		(Marazza et al., 1980)
PrPdBi	MgAgAs	<i>cF</i> 12	6.794		(Riani et al., 1995)
PrPdBi	MgAgAs	<i>cF</i> 12	6.797(1)		(Haase et al., 2002)
NdPdBi	MgAgAs	<i>cF</i> 12	6.778		(Marazza et al., 1980)
SmPdBi	MgAgAs	<i>cF</i> 12	6.757		(Riani et al., 1995)
SmPdBi	MgAgAs	<i>cF</i> 12	6.719(2)		(Haase et al., 2002)
GdPdBi	MgAgAs	<i>cF</i> 12	6.698		(Marazza et al., 1980)
TbPdBi	MgAgAs	<i>cF</i> 12	6.650		(Riani et al., 1995)
TbPdBi	MgAgAs	<i>cF</i> 12	6.660(1)		(Haase et al., 2002)
DyPdBi	MgAgAs	<i>cF</i> 12	6.643		(Marazza et al., 1980)
HoPdBi	MgAgAs	<i>cF</i> 12	6.610		(Marazza et al., 1980)
ErPdBi	MgAgAs	<i>cF</i> 12	6.594(1)		(Haase et al., 2002)
TmPdBi	MgAgAs	<i>cF</i> 12	6.564(1)		(Haase et al., 2002)
YbPdBi	MgAgAs	<i>cF</i> 12	6.592		(Marazza et al., 1980)

continued on next page

Table 17, *continued*

Compound	Structure type	Pearson symbol	a (Å)	c (Å)	Reference
YbPdBi	MgAgAs	$cF12$	6.590		(Dhar et al., 1988)
YbPdBi	MgAgAs	$cF12$	6.5975(5)		(LeBras et al., 1995)
YbPdBi	MgAgAs	$cF12$	6.5934(3)		(Kaczorowski et al., 1999)
LuPdBi	MgAgAs	$cF12$	6.566(1)		(Haase et al., 2002)
YPd ₂ Bi	MnCu ₂ Al	$cF16$	6.825		(Riani et al., 1995)
PrPd ₂ Bi	MnCu ₂ Al	$cF16$	6.928		(Riani et al., 1995)
SmPd ₂ Bi	MnCu ₂ Al	$cF16$	6.882		(Riani et al., 1995)
GdPd ₂ Bi	MnCu ₂ Al	$cF16$	6.865		(Riani et al., 1995)
TbPd ₂ Bi	MnCu ₂ Al	$cF16$	6.838		(Riani et al., 1995)
DyPd ₂ Bi	MnCu ₂ Al	$cF16$	6.824		(Riani et al., 1995)
HoPd ₂ Bi	MnCu ₂ Al	$cF16$	6.817		(Riani et al., 1995)
ErPd ₂ Bi	MnCu ₂ Al	$cF16$	6.798		(Riani et al., 1995)
YbPd ₂ Bi	MnCu ₂ Al	$cF16$	6.893		(Riani et al., 1995)
Y ₅ Pd ₂ Bi	Mo ₅ B ₂ Si	$I32$	7.779(1)	13.699(5)	(Mozharivskiy and Franzen, 2000)
Gd ₅ Pd ₂ Bi	Mo ₅ B ₂ Si	$I32$	7.864(2)	13.644(4)	(Mozharivskiy and Franzen, 2000)
Tb ₅ Pd ₂ Bi	Mo ₅ B ₂ Si	$I32$	7.820(1)	13.585(2)	(Mozharivskiy and Franzen, 2000)
Dy ₅ Pd ₂ Bi	Mo ₅ B ₂ Si	$I32$	7.770(2)	13.558(5)	(Mozharivskiy and Franzen, 2000)
Ho ₅ Pd ₂ Bi	Mo ₅ B ₂ Si	$I32$	7.719(1)	13.563(5)	(Mozharivskiy and Franzen, 2000)
Er ₅ Pd ₂ Bi	Mo ₅ B ₂ Si	$I32$	7.695(1)	13.527(4)	(Mozharivskiy and Franzen, 2000)
Tm ₅ Pd ₂ Bi	Mo ₅ B ₂ Si	$I32$	7.652(1)	13.474(4)	(Mozharivskiy and Franzen, 2000)
Lu ₅ Pd ₂ Bi	Mo ₅ B ₂ Si	$I32$	7.586(2)	13.440(6)	(Mozharivskiy and Franzen, 2000)
Ce ₈ Pd ₂₄ Bi	Ce ₈ Pd ₂₄ Sb	$cP33$	8.4601(8)		(Gordon et al., 1996)

^aEuPd₂Bi₂: CaBe₂Ge₂-type, space group $P4/nmm$ (No. 129), $Z = 2$. Presumed atomic parameters: Eu in $2c$ ($1/4, 1/4, \sim 0.27$), Pd1 in $2b$ ($3/4, 1/4, 1/2$), Pd2 in $2c$ ($1/4, 1/4, \sim 0.88$), Bi1 in $2c$ ($1/4, 1/4, \sim 0.64$), Bi2 in $2a$ ($3/4, 1/4, 0$).

^bRPdBi: MgAgAs-type (“half-Heusler”), space group $F\bar{4}3m$ (No. 216), $Z = 4$; R in $4b$ ($1/2, 1/2, 1/2$), Pd in $4c$ ($1/4, 1/4, 1/4$), Bi in $4a$ ($0, 0, 0$).

^cRPd₂Bi: MnCu₂Al-type (ordered BiF₃-type, “Heusler”), space group $Fm\bar{3}m$ (No. 225), $Z = 4$; R in $4b$ ($1/2, 1/2, 1/2$), Pd in $8c$ ($1/4, 1/4, 1/4$), Bi in $4a$ ($0, 0, 0$).

^dR₅Pd₂Bi: Mo₅B₂Si-type, space group $I4/mcm$ (No. 140), $Z = 4$. Atomic parameters for isostructural Ho₅Ni₂Bi: Ho1 in $4c$ ($0, 0, 0$), Ho2 in $16l$ ($0.1555(2), x + 1/2, 0.1372(1)$), Ni in $8h$ ($0.3706(6), x + 1/2, 0$), Bi in $4a$ ($0, 0, 1/4$) (Mozharivskiy and Franzen, 2000).

^eCe₈Pd₂₄Bi: Ce₈Pd₂₄Sb-type, space group $Pm\bar{3}m$ (No. 221), $Z = 1$. Atomic parameters for isostructural Ce₈Pd₂₄Sb: Ce in $8g$ ($0.25140(3), x, x$), Pd1 in $6f$ ($0.25552(8), 1/2, 1/2$), Pd2 in $6e$ ($0.31118(11), 0, 0$), Pd3 in $12h$ ($0.26675(7), 1/2, 0$), Sb in $1a$ ($0, 0, 0$) (Gordon and DiSalvo, 1996).

5.6.1. RPd_2Bi_2

The only known representative is $EuPd_2Bi_2$, for which only cell parameters refined from a Guinier powder pattern are available (Hofmann and Jeitschko, 1985). A $CaBe_2Ge_2$ -type structure was proposed. Because the structure of the corresponding antimonide, $EuPd_2Sb_2$, refined from single-crystal data shows no anomalies, it is assumed that $EuPd_2Bi_2$ also suffers from no deficiencies in the Pd sites, but this has not been confirmed. Given the close relationship of the $CaBe_2Ge_2$ -type structure to the defect or stuffed $HfCuSi_2$ -type phases so prevalent among other ternary rare earth pnictides ($RM_{1-x}Pn_2$ or $RM_{1+x}Pn_2$), it is curious that no $RPd_{1-x}Bi_2$ or $RPd_{1+x}Bi_2$ phases have yet been prepared.

5.6.2. $RPdBi$

The equiatomic compounds $RPdBi$ ($R = Y, Ce, Pr, Nd, Sm, Gd, Tb, Dy, Ho, Yb$) were prepared by melting of the elements placed in sealed Ta crucibles within an induction furnace (Marazza et al., 1980; Riani et al., 1995). Analysis of the powder X-ray diffraction patterns revealed these phases to have the $MgAgAs$ -type structure, shown in fig. 12a, in which Pd atoms enter half the octants within the cubic unit cell. Given the clear relationship to the NaCl-type structure of the binary rare earth bismuthides RBi , the solubility of Pd was examined. Metallographic and X-ray diffraction analysis of several $GdPd_xBi$ samples showed that they were heterogeneous, implying negligible solubility of Pd in RBi phases (Marazza et al., 1980), in contrast to that of Ni (Dwight, 1974). The remaining members of the $RPdBi$ series ($R = Sc, La, Pr, Sm, Tb, Er, Tm, Lu$) were prepared by annealing cold-pressed pellets of the elements in evacuated silica tubes at $600^\circ C$ for 3 h, followed by melting in a high-frequency furnace (Haase et al., 2002).

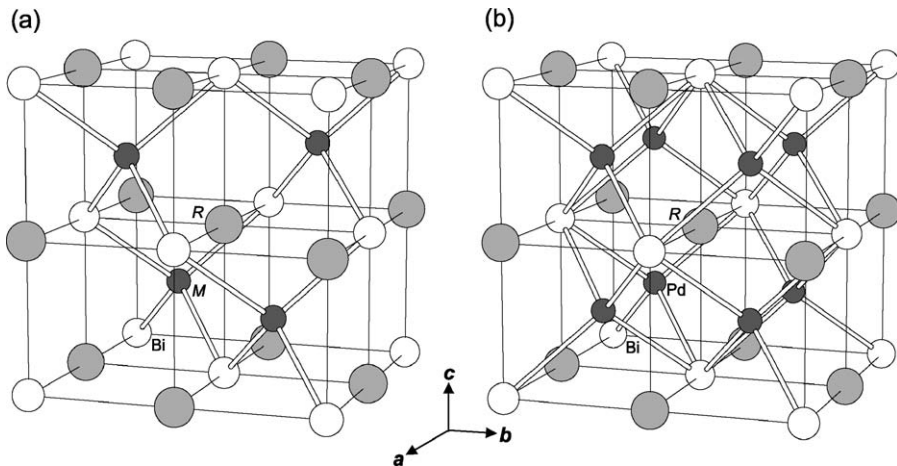


Fig. 12. Structures of (a) $RMBi$ ($M = Ni, Pd, Pt$) ($MgAgAs$ -type) and (b) RPd_2Bi ($MnCu_2Al$ -type).

5.6.3. RPd_2Bi

As with the $RPdBi$ series, the compounds RPd_2Bi ($R = Y, Pr, Sm, Gd, Tb, Dy, Ho, Er, Yb$) were also prepared by melting of the elements placed in sealed Ta crucibles within an induction furnace, following by annealing at 750 °C for 1 week (Riani et al., 1995). The RPd_2Bi compounds adopt the $MnCu_2Al$ -type structure, shown in fig. 12b, which illustrates the relationship to the $MgAgAs$ -type structure adopted by $RPdBi$. In RPd_2Bi , the Pd atoms enter *all* the octants within the cubic unit cell. Analysis of the cell parameters for samples along the $GdBi$ – $GdPd_2Bi$ section clearly indicate that $GdPdBi$ and $GdPd_2Bi$ are strictly stoichiometric.

5.6.4. *Properties of $RPdBi$ and RPd_2Bi*

The compounds $RPdBi$ and RPd_2Bi belong to two larger series known as half-Heusler and Heusler alloys, respectively. Given the existence of other erbium-based intermetallics that are magnetic superconductors, Kaczorowski et al. (2005) have recently investigated the properties of $ErPdBi$ and $ErPd_2Bi$. The samples were prepared by arc melting followed by annealing at 800–1000 °C for several weeks. Properties were measured directly on the as-cast sample of $ErPdBi$ owing to problems of decomposition after annealing. Both $ErPdBi$ and $ErPd_2Bi$ are paramagnetic due to Er^{3+} ions, obeying the Curie–Weiss law with no apparent transitions in the magnetic susceptibility curves down to 1.7 K. However, the electrical resistivity shows complicated dependence with temperature. For $ErPdBi$, the resistivity varies only slightly, reaching a broad maximum of 1000 $\mu\Omega$ cm near 160 K but dropping suddenly below 7.5 K. For $ErPd_2Bi$, the resistivity at 300 K is about 140 $\mu\Omega$ cm but displays several anomalies upon cooling, including one at 168 K that was attributed to a first-order structural phase transition to a lower symmetry. The behaviour of both these compounds was speculated to arise from the formation of narrow gaps near the Fermi level.

$YbPdBi$ has been studied extensively. It was first identified as a possible mixed-valent heavy-fermion compound, with evidence from magnetic susceptibility and heat capacity measurements showing a lower than expected magnetic moment of 4.04 μ_B/Yb (cf., 4.54 μ_B for trivalent Yb) and a large γ value of 470 mJ/mol K² (Dhar et al., 1988). A later analysis revealed an effective magnetic moment closer to 4.4 μ_B , a second-order magnetic ordering transition near 1 K, and a non-cubic symmetry around the Yb site (LeBras et al., 1995). From a re-measurement of the heat capacity, the earlier γ value was challenged, but the heavy fermion behaviour was clearly supported by the electrical resistivity curve, which reveals a broad maximum near 25 K followed by a sharp drop and T^2 -dependence at low temperatures (Kaczorowski et al., 1999). The magnetoresistance follows scaling consistent with Kondo-impurity behaviour, and the anomaly in the specific heat was attributed to antiferromagnetic ordering (Pietri et al., 2000). X-ray photoemission spectroscopy and tight-binding LMTO measurements were carried out recently, and these support the presence of a mixed valence state for Yb, which has an effective valence of ~ 2.74 (Szytuła et al., 2003).

5.6.5. R_5Pd_2Bi

In analogy to R_5Ni_2Bi compounds, the series R_5Pd_2Bi ($R = Y, Gd, Tb, Dy, Ho, Er, Tm, Lu$) was prepared by arc melting of 1 g stoichiometric mixtures of R , Pd, and Bi, followed by annealing in evacuated silica tubes at 800 °C for 10 d (Mozharivskiy and Franzen, 2000). Only

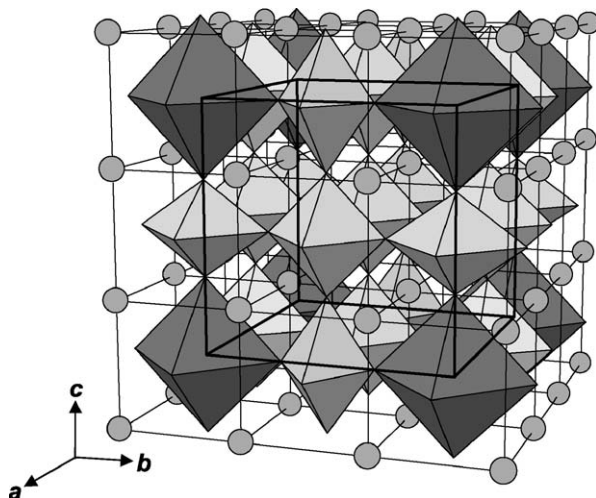


Fig. 13. Structure of $\text{Ce}_8\text{Pd}_{24}\text{Bi}$, consisting of octahedral Pd_6 clusters that are either empty (lightly shaded) or centred by Bi atoms (heavily shaded polyhedra). Ce atoms are represented by spheres.

cell parameters refined from powder X-ray diffractometer data are available. The $R_5\text{Pd}_2\text{Bi}$ compounds are assumed to be fully stoichiometric and to adopt the $\text{Mo}_5\text{B}_2\text{Si}$ -type structure, described earlier in the context of $R_5\text{Ni}_2\text{Bi}$ compounds (section 5.5.4). No physical properties have been measured so far.

5.6.6. $R_8\text{Pd}_{24}\text{Bi}$

The compound $\text{Ce}_8\text{Pd}_{24}\text{Bi}$ is a member of a series of $\text{Ce}_8\text{Pd}_{24}X$ compounds where X can be one of several p-block elements. It was prepared by arc melting of the elements in the desired ratio, with a less than 2 wt.% excess of Bi, followed by annealing at 900°C in Ta tubing within evacuated silica tubes for 2 weeks (Gordon et al., 1996). The compound may be considered to be derived by filling the centres of one-eighth of the empty Pd_6 octahedral clusters within the cubic CePd_3 structure with Bi atoms, resulting in an ordered superstructure (fig. 13). Some of the remaining empty Pd_6 clusters must be compressed to accommodate a reasonable Pd–Bi distance of $\sim 2.6 \text{ \AA}$ within the filled clusters. Magnetic measurements revealed antiferromagnetic ordering at $T_N = 5 \text{ K}$. Fitting of the high-temperature magnetic susceptibility data to the modified Curie–Weiss law led to $\theta_p = -11 \text{ K}$ and an effective moment of $2.49(3) \mu_B/\text{Ce}$, corresponding to trivalent cerium. The electrical resistivity exhibits a broad “roll-over” upon cooling, and a sharp decrease at T_N . Specific heat measurements also showed a sharp peak at 4.6 K , close to the ordering temperature, in the plot of (C_{el}/T) vs T^2 (Cho et al., 1998).

5.7. $R\text{–Pt–Bi}$

The Pt-containing phases show many similarities to their Pd analogues. Property measurements have been very extensive. Crystallographic data are listed in table 18.

Table 18
 Crystallographic data for R–Pt–Bi compounds^{a,b,c}

Compound	Structure type	Pearson symbol	<i>a</i> (Å)	<i>c</i> (Å)	Reference
La ₃ Pt ₃ Bi ₄	Y ₃ Au ₃ Sb ₄	<i>cI40</i>	10.130		(Severing et al., 1991)
Ce ₃ Pt ₃ Bi ₄	Y ₃ Au ₃ Sb ₄	<i>cI40</i>	9.998(5)		(Hundley et al., 1990)
Ce ₃ Pt ₃ Bi ₄	Y ₃ Au ₃ Sb ₄	<i>cI40</i>	10.051		(Severing et al., 1991)
YPtBi	MgAgAs	<i>cF12</i>	6.66		(Canfield et al., 1991)
YPtBi	MgAgAs	<i>cF12</i>	6.640(1)		(Haase et al., 2002)
LaPtBi	MgAgAs	<i>cF12</i>	6.867		(Jung et al., 2001)
LaPtBi	MgAgAs	<i>cF12</i>	6.829(1)		(Haase et al., 2002)
CePtBi	MgAgAs	<i>cF12</i>	6.815(2)		(Marazza et al., 1980)
CePtBi	MgAgAs	<i>cF12</i>	6.84		(Canfield et al., 1991)
CePtBi	MgAgAs	<i>cF12</i>	6.841		(Jung et al., 2001)
CePtBi	MgAgAs	<i>cF12</i>	6.779(1)		(Haase et al., 2002)
PrPtBi	MgAgAs	<i>cF12</i>	6.78		(Canfield et al., 1991)
PrPtBi	MgAgAs	<i>cF12</i>	6.799		(Suzuki et al., 1997)
NdPtBi	MgAgAs	<i>cF12</i>	6.76		(Canfield et al., 1991)
SmPtBi	MgAgAs	<i>cF12</i>	6.74		(Canfield et al., 1991)
SmPtBi	MgAgAs	<i>cF12</i>	6.722		(Kim, M.-S., 2001)
GdPtBi	MgAgAs	<i>cF12</i>	6.680		(Dwight, 1974)
TbPtBi	MgAgAs	<i>cF12</i>	6.66		(Canfield et al., 1991)
TbPtBi	MgAgAs	<i>cF12</i>	6.662(1)		(Haase et al., 2002)
DyPtBi	MgAgAs	<i>cF12</i>	6.644		(Dwight, 1974)
HoPtBi	MgAgAs	<i>cF12</i>	6.631		(Dwight, 1974)
ErPtBi	MgAgAs	<i>cF12</i>	6.616		(Dwight, 1974)
TmPtBi	MgAgAs	<i>cF12</i>	6.601		(Canfield et al., 1991)
TmPtBi	MgAgAs	<i>cF12</i>	6.588(1)		(Haase et al., 2002)
YbPtBi	MgAgAs	<i>cF12</i>	6.595(2)		(Marazza et al., 1980)
YbPtBi	MgAgAs	<i>cF12</i>	6.60		(Canfield et al., 1991)
YbPtBi	MgAgAs	<i>cF12</i>	6.59533(1)		(Robinson et al., 1994)
YbPtBi	MgAgAs	<i>cF12</i>	6.584(1)		(Haase et al., 2002)
LuPtBi	MgAgAs	<i>cF12</i>	6.59		(Canfield et al., 1991)
LuPtBi	MgAgAs	<i>cF12</i>	6.574(1)		(Haase et al., 2002)
Y ₅ Pt ₂ Bi	Mo ₅ B ₂ Si	<i>tI32</i>	7.735(4)	13.661(5)	(Mozharivskyj and Franzen, 2001)
Gd ₅ Pt ₂ Bi	Mo ₅ B ₂ Si	<i>tI32</i>	7.851(2)	13.687(7)	(Mozharivskyj and Franzen, 2001)
Tb ₅ Pt ₂ Bi	Mo ₅ B ₂ Si	<i>tI32</i>	7.783(3)	13.599(9)	(Mozharivskyj and Franzen, 2001)
Dy ₅ Pt ₂ Bi	Mo ₅ B ₂ Si	<i>tI32</i>	7.744(2)	13.557(9)	(Mozharivskyj and Franzen, 2001)
Ho ₅ Pt ₂ Bi	Mo ₅ B ₂ Si	<i>tI32</i>	7.710(2)	13.576(8)	(Mozharivskyj and Franzen, 2001)

continued on next page

Table 18, *continued*

Compound	Structure type	Pearson symbol	a (Å)	c (Å)	Reference
Er ₅ Pt ₂ Bi	Mo ₅ B ₂ Si	$I\bar{4}32$	7.6982(8)	13.561(3)	(Mozharivskyj and Franzen, 2001)
Tm ₅ Pt ₂ Bi	Mo ₅ B ₂ Si	$I\bar{4}32$	7.642(2)	13.491(8)	(Mozharivskyj and Franzen, 2001)

^aR₃Pt₃Bi₄: Y₃Au₃Sb₄-type, space group $I\bar{4}3d$ (No. 220), $Z = 4$; R in $12a$ (3/8, 0, 1/4), Pt in $12b$ (7/8, 0, 1/4), Bi in $16c$ (x, x, x), $x = \sim 0.086$ (Kwei et al., 1992).

^bRPtBi: MgAgAs-type, space group $F\bar{4}3m$ (No. 216), $Z = 4$; R in $4b$ (1/2, 1/2, 1/2), Pt in $4c$ (1/4, 1/4, 1/4), Bi in $4a$ (0, 0, 0).

^cR₅Pt₂Bi: Mo₅B₂Si-type, space group $I4/mcm$ (No. 140), $Z = 4$. Atomic parameters for Er₅Pt₂Bi: Er1 in $4c$ (0, 0, 0), Er2 in $16l$ (0.1558(2), $x + 1/2$, 0.1379(1)), Pt in $8h$ (0.3612(2), $x + 1/2$, 0), Bi in $4a$ (0, 0, 1/4) (Mozharivskyj and Franzen, 2001).

5.7.1. R₃Pt₃Bi₄

La₃Pt₃Bi₄ and Ce₃Pt₃Bi₄ were prepared as large single crystals grown from a Bi flux (Hundley et al., 1990) or with the Bridgman method (Katoh and Takabatake, 1998). The entire solid solution (La _{x} Ce _{$1-x$})₃Pt₃Bi₄ can also be prepared (Hundley et al., 1994). These compounds adopt the cubic Y₃Au₃Sb₄-type structure (Dwight, 1977), a filled variant of the Th₃P₄-type structure, in which Pt atoms enter tetrahedral sites within the “R₃Bi₄” framework. There is only one free positional parameter, corresponding to the x coordinate for the Bi atom at $16c$ (x, x, x), which has been determined from neutron powder diffraction to be 0.0853 at room temperature for Ce₃Pt₃Bi₄ (Kwei et al., 1992).

Since its initial discovery as a prototypical “Kondo insulator” (Hundley et al., 1990; Severing et al., 1991), Ce₃Pt₃Bi₄ has elicited substantial attention. Unlike most other f-electron intermetallics, this compound is not metallic; instead, its resistivity shows activated behaviour corresponding to a narrow band gap on the order of 5 meV. The gap is believed to arise from the hybridization of f electrons with the conduction band. Considerable effort has gone into further characterizing this compound (which is generally formulated as “Ce₃Bi₄Pt₃” in the physics literature), but this is beyond the scope of the present review.

5.7.2. RPtBi

The equiatomic compounds RPtBi probably represent the most exhaustively studied set of ternary rare earth bismuthides to date. Credit for the initial discovery of this family of compounds really goes to Dwight (1974), who prepared the Gd, Dy, Ho, and Er members by arc melting. Marazza et al. (1980) also prepared the Ce and Yb members by melting in an induction furnace followed by annealing at 500 °C for one week. Subsequent preparation of the remaining members of this series generally involves arc melting of the elements in the ideal ratios followed by annealing (e.g., 800 °C for 7 d within silica tubes (Haase et al., 2002)) to form polycrystalline samples, or use of a Bi flux to form single crystals (Canfield et al., 1991). For the La, Ce, and Pr members, the competing R₃Pt₃Bi₄ phase is favoured, and care has to be taken to avoid its preferential formation. Crystals of CePtBi and PrPtBi were grown from a Pb flux instead of a Bi flux (Canfield et al., 1991). Large single crystals of LaPtBi and CePtBi

were grown with the Bridgman technique starting from a mixture of the binary alloys LaPt or CePt with Bi placed within a Mo crucible, which was heated at 1350 °C and slowly cooled by moving it out of the furnace at 1 mm/h (Goll et al., 2002). A similar procedure was applied to produce SmPtBi crystals (Kim, M.-S. et al., 2001).

Dwight (1974) had already correctly characterized the structure (MgAgAs-type, or “half-Heusler”) of the $RPtBi$ compounds from Debye–Scherrer powder X-ray diffraction patterns, in analogy with $RNiSb$, despite later confusion that arose from misassignment of the atomic positions (Robinson et al., 1994). Within the space group $F\bar{4}3m$ (No. 216), the atoms occupy three different sites, each of fourfold multiplicity and site symmetry $\bar{4}3m$. However, their placement is not arbitrary as the coordination environments around each site differ. For example, in YbPtBi, the Pt atom occupies what has popularly been called the “unique” site, in that it is eightfold coordinated (tetrahedrally by four Bi atoms at 2.86 Å and tetrahedrally by four Yb atoms at 2.86 Å), unlike the other two sites which have only four nearest neighbours. Some early papers placed the Bi atom in the “unique” site, which would have led to Bi–Yb distances (2.86 Å) that are unreasonably short compared to more typical distances of ~ 3.3 Å. Total energy calculations on LaPtBi also demonstrate convincingly that Pt resides on this site (Oguchi, 2001). Since the origin can be translated arbitrarily (along the body diagonal of the unit cell along $1/4, 1/4, 1/4$; $1/2, 1/2, 1/2$; or $3/4, 3/4, 3/4$) or the positions can be inverted, there are eight possible correct settings for listing the atomic positions. Although it has become common in the literature to place the Pt atom at (0, 0, 0), a standardization of the crystal structure, with an origin shift along $1/4, 1/4, 1/4$ (see footnote b in table 18) gives a representation that clearly shows the relationship of $RPtBi$ to the rocksalt-type structure of the parent binary RBi , with Pt atoms entering tetrahedral sites (fig. 14).

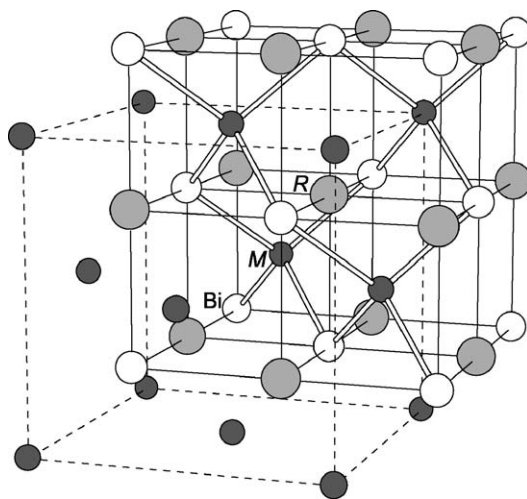


Fig. 14. Structure of $RMBi$ ($M = Ni, Pd, Pt$) (MgAgAs-type). The cell outlined in dashed lines corresponds to an alternative choice of origin.

The bonding in all these MgAgAs-type $RMBi$ ($M = Ni, Pd, Pt$) compounds can be rationalized in a straightforward manner. The tetrahedral geometry of Bi atoms around the M atoms implies sp^3 hybridization, consistent with the coordination preferences of zero-valent (d^{10}) M . The stability of these $RMBi$ compounds can be regarded as being derived from adherence to the eighteen electron rule, as indicated by the $VEC = 3 + 10 + 5 = 18$. The closed shell electronic configuration should thus lead to semiconducting behaviour, in principle.

With the availability of large single crystals grown from Bi flux, investigation of the physical properties of the $RPtBi$ series could begin in earnest. On proceeding from the early to the late rare earth members, there is a general trend from semiconducting to metallic behaviour (Canfield et al., 1991). Lattice constants and magnetic properties are consistent with the presence of trivalent rare earths.

5.7.2.1. *YPtBi* The nonmagnetic member $YPtBi$ has been primarily exploited as a host in which various other rare earth ions such as Nd, Gd, Er, and Yb have been doped (Martins et al., 1996; Pagliuso et al., 1999; Güner et al., 2003a, 2003b). From electron-spin resonance spectra, crystal-field splitting parameters for the rare earth site have been estimated.

5.7.2.2. *LaPtBi* Transport and thermoelectric properties have been measured on single crystals of $LaPtBi$ (Jung et al., 2001). With only a weakly temperature dependent resistivity ($1.2 \text{ m}\Omega \text{ cm}$ at room temperature) and a small positive Hall coefficient ($1.4 \text{ cm}^3/\text{C}$ at 4.2 K), $LaPtBi$ is a low hole-carrier concentration semimetal. The band structure and Fermi surface have been calculated (Oguchi, 2001).

5.7.2.3. *CePtBi* Transport, magnetic, and thermal measurements on a large single crystal of $CePtBi$ have been measured (Pietrus et al., 2000; Jung et al., 2001). The resistivity of $CePtBi$ shows a strong temperature dependence and reaches a maximum at 27 K. The dc magnetic susceptibility follows the Curie–Weiss law above 100 K, and a maximum in the ac magnetic susceptibility below 1 K was attributed to the onset of antiferromagnetic ordering. A γ value of $25 \text{ }\mu\text{J}/\text{mol K}^2$ was extracted from the specific heat curve. The Hall coefficient changes sign from positive to negative as the temperature is increased above 170 K. The thermoelectric power is positive from 4 to 300 K, reaching a maximum of $115 \text{ }\mu\text{V}/\text{K}$ at 100 K. A strong dependence of the Shubnikov–de Haas frequency is observed in the field-dependent resistivity up to 28 T (Goll et al., 2002), but vanishes at higher fields up to 60 T (Wosnitza et al., 2004).

5.7.2.4. *PrPtBi* Measurements were initially made on powder samples prepared by arc melting (Suzuki et al., 1997). The electrical resistivity ($\sim 1 \text{ m}\Omega \text{ cm}$ at 300 K) and Hall coefficient ($\sim 0.7 \text{ cm}^3/\text{C}$ at low temperatures) are consistent with semiconductivity. The magnetic susceptibility follows the Curie–Weiss law above 50 K but tends to become temperature-independent below 50 K. The specific heat curve shows a prominent anomaly at 1.35 K. A crystalline electric field (CEF) level scheme was derived from inelastic neutron scattering

experiments (Kasaya et al., 2000). From low-temperature X-ray diffraction and elastic constant measurements, a ferro-quadrupolar transition was proposed to account for the 1.35 K feature (Naher et al., 2003; Suzuki, H. et al., 2004; Suzuki, O. et al., 2004).

5.7.2.5. *NdPtBi* Transport and magnetic properties have been measured on single crystals of NdPtBi (Morelli et al., 1996). The resistivity rises from room temperature ($\sim 1 \text{ m}\Omega \text{ cm}$) to tenfold this value at low temperatures. The dc magnetic susceptibility reveals an antiferromagnetic transition at 2.2 K. The resistivity is strongly field-dependent, and the Hall coefficient suggests n-type carriers at room temperature and p-type carriers at low temperature, consistent with NdPtBi being a semimetal with a small overlap of valence and conduction bands.

5.7.2.6. *SmPtBi* Measurements have been made on powder samples of SmPtBi, which is a semimetal (Kim, M.-S. et al., 2001). The electrical resistivity shows a broad maximum of $1.7 \text{ m}\Omega \text{ cm}$ at 80 K, and the thermoelectric power also reaches a maximum of $60 \mu\text{V}/\text{K}$ at 126 K. The Hall coefficient is positive below 200 K and negative above 200 K. Antiferromagnetic ordering at 2.2 K is manifested by peaks in the dc magnetic susceptibility and specific heat curves.

5.7.2.7. *YbPtBi* No other member has been studied so thoroughly as YbPtBi, which was identified to be a “super-heavy-fermion” material with an electronic specific heat coefficient of $\gamma = 8 \text{ J/mol K}^2$ at low temperatures (Fisk et al., 1991). At 0.4 K, there is an anomaly in the specific heat coincident with a transition seen in the ac magnetic susceptibility (Fisk et al., 1991). Earlier LMTO calculations indicated that the band gap which occurs in other RPtBi members (such as YPtBi) closes in YbPtBi as a result of broadening and overlap of the Yb d and Pt d bands, giving rise to a low but non-zero density of states at the Fermi level (Eriksson et al., 1992), and the form of the Fermi surface was found to be rather simple (McMullan and Ray, 1992). A later band structure calculation pointed to the importance of pinning of an Yb 4f state to the Fermi level (Oppeneer et al., 1997). The presence of a disordered static Yb magnetism, with a moment no larger than $0.1 \mu_B$, along with a paramagnetic component, was suggested from μSR measurements (Amato et al., 1992). Further specific heat studies conducted on “diluted” YbPtBi, in which Yb was gradually replaced by non-magnetic Y in the solid solution $\text{Yb}_{1-x}\text{Y}_x\text{PtBi}$, showed that the specific heat feature remains fixed at 0.4 K (Thompson et al., 1993). To account for the large value of γ at the 0.4 K anomaly, several models have been proposed for how the eightfold-degenerate $J = 7/2$ state of Yb^{3+} is split by crystal field effects into several low-energy excitation levels, from the interpretation of inelastic neutron scattering data (Robinson et al., 1993, 1995, 1999; Canfield et al., 1994). Effects of pressure and applied field on the electrical resistivity were suggested to arise from the formation of a spin density wave at 0.4 K (Movshovich et al., 1994a, 1994b). A powder neutron diffraction study provided the corrected crystal structure, and indicated that any ordered magnetic moment present at low temperature must be less than $0.25 \mu_B$ (Robinson et al., 1994). A review of the ground state properties of YbPtBi was presented in terms of competing energy scales (Canfield et al., 1994), but a unified picture remains elusive. Hall effect and thermoelectric power measurements demonstrated that these

properties stem from YbPtBi being a low-carrier concentration semimetal (Hundley et al., 1997).

5.7.3. R_5Pt_2Bi

The series R_5Pt_2Bi ($R = Y, Gd, Tb, Dy, Ho, Er, Tm$) was prepared by arc melting of 0.5 g stoichiometric mixtures of the elements followed by annealing in evacuated silica tubes at 800 °C for 10 d (Mozharivskiy and Franzen, 2001). From powder X-ray diffraction data, a Rietveld refinement was performed on Er_5Pt_2Bi and cell parameters were determined for the remaining members. They adopt the Mo_5B_2Si -type structure, which has been described earlier for the isostructural R_5Ni_2Bi (section 5.5.4) and R_5Pd_2Bi series (section 5.6.4). Magnetic properties have been measured only for Er_5Pt_2Bi , which follows the Curie–Weiss law above 50 K ($\theta_p = -6.7(7)$ K; $\mu_{\text{eff}} = 9.8(1) \mu_B/Er$) and orders antiferromagnetically below 10.5 K. At 2 K, a metamagnetic transition occurs at 25 kOe.

5.8. $R-Cu-Bi$

The Cu-containing systems do not appear to have been extensively investigated yet, and it may be promising to find new phases here. Crystallographic data are listed in table 19.

5.8.1. $RCu_{1-x}Bi_2$

Powder samples of $RCu_{1-x}Bi_2$ were first prepared for $R = Ce$ (Flandorfer et al., 1996) and recently extended to $R = La, Gd, Dy$ (Lu et al., 2004), through arc melting of the elements followed by annealing at 600 °C. The extent of R substitution has not yet been fully investigated. Large plate-shaped single crystals of $CeCu_{1-x}Bi_2$ have been grown through use of excess bismuth as a self-flux (Ye et al., 1996), and samples with dimensions of several mm were obtained upon cooling from 1000 °C to 650 °C over four weeks followed by centrifuging (Thamizhavel et al., 2003). $CeCu_{1-x}Bi_2$ has been reported to be somewhat moisture-sensitive (Flandorfer et al., 1996; Ye et al., 1996).

The structure of $CeCu_{1-x}Bi_2$ was found to be deficient in Cu from refinement of X-ray diffraction data on powder ($CeCu_{0.9}Bi_2$ (Flandorfer et al., 1996)) and on single-crystal samples ($CeCu_{0.71}Bi_2$ (Ye et al., 1996)). Like $RNi_{1-x}Bi_2$ (section 5.5.2), the $RCu_{1-x}Bi_2$ series adopts the defect $HfCuSi_2$ -type structure (also known as $ZrCuSi_2$ - or $CaMnBi_2$ -type) (fig. 10a), but the precise deficiency and homogeneity ranges still need to be clarified. In $CeCu_{0.71}Bi_2$, layers of edge-sharing $CuBi_4$ tetrahedra ($Cu-Bi$, 2.7093(8) Å) are separated from square nets of Bi atoms ($Bi-Bi$, 3.221(2) Å) by the Ce atoms (Ye et al., 1996). A refinement of powder X-ray diffraction data was also performed for $LaCu_{1-x}Bi_2$, but no significant deviation from full occupancy for Cu site was observed (Lu et al., 2004).

Magnetic susceptibility measurements on a powder sample of $CeCu_{0.9}Bi_2$ revealed antiferromagnetic ordering below $T_N = 12$ K (Flandorfer et al., 1996). An effective magnetic moment of 2.3 $\mu_B/f.u.$ was derived from the Curie–Weiss law, in good agreement with trivalent cerium, as supported by a valence of 3.1 calculated from the L_{III} edge in the X-ray absorption spectrum. More detailed measurements were made on a large single crystal of $CeCu_{1-x}Bi_2$ oriented parallel or perpendicular to the c axis (Thamizhavel et al., 2003), confirming antiferromagnetic ordering ($T_N = 11.3$ K) with the easy magnetization axis along c and highly

Table 19
Crystallographic data for R–Cu–Bi compounds^{a,b,c}

Compound	Structure type	Pearson symbol	<i>a</i> (Å)	<i>b</i> (Å)	<i>c</i> (Å)	Reference
LaCuBi ₂	HfCuSi ₂	<i>tP</i> 8	4.57946(4)		9.8858(2)	(Lu et al., 2004)
CeCu _{0.9} Bi ₂	HfCuSi ₂	<i>tP</i> 8	4.5496(7)		9.883(3)	(Flandorfer et al., 1996)
CeCu _{0.71} Bi ₂ ^d	HfCuSi ₂	<i>tP</i> 8	4.555(2)		9.772(6)	(Ye et al., 1996)
GdCuBi ₂	HfCuSi ₂	<i>tP</i> 8	4.49279(9)		9.5958(4)	(Lu et al., 2004)
DyCuBi ₂	HfCuSi ₂	<i>tP</i> 8	4.47680(7)		9.5124(3)	(Lu et al., 2004)
UCuBi ₂	HfCuSi ₂	<i>tP</i> 8	4.526		9.376	(Kaczorowski, 1992)
EuCuBi	ZrBeSi	<i>hP</i> 6	4.622		8.536	(Tomuschat and Schuster, 1981)
YbCuBi ^d	ZrBeSi	<i>hP</i> 6	4.594(4)		7.928(6)	(Tkachuk et al., 2006a)
YbCuBi	LiGaGe	<i>hP</i> 6	4.572(1)		7.860(1)	(Merlo et al., 1990)
YbCuBi	LiGaGe	<i>hP</i> 6	4.5829(9)		7.854(3)	(Kaczorowski et al., 1999)
YbCuBi ^d	LiGaGe	<i>hP</i> 6	4.5821(3)		7.8107(8)	(Tkachuk et al., 2006a)
La ₅ CuBi ₃	Hf ₅ Sn ₃ Cu	<i>hP</i> 18	9.695(8)		6.662(7)	(Hohnke and Parthé, 1969)
Ce ₅ CuBi ₃	Hf ₅ Sn ₃ Cu	<i>hP</i> 18	9.59(2)		6.59(1)	(Hohnke and Parthé, 1969)
Pr ₅ CuBi ₃	Hf ₅ Sn ₃ Cu	<i>hP</i> 18	9.493(10)		6.548(8)	(Hohnke and Parthé, 1969)
Nd ₅ CuBi ₃	Hf ₅ Sn ₃ Cu	<i>hP</i> 18	9.476(7)		6.519(4)	(Hohnke and Parthé, 1969)
Gd ₅ CuBi ₃	Hf ₅ Sn ₃ Cu	<i>hP</i> 18	9.265(8)		6.424(6)	(Hohnke and Parthé, 1969)
Tb ₅ CuBi ₃	Hf ₅ Sn ₃ Cu	<i>hP</i> 18	9.200(9)		6.383(5)	(Hohnke and Parthé, 1969)
Ho ₅ Cu _{0.7} Bi _{2.3}	β -Yb ₅ Sb ₃ ?	<i>oP</i> 32	11.936(2)	9.151(1)	8.023(1)	(Morozkin et al., 2005)

^aRCu_{1-x}Bi₂: Defect HfCuSi₂-type, space group *P4/nmm* (No. 129), *Z* = 2; *R* in 2*c* (1/4, 1/4, *z*₁), Cu in 2*b* (3/4, 1/4, 1/2), Bi1 in 2*c* (1/4, 1/4, *z*₂), Bi2 in 2*a* (3/4, 1/4, 0). For LaCu_{1-x}Bi₂, *z*₁ = 0.2538 and *z*₂ = 0.6487 (Lu et al., 2004). For CeCu_{0.71}Bi₂, *z*₁ = 0.26444(9) and *z*₂ = 0.65015(8) (Ye et al., 1996).

^bRCuBi: ZrBeSi-type, space group *P6₃/mmc* (No. 194), *Z* = 2; *R* in 2*a* (0, 0, 0), Cu in 2*c* (1/3, 2/3, 1/4), Bi in 2*d* (1/3, 2/3, 3/4). LiGaGe-type, space group *P6₃mc* (No. 186), *Z* = 2; *R* in 2*a* (0, 0, ~0), Cu in 2*b* (1/3, 2/3, ~0.29), Bi in 2*b* (1/3, 2/3, ~0.74) for low-temperature YbCuBi (Tkachuk et al., 2006a).

^cR₅CuBi₃: Hf₅Sn₃Cu-type, space group *P6₃/mcm* (No. 193), *Z* = 2; *R*1 in 6*g* (*x*₁, 0, 1/4), *R*2 in 4*b* (1/3, 2/3, 0), Cu in 2*b* (0, 0, 0), Bi in 6*g* (*x*₂, 0, 1/4). For Gd₅CuBi₃, *x*₁ = 0.266(8) and *x*₂ = 0.606(5).

^dSingle-crystal data.

anisotropic magnetization with the occurrence of four metamagnetic transitions. The electrical resistivity is also highly anisotropic ($\rho_{\parallel[001]} \approx 200 \mu\Omega \text{ cm}$, $\rho_{\parallel[100]} = 50 \mu\Omega \text{ cm}$ at room temperature) and shows a sharp drop at *T_N*. From specific heat measurements, a γ value of 20 mJ/mol K² was obtained.

5.8.2. $RCuBi$

The only known equiatomic compounds in this series, $EuCuBi$ and $YbCuBi$, are formed with the divalent rare earths. $EuCuBi$ was first prepared by reaction of the elements in stoichiometric ratio in an alumina crucible jacketed in a silica tube at 1000°C , followed by regrinding and reheating at 1100°C (Tomuschat and Schuster, 1981, 1984). $YbCuBi$ was prepared by melting of the elements within Ta crucibles in an induction furnace, followed by annealing at 450°C (Merlo et al., 1990, 1995). Conventional arc melting in the presence of excess Yb and Bi, followed by annealing at 600°C , was also used to prepare $YbCuBi$ for transport measurements (Kaczorowski et al., 1999).

$EuCuBi$ and high-temperature $YbCuBi$ adopt the $ZrBeSi$ -type (ordered Ni_2In -type) structure, whereas low-temperature $YbCuBi$ adopts the $LiGaGe$ -type (ordered $CaIn_2$ -type) structure (Tomuschat and Schuster, 1981, 1984; Merlo et al., 1995; Tkachuk et al., 2006a). These hexagonal structures are closely related in that both consist of R atoms separating hexagonal $\infty^2[CuBi]$ nets stacked along the c direction. In $YbCuBi$, the phase transition occurs at 375 K , as seen by kinks in the temperature dependence of the lattice parameters and the electrical re-

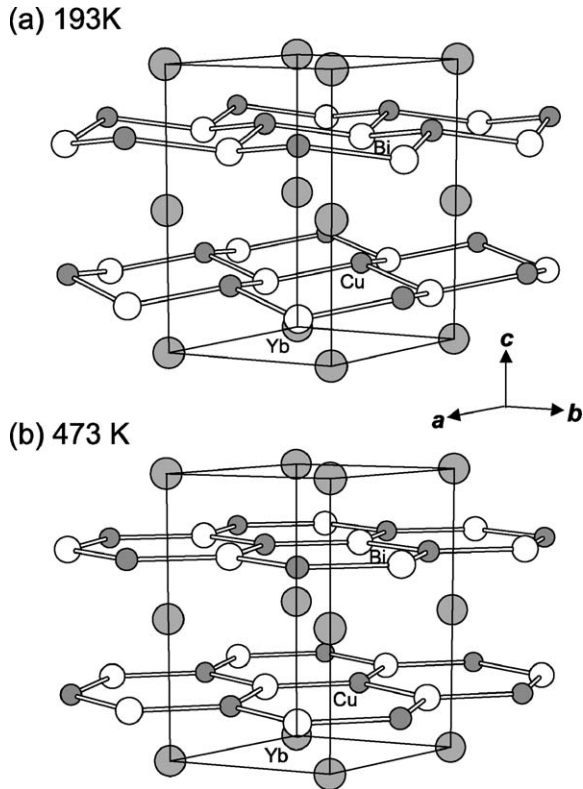


Fig. 15. Structures of (a) low- ($LiGaGe$ -type) and (b) high-temperature $YbCuBi$ ($ZrBeSi$ -type).

sistivity (Merlo et al., 1995). Variable-temperature structure determination on a single crystal of YbCuBi confirmed that the ∞^2 [CuBi] nets are strictly planar in the high-temperature phase (ZrBeSi-type) but become buckled in the low-temperature phase (LiGaGe-type) (fig. 15) (Tkachuk et al., 2006a). The Cu atoms transform from trigonal planar to tetrahedral geometry (Cu–Bi 2.7 Å) with the formation of a fourth, long Cu–Bi distance (3.5 Å). The highly elongated displacement ellipsoids of the Cu atoms are characteristic of these and related structures. The structures of both EuCuBi and YbCuBi are compatible with an electron-precise Zintl formulation in which the rare earth atoms are divalent, $R^{2+}Cu^+Bi^{3-}$.

EuCuBi is antiferromagnetic at low temperature ($T_N = 18$ K) and follows the Curie–Weiss law at high temperatures, with an effective magnetic moment ($\mu_{\text{eff}} = 7.65 \mu_B$) somewhat smaller than that expected for Eu^{2+} ($7.94 \mu_B$) (Tomuschat and Schuster, 1981, 1984). The electrical resistivity of a pressed pellet of YbCuBi shows metallic behaviour ($\rho_{300\text{ K}} = 0.3 \text{ m}\Omega \text{ cm}$) but displays a kink around the structural phase transition at 375 K (Merlo et al., 1995). The magnetic susceptibility is temperature-independent ($1.6 \times 10^{-4} \text{ emu/mol}$) with a Curie tail at low temperature attributed to the presence of less than 2% paramagnetic Yb^{3+} impurities (Kaczorowski et al., 1999).

5.8.3. R_5CuBi_3

The rare earth rich compounds R_5CuBi_3 have been prepared for $R = \text{La, Ce, Pr, Nd, Gd, Tb}$ by arc melting mixtures of the elements (Hohnke and Parthé, 1969). Only powder X-ray diffraction data are available. The structure of the Gd member was deduced by comparison with that of the binary bismuthide Gd_5Bi_3 , and in fact, Gd_5CuBi_3 can be regarded as being derived from the filling of octahedral sites by Cu atoms within Gd_5Bi_3 (fig. 16). The structure

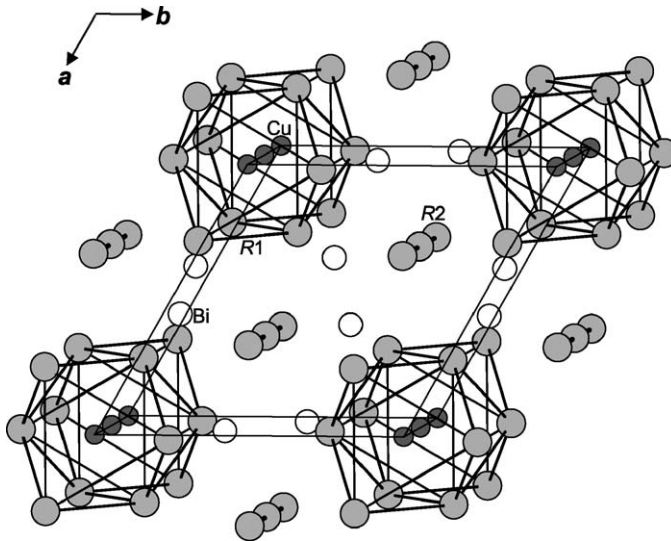


Fig. 16. Structure of R_5CuBi_3 ($R = \text{La, Ce, Pr, Nd, Gd, Tb}$) (Hf_5Sn_3Cu -type).

is the well-known hexagonal $\text{Hf}_5\text{Cu}_3\text{Sn}$ -type. Besides the octahedral Gd_6 clusters, there are also chains of Gd atoms aligned along the c direction, containing rather short Gd–Gd distances of 3.21 Å. The Bi atoms are ninefold-coordinated by Gd atoms at distances of 3.15–3.42 Å, and the structure can be derived alternatively from Bi-centred trigonal prisms.

5.8.4. $R_5\text{Cu}_{1-x}\text{Bi}_{2+x}$

The compound $\text{Ho}_5\text{Cu}_{0.7}\text{Bi}_{2.3}$ was recently prepared by arc melting of the elements followed by annealing at 830 °C for 240 h and quenching in water (Morozkin et al., 2005). It was suggested to adopt a β - Yb_5Sb_3 -type structure (Pearson symbol $oP32$, space group $Pnma$ (No. 62), $Z = 4$).

5.8.5. Actinide compounds

UCuBi_2 has been prepared by reaction of UBi_2 and Cu at 700 °C for 2 weeks (Kaczorowski, 1992). Powder X-ray diffraction data indicate that it adopts the HfCuSi_2 -type structure. The magnetic susceptibility shows two maxima, one at 51 K attributed to antiferromagnetic ordering, and another at 15 K of uncertain origin. In the paramagnetic regime, the susceptibility can be fit to the modified Curie–Weiss law giving an effective magnetic moment of 2.94 μ_{B}/U , $\theta_{\text{p}} = 31$ K, and $\chi_0 = 2.5 \times 10^{-4}$ emu/mol.

5.9. $R\text{-Ag-Bi}$

The $R\text{AgBi}_2$ series ($R = \text{La, Ce, Pr, Nd, Sm, Gd}$) represents the only known compounds in the $R\text{-Ag-Bi}$ systems so far (Petrovic et al., 2003). Large plate-shaped malleable single crystals were prepared from reaction of the elements in excess Bi, starting from compositions “ $R_{0.14}\text{Ag}_{0.14}\text{Bi}_{0.72}$ ” ($R = \text{La, Ce, Pr, Nd, Sm}$) or “ $\text{Gd}_{0.045}\text{Ag}_{0.091}\text{Bi}_{0.864}$ ”, in alumina crucibles within silica tubes cooled from 1000 °C to 400 °C over 130–160 h. Only approximate cell parameters were refined from the powder X-ray diffraction patterns, but the structure is assumed to correspond to the HfCuSi_2 -type.

With the availability of these large crystals, extensive characterization of the electrical and magnetic properties was performed, as summarized in table 20 (Petrovic et al., 2003). LaAgBi_2 is a diamagnetic metal with little anisotropy. Isothermal magnetization curves below 36 K under applied fields parallel to the c axis revealed de Haas van Alphen oscillations corresponding to very light effective electronic mass. All other members (except PrAgBi_2) are metallic and undergo antiferromagnetic ordering, with $\chi_a > \chi_c$, but the Néel temperatures scale poorly with the de Gennes factor. In general, fits of the high-temperature magnetic susceptibility to the Curie–Weiss law gave values of μ_{eff} that are consistent with the theoretical free-ion values, and no large magnetoresistance effects were observed. CeAgBi_2 shows weakly anisotropic metamagnetism, with two field-dependent transitions observed at 2 K under applied fields parallel to c . The resistivity drops sharply below 25 K. PrAgBi_2 probably has a non-magnetic ground state. NdAgBi_2 is a well-defined local moment member of the series. SmAgBi_2 exhibits non-Curie–Weiss behaviour, and the resistivity shows a feature at $T_{\text{N}} = 8$ K consistent with the loss of spin-disorder scattering. GdAgBi_2 has a complex magnetic structure, and a spin-reorientation process has been proposed.

Table 20
Crystallographic data and physical properties for $R\text{AgBi}_2$ compounds (Petrovic et al., 2003)

Compound ^a	a (Å)	c (Å)	μ_{eff} (μ_{B}/R^{3+})	μ_{RS} (μ_{B}/R^{3+})	θ_{p} (K)	T_{N} (K)	$\rho_{300\text{K}}/\rho_{2\text{K}}$
LaAgBi_2	4.60(1)	10.36(2)	diamagnetic				25
CeAgBi_2			2.25	2.53	22.6	6.1	15
PrAgBi_2			3.56	3.57	−3		65
NdAgBi_2	4.52	10.23	3.63	3.61	−25.1	3.9	34
SmAgBi_2	4.44(4)	10.32(5)	non-Curie–Weiss			8.0	5
GdAgBi_2			7.64	7.93	−52	16	2

^a $R\text{AgBi}_2$: HfCuSi_2 -type, space group $P4/nmm$ (No. 129), $Z = 2$; R in $2c$ (1/4, 1/4, ~ 0.27), Ag in $2b$ (3/4, 1/4, 1/2), Bi1 in $2c$ (1/4, 1/4, ~ 0.64), Bi2 in $2a$ (3/4, 1/4, 0).

Table 21
Standardized positional parameters for $\text{Ce}_6\text{ZnBi}_{14}$ (Tkachuk et al., 2006c)^a

Atom	Wyckoff position	Occupancy	x	y	z
Ce1	8l	1	0	0.14195(6)	0.36665(5)
Ce2	4i	1	0	0	0.17114(7)
Zn	4j	0.500	1/2	0	0.4323(3)
Bi1	8l	1	0	0.21146(4)	0.19673(4)
Bi2	8l	1	0	0.36165(4)	0.41028(4)
Bi3	4j	1	1/2	0	0.29837(5)
Bi4	4g	1	0	0.32737(6)	0
Bi5	4f	0.500	0.3942(4)	1/2	0
Bi6	2a	1	0	0	0

^a $\text{Ce}_6\text{ZnBi}_{14}$: Own type, Pearson symbol $oI42$, space group $Immm$ (No. 71), $Z = 2$, $a = 4.3916(4)$ Å, $b = 15.399(1)$ Å, $c = 19.315(2)$ Å.

5.10. $R\text{–Zn–Bi}$

Investigation of the $R\text{–Zn–Bi}$ systems has not been extensive, but there is good potential here for finding new phases.

5.10.1. $R_6\text{ZnBi}_{14}$

The Bi-rich compound $\text{Ce}_6\text{ZnBi}_{14}$ was prepared by stoichiometric reaction of the elements placed in a silica tube, heated at 500 °C for 48 h and 950 °C for 48 h, and then cooled to room temperature over 130 h (Tkachuk et al., 2006c). Standardized positional parameters, refined from single-crystal X-ray diffraction data, are given in table 21. The orthorhombic structure is of a new type (fig. 17). An extensive anionic network of Bi atoms is constructed from four-atom-wide (Bi2–Bi1–Bi1–Bi2) and three-atom-wide (Bi4–Bi5–Bi4) ribbons extending along the a direction. Single Bi6 atoms connect the four-atom-wide ribbons, outlining large channels that contain face-sharing columns of Ce_6 trigonal prisms centred by Bi3 atoms. Square pyramidal sites are partially occupied by Zn atoms, but because of their

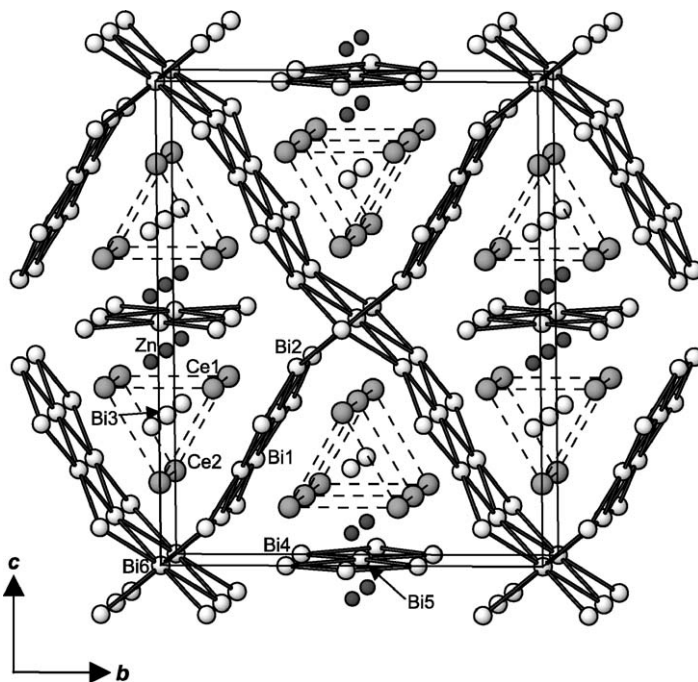


Fig. 17. Structure of $\text{Ce}_6\text{ZnBi}_{14}$ (own type).

proximity to nearby Bi5 sites, both the Zn and Bi5 sites must be half-occupied. This entails disorder within the three-atom-wide ribbons, which consist of large or small rhombi of Bi atoms linked in the a direction. Fig. 18 shows one possible local ordering, in which reasonable Zn–Bi distances are attained only if the larger rhombi are capped by Zn atoms. The structure of $\text{Ce}_6\text{ZnBi}_{14}$ can be considered to be a stuffed variant of $(\text{U}_{0.5}\text{Ho}_{0.5})_3\text{Sb}_7$ (Schmidt and Jeitschko, 2001). Bonding is difficult to rationalize in this polybismuthide structure. Other rare earth substitutions are probably possible, and physical properties remain to be measured.

5.10.2. $R_9\text{Zn}_4\text{Bi}_9$

The only other known compound in the R –Zn–Bi systems so far is $\text{Yb}_9\text{Zn}_4\text{Bi}_9$, which was initially found in a reaction of Yb, Zn, and Bi in a 1 : 2 : 2 atomic ratio in a graphite crucible within a silica tube heated at 950 °C for one day and cooled to room temperature over one day, but can also be prepared from stoichiometric reaction (Kim, S.-J. et al., 2001). Standardized positional parameters are given in table 22. $\text{Yb}_9\text{Zn}_4\text{Bi}_9$ is isotypic with $\text{Ca}_9M_4\text{Bi}_9$ ($M = \text{Mn}, \text{Zn}$) (Brechtel et al., 1979). The structure is built up of ribbons of corner-sharing ZnBi_4 tetrahedra (Zn–Bi, 2.748(3)–3.085(3) Å) separated by Yb atoms (fig. 19). Magnetic measurements revealed Curie–Weiss behaviour with an effective magnetic moment of 4.04(2) μ_B

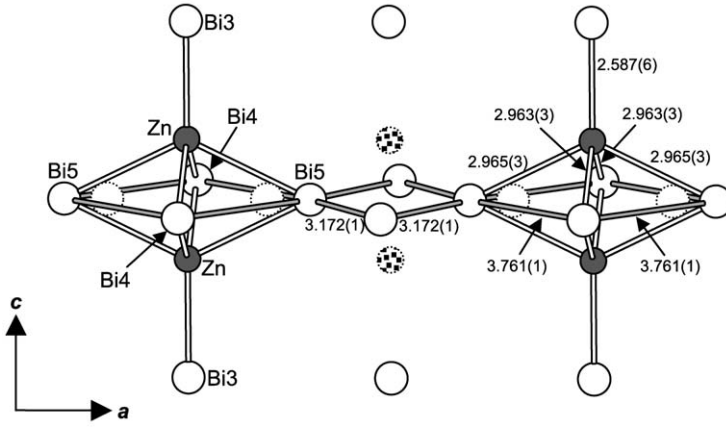


Fig. 18. Possible local ordering near three-atom-wide Bi ribbons in $\text{Ce}_6\text{ZnBi}_{14}$.

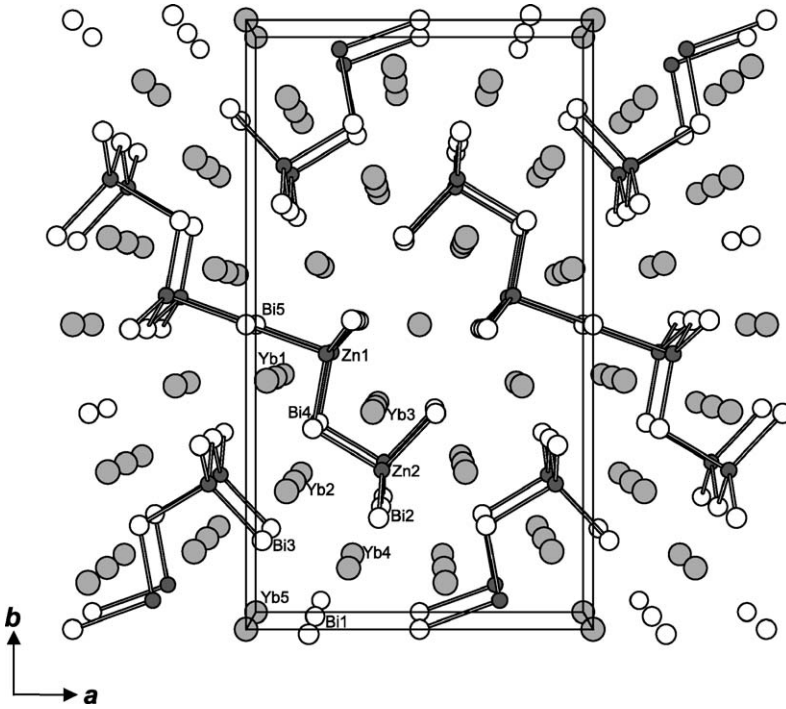


Fig. 19. Structure of $\text{Yb}_9\text{Zn}_4\text{Bi}_9$ (Ca₉Mn₄Bi₉-type).

Table 22
Standardized positional parameters for Yb₉Zn₄Bi₉ (Kim, S.-J. et al., 2001)^a

Atom	Wyckoff position	<i>x</i>	<i>y</i>	<i>z</i>
Yb1	4 <i>h</i>	0.07225(8)	0.41094(5)	1/2
Yb2	4 <i>h</i>	0.12823(8)	0.23466(5)	1/2
Yb3	4 <i>h</i>	0.36925(8)	0.36127(5)	1/2
Yb4	4 <i>g</i>	0.29530(9)	0.10044(5)	0
Yb5	2 <i>a</i>	0	0	0
Zn1	4 <i>g</i>	0.2306(3)	0.4522(1)	0
Zn2	4 <i>g</i>	0.3914(3)	0.2611(1)	0
Bi1	4 <i>h</i>	0.18975(7)	0.00714(4)	1/2
Bi2	4 <i>h</i>	0.38573(7)	0.19236(4)	1/2
Bi3	4 <i>g</i>	0.04622(7)	0.14546(4)	0
Bi4	4 <i>g</i>	0.19175(7)	0.32941(4)	0
Bi5	2 <i>c</i>	0	1/2	0

^aYb₉Zn₄Bi₉: Ca₉Mn₄Bi₉-type, Pearson symbol *oP44*, space group *Pbam* (No. 55), *Z* = 2, *a* = 12.5705(13) Å, *b* = 22.028(2) Å, *c* = 4.6401(5) Å.

per formula unit of Yb₉Zn₄Bi₉. Compared with the expected moment for one free Yb³⁺ ion (4.50 μ_B), this was interpreted as evidence for mixed-valent ytterbium in Yb₉Zn₄Bi₉, as implied by the formulation (Yb³⁺)(Yb²⁺)₈(Zn²⁺)₄(Bi³⁻)₉. Band structure (DFT) calculations show a large contribution of Yb *f* states mixed with Zn and Bi *p* states near the Fermi level. Yb₉Zn₄Bi₉ is weakly metallic and the carrier type changes from p-type at room temperature to n-type below 225 K.

6. Ternary *R*-*p*-element-Bi systems

Ternary rare earth bismuthides containing a post-transition metal are still rather sparse, suggesting opportunities for further investigation. A few known examples tend to show similarities to ternary rare earth transition-metal bismuthides, described above. When the systems contain a chalcogen as the third component, the bonding character changes dramatically. In these instances, the bismuth atoms can be regarded as cationic, and are always coordinated by the more electronegative chalcogen atoms. Usually there is some limited mutual solubility of *R* and Bi in the parent binary chalcogenides, leading to solid solutions (R_{1-x}Bi_x)₂Q₃ (*Q* = S, Se, Te) at both extremes.

6.1. *R*-*trial*-*Bi*

Systems containing post-transition metals such as the heavier triels (group 13 elements) might be expected to show analogies to those containing d-block elements, but so far little work has been done in this area.

6.1.1. *R–Al–Bi*

La–Al–Bi melts prepared in silica tubes at temperatures between 700 °C and 750 °C were examined to determine various thermodynamic properties such as the distribution coefficient of La within the Al and Bi liquid layers (Degtyar et al., 1971).

As part of a study on magnetically ordered Laves phases, the solid solution $\text{Gd}(\text{Al}_{1-x}\text{Bi}_x)_2$ was prepared for $0 < x < 0.2$ by arc melting. All samples were found to adopt the cubic MgCu_2 -type structure (Pearson symbol $cF24$, space group $Fd\bar{3}m$, $Z = 8$) with Gd at $8b$ ($3/8, 3/8, 3/8$) and Al/Bi at $16c$ ($0, 0, 0$), but surprisingly the cell parameters were reported to be independent of the Bi content (ranging from $a = 7.898$ to 7.900 Å) (Jarosz et al., 1990). On going from GdAl_2 to $\text{Gd}(\text{Al}_{0.8}\text{Bi}_{0.2})_2$, the paramagnetic Curie temperature decreases from 171 to 124 K and the spin-disorder resistivity decreases from 55 to 35 $\mu\Omega$ cm (Chełkowska, 1994), while μ_{eff} increases slightly from 7.9 to 8.3 μ_B . Attempts were made to fit the trends through a multiband model (Matlak and Zieliński, 1991) and LMTO calculations (Ufer et al., 1994). XPS spectra were also measured (Chełkowska et al., 1994).

6.1.2. *R–Ga–Bi*

The only known compound so far in the *R–Ga–Bi* system is LaGaBi_2 , which was prepared by stoichiometric reaction of the elements, although use of excess Ga as a flux may be helpful (Morgan et al., 2003). The structure is of a new type and positional parameters are given in table 23. The hexagonal structure contains an extensive anionic network built up of three-atom-wide Bi ribbons (Bi1–Bi2–Bi1) connected by six-membered rings of Ga atoms (fig. 20). Within the hexagonal channels outlined by this network are face-sharing columns of La_6 trigonal prisms centred by Bi3 atoms. The Bi4 atom lies sandwiched between pairs of Ga_6 rings. Bonding has been analyzed through a “retrotheoretical” approach in which the electronic structures of smaller fragments of the structures were examined separately. Weak multicentre bonding involving $3c-2e^-$ Ga–Bi and $2c-1e^-$ Bi–Bi bonds coexists with strong, perhaps multiple, bonding in the Ga–Ga bonds. Binding energies for Ga and Bi in LaGaBi_2 obtained from XPS spectra are close to those in the elements. Resistivity measurements reveal metallic behaviour ($\rho_{300\text{K}} = 30 \mu\Omega$ cm, $\rho_{5\text{K}} = 5 \mu\Omega$ cm).

Table 23
Standardized positional parameters for LaGaBi_2 (Morgan et al., 2003)^a

Atom	Wyckoff position	<i>x</i>	<i>y</i>	<i>z</i>
La	<i>6m</i>	0.22530(3)	0.45059(6)	1/2
Ga	<i>6k</i>	0.18199(13)	0	1/2
Bi1	<i>6j</i>	0.32457(5)	0	0
Bi2	<i>3g</i>	1/2	0	1/2
Bi3	<i>2c</i>	1/3	2/3	0
Bi4	<i>1a</i>	0	0	0

^a LaGaBi_2 : Own type, Pearson symbol $hP24$, space group $P6/mmm$ (No. 191), $Z = 6$, $a = 13.5483(4)$ Å, $c = 4.3937(1)$ Å.

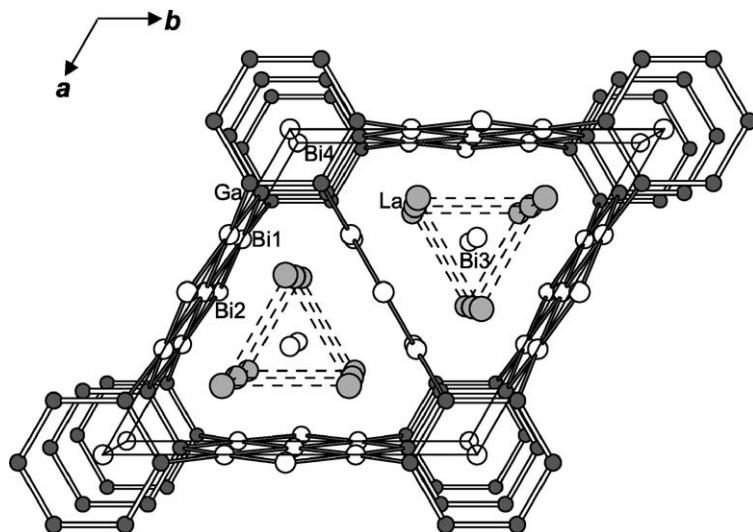


Fig. 20. Structure of LaGaBi_2 (own type).

6.1.3. *R-In-Bi*

The compound $\text{Eu}_{14}\text{InBi}_{11}$ was prepared in polycrystalline form by reaction of the elements in a Ta tube jacketed by a silica tube, heated at 1000°C for up to 5 days (Chan et al., 1997). It is isostructural to the Zintl phase $\text{Eu}_{14}\text{MnBi}_{11}$ (discussed in section 5.1.2), with the $\text{Ca}_{14}\text{AlSb}_{11}$ -type structure (Pearson symbol $tI208$, space group $I4_1/acd$ (No. 142), $Z = 8$). Since single crystals were unavailable, only cell parameters were refined ($a = 17.672(6) \text{ \AA}$, $c = 23.11(1) \text{ \AA}$). Magnetic measurements show that $\text{Eu}_{14}\text{InBi}_{11}$ undergoes an antiferromagnetic transition near 10 K. At high temperatures, the magnetic susceptibility was fit to the Curie–Weiss law, giving $\theta_p = -14.2(2) \text{ K}$ and $\mu_{\text{eff}} = 30.1(1) \mu_B/\text{f.u.}$ (in good agreement with the value expected for 14 Eu^{2+} ions).

The isothermal section of the La–In–Bi phase diagram at 600°C has been investigated (Désévéday et al., 2004). There do not appear to be any ternary compounds in this system, apart from perhaps a phase with tentative composition “ La_5InBi_3 ”.

6.2. *R-tetrel-Bi*

Because tetrels (group 14 elements) have similar electronegativities as Bi, both components will compete equally for electrons transferred from the *R* component. However, few compounds are known; crystallographic data are listed in table 24.

6.2.1. *R-Si-Bi*

A compound of approximate composition “ Ce_5SiBi_2 ” was identified as a byproduct in the course of investigating the Ce–Zn–Bi phase diagram, presumably as a result of reaction with

Table 24
Crystallographic data for *R*-tetrel–Bi compounds

Compound	Structure type	Pearson symbol	<i>a</i> (Å)	<i>c</i> (Å)	Reference
CeGeBi ₂	SrZnBi ₂	<i>tI</i> 16	4.738(1)	15.484(7)	(Stetskiv et al., 1998)
Ce ₃ GeBi	La ₃ GeIn	<i>tI</i> 80	12.257(3)	16.200(5)	(Stetskiv et al., 1998)
La ₄ SnBi ₂	anti-Th ₃ P ₄	<i>cI</i> 28	9.686(2)		(Hulliger and Ott, 1977)
La ₄ (Pb _{<i>x</i>} Bi _{1–<i>x</i>}) ₃	anti-Th ₃ P ₄	<i>cI</i> 28	9.795(2) (<i>x</i> = 0.167) to 9.809(2) (<i>x</i> = 0.667)		(Hulliger and Ott, 1977)

Table 25
Standardized positional parameters for CeGeBi₂ (Stetskiv et al., 1998)

Atom	Wyckoff position	<i>x</i>	<i>y</i>	<i>z</i>
Ce	4 <i>e</i>	0	0	0.1285(2)
Ge	4 <i>e</i>	0	0	0.3675(7)
Bi1	4 <i>d</i>	0	1/2	1/4
Bi2	4 <i>c</i>	0	1/2	0

the silica tube (Tkachuk and Mar, 2004). Preliminary characterization suggests that it adopts an ordered version of the orthorhombic β -Yb₅Sb₃-type structure.

6.2.2. *R*–Ge–Bi

The ternary Ce–Ge–Bi system has been investigated through analysis of samples prepared by arc melting of the elements followed by annealing at 400 °C for 500 h (Stetskiv et al., 1998). Two ternary compounds, CeGeBi₂ and Ce₃GeBi, were identified, and their structures were refined by Rietveld analysis of powder X-ray diffraction data. CeGeBi₂ is isostructural to SrZnBi₂ (Cordier et al., 1976), an ordered ZrAl₃-type structure (Pearson symbol *tI*16, space group *I4/mmm* (No. 139), *Z* = 4). Table 25 lists standardized positional parameters. Fig. 21 shows that the structure consists of Ce atoms separating square nets of Bi atoms (Bi2–Bi2, 3.350 Å) and layers built up of condensed BiGe₄ tetrahedra (Bi1–Ge, 2.987 Å). Ce₃GeBi was reported to adopt the La₃GeIn-type structure (Guloy and Corbett, 1996), but the listed atomic positions appear to be inconsistent with the tetragonal space group (*I4/mcm*) proposed.

6.2.3. *R*–Sn–Bi and *R*–Pb–Bi

La₄SnBi₂ and La₄(Pb_{*x*}Bi_{1–*x*})₃ (0.167 < *x* < 0.667) have been reported, which were prepared by reaction of the elements in a Ta tube (Hulliger and Ott, 1977). Powder X-ray diffraction indicated a cubic anti-Th₃P₄-type structure in which the tetrel and Bi atoms are assumed to be disordered over the same site (space group *I $\bar{4}$ 3*d* (No. 220), *Z* = 4; La in 16*c* (~0.06, ~0.06, ~0.06), Sn/Pb and Bi in 12*a* (3/8, 0, 1/4)). La₄(Pb_{*x*}Bi_{1–*x*})₃ is superconducting with *T*_c increasing from 2.3 K (La₄PbBi₂) to 2.5 K (La₄Pb₂Bi) as the number of valence electrons increases.*

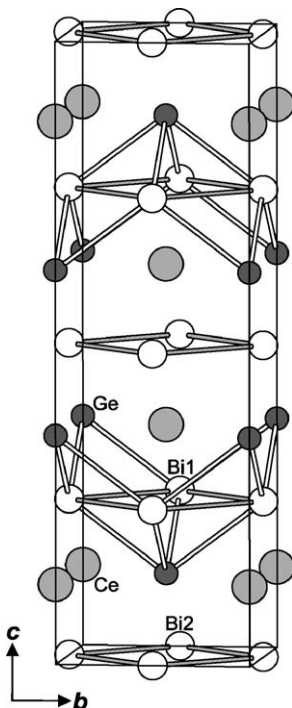


Fig. 21. Structure of CeGeBi_2 (SrZnBi_2 -type).

6.3. R - Pn - Bi

Mixed pnictogen systems such as these are likely to show disorder in their structures. Crystallographic data are listed in [table 26](#).

6.3.1. R - Sb - Bi

The solid solutions $\text{Sm}_4(\text{Sb}_x\text{Bi}_{1-x})_3$ and $\text{Gd}_4(\text{Sb}_x\text{Bi}_{1-x})_3$ have been prepared, both adopting the cubic anti- Th_3P_4 -type structure corresponding to the parent binaries. Since Sm_4Bi_3 undergoes a structural transition from a mixed-valent to a trivalent state above 260 K, single crystals of $\text{Sm}_4(\text{Sb}_x\text{Bi}_{1-x})_3$ for $x = 0.1$ – 0.7 were grown by a flux method in order to simulate pressure effects ([Aoki et al., 1999](#)). As x is increased from 0.1 to 0.7, the charge ordering temperature increases slightly.

Investigation of the complete solid solution $\text{Gd}_4(\text{Sb}_x\text{Bi}_{1-x})_3$ focused initially on the magnetic and electrical properties ([Holtzberg et al., 1964](#)) and was later superseded by a more extensive study, including measurement of thermal properties, on samples prepared by reaction of the elements within Ta crucibles in an induction furnace ([Niu et al., 2001](#)). A slightly negative deviation from Vegard's law was observed in the evolution in the lattice parameter with x . Atomic positions were determined from Rietveld refinements for $x = 0, 0.25,$

Table 26
Crystallographic data for R–Pn–Bi compounds^{a,b}

Compound	Structure type	Pearson symbol	<i>a</i> (Å)	<i>c</i> (Å)	Reference
Sm ₄ (Sb _{<i>x</i>} Bi _{1–<i>x</i>}) ₃	anti-Th ₃ P ₄	<i>cI28</i>			(Aoki et al., 1999)
Gd ₄ (Sb _{<i>x</i>} Bi _{1–<i>x</i>}) ₃	anti-Th ₃ P ₄	<i>cI28</i>	9.383 (<i>x</i> = 0) to 9.224 (<i>x</i> = 1)		(Holtzberg et al., 1964)
Gd ₄ (Sb _{<i>x</i>} Bi _{1–<i>x</i>}) ₃	anti-Th ₃ P ₄	<i>cI28</i>	9.3906(3) (<i>x</i> = 0) to 9.2328(2) (<i>x</i> = 1)		(Niu et al., 2001)
USbBi	anti-Cu ₂ Sb	<i>tP6</i>	4.28	8.72	(Chechernikov et al., 1990)
U ₂ N ₂ Bi	ThCr ₂ Si ₂	<i>tI10</i>	3.9292(5)	12.548(2)	(Benz and Zachariassen, 1970)
U ₂ N ₂ Bi	ThCr ₂ Si ₂	<i>tI10</i>	3.95(1)	12.65(4)	(Żolnierek and Troć, 1978)
Th ₂ N ₂ Bi	ThCr ₂ Si ₂	<i>tI10</i>	4.075(1)	13.620(1)	(Benz and Zachariassen, 1970)

^aR₄(Sb_{*x*}Bi_{1–*x*})₃: Anti-Th₃P₄-type, space group $I\bar{4}3d$ (No. 220), *Z* = 4; R in 16*c* (*x*, *x*, *x*), Pn in 12*a* (3/8, 0, 1/4). For Gd₄(Sb_{0.5}Bi_{0.5})₃, *x* = 0.07214(9) (Niu et al., 2001).

^bU₂N₂Bi and Th₂N₂Bi: ThCr₂Si₂-type, space group *I4/mmm* (No. 139), *Z* = 2; U or Th in 4*e* (0, 0, ~0.344), N in 4*d* (0, 1/2, 1/4), Bi in 2*a* (0, 0, 0) (Benz and Zachariassen, 1970).

0.50, 0.75, 1.00 from X-ray powder diffraction data (Niu et al., 2001). Magnetic susceptibility (ac and dc) and heat capacity measurements showed that all members of the solid solution order ferromagnetically, with *T_c* increasing monotonically from 266 K (Gd₄Sb₃) to 332 K (Gd₄Bi₃). The magnetocaloric effect is moderate, and the peak temperatures increase linearly with higher Bi content.

6.3.2. Actinide compounds

Investigation of actinide–Pn–Bi systems is more developed than in the rare earth systems.

6.3.2.1. *Actinide–Sb–Bi* The only known compound in this system so far is USbBi, which was prepared either by reaction of uranium binaries at 900 °C (Troć and Żolnierek, 1979) or by reaction of the elements at 930 °C (Chechernikov et al., 1990). It adopts the tetragonal anti-Cu₂Sb-type structure (Pearson symbol *tP6*, space group *P4/nmm* (No. 129), *Z* = 2), the same as the constituent binaries USb₂ and UBi₂, but the atomic positions and site distribution have not been determined. Although the magnetic susceptibility of USbBi has been measured from 4.2 to 900 K (Troć and Żolnierek, 1979) and from 80 to 300 K (Chechernikov et al., 1990), the conclusions are somewhat unclear, with ferromagnetism (*T_c* = 140 K) being cited by the former and antiferromagnetism (*T_N* = 230 K) by the latter.

6.3.2.2. *Actinide–N–Bi* The two actinide compounds U₂N₂Bi and Th₂N₂Bi could be prepared by two methods: (i) reaction of cold-pressed powder mixtures of the binaries UBi and UN (or ThBi and ThN) in a tungsten crucible, in nitrogen atmosphere at 1000 °C for 16 h, or

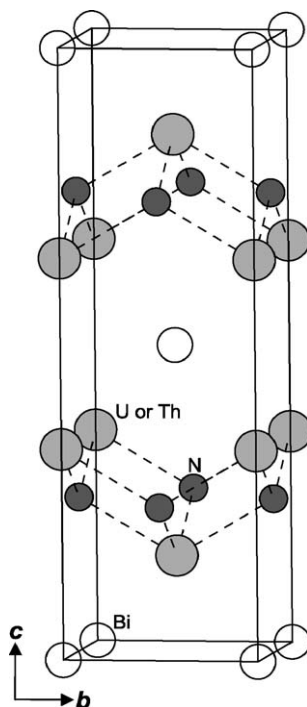


Fig. 22. Structure of U_2N_2Bi or Th_2N_2Bi ($ThCr_2Si_2$ -type).

(ii) reaction of the mononitride UN (or ThN) with Bi in a silica tube at $1000^\circ C$ for one month (Benz and Zachariassen, 1970). They adopt a ternary $ThCr_2Si_2$ -type derivative of the common tetragonal $BaAl_4$ -type structure, consisting of layers of edge-sharing tetrahedra centred by N atoms and coordinated by U or Th atoms (U–N, 2.29 Å; Th–N, 2.41 Å), alternating with square nets of Bi atoms, stacked along the c direction (fig. 22). The nitrogen atoms in Th_2N_2Bi can be partially replaced by oxygen atoms to form $Th_2(N,O)_2Bi$. The magnetic properties of U_2N_2Bi have been investigated (Żolnierok and Troć, 1978). Magnetic susceptibility measurements from 4.2 to 1000 K revealed that U_2N_2Bi orders ferromagnetically with $T_c = 154$ K, with a doublet ground state for U^{4+} .

6.4. R -Bi-S

The R -Bi-S systems are very rich. However, not all phases have been well characterized and there are still many ambiguities about their structures. Crystallographic data are listed in table 27.

Table 27
Crystallographic data for R–Bi–S compounds

Compound	Structure type	Pearson symbol	<i>a</i> (Å)	<i>b</i> (Å)	<i>c</i> (Å)	Reference
SmBi ₄ S ₇	unknown	<i>o</i> **	12.61	14.20	4.70	(Sadygov et al., 1989)
EuBi ₄ S ₇	unknown	<i>o</i> **	12.53	14.10	4.06	(Aliev et al., 1986)
Ce _{1.25} Bi _{3.78} S ₈	Ce _{1.25} Bi _{3.78} S ₈	<i>oP</i> 52	16.55(1)	4.053(2)	21.52(1)	(Céolin et al., 1977)
SmBi ₂ S ₄	PbBi ₂ S ₄ ?	<i>oP</i> 28 ?	12.55	14.11	4.12	(Sadygov et al., 1989)
EuBi ₂ S ₄	PbBi ₂ S ₄ ?	<i>oP</i> 28 ?	11.22	14.06	3.59	(Rustamov et al., 1977a; Godzhaev et al., 1977)
EuBi ₂ S ₄	PbBi ₂ S ₄ ?	<i>oP</i> 28 ?	12.50	14.03	4.07	(Aliev et al., 1986)
YbBi ₂ S ₄	PbBi ₂ S ₄ ?	<i>oP</i> 28 ?	12.47	14.00	4.05	(Aliev et al., 1986)
Eu _{1.1} Bi ₂ S ₄	Eu _{1.1} Bi ₂ S ₄	<i>hP</i> 85	24.820(8)		4.080(1)	(Lemoine et al., 1986)
PrBiS ₃	Sb ₂ S ₃ ?	<i>oP</i> 20 ?	11.20	11.28	3.96	(Garibov et al., 1993a)
NdBiS ₃	Sb ₂ S ₃ ?	<i>oP</i> 20 ?	11.40	11.27	3.94	(Tanryverdiev et al., 1997)
SmBiS ₃	Sb ₂ S ₃ ?	<i>oP</i> 20 ?	11.15	10.77	3.85	(Sadygov et al., 1989)
Eu ₃ Bi ₄ S ₉	unknown	<i>o</i> *	16.50	23.86	4.00	(Aliev et al., 1986)
La ₄ Bi ₂ S ₉	La ₄ Bi ₂ S ₉	<i>oP</i> 60	28.55	4.06	12.82	(Ecrepont et al., 1988; Garibov et al., 1993b)
La ₄ Bi ₂ S ₉	La ₄ Bi ₂ S ₉	<i>oP</i> 60	28.60	4.06	12.80	(Tanryverdiev et al., 1997)
Ce _{3.7} Bi _{2.3} S ₉	La ₄ Bi ₂ S ₉	<i>oP</i> 60	28.44	4.045	12.80	(Ecrepont et al., 1988)
Ce ₄ Bi ₂ S ₉	La ₄ Bi ₂ S ₉	<i>oP</i> 60	28.52	4.06	12.80	(Garibov et al., 1993b)
Ce ₄ Bi ₂ S ₉	La ₄ Bi ₂ S ₉	<i>oP</i> 60	28.50	4.02	12.78	(Tanryverdiev et al., 1997)
Pr ₄ Bi ₂ S ₉	La ₄ Bi ₂ S ₉	<i>oP</i> 60	28.30 ?	4.04	12.40 ?	(Garibov et al., 1993a)
Pr ₄ Bi ₂ S ₉	La ₄ Bi ₂ S ₉	<i>oP</i> 60	28.50	4.04	12.76	(Garibov et al., 1993b)
Pr ₄ Bi ₂ S ₉	La ₄ Bi ₂ S ₉	<i>oP</i> 60	28.40	4.02	12.74	(Tanryverdiev et al., 1997)
Nd ₄ Bi ₂ S ₉	La ₄ Bi ₂ S ₉	<i>oP</i> 60	28.46	4.02	12.72	(Garibov et al., 1993b)
Nd ₄ Bi ₂ S ₉	La ₄ Bi ₂ S ₉	<i>oP</i> 60	28.36	4.00	12.67	(Tanryverdiev et al., 1997)
Eu ₂ BiS ₄	PbBi ₂ S ₄	<i>oP</i> 28	11.579(9)	4.089(1)	14.523(8)	(Lemoine et al., 1982)

6.4.1. Phase diagrams

Phase diagrams have been determined for several quasibinary systems R_2S_3 – Bi_2S_3 ($R = La, Ce, Pr, Nd, Sm$) as a function of composition and temperature, through examination of products prepared by reaction of the elements in silica tubes by powder X-ray diffraction, differential thermal analysis, microstructural analysis, and microhardness measurements (Ecrepont et al., 1988; Tanryverdiev et al., 1997; Garibov et al., 1993a; Sadygov et al., 1989). The R_2S_3 – Bi_2S_3 phase diagrams for $R = La$ – Nd are all very similar. Solid solutions are formed with the end members, viz., $(R_{1-x}Bi_x)_2S_3$ with $0 < x < \sim 0.15$ adopts the parent R_2S_3 structure, and $(R_{1-x}Bi_x)_2S_3$ with $\sim 0.9 < x < 1$ has the Bi_2S_3 structure. The existence of two ternary phases with nominal compositions $R_4Bi_2S_9$ and $RBiS_3$ was also revealed, which were proposed to be formed by peritectic reactions: (i) liquid + $R_2S_3 = R_4Bi_2S_9$, and (ii) liquid + $R_4Bi_2S_9 = RBiS_3$.

In the Ce-containing system, the existence of “ $Ce_{1.2}Bi_{0.8}S_3$ ” (which is likely the same phase as “ $Ce_4Bi_2S_9$ ”) and $CeBiS_3$ has been reported (Ecrepont et al., 1988). A third non-equilibrium phase, $Ce_{1.25}Bi_{3.78}S_8$, was identified but it does not really belong to the Ce_2S_3 – Bi_2S_3 section and had been previously characterized by single-crystal X-ray diffraction (Céolin et al., 1977).

In the Sm_2S_3 – Bi_2S_3 section, unlike the other systems above, only one ternary phase, $SmBiS_3$, was found. In the SmS – Bi_2S_3 section, two ternary phases, $SmBi_2S_4$ and $SmBi_4S_7$, were found (Sadygov et al., 1989).

6.4.2. $Ce_{1.25}Bi_{3.78}S_8$

Single crystals of $Ce_{1.25}Bi_{3.78}S_8$ were obtained from a reaction mixture of composition “ $CeBiS_3$ ” in a KCl/KI flux heated at 750 °C for 15 days (Céolin et al., 1977). The structure has been determined by single-crystal X-ray diffraction (Pearson symbol $oP52$, space group $Pnma$ (No. 62), $Z = 4$). Standardized positional parameters are listed in table 28, and the structure is shown in fig. 23. The three-dimensional framework is built up of Bi-centred polyhedra (CN6 for Bi2, Bi3, Bi4; CN7 for Bi1) coordinated by S atoms. These polyhedra are highly irregular, and in view of some long distances (e.g., Bi3–S1, 3.253(6) Å; Bi4–S8, 3.611(6) Å), some of the Bi atoms are perhaps better viewed as being pentacoordinate. Tunnels encapsulated by this framework are occupied by the Ce atoms. Note the partial occupancy of the Ce1 (0.25) and Bi1 (0.78) sites, which accounts for the non-stoichiometric formula.

6.4.3. RBi_2S_4 and related Eu – Bi – S phases

Phases with the composition RBi_2S_4 have been reported for $R = Sm, Eu, Yb$, that is, those rare earths that are potentially divalent (Sadygov et al., 1989; Rustamov et al., 1977a; Aliev et al., 1986). They are probably related to the structure of Eu_2BiS_4 ($PbBi_2S_4$ -type) described below.

The first report of a compound with apparent composition $EuBi_2S_4$, which was prepared by reaction of the elements or of binaries at 1100–1150 °C in silica tubes (Rustamov et al., 1977a), indicated orthorhombic cell parameters that differed somewhat from those appearing in a later report (Aliev et al., 1986). In both instances, these parameters are similar to those of Eu_2BiS_4 , which was prepared by stoichiometric reaction of Bi_2S_3 and Eu_3S_4 in an evacuated silica tube at 950 °C followed by slow cooling (Lemoine et al., 1982). The

Table 28
Standardized positional parameters for $\text{Ce}_{1.25}\text{Bi}_{3.78}\text{S}_8$ (Céolin et al., 1977)^a

Atom	<i>x</i>	<i>z</i>
Ce1 ^b	0.1993(4)	0.2416(3)
Ce2	0.29149(9)	0.04492(7)
Bi1 ^b	0.03496(7)	0.40846(6)
Bi2	0.04299(6)	0.74156(4)
Bi3	0.34936(5)	0.39686(4)
Bi4	0.42754(5)	0.58436(4)
S1	0.0261(4)	0.1693(3)
S2	0.0727(3)	0.5438(3)
S3	0.1879(4)	0.8208(3)
S4	0.2090(3)	0.4477(3)
S5	0.2826(3)	0.6238(3)
S6	0.3929(3)	0.1747(3)
S7	0.4101(3)	0.8285(3)
S8	0.6174(4)	0.5017(3)

^aAll atoms in Wyckoff position 4c (*x*, 1/4, *z*) of space group symmetry *Pnma*.

^bOccupancy of 0.25 in Ce1 and 0.78 in Bi1.

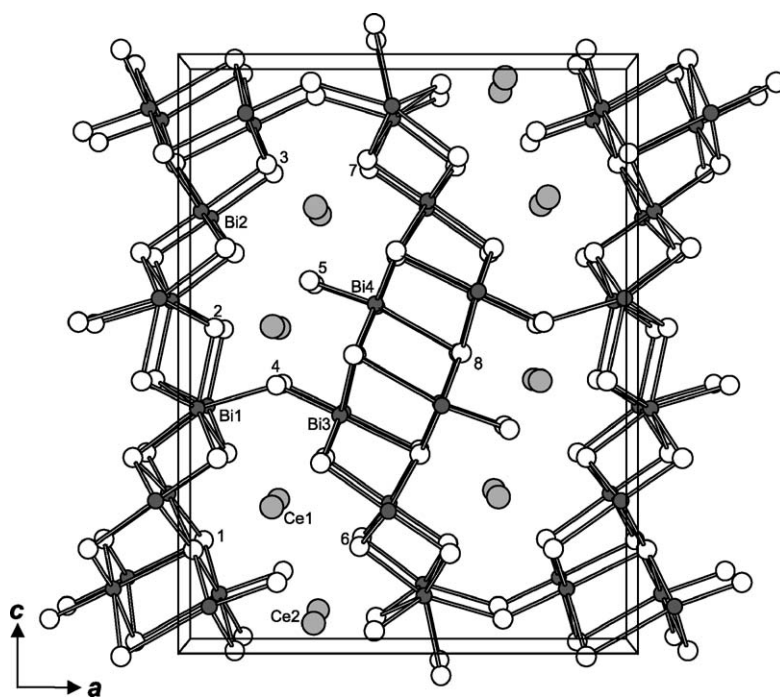


Fig. 23. Structure of $\text{Ce}_{1.25}\text{Bi}_{3.78}\text{S}_8$ (own type). The S atoms are numbered but unlabeled.

Table 29
Standardized positional parameters for Eu_2BiS_4 (Lemoine et al., 1982)^a

Atom	x	z
Eu1	0.2702(2)	0.6537(1)
Eu2	0.6117(2)	0.5952(1)
Bi1	0.0651(1)	0.3903(1)
S1	0.0129(8)	0.7144(6)
S2	0.0518(7)	0.0902(5)
S3	0.2635(8)	0.3044(5)
S4	0.3244(9)	0.0111(6)

^aAll atoms in Wyckoff position $4c$ ($x, 1/4, z$) of space group symmetry $Pnma$.

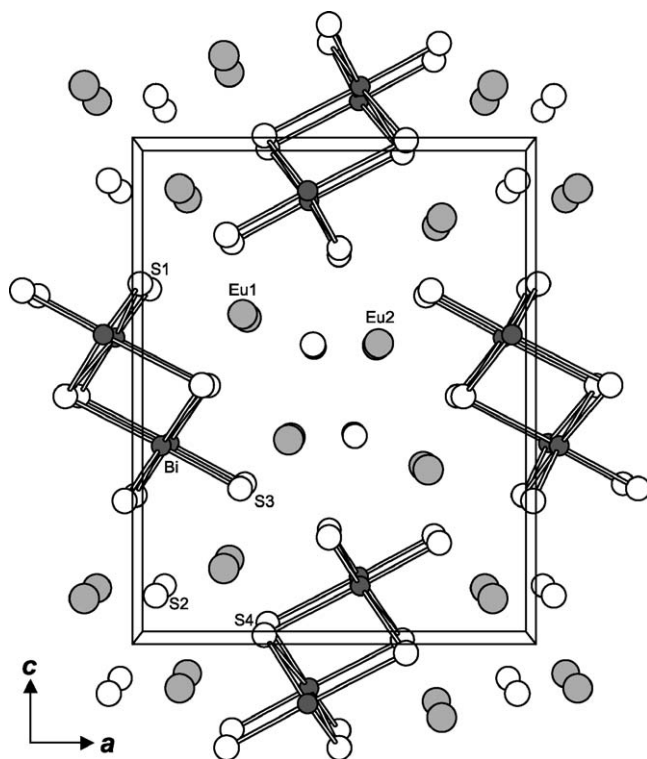


Fig. 24. Structure of Eu_2BiS_4 (PbBi_2S_4 -type).

structure of Eu_2BiS_4 was determined by single-crystal X-ray diffraction (Pearson symbol $oP28$, space group $Pnma$ (No. 62), $Z = 4$). Standardized positional parameters are listed in table 29, and the structure is shown in fig. 24. The structure corresponds to the PbBi_2S_4

Table 30
Standardized positional parameters for $\text{Eu}_{1.1}\text{Bi}_2\text{S}_4$ (Lemoine et al., 1986)^a

Atom	<i>x</i>	<i>y</i>
Eu1	0.3553(1)	0.1232(1)
Eu2	0.5572(1)	0.2337(1)
Eu3 ^b	0	0
Bi1	0.0207(1)	0.1776(1)
Bi2	0.0534(1)	0.5909(1)
Bi3	0.1487(1)	0.4954(1)
Bi4	0.3328(1)	0.2742(1)
S1	0.1197(7)	0.3082(7)
S2	0.1344(15)	0.0754(9)
S3	0.2195(6)	0.2553(7)
S4	0.2522(6)	0.5952(6)
S5	0.3039(6)	0.4562(6)
S6	0.3679(6)	0.0027(7)
S7	0.4511(6)	0.2653(7)
S8	0.5512(7)	0.0993(6)

^aAll atoms in Wyckoff position $6h$ ($x, y, 1/4$), except for Eu3, which is in $2a$ ($0, 0, 1/4$). Space group symmetry is $P6_3/m$.

^bOccupancy 0.50.

(galenobismutite) type (Iitaka and Nowacki, 1962). Double chains of edge-sharing Bi-centred octahedra coordinated by S atoms are extended along the *b* direction, between which lie isolated Eu and S atoms. The Eu1–S distances (3.020(6)–3.400(10) Å) are distinctly longer than the Eu2–S distances (2.780(8)–2.992(8) Å), evidence for the presence of mixed-valent europium ((Eu1)²⁺, (Eu2)³⁺) and in good agreement with the valence-precise formulation (Eu²⁺)(Eu³⁺)(Bi³⁺)(S²⁻)₄. With this reasoning, it is possible that the EuBi₂S₄ compound (or its Sm and Yb analogues) described above corresponds to a similar structure but with Eu³⁺ being substituted by Bi³⁺, although this needs to be confirmed.

Curiously, there exists a compound of composition $\text{Eu}_{1.1}\text{Bi}_2\text{S}_4$ that is not the same as the EuBi_2S_4 compound noted above. It can be prepared by reaction of EuS and Bi₂S₃ (or 2Bi + 3S) at 800 °C in evacuated silica tubes, or by reaction of a mixture of EuS + 2Bi under H₂S flow at 600–700 °C (Lemoine et al., 1986). Standardized positional parameters are listed in table 30. The hexagonal structure (Pearson symbol *hP*85, space group $P6_3/m$ (No. 176), *Z* = 12) is shown in fig. 25. It is built up of Bi-centred polyhedra in motifs similar to those seen in the previous structures (especially Ce_{1.25}Bi_{3.78}S₈ (fig. 23)), except that the arrangement leads to large tunnels aligned along the sixfold axis. Within these tunnels are additional sites that are half-occupied by Eu3 atoms. As before, some of the Bi-centred octahedra are highly distorted and should be really considered to be pentacoordinate, if long distances (e.g., Bi2–S8, 3.630(2) Å) are neglected.

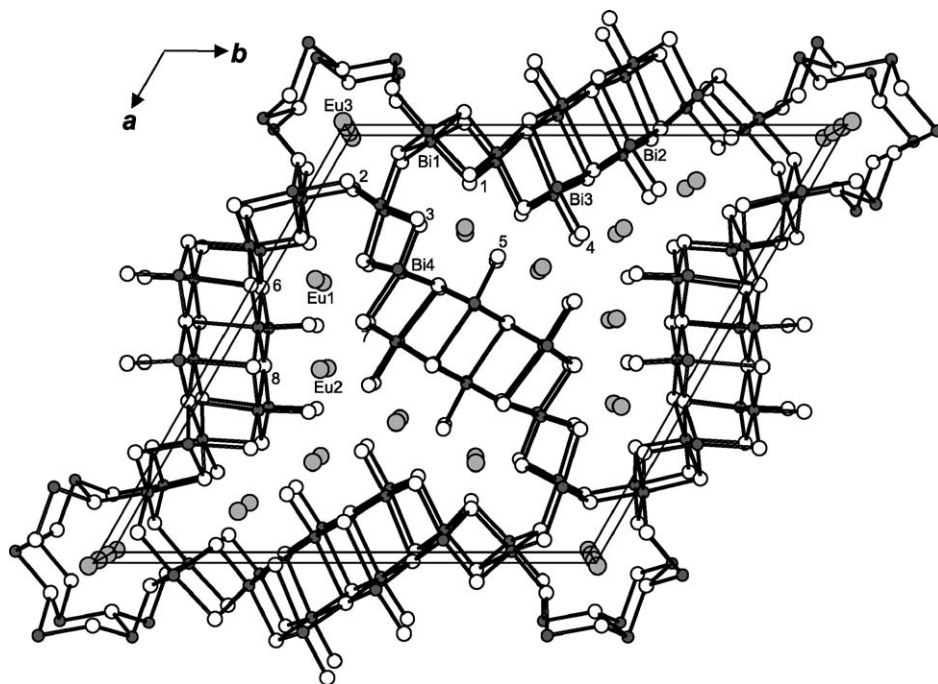


Fig. 25. Structure of $\text{Eu}_{1.1}\text{Bi}_2\text{S}_4$ (own type). The S atoms are numbered but unlabeled.

6.4.4. $R\text{BiS}_3$

Despite their relative ease of formation, not much is known about these phases (formed for $R = \text{La}, \text{Ce}, \text{Pr}, \text{Nd}, \text{Sm}$) beyond the orthorhombic cell parameters for some and microhardness for others (Ecrepont et al., 1988; Tanryverdiev et al., 1997; Garibov et al., 1993a; Sadygov et al., 1989). They may be related to the stibnite (Sb_2S_3 -type) structure, but this requires confirmation.

6.4.5. $R_4\text{Bi}_2\text{S}_9$

The compounds $R_4\text{Bi}_2\text{S}_9$ can be prepared from the constituent elements, below their incongruent melting temperatures ($\text{La}_4\text{Bi}_2\text{S}_9$, 890 °C; $\text{Ce}_4\text{Bi}_2\text{S}_9$, 900 °C; $\text{Pr}_4\text{Bi}_2\text{S}_9$, 950 °C; $\text{Nd}_4\text{Bi}_2\text{S}_9$, 890 °C) (Ecrepont et al., 1988; Tanryverdiev et al., 1997). Alternative routes including decomposition of a precursor (prepared from R and Bi nitrates), reaction of Bi_2S_3 with R and S, and use of vapour transport agents, have also been reported (Garibov et al., 1993b). The structure of $\text{La}_4\text{Bi}_2\text{S}_9$ (Pearson symbol $oP60$, space group $Pnma$ (No. 62), $Z = 4$) has been determined by refinement of powder X-ray diffraction data (Ecrepont et al., 1988), and standardized positional parameters are listed in table 31. The structure, shown in fig. 26, consists of undulating layers built up of Bi-centred polyhedra (CN6 and CN7) coordinated by S atoms, between which lie isolated R and S atoms. Structural relationships between $\text{La}_4\text{Bi}_2\text{S}_9$ and other

Table 31
Standardized positional parameters for $\text{La}_4\text{Bi}_2\text{S}_9$ (Ecrepont et al., 1988)^a

Atom	x	z
La1	0.1759	0.739
La2	0.1988	0.093
La3	0.3163	0.904
La4	0.4441	0.743
Bi1	0.0625	0.5572
Bi2	0.4349	0.4238
S1	0.006	0.380
S2	0.042	0.095
S3	0.056	0.785
S4	0.120	0.379
S5	0.231	0.546
S6	0.244	0.267
S7	0.351	0.399
S8	0.352	0.688
S9	0.366	0.106

^aAll atoms in Wyckoff position $4c$ ($x, 1/4, z$) of space group symmetry $Pnma$.

complex chalcogenides have been developed in terms of crystallographic planes (Borisov et al., 2000). Consistent with the valence-precise formulation $(R^{3+})_4(\text{Bi}^{3+})_2(\text{S}^{2-})_9$, all of these compounds are semiconductors with band gaps around 1.3 eV (Garibov et al., 1993b).

6.4.6. Other phases

SmBi_4S_7 , EuBi_4S_7 , and $\text{Eu}_3\text{Bi}_4\text{S}_9$ have been reported, but little is known about their structures except that they are orthorhombic (Sadygov et al., 1989; Aliev et al., 1986). Some electrical properties have been measured for these Eu compounds, which are semiconductors with ~ 1 eV band gaps (Aliev et al., 1986).

6.5. $R\text{-Bi-Se}$

Although not as thoroughly investigated, the phases formed in the $R\text{-Bi-Se}$ systems are assumed to be the same as their sulfide analogues. Crystallographic data are listed in table 32, but much of this requires confirmation.

6.5.1. Phase diagrams

Phase diagrams have been determined for sections of the $R\text{-Bi-Se}$ ($R = \text{Ce}, \text{Sm}, \text{Tm}$) systems as a function of composition and temperature, through powder X-ray diffraction, differential thermal analysis, microstructural analysis, and microhardness measurements.

6.5.1.1. Ce-Bi-Se In the $\text{CeSe-Bi}_2\text{Se}_3$ section, a solid solution designated as “ α ” is formed with Bi_2Se_3 (up to 5 mol% CeSe) and a hexagonal ternary phase $\text{Ce}_2\text{Bi}_2\text{Se}_5$ of unknown structure is formed by peritectic reaction of α and CeSe at 330 °C (Mamedova et al., 2003).

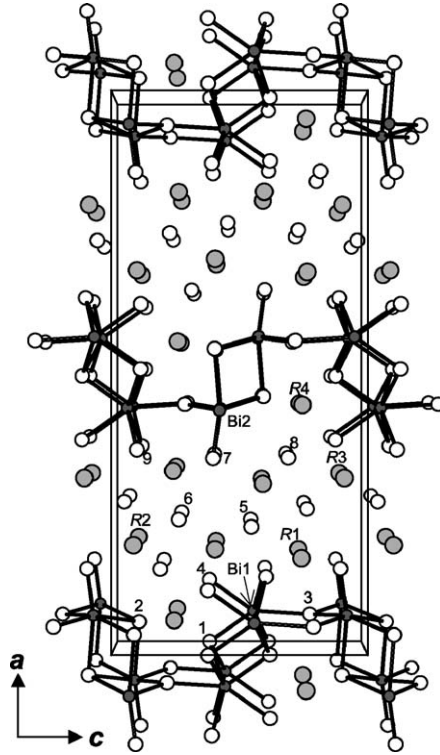


Fig. 26. Structure of $R_4Bi_2S_9$ ($R = La, Ce, Pr, Nd$) ($La_4Bi_2S_9$ -type). The S atoms are numbered but unlabeled.

6.5.1.2. *Sm–Bi–Se* The phase diagram is quite complex, with three ternary phases revealed: $SmBiSe_3$, $SmBi_2Se_4$, and $SmBi_4Se_7$ (Sadygov, 1993). $SmBiSe_3$ probably adopts a Sb_2S_3 -type structure. $SmBi_2Se_4$ was reported to adopt a $FeSb_2S_4$ -type structure, but the possibility of a $PbBi_2S_4$ -type structure also needs to be considered. $SmBi_4Se_7$ has an unknown structure.

6.5.1.3. *Tm–Bi–Se* Several sections have been examined, revealing three ternary phases: $TmBiSe_3$, $TmBi_2Se_4$, and $TmBi_4Se_7$ (Sadygov et al., 2001; Dzhaferova et al., 2002). The powder X-ray diffraction pattern reported for $TmBiSe_3$ appears to be consistent with an Sb_2S_3 -type structure (Sadygov et al., 2001). $TmBi_2Se_4$ and $TmBi_4Se_7$ probably have structures related to Sb_2S_3 , but by analogy to other systems, the former may adopt the $PbBi_2S_4$ -type structure.

6.5.2. *Eu–Bi–Se*

The ternary compounds $EuBi_2Se_4$, $EuBi_4Se_7$, and $Eu_3Bi_4Se_9$ have been identified (Rustamov et al., 1977a; Godzhaev et al., 1977; Aliev et al., 1986). $EuBi_2Se_4$ probably has the $PbBi_2Se_4$ -

Table 32
Crystallographic data for *R*-Bi-*Se* compounds

Compound	Structure type	Pearson symbol	<i>a</i> (Å)	<i>b</i> (Å)	<i>c</i> (Å)	mp ^a (°C)	Reference
SmBi ₄ Se ₇	unknown	<i>o</i> **	11.95	14.24	4.13		(Sadygov, 1993)
EuBi ₄ Se ₇	unknown	<i>o</i> **	12.64	14.97	4.17		(Aliev et al., 1986)
TmBi ₄ Se ₇	unknown	<i>o</i> **	12.69	14.13	4.71	750	(Dzhafarova et al., 2002)
SmBi ₂ Se ₄	PbBi ₂ S ₄ ?	<i>oP</i> 28 ?	11.59	14.18	4.12		(Sadygov, 1993)
EuBi ₂ Se ₄	PbBi ₂ S ₄ ?	<i>oP</i> 28 ?	11.26	14.16	3.73		(Godzhaev et al., 1977)
EuBi ₂ Se ₄	PbBi ₂ S ₄ ?	<i>oP</i> 28 ?	12.64	14.48	4.11		(Aliev et al., 1986)
TmBi ₂ Se ₄	PbBi ₂ S ₄ ?	<i>oP</i> 28 ?	12.50	14.79	4.30	740 (i)	(Dzhafarova et al., 2002)
SmBiSe ₃	Sb ₂ S ₃ ?	<i>oP</i> 20 ?	11.71	11.84	4.10		(Sadygov, 1993)
TmBiSe ₃	Sb ₂ S ₃ ?	<i>oP</i> 20 ?	11.62	11.71	4.04	750 (i)	(Sadygov et al., 2001)
Eu ₃ Bi ₄ Se ₉	unknown	<i>o</i> **	17.60	24.74	4.12		(Aliev et al., 1986)
Ce ₂ Bi ₂ Se ₅	unknown	<i>h</i> **	4.20		17.14	330 (i)	(Mamedova et al., 2003)

^a(i) means “incongruently melting”.

type structure, whereas the other two have unknown structures. All are semiconductors with band gaps of 0.8–0.9 eV.

6.5.3. *Gd*-*Bi*-*Se*

A single crystal of Bi₂Se₃ lightly doped (0.12%) by Gd, which substitutes at sites of hexagonal symmetry, was prepared by the Bridgman technique, and its EPR spectra was analyzed to obtain spin-Hamiltonian parameters (Gratens et al., 1997).

6.6. *R*-*Bi*-*Te*

Although many of the phases in the *R*-*Bi*-*Te* systems have the same nominal compositions as in the corresponding sulfide and selenide systems, they have different structures. Crystallographic data are listed in table 33. Some of these tellurides may be good candidates for thermoelectric materials.

6.6.1. Phase diagrams

Phase diagrams have been determined for sections of various *R*-*Bi*-*Te* systems as a function of composition and temperature, through powder X-ray diffraction, differential thermal analysis, and microstructural analysis. In general, sections of these diagrams are similar for various *R*.

The *R*₂Te₃-Bi₂Te₃ sections (*R* = Y, La, Ce, Sm, Dy, Tm) contain the trigonal ternary phase *R*BiTe₃, which was proposed to be formed by the peritectic reaction: liquid + *R*₂Te₃ = *R*BiTe₃ (Rustamov et al., 1977b, 1978, 1979a; Sadygov et al., 1985, 1987a, 1987b). This phase can be formed for other *R*, but not through reaction of the elements (section 6.6.3).

Table 33
Crystallographic data for R–Bi–Te compounds

Compound	Structure type	Pearson symbol	<i>a</i> (Å)	<i>b</i> (Å)	<i>c</i> (Å)	mp ^a (°C)	Reference
SmBi ₄ Te ₇	Th ₃ P ₄ ?	<i>cI28</i> ?	10.81			600	(Sadygov et al., 1988)
EuBi ₄ Te ₇	Th ₃ P ₄ ?	<i>cI28</i> ?	10.60			590	(Aliev and Rustamov, 1978; Aliev et al., 1986)
TmBi ₄ Te ₇	Th ₃ P ₄ ?	<i>cI28</i> ?	9.94			780	(Sadygov et al., 1996)
YbBi ₄ Te ₇	Th ₃ P ₄ ?	<i>cI28</i> ?	10.64			650	(Aliev and Rustamov, 1978; Aliev et al., 1986)
SmBi ₂ Te ₄	Th ₃ P ₄ ?	<i>cI28</i> ?	10.57			530 (i)	(Sadygov et al., 1988)
EuBi ₂ Te ₄	Th ₃ P ₄ ?	<i>cI28</i> ?	10.48			550 (i)	(Aliev and Rustamov, 1978; Aliev et al., 1986)
TmBi ₂ Te ₄	Th ₃ P ₄ ?	<i>cI28</i> ?	9.46			680 (i)	(Sadygov et al., 1996)
YbBi ₂ Te ₄	Th ₃ P ₄ ?	<i>cI28</i> ?	10.48			600 (i)	(Aliev and Rustamov, 1978; Aliev et al., 1986)
YBiTe ₃	Bi ₂ Te ₃ ?	<i>hR15</i> ?	4.46		31.63	710 (i)	(Rustamov et al., 1978)
CeBiTe ₃	Bi ₂ Te ₃ ?	<i>hR15</i> ?	4.19		31.16	680 (i)	(Rustamov et al., 1979a)
SmBiTe ₃	Bi ₂ Te ₃ ?	<i>hR15</i> ?	4.22		32.91	800 (i)	(Rustamov et al., 1977b)
TbBiTe ₃	Bi ₂ Te ₃ ?	<i>hR15</i> ?	4.30		31.60		(Rustamov et al., 1979b)
DyBiTe ₃	Bi ₂ Te ₃ ?	<i>hR15</i> ?				700 (i)	(Sadygov et al., 1987a)
HoBiTe ₃	Bi ₂ Te ₃ ?	<i>hR15</i> ?	4.28		31.49		(Rustamov et al., 1979b)
TmBiTe ₃	Bi ₂ Te ₃ ?	<i>hR15</i> ?	4.20		31.11	870 (i)	(Sadygov et al., 1985)
LuBiTe ₃	Bi ₂ Te ₃ ?	<i>hR15</i> ?	4.18		30.88		(Rustamov et al., 1979b)
Tb ₃ Bi ₄ Te ₉	unknown	<i>o</i> **	17.622	24.770	4.147	730 (i)	(Rustamov et al., 1985)
LaBiTe	unknown	<i>oP</i> *	7.20	7.08	18.20		(Asadov et al., 1995)
Sm ₄ Bi ₂ Te	anti-Th ₃ P ₄	<i>cI28</i>	9.899(3)				(Hulliger, 1979b)
Eu ₄ Bi ₂ Te	anti-Th ₃ P ₄	<i>cI28</i>	9.926(2)				(Hulliger, 1979b)
Yb ₄ Bi ₂ Te	anti-Th ₃ P ₄	<i>cI28</i>	9.571(2)				(Hulliger, 1979b)
Sc ₆ Bi _{1.68} Te _{0.80}	Fe ₂ P	<i>hP9</i>	7.6821(3)		4.0815(4)		(Chen and Corbett, 2004)

^a(i) means “incongruently melting”.

The $R\text{Te}-\text{Bi}_2\text{Te}_3$ sections ($R = \text{Sm}, \text{Eu}, \text{Tm}, \text{Yb}$) contain two cubic ternary phases (Aliev and Rustamov, 1978; Aliev and Maksudova, 1986; Sadygov et al., 1988, 1996; Sadygov and Aliev, 1989). One phase, $R\text{Bi}_2\text{Te}_4$, is formed by the peritectic reaction: liquid + $R\text{Te} = R\text{Bi}_2\text{Te}_4$. The other phase, $R\text{Bi}_4\text{Te}_7$, is congruently melting. YbBi_4Te_7 undergoes a phase transformation from a low- (α) to a high-temperature form (β) at 400°C (Aliev and Rustamov, 1978; Aliev and Maksudova, 1986).

The $\text{TbTe}-\text{Bi}_2\text{Te}_3$ section appears to be somewhat different, revealing only one ternary phase, $\text{Tb}_3\text{Bi}_4\text{Te}_9$, that is incongruently melting and has an orthorhombic structure (Rustamov et al., 1985). However, another ternary phase, TbBiTe_3 , can be prepared but not through reaction of the elements (section 6.6.3), and it does not appear in this phase diagram section studied.

In the $\text{La}-\text{Bi}-\text{Te}$ phase diagram, an equiatomic phase LaBiTe was identified (orthorhombic but of unknown structure) and rationalized by calculation of thermodynamic quantities (Asadov et al., 1995).

6.6.2. $R\text{Bi}_2\text{Te}_4$ and $R\text{Bi}_4\text{Te}_7$

These were identified in several phase diagrams, described above. They have been proposed to be related to the cubic Th_3P_4 -type structure (Pearson symbol $cI28$, space group $I\bar{4}3d$ (No. 220), $Z = 4$), in which atoms occupy only two sites (12a and 16c). For $R\text{Bi}_2\text{Te}_4$, this implies disorder of the R and Bi atoms. For $R\text{Bi}_4\text{Te}_7$, partial occupancy would have to be involved as well. Transport properties have been measured for the Eu and Yb members, which are semiconductors with band gaps of 0.3–0.5 eV (Godzhaev et al., 1977; Aliev et al., 1986; Maksudova et al., 1988).

6.6.3. $R\text{BiTe}_3$

Identified for some members from phase diagrams described above, these compounds were prepared for many other rare earths ($R = \text{Y}, \text{La}, \text{Ce}, \text{Pr}, \text{Nd}, \text{Sm}, \text{Tb}, \text{Ho}, \text{Tm}, \text{Lu}$) by equimolar reaction of Bi_2Te_3 and $R\text{Cl}_3$ (Rustamov et al., 1979b, 1984). The cell parameters for LaBiTe_3 have not been determined. They were assumed to adopt the trigonal Bi_2Te_3 -type (tetradymite) structure (Pearson symbol $hR15$, space group $R\bar{3}m$ (No. 166), $Z = 3$). Electrical conductivity, Seebeck coefficient, and Hall effect measurements revealed that these compounds are n -type semiconductors with band gaps of about 0.2 eV.

6.6.4. $R_4\text{Bi}_2\text{Te}$

These compounds were prepared with divalent rare earths ($R = \text{Sm}, \text{Eu}, \text{Yb}$) by reaction of elements or binaries (Hulliger, 1979b). They adopt the anti- Th_3P_4 -type structure (Pearson symbol $cI28$, space group $I\bar{4}3d$ (No. 220), $Z = 4$) and are assumed to be semiconducting. $\text{Eu}_4\text{Bi}_2\text{Te}$ orders antiferromagnetically at $T_N = 36\text{ K}$.

6.6.5. $\text{Sc}_6\text{Bi}_{1.68}\text{Te}_{0.80}$

A “few” crystals of $\text{Sc}_6\text{Bi}_{1.68}\text{Te}_{0.80}$ were extracted from the surface of Mo foil after an annealing treatment at 1300°C of an arc melted pellet in a reaction intended to prepare “ Sc_6BiTe_2 ” (Chen and Corbett, 2004). The structure was refined from single-crystal X-ray diffraction data.

It is based on the Fe₂P-type and contains two types of Sc₆ trigonal prisms, the larger of which is centred by Bi atoms and the smaller by Te atoms. The Bi and Te sites are each partially occupied at about 0.80. Band structure calculations were performed, showing the importance of Sc–Bi bonding.

6.6.6. Other data

The examples below illustrate how Bi can be partially substituted either by *R* or by Te.

6.6.6.1. *CeBi_{1-x}Te_x* Solid solutions of CeBi_{1-x}Te_x with the rocksalt structure have been prepared throughout the entire range. Magnetic and transport measurements show a transition from ferromagnetic to paramagnetic behaviour, and a ground state reversal as *x* increases to 0.2 (Sera et al., 1985). The magnetic properties of these solutions have been followed as a function of pressure (Bartholin et al., 1987), and the electronic structure of CeBi_{0.7}Te₃ has been examined by XPS (Oh et al., 1992).

6.6.6.2. *(R_xBi_{1-x})₂Te₃* Single crystals of Bi₂Te₃ doped with 1–5 mol% Gd were prepared by the Bridgman technique; EPR measurements confirmed that Gd substitutes for Bi atoms at sites of 3*m* symmetry, and magnetization measurements suggested an antiferromagnetic coupling of the Gd³⁺ ions (El Kholdi et al., 1994). Powders of Bi₂Te₃ doped with about 4 mol% of rare earth (*R* = La, Ce, Sm, Er) were prepared through a solvothermal route from rare earth oxides or chlorides, BiCl₃, and Te in basic aqueous solution in the presence of NaBH₄ (Zhao et al., 2004; Ji et al., 2005). From measurement of transport properties, these powders were found to have thermoelectric figures of merit up to $ZT = \sim 0.2$.

6.7. *R–Bi–halogen*

Table 34 lists crystallographic data for the few known examples in these systems.

The only ternary phases containing *R*, Bi, and a halogen known so far are *R*₅Bi₃Br (*R* = La, Pr), which were prepared in about 90% yield by stoichiometric reaction of *R*, *R*Br₃, and Bi in metal tubes (Nb or Ta) placed within silica tubes at 950 °C for two weeks (Jensen et al., 1999) or at 850 °C for two months (Zheng et al., 2002). They adopt a Hf₅Cu₃Sn-type (or stuffed Mn₅Si₃-type) structure (Pearson symbol *hP*18, space group *P*6₃/*mcm* (No. 193), *Z* = 2). From a single-crystal X-ray diffraction study on La₅Bi₃Br, the standardized positional parameters are: La1 in 6*g* (0.2728(3), 0, 1/4); La2 in 4*d* (1/3, 2/3, 0); Bi in 6*g*

Table 34
Crystallographic data for *R–Bi–halogen* compounds

Compound	Structure type	Pearson symbol	<i>a</i> (Å)	<i>c</i> (Å)	Reference
La ₅ Bi ₃ Br	Hf ₅ Cu ₃ Sn	<i>hP</i> 18	9.718(5)	6.753(6)	(Jensen et al., 1999)
La ₅ Bi ₃ Br ^a	Hf ₅ Cu ₃ Sn	<i>hP</i> 18	9.742(2)	6.795(2)	(Zheng et al., 2002)
Pr ₅ Bi ₃ Br	Hf ₅ Cu ₃ Sn	<i>hP</i> 18	9.528(4)	6.618(7)	(Jensen et al., 1999)

^aSingle-crystal data.

(0.6171(2), 0, 1/4); Br in $2b$ (0, 0, 0) (Zheng et al., 2002). The structure is similar to that depicted for Gd_5CuBi_3 (see fig. 16 in section 5.8.3), with chains of face-sharing La_6 octahedra (whose centres are filled by Br atoms and whose edges are bridged by Bi atoms) and chains of La atoms extending along the c direction. The existence of $\text{Ce}_5\text{Bi}_3\text{X}$ ($\text{X} = \text{Cl}, \text{Br}$) analogues has also been mentioned briefly (Hurng and Corbett, 1989). It is likely that many presumed binary R_5Bi_3 phases could well be similar ternary compounds stabilized by interstitial impurities (Jensen et al., 1999).

7. Conclusion

Ternary rare earth bismuthides share many similarities with the corresponding antimonides, but their chemistry and physics remain much less investigated. Many of the structure types found in these bismuthides are the same as in the antimonides. Thus, simple structures derived from rocksalt (RMBi ($M = \text{Ni}, \text{Pd}, \text{Pt}$), MgAgAs -type; RPd_2Bi , MnCu_2Al -type) or Fe_2P variants (RMBi ($M = \text{Mn}, \text{Fe}, \text{Co}, \text{Rh}$)) are adopted by both antimonides and bismuthides. Because most studies have so far focused on metal-rich systems, many dense, cluster-type structures are found. In general, these types of structures are made amenable by the large sizes of both the R and Bi atoms, which can take on high CN geometries. The more metal-rich the compound, the more likely this will occur. This trend is nicely seen on examining the coordination around Bi atoms on progressing from $\text{R}_5\text{M}_2\text{Bi}$ ($M = \text{Ni}, \text{Pd}, \text{Pt}$) (CN8 tetragonal antiprismatic), $\text{R}_8\text{Pd}_{24}\text{Bi}$ (CN10 bicapped square antiprismatic), and finally to $\text{R}_{12}\text{Co}_5\text{Bi}$ (CN12 icosahedral). Moreover, whereas the first two of these compounds have antimonide analogues, $\text{R}_{12}\text{Co}_5\text{Bi}$ (which is the most metal-rich rare earth bismuthide to date) is so far unique to bismuthides.

At the other extreme are Bi-rich systems, where fewer examples are known, probably because of the greater difficulties in synthesis. It is possible that some of these compounds are formed under non-equilibrium conditions. Again, some of these compounds have antimonide analogues, such as RMBi_2 ($M = \text{Ni}, \text{Cu}, \text{Ag}$) (HfCuSi_2 -type) and Ce_3MnBi_5 (anti- $\text{Hf}_5\text{Cu}_3\text{Sn}$ -type). These structures necessarily contain Bi–Bi bonding networks, in the form of two-dimensional square nets in RMBi_2 or one-dimensional linear chains in Ce_3MnBi_5 . Intermediate between these are finite Bi ribbons, either three- or four-atoms wide, that occur in $\text{Ce}_6\text{ZnBi}_{14}$ and LaGaBi_2 . This concept of pnictogen ribbons has proven useful in systematizing the structures of rare earth Sb-rich phases (Mills et al., 2002), so it may be worthwhile exploring whether it also applies to bismuthides. New examples of such bismuthides would be significant in extending our understanding of homoatomic Bi–Bi bonding.

The rare earth bismuth chalcogenides are quite different from the other systems, and really belong in a separate category. Where structures have been resolved, these are found to be valence-precise compounds containing formally Bi^{3+} and are expected to be semiconductors.

Fig. 27 summarizes the extent of known, well-defined ternary rare earth bismuthides. As can be seen, only a few systems have been relatively well studied, namely those containing the late first-row transition metals, the Ni triad, and the chalcogens. Notably lacking are examples of rare earth bismuthides containing early transition metals or the post-transition metals,

H $R_5\text{Bi}_3\text{H}$												B	C	N	O	F	
Li $RL_3\text{Bi}_2$ $RL\text{Bi}_2$ $RL\text{Bi}$	Be																
Na	Mg $R_3\text{MgBi}_5$												Al	Si $R_5\text{SiBi}_2?$	P	S $R\text{Bi}_4\text{S}_7$ $R_{1,2}\text{Bi}_{3,6}\text{S}_8$ $R\text{Bi}_2\text{S}_4$ $R_{1,1}\text{Bi}_2\text{S}_4$ $R\text{BiS}_3$ $R_3\text{Bi}_4\text{S}_9$ $R_4\text{Bi}_2\text{S}_9$ $R_2\text{BiS}_4$	Cl
K	Ca	Sc	Ti	V	Cr	Mn $R_3\text{MnBi}_5$ $R_{1,4}\text{MnBi}_{11}$ $R_6\text{MnBi}_2$	Fe $R_9\text{FeBi}_2$ $R_6\text{FeBi}_2$ $R_6\text{Fe}_{13}\text{Bi}$	Co $R_5\text{CoBi}_2$ $R_6\text{CoBi}_2$ $R_6\text{Co}_{13}\text{Bi}$ $R_{12}\text{Co}_9\text{Bi}$	Ni $R\text{NiBi}_2$ $R\text{NiBi}$ $R_5\text{Ni}_2\text{Bi}$ $R_5\text{NiBi}_2$	Cu $RCuBi_2$ $RCuBi$ $R_5\text{CuBi}_3$ $R_5\text{CuBi}_2$	Zn $R_6\text{ZnBi}_{14}$ $R_9\text{Zn}_4\text{Bi}_9$	Ga $RGaBi_2$	Ge $RGeBi_2$ $R_3\text{GeBi}$	As	Se $R\text{Bi}_4\text{Se}_7$ $R\text{Bi}_2\text{Se}_4$ $R\text{BiSe}_3$ $R_3\text{Bi}_4\text{Se}_9$ $R_2\text{Bi}_2\text{Se}_5$	Br $R_5\text{Bi}_3\text{Br}$	
Rb	Sr	Y	Zr	Nb	Mo	Tc	Ru	Rh $RRh\text{Bi}$	Pd $RPd_2\text{Bi}_2$ $RPd\text{Bi}$ $RPd_2\text{Bi}$ $R_3\text{Pd}_2\text{Bi}$ $R_3\text{Pd}_{24}\text{Bi}$	Ag $R\text{AgBi}_2$	Cd	In $R_{14}\text{InBi}_{11}$ $R_5\text{InBi}_3?$	Sn $R_4\text{SnBi}_2$	Sb	Te $R\text{Bi}_4\text{Te}_7$ $R\text{Bi}_2\text{Te}_4$ $R\text{BiTe}_3$ $R_3\text{Bi}_4\text{Te}_9$ $R\text{BiTe}$ $R_4\text{Bi}_2\text{Te}$ $R_6\text{Bi}_{1,7}\text{Te}_{0,8}$	I	
Cs	Ba	La	Hf	Ta	W	Re	Os	Ir	Pt $R_3\text{Pt}_3\text{Bi}_4$ $R\text{PtBi}$ $R_5\text{Pt}_2\text{Bi}$	Au	Hg	Tl	Pb	Bi	Po	At	

Fig. 27. Known ternary rare earth bismuthides.

but this scarcity probably reflects the absence of attention paid to these systems than to any inherent instability. The development of current research in the bismuthides parallels but lags behind that of the antimonides. With new opportunities in this area identified in this review, additional compounds are expected to be forthcoming in the future.

Acknowledgements

Much of the writing was completed during part of a sabbatical leave, supported by the University of Alberta, at the Université de Rennes 1, kindly hosted by Dr. Henri Noël and Dr. Olivier Tougaït. I am grateful to Dr. Andriy V. Tkachuk for his meticulous reading and helpful criticism of this manuscript.

References

- Abdusalyamova, M.N., Chuiko, A.G., Shishkin, E.I., Rachmatov, O.I., 1996. *J. Alloys Compd.* **240**, 272–277.
- Abdusalyamova, M.N., Rachmatov, O.I., 2002. *Z. Naturforsch. A* **57**, 98–100.
- Abulkhaev, V.D., 1992a. *Inorg. Mater.* (Translation of *Izv. Akad. Nauk SSSR, Neorg. Mater.*) **28**, 1511–1514.
- Abulkhaev, V.D., 1992b. *Inorg. Mater.* (Translation of *Izv. Akad. Nauk SSSR, Neorg. Mater.*) **28**, 1717–1720.
- Abulkhaev, V.D., 1993a. *Russ. Metall.* (Translation of *Izv. Akad. Nauk SSSR, Metall.*) (1), 152–155.
- Abulkhaev, V.D., 1993b. *Russ. Metall.* (Translation of *Izv. Akad. Nauk SSSR, Metall.*) (2), 169–172.
- Abulkhaev, V.D., Ganiev, I.N., 1995. *Russ. Metall.* (Translation of *Izv. Akad. Nauk SSSR, Metall.*) (2), 142–145.
- Aliev, O.M., Maksudova, T.F., 1986. *Russ. J. Inorg. Chem.* **31**, 1523–1525. *Zh. Neorg. Khim.* **23** (1986) 2639–2642 (in Russian).
- Aliev, O.M., Rustamov, P.G., 1978. *Russ. J. Inorg. Chem.* **23**, 1551–1553. *Zh. Neorg. Khim.* **23** (1978) 2800–2803 (in Russian).
- Aliev, O.M., Maksudova, T.F., Samsonova, N.D., Finkel'shtein, L.D., Rustamov, P.G., 1986. *Neorg. Mater.* **22**, 29–32.
- Allemand, J., Letant, A., Moreau, J.M., Nozières, J.P., Perrier de la Bâthie, R., 1990. *J. Less-Common Met.* **166**, 73–79.
- Alonso, J.A., Boucherle, J.X., Rossat-Mignod, J., Schweizer, J., Suzuki, T., Kasuya, T., 1992. *J. Magn. Magn. Mater.* **103**, 179–193.
- Amato, A., Canfield, P.C., Feyerherm, R., Fisk, Z., Gy-gax, F.N., Heffner, R.H., MacLaughlin, D.E., Ott, H.R., Schenck, A., Thompson, J.D., 1992. *Phys. Rev. B* **46**, 3151–3154.
- Aoki, H., Ochiai, A., Suzuki, T., 1999. *Physica B* **259–261**, 349–350.
- Asadov, M.M., Babaeva, I.G., Aliev, O.M., 1995. *Russ. J. Inorg. Chem.* **40**, 813–814. *Zh. Neorg. Khim.* **40** (1995) 842–843 (in Russian).
- Bartholin, H., Sera, M., Haen, P., Kasuya, T., 1987. *J. Magn. Magn. Mater.* **63–64**, 46–48.
- Benz, R., Zachariasen, W.H., 1970. *Acta Crystallogr. Sect. B* **26**, 823–827.
- Bodak, O., Stepien-Damm, J., Galdecka, E., 2000. *J. Alloys Compd.* **298**, 195–197.
- Bolotaev, A.G., Koroliuk, A.L., Morozkin, A.V., Niki-forov, V.N., 2004. *J. Alloys Compd.* **373**, L1–L2.
- Borisov, S.V., Magarill, S.A., Pervukhina, N.V., Pod-berezskaya, N.V., 2000. *J. Struct. Chem.* **41**, 263–271. *Zh. Strukt. Khim.* **41** (2000) 324–334 (in Russian).
- Borzone, G., Ferro, R., Parodi, N., Saccone, A., 1995. *Gazz. Chim. Ital.* **125**, 263–270.
- Brechtel, E., Cordier, G., Schäfer, H., 1979. *Z. Naturforsch. B: Anorg. Chem. Org. Chem.* **34**, 1229–1233.
- Canfield, P.C., Thompson, J.D., Beyermann, W.P., Lacerda, A., Hundley, M.F., Peterson, E., Fisk, Z., Ott, H.R., 1991. *J. Appl. Phys.* **70**, 5800–5802.
- Canfield, P.C., Movshovich, R., Robinson, R.A., Thompson, J.D., Fisk, Z., Beyermann, W.P., Lacerda, A., Hundley, M.F., Heffner, R.H., MacLaughlin, D.E., Trouw, F., Ott, H.R., 1994. *Physica B* **197**, 101–108.

- Céolin, R., Toffoli, P., Khodadad, P., Rodier, N., 1977. *Acta Crystallogr. Sect. B* **33**, 2804–2806.
- Chan, J.Y., Wang, M.E., Rehr, A., Kauzlarich, S.M., Webb, D.J., 1997. *Chem. Mater.* **9**, 2131–2138.
- Chan, J.Y., Kauzlarich, S.M., Klavins, P., Shelton, R.N., Webb, D.J., 1998a. *Phys. Rev. B* **57**, R8103–R8106.
- Chan, J.Y., Olmstead, M.M., Kauzlarich, S.M., Webb, D.J., 1998b. *Chem. Mater.* **10**, 3583–3588.
- Chechernikov, V.I., Martynova, L.F., Kuznetsov, N.T., Slovyanskikh, V.K., Gracheva, N.V., 1990. *Izv. Akad. Nauk SSSR, Neorg. Mater.* **26**, 2222.
- Chen, L., Corbett, J.D., 2004. *Inorg. Chem.* **43**, 436–442.
- Chefkowska, G., 1994. *Solid State Commun.* **91**, 803–806.
- Chefkowska, G., Chefkowski, A., Borstel, G., Neumann, M., 1994. *Electron Technology* **27**, 161–165.
- Cho, B.K., Gordon, R.A., Jones, C.D.W., DiSalvo, F.J., Kim, J.S., Stewart, G.R., 1998. *Phys. Rev. B* **57**, 15191–15196.
- Coey, J.M.D., Qi, Q., Knoch, K.G., Leithe-Jasper, A., Rogl, P., 1994. *J. Magn. Magn. Mater.* **129**, 87–97.
- Corbett, J.D., Leon-Escamilla, E., 2003. *J. Alloys Compd.* **356–357**, 59–64.
- Cordier, G., Eisenmann, B., Schäfer, H., 1976. *Z. Anorg. Allg. Chem.* **426**, 205–214.
- Dai, D., Fang, R., Long, P., Zhang, S., Ma, T., Dai, C., Zhang, X., 1992. *J. Magn. Magn. Mater.* **115**, 66–76.
- Degtyar, V.A., Vnuchkova, L.A., Bayanov, A.P., Serebrennikov, V.V., 1971. *Izv. Akad. Nauk SSSR, Metall* (6), 86–88.
- Désévéday, F., Tkachuk, A.V., Mar, A., 2004. Unpublished work.
- Dhar, S.K., Nambudripad, N., Vijayaraghavan, R., 1988. *J. Phys. F: Met. Phys.* **18**, L41–L44.
- Drzyzga, M., Szade, J., 2001. *J. Alloys Compd.* **321**, 27–34.
- Drzyzga, M., Szade, J., Deniszczyk, J., Michalecki, T., 2003. *J. Phys.: Condens. Matter* **15**, 3701–3706.
- Dwight, A.E., 1974. *Proc. 11th Rare Earth Res. Conf.* **2**, 642–650.
- Dwight, A.E., 1977. *Acta Crystallogr. Sect. B* **33**, 1579–1581.
- Dzhafarova, E.K., Sadygov, F.M., Babaev, Ya.N., Babanly, M.B., 2002. *Russ. J. Inorg. Chem.* **47**, 1572–1574. *Zh. Neorg. Khim.* **47** (2002) 1713–1715 (in Russian).
- Ecrepont, C., Guittard, M., Flahaut, J., 1988. *Mater. Res. Bull.* **23**, 37–42.
- El Kholdi, M., Averous, M., Charar, S., Fau, C., Brun, G., Ghoumari-Bouanani, H., Deportes, J., 1994. *Phys. Rev. B* **49**, 1711–1715.
- Eriksson, O., Wills, J.M., Boring, A.M., 1992. *J. Alloys Compd.* **185**, 145–149.
- Fang, R., Li, D., Ma, T., Dai, D., Zhang, X., 1991. *IEEE Trans. Magn.* **27**, 5133–5135.
- Fang, R., Dai, D., Zhang, S., Long, P., Ma, T., Dai, C., Zhang, X., 1992. *J. Magn. Magn. Mater.* **104–107**, 1031–1032.
- Fang, R., Fang, Q., Zhang, S., Peng, C., Dai, D., 1994. *J. Appl. Phys.* **76**, 6769–6771.
- Fang, R., Fang, Q., Zhang, S., Peng, C., Dai, D., 1995. *J. Appl. Phys.* **77**, 1178–1183.
- Fang, Q., Fang, R., Zhang, S., Dai, D., 1998. *J. Magn. Magn. Mater.* **188**, 241–245.
- Fang, Q., Fang, R., Zhang, S., Dai, D., 1999. *J. Appl. Phys.* **86**, 3878–3880.
- Ferguson, M.J., Hushagen, R.W., Mar, A., 1997. *J. Alloys Compd.* **249**, 191–198.
- Fisher, P., Hälgl, W., Hulliger, F., 1985. *Physica B/C* **130**, 551–554.
- Fisk, Z., Canfield, P.C., Beyermann, W.P., Thompson, J.D., Hundley, M.F., Ott, H.R., Felder, E., Maple, M.B., Lopez de la Torre, M.A., Visani, P., Seaman, C.L., 1991. *Phys. Rev. Lett.* **67**, 3310–3313.
- Flandorfer, H., Sologub, O., Godart, C., Hiebl, K., Leithe-Jasper, A., Rogl, P., Noël, H., 1996. *Solid State Commun.* **97**, 561–565.
- Gambino, R.J., 1967. *J. Less-Common Met.* **12**, 344–352.
- Garibov, F.A., Aliev, F.G., Aliev, O.M., Mamedov, V.N., Kuliev, A.G., 1993a. *Zh. Neorg. Khim.* **38**, 173–174.
- Garibov, F.A., Aliev, O.M., Aliev, F.G., Mamedov, V.N., Albendov, A.A., 1993b. *Neorg. Mater.* **29**, 432–433.
- Gelato, L.M., Parthé, E., 1987. *J. Appl. Crystallogr.* **20**, 139–143.
- Godzhaev, E.M., Rustamov, P.G., Guseinov, M.S., Aliev, O.M., 1977. *Neorg. Mater.* **13**, 624–626.
- Goll, G., Hagel, J., von Löhneysen, H., Pietrus, T., Wanka, S., Wosnitza, J., Zwicky, G., Yoshino, T., Takabatake, T., Jansen, A.G.M., 2002. *Europhys. Lett.* **57**, 233–239.
- Gordon, R.A., DiSalvo, F.J., 1996. *Z. Naturforsch. B* **51**, 52–56.
- Gordon, R.A., Jones, C.D.W., Alexander, M.G., DiSalvo, F.J., 1996. *Physica B* **225**, 23–32.
- Gratens, X., Isber, S., Charar, S., Fau, C., Averous, M., Misra, S.K., Golacki, Z., Ferhat, M., Tedenac, J.C., 1997. *Phys. Rev. B* **55**, 8075–8078.
- Grund, I., Schuster, H.-U., Müller, P., 1984. *Z. Anorg. Allg. Chem.* **515**, 151–158.
- Grund, I., Zwiener, G., Schuster, H.-U., 1986. *Z. Anorg. Allg. Chem.* **535**, 7–12.
- Guloy, A.M., Corbett, J.D., 1996. *Inorg. Chem.* **35**, 2616–2622.

- Güner, S., Rameev, B., Aktaş, B., 2003a. *J. Magn. Magn. Mater.* **258–259**, 372–375.
- Güner, S., Rameev, B., Aktaş, B., 2003b. *Phys. Stat. Solidi* **236**, 645–650.
- Haase, M.G., Schmidt, T., Richter, C.G., Block, H., Jeitschko, W., 2002. *J. Solid State Chem.* **168**, 18–27.
- Hansen, P., Urner-Wille, M., 1979. *J. Appl. Phys.* **50**, 7471–7476.
- Hartmann, M., McGuire, T.R., 1983. *Phys. Rev. Lett.* **51**, 1194–1197.
- Hartmann, M., Witter, K., Willich, P., 1985. *IEEE Trans. Magn.* **21**, 2044–2046.
- Heitmann, H., Sander, I., Urner-Wille, M., Witter, K., 1980. *J. Magn. Magn. Mater.* **21**, 233–238.
- Hofmann, W.K., Jeitschko, W., 1985. *Monatsh. Chem.* **116**, 569–580.
- Hofmann, W.K., Jeitschko, W., 1988. *J. Less-Common Met.* **138**, 313–322.
- Hohnke, D., Parthé, E., 1966. *Acta Crystallogr.* **21**, 435–437.
- Hohnke, D., Parthé, E., 1969. *J. Alloys Compd.* **17**, 291–296.
- Holm, A.P., Kauzlarich, S.M., Morton, S.A., Waddill, G.D., Pickett, W.E., Tobin, J.G., 2002. *J. Am. Chem. Soc.* **124**, 9894–9898.
- Holtzberg, F., McGuire, T.R., Methfessel, S., Suits, J.C., 1964. *J. Appl. Phys.* **35**, 1033–1038.
- Hulliger, F., 1979a. In: Gschneidner Jr., K.A., Eyring, L. (Eds.), *Handbook on the Physics and Chemistry of Rare Earths*, vol. **4**. North-Holland Publishing, Amsterdam, pp. 153–256.
- Hulliger, F., 1979b. *Mater. Res. Bull.* **14**, 259–262.
- Hulliger, F., 1980. *J. Magn. Magn. Mater.* **15/18**, 1243–1244.
- Hulliger, F., Ott, H.R., 1977. *J. Less-Common Met.* **55**, 103–113.
- Hulliger, F., Stucki, F., 1978. *Z. Phys. B: Condens. Matter* **31**, 391–393.
- Hundley, M.F., Canfield, P.C., Thompson, J.D., Fisk, Z., Lawrence, J.M., 1990. *Phys. Rev. B* **42**, 6842–6845.
- Hundley, M.F., Canfield, P.C., Thompson, J.D., Fisk, Z., 1994. *Phys. Rev. B* **50**, 18142–18146.
- Hundley, M.F., Thompson, J.D., Canfield, P.C., Fisk, Z., 1997. *Phys. Rev. B* **56**, 8098–8102.
- Hurng, W.-M., Corbett, J.D., 1989. *Chem. Mater.* **1**, 311–319.
- Iitaka, Y., Nowacki, W., 1962. *Acta Crystallogr.* **15**, 691–698.
- Jarosz, J., Ślebarski, A., Chelkowski, A., 1990. *J. Phys.: Condens. Matter* **2**, 7181–7186.
- Jemetio, J.-P., Doert, Th., Rademacher, O., Böttcher, P., 2002. *J. Alloys Compd.* **338**, 93–98.
- Jensen, E.A., Hoistad, L.M., Corbett, J.D., 1999. *J. Solid State Chem.* **144**, 175–180.
- Ji, X.H., Zhao, X.B., Zhang, Y.H., Lu, B.H., Ni, H.L., 2005. *J. Alloys Compd.* **387**, 282–286.
- Jung, M.H., Yoshino, T., Kawasaki, S., Pietrus, T., Bando, Y., Suemitsu, T., Sera, M., Takabatake, T., 2001. *J. Appl. Phys.* **89**, 7631–7633.
- Jung, M.H., Lacerda, A.H., Takabatake, T., 2002. *Phys. Rev. B* **65**, 132405-1–132405-3.
- Kaczorowski, D., 1992. *J. Alloys Compd.* **186**, 333–338.
- Kaczorowski, D., Leithe-Jasper, A., Rogl, P., Flandorfer, H., Cichorek, T., Pietri, R., Andraka, B., 1999. *Phys. Rev. B* **60**, 422–433.
- Kaczorowski, D., Gofryk, K., Plackowski, T., Leithe-Jasper, A., Grin, Yu., 2005. *J. Magn. Magn. Mater.* **290–291**, 573–579.
- Kasaya, M., Suzuki, H., Tazawa, D., Shirakawa, M., Sawada, A., Osakabe, T., 2000. *Physica B* **281–282**, 579–580.
- Kasuya, T., Sera, M., Suzuki, T., 1993. *J. Phys. Soc. Jpn.* **62**, 2561–2563.
- Kasuya, T., Sera, M., Okayama, Y., Haga, Y., 1996. *J. Phys. Soc. Jpn.* **65**, 160–171.
- Katoh, K., Takabatake, T., 1998. *J. Alloys Compd.* **268**, 22–24.
- Katz, H.M., Hill, F.B., Speirs, J.L., 1960. *Trans. Metall. Soc. AIME* **218**, 770–775.
- Kawasaki, Y., Kishimoto, Y., Imai, N., Ohno, T., Kubo, H., Yoshii, S., Kasaya, M., 2004. *J. Phys. Soc. Jpn.* **73**, 694–697.
- Kim, M.-S., Sasakawa, T., Suemitsu, T., Bando, Y., Umeo, K., Iga, F., Mitamura, H., Goto, T., Takabatake, T., 2001. *J. Phys. Soc. Jpn.* **70**, 3650–3653.
- Kim, S.-J., Salvador, J., Bilc, D., Mahanti, S.D., Kanatzidis, M.G., 2001. *J. Am. Chem. Soc.* **123**, 12704–12705.
- Kleinke, H., 1997. *J. Alloys Compd.* **252**, L29–L31.
- Kleinke, H., 1998. *J. Alloys Compd.* **270**, 136–141.
- Kuz'ma, Y., Chykhrij, S., 1996. In: Gschneidner Jr., K.A., Eyring, L. (Eds.), *Handbook on the Physics and Chemistry of Rare Earths*, vol. **23**. Elsevier, Amsterdam, pp. 285–434.
- Krypyakevich, P.I., Burnashova, V.V., Markiv, V.Ya., 1970. *Dopov. Akad. Nauk Ukr. RSR, Ser. A: Fiz.-Tekhn. Mat. Nauki* **32**, 828.
- Kwei, G.H., Lawrence, J.M., Canfield, P.C., Beyermann, W.P., Thompson, J.D., Fisk, Z., Lawson, A.C., Goldstone, J.A., 1992. *Phys. Rev. B* **46**, 8067–8072.
- Kwon, Y.-U., Sevov, S.C., Corbett, J.D., 1990. *Chem. Mater.* **2**, 550–556.

- Larson, P., Mahanti, S.D., Sportouch, S., Kanatzidis, M.G., 1999. *Phys. Rev. B* **59**, 15660–15668.
- LeBras, G., Bonville, P., Hodges, J.A., Hammann, J., Besnus, M.J., Schmerber, G., Dhar, S.K., Aliev, F.G., André, G., 1995. *J. Phys.: Condens. Matter* **7**, 5665–5680.
- Léger, J.M., Oki, K., Rossat-Mignod, J., Vogt, O., 1985. *J. Phys. (Paris)* **46**, 889–894.
- Lemoine, P., Carré, D., Guittard, M., 1982. *Acta Crystallogr. Sect. B* **38**, 727–729.
- Lemoine, P., Carré, D., Guittard, M., 1986. *Acta Crystallogr. Sect. C* **42**, 259–261.
- Leon-Escamilla, E., Corbett, J.D., 1994. *J. Alloys Compd.* **206**, L15–L17.
- Leon-Escamilla, E., Corbett, J.D., 1998. *J. Alloys Compd.* **265**, 104–114.
- Leon-Escamilla, E.A., Hurng, W.-M., Peterson, E.S., Corbett, J.D., 1997. *Inorg. Chem.* **36**, 703–710.
- Li, Z., Luo, H., Lai, W., Zeng, Z., Zheng, Q., 1991. *Solid State Commun.* **79**, 791–794.
- Li, G.-R., Tong, Y.-X., Liu, G.-K., 2004a. *J. Electrochem. Soc.* **151**, C412–C417.
- Li, G.-R., Tong, Y.-X., Liu, G.-K., 2004b. *Mater. Lett.* **58**, 3839–3843.
- Lu, Y.M., Yang, X.X., Chen, H.H., Zhao, J.T., 2004. *J. Rare Earths* **22**, 746–748.
- Lu, Y.-M., Liang, Y., Yang, X.-X., Chen, H.-H., Zhao, J.-T., 2005. *Jiegou Huaxue* **24**, 769–772.
- Maksudova, T.F., Rustamov, P.G., Aliev, O.M., 1985. *J. Less-Common Met.* **109**, L19–L23.
- Maksudova, T.F., Alieva, O.A., Aliev, O.M., 1988. *Neorg. Mater.* **24**, 1393–1394.
- Mamedova, S.G., Sadygov, F.M., Gasymov, V.A., Babanly, M.B., 2003. *Russ. J. Inorg. Chem.* **48**, 422–424. *Zh. Neorg. Khim.* **48** (2003) 492–494 (in Russian).
- Marazza, R., Rossi, D., Ferro, R., 1980. *Gazz. Chim. Ital.* **110**, 357–359.
- Marchand, R., 1998. In: Gschneidner Jr., K.A., Eyring, L. (Eds.), *Handbook on the Physics and Chemistry of Rare Earths*, vol. **25**. Elsevier, Amsterdam, pp. 51–99.
- Martins, G.B., Rao, D., Barberis, G.E., Rettori, C., Duro, R.J., Sarrao, J., Fisk, Z., Oseroff, S., Thompson, J.D., 1996. *Physica B* **223–224**, 396–398.
- Matlak, M., Zieliński, J., 1991. *Acta Phys. Polon. A* **79**, 717–719.
- McGuire, T.R., Hartmann, M., 1985. *IEEE Trans. Magn.* **21**, 1644–1646.
- McMullan, G.J., Ray, M.P., 1992. *J. Phys.: Condens. Matter* **4**, 7095–7101.
- Merlo, F., Pani, M., Fornasini, M.L., 1990. *J. Less-Common Met.* **166**, 319–327.
- Merlo, F., Pani, M., Fornasini, M.L., 1995. *J. Alloys Compd.* **221**, 280–283.
- Mills, A.M., Lam, R., Ferguson, M.J., Deakin, L., Mar, A., 2002. *Coord. Chem. Rev.* **233–234**, 207–222.
- Milner, G.W.C., Edwards, J.W., 1958. *Anal. Chim. Acta* **18**, 513–519.
- Milner, G.W.C., Nunn, J.H., 1957. *Anal. Chim. Acta* **17**, 494–499.
- Morelli, D.T., Canfield, P.C., Drymiotis, P., 1996. *Phys. Rev. B* **53**, 12896–12901.
- Morgan, M.G., Wang, M., Chan, W.Y., Mar, A., 2003. *Inorg. Chem.* **42**, 1549–1555.
- Morozkin, A.V., 2003a. *J. Alloys Compd.* **358**, L9–L10.
- Morozkin, A.V., 2003b. *J. Alloys Compd.* **360**, L1–L2.
- Morozkin, A.V., 2003c. *J. Alloys Compd.* **360**, L7–L8.
- Morozkin, A.V., Nirmala, R., Malik, S.K., 2005. *J. Alloys Compd.* **394**, L9–L11.
- Movshovich, R., Lacerda, A., Canfield, P.C., Arms, D., Thompson, J.D., Fisk, Z., 1994a. *Physica* **199–200**, 67–69.
- Movshovich, R., Lacerda, A., Canfield, P.C., Thompson, J.D., Fisk, Z., 1994b. *Phys. Rev. Lett.* **73**, 492–495.
- Mozharivskii, Yu.A., Kuz'ma, Yu.B., Sichevich, O.M., 1998. *Inorg. Mater. (Translation of Neorg. Mater.)* **34**, 707–710.
- Mozharivsky, Yu.A., Kuz'ma, Yu.B., 1999. *Russ. Metall. (Translation of Metallurgy)* **4**, 166–169.
- Mozharivskiy, Y. 2005. Private communication.
- Mozharivskiy, Y., Franzen, H.F., 2000. *J. Solid State Chem.* **152**, 478–485.
- Mozharivskiy, Y., Franzen, H.F., 2001. *J. Alloys Compd.* **327**, 78–81.
- Naher, S., Suzuki, H., Mizuno, M., Xue, Y., Kasaya, M., Kunii, S., Kitai, T., 2003. *Physica B* **329–333**, 631–632.
- Niu, X.J., Gschneidner Jr., K.A., Pecharsky, A.O., Pecharsky, V.K., 2001. *J. Magn. Magn. Mater.* **234**, 193–206.
- Nomura, K., Hayakawa, H., Ono, S., 1977. *J. Less-Common Met.* **52**, 259–269.
- Oguchi, T., 2001. *Phys. Rev. B* **63**, 125115-1–125115-5.
- Oh, S.-J., Suga, S., Saito, Y., Kakizaki, A., Ishii, T., Taniguchi, M., Fujimori, A., Miyahara, T., Kato, H., Ochiai, A., Suzuki, T., Kasuya, T., 1992. *Solid State Commun.* **82**, 581–586.
- Oppeneer, P.M., Antonov, V.N., Yaresko, A.N., Perlov, A.Ya., Eschrig, H., 1997. *Phys. Rev. Lett.* **78**, 4079–4082.
- Oyamada, A., Isobe, A., Kitazawa, H., Ochiai, A., Suzuki, T., Kasuya, T., 1993. *J. Phys. Soc. Jpn.* **62**, 1750–1757.

- Pagliuso, P.G., Rettori, C., Torelli, M.E., Martins, G.B., Fisk, Z., Sarrao, J.L., Hundley, M.F., Oseroff, S.B., 1999. *Phys. Rev. B* **60**, 4176–4180.
- Pan, D.-C., Sun, Z.-M., Mao, J.-G., 2006. *J. Solid State Chem.* **179**, 1016–1021.
- Parodi, N., Borzone, G., Balducci, G., Brutti, S., Ciccioli, A., Gigli, G., 2003. *Intermetallics* **11**, 1175–1181.
- Parthé, E., Gelato, L.M., 1984. *Acta Crystallogr. Sect. A* **40**, 169–183.
- Pecharsky, A.O., Gschneidner Jr., K.A., 1999. *J. Alloys Compd.* **287**, 67–70.
- Petrovic, C., Bud'ko, S.L., Canfield, P.C., 2002. *J. Magn. Magn. Mater.* **247**, 270–278.
- Petrovic, C., Bud'ko, S.L., Strand, J.D., Canfield, P.C., 2003. *J. Magn. Magn. Mater.* **261**, 210–221.
- Pietri, R., Andracka, B., Kaczorowski, D., Leithe-Jasper, A., Rogl, P., 2000. *Phys. Rev. B* **61**, 12169–12173.
- Pietrus, T., Mioković, T., Schröder, A., von Löhneysen, H., Yoshino, T., Takagi, K., Umeo, K., Takabatake, T., 2000. *Physica B* **281–282**, 745–746.
- Prill, M., Mosel, B.D., Müller-Warmuth, W., Albering, J., Ebel, T., Jeitschko, W., 2002. *Solid State Sci.* **4**, 695–700.
- Reiswig, R.D., Mack, D.J., 1955. *J. Metals* **7**, 315–316.
- Riani, P., Mazzone, D., Zanichi, G., Marazza, R., Ferro, R., 1995. *Z. Metallkd.* **86**, 450–452.
- Robinson, R.A., Kohgi, M., Osakabe, T., Canfield, P.C., Kamiyama, T., Nakane, T., Fisk, Z., Thompson, J.D., 1993. *Physica B* **186–188**, 550–552.
- Robinson, R.A., Purwanto, A., Kohgi, M., Canfield, P.C., Kamiyama, T., Ishigaki, T., Lynn, J.W., Erwin, R., Peterson, E., Movshovich, R., 1994. *Phys. Rev. B* **50**, 9595–9598.
- Robinson, R.A., Kohgi, M., Osakabe, T., Trouw, F., Lynn, J.W., Canfield, P.C., Thompson, J.D., Fisk, Z., Beyermann, W.P., 1995. *Phys. Rev. Lett.* **75**, 1194–1197.
- Robinson, R.A., Christianson, A., Nakotte, H., Beyermann, W.P., Canfield, P.C., 1999. *Physica B* **259–261**, 138–139.
- Rossat-Mignod, J., Burlet, P., Quezel, S., Effantin, J.M., Delacote, D., Bartholin, H., Vogt, O., Ravot, D., 1983. *J. Magn. Magn. Mater.* **31/34**, 398–404.
- Rustamov, P.G., Godzhaev, E.M., Guseinov, M.S., Aliev, O.M., 1977a. *Russ. J. Inorg. Chem.* **22**, 298–299. *Zh. Neorg. Khim.* **22** (1977) 540–542 (in Russian).
- Rustamov, P.G., Sadygov, F.M., Melikova, Z.D., Saforov, M.G., 1977b. *Russ. J. Inorg. Chem.* **22**, 585–586. *Zh. Neorg. Khim.* **22** (1977) 1062–1064 (in Russian).
- Rustamov, P.G., Sadygov, F.M., Melikova, Z.D., Saforov, M.G., 1978. *Russ. J. Inorg. Chem.* **23**, 471–472. *Zh. Neorg. Khim.* **23** (1978) 849–850 (in Russian).
- Rustamov, P.G., Sadygov, F.M., Melikova, Z.D., Cherstvova, V.B., 1979a. *Russ. J. Inorg. Chem.* **24**, 426–428. *Zh. Neorg. Khim.* **24** (1979) 764–766 (in Russian).
- Rustamov, P.G., Sadygov, F.M., Melikova, Z.D., Alidzhanov, M.A., Ali-Zade, M.Z., 1979b. *Neorg. Mater.* **15**, 775–777.
- Rustamov, P.G., Sadygov, F.M., Abilov, Ch.I., 1984. *Phys. Stat. Solidi A* **86**, K113–K115.
- Rustamov, P.G., Sadygov, F.M., Aliev, I.I., 1985. *Russ. J. Inorg. Chem.* **30**, 148–150. *Zh. Neorg. Khim.* **30** (1985) 263–265 (in Russian).
- Sadigov, F.M., Aliyev, O.M., Rustamov, P.G., 1985. *J. Less-Common Met.* **113**, 17–19.
- Sadygov, F.M., 1993. *Russ. J. Inorg. Chem.* **38**, 986–991. *Zh. Neorg. Khim.* **38** (1993) 1065–1071 (in Russian).
- Sadygov, F.M., Aliev, O.M., 1989. *Neorg. Mater.* **25**, 1283–1286.
- Sadygov, F.M., Abilov, Ch.I., Rustamov, P.G., 1985. *Russ. J. Inorg. Chem.* **30**, 1806–1808. *Zh. Neorg. Chem.* **30** (1985) 3177–3180 (in Russian).
- Sadygov, F.M., Rustamov, P.G., Il'yasov, T.M., Cherstvova, V.B., 1987a. *Neorg. Mater.* **23**, 545–549.
- Sadygov, F.M., Bakhtiyarov, I.B., Geidarova, E.A., 1987b. *Neorg. Mater.* **23**, 1988–1992.
- Sadygov, F.M., Geidarova, E.A., Aliev, I.I., 1988. *Russ. J. Inorg. Chem.* **33**, 1238–1240. *Zh. Neorg. Khim.* **33** (1988) 2167–2169 (in Russian).
- Sadygov, F.M., Aliev, I.I., Aliev, O.M., 1989. *Russ. J. Inorg. Chem.* **34**, 602–604. *Zh. Neorg. Khim.* **34** (1989) 1071–1074 (in Russian).
- Sadygov, F.M., Rustamov, P.G., Mirzoeva, R.D., 1996. *Russ. J. Inorg. Chem.* **41**, 289–291. *Zh. Neorg. Chem.* **41** (1996) 302–304 (in Russian).
- Sadygov, F.M., Dzhafarova, E.K., Babanly, M.B., Kuliev, F.I., 2001. *Russ. J. Inorg. Chem.* **46**, 1244–1246. *Zh. Neorg. Khim.* **46** (2001) 1379–1381 (in Russian).
- Saha, S., Huang, M.Q., Thong, C.J., Zande, B.J., Chandhok, V.K., Simizu, S., Obermyer, R.T., Sankar, S.G., 2000. *J. Appl. Phys.* **87**, 6040–6042.
- Saiki, K., Onishi, K., Inokuchi, S., Sakurai, Y., 1985. *Japan. J. Appl. Phys.* **24**, 552–556.
- Salamakha, P., Sologub, O., Suemitsu, T., Takabatake, T., 2000. *J. Alloys Compd.* **313**, L5–L9.
- Schmidt, F.A., McMasters, O.D., Lichtenberg, R.R., 1969. *J. Less-Common Met.* **18**, 215–220.

- Schmidt, T., Jeitschko, W., 2001. *Inorg. Chem.* **40**, 6356–6361.
- Sera, M., Haen, P., Laborde, O., Bartholin, H., Kasuya, T., 1985. *J. Magn. Magn. Mater.* **47–48**, 89–92.
- Severing, A., Thompson, J.D., Canfield, P.C., Fisk, Z., Riseborough, P., 1991. *Phys. Rev. B* **44**, 6832–6837.
- Sichevich, O.M., Lapunova, R.V., Sobolev, A.N., Grin, Ya.N., Yarmolyuk, Ya.P., 1985. *Kristallografiya* **30**, 1077–1080.
- Smith, F.J., Ferris, L.M., 1970. *J. Inorg. Nucl. Chem.* **32**, 2863–2868.
- Sologub, O.L., Salamakha, P.S., 2003. In: Gschneidner Jr., J.-C.G., Bünzli, K.A., Pecharsky, V.K. (Eds.), *Handbook on the Physics and Chemistry of Rare Earths*, vol. **33**. Elsevier, Amsterdam, pp. 35–146.
- Steinberg, G., Schuster, H.-U., 1979. *Z. Naturforsch.* **B 34**, 1165–1166.
- Stetskiv, A.O., Pavlyuk, V.V., Bodak, O.I., 1998. *Ukr. Khim. Zh.* **64**, 22–24.
- Suzuki, H., Kasaya, M., Miyazaki, T., Nemoto, Y., Goto, T., 1997. *J. Phys. Soc. Jpn.* **66**, 2566–2568.
- Suzuki, H., Xue, Y., Naher, S., Yamauchi, R., Asada, S., Mizuno, M., Abe, S., Kunii, S., Kasaya, M., 2004. *Physica B* **345**, 239–242.
- Suzuki, O., Suzuki, H., Takamasu, T., Kitazawa, H., Kido, G., 2004. *Physica B* **346–347**, 416–420.
- Szytuła, A., Jezierski, A., Penc, B., Winiarski, A., Leithe-Jasper, A., Kaczorowski, D., 2003. *J. Alloys Compd.* **360**, 41–46.
- Tanryverdiev, V.S., Aliev, O.M., Aliev, I.G., 1997. *Russ. J. Inorg. Chem.* **42**, 287–291. *Zh. Neorg. Khim.* **42** (1997) 346–350 (in Russian).
- Thamizhavel, A., Galatanu, A., Yamamoto, E., Okubo, T., Yamada, M., Tabata, K., Kobayashi, T.C., Nakamura, N., Sugiyama, K., Kindo, K., Takeuchi, T., Settai, R., Ōnuki, Y., 2003. *J. Phys. Soc. Jpn.* **72**, 2632–2639.
- Thompson, J.D., Canfield, P.C., Lacerda, A., Hundley, M.F., Fisk, Z., Ott, H.-R., Felder, E., Chernikov, M., Maple, M.B., Visani, P., Seaman, C.L., Lopez de la Torre, M.A., Aeppli, G., 1993. *Physica B* **186–188**, 355–357.
- Tkachuk, A.V., Mar, A. 2004. Unpublished results.
- Tkachuk, A.V., Mar, A., 2005. *Inorg. Chem.* **44**, 2272–2281.
- Tkachuk, A.V., Mozharivskyj, Y., Mar, A., 2006a. *Z. Kristallogr.* **221**, 539–542.
- Tkachuk, A.V., Muirhead, C.P.T., Mar, A., 2006b. *J. Alloys Compd.* **418**, 39–44.
- Tkachuk, A.V., Tam, T., Mar, A., 2006c. *J. Alloys Compd.*, submitted for publication.
- Tomuschat, C., Schuster, H.-U., 1981. *Z. Naturforsch.* **B 36**, 1193–1194.
- Tomuschat, C., Schuster, H.-U., 1984. *Z. Anorg. Allg. Chem.* **518**, 161–167.
- Troć, R., Żolnierek, Z., 1979. *J. Phys., Colloque* **40** (4), 79–81.
- Turberfield, K.C., Passell, L., Birgeneau, R.J., Bucher, E., 1971. *J. Appl. Phys.* **42**, 1746–1754.
- Ufer, H., Chelkowska, G., Borstel, G., 1994. *Solid State Commun.* **92**, 751–754.
- Urner-Wille, M., Kobs, R., Witter, K., 1981. *IEEE Trans. Magn.* **17**, 2621–2623.
- Wang, M., McDonald, R., Mar, A., 1999. *J. Solid State Chem.* **147**, 140–145.
- Wang, M.E., Chang, J.T., Kauzlarich, S.M., 1996. *Z. Anorg. Allg. Chem.* **622**, 432–436.
- Wang, Y., Gabe, E.J., Calvert, L.D., Taylor, J.B., 1976. *Acta Crystallogr. Sect. B* **32**, 1440–1445.
- Washko, S., Gerboc, J., Orehotsky, J., 1976. *IEEE Trans. Magn.* **12**, 974–976.
- Weitzer, F., Leithe-Jasper, A., Rogl, P., Hiebl, K., Noël, H., Wiesinger, G., Steiner, W., 1993. *J. Solid State Chem.* **104**, 368–376.
- Wells, A.F., 1977. *Three-Dimensional Nets and Polyhedra*. Wiley, New York.
- Wosnitza, J., Hagel, J., Kozlova, N., Eckert, D., Müller, K.-H., Mielke, C.H., Goll, G., Yoshino, T., Takabatake, T., 2004. *Physica B* **346–347**, 127–131.
- Ye, J., Huang, Y.K., Kadowaki, K., Matsumoto, T., 1996. *Acta Crystallogr. Sect. C* **52**, 1323–1325.
- Yoshihara, K., Taylor, J.B., Calvert, J.D., Despault, J.G., 1975. *J. Less-Common Met.* **41**, 329–337.
- Yoshii, S., Kasaya, M., Takahashi, H., Mori, N., 1996. *Physica B* **223–224**, 421–425.
- Yoshii, S., Tazawa, D., Kasaya, M., 1997. *Physica B* **230–232**, 380–382.
- Zeng, L., Franzen, H.F., 1998. *J. Alloys Compd.* **266**, 155–157.
- Zhao, X.B., Zhang, Y.H., Ji, X.H., 2004. *Inorg. Chem. Commun.* **7**, 386–388.
- Zheng, C., Mattausch, H., Simon, A., 2002. *J. Alloys Compd.* **347**, 79–85.
- Zhuravlev, N.N., Smirnova, E.M., 1962. *Sov. Phys. Crystallogr. (Translation of Kristallografiya)* **7**, 243–244.
- Żolnierek, Z., Troć, R., 1978. *J. Magn. Magn. Mater.* **8**, 210–222.
- Zwiener, G., Neumann, H., Schuster, H.-U., 1981. *Z. Naturforsch. B* **86**, 1195–1197.

Chapter 228

SWITCHABLE METAL HYDRIDE FILMS

I. ARUNA, L.K. MALHOTRA and B.R. MEHTA

*Thin Film Laboratory, Department of Physics, Indian Institute of Technology Delhi,
New Delhi 110 016, India*

E-mail: lalit@physics.iitd.ernet.in

Contents

Symbols and abbreviations	84	2.5.3. Isotope effect	203
1. Introduction	87	2.5.4. Evidence of ionic bonding in YH _{3-δ} : Infrared transmittance studies	206
1.1. Switchable mirror effect: The discovery	88	2.6. Theoretical models for first generation switchable mirrors	207
1.2. Fabrication	90	2.6.1. The “weak correlation” model: Broken symmetry structure	209
1.2.1. R film deposition	90	2.6.2. The “strong correlation” model	212
1.2.2. Requirement of a cap layer	91	2.6.3. Recent calculations	215
1.3. Hydrogenation techniques	93	3. Second generation switchable mirrors	226
1.3.1. Gas phase loading	93	3.1. R–Mg alloy films	227
1.3.2. Electrochemical loading	93	3.1.1. Y–Mg alloy	228
1.3.3. Chemical technique	97	3.1.2. La–Mg alloy	235
1.4. Hydrogen concentration determination	98	3.1.3. Sm–Mg alloy	239
2. First generation switchable mirrors	101	3.1.4. Gd–Mg alloy	241
2.1. Polycrystalline rare earth films: Homoge- neous switching	101	3.1.5. Er–Mg alloy	249
2.1.1. Yttrium films	103	3.2. R–Mg multilayer films	249
2.1.2. Lanthanum films	120	3.2.1. Y–Mg multilayers	250
2.1.3. Praseodymium films	122	3.2.2. Gd–Mg multilayers	252
2.1.4. Samarium films	128	4. New generation rare earth nanoparticle based switchable mirrors	255
2.1.5. Gadolinium films	139	4.1. Y nanoparticle layers	255
2.1.6. Dysprosium films	145	4.2. Gd nanoparticle layers	260
2.2. Epitaxial switchable mirrors: Pixel switching	146	5. Applications of switchable rare earth hydride films	266
2.3. Effect of Pd over layer thickness	163	5.1. Electrochromic devices	266
2.4. Hysteresis	180	5.2. Indicator layers	269
2.4.1. R–R alloy films: La–Y alloy films	186	5.3. Tunable magnetic layers	271
2.4.2. RH ₂ films: YH ₂ films	194	5.4. Hydrogen sensors	272
2.5. Diffusion, electromigration experiments and isotope effect	197	6. Summary and outlook	273
2.5.1. Diffusion and electromigration of H	197	References	275
2.5.2. Electronic structure of YH _{3-δ} : Angle resolved photoemission spectroscopy studies	201		

Symbols and abbreviations

A	symmetry point	d	interplanar distance
AES	Auger electron spectroscopy	dhcp	double hexagonal closed pack
AFM	atomic force microscopy	d_{coh}	out-of-plane coherence length
ARPES	angle resolved photoemission spectroscopy	d_{\perp}	separation between consecutive hexagonal planes
ARUPS	angle resolved ultraviolet photoelectron spectroscopy	d_{\parallel}	nearest neighbor distance within the hexagonal planes
A_{opt}	optical absorption	E	electric field
A	film area	EMA	effective mass approximation
a	lattice parameter	ERDA	elastic recoil detection analysis
Δa	change in the lattice parameter a	EXAFS	extended X-ray absorption fine structure
$B(T)$	magnetic field	E_{F}	Fermi energy
C_{H}	Hall coefficient	E_{g}	optical band gap
C_{H0}	initial value of Hall coefficient before hydrogenation	$E_{\text{g}}(\text{eff})$	effective optical gap (defined arbitrarily as the energy at which T_{opt} falls to 30%)
c	lattice parameter	E_{Pd}	energy at the surface of the Pd over layer measured in RBS
c_{dhcp}	lattice parameter (of double hexagonal closed packed structure, corresponding to c in hcp structure)	E_{vac}	energy of the reference vacuum level
c_{Sm}	lattice parameter (of samarium structure, corresponding to c in hcp structure)	$E(\bar{\Gamma}), E(\bar{K})$	energies of hydrogen induced split-off states of Pd (111)
Δc	change in the lattice parameter c	ΔE_0	adjustable shift to account for uncertainties in chemical bonding and core relaxation effects
CCD	charge coupled device	E_e	electrochemical potential
D	film thickness	e	electronic charge
DFT	density functional theory	FEES	free-electron-final state
DL	Drude–Lorentz	FWHM	full width at half maxima
DO	Drude oscillator	F_{d}	direct force on H atoms in the presence of external electric field
DOS	density of states	F_{wind}	“wind force” (force due to the momentum transfer to the H atoms acting as scattering centers)
D_1	critical Pd over layer thickness for a functional switchable mirror	F	Faraday’s constant
D_2	minimum Pd thickness necessary to cover the rare earth film completely	fcc	face centered cubic
D_{Al}	Al buffer layer thickness	GAXRD	glancing angle X-ray diffractometer
D_{f}	diffusion coefficient		
D_{Pd}	Pd over layer thickness		
D_{Y}	Y film thickness		

GGA	generalized gradient approximation	LEED	low energy electron diffraction
GITT	galvanostatic intermittent titration	LMTO	linear–muffin–tin–orbital
GW	Green’s function G and the screened Coulomb interaction W	LO	Lorentz oscillator
g	Gutzwiller factor	l_{coh}	X-ray coherence length
g_{o}	Gutzwiller factor for octahedral H	M	symmetry point
g_{t}	Gutzwiller factor for tetrahedral H	MBE	molecular beam epitaxy
H	symmetry point	ML	monolayer
HRTEM	high resolution transmission electron microscopy	\bar{M}	symmetry point
H_{ad}	adsorbed hydrogen species	$m_{\text{e(h)}}^*$	electron (hole) effective mass
H_{Oct}	neutral H atom occupying octahedral interstitial site	N	coordination number
H_{tetra}	neutral H atom occupying tetrahedral interstitial site	N_{coh}	number of coherent layers
ΔH	partial molar heat of solution	n	the refractive index
$\Delta \bar{H}$	partial molar enthalpy	n	charge carrier concentration
$\Delta H_{\alpha \rightarrow \beta}$	heat of formation for the $\alpha \rightarrow \beta$ transformation	n_{c}	critical carrier concentration
$\Delta H_{\beta \rightarrow \gamma}$	heat of formation for the $\beta \rightarrow \gamma$ transformation	n_{e}	number of electrons involved in the hydrogen evolution reaction
h	Planck’s constant	PIXE	proton induced X-ray emission
hcp	hexagonal close packed	PLA	pulsed laser ablation
ITO	indium tin oxide	PLD	pulsed laser deposition
$I_{\text{RH}_x(hkl)}$	intensity of the XRD peak with Miller indices (hkl) in RH_x	ppm	parts per million
I	current	p_{H_2}	partial pressure of hydrogen
J_{e}	electron flux	R	resistance
J_{H}	hydrogen flux	R	rare earth (elements of the lanthanide series, scandium and yttrium)
j	current density	RBS	Rutherford backscattering
K	symmetry point	RHEED	reflection high-energy electron diffraction
K_{opt}	mobility of the diffusion front (or the optical transition)	RT	room temperature
\bar{K}	symmetry point	R_0	initial resistance of the film before hydrogenation
K	wind force coefficient	R	gas constant
k	wave vector	r	interatomic distance
k	extinction coefficient	SAED	selected area electron diffraction
k	wave number	SMSI	strong metal-support interaction
L	symmetry point	s	spin quantum number
L	nanoparticle size	sccm	standard cubic centimeters
LDA	local density approximation	sX-LDA	self-consistent local density approximation
		TEM	transmission electron microscopy
		T_{DL}	transmittance of deloaded film

T_L	transmittance of hydrogen loaded film	z_{opt}	distance of the hydrogen front in the uncovered region of the rare earth metal film from the edge of the Pd overlayer
T_{opt}	optical transmittance		
T	temperature		
T_C	Curie temperature	α	absorption coefficient
T_c	critical temperature	α	solid solution
T_N	Néel temperature	β	dihydride phase
T_{sub}	substrate temperature	γ	trihydride phase
t	hydrogen exposure time	γ_{Pd}	surface energy of Pd
t_L	time taken by the diffusion front to cover the whole lateral length (L) of the R film uncapped with Pd	γ_Y	surface energy of Y
		δ	H concentration in $\text{RH}_{3-\delta}$ where $3 > \delta \geq 0$
U	electrode potential	σ	conductivity
UHV	ultra-high vacuum	$\Delta\sigma^2$	standard deviation
U	energy increase due to Coulomb repulsion	ρ	resistivity
V_H	Hall voltage	$\Delta\rho/\rho(0)$	magnetoresistance
V	voltage	χ	normalized oscillatory part of absorption coefficient
V_{bias}	bias voltage		
V_m	molar volume of $\text{La}_{1-y}\text{Y}_y\text{H}_x$	$\Delta\chi$	surface potential difference/chi potential difference
V_Y	the molar volume of yttrium	ε	dielectric function
W	symmetry point	ε_1	real part of the dielectric function
WDA	weighted density approximation	ε_2	imaginary part of the dielectric function
X	symmetry point		
XAFS	X-ray absorption fine structure spectroscopy	ε_d	energy of the Pd d-band centroid
XDAP	X-ray absorption data analysis program	ε_d'	shifted energy of the Pd d-band centroid due to nanoparticle nature
XPS	X-ray photoelectron spectroscopy	e_g and t_{2g}	molecular orbitals
XRD	X-ray diffractometry	Γ	symmetry point
x	hydrogen concentration (e.g. in YH_x , $x = [\text{H}]/[\text{Y}]$, $x \leq 3$)	$\bar{\Gamma}$	symmetry point
Δx	change in the hydrogen concentration	$\bar{\Gamma}\bar{K}$	direction of the surface Brillouin zone
y	Y concentration in the $\text{La}_{1-y}\text{Y}_y$ alloys	$\bar{\Gamma}\bar{M}$	direction of the surface Brillouin zone
Z^*	effective valance (= $Z_d + Z_{\text{wind}}$) on H atom in $\text{YH}_{3-\delta}$ where Z_d corresponds to the direct force and Z_{wind} to the wind force	τ_s	switching (or response) time
		τ_R	recovery time
		λ	wavelength
z	Mg concentration in the $\text{R}_{1-z}\text{Mg}_z$ alloys	η	intensity ratio of the (002) XRD peak of YH_3 and (111) peak of the YH_2
		ω_p	plasma frequency

ξ	H concentration in $\text{RH}_{2\pm\xi}$, $0 \leq \xi \leq 1$	ζ_2	overlap integral between neighbouring Y atoms
ζ_1	overlap integral of neutral H atom with the neighbouring Y atoms	ψ and Δ	ellipsometry parameters

1. Introduction

Since the first work by [Winkler \(1891\)](#), studies on rare earth hydrides (RH_x) have been carried out more or less continuously for more than a century now. The reasons for the researchers constant endeavor are manifold and stem from both scientific curiosity and technological applications. The important reasons for the interest in rare earth metals R (R: elements of the lanthanide series, scandium and yttrium) have been their relatively high hydrogen retention capacity [the largest possible hydrogen-to-metal ratio (up to 3) among elements] and hydrogen-induced modifications in structural, electronic, magnetic, and optical properties. The hydrogen-induced modification of the basic material properties in bulk rare earth metals have been reviewed by many authors; [Mueller et al. \(1968\)](#), [Libowitz and Macland \(1979\)](#), [Arons \(1982, 1991\)](#), [Wiesinger and Hilscher \(1991\)](#), [Schlapbach \(1992\)](#), [Vajda and Daou \(1993\)](#) and [Vajda \(1995\)](#). One of the problems encountered in various studies on RH_x have been the instability of the trihydride state. Excessive stresses build up in rare earth hydrides (RH_x) near the trihydride state (x approaching 3) due to repulsive H–H interaction between the hydrogen atoms. These stresses get relieved by converting the bulk RH_x into powder ([Mueller et al., 1968](#); [Vajda, 1995](#)). Another problem, which complicated the measurements, has been the rapid oxidation rate of the parent metals. Though there are reports on the measurement of electrical resistivity on single crystals of RH_x , most of the investigations have been carried out on bulk RH_x powders in the form of compressed pellets ([Vajda, 1995](#)). To avoid the problem of the extreme oxidation sensitivity of the R metals, measurements were carried out in dry and inert ambient. [Libowitz \(1973\)](#) performed electrical measurements directly on single crystals of R metals but only up to composition of $\text{RH}_{2.75}$. [Maier-Komor \(1985\)](#) carried out resistivity measurements for $\text{LaH}_{2+\xi}$ with higher hydrogen concentrations ($0.80 < \xi < 0.90$), but the absolute resistivity values were reported to be accurate only within a factor of 2 or 3. The existence of metal to semiconductor (M–S) transition has been reported in a number of rare earth hydrides for compositions lying between the di- and trihydride state e.g., in $\text{CeH}_{2+\xi}$ in the range $0.7 \leq \xi \leq 0.8$ ([Libowitz and Pack, 1969](#)), $\text{LaH}_{2+\xi}$ for $0.8 \leq \xi \leq 0.9$ ([Shinar et al., 1988, 1989, 1990](#)) and in $\text{GdH}_{2+\xi}$, $\text{HoH}_{2+\xi}$, $\text{ErH}_{2+\xi}$, and in $\text{YH}_{2+\xi}$ with $\xi \approx 0.1\text{--}0.3$ ([Vajda, 1995](#)). Optical measurements on the other hand were limited to a select few dihydrides. For example, [Weaver et al. \(1978, 1979a, 1979b\)](#) measured in detail the reflectivity of the dihydrides of Sc, Y, and Lu but could not extend their interesting measurements to the trihydrides. Thus, although the M–S transitions had been observed in RH_x there were no reports on the simultaneous measurement of the optical properties during the transition. In hindsight, this appears unfortunate and the discovery of “switchable mirror effect” had to wait till 1996, when [Huiberts et al.](#) showed that remarkable changes in optical properties in the visible part of electromagnetic spectrum accompany the hydrogen induced M–S transition in YH_x (LaH_x),

$2 < x < 3$. Huiberts et al. showed that it was possible to obtain stoichiometric YH_3 at 25 GPa and $\text{YH}_{2.86 \pm 0.02}$ could be obtained even at 10^5 Pa, using thin films of Y metal capped with a Pd over layer. Since the effective attractive H–H interaction in metal hydrides is essentially of elastic origin (Alefeld, 1972); therefore partial clamping of films to substrate weakens the H–H repulsive interactions thus avoiding the instability of the trihydrides (Huiberts, 1996a, 1996b). Moreover, the presence of protective Pd over layer helped in performing all *ex situ* measurements (e.g., electrical resistivity, magnetoresistance, photoconductivity, Hall effect and optical transmittance and reflectance, etc.) preventing the R metal from oxidation.

1.1. Switchable mirror effect: The discovery

In the quest for high T_c superconductors, Griessen and co-workers chose to dissolve hydrogen in yttrium to break the molecular bond, and then compress the sample under moderately high pressures to increase its metallic character (Griessen, 2001). Rough estimates suggested that around a pressure of 0.5 Mbar, YH_3 should become superconducting with a T_c close to room temperature. This goal was never realized. Instead, they discovered (Huiberts et al., 1996a, 1996b) what is now called the “switchable mirror effect”. It was observed that a 500 nm yttrium film deposited on one of the diamonds of the high pressure diamond-anvil-cell changed from a shiny metallic state to a transparent yellow state upon hydrogen uptake under several thousands of atmosphere around 240 K. Although as mentioned earlier, M–S transition had been reported in various studies on rare earth hydrides, no reports whatsoever existed about such drastic changes in the optical properties in the visible part of the electromagnetic spectrum. The diamond-anvil-cell allowed Griessen and co-workers to optically monitor the hydrogen absorption *in situ*. The same transitions were observed at room temperature and low hydrogen pressures (typically 1 bar) provided the underlying film was protected by a thin palladium over layer (5–20 nm). It was observed that yttrium (Y) and lanthanum (La) films capped with a palladium (Pd) over layer exhibit reversible optical and electronic properties on hydrogen loading and subsequent deloading. For example, Y film transforms from its shiny metallic state (Y) to a dark blue reflecting dihydride state ($\text{YH}_{2 \pm \xi}$) on hydrogen exposure and finally approaches the yellow transparent semiconducting trihydride state ($\text{YH}_{3-\delta}$) on further uptake of the hydrogen. Due to the small heat of formation of $\text{YH}_{3-\delta}$ [–41.8 kJ/mole H (Flotow et al., 1963); –44.9 kJ/mole H (Yannopoulos et al., 1965)] as compared to that of $\text{YH}_{2 \pm \xi}$ [–114 kJ/mole H (Yannopoulos et al., 1965)], optical and electronic properties could be switched between the mirror like reflecting dihydride and the transparent semiconducting trihydride states by subsequent loading and deloading of hydrogen and hence the name “switchable mirror effect”.

The evolution of electrical resistivity (ρ) and optical transmittance (T_{opt}) for red light as a function of hydrogen exposure time for a representative switchable mirror are shown in fig. 1. As the hydrogen concentration increases, there is an initial weak rise in ρ due to impurity scattering, and there after it decreases steadily until it reaches a minimum in the dihydride phase. At this point, YH_2 has a resistivity that is 5 times lower than that of pure Y. At higher H concentrations, ρ increases by several orders of magnitude and is only limited by the conductivity of the Pd over layer. The optical transmittance remains low until in the dihydride

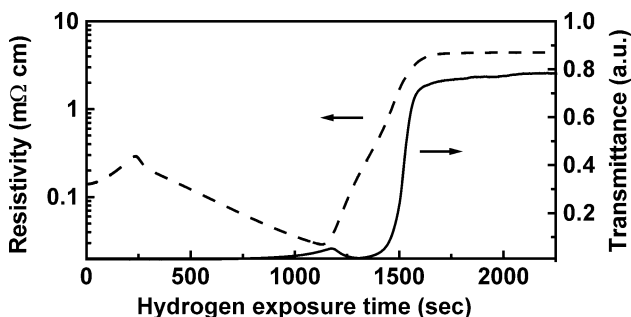


Fig. 1. The variation in electrical resistivity (dashed line) and optical transmittance (solid line) as a function of hydrogen exposure time for a 300 nm yttrium film capped with 20 nm of Pd over layer on exposure to H_2 gas at 10^5 Pa pressure at room temperature (Huiberts et al., 1996a; Griessen, 2001).

phase a weak maximum (at $h\nu = 1.9$ eV) occurs at approximately the same time as the minimum in resistivity is reached. The film transmittance suddenly rises and stays high as H concentration is increased from 2 to 3. These remarkable switchable optical and electrical properties have since been observed in R metals where there is a structural transition in going from the dihydride to trihydride state (heavy R metals: Y, Sm, Eu, Gd, Tb, Dy, Ho, Er, Tm, Yb, and Lu) as well as in those where the structure remains unaffected (light R metal: La, Ce, Pr, Nd) confirming thereby that the phenomenon is of electronic origin.

Though the discovery of “switchable mirrors effect” is an example of serendipity, the careful detailed analysis of the remarkable observations by the discoverers has triggered renewed research interest in rare earth metal hydride films both for understanding the basic physics underlying the phenomenon and the quest for potential technological applications. The extensive research in “switchable mirrors” based on R metals has lead to the following generations of switchable mirrors:

- (1) The “*First generation switchable mirrors*” typically consist of polycrystalline or epitaxial R metal films (as the active layer) capped with a Pd over layer, deposited on a transparent substrate. Although almost all the R metals [e.g., (La, Y: Huiberts et al. (1996a)), (La, Ce, Pr, Nd, Sm, Eu, Gd, Tb, Ho, Er, Tm, Yb, and Lu: van der Sluis et al. (1997)), (Pr: Mor and Malhotra (2000)), (Gd: Lee and Lin (2000)), (Dy: Azofeifa and Clark (2000)), and (Sm: Kumar et al. (2002))] have been observed to exhibit the switchable mirror property, Y is the most widely investigated metal and becomes the archetypical material for the first generation switchable mirrors. The R–R alloy (La–Y: van Gogh et al. (2001)) films are also categorized in this generation of switchable mirrors. It is interesting to note that where as on a macroscopic scale, both polycrystalline and epitaxial switchable mirrors exhibit similar properties, the latter forms an extended self organized ridge network of optically resolvable micron sized triangular domains that switch one-by-one homogeneously and independently during hydrogen absorption (Nagengast et al., 1999a). A detailed review on the structural, optical and electronic properties of these switchable mirrors and the theoretical studies attempted in explaining the observed phenomenon is given in section 2.

- (2) One of the major limitations of the first generation switchable mirrors was colored trihydride state. The quest to attain color neutral transparent trihydride state (constant transmittance in the visible region) lead to the so-called “*Second generation switchable mirrors*”. The active layer in these switchable mirrors is a thin film of a R–Mg alloy [e.g., (Gd, Sm, Lu, Y: van der Sluis et al. (1997)), (Er, Gd, Sm and Y: von Rottkay et al. (1999a, 1999b)), (La: Isidorsson et al. (2001)), (Y: Giebels et al. (2002a, 2004))] or R–Mg multilayers [(Gd: van der Sluis (1998)), (Y: Giebels et al. (2002b))]. In these switchable mirrors, the band gap of the trihydride state can be tuned by varying the Mg concentration. In addition to the shiny reflecting and transparent insulating states, strongly absorbing black intermediate state has also been observed in the R–Mg alloy based switchable mirrors. Section 3 gives details of the structural, optical and electronic properties of these films.
- (3) A distinct extension to the class of switchable mirrors avoiding the use of R metals and based on the hydrides of magnesium-transition metal alloys was introduced by Richardson et al. (2001). These are categorized as the “*Third generation switchable mirrors*”. So far alloys of Mg with Ni, Co, Fe, Mn and V have been observed to exhibit hydrogen induced switchable mirror properties (Richardson et al., 2002). The Mg-transition metal switchable mirrors were observed to exhibit similar optical states as observed in R–Mg alloys, viz., shiny metallic state, highly transparent state and highly absorbing state (Isidorsson et al., 2002; Yoshimura et al., 2002; Enache et al., 2004; van Mechelen et al., 2004), etc. A detailed discussion on this generation of switchable mirrors lies outside the scope of this chapter.
- (4) Recently, R nanoparticle layers [e.g., Y: Bour et al. (2001), Gd: Aruna et al. (2004)] have also been utilized as the active layer in the switchable mirrors. In these “*New generation switchable mirrors*”, in addition to the size dependent switchable properties, utilization of nanoparticle layers showed that it was possible to tune the band gap of the trihydride state by varying the nanoparticle size (Aruna et al., 2004) and sense very low concentrations of hydrogen (Bour et al., 2001). In a recent study, the use of Pd nanoparticle over layer to enhance the hydrogen induced switching properties of the Gd polycrystalline films has been reported (Aruna et al., 2005c). The studies are discussed in detail in section 4.

1.2. Fabrication

1.2.1. R film deposition

The deposition and electrical characterization of R metal and R hydride films have been reported in the seventies (e.g., Curzon and Singh (1978, 1979)). Since the discovery of the switchable mirror effect, a variety of techniques have been utilized to deposit R metal polycrystalline and epitaxial films e.g., molecular beam deposition (e.g., Huiberts et al. (1996b)), sputter deposition (e.g., van der Sluis et al. (1997), van der Sluis and Mercier (2001), Mercier and van der Sluis (2001)), pulsed laser deposition (e.g., Dam et al. (2003)) and thermal evaporation (e.g., Mor and Malhotra (2000)). Typically for pure R metals films, a base pressure of 10^{-5} Pa, is an essential requirement (Huiberts et al., 1996b; Wildes et al., 1996). Where as room temperature deposition resulted in polycrystalline films, a higher substrate temperature was utilized for depositing epitaxial films. Due to the higher

deposition temperature, the hydrogen incorporation during deposition of the epitaxial films is much lower $\{x = [H]/[Y] = 0.01-0.03$ (Wildes et al., 1996)} as compared to polycrystalline films $\{x = [H]/[Y] = 0.08$ (Huiberts et al., 1996b)}. For the growth of polycrystalline films, the choice of substrate was not crucial and a variety of substrates (diamond, suprasil, mylar, glass, quartz, GaAs, Al_2O_3) have been utilized. On the other hand the choice of substrate [(W(110): Hayoz et al. (1998)), (Nb/W: Remhof et al. (1997)), (CaF₂: Nagengast et al. (1999a)), (BaF₂: Jacob et al. (2002))] played an important role in the growth of epitaxial layers as the large lattice mismatch ($\sim 5\%$ in case of CaF₂ and $\sim 20\%$ in case of BaF₂) causes the coherent film to relax after a certain thickness. Borgschulte et al. (2003) showed that this relaxation process is responsible for the so-called ridge formation. A variety of techniques have been utilized for R–Mg alloy film depositions viz., sputter deposition (von Rottkay et al., 1999a), co-deposition from electron beam guns (e.g., von Rottkay et al. (1999b), Isidorsson et al. (2001)) and evaporation (e.g., van der Sluis et al. (1997), Di Vece et al. (2001)). R–Mg multilayers have been deposited by sputtering in Ar or by evaporation (van der Sluis, 1998; Giebels et al., 2002a, 2002b). For depositing nanoparticle layers, laser ablation (Bour et al., 2001) and inert gas evaporation technique (Aruna et al., 2004) have been utilized.

1.2.2. Requirement of a cap layer

Severe oxidation sensitivity was one of the nagging problems for the *ex situ* measurements of the rare earth films. Due to the enormous heat of formation of the oxidation reaction (e.g. for Y: $\Delta H_f \approx -2$ MJ/mole Y_2O_3), oxidation is much more favorable than hydrogenation. In earlier measurements on trihydride films of Y, Tb, Ho and Er, hydrogen loading was carried out in ultra high vacuum (UHV) conditions by exposing the as-deposited films to hydrogen ambient at either room temperature (Curzon and Singh, 1978, 1979; Bracconi et al., 1988), or at elevated temperatures (around 570 K) (Rahman Khan et al., 1981, 1987, 1984). The loading times to reach the trihydride state at room temperature were extremely long (days) while at high temperatures the films turned into powder before reaching the trihydride state. Furthermore, above the dihydride phase the hydrogen uptake slowed down considerably, possibly due to oxidation of the surface. Based on the idea first proposed by Pick et al. (1979), Huiberts et al. (1996a) showed that utilizing Pd over layer on the rare earth films could circumvent the above-mentioned difficulties. They showed that Pd over layer protects the R film against oxidation and catalyses the dissociative adsorption and associative desorption of the H₂ molecule at the film surface. Also, the surface of Pd over layer does not provide any activation barrier to the adsorption of H₂ molecules and it increases the hydrogen-sticking coefficient (Huiberts, 1996a, 1996b). In a few studies, Au (Wildes et al., 1996) and Pt over layers have also been used.

The main drawback of the Pd over layer is that it diffuses into the rare earth layer and consequently loses its protective and catalytic property (van der Molen et al., 1999). The surface energy of Pd ($\gamma_{Pd} = 2000$ mJ/m²) is larger than that of rare earth metals (e.g. $\gamma_Y = 1000$ mJ/m²). In addition, the heat of solution of Pd in Y for small concentrations is $\Delta H_{sol} \cong -287$ kJ/mol (Meidema, 1978). The different surface energies and the strong negative heat of solution are the driving forces for the interdiffusion of Pd and Y. Using angle

resolved ultraviolet photoelectron spectroscopy, Borgschulte et al. (2001) showed that the formation of interfacial Y–Pd alloy hinders hydrogen adsorption due to oxygen induced surface segregation of the Y–Pd alloy on air exposures. An intermediate YO_x layer (van der Molen et al., 1999) or the presence of AlO_x buffer layer (van Gogh et al., 2000b) has been observed to prevent the Pd diffusion, thereby preventing the interfacial alloy formation. Other limitation of the Pd over layer is that it limits the transmittance of the rare earth trihydride to about 35–40% (von Rottkay et al., 1999a, 1999b). Using ellipsometric measurements von Rottkay et al. investigated the optical constants of Pd on the R–Mg alloy films by depositing Pd layers (5–50 nm) on indium tin oxide (ITO) coated glass. It was assumed that optical properties of Pd on R–Mg alloy are similar to those of Pd on ITO. It was observed that whereas the real parts of the refractive index are rather similar, the extinction coefficient apparently approaches the bulk value for thickness >10 nm. The optical properties of Pd were observed to undergo reversible changes under the influence of hydrogen e.g., the extinction coefficient decreased from 3.78 to 2.78 upon hydrogenation.

One of the issues in the research on switchable mirrors has been to optimize the Pd over layer thickness (Huiberts et al., 1996b; van der Molen et al., 1999; Kremers et al., 1998; van Gogh et al., 2000a; Mor et al., 2001; Mor and Malhotra, 2003; Borgschulte et al., 2004; Kumar et al., 2002; Kumar and Malhotra, 2004a, 2004b). On the one hand, this layer needs to be thin as Pd limits the transmittance of the hydride to about 35–40% (von Rottkay et al., 1999a). On the other hand, it should form a closed layer and provide complete coverage as oxide formation deteriorates the R layer and hinders hydrogenation (Huiberts et al., 1996b). Since the effect of hydrogen on the resistivity of Pd is quite small (it only increases by a factor of 1.7 at room temperature, while the material stays metallic), a thick Pd over layer electrically short-circuits the underlying RH_x layer. Thus the optimal Pd over layer thickness for electrical measurements corresponds to the thickness for which there occurs largest change in electrical resistivity and for which Pd over layer has no influence on the resistivity of the hydride. Huiberts et al. (1996b) have shown that a Pd over layer of thickness 5 nm gives a maximum change in electrical resistivity (by a factor of 220 upon hydrogen loading) for 500 nm Y film. However at this thickness Pd films were observed to form islands electrically separated by oxidized yttrium. Mor and Malhotra (2000) used a different approach to avoid the effect of continuous Pd over layer. They studied the usage of Pd dots of varying diameters (3.5–0.5 μm) of different thickness (8–18 nm) over Pr films of thickness 28 nm, and showed that relatively faster transitions were observed with Pd dots of smallest thickness and covering the largest area of the underlying film. Using matrix samples with a staircase of Y capped with a staircase of Pd, van der Molen et al. (1999) concluded that there is a strong dependence of switching performance on Pd thickness, described by three regimes A, B, and C. In the regime A, it was shown that independent of the underlying Y thickness, for Pd thickness (D_{Pd}) less than the critical thickness (D_1) of 4 nm hydrogenation was not possible at all. Pd–Y interdiffusion in UHV followed by oxidation in air was attributed for the existence of this inactive regime. In regime B (defined by $D_1 < D_{Pd} < D_2$) the switching time (of a plaquette $0.2 \times 0.1 \text{ mm}^2$, defined as the time needed to reach the largest slope in the transmittance versus time curve) was observed to decrease with increasing Pd thickness to a constant minimum value. The lowest switching time was observed at a Pd over layer thickness

(D_2) necessary to just cover the Y layer. In the regime C, defined by $D_{Pd} > D_2$, any extra Pd on top of the already closed cap layer introduces a negligible increase in switching times. Van Gogh et al. (2000a) reported a decrease in the critical thickness to 2.7 nm in the presence of an intermediate YO_x layer and to 0.5 nm with an AlO_x buffer layer. Borgschulte et al. (2004) used scanning tunneling microscopy and spectroscopy studies to show that the critical thickness of the cap layer is related to the inactivation of the Pd islands due to encapsulation by the YO_x layer. In an interesting observation, Mor and Malhotra (2003) showed that *in situ* hydrogenation of 170 nm Pr films covered with very thin Pd over layers ($D_{Pd} \leq 9$ nm) leads to formation of nanocrystalline $PrH_{3-\delta}$ due to stress induced rearrangement of initially large crystallites yielding a low energy configuration. Recently, Aruna et al. (2005c) showed that the enhanced catalytic properties of Pd at nanodimensions can be utilized by using continuous Pd nanoparticle over layer on Gd polycrystalline films, which avoids the problem of partial oxidation of the uncovered rare earth layer encountered at smaller Pd over layer thickness.

1.3. Hydrogenation techniques

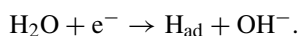
1.3.1. Gas phase loading

The most common and the fastest techniques for hydrogenation of the rare earth metals is by gas phase loading where H_2 is injected into the chamber with the rare earth metal film and pumped out periodically. The hydrogenation performed in H_2 ambient is better reproducible, and well suited for exploratory work but suffers from the disadvantage that the quantitative monitoring of the amount of hydrogen getting incorporated in the film on an absolute scale is not possible. Moreover it is not practical for device operation.

1.3.2. Electrochemical loading

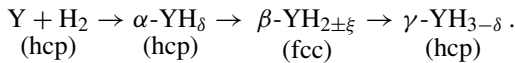
The disadvantage of the gas phase loading can be taken care of by the electrochemical loading. Notten et al. (1996) first demonstrated this technique of hydrogen loading via electrolytic reduction of proton donating species, such as water. Since R metals are extremely base metals, with more negative electrode potentials (e.g., Y: $E^\circ = -1.981$ V), and are expected to dissolve easily in acidic solution, alkaline solutions ($pH \leq 12$) were found to be more promising with respect to stability in electrolyte solution. 1–6 M KOH (Notten et al., 1996; Kooij et al., 1999) and NaOH (von Rottkay et al., 1999a, 1999b; Parkhutik and Matveeva, 2002; Matveeva et al., 2002a; Matveeva and Parkhutik, 2002b) are commonly used liquid electrolytes. Matveeva et al. (2002a) also utilized organic solvent (ethylene glycol) and observed that colored products were formed in the vicinity of ITO anode due to oxidation of ethylene glycol. In addition, the lifetime of the cathode in contact with ethylene glycol based solution was short and Pd–Y was observed to dissolve in less than an hour.

The charge transfer reaction at the film/electrolyte interface is represented by



The adsorbed hydrogen species, H_{ad} , diffuse into the R metal leading to the hydrogenation of the film. There is a direct relation between the integrated current and the amount of hydrogen adsorbed. This method has the advantage that the hydrogen concentration can be carefully

controlled by controlling the electric current. Extremely low hydrogen concentrations can thus be incorporated in the R metal films. The presence of thin Pd over layer is essential for providing a sufficiently high electrocatalytic activity for the electrochemical charge transfer reaction. As the room temperature plateau pressure of the Pd over layer is over 1 mbar, the absorption of hydrogen by this thin over layer is negligible. Using a conventional three-electrode configuration, i.e., Pd (0–20 nm) capped Y (200–500 nm) film as the working electrode, Pt as counter electrode and Hg/HgO/6 M KOH as reference electrode, in both the galvanostatic (constant reduction current) and potentiostatic (constant reduction potential) configurations, Notten et al. (1996) demonstrated the possibility of cathodically polarizing and depolarizing the Y films. *In situ* optical transmittance measurements of the films were performed by illuminating the electrodes from the back of the samples and detecting the light intensity at the front, using a white light source in combination with a photodetector. Fig. 2 shows a typical example of (a) the electrode potential and (b) accompanying electrode transmittance for a 500 nm Y film electrode capped with a 5 nm Pd over layer during galvanostatic hydriding (current = 1 mA) in 6 M KOH solution. The hydrogen concentration (x) calculated from the amount of electrical charge is shown in the upper part of fig. 2. The various crystallographic regions correspond well with the various stages electrochemically observed:



In line with the theoretical considerations, the voltage plateau corresponds to the two-phase regions, where as the steeper parts to the solid solutions. Y electrode remains optically closed for $x < 2.7$. The electrode starts to become transparent at a hydride composition where all the β -phase has been converted into γ -phase. Using cyclic voltametry (dynamic current-potential measurements), Notten et al. showed that where as the reversible hydride formation is a single-step process, the decomposition reaction is a two-step process. In addition it has been shown that the $\text{YH}_{3-\delta}$ is unstable under open circuit conditions. The loss of the reversible part of the stored hydrogen under these conditions has been attributed to an electroless reaction of oxygen dissolved in the electrolyte and the hydride. The chemical stability is also poor when the Y electrodes are exposed to highly energetic light ($>$ the band gap of the trihydride), suggesting that the $\text{YH}_{3-\delta}$ is photoanodically converted to the oxidic form of the Y electrode.

The electrochemical potential is related to an effective hydrogen gas pressure,

$$E_e = -\frac{RT}{n_e F} \ln p_{\text{H}_2} - 0.926 \quad [\text{V vs. Hg/HgO}],$$

where R is the gas constant, T the temperature, F the Faraday constant, and n_e the number of electrons involved in the hydrogen evolution reaction. This offers a possibility of studying the thermodynamic and electrochemical properties of the rare earth metal hydride system. With an oxygen free electrolyte it can be used to measure the hydrogen concentration in the films quantitatively and to determine pressure-composition isotherms. Kooij et al. (1999) have constructed pressure-composition isotherm for yttrium–hydrogen system on the basis of electrode potential, transmittance and resistivity measured during *in situ* electrochemical hydrogenation of the film; their results are shown in fig. 3. The nature of the transmittance

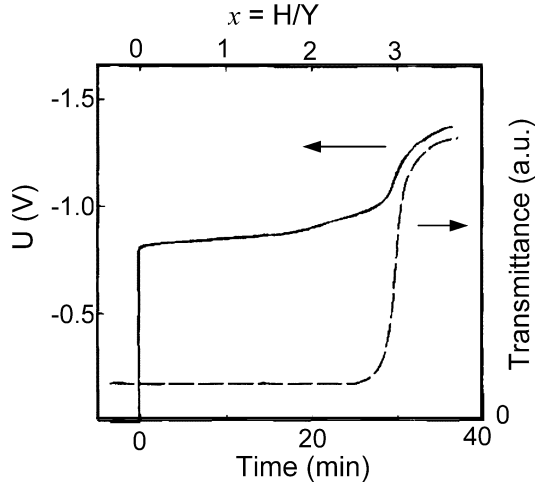


Fig. 2. Evolution of the electrode potential (U) and optical transmittance as a function of time and the hydrogen concentration in Pd (5 nm) capped Y (500 nm) film during galvanostatic hydriding (Kooij et al., 1999).

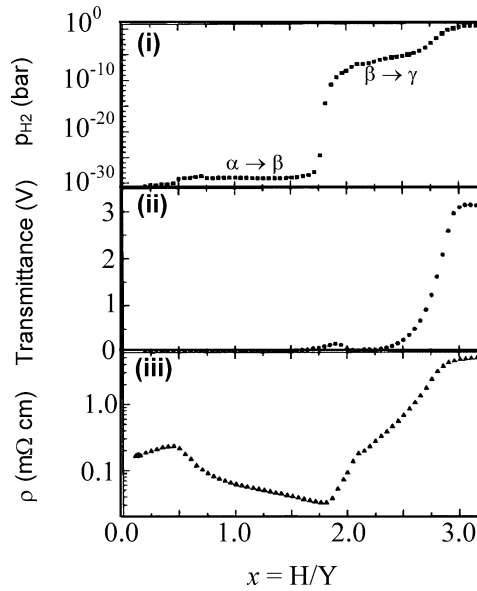


Fig. 3. Variation in (i) pressure, (ii) transmittance and (iii) resistivity of Pd (15 nm) capped Y (300 nm) film as a function of hydrogen concentration x (Kooij et al., 1999).

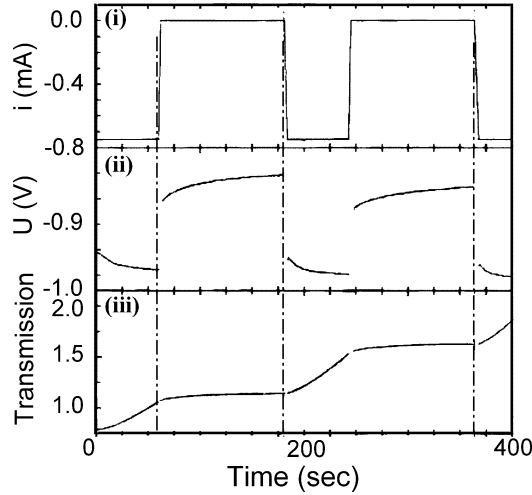


Fig. 4. Time evolution of (i) current, (ii) electrode potential (with respect to Hg/HgO electrode) and (iii) transmission (at 635 nm) of Pd (15 nm) capped Y (300 nm) in 1 M KOH during galvanostatic loading experiment. The vertical lines (dash dot) indicate the equilibrium potential U_{eq} (Kooij et al., 1999).

and resistivity curves shows similarity with those obtained for gas phase loading (Huiberts et al., 1996a). At concentrations below $x \approx 0.4$, the system is in α -YH_x solid solution phase. Between $0.5 < x < 0.7$, there is a plateau corresponding to the coexistence of hcp α -YH_δ and fcc β -YH_{2±δ}. In the β -YH_{2±ξ} phase (corresponding to the minimum in resistivity and a small maximum in transmittance) a strong rise in the pressure is observed, followed by a sloping plateau corresponding to the transition of β -YH_{2±ξ} to γ -YH_{3-δ}. To avoid the problems related to the polarizing current in the resistivity methods, Kooij et al. (1999) had utilized galvanostatic intermittent titration (GITT) technique for the absorption of the hydrogen between the β -YH₂ and γ -YH₃. In GITT a constant current is applied for some time to change the hydrogen concentration by a certain amount. Whether the hydrogen is absorbed or desorbed depends on the sign of the current. After the current pulse, the system is allowed to relax in the open circuit conditions, while the potential, resistivity and optical transmittance are monitored *in situ*. Fig. 4 gives the variation in the current, electrode potential and transmittance (at 635 nm) for a Pd (15 nm) capped Y (300 nm) film. Under equilibrium conditions at room temperature the equilibrium potential U_{eq} (in volts) of the electrode with respect to Hg/HgO is related to the partial hydrogen pressure p_{H_2} (in bar) at the solid/electrolyte interface by Nernst equation

$$U_{eq} = -\frac{RT}{2F} \ln p_{H_2} - 0.926,$$

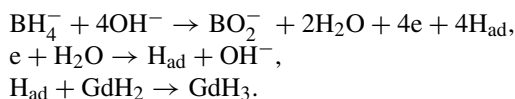
where $R = 8.314$ J/K mol is the gas constant and $F = 96487$ C/mol is the Faraday constant. During a current pulse, a considerable potential drop and an overpotential are superimposed on the equilibrium potential. Kooij et al. (1999) observed that the open circuit potential of the

Y/Pd electrode was solely determined by the solid/liquid interface. Excess amount of hydrogen in the palladium cap layer was expected, immediately after the application of the current pulse. Towards equilibrium the surface hydrogen concentration was observed to decrease with time due to hydrogen diffusion into the film, leading to a less negative open circuit potential. On the other hand, optical transmittance was observed to increase in intensity during the current pulse, revealing the hydrogen concentration throughout the film. Under open-circuit conditions the afore-mentioned in-diffusion of hydrogen was observed to lead to a slightly higher hydrogen concentration within the film, which accounts for the slight increase of the optical transmittance during the equilibration period.

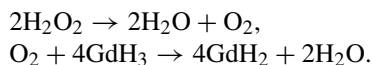
Since the first demonstration by Notten et al. (1996), electrochemical hydrogenation has been utilized not only to study the reversible optical and electrical properties and the corresponding thermodynamic properties of first-generation switchable mirrors [e.g., (Y: Kremers et al. (1998), Kooij et al. (1999), Parkhutik and Matveeva (2002)), (La–Y alloy: van Gogh et al. (2001)), (Gd, Y: Di Vece et al. (2002, 2003c)), (Sm: von Rottkay (1999a, 1999b), Kumar and Malhotra (2004a, 2004b))] but also in second-generation switchable mirrors [(Sm–Mg, Y–Mg and Gd–Mg: Ouwerkerk (1998)), (Sm–Mg, Gd–Mg alloys: von Rottkay et al. (1999a, 1999b)), (Gd–Mg: Di Vece et al. (2002))]. One of the major disadvantages of the electrochemical loading is its wet and corrosive environment and the applicability, limited in a temperature window; between the freezing and boiling points of the electrolyte. In order to avoid wet ambient, solid electrolytes such as ZrO_2H_x (Armitage et al., 1999; van der Sluis and Mercier, 2001) and conducting polymer Nafion[®] 117 membrane (Matveeva et al., 2002a; Matveeva and Parkhutik, 2002b) have been utilized. The disadvantage of the polymer exchange membrane is that the membrane must be solvated (by water or other small molecules) to start conducting. In the dry state, the polymer ion-exchange membranes are not conductive (Matveeva et al., 2002a; Matveeva and Parkhutik, 2002b).

1.3.3. Chemical technique

Van der Sluis (1999) has demonstrated a new chemical technique for hydrogenation of R metals. It has been shown that by immersion in aqueous KOH-solution containing NaBH_4 , 200 nm Gd films capped with 10 nm Pd over layer can be switched to transparent GdH_3 state. The following electroless reactions are observed to take place:



The attractive feature of this technique is that it leads to almost stoichiometric trihydrides due to the high redox potential differences. The unloading to GdH_2 has been achieved by immersion in a 0.3% H_2O_2 aqueous solution.



Van der Sluis (1999) showed that the optical properties of these chemically switched Pd capped Gd film samples are similar to the films switched by gas phase or by electrochemical means.

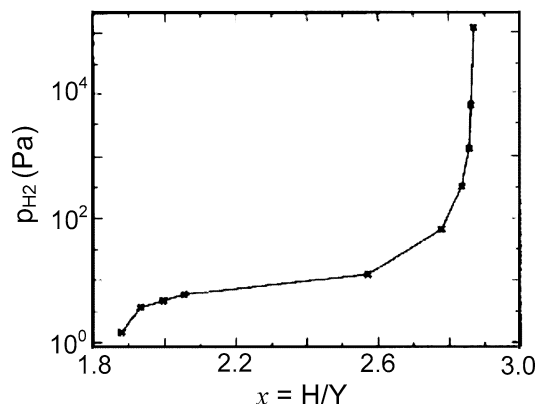


Fig. 5. Pressure-composition isotherm of Y (530 nm) film capped with Pd (52 nm) measured with quartz crystal microbalance during hydrogen absorption at 288 K (Huiberts et al., 1996b).

1.4. Hydrogen concentration determination

Hydrogen concentration in switchable mirrors has been measured under in-situ conditions during gas phase loading using quartz crystal monitor (QCM) (Y: Huiberts et al. (1996b), Griessen et al. (1997); Dy: Azoifeifa and Clark (2000)) and during electrochemical loading (e.g. Y: Kremers et al. (1998), Kooij et al. (1999); SmMg: Ouwerkerk (1998); La and LaY: van Gogh et al. (2001); Y, YMg: Giebels et al. (2002a, 2002b); Gd and GdMg: Di Vece et al. (2002); Sm: Kumar and Malhotra (2004a)). Nuclear reaction analysis (NRA) [Y: Huiberts et al. (1996b)] and elastic recoil detection analysis (ERDA) [Y: Huisman et al. (1999, 2001); Gd: Aruna et al. (2005b)] have been used under *ex situ* conditions.

By applying a high frequency electric field a quartz crystal can be brought into fundamental resonant mode typically at 6 MHz. This frequency depends on the mass, which is mechanically connected to the crystal. In QCM method, the total mass change is determined by measuring the shift in frequency of the oscillator. It is thus possible to measure small mass changes by monitoring the shift in the resonance frequency. Huiberts et al. (1996b) determined the amount of Y atoms as well as the amount of H atoms using this technique. Corrections were made to the observed resonance frequency shift due to the change in the coupling of the crystal with the surroundings because of the increase in hydrogen gas pressure. Noise in the frequency measurement and error in thickness values can produce uncertainty ($\sim 1.5\%$) in the value of hydrogen concentration determined by QCM method. Structural changes in heavy rare earth metals upon hydrogenation changes the elastic properties of the material and this can also cause a frequency shift. Huiberts et al. showed that the error due to the structural transitions can be as large as 3% for a shift in the measured frequency by 0.09. The H contamination in the as deposited films was estimated by analyzing the resistivity data before loading and by X-ray measurements of a similar film after evaporation under the same conditions. The H concentration in the Pd over layer was established from the measurements on the Pd thin films (fig. 5).

During electrochemical loading, measurement of the charge transferred during loading can be used to estimate the concentration of hydrogen. For a sample (e.g., Y) of area A and thickness D , the change Δx in the hydrogen concentration can be calculated from the transferred charge using the relation

$$\Delta x = -\frac{V_Y}{ADF} \int i(t) dt$$

with F being the Faraday's constant and V_Y the molar volume of yttrium. Since the electrochemical loading has the advantage of monitoring the absolute hydrogen concentration in the films, this technique has been the most widely used technique for hydrogen concentration determination in switchable mirrors. However, the presence of oxygen in the solution, H_2 formation, partial oxidation of R metal layer and the hydrogen absorbed in the palladium during electrochemical loading were observed to result in slightly higher estimates. [Kremers et al. \(1998\)](#) estimated the error in the hydrogen concentration due to the aforementioned reasons to be of the order of 3%. Kremers et al. argued that although the Pd also forms a hydride, the amount of hydrogen in the Pd cap layer can be neglected, because it is relatively thin and the enthalpy of formation of PdH_x is much less negative than that of YH_x . The resulting error in the hydrogen concentration was estimated to be not larger than 0.1 for $x = 3$.

^{15}N technique makes use of a nuclear reaction between H and high-energy nitrogen (^{15}N) ions. Hydrogen concentration at the sample surface is determined from the yield of reaction products and depth information can be estimated from the energy of the projectile species. To check the concentrations measured by QCM technique, [Huiberts et al. \(1996b\)](#) determined the hydrogen concentration using ^{15}N technique. The main difference between the QCM and ^{15}N technique was the more local nature of the latter. In QCM the complete mass change (due to hydrogen absorption) at any moment during absorption is measured where as in the ^{15}N technique, hydrogen concentration is measured at a certain depth depending on the incident energy of the impinging nitrogen ions and gives an average over a depth interval. The depth interval was observed to increase due to straggling effect as the incident ion energy is increased to probe farther from the surface. Since the hydrogen concentrations are measured in vacuum, [Huiberts et al. \(1996b\)](#) quenched the samples down to $T \sim 180$ K to stop the hydrogen escaping from the samples before the measurements. [Fig. 6](#) gives the hydrogen depth profiles determined by means of nuclear ^{15}N method for a Pd (5 nm) capped Y (500 nm) film. The overall concentration x for the sample after hydrogenating at 10^5 Pa pressure [curve (a)] was estimated to be 2.86 ± 0.02 , where as the concentration profile obtained for the sample [curve (b)] for which the resistivity has reached its minimum during loading (after correction for straggling was included) was found to be close to $x = 1.9$. The lower hydrogen concentration at a depth of ~ 200 nm was attributed to be due to the partial oxidation of the surface and the apparently large thickness (620 nm corresponding to the dihydride state and 693 nm to that of the trihydride state) was related to the straggling effects and the strong surface roughness. The increase in the thickness ($\sim 11\%$) in going from the di- to the trihydride state was found to be close to the value calculated from the X-ray diffraction measurements on bulk samples ($\sim 10.4\%$), indicating that the entire volume expansion that occurs in bulk materials occurs in the form of a one-dimensional expansion perpendicular to the substrate.

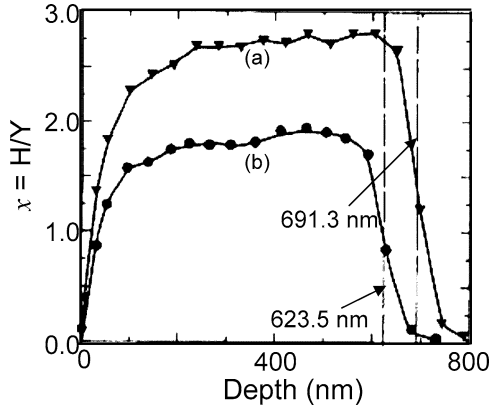


Fig. 6. Hydrogen depth profiles of Pd (5 nm) capped YH_x (500 nm) films with (a) $x = 2.86$ and (b) $x \sim 1.9$, determined by ^{15}N method. Vertical dotted lines represent the apparent thickness of the films (Huiberts et al., 1996b).

In the ERDA technique, the sample to be analyzed is irradiated by high-energy ion beam and energy distribution of the H recoil is measured. A detector in the forward direction detects the recoiling hydrogen atoms, while the scattered projectiles and heavier recoils are absorbed in a stopper foil between target and detector. The depth profile information is obtained from the energy of the recoil and the energy loss of the projectiles in the samples. Huisman et al. (1999) performed ERDA measurements using $^4\text{He}^{2+}$ ion beam 5 MeV of energy to correlate the hydrogen concentration with optical transmittance using double-diffusion sample geometry where two Pd strips were evaporated on the Y layer, one at each short side of the sample (surface area $0.5 \times 1.0 \text{ cm}^2$). Simultaneous Rutherford backscattering (RBS) and proton induced X-ray emission (PIXE) measurements were also carried out. The hydrogen diffusion profile in a switchable mirror of YH_x was measured by continuous translation of the sample in the $\pm z$ -direction between the two Pd strips. The scale length was taken to be 6.5 mm, placing the end points of the scan on the Pd strips. The X-ray signal was used to identify the Pd edges on the sample, in order to define the origin for the line scan. Since there was no general consensus upon the magnitude of the different relevant stopping factors and ERDA cross-sections in the energy range suitable for the rare earth materials, Huisman et al. performed internal calibration of the microbeam setup used in the experiment. The hydrogen concentration x in YH_x was evaluated based on the ERDA and RBS measurements. The hydrogen concentration in the as-deposited film was found to be $x \sim 0.2$. The films were hydrogenated for three days at room temperature in 1 bar of hydrogen gas. Fig. 7 gives the hydrogen concentration x as a function of the distance z (μm) for the hydrogen loaded Y-film in the uncovered region of the sample (the Pd covered regions at $z_{\text{opt}} < 0$ and $z_{\text{opt}} > 3900 \mu\text{m}$, are not shown). The transmittance measurements [intensity profiles of the red (a) and blue (b) output signals of the 3-CCD camera] performed at the same place in the sample are also shown (solid lines). Upon hydrogen loading, the hydrogen concentration in the α -phase (between $750 < z_{\text{opt}} (\mu\text{m}) < 3150$) was found to increase from $x \sim 0.2$ to $x \sim 0.45$. The inspec-

tion of the corresponding optical transmittance in the same region at the sample place shows that the β -phase has not precipitated. It was argued that this higher x in the α -phase was a consequence of the hydrogen leaking through the oxide layer, resulting in higher hydrogen concentration. From the discontinuities in the red and blue optical transmittance profiles (at $z_{\text{opt}} = 600$ and $z_{\text{opt}} = 3300 \mu\text{m}$) where the hydrogen concentration remained nearly constant, it was concluded that the β -phase extends over $z \sim 150 \mu\text{m}$. These phase boundaries were attributed to the β - γ coexistence region. In the γ phase region, the hydrogen concentration was observed to increase from $x = 1.5$ to $x = 2.0$, accompanied by a more or less gradual increase in the blue optical transmittance signal. From the above-mentioned observations and the results of Kooij et al. (2000), it was concluded that although there must be three thermodynamically stable phases in the YH_x system ($0 < x < 3$), the phase diagram of YH_x thin film may be different compared to the bulk phase diagram, with the phase boundaries shifted towards lower x in case of the former as compared to the later. The unexpected presence of oxygen profile necessitated a careful interpretation of local hydrogen concentration differences in the YH_x sample. Huisman et al. (2001) carried out careful analysis of the oxidation and hydrogenation of YH_x thin films. The lateral hydrogen concentration on the micro-scale was measured using $^1\text{H}(^4\text{He}, ^1\text{H})^4\text{He}$ ERDA at 5 MeV and the degree of oxidation of the uncovered part of the YH_x layer was obtained using $^{16}\text{O}(^4\text{H}, ^4\text{H})^{16}\text{O}$ resonant backscattering around 3.036 MeV. The lateral hydrogen concentration and the normalized oxygen profiles measured on Y (200 nm) film covered on both side by Pd (30 nm) strips [leaving $4 \times 5 \text{mm}^2$ of the Y area which is superficially oxidized] and hydrogenated for few weeks at 373 K, is shown in fig. 8. The measured hydrogen concentration profiles were in agreement with those of Kooij et al. (2000). The measured oxygen lateral concentration profiles indicated a lower oxygen density in the more H rich parts of the YH_x layer. By measuring the oxygen profiles at different beam energies, it was concluded that the stoichiometry of YO_yH_x was different between different phases. It was concluded that the hydrogen concentrations given in fig. 8 are to be considered as lower estimates, due to the presence of switchably inactive oxide layers at the surface of the YH_x films which might influence the effective Y thickness available for hydride formation.

2. First generation switchable mirrors

As introduced in the previous section, the first generation switchable mirrors typically consist of polycrystalline or epitaxial R metal films (as the active layer) capped with a Pd over layer, deposited on a transparent substrate.

2.1. Polycrystalline rare earth films: Homogeneous switching

The research into this class of films was triggered by the remarkable discovery by Huiberts et al. (1996a). Since then, almost all the rare earth metals have been studied for the modification in the hydrogen induced optical and electrical switching properties. This section reviews the changes in the optical, electrical and structural properties upon hydrogenation, reported for

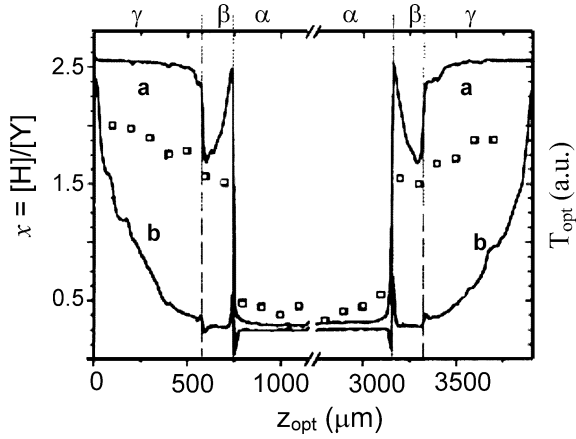


Fig. 7. Results of the line scan on a double diffusion sample: The hydrogen concentration as a function of z_{opt} (\square). The solid lines represent the transmission measurements along the same line showing both the red (a) and blue (b) signals of the 3-CCD camera. Vertical lines indicate the various phase boundaries in the sample (Huisman et al., 1999).

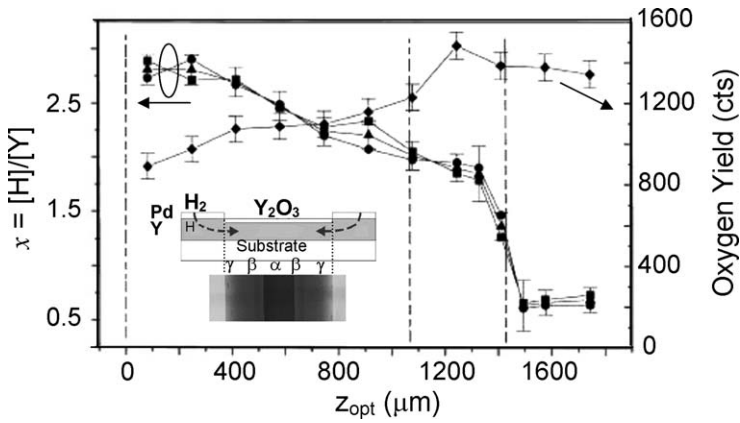


Fig. 8. Variation of the lateral hydrogen concentration and normalized oxygen concentration as a function of distance from the edges of Pd strips. The plot for the lateral hydrogen concentration from the left (\blacksquare) and the right (\bullet) Pd strips (schematic diagram of the sample and the corresponding optical image after a few weeks of H loading at 373 K is shown in the inset) and the average H profile (\blacktriangle) are shown. The different YH_x phases have been indicated by vertical lines (Huisman et al., 1999).

the polycrystalline rare earth films. The effect of the Pd over layer thickness on the switching properties is reviewed later in section 2.3.

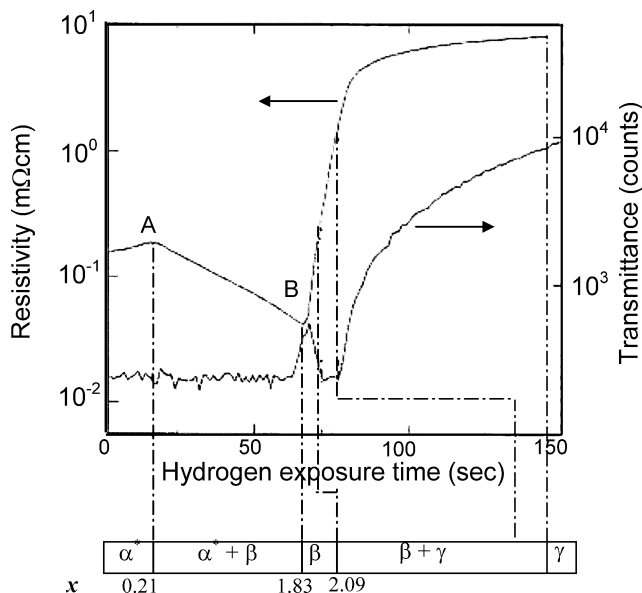


Fig. 9. Variation in the electrical resistivity and optical transmittance (at $h\nu = 1.8$ eV) during hydrogen loading (p_{H_2} increased to 0.9×10^5 Pa) at room temperature in Pd (20 nm) capped Y (~ 500 nm) film deposited on an Al_2O_3 substrate is compared with the bulk phase diagram (Huiberts et al., 1996a).

2.1.1. Yttrium films

Yttrium, being the first of the metals studied for the switchable mirror effects, is the most widely explored among the rare earth metals and hence forms the representative material for the first generation switchable mirrors. The switchable mirror effect has been studied in polycrystalline Y films using both gas phase loading (Huiberts et al., 1996a, 1996b, 1997; Griessen et al., 1997; Kremers et al., 1998; den Broeder et al., 1998; van der Molen et al., 1999, 2000, 2002a, 2002b; van Gogh et al., 1999, 2000a; Huisman et al., 1999, 2001; Kooij et al., 2000; Borgschulte et al., 2001, 2004; Remhof et al., 2002a, 2002b; Schoenes et al., 2003), and electrochemical loading (Notten et al., 1996; Kremers et al., 1998; Kooij et al., 1999, 2000; Lee and Shin, 1999; Lee et al., 2001; Hoekstra et al., 2001; Remhof et al., 2002a, 2003a, 2003b; Parkhutik and Matveeva, 2002; Matveeva et al., 2002a; Matveeva and Parkhutik, 2002b; Giebels et al., 2002a; Di Vece and Kelly, 2003a; Di Vece et al., 2003b, 2003c; Dornheim et al., 2003). Chemical loading (van der Sluis, 1999) has also been reported. The general behavior in the electrical resistivity and optical transmittance at red light as a function of hydrogen loading time for typical Pd capped Y film has been introduced in section 1. This section briefly reviews the details of various studies carried out on Y films to explore the hydrogen-induced modifications in the basic material properties.

Fig. 9 shows the variation in the electrical resistivity and optical transmittance (at $h\nu = 1.8$ eV) during hydrogen loading (p_{H_2} increased to 0.9×10^5 Pa) at room temperature in Pd (20 nm) capped Y (~ 500 nm) film deposited on an Al_2O_3 substrate (Huiberts et al., 1996a,

1996b). The resistivity was calculated from the measured resistance value taking into account the effective film thickness (calculated by requiring that the slope of the $d\rho/dT$ obtained from the resistivity versus temperature characteristics of the film before hydrogen loading matches the measured slope from bulk). The resistivity was observed to increase (in α phase) immediately after exposure to hydrogen and attributed to a decrease in the number of free electron charge carriers and additional electron scattering due to randomly distributed hydrogen. As the hydrogen concentration was increased, the dihydride phase precipitates at point A and this results in decreased resistivity. The resistivity minima at point B was attributed to β -YH₂ that has resistivity five times lower than pure yttrium. The optical transmittance was observed to have a small maxima ($\sim 1\%$ transmittance) in the small interval around the resistivity minima. At slightly higher concentrations the transmittance was observed to drop again due to the extra absorption related to the octahedral site occupancy. Thereafter, the resistivity and the transmitted intensity were observed to increase rapidly due to the increased octahedral occupation in the β -YH₂ phase and further due to formation of semiconducting trihydride state (γ -YH_{3- δ}). Huiberts et al. (1996b) showed that the choice of the substrate was not crucial for the observed hydrogen induced optical and electrical switching properties. As mentioned in section 1, similar variations in the electrical resistivity and optical transmittance (at 635 nm) measured simultaneously during electrochemical loading have been observed. Notten et al. (1996) showed that the optical appearance of the Y film electrodes could be electrochemically switched from the mirror like state to the highly transparent state. A strong alkaline solution was observed to be a suitable electrolyte providing a sufficiently high electrocatalytic activity for the electrochemical charge-transfer reaction. Pd (0–20 nm) capped Y (200–500 nm) films were hydrogenated via constant galvanostatic, potentiostatic and dynamic current-potential measurements, in 6 M KOH using Hg/HgO as the reference electrode and Pt as the counter electrode. It was concluded that hydrogen is irreversibly bound in yttrium dihydride and reversibly bound in the trihydride. The optical changes were observed to occur within a narrow hydrogen concentration range of YH_{2.7} and YH_{3.0}, at relatively high hydrogen partial pressures. It was observed that the rate of optical switching from the transparent trihydride to the mirror like dihydride state was accomplished within few seconds, whereas the reverse process was observed to take time, of the order of minutes. Notten et al. argued that this observed dependence of the rate of switching on the history of the process was related to the applied overpotential, indicating that the rate of the electrochemical surface reaction plays an important role.

Kremers et al. (1998) investigated the optical transmittance of YH_x spectroscopically as a function of hydrogen concentration during electrochemical loading of a series of Y (500 nm) film electrodes, and covered with Pd over layer of varying thickness deposited on quartz substrates. The electrochemical loading was carried out in 6 M KOH using Hg/HgO as the reference electrode and Pt as the counter electrode. The contribution from the Pd over layer to the optical transmittance of YH_{3- δ} was estimated using the macroscopic thin film optics. It was shown that the effect of Pd over layer could be corrected to determine the intrinsic optical transmittance of YH_x for $0 \leq x < 3$ in the photon energy range $1.1 \text{ eV} \leq h\nu \leq 2.0 \text{ eV}$. The electrochemical results were compared with the combined measurements of both the optical transmittance (at 632.8 nm) and electrical resistivity performed on as-deposited uncapped Y

films during *in situ* hydrogen absorption. The measured optical transmittance, corrected for the contribution from the Pd over layer, was observed to compare well with the results obtained for *in situ* gas phase loaded uncapped Y films. It was shown that both the data could be described consistently with the simple optical decay lengths such as 277.8 nm for $\text{YH}_{3-\delta}$ and 15.1 nm for Pd at $h\nu = 1.96$ eV. For 500 nm films, the maximum transmittance of yttrium dihydride at $h\nu = 1.8$ eV was observed to be 0.25% and that of substoichiometric trihydride to be 16%. From the optical transmittance and electrical resistivity measurements, it was concluded that for $x \leq 1.7$, the film is in the α - β coexistence region. For $1.75 \leq x \leq 2.1$, the film is predominantly in the β - YH_2 phase. At $x = 2.1$, the β - γ coexistence region starts and for $x \geq 2.75$, the film consists of purely γ - $\text{YH}_{3-\delta}$ phase. Based on the absorptivity measurements by Weaver et al. (1979a, 1979b) on $\text{YH}_{1.73}$ and self-consistent band structure calculations by Peterman et al. (1979) for the stoichiometric YH_2 with all the tetrahedral sites filled by the hydrogen, Kremers et al. (1998) gave the qualitative explanation for the observed reddish transmittance of yttrium dihydride (at $1.75 \leq x \leq 2.1$, centered at $h\nu = 1.8$ eV) in terms of the interband and intraband transitions. For $h\nu < 1.5$ eV, no transmittance was observed as almost all of the light is reflected by the electrons in the band crossing the Fermi level – a behavior typical of a Drude-like free electron plasma (intraband transitions). The corresponding plasmon is screened by the occurrence of the interband transitions. Kremers et al. (1998) argued that although the density of states is not negligible above the Fermi energy, the onset of interband transitions is calculated to be roughly at 2.0 eV. Therefore the absorption of photons became appreciable only for energies $h\nu \geq 2$ eV. In the region $1.5 \leq h\nu \leq 2$ eV there was thus neither strong absorption nor reflection of light and photons could be transmitted. The measured optical transmittance was mapped on to the hydrogen concentrations measured using the results of the electrochemical loading experiments. In this way the intrinsic hydrogen concentration dependence of the resistivity was also determined for uncapped YH_x films. For $x > 2.73$, in the γ - $\text{YH}_{3-\delta}$ phase, a linear dependence of intrinsic resistivity and transmittance (at 632.8 nm) was found. In the β - γ coexistence region on the other hand, the resistivity was observed to lag behind the transmittance.

Kooij et al. (1999) showed that it was possible not only to study the thermodynamics of the RH_x system, but also carry out the simultaneous measurements of the electrical properties as function of hydrogen concentration during electrochemical loading. The conduction through the electrolyte was found to be negligible but the Pd over layer was observed to dominate the electrical characteristics when the resistivity of the underlying YH_x layer became larger at high hydrogen concentrations. By placing the electrochemical cell used for resistivity measurements in an optical spectrometer, simultaneous optical spectroscopy could be performed. Fig. 10 shows the optical transmittance and reflection spectra, measured during the equilibration time during GITT (section 1) in a Pd (15 nm) capped Y (300 nm) film deposited on quartz substrate and hydrogenated in 1 M KOH with Hg/HgO as reference electrode and Pt as counter electrode for the hydrogen concentrations between $x = 2$ and $x = 3$. In the β - YH_2 phase, the characteristic transparency window is observed in the transmittance near photon energies of 1.8 eV. Upon increasing hydrogen concentration, the maximum was observed to shift to lower energies while the intensity decreased markedly. When the hydrogen concentration was increased further to values $x > 2.2$, the film was observed to open optically

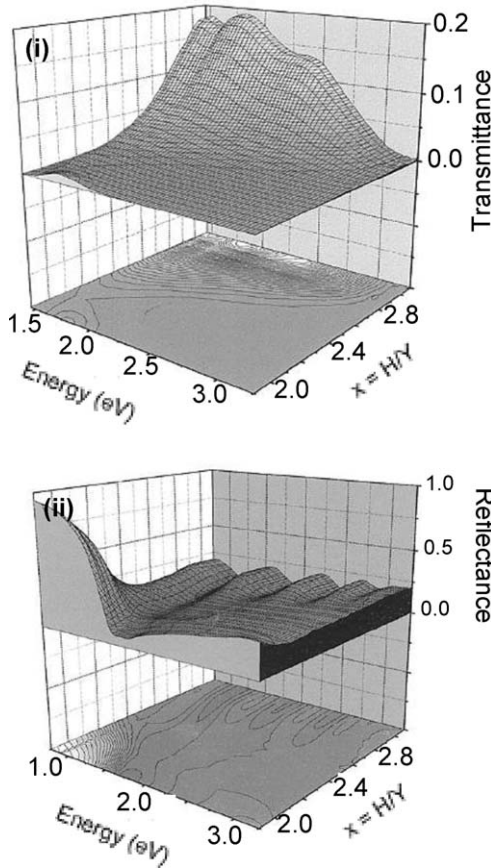


Fig. 10. Optical transmittance (i) and reflectance (ii) spectra of a Pd (15 nm) capped Y (300) film as a function of hydrogen concentration during the second galvanostatic loading from the dihydride to trihydride. The corresponding contours are plotted in the lower part of the graphs (Kooij et al., 1999).

and the characteristic trihydride transmittance was found. At energies >2.8 eV the absorption in $YH_{3-\delta}$ was observed to become considerable resulting in a strong decrease in transmittance. On the low energy side of the spectrum (<1.4 eV) light was absorbed in the aqueous electrolyte solution, limiting the accuracy of the transmittance measurements. The wavelike behavior of the transmittance in the transparent state was attributed to the interference of light reflected from the substrate/Y and Y/Pd interfaces. The reflection spectra clearly show a transition from a metallic state to a semiconducting transparent state as hydrogen concentration changes from $x = 2.0$ to $x = 3.0$. At hydrogen concentrations close to the dihydride phase a strong reflection was observed at energies <1.8 eV, characteristic of free electrons in the film. Upon further hydrogenation, the sample becomes more semiconducting and the reflec-

tion due to free electrons was observed to shift to lower energies. Approaching the trihydride phase the film becomes increasingly more transparent and consequently interference fringes were observed, similar to those observed in the transmittance.

Huiberts et al. (1996a, 1996b, 1997) established the semiconducting nature of the trihydride phase from the low carrier density ($\sim 10^{19} \text{ cm}^{-3}$) determined from the Hall measurements for the samples with a typical hydrogen concentration of $2 \times 10^{21} \text{ cm}^{-3}$ (corresponding to $\text{YH}_{2.9}$), the negative temperature coefficient of the electrical resistivity ($d\rho/dT$) for $2 \text{ K} < T < 350 \text{ K}$, the weak magnetoresistance in fields up to $7T$ at temperatures between 4.2 and 300 K, the two orders of variation in the observed electrical resistivity between the dihydride and trihydride states, and the optically measured band gap of 1.8 eV, with an edge extending up to 2.8 eV for $\text{YH}_{3-\delta}$. The value of the Hall coefficient estimated from room temperature measurements in the as-deposited sample ($x \sim 0.08$) was observed to be $-6.2 \times 10^{-11} \text{ m}^3 \text{ C}^{-1}$. For the dihydride phase, the Hall coefficient (C_H) for two different measurements around the resistivity minimum were observed to be $-2.5 \times 10^{-12} \text{ m}^3 \text{ C}^{-1}$ and $+1.25 \times 10^{-11} \text{ m}^3 \text{ C}^{-1}$. It was argued that this was in agreement with the fact that the band gap at the Fermi level is exactly half filled, and as a result, the Hall coefficient was either positive (more than half occupation) or negative (less than half occupation). This behavior was similar to that Hall coefficient measured by Heckman (1967) for CeH_2 . The values for the trihydride state ($-3.2 \times 10^{-7} \text{ m}^3 \text{ C}^{-1}$ for $x = 2.873$, $-4.0 \times 10^{-7} \text{ m}^3 \text{ C}^{-1}$ for $x = 2.887$, and $-4.6 \times 10^{-7} \text{ m}^3 \text{ C}^{-1}$ for $x = 2.898$) indicated a strong lowering of the charge density due to the opening of semiconducting gap. It was observed that the charge density in $\text{YH}_{3-\delta}$ was much smaller than expected on the basis of the large concentration of the octahedral vacancies, which act as donors, a fact explained by Eder et al. (1997) and Ng et al. (1997, 1999). The hydrogen concentration in the hydrogen saturated trihydride state and dihydride state was estimated from the QCM as well as ^{15}N techniques and was found to be $x = 2.86 \pm 0.02$ and 1.98, respectively. Huiberts et al. (1997) investigated the temperature dependence of electrical resistivity, the Hall coefficient and the magnetoresistance as a function of δ in Pd (5 nm) capped $\text{YH}_{3-\delta}$ ($\sim 500 \text{ nm}$) films. Fig. 11 shows the temperature dependence of the resistivity of the film for four different values of δ . It was observed that the resistivity increases with decrease in hydrogen deficiency according to $\rho \propto \delta^{-1}$. For all $\delta < 0.15$ (top three curves) the same general temperature dependence was observed. At $T < 20 \text{ K}$, a regime (A) was found where the resistivity tends to diverge exponentially with decreasing temperature, typical for insulator. At lower temperatures, in the ordered phase, a regime (B) was observed with a limited negative ($d\rho/dT$) (which becomes more pronounced at higher hydrogen content), followed by an order-disorder transition (C). For $T > 300 \text{ K}$ a high-temperature regime (D) characterized by thermally activated transport was observed. The Hall coefficient C_H measured for four samples with $\delta < 0.15$ (fig. 12) was also observed to exhibit different regimes. Huiberts et al. argued that the sharp decrease in C_H for $T < 20 \text{ K}$ was consistent with the freezing of the charge carriers into localized states. The presence of predominant electron-electron interaction effects for $T > 20 \text{ K}$ was ruled out since C_H in this regime was observed to be independent of the temperature. The hysteresis observed in the resistivity and the Hall coefficient values was attributed to the order-disorder transition. The weak magnetoresistance varies approximately quadratically with the applied field for an $\text{YH}_{3-\delta}$ film with $\delta \approx 0.01$

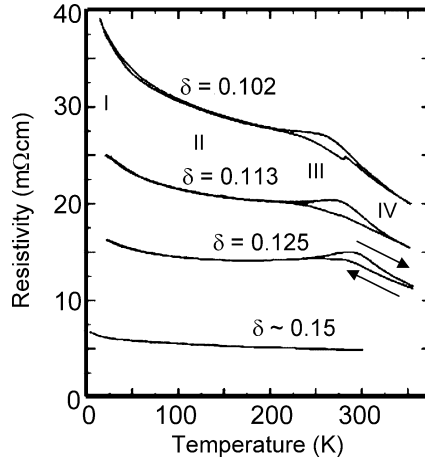


Fig. 11. Temperature dependence of resistivity in a Pd (5 nm) capped $\text{YH}_{3-\delta}$ (500 nm) film for four different values of δ (Huiberts et al., 1997).

(fig. 13). The detailed transport measurements revealed a remarkable logarithmic temperature dependence of the electrical resistivity within a large temperature range ($20 \leq T \leq 200$ K) for the hydrogen deficient films with $0.01 < \delta < 0.15$. Huiberts et al. (1997) related this dependence to the two-dimensional weak localization or Kondo scattering of the conduction electrons. It was argued that the interpretation of the logarithmic temperature dependence in terms of 2D weak localization or in terms of Kondo scattering requires the persistence of metallic conduction for small hydrogen deficiencies δ . A plausible explanation for this metallic conduction was argued to rely on the formation of a stratified superstructure in the $\text{YH}_{3-\delta}$, where conducting sheets with a high hydrogen vacancy density provide metallic conduction even for very low overall vacancy densities. Insulating YH_3 sheets, which were observed to dominate the optical properties for $\delta < 0.15$, separated the metallic sheets. It was argued that the metallic conduction process with a logarithmic temperature dependence of the resistivity was no longer effective at lower temperature $T < 20$ K and was replaced with a hopping like conduction process. At the same time, the Hall coefficient was interpreted in terms of the onset of a freezeout of the charge carriers, while the magnetoresistance becomes strongly positive.

Hoekstra et al. (2001, 2003), Voss (2001), Roesnbaum and Hoekstra (2002), and Roy et al. (2002) showed that it was possible to hydrogenate rare earth films *in situ* even at very low temperatures under ultraviolet illumination. A systematic investigation of the magnetotransport properties of Pd (5 nm) capped Y (550 nm) films was carried out for temperatures between 0.35 and 293 K in magnetic fields up to 14T and for chosen values of x . Hoekstra et al. observed that the charge carriers created by UV irradiation at $T < 1$ K would persist for days at temperatures as high as 200 K. The photodoping was observed to change the charge carrier concentration n ($T = 0.35$ K) from 5.0×10^{18} to $7.5 \times 10^{18} \text{ cm}^{-3}$ (fig. 14). This persistent photoconductivity enabled to fine-tune the conductivity (σ) and Hall coeffi-

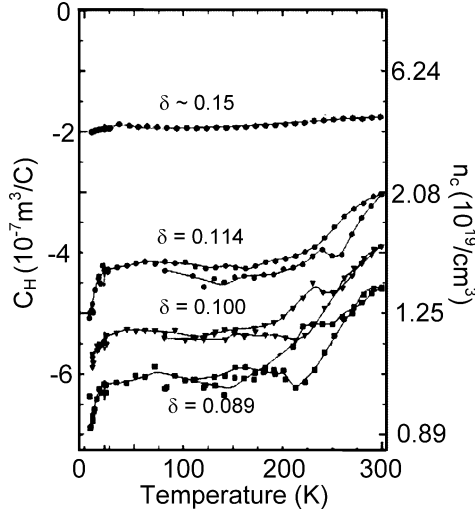


Fig. 12. Variation in the Hall coefficient and the corresponding carrier concentration as a function of temperature in Pd (5 nm) capped $\text{YH}_{3-\delta}$ (500 nm) for four different values of δ (Huiberts et al., 1997).

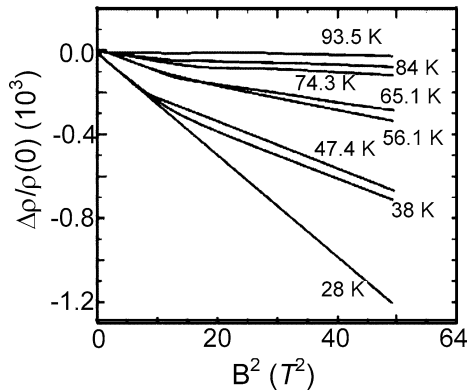


Fig. 13. Variation in magnetoresistance as a function of magnetic field for $\text{YH}_{2.99}$ film at different temperatures (Huiberts et al., 1997).

cient (C_H) through the quantum critical points. The metal insulator transitions were tuned by a combination of hydrogen gas loading (curves upto 300 K) and UV illumination (curves upto 50 K). Fig. 15 gives the resulting $\sigma(T)$ curves on a log-log scale. The upper most three curves with $n > 10^{22} \text{ cm}^{-3}$ were associated to the metallic state while the bottom three with $n < 10^{19} \text{ cm}^{-3}$ to the insulating state. This was based on the study of the temperature dependence of Hall voltage (V_H). Fig. 16 shows $V_H(H)$ at $T = 0.35$ and 4.2 K for YH_x

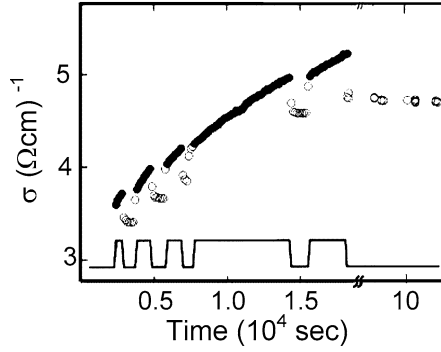


Fig. 14. Variation in photoconductivity in YH_x film (at $T = 0.35$ K) as a function of ultraviolet light ($\sim 220\text{--}700$ nm) illumination time. As the UV light is switched on and off (solid line), the sample warms to 0.4 K, but returns to a higher, stable value of the conductivity upon cooling (open circles) (Hoekstra et al., 2001).

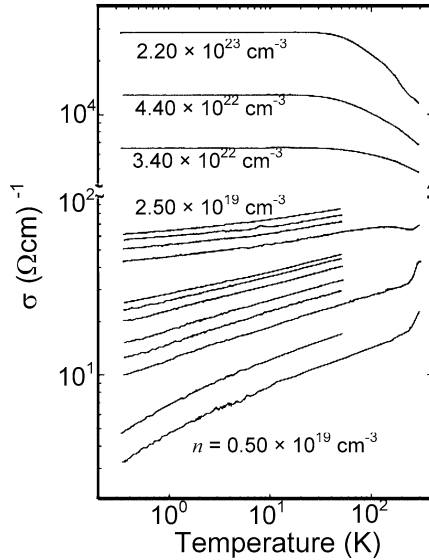


Fig. 15. Temperature dependence of the conductivity for a YH_x film at different values of the carrier concentration ($T = 0.35$ K). The unlabelled curves have $n = (0.75, 0.89, 1.07, 1.18, 1.45, 1.51, 1.64, 1.88, 2.12, \text{ and } 2.32) \times 10^{19} \text{ cm}^{-3}$ (Hoekstra et al., 2001).

sample with $n(T = 0.35 \text{ K}) = 8.9 \times 10^{18}$ and $3.4 \times 10^{22} \text{ cm}^{-3}$, respectively. For the curves $10 \text{ (}\Omega \text{ cm)}^{-1} < \sigma(T = 0.35 \text{ K}) < 70 \text{ (}\Omega \text{ cm)}^{-1}$, Hoekstra et al. observed that σ varies linearly with $T^{1/6}$ over more than two decades in T in the immediate vicinity of the metal insulator transition, with an extrapolated value for the critical density (n_c) between 1.18 and

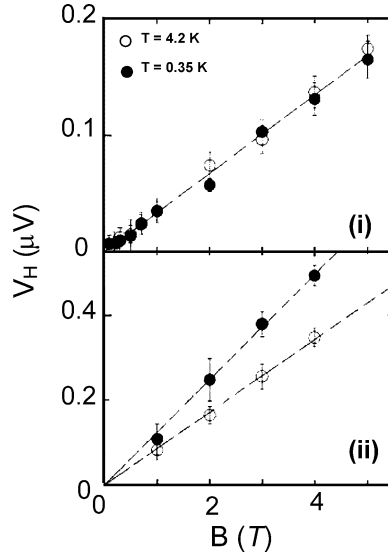


Fig. 16. Variation of Hall voltage as a function of magnetic field for metallic (i) dihydride ($n = 3.40 \times 10^{22} \text{ cm}^{-3}$) and (ii) insulating trihydride ($n = 0.89 \times 10^{19} \text{ cm}^{-3}$) states (Hoekstra et al., 2001).

$1.45 \times 10^{19} \text{ cm}^{-3}$ (fig. 17). The anomalously small (1/6) power dependence of σ on T was ascribed to the influence of the quantum critical point. The hydrogen concentration was determined for the curves running up to 300 K by comparing the $\sigma(T = 293)$ values with those from the electrochemical loading experiments (Kooij et al., 1999), giving critical hydrogen concentration between 2.83 and 2.90. From these results, Hoekstra et al. argued that the metal–insulator transition is not accompanied by a structural transition since it takes place within the purely hcp γ phase of YH_x which exists for $x > 2.7$. Qualitative agreement with the finite-size scaling picture of the quantum phase, but with an anomalously large product of the static and dynamic critical exponents ($= 6.0 \pm 0.5$) was found for the metallic state. It was argued that this unusually large product of the static and dynamic critical exponents appeared to mark the continuous M–I transitions and highlighted the important role played by electron–electron correlations. Roy et al. symmetrically mapped out the low temperature electrical transport from deep in the insulator to the quantum critical point using the persistent photoconductivity as a drive parameter. It was shown that both the activated hopping over a Coulomb gap and power-law quantum fluctuations must be included to describe the data.

In order to understand the physics underlying the remarkable transitions observed in RH_x , it was important to realize how the optical properties varied with the M–I transitions for various optical spectral ranges. Lee and Shin (1999), Lee et al. (2001) studied in detail the optical properties of $\gamma\text{-YH}_{3-\delta}$ films, in the energy range 0.05–6 eV at room temperature. Pd (15 nm) capped Y films (48, 80, 160, and 320 nm) deposited on two different kinds of substrates were used for different spectral-range measurements (Al_2O_3 , for 0.2–6 eV) and (GaAs, for 0.05–0.2 eV). The visible and near infrared measurements (0.2–6 eV) were carried with a grating

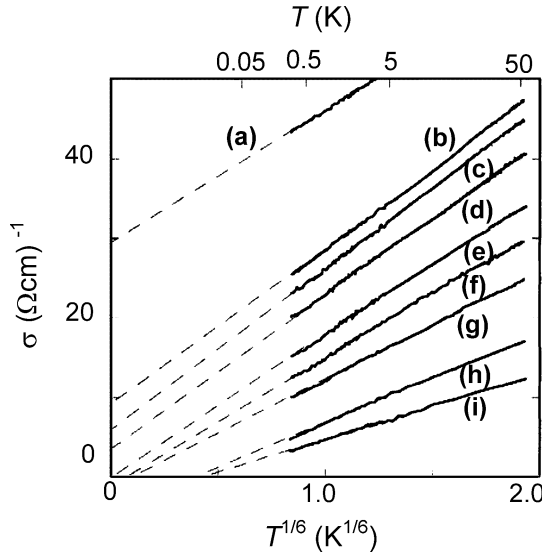


Fig. 17. Near quantum critical point (n_c) conductivity varies as $1/6$ power of temperature. The curves are extrapolated to $T = 0$, giving $1.18 < n_c < 1.45 \times 10^{19} \text{ cm}^{-3}$ (dashed lines). The curves (a)–(i) correspond to $n = (1.88, 1.64, 1.51, 1.45, 1.18, 1.07, 0.89, 0.75, 0.50) \times 10^{19} \text{ cm}^{-3}$ (Hoekstra et al., 2001).

monochromator, whereas rapid scan Fourier transform spectrometer was used for mid infrared spectra (0.05–0.2 eV). The films were hydrogenated via gas phase loading at 1 atm. Based on the pressure composition isotherms proposed by Huiberts et al. (1996b), Lee et al. assigned a value of $x \cong 2.87$ for the hydrogen concentration (at $p_{\text{H}_2} = 1 \text{ atm}$) in their films. Fig. 18(i) shows the transmittance spectra for two thicknesses of $\text{YH}_{3-\delta}$ films in the energy range from 0.05–6 eV. The enlarged spectrum for low energy range (0.05–0.2 eV) for a film of thickness 58 nm is shown in fig. 18(ii). Lee et al. attributed the observed absorption peaks in the transmittance spectra to optical excitations. The most prominent peak at 3.0 eV was attributed to the fundamental absorption from the valence band to conduction band edge, whereas the possible origin for the weak mid infrared absorption edge peaks (0.67 eV, 0.34 eV and 0.24 eV) were thought to be the transitions between the impurities and bands. The estimated band gap in $\text{YH}_{2.87}$ was 2.66 eV. The absorption coefficient [fig. 19(i)] was estimated from the slope of the $\ln T_{\text{opt}}$ versus film thickness (Lambert's law) [fig. 19(ii)]. Based on the observations of Libowitz (1972) and Heckman (1967) [$\text{CeH}_{3-\delta}$ a compensated semiconductor (n-type for $\delta < 0.2$ and p-type for $\delta > 0.2$)] and the fact that all RH_x exhibit similar properties; Lee et al. postulated that $\text{YH}_{3-\delta}$ was a compensated semiconductor and that the peak at 0.67 eV was due to transition from the donor level to the conduction band whereas the peaks appearing at 0.34 eV and 0.24 eV (of a comparatively smaller intensity) were due to transitions associated with donors. Lee et al. attributed the peaks appearing in the region 0.05–0.2 eV (three strong peaks at 77, 112 and 159 meV, each associated with two weak peaks) to the local vibration modes of hydrogen in the $\text{YH}_{3-\delta}$ lattice. This interpretation was based on the results of the

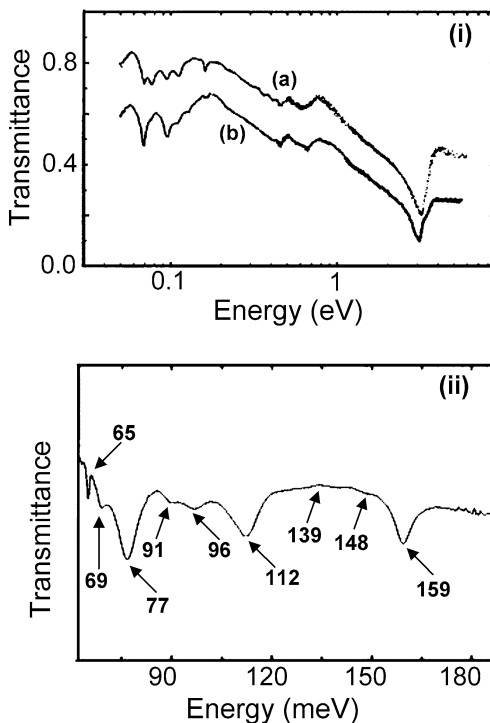


Fig. 18. (i) Optical transmittance vs. photon energy for $\text{YH}_{3-\delta}$ films of thickness (a) 80 nm and (b) 160 nm. (ii) Enlarged spectrum for the low energy region for film of thickness 58 nm (Lee and Shin, 1999).

inelastic neutron scattering experiments (Rush et al., 1966; Anderson et al., 1986; Udovic et al., 1997a, 1997b), according to which the 82 meV peak corresponds to the H vibration modes at the octahedral sites and the 156 and 120 meV peaks correspond to the local modes at the tetrahedral sites. The extinction coefficient (k), the refractive index (n) and dielectric function (ϵ) were obtained using Kramer–Kronig analysis (fig. 20). The optical conductivity was modeled by a dielectric function (expressed by a Drude term and five Lorentzian oscillators) including the contributions from free charge carriers, interband and impurity-related transitions. In the lower energy range, the extinction coefficient as well as optical conductivity were observed to increase sharply with decreasing frequency indicating strong free charge carrier absorption in the $\text{YH}_{3-\delta}$ films. In addition, the plasma frequency ($\omega_p = 0.16$ eV), effective carrier density ($3.1 \times 10^{21} \text{ cm}^{-3}$) and donor ionization energy ($3.3 \times 10^{21} \text{ cm}^{-3}$ at $\delta = 0.13$) were also estimated. Lee et al. observed that the values of carrier density, and donor ionization energy estimated from the optical results correlated well with those obtained by Huiberts et al. (1996a, 1996b) from the Hall measurements. Based on these results, it was concluded that $\text{YH}_{3-\delta}$ is a highly doped, wide-gap semiconductor with an energy gap of 2.6 eV. Later, Lee et al. (2001) studied the infrared transmittance properties in all the three hydrogenation states

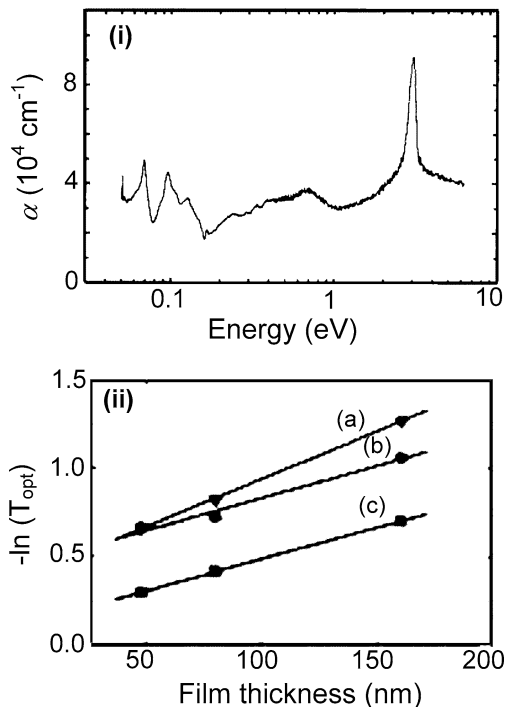


Fig. 19. (i) Absorption coefficient (α) vs. photon energy for $\text{YH}_{3-\delta}$ film. (ii) Logarithm of the optical transmittance vs. film thickness at (a) $\lambda = 200$ nm, (b) 800 nm and (c) 1600 nm (Lee and Shin, 1999).

of YH_x films (as deposited, di- and trihydride), in the frequency range $500\text{--}4000\text{ cm}^{-1}$. It was observed that the transmittance slightly decreases in the β phase followed by a significant increase during $\beta \rightarrow \gamma$ transition (fig. 21). The transmittance spectra were modeled by a Drude-like dielectric function, neglecting the hydrogen local modes (the dotted line in fig. 21). The carrier concentration estimated from the fit was observed to decrease ($1.5 \times 10^{22}\text{ cm}^{-3}$ in as-deposited, $2.4 \times 10^{21}\text{ cm}^{-3}$ in β phase and $2.0 \times 10^{20}\text{ cm}^{-3}$ in γ phase) whereas the carrier relaxation time was observed to increase ($2.5 \times 10^{-16}\text{ s}^{-1}$ in as-deposited, $2.3 \times 10^{-15}\text{ s}^{-1}$ in β phase and $1.0 \times 10^{-15}\text{ s}^{-1}$ in γ phase) with hydrogen concentration. The increase in the relaxation time was attributed to the large reduction in the electron–phonon scattering. The high-frequency limiting dielectric function ϵ_∞ for the as deposited and β phase was found to be ≈ 1 , a typical value for metals whereas in the γ phase, its value was found to be 14, a value typical for semiconductors. By studying the variations in the infrared transmittance spectra during $\beta \rightarrow \gamma$ transition, it was observed that the hydrogen vibration modes at the tetrahedral sites were undetected in β phase. This was interpreted in terms of the electrostatic screening effect due to the free charge carriers in the yttrium hydride. It was argued that when the system was near the β phase, it is metallic and the screening effect is profound. As the system transforms from the β to γ phase, the electron density decreases reducing the screen-

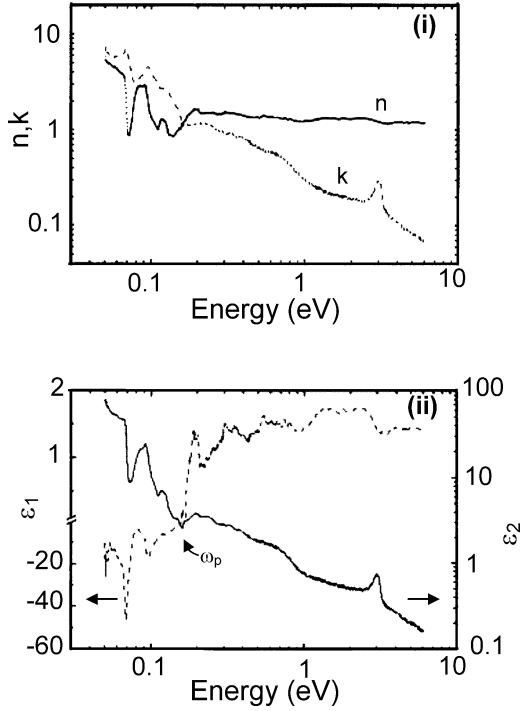


Fig. 20. (i) Refractive index (n) and extinction coefficient (k) vs. photon energy for $\text{YH}_{3-\delta}$ film. (ii) Real (ϵ_1) and imaginary (ϵ_2) parts of dielectric function vs. photon energy (Lee and Shin, 1999).

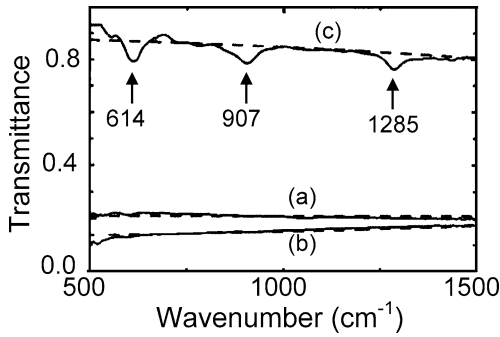


Fig. 21. Infrared transmittance spectra for a YH_x film corresponding to the (a) as-deposited, (b) dihydride and (c) trihydride phases (Lee et al., 2001).

ing effect and as a result, the partially screened local modes appear as weak signals. In the γ phase, the system is insulating and screening is weak and thus the H modes behave like

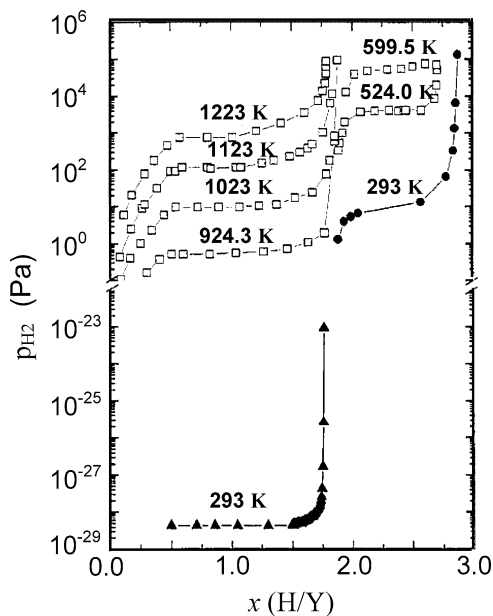


Fig. 22. Pressure composition isotherms of Pd (10 nm) capped YH_x (500 nm) determined from potentiostatic electrolytic (\blacktriangle) and QCM (\bullet) measurements. For comparison the isotherms for bulk Y are also depicted (Griessen et al., 1997; Yannopoulos et al., 1965).

unscreened oscillators. Based on these results, it was concluded that the screening effect can be continuously tuned by simply varying the hydrogen content in the YH_x system and that the absorption intensity of the vibration mode depends on the carrier concentration.

The optical properties of the YH_x as a function of hydrogen concentration were also studied by van Gogh et al. (2001), Rode et al. (2001) and Schoenes et al. (2003). From the analysis of the IR spectra, the Szigeti effect charge was derived. It was found that in the insulating γ phase, the hydrogen is negatively charged with a transfer of about $0.5e$ to every hydrogen atom. Raman scattering spectra display one line in the YH_2 and up to 13 lines in YH_3 . The hydrogen vibrations were identified by comparing the spectra with the deuterated samples. An analysis of the polarization showed that the structure was non-centrosymmetric. The results were observed to support the models, which assume strong electron correlations for the electronic structure (see sections 2.5 and 2.6 for details).

The absorption/desorption properties of hydride forming metals/compounds are generally characterized by the pressure-composition isotherms. The pressure composition isotherms have been determined for the Pd capped YH_x films using the hydrogen concentration determined *in situ* from the QCM and ERDA measurements and/or estimated from the current during the electrochemical loading (Huiberts et al., 1996b; Griessen et al., 1997; Kooij et al., 1999, 2000; Huisman et al., 1999). These pressure composition isotherms were observed to be different from their bulk counterparts. Fig. 22 shows a typical pressure-composition isotherm

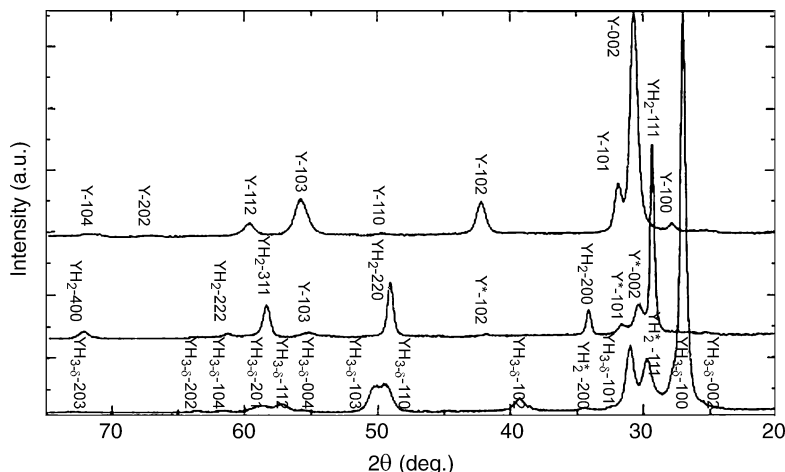


Fig. 23. X-ray diffractograms of YH_x film (570 nm) corresponding to (a) α -Y, (b) β -YH₂, and (c) γ -YH_{3- δ (Huiberts et al., 1996b).}

for Pd (10 nm) capped Y (500 nm) films. The electrolytic method was used for obtaining the plateau pressure for the $\alpha \rightarrow \beta$ coexisting phases, and a QCM method for isotherms at higher concentrations (Griessen et al., 1997). The heat of formation for the $\alpha \rightarrow \beta$ transformation (at $p_{\text{H}_2} \approx 10^{-28}$ Pa) was estimated to be $\Delta H_{\alpha \rightarrow \beta} = -114$ kJ/mol, which was in good agreement with the bulk value [-114 kJ/mol, Behrens et al. (1976)]. For the $\beta \rightarrow \gamma$ transformation (with $p_{\text{H}_2} = 9.2$ Pa in the plateau region) $\Delta H_{\beta \rightarrow \gamma}$ was estimated to be -31 kJ/mol, which was less negative than the bulk value [-41.8 kJ/mol, Flotow et al. (1963); -44.9 kJ/mol, Yannopoulos et al. (1965)]. Huiberts et al. argued that the relatively large plateau observed in the Y thin films indicates that the heat of formation is less negative in the thin films as compared to bulk, or equally, yttrium di- and trihydride films were slightly less stable than their bulk counterparts. From ERDA measurements and the results of Kooij et al. (2000), Huisman et al. (1999) concluded that although there must be three thermodynamically stable phases in the YH_x system ($0 < x < 3$) as in bulk, phase diagram of YH_x thin film may be different compared to the bulk phase diagram, with the phase boundaries shifted towards lower x in case of the former as compared to the later.

Bulk Y crystallizes in the hcp structure. At low hydrogen concentrations, α phase (a single solid solution of H in Y) is formed where hydrogen enters the tetrahedral sites of the Y lattice. At intermediate hydrogen concentrations β phase is formed where hydrogen occupies all the tetrahedral sites. At higher hydrogen concentrations, the octahedral sites start getting filled up and the γ phase precipitates. The α phase has hcp structure, β phase has fcc structure and the structure transforms back to hcp in the γ phase (Muller et al., 1968; Vajda, 1995). Udovic et al. (1996) and Remhof et al. (1999), on the other hand, showed by means of neutron diffraction measurements that YH₃ has HoD₃ ($P\bar{3}c1$) structure. However the small displacements of the yttrium atoms and the positions of the hydrogen atoms were not discernable from X-

Table 1

Lattice constants (a and c), calculated distances d_{\perp} (between the hexagonal planes) and d_{\parallel} (nearest neighbor distances) and molar volume for yttrium, yttrium dihydride and yttrium trihydride reported for bulk (Kooij et al., 2000) and thin films (Huiberts et al., 1996b). The values corresponding to thin films are bolded

Phase	a (Å)	c (Å)	d_{\perp} (Å)	d_{\parallel} (Å)	\bar{V}_{YH_x} (cm ³)
hcp Y	3.650	5.737	2.8685	3.650	19.924
	3.664	5.790	2.8950	3.664	–
fcc YH ₂	5.199	–	3.0016	3.6762	21.149
	5.205	–	3.0051	3.6805	21.222
	5.201	–	3.0028	3.6777	21.174
	5.209	–	3.0074	3.6833	21.272
	5.219	–	3.0133	3.6909	–
hcp YH ₃	3.672	6.659	3.3295	3.672	23.405
	3.674	6.599	3.2995	3.674	23.220
	3.672	6.625	3.3125	3.672	23.285
	3.686	6.602	3.3010	3.686	–
	–	–	–	–	–

ray diffraction measurement. Huiberts et al. (1997), studied the hydrogen induced changes in the structural properties of Y thin films by X-ray diffraction measurements carried out *ex situ*. Kooij et al. (2000), van Gogh et al. (2000a), and Remhof et al. (2002a) performed *in situ* XRD measurements during hydrogenation. Fig. 23 shows the X-ray diffractograms of Y films (570 nm) at different stages of hydrogenation (Huiberts et al., 1997). From the measured value of the increase in the lattice parameter of the as-deposited films ($\Delta a = 0.007$ Å and $\Delta c = 0.022$ Å) and from the reported value of lattice parameters for YH_{0.19} ($a = 3.664$ Å and $c = 5.790$ Å), Huiberts et al. estimated the amount of hydrogen incorporated in the films during deposition to be 8.0%. The calculated lattice parameters reported for the bulk and for the thin film of Y at different stages of hydrogenation are tabulated in table 1. The separation d_{\perp} between consecutive hexagonal planes (hcp: $d_{\perp} = c/2$; fcc: $d_{\perp} = a/\sqrt{3}$), the nearest neighbor distance d_{\parallel} within these planes (hcp: $d_{\parallel} = a$; fcc: $d_{\parallel} = a/\sqrt{2}$) and the yttrium molar volume V_Y are also given in table 1. Kooij et al. (2000) mapped the X-ray diffraction results measured *in situ* during gas phase hydrogen loading of Pd (15 nm) capped Y (300 nm) films onto the electrochemical results via the electrical resistivity which was measured simultaneously in the X-ray diffraction experiment as well as in the electrical/optical experiments during electrochemical loading, to get information about the concentration dependence of the crystallographic structure. During hydrogen loading, a narrow co-existence region of the cubic and hexagonal phases was observed to exist for $1.9 \leq x \leq 2.1$. Above $x = 2.1$, the film was observed to remain in the hcp phase with no further lattice expansion till $x = 3$, which was in strong contrast to the observations in bulk. During deloading, on the other hand, the films were observed to exhibit bulk like behavior. From $x = 2.7$ down to 2.0, fcc YH_{2±ξ} and YH_{3-δ} phases were observed to coexist. The anomalously large difference in the phase coexistence region in the films and in bulk claimed by Kooij et al. motivated Remhof et al. (2002a) to perform a series of new experiments where the optical, electrical and structural properties were all measured simultaneously on a single sample. Remhof et al. (2002a) could not con-

firm the narrow β - γ co-existence region in their experiments. Their results are discussed in detail in section 2.4.1.

As demonstrated by various workers, an interesting feature of the RH_x films is their mechanical stability as compared to bulk. While the bulk Y-H becomes powder before reaching the trihydride state during the first loading, Y-H films could be loaded and deloaded easily and very often without deterioration of the film quality. Dornheim et al. (2003) performed stress measurements during hydrogen loading of polycrystalline (0002)-textured Y films (50–500 nm) deposited on sapphire substrate capped with a Pd (15–30 nm) over layer and loaded via electrochemical means in 1 M KOH solution. The hydrogen concentration in the films was calculated from the measured electric charge by using Faraday's law. The apparent phase boundaries were determined by *in situ* X-ray diffraction measurements. The stresses, which build up during hydrogenation of the films, were measured *in situ* using an optical two-laser beam deflection setup for measuring the substrate curvature and described by one-dimensional linear elastic model using the bulk Y-H data. It was observed that the basic properties of the bulk Y-H phase diagram and the elastic constants resembled the measured values of the thin films. Compressive stresses were observed to build up during hydrogen loading in the α phase and in the α - β two-phase region, showing an increase of -1.3 GPa per hydrogen concentration (compressive stress). It was shown that, in contrast to bulk Y-H samples, which are known to undergo contraction in the β phase, thin films showed no evidence for such a contraction during the first loading cycle. The observed constant stresses in the bulk β phase concentration range ($=0.1$ H/Y), were attributed to the narrow β phase field (0.02 H/Y) of the thin film during the first loading. Only the films, which were kept at a hydrogen concentration of about 1.5 H/Y for weeks, were observed to exhibit tensile stresses in the concentration range of the bulk β phase. A stress increase of about $+0.5$ GPa per hydrogen concentration was measured in the β - γ two-phase region. This was attributed to the smaller in plane nearest neighbor distance in the γ phase compared to the β phase. In the γ phase the compressive stresses were observed to build up again (it increases by -1.3 GPa per hydrogen concentration), compensating the tensile stress. Dornheim et al. concluded that in total the net stress remains comparatively small, leading to the observed good mechanical stability of the RH_x thin films.

For practical applications, the optimization of parameters such as switching time, lifetime, and optical contrast ratio are of importance. Van der Molen et al. (1999) investigated the dependence of the hydrogenation properties of the switchable mirrors on the thickness of both the Y and Pd layers. The results are discussed in detail in section 2.4.1. Van der Molen et al. (1999) determined the mobility coefficients for the lateral transport of hydrogen in the Y thin films using optical measurements carried out during loading via the gas phase. The hydrogen diffusion perpendicular to the matrix sample surface was compared with lateral transport of hydrogen. It was shown that the switching time and the morphology of the film depend strongly on the film thickness. Since hydrogen diffusion coefficient (D_f) was observed to depend strongly on the film thickness Li and Cheng (1996), Di Vece and Kelly (2003a) determined the relation between the switching time (τ_s) and diffusion coefficient. The switching of Pd (10 nm) capped Y (200 nm) films deposited on chromium (2.5 nm) coated glass substrate, was studied by potential step experiments in which both the current and transmittance were

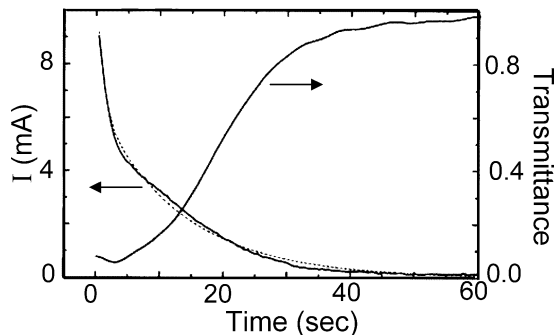


Fig. 24. Transient of current (solid line) with fit (dotted line) and of optical transmittance (normalized) for Y film after a potential step of 0.2 V to -0.95 V was applied (Di Vece and Kelly, 2003a; Di Vece et al., 2003b, 2003c).

followed as a function of time. All the electrochemical experiments were carried out in 1 M KOH solution at room temperature using Hg/HgO as reference electrode and Pt as counter electrode. Fig. 24 shows the current and transmittance transients measured simultaneously after a step from 0.2 V to -0.95 V. Two different time domains ($t \leq 100$ ms and $1 \leq t \leq 60$ s) were investigated. In the first few seconds, a fast decay in the current was observed, followed by a much slower decay, which was observed to be accompanied by the main changes in the optical transmittance. The current transients were fitted using double exponential function and the effective diffusion coefficients were determined from the time dependence of the current. Di Vece argued that the presence of double decay process could be understood in terms of the different phases through which loading occurs in YH_x ($2 < x < 3$). The first decay was related to the filling of the β phase with a higher diffusion coefficient where as the slow decay in the transient was related to the transformation from the $\beta \rightarrow \gamma$ phase. It was observed that the fast exponential decay clearly visible in the current transients in the first few seconds, was absent if some additional charge (Δx) was introduced before the potential step. The diffusion coefficients were observed to be concentration dependent. An increase in the diffusion coefficient was observed as a function of concentration (fig. 25). Experiments at different temperatures showed Arrhenius dependence of both the diffusion coefficients and switching time. The activation energies estimated from the slopes (0.39 and 0.34 eV) were in good agreement with the value of 0.37 eV estimated for the $\beta \rightarrow \gamma$ phase by den Broeder et al. (1998) from the lateral gas phase loading experiments on Y thin film.

2.1.2. Lanthanum films

The hydrogen induced optical, electrical and structural properties of Pd capped La film has been studied by Huijberts et al. (1996a), Griessen et al. (1997) and by van Gogh et al. (2001). Fig. 26 shows the variation in electrical resistivity and optical transmittance (at 1.8 eV) as a function of hydrogen exposure time for a Pd (20 nm) capped La (500 nm) film. The relation between the thermodynamic phases and the hydrogen concentration at room temperature as deduced from the experimentally determined phase diagram for the bulk La-H system is also

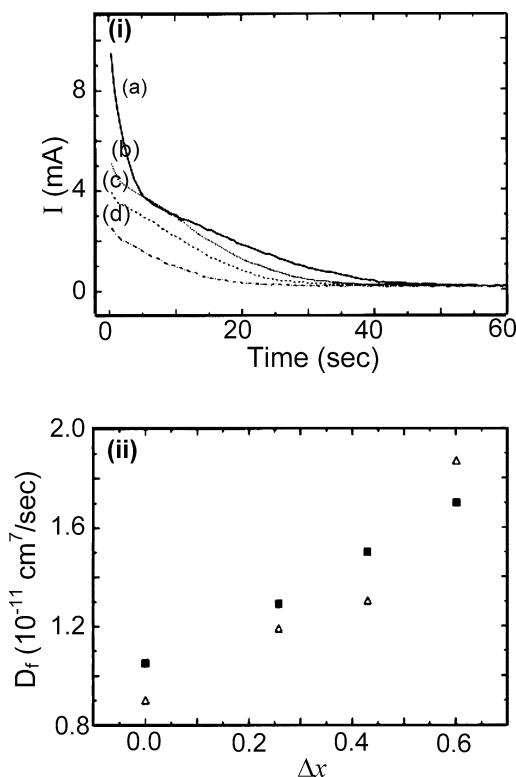


Fig. 25. (i) Currents transients after adding (a) $\Delta x = 0$, (b) $\Delta x = 0.26$, (c) $\Delta x = 0.43$, and (d) $\Delta x = 0.60$. (ii) Diffusion coefficients calculated from the current transients using exponent factor (Δ) and the pre-exponential factor (\blacksquare) (Di Vece and Kelly, 2003a).

depicted. The resistivity and optical transmittance are observed to exhibit similar variation as function of hydrogen intake as observed in YH_x , except that no transparency window was observed near LaH_2 and the optical switching in LaH_x was observed to be more gradual than for YH_x . In addition, LaH_x was observed to remain in the cubic fcc phase over the whole concentration range ($2 < x < 3$) at temperatures above ~ 300 K, revealing the electronic origin of the observed M–I transition. In contrast to the observations of Huiberts et al. (1996a), van Gogh et al. (2001) observed the optical window in the optical transmittance spectra (at 1.52 eV) of La (300 nm) film capped with AlO_x/Pd over layer (1.5 nm AlO_x , 15 nm Pd) near the dihydride phase (fig. 27). The optical properties studied by van Gogh et al. (2001) are described in detail in section 2.4.1.

Van Gogh et al. performed the X-ray diffraction measurements on La (300 nm) film capped with AlO_x/Pd over layer during *in situ* hydrogenation. The films were hydrogenated by exposing to 10^5 Pa hydrogen gas at room temperature and deloaded at 100°C . As-deposited La film was observed to have dhcp structure, with lattice parameters $a = 3.769 \text{ \AA}$ and $c = 6.102 \text{ \AA}$.

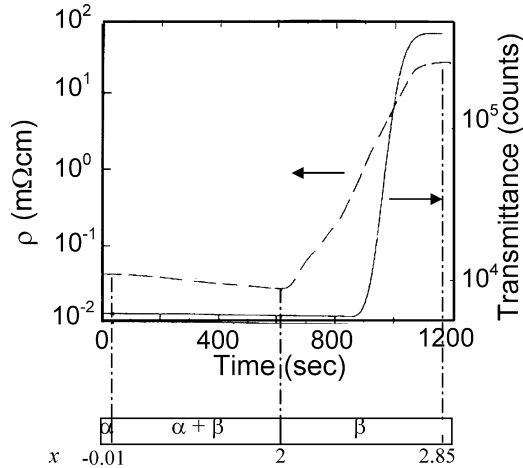


Fig. 26. Variation in the electrical resistivity and optical transmittance (at $h\nu = 1.8$ eV) during hydrogen loading (p_{H_2} increased to 0.9×10^5 Pa) at room temperature in Pd (20 nm) capped La (500 nm) film deposited on Al_2O_3 substrate is compared with the bulk phase diagram (Huiberts et al., 1996a).

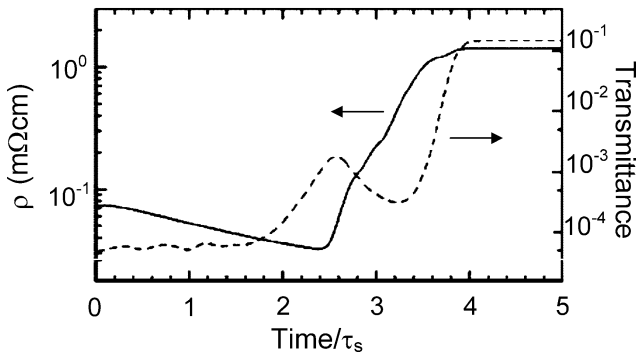


Fig. 27. Time dependence of the optical transmittance (at 1.52 eV) and resistivity for LaH_x after 1000 mbar of H_2 is applied at time = 0. The time is scaled with the switching time of 20.5 s (van Gogh et al., 2001).

The dihydride was observed to have fcc structure with $a = 5.694$ Å. La was observed to remain in the fcc phase in the trihydride phase with lattice parameter $a = 5.616$.

2.1.3. Praseodymium films

Mor et al. (2000, 2001, 2003) studied the hydrogen induced electrical, optical and structural properties of praseodymium (28–170 nm) films with and with out Pd over layer. The films were deposited by thermal evaporation onto Corning 7059 substrates. A metal to insulator transition was observed in the uncapped Pr films (28–90 nm) during *in situ* hydrogen loading

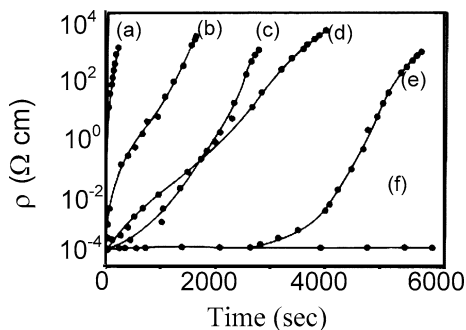


Fig. 28. Time evolution of resistivity of Pr films of various thickness and deposition and loading temperatures, after exposure to hydrogen gas at 1.015×10^5 Pa, (a) 28 nm, 373 K, (b) 28 nm, 323 K, (c) 60 nm, 373 K, (d) 60 nm, 323 K, (e) 90 nm, 373 K and (f) 90 nm, 323 K (Mor and Malhotra, 2000).

only for temperatures ≥ 323 K. For studying the transition at room temperature different Pd over layer configurations were utilized viz., Pd dots of various diameters (0.5–3.5 mm) and various thickness (8–18 nm) on the Pr films of thickness 28 nm; and Pd over layer of various thickness (5–19 nm) on Pr films of thickness 170 nm.

A metal to semiconductor transition was observed in uncapped Pr films during *in situ* hydrogen loading at temperatures ≥ 353 K. Fig. 28 shows the variation in electrical resistivity as a function of hydrogen exposure time for Pr films of various thickness hydrogenated at different temperatures. It was observed that higher substrate temperature and low thickness of Pr film facilitates a fast M–I transition. Films of thickness 28 nm, 60 nm and 90 nm deposited at 373 K and those of thickness 28 nm and 60 nm deposited at 323 K were observed to exhibit M–I transition with resistivity changing by six orders of magnitude. The time required for M–I transition was found to be minimum (285 s) for 28 nm Pr film deposited and hydrogenated at 373 K. Fig. 29 shows the transmittance and reflectance as a function of wavelength of the hydrogenated Pr films deposited and hydrogenated *in situ* at 373 K. Using the observed transmittance, reflectance, and thickness of the films, the refractive index and extinction coefficient were evaluated using Tomlin's algorithm. The absorption coefficient was evaluated using the extinction coefficient and the optical band gap corresponding to direct transition estimated from the Tauc's plot was observed to be 3.0 eV. X-ray diffraction studies of the Pr (90 nm) films deposited and hydrogenated at 373 K revealed fcc, CaF_2 type structure with average lattice parameter of 5.611 Å.

By capping Pr films (28 nm) with Pd dots of various diameters, M–I transition was realized at room temperature. Mor et al. argued that the use of Pd dots avoided the problem encountered during the use of a continuous Pd over layer (Huiberts et al., 1996b) while still making monoatomic hydrogen available for reaction with underlying film. Dots of various diameters 3.5, 1.5 and 0.5 mm and each of thickness 12 nm were vacuum evaporated on 28 nm Pr films. The total time required in getting six-fold change in magnitude of resistivity was minimum for the mask, which covered the maximum area (dots of diameter, 3.5 mm) [fig. 30(i)]. Us-

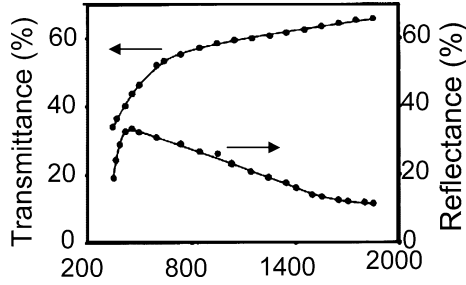


Fig. 29. Transmittance and reflectance spectra of uncapped Pr film (28 nm), deposited and exposed to hydrogen gas *in situ* at 373 K (Mor and Malhotra, 2000).

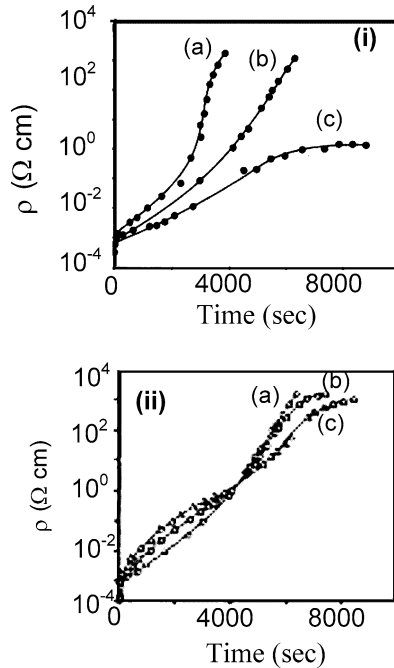


Fig. 30. (i) Variation of resistivity as a function of time for room temperature deposited Pr films (28 nm) covered with Pd (12 nm thickness) dots of area (a) 77.16 mm², (b) 19.44 mm² and (c) 21.2 mm² on exposure to hydrogen gas at 1.015 × 10⁵ Pa pressure. (ii) Resistivity change during hydrogen loading for a 28 nm Pr film covered with (a) 8 nm, (b) 12 nm and (c) 18 nm thick Pd dots (of diameter 3.5 mm) at room temperature as a function of time. The surface area of Pr films was 144 mm² (Mor and Malhotra, 2000).

ing the mask for dots of diameter 3.5 mm, different thickness (8, 12 and 18 nm) of Pd were deposited and it was observed that relatively fast transitions were observed for Pr films cov-

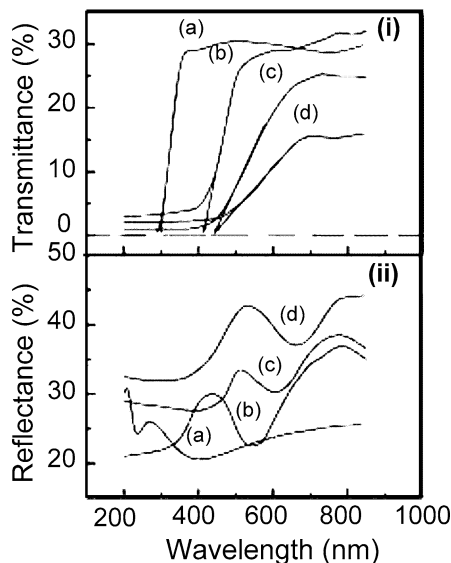


Fig. 31. Transmittance (i) and reflectance (ii) spectra of $\text{PrH}_{3-\delta}$ (120 nm) capped with Pd overlayer of thickness (a) 5 nm, (b) 9 nm, (c) 12 nm and (d) 19 nm (Mor and Malhotra, 2003).

ered with 8 nm Pd dots during the hydrogen loading [fig. 30(ii)]. Though the M–I transition was observed in the Pr films covered with Pd dots as well as without any Pd over layer, the transitions were not reversible. On using Pd over layers with selected covered area geometry, the transition or switching time in seconds was achieved. Increase in Pd cap thickness was found to significantly affect the magnitude of the transmittance of PrH_x films. The transmittance edge of the hydrogen saturated Pr films stayed at 2.82 eV provided the thickness of the over layer was ≥ 12 nm. With decrease in the Pd over layer thickness a blue shift in the transmittance edge has been observed (Mor and Malhotra, 2003). Fig. 31 shows the transmittance and reflectance spectra of $\text{PrH}_{3-\delta}$ films capped with Pd over layers of various thickness. On desorbing hydrogen from hydrogen saturated films a red shift in the transmittance edge was observed. The magnitude of the shift was observed to increase with increase in the cap layer thickness. Ellipsometric measurements were performed to determine the dielectric constants of the Pd capped deloaded PrH_x films (Mor et al., 2001). Experimental ψ and Δ spectra were fitted to an optical model consisting of the air/Pd/ PrH_x /glass substrate in order to generate the dielectric constants of the underlying hydrided films. The dielectric function $\epsilon(\omega)$ for PrH_x films was modeled using a sum of five Lorentz oscillators (LO) and one Drude oscillator (DO). The first LO represented higher energy band transitions, second the LO described the transition between the valence and the conduction band of PrH_x films, the third LO represented the transition involving localized states formed near to conduction band upon hydrogen desorption, and the fifth LO of PrH_x represented the transition between the acceptor levels to conduction band and/or valence band to donor levels. The variation of parameters of the DO

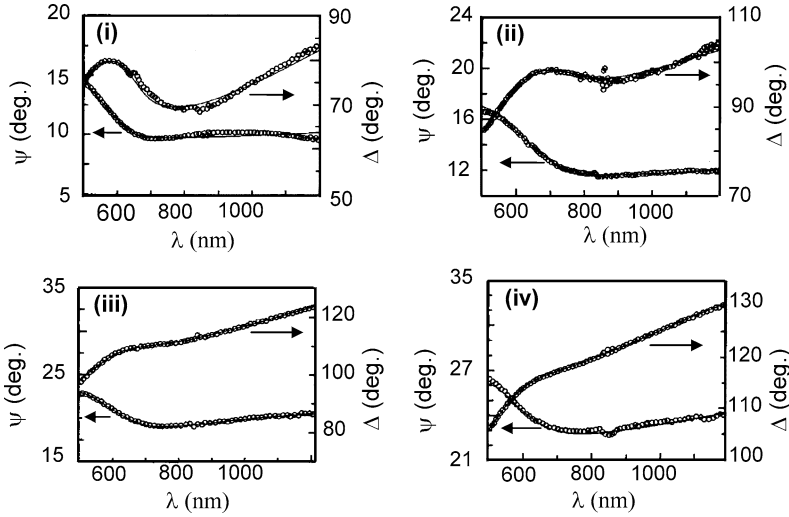


Fig. 32. ψ and Δ spectra of deloaded PrH_x films capped with Pd over layer of thickness (i) 9 nm, (ii) 12 nm, (iii) 15 nm and (iv) 18 nm. Both the experimentally observed data ($\circ \circ \circ$) and the theoretical fit (---) are shown (Mor et al., 2001).

was found to affect the strength of the fifth LO. The plasma energy given in the Drude term was found to be small in hydrogen-saturated films. Fig. 32 gives the experimental and theoretically fitted Ψ and Δ spectra of the deloaded PrH_x films covered with Pd over layer of different thickness, showing a reasonable good fit between the experimental and theoretical data. Using these data the refractive index (n) and extinction coefficient (k) and the real (ϵ_1) and imaginary parts (ϵ_2) of the dielectric constant were calculated (fig. 33). The value of refractive index was observed to lie between 1–2.2 and the extinction coefficient varied between 0.15–1.2 for PrH_x films. Mor et al. attributed the change in the position and broadening of the ϵ_2 peak to the roughness of the film. It was observed that with decrease in the thickness of the Pd over layer on the PrH_x films, the ϵ_2 peak decreased in height and broadened and shifted towards higher wavelength, indicating that a continuous smooth Pd film was achieved only for thickness exceeding 18 nm. The band gap of the deloaded PrH_x films as a function of the Pd over layer thickness was estimated from the Tauc's plots (fig. 34). From the estimated values, it was concluded that increased thickness of the Pd capped layer leads to a decrease in the value of x in PrH_x films during deloading. This was similar to the results of Kooij et al. (2000) who demonstrated a shift in the transmittance edge of YH_x films towards lower energy with a decrease in concentration of hydrogen in the films. Mor et al. (2001) observed additional features in the Tauc's plot with decrease in the Pd over layer thickness (fig. 34), which was attributed to the transitions involving the localized states formed between the conduction band and valence band after deloading hydrogen from the hydride films. The average transition energy due to the vacancy states (1.62 eV) observed by Mor et al. (2001) was close to the value of 1.9 eV estimated theoretically by Ng et al. (1999). The slight disagreement with in

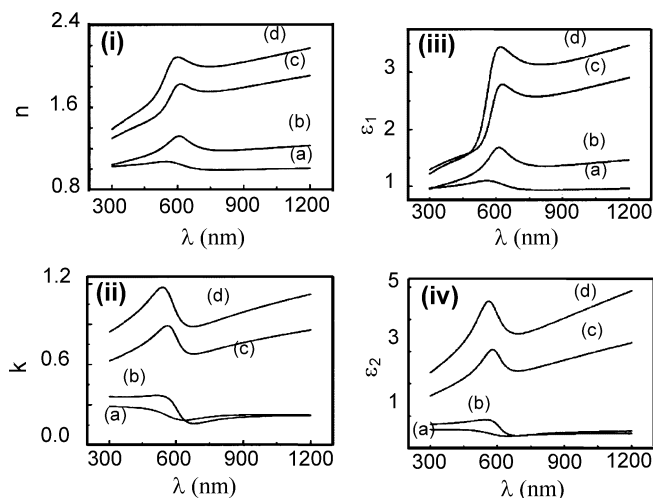


Fig. 33. Variation of (i) n , (ii) k , (iii) ϵ_1 , (iv) ϵ_2 in deloaded PrH_x films capped with Pd over layer of thickness (a) 9 nm, (b) 12 nm, (c) 15 nm and (d) 18 nm (Mor et al., 2001).

the values was related to the contribution of Coulomb attraction between the H vacancy and extra electron in the latter case, which was not taken into account. It was argued that with an increase in the Pd over layer thickness the amount of hydrogen deloaded will be large and hence the concentration of localized states within the band gap will be higher. When these localized states substantially overlap each other, hydrogen deloaded films start moving towards a more metallic character. Similar observations of the formation of strongly localized states near the conduction band during hydrogen deloading from the YH_x were reported by Kooij et al. (2000) who interpreted the concentration dependence of optical and electrical properties of $\gamma\text{-YH}_x$ phase using the Ng et al. (1999) theory for LaH_x . Mor et al. (2001, 2003) observed that for PrH_x films covered with a Pd over layer of thickness ≤ 9 nm, hydrogen desorption was not possible. It was argued that this was due to the non-permeable oxide layer formed on the uncovered portion of the Pr films and that the binding energy of hydrogen chemisorbed on the surface is higher than that of hydrogen absorbed at the interstitial sites on the Pd clusters formed at such low thicknesses. Interesting observations were reported for Pr (170 nm) films covered with Pd over layer of thickness ≤ 9 nm. Using XRD, TEM and AFM measurements it was shown that hydrogenation of such films led to the transformation of polycrystalline Pr films into nanocrystalline $\text{PrH}_{3-\delta}$ films. These films showed a blue shift in their transmittance edge with respect to position of the edge of $\text{PrH}_{3-\delta}$ films capped with 19 nm thick Pd layer (fig. 31). Using EMA theory, the approximate size of nanocrystallites calculated from the blue shift of 1.36 and 0.24 eV for a cap layer of 5 nm and 9 nm was found to be 19 nm and 32 nm, respectively.

The structural characterization of the Pd capped Pr films revealed that the room temperature deposited films were polycrystalline in nature. The structure of Pr film was found to

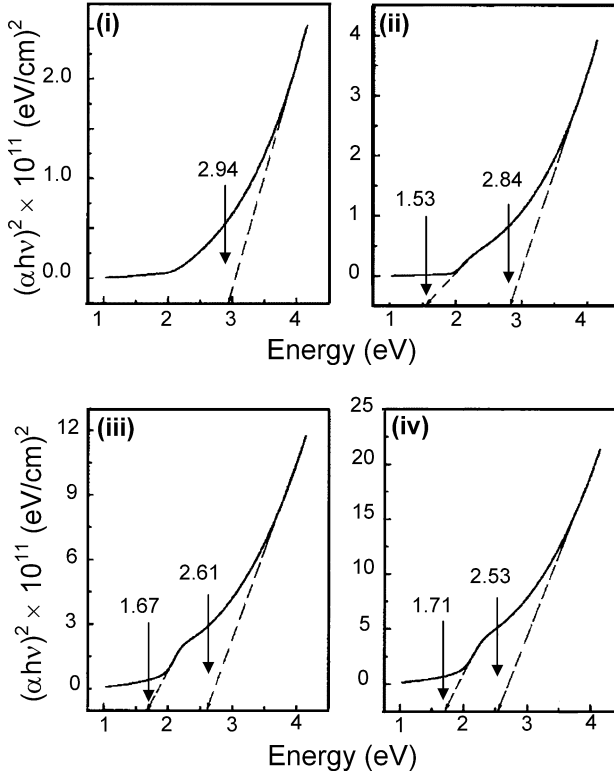


Fig. 34. Tauc's plot of deloaded Pr (170 nm) films capped with Pd over layer of thickness (i) 9 nm, (ii) 12 nm, (iii) 15 nm and (iv) 18 nm (Mor et al., 2001).

be double hexagonal and was observed to exhibit a preferential orientation with [004] direction perpendicular to the substrate. The average lattice parameter of Pr film were obtained to be $a = 3.688 \text{ \AA}$ and $c = 11.742 \text{ \AA}$. Upon hydrogenation no structural transformation was observed, both $\text{PrH}_{2\pm\xi}$ and $\text{PrH}_{3-\delta}$ remaining fcc. The lattice constant of the dihydride was found to decrease until the trihydride state was reached. It was found that the in-plane and out of plane expansion were about 9.3% and 6.2% respectively between the Pr and its dihydride phase, whereas in-plane and out-of-plane contraction of approximately 1.3% was observed to occur between the dihydride and the trihydride phases. Fig. 35 shows the X-ray diffractograms of a typical as deposited, and hydrogen loaded Pd (18 nm) capped Pr (90 nm) film.

2.1.4. Samarium films

Von Rottkay et al. (1999a) studied the changes in the optical and electrical properties of Pd (15 nm) capped Sm (67 nm) films, sputter deposited on glass substrates coated with conducting tin oxide or ITO, during electrochemical hydrogen loading in 5 M NaOH with two Pt

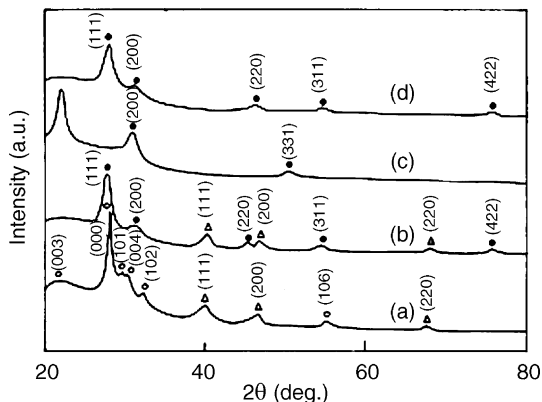


Fig. 35. X-ray diffractograms of the Pd capped Pr films as deposited (a) and hydrogenated at room temperature (b). The X-ray diffractograms of uncapped Pr films deposited and hydrogen loaded at 373 K for 30 min (c) and 3 h (d) are also shown (Mor and Malhotra, 2000).

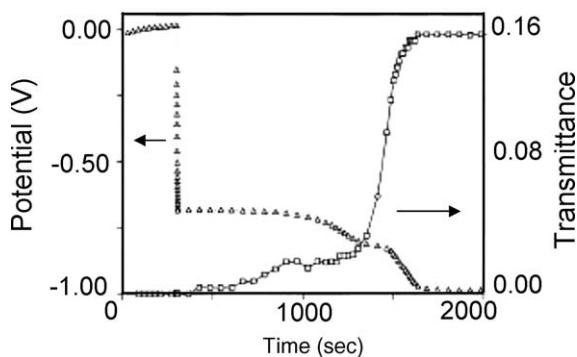


Fig. 36. Initial galvanostatic loading in 5 M NaOH of a Sm (67 nm) capped Pd (15 nm) film (von Rottkay et al., 1999a).

electrodes (one as counter electrode and other as pseudo-reference electrode). The electrochemical measurements were carried out in fused silica cell mounted in an optical bench for simultaneous optical transmittance measurements. Kumar et al. (2002, 2004a, 2004b, 2004c, 2004d) studied the effect of Pd over layer thickness on the hydrogen-induced changes in the electrical and optical properties of Pd capped Sm films deposited by thermal evaporation and hydrogenated via both gas phase loading and electrochemical loading.

Fig. 36 shows the time evolution of the electrode potential and transmittance during the initial galvanostatic loading of a Pd (15 nm) capped Sm (67 nm) film hydrogenated via electrochemical loading in 5 M NaOH (von Rottkay et al., 1999a). Two plateaus were observed, one at -690 mV and another one at -820 mV, after which the potential was observed to drop

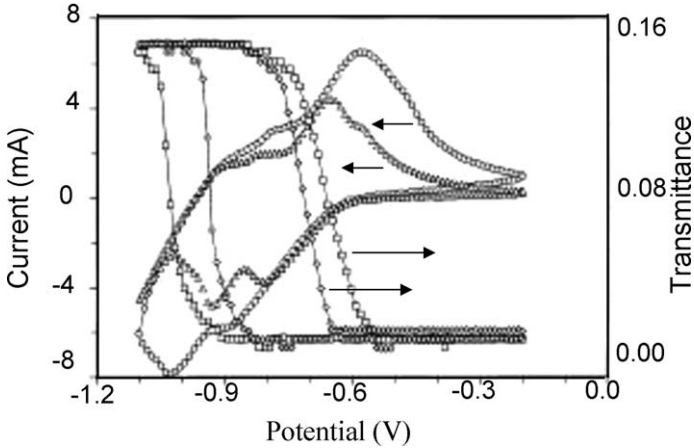


Fig. 37. CV at 5 (Δ) and 10 mV s^{-1} (\circ) in 5 M NaOH of a Pd (15 nm) capped Sm (67 nm) film. Simultaneously measured transmittance [\diamond : 5 mV s^{-1} , \square : 10 mV s^{-1}] is also shown (von Rottkay et al., 1999a).

rapidly before reaching the hydrogen evolution limit. Von Rottkay et al. argued that though the second plateau was less marked than the first one, it was possible to discern a 2/3–1/3 relation in the plateau lengths corresponding to the cubic SmH_2 and the hexagonal SmH_3 stages. During the first potential step the transmittance was observed to rise up to 2% and then reaches 16% at the end of the second plateau, with the maximum transmittance limited only by the Pd over layer. Once the film was loaded with hydrogen it was cycled between the dihydride and trihydride states. The CV measurements (cycles at 5 and 10 mV s^{-1} between -0.2 and -1.1 V) and the simultaneously measured transmittance are shown in fig. 37. Cathodic half cycle showed two peaks where as anodic scan was observed to have one peak with a small shoulder. This was attributed to the two-step conversion from SmH_3 to SmH_2 . Von Rottkay et al. also performed the potential step experiments where the samples was held at -0.2 V for 60 s and then at -1.0 V for 60 s. The response time in Pd (15 nm) Pd capped Sm (67 nm) film was observed to be 20 s for the transition from reflecting metallic dihydride state to the transparent semiconducting trihydride state where as less than 10 s for the reverse transition.

Kumar et al. (2002) studied the electrical and optical switching of Sm films (55 nm) capped with different thickness (9–15 nm) of Pd over layer on gas phase hydrogenation. Fig. 38 shows the variation in resistance as a function of hydrogen exposure time. As reported by Azofeifa and Clark (2000) for Dy films, Sm films did not show the initial rise in the resistance upon hydrogen exposure; instead the resistance was observed to decrease indicating the precipitation of SmH_2 . After a minima (signature of the dihydride formation) a steep rise in the resistance was observed followed by a saturation corresponding to the formation of $\text{SmH}_{3-\delta}$. The over layer thickness was shown to control the response time (defined as the time required for the initial resistance to reach 90% of the saturation value) and recovery time (time required for the saturated resistance value to fall to 90% of minimum value), a higher thickness facilitating faster response and recovery time. Kumar and Malhotra (2004d) showed that Pd capped Sm

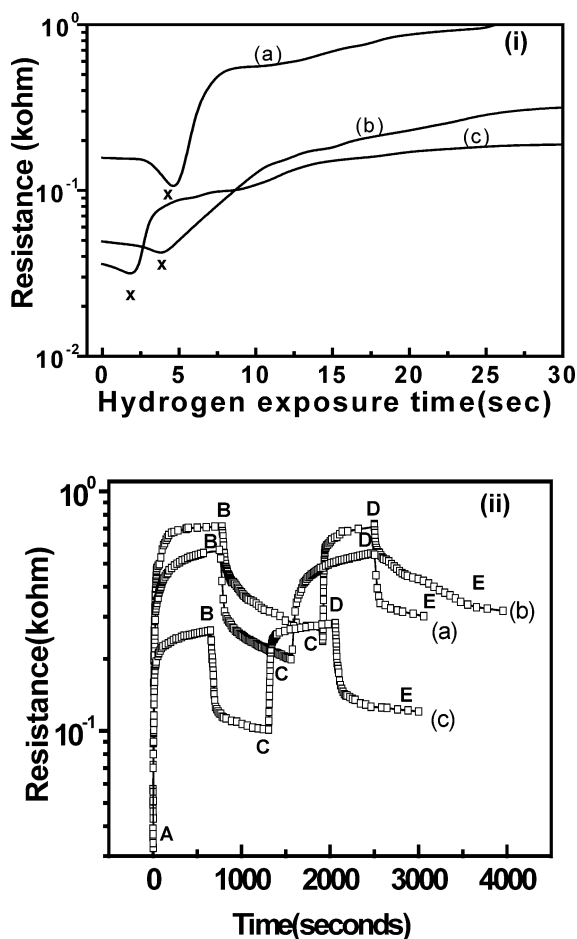


Fig. 38. (i) Time evolution of resistance during hydrogen loading of Sm (55 nm) films capped with Pd overlayer of thickness (a) 9 nm, (b) 12 nm and (c) 15 nm during hydrogen loading ($p_{H_2} = 1.01 \times 10^5$ Pa). The decrease in resistance to point *x* is indicative of the formation of dihydride phase. (ii) The corresponding variation in resistance during hydrogen loading (AB, CD) and deloading (BC, DE) (Kumar et al., 2002).

films could be used as an efficient sensor for hydrogen detection as the films exhibit a very high absorption and desorption efficiency for hydrogen at room temperature without any need for an external source and could detect low concentrations of hydrogen, suggesting the use as a potential base material for hydrogen sensing applications without worrying about cross sensitivity problems (see section 5 for details).

The effect of Pd over layer thickness on the hydrogenation of Sm (55 nm) films capped with Pd over layer of different thicknesses was also carried out using electrochemical loading (Kumar et al., 2004a, 2004b, 2004c). Charging (loading) and discharging (deloading) of hydrogen

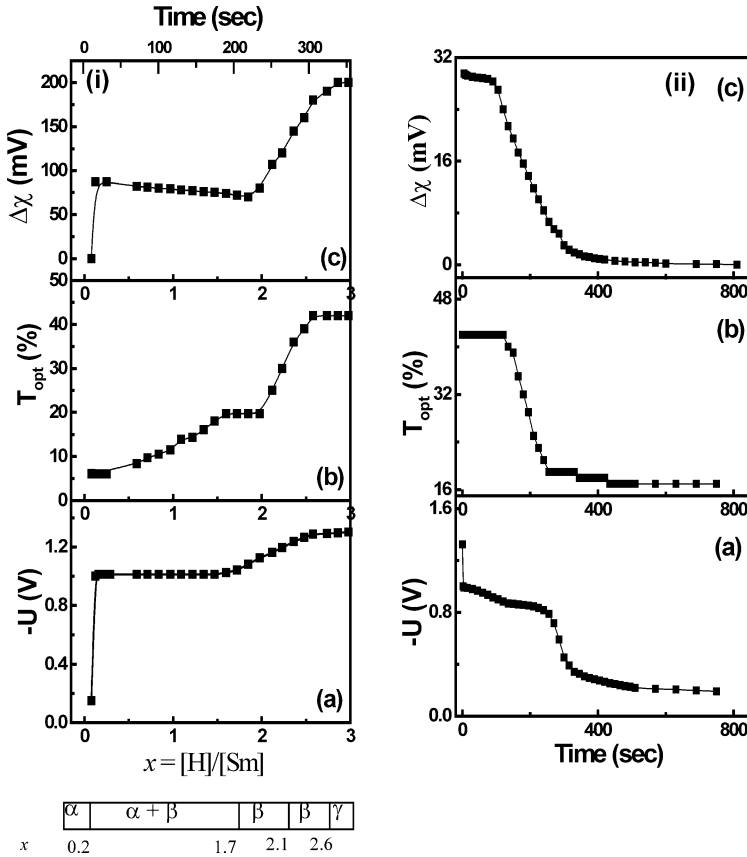


Fig. 39. (i) Variation in (a) Electrode potential (b) transmittance, and (c) surface potential difference of a Pd (7 nm) capped Sm (50 nm) film as a function of hydrogen concentration $x = [H]/[Sm]$ determined from galvanostatic loading experiments. The proposed phase diagram is also depicted. (ii) Variation in (a) Electrode potential (b) transmittance, and (c) surface potential difference as a function of time on spontaneous discharge (Kumar and Malhorta, 2004a).

into/from Pd capped Sm films (used as working electrode in the electrolytic cell) was achieved by cathodically polarizing/depolarizing the working electrode. The electrochemical measurements were performed in an aqueous 1 M KOH solution using Pt trip as a counter electrode and Hg/HgCl₂ (Kumar et al., 2004a, 2004b) or Hg/HgO (Kumar and Malhorta, 2004c) as reference electrode. By monitoring the working electrode potential, the transmittance (at 650 nm) and the chi potential difference ($\Delta\chi$, which was related to the resistance of the films), Kumar and Malhorta (2004a) estimated the different phases present in the Pd (7 nm) capped Sm (50 nm) films during the hydrogen loading and proposed the phase diagram for Sm-H system [fig. 39(i)]. Using Faraday's law and taking the film thickness, the electrode surface area, and the integrated charge into account, Kumar and Malhorta (2004a) calculated the hydrogen

concentration in Sm film assuming an initial hydrogen concentration of $x = 0.08$ [which gets incorporated into the film during deposition, [Huiberts et al. \(1996b\)](#)]. These calculations showed that the observed transitions in transmittance and $\Delta\chi$ curves correspond to hydrogen content of about 0.25, 1.7, 2.1 and 2.6 respectively in Sm films. Based on the experimental results and calculations, the reported phase diagram for bulk Sm–H system ([Mueller et al., 1968](#)) and the published data on similar studies on rare earth metal films ([Huiberts et al., 1996a](#); [Notten et al., 1996](#); [Kooij et al., 1999](#)) it was inferred that for hydrogen concentrations $x \leq 0.25$, the transmittance remains constant and $\Delta\chi$, after an initial rise from 0 mV to 87 mV also remains constant. Constant transmittance and $\Delta\chi$ are signatures of a single-phase solid solution of hydrogen in samarium. For $0.25 < x < 1.7$, $\Delta\chi$ decreases gradually which indicates transition towards dihydride. The rise in transmittance in this region was attributed to the small thickness (55 nm) of the Sm film. The transmittance remained constant for $1.7 < x < 2.1$ and the minima in $\Delta\chi$ occurs at 1.85 which was considered as indication of the formation of the dihydride state at that composition. Thereafter all three curves were observed to exhibit a sharp rise and attaining a constant values beyond $x = 2.6$ which was considered as an indication of the formation of trihydride state. By increasing the hydrogen concentration x in SmH_x at room temperature, three stable hydride phases were observed viz., α (a single phase solid solution of hydrogen in samarium), β (the dihydride phase), and γ (the trihydride phase) in addition to the two phase ($\alpha + \beta$ and $\beta + \gamma$) coexisting regions. [Fig. 39\(ii\)](#) shows the variation in working electrode potential (U), transmittance (T_{opt}), and $\Delta\chi$ during spontaneous discharging of the films. The electrode potential was observed to increase immediately from -1.3 V to -1.0 V. Four regions, subsequently encountered are regions of gradual increase, a near constant region followed by a sharper increase and then a slow increase to attain a constant value. The occurrence of these regions was explained in terms of the variation in the simultaneously measured transmittance and $\Delta\chi$. It was argued that in the first region, 0 to 120 seconds, the excess charge (H^+ ion) accumulated at working electrode/electrolyte interface starts to diffuse slowly through the electrolyte. The slow increase of working electrode potential indicated that the capacitive layer diffuses towards the anode, however no deloading of hydrogen from the working electrode was occurring. This was clear from the almost constant values of T_{opt} (42%) and $\Delta\chi$ (26 mV). In the second region, between 120 to 260 seconds, the potential was observed to become approximately constant but a drastic change in transmittance from 42% to 19% and in $\Delta\chi$ from 26 mV to 6.5 mV was observed. It was argued that the nearly constant transmittance reflects that the hydrogen discharged from the working electrode stays at the interface. In the range between 260 to 400 seconds, the potential increases sharply from -0.790 V to -0.270 V, indicating that the accumulated hydrogen on the working electrode starts to diffuse through the electrolyte and a small change in transmittance and $\Delta\chi$ occurs. In the fourth region beyond 400 seconds, all three curves stay almost constant, which indicate that the dihydride state has been attained, and no hydrogen can then be deloaded. [Kumar and Malhotra \(2004a\)](#) argued that though the potential on deloading falls to about 0.2 V a value comparable to that obtained (corresponding to α phase) during loading, it does not mean reaching the α phase during deloading. The nearly equal potential values in the two phases was due to their comparable electrical conductivity; however the transmittance (a distinguishing feature between the two phases) on deloading $\sim 16\%$ was much higher than

that obtained on loading the α phase $\sim 6\%$. The transition between the di- and trihydride state was reversible. The dark brownish color of dihydride state was observed to change reversibly to the golden greenish color of the trihydride state by changing the hydrogen concentration in the films.

Fig. 40 shows the development of electrode potential on charging and discharging of the working electrode and the corresponding, *in situ* measured, variation of transmittance (at 650 nm) for Sm films (55 nm) capped with Pd over layers of thicknesses 5, 8, and 11 nm respectively (Kumar and Malhotra, 2004c). The potential was observed to fall sharply in each case during cathodic polarization of the working electrode. The fall in potential and the corresponding changes in the transmittance (indicated by the portion AB) represents the transformation of the Sm films from the metallic state to the nearly trihydride state as also confirmed by measurement of resistance. The switching time (defined as the time required to reach 90% of the maximum transmittance) was observed to vary with the Pd over layer thickness, with 38, 30, and 22 s obtained respectively for Pd over layers of thicknesses 5, 8 and 11 nm. No change in the transmittance and potential curves (at the portion B to C) after the formation of nearly trihydride state was observed even though current density was maintained at the initial value of 3.057 mA/cm^2 . At point C, the films were anodically discharged by changing the polarity. Comparison of transmittance curves showed that the discharging (deloading) is very slow in films covered with Pd over layer of thickness 5 nm. The rate of discharging increases with the increase in the Pd over layer thickness. The slow discharge of hydrogen in Sm films capped with low thickness of Pd overlayer was explained in terms of the low coverage of the underlying Sm films at small thickness Pd over layer and the inability of Pd clusters formed at small thickness to show reversible hydrogen deloading capacity as given by Mor and Malhotra (2003). The reversibility between the charged and discharged states was also observed to become better with increase in Pd layer thickness. No degradation of the films was observed even after 40 cycles of charging (loading)/discharging (unloading) in 15 nm Pd covered film and there was no trace of any bubble formation. It was observed that the reversible switching between dihydride and trihydride states occurred within 6 seconds and was reproducibly observed for 40 cycles. In all the three cases discussed above, the large fall in potential was found and was attributed to the high-applied current density between working and counter electrodes. If current density is high, then the rate of evolution of hydrogen ions at the electrode surface will be high, resulting in a high chemical potential generated in the solution. The switching time was observed to decrease with increase in current density, the variation being in agreement with the predictions of the Sand equation (Gileadi et al., 1975) and was interpreted in terms of the increased rate of reaction on the surface of the working electrode because of a higher driving force at high current density. Kumar and Malhotra (2004c) argued that in addition to thickness of Pd over layer, the current density, and the interface between Sm and Pd films plays an important role in controlling the switching time as well as their chemical stability in the electrolyte and cycle durability. The time duration between deposition of Sm and Pd was found to be an important factor.

The transmittance and reflectance of $\text{SmH}_{3-\delta}$ film (55 nm) capped with Pd (2.5 nm) hydrogenated via gas phase loading is given in fig. 41. Neglecting the contribution from the Pd over layer, the refractive index and extinction coefficient were determined from the measured

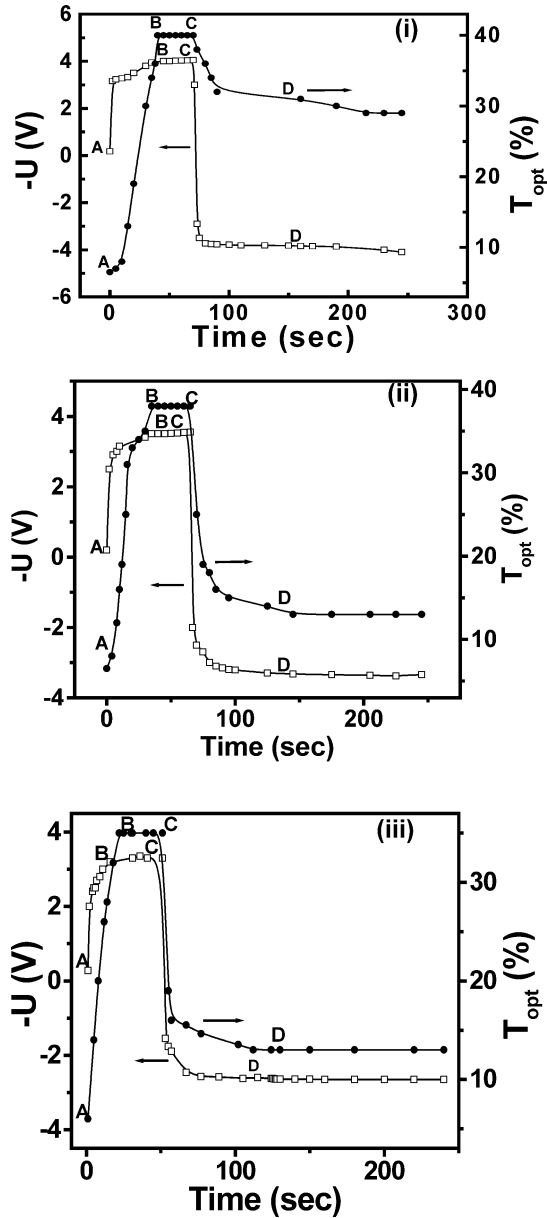


Fig. 40. Development of electrode potential E and *in situ* measured optical transmittance as a function of time for 55 nm Sm film (working electrode) covered Pd overlayer of thickness (i) 5 nm, (ii) 8 nm, and (iii) 11 nm, during galvanostatic hydrogen loading and unloading at current density 3.057 mA/cm^2 in 1 M KOH (Kumar and Malhorta, 2004c).

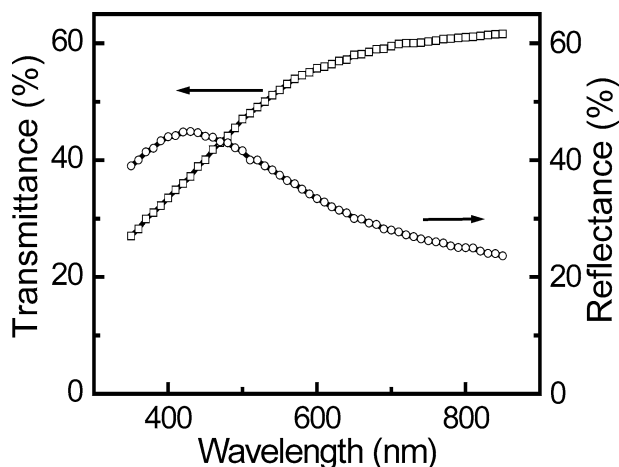


Fig. 41. Transmittance and reflectance spectra of Pd (2.5 nm) capped $\text{SmH}_{3-\delta}$ (55 nm) (Kumar et al., 2002).

transmittance and reflectance and film thickness. Optical gap estimated from the Tauc's plot for $\text{SmH}_{3-\delta}$ revealed a direct allowed transition with a band gap of 3.0 eV. The effect of Pd over layer on the desorption of hydrogen from fully hydrogenated $\text{SmH}_{3-\delta}$ (55 nm) films was studied by using *ex situ* optical measurements on the films hydrogenated via electrochemical loading and deloaded by changing the polarity of the films. Fig. 42 shows the variation in the optical transmittance and reflectance as a function of wavelength for the Sm (55 nm) film capped with Pd over layer of different thickness. The differences in optical responses at low and high energies are clearly seen in the reflectance spectra. At low energies (≥ 750 nm), the dihydrides were observed to be highly reflecting due to the free electron optical response while the features at higher photon energies were related to the interband transition, as explained by Kooij et al. (2000). At low energies, the magnitude of reflectance was observed to increase with increasing thickness of the Pd over layer. Based on the arguments by Kooij et al. (2000), Mor et al. (2001) and theoretical predictions by Ng et al. (1999), it was argued that more hydrogen desorption occurs at higher Pd over layer thicknesses, which leads to the delocalization of the electrons at the hydrogen atom sites. The transmittance was observed to decrease as the palladium overlayer thickness increases, as a higher thickness of palladium film limits the transmittance (Huiberts et al., 1996a, 1996b; von Rottkay et al., 1999b). The increase in cap layer thickness leads to a red shift of the transmittance edge upon unloading of hydrogen, which was explained to be due to the increased hydrogen desorption at higher thicknesses of the Pd over layer as explained by Mor et al. (2001). The band gap of the deloaded SmH_x obtained from the Tauc's plot using the absorption coefficient derived from the transmittance and reflectance values showed a dependence on the Pd over layer thickness (fig. 43) as also observed by Mor et al. (2001). The tail in Tauc plots was attributed to a transition involving localized states as explained by Mor et al. (2001) and as predicted by Ng et al. (1999). The shifting of the band gap towards lower energy in these films upon unloading

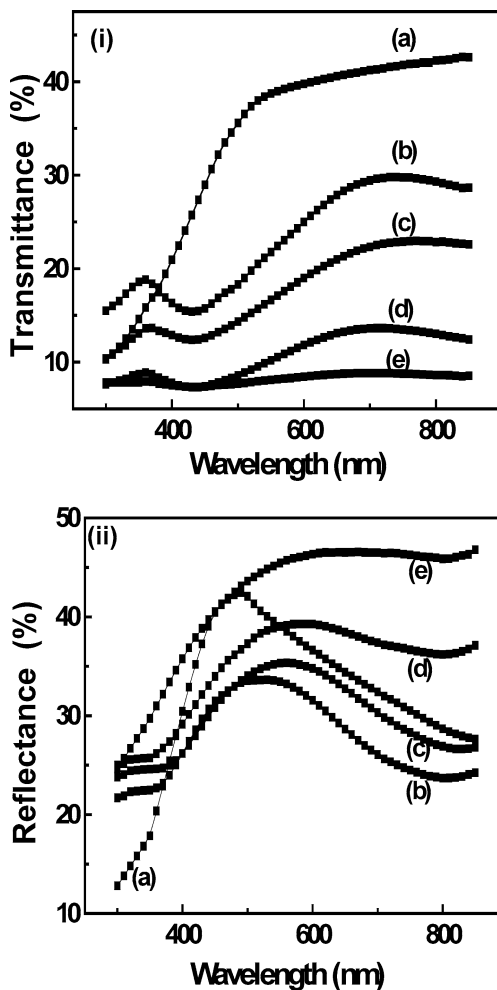


Fig. 42. Transmittance (i) and Reflectance (ii) spectra for 55 nm SmH_x films covered with (a) 5.0 nm, (b) 8.0 nm, (c) 11.0 nm, and (d) 15.0 nm palladium over layers. The transmittance and reflectance spectra of a typical metallic samarium film covered with Pd overlayer of thickness 5.0 nm is shown in (e) (Kumar and Malhotra, 2004b).

was also in accord with the reported observation by Kooij et al. (2000) who demonstrated the shift in transmittance edge of YH_x films towards lower energy with decreasing hydrogen concentration in the films.

Hall effect measurements performed on the Pd capped Sm films during *ex situ* hydrogen loading and deloading provide insight into the changes occurring in the band structure of the Sm upon hydrogen loading and deloading (Kumar et al., 2002). From an electron dominated conduction with a metal-like $C_H = -14.9 \times 10^{-10} \text{ C}^{-1} \text{ m}^3$, the magnitude of C_H was ob-

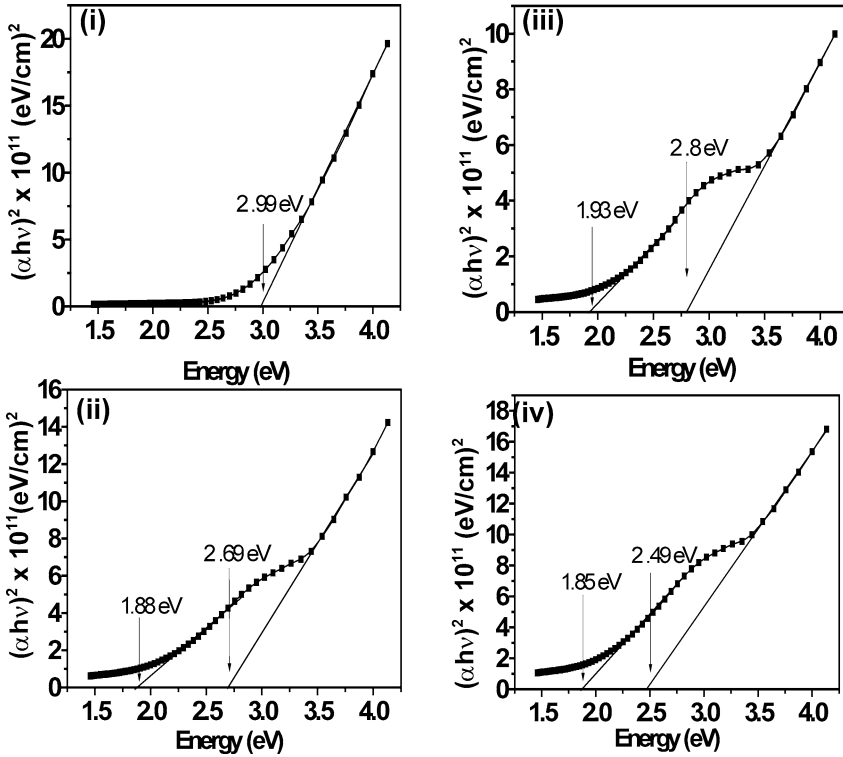


Fig. 43. $(\alpha h\nu)^2$ vs. $h\nu$ plots for deloaded SmH_x films covered with Pd over layer of thickness (i) 5.0 nm, (ii) 8.0 nm, (iii) 11.0 nm, and (iv) 15.0 nm (Kumar and Malhotra, 2004b).

served to increase as hydrogen is absorbed reaching $C_H = -1081.8 \times 10^{-10} \text{ C}^{-1} \text{ m}^3$ for hydrogen saturated Pd capped Sm films ($\text{SmH}_{3-\delta}$). On unloading hydrogen, the C_H changes and was observed to attain a value $C_H = -3.85 \times 10^{-10} \text{ C}^{-1} \text{ m}^3$ at the dihydride composition. This decrease in the value of C_H towards zero was an indication of the existence of holes in the dihydride films as argued by (Azofeifa and Clark, 2000). Loading of hydrogen into the hydrogen-desorbed films again raises the magnitude of C_H , its sign still remaining negative and this increase/decrease was repeatedly observed as reversible cycles of loading and unloading were performed.

X-ray diffractograms of the as deposited, hydrogen loaded and deloaded Pd capped Sm film are shown in fig. 44. As-deposited Sm films were observed to be polycrystalline with rhombohedral structure and an average lattice parameter of $a = 8.989 \text{ \AA}$, slightly larger than the value reported for bulk (Mueller et al., 1968) attributed to the small amount of hydrogen incorporated in the Sm films during deposition. Hydrogen saturated Sm films ($\text{SmH}_{3-\delta}$) were observed to have hexagonal structure with average lattice parameter of $a = 3.775 \text{ \AA}$ and $c = 6.743 \text{ \AA}$ and the deloaded film was observed to have fcc, CaF_2 structure with an average

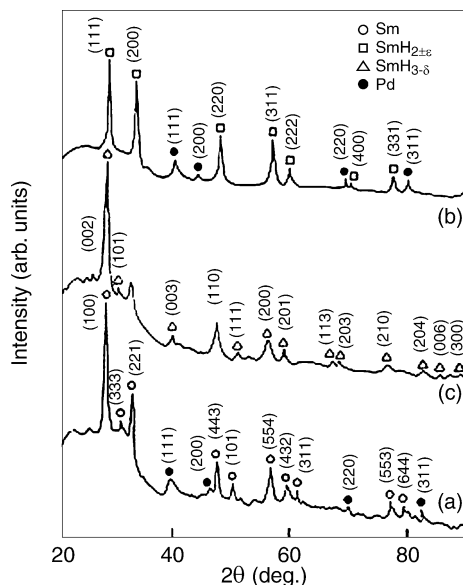


Fig. 44. X-ray diffractograms of (a) Sm (55 nm) films covered with Pd over layer of thickness 9 nm, (b) $\text{SmH}_{3-\delta}$ film covered with Pd over layer of thickness 2.5 nm, and (c) deloaded $\text{SmH}_{2\pm\epsilon}$ film (Kumar et al., 2002).

lattice parameter of 5.372 \AA , in close proximity with the reported values for bulk $\text{SmH}_{3-\delta}$ and SmH_2 respectively (Mueller et al., 1968).

2.1.5. Gadolinium films

The optical properties of the gas phase loaded $\text{GdH}_{3-\delta}$ were studied in detail by Lee and Lin (2000). Di Vece et al. (2002, 2003c) studied the changes in the electrical, optical and thermodynamic properties in polycrystalline Pd capped Gd films upon hydrogenation via electrochemical loading. The galvanostatic loading was performed on Pd (10 nm) capped polycrystalline Gd (57, 100, 200, 300, and 400 nm) films, deposited on ITO substrates top coated with 0.5 nm Mg layer, in 1 M KOH solution at room temperature using Hg/HgO as reference electrode and Pt as counter electrode. Fig. 45 shows the pressure composition isotherm together with the transmittance (at 670 nm) as a function of hydrogen concentration in Pd (10 nm) capped Gd (200 nm). The Gd film was observed to display a plateau pressure up to $x = 1.2$. The heat of formation obtained from this low hydrogen concentration plateau (-107 kJ/mol H) was observed to be in good agreement with the reported value for bulk GdH_2 (Libowitz and Macland, 1979). Between $1.3 < x < 1.7$, a transmittance window was observed. This optical transition was accompanied by a drastic increase in the pressure as the $\alpha \rightarrow \beta$ transition is completed. After the sharp pressure increase, the $\beta \rightarrow \gamma$ transition was observed. Fig. 46 shows the current and transmittance transients of the Gd films recorded simultane-

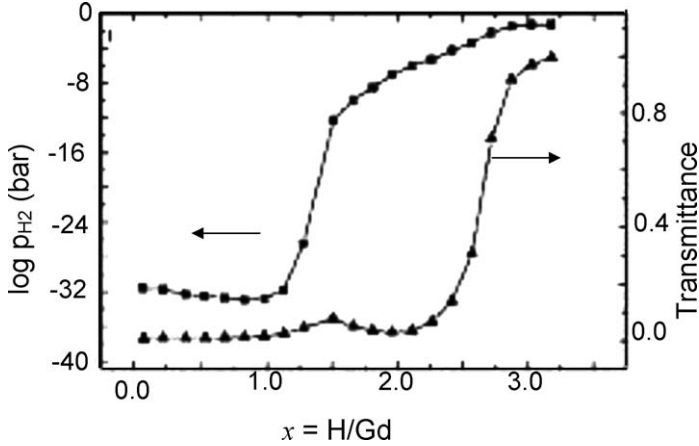


Fig. 45. Pressure composition isotherm (■) (determined using GITT) and normalized optical transmittance (▲) of Gd (200 nm) film capped with a Pd (10 nm) over layer (Di Vece et al., 2002).

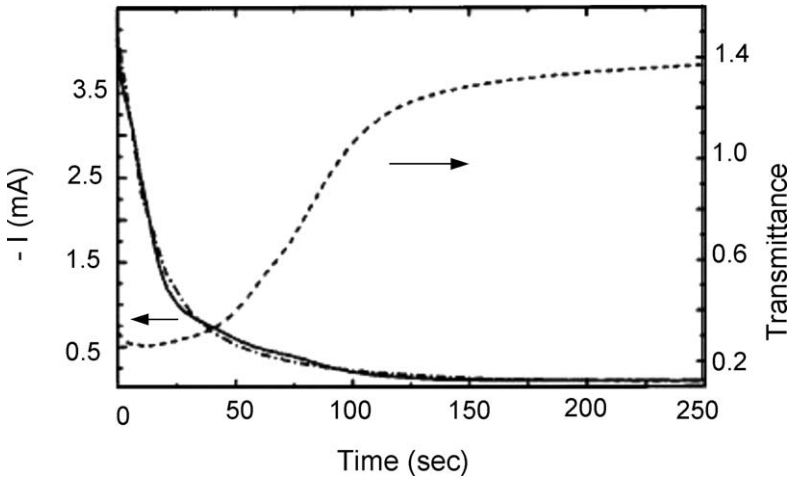


Fig. 46. Transient of current (solid line) with fit (dotted line) and of optical transmittance (normalized) for Gd film after a potential step of 0.2 V to -0.95 V was applied (Di Vece et al., 2003c).

ously after a potential step (from 0.2 to -0.95 V) was applied. In the first few seconds, a rapid decay in the current and a small initial decrease in the transmittance were observed. The initial decrease in the optical transmittance was attributed to the presence of the optical window. A much slower decay in the current transient was accompanied by the main optical change. The transmittance was observed to increase until the hydrogen concentration was uniformly distributed within the film and the electrochemical potential corresponds to the applied

potential. The current was observed to reach a low steady-state value, which corresponds to the hydrogen evolution. Di Vece et al. showed that a simple diffusion model can be used to describe consistently the switching kinetics of a Gd thin film upon hydrogenation. The time constants of the current and transmittance transients were observed to be directly related to the diffusion coefficient, pertaining to the reversible loading of the Gd film. The two time domains observed (double exponential decay) were attributed to the different structural phases involved in the transition from the dihydride to the trihydride state. A clear dependence of the switching time (τ) and the diffusion coefficient (D_f) on temperature, potential, concentration, and film thickness was observed. Fig. 47(i) shows variation of the logarithm of the diffusion coefficient and the measured switching time (defined as the maximum of the derivative of the transmittance with respect to time) as a function of reciprocal of temperature for the slow process in a Pd (10 nm) capped Gd (200 nm) film determined from the exponential current decay fit. The diffusion coefficient for the slow process was observed to range from 4.5×10^{-12} to $2.0 \times 10^{-11} \text{ cm}^2 \text{ s}^{-1}$ in the temperature interval from 25 to 65 °C; the corresponding activation energy was observed to be 0.32 eV. The fast decay was observed to give activation energy of ~ 0.29 eV. The activation energy calculated from the slope of the reciprocal switching time versus reciprocal temperature plot was obtained to be 0.29. From the gas phase loading experiments on the Y films loaded by lateral hydrogen transport, activation energy of 0.37 eV for the $\beta \rightarrow \gamma$ transition was reported by den Broeder et al. (1998). Di Vece et al. argued that the markedly good agreement between the activation energies independently determined from the current and transmittance transients and the good agreement of the activation energies for hydrogen diffusion in Y films with literature values provided strong evidence in support of the diffusion limited kinetics. A significant increase in the diffusion coefficient with increase in hydrogen concentration and decreasing applied potential was found. The diffusion coefficient was observed to increase from 3.2×10^{-12} to $6.9 \times 10^{-12} \text{ cm}^2 \text{ s}^{-1}$ with increase in hydrogen concentration from 0.01 to 0.06, whereas the optical switching time was observed to decrease [fig. 47(ii)]. It was suggested that the change in the electronic structure at higher hydrogen concentrations, apparent from the optical changes, could give rise to lower diffusion barriers at higher hydrogen concentrations. The optical switching time was also observed to decrease if some initial hydrogen is present in the before the potential step. An increase in diffusion coefficient from 1.4×10^{-11} to $1.3 \times 10^{-10} \text{ cm}^2 \text{ s}^{-1}$ and a decrease in the switching time from 100 to 10 s was observed with increase in the potential range -0.91 to -1.2 V [fig. 47(iii)]. A thickness dependence of the switching time and diffusion coefficient was also found. For potential step of -1.0 V, the diffusion coefficient was observed to increase from 3.2×10^{-12} to $2.1 \times 10^{-11} \text{ cm}^2 \text{ s}^{-1}$ as the film thickness increased from 57 to 400 nm. The diffusion coefficient for the potential step to -1.1 V was observed to be higher, but showed the same trend with increasing film thickness [fig. 47(iv)]. From the nonlinear dependence of the switching time on the film thickness [fig. 47(iv)] Di Vece et al. concluded that role of diffusion in the switching kinetics was more important than the role of surface processes.

Similar to the analysis on $\text{YH}_{3-\delta}$ thin films, Lee and Lin (2000) determined the optical constants of the γ -phase GdH_3 thin films. A sapphire disc was used as substrate for higher energy range (0.2–2.9 μm), and GaAs wafer for the low energy range (2.5–25 μm) measurements. Pd (15 nm) capped Gd (32, 68, and 98 nm) films were hydrogenated via gas phase loading

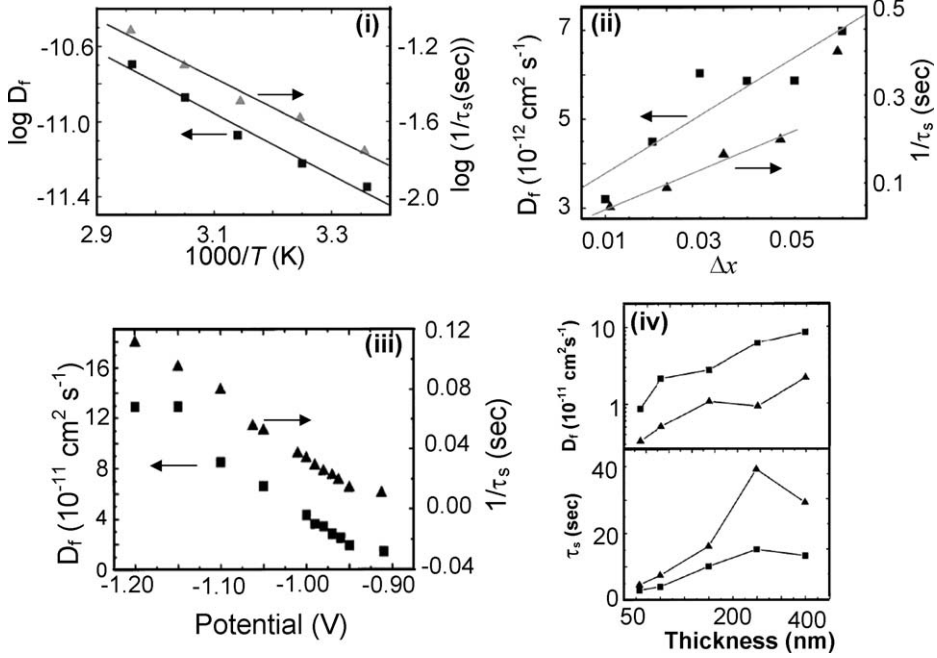


Fig. 47. (i) Arrhenius plot of diffusion coefficient (D_f) and the reciprocal switching time (τ_s) in a Gd film. (ii) Variation in diffusion coefficient and switching time as a function of added hydrogen. (iii) Potential dependence of diffusion coefficient and reciprocal switching time. (iv) Variation in diffusion coefficient and reciprocal switching time as a function of film thickness for two applied potentials, 1.0 V (square) and 1.1 V (triangle) (Di Vece et al., 2003c).

(10 Torr). After few minutes, the Gd film was observed to change from a highly reflecting to a transparent state, indicating that the film had undergone the $\alpha \rightarrow \beta \rightarrow \gamma$ phase transition. The phase transformations were supported by resistivity measurements. The optical transmittance of GdH_3 thin films was then measured over a broad spectral range 0.05–6 eV (fig. 48). The frequency dependent absorption coefficient (α) was determined from the measured transmittance spectra using the Lambert's law (fig. 49). The most pronounced peak in the high-energy range 1–6 eV, appearing at photon energy of 3.06 eV, was assigned to the fundamental absorption from the valance band edge to the conduction band edge. The two shoulders at slightly lower energies at 2.6 eV and 2.0 eV were attributed to transitions between an impurity and a band. The analysis indicated that GdH_3 is a wide band gap semiconductor with an energy gap of 2.55 eV. The three large absorption peaks appearing in the low-energy region (0.05–0.2 eV), at 75.9, 110.6 and 157 meV were attributed to the local vibration modes of hydrogen in GdH_3 . The extinction coefficient was evaluated from the estimated absorption coefficient where as the refractive index was estimated using Kramers–Kronig analysis [fig. 50(i)]. Using the estimated values of frequency dependent refractive index and extinction coefficient, the complex dielectric constant has been evaluated [fig. 50(ii)]. In addition, the frequency dependent op-

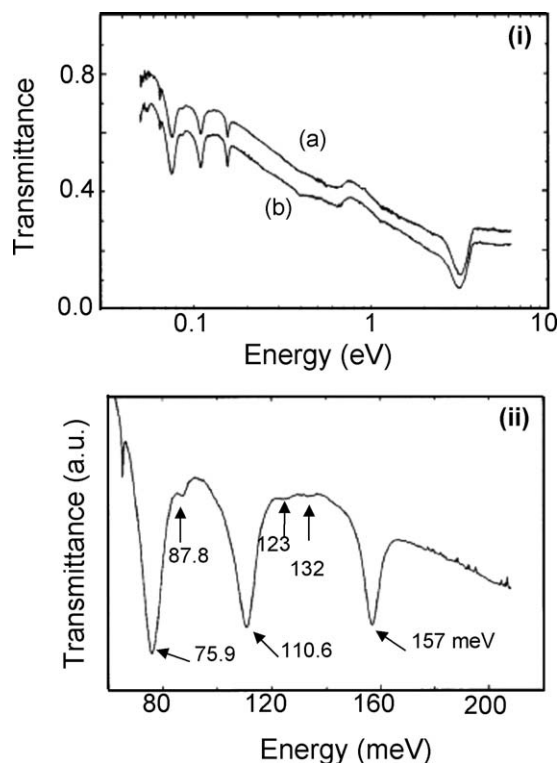


Fig. 48. (i) Optical transmittance vs. photon energy for $\text{GdH}_{3-\delta}$ films of thickness (a) 68 nm and (b) 96 nm. (ii) Enlarged spectrum for the low energy region (Lee and Lin, 2000).

tical conductivity, free carrier density and plasma frequency associated with the free carriers were also determined. The optical conductivity was modeled by two-component dielectric function (a Drude term and five Lorentzian oscillator). The plasma frequency was estimated to be 0.725 eV and the carrier density $3.7 \times 10^{20} \text{ cm}^{-3}$. Lee et al. argued that the relatively large free carrier density indicates the GdH_3 was a highly doped semiconductor and as a result there was a strong free-carrier absorption effects at long wavelengths. The monotonically decreasing base line in the transmittance spectra and the monotonically decreasing extinction coefficient reveal strong absorption effects.

The changes in the optical and electrical properties of the rare earth metal upon hydrogen loading is accompanied by volume changes which can lead to considerable stresses causing property deterioration. Leervad Pedersen et al. (2003) compared different materials that exhibit hydrogen induced switching to determine the material best suited to meet the requirements of gasochromic applications in terms of process stability and reversibility. The measurements were carried out using a wafer curvature setup, which allows simultaneous measurements of the mechanical stress and optical transmittance and reflection of the coatings.

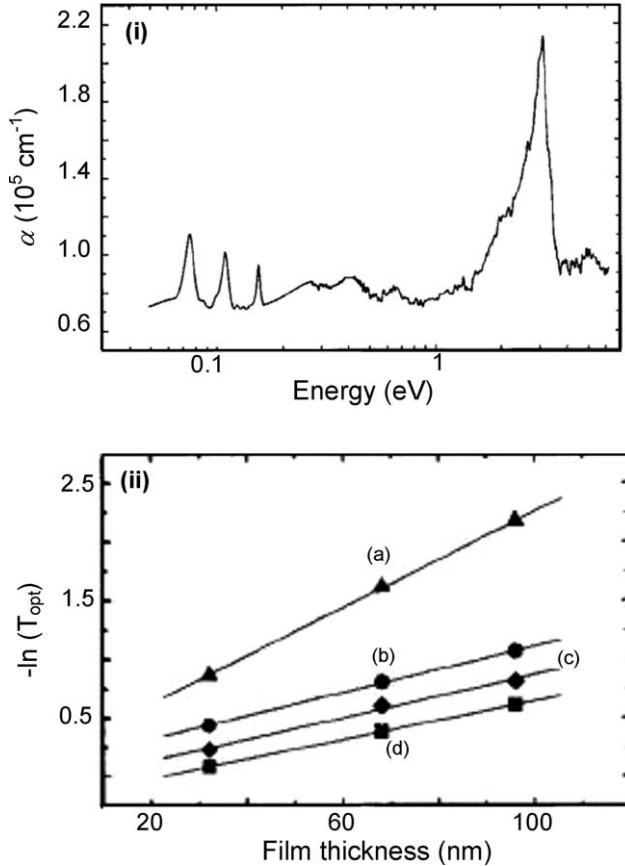


Fig. 49. (i) Absorption coefficient vs. photon energy for $\text{GdH}_{3-\delta}$ film. (ii) Logarithm of the optical transmittance vs. film thickness at $\lambda = 400 \text{ nm}$ (a), 298 nm (b) 980 nm (c) and 2000 nm (d) (Lee and Lin, 2000).

It was shown that mechanical stress measurements provide crucial information on the reversibility of the process involved in optically switchable thin coatings and possible material limitations. The stress changes of several GPa were observed in the switching of a Gd (50 nm) film capped with Pd (10 nm). Gd was observed to exhibit irreversible stress changes upon the first switching and reversible behavior upon subsequent cycles. In contrast to this, Pd (10 nm) capped Mg (150 nm) film, which was observed to exhibit stress changes of several hundreds of MPa, showed irreversible switching with hampered durability due to oxidation which was accelerated by the stress induced defect formation in the films. In the case of WO_x (100 nm) capped with Pd (10 nm) stress changes of only the order of 100 MPa were found and the films were observed to exhibit reversible switching.

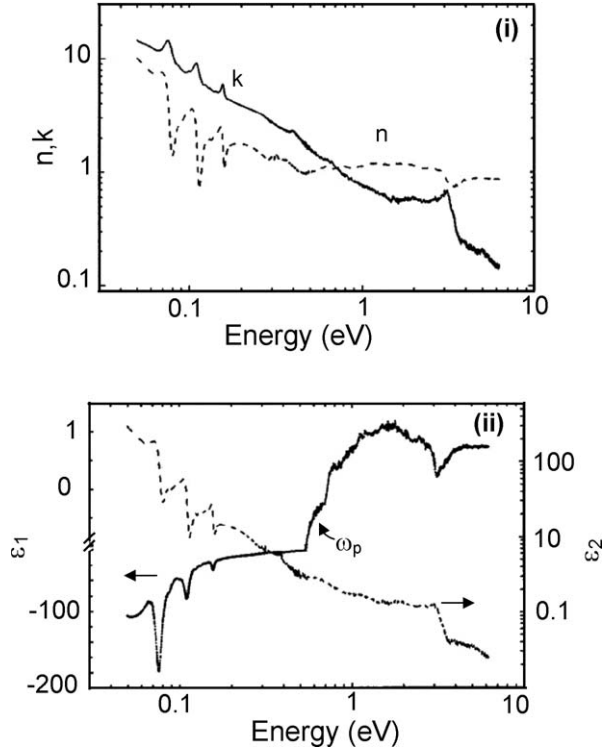


Fig. 50. (i) Refractive index (n) and extinction coefficient (k) vs. photon energy for $\text{GdH}_{3-\delta}$ film. (ii) Real (ϵ_1) and imaginary (ϵ_2) parts of dielectric function vs. photon energy (Lee and Lin, 2000).

2.1.6. Dysprosium films

Azofeifa and Clark (2000) studied the optical and electrical switching properties as a function of hydrogen concentration in the Pd (20 nm) capped Dy (250–300 nm) films. The Dy films were deposited on glass substrates using electron beam evaporation. The hydrogenation was achieved by gas phase loading and the hydrogen pressure was varied in two different ways; firstly by introducing hydrogen in small steps into the chamber, allowing for the equilibrium pressure to reach at each step, and continue till the desired saturation pressure had been attained and secondly by raising the pressure at once above threshold and monitoring the change in the electrical (four point method) and optical properties (at $\lambda = 632.8$ nm) as a function of hydrogenation time. The hydrogen concentration, $x = [\text{H}]/[\text{Dy}]$ was measured by means of calibrated quartz crystal microbalance. It was observed that the Pd capped Dy films absorb large amounts of hydrogen, achieving hydrogen concentrations close to 3, with relatively low hydrogen pressures (<5 Torr). The optical transmittance of Pd (21 nm) capped Dy film (257 nm) as a function of hydrogen exposure time was observed to exhibit a behavior similar to that observed in YH_x films, with a small local maxima corresponding to the com-

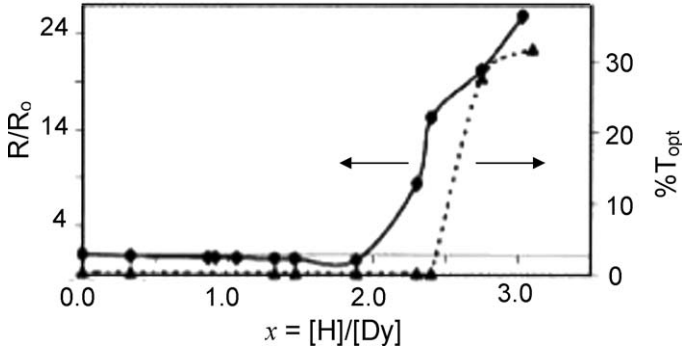


Fig. 51. Variation of electrical resistance normalized to its initial value R_0 before hydrogenation, and optical transmittance (at $\lambda = 638.2$ nm) as a function of hydrogen concentration of a Pd (19 nm) capped Dy (300 nm) (Azofeifa and Clark, 2000).

pletion of β phase, before the final maxima. For $x < 2.4$, there were no measurable changes in transmittance and the onset of large change in transmittance occurred at a concentration between 2.5 and 2.6 which were reached at hydrogen pressures between 3.2 and 3.7 Torr. The electrical resistance was observed to remain low and essentially constant till $x < 1.8$. A small minima at $x \sim 1.8$ indicated the formation of dihydride phase. No initial rise in resistance as expected for the light rare earths was observed. For $x > 1.8$, a drastic increase in the resistance with change of the order of 25 has been observed, indicating the precipitation of trihydride phase. The variation in electrical resistance normalized to its initial value and optical transmittance for Pd (19 nm) capped Dy (300 nm) film as a function of hydrogen concentration is shown in fig. 51. Azofeifa et al. measured the Hall coefficient (C_H) to get insight into the changes occurring in the band structure of Dy as a function of hydrogen intake. The C_H was observed to evolve from an electron dominated conduction with a metal-like value of $2.0 \times 10^{-10} \text{ C}^{-1} \text{ m}^{-3}$, to zero as hydrogen concentration reached a value between 1.5 and 1.8 for different samples. The value $C_H = 0$ indicates the formation of holes in a proportion such that their contribution to V_H neutralizes that of the electrons. As more hydrogen is absorbed these holes are filled and the electrons again dominate the conduction. The evolution of C_H as a function of hydrogen concentration, from the initial negative value to zero and then to large negative values (fig. 52) indicated that the band structure of Dy evolved as expected in the anionic picture of hydrogen inside the rare earths.

2.2. Epitaxial switchable mirrors: Pixel switching

Since its discovery, most of the work on switchable mirror effect has been devoted to the study of hydrogen-induced changes in optical, electronic and structural properties in polycrystalline R metal films, as summarized in the previous section. Though some studies have been reported on single-crystalline films, for example Y films on (110) W substrates (Hayoz et al., 1998) and epitaxial Y films deposited on Nb coated (110) Al_2O_3 substrates (Wildes et al., 1996; Remhof et al., 1997, 1999), these samples were not suitable for optical and elec-

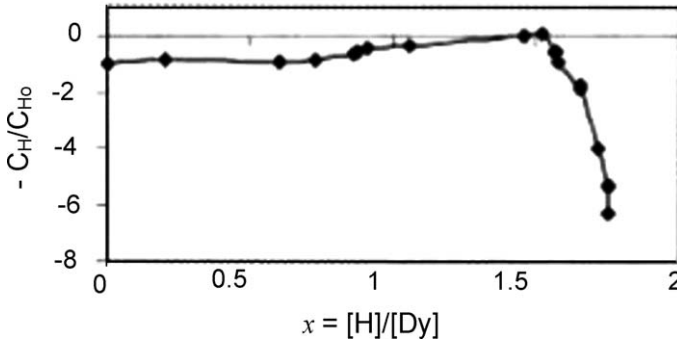


Fig. 52. Variation in Hall coefficient (normalized with respect to the initial value before hydrogenation) as a function of hydrogen concentration (Azofeifa and Clark, 2000).

trical measurements because of the metallic substrate or the presence of metallic buffer layer. Nagengast et al. (1999a) were the first to demonstrate that high quality epitaxial films suitable for studying switchable mirror properties could be deposited on transparent insulating (111)-CaF₂ substrate, without any intermediate buffer layer, by e-beam evaporation. Later Jacob et al. (2002) showed that epitaxial Y films having similar quality as those obtained on (111)-CaF₂ substrates could also be deposited on (111)-BaF₂ substrates.

As mentioned in the previous sections, remarkable hydrogen induced changes in optical and electrical properties are observed in polycrystalline R metal films. The occurrence of equally spectacular reversible effects resulting from hydrogen induced structural transitions, the so-called “Manhattan effect”, was discovered in epitaxial switchable mirrors. In contrast to the polycrystalline R metal films, which are optically homogeneous, epitaxial R films were observed to exhibit “pixel switching”. During the initial hydrogen exposure, the switchable mirror surface was observed to self organize into an ensemble of micrometer-sized domains, defined by permanent triangular ridge network (Y/CaF₂: Nagengast et al. (1999a), Kersemakers et al. (2000); Ho/ α -Al₂O₃: Grier et al. (2000); Gd/W: Pundt et al. (2000)). These individual pixels switch homogeneously at an individual rate during the subsequent hydrogen loading/deloading cycles. The large structural changes proceed domain-wise leading to a dynamic “Manhattan skyline” of expanding and contracting domains. Manhattan switching results from the complex interplay between hydrogen concentration, stress and structural changes in the switchable mirrors as summarized in the following paragraphs. It is important to note that though the structural transitions also accompany the hydrogen induced optical and electrical effects in polycrystalline films, the above mentioned microscopic optical effects are not observed because the domains are smaller than the visible light wavelength (Kersemakers et al., 2002b).

Fig. 53(i) shows a typical example of a regular triangular optical pattern that occur in epitaxial switchable mirrors for a Pd (7 nm) capped Y (400 nm) film imaged in transmitted light while it was slowly deloading from its YH_{3- δ} state (Kersemakers et al., 2000). A dense micrometer-spaced network of opaque lines, defining the domains that are observed to be ei-

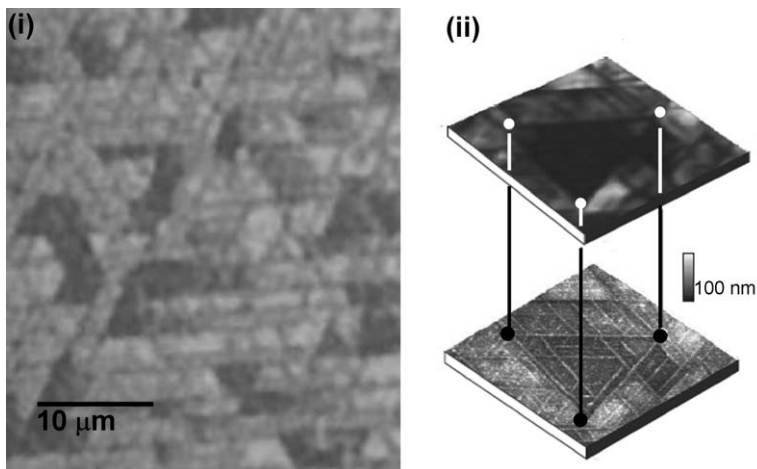


Fig. 53. (i) Optical transmittance image of Pd (7 nm) capped epitaxial YH_x film (400 nm) showing the triangular network of dark ridges, bounding domain which are either transparent $\text{YH}_{3-\delta}$ or dark YH_2 . (ii) Optical micrograph (upper image) in the transmitted light of a dihydride/trihydride mixed phase ($12.5 \times 12.5 \mu\text{m}^2$) and the corresponding AFM micrograph (lower image) of Pd (20 nm) capped Y (150 nm) film (Kerssemakers et al., 2000).

ther yellowish transparent or reddish opaque, oriented along the main hexagonal directions of the epitaxial Y film was observed. A ridge network was earlier reported in films of varying Y thickness (24–400 nm) (Nagengast et al., 1999a). A remarkable characteristic of the domain switching is a correspondence between the height of the domains and their optical transmittance. Fig. 53(ii) shows a direct comparison between the optical transmittance and topographical texture of a specific area in (20 nm) Pd capped (150 nm) YH_x film. In order to understand the one-to-one correspondence between the observed remarkable changes in structural properties resulting in changes in topographical texture with the optical and electrical properties, Kerssemakers et al. (2002a, 2002b) measured the resistivity (using four point configuration) and optical transmittance (using the built-in laser of the AFM and a photodiode at the back of the sample) while simultaneously capturing the AFM images of Pd (5 nm) capped (350 nm) epitaxial YH_x film during loading/deloading cycles. Hydrogen loading was carried out in a continuous flow of a mixture of H_2 and ambient air in the standard “fluid cell” equipped with the AFM. Deloading was performed by flowing the cell with air. Fig. 54(i) shows the optical transmittance vs. resistivity curves of the second loading/deloading cycle (Kerssemakers et al., 2002a). Some of the representative AFM images recorded at different stages marked by points (I–VI) are shown in fig. 54(ii). The optical transmittance curve is similar to that observed in polycrystalline YH_x films with strong hysteresis (Kooij et al., 2000). As the hydrogen concentration was increased the optical transmittance was observed to decrease from point (I) of the lowest possible H-concentration ($x \approx 1.9$) towards a local optical minima. Based on an earlier report (Kooij et al., 2000), this corresponds to $x = 2.1$. The AFM image (I) shows clearly the triangular ridge network. As the hydrogen concentration was increased ($x > 2.1$) the domains

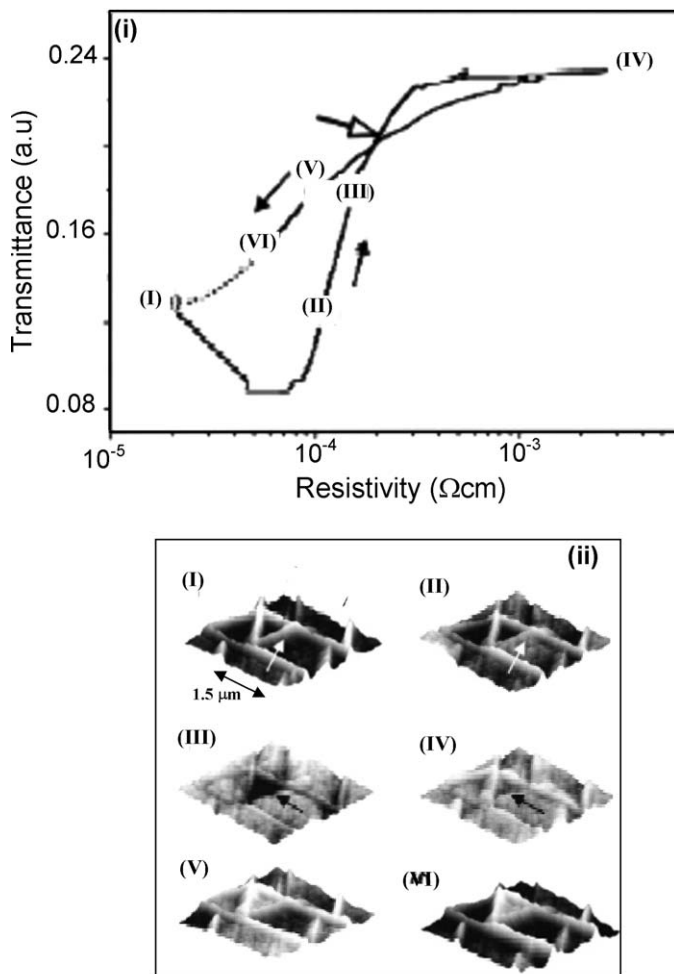


Fig. 54. (i) Optical transmittance vs. resistivity measured during second hydrogen loading and subsequent deloading of Pd (5 nm) capped epitaxial YH_x (350 nm) film. (ii) The corresponding cyclic structural changes (AFM images) measured *in situ* continuously during hydrogenation (Kerssemakers et al., 2002a).

exhibit the “Manhattan effect”. The domains start rising as is clear from the relative lowering of the ridges (II). The rising of domain indicates hydrogen induced lattice expansion occurring during the fcc (β) to hexagonal (γ) phase transition. In contrast to polycrystalline films for which fcc to hexagonal phase transition ends at the transmittance minima (Kooij et al., 2000), the epitaxial YH_x films are observed to undergo no structural transitions before the films have the minima in the optical transmittance. As the hydrogenation proceeds, except for one domain in lowered β phase (indicated by an arrow in image III), almost all the domains are fully

switched to the γ phase. This domain also switches to the γ phase in the subsequent loading (image IV). During *domain switching* (I–III) the ridge pattern remains unchanged. However, immediately after the last domains have reached the fully expanded γ phase, *ridge switching* (with the ridges protruding again) occurs within a very narrow range of overall resistivity and transmittance. During deloading, an inversion of the domain height distribution occurs with the domains, which switch relatively slow from β to γ phase, showing similar retarded kinetics in switching back from γ to β phase. In comparison to the domain switching, ridges show no sharp change during deloading. It was observed that the phase growth in the domain and the local orientation of the ridges were related. The switching was observed to be fastest on the shallow side of the ridges. The difference in the switching kinetics has been explained in terms of expansion-induced stress potential (for loading) around a ridge (linked to the asymmetric structure of a ridge). This leads to a “potential landscape” linked to the ridge pattern for each ridge, a relatively unfavorable “hard” side and a relatively favorable “soft” side for hydrogen entry (Kerssemakers et al., 2002a). In addition it has been shown (Kerssemakers et al., 2002b) that each of the domains cross three regimes during loading from YH_2 to YH_3 , (i) a single-phase regime close to stoichiometric YH_2 , with optical transmittance decreasing with increase in H concentration, (ii) a two-phase coexistence regime in which the transmittance rises with the fraction of γ phase present locally, and (iii) a single-phase γ regime in which still significant optical changes occur. For obtaining the above-mentioned correlation between the optical transmittance and the phase fraction, the latter was established from the measured hydrogen induced local relative height changes in the domain regions. The ridges were excluded as they divert in topography as well as optical properties and do not represent the undeformed material. Fig. 55 shows a scatter plot of transmittance versus relative height obtained by comparing a large number of points on the domain surfaces both in optical and in the AFM micrographs, all taken in the same hydrogenation state of the YH_x film. The range of heights, expressed in % of the film thickness covers the 10% expansion difference between the full β and the full γ phases; indicating that the left most points represent points on the surface which are fully β phase and the right most points correspond to the fully hexagonal γ phase. Fig. 55 clearly shows that a wide range of transmittance values exist for the γ phase indicating that $\sim 50\%$ of the optical switching takes place at an essentially constant height i.e., a single phase. To correlate the structural and optical dynamics, Kerssemakers et al. (2002b) converted the image series into height and transmittance histograms, respectively. Fig. 56(i) shows two typical height histograms: one from the surface of film in dihydride phase (peak I) and the other (peak II) from the same area but taken at the end of the two-phase coexistence regime, with the narrow peaks correspond to the domains whereas the tails correspond to the ridges. The changes in the topographical and transmittance histograms during hydrogen loading are indicated in fig. 56(ii) and (iii), respectively. A number of interesting implications were observed to arise from a comparison of these plots: (i) The onset of structural coexistence region was observed to coincide with the minimum in the optical transmittance (dashed line A), indicating that the darkening of the films occurs in a single phase regime, in contradiction to the observations by Kooij et al. (2000), (ii) The maximum spread in the film transmittance was observed near the end of the two-phase co-existence region, indicating a large spread in both the pixel kinetics and hexagonal γ -phase transmittance.

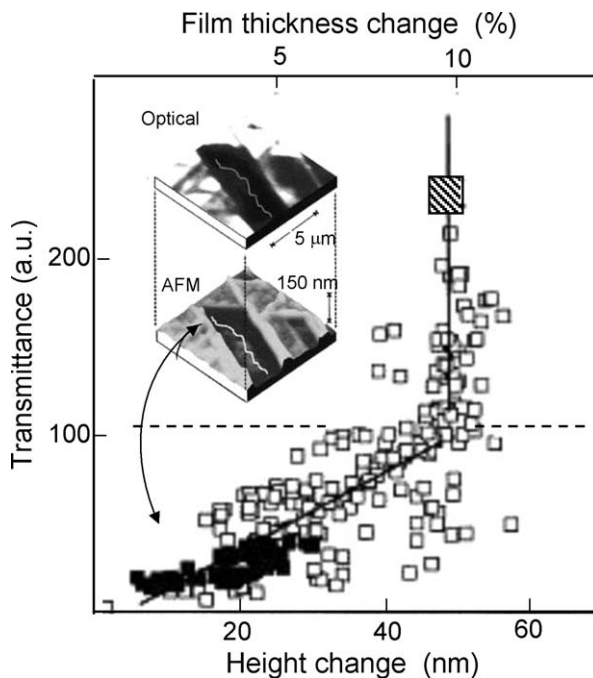


Fig. 55. Optical transmittance versus local height change of Pd (3 nm) capped epitaxial YH_x (500 nm) film at a hydrogen concentration of $x \sim 2.5$ during slow unloading. The small open and solid squares represent local points on the film surface (excluding the ridges), all taken in the same hydrogenation state of the YH_x film. The correlation between the structural and optical switching is shown in the inset. The maximum optical transmittance of the mirror at 1 bar of the H_2 pressure is indicated by the large shaded square (Kerssemakers et al., 2002b).

Nagengast et al. (1999a) and Kerssemakers et al. (2000) interpreted the ridge formation in terms of the in-plane thermal expansion differences between the film and the substrate and the in-plane expansion of the Y lattice during the H adsorption – a fact confirmed by detailed X-ray diffraction (Nagengast et al., 1999a; Kerssemakers et al., 2002a, 2002b), Rutherford backscattering (RBS) (Kerssemakers et al. 2002a, 2002b), and high resolution transmittance electron microscopy (HRTEM) (Kooi et al., 2002) measurements. Borgschulte et al. (2003) using reflection high-energy electron diffraction (RHEED) and Auger electron spectroscopy (AES) measurements on the other hand showed that a strong interdiffusion between the film and the substrate occurs leading to the compressive in-plane strain which are relaxed via misfit glides during the film growth resulting in the formation of the ridge network.

Nagengast et al. (1999a) showed using X-ray diffraction analysis that irrespective of the large lattice expansion which occurs on hydrogenation, the structural coherence in all the spatial directions as well as the epitaxial relation to the substrate was preserved in these films – a finding consistent with the observations of Hayoz et al. (1998) and Remhof et al. (1997, 1999). Fig. 57(i) shows the development of Y (002) reflection upon hydrogen loading. The FWHM

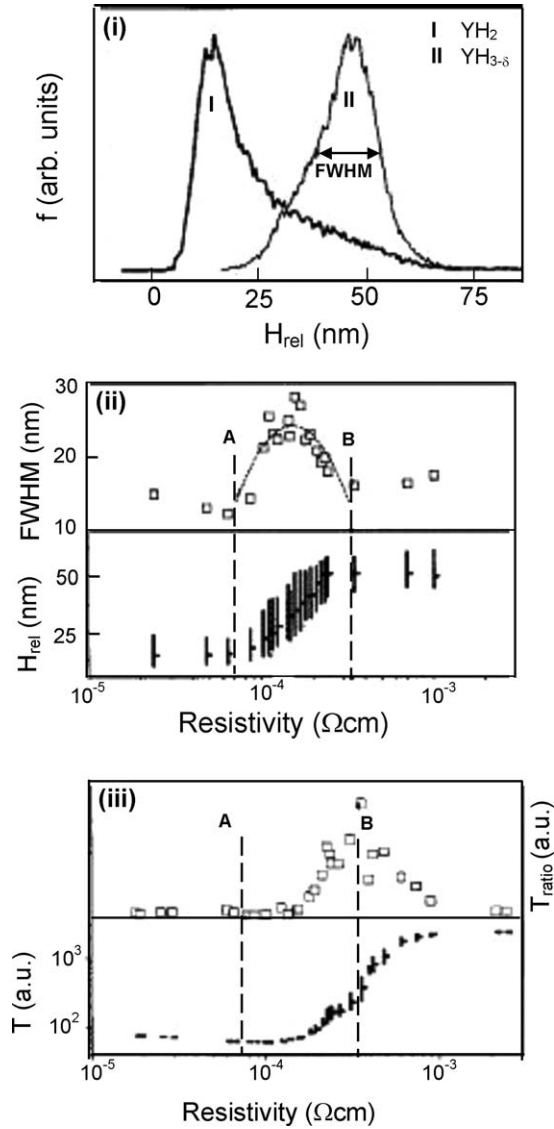


Fig. 56. A comparison of local and average measurements during hydrogen loading. (i) Height histogram. Changes in the (ii) topographical and (iii) transmittance histograms. The peak values and FWHM values of both the topography (A in ii) and transmittance (A in iii) are used to compare the local dynamic behavior in terms of phase coexistence (B in ii) and optical transmittance (B in iii) (Kerssemakers et al., 2002b).

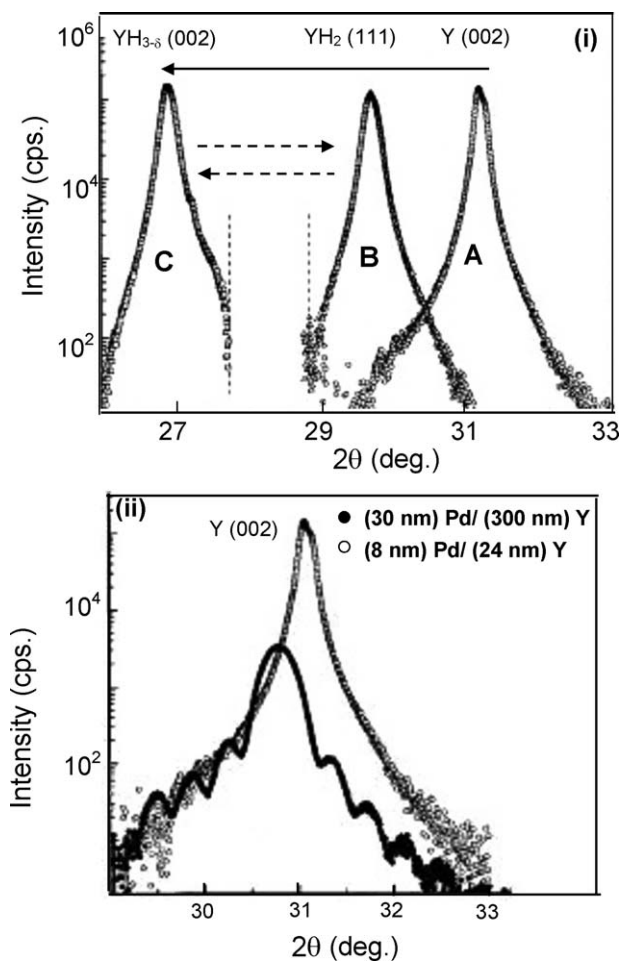


Fig. 57. (i) Development of (002) reflection of Pd (30 nm) capped epitaxial Y (300 nm) film upon hydrogen loading: as-deposited (A), after loading with 1 bar H_2 (B) and after unloading at $100^\circ C$ in air. (ii) Y (002) reflection for switchable mirrors having different thickness of Pd and Y (Nagengast et al., 1999a).

width (0.06°) and the shape of the Bragg reflections [Y (002) in the as deposited state, $YH_{3-\delta}$ (002) in the loaded state and YH_2 (111) in the deloaded state] remains same revealing that the hydrogenation process does not affect the out-of-plane coherence of the film. Apart from the substrate and the Pd over layer, only the (00 l) Bragg reflections are observed in the X-ray diffractograms of these films [as shown in fig. 57(ii)] revealing that the films are oriented with the c -axis of the hexagonal unit cell perpendicular to the substrate. With thick films, a sharp peak was observed where as for thin films (≤ 80 nm) finite size oscillations are observed. In addition the c -axis lattice constant appeared to be significantly larger in thin Y films as compared

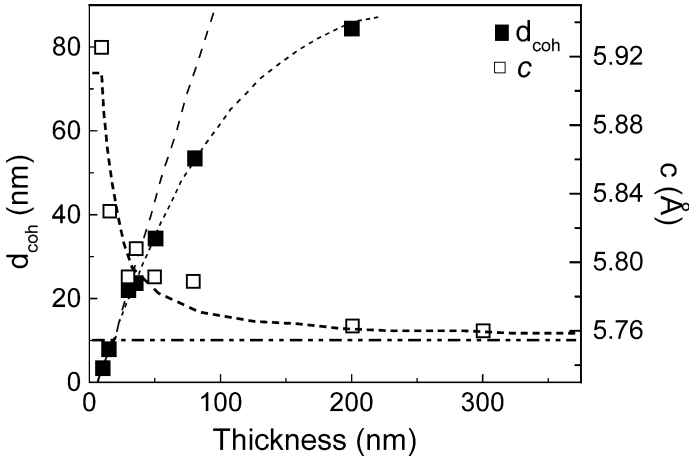


Fig. 58. Variation of coherence length (d_{coh}) and out-of-plane lattice parameter (c) as a function of film thickness. The dotted lines are guide to eye and the dash line has a slope of 1. The dash-dotted line represents the bulk c value for a film with an initial hydrogen concentration of $x \sim 0.08$ H/Y (Kooij et al., 2002).

to thick films indicating an out-of plane strain of 1.22%. As the hydrogen incorporation during deposition cannot cause such a large lattice expansion, the clamping of the substrate was understood to be the possible reason for the effect. The absence of any sign of tensile stresses in spite of the large lattice mismatch (5.4%) between the YH_x basal plane and the (111)- CaF_2 plane clearly indicates that the film relaxes in the first stage of the growth and the epitaxial nature was maintained during hydrogenation [fig. 57(ii)]. Similar results have been established by Kooij et al. (2002) by utilizing Rutherford backscattering (RBS) ion channel measurements and X-ray diffraction analysis of the as-deposited and hydrogenated Pd (7–30 nm) capped epitaxial Y (10–400 nm) films deposited on (111)- CaF_2 . Out-of-plane measurements were carried out along the growth direction by using the high angle X-ray scattering whereas the glancing incidence X-ray diffraction has been utilized for in-plane measurements. Scans were carried out in two different directions of reciprocal space viz., rocking or the transverse (θ) scans by rotating the scattering vector through a Bragg point and the radial or the longitudinal ($\theta-2\theta$) scans. The out-of-plane X-ray diffraction measurements (in the $\theta-2\theta$ geometry with the scattering vector perpendicular to the substrate) showed similar results as obtained by Nagengast et al. (1999a) with finite size oscillation for thin films (≤ 80 nm) and a sharp peak for thick films. Fitting the finite size oscillations to the Laue equation, the number of coherent layers N_{coh} (described by a Gaussian distribution) and the out-of-plane coherence length d_{coh} [which is product of the number of layers (N_{coh}) and the interlayer distance ($d_{\perp} = c/2$)] were obtained. The variation of coherence length and out-of-plane lattice parameter c as a function of film thickness is shown in fig. 58. The linear relation between the coherence length and the layer thickness deviates with increasing thickness. In addition a remarkably strong increase of the c -axis lattice parameter of the as-deposited yttrium with decrease in the film thickness was observed. This out of plane lattice expansion was observed to be much larger

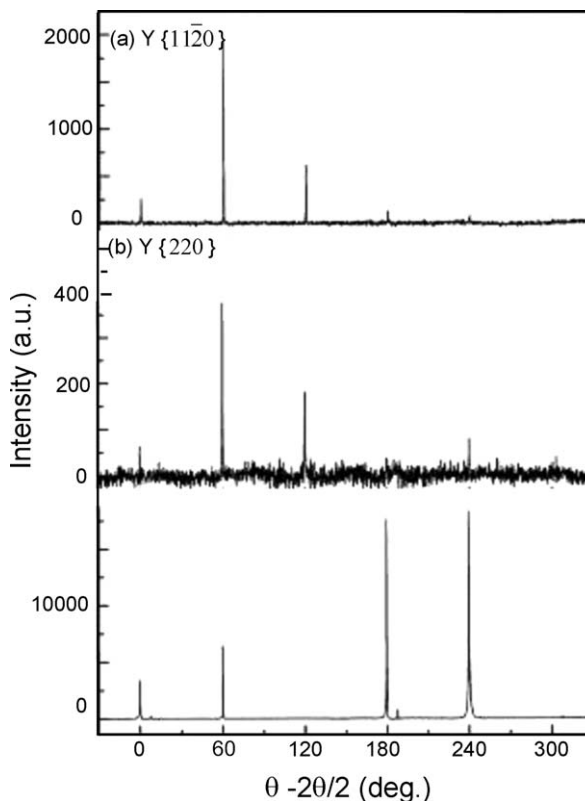


Fig. 59. 360° in-plane rocking scans of the (a) Y {11 $\bar{2}$ 0}, (b) YH₂ {220} and (c) CaF₂ {220} reflections from Pd (15 nm) capped (300 nm) Y film before and after hydrogen loading. The 2θ angles for the three scans were fixed at 50.10, 49.67 and 47.06°, respectively (Kooij et al., 2002).

than the maximum value expected from an increase in hydrogen concentration (5.803 Å) and was thus ascribed to the difference in thermal expansion coefficient of the Y ($6.0 \times 10^{-6} \text{ K}^{-1}$ (Lide, 1996) and CaF₂ ($17.8 \times 10^{-6} \text{ K}^{-1}$ (Lide, 1996)) (substrate shrinks more than the film leading to the in-plane compression of the Y lattice during cooling down to room temperature after deposition at 700 °C). This indicates that for films thicker than 100 nm the stress related to the film/substrate interaction was completely relaxed. In this region, the coherence length was of the same order as the film thickness. Glancing angle diffraction with the scattering angle parallel to the substrate was used to obtain information on the in-plane crystal structure and to study the epitaxial relation between the film and the substrate. A small in-plane lattice expansion was observed as indicated by the shift of the YH₂ (220) peak to smaller angles with respect to Y (11 $\bar{2}$ 0) reflection and 0.22% compression in the lattice parameter in the YH₂ phase. Fig. 59 shows the 360° rocking scans of the Y {11 $\bar{2}$ 0}, YH₂ {220} and CaF₂ {220} reflections from a Pd (15 nm) capped Y (300 nm) film before and after hydrogenation.

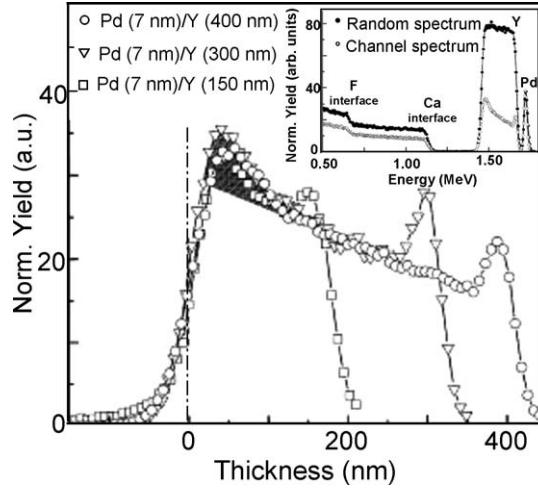


Fig. 60. Yttrium channel spectra of Pd (7 nm) capped epitaxial Y films of different thicknesses, along Y [0002] direction for 2 MeV $^4\text{He}^+$ ions as function of distance from the film/substrate interface. The shaded region indicates the extra upturn of the signal, related to the mismatch-induced strain at the film/substrate interface. The inset shows the full Rutherford backscattering spectra for Y film of thickness 400 nm deposited $\text{CaF}_2(111)$ substrate (Kooij et al., 2002).

The exactly equal 60° spacing of the peaks reflect the perfect six-fold symmetry in the plane parallel to the substrate. The good crystalline quality of the films was also indicated by the low channeling yield in the RBS spectra (fig. 60) where as the unique epitaxial relation between the film and the substrate was clearly revealed by the alignment of the axial as well as planar channeling scans (fig. 61). The yttrium yield from films of various thickness as a function of distance from the film-substrate interface is shown in fig. 60. All the spectra show a surface peak at a distance corresponding to the film thickness followed by an upturn due to increased dechanneling with increasing depth in the film. Near the interface an extra upturn was observed to be present in all the spectra over a distance of ~ 100 nm from the interface. This extra displacement of the yttrium atoms from the [0002] axis indicated that there was an interface layer with considerable lattice mismatch, independent of film thickness. The rocking curves (from axial channel dip measurements) for various yields performed by scanning the tilt angle θ from -3.5° to $+3.5^\circ$ with respect to the Y [0002] and the $\text{CaF}_2 \langle 111 \rangle$ directions with a 0.1° step increment shown in fig. 61(i), clearly show that various channel dips do not shift revealing the good alignment between the film and the substrate. The backscattering intensity from Pd (7 nm) capped Y (400 nm) film and from the substrate as a function of the spin angle over a 180° rotation around the Y [0002] direction is shown in fig. 61(ii). The six-fold symmetry due to the $\text{CaF}_2 \{220\}$ planes in the (111) plane was clearly exhibited by the 60° spacing of the corresponding channel minima. The yttrium signal exhibits a 12-fold symmetry as a result of the six-fold symmetry of both the $\{11\bar{2}0\}$ and the $\{10\bar{1}0\}$ planes in the (0002) plane, rotated 30° with respect to each other. The planar channeling measurement

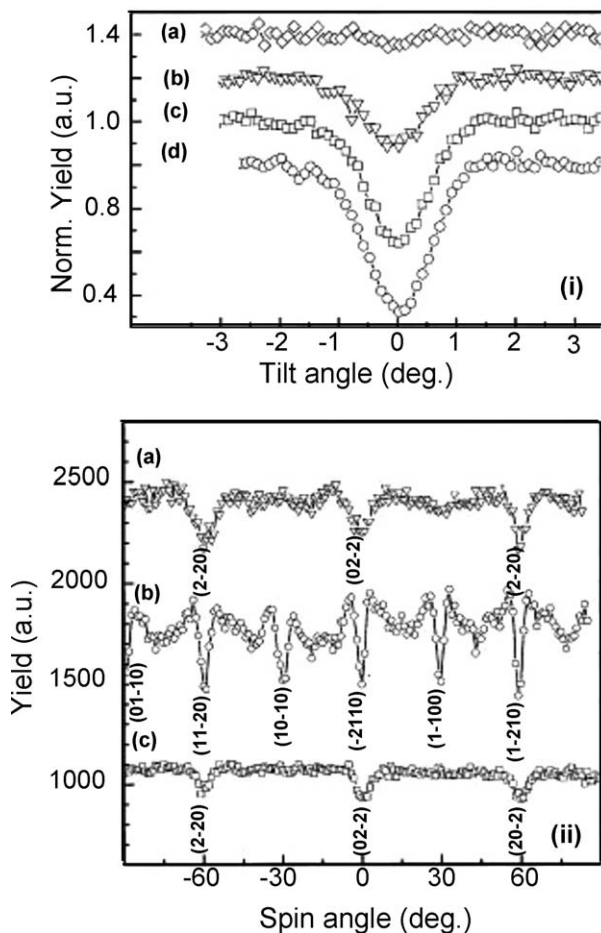


Fig. 61. (i) Angular yield profile along the Y [0002] axis of the Y yield from the regions (a) near the surface (1.56–1.67 MeV) and (b) near the film/substrate interface (1.47–1.56 MeV), (c) of the Ca yield from the CaF₂ substrate (0.70–1.10 MeV) and (d) of the Pd yield from the cap layer (1.68–1.76 MeV) as a function of tilt angle. (ii) Angular dependence of the (a) Ca backscattering, (b) the near surface Y yield from as-deposited film, and (c) Y yield from the hydrogenated film as a function of samples rotation angle (Kooij et al., 2002).

on an fcc-YH₂ film, which has been loaded and deloaded several times, is also presented in fig. 61(ii). The 60° spacing between the channel dips was a result of the six fold symmetry of the YH₂ {220} planes in the (111) plane, similar to the signal of the fcc-CaF₂.

From the fact that the steep facet ridges make an average angle of $5.8^\circ \pm 0.2^\circ$, Kerssemakers et al. (2000) concluded that the ridge pattern occurs due to the $(10\bar{1}\bar{2})$ twinning. Kooi et al. (2002) gave detailed explanation of the mechanism of phase transformations using HRTEM as an investigation tool. It was shown that prior to α -Y to β -YH₂ transformation, a triangular

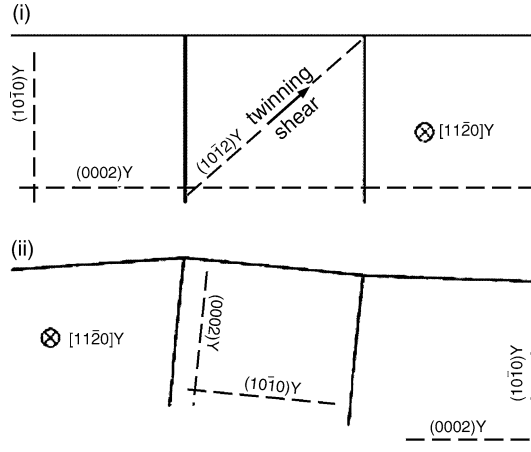


Fig. 62. Schematic representation of $(10\bar{1}2)$ twinning in Y where (i) the boundaries between the twins and the domains are initially parallel to the $(10\bar{1}0)$ and (ii) the Y during twinning is rotated 5.6° (Kooi et al., 2002).

network develops due to $(10\bar{1}2)$ twinning that occurs in α -Y in order to relax the compressive strain buildup due to H intake. The compressive stresses in the as-deposited Y films on CaF_2 arise due to the difference in their thermal expansion coefficient. During twinning the basal plane (0002) that was originally parallel to the film/substrate interface rotates by 5.6° and transforms into a prismatic plane $(10\bar{1}0)$ that has 10.3% larger d spacing. Similarly the vertical prismatic plane was replaced by the basal plane corresponding to an in plane contraction of 9.4% giving an overall crystal reorientation for the ridge of 95.6° (fig. 62). The evidence that the ridges are a result of the $(10\bar{1}2)$ twinning was clear from the 95° rotation of the orientation of the Y ridges (compared to the domains) around the common $(10\bar{1}2)$ twinning axis that was parallel to the length of the ridges as observed by SAED pattern shown in fig. 63. The transformations between the hexagonal (α and γ) and fcc (β) phases proceed by the glide of Shockley partial dislocations on each second basal plane. To prevent macroscopic shape changes in the domains, a larger number of horizontal $\Sigma 3\{111\}$ twin boundaries develop within the YH_2 . Fig. 64 shows the cross-sectional HRTEM image showing the $\Sigma 3\{111\}$ twin boundaries in hydrogen loaded (500 nm) Y film epitaxially grown on a (5 nm) Nb coated α - Al_2O_3 ($11\bar{2}0$) substrate. It was observed that the films consist of thin (~ 15 – 40 nm) horizontal lamellae of (111) fcc planes separated by planar defects running parallel to the substrate both before and after cycling to YH_3 , suggesting that the reversible β - γ transformations develop in a planar fashion possibly by incorporating Shockley-type partial dislocations. The large number of Shockley partial dislocations present at the boundaries between the two variants in the domains greatly facilitates the reversible β - γ transformation and their presence avoids the need for nucleating these partials. After the initial α - β transformation, nearly vertical twin boundaries arise in the ridges. During phase transformations, considerable anisotropic lattice expansions occur due to the hydrogen intake. The dominant expansion occurs along the c axes of the hexagonal α -Y and γ - $\text{YH}_{3-\delta}$ phases and during the β - γ transformations, both

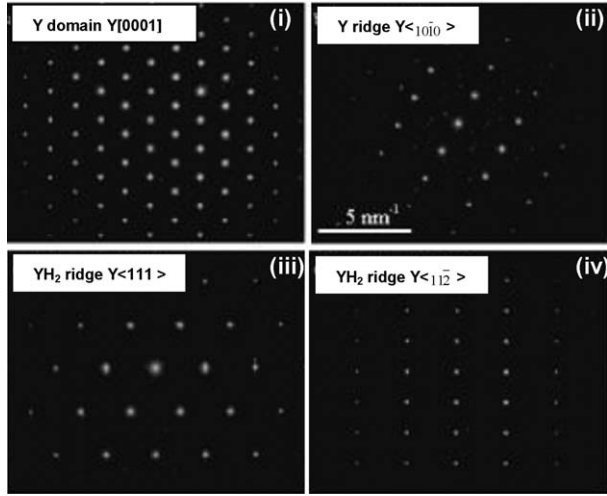


Fig. 63. SAED pattern for the (i) Y domains, (ii) Y ridges, (iii) YH₂ domains and (iv) YH₂ ridges (Kooi et al., 2002).

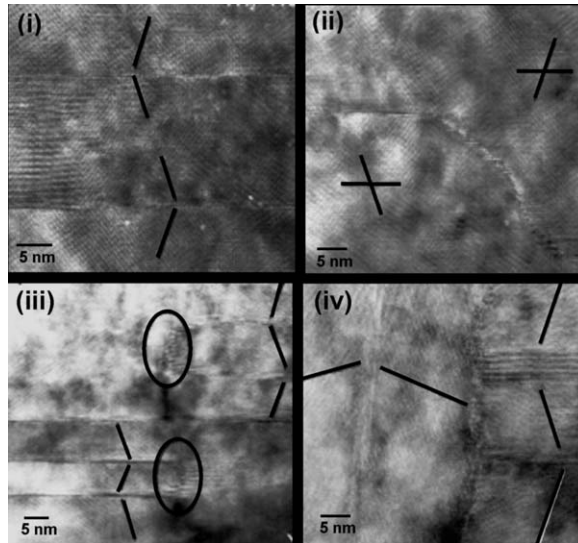


Fig. 64. Cross-sectional HRTEM images showing (i) overlap of two twinning variants, (ii) superledge present on the twinning boundary with a height parallel to the substrate/film interface normal, (iii) abruptly ending twin lamella bounded by $\Sigma 3\{111\}$ boundaries and (iv) vertical $\Sigma 3\{111\}$ twin boundaries in a YH₂ domain containing horizontal $\Sigma 3\{111\}$ twin boundaries (Kooi et al., 2002).

the domains and the ridges choose to keep this c axis as perpendicular as possible to the free surface. A delayed β - γ transformation was observed in the ridges as compared to domains, a feature also observed by Kerssemakers et al. (2002a, 2002b). This was explained in terms of the in-plane expansion of the ridges hampering their transformation. The domains on the other hand were observed to expand 10.6% perpendicular to the surface. The vertical twin boundaries in the ridges were observed to act as hinges allowing for the largest differences in the expansion between the ridges and domains to be absorbed.

The extra channeling near the interface observed in the yttrium yield in the RBS spectra (fig. 60) may also result from small amounts of fluorine from the CaF_2 substrate, diffusing into the film during deposition at 700°C . However the absence of significant bulk fluorine contribution in the RBS spectra rules out this possibility. Hayoz et al. (2001) on the other hand observed large amounts of fluorine (20%) contaminants on the surface of the films using X-ray photoelectron spectroscopy, X-ray photoelectron diffraction, and low energy electron diffraction measurements. High-quality epitaxial hcp (0001) oriented films were observed for Y deposition at 700°C . However these films were observed to be rich in F on the surface. On the other hand when the deposition temperature was chosen so low that the LEED reflexes were very broad, no F contamination was detected indicating strongly the role of F as a surfactant. Fig. 65 shows the F 1s and Y 3d XPS spectra for different Y films (the preparation conditions are mentioned in table 2). The intense F 1s peak in the near surface region reveals surface F contamination [fig. 65(I)]. Upon lowering the substrate temperature, very little changes are visible in the XPS spectra [fig. 65(II)]. However deposition at room temperature and followed by contamination with oxygen, reduces the F on the surface [fig. 65(III)] and results in poorly ordered surface as indicated by diffused LEED reflexes [table 2]. Annealing these films to high 700°C restores the highly ordered surface but the F contamination was also restored. At room temperature under a H_2 partial pressure of 5×10^{-6} mbar, the formation of F-free transparent $\text{YH}_{2.3}$ films of a red/yellow color and poor crystallinity were observed [fig. 65(IV)]. Using a model based on line shape and peak position analysis of the Y 3d core level it has been shown that the hydrogen concentration in these samples was $x = 2.3$. This was in contrast to the single crystalline dihydride films ($x = 1.99$) grown under the same H_2 partial pressure on W (110) (Hayoz et al., 1998). The large hydrogen concentration in the former case as compared to the latter has been attributed to the large c -axis lattice expansion and the possibility of catalytic activity of the F atoms towards H_2 dissociation. Upon deloading at 600°C , the films were observed to lose their transparency and get converted from the poorly ordered fcc (111) lattice to a well-ordered hcp (0001) lattice with restored F contamination [fig. 65(V)]. The evidence of preferential location of F at the surface emerges from the line shape and peak position analysis of the F 1s singlet and Y 3d doublet. The line width and line shape of the F 1s XPS spectrum was broad (FWHM ~ 3.4 eV) and slightly asymmetric in case of films I, II, and III whereas for films IV and V, the line width was reduced (FWHM ~ 3.0 eV) and the line shape was almost symmetric. In addition the F 1s peak shift to higher energy in films IV and V as compared to I, II, and III, indicating that the F 1s spectrum was composed of two peaks (labeled A and B). The F 1s B component was attributed to F atoms floating at the surface (also confirmed by the XPD analysis) while the A component

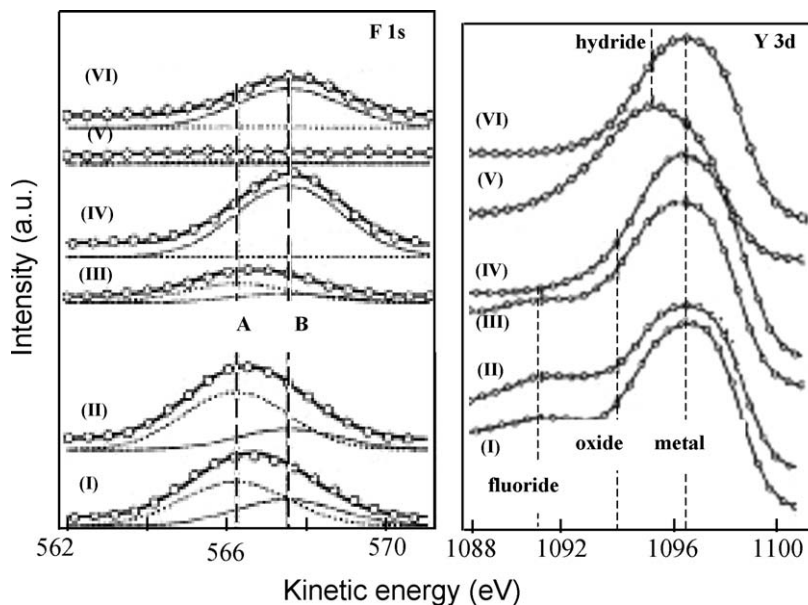


Fig. 65. XPS spectra showing F 1s singlet and Y 3d doublet for the different Y films (table 2 gives the preparation conditions). For F 1s the solid lines are the best fits to the data using two Gaussian functions (A and B). For Y 3d the solid lines are just a guide for the eye. The dotted lines indicate the peak positions of the 3d doublet for Y in different chemical environments (Hayoz et al., 2001).

Table 2

Summary of preparation procedure and respective results of LEED, XPD and XPS line shape and peak position analysis given in fig. 65 (Hayoz et al., 2001)

Film	Preparation	XPD	LEED quality	F in Y 3d emission	F 1s intensity relative to Y 3d			
					A + B	A	B	O 1s
I	55 nm, 700 °C	hcp (0001)	sharp	Yes	14.3	9.0	5.3	0.0
II	+25 nm, 350 °C	hcp (0001)	broad	Yes	13.2	9.8	3.5	0.6
III	+20 nm, RT	hcp (0001)	diffuse	?	5.7	3.9	1.8	1.7
IV	annealed 700 °C	hcp (0001)	very sharp	No	13.0	0.0	13.0	0.2
V	50 nm, RT, under 5×10^{-6} mbar H ₂	fcc (111)	no spot	No	0.0	0.0	0.0	0.0
VI	annealed 600 °C	hcp (0001)	very sharp	No	8.5	0.0	8.5	0.9

was caused by F atoms below the surface (with the peak position coinciding with that of F 1s in YF₃).

By means of *in situ* RHEED and AES, Borgschulte et al. (2003) explained the ridge formation in terms of the strain relaxation that results from the chemical interaction of Y and F at the initial stages of growth. Fig. 66 shows the RHEED pattern of the initial stages of the growth

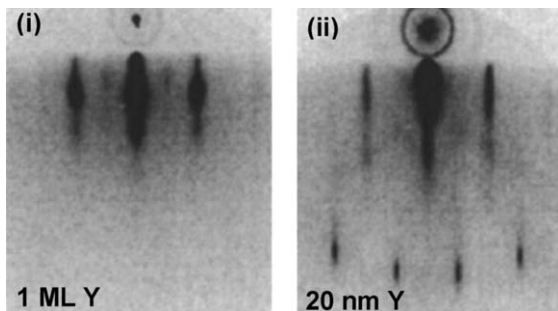


Fig. 66. RHEED patterns revealing a smooth Volmer–Weber growth for Y [(i) 1 ML Y and (ii) 20 nm Y] on CaF₂(111) (Borgschulte et al., 2003).

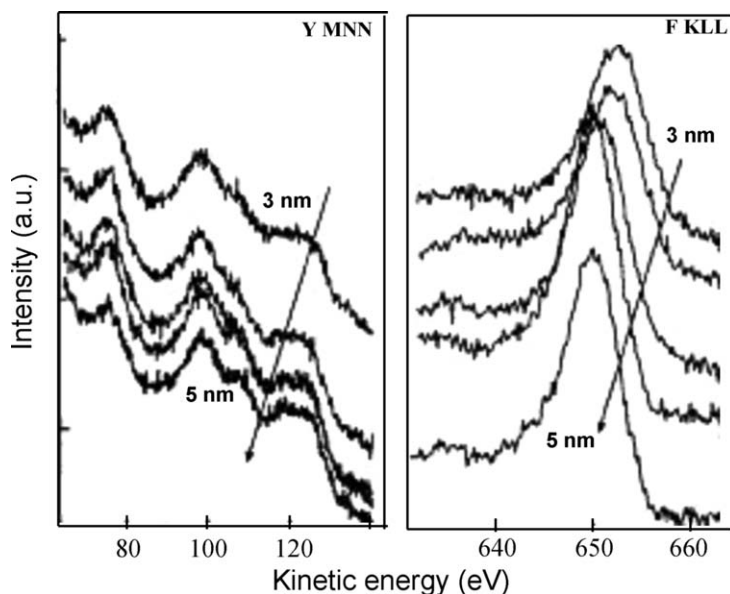


Fig. 67. Auger electron spectra of Y MNN and F KLL lines on a wedge sample of Y on CaF₂ for various Y thickness (from 3 nm to 5 nm) (Borgschulte et al., 2003).

revealing the Volmer–Weber growth mode. The spacing of the streaks in RHEED pattern was inversely proportional to the in-plane lattice constant of the films. The in-plane lattice parameter during growth derived from the RHEED patterns showed 2.4% compressive strain in the epitaxial Y films as compared to the bulk. The large compressive strain has been explained in terms of the reaction of fluorine atoms with the yttrium atoms at the interface as confirmed from the AES measurements. Fig. 67 shows the variation in the intensity of Y MNN and F

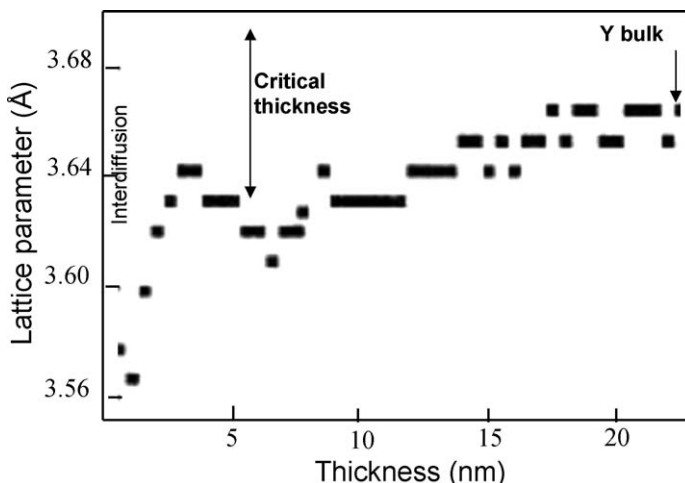


Fig. 68. Changes in the in-plane lattice parameter as a function of film thickness during the epitaxial growth (Borgschulte et al., 2003).

KLL Auger lines as a function of film thickness (3–5 nm). A shift in the peak position and a change in FWHM of the F KLL in addition to splitting of the Y MNN lines indicate the change in oxidation state of the Y atoms with increase in film thickness. Fig. 68 shows the evolution of the lattice parameter as a function of film thickness during the epitaxial growth. The large reduction in the lattice parameter in the first Y monolayer compared to the bulk was explained in terms of the electron transfer from the Y to neighboring F atoms (charged Y ions being smaller than the neutral Y atoms). Successive Y layers were less F-influenced, leading to an increase of the lattice parameter.

In summary, the epitaxial R films exhibit pixel switching. During the initial hydrogen exposure, the film self-organizes itself into an ensemble of pixels, each pixel being a micrometer sized domain surrounded by a permanent triangular ridge network. The pixels switch homogeneously at an individual rate, accompanied by large structural changes during subsequent hydrogen loading and deloading cycles. This causes a dynamic “Manhattan skyline” of expanding and contracting domains. A correlation between the height of the domain and their optical transmittance has been reported. The ridge pattern remains unchanged during the domain switching but changes slightly after the last domain switches completely into the γ phase. Various experimental studies have indicated that a complex interplay between hydrogen concentration, stress and structural changes may be responsible for the “Manhattan effect”.

2.3. Effect of Pd over layer thickness

As discussed in section 1, in a number of studies the hydrogen induced switching properties have been studied in terms of the Pd over layer thickness. Among the various studies reported (Huiberts et al., 1996b; Kremers et al., 1998; van der Molen et al., 1999; van Gogh et al., 2000a; Mor et al., 2001; Mor and Malhotra, 2003; Borgschulte et al., 2004; Kumar et al.,

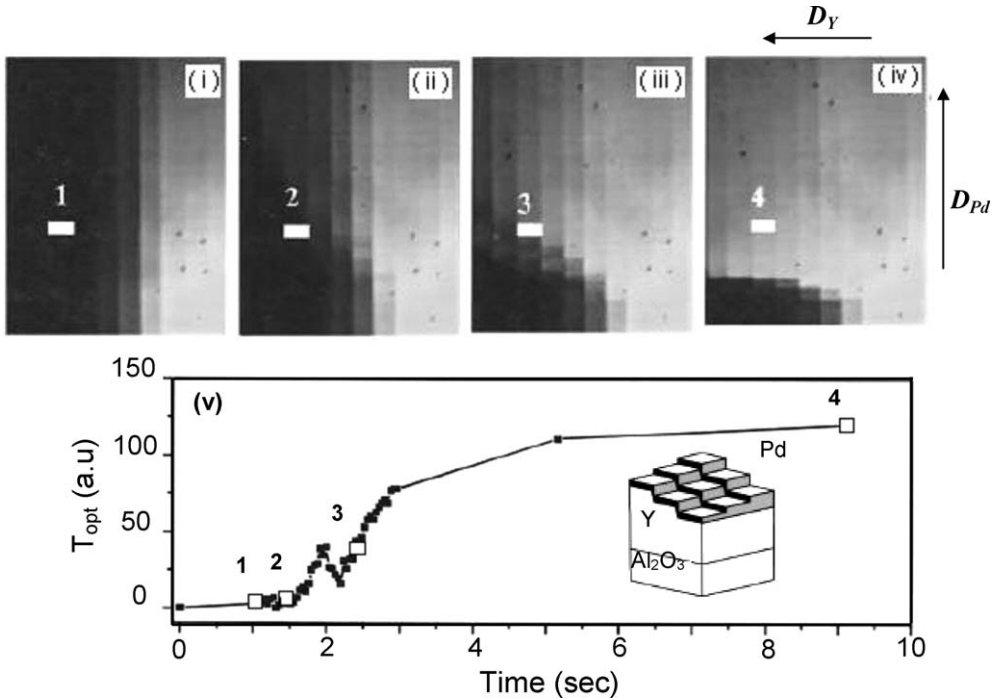


Fig. 69. Optical transmittance images of Pd/Y matrix sample [schematic representation shown in inset of (v)] at (i) 1, (ii) 1.5, (iii) 2.5, and (iv) 9.2 s after exposure to 1 bar of H_2 . In the area depicted D_Y and D_{Pd} increases stepwise from 0 to 150 nm and 1 to 25 nm, respectively. (v) Optical transmittance vs. time curve for a typical plaquette (marked white, with $D_{Pd} = 10$ nm, $D_Y = 100$ nm). The points marked 1–4 are taken from (i)–(iv), respectively (van der Molen et al., 1999).

2002; Kumar and Malhotra, 2004a, 2004b); van der Molen et al. (1999), studied the effect of Pd and the underlying Y film thickness on the switching kinetics using maximum number of combinations of Pd and Y thickness deposited on the same sample. This was achieved by using a matrix like sample. The matrix of yttrium and palladium on sapphire substrate were deposited by using mutually perpendicular mask directions for Pd and Y deposition with shadow of the mask edge creating a step width between two plaquettes of typically 20 μm . The hydrogen loading behavior per plaquette was monitored by exposing the whole sample to 1 bar of hydrogen gas in an optical microscope and capturing the images sequentially. The transmitted intensity of the individual plaquette (0.2×0.1 mm²) was observed to be a function of the thickness of Pd (D_{Pd}) and Y (D_Y) and of the hydrogen concentration x . Following a single image pixel within the plaquette as a function of time, the variation in optical transmittance of each plaquette was obtained. One such curve for a plaquette with $D_Y = 100$ nm and $D_{Pd} = 10$ nm clearly showing the characteristic behavior of the hydrogenation curve is shown in fig. 69. Extending this procedure to all the plaquettes on the matrix, the time evolution of

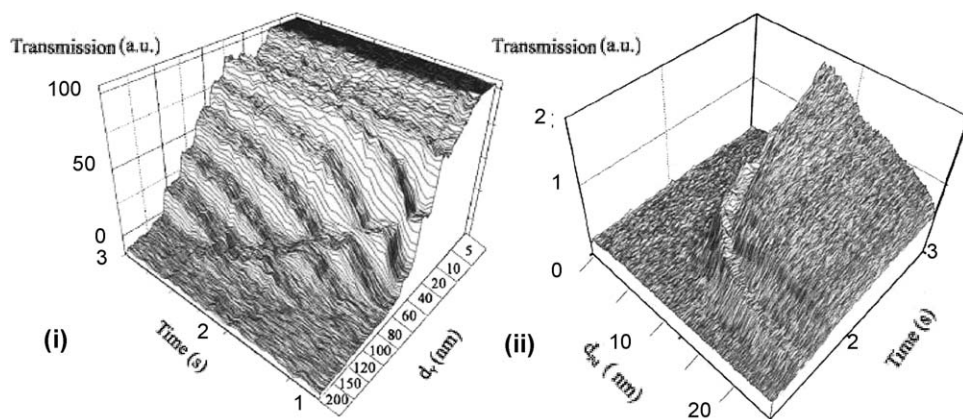


Fig. 70. (i) Optical transmittance curves taken along (i) Y stair at constant Pd thickness (10 nm) [corresponding to the horizontal strip crossing the marked plaquette in fig. 69(i)–(iv)] and (ii) Pd stair at constant Y thickness (80 nm) [corresponding to a vertical strip in fig. 69(i)–(iv)], during hydrogen loading of Pd/Y matrix sample in 1 bar H_2 at RT (van der Molen et al., 1999).

the rows and column of the plaquettes was followed simultaneously. A line scan taken across the Y stair at a constant Pd thickness (10 nm) was observed to result in parallel series of loading curves (25 loading curves corresponding to the 25 pixels per plaquette), one for each pixel of the set of images recorded during hydrogenation [fig. 70(i)]. Following similar procedure for a column of plaquettes along Pd stair at constant Y (80 nm) thickness, a continuous surface was observed [fig. 70(ii)]. Using all the possible Y and Pd thickness combinations, van der Molen et al. found interesting and complicated dependence of switching time τ_s (defined as the time needed to reach the largest slope dT_{opt}/dt in the transmittance versus time curve) on the Pd and Y thickness. As shown in fig. 71, the switching behavior was divided into three regions (A, B and C) separated by characteristic Pd thickness D_1 and D_2 . In the region with $D_{Pd} < D_1$ (region A), no switching was observed. The critical Pd thickness (D_1) needed for a functional device was observed to be independent of D_Y and the storage time in air and was observed to depend on the substrate temperature. The impossibility to load below D_1 was related to the H_2 dissociation problem at the inactive surface layer, resulting mainly due to the Pd–Y interfacial alloy, consuming all Pd within the UHV followed by surface oxidation in air. Van der Molen et al. found that values of D_1 found from switching curves were consistent with $D_{overlap}$, the penetration depth of Pd in Y, $D_{overlap}$ (estimated from the extra overlap in the Y and Pd RBS peaks). From switching curves, $D_1 (T_{sub} = RT) = 4$ nm, $D_1 (T_{sub} = 330^\circ C) \approx 27$ nm, and $D_1 (T_{sub} = 550^\circ C) > 30$ nm were observed. Whereas from RBS spectra the estimated values were $D_{overlap} (T_{sub} = RT) = 5 \pm 5$ nm, $D_{overlap} (T_{sub} \geq 300^\circ C) = 20 \pm 5$ nm, and $D_{overlap} (T_{sub} = 550^\circ C) \geq 30$ nm. For $D_{Pd} > 4$ nm, the switching time for all Y thicknesses was observed to exhibit general trend. In the region with $D_1 \leq D_{Pd} \leq D_2$, where D_2 correspond to the minimal Pd layer thickness necessary to cover the Y layer (which is an increasing function of D_Y), the switching time τ_s was ob-

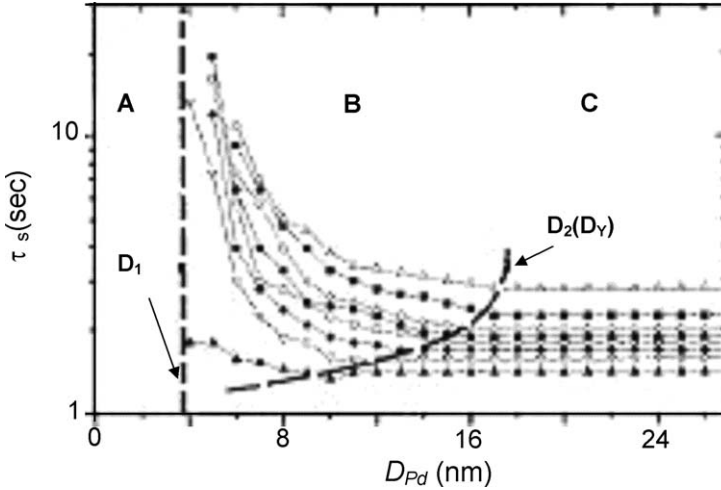


Fig. 71. Pd thickness dependence of switching time for Pd/Y matrix sample of various Y thickness ($-\blacktriangle-$, $-\nabla-$, $-\blacklozenge-$, $-\square-$, $-\bullet-$, $-\circ-$, $-\blacksquare-$, $-\triangle-$; correspond to 20, 40, 60, 80, 100, 120, 150, 200 nm) for the first hydrogen loading cycle (van der Molen et al., 1999).

served to decrease with increase in the D_{Pd} , Huiberts et al. (1996a) found similar results. For example, for 500 nm Y film capped with 20 nm of Pd over layer a switching time of 125 s has been reported in comparison to 20–40 h for a cap layer of 5 nm. AFM studies carried out on samples showed that Pd forms electrically disconnected clusters having 5–10 nm height and 10 nm width. STM studies on pre-oxidized 400 nm Y layer capped with 3 nm Pd showed unconnected clusters of average diameter 4 nm, whereas 10 nm Pd deposits were observed to form a continuous film (Borgschulte et al., 2004). Van der Molen et al. argued that the Pd does not form a closed layer below the thickness D_2 (in region B). The resulting local oxide on the uncovered portions acts as a barrier to hydrogenation, resulting in higher switching times. Van der Molen et al. argued that the D_2 depend not only on D_Y , but also on the morphology of the Y films with rough Y surface likely to increase the cap layer thickness. The morphology of Y films was observed to depend sensitively on the film thickness (fig. 72). Finally in region C ($D_2 > D_{Pd}$), τ_s was observed to be constant within the accuracy of the measurements and any extra Pd on top of already closed cap layer was observed to introduce negligible increase in the switching time. In the second cycle of loading, a slightly different dependence of τ_s on Pd thickness was observed. Though no switching was observed below a sharply defined value of D_1 , for $D_{Pd} > D_1$ the switching time was observed to decrease faster with increase in D_{Pd} in comparison to the first cycle. For $D_{Pd} > 8$ nm, the switching time was observed to be independent of D_{Pd} . This was interpreted in terms of the possible enhancement in the dissociation kinetics at the heterogeneous oxide-Pd surface and to the crystalline orientation of the sample.

The switching time was observed to increase as a function of Y thickness (D_Y), for any constant Pd thickness (D_{Pd}), suggesting diffusion-controlled hydrogen loading behavior of

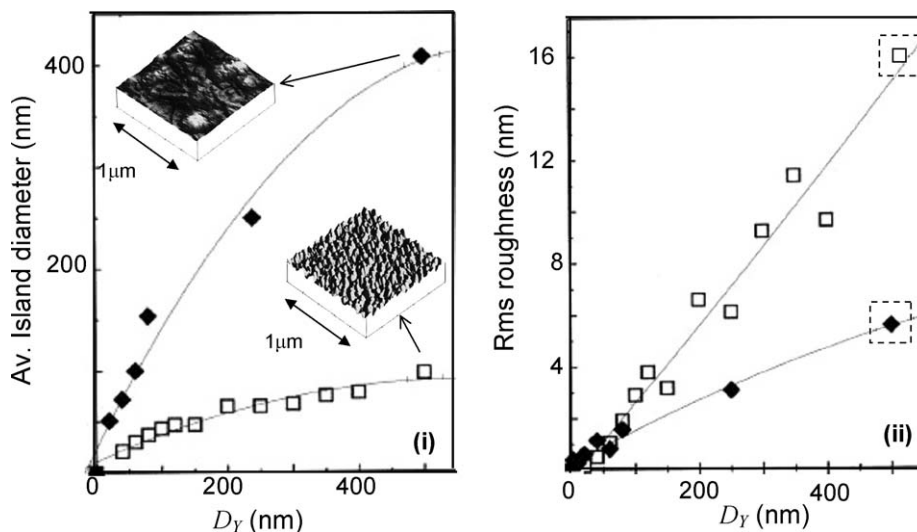


Fig. 72. The average island diameter (i) and the rms roughness (ii) of two typical Y films grown at $T_{\text{subs}} = 293$ K (\square) and $T_{\text{subs}} = 600$ K (\blacklozenge). The AFM images of Pd/Y matrix samples deposited at the above-mentioned temperatures with $D_Y = 500$ nm are shown in the inset of (i) (van der Molen et al., 1999).

the films. Den Broeder et al. (1998), van der Molen et al. (2000, 2002a, 2002b) showed using electromigration experiments that hydrogen migration in YH_x is diffusion controlled. Van der Molen et al. compared the lateral and normal diffusion in simultaneously deposited but differently patterned Pd/Y matrix samples. It was observed that the mobility of the diffusion front ($K_{\text{opt}} = z_{\text{opt}}^2/t$, where z_{opt} is the distance of the diffusion front from the Pd edge and t is the time) the optical transition strongly depended on the Y thickness (fig. 73). The thinner the Y film, the lower the mobility. Whereas $\beta\text{-YH}_{2\pm\epsilon}$ phase was observed to grow very fast even in 10 nm Y films, for $D_Y < 20$ nm, the $\gamma\text{-YH}_{3-\delta}$ phase does not grow which was attributed to stresses in the films.

The strongest limiting factor in the switchable mirror kinetics was observed to be the oxidation of the active R metal layer. Huiberts et al. (1996b) showed using RBS measurements on Pd (5 nm) capped (570 nm) Y films that oxygen was detectable up to a depth of 175 nm. It was argued that the total amount of oxygen in the sample was relatively low (few percent in the top layer) resulting from oxygen diffusing along the grain boundaries of the polycrystalline film and subsequent obstruction of further diffusion by the formation of the Y_2O_3 phase. Van der Molen et al. (1999) showed using optical transmittance measurements that the Y grains were only oxidized down to approximately 5 nm. However, along the grain boundaries oxygen was present down to 150 nm. In an interesting observation, van der Molen et al. found that the hydrogenation experiments on matrix samples consisting of preoxidized Y capped with Pd showed that the oxide does not completely block the atomic H diffusion. The preoxidized Pd/ Y_2O_3 /Y matrix sample was observed to switch with a 3 nm Pd over layer, whereas unoxidized Y needed at least 5 nm of Pd over layer for hydrogenation (fig. 74). It was argued that

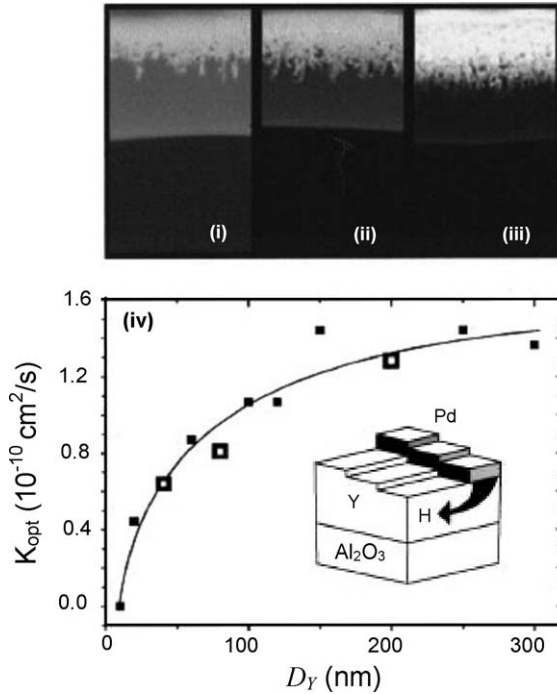


Fig. 73. Optical microscope images (i)–(iii) in the transmitted light of Pd/Y matrix sample with lateral diffusion geometry [schematic representation shown in the inset of (iv)] in 1 bar H_2 at room temperature, for three different Y thicknesses, 40, 80, and 200 nm. The Pd strip located at the top of the picture is not shown for clarity. The mobility of optical transition K_{opt} as a function of D_Y is shown in (iv). The open squares correspond to images (i)–(iii) (van der Molen et al., 1999).

the Pd–Y interdiffusion was hindered by the oxide buffer layer as seen from the RBS spectra (fig. 75). Borgschulte et al. (2001) investigated the alloy formation at the Y–Pd interface by photoemission and electron diffraction measurements. Pd over layer was grown on epitaxial Y (0001) films at different temperatures. It was observed the Pd grows as polycrystalline over layer for deposition at room temperature where as a monocrystalline epilayer was formed at 300 °C. For Pd deposition at room temperature, a complete coverage was observed for thicknesses as small as 3 nm. However, deposition at high temperatures resulted in an ordered Y–Pd alloy at the surface as confirmed by RHEED (fig. 76). Fig. 77 shows the Auger spectra for Y films capped with Pd (3 nm) at RT and 300 °C. The room temperature deposited film shows only Pd MNN lines indicating a fully covered Pd surface with no Y impurities. The surface diffusion was observed to be enhanced at high temperatures, as shown in the RHEED reflexes [fig. 76(ii)]. The different lattice plane spacing and superstructure line indicated an ordered Y–Pd alloy. The Auger spectra of the sample with Pd over layer deposited at 300 °C was observed to exhibit both Pd and Y lines with Pd lines. The form of Pd lines was observed to be slightly different from that of pure Pd and was observed to be shifted to higher energies.

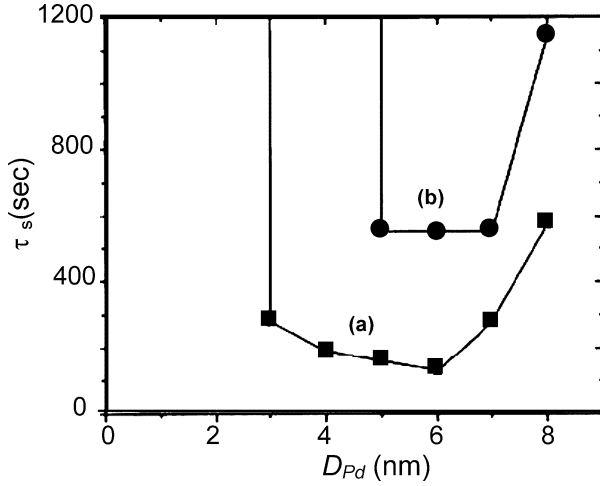


Fig. 74. Dependence of switching time (τ_s) on Pd thickness (D_{Pd}) for 40 nm Y layer in (a) Pd/Y₂O₃/Y matrix sample (oxidation carried out in air ambient for 10 min) and (b) Pd/Y matrix sample. Note that for $3 \leq D_{Pd} \leq 4$ nm the preoxidised sample exhibit switching where as the normal Pd/Y sample does not (van der Molen et al., 1999).

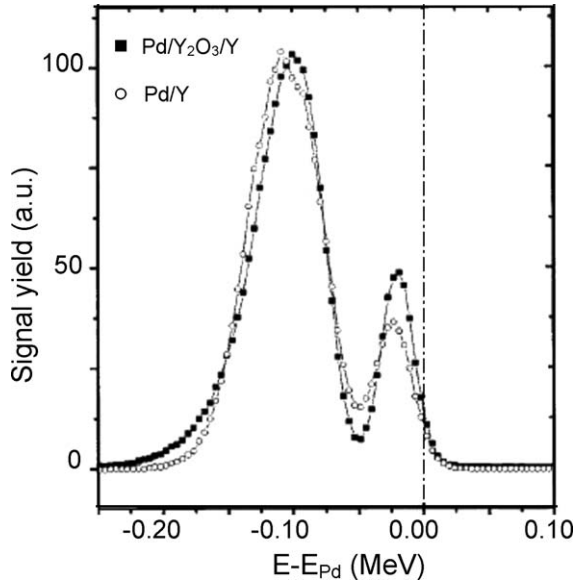


Fig. 75. RBS spectra of Pd/Y₂O₃/Y (■) and Pd/Y (○) matrix samples. The curves are aligned at the surface edge of E_{Pd} . Clearly, the direct evaporation of Pd on Y yields a lower Pd surface peak, with higher overlap with Y peak than the Pd evaporated on preoxidized Y surface does, indicating that the oxide layer prevents the Pd from intermixing with the Y (van der Molen et al., 1999).

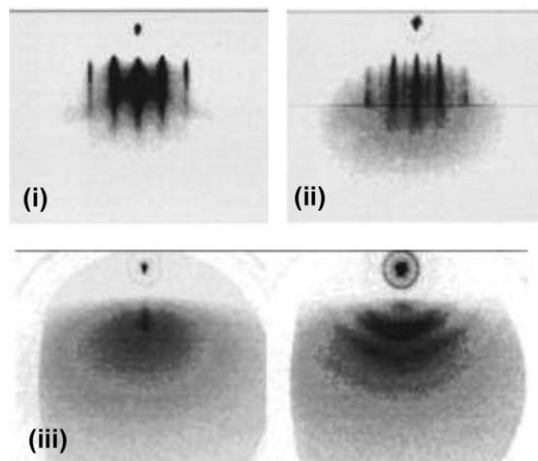


Fig. 76. (i) RHEED pattern of $[10\bar{1}0]$ direction of an epitaxial Y (0001) film taken at 20 kV. (ii) The corresponding RHEED pattern of the sample films after deposition of 5 nm of Pd over layer at 300 °C. The superstructure peaks indicates an ordered Pd–Y alloy whereas the V form of the streaks indicate faceted surface. (iii) The RHEED pattern after depositing 0.5 nm (left pattern) and 5 nm of Pd at RT. The original Y reflexes are observed to vanish immediately after deposition of 0.5 nm of Pd and an amorphous/polycrystalline overlayer is formed (Borgschulte et al., 2001).

It was argued that the different surface energies and the strong negative heat of solution of Pd in Y provide the driving force for the interdiffusion of Pd into Y. Using IR spectroscopy Borgschulte et al. showed that Y films capped with Y–Pd alloy do not switch from the metallic to insulating hydride state when exposed to a hydrogen atmosphere at room temperature. To study the origin of the reduced hydrogenation the electronic properties of Pd-rich Y–Pd surfaces were investigated by angle resolved ultraviolet spectroscopy (ARUPS). Fig. 78 shows the angle resolved energy distribution curves at various photon emission angles, measured at room temperature in the $[10\bar{1}]$ direction for Pd (111), $Y_{15}Pd_{85}$ and $Y_{25}Pd_{75}$ films excited with He I resonance line. The spectra of $Y_{25}Pd_{75}$ surface was observed to have three dominant features at 0.7, 1.5 and 2.5 eV binding energy. Upon varying the emission angle these features were observed to exhibit no dispersion and only intensity modulation. On the other hand the total width of the energy distribution curves were observed to be smaller for Pd and $Y_{15}Pd_{85}$ surfaces, revealing that band dispersion is reduced in $Y_{25}Pd_{75}$. In contrast to $Y_{25}Pd_{75}$, ARUP spectra of Pd (111) and $Y_{15}Pd_{85}$ showed stronger dispersions of the valence band features. The dispersion in the bands was observed to decrease with increase in Y content where as the energy of the d-band center was observed to remain constant. The alloying of Pd with Y was discussed in the framework of qualitative tight-binding approximation. The idea was taken from the work by Schneider et al. (1998). It was argued that the charge transfer between Pd and Y was governed by the electron densities and the contact potential, which were related to the individual densities of states (DOS) and work functions, respectively (fig. 79). With about nine d electrons per atom, the Pd 4d band is almost filled, while for Y the 5d band occupation is close to 1, and the Fermi energy lie close to the bottom of this band. When these metals are

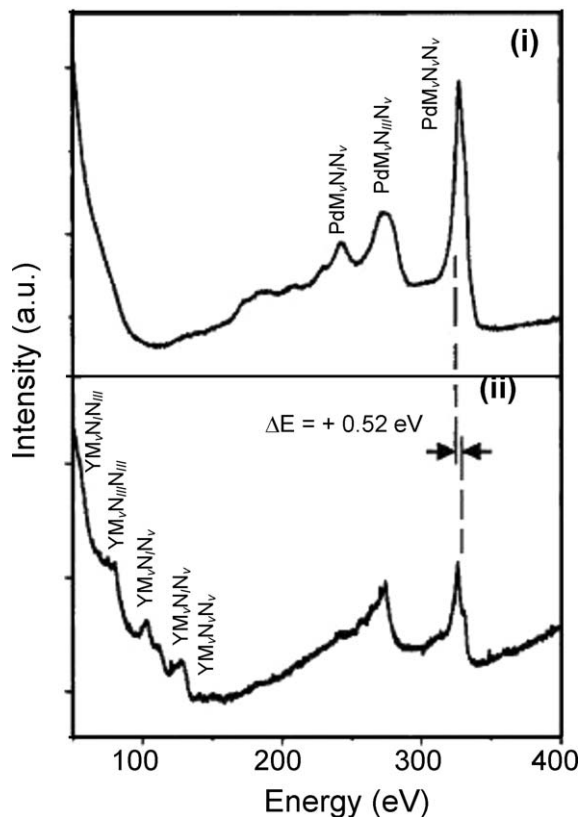


Fig. 77. The Auger spectra of Y films capped with Pd (3 nm) overlayer at (i) RT and (ii) at 300 °C. The main Pd MNN peak is shifted towards higher energy side in the sample deposited at 300 °C (Borgschulte et al., 2001).

brought to into contact, the contact potential leads to a charge transfer from Y to Pd until a common Fermi energy is established. The shifting of Pd Auger peaks towards higher energies indicates charge transfer from Y towards Pd. Since in photoemission experiments the binding energies are measured relative to the Fermi energy, this charge transfer was reflected in the photoemission spectra by a shift of the Pd 4d band to higher binding energy. It was argued that in addition to the charge transfer, compound formation also results in band narrowing that occurs due to the reduced coordination with equivalent atoms. Hybridization between the Pd and Y states and the disordered crystal structure may reduce the narrowing effects. The reactivity of the Y–Pd alloy surfaces was estimated in using the chemisorption model of Hammer and Norskov (Hammer and Norskov, 1995), which predicted a better chemisorption of hydrogen and oxygen. Fig. 80 shows the Auger spectra of Y films capped with Pd at RT and at a substrate temperature of 300 °C before and after exposure to air for 2 min. The films capped with Pd at RT showed no significant change in the two spectra. No oxygen peak was observed

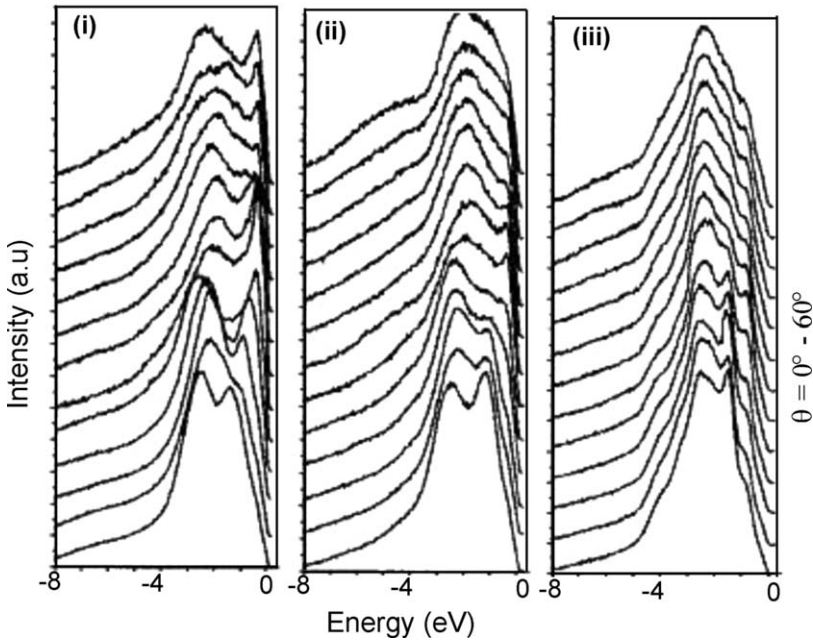


Fig. 78. Angular resolved photoemission spectra for (i) Pd (111), (ii) $Y_{15}Pd_{85}$, and (iii) $Y_{25}Pd_{75}$ films measured at room temperature and various emission angles ($0-60^\circ$) and excited with He I resonance line (Borgschulte et al., 2001).

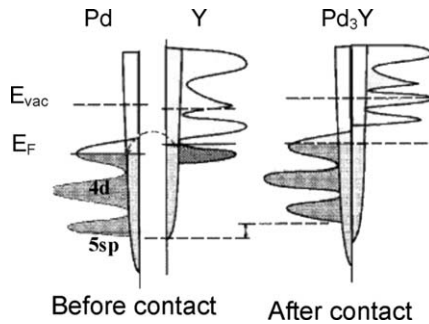


Fig. 79. The schematic diagram showing the partial sp and d DOS of pure Y and Pd metals before and after the contact has been made. After the contact has been made the Fermi levels adjust by charge transfer. A decrease of the number of next nearest neighbors leading to narrowing of the bands is illustrated by a smaller bandwidth, whereas the changes of the dispersion (e.g., splitting of the states due to hybridization are not included (Borgschulte et al., 2001)).

at 510 eV. In contrast, the Y films with Pd deposited at higher temperature showed oxygen contamination at the surface after about 2 h in UHV, which was observed to increase sharply

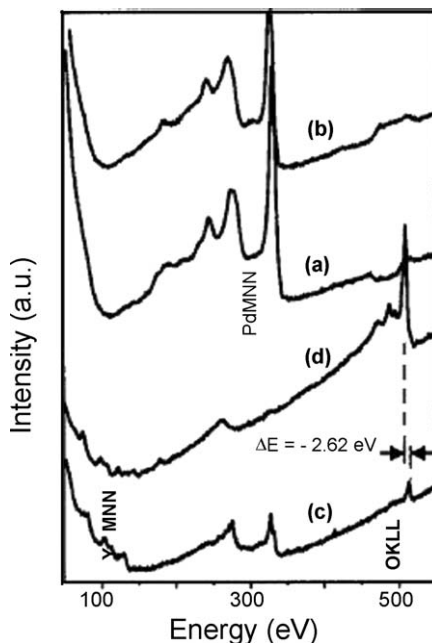


Fig. 80. The Auger spectra of Y films capped with Pd overlayer at RT (a, b) and at 300 °C (c, d), before (a, c) and after (b, d) exposure to air for 2 min (Borgschulte et al., 2001).

after exposure to air. The main peak was observed to shift towards lower energy, indicating a chemical oxidation of the Y compared to weak absorption of oxygen on the Y–Pd alloy in UHV. The Y MNN peak was observed to split whereas the Pd MNN peaks disappeared upon exposure to air. Borgschulte et al. argued that the high negative oxidation enthalpy of Y, which is higher than the heat of solution of Y in Pd, an oxygen induced surface segregation occurs. Yttrium oxide having smaller surface energy compared to Y and Pd, diffuses to the surface. The oxidized surfaces are initially inert to H_2 and thus the kinetic of hydrogen chemisorption of the Y–O–Pd surface becomes extremely slow and hydrogenation of the underlying Y is nearly impossible.

Van Gogh et al. (2000a) showed that instead of pre-oxidized R layer, the presence of AlO_x , buffer layer between the Pd over layer and the optically active R layer, drastically improves the optical properties and life time of switchable mirrors. Pd/ AlO_x /Y (or La) matrix samples with ~ 100 combinations of (partly oxidized) Al and Pd layer thickness D_{Al} and D_{Pd} with $0 \leq D_{Al}, D_{Pd} \leq 10$ nm were studied. Fig. 81 shows the dependence of switching time τ_s (defined as the time at which the light intensity reaches half of its final maximum value) on the Pd over layer in 150 nm Y film deposited on CaF_2 (i) and 100 nm La deposited on SiO_2 capped (ii), with AlO_x buffer layer. The buffer layer was observed to lower the minimum Pd thickness necessary for hydrogenation to ~ 1 nm, resulting in $\approx 20\%$ increase of the maximum transmittance. It is generally observed that Y films can be reversibly switched ~ 100 times,

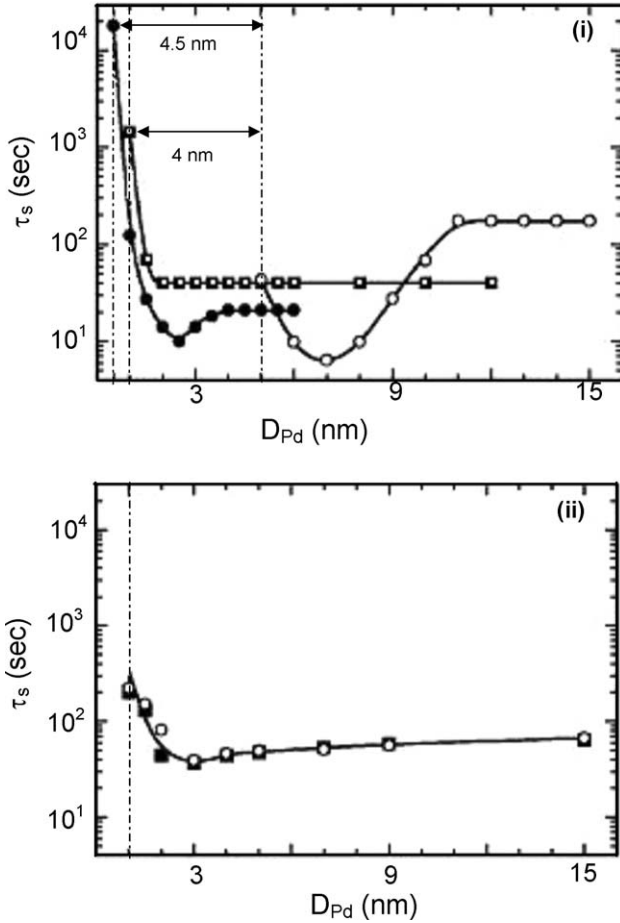


Fig. 81. Dependence of optical switching time on Pd thickness for (i) 150 nm Y deposited on CaF_2 capped with Pd (●), Pd/native YO_x (□), and Pd/ 1.2 nm AlO_x (●) and (ii) 100 nm La on SiO_2 capped with Pd/ 0.9 nm AlO_x (○) and Pd/ 1.2 nm AlO_x (■) (van Gogh et al., 2000a).

whereas La could only be switched once. In addition as oxidation of La does not stop on the microscopic length scale, a La film covered with Pd, was observed to fully deteriorate within a few hours in air at room temperature. Effort has been made to circumvent this problem by growing an AlO_x buffer layer in between the Pd and R metals layer. In case of Y films, the Pd/ AlO_x composite cap layer was observed to give marginally better results compared with a Pd/ YO_x layer. However for La films, as compared to the native oxide or even YO_x buffer layer, the films covered with AlO_x were observed to exhibit large improvement in switching properties and lifetime. Van Gogh et al. (2000a) interpreted the role of AlO_x in terms of coupled-currents approach of Fromhold in the “very thin film regime” (Fromhold, 1976). It

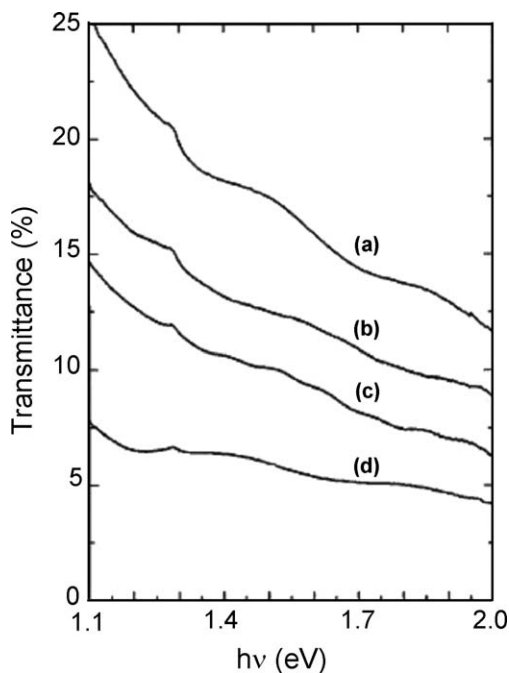


Fig. 82. Transmittance spectra of 500 nm $\text{YH}_{3-\delta}$ films capped with Pd overlayer of thickness (a) 5 nm, (b) 9 nm, (c) 14 nm, and (d) 20 nm (Kremers et al., 1998).

was argued that when the entire Al was oxidized, the kinetic potential which drives the cation and electron transport, increases because of the lower work function of Y (or La) as compared to Al. Further oxidation was observed to depend on the resulting current of Y (or La) cations towards the AlO_x -gas surface. This current was proportional to the exponential of negative of activation energy of Y (La) cation diffusion in AlO_x . It was argued that since the radii of Y^{3+} and La^{3+} were 1.7 and 1.9 times larger than that of Al^{3+} , the activation energy was expected to be much larger than for the Al ion and thus AlO_x blocks the Y^{3+} (La^{3+}) diffusion, and consequently further oxidation. It is interesting to note here that Gd nanoparticles synthesized by inert gas evaporation technique were observed to have thin oxide shell around the Gd core which prevents the Pd-Gd interfacial alloy formation resulting in enhanced switching properties in Gd nanoparticle based switchable mirrors (Aruna et al., 2004, 2005c).

The effect of the Pd over layer thickness on the optical transmittance and hence the hydrogen uptake has been studied by number of authors (Kremers et al., 1998; van der Molen et al., 1999; van Gogh et al., 2000a; Mor et al., 2001; Mor and Malhotra, 2003; Borgschulte et al., 2004; Kumar et al., 2002; Kumar and Malhotra, 2004a, 2004b). Fig. 82 shows the variation in optical transmittance spectra for $\text{YH}_{3-\delta}$ films (500 nm) capped with 5-, 9-, 14-, 20 nm of Pd over layer of thickness, clearly showing an increase in the optical transmittance with decrease in the Pd over layer thickness. Similar trend was observed by Mor and Malhotra (2003) for

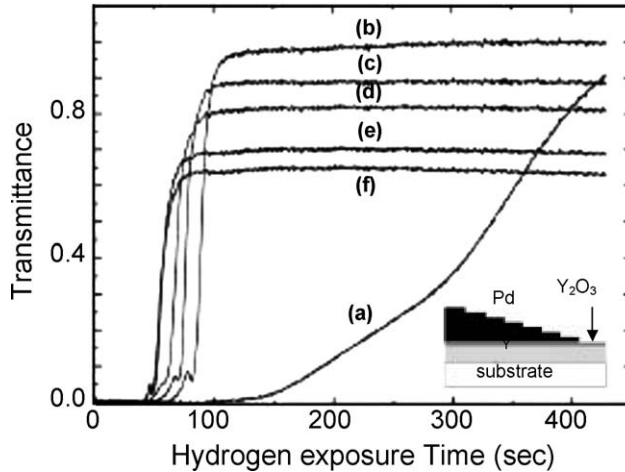


Fig. 83. Normalized optical transmittance of Y (200 nm) film capped with Pd over layer of thickness 3–8 nm (a–f) in steps of 1 nm (schematic shown in the inset) as a function of hydrogen exposure time (1 bar H_2 , at RT). The curves are arbitrarily normalized to the asymptotic value of 4 nm sample. The small peak is due to the infrared transparency window of the YH_2 (Borgschulte et al., 2001).

hydrogen loaded Pr (170 nm) films capped with Pd over layer of thickness 5-, 9-, 12- 19 nm; Borgschulte et al. (2004) for hydrogenated Y (200 nm) films capped with 3-, 4-, 5-, 6-, 7-, 8 nm; and Kumar and Malhotra (2004b) for 55 nm Sm films in the fully loaded state capped with Pd over layer of thickness 5-, 8-, 11-, 15 nm. Mor et al. observed that in addition to increase in the transmittance, the transmittance edge was observed to exhibit a blue shift for films capped with Pd of thickness 5 nm and 9 nm, in comparison to films capped with Pd of thickness 12 nm and 19 nm which show a transmittance edge of 2.82 eV Mor and Malhotra (2003) It was observed that the reversible hydrogen induced switching occurs only in Pr (170 nm) films capped with Pd of thickness ≥ 12 nm which was attributed to the non-uniform coverage of the underlying Pr films and the decreased reversible hydrogen absorption capacity of the Pd clusters which are formed at low Pd thickness (due to its relatively higher surface energy than any R metal). It was observed that for $D_{Pd} \leq 9$ nm, *in situ* hydrogen loading of 170 nm Pr films results in nanocrystalline size $PrH_{3-\delta}$ films due to structural rearrangement caused by hydrogen induced stresses (Mor and Malhotra, 2003), resulting in increased band gap. The band gap of PrH_x films estimated from spectroscopic ellipsometry was observed to decrease with increase in the Pd over layer thickness and has been attributed to the increase in hydrogen desorption at higher Pd thickness (Mor et al., 2001). Similar results were observed by Kumar and Malhotra (2004b) on Sm (55 nm) films capped with Pd of different thickness (see section 2.1.6 for details)

Borgschulte et al. (2004) studied the relation between the hydrogen uptake kinetics in switchable mirrors and the morphology and the electronic properties of the over layer at different Pd thickness. Fig. 83 shows the variation of the optical transmittance of a surface oxidized

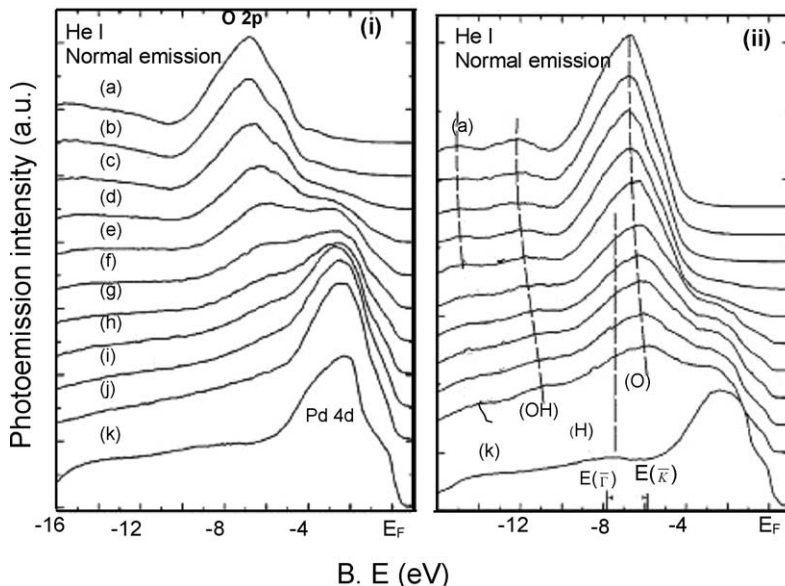


Fig. 84. Photoemission spectra of (i) as deposited and (ii) hydrogenated (1800 L H₂) Pd capped surface oxidized polycrystalline Y films. The curves (a)–(k) correspond to the films covered with Pd of thickness 0, 0.66, 1.33, 2.0, 2.66, 3.33, 4.0, 4.66, 5.33, 6.0, and 10 nm, respectively. In (ii) the (OH) and (O) correspond to the hydroxide and the oxide states, respectively. E($\bar{\Gamma}$), E(\bar{K}) indicate the energies of the hydrogen induced split-off states of the Pd (111) (Borgschulte et al., 2001).

Y (200 nm) film capped with Pd over layer of various thicknesses, as function of hydrogen exposure time. The switching time (defined as the time between the opening of the H₂ valve and the maximum slope of the transmittance-time function, corresponding to the trihydride formation) was observed to depend strongly on Pd thickness in agreement with van der Molen et al. (1999). It was observed to be minimum for 8 nm and increase drastically for smaller thickness values. The film covered with less than 3 nm of Pd were observed to exhibit no switching properties. It was argued from the AES measurements that the surface oxidized Y was totally covered for $D_{Pd} > 8$ nm. The electronic structure of as grown Pd clusters was observed to show minor dependence on thickness [fig. 84(i)]. However, strong changes of the photoemission spectra were found after hydrogenation, in particular the oxide peak was observed to shift and the Pd peak was observed to vanish. Fig. 84(ii) shows the photoemission spectra of surface oxidized Y (200 nm) films capped with Pd over layer of different thickness after exposure to 1800 L of hydrogen. The spectra of films with 10 nm Pd cap layer were observed to be similar to the bulk Pd. Photoemission spectra of films covered with thinner Pd over layer was observed to show O 2p peak at -6.5 eV, which was observed to shift with increase in thickness. The intensity of O 2p peaks was observed to be much larger than the Pd 4d peaks, which were strongly reduced as compared to the as-deposited films. The pure YO_x surface was observed to show additional peaks at around -2 eV and -14 eV, which were

attributed to the OH group on the oxide surface. The observed phenomenon was explained in terms of the strong metal-support interaction (SMSI) state, characterized by encapsulation of the Pd clusters by the yttrium hydroxide (formed by reduction of yttrium oxide in presence of hydrogen) layer. It was argued that as a result of SMSI the catalytically active surface of the Pd clusters was covered and the thickness effect of the hydrogen absorption corresponds to the thickness dependence of the amount of free Pd surface as the degree of encapsulation decreases with increase in Pd thickness. Borgschulte et al. (2004) concluded that the critical thickness D_1 required for fast hydrogen uptake correspond to the thickness below which the Pd clusters are completely covered with the yttrium oxide (-hydroxide) layer. The SMSI state of the small clusters was confirmed by the scanning tunneling spectroscopy. Fig. 85 shows the topography and current image of surface oxidized Y (200 nm) film capped with Pd over layer of thickness 3 nm. The as measured I-V curves and the estimated DOS $[-(dI/dV)(V/I)]$ at two different regions on the surface are also shown. A comparison of the topography and the DOS clearly shows that, the white region correspond to oxides (showing a DOS gap characteristic of the insulators) where as the dark region are metallic, confirming the SMSI state of Pd clusters at small thickness.

Recently the enhanced catalytic properties of Pd at reduced dimensions have been utilized in switchable mirror applications to improve the switching properties of Pd nanoparticle capped Gd switchable mirrors. Aruna et al. (2005c) studied the effect of nanoparticle nature of the Pd over layer on the performance of Gd based switchable mirrors. Pd nanoparticle over layer was deposited by inert gas evaporation technique. It was shown that by using a continuous Pd nanoparticle over layer it was possible to carry out an unambiguous study of the size dependent effects with out any interference due to reduced and incomplete coverage of the R metal layer. Deposition of 10 nm thick Pd over layer consisting of nanoparticles of 9 nm size was observed to result in a large increase in optical and electrical contrast [fig. 86(iv)] and a substantial decrease in response and recovery time [fig. 87(i), (ii)] in Gd switchable mirrors. The optical absorption edge was observed to be 2.72 eV, 2.61 eV and 2.55 eV for Gd polycrystalline films capped with Pd nanoparticle over layer with an average particle size of 9 nm, 14 nm and 26 nm, respectively [fig. 86(iii)]. A uniformly deposited nanoparticle layer was shown to be crucial for improving hydrogen recovery time. A large decrease in the recovery time (24.6 min to 1.8 min) and response time (3.3 min to 2.3 min) of Gd films with the decrease in the Pd nanoparticle size (26 nm to 9 nm) was observed [fig. 87(i), (ii)]. An increase in surface area (fig. 86), lattice contraction [fig. 87(iii)] and shift in Pd d-band centroid [fig. 87(iv)] were shown to play an important role in improving the catalytic properties of the nanoparticle Pd over layer. It was argued that the increase in crystal field due to lattice contraction on reduction of size of Pd nanoparticles increases the d-band coupling matrix element and cause a shift in the d-band centroid resulting in enhanced reactivity of Pd towards H at smaller sizes as shown in the energy level diagram of H-Pd system [fig. 87(iv)].

In summary, the kinetics of switching is controlled by a combination of the underlying R film thickness and the thickness of the Pd over layer. For each combination a critical Pd thickness exists below which switching is not possible. Slower switching kinetics have been attributed to oxidation of the uncovered portion of R film and the Pd-R alloy formation.

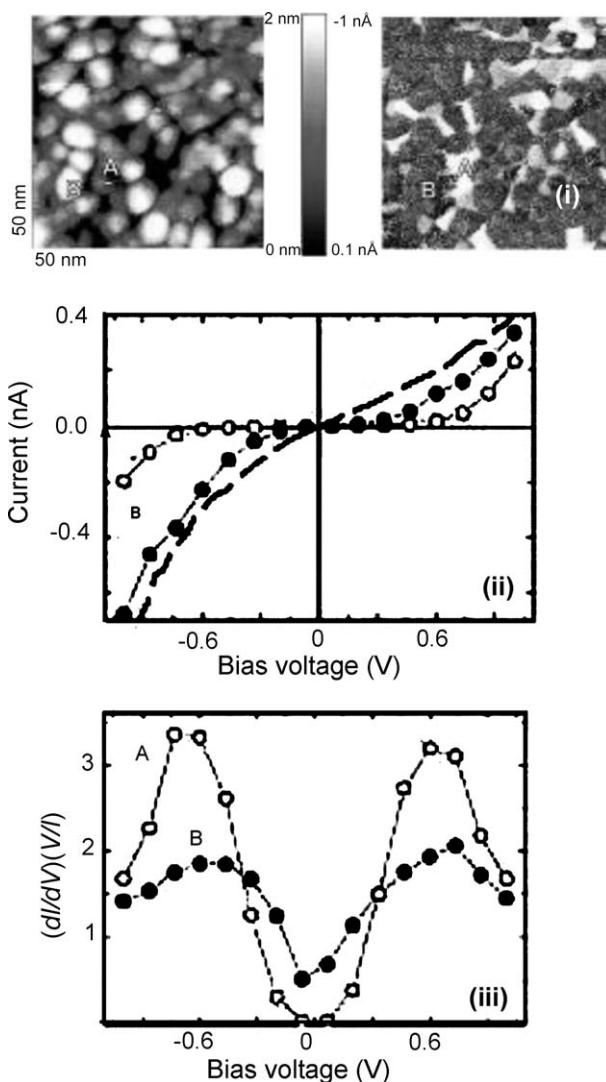


Fig. 85. (i) Topography (left $V_{\text{bias}} = +1$ V) and current (right $V_{\text{bias}} = -1$ V) image of Pd (3 nm) capped Y (0001) film deposited on CaF_2 (111) after exposure to 10–4 mbar H_2 . (ii) The I–V curves (obtained by current imaging tunneling spectroscopy) and the (iii) calculated DOS = $(dI/dV)(V/I)$ corresponding to two different locations (A and B) on the film. For comparison the I–V curve for a 10 nm Pd layer [dotted line in (ii)] is also included (Borgschulte et al., 2001).

Increase in thickness of the Pd over layer takes care of the oxidation problem and also leads to a reduction of switching time. The use of a buffer layer between Pd and R film has been suggested to prevent alloy formation. It has also been suggested that using nanoparticle films

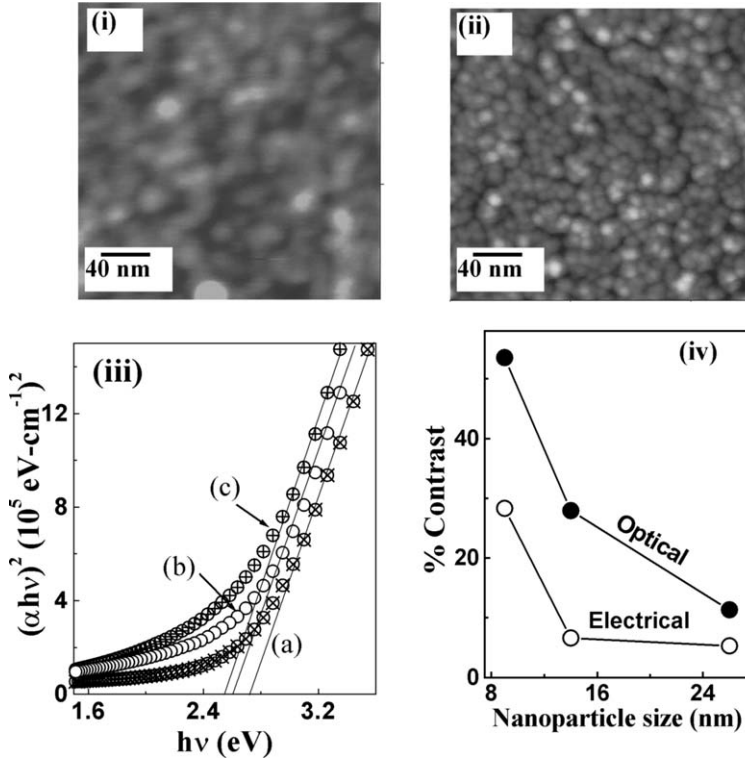


Fig. 86. AFM images ($250 \text{ nm} \times 250 \text{ nm}$) showing the change in surface morphology of Gd films capped with Pd nanoparticles of average size (i) 26 nm and (ii) 9 nm. (iii) Tauc's plot of the hydrogenated Gd films capped with Pd nanoparticles of size (a) 9 nm, (b) 14 nm, and (c) 26 nm. (iv) Variation in optical contrast (at $\lambda = 500 \text{ nm}$) and electrical contrast as a function of Pd nanoparticle size. The optical contrast is defined as $(T_L - T_{DL})/T_L$ where T_L and T_{DL} are the transmittance values of loaded and deloaded samples respectively and the electrical contrast is defined as the ratio of the saturation value of resistance to the minimum value of resistance (Aruna et al., 2005c).

of R metal and Pd not only prevents alloy formation but also enhances the catalytic properties of Pd leading to an improvement in switching characteristics.

2.4. Hysteresis

On the basis of the optical transmittance and electrical resistivity measured *in situ* during the electrochemical hydrogenation, and the crystal structure determined by X-ray diffraction measurements in a separate gas phase loading experiment carried out together with simultaneous resistivity measurements; Kooij et al. (2000) showed that switchable mirrors based on yttrium hydride exhibit extraordinarily large hysteresis effects in the hydrogen induced optical, electrical, and structural properties during hydrogen absorption and desorption in the reversible concentration range ($1.9 \leq x < 3.0$). It was observed that the optical transmit-

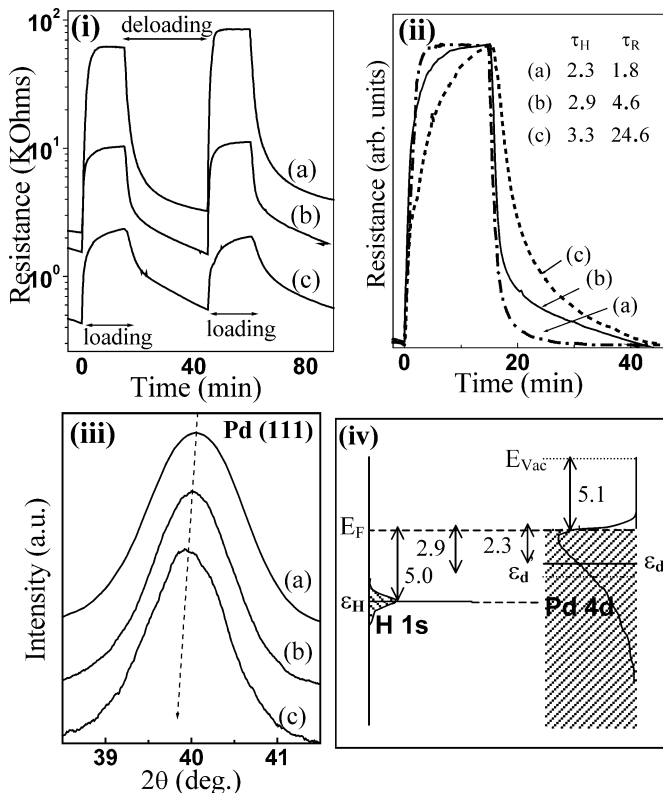


Fig. 87. (i) Changes in electrical resistance during hydrogen loading–deloading cycles in Gd films capped with Pd nanoparticles with size (a) 9 nm, (b) 14 nm, and (c) 26 nm. (ii) Normalized resistance curves for different samples showing decrease in response (τ_s) and recovery times (τ_R) with reduction in Pd nanoparticle size. τ_s is defined as the time required to reach 90% of the saturation value of the resistance and τ_R is defined as the time needed for the resistance to fall up to 30% of the saturation value. (iii) Slow scanned Pd (111) XRD peak in Gd films capped with Pd nanoparticles with size (a) 9 nm, (b) 14 nm, and (c) 26 nm. (iv) A schematic energy level diagram of H–Pd system showing increased overlap of H 1s and Pd 4d levels due to size-induced shift of d-band centroid (ϵ_d to ϵ'_d) (Aruna et al., 2005c).

tance (at 1.96 eV) exhibits a distinct minimum upon loading the film from the dihydride to the trihydride state; however, on deloading this minimum was absent. Fig. 88(i) shows the variation in optical transmittance as a function of hydrogen concentration x for Y polycrystalline film (300 nm) capped with Pd (15 nm) over layer. The film was hydrogenated via electrochemical loading in 1 M KOH utilizing constant galvanostatic loading at a constant current $|j| = 0.2 \text{ mA/cm}^2$ ($j < 0$ for loading and $j > 0$ for deloading). For the full loading and deloading cycle three linear regimes were observed; during loading for $1.9 \leq x < 2.1$, the transmittance decreases by about one order of magnitude; followed by a strong increase of the transmittance by more than two orders of magnitude; and then a linear decrease in trans-

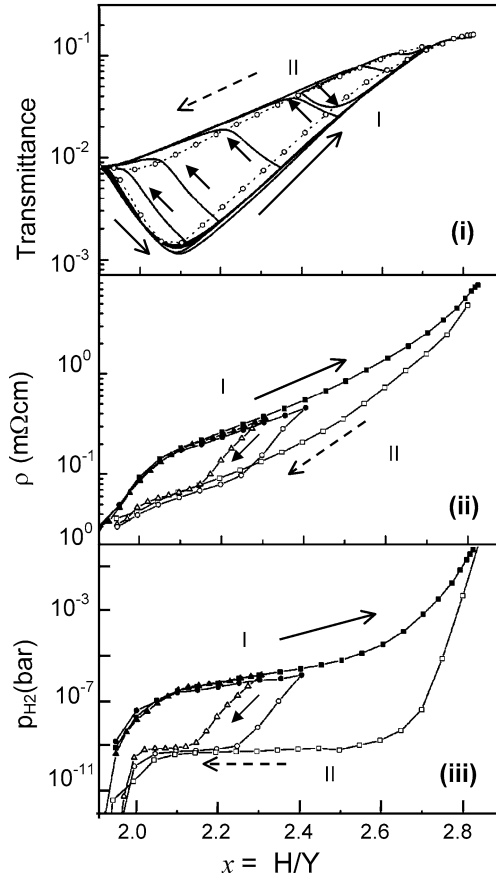


Fig. 88. (i) Optical transmittance at 1.96 eV (solid lines obtained using continuous galvanostatic loading and open circles obtained from GITT) and (ii) resistivity (obtained from GITT measurements and corrected for Pd over layer) as a function of hydrogen concentration in Pd (15 nm) capped Y (300 nm) films. (iii) Pressure composition isotherms obtained from GITT for the same film (Kooj et al., 2000).

mittance during deloading. By changing the current, the hydrogenation and dehydrogenation rates were varied but no marked influence on the aforementioned behavior was observed. To eliminate the effects related to the kinetics of hydrogenation, the galvanostatic intermittent titration technique (GITT) (explained in section 1) was utilized and the physical properties of the electrochemically loaded switchable yttrium hydride films were studied under equilibrium conditions. Although the optical transmittance measured under equilibrium conditions using GITT [fig. 88(i)] exhibits less hysteresis, the results were essentially similar to that for the continuous loading/deloading experiment confirming that the hysteresis effect was not a result of the slow kinetics of the system. The pressure composition isotherms of the YH_x system between $x = 2$ and 3 for loading and deloading, determined electrochemically using

GITT, differ by approximately three orders of magnitude [fig. 88(iii)]. The hydrogen pressure was calculated from the measured equilibrium potential using Nernst equation (section 1). No plateau was observed in the pressure-composition isotherm during loading. A strong increase in pressure (logarithmic) was observed between $x = 1.9$ and 2.1 , followed by a much slower, almost linear increase between $x = 2.1$ and 2.55 , and then a rapid increase for $x > 2.6$. During deloading, after a sharp decrease of the pressure, an almost flat plateau was found between $x = 2.6$ and 2.0 , followed by a very rapid decrease near $x = 1.9$. The desorption data were in good agreement with the literature data on bulk yttrium but the absorption results showed a variation. From the plateau pressure in the desorption isotherms, which corresponds to a two-phase coexistence region, the enthalpy of formation ($\Delta H_{\alpha \rightarrow \beta}$) of dihydride was determined to be -44.8 kJ/mol H; which were in agreement with the value determined for bulk (Flotow et al., 1963). Yannopoulos et al. (1965) measured the pressure-composition isotherms in the range 250 – 350 °C, and from a fit to the plateau pressure as a function of temperature obtained the values of -43.1 kJ/mol H and -42.2 kJ/mol H for absorption and desorption, respectively. Kooij et al. (2000) on the other hand estimated the partial molar enthalpy to have a value between $\Delta \bar{H} = -37.4$ and -32.7 kJ/mol H from the pressure values at $x = 2.1$ and 2.55 . These enthalpies were close to the value ($\Delta \bar{H} = -30.0$ kJ/mol H) obtained by Huiberts et al. (1996b) from the sloping of the plateau in the absorption isotherm measured by means of quartz crystal microbalance but were significantly higher than the values for bulk mentioned above. Fig. 88(ii) shows the variation in resistivity as a function of hydrogen concentration measured simultaneously while determining the pressure-composition isotherms, clearly revealing the hysteresis in the loading and deloading curves. By starting deloading (loading) after the film has been loaded (deloaded) to an intermediate composition, a transition has been observed from curve I to II (II to I) in each of the optical transmittance, resistivity and pressure-composition isotherm measurements (fig. 88). *In situ* X-ray diffraction measurements also exhibit hysteresis behavior. It has been observed that during the hydrogen loading (from $x = 1.9$ to $x = 2.1$) the intensity ratio $\eta = I_{\text{YH}_3(002)}/I_{\text{YH}_2(111)}$ increases by five orders of magnitude, indicating a rapid transformation from fcc to hcp. For $x > 2.1$, YH_x remained in a single hcp phase. This was in sharp contrast to the behavior observed in bulk (Mueller et al., 1968). The separation into two regimes was also revealed from the transmittance minima at $x = 2.1$ [fig. 88(i)], and a sudden change of the slope in the resistivity near $x = 2.1$ [fig. 88(ii)]. However the pressure-composition isotherms do not show a plateau for $1.9 < x < 2.1$, though a change in slope below and above $x = 2.1$ was observed [fig. 88(iii)]. Upon deloading, the fcc phase precipitates immediately at high hydrogen concentrations ($x \sim 2.7$) and both the fcc and hcp phases coexist (from $x = 2.7$ down to $x = 2.1$) until the stable dihydride configuration is reached at lower hydrogen concentrations, as also observed in bulk. The evidence of the coexistence of the two-phase region during deloading was also obtained from the pressure-composition isotherm, which exhibits a plateau in this concentration range. In addition the transmittance and resistivity measured in the coexisting phase region were related to the optical and electrical properties of the two separate phases. Kooij et al. (2000) interpreted the observed hysteresis in terms of the large strain and consequently stress at the interface between fcc $\text{YH}_{1.9}$ and hcp $\text{YH}_{x \geq 2.1}$. On the basis of the experiments on more flexible substrates and a comparison of the lattice constants in

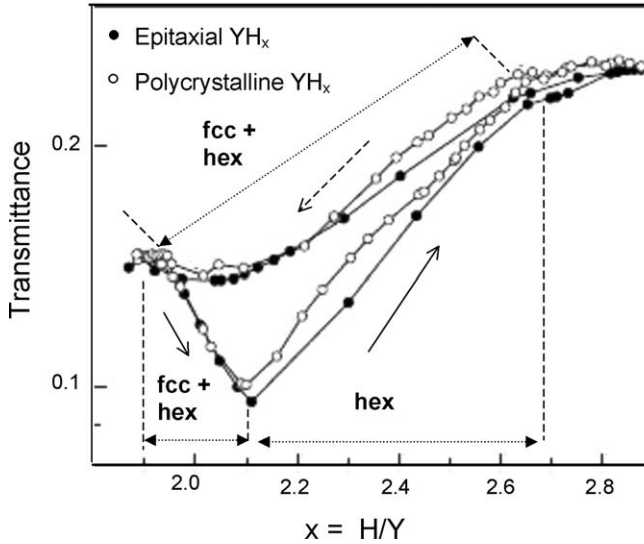


Fig. 89. Optical transmittance (at 1.78 eV) as a function of hydrogen concentration in Pd (10 nm) capped 60 nm epitaxial (-○-) and 50 nm polycrystalline (-●-) Y film (van Gogh et al., 2000a).

bulk and thin films, it was argued that the stress is not related to the clamping of the film to the substrate. According to Kooij et al., some grains (with average diameter <70 nm) in 300 nm YH_x films transform from cubic to a hexagonal structure upon absorption of small amount of hydrogen. As a result of the elastic interaction between neighboring crystallites, the entire film transforms into the hcp phase at concentrations as low as $x = 2.1$. During desorption, such interactions were absent allowing individual crystallites to transform back to the fcc phase, while other crystallites remain in the comparatively expanded hcp phase. This interpretation was supported by the X-ray diffraction analysis. It was shown that as-deposited films were polycrystalline with a preferred orientation with [002] direction perpendicular to the substrate surface. However upon hydrogenation, expansion of grains with the [002] direction parallel to the substrate was hindered by neighboring material resulting in the stress in the film. This leads to plastic deformation and a reorientation of the crystal grains in such a way that the [002] directions of the different crystals align perpendicular to the substrate. This was expressed by a marked increase of the ratio of the (002) and (101) peak intensities upon hydrogenation of hcp Y [$I_{Y(002)}/I_{Y(101)} \approx 1.9$] to hcp YH_3 [$I_{YH_3(002)}/I_{YH_3(101)} \approx 20$].

Van Gogh et al. (2000b) performed similar *in situ* optical and electrical measurements in gas phase loading experiments on polycrystalline and epitaxial YH_x films and observed that both the films exhibit large hysteresis in the properties indicating that hysteresis was an intrinsic thin film effect and that a texture with the hexagonal planes parallel to the substrate was generated by first H-absorption in the polycrystalline films. Fig. 89 shows the variation in optical transmittance as a function of hydrogen concentration for Pd (10 nm) capped epitaxial (60 nm) and polycrystalline (50 nm) Y films during loading and deloading.

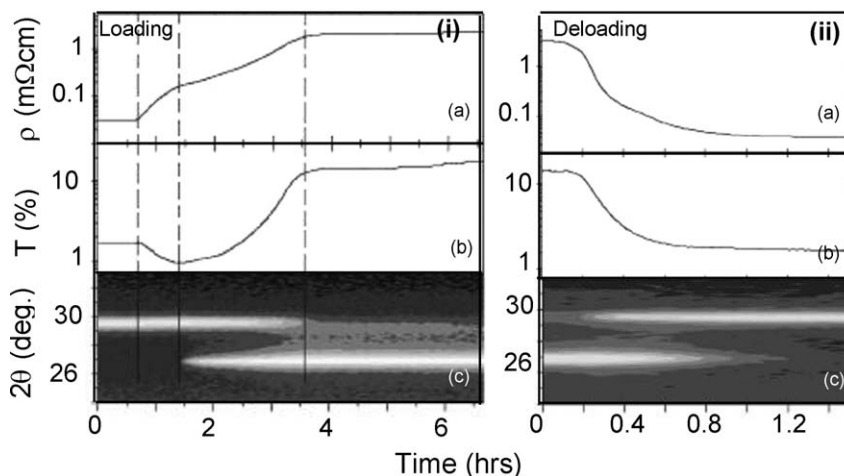


Fig. 90. Sequence of longitudinal X-ray scans (c), simultaneously measured optical transmittance (at 640 nm) (b) and electrical resistivity (a) of a Pd (10 nm) capped Y (300 nm) film grown on amorphous quartz during gas phase hydrogen loading (i) and deloading (ii) (Remhof et al., 2002a).

In contrast to the observations by Kooij et al. (2000) and van Gogh et al. (2000b), Remhof et al. (2002a) in their studies on Pd (10 nm) capped Y (300 nm) polycrystalline film sample did not confirm the existence of the small β - γ coexistence region (for $1.9 < x < 2.1$). During hydrogen loading above $x = 1.9$, the films were observed to stay in the metallic fcc β phase until $x = 2.1$. Upon further hydrogen intake the system crosses the miscibility gap in which the fcc β phase coexists with the hcp γ phase before hydrogen saturation was reached in the pure γ hcp phase. During deloading the coexistence of the β and γ phases was observed for $1.9 < x < 2.7$. Fig. 90 shows the variation in optical transmittance (at 1.96 eV), electrical resistivity and simultaneously measured sequence of longitudinal X-ray scans during gas phase loading (in 1 bar hydrogen) and deloading (at 120 °C in ambient air) respectively for a Pd (10 nm) capped (300 nm) Y film. It was observed that the lattice constant of the fcc β phase with in the two phase coexistence region depends on whether the measurement was carried out during loading or deloading. During hydrogenation, the β phase first shrinks until the γ phase starts to precipitate. When both phases coexist the β phase stays with a compressed lattice. During the whole unloading process, on the other hand, the β phase always exhibits its uncompressed lattice constant. Since the lattice parameter in the β phase was directly related to the hydrogen concentration, it was concluded that, during hydrogen loading, the γ phase coexists with the dark, high concentration ($x = 2.1$) β phase while upon deloading, the γ phase coexists with the low concentration ($x = 1.9$) fairly transparent β phase. The schematic phase diagram of the polycrystalline thin YH_x (300 nm) at 70 °C during hydrogen loading and deloading as proposed by Remhof et al. (2002a) is depicted in fig. 91. The hysteresis effects observed in optical transmittance and electrical resistivity were explained in terms of the difference in properties of the low concentration fcc phase $YH_{1.9}$ and the high concentration fcc phase $YH_{2.1}$ on the basis of the bulk phase diagram. Though the unit cell volume of the hcp γ

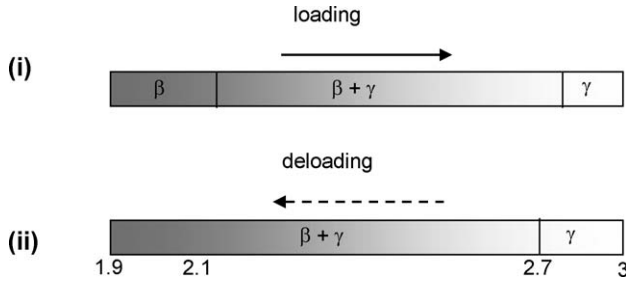


Fig. 91. Schematic phase diagram of a polycrystalline Y (300 nm) film at 70 °C during hydrogen loading (i) and deloading (ii) (Remhof et al., 2002a).

phase is about 10% larger than that of the fcc β phase, the in-plane lattice parameter of the γ phase is slightly smaller than the in-plane lattice parameter of the β phase. During hydrogen loading, the Y–Y distance within the basal plane first contracts before the system enters the miscibility gap, thus reducing the compressive in-plane stress in the β – γ coexistence region. In addition, the in-plane lattice parameter of the γ phase expands with increasing hydrogen pressure. Therefore in order to reduce the resulting mechanical stress, a high concentration γ phase was favored. During deloading, the γ phase unloads below its equilibrium value before β phase nucleates. This lower concentration γ phase contracts beyond its equilibrium value and was therefore under tensile stress. Precipitation of the expanded, low concentration β phase leads to compressive in-plane stresses, which stabilizes the low concentration γ phase. In-plane stress during loading and deloading, result in observed hysteresis effects in the optical and electronic properties and in the pressure composition isotherms. The explanations given by Remhof et al. (2002a) as mentioned above were in contradiction to the earlier interpretations of hysteresis in thin film YH_x based on non-simultaneous measurements of the optical and structural properties on different films by Kooij et al. (2000).

2.4.1. R–R alloy films: La–Y alloy films

To investigate the influence of structural phase transitions on the observed hysteresis effects in the hydrogen induced structural, optical, electrical properties and in the pressure-composition isotherms in YH_x films in the reversible hydrogen concentration range, van Gogh et al. (2000a, 2000b, 2001) studied the aforementioned properties in the polycrystalline $La_{1-y}Y_yH_x$ alloy films. La and Y are chemically similar as both have the d^1s^2 valence electron configuration. However, they exhibit structural dissimilarity upon hydrogenation. LaH_x stays fcc and undergoes lattice contraction for $2 < x < 3$, where as YH_x undergoes structural transition from fcc to hcp with a large lattice expansion (Mueller et al., 1968). The chemical similarity and structural difference between La and Y make the $La_{1-y}Y_yH_x$ system particularly suitable for studying of the role of the structural phase transitions on the properties of switchable mirrors.

Fig. 92 shows the X-ray diffractograms of the as-deposited, dihydride and trihydride phases of $La_{1-y}Y_yH_x$ alloy films, for $y = 0, 0.52$ and 1. The samples were mounted in a gas cell with Be windows to enable *in situ* hydrogenation. The crystal structure, the lattice parameters

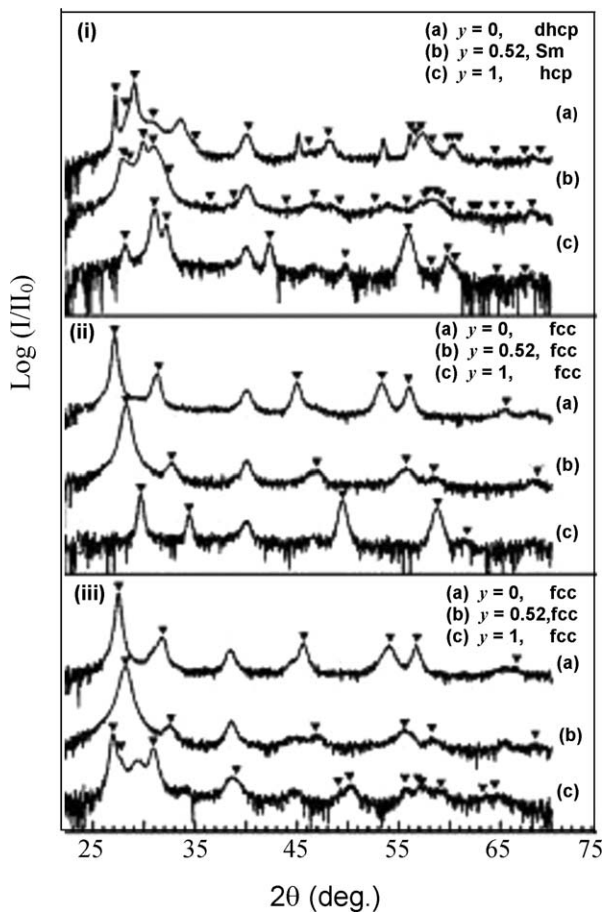


Fig. 92. X-ray diffractograms of $\text{La}_{1-y}\text{Y}_y\text{H}_x$ with (a) $y = 0$, (b) $y = 0.52$, and (c) $y = 1$ for (i) as deposited, (ii) dihydride ($x = 2$) and (iii) trihydride ($x = 3$) state (van Gogh et al., 2001).

and the molar volume of as deposited, hydrogen loaded and deloaded $\text{La}_{1-y}\text{Y}_y\text{H}_x$ alloy films for $0 < y < 1.0$ are shown in fig. 93. All the polycrystalline $\text{La}_{1-y}\text{Y}_y$ alloy films were found to be c -axis oriented. No disproportionation occurs upon hydrogen loading, and the preferential orientation was enhanced after the first loading. As-deposited $\text{La}_{1-y}\text{Y}_y\text{H}_x$ films ($x \approx 0.16$) were observed to have dhcp structure for $0 \leq y \leq 0.30$, Sm structure for $y = 0.46$, hcp + Sm structure for $y = 0.52$ and hcp structure for $0.67 \leq y \leq 1$. For comparing the lattice parameters as shown in fig. 93, $c = c_{\text{dhcp}}/2$ and $c = 2c_{\text{Sm}}/9$ were used. All the dihydrides were observed to have fcc structure. The lattice parameters of the dihydrides were compared with those of the as deposited and trihydride samples by defining $a = a_{\text{fcc}}/\sqrt{2}$ and $c = 2a_{\text{fcc}}/\sqrt{3}$. The trihydrides were observed to exhibit structural phase transition, for

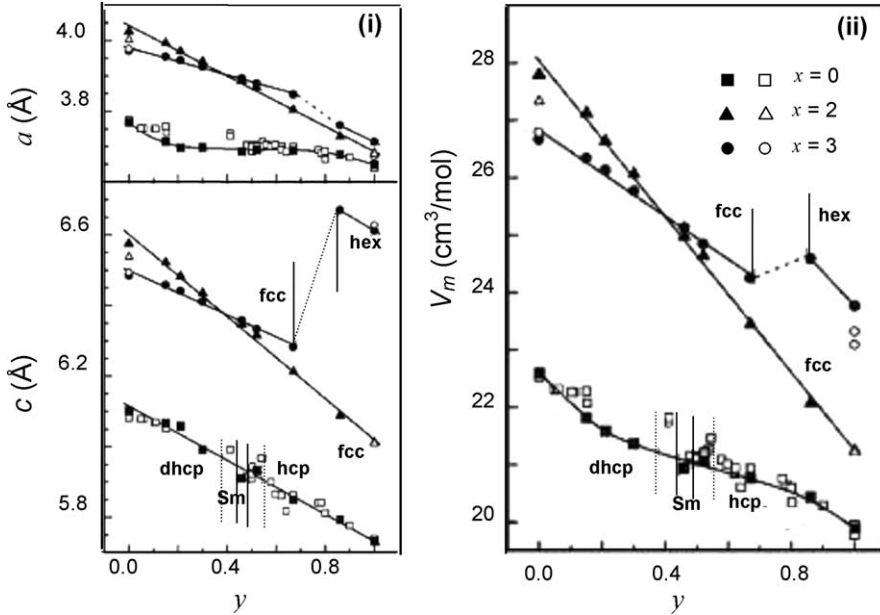


Fig. 93. Yttrium concentration (y) dependence of the (i) lattice parameters (a , c) and (ii) molar volume of $\text{La}_{1-y}\text{Y}_y\text{H}_x$ (V_m) for the as-deposited, dihydride and trihydride states. The open symbols are the literature values (Gschneidner and Calderwood, 1982; Mueller et al., 1968). The vertical lines represent the phase boundaries for the various structural phases (solid lines) and mixed phase region (dotted lines) (van Gogh et al., 2001).

$y < 0.67$ the films were fcc and for $y > 0.81$ the films were hexagonal. The hexagonal trihydrides ($y \geq 0.86$) were observed to have anomalously large c/a ratio, indicating structure different from hcp.

The variation in optical transmittance as a function of simultaneously measured resistivity in $\text{La}_{1-y}\text{Y}_y\text{H}_x$ alloy films is shown in fig. 94. For $y \leq 0.30$, the films were completely hysteresis free and have a sharp optical transition, whereas for $0.46 \leq y \leq 0.67$, the optical transition proceeds more gradually and some hysteresis was present. The films with $y \geq 0.86$, exhibit large hysteresis effects. Except for the film with $y = 0.67$ (not shown in the figure), which was on the borderline of the fcc-hex phase transition, for all other films the transmittance versus resistivity curves were observed to reach the final shape after the first absorption-desorption cycle. For the film with $y = 0.67$, the cycle was observed to become reproducible from the third loading cycle onwards.

The pressure-composition isotherm for a typical $\text{La}_{1-y}\text{Y}_y\text{H}_x$ ($\text{La}_{0.55}\text{Y}_{0.45}\text{H}_x$) is shown in fig. 95. In agreement with the optical and X-ray diffraction measurements, the isotherms were observed to be hysteresis free and without any plateau, indicating that these alloy films remain fcc for all $x > 2$. Van Gogh et al. (2001), fitted the isotherms to the Lacher's equation (Lacher, 1938) and calculated the partial molar heat of solution ΔH . For example for $\text{La}_{0.54}\text{Y}_{0.46}\text{H}_x$ alloy, the heat of solution ΔH was found to be -38.1 kJ/mole H.

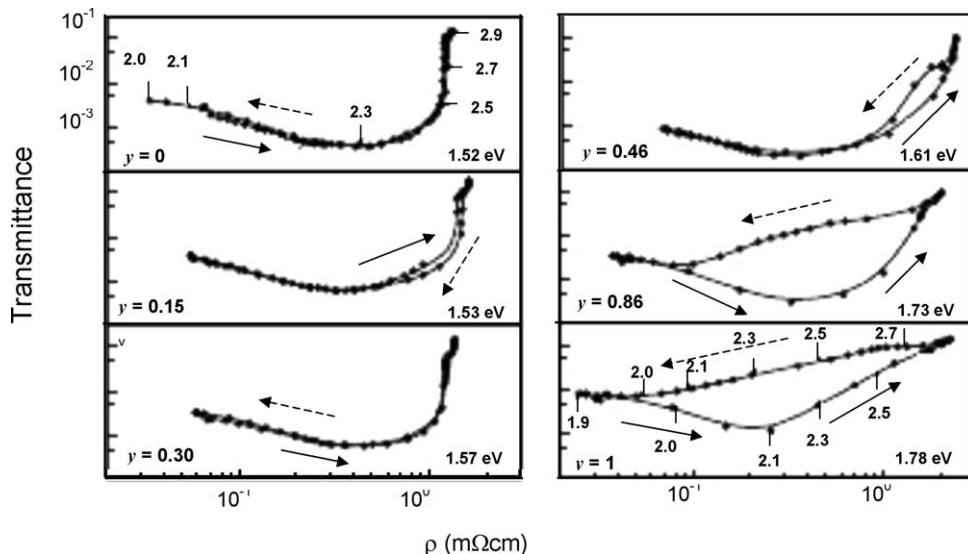


Fig. 94. Variation in optical transmittance as a function of resistivity during gas phase loading of $\text{La}_{1-y}\text{Y}_y$ (300 nm) films [having different values of y] during the second loading cycle. The transmittance for the photon energy for which the dihydride transmittance has its maximum are given. The hydrogen concentrations as determined electrochemically are given for $y = 0$ and $y = 1$ (van Gogh et al., 2000a, 2000b).

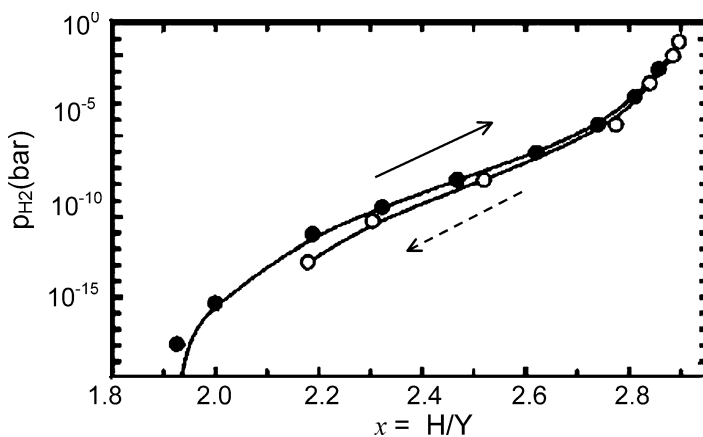


Fig. 95. Pressure-composition isotherms for $\text{La}_{0.55}\text{Y}_{0.45}\text{H}_x$ alloy at 295 K (van Gogh et al., 2001).

The dielectric function $\epsilon(\nu)$ of the as-deposited $\text{La}_{1-y}\text{Y}_y$ alloys obtained from ellipsometry after correction for the substrate and the Pd over layer are shown in fig. 96(i). To analyze the data quantitatively, van Gogh et al. modeled $\epsilon(\nu)$ using a sum of one Drude and three Lorentz

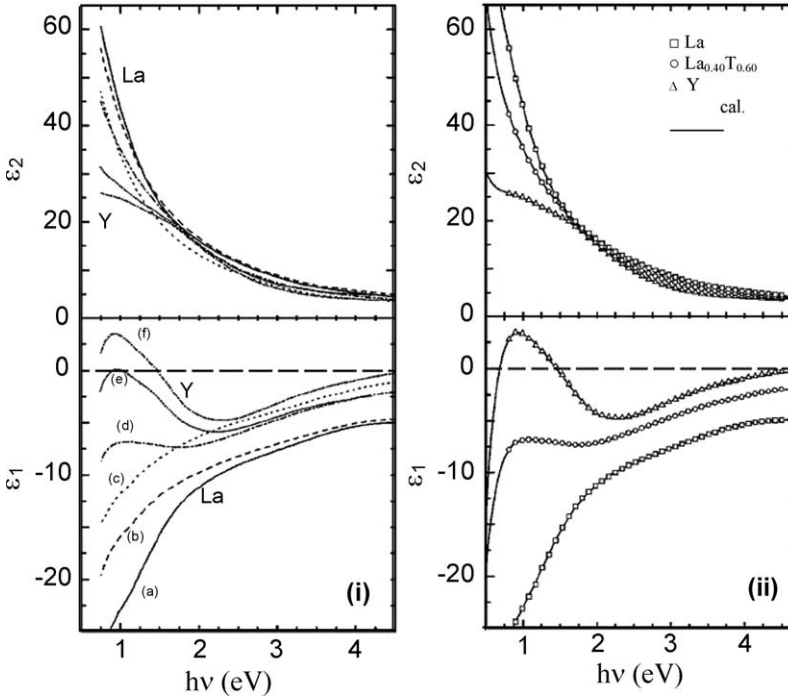


Fig. 96. (i) Real (ϵ_1) and imaginary (ϵ_2) parts of the dielectric constant of the as deposited $\text{La}_{1-y}\text{Y}_y$ films with $y = 0$ (a), $y = 0.25$ (b), $y = 0.46$ (c), $y = 0.50$ (d), $y = 0.81$ (e) and $y = 1$ (f) as determined from ellipsometry. (ii) The results of the fit using DL parametrization (solid lines) along with the measured values (open symbols) for films with three different Y compositions (van Gogh et al., 2001).

oscillators (LO). The results of the fit for three representative compositions are shown in the fig. 96(ii). After decomposition of $\epsilon(\nu)$ into free- and bound-electron contributions, it was observed that the interband properties were similar in La and Y. The difference in $\epsilon(\nu)$ was only caused by the interplay of the contribution of Drude and First LO. Both contributions were observed to be large and to have opposite signs in $\epsilon_1(\nu)$. The y dependence of the various Drude–Lorentz parameters was observed to exhibit a clear trend. First, the plasma frequency was observed to decrease linearly with y . Secondly, a non-linear behavior in the relaxation time was observed due to disorder. Third, the interband absorption was observed to shift monotonically towards blue upon increasing y , indicating a narrowing of bands caused by the 14% larger volume of La compared to Y. Van Gogh et al. argued that the volume effect was much larger than the broadening effect due to larger radii of 4sp5d orbitals of La as compared to the 3sp4d orbitals of Y. Similar effects have been observed in the dihydrides. Fig. 97(i) shows the dielectric functions for the $\text{La}_{1-y}\text{Y}_y\text{H}_2$ films obtained from the ellipsometry after correction for the substrate and the Pd over layer. To analyze the optical properties of $\text{La}_{1-y}\text{Y}_y\text{H}_2$, Drude Lorentz parametrization for $\epsilon(\nu)$ was performed [fig. 97(ii)]. For all alloys, the interband ab-

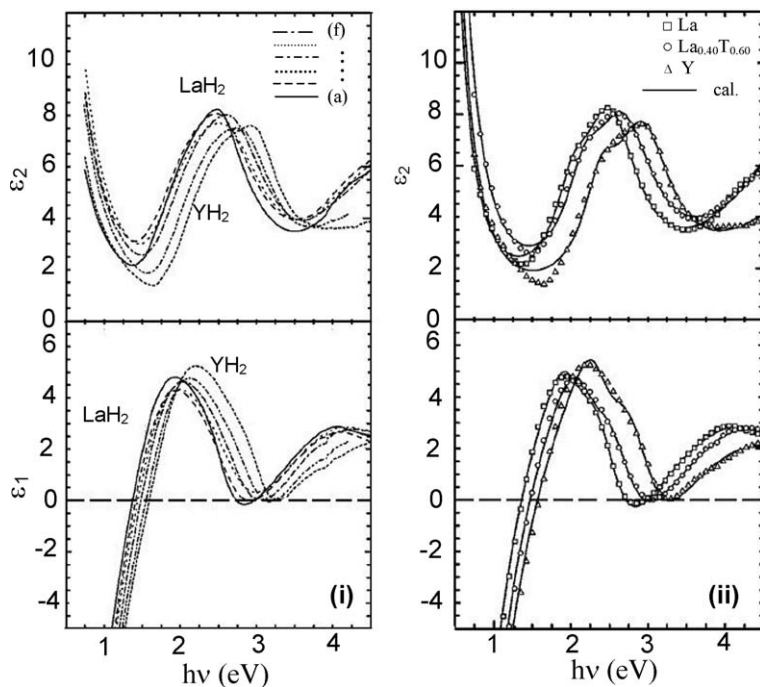


Fig. 97. (i) Real and imaginary parts of the dielectric constant of $\text{La}_{1-y}\text{Y}_y\text{H}_2$ films with $y = 0$ (a), $y = 0.25$ (b), $y = 0.46$ (c), $y = 0.50$ (d), $y = 0.81$ (e) and $y = 1$ (f). (ii) The results of the fit using DL parametrization (solid lines) along with the measured values (open symbols) for films with three different Y compositions (van Gogh et al., 2001).

sorptions were observed to exist below the plasma energy (which was typically at 4 eV). At low energy, a free-electron behavior was observed and around 2.5 eV interband absorptions were discerned. Around 4.0 eV, the onset of another interband transition was observed. As observed for the as-deposited state, the typical features were observed to shift to higher energies in the dielectric function of the dihydrides on increasing y . The structure in ϵ_2 around 2.5 eV was attributed to interband absorptions within the d-like complex band along Q, W–K and Σ in the first Brillouin zone. From the calculated band structures for YH_2 (Peterman et al., 1979) and LaH_2 (Ng et al., 1999) the onset for the interband transitions of 2.1 and 1.3 eV (i.e., a difference of 0.8 eV) were estimated, whereas from the Drude–Lorentz fits (van Gogh et al., 2001), a difference of 0.4 eV was estimated. The absorption above 3.5 eV was attributed to the interband transitions mainly between the parallel bands along Σ , where the lower band was d–s-like and the upper band was d-like (Weaver et al., 1979b). The sharp structure in ϵ_2 around 5 eV was attributed to the flatness of the lower d–p band near the K point. To investigate the effect of alloying on the optical window observed in YH_2 , van Gogh et al. (2000b, 2001) measured directly the optical transmittance and reflectance of the dihydrides for different alloys. Although the transmittance window was observed for all alloys, its magnitude was

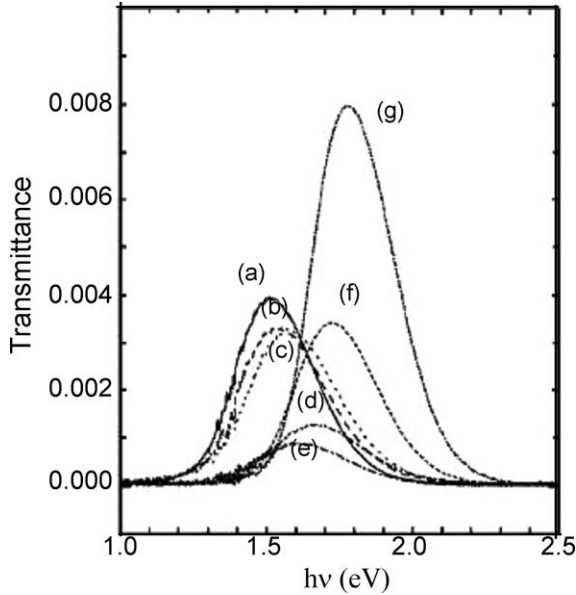


Fig. 98. Dihydride transmittance window for $\text{La}_{1-y}\text{Y}_y\text{H}_2$ films with $y = 0$ (a), $y = 0.15$ (b), $y = 0.30$ (c), $y = 0.46$ (d), $y = 0.67$ (e), $y = 0.86$ (f) and $y = 1$ (g) (van Gogh et al., 2001).

strongly suppressed upon alloying (fig. 98). A monotonic shift in the transmittance maximum from 1.52 eV for LaH_2 to 1.78 eV for YH_2 has been observed. The amplitude minimum, with an order of magnitude lower than for YH_2 or LaH_2 , was observed for $y = 0.46$. From the trend of the calculated transmittance of a Pd (15 nm)/ $\text{La}_{1-y}\text{Y}_y\text{H}_x$ (300 nm)/Suprasil stack using Drude–Lorentz parametrization of $\varepsilon(\nu)$, van Gogh concluded that the suppression of the dihydride window in $\text{La}_{1-y}\text{Y}_y\text{H}_2$ was caused by disorder with largest contribution coming from the optical absorption at energies much larger than 4.5 eV. Upon hydrogenation from $x = 2$, the variation in $\varepsilon(\nu)$ for two typical alloys and YH_x are shown in fig. 99, indicating qualitative similarity in the behavior of all alloys. The main trends followed are indicated by arrows in the figures. First, the free electron optical response was observed to disappear with increasing x (A). Second, the interband absorption around 2.5 eV was observed to be suppressed (B). Third, the second interband absorption peak in ε_2 was observed to shift to lower energies (C). Van Gogh et al. (2001) argued that the systematic lowering in energy of the interband transitions was not caused by the volume changes since LaH_x contracts for $x = 2 \rightarrow 3$, $\text{La}_{0.54}\text{Y}_{0.46}\text{H}_x$ expands slightly where as YH_x was observed to expand by large amounts. The origin of the trends was explained in terms of the band structures of LaH_2 and LaH_3 calculated by Ng et al. (1999). Firstly, it was argued that the decrease in the plasma frequency was consistent with the Kondo insulator picture of Ng et al. according to which for $x > 2$, every additional hydrogen binds an electron to the host metal into a sort of Zhang–Rice singlet, leading to a linear depletion of the free electron density. Secondly, the weakening and

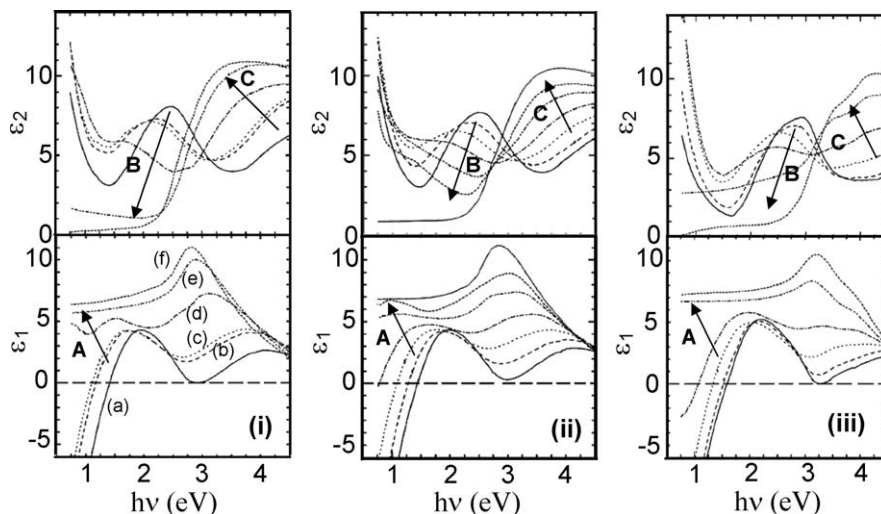


Fig. 99. Variation of real and imaginary parts of the dielectric constant as a function of hydrogen concentration [for $x = 2.0$ (a), $x = 2.3$ (b), $x = 2.4$ (c), $x = 2.5$ (d), $x = 2.8$ (e) and $x = 2.9$ (f)] of the $\text{La}_{1-y}\text{Y}_y\text{H}_x$ films with (i) $y = 0.25$, (ii) $y = 0.54$ and (iii) $y = 1$, upon hydrogen loading from the dihydride state. The main trends A, B and C in these curves indicated by the arrows are explained in the text (van Gogh et al., 2001).

downward shift in energy of the interband absorptions around 2.5 eV were attributed to the transitions between the d band along Q, W–K and Σ . It was argued that hydrogen addition causes the d band states to hybridize to much lower energies resulting in disappearance of the optical interband transitions. Adding hydrogen was observed to cause more and more disorder leading to band flattening, and consequently a red shift of the interband absorptions. The third effect observed was that the interband absorptions present in the dihydride at higher energies (>3.5 eV) shift towards lower energy upon increasing x . It was argued that the onset of these transitions determine the final appearance of trihydride state. The increased strength of the high-energy interband transitions was argued to originate from the flatness of the new band near Γ . The dielectric functions of the alloy in the trihydride state are shown in fig. 100. ϵ_2 was observed to increase strongly when the energy approaches the band gap. For $y = 0.81$ and $y = 1$ an extra absorption above the optical gap (near 4.2 eV) was observed. Depending on y , absorption below the optical gap was observed to extend to 1–1.8 eV below the optical gap. Similar effects were observed in the measured transmittance and have been attributed to the lattice defects. It was argued that in agreement with the *GW* calculations (van Gelderen et al., 2000) the dipole forbidden transitions become allowed because of the disorder. Van Gogh et al. estimated the optical band gap of the $\text{La}_{1-y}\text{Y}_y\text{H}_{3-\delta}$ both from ellipsometry measurements (by extrapolating ϵ_2 to zero) as well as modeling the transmittance edge (using Tauc's plots) [fig. 101]. The optical gap was observed to increase monotonically with y from 1.87 ± 0.03 eV for LaH_3 to 2.63 ± 0.03 eV for YH_3 . The discontinuity between $y = 0.67$ and 0.81 was observed to coincide with the structural phase transitions from fcc to hexagonal.

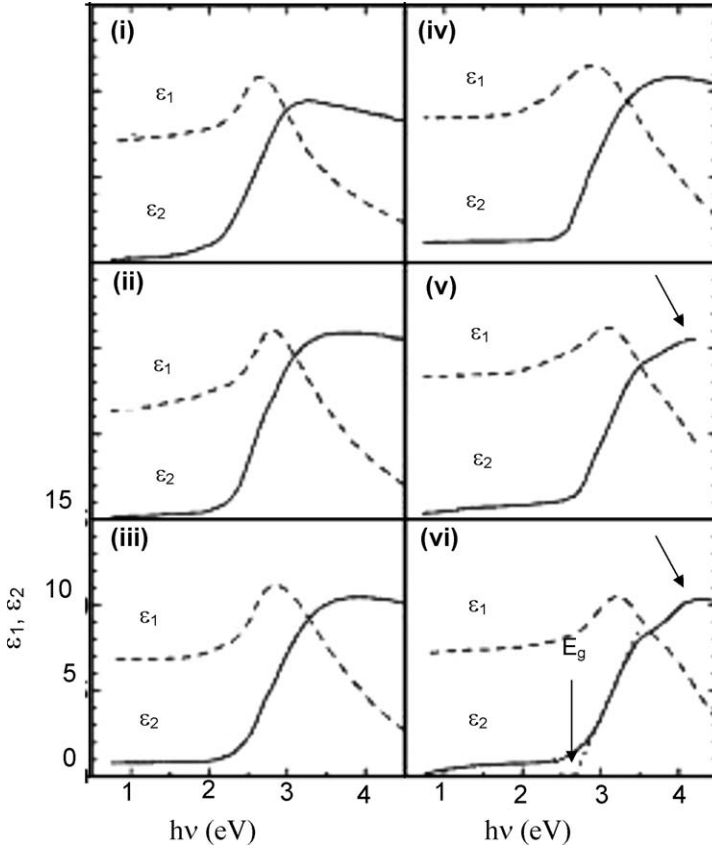


Fig. 100. Real (ϵ_1) and imaginary (ϵ_2) parts of the dielectric constants for the $\text{La}_{1-y}\text{Y}_y\text{H}_{2.9}$ films with $y = 0$ (i), $y = 0.25$ (ii), $y = 0.46$ (iii), $y = 0.60$ (iv), $y = 0.81$ (v), and $y = 1$ (vi) (van Gogh et al., 2001).

For the fcc trihydride region ($y \leq 0.67$) the optical gap was observed to increase non-linearly with increasing y , and a value of 2.33 eV was observed for $y = 0.67$. Van Gogh et al. argued that the shift in the band gap was due to volume effects because within one phase the band gap was observed to increase monotonically with decreasing molar volume and the discontinuity in the molar volume coincides with the discontinuity in the band gap.

2.4.2. RH_2 films: YH_2 films

By depositing a switchable mirror directly in the hydrided state, the stress development induced by the very first loading may be avoided and lower stresses were anticipated during subsequent cycling. Though Hayoz et al. (2000) deposited high quality epitaxial YH_2 films *in situ* at 227 °C on W(110) substrate in molecular beam deposition (MBD) system by utilizing ultra-clean atomic hydrogen source, the hydrogen induced optical and electrical switching in

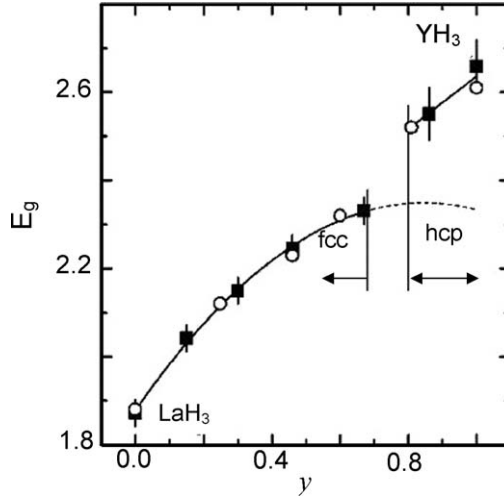


Fig. 101. Yttrium concentration dependence of optical band gap (E_g) of $\text{La}_{1-y}\text{Y}_y\text{H}_3$ determined by modeling the transmittance edge (■) and by taking the axis cutoff of ϵ_2 (○). The solid (dash) lines represent the second-order polynomial fit to the data with $y < 0.67$ suggesting an optical gap of 2.32 eV for the fcc YH_3 (Van Gogh et al., 2001).

these films was not studied. Dam et al. (2003) and Lokhorst et al. (2003) studied the hydrogen induced optical and electrical switching properties in pulsed laser deposited epitaxial [on (111)- CaF_2 at substrate temperature 500°C] and nanocrystalline [on quartz substrate at room temperature] YH_2 films and compared them with the MBE films. The as grown YH_2 films (100–300 nm) were capped with Pd over layer (10 nm). Dam et al. (2003) showed that using pulsed laser deposition (PLD) technique YH_2 films could be deposited without adding hydrogen to the deposition chamber. The dihydride formation occurs due to the hydrogen dissolved in the Y-target, which was preferentially liberated during the ablation process. AFM studies on the samples showed that the nanocrystalline films deposited at room temperature on quartz substrate have the lower surface roughness as compared to the epitaxial PLD and MBE films (Lokhorst et al., 2003). XRD studies of the YH_2 films grown on CaF_2 shows the preferential 111-orientation of the fcc structure and the texture analysis (a ϕ - ψ scan with 2θ fixed at the 111 reflection of YH_2) shows the six symmetry equivalent 111-directions, confirming the epitaxial nature of the films. The XRD measurements of nanocrystalline YH_2 reveal fcc structure of as deposited films. The textured measurements show a very broad band of symmetry equivalent 111-reflections, indicating that these YH_2 films were randomly oriented with only slight preference for a 111-surface orientation (Dam et al., 2003). From the comparison of the switching behavior in the MBE grown and *ex situ* loaded films with those of the PLD films, it was observed that both the electrical and optical contrast were reduced in the later as compared to the former due to the presence of $\text{Y}(\text{OH})_3$. On the other hand the nanocrystalline PLD films were observed to exhibit quenched hysteresis effects. A comparison of the plots combining the optical transmittance (at 1.9 eV) and electrical resistivity (fig. 102), mea-

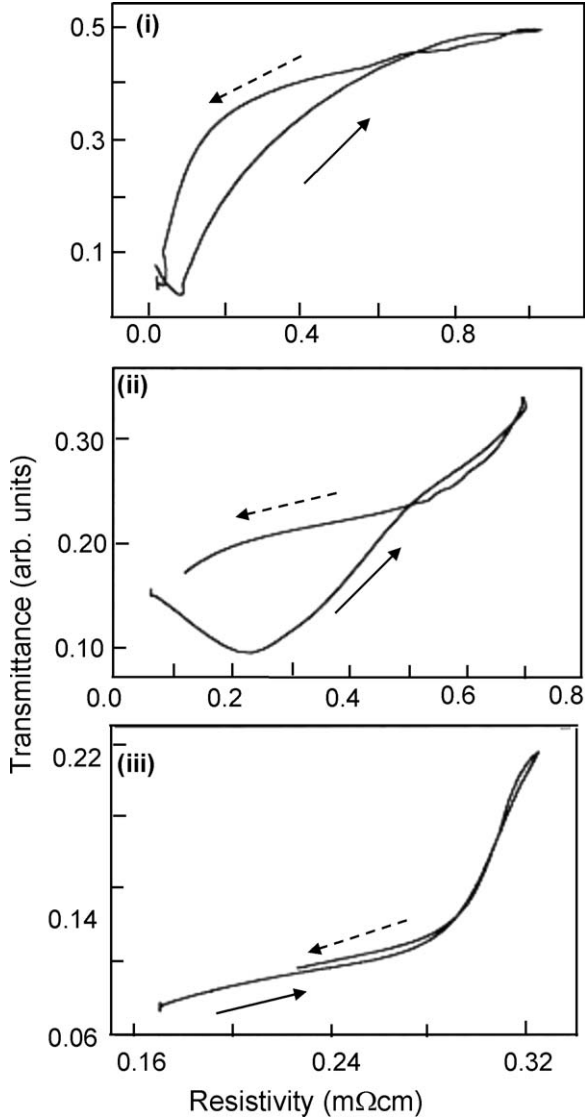


Fig. 102. Variation of optical transmittance (at 635 nm) as a function of electrical resistivity during hydrogen loading and deloading of Pd (10 nm) capped (i) Epitaxial MBE, (ii) Epitaxial PLD and (iii) Nanocrystalline PLD Y films (Lokhorst et al., 2003).

sured simultaneously during gas phase hydrogen loading and deloading, in the PLD films with the MBE grown and *ex situ* loaded YH₂ films clearly shows the absence of hysteresis in the nanocrystalline YH₂ films. The absence of hysteresis in the nanocrystalline films was

attributed to the absence of hydrogen induced structural phase transitions resulting in reduced stresses in the films.

It is worth mentioning that the cycle lifetime of a GdMgH_x films deposited by co-sputtering the metals in a 5 : 1 hydrogen/argon atmosphere (van der Sluis and Mercier, 2001; Mercier and van der Sluis, 2001; Janner et al., 2001) at room temperature was observed to be about 10 times better than a GdMg metal film (Janner et al., 2001) strongly indicating that the stresses and strains induced by the hydrogen loading and deloading were a major factor in the degradation of switchable mirrors.

2.5. Diffusion, electromigration experiments and isotope effect

2.5.1. Diffusion and electromigration of H

The first study of the diffusion and electromigration of hydrogen in RH_x was carried out by den Broeder et al. (1998). The dependence of optical properties and on hydrogen concentration and the high hydrogen mobility in metals was used for a real time visualization of hydrogen migration in rare earth metals. The experiments were done on Y films evaporated under ultrahigh vacuum conditions onto a transparent substrate (Sapphire or quartz) and capped with Pd over layer in such a way that some portion of Y was covered with Pd while others were uncovered. In their experiments, den Broeder et al. evaporated Pd in the form of a disc or one or more strips. Upon exposure to air, the uncovered portion of Y film was oxidized resulting in the formation of an impermeable Y_2O_3 layer. Areas covered with Pd were not oxidized and remained permeable for hydrogen. In a typical experiment, hydrogen gas (10^5 Pa) was introduced into the chamber containing the sample and equipped with optical window and a temperature control system. Using a white lamp behind this arrangement, the optical transmittance changes were monitored optically. Den Broeder et al. (1998) observed that upon hydrogen intake, the Y film underneath the Pd pattern immediately starts absorbing hydrogen atoms and within a few seconds yellowish transparent $\text{YH}_{3-\delta}$ was formed under the Pd covered region. It was argued that further hydrogen intake could only occur if H diffuses laterally into the Y underneath the impermeable Y_2O_3 layer. For the disc geometry chosen, hydrogen was observed to diffuse radially. As the hydrogen concentration x decreased from $x = 3$ beneath the Pd disc to $x = 0$ far from it, several hydride phases were formed. As each phase has a characteristic optical transmittance, H diffusion was observed to result in the formation of typical rings that expand with time t as \sqrt{t} . The inner ring corresponds to the transparent $\gamma\text{-YH}_{3-\delta}$ phase and the outer ring to the weakly transparent $\beta\text{-YH}_2$ phase (fig. 103).

Similar techniques were used to study the electromigration in switchable mirrors (den Broeder et al., 1998; van der Molen et al., 2000, 2002a, 2002b). Den Broeder et al. (1998) argued that the optical methods used for studying the hydrogen diffusion could be applied to the case of hydrogen migration in the presence of an electric field. In electromigration experiments the motion of hydrogen was influenced in two ways. Firstly, electric field was observed to exert a direct force ($\mathbf{F}_d = \mathbf{Z}_d e \mathbf{E}$) on H atoms; secondly, the charge carriers were observed to transfer momentum to hydrogen atoms, which act as scattering centers, resulting in the so-called wind force ($\mathbf{F}_{\text{wind}} = \mathbf{Z}_{\text{wind}} e \mathbf{E}$). In $\gamma\text{-YH}_{3-\delta}$ the direct force was expected to be

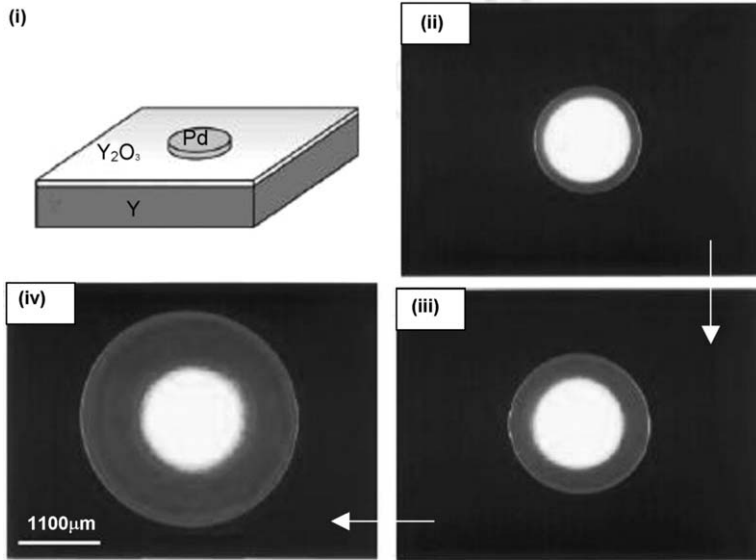


Fig. 103. (i) Schematic diagram of the sample (300 nm Y film covered with a Pd disc of 1.1 mm diameter and 30 nm thickness) used for radial hydrogen diffusion. The optical microscope images of the sample at various times [(ii) 1 day, (iii) 5 days, and (iv) 23 days] after exposure to hydrogen (10^5 Pa, 60°C) (den Broeder et al., 1998).

the dominant mechanism because of the relatively large electrical resistivity and hence was expected to provide information about the electronic state of the hydrogen in the $\gamma\text{-YH}_{3-\delta}$. Fig. 104 shows the electromigration of hydrogen in Y (200 nm thick, 1.5 mm wide) covered on left and right by Pd strips (30 nm), hydrogenated in 1 bar H_2 atmosphere at 110°C for 12 h and 10 min. In the absence of an electric field, the diffusion pattern was observed to be symmetric [fig. 104(ii)]. In the presence of an electric field, on the other hand, the diffusion fronts were observed to be asymmetric with much faster migration of γ -phase on the side of the negative electrode than on the positive electrode, confirming that hydrogen behaves as negatively charged impurity in $\text{YH}_{3-\delta}$. The conclusion was in agreement with the strong-electron-correlation theories by Ng et al. (1997, 1999) and Eder et al. (1997).

Van der Molen et al. (2000, 2002a, 2002b) extended the optical method of den Broeder et al. (1998) and studied electromigration of hydrogen in $\text{YH}_{3-\delta}$. The electromigration was studied in the deloaded polycrystalline YH_x films (200 nm) covered partially on one side with Pd (30 nm) and having a partially uncovered oxidized portion, during hydrogenation. From the local reduction of transmittance, the local hydrogen concentration was determined. Fig. 105 gives a plot of the evolution of hydrogen distribution in the presence of an electric field, clearly revealing that the distribution moves towards the negative pole and spreads out as a result of diffusion. Van der Molen et al. (2000, 2002a) analyzed the process by solving a linearized partial differential equation describing the process, and found good agreement between the experimental curves and analytical solutions. The effective valence Z^* ($=Z_d + Z_{\text{wind}}$) of H

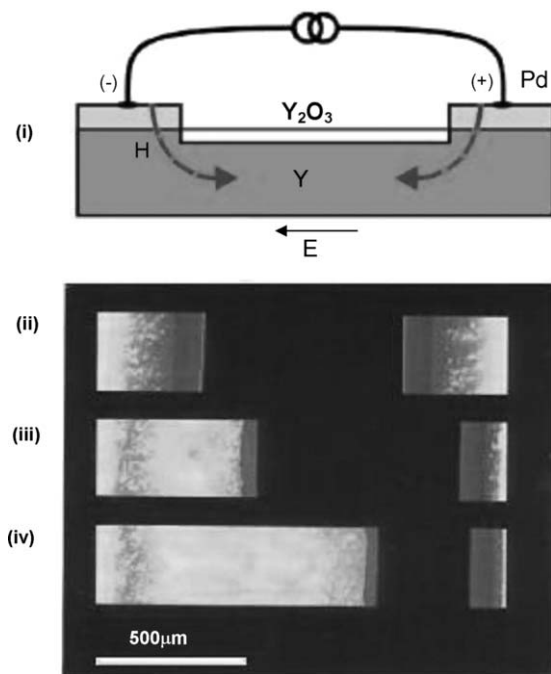


Fig. 104. (i) Schematic diagram of the sample (200 nm thick, 1.5 mm wide Y film covered with Pd strips of 30 nm thickness) used for lateral hydrogen diffusion. The optical microscope images of the sample after exposure to hydrogen (10^5 Pa, 110 °C for 12 h 10 min) in the absence of electric current (ii). The corresponding images when a dc current [(iii) 20 mA and (iv) 40 mA] was applied from right (+) to left (-) (den Broeder et al., 1998).

in $\text{YH}_{3-\delta}$ was found to be negative and its value was observed to be dominated by a huge wind-force term i.e., $Z^* \approx K/\rho$, with $K \sim -60$ m Ω cm which was three orders of magnitude as compared to that for a typical H in metals. It was observed that in an Arrhenius plot, the ratio of hydrogen (J_{H}) and electron fluxes (J_{e}) extrapolates to unity at infinite temperatures (fig. 106), indicating a one-to-one correlation of the hydrogen and electron hopping. Van der Molen et al. explained their results in terms of the strong electron correlation theories (Eder et al., 1997; Ng et al., 1997, 1999) which predicted each proton to bind two electrons in similar way as Zhang–Rice singlet. Another interesting observation, the so-called “hydrogen traffic jam”, was made during lateral electromigration experiments of the β -phase and γ -phase in the samples with an Al strip deposited opposite to Pd strip on the substrate prior to Y deposition (van der Molen et al., 2002b). It was observed that after an initial diffusion dominated behavior, both the fronts moved with the same velocity (fig. 107). Van der Molen et al. (2002b) explained this within the theory of irreversible thermodynamics, demanding continuity at the phase boundaries. It was observed that once the γ -front reached a local discontinuity in the electric field, H piles up in a highly concentrated trihydride region and a sort of H traffic jam is formed (fig. 108). This phenomenon was well described using a non-linear

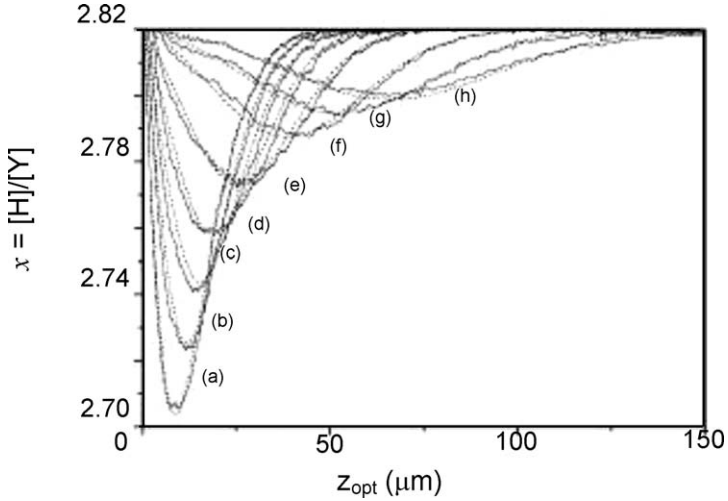


Fig. 105. Evolution of local hydrogen concentration (in 200 nm $\text{YH}_{3-\delta}$ film covered on left by a Pd strip of thickness 30 nm) as a function of diffusion front distance (z_{opt}) from the edge of the Pd strip taken at times (a) 0, (b) 62, (c) 155, (d) 279, (e) 527, (f) 1085, (g) 1705, and (h) 2387 s after the sample has been exposed to H_2 (1 bar, 70 °C) (van der Molen et al., 2000).

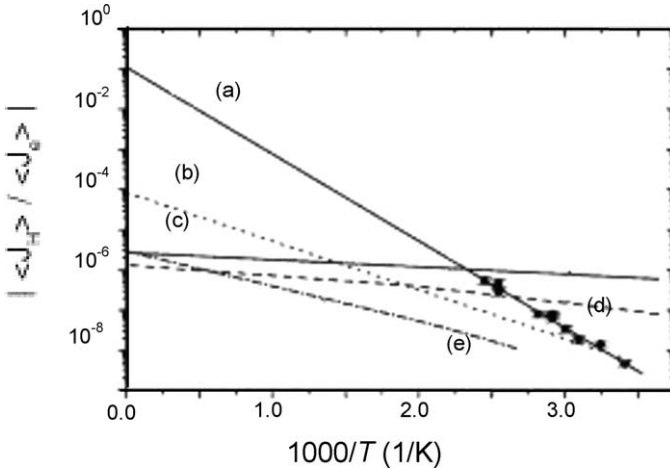


Fig. 106. Arrhenius plot of the ratio of hydrogen (J_{H}) and electron fluxes (J_{e}) for electromigration in $\text{YH}_{3-\delta}$ (a). For comparison, the plot for (b) $\text{PdH}_{0.1}$, (c) $\text{VH}_{0.01}$, (d) $\text{NdH}_{0.01}$, and (e) $\text{TaH}_{0.01}$ are also shown (van der Molen et al., 2000).

differential equation. Comparing the analytical solution to the experiment, an anomalously large wind force coefficient $K \approx -23 \text{ m}\Omega \text{ cm}$, which was much larger than the value usually observed in metal hydrides, was found. It was observed that in steady state conditions, very

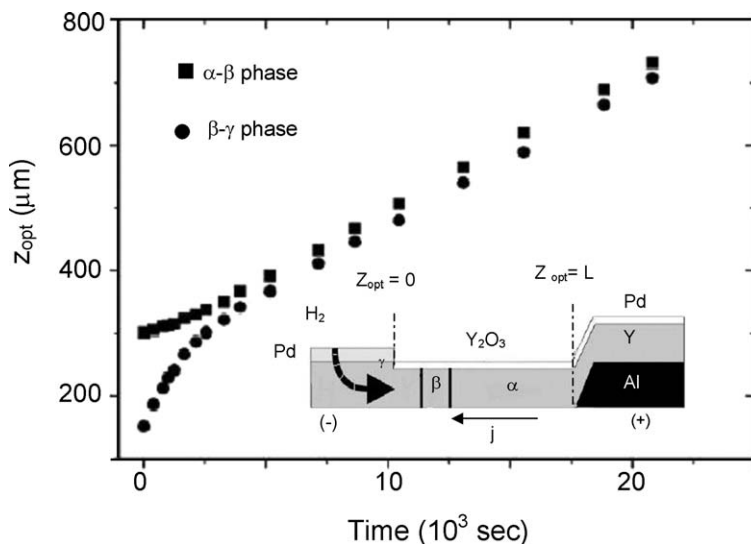


Fig. 107. Evolution of the diffusion fronts corresponding to the α - β phase boundary (■) and the β - γ phase boundary (●) in Pd (30 nm) capped Y (200 nm) film (deposited in the configuration shown in the schematic in the inset) when a current of $j = 1.37 \times 10^4$ A/cm² at 383 K is applied after the α - β phase boundary and the β - γ phase boundary were initially tuned to $z = 302$ μ m and 152 μ m, respectively in 1 bar H₂ (van der Molen et al., 2002b).

high chemical potentials, comparable to those in high-pressure experiments could be reached in the traffic jam regions.

2.5.2. Electronic structure of $YH_{3-\delta}$: Angle resolved photoemission spectroscopy studies

Hayoz et al. (2003) performed the angle resolved photoemission spectroscopy (ARPES) experiments on uncapped single crystalline Y (20 nm) films in the trihydride phase grown on W(110). The films were observed to exhibit well-defined low energy electron diffraction spots according to the hexagonal arrangement of Y in HoD₃-type structure but the H-induced superstructures were not present due to the weak scattering from H. ARPES measurements were performed with monochromatized He I $_{\alpha}$ line at room temperature with an energy resolution of 35 meV. The hydrogen composition in the films was determined via photoelectron diffraction and X-ray photoelectron spectroscopy and was found to be $x = 2.9$ (Hayoz et al., 2000). Fig. 109 shows the ARPES data measured along two high symmetry directions of the surface Brillouin zone. The dispersion was observed to be relatively weak in the $\bar{\Gamma}K$ and $\bar{\Gamma}M$ directions of the surface Brillouin zone. The d states that appear in Y and YH₂ were not observed in the YH₃ spectra. Five dispersion features were discernible (labeled a–e) with a broad and almost dispersion less maxima between 5.5 and 8.3 eV were observed for all angles. For comparing the experimental observations with theoretical calculations, Hayoz et al. (2003) also performed the band structure calculations using the full-potential linearized augmented plane-wave method within the generalized gradient approximation for the HoD₃-type struc-

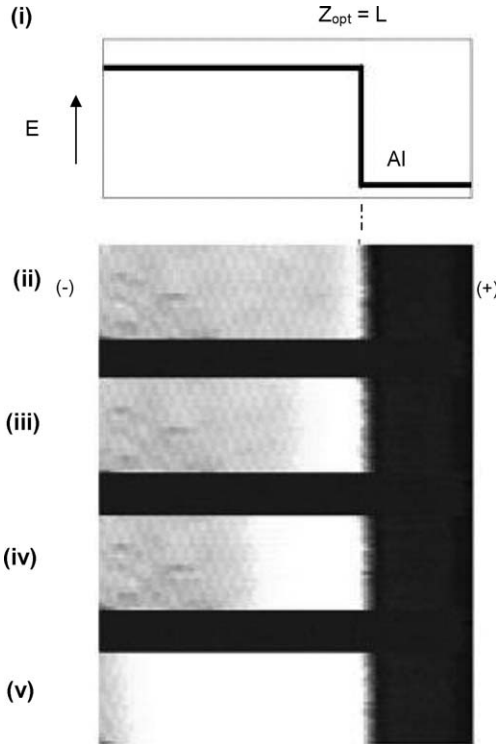


Fig. 108. The local electric field $E(z)$ has a discontinuity at $z = L$ as shown schematically in (i). When the γ -front reaches $z = L$, a “traffic jam” of H becomes visible, its tail moving opposite to the direction of the incoming H. (ii)–(v) Optical microscope images at $t - t_L = 130, 580, 990, 2370$ s ($j = 1.02 \times 10^4$ A/cm², $T = 383$ K) (van der Molen et al., 2002b).

ture (fig. 110). The band structure calculations were in good agreement with those proposed by Kelly et al. (1997a). However a set of flat H-induced bands between 1.8 eV and 4.6 eV, extending over the whole of the Brillouin zone, were observed. Hayoz et al. argued that the such set of flat bands gives rise to high density of states in this energy range, and thus lead to the high intensity features (shaded region in fig. 109) observed in the experiment. The energy width of the region in the experiment was observed to be in good agreement with the energy interval of the flat bands in the LDA band structure calculations. The only differences were a rigid shift in the valence band by ~ 1.5 eV (inferred from the free-electron-final state approximation) and the position of the flat bands (experimental occur 3.7 eV higher in binding energy). The conclusions from ARPES experiments were in good agreement with the LDA calculations but were in contrast to the model by Ng et al. (1999) according to which the strong electron correlation induced a band narrowing. Hayoz et al. (1998) argued that it was not possible to identify every individual band from the experiment due to the presence of large number of bands. Furthermore, based on the FEFS approximation, a rigid shift of the

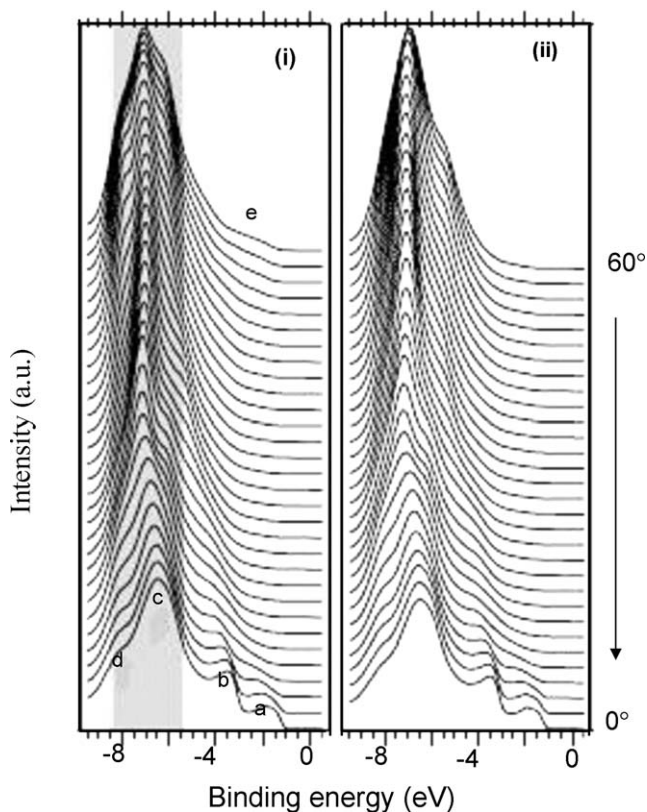


Fig. 109. Energy distribution curves taken along the (i) $\bar{\Gamma}\bar{K}$ and (ii) $\bar{\Gamma}\bar{M}$ directions of the surface Brillouin zone, collecting spectra up to 60° off-normal emission. Normal emission (0°) corresponds to $\bar{\Gamma}$; the \bar{K} and \bar{M} points are reached at approximately 17° and 15° off-normal emission, respectively, at 0 eV binding energy (Hayoz et al., 2001).

valence band towards higher binding energy by more than 1 eV was inferred, which was consistent with the *GW* calculations, and the opening of a gap. The downward shift of flat bands observed in the ARPES spectra was observed to support the model proposed by Eder et al. predicting a shift of the potential at H sites and retaining the broad H band.

2.5.3. Isotope effect

To verify the existence of broken symmetry structure as proposed by Kelly et al. (1997a, 1997b) (section 2.6), van Gogh et al. (1999) studied the optical and electrical properties upon H (D) loading in Pd (10 nm) capped Y (50 nm) films. Kelly et al. (1997a, 1997b) had argued that the zero point energy motion of the H (D) atoms is comparable to the symmetry breaking H (D) displacements. According to Kelly et al. the total energy difference between the metallic HoD₃-type structure and the broken symmetry structures was 11.7 meV per YH₃, which was

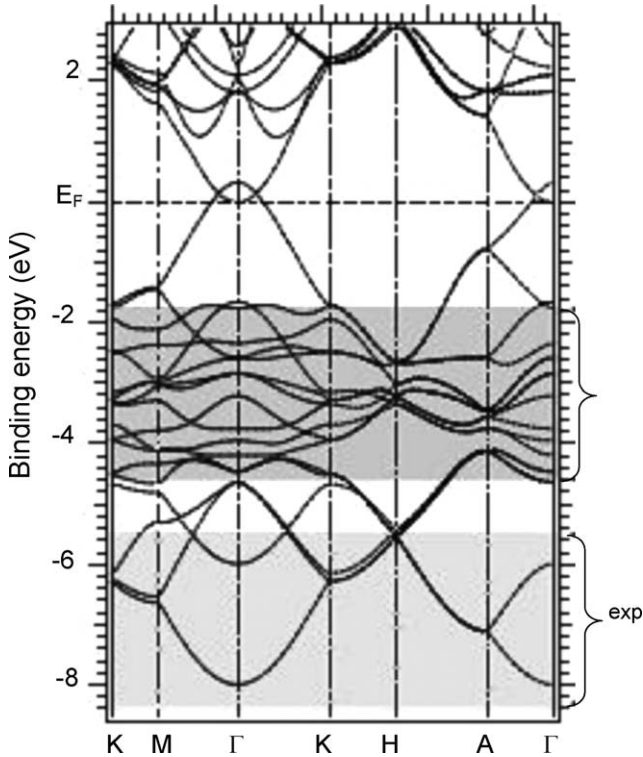


Fig. 110. LDA based band structure calculation for the HoD_3 -type structure. The region of flat H-induced bands are indicated by dark shaded region and the region where the experiment shows high density of states is indicated by light shaded region (Hayoz et al., 2001).

much smaller than the 57 eV of optical phonon modes in YH_3 corresponding to the motion along c -axis of the metal- and near-metal plane H atoms (which were mainly responsible for energy lowering in the broken symmetry structure). In YD_3 , the aforementioned optical phonon energies were ≈ 16 meV lower than in YH_3 , indicating a large isotope effect in the observed optical and electrical properties.

Van Gogh et al. (1999) loaded the films with H_2 (D_2) at 190 Pa and measured alternatively the optical transmittance and reflectance of the films, measuring simultaneously resistivity (using the *van der Pauw* technique). Once the stabilization in the hydrogen-induced properties was observed, the H_2 (D_2) gas pressure was increased in steps to 10^5 Pa. The H (D) concentration x in the YH_x (YD_x) film was estimated by relating the measured resistivity ρ with the $x(\rho)$ measured using the electrochemical method described by Kooij et al. (1999). Fig. 111 shows a comparison of optical reflectance and transmittance spectra as a function of hydrogen (deuterium) concentration in YH_x (YD_x) films. The H (D) concentration dependence of the electrical resistivity, as determined electrochemically is shown in fig. 112. Although the

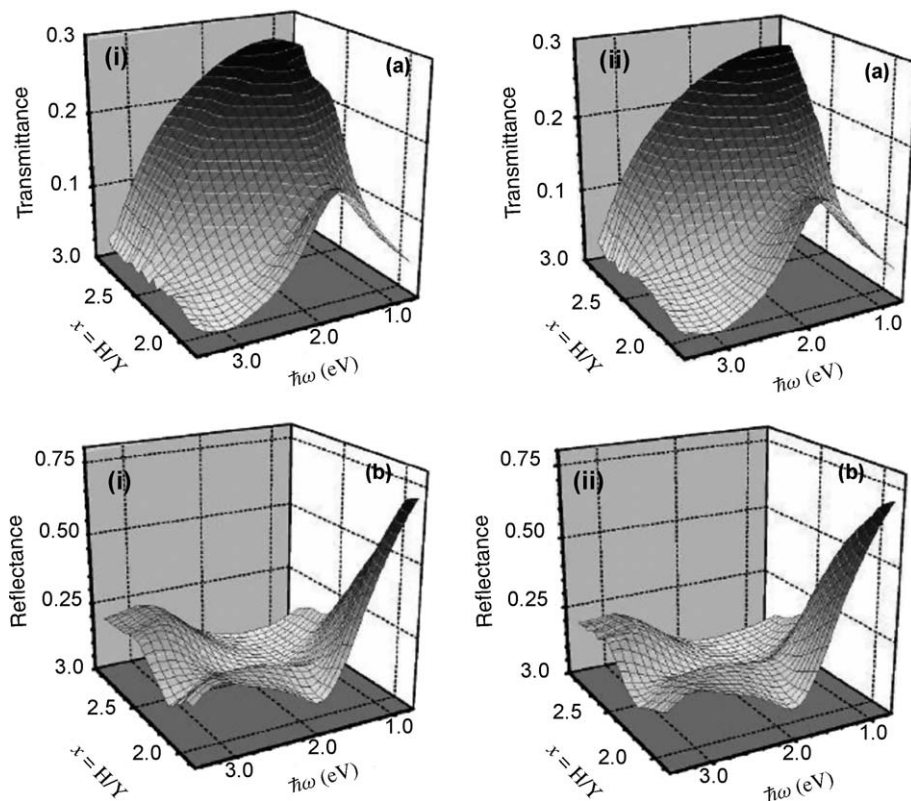


Fig. 111. Variation of optical transmittance (a) and reflectance (b) as a function of hydrogen concentration x for a Pd (10 nm) capped (i) YH_x (50 nm) film and (ii) YD_x (50 nm) film hydrogenated at RT in H_2 atmosphere (van Gogh et al., 1999).

resistivity of YD_x was systematically higher than that of YH_x , qualitatively both the materials were observed to behave similarly. In the dihydride state ($x \approx 2$), the reflectance was observed to have a minimum for $h\nu = 1.96$ eV. The high reflectivity at low energies was attributed to free electron (intraband transitions). The screened plasma energy of YH_2 at 1.64 eV (Weaver et al., 1979a) explains the sharp decrease of the reflectance around this energy. It was argued that at higher energies, the reflectance was caused by the interband absorptions from the conduction band into the higher d-derived bands as shown earlier by Peterman et al. (1979). As a result, at intermediate photon energies, neither a strong reflectance nor a strong absorption was observed, giving rise to the transmittance window, with a maximum at $h\nu = 1.80$ eV. With increasing x , the low energy reflectance decreases because the additional hydrogen atoms bind more and more free electrons. Finally, the transparent trihydride state is reached, having an absorption edge at ≈ 2.8 eV, which gives $\text{YH}_{3-\delta}$ its typical yellow color. From the detailed analysis of the optical reflectance near $h\nu = 3.1$ eV for $x_{\text{H(D)}} > 2.7$, van Gogh et al. (1999)

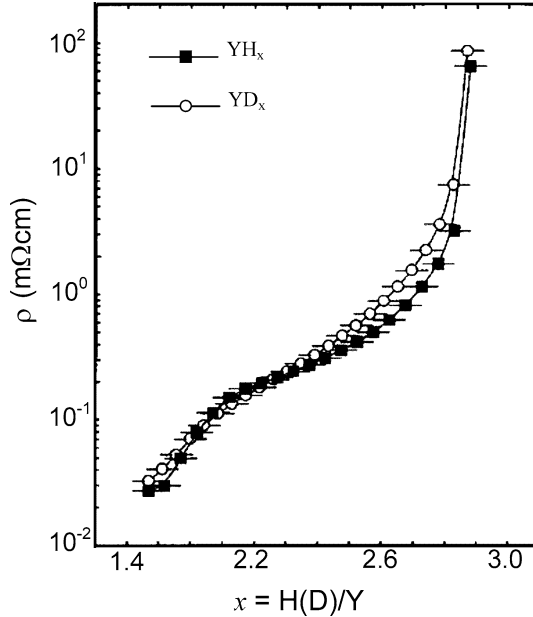


Fig. 112. Dependence of electrical resistivity on the hydrogen concentration in YH_x and YD_x (van Gogh et al., 1999).

found that the optical band gap of $\text{YD}_{3-\delta}$ was 35 ± 13 meV larger than that for $\text{YH}_{3-\delta}$. The difference in the band gap was explained in terms of the electron correlation approach proposed by Ng et al. (1999). Based on the theoretical calculations a difference in the optical gap of 39 meV between YD_3 and YH_3 was calculated. From the observations on the optical and electrical properties on YH_x and YD_x , van Gogh et al. (1999) concluded that the semiconducting nature of YH_3 (YD_3) is robust and is unlikely due to the rearrangement of the H (D) atoms in the Y-lattice as proposed by Kelly et al. (1997a, 1997b).

2.5.4. Evidence of ionic bonding in $\text{YH}_{3-\delta}$: Infrared transmittance studies

Electromigration studies discussed above showed that hydrogen in insulating $\text{YH}_{3-\delta}$ behaves as negative ion. However, the precise amount of charge transfer was not determined in these experiments. Y 3d core-level shift experiments by Osterwalder (1985) indicated charge transfer of 0.19 and 0.29 units per hydrogen atom in YH_2 and YH_3 , respectively. However, the technique used was surface sensitive and the measurements were performed in UHV so the stoichiometry of the compounds was questionable. Size arguments for the migrating hydrogen and the results of the less surface sensitive techniques like soft X-ray emission and absorption measurements were interpreted in terms of positively charged hydrogen (Hjörvarsson et al., 1999). To find the answer to questions regarding the sign and magnitude of charge transfer between Y and H, Rode et al. (2001) looked at the excitation of one-phonon modes by infrared

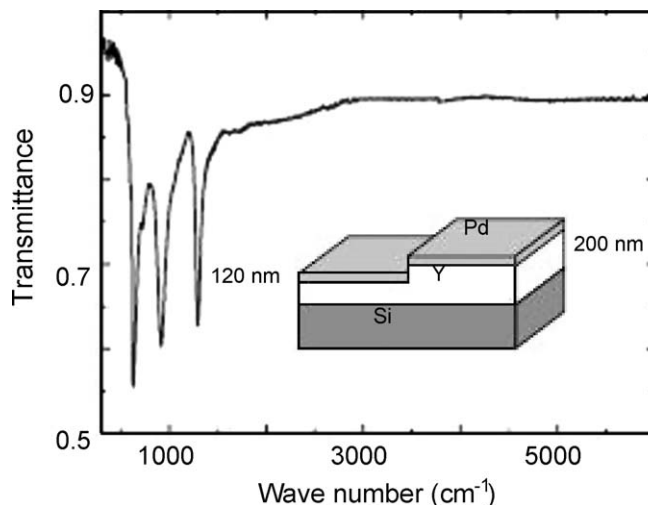


Fig. 113. Optical transmittance for the ratio of the transmittance spectra for $\text{YH}_{3-\delta}$ films of thickness 200 nm and 120 nm. The sample configuration is shown in the inset (Rode et al., 2001).

radiation. Rode et al. argued that the oscillator strength of the one-phonon excitations, the so-called Reststrahlen, was related to the difference of the dielectric function at frequencies far below and far above the phonon frequencies, which, in turn, was a measure of the effective atomic charge. The infrared transmittance spectra of $\text{YH}_{3-\delta}$ and $\text{YD}_{3-\delta}$ thin films were measured in the energy range from 300–6000 cm^{-1} , and the optical constants were evaluated by Kramers–Kronig analysis. To eliminate the effect of Pd overlayer and the substrate, the samples were prepared with the configuration shown schematically in the inset of fig. 113. Fig. 113 shows the transmittance for the ratio of the transmittance spectra for $\text{YH}_{3-\delta}$ films of thickness 200 nm and 120 nm. The estimated dielectric functions are shown in fig. 114. It was observed that the optical spectrum of $\text{YH}_{3-\delta}$ in the mid-infrared region was dominated by infrared-active one-phonon excitations. From the fit of the frequency-dependent dielectric conductivity and the dielectric loss functions with one Drude term and five Lorentz oscillators, the longitudinal and transverse optical-phonon frequencies were determined (fig. 115). The Born and Szigeti effective charges were calculated and the ionicities of the ions in the $\text{YH}_{3-\delta}$ were derived. Based on their experimental observations, Rode et al. concluded that the hydrogen does not enter as proton in $\text{YH}_{3-\delta}$ but that it is negatively charged, with a Szigeti effective charge of nearly $0.5e$.

2.6. Theoretical models for first generation switchable mirrors

The observation of the metal insulator transitions in RH_x thin films was not surprising as it had been predicted for the bulk samples by the pioneering work of Libowitz and Pack (1969, 1972), Vajda (1995), Shinar et al. (1988, 1990) and the early bandstructure calculations of Switendick (1970, 1971). Switendick (1970) calculated the electronic structure of YH_3 using

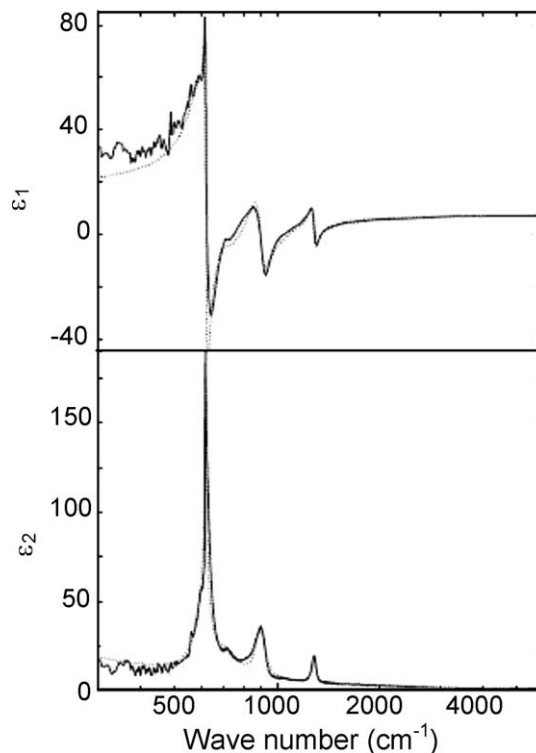


Fig. 114. Dielectric function of $\text{YH}_{3-\delta}$ in the near and mid infrared region (solid line). The fitted spectrum are shown by dotted line (Rode et al., 2001).

a non-self-consistent approximation and found an energy gap of 1.5 eV. However, a more sophisticated state-of-art self-consistent local density approximation (LDA), of the density functional theory (DFT), calculations by Dekker et al. (1993) and Wang and Chou (1993, 1994, 1995) predicted LaH_3 and YH_3 to be metals or semimetals. Wang et al. performed calculations showing that YH_3 in the so-called HoD_3 -type structure has a lower energy. In this structure, H atoms formerly at the octahedral sites move towards the metal atom planes, one being $0.07c$ above the plane, one being in the plane and one being $0.07c$ below it (the so-called Peierls distortion). The inequivalence of the three near-metal-plane H-atoms leads to a tripled unit cell and consequently to a three times smaller Brillouin zone. The DFT-LDA calculations for YH_3 in the HoD_3 -type structure, predicted a large overlap (~ 1.5 eV) of yttrium and hydrogen bands at the Fermi level (Dekker et al., 1993; Wang and Chou 1993, 1994, 1995). Similarly the best LDA calculations available for the LaH_3 predicted a tiny indirect band gap of 3 meV and a direct gap of 0.17 eV or a small band overlap (Dekker et al., 1993). Thus the observations by Huiberts et al. (1996a) of the large optical gap in YH_3 and LaH_3 and the observed increase in resistivity with decreasing temperature, which

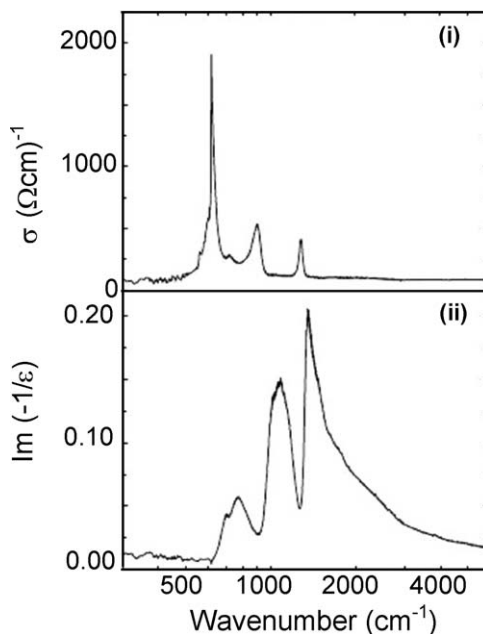


Fig. 115. Frequency dependent conductivity (i) and dielectric loss (ii) (Rode et al., 2001).

were incompatible with a metallic character, stimulated theorists to reconsider the nature of the band gap in YH_x and LaH_x systems in detail. The relevant models and calculations that have been developed to explain the semiconducting nature of the rare earth trihydrides are summarized below.

2.6.1. The “weak correlation” model: Broken symmetry structure

In the “weak interaction” proposal, Kelly et al. (1997a, 1997b) argued that the zero-value band gap found for LaH_3 made it very similar to Ge, which also has a vanishing gap in LDA. The reasons for the discrepancy resulted from the unjustified interpretation of the Kohn–Sham eigenvalues of the DFT as excitation energies. It was suggested that to calculate single particle excitation energies, a quasiparticle equation is to be solved in which the local, energy-independent exchange–correlation potential of DFT has to be replaced by a non-local, energy-dependent self-energy. By analogy with the conventional semiconductor, Kelly et al. (1997a, 1997b) argued that such a correlation should result in a band gap for the LaH_3 but would by itself be insufficient to resolve the much larger discrepancy found in YH_3 . Therefore it was suggested that in addition to quasiparticle correction, the electron–phonon coupling played a role in YH_3 . LDA total energy calculations in which the lattice structure is optimized predict that a symmetry lowering of HoD_3 -type structure leads to a slightly lower total energy without increasing the unit cell size. It was demonstrated that the lowest energy structure for YH_3 is one in which the metal plane H atoms are modulated in yet another way. It was shown that

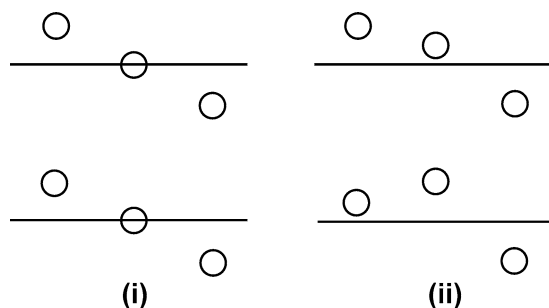


Fig. 116. Schematic outline of the location of the hydrogen atom in (i) the HoD₃-type structure and (ii) broken symmetry structure (van Gelderen et al., 2001).

two of the H atoms are still at $+0.07c$ and $-0.07c$ from the metal plane, but the remaining one is $0.03c$ from the plane. This structure was observed to have an energy of 70 meV per unit cell lower than that of HoD₃-type structure. Fig. 116 shows schematically the HoD₃-type structure and the broken symmetry structure proposed by Kelly et al.

Kelly et al. (1997a, 1997b) determined the ground state of YH₃ using the DFT with the LDA approximation and Car–Parrinello method. The calculations were carried out within the LDA for exchange and correlation. The valence electron wave functions were expanded in a plane wave basis and soft fully separable non-conserving pseudopotentials were used to describe the interaction of the valence electrons with the Y core electrons. The Y 4p states were included in the core and the non-linear core corrections were made in the treatment of the exchanged-correlation potential. The calculations were carried with the tripled unit cell containing 6 Y and 18 H atoms. The band structures calculated by Kelly et al. (1997a, 1997b) for YH₃ in the HoD₃-type and the broken symmetry structures are depicted in fig. 117. It was found that in the Jahn–Teller-like distortion of H atoms yielding the *P*6₃ structure, in which the threefold symmetry was conserved but both the inversion and the glide symmetries were broken, lead to a large gap in the band structure. The valence band maximum and the conduction band minimum were found along ΓA and ΓM , respectively, but the indirect gap of 0.75 eV was observed to differ only slightly from the direct gap of 0.8 eV along ΓM . As LDA calculations are known to systematically underestimate the band gaps of semiconductors and insulators by about 1 eV, and even predict a material to be a metal rather than a semiconductor as in the case of Ge, the band gap calculated by Kelly et al. was considered to be in qualitative agreement with the experimental data. However, the calculated symmetry-breaking hydrogen displacements were not confirmed by neutron diffraction experiments neither in bulk (Udovic et al., 1997a) nor in thin films (Remhof et al., 1997, 1999), whereas the HoD₃-type structure was deduced experimentally by various workers viz., Udovic et al. (1996), Miron et al. (1972), and Mannsman and Wallace (1964). This lead Kelly et al. (1997a, 1997b) to argue that the large zero point motion of hydrogen might blur the neutron diffraction measurements. In other words, it was argued that as the zero point energy of hydrogen is larger than the energy barrier separating the global energy minima in parameter space, the H atoms probe the minima (which corresponds to an insulating state) as well as the maxima (which correspond to a metallic state)

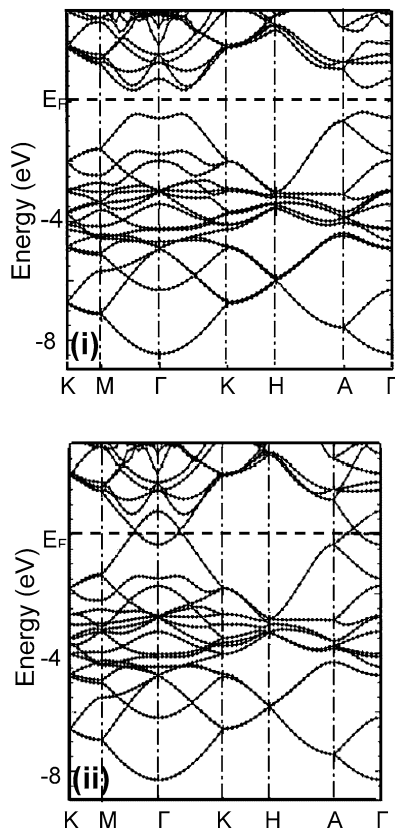


Fig. 117. Band structure for YH_3 for (i) the HoD_3 -type structure and (ii) broken symmetry structure (Kelly et al., 1997a, 1997b).

leading to a state which is insulating but in which the hydrogen atoms are, on an average, in positions apparently corresponding to the HoD_3 -type structure. However, van Gogh et al. (1999) argued that if the zero point motion was the key ingredients to explain the neutron diffraction results, then one expects to see a clear difference between YH_3 and YD_3 . In sharp contradiction to this, van Gogh et al. (1999) observed negligible difference in the metal-insulator transitions as well as the optical properties of the insulating state on the hydrogen mass, questioning the importance of the broken symmetry structure for the insulating ground state of YH_3 . Later van Gelderen et al. (2001, 2003a, 2003b) showed that neutron diffraction spectroscopy data could be more easily interpreted in terms of a broken symmetry structure than in terms of the HoD_3 -type structure. Kierey et al. (2001) were the first to give evidence of the broken symmetry structure based on the Raman effect studies of optical phonons in YH_3 and YD_3 . However, van der Molen et al. (2001) observed that the yttrium trihydride formed due to disproportionation of the $\text{Y}_{1-z}\text{Mg}_z$ alloy films upon hydrogenation has fcc structure

and is transparent insulator with properties similar to the hcp $\text{YH}_{3-\delta}$, suggesting that there is probably very little connection between the structure and optical transitions.

2.6.2. The “strong correlation” model

A much different approach was introduced by Eder et al. (1997) and Ng et al. (1997, 1999). Both the groups utilized the rather special properties of the H^- ion. The trihydrides were viewed as an H^- lattice embedded in the rare earth metal lattice. It was expected that, as a direct consequence of the large on-site repulsion between the two electrons near the same proton in H^- ion, strong correlation effects would be especially large in YH_x and similar rare-earth hydrides. This repulsion is reflected in the radius of the H^- ion that is about 3 times larger than for a neutral H atom and its ionization potential, which is only 0.7 eV as compared to 13.6 eV for neutral H. Taking LaH_x as a prototype for these compounds, Ng et al. (1997, 1999) used the special properties of the H^- ion in two ways. First, it was assumed that H^- was a bound state within LaH_3 and the Chandrasekhar wave function was then used to calculate the hopping integral within the sublattice of H^- ions. In this way, the correlation effects were incorporated in the width of the H-like bands. Second, Ng et al. (1999) postulated that each H site is occupied by at least one electron. This was justified by the large binding energy of electron in a neutral H atom. Ng et al. (1999) developed a many-body theoretical model to describe the H^- ion lattice in rare earth hydrides by using LaH_x as a prototype for these compounds. The electronic structure of the metal hydrides was described in the large U -limit Anderson lattice model. To calculate the band structure of LaH_3 , Ng et al. (1999) used tight binding fit to LDA band structure to find the essential parameters. Then, the H–H hopping integrals were replaced with the values for the H^- sublattice that they calculated. Since the latter were smaller, it lead to smaller width of the H-like bands. To determine the ground state of LaH_3 subjected to the constraints mentioned above, the so-called Gutzwiller method was utilized. In this variational approach, the hydrogen hopping integrals were renormalized by a Gutzwiller factor g . Since $0 \leq g \leq 1$ ($g_t = 0.78$ for tetrahedral H; $g_o = 0.70$ for octahedral H), the width of the H^- like bands were further reduced. This resulted from the restricted freedom in excursions caused by the constraints. The main difference between the band structure by Ng et al. and the LDA results lies in the width of the H^- like valence bands. In Ng’s calculations, the correlation effects caused the electrons to “stay away” from each other, resulting in the H^- like bands to be so narrow that the overlap with the Y-like conduction band was removed. Fig. 118 gives the band structure of the LaH_3 calculated by Ng et al. (1999) by taking into account the strong correlation effects. The resulting gap was between 1.5 and 2.1 eV for LaH_3 depending on whether the crystal field was included in estimating the H–H hopping integrals or not [fig. 118(i) and (ii), respectively]. Ng et al. argued that the opening of the energy gap at the chemical potential was primarily due to the strong electron correlations in the H^- ions, which reduces the H^- bandwidth. In addition, the large electron–electron Coulomb repulsion on the H^- ion that restricts the electronic state to exclude the empty electron state at any H site, further reduces the H^- bandwidth. Ng et al. (1999) also studied the variation of band gap in LaH_3 as a function of lattice constant. It was observed that with decrease in the lattice constant, there was an increase in the electron hopping matrix elements between the H ions and thus in the H^- bandwidth leading to reduction

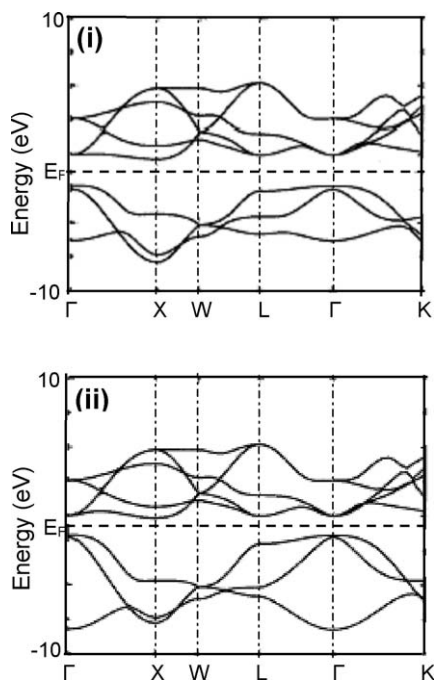


Fig. 118. Band structure for LaH_3 calculated by Ng et al. if (i) the crystal field is included in estimating the H–H hopping integral and if (ii) the crystal field effect is not included (Ng et al., 1999).

of the gap and eventually to the closing of the gap indicating that under pressure LaH_3 would undergo a insulator to metal transition. Based on the strong electron correlation model, Ng et al. proposed that the mechanism of the metal–insulator transition in LaH_3 could be understood by approaching from either the metallic dihydride (by introducing an extra H atom in LaH_2) or from the insulating trihydride (by localized vacancy state in LaH_3). It was argued that starting from LaH_2 , introduction of a neutral H atom into the H_{oct} site creates an $s = 1/2$ magnetic impurity that couples the conduction electron spins. The hybridization between the H and La orbitals results in the outer electron in H^- ion to fluctuate between the H_{oct} site and the surrounding La site. Because of the symmetry, only two La 5d e_g orbitals are coupled to the H 1s (H_{oct}) electron density. In this description, the material with all the octahedral sites occupied (LaH_3) was viewed as Kondo insulator with a large band gap. This conclusion was consistent with the model proposed by Eder et al. (1997). In the second approach, removal of neutral H atoms introduces vacancies at octahedral sites, which donate electrons to the conduction band. The elementary entity when a H atom is removed from the insulating LaH_3 was considered to be the octahedral vacancy, which is highly localized electronically due to the strong hybridization between the H 1s and its neighboring La 5d e_g orbitals. In a conventional semiconductor, the impurity state is described by an effective-mass theory, and the result is a hydrogen like bound state with effective Bohr radius ~ 10 nm due to the light effective elec-

tron mass and the large dielectric constant. The critical impurity concentration at which the system becomes metallic is given by the Mott criterion. And since the interatomic distances were smaller than the Bohr radius, the critical impurity concentration is very small ($\sim 10^{-3}$). Ng et al. argued that the vacancy state in $\text{LaH}_{3-\delta}$ was very different. Experiments of Huiberts et al. (1996a, 1996b) and Shinar et al. (1990) showed that the semiconducting states extend to a critical impurity concentration of 0.25 for $\text{LaH}_{3-\delta}$ and still larger for $\text{YH}_{3-\delta}$, suggesting very localized impurity states. Ng et al. (1997) proposed that vacancy states in $\text{LaH}_{3-\delta}$ were very localized La 5d e_g orbitals centered at the vacancy with the s-wave symmetry. It was argued that the La 5d e_g and H_{oct} electrons hybridize strongly to form bonding (mainly H) and antibonding (mainly e_g) states. A vacancy of H_{oct} breaks the bonds locally and the e_g electron becomes locally non-bonding, which has much lower energy than the antibonding e_g states away from the vacancy. As a result, in addition to serving as a positive charge center as in conventional n -type semiconductor, the octahedral H vacancy creates a potential well for the e_g state electron. The latter is non-perturbative and is responsible for the unusual concentration dependence of the semiconductor. It was concluded that the H_{oct} vacancy electron states were highly localized and they were well within the band gap. It was found that the s-symmetric octahedral e_g state has an energy -0.38 eV below the La 5d conduction band at the Γ point which is a t_{2g} state and was decoupled from the vacancy state and therefore the electrons were supposed to occupy the less energetic vacancy state instead of the conduction band, implying an insulating ground state for $x \leq 3$. It was argued that when more number of vacancies were created, more localized states were formed within the band gap and the material would become metallic when the localized states start to overlap with each other.

Eder et al. (1997) investigated the influence of electron correlations in H^- on the overlap between the Y and H orbitals. The key ingredient in their approach was the size of the hydrogen orbital, which depends strongly on the electron occupation; H^- ion being much larger in size as compared to the neutral H atom. A neutral H atom in YH_3 lattice has (due to small spatial extent of the one-electron orbital) relatively small overlap integral (ζ_1) with Y neighbors, i.e., there is not much gain due to hybridization. If the H atom captures an electron from the Y-like conduction band to form the H^- ion, the overlap with the neighboring Y atoms is significantly increased ($\zeta_2 > \zeta_1$) due to the much larger extent of the two-electron wave function. Simultaneously there is some energy loss due to the extra Coulomb repulsion at the H-site. Eder et al. argued that the lowering of the kinetic energy due to the extra hybridization could be larger than the energy increase due to Coulomb repulsion (U). In other words due to the so-called “breathing” property of H, the configuration consisting basically of the H^- like ions and Y^{3+} ions is stable. Since there are no electrons left in the Y-like conduction band, this system was expected to be insulating. The gap was determined by the energy difference between the two-electron state on one hand and the situation in which one electron is at the H site and one is in the Y-like conduction band on the other. For more explicit calculations, Eder et al. (1997) employed a Hamiltonian in which the occupation dependence of the Y–H overlap was introduced. It was shown that for reasonable values of U and ζ_2/ζ_1 ($0.5 \text{ eV} < U < 10 \text{ eV}$ and $\frac{5}{4} < \frac{\zeta_2}{\zeta_1} < 5$) the new Hamiltonian “induces” a gap in the YH_3 band structure.

On comparing the electron addition and removal picture as proposed by Eder et al. with the LDA band picture, one can clearly observe that the valence band has moved down by several

eV so that a gap has opened. This was in clear contrast with the results of Ng et al., which implied a narrowing of the H^- like bands. This demonstrated that though both groups started with a similar picture of H^- ion, different aspects of the electron correlation in H^- were used to arrive at an insulating trihydride state. Ng et al. stress on H^- – H^- overlap where as Eder et al. make use of the Y–H overlap. The advantage of the models by Ng et al. and Eder et al. is that they provide a real space microscopic picture of the H^- like states as well as of the H vacancy states in $LaH_{3-\delta}$ and $YH_{3-\delta}$. In the H^- like state, one electron is rather localized close to the proton whereas the other is at a much larger radius, “race tracking” the neighboring Y orbitals. This situation is somewhat similar to the Zhang–Rice singlet binding two holes in the CuO_2 planes of the high- T_c superconductors. When H atom is removed from the YH_3 , one electron is left at the H vacancy site, trapped in a s-like orbital formed by the ligand orbitals. The radius of this state is approximately half a lattice spacing that is very small compared to the situation usually encountered for donors in semiconductors. To induce the insulator–metal transition, one needs significant overlap of the vacancy wave functions. Due to the small spatial extent of the vacancy states, this happens at very high vacancy concentrations only. This is consistent with the experimental data, which show that $YH_{3-\delta}$ is insulating even for δ as large as $\delta \approx 0.2$.

As already discussed in the previous sections, electromigration experiments by den Broeder et al. (1998) and van der Molen et al. (2000, 2002a, 2002b) confirm that hydrogen in $YH_{3-\delta}$ behaves like a negative ion. Infrared transmission spectra by Rode et al. (2001) also lead to conclusions that significant charge transfer from yttrium to hydrogen takes place. It was found that hydrogen does not enter as proton in the compound, but that it is negatively charged, with an effective charge of approximately $-0.5e$. In addition, angular resolved photoemission spectroscopy (ARPES) studies by Hayoz et al. (2003) bear the signature of strongly correlated electron system. Hoekstra et al. (2001, 2003) and Roy et al. (2002), found unusually large critical exponents in scaling that hint to strong electron correlations.

2.6.3. Recent calculations

The importance of electron correlation effects were taken into account in *ab initio* band structure calculations based on *GW* approximation which explicitly included many-body effects. In this approach, the electron self energy was computed via a truncated expansion in terms of a Green’s function G and the screened Coulomb interaction W .

Miyake et al. (2000) studied YH_3 in the cubic BiF_3 -type and hexagonal LaF_3 -type structures using electronic structure data derived from the linear–muffin–tin–orbital (LMTO) method within the atomic-sphere approximation. They calculated the quasiparticle band structure within the *GW* approximation. In addition to the non-self consistent procedure, a semi-self consistent procedure was employed in calculating the self-energy. It was found that the main effect of self-energy was to raise the Y-4d like conduction band. The response function and the self-energy were expressed as the product of the wave functions. For BiF_3 -type structure, the band structure was calculated with an $8 \times 8 \times 8$ k -point mesh and for LaF_3 -type structure with a larger unit cell, $6 \times 6 \times 4$ k -point mesh was utilized. In BiF_3 -type structure, the Y atoms form the fcc structure. Two hydrogen atoms (per each Y atom) are at tetrahedral interstitial sites and the third occupies the octahedral interstitial site. LDA density of states for YH_3 in this structure showed that the valence band was predominantly hydrogen 1s with a

mixture of Y (5s, 5p and 4d) whereas the conduction band was dominated by Y 4d with some mixing of hydrogen 1s. The hydrogen band was quite broad with a width extending to about 10 eV, in sharp contrast to the value of U estimated by Eder et al. (1997). The band structure obtained from the LDA and the GW approximation are given in fig. 119(i). It was observed that the GW correction does not change the valence band too much, whereas the self-energy correction was observed to be much larger for conduction band (~ 2 eV). LDA band structure showed band overlap at the Γ point of 0.8 eV. The highest occupied state, which was triply degenerate and of the Y 4d character, was observed to show an upshift of 2.2 eV upon adding self-energy contribution in the GW approximation. On the other hand, the lowest unoccupied state with the H 1s character was observed to change by 0.3 eV, resulting in reversal of the order of the two states and consequently the quasi particle band becoming insulating with a gap at Γ point of 1.2 eV. Since the starting Hamiltonian was with a band overlap of almost 1 eV, Miyake et al. (2000) shifted the Y 4d LMTO orbital after self-consistent LDA calculations and did an extra calculation for one iteration. Starting from the *shifted* Hamiltonian, the self-energy correction was estimated and correction was added to the *unshifted* LDA eigen values. It was observed that in the quasiparticle band structure calculated by this procedure, the valence band was unchanged while the conduction band was raised resulting in a band gap of 1.9 eV. A study of the shift in the GW gap as a function of the gap of the shifted Hamiltonian (from which self-energy is calculated) showed a monotonic increase in the former as a function of later. At a large gap in the *shifted* Hamiltonian, the self-energy and hence the GW gap was observed to decrease. The two gaps were observed to match at a value of 3.2 eV. For the *shifted* and the *unshifted* case, the valence bandwidth was observed to be 10.5 eV and 10.2 eV, respectively as compared to that of 10.7 eV for LDA. To investigate whether the semiconducting state was structure dependent, Miyake et al. (2000) performed similar calculations for YH_3 in LaF_3 -type structure, in which the Y atoms form a hcp lattice, and among the three hydrogen atoms per each Y atom one is on the metal plane and the other two occupy the tetrahedral sites between the two metal planes. The band structure calculated is shown in fig. 119(ii). LDA bands were observed to be semimetallic with a band overlap of 1.4 eV. As observed for the BiF_3 -type structure, the conduction band was observed to shift (by 2 eV) by the self-energy, whereas the valence band was observed to remain unchanged. However, the shape of the band was modified in the occupied part of the H-K and M-L lines. It was found that the self-energy correction raises the energy by about 1 eV when the state was of tetrahedral hydrogen character while a downward shift occurs if the state has little tetrahedral hydrogen component. The net contribution of the self-energy contribution was observed to decrease the band overlap from 1.4 eV (LDA) to 0.8 eV (GW approximation). The decrease of the band overlap was observed to change the charge density and hence the Hamiltonian was shifted so that the initial band structure is close to the real one. This procedure resulted in a gap between the Γ point (valence state) and the K point (conduction state) of 1.1 eV. Interestingly, the opening up of the gap was found to be as a result of the raise in the unoccupied Y 4d-like conduction band rather than due to narrowing of H-like valence band. Miyake et al. (2000) argued that YH_3 was a normal semiconductor comparable to Si. It was argued that the failure of the LDA was not due to the presence of strong correlations, but merely an effect of poor starting Hamiltonian and that the band gap was controlled mostly by the

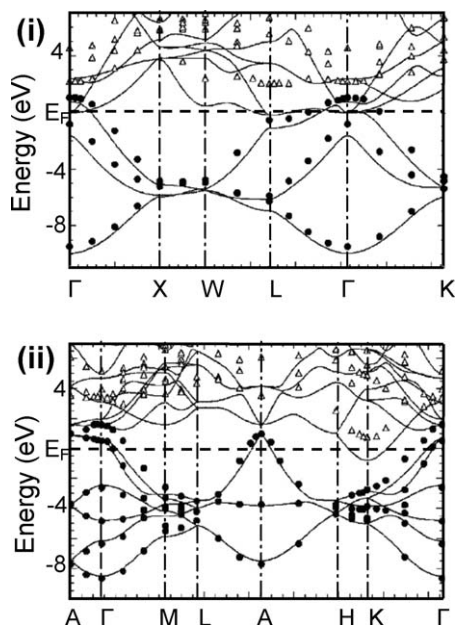


Fig. 119. The quasiparticle band structure for YH₃ with (i) BiF₃-type and (ii) LaF₃-type structures. The filled circles (empty triangles) denote the valence (conduction) bands. The solid lines represent the LDA band (Miyake et al., 2000).

electronic interactions rather than by the crystal structure. The calculated dielectric function agreed reasonably well with the experimental data obtained by van Gogh et al. (2001).

Van Gelderen et al. (2000, 2002) obtained YH₃ band structure employing parameter-free quasi-particle calculations with the *GW* approximation and using the space-time approach for three different hexagonal configurations: the LaF₃-type, HoD₃-type (with $P\bar{3}c1$ symmetry) and the broken symmetry structures (with $P6_3$ symmetry). The input data for *GW* calculations consisted of the electronic wave functions and energies obtained from the LDA calculations. For the Y₂H₆ unit cell with the so-called LaF₃-type structure, van Gelderen et al. used a $(6 \times 6 \times 4)$ *k*-set, an $(8 \times 8 \times 14)$ real-space grid, and a total of 200 bands in the *GW* calculations. By varying the size of the real space and reciprocal space grids, the quasiparticle energies were estimated to be converged within 0.1 eV. For the Y₆H₁₈ unit cell (the HoD₃-type structure) the $(4 \times 4 \times 4)$ *k*-set, a $(12 \times 12 \times 12)$ real-space grid and 300 bands were used. The effect of including the non-diagonal matrix elements of the self-energy operator (using LDA functions as the basis set) while solving the quasiparticle equation was also studied. It was observed that the quasiparticle wave functions were practically identical to their LDA counterparts. The *GW* scheme was iterated by updating the quasiparticle energies in both the *G* and *W*. The electron bands for YH₃ in the LaF₃-type, tripled LaF₃-type and HoD₃-type structures estimated using the LDA and the *GW* calculations are depicted in fig. 120. In the LDA band structure for YH₃ in LaF₃-type structure, the bands around the Fermi level (marked

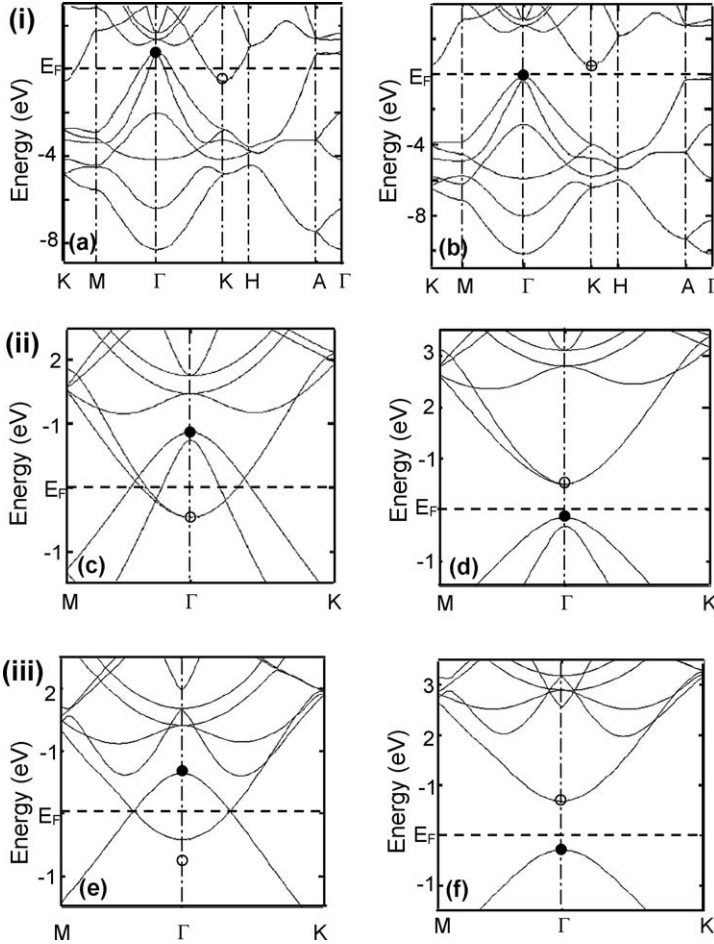


Fig. 120. Electron bands for YH_3 in (i) the LaF_3 -type structure, (ii) the tripled LaF_3 -type structure, and (iii) the HoD_3 -type structure, calculated within LDA (a, c and e) and *GW* band structures (b, d and f) (van Gelderen et al., 2002).

by solid and open circles) through out the Brillouin zone were well separated by a direct gap (0.6 eV at Γ and 2.3 eV at K). However, since the minimum of the upper band at K was lower than the maximum of the lower band at Γ , LDA predicted it to be a semimetal. When the LaF_3 unit cell was tripled, in addition to the original LDA bands at Γ , van Gelderen et al. observed two new bands at Γ which resulted from the folding in the bands from K in the original larger Brillouin zone. It was observed that the indirect overlap between Γ and K in LaF_3 -type unit cell becomes a direct overlap at Γ in the Brillouin zone of the tripled unit cell. In HoD_3 -type, the symmetry-breaking hydrogen displacements moved one pair of bands, which overlapped

at Γ , away from the Fermi level. Compared to the results of LDA calculations, the band structure of YH_3 in LaF_3 -type structure predicted from the GW calculations showed an increase in the separation between the valence and conduction bands, resulting in an indirect gap of 0.6 eV between Γ and K. Van Gelderen et al. (2000, 2002) argued that the small indirect gap is not easily measured in the optical experiments since the strongest optical transitions were k conserving. The direct gap at Γ (2.9 eV) was in agreement with the experimentally observed optical gap. In the Brillouin zone of tripled unit cell on the other hand, van Gelderen et al. (2000, 2002) observed that the small indirect Γ K gap was folded into a direct gap at Γ . In the absence of structural change, the dipole matrix elements connecting the folded highest valence and lowest conduction band were observed to vanish, leading to an optical gap of 2.9 eV between the highest valence band and the third conduction band at the Γ point in the reduced Brillouin zone. GW calculations performed on YH_3 in HoD_3 -type structure showed an upward shift in the conduction bands and a downward shift in valence bands. This was in contrast to the calculation by Ng et al. (1997, 1999) who found a large decrease in the valence bandwidth leading to a gap in LaH_3 . The GW calculations gave a direct gap at Γ of 1.0 eV for the YH_3 in the HoD_3 -type structure. It was argued that the symmetry breaking hydrogen displacements in the HoD_3 -type structure push some of the GW bands away from the Fermi level. The quasiparticle wave functions were observed to be practically identical to the LDA wave functions, implying that in the absence of the strong excitonic effects, the matrix elements for the optical transitions were unchanged. The symmetry-breaking hydrogen was observed to induce additional oscillator strength between some pairs of the bands, but not between the highest valence and the lowest conduction band. Between these states, the dipole transitions were observed to remain forbidden. The optical gap (of 2.9 eV at Γ) was thus calculated from the energy separation between the highest valence band and the second conduction band, between which the electric dipole transition was allowed. For the YH_3 in the broken symmetry structure, van Gelderen et al. (2000, 2002) observed that it was important to include the non-diagonal elements of the self-energy in the LDA basis while solving the quasiparticle equation. Fig. 121 gives a comparison between the LDA and GW bands along the $A\Gamma$ direction for the HoD_3 -type structure and the broken symmetry structure. Breaking the symmetry introduces additional interactions between the bands leading to band gaps in LDA spectrum. On the other hand, in addition to an increase in the band gap of the broken symmetry structure as a result of the GW corrections, important changes in the shape of the bands near the Fermi energy were observed as compared to the LDA bands. It was argued that since the quasiparticle corrections of these bands were k dependent, the interpolation scheme used to plot the GW bands for the HoD_3 -type structure could not be used for the broken symmetry structure. The GW bands of the broken symmetry structure were observed to closely resemble the GW bands of the HoD_3 -type structure. The final gap of 1.4 eV was observed in the GW bands of the broken symmetry structure. The picture of YH_3 that van Gelderen et al. (2000, 2002) derived from the parameter free calculations was that of a simple compound semiconductor in which the on-site Coulomb correlations played a minor role and could be treated within the GW formulation of many-body perturbation theory. The opening up of band gap by using the GW corrections was explained in the following way: When a solid is constructed starting with neutral Y and H atoms, charge would be transferred

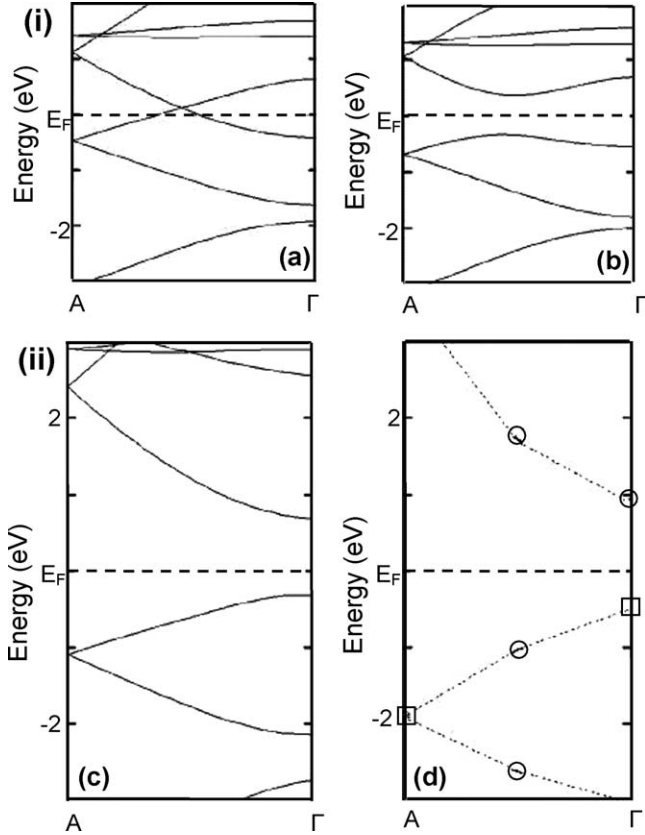


Fig. 121. Band structure for YH_3 for (i) the HoD_3 -type structure and (ii) the broken symmetry structure, calculated by LDA (a and c) and GW calculations (b and d) (van Gelderen et al., 2002).

from the Y to H (the ionization energy of the later being twice as large as the former) upon atomic interactions, resulting in an upshift of the levels derived from the H 1s and downshift of the Y levels. The overlap of valence orbitals on neighboring atoms would lead to a covalent interaction and the atomic levels would broaden into bands. In addition, the charge transfer to the hydrogen would cause the atomic orbital to delocalize leading to an increase in the bandwidth. Van Gelderen et al. (2002) argued that these effects were fully accounted for in the self-consistent band model. In addition to calculating the band structures for YH_3 in different structures, van Gelderen et al. (2001, 2003a, 2003b) gave evidence for the existence of the broken symmetry structure using the phonon spectrum of YH_3 . They calculated the lattice vibrational properties of YH_3 and YD_3 with the harmonic approximation for the three proposed structures.

On the basis of the quasiparticle calculations in the GW approximation performed on LaH_3 including the f states and the d states, Chang et al. (2001) concluded that LaH_3 is a band

insulator with a direct dipole forbidden band gap of 1.1 eV. It was shown that the *f* states were unimportant in the calculations on the optical transmission from 0 to 3 eV. Chang et al. also performed the DFT calculation within the LDA using the standard norm-conserving pseudopotentials and including the 4*d*, 5*s*, and 5*p* semicore states in the sets of valence bands and obtained the band structure which was in agreement with those predicted by Dekker et al. (1993). It was argued that the symmetry of the wavefunctions associated with the electronic levels indicated that the threefold states just below the Fermi energy at Γ were predominantly La 5*d* in character and the non-degenerate state just above the Fermi energy at Γ was H 1*s* in character, with both on the tetrahedral and octahedral sites. Chang et al. observed that when the 4*f* states were included in the valence shell, the flat conduction bands located 2–3 eV above the Fermi level were La-4*f* like; however the band structure around the Fermi level was hardly modified. At Γ , the La-5*d* states were located 0.1 eV below the Fermi energy and the non-degenerate H-1*s* level 0.2 eV above the Fermi energy. It was observed that, even upon inclusion of the 4*f* states in the valence shell with the LDA, the LaH₃ was predicted to be metallic with a band overlap of 0.3 eV at Γ in contrast to the experimental observations. To predict the band structure with better agreement with the experimental observations, Chang et al. performed quasiparticle calculations in the *GW* approximation on LaH₃. The self-energy was calculated for the system including both the *f* states and the *d* states. To calculate the dielectric screening at non-zero frequencies Chang et al. applied the generalized plasma-pole model and used the Kramer–Kronig relations and the *f* sum rule, using the valence charge density but without including the contribution due to the semicore states, to solve for the unknown parameters in the dielectric screening. The *GW* calculations were performed to compute the quasiparticle energies at Γ and it was concluded that the quasiparticle correction opens up a gap at Γ . Further, it was concluded that the fundamental gap which was indirect within the DFT-LDA became direct at Γ . The magnitude of the *GW* correction was found to be exceptionally large in the present case. Both the ~ 1.1 eV opening of the band gap and the ~ 4 eV corrections in the case of the 4*f* states clearly showed that the Kohn–Sham eigen values were dramatically different from the quasiparticle energies for such systems. In order to compare the theoretical results with the experimental observations, Chang et al. (2001) measured the frequency-dependent complex dielectric function using the random phase approximation, neglecting the effects of local fields. It was argued that the optical threshold does not necessarily correspond to the transitions at the Γ point from the top of the valence band to the two-fold degenerate 5*d* states located roughly 3.5 eV above the Fermi level, as it does not take into account the dependence on thickness of the film and the detailed nature of the absorption edge.

Alford et al. (2003) calculated the quasiparticle band structures for the cubic YH₃ and LaH₃ by evaluating the self-energy in the *GW* approximation using *ab initio* pseudopotentials and plane waves. For Y, the wavefunction of the outer core states (4*s* and 4*p*) had a substantial overlap with that of the valence states (5*s* and 4*d*). Similar situation occurred for La. It was argued that in order to obtain good structural properties with LDA, either the semicore states were to be included explicitly in the pseudopotential calculations or the partial-core corrections were to be employed to take into account the non-linear nature of the exchange-correlation functions. Since the quasiparticle calculations required an accurate determination

of screening, a careful examination of the effect due to semicore states was needed. Alford et al. (2003) noted that in general, the exchange and correlation effects between the core and valence electrons were non-local and energy dependent. The effective interaction between the valence electrons was modified by the interaction of core dipoles with the fluctuating valence charge. In addition, Alford et al. (2003) noted that the *GW* calculations, previously reported, typically used single-particle wavefunctions and eigen values from LDA calculations to construct the initial one-particle propagator and the screened interaction separately. Since the LDA calculations yielded a semimetal for these trihydrides with an overlapping valence and conduction bands, it was clear that the dielectric function calculated from a semimetal would not properly represent the screening in semiconductor. To circumvent these problems, Alford et al. (2003) performed two pseudopotential quasiparticle calculations for both the cubic LaH_3 and YH_3 : One including the semicore states explicitly and the other dealing with the three valence electrons in Y or La only, but handling the non-linear exchange correlation between the core and valence electrons through the partial-core correction at the LDA level. The quasiparticle band gaps were analyzed as a function of an initial shift in the LDA bands used to evaluate the random-phase approximation screening in constructing the self-energy. It was observed that the quasiparticle band gaps were not sensitive to the initial shift in the LDA bands. The effects of the outer core electrons in the Y or La were examined by either explicitly including them as valence states or by employing the partial-core correction. Since the results for the quasiparticle energies were observed to differ only by 0.1 eV, it was suggested that in these cases the exchange and correlation between the semicore and valence states could be treated through the partial-core correction without having to include the semicore states explicitly. It was shown that the self-energy corrections to the LDA open a gap at Γ of 0.2–0.3 eV and 0.8–0.9 eV for YH_3 and LaH_3 , respectively. Alford et al. (2003) found that the fundamental gap at Γ in cubic YH_3 was 0.5 eV smaller than that in LaH_3 [fig. 122(i) and(ii)]. This difference has been attributed to the larger original overlap between the LDA valence and conduction bands in YH_3 , leading to the mixing of the LDA states near the gap region inducing a finite oscillator strength in the YH_3 transition matrix calculations producing a spurious low-energy peak in the imaginary part of the dielectric function and making it difficult to accurately determine the optical-absorption threshold. The valence-band narrowing suggested by Ng et al. (1999) was not observed in the quasiparticle band structure calculated by Alford et al. (2003) and the valence bandwidth was too broad for the Coulomb repulsion (U) value of 2 eV as speculated by Eder et al. (1997). The fundamental gap obtained for cubic YH_3 was observed to be much smaller than that reported by Miyake et al. (2000). It was argued that this difference results from the inaccuracy of the basis functions used in *GW* calculations (based on the LMTO method within the atomic-sphere approximation) for representing the electron–electron interactions in the interstitial regions.

Wolf and Herzog (2002, 2003) using screened exchange LDA (sX-LDA) demonstrated that the direct gap of YH_3 (YD_3) was insensitive to the chosen structure. Wolf et al. explored the phase stability, the band structures and optical properties of three different structures of YH_3 viz., the HoD_3 -type structure with its $P\bar{3}c1$ symmetry, a non-centrosymmetric structure with $P6_3cm$ symmetry [as assumed by Udovic et al. (1998, 2000)] and a broken symmetry structure with space group $P6_3$ [as proposed by Kelly et al. (1997a, 1997b)], by total energy cal-

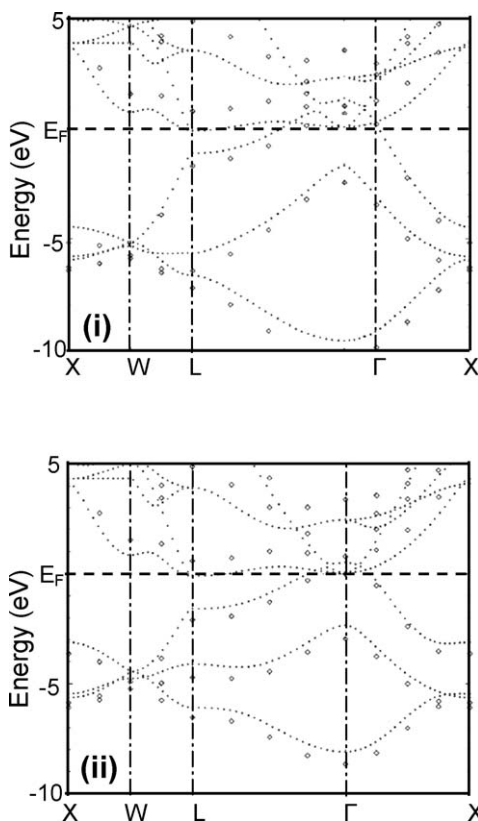


Fig. 122. Band structure of (i) YH_3 and (ii) LaH_3 in the cubic BiF_3 -type structure. The diamonds (dots) denote the GW quasiparticle (LDA) results (Alford et al., 2003).

culations based on the structural parameters as characterized experimentally and as calculated by minimization of atomic forces and stress tensors. In order to overcome the inadequacy of the standard DFT to describe the band gaps and optical excitations, the self-consistent sX-LDA was applied. In the sX-LDA approach, a part of the purely local approximation to exchange and correlation was replaced by a non-local screened Hartree-Fock operator. The $P6_3$ structure was found to yield the lowest energy followed by $P6_3cm$ and $P\bar{3}c1$ structures, though the energy differences between these structures was of the order of 0.01 eV. A comparison of the electric field gradients for D and Y atoms calculated by applying the structural parameters with the experimental data obtained from the deuteron magnetic resonance for the YD_3 as well as substitutions for the Y nucleus, showed best agreement for the structure with $P6_3cm$ symmetry. Wolf et al. observed that whereas the LDA band structures for $P\bar{3}c1$ and $P6_3cm$ structures exhibit a band overlap at the Γ point resulting in a negative band gap of about -0.7 eV, the $P6_3$ structure showed a positive band gap of 1.0 eV indicating it to be

a semiconductor as demonstrated by Kelly et al. (1997a, 1997b). It was argued that whereas for the first two structures the valence and conduction bands belong to different irreducible representations and thus were allowed to cross, in the broken symmetry structure, the corresponding bands belong to the same irreducible representation. Consequently the band crossing was forbidden and a band gap opened for symmetry reasons. The fact that the bands approach each other very closely in the gap region results in quite unusual inverse curvature of bands around the Γ point. Wolf and Herzig (2002, 2003) argued that the non-local screened interaction within sX-LDA in general causes the valence and conduction bands to be pulled apart and thus removes the band overlap for the $P\bar{3}c1$ and $P6_3cm$ structures. Wolf and Herzig (2002, 2003) observed that for all the three structural types the sX-LDA band structures were quite similar in the whole energy range, and the peculiar features of $P6_3$ structure model with the LDA disappeared. Also, the fundamental gaps were almost of the same magnitude, i.e., in the range 1.8–2.1 eV, and were in agreement with the values observed in optical measurements [1.8 eV, Huiberts et al. (1996a, 1996b); 1–1.8 eV, van Gogh et al. (2001)]. The same was true for the gap of 2.9–3.0 eV bridging the second highest excitation, which was close to the optical band gap reported from the transmission and reflectance experiments [2.3–2.8 eV, Huiberts et al. (1996a, 1996b), Griessen et al. (1997), van Gogh et al. (1999, 2001)]. Fig. 123 gives the band structure of YH_3 calculated by Wolf and Herzig (2002, 2003) for the three different structures. It was concluded from these results that as compared to other structures, the broken symmetry $P6_3$ structure was not better suited to explain the insulating trihydride state as reported by Kelly et al. (1997a, 1997b). Because of the small energy differences which were within the estimated errors of the applied methods, comparison of the calculated and measured optical spectra were not suitable to discriminate between the different structures.

Recently, Wu et al. (2004) studied the band structures of the hexagonal YH_3 and cubic YH_3 and LaH_3 within the weighted density approximation (WDA) using four different pair distribution functions and compared them with their LDA calculations (in which the Hedin–Lundqvist exchange correlation function was used instead of the Wigner ansatz used previously by Wang and Chou (1993, 1995)). Although WDA used the exact form of exchange correlation energy, the exchange energy between the core and valence states were not well described due to the approximate model of the pair distribution function. Based on this observation Wu et al. proposed a shell partitioning approach to guarantee the correct behavior of the core–valence exchange correlation interaction, in which the valence–valence interactions were treated with the WDA while the core–core and core–valence interactions with the LDA. It was observed that WDA band structure was sensitive to the choice of the pair distribution function and best results (larger band gaps) were obtained for the pair distribution function that has shorter range similar to that tested by Rushton et al. (2002). The band structures calculated using WDA were in good agreement with those of the *GW* calculations. For hexagonal YH_3 , Wu et al. (2004) studied a simplified hexagonal LaF_3 -type structure with a Y_2H_6 unit cell in which Y atoms form a hcp structure and optimized the H positions and the equilibrium volume with a fixed *c/a* ratio. The WDA calculations predicted a direct Γ gap of 2.2 eV and a fundamental gap of 0.41 eV between Γ and K, in agreement with the *GW* calculations by van Gelderen et al. (2000) who obtained a fundamental gap of 0.6 eV and a direct Γ gap of 2.9 eV. Their LDA predicted a direct band gap of 1.0 eV at Γ and an overlap

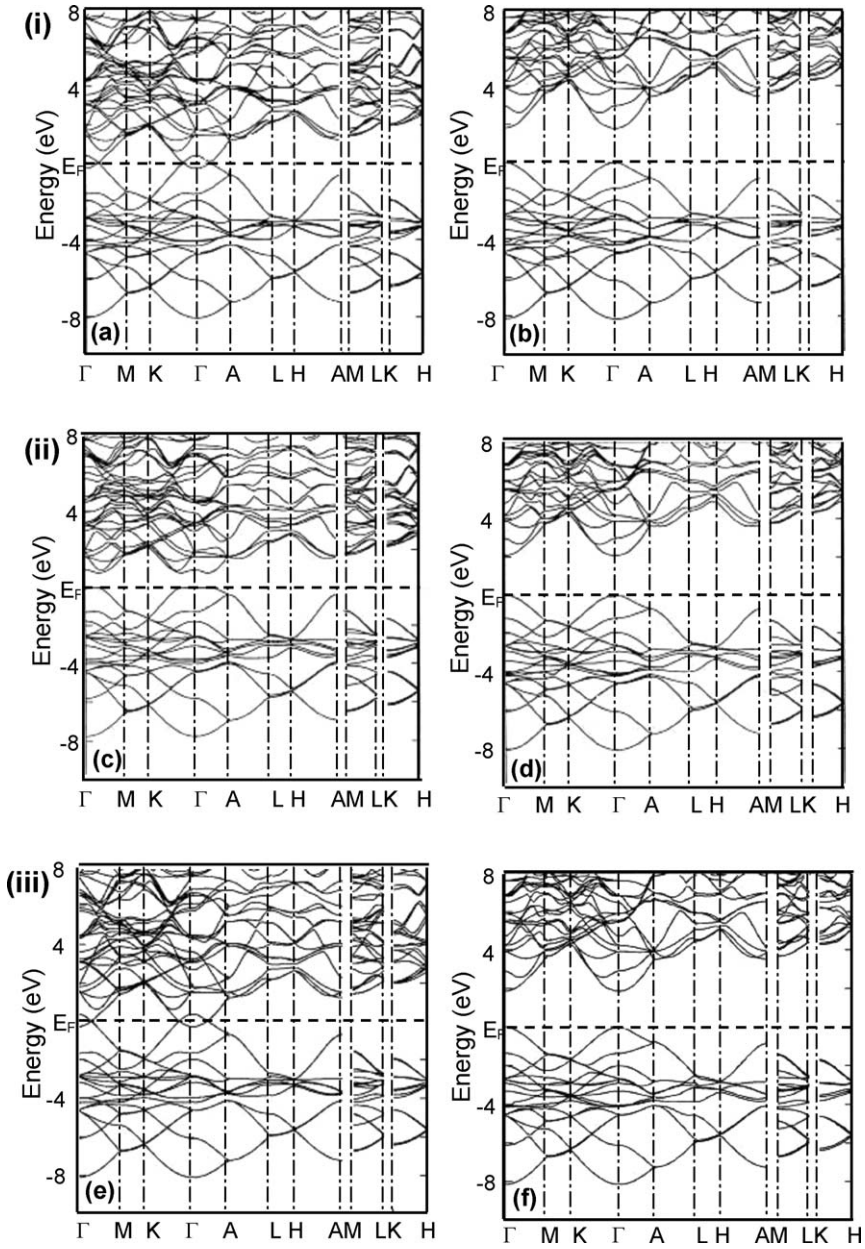


Fig. 123. Electronic band structure for YH_3 for space groups (i) $P\bar{3}c1$, (ii) $P6_3$ and (iii) $P6_3cm$, calculated within LDA (a, c and e) and sX-LDA (b, d and f) (Wolf and Herzig, 2002, 2003).

of 0.93 eV between Γ and K, leading to a semimetal. These results were different from the previous LDA (which predicted 0.6 eV for the direct Γ gap and 1.3 eV for the overlap) calculations by Wang and Chou (1993, 1995) due to the different exchange correlation functions used. Comparing their results with those of Wang and Chou (1993, 1995), and van Gelderen et al. (2000), Wu et al. (2004) argued that in the Brillouin zone of the more complicated tripled HoD₃-type structure, the indirect Γ -K gap is folded to form a direct gap at the Γ point which are roughly of the same order, implying that a small gap between the Γ and K in the simple hexagonal structure would make YH₃ a semiconductor even in the complicated HoD₃-type structure. Fig. 124(i) gives the band structure of hexagonal YH₃ calculated by LDA and WDA. The WDA calculation performed on cubic BiF₃-type structure of YH₃ and LaH₃, in which the Y or La atoms constituted a fcc lattice with H atoms located at the tetrahedral and octahedral sites, predicted both hydrides to be semiconductors with direct Γ gaps of 0.19 eV and 0.80 eV for YH₃ and LaH₃, respectively. It was argued that the fundamental gaps were about 0.1 eV smaller, because the energy of lowest conduction band at L was slightly lower than that at Γ . The LDA calculations by Wu et al. predicted both cubic YH₃ and LaH₃ to be metals (with direct overlap of 1.0 eV for YH₃ and 0.46 eV for LaH₃ at Γ point) in agreement with the previous calculations by Miyake et al. (2000) and van Gogh et al. (2001). Fig. 124(ii) and (iii) gives the band structures of cubic YH₃ and LaH₃ respectively, calculated by LDA and WDA. Based on their results Wu et al. argued that the insulating property of the rare earth trihydrides was of electronic origin rather than of structural origin and that there was no strong correlation in the H 1s states, and the absence of the self-interaction in H 1s was crucial in obtaining correct band structure. It was concluded that the gap problem was not due to unusual correlations or quasiparticle corrections, but was a problem with the LDA and the generalized gradient approximation (GGA) exchange correlation functions. Although WDA band gaps calculated by Wu et al. (2004) were in agreement with the *GW* calculations, the values were 1.0–2.0 eV smaller than the experimental values. Van Gelderen et al. (2000) argued that the fundamental gap of the hexagonal YH₃ was not the measured optical gap due to the forbidden transition between the highest valence and lowest conduction bands. It was concluded that the measured value corresponds to the direct gap at Γ of the hexagonal LaF₃-type structure and that the real hexagonal YH₃ was more complex and it may have lower symmetry so that the dipole matrix element may not be zero. Wu et al. (2004) argued that their WDA calculations underestimated the band gaps due to the DFT gap discontinuity at the Fermi level.

3. Second generation switchable mirrors

The major limitation of the first generation switchable mirrors for large-scale technological applications was the colored trihydride state. All the R metals tested for switchable mirror effect (La, Ce, Pr, Nd, Sm, Eu, Gd, Tb, Dy, Ho, Er, Tm, Yb, and Lu) are yellow to red in transmittance in the transparent trihydride state. An important step forward for technological applications was the discovery that color neutral switchable mirrors could be fabricated by alloying the R metals with Mg. Later, R-Mg multilayers were also shown to exhibit tunable constant transmittance in the visible range in the high hydrogen content state.

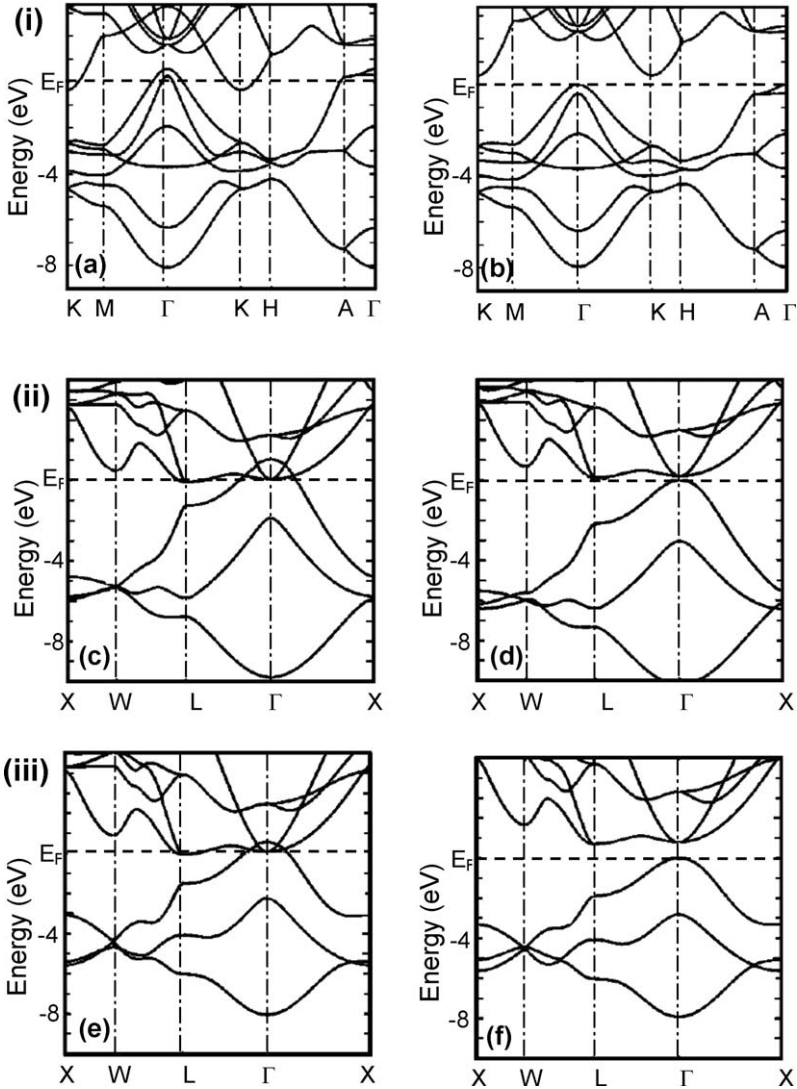


Fig. 124. Electron bands for (i) hexagonal YH_3 , (ii) cubic YH_3 , and (iii) cubic LaH_3 , calculated within LDA (a, c and e) and WDA with G-J4 type of G (b, d and f) (Wu et al., 2004).

3.1. R-Mg alloy films

Van der Sluis et al. (1997) first demonstrated the possibility to attain color neutrality (constant transmittance in the fully hydrogenated state) by alloying R metals (Y, Sm, Gd, and Lu) with Mg. It was shown that by varying the Mg concentration in the R-Mg alloy, one could fine-tune

the band gap and hence extend the constant transmittance region of the trihydrides to lower wavelengths. The choice of Mg for this purpose stemmed because of the following reasons:

1. The heat of formation of magnesium hydride (-33 kJ/mol H) is similar to that of the transition between the rare earth dihydride and trihydride. This was essential to keep the hydrogen uptake reversible.
2. Magnesium hydride is a large band gap material (~ 6 eV). This was essential for attaining fully transparent hydride.

The following sections describe briefly the optical, electronic and structural properties of the R–Mg alloy films reported to date.

3.1.1. Y–Mg alloy

Nagengast et al. (1999b) and van der Molen et al. (2001) carried out structural, optical transmittance and electrical resistivity measurements on a series of Y–Mg alloy films. They showed that the enhanced contrast between the transparent insulating state and the reflecting metallic state was due to compositional disproportionation of the alloy during hydrogen loading. This disproportionation was attributed to the great affinity of the R metals towards hydrogen. The details of the *in situ* X-ray measurements on a Pd (15 nm) capped $Y_{0.5}Mg_{0.5}$ alloy film (400 nm) on Al_2O_3 substrate during hydrogen loading at 10^3 Pa at room temperature is shown in fig. 125. As deposited film (curve a) consists of a preferentially (110) oriented, single-phase γ -YMg alloy with a lattice constant $a = 3.806$ Å. At low concentrations (stage A), lattice expansion was observed as indicated by a shift in the (110) peak towards lower angles (curve b). With increase in H concentration, (curves c–f) the intensity of the γ -YMg (110) peak decreases where as new reflections at 32° [corresponding to Mg (100)], 29.6° and 34.1° [corresponding to YH_2 (111) and (200)] appear, indicating disproportionation of γ -YMg into YH_2 and Mg clusters upon initial H intake. In stage B, the intensity of YH_2 remains unchanged whereas that of Mg (100) peak decreases indicating the formation of orthorhombic primitive MgH_2 . Upon further H intake (stage C), the shift in the diffraction peaks to smaller angles reflects a gradual lattice expansion. Apparently, cubic $YH_{3-\delta}$ was formed with $a = 5.25$ Å. The phase disproportionation was also reflected in the simultaneous electrical resistivity (ρ) measurements [fig. 126(i)]. At low hydrogen concentrations, the increase in ρ was similar to that in α - YH_x , and was mainly due to the electron scattering from the randomly distributed H atoms. In contrast to the pure R dihydrides, in γ - $Y_{0.5}Mg_{0.5}H_x$ the formation of YH_2 (stage A) results in concomitant increase in the disorder of the host metal lattice resulting in further over all increase in the ρ . In stage B, the formation of insulating MgH_2 phase causes further increase in the resistivity while the formation of cubic $YH_{3-\delta}$ changes the slope of the resistivity at high H concentrations (stage C). Fig. 126(ii) shows the corresponding H induced changes in the optical transmittance at photon energies 1.8 eV and 2.5 eV, clearly revealing that Mg acts as a microscopic optical shutter. Two-step disproportionation of the $Y_{0.5}Mg_{0.5}$ alloy during hydrogen absorption results in quenching the YH_2 transmittance window. In the first step, YH_2 was formed leaving the Mg clusters in the matrix. In the second step, the concentration of YH_2 increases gradually but the optical transmittance remains low until highly transparent MgH_2 was formed. From there on optical properties of $Y_{0.5}Mg_{0.5}H_x$ are similar to that of YH_x .

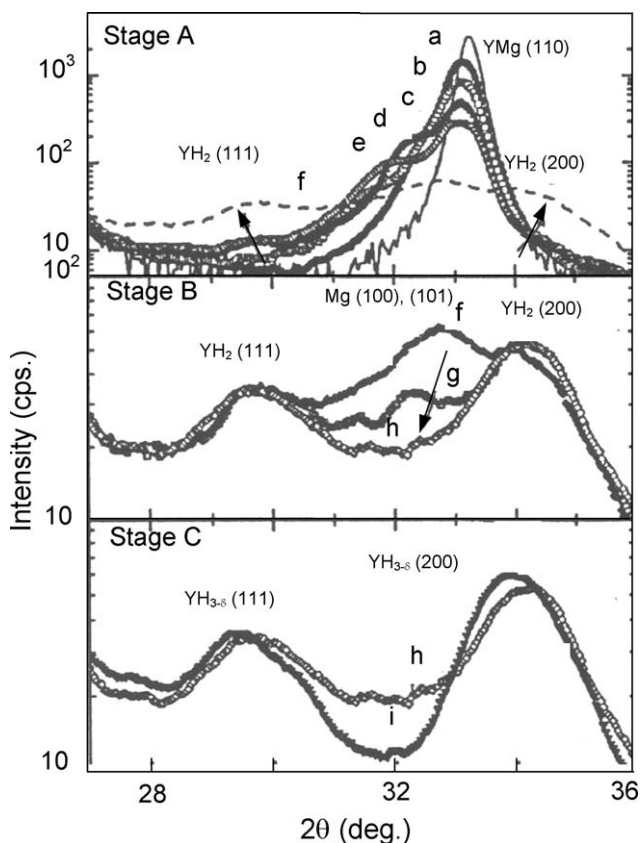


Fig. 125. Time evolution of the XRD peaks in Pd (15 nm) capped $Y_{0.5}Mg_{0.5}$ film showing different stages (A, B and C) during *in situ* hydrogen loading at 10^3 Pa at room temperature. The various alphabets (a–i) specify the measurements at times in increasing order [e.g. (a) as-deposited at 0 min, (b) 20 min, (c) 40 min, etc.] (Nagengast et al., 1999b).

The crystal structure of $YH_{3-\delta}$ formed in the final state of disproportionation of the $Y_{1-z}Mg_z$ alloy during hydrogen absorption was observed to depend on the Mg concentration (van der Molen et al., 2001). For $z < 0.10$ both hcp and fcc $YH_{3-\delta}$ are observed where as for higher concentrations ($z \geq 0.10$) only cubic $YH_{3-\delta}$ was formed. Fig. 127 shows the volume per $YH_{3-\delta}$ formula unit as a function of Mg concentration in the fully hydrogenated Pd (15 nm) capped $Y_{1-z}Mg_z$ alloy (300 nm) films on Al_2O_3 loaded at room temperature with hydrogen at 1 bar pressure. For $z < 0.10$, the unit cell volume of both the fcc and hcp structures are approximately independent of z . For $z \geq 0.10$ where only fcc $YH_{3-\delta}$ exists, unit cell volume decreases with increase in the Mg concentration. These phenomena have been explained by considering the large stresses induced by the enormous volume expansions of Y ($\sim 17\%$ for transformation to $YH_{3-\delta}$ in bulk Y) and Mg ($\sim 32\%$ up on MgH_2 formation

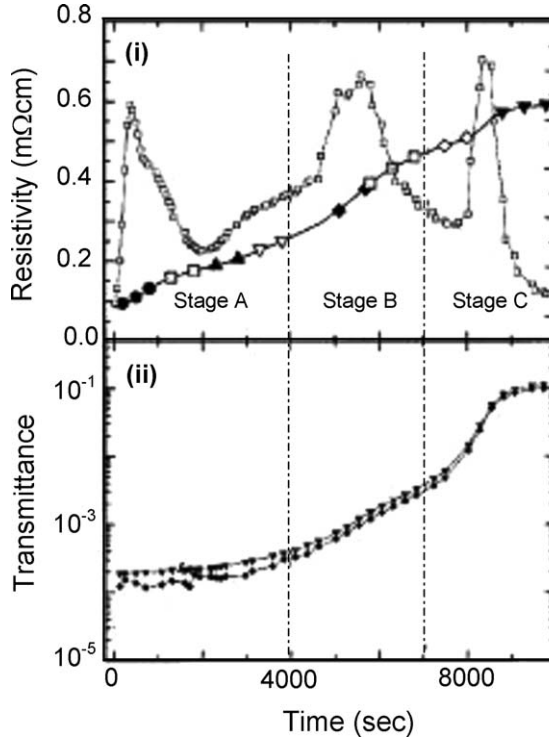


Fig. 126. Time evolution of electrical resistivity (i) and optical transmittance [at 1.8 eV (\blacktriangledown) and 2.5 eV (\blacklozenge)] (ii) of Pd (15 nm) capped $Y_{0.5}Mg_{0.5}$ (400 nm) film during hydrogen loading at 10^3 Pa at room temperature. The open symbols in (i) represent the derivative of the resistivity. The various symbols used in (i) correspond to the X-ray measurements shown in fig. 125 (Nagengast et al., 1999b).

in bulk Mg) during hydrogenation. For $z < 0.10$, the system was able to reduce the internal pressures by transforming hcp $YH_{3-\delta}$ to fcc $YH_{3-\delta}$ where as for $z \geq 0.10$, this was no longer possible and the fcc $YH_{3-\delta}$ was compressed with increasing Mg concentration. The volume of fcc YH_2 determined after deloading the films is also shown in fig. 127. In contrast to LaH_x as well as theoretical predictions, fcc $YH_{3-\delta}$ has larger unit cell volume as compared to that of fcc YH_2 .

The variation in the optical transmittance (T_{opt}) as a function of photon energy for $Y_{1-z}Mg_z$ alloy films ($z = 0.01, 0.15, 0.30$) in equilibrium with 1 bar hydrogen at room temperature are shown in fig. 128(i). As the Mg concentration increases, the switchable mirrors become more transparent and more color neutral. The variation in effective optical band gap $E_{g(eff)}$ (defined arbitrarily as the energy at which T_{opt} falls to 30%) with the increase in Mg concentration is shown in fig. 128(ii). In the two phase (fcc-hcp YH_3) region, the optical gap does not change significantly with z , although hcp $YH_{3-\delta}$ was continuously replaced by fcc $YH_{3-\delta}$ indicating that optical properties of fcc $YH_{3-\delta}$ are comparable to those of the hcp $YH_{3-\delta}$. In

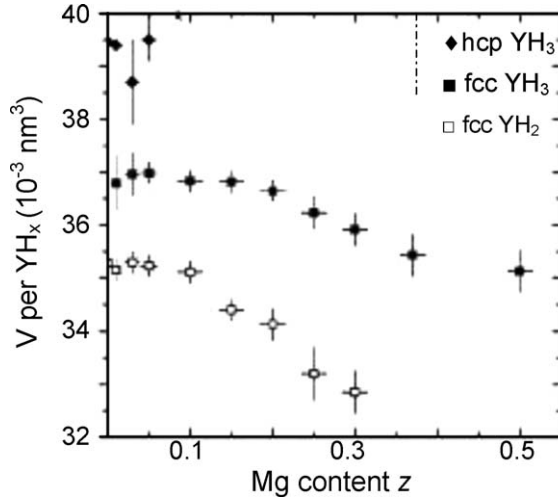


Fig. 127. Volume of YH_3 per formula unit (\blacklozenge , \blacksquare) in fully hydrogenated $Y_{1-z}Mg_z$ alloys as a function of Mg concentration z ($p_{H_2} = 1$ bar, at room temperature). Upon deloading the change in the volume of YH_2 (per formulae unit) (\square) as a function of z is also depicted (van der Molen et al., 2001).

the region with $z \geq 0.10$, the optical gap increases nearly linearly with z . The insulating nature of the hydrided samples was confirmed by a series of resistivity measurements performed on $Y_{1-z}Mg_z$ alloy films partly covered by Pd with uncovered part superficially oxidized in air. The variation in the electrical resistivity of the transparent region as a function of Mg concentration is shown in fig. 129 clearly revealing an exponential increase in ρ with z . The increase in ρ with increase in z when hcp $YH_{3-\delta}$ was substituted by fcc $YH_{3-\delta}$ ($z < 0.10$) clearly reveals that resistivity of fcc $YH_{3-\delta}$ was equal to or larger than that of hcp $YH_{3-\delta}$. From the results of the optical transmittance and electrical resistivity measurements on fully hydrogenated $Y_{1-z}Mg_z$ alloy films by van der Molen et al. (2001), it was concluded that the fcc $YH_{3-\delta}$ was an insulator with a gap comparable to that of hcp $YH_{3-\delta}$. These results are consistent with the GW calculations (van Gelderen et al., 2000; Miyake et al., 2000) described earlier, which showed that $YH_{3-\delta}$ was insulating in four different structures, as well as in good agreement with the strong electron correlation model given by Ng et al. (1997, 1999) and Eder et al. (1997). However, the results are contradictory to the predictions by Ahuja et al. (1997) that a transition from hcp to fcc $YH_{3-\delta}$ was accompanied by an insulator to metal transition. The increase in the effective optical band gap in addition to the exponential increase in ρ with increase in the Mg concentration has been explained by quantum confinement effects in the fcc $YH_{3-\delta}$ clusters. Fig. 130 shows the variation in the change in the band gap (right axis) as a function of the Mg concentration estimated from the following expression:

$$\Delta E_g \approx \frac{h^2}{2L^2} \left(\frac{1}{m_c^*} + \frac{1}{m_h^*} \right),$$

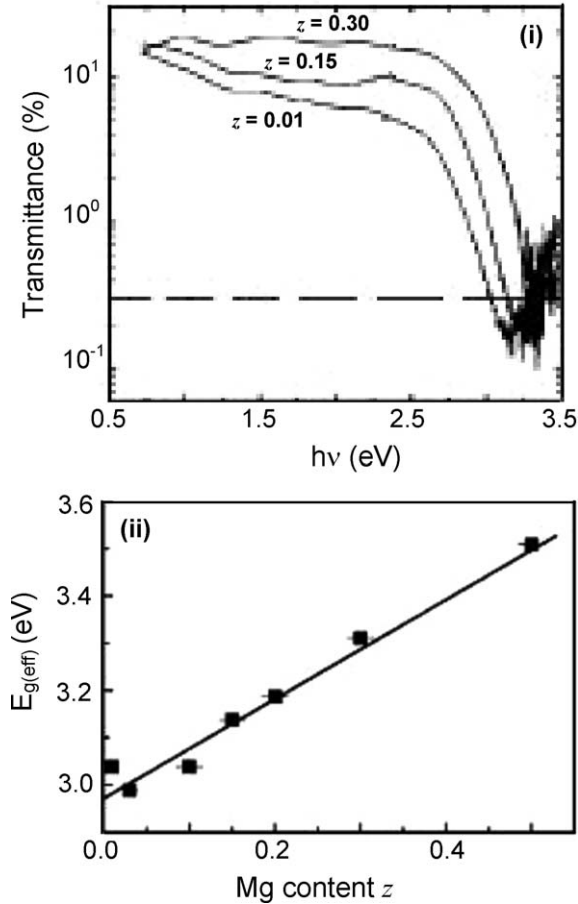


Fig. 128. (i) Optical transmittance as a function of photon energy for three hydrogenated films. (ii) Variation in effective optical gap as a function of Mg content z (van der Molen et al., 2001).

where $m_{e(h)}^*$ denotes the electron (hole) effective mass and L is the diameter of the $\text{YH}_{3-\delta}$ clusters. X-ray coherence length (l_{coh}) determined from the width of the XRD peaks using Debye–Scherrer formulae has been used for estimating L [as shown in fig. 131 (left axis), l_{coh} decreases from 18 nm for $z = 0$ to 4 nm for $z = 0.3$] and the GW band structure calculations have been used to obtain the effective masses $m_e^* \approx 0.35 m_e$ and $m_h^* \approx -0.74 m_e$. Assuming that $L = l_{\text{coh}}$, fig. 130 shows that with increase in the Mg concentration, diameter of the fcc $\text{YH}_{3-\delta}$ clusters decreases resulting in the increase in the optical gap.

Apart from the reflecting and a transparent state, R–Mg alloys exhibit a highly absorbing, black state during loading with hydrogen. This black state has been reported for example in $\text{Y}_{1-z}\text{Mg}_z\text{H}_x$ alloys (Nagengast et al., 1999b; van der Molen et al., 2001), $\text{La}_{0.5}\text{Mg}_{0.5}\text{H}_x$

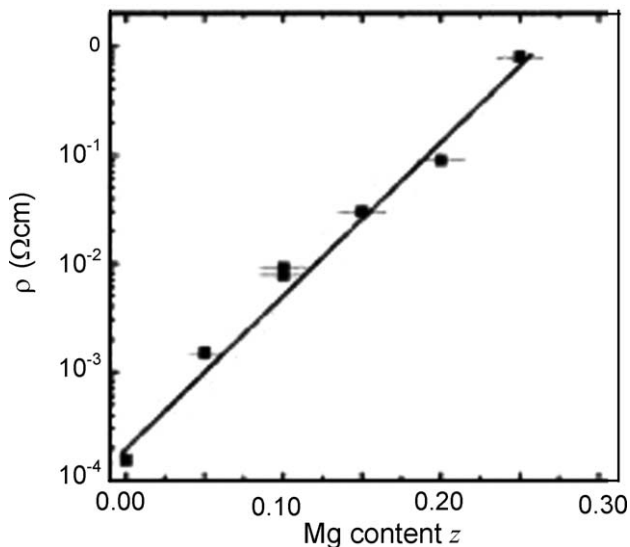


Fig. 129. Variation of resistivity of the uncapped $Y_{1-z}Mg_z$ layer in the lateral geometry as a function of Mg content (van der Molen et al., 2001).

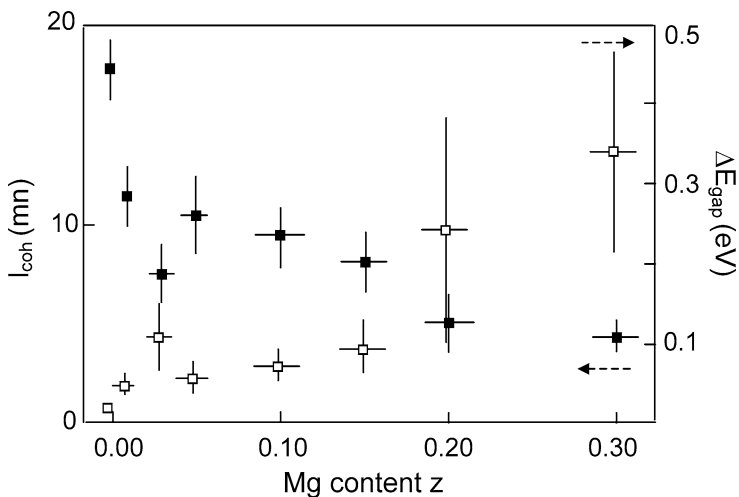


Fig. 130. Variation in X-ray coherence length of the YH_3 clusters (■) and band gap (□) of fully hydrogenated $Y_{1-z}Mg_z$ alloy as a function of Mg content z (van der Molen et al., 2001).

(Isidorsson et al., 2001) and in $Gd_{1-z}Mg_zH_x$ with $z > 0.50$ (van der Sluis et al., 1997; Armitage et al., 1999). Fig. 131 shows the variation in the measured transmittance and reflectance

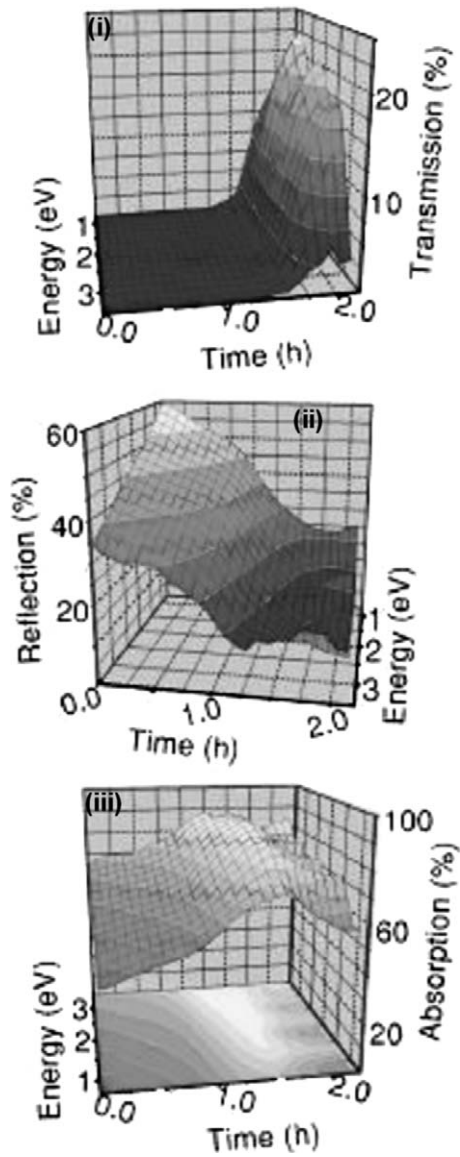


Fig. 131. (i) Transmittance, (ii) reflection, and (iii) absorption during hydrogen loading (in 10 mbar H_2) of a Pd (10 nm) capped YMg alloy film (200 nm). After 2.2 h the sample was observed to be in fully hydrogenated state with an overall composition of $YMgH_{4.9}$ (Giebels et al., 2004).

tion and the estimated absorption ($1 - T_{\text{opt}} - R_{\text{opt}}$) of $Y_{1-z}Mg_z$ (200 nm) film capped with Pd (10 nm) over layer deposited on a quartz substrate during hydrogen loading at 10 mbar H_2 . Apart from the reflecting and transparent state, the existence of highly absorbing state was clearly evident. The black state was observed not only during hydrogen loading but also during deloading. The black state (corresponding to the hill in A_{opt}) was observed when the reflection was low and the film was just becoming transparent. In the black state, absorption of 70–80% (after correcting for the Pd cap layer and the quartz substrate) was observed over the entire visible spectrum. Giebels et al. (2004) argued that the black state was a fundamental property of all R–Mg alloys with considerable amount of Mg and gave a quantitative description of the mechanism responsible for the existence of the black state. Since the R–Mg alloys were observed to disproportionate into small nanosized grains upon hydrogen loading, using Bruggeman effective medium approximation (Bruggeman, 1935), Geibels et al. modeled the optical properties of the system consisting of heterogeneous mixtures of RH_x , Mg and MgH_2 . By using Bruggeman effective medium approximation in combination with the transfer matrix method, it was shown that the theoretically predicted optical properties match the experimental observations only if the coexistence of the small Mg and MgH_2 grains was considered. Since the black state was also observed in multilayers with Mg and in pure Mg films (Giebels et al., 2004), it was argued that the R metals were not playing any role in the observed black state. The R metal serves to disproportionate the film into small grains of $RH_{2\pm\delta}$ and Mg during the first hydrogen loading, which switching independently on further hydrogen uptake. It was shown that the bulk plasmon frequency of the metal determines the photon energy at which the absorption due to cluster resonances vanishes, similar to the absorption phenomenon of light observed in metal-dielectric composites such as Au-glass, Ag-glass and Co- Al_2O_3 .

In addition to the modified properties of the $Y_{1-z}Mg_z$ alloys described above, large difference in the thermochromic properties are observed in $YMgH_x$ alloys as compared to pure YH_x (Giebels et al., 2002a). The transmittance of Pd (9 nm) capped $Y_{0.9}Mg_{0.1}H_{2.9-\delta}$ alloy films (260 nm) was observed to decrease by 64% to 83% between 30 °C and 160 °C as compared to the decrease of 9% to 36% in pure $YH_{3-\delta}$ (280 nm) films (fig. 132). This thermochromic effect was caused by hydrogen desorption on increase in temperature. Both the films show a continuous decrease in the transmittance with temperature. In pure $YH_{3-\delta}$, the minimal change in of the transmittance with temperature occurs at ≈ 800 nm whereas in $Y_{0.9}Mg_{0.1}H_{2.9-\delta}$ a maximal change of transmittance with temperature occurs at ≈ 550 nm. The difference in the thermochromic effects has been assigned to the absence of the fcc to hcp phase transition in the phase segregated YH_x for $x \geq 2$, leading to the non-appearance of the plateaus in the pressure-composition isotherms of $Y_{0.9}Mg_{0.1}H_x$ and the increase in the steepness of the optical transition upon hydrogen desorption (fig. 132).

3.1.2. La–Mg alloy

Isidorsson et al. (2001) have investigated the influence of Mg on the structural, electronic and optical properties of the lanthanum hydride films. Fig. 133 shows the X-ray diffractograms of the Pd (10 nm) capped $La_{0.55}Mg_{0.45}$ alloy film (584 nm) on quartz in the as deposited (at 300 °C), loaded (at room temperature in 1 bar hydrogen pressure) and deloaded (in air

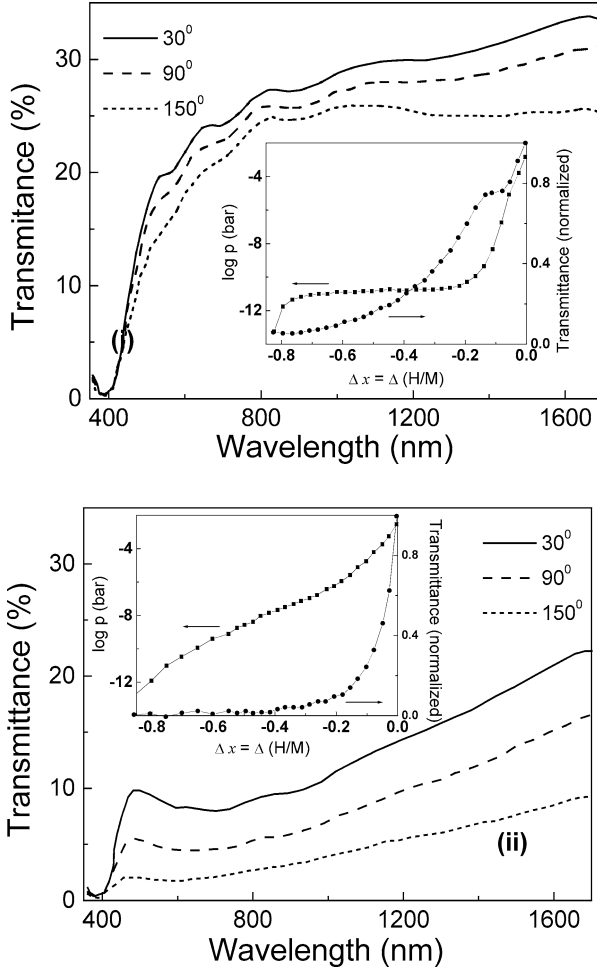


Fig. 132. Temperature dependence of transmittance of (i) 260 nm $\text{YH}_{3-\delta}$ and (ii) 280 nm $\text{Y}_{1-z}\text{Mg}_z\text{H}_{2.9-\delta}$ (capped with Pd over layer of thickness 9 nm) in 1 bar of H_2 . The corresponding pressure composition isotherms are shown in the inset (Giebels et al., 2002a).

at 50–150 °C) states. In the as-deposited film the peaks corresponding to LaMg intermetallic compound with CsCl-type structure along with those of high temperature fcc β -La phase, $\text{LaH}_{2-\xi}$, and Pd are observed. The lattice parameter of LaMg phase was estimated to be 3.969 Å. In the hydrogen-loaded state ($\text{La}_{0.55}\text{Mg}_{0.45}\text{H}_{2.55}$) the LaMg disproportionates into fcc $\text{LaH}_{3-\delta}$ and hcp MgH_2 . Whereas LaH_x was observed to undergo a lattice contraction of 1.02% and MgH_2 by 2.9% along the a axis, Pd was observed to expand by 3.6% during loading. The deloaded samples ($\text{La}_{0.55}\text{Mg}_{0.45}\text{H}_2$) consist of peaks corresponding to LaH_2 , MgH_2 and Pd. The grain size estimated from the coherence length using Debye-Scherrer

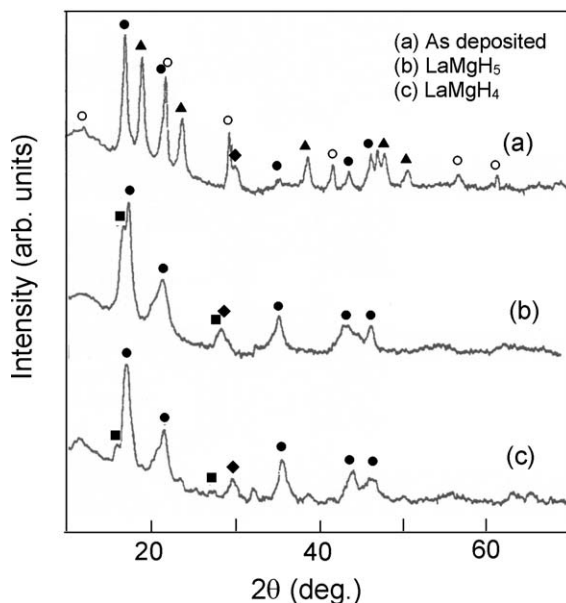


Fig. 133. X-ray diffractograms of Pd (10 nm) capped LaMgH_x (584 nm) film in the (a) as-deposited, (b) loaded (in 1 bar H₂, $x \approx 5$), and (c) deloaded ($x \approx 4$). The symbols ●, ▲, ○, ■, ◆, correspond to LaH_x, La, LaMg, MgH₂, and Pd, respectively. Symbol ● corresponds to XRD peaks due to LaH₂ in curve (b) and to LaH₃ in curve (c) (Isidorsson et al., 2001).

Table 3

Grain size (in nm) estimated from the coherence length for La_{0.55}Mg_{0.45}, La_{0.55}Mg_{0.45}H_{2.55}, La_{0.55}Mg_{0.45}H_{2.55} (loaded) and La_{0.55}Mg_{0.45}H₂ (deloaded) (Isidorsson et al., 2001)

Material	As-deposited	Loaded	Deloaded
LaMg (110)	35		
β-La (111)	18		
α-LaH _{2-δ} (111)	21		
γ-LaH _{3-δ} (111)		17	
β-LaH _{2-δ} (111)			12
MgH ₂ (110)		13	13
Pd (111)	12	6	6

formulae are tabulated in table 3. It is interesting to note the disproportionation of 35 nm intermetallic LaMg to LaH_x and the decrease in size to 17 nm and then to 12 nm after the first loading and deloading, respectively.

The evolution of the optical transmittance and reflectance spectra during hydrogen loading of a Pd capped (2.5 nm) La_{0.51}Mg_{0.49} alloy film (50 nm) with a thin AlO_x buffer layer in between are shown in fig. 134. The important features of the transmittance spectra include a flat

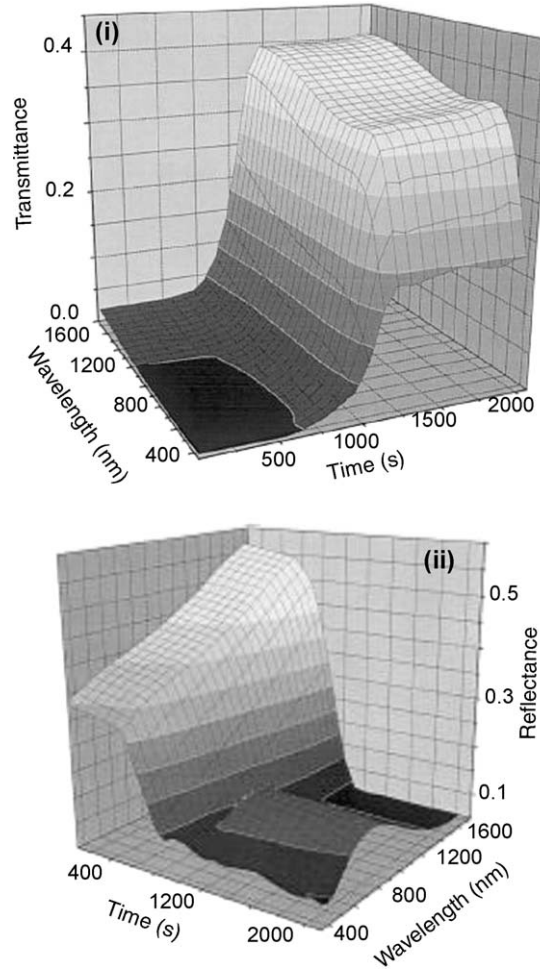


Fig. 134. Evolution of optical transmittance and reflectance of Pd (2 nm) capped $\text{La}_{0.51}\text{Mg}_{0.49}$ film (50 nm) having AlO_x buffer layer during hydrogenation (Isidorsson et al., 2001).

plateau in the transmitting state and absorption edge close to 400 nm (leading to color neutral transmitting state) along with large total transmittance change upon loading. In the reflectance spectra the specific feature to note is the high absorbance ($A_{\text{opt}} = 1 - T_{\text{opt}} - R_{\text{opt}}$) at ≈ 1000 s, which occurs after the metallic state with high reflectance, but before the transmitting state was reached where the reflectance again increases at certain wavelengths (≈ 800 nm) due to interference. The optical band gap estimated from analyzing the transmittance spectra using Lambert–Beer law gives $E_g = 3.0$ eV for a 50 nm thick $\text{LaMgH}_{2.5}$ film which was large in contrast to 2.2 eV for 60 nm pure $\text{LaH}_{3-\delta}$ film.

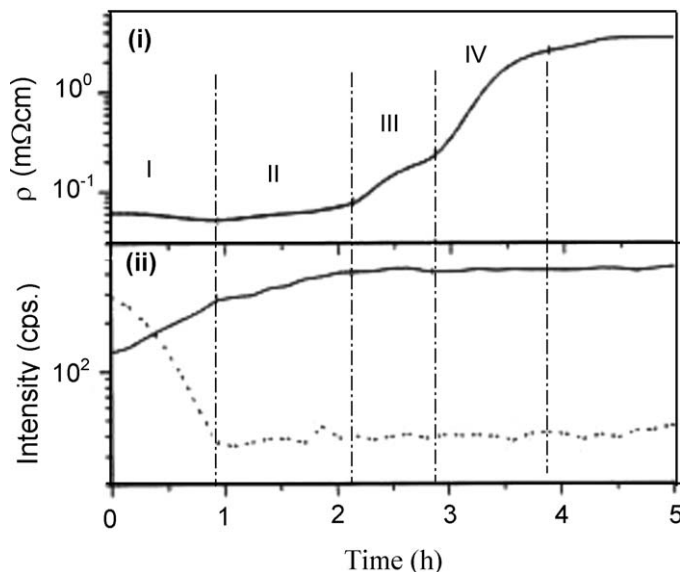


Fig. 135. Time evolution of (i) resistivity and (ii) X-ray intensity of two dominant peaks [LaH_x fcc (111): solid line; β -La fcc (111)] in the indicated crystal structure in LaMg alloy film capped with Pd. The different region I–IV are explained in the text (Isidorsson et al., 2001).

The time evolution of resistivity of 584 nm LaMg alloy film capped with 10 nm Pd over layer was shown together with the optical transmittance at $\lambda = 560$ nm and the X-ray intensity at angles of diffraction pertaining to the β -La (111) and LaH_x (111) peaks are shown in fig. 135. There are four regimes: (I) after ≈ 1 h β -La phase disappears and ρ decreases, as LaH_2 was a better conductor than β -La; (II) until ≈ 2 h the intensity of the $\text{LaH}_{2-\xi}$ phase saturates while the resistivity increases only marginally; (III) in this region the reflectance of the film decreases as the absorption increases. The ρ exhibits local features due to the mixed phases of conducting $\text{LaH}_{2+\xi}$, the insulating $\text{LaH}_{3-\delta}$ and MgH_2 phases; (IV) in this region $\text{LaH}_{3-\delta}$ phase goes through the metal–insulator transition, the ρ increase drastically and the film becomes transparent.

3.1.3. Sm–Mg alloy

Using potentiostatic and galvanostatic techniques of electrochemical loading (Ouwkerk, 1998) and gas phase loading (von Rottkay et al., 1999a, 1999b) Sm–Mg alloy films have been studied for the hydrogen induced modified properties. The variation in the electrode potential, measured with respect to the Hg/HgO reference electrode, and the log of optical transmittance as a function of the hydrogen content measured from the integrated current for a 195 nm $\text{Sm}_{0.34}\text{Mg}_{0.66}$ alloy film (dotted line) and 870 nm $\text{Sm}_{0.32}\text{Mg}_{0.68}$ alloy film (solid line) capped with 10 nm Pd over layer during the initial galvanostatic hydrogen loading (at a constant current of 0.308 mA/cm^2) in 2 M KOH is shown in fig. 136. Since the initial

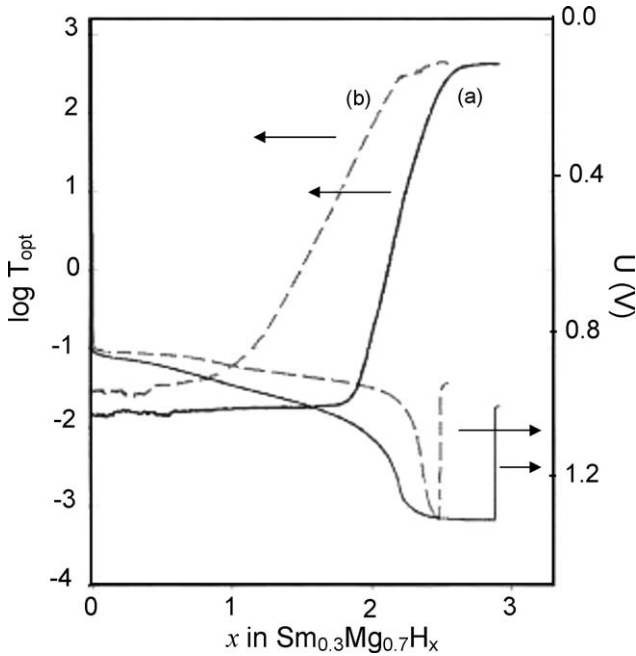


Fig. 136. Variation in logarithm of optical transmittance and the electrode potential (vs. Hg/HgO) as a function of hydrogen concentration for Pd (10 nm) capped (a) $\text{Sm}_{0.30}\text{Mg}_{0.70}$ (870 nm) film and (b) $\text{Sm}_{0.30}\text{Mg}_{0.70}$ (195 nm) film. The compositions are approximate (Ouwkerk, 1998).

composition of the films was similar (i.e., approximately $\text{Sm}_{0.30}\text{Mg}_{0.70}$) and the final composition was the hydrogen saturated samarium magnesium hydride, the electrode potential at the onset of the loading and the end voltage are same in both the films. However due to larger lateral resistance of the thicker film and the different composition in the intermediate phases of hydrogen loading in two films, the 870 nm layer has larger overpotential as compared to the 195 nm film. Though the ratio of the film thickness was 4.5, the optical transmittance of both the films after hydrogen loading was observed to be same ($\sim 33\%$), revealing that the absorption by the approximate $\text{Sm}_{0.30}\text{Mg}_{0.70}\text{H}_x$ alloy films was close to zero and the reflection losses or absorption in the palladium hydride layer are the main cause for the less than 100% transmittance. The maximum attainable dynamic range was observed to be highly dependent on the film thickness (10^4 for 195 nm $\text{Sm}_{0.34}\text{Mg}_{0.66}$ film and 10^{16} for 870 nm thick film). The optical transmittance of 200 nm $\text{Sm}_{0.48}\text{Mg}_{0.52}$ capped with 10 nm of Pd over layer hydrogenated by gas phase loading (10^5 Pa hydrogen) is shown in fig. 137 (von Rottkay et al., 1999b). The complex refractive index in the as-deposited, hydrogen loaded and deloaded states are given in the inset. By coulometry, the hydrogen introduced during the first loading of the film of approximate composition $\text{Sm}_{0.30}\text{Mg}_{0.70}$ was estimated to be about 2.3 mole hydrogen per mole of the alloy, whereas on deloading 1.7 mole of hydrogen was removed leaving 0.6 mole of hydrogen per mole of the alloy. Fig. 138 shows a complete potentiosta-

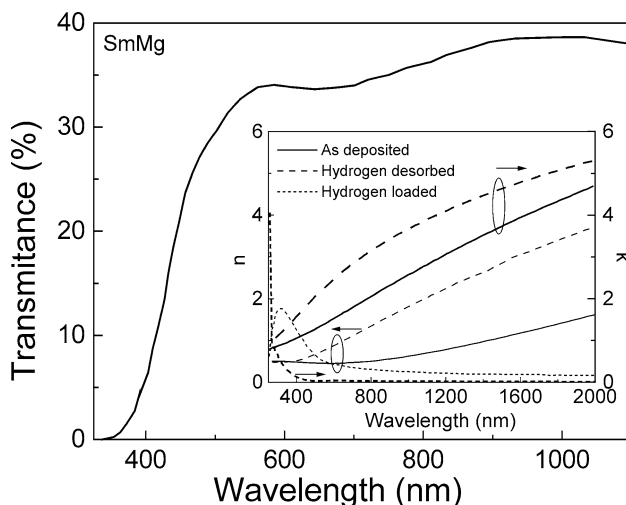


Fig. 137. Optical transmittance of a hydrogen loaded $\text{Sm}_{0.48}\text{Mg}_{0.52}$ film. The inset shows the real (n) and imaginary (k) parts of the complex refractive index of the $\text{Sm}_{0.48}\text{Mg}_{0.52}$ film in the as deposited, hydrogen loaded and deloaded states (von Rottkay et al., 1999a, 1999b).

tic switching cycle of one such film of thickness 195 nm. The hydrogen loading takes about 1 min where as deloading takes 3 min. The lateral resistance of the film, which increases upon hydrogen intake, limits the rate of hydrogen loading and deloading [e.g., the lateral resistance of a 200 nm film of this composition was found to be 96Ω in the fully hydrogenated state ($x = 2.3$) as compared to 7Ω in the deloaded state ($x = 0.6$)]. Fig. 139 gives the current-voltage curve for the $\text{Sm}_{0.34}\text{Mg}_{0.66}\text{H}_x$ film that has been loaded and deloaded with hydrogen previously and brought to equilibrium at $+5 \text{ V}$ vs. Hg/HgO . The peaks in the hydriding curve at -0.8 and -1.1 V are ascribed to the hydriding of SmH_2 and Mg respectively (both shifted by overpotential, with the overpotential for the hydrogen loading of SmH_2 lower than that of Mg) indicating the disproportionation of the alloy upon hydrogenation. The shape of the dehydriding curve was more complex than the hydriding curve. Apart from the dehydriding SmH_3 and MgH_2 the release of hydrogen gas adsorbed at the surface also contributes to the curve.

X-ray diffraction studies showed the amorphous nature of the film with approximate composition $\text{Sm}_{0.30}\text{Mg}_{0.70}\text{H}_x$ capped with crystalline Pd over layer in agreement with the studies on $\text{Gd}_{1-z}\text{Mg}_z$ alloy films which show the amorphous nature for $z > 0.50$ (van der Sluis, 1998).

3.1.4. Gd–Mg alloy

The modifications in the hydrogen induced optical, electronic and structural properties of Gd–Mg alloy films have been studied by utilizing both the gas phase loading as well as electrochemical loading. The $\text{Gd}_{1-z}\text{Mg}_z$ alloy films (200 nm) with $0.1 < z < 0.9$, capped with

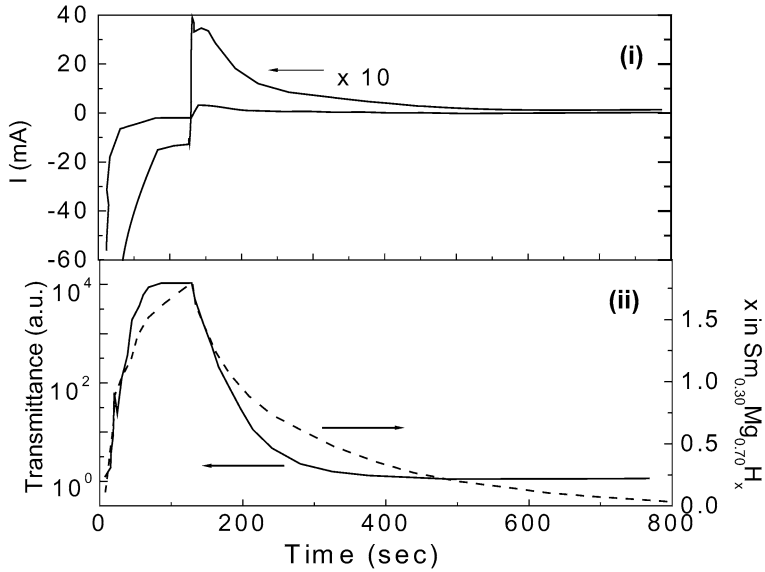


Fig. 138. (i) Evolution of current at constant potential of -1.25 V vs. Hg/HgO during charging and $+0.20$ V vs. Hg/HgO during discharging of hydrogen and (ii) variation of optical transmittance (solid line) and hydrogen concentration (dotted line) during charging and discharging of hydrogen for 195 nm thick films of approximate composition $\text{Sm}_{0.30}\text{Mg}_{0.70}\text{H}_x$ capped with 10 nm Pd over layer (Ouwkerk, 1998).

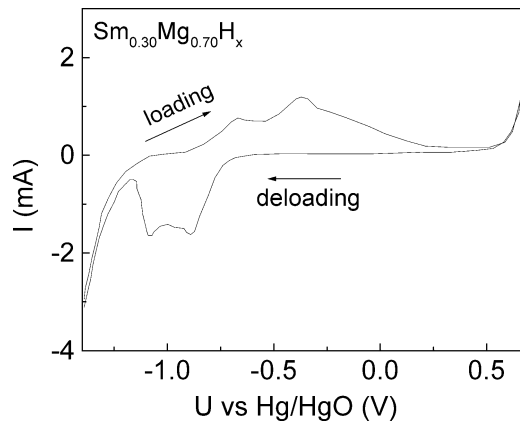


Fig. 139. CV curve for a Pd (10 nm) capped 195 nm thick film of approximate composition $\text{Sm}_{0.30}\text{Mg}_{0.70}\text{H}_x$ measured at 1 mV s^{-1} (Ouwkerk, 1998).

Pd over layer (10 nm) deposited by conventional thermal evaporation technique and loaded with 5 bar H_2 show interesting hydrogen induced changes in optical properties (van der Sluis

et al., 1997). In the fully hydrogenated state, there was a shift in the absorption spectra to shorter wavelength with increasing Mg concentration, with the sample becoming more or less color neutral for $z \approx 0.5$. The transmittance of the Gd–Mg alloy films was higher than that of $\text{GdH}_{3-\delta}$ films and the H_2 pressure at which maximum transmittance was attained decreases with increasing Mg content. In the deloaded state (obtained by subsequently deloading the samples in air), the transparency window at 700 nm shifts slowly towards shorter wavelengths and gradually disappears with increasing Mg content leading to an increase in the transmittance ratio (transmittance of hydrided state/transmittance of dehydrided state) to more than 3000 for $\text{Gd}_{1-z}\text{Mg}_z$ alloy with $z \leq 0.3$ in contrast to 13 for Gd. Fig. 140 shows the variation in the transmittance of some representative Pd (10 nm) capped Gd–Mg alloy films (200 nm) in (a) hydrogen loaded state and (b) hydrogen desorbed state. Another interesting effect found in R–Mg alloy films was that, unlike the pure R metals, where the reversible transition was between a phase with a hydrogen to metal ratio $\text{H}/\text{M} \sim 2$ to that with $\text{H}/\text{M} \sim 3$ with the former normally having a low reflection (of the order of 10%), R–Mg alloy films with a substantial amount of Mg (e.g. for $\text{Gd}_{1-z}\text{Mg}_z$ alloy with $z > 0.5$) three different optical states can be discerned depending on the amount of absorbed hydrogen. In fully hydrogenated state, R–Mg alloy was in the nearly color neutral transparent state. A non-transparent dark (low reflecting) state, optically resembling the R dihydride phase, was obtained when a part of hydrogen was desorbed. If the desorption was continued, a non-transparent and highly reflecting phase, with considerable amount of hydrogen, optically resembling the original metal layer was obtained. Giebels et al. (2004) gave a quantitative description of the mechanism responsible for the existence of this highly absorbing black state. This is described later in the section.

Von Rottkay et al. (1999a, 1999b), investigated the optical switching effect in R–Mg alloy films in terms of the changes in the complex refractive index as determined by the variable angle-spectroscopic ellipsometric and normal-incidence radiometric measurements over the solar spectrum. A Lorenz oscillator model was used to represent the dispersion for the Pd capped $\text{Gd}_{0.42}\text{Mg}_{0.58}$ (also for $\text{Sm}_{0.48}\text{Mg}_{0.52}$ and $\text{Er}_{0.42}\text{Mg}_{0.58}$ films) in order to guarantee the Kramer–Kronig consistency of the spectral optical indices. Only time dependent dynamic data taken at a single wavelength were fitted point by point. Ellipsometric and radiometric data were fitted together weighing both data types according to their standard deviations. The numerical iterations were performed using Levenberg–Marquardt algorithm (Preuss et al., 1989). The real and imaginary parts (n and k) of the complex refractive index of the $\text{Gd}_{0.42}\text{Mg}_{0.58}$ film sputter deposited on silica in the as deposited, hydrogen loaded and deloaded states are given in the inset of fig. 141. In the deloaded state the extinction coefficient increases at higher wavelengths due to the free electron contributions, clearly revealing the metallic character. The hydrided state shows a dielectric optical response in the visible range. It was observed that the complex refractive index changes significantly from the as-deposited state to the dehydrided state after one cycle and stays constant after subsequent cycles. This effect was related to the significant residual hydrogen that can be found in the samples after one hydrogen cycle. For example, in $\text{Gd}_{0.5}\text{Mg}_{0.5}$ alloy films, it was observed that hydrogen is trapped up to a ratio of 0.8 H/M (as obtained from Rutherford backscattering and elastic recoil detection analysis measurements). As a consequence, the visible reflectance of the magnesium rich alloy films was lowered from about 65% to 60%. For $\text{Gd}_{0.42}\text{Mg}_{0.58}$ alloy film, the extinction coefficient

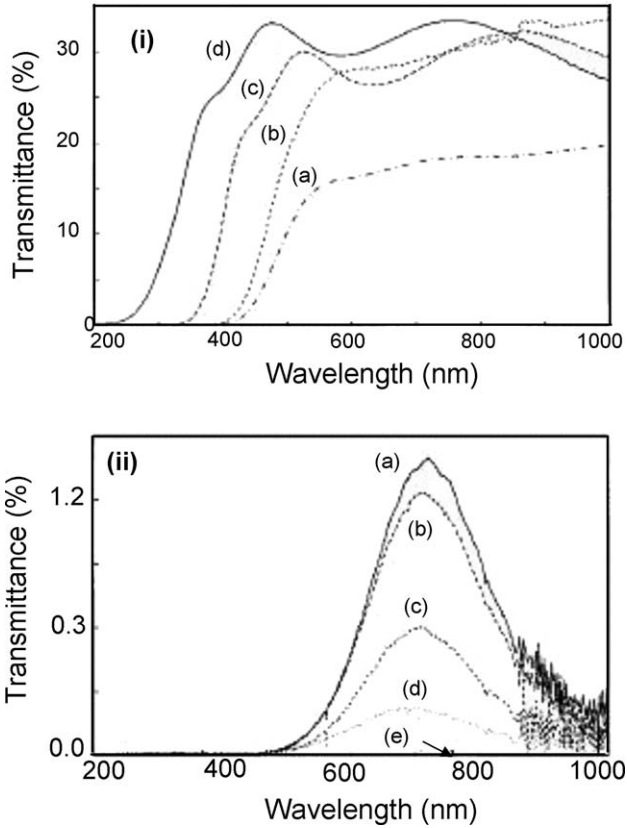


Fig. 140. (i) Optical transmittance of Pd (10 nm) capped $Gd_{1-z}Mg_z$ (200 nm) films with (a) $z = 0$, (b) $z = 0.20$, (c) $z = 0.50$ and (d) $z = 0.90$ in the hydrogen loaded state (at $p_{H_2} = 5$ bar). (ii) The dihydride transmittance window for films with (a) $z = 0$, (b) $z = 0.01$, (c) $z = 0.03$, (d) $z = 0.10$, and (e) $z = 0.30$ (van der Sluis et al., 1997).

at 550 nm in the hydrided state was about 10^{-3} , implying that it was the Pd cap layer, which limits the visible transparency in the hydrogen-loaded state. Thus if the protective layer of Pd could be eliminated, a visible transparency close to 90% seems to be achievable with a 240 nm thick R-Mg alloy films.

The electrochemical loading of the Pd capped Gd-Mg films (deposited on substrate coated with transparent conducting oxide, e.g. $SnO_2:F$ or $In_2O_3:Sn$) have been carried out using galvanostatic, potentiostatic (von Rottkay et al., 1999b), and galvanostatic intermittent titration (GITT: Di Vece et al. (2002)) techniques. In addition to obtaining the direct correlation between the observed changes in optical properties (transmittance in particular) with the hydrogen concentration in the films, the pressure-composition isotherms and the corresponding thermodynamic quantities have also been evaluated utilizing electrochemical loading. Fig. 142 shows the pressure-composition isotherms determined with the

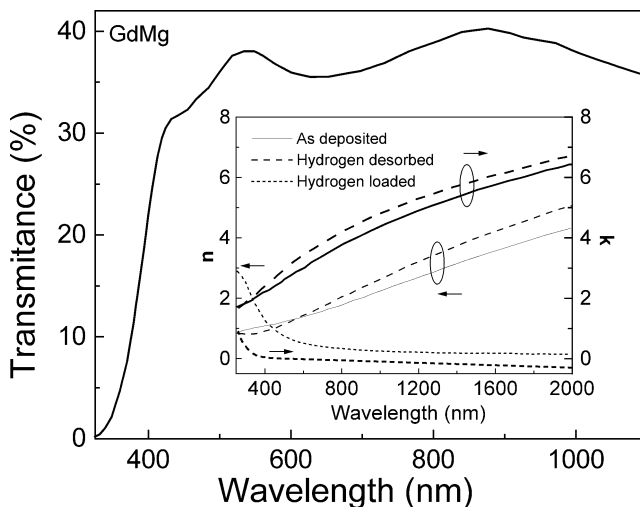


Fig. 141. Optical transmittance of a hydrogen loaded $Gd_{0.42}Mg_{0.58}$ film. Inset shows the real (n) and imaginary parts (k) of the complex refractive index of the $Gd_{0.42}Mg_{0.58}$ film in the as deposited, hydrogen loaded and de-loaded states (von Rottkay et al., 1999a, 1999b).

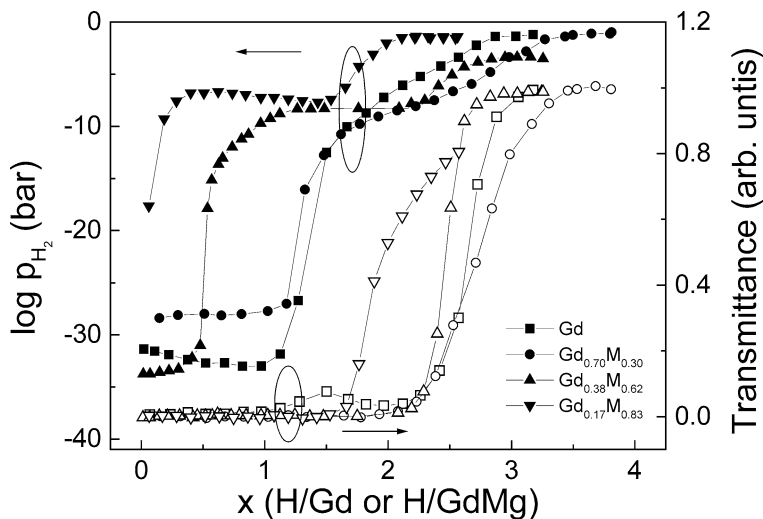


Fig. 142. Pressure-composition isotherms for $Gd_{1-z}Mg_z$ alloys determined with GITT. The simultaneously measured optical transmittance is also shown (Di Vecce et al., 2002).

GITT and the corresponding normalized transmittance as a function of concentration for some representative Pd capped (10 nm) Gd–Mg alloy films (200 nm), deposited by con-

ventional evaporation technique on Mg coated (0.5 nm) ITO films. For $\text{Gd}_{0.7}\text{Mg}_{0.3}$ and $\text{Gd}_{0.38}\text{Mg}_{0.62}$ alloy films the formation enthalpies calculated from the first plateau in the pressure-composition isotherms (-96 kJ/mol and -108 kJ/mol respectively) are close to the formation enthalpy of GdH_2 (-104 kJ/mol for bulk (Libowitz and Macland, 1979); -107 kJ/mol for thin film (Di Vece et al., 2002)), indicating the disproportionation of these GdMg alloys resulting in gadolinium dihydride and magnesium. The hydrogen induced compositional disproportionation was first reported for Y-Mg alloy films (Nagengast et al., 1999b; van der Molen et al., 2001). Nagengast et al. suggested that the Mg clusters which are formed as a result of compositional disproportionation act as microscopic optical shutter (described later in the section) resulting in enhanced optical contrast between the switchable states. From the pressure composition isotherms, Di Vece et al. concluded that the GdH_2 clusters are formed for Gd concentration >0.38 . The formation enthalpy calculated from the second plateau (clearly visible between $x = 1$ to $x = 2.1$) for $\text{Gd}_{0.38}\text{Mg}_{0.62}$, -41 kJ/mol, was in good agreement with corresponding value of -42 kJ/mol for MgH_2 in a stressed thin film (Nagengast et al., 1999b). Though the formation enthalpies of GdH_3 (-46 kJ/mol for bulk (Libowitz and Macland, 1979)) and MgH_2 are similar, the large extent of the second plateau ($\Delta x = 1.1$) in the pressure composition isotherm of $\text{Gd}_{0.38}\text{Mg}_{0.62}$ in comparison to that for GdH_3 ($\Delta x = 0.4$) indicates that the second plateau can be ascribed largely to the MgH_2 formation. From the onset of the optical transmittance measured simultaneously, it was concluded that the formation of GdH_3 was the final stage in the switching process i.e., the main optical changes occurs when the films are with in 10% of the final concentration corresponding to the GdH_3 .

It is interesting to note that the switching/response time (defined as 90% of the optical transition) was observed to decrease with an increase in the Mg concentration. For example, for Pd (10 nm) capped $\text{Gd}_{0.6}\text{Mg}_{0.4}$ film (100 nm) switching time of 0.65 s was observed in contrast to 20 min for $\text{Gd}_{0.8}\text{Mg}_{0.2}$ film (van der Sluis, 1998). For a 204 nm $\text{Gd}_{0.5}\text{Mg}_{0.5}$ film capped with 5 nm Pd over layer, the switching time was observed to be 10 s whereas the transition back to the reflecting state took four times (45 s) longer (von Rottkay et al., 1999a). It is important to note that the kinetics of switching depends on the thickness of the Pd over layer, the hydrogenation pressure and the time between the deposition and measurements (von Rottkay et al., 1999a, 1999b).

Janner et al. (2001), studied the cyclic durability [number of cycles after which the variation in optical transmittance was decreased to half] and degradation mechanism of the differently prepared Gd-Mg alloy films [Pd capped (10 nm) $\text{Gd}_{0.4}\text{Mg}_{0.6}$ metal films (200 nm) deposited by evaporation at 10^{-8} mbar base pressure and Pd capped (15–20 nm) $\text{Gd}_{1-z}\text{Mg}_z\text{H}_x$ films (133–220 nm) deposited by RF Magnetron sputtering with a deposition pressure of 86 μbar in Ar/ H_2 (in the ratio of 1 : 5)] with electrochemical switching in 1 M KOH solution. Degradation in terms of elemental segregation, delamination and growth of a GdMg (hydro)oxide layer upon cycling leading to slower kinetics has been observed. Similar switching kinetics and probable growth of GdMg hydro(oxide) was also observed in the all-solid state switchable mirror device (van der Sluis and Mercier, 2001; Mercier and van der Sluis, 2001). Janner et al. (2001), observed that contacting the sample at the back of the GdMg metal film on a conducting ITO substrate in combination with a 1 nm

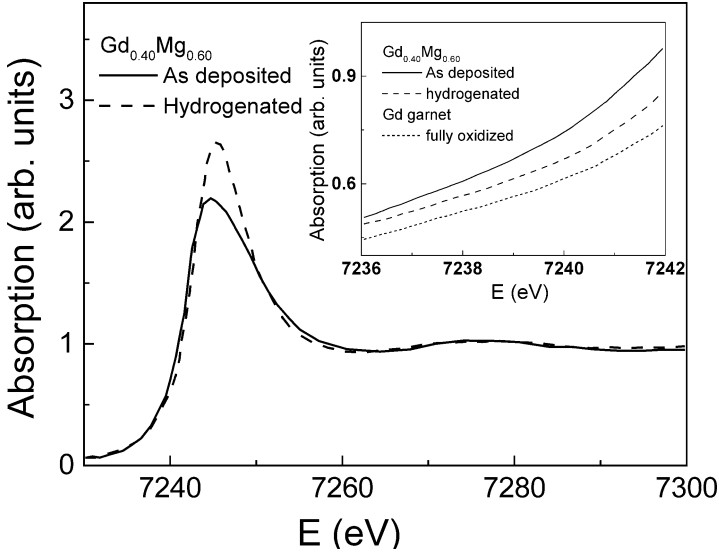


Fig. 143. The X-ray absorption spectra of $\text{Gd}_{0.40}\text{Mg}_{0.60}$ thin film in the as deposited and hydrogenated states. The inset shows the enlarged edge region (Di Vece et al., 2003b).

Mg adhesion layer, increased the cyclic durability by a factor of two where as switchable mirrors that had been deposited in the presence of hydrogen ($\text{Gd}_{1-z}\text{Mg}_z\text{H}_x$) were observed to have improvement by a factor of 10. In contrast, no improvement in cyclic lifetime was observed in the presence of an extra buffer layer (Al, AlO_x , GdMg oxide, CaF_2 and Nb).

Van der Sluis (1998) studied the structural properties of GdMg alloy films using high angle X-ray diffraction analysis. It was observed that up to Mg concentrations near 0.50, GdMg films consist of solid solutions with lattice parameters in reasonable good agreement with linear interpolation between the Gd and Mg lattice parameters. For concentrations near 0.50, the GdMg intermetallic, which has CsCl structure, was observed. Higher Mg concentrations were observed to result in amorphous films. Di Vece et al. (2003b) on the other hand studied the structural and electronic properties of GdMg switchable mirrors [polycrystalline $\text{Gd}_{0.4}\text{Mg}_{0.6}$ films (1 μm) capped with Pd over layer (50 nm)] with X-ray absorption fine structure spectroscopy (XAFS) at the Gd- L_3 edge. Fig. 143 shows the normalized L_3 near-edge X-ray absorption spectra for the GdMg alloy film in the as-deposited state and after hydrogenation. In addition to increase in the intensity of the absorption edge, there was a shift of 0.5 eV (inset of fig. 143) in the hydrogenated film as compared to the as-deposited film. This was directly related to an increase in the number of holes in the d band. A comparison of the edge shift in a fully hydrogenated film to that for the fully oxidized gadolinium (0.9 eV in gadolinium garnet), shows that only 55% of the three conduction electrons are transferred to hydrogen atoms and this may be important for the main optical transitions. Similar evidence of partial charge transfer (an effective charge of $0.5e$ on the hydrogen atoms) has been observed by Rode et al. (2001) from infrared spectroscopy studies in yttrium thin films. From

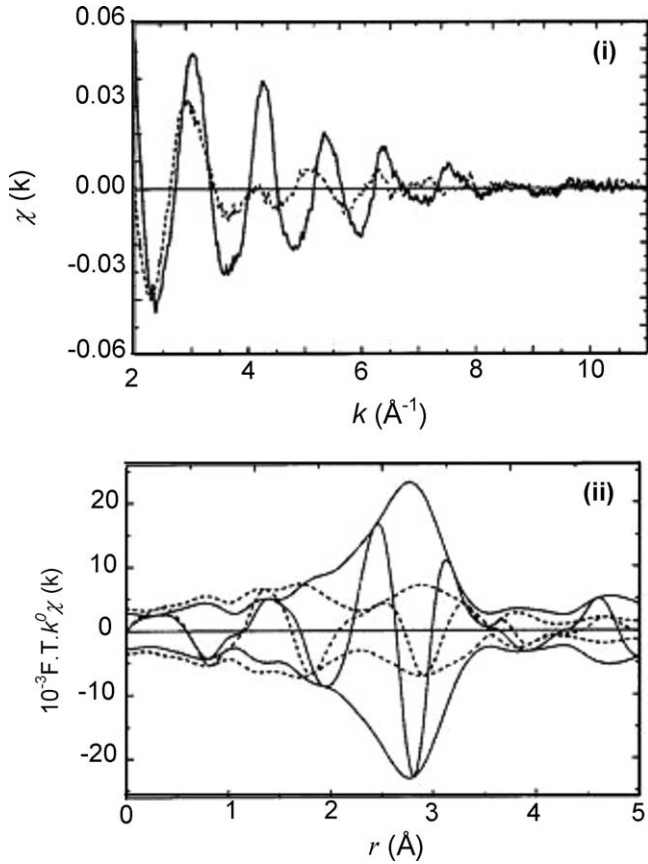


Fig. 144. (i) The normalized EXAFS data and (ii) the Fourier transform (k^0 , $\Delta k = 2.5\text{--}11 \text{\AA}^{-1}$) for the as deposited (solid line) and hydrogenated (dotted line) $\text{Gd}_{0.40}\text{Mg}_{0.60}$ film (Di Vece et al., 2003b).

the EXAFS (extended X-ray absorption fine structure), information about the local structure in the GdMg alloys such as the nature and number of surrounding atoms and interatomic distances were obtained. Fig. 144 gives the normalized EXAFS data for the as deposited (solid line) and the loaded film (dotted line). An abrupt decrease in the absorption after $k = 4$ in the loaded film as compared to the gradual decrease in the as deposited film indicates the dominant presence of hydrogen as scatterer. To emphasize on the low- k region of the EXAFS spectrum (where the hydrogen and oxygen contributions are dominant), the k^0 weighed Fourier transforms of EXAFS spectra of both as deposited and hydrogenated GdMg alloy films have been studied by fitting the data using XDAP data analysis program utilizing four absorber-backscatterer combinations (Gd–Gd, Gd–Mg, Gd–O and Gd–H). Table 4 summarizes the results of the EXAFS analysis of the as deposited and the hydrogenated GdMg alloy films, respectively. The low Gd–Mg and high Gd–Gd coordination numbers in $\text{Gd}_{0.4}\text{Mg}_{0.6}$

Table 4

Summary of results of EXAFS analysis ($2.5 < k < 11 \text{ \AA}^{-1}$, k^0 weighing) of Pd capped $\text{Gd}_{0.40}\text{Mg}_{0.60}$ film in the as deposited and fully hydrogen loaded state. Here N is the coordination number, r interatomic distance, $\Delta\sigma^2$ standard deviation, ΔE_0 adjustable shift to account for uncertainties in chemical bonding and core relaxation effects, and k the wave number (Di Vece et al., 2003b)

Absorber–backscatterer		N	r (\AA)	$\Delta\sigma^2$ (10^{-3} \AA^2)	ΔE_0 (eV)	k variance	
						imaginary	real
Gd–Gd	As-deposited	8.9	3.45	6.8	13.0	0.18	0.08
	loaded	5.2	3.59	6.0	9.5	0.52	0.25
Gd–Mg	As-deposited	2.7	3.23	3.6	–5.1		
	loaded	0.6	3.54	18.0	–8.0		
Gd–O	As-deposited	0.2	2.40	5.0	–7.0		
	loaded	1.0	2.36	8.0	–7.9		
Gd–H	As-deposited	1.5	2.26	5.0	3.0		
	loaded	4.1	2.43	2.6	2.4		

films indicate that the as-deposited film are phase segregated and the segregation was enhanced on hydrogen loading. The small nearest neighbor distances for Gd–Gd and Gd–Mg and a total coordination (Gd + Mg) of 12 around Gd indicate an α -Gd hcp structure in the as deposited $\text{Gd}_{0.4}\text{Mg}_{0.6}$ films. The γ -GdH₃ structure has a c -axis elongation, resulting in larger distances between the planes. Thus instead of 12 nearest neighbors in an ideal hcp structure, only the six nearest gadolinium neighbors within the metal plane are expected to be included in the coordination number. Comparing this value with the total coordination (Gd + Mg) of six present in the hydrogenated $\text{Gd}_{0.4}\text{Mg}_{0.6}$ alloy film, shows that phase segregated Gd clusters have γ -GdH₃ hcp structure in fully hydrogenated state. However the Gd–H coordination of 4 in the hydrogenated films suggested a structure with the octahedral hydrogen shifted to the metal plane in the gadolinium trihydride, as also reported for yttrium trihydride (section 2.1.1).

3.1.5. Er–Mg alloy

Using ellipsometry von Rottkay et al. (1999b) studied the hydrogen induced modifications in the optical properties of the gas-phase loaded Pd (10 nm) capped $\text{Er}_{0.42}\text{Mg}_{0.58}$ alloy films (200 nm), in addition to the $\text{Gd}_{0.42}\text{Mg}_{0.58}$ and $\text{Sm}_{0.48}\text{Mg}_{0.52}$ alloy films. The optical transmittance of the fully hydrogenated sample and the complex refractive indices of the as deposited, hydrogen loaded and deloaded samples are shown in fig. 145.

3.2. R–Mg multilayer films

As reviewed above, the addition of Mg enhanced the reflectivity and lowered the transmittance in the opaque state and enhanced the transmittance and improved the color neutrality of the transparent state in the R–Mg alloy films. However the kinetics of these alloy films were observed to be significantly slower than that of pure R metal based first generation switch-

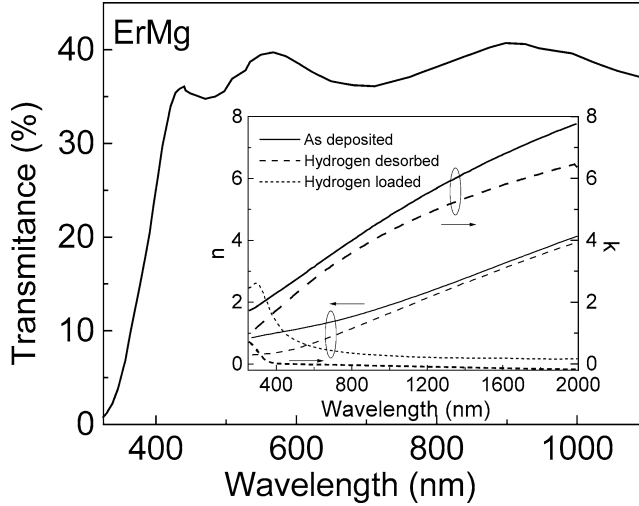


Fig. 145. Optical transmittance of a hydrogen loaded $\text{Er}_{0.42}\text{Mg}_{0.58}$ film. The inset shows the real (n) and imaginary (k) parts of the complex refractive index of the $\text{Er}_{0.42}\text{Mg}_{0.58}$ film in the as deposited, hydrogen loaded and deloaded states (von Rottkay et al., 1999a, 1999b).

Table 5
Effective optical bandgap of YH_3 , $\text{Y}_{0.4}\text{Mg}_{0.6}\text{H}_{2.4}$ alloy and $\text{Y/Mg-H}_{2.4}$ multilayers (Giebels et al., 2002b)

Sample	E_g (± 0.1 eV)
$\text{Y}_{0.4}\text{Mg}_{0.6}\text{H}_{2.4}$ alloy	3.1
$38 \times (2 \text{ nm Mg} + 2 \text{ nm Y})$	2.9
$13 \times (6 \text{ nm Mg} + 6 \text{ nm Y})$	2.7
$15 \times (10 \text{ nm Mg} + 10 \text{ nm Y})$	2.7
$15 \times (10 \text{ nm Y} + 10 \text{ nm Mg}) + 10 \text{ nm Y}$	2.7
YH_3	2.6

able mirrors. In 1998 van der Sluis showed that utilizing multilayer structures consisting of alternating Mg and Gd layers, it was possible to address the problem of slower hydrogenation kinetics. Later, Giebels et al. (2002b) studied Y–Mg multilayer films.

3.2.1. Y–Mg multilayers

The optical, electrical, structural, and thermodynamic properties of the Pd (10 nm) capped Y–Mg multilayers with increasing layer thickness and constant overall composition (near $\text{Y}_{0.40}\text{Mg}_{0.60}$) have been studied and compared with those of hydrogenated $\text{Y}_{0.40}\text{Mg}_{0.60}$ alloy and pure Y films (Giebels et al., 2002b). The transmittance and reflectance of polycrystalline Y–Mg multilayers [$38 \times (2 \text{ nm Y} + 2 \text{ nm Mg})$, $13 \times (6 \text{ nm Y} + 6 \text{ nm Mg})$, $15 \times (10 \text{ nm Y} + 10 \text{ nm Mg})$, $15 \times (10 \text{ nm Y} + 10 \text{ nm Mg}) + 10 \text{ nm Y}$] are compared

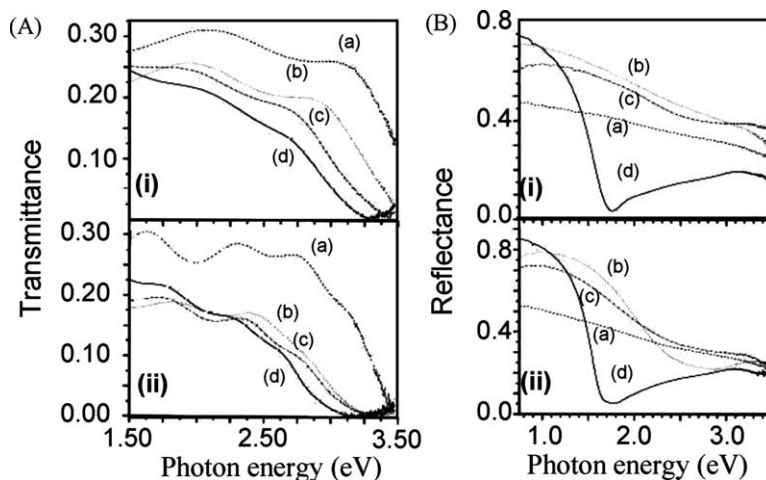


Fig. 146. Transmittance (A) and reflectance (B) spectra of (a) $Y_{0.4}Mg_{0.6}$ alloy, (b) $38 \times (2 \text{ nm Mg} + 2 \text{ nm Y})$, (c) $13 \times (6 \text{ nm Mg} + 6 \text{ nm Y})$, and (d) YH_3 film with total thickness of (i) 150 nm; and (a) $Y_{0.4}Mg_{0.6}$ alloy, (b) $15 \times (10 \text{ nm Mg} + 10 \text{ nm Y})$, (c) $15 \times (10 \text{ nm Mg} + 10 \text{ nm Y}) + 10 \text{ nm Y}$, and (d) YH_3 film with total thickness of (ii) 300 nm (Giebels et al., 2002b).

with those of the Y–Mg alloy and pure Y in the hydrogen loaded and deloaded states respectively (fig. 146). The effective optical absorption edge was estimated from the Lambert–Beer law and is tabulated in table 5. In contrast to the Gd–Mg multilayers (van der Sluis, 1998), it has been observed that the transmittance and the absorption edge of the Y–Mg multilayers depend non-trivially on the distribution of Mg in the film. With an increase in the Mg content, the optical absorption edge of the $YMgH_{2.4}$ multilayers shifts from the edge of the alloy $Y_{0.40}Mg_{0.60}H_{2.4}$ towards the pure YH_3 . The transmittance was also decreased with respect to the alloy films, whereas a comparison of the reflectance spectra of the $YMgH_{0.8}$ multilayer in the deloaded state with those of the YH_2 and $Y_{0.40}Mg_{0.60}H_{0.8}$ alloy shows a large enhancement of reflectance in the former. The variation in the structural, optical and electrical properties of the multilayer film is depicted typically in fig. 147. In region I, the resistivity drops slightly due to the formation of fcc YH_2 . In region II, resistivity increases again before the rise in transmittance, region III. Together with this increase, the YMg intermetallic (with CsCl-like structure) and hcp Mg phases disappear. At the onset of the transmittance, both these phases disappear and the hcp YH_3 peak appears. From the *in situ* XRD and thermodynamic measurements combined with the transmittance measurements, it has been concluded that the Mg and YH_2 transform almost at the same time to MgH_2 and YH_3 , respectively, with a heat of formation of -30.9 kJ/mol H in absorption and -36.6 kJ/mol H in desorption. In addition to this hysteresis effects observed in pure YH_3 films are absent in the multilayer films (fig. 148).

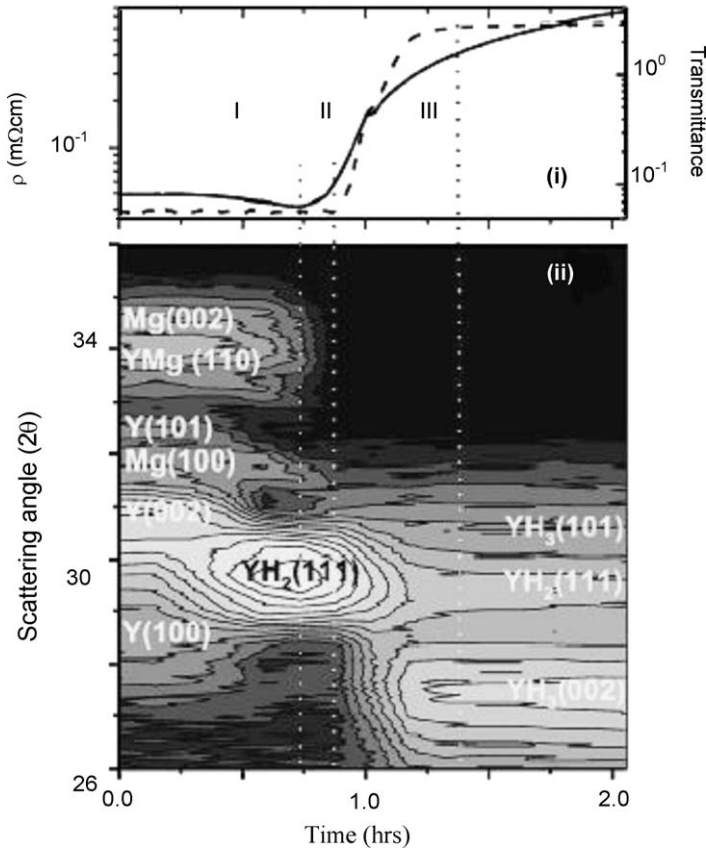


Fig. 147. Time evolution of (i) transmittance (at 1.96 eV) (dashed line) and resistivity (solid line); (ii) Contour plots of the X-ray intensity as a function of time for $13 \times (6 \text{ nm Mg} + 6 \text{ nm Y})$ multilayer capped with Pd (10 nm). At $t = 0.18 \text{ h}$ hydrogen was introduced into the system. The gray scale correspond to a logarithmic intensity scale (Giebels et al., 2002b).

3.2.2. Gd–Mg multilayers

Van der Sluis (1998) studied the structural and optical properties of Pd capped (10 nm) Gd–Mg multilayers with average composition close to $\text{Gd}_{0.60}\text{Mg}_{0.40}$ and approximate thickness of $200 \times (0.21 \text{ nm Gd} + 0.14 \text{ nm Mg})$, $100 \times (0.42 \text{ nm Gd} + 0.28 \text{ nm Mg})$, $50 \times (0.84 \text{ nm Gd} + 0.56 \text{ nm Mg})$, $25 \times (1.68 \text{ nm Gd} + 1.12 \text{ nm Mg})$, $12 \times (3.36 \text{ nm Gd} + 2.24 \text{ nm Mg})$, and $6 \times (6.72 \text{ nm Gd} + 4.48 \text{ nm Mg})$. High angle X-ray diffraction studies showed that in all cases, Gd like diffractograms were obtained with peaks shifted towards lower angles. The origin of the small shift has been interpreted in terms of the residual compressive stresses (in-plane) induced by the intermediate Mg layers or by the dissolution of hydrogen in the metal phase during sputtering. The absence of Mg peaks has been attributed

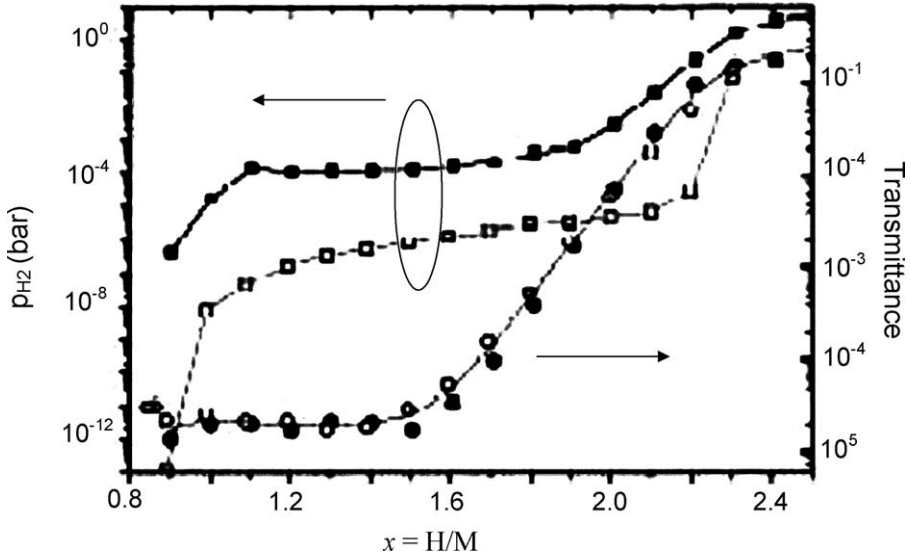


Fig. 148. Pressure-composition isotherm of a $15 \times (10 \text{ nm Mg} + 10 \text{ nm Y})$ multilayer capped with 10 nm Pd between the low (YH_2 and Mg) (\square) and high hydrogen phase (YH_3 and MgH_2) (\blacksquare) as a function of the hydrogen concentration per metal atom, $x = H/M$. The transmittance (at 1.96 eV) spectra as a function of hydrogen concentration for the low (\circ) and the high (\bullet) hydrogen phases (Giebels et al., 2002b).

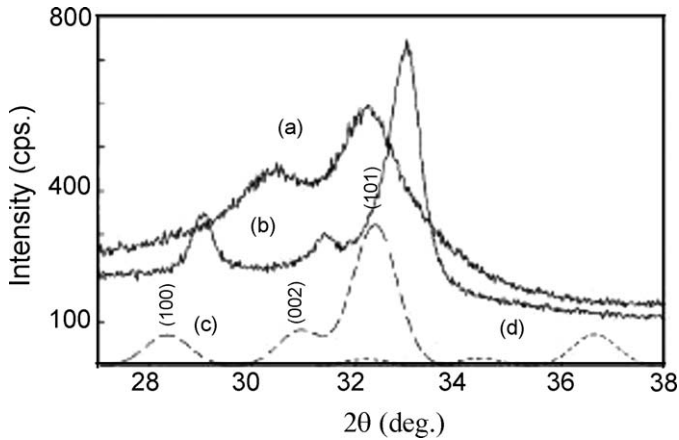


Fig. 149. X-ray diffractogram of Gd-Mg multilayer [$25 \times (1.68 \text{ nm Gd} + 1.12 \text{ nm Mg})$] (a). For comparison the diffractograms of the $Gd_{0.80}Mg_{0.20}$ alloy (b) and calculated diffractograms for pure Gd (c) and pure Mg (d) are also shown (van der Sluis, 1998).

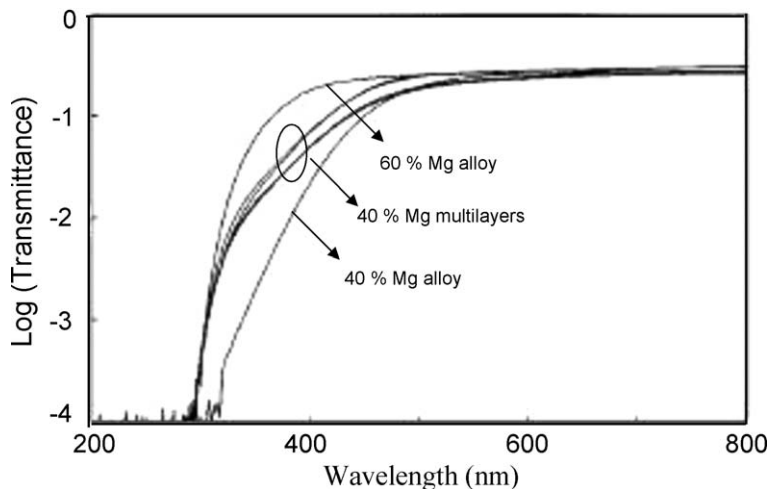


Fig. 150. Log (transmittance) as a function of wavelength for Gd–Mg multilayers (with constant average composition 40% and varying periodicities) along with those of $\text{Gd}_{0.80}\text{Mg}_{0.20}$ and $\text{Gd}_{0.40}\text{Mg}_{0.60}$ alloy films in the fully hydrogenated state (van der Sluis, 1998).

to its low scattering factor. Fig. 149 shows the X-ray diffractogram of a typical Gd–Mg multilayer [$25 \times (1.68 \text{ nm Gd} + 1.12 \text{ nm Mg})$]. For comparison, the diffractograms of the $\text{Gd}_{0.80}\text{Mg}_{0.20}$ and calculated diffractograms for pure Gd and pure Mg are also shown. Low angle X-ray reflectivity measurements on the multilayer films showed that the multilayer structure was preserved and the multilayer expands irreversibly by 15% during the hydrogen induced switching. The log of transmittance spectra of the Gd–Mg multilayers along with those of $\text{Gd}_{0.80}\text{Mg}_{0.20}$ and $\text{Gd}_{0.40}\text{Mg}_{0.60}$ alloy films in the fully hydrogenated state are shown in fig. 150 revealing a high transmittance at long wavelengths (limited by the Pd over layer) and a drop in the transmittance at a specific wavelength (corresponding to the band gap). All the multilayer spectra appear identical irrespective of the periodicity and fall between those of the $\text{Gd}_{0.80}\text{Mg}_{0.20}$ and $\text{Gd}_{0.40}\text{Mg}_{0.60}$ alloy films. The inset of fig. 151 compares the transmittance as a function of the hydrogen exposure time for a $25 \times (1.68 \text{ nm Gd} + 1.12 \text{ nm Mg})$ multilayer with composition close to $\text{Gd}_{0.60}\text{Mg}_{0.40}$ and that of a 100 nm alloy film of same composition, clearly showing faster switching kinetics of the multilayer as compared to alloy film. The enhanced switching kinetics was even more pronounced for higher Mg contents, e.g., the $\text{Gd}_{0.20}\text{Mg}_{0.80}$ alloy film has a switching time from metal to fully hydrogenated state of about 20 min as compared to 70 s in case of a multilayer film with same average composition [$53 \times (0.21 \text{ nm Gd} + 1.12 \text{ nm Mg})$]. The switching kinetics of the Gd–Mg multilayers depends on the periodicity. Fig. 151 also shows the variation in the switching times (defined as 90% of the optical effects from metal to high hydrogen state) for the multilayers with constant average composition and varying periodicities, clearly showing fastest switching for intermediate Mg concentrations.

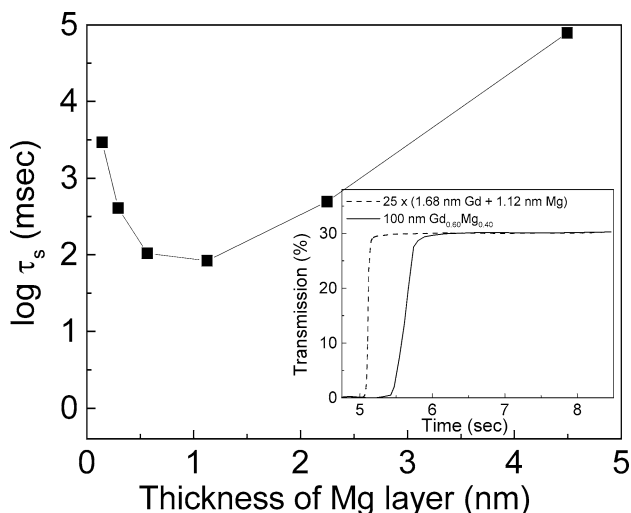


Fig. 151. Variation of switching time (defined as 90% of the optical effects from metal to high hydrogen state) for the Gd–Mg multilayers with constant average composition [$25 \times (1.68 \text{ nm Gd} + 1.12 \text{ nm Mg})$] and varying periodicities. The inset compares the transmittance as a function of the hydrogen exposure time for a $25 \times (1.68 \text{ nm Gd} + 1.12 \text{ nm Mg})$ multilayer with composition close to $\text{Gd}_{0.60}\text{Mg}_{0.40}$ and that of a 100 nm alloy film of same composition, clearly showing faster switching kinetics of the multilayer (0.08 s) as compared to alloy film (0.65 s) (van der Sluis, 1998).

4. New generation rare earth nanoparticle based switchable mirrors

Recently, a “nanoparticle route” has been utilized to improve switchable mirror properties. It has been shown that it is possible to tune the hydrogen induced structural, optical and electrical properties by varying the nanoparticle size. Bour et al. (2001) and Stepanov et al. (2002a, 2002b) studied the optical and electrical properties of Y nanoparticle layer deposited by pulsed laser ablation. Aruna et al. (2004, 2005a, 2005b, 2005c) investigated the effect of reducing the nanoparticle size in both Gd layer and catalytic Pd over layer deposited by inert gas evaporation on the switchable mirror characteristics.

4.1. Y nanoparticle layers

Y nanoparticles prepared from a bulk metal target by pulsed laser ablation (PLA) using a pulsed Nd:YAG laser in an Ar background atmosphere were deposited on quartz substrates or carbon coated grids by adiabatic expansion of the metal clusters through a nozzle with Ar as carrier gas (Gartz et al., 1999; Bour et al., 2001; Stepanov et al., 2002a, 2002b). The nanoparticles deposited at 0.6 bar Ar pressure were observed to have an average size of 25 nm where as those deposited at 1.2 bar had 30 nm average size (fig. 152) (Stepanov et al., 2002a, 2002b). It was observed that the nanoparticles deposited at higher background pressure were surrounded by a shell (fig. 153), which was assumed to be that of Y_2O_3 . To examine this

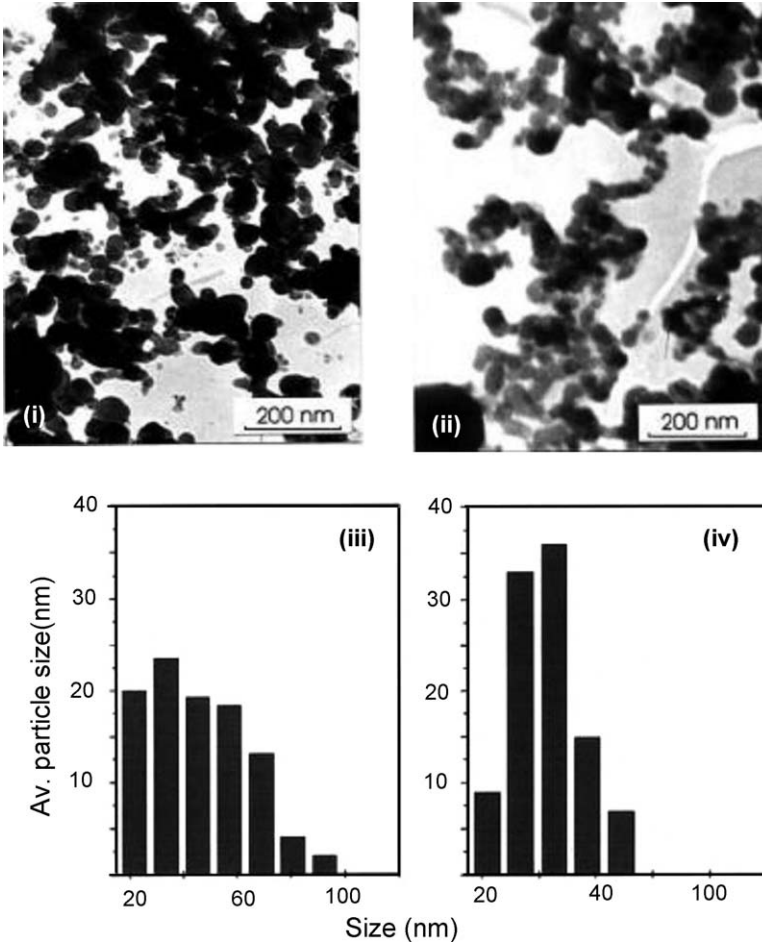


Fig. 152. TEM micrographs of Y nanoparticles prepared by PLA at (i) 0.6 bar and (ii) 1.2 bar Ar pressure. The corresponding particle size histograms are respectively shown in (iii) and (iv), revealing an average size of 25 nm with standard deviation of 68 nm and 30 nm with deviation of 19 nm (Stepanov et al., 2002a).

suggestion, the optical extinction spectra of the deposited clusters on quartz substrate were measured *in situ* in UHV. Stepanov et al. (2002b) applied the Mie scattering theory to calculate the extinction spectra of Y core clusters with Y_2O_3 shell on the surface of silica using recursion formalism. In this modeling the size of the core was kept constant at 16 nm and the thickness of the shell was monotonically varied from 0 to 20 nm. The experimental observations as well as the calculations clearly revealed that an increase in the thickness of the shell moved the optical extinction peak of the Mie resonance to lower photon energies and yielded an extinction increasing in the ultraviolet region. Stepanov et al. (2002b) argued that though

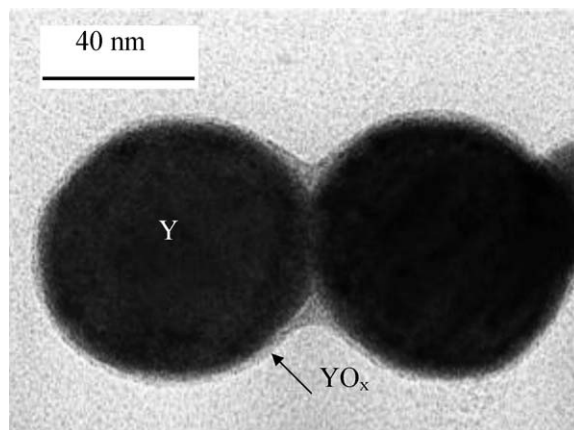


Fig. 153. HRTEM micrograph of Y nanoparticles clearly revealing a distinguishable shell presumably consisting of yttrium monoxide (Bour et al., 2001).

the high extent of aggregation and the broad size distributions were not taken into account in Mie theory, their results give qualitative information about the optical behavior and some agreement with the experimental observations.

Y nanoparticle layers were covered by a Pd over layer (1–2 nm) and hydrogenated at room temperature and different background pressures (3×10^{-6} to 5 mbar). It was possible to observe hydrogenation effects both optically and electrically, even with the oxide shells, revealing that these shells do not hinder hydrogenation/dehydrogenation process. In the first step metallic YH_2 was formed and in the second step additional H formed $\text{YH}_{3-\delta}$ ($\delta < 1$ to $\delta \ll 1$). Aruna et al. (2005a) also observed the presence of hydrogen permeable oxide shell around the Gd nanoparticles deposited by inert gas evaporation technique. It was observed that, in addition to the unhindered hydrogenation/dehydrogenation, the oxide shell acts as protective cover against further oxidation of the core in the absence of Pd over layer (Aruna et al., 2005a). Bour et al. argued that though the films were percolated as required for the electrical measurements, the nanoparticles could be assumed as separate (alienated by the oxide shell) and hence Mie's theory could be applied as an acceptable approximation. The phase composition of the hydrogenated nanoparticles was determined by the optical density measurements performed *in situ*. The measurements were performed at room temperature in a wavelength range from 250 to 1000 nm using a single-beam optical fiber setup based on an MSC 400 spectrometer. It was argued that the comparison of the experimental optical data with the basic Mie theory could be used to discriminate between the two metallic phases, which exhibit different Mie peaks and the dielectric phases, which do not show any plasmon peak. On going from Y to $\text{YH}_{\approx 2}$, Mie resonance peak was observed first at 3.25 eV and then at 1.26 eV [fig. 154(i)] (Bour et al., 2001, Stepanov et al., 2002a, 2002b). The experimental data was fitted with the theoretical Mie calculations using bulk dielectric functions and the best fit was observed for $\text{YH}_{2.2}$ assuring a quantitatively correct ratio between the peaks at 1.3 eV and 3.3 eV [fig. 154(ii)]. As

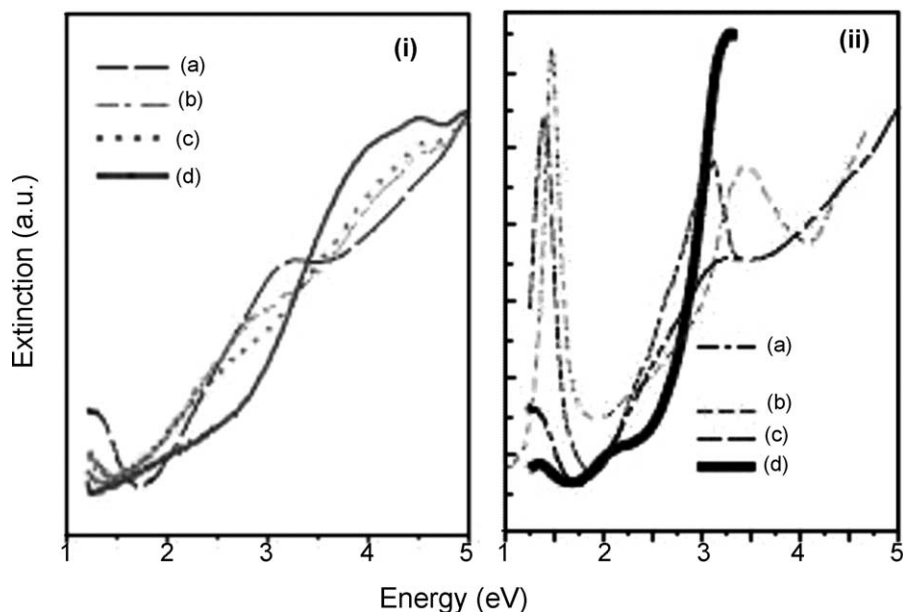


Fig. 154. (i) Variation in extinction coefficient of $\text{YH}_{\approx 2}$ (a) with increase in hydrogen pressure (b) 5.0×10^{-3} , (c) 2.1×10^{-1} , (d) 8.8×10^0 mbar H_2 . (ii) Calculated spectra (b–d) using theoretical Mie calculations for $\text{YH}_{\approx 2}$ (a) assuming (b) $\text{YH}_{1.73}$, (c) $\text{YH}_{1.81}$, and (d) $\text{YH}_{2.2}$ (Bour et al., 2001).

the hydrogen concentration was increased in $\text{YH}_{\approx 2}$, two noticeable changes were observed: (i) the peak at 1.26 eV disappeared rapidly and vanished at 2.1×10^{-1} mbar external H_2 pressure and (ii) the peak at 3.25 eV remained visible longer but faded at 8.8 mbar indicating the formation of the insulating trihydride state. From the slope of the interband edge at 8.8 mbar, Bour et al. estimated the band gap of the trihydride state to be 2.51 eV.

The changes in electrical resistivity as a function of H_2 pressure during loading is shown in fig. 155(i). For the initial rise in pressure from 3×10^{-6} mbar (base pressure) to 2×10^{-5} mbar, a minor change of 16 Ω in resistivity was observed over 30 min (first inset in fig. 155). The second increase in the H_2 partial pressure to 1×10^{-5} mbar was observed to produce a more pronounced change of 146 Ω over 47 minutes (second inset does not show any sign of having reached equilibrium as the curve still increases further). Afterwards, every increase in H_2 pressure was observed to have pronounced effects on resistivity. At 1×10^{-3} mbar and 1×10^{-2} mbar respectively, equilibrium was reached within 30 min. For higher pressures, a rapid change within minutes followed by a gradual increase was observed indicating the presence of more than one diffusion mechanism. Similar time dependence was observed during deloading [fig. 155(ii)]. First a rapid decrease in resistivity was observed. After 30 min, the pressure was observed to reach below 1×10^{-5} mbar. However it took 21 hours to reach to the initial resistivity value. The cyclic variation in the resistance of the Pd capped Y nanoparticle layers in response to the variation to hydrogen pressure is shown in fig. 156. The solid lines

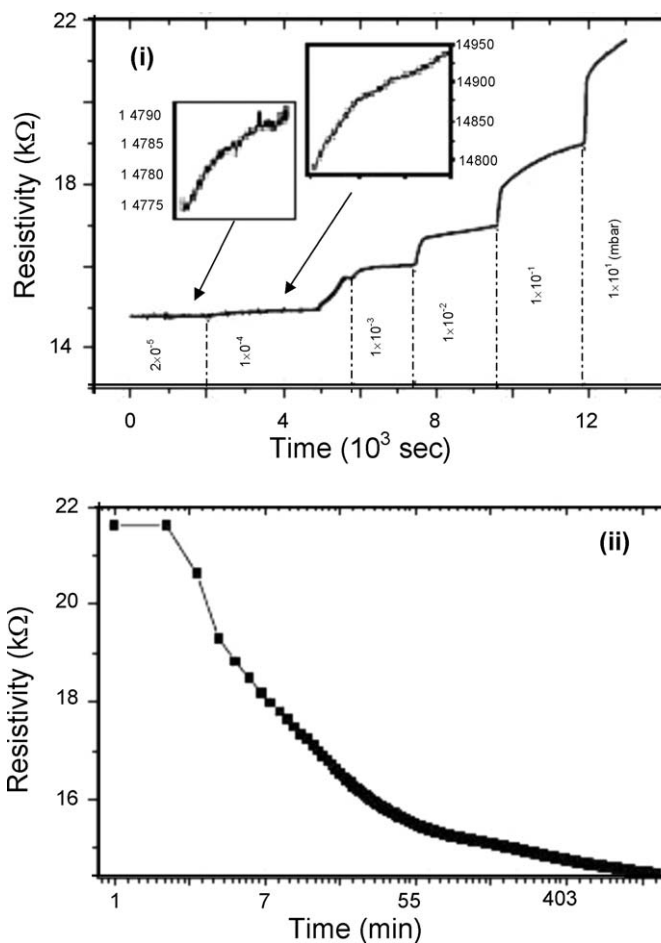


Fig. 155. Variation in resistivity of Y nanoparticles as a function of hydrogen exposure time during hydrogen (i) loading and (ii) deloading. The dependence of the change in electrical resistivity on hydrogen pressure is shown in (i). The vertical lines in (i) indicate the hydrogen pressure. The two insets in (i) show a more detailed view of the resistivity variation in the two regions indicated by arrows (Bour et al., 2001).

show the increase in resistance upon increase in the H_2 pressure to 10 mbar and the dotted curve shows the change in resistance on subsequent evacuation of the working chamber to 10^{-6} mbar. Bour et al. and Stepanov et al. argued that the sensitivity of the Y nanoparticles to low amounts of hydrogen makes the future application as optical and/or hydrogen sensor feasible. It was argued that Y nanoparticles have the advantage of increased efficacy of interaction with hydrogen due to increased surface area and higher stability with respect to mechanical stresses and fracture as compared to Y films.

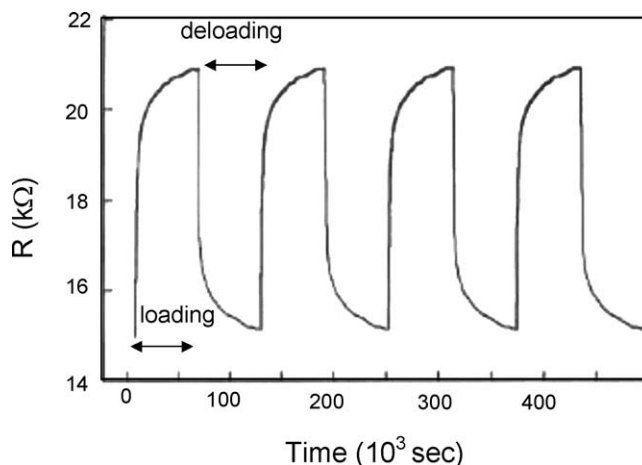


Fig. 156. Cyclic variation in resistance of Pd capped Y nanoparticle layer during hydrogen loading (pressure increases to 10 mbar) and deloading (subsequent evacuation of the chamber) (Stepanov et al., 2002b).

It may be mentioned that Lokhorst et al. (2003) studied the hydrogen induced changes in the structural, optical and electrical properties of directly deposited nanocrystalline YH₂ films deposited on quartz substrate at room temperature using PLD technique (see section 2.4.2 for details).

4.2. Gd nanoparticle layers

Gd nanoparticle films were synthesized using inert gas evaporation technique (Aruna et al., 2004, 2005a, 2005b). High purity Gd (99.9%) was evaporated in inert gas (Ar) ambient using a resistively heated tungsten boat. The working pressure, gas flow rate and substrate temperature were varied to vary the particle size in Gd nanoparticle films. Different substrates such as glass, quartz, NaCl, silicon, and carbon coated copper grid were used for characterizing these nanoparticle films using several complementary techniques such as glancing angle X-ray diffractometer (GAXRD), transmission electron microscopy (TEM), high resolution transmission electron microscopy (HRTEM), atomic force microscopy (AFM), UV-VIS-NIR spectrophotometer, X-ray photoelectron spectrometer (XPS) and elastic recoil detection analysis (ERDA). For fabricating Gd nanoparticle film based switchable mirrors, Gd nanoparticle layers (30 nm) deposited on transparent substrate were capped with a Pd over layer (10 nm). Gd nanoparticle films were loaded with hydrogen via gas phase loading by introducing H₂ into the chamber at 30 sc cm (standard cubic centimeter) until a pressure of 760 Torr was attained. For deloading, the chamber was evacuated using a mechanical rotary pump. Fig. 157 shows a comparison of the X-ray diffractograms of the Pd capped Gd nanoparticle film deposited at an argon pressure of 1.7×10^{-3} Torr (with an average particle size of 8 nm) and Pd capped Gd polycrystalline film deposited in vacuum at a base pressure of 1.0×10^{-6} Torr. The inset shows a typical TEM micrograph of Gd nanoparticle sample with an average particle size

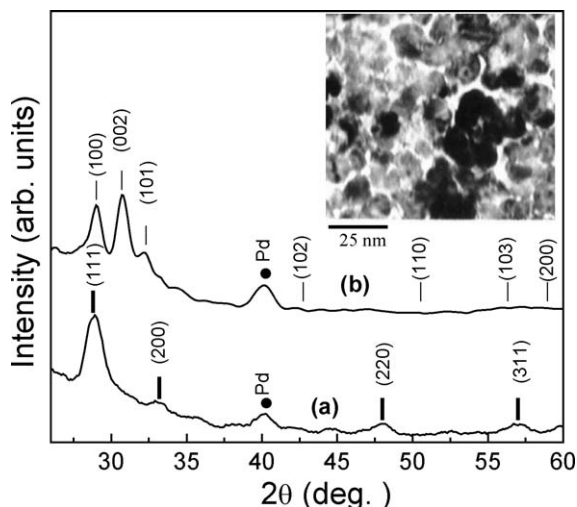


Fig. 157. X-ray diffractograms of as-deposited Gd (a) nanoparticle and (b) polycrystalline films capped by a Pd layer. The thick vertical lines represent the calculated (hkl) values corresponding to the f.c.c. structure and the thin lines represent the (hkl) values corresponding to the h.c.p. structure of Gd. The XRD peak at $2\theta = 40.1^\circ$ corresponds to the (111) plane of f.c.c. structure of Pd. The inset shows the TEM micrograph of Gd film nanoparticle film with an average particle size of 8 nm (Aruna et al., 2004).

of 8 nm. The X-ray diffractogram of Gd nanoparticles, revealed face centered cubic (f.c.c.) structure with $a = 5.37 \text{ \AA}$. The observed 2θ and “d” values and calculated (hkl) planes were: $2\theta = 28.8^\circ$, $d = 3.099 \text{ \AA}$, (111); $2\theta = 33.2^\circ$, $d = 2.697 \text{ \AA}$, (200); $2\theta = 48.0^\circ$, $d = 1.895 \text{ \AA}$, (220) and $2\theta = 57.0^\circ$, $d = 1.615 \text{ \AA}$, (311). Gd polycrystalline film on the other hand showed predominant XRD peaks corresponding to h.c.p. structure. The observed 2θ and “d” values were: $2\theta = 29.1^\circ$, $d = 3.066 \text{ \AA}$; $2\theta = 30.7^\circ$, $d = 2.910 \text{ \AA}$, and $2\theta = 32.2^\circ$, $d = 2.778 \text{ \AA}$, corresponding to (100), (002), and (101) planes of h.c.p. structure with $a = 3.54 \text{ \AA}$ and $c = 5.82 \text{ \AA}$. The size-induced structural transitions were observed in both bare and Pd layer capped Gd nanoparticle films (Aruna et al., 2004, 2005a). The size-induced structural transformations in nanoparticles have been explained as being due to the modified surface structure, and/or a large concentration of defects present in the nanophase and/or the change in Gibbs free energy due to the surface energy term. GAXRD measurements were also carried out in the hydrogen loaded and deloaded Gd nanoparticle films in order to study the hydrogen induced structural changes. Gd nanoparticle films having the fcc structure were observed to remain fcc in the dihydride and the trihydride phases. In contrast to this, the polycrystalline Gd films were observed to undergo a structural transition from hcp structure (metal) to fcc (dihydride) and finally become fcc (trihydride) (Aruna et al., 2005b) (fig. 158).

The hydrogen-induced optical and electrical switching behavior were studied in Gd nanoparticle and polycrystalline films (30 nm) capped with a Pd over layer (10 nm) (Aruna et al., 2004). In comparison with the polycrystalline Gd films, Gd nanoparticle films were observed to show improved optical and electrical switching behavior. First, the optical trans-

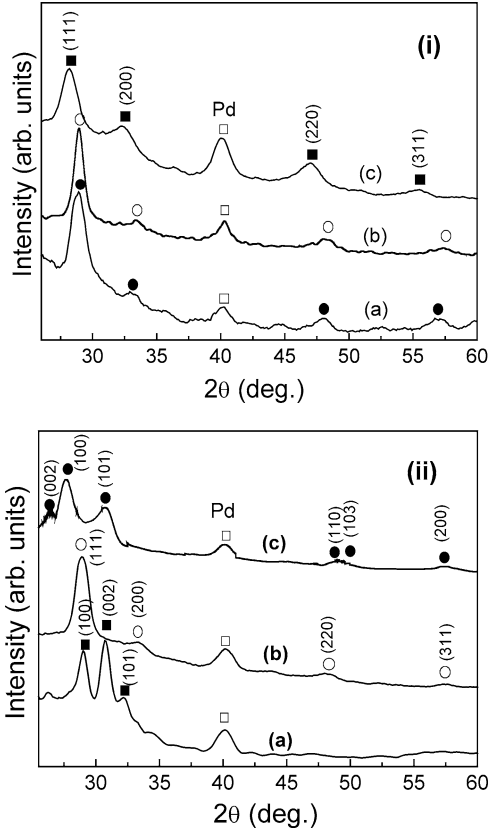


Fig. 158. X-ray diffractograms of as-deposited (a), hydrogen loaded (c) and deloaded (b) Gd nanoparticle (i) and polycrystalline (ii) films capped with Pd over layer (Aruna et al., 2005b).

mittance of the trihydride state of the nanoparticle films showed an extended constant transmittance region in the visible energy with decrease in the nanoparticle size as a consequence of size-induced blue shift. Secondly, the optical contrast $[OC = (T_L - T_{DL})/T_L]$, where T_L and T_{DL} are the transmittance values of loaded and deloaded samples, respectively] was also observed to increase with decrease in the nanoparticle size. Finally, the electrical switching time upon hydrogenation (time taken for the resistance to reach to 90% of its final value) of Gd nanoparticle films was observed to be size-dependent and become better with a decrease in the Gd nanoparticle size as compared to polycrystalline Gd films (fig. 159). Using the transmittance, reflectance, and thickness data of hydrogenated Pd capped Gd films and accounting for the transmittance and reflectance of the Pd over layer, the optical absorption coefficient (α) of $GdH_{3-\delta}$ was evaluated. The best linear relationship obtained for $(\alpha h\nu)^2$ vs. $h\nu$ plots, indicated a direct allowed transition. The intercept of linear fit to the abscissa at $\alpha = 0$ was used to estimate the optical absorption edge of 2.89 eV, 2.64 eV and 2.55 eV for hydrogen loaded

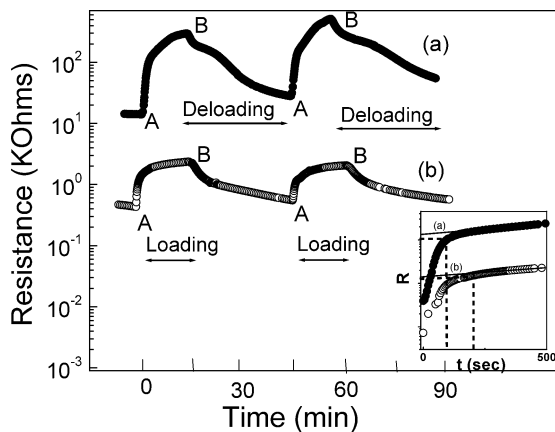


Fig. 159. Cyclic variation in resistance of Pd capped Gd nanoparticle sample (a) and polycrystalline sample (b) between dihydride (A) and trihydride (B) states. For clarity, the first transition point between A and B shown in the figure is marked as the starting point ($t = 0$). The inset shows a magnified part of the electrical switching curves [resistance (R) as a function of hydrogen exposure time (t)] for the two films. The values of time required for attaining 90% of the final resistance value from the initial value are marked as vertical dotted lines (Aruna et al., 2004).

Gd nanoparticle film having average particle size 8 nm, 10 nm and Gd polycrystalline film, respectively (fig. 160). For measuring hydrogen concentration in the dihydride and trihydride states of Gd nanoparticle and polycrystalline layers Aruna et al. (2005b) performed the ERDA measurements using 40 MeV $^{28}\text{Si}^{5+}$ ions. Along with ERDA measurements, Rutherford back scattering spectroscopy (RBS) was carried out to determine the Pd and Gd composition and thickness. The variation of hydrogen concentration (estimated from the area under the H recoil curve) as a function of ion dose, in case of hydrogen loaded and deloaded states of the Pd capped Gd nanoparticle and polycrystalline films is shown in fig. 161. The absolute hydrogen concentration in the films was estimated by extrapolating the curves to zero ion fluence. The results of this study clearly showed that the improvements in optical and electrical switching characteristics of Gd nanoparticle based switchable mirrors were directly related to large changes in H concentration during loading–deloading cycles in case of nanoparticle samples. Nanoparticle sample were observed to exhibit a larger difference in the $[\text{H}]/[\text{Gd}]$ values (2.9 and 1.7) in comparison to polycrystalline sample (2.4 and 2.0) in the loaded and deloaded states. H depth profile analysis showed that hydrogenation/dehydrogenation process was limited to about 100 nm thickness in polycrystalline samples whereas the complete 120 nm thickness is active in case of nanoparticle sample (fig. 162). These results have been explained in terms of enhanced surface area, large number of inter particle boundaries, a relatively slack Gd layer and the reduced interlocking of grains due to di- and trihydride phases having similar crystal structures in case of nanoparticle sample.

A detailed X-ray photoelectron spectroscopy study was carried out to understand the effect of nanoparticle nature on the Pd–Gd interface. In case of Gd polycrystalline films, Pd 4d peak was observed to become narrow (FWHM of the Pd 4d peak decreases from 4.78 eV to

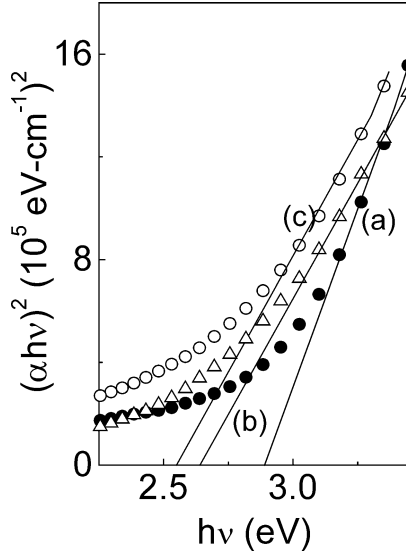


Fig. 160. Tauc's plots of the hydrogenated Gd nanoparticle film with average size (a) 8 nm and (b) 10 nm, and (c) Gd polycrystalline film (Aruna et al., 2004).

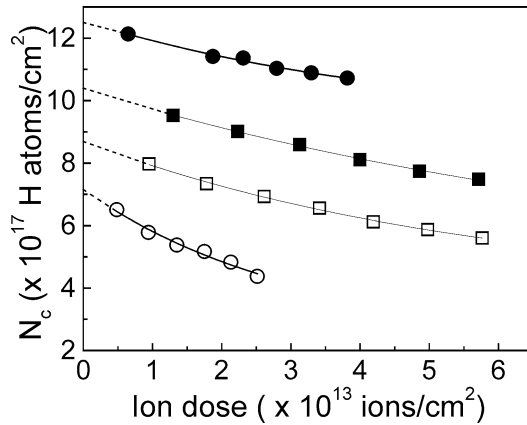


Fig. 161. Variation of the hydrogen concentration as a function of ion fluence in nanoparticle and polycrystalline films in the fully loaded state (●-, ■-, respectively) and in the deloaded state (-○-, -□-, respectively) (Aruna et al., 2005b).

3.59 eV) and shift towards higher energy (from 1.68 eV to 3.15 eV) with respect to Fermi level at Gd-Pd interface (fig. 163). A similar narrowing and shifting of transition metal d bands to higher binding energy value was observed in Gd_xT_y ($T = Ni, Rh, Ir, Pd$) compounds and

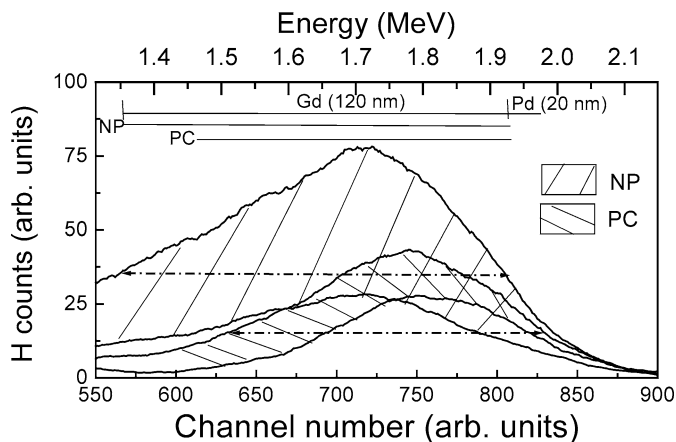


Fig. 162. Typical H recoil spectra of hydrogen loaded (NPT, PCT) and deloaded (NPD, PCD) Gd nanoparticle (NP) and polycrystalline (PC) films. (NPT: 2.3×10^{13} ion/cm², NPD: 2.5×10^{13} ion/cm², PCT: 2.2×10^{13} ion/cm², PCD: 2.6×10^{13} ion/cm²). The dotted lines represent the active thickness of the Gd layer (in NP 120 nm and in PC ~ 100 nm) participating in hydrogenation/dehydrogenation (Aruna et al., 2005b).

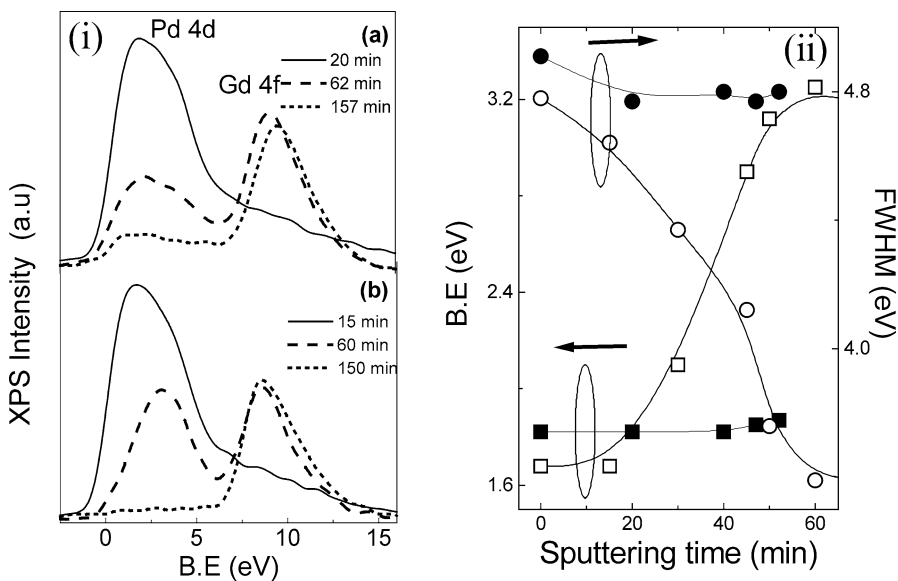


Fig. 163. (i) Valence band spectra of Pd capped Gd nanoparticle (a) and (b) polycrystalline films at different sputtering times. Intensity of Gd 4f peak increases and that of Pd 4d decreases on going from Pd to Gd at Pd-Gd interface. (ii) Change in FWHM and binding energy of Pd 4d electrons as a function of sputtering time for nanoparticle (solid symbols) and polycrystalline (hollow symbols) films (Aruna et al., 2004).

the observed band narrowing on compound formation was attributed to reduced coordination with equivalent atoms (Talík et al., 1998). The narrowing of Pd 4d band was also explained in terms of the hybridization of almost empty Gd 5d band with the nearly full Pd 4d band. The shift in the binding energy position of Pd 4d electrons in Gd₃Pd compounds was attributed to the charge transfer from Gd 6s to Pd 4d states. The FWHM (4.91–4.98 eV) and binding energy (1.82–1.87 eV) of Pd 4d peak in case of Gd nanoparticle film, on the other hand, was observed to remain almost constant, clearly revealing the absence of Pd–Gd alloy formation at the interface (fig. 163). These results were explained in terms of a Gd₂O₃ shell around the Gd nanoparticle core. It was argued that the presence of the oxide shell hinders the charge transfer from Gd to Pd preventing the Gd–Pd interface alloy formation resulting in the improvement of the Pd coverage and hence the enhanced switchable mirror characteristics of the Gd nanoparticle film.

5. Applications of switchable rare earth hydride films

In addition to opening up some unfathomable challenges for physicists, rare earth metal hydride films offer a number of interesting possibilities for technological applications. Besides the gas-phase hydrogenation of rare earth metals, liquid and solid state materials have been reported as suitable media to stimulate such optical switching under electrochemical polarization, indicating the possibility of many technological devices based on electrochromism. The possibility of real time visualization of the optical transitions reported in the lateral diffusion experiments (den Broeder et al., 1998; van der Molen et al., 2000, 2002a, 2002b) revealed promising application of the rare earth hydride films in indicator layers and display devices. Epitaxial switchable mirrors may offer additional possibilities through their self-organized, pixel-by-pixel switchable domain pattern (e.g., Nagengast et al. (1999a), Kerssemakers et al. (2000, 2002a)). UV light triggered switchable mirrors (Hoekstra et al., 2001, 2003; Voss, 2001; Roesnbaum and Hoekstra, 2002; Roy et al., 2002) hint at the possibility of light controlling light and the usage in optoelectronics. The fast response times of the rare earth films even at small H₂ pressures (Bour et al., 2001; Kumar and Malhotra, 2004c) offer the possibility for sensor applications. Recent study of the nanoparticle based switchable mirrors (Aruna et al., 2004, 2005b) offer the possibility of fabricating switchable mirror devices at nanoscale. Other potential applications of switchable rare earth hydride films include high-tech window shades with solar heat control, variable reflectance rear-view mirrors in cars, variable transmittance glasses, computer displays, antireflection coatings for TV screens and monitors, tunable magnetic layers, smart light bulbs with adaptive optics, optical logic gates, and in optical computing and fiber-optical network switching. Though all the above-mentioned applications have not been looked into, some of them reported in literature are discussed in the following sections.

5.1. Electrochromic devices

Electrochromism is the reversible change in the optical properties that occur when a material is electrochemically oxidized or reduced. The device consists, of the active electrochromic layer,

an electrolyte and a counter electrode, which may or may not be electrochromic. The electrolyte should be good ionic conductor and electrically insulating in order to be non-volatile.

Since the first report on the possible hydrogenation of the R metal layers via electrochemical loading, most of the efforts from application point of view were dedicated towards fabricating all solid state electrochromic devices for smart optical windows. The feasibility of all-solid-state devices based on R metal-hydride switchable mirrors was first demonstrated by Armitage et al. (1999). The device was based on Gd–Mg hydride, Pd, hydrated zirconium oxide proton conductor, H storage layer, and an ITO layer deposited on glass substrate. The schematic diagram is shown in fig. 164(i). WO_3 that switches from transparent to blue when protonated (complementing the transition in the RH_x) was used as the H storage layer. When the hydride was kept at -3.0 V relative to the WO_3 all the layers were transparent where as when it was at $+3.0$ V the reverse process occurred and the device was observed to become absorbing and reflecting. As the potential was varied through this range, the H content in the hydride was varied, yielding intermediate optical properties. The device was observed to switch reversibly from reflecting ($\sim 35\%$ R, $<0.05\%$ T) to transparent ($>25\%$ T at 650 nm), with intermediate properties between these two states [fig. 164(ii) and (iii)]. Although the optical switching characteristics and the stability of the prototype switching mirror were encouraging, the switching time was observed to be too high for practical applications. The device was observed to take 16 h for the reflecting–transparent–reflecting cycle in contrast to 3 min for Gd–Mg hydride film upon electrochemical loading (von Rottkay et al., 1999a) which was attributed to the shorting and unexpectedly high resistance of the hydrated ZrO_2 . Using an inverted configuration (WO_3 as the bottom electrode and consisting of GdMgH_5 electrochromic layer) as depicted in schematic in fig. 165, van der Sluis et al. showed that the switching times could be reduced to 5 min, although the full switching cycle was still of the order of 1 h. The device was observed to switch reversibly up to ~ 500 times. Switching was carried out with ± 1 V over the device. When $+1$ V was applied to the GdMgH_5 layer, the hydrogen moved towards the WO_3 which was observed to become blue while the GdMgH_5 layer was observed to become metallic (GdMgH_2) resulting in a non-transparent stack. When -1 V was applied to GdMgH_2 layer, the hydrogen moved back to the GdMgH_2 layer and both the electrochromic layers become transparent. A maximum transparency of 65% was observed in this study as compared to 20% in the all solid-state prototype device reported by Armitage et al. (1999). Mercier and van der Sluis (2001) studied a “symmetric GdMg stack” i.e., $\text{GdMgH}_x/\text{Pd}/\text{ZrO}\cdot(\text{H}_2\text{O})_x\cdot[\text{H}_2]_y/\text{Pd}/\text{GdMg}/\text{Pd}$ (where symmetrically placed GdMg was used as H storage layer instead of WO_3) as the all-solid-state device. The top hydrogen storage GdMg layer covered by Pd hydrogenated into transparent state remained in that state as long as H_2 was present in the atmosphere. When potential was applied between the bottom and top electrodes, it was possible to reversibly transport H ions through the electrolyte into the bottom metal hydride. The presence of three Pd layers was observed to limit the transmission of the stack to 6% at the end of cathodic step and to 0.5% at the end of anodic potential step. Although, many material problems still remain to be solved, such all-solid-state devices are an important step towards large-scale application of switchable mirrors. Matveeva et al. (2002a) and Parkhutik and Matveeva (2002) studied the electrochemical behavior of the Y/Pd cathode and its reversible optical switching and addressed some of the common problems that

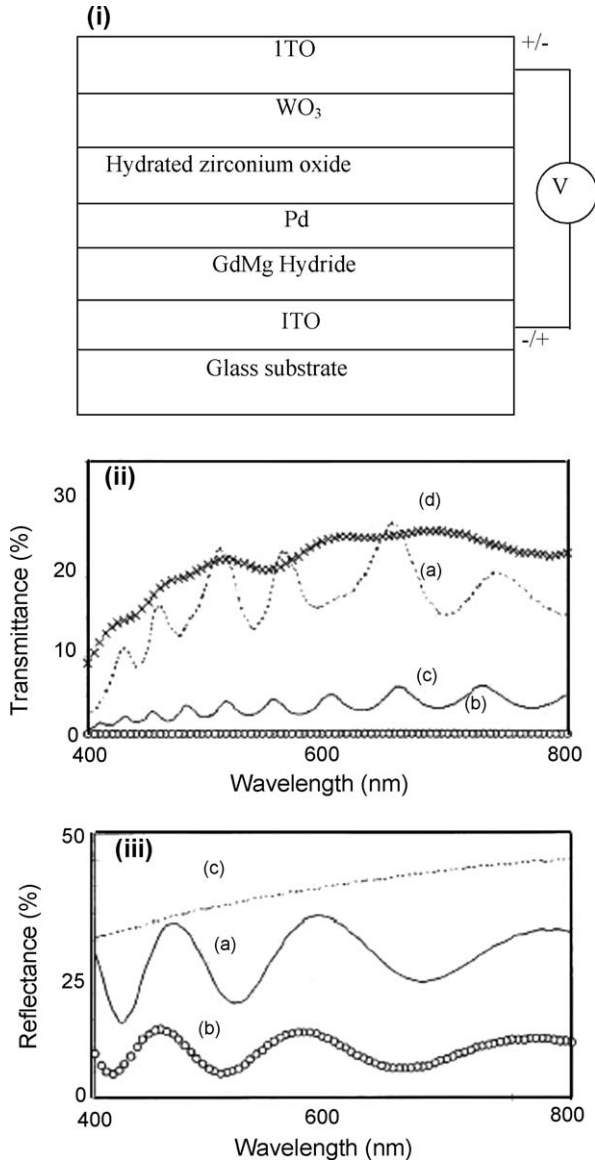


Fig. 164. (i) Schematic cross-section of the Gd–Mg hydride based optical switch. (ii) Transmittance of the device in the (a) transparent, (b) absorbing and (c) intermediate optical states along with (d) maximum transmittance of a similar Pd/Gd–Mg hydride film. (iii) Reflectance (measured through the substrate) for the device in the (a) reflecting and (b) absorbing states, and (c) a comparable Pd/Gd–Mg film in the hydrogen-deficient phase (Armitage et al., 1999).

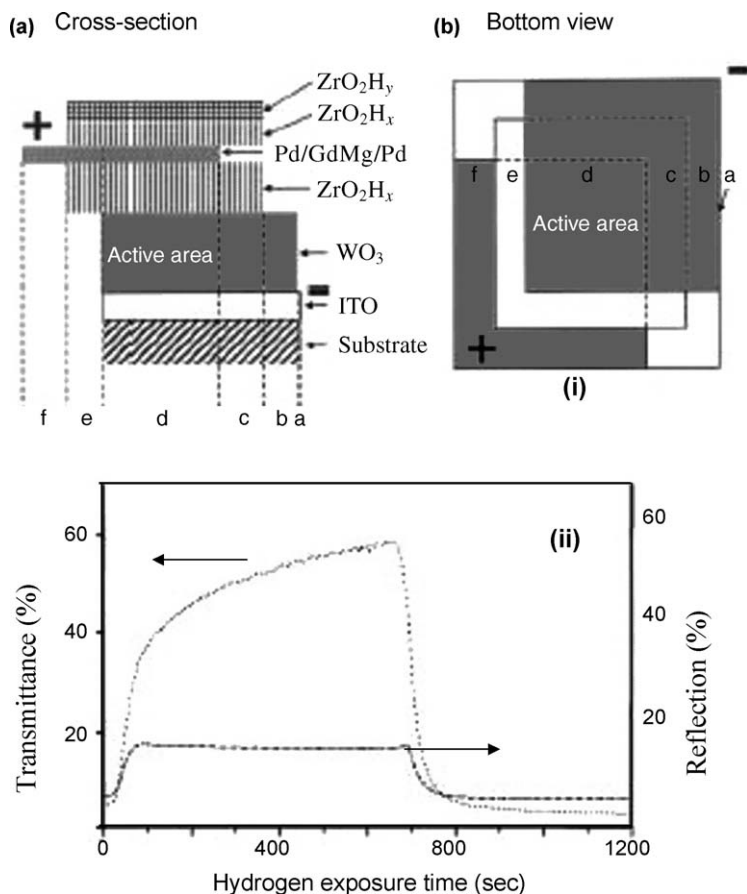


Fig. 165. (i) Schematic diagram of the device in (a) cross-sectional and (b) bottom view. Area **a** is covered with ITO, **b** with ITO:WO₃, **c** with ITO:WO₃:ZrO₂H_x:ZrO₂H_x:ZrO₂H_y, **d** with the complete stack, **e** with ZrO₂H_x:Pd:GdMg:Pd:ZrO₂H_x:ZrO₂H_y and **f** with Pd:GdMg:Pd. (ii) The variation in transmission and reflection from the bottom side of the device during hydrogenation–dehydrogenation cycle (van der Sluis and Mercier, 2001).

might affect the device function. The possible design and optimum operational conditions of the planar electrochemical cell, type of electrolyte used in the cell (liquid, solid or polymeric), role and design of anodic electrode and the anodic process accomplished on it, the sealing problems in obtaining a hermetically closed cell with a liquid electrolyte inside and a possible gas evolution methodology were discussed.

5.2. Indicator layers

The fact that switchable rare earth hydride films have optical properties that depend strongly on hydrogen concentration offers the possibility to use them as two-dimensional hydrogen

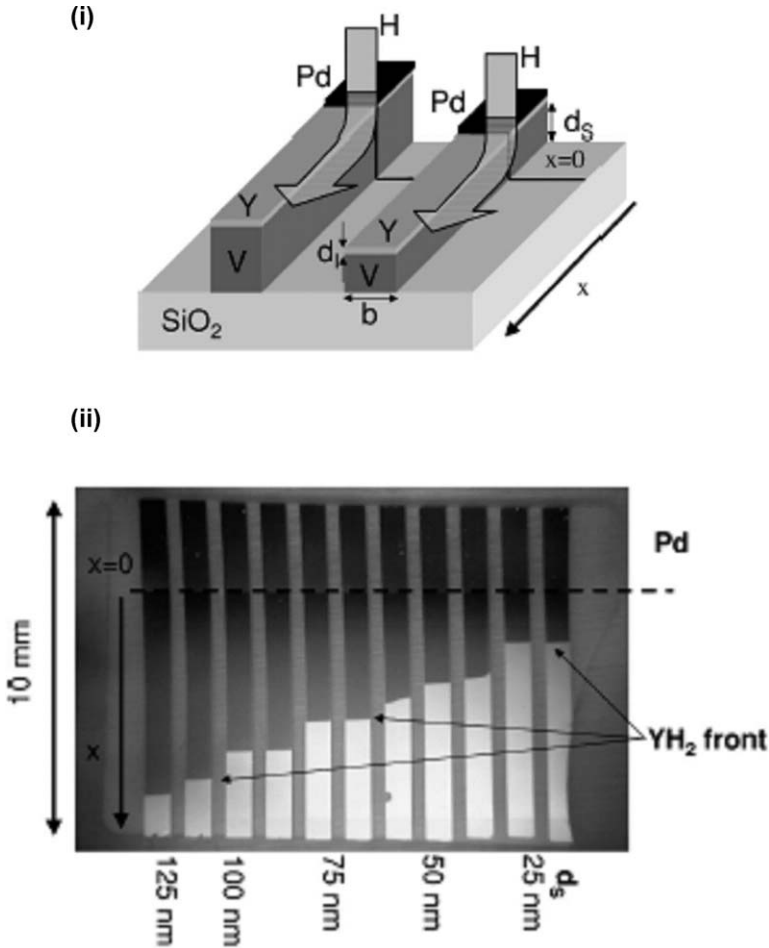


Fig. 166. (i) Schematic diagram of the sample used. Y covered vanadium strips ($1 \times 10 \text{ mm}^2$) of thickness 25–125 nm are deposited onto an $\alpha\text{-SiO}_2$ substrate ($15 \times 10 \times 0.53 \text{ mm}^3$). The strips are partially covered with Pd overlayer. In the actual sample there are 11 strips. (ii) Optical image of sample loaded in hydrogen atmosphere (1 mbar, 473 K) for 10^4 s (Remhof et al., 2002b).

concentration indicators. The simplest application is to monitor hydrogen diffusion in switchable mirrors as described in section 2.5. Another possibility is to deposit a thin switchable rare earth layer on a sample of interest that might be opaque. In such a configuration hydrogen diffusion could be observed through the coloration change in the switchable mirror indicator. Remhof et al. (2002b) demonstrated that hydrogen diffusion in materials such as vanadium could be monitored optically in reflection by using samples such as depicted in fig. 166(i). A vanadium strip of 10 mm length, 1 mm width and a typical thickness of 100 nm was covered with a thin layer of Y (30 nm) as an optical indicator for hydrogen diffusion.

One end of this V–Y bilayer was covered *in situ* with Pd (10 nm) film. The surface of the uncovered portion was oxidized when exposed to air, leaving the Pd covered portions permeable to hydrogen. Hydrogen loading could thus proceed via Pd strip and the subsequent lateral hydrogen diffusion was observed to occur mainly through vanadium, since the hydrogen diffusion is several orders of magnitude faster in vanadium than in yttrium. The lateral migration of hydrogen in vanadium away from the Pd covered region could be monitored optically as a change in the reflection of the Y indicator layer. Fig. 166(ii) shows the optical images taken 10^4 s after the film was exposed to hydrogen (10^2 Pa at $T = 473$ K). The optical discontinuity within the indicator corresponds to the boundary between the silvery gray low concentration α -YH_{0.2} phase and the blue dihydride phase (β -YH_{1.9}). This diffusion front was observed to move by 0.9 cm in 10^4 s, indicating that the diffusion coefficient is high of the order of 10^{-4} – 10^{-5} cm²/s. Remhof et al. (2002b) estimated the diffusion coefficient $D = 1.2 \times 10^{-5}$ cm²/s at $T = 473$ K for a hydrogen concentration $H/V = 0.62$, from the simultaneous optical measurements on Y–V bilayers with various thickness ratios (in order to taken into account the hydrogen leaking from the film to the indicator layer). It was observed that the overall diffusion rate of hydrogen in Y–V bilayer depends on the thickness ratio of the two metallic layers, indicating a possibility to tune the effective diffusion coefficient of a film. In patterned thin films this opened up the opportunity to locally vary the hydrogen mobility and to investigate the behavior of hydrogen diffusion fronts when they cross the interface between two media with different diffusion coefficients (Remhof et al., 2003a, 2003b). Fig. 167 shows the schematic representation of the sample used to investigate the hydrogen diffusion (a circular diffusion front) from a slow medium to a fast medium (Remhof et al., 2003a). When the diffusion front generated in the “slow” medium hits the boundary with a “fast” medium the front was observed to bulge out into a mushroom shaped pattern. Based on these observations, Remhof et al. showed that there were some analogies between the diffusion and geometric optics.

5.3. Tunable magnetic layers

In addition to the hydrogen induced structural, optical and electrical properties, some R metals also exhibit remarkable changes in magnetic properties. For example, Gd is a metallic ferromagnet with Curie temperature $T_C \approx 293$ K, its dihydride is antiferromagnetically ordered metal with $T_N \approx 20$ K, and its trihydride is semiconducting antiferromagnet with substantially lower Néel temperature ($T_N \approx 1.8$ K). Using these tunable magnetic properties, Miniotas et al. (2002) have carried out the transport and magnetization measurements on GdH_{3- δ} . The schematic cross-section of the sample used is shown in the inset of fig. 168. Epitaxial Gd film (500 nm) 10×10 mm in dimension capped with Pd strips of 1 mm width separated by 2 mm, were hydrogenated at 10^5 Pa H₂ at 600 K at UHV after initial exposure to air. The Pd contacts served as hydrogen windows during the hydrogen loading. Hydrogen diffused laterally in the Gd film forming a transparent semiconducting trihydride state between the contacts. When removed from the hydrogenation chamber, hydrogen desorbs from the sample below the Pd contacts resulting in a metallic Gd dihydride phase. This ensures ohmic contact to the trihydride part of the sample (see inset in fig. 168). Lateral hydrogen diffusion is extremely slow at room temperature and hydrogen was therefore trapped in the regions between the Pd contacts.

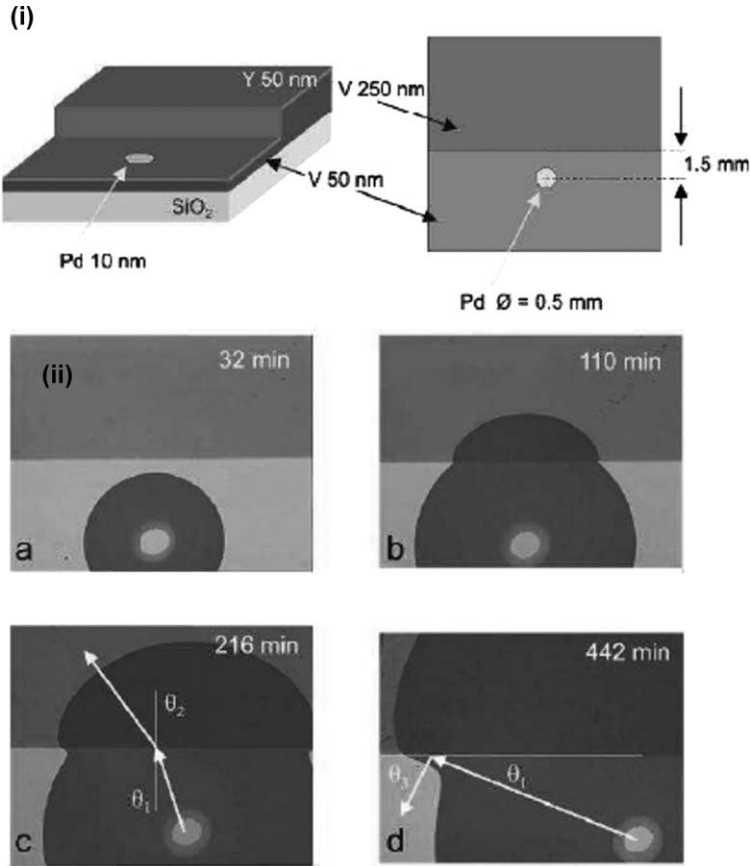


Fig. 167. (i) Schematic representation of the sample used to investigate hydrogen diffusion from slow to fast medium. (ii) Optical microscope images of the hydrogen diffusion fronts. Each image covers a $5.6 \times 4.5 \text{ mm}^2$ area of the sample. The images (a)–(d) are recorded 32, 110, 216, 442 min after the sample has been exposed to hydrogen ambient of 10^5 Pa at 373 K (Remhof et al., 2003a).

Fig. 168 shows the temperature dependence of the resistivity of GdH_3 thin films with low (a) and high (b) hydrogen vacancies in a magnetic field of 120 kOe and in zero field. The zero field semiconductor-like behavior in the resistivity was found to be suppressed in a magnetic field of 120 kOe.

5.4. Hydrogen sensors

Detection of hydrogen using bulk rare earth metal hydrides was proposed as far back as 1973, however the proposed approach was specific to steel industry but not adapted for other applications (Toy and Phillips, 1973). The discovery of hydrogen induced remarkable changes

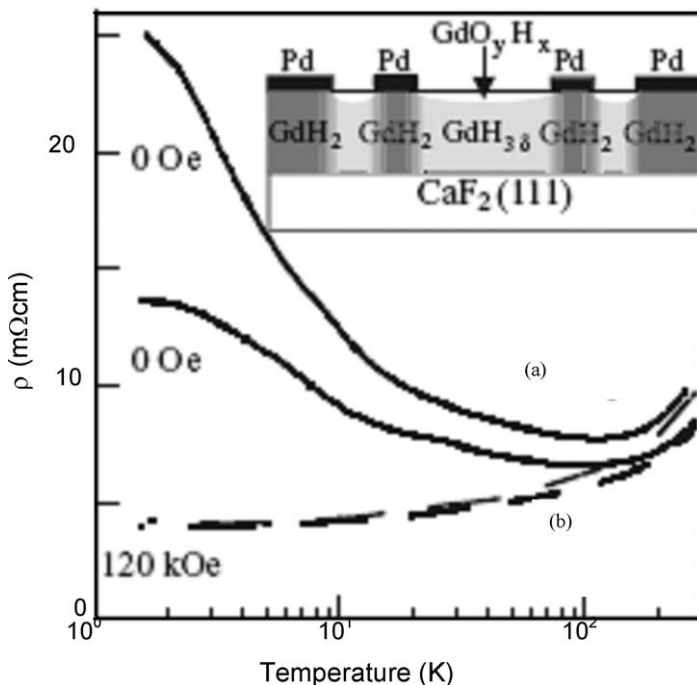


Fig. 168. Temperature dependence of resistivity of the $\text{GdH}_{3-\delta}$ thin films with low (a) and high (b) vacancy concentrations in a magnetic field of 120 kOe and in zero field. The inset shows a schematic cross-section of the sample (Miniotas et al., 2002).

in the optical and electrical properties in Pd capped R metal films has triggered quest for many technological applications. Kumar and Malhotra (2004b) for example showed that a Pd capped Sm films can be used as efficient sensor materials for hydrogen detection at room temperature. The response time was observed to depend upon the hydrogen concentration, varying from 6 s to 30 s for variation from 194 ppm to 10 000 ppm, respectively [fig. 169(i), (ii)]. However very fast hydrogen desorption (2 s) was observed at room temperature, making the sensing element ready for quick reuse. It was shown that hydrogen concentrations as low as 194 ppm could be detected without any cross sensitivity problem [fig. 169(iii)]. In contrast to a normal sensor element, which after detection needed some external source to restore to the original state (e.g. temperature, power, etc.), no external source was observed to be needed with this sensor element.

6. Summary and outlook

This review summarize various studies carried out on different generations of rare earth metal switchable mirrors based on polycrystalline, epitaxial layers, rare earth–Mg alloys, rare earth–

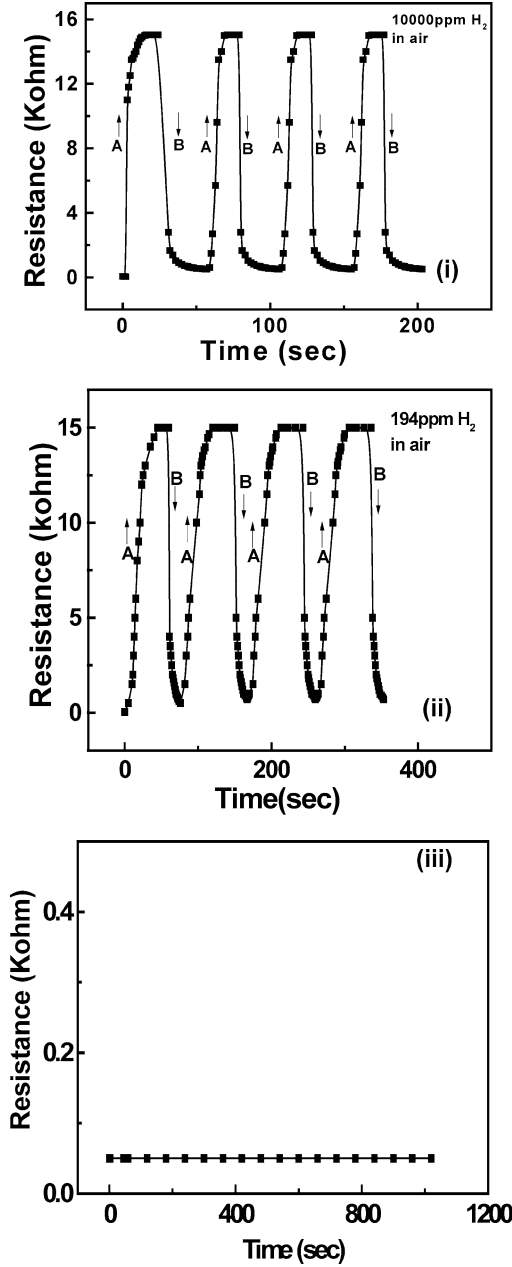


Fig. 169. Response of the sensing element in the presence of (i) 194 ppm and (ii) 10 000 ppm hydrogen in air. A – absorption, B – desorption. (iii) Resistance versus time curve, for a 55 nm Sm film capped with Pd overlayer, on exposure to 10 000 ppm of CO₂, H₂S, argon plus CH₄ and argon plus C₂H₅OH (Kumar et al., 2002).

Mg multilayers structures and nanoparticles. In the vast amount of reported literature, especially in case of polycrystalline and epitaxial rare earth metals, switching behavior measured in terms of optical and electrical contrast, switching and recovery times and transparency and colour neutrality of the trihydride state has been explained in terms of intrinsic effects like crystal structure change, phase modification, lattice contraction/expansion, lateral and longitudinal H diffusion during hydrogenation and dehydrogenation. Extrinsic effects like the presence of grain boundaries, mixing and alloy formation at the R metal–Pd interface, resistance to phase change due to interlocked topography, presence of oxide surface layer make the switching process quite complicated. Despite the oxidation prone nature of rare earth metals, which makes the *ex situ* characterization challenging difficult, a number of characterization techniques have been successfully used to investigate switching phenomenon. As mentioned in the beginning, a large scope for fabricating a variety of devices based on hydrogen induced structural, optical and electrical changes and the possibility of new physics required to explain the intriguing phenomenon accompanying the switchable mirror effect – provided the necessary impetus for applied and basic research in this area. These two factors continue to provide the driving force to undertake more research activities. In fact, due to advancement in science and technology, possibilities have increased and the work on rare earth switchable mirrors will definitely carry forward to cover more directions. A study of switching phenomenon using nanotechnological route is one such direction. Innovations can be both in terms of synthesizing rare earth materials in nanoparticle forms and also for utilizing nanotechnological tools like scanning tunnelling and atomic force microscopy for carrying out investigations on nano scale under insitu conditions. The initial work carried out in this direction has shown positive results. Synthesis of rare earth nanoparticle having well defined sizes with narrow size distribution for switchable mirrors applications will be quite useful. Pd over layer plays an important role during hydrogenation and dehydrogenation. More work needs to be carried out to understand R metal–Pd interface. Use of Pd nanoparticles has been shown to improve the switching properties and It may also be possible to modify Pd layers by other means. It may also be possible to use chemical methods for growing rare earth layer.

References

- Ahuja, R., Johansson, B., Willis, J.M., Eriksson, O., 1997. *Appl. Phys. Lett.* **71**, 3498.
- Alefeld, G., 1972. *Ber. Bunsen-Ges. Phys. Chem.* **76**, 746.
- Alford, J.A., Chou, M.Y., Chang, K.E., Louie, S.G., 2003. *Phys. Rev. B* **67**, 125110.
- Anderson, I.S., Rush, J.J., Udovic, T., Rowe, J.M., 1986. *Phys. Rev. Lett.* **57**, 2822.
- Armitage, R., Rubin, M., Richardson, T., O'Brien, N., Chen, Y., 1999. *Appl. Phys. Lett.* **75**, 1836.
- Arons, R.R., 1982. Rare earth hydrides. In: Hellwege, K.H. (Ed.), *Landolt–Börnstein New Series*, vol. **12c** (chapter 6.3).
- Arons, R.R., 1991. Rare earth hydrides. In: Wijn, H.P.J. (Ed.), *Landolt–Börnstein New Series*, vol. **19d1** (chapter 2.3).
- Aruna, I., Mehta, B.R., Malhotra, L.K., Shivaprasad, S.M., 2004. *Adv. Mater.* **16**, 169.
- Aruna, I., Mehta, B.R., Malhotra, L.K., Shivaprasad, S.M., 2005a. *Adv. Funct. Mater.* **15**, 131.
- Aruna, I., Mehta, B.R., Malhotra, L.K., Khan, S.A., Avasthi, D.K., 2005b. *J. Nanosci. Nanotech.* **5**, 1728.
- Aruna, I., Mehta, B.R., Malhotra, L.K., 2005c. *Appl. Phys. Lett.* **87**, 103101.
- Azofeifa, D.E., Clark, N., 2000. *J. Alloys Compd.* **305**, 32.

- Behrens, H., Ebel, G., 1976. In: Behrens, H., Ebel, G. (Eds.), *Gases and Carbon in Metals*, Physics Data Services, vol. 5. Fachinformationszentrum Energies, Physik, Mathematik, Karlsruhe.
- Borgschulte, A., Rode, M., Jacob, A., Schoenes, J., 2001. *J. Appl. Phys.* **90**, 1147.
- Borgschulte, A., Weber, S., Schoenes, J., 2003. *Appl. Phys. Lett.* **82**, 2898.
- Borgschulte, A., Westerwaal, R.J., Rector, J.H., Dam, B., Griessen, R., Schoenes, J., 2004. *Phys. Rev. B* **70**, 155414.
- Bour, G., Reinholdt, A., Stepanov, A.L., Keutgen, C., Kreibig, U., 2001. *Eur. Phys. J. D* **16**, 219.
- Bracconi, P., Pörschke, E., Lässer, R., 1988. *Appl. Surf. Sci.* **32**, 392.
- Bruggeman, D.A.G., 1935. *Ann. Phys. (Leipzig)* **24**, 636.
- Chang, K.E., Xavier, B., Louie, S.G., 2001. *Phys. Rev. B* **64**, 155108.
- Curzon, A.E., Singh, O., 1978. *J. Phys. F: Metal Phys.* **8**, 1619.
- Curzon, A.E., Singh, O., 1979. *Thin Solid Films* **57**, 157.
- Dam, B., Lokhorst, A.C., Remhof, A., Heijna, M.C.R., Rector, J.H., Borsari, D., Kerssemakers, J.W.J., 2003. *J. Alloys Compd.* **356–357**, 526.
- Dekker, J.P., van Ek, J., Lodder, A., Huiberts, J.N., 1993. *J. Phys.: Condens. Matter* **5**, 4805.
- den Broeder, F.J.A., van der Molen, S.J., Kremers, M., Huiberts, J.N., Nagengast, D.G., van Gogh, A.T.M., Huisman, W.H., Koeman, N.J., Dam, B., Rector, J.H., Plota, S., Haaksma, M., Hanzen, R.M.N., Jungblut, R.M., Duine, P.A., Griessen, R., 1998. *Nature* **394**, 656.
- Di Vece, M., van der Sluis, P., Janner, A.-M., Kelly, J.J., 2001. *J. Electrochem. Soc.* **148**, G576.
- Di Vece, M., Zevenhuisen, S.J.M., Kelly, J.J., 2002. *Appl. Phys. Lett.* **81**, 1213.
- Di Vece, M., Kelly, J.J., 2003a. *J. Alloys Compd.* **356–357**, 156.
- Di Vece, M., van der Eerden, A.M.J., van Bokhoven, J.A., Lemaux, S., Kelly, J.J., Koningsberger, D.C., 2003b. *Phys. Rev. B* **67**, 035430.
- Di Vece, M., Swart, I., Kelly, J.J., 2003c. *J. Appl. Phys.* **94**, 4659.
- Dornheim, M., Pundt, A., Kirchheim, R., van der Molen, S.J., Kooij, E.S., Kerssemakers, J., Griessen, R., Harms, H., Geyer, U., 2003. *J. Appl. Phys.* **93**, 8958.
- Eder, R., Pen, H.F., Sawatsky, G.A., 1997. *Phys. Rev. B* **56**, 10115.
- Enache, S., Lohstroh, W., Griessen, R., 2004. *Phys. Rev. B* **69**, 115326.
- Flotow, H.E., Osborne, D.W., Otto, K., Abraham, B.M., 1963. *J. Chem. Phys.* **38**, 2620.
- Fromhold Jr., A.T., 1976. In: Fromhold Jr., A.T. (Ed.), *Theory of Metal Oxidation*, vol. 1. North-Holland, Amsterdam.
- Gartz, M., Keutgen, C., Kuenneke, S., Kreibig, U., 1999. *Eur. Phys. J. D* **9**, 127.
- Giebels, I.A.M.E., van der Molen, S.J., Griessen, R., Di Vece, M., 2002a. *Appl. Phys. Lett.* **80**, 1343.
- Giebels, I.A.M.E., Isidorsson, J., Kooij, E.S., Remhof, A., Koeman, N.J., Rector, J.H., van Gogh, A.T.M., Griessen, R., 2002b. *J. Alloys Compd.* **330–332**, 875.
- Giebels, I.A.M.E., Isidorsson, J., Griessen, R., 2004. *Phys. Rev. B* **69**, 205111.
- Gileadi, E., Kirova Eisner, E., Penciner, J., 1975. In: Gileadi, E., Kirova Eisner, E., Penciner, J. (Eds.), *Interfacial Electrochemistry: An Experimental Approach*. Addison-Wesley, Reading, MA, pp. 47, 64.
- Grier, E.R., Kolosov, O., Petford-Long, A.K., Ward, R.C.C., Wells, M.R., Hjörvarsson, B., 2000. *J. Phys. D* **33**, 894.
- Griessen, R., Huiberts, J.H., Kremers, M., van Gogh, A.T.M., Koeman, N.J., Dekker, J.P., Notten, P.H.L., 1997. *J. Alloys Compd.* **253–254**, 44.
- Griessen, R., 2001. *Europhys. News* **32**, 42.
- Gschneidner Jr., K.A., Calderwood, F.W., 1982. *Bull. Alloy Phase Diagrams* **3**, 94.
- Hammer, B., Norskov, J.K., 1995. *Nature (London)* **376**, 238.
- Hayoz, J., Sarbach, S., Pillo, Th., Boschung, E., Naumović, D., Aebi, P., Schlapbach, L., 1998. *Phys. Rev. B* **58**, 4270.
- Hayoz, J., Pillo, Th., Bovet, M., Züttel, A., Guthrie, St., Schlapbach, L., Aebi, P., 2000. *J. Vac. Sci. Technol. A* **18**, 2417.
- Hayoz, J., Aebi, P., Schlapbach, L., Schoenes, J., 2001. *J. Appl. Phys.* **90**, 3925.
- Hayoz, J., Koitzsch, C., Bovet, M., Naumović, D., Schlapbach, L., Aebi, P., 2003. *Phys. Rev. Lett.* **90**, 196804.
- Heckman, R.C., 1967. *J. Chem. Phys.* **46**, 2158.
- Hjörvarsson, B., Guo, J.-H., Ahuja, R., Ward, R.C.C., Andersson, G., Eriksson, O., Wells, M.R., Sâthe, C., Agui, A., Butori, S.M., Nordgren, J., 1999. *J. Phys.: Condens. Matter* **11**, 119.
- Hoekstra, A.F.Th., Roy, A.S., Rosenbaum, T.F., Griessen, R., Wijngaarden, R.J., Koeman, N.J., 2001. *Phys. Rev. Lett.* **86**, 5349.
- Hoekstra, A.F.Th., Roy, A.S., Rosenbaum, T.F., 2003. *J. Phys.: Condens. Matter* **15**, 1405.
- Huiberts, J.H., Griessen, R., Rector, J.H., Wijngaarden, R.J., Dekker, J.P., de Groot, D.G., Koeman, N.J., 1996a. *Nature (London)* **380**, 231.

- Huiberts, J.H., Rector, J.H., Wijngaarden, R.J., Jetten, S., de Groot, D.G., Dam, B., Koeman, N.J., Griessen, R., Hjörvarsson, B., Olafsson, S., Cho, Y.S., 1996b. *J. Alloys Compd.* **239**, 158.
- Huiberts, J.H., Griessen, R., Wijngaarden, R.J., Kremers, M., 1997. *Phys. Rev. Lett.* **79**, 3724.
- Huisman, M.C., van der Molen, S.J., Vis, R.D., 1999. *Nucl. Instrum. Methods Phys. Res. B* **158**, 451.
- Huisman, M.C., Jongerden, M.R., van der Molen, S.J., Vis, R.D., 2001. *Nucl. Instrum. Methods Phys. Res. B* **181**, 389.
- Isidorsson, J., Giebels, I.A.M.E., Kooij, E.S., Koeman, N.H., Rector, J.H., van Gogh, A.T.M., Griessen, R., 2001. *Electrochim. Acta* **46**, 2179.
- Isidorsson, J., Giebels, I.A.M.E., Griessen, R., Di Vece, M., 2002. *Appl. Phys. Lett.* **80**, 2305.
- Jacob, A., Borgschulte, A., Schoenes, J., 2002. *Thin Solid Films* **414**, 39.
- Janner, A.-M., van der Sluis, P., Mercier, V., 2001. *Electrochim. Acta* **46**, 2173.
- Kelly, P.J., Dekker, J.P., Stumpf, R., 1997a. *Phys. Rev. Lett.* **78**, 1315.
- Kelly, P.J., Dekker, J.P., Stumpf, R., 1997b. *Phys. Rev. Lett.* **79**, 2921.
- Kerssemakers, J.W.J., van der Molen, S.J., Gunther, R., Koeman, N.J., Griessen, R., 2000. *Nature* **406**, 489.
- Kerssemakers, J.W.J., van der Molen, S.J., Gunther, R., Dam, B., Griessen, R., 2002a. *J. Alloys Compd.* **330–332**, 342.
- Kerssemakers, J.W.J., van der Molen, S.J., Gunther, R., Dam, B., Griessen, R., 2002b. *Phys. Rev. B* **65**, 075417.
- Kierzy, H., Rode, M., Jacob, A., Borgschulte, A., Schoenes, J., 2001. *Phys. Rev. B* **63**, 134109.
- Kooij, B.J., Zoestbergen, E., De Hosson, J.Th.M., Kerssemakers, J.W.J., Dam, B., Ward, R.C.C., 2002. *J. Appl. Phys.* **91**, 1901.
- Kooij, E.S., van Gogh, A.T.M., Griessen, R., 1999. *J. Electrochem. Soc.* **146**, 2990.
- Kooij, E.S., van Gogh, A.T.M., Nagengast, D.G., Koeman, N.J., Griessen, R., 2000. *Phys. Rev. B* **62**, 10088.
- Kooij, E.S., Rector, J.H., Magengast, D.G., Kerssemakers, J.W.J., Dam, B., Griessen, R., Remhof, A., Zabel, H., 2002. *Thin Solid Films* **402**, 131.
- Kremers, M., Koeman, N.J., Griessen, R., Notten, P.H.L., Tolboom, R., Kelly, P.J., Duine, P.A., 1998. *Phys. Rev. B* **57**, 4943.
- Kumar, P., Philip, R., Mor, G.K., Malhotra, L.K., 2002. *Jpn. J. Appl. Phys.* **41**, 6023.
- Kumar, P., Malhotra, L.K., 2004a. *Jpn. J. Appl. Phys.* **43**, 909.
- Kumar, P., Malhotra, L.K., 2004b. *Appl. Surf. Sci.* **236**, 461.
- Kumar, P., Malhotra, L.K., 2004c. *Electrochim. Acta* **49**, 3355.
- Kumar, P., Malhotra, L.K., 2004d. *Mater. Chem. Phys.* **88**, 106.
- Lacher, P.R., 1938. *Proc. R. Soc. London, Ser. A* **161**, 525.
- Lee, M.W., Shin, W.P., 1999. *J. Appl. Phys.* **86**, 6798.
- Lee, M.W., Lin, C.H., 2000. *J. Appl. Phys.* **87**, 7798.
- Lee, M.W., Kuo, C.Y., Lin, H.C., Wang, H.C., 2001. *J. Appl. Phys.* **89**, 6135.
- Leervad Pedersen, T.P., Salinga, C., Weis, H., Wutting, M., 2003. *J. Appl. Phys.* **93**, 6034.
- Li, Y., Cheng, Y.T., 1996. *Int. J. Hydrogen Energy* **21**, 281.
- Libowitz, G.G., Pack, J.G., 1969. *J. Chem. Phys.* **50**, 3557.
- Libowitz, G.G., Macland, A.G., 1979. Hydrides. In: Gschneidner Jr., K.A., Eyring, L. (Eds.), *Handbook on the Physics and Chemistry of Rare Earths*, vol. 3. North-Holland, Amsterdam (chapter 26).
- Libowitz, G.G., 1972. *Ber. Bunsen-Ges. Ges.* **76**, 837.
- Libowitz, G.G., 1973. *Ber. Bunsen-Ges. Ges.* **77**, 837.
- Lide, D.R., 1996. In: Lide, D.R. (Ed.), *CRC Handbook of Chemistry and Physics*, Seventy seventh ed. CRC Press, Boca Raton, FL, USA.
- Lokhorst, A.C., Heijna, M.C.R., Rector, J.H., Giebels, I.A.M.E., Koeman, N.J., Dam, B., 2003. *J. Alloys Compd.* **356–357**, 536.
- Maier-Komor, P., 1985. *Nucl. Instrum. Methods Phys. Res. A* **234**, 641.
- Mannsmann, M., Wallace, W.E., 1964. *J. Phys. (Paris)* **25**, 454.
- Matveeva, E.S., Ortega Ramiro, R.J., Sanchez Bolinchez, A., Ferrer Jiménez, C., Parkhutik, V.P., 2002a. *Sens. Actuators B* **84**, 83.
- Matveeva, E.S., Parkhutik, V., 2002b. *J. Electrochem. Soc.* **149**, 148.
- Meidema, A.R., 1978. *Z. Metallkd.* **69**, 287.
- Mercier, V.M.M., van der Sluis, P., 2001. *Solid State Ionics* **145**, 17.
- Miniotas, A., Norblad, P., Andersson, M., Hjörvarsson, B., 2002. *Europhys. Lett.* **58**, 442.
- Miron, N.F., Shcherbak, V.I., Bykov, V.N., Levdiuk, V.A., 1972. *Sov. Phys. Crystallogr.* **17**, 342.
- Miyake, T., Aryasetiawan, R., Kino, H., Terakura, K., 2000. *Phys. Rev. B* **61**, 16491.
- Mor, G.K., Malhotra, L.K., 2000. *Thin Solid Films* **359**, 28.
- Mor, G.K., Malhotra, L.K., Bhattacharyya, D., 2001. *J. Appl. Phys.* **90**, 1.

- Mor, G.K., Malhotra, L.K., 2003. *Solid State Commun.* **125**, 523.
- Mueller, W.M., Blackledge, J.P., Libowitz, G.G., 1968. The rare-earth hydrides, Yttrium and scandium hydrides. In: Mueller, W.M., Blackledge, J.P., Libowitz, G.G. (Eds.), *Metal Hydrides*. Academic Press, New York (chapters 9, 10).
- Nagengast, D.G., Kerssemakers, J., van Gogh, A.T.M., Dam, B., Griessen, R., 1999a. *Appl. Phys. Lett.* **75**, 1724.
- Nagengast, D.G., van Gogh, A.T.M., Kooij, E.S., Dam, B., Griessen, R., 1999b. *Appl. Phys. Lett.* **75**, 2050.
- Ng, K.K., Zhang, F.C., Anisimov, V.I., Rice, T.M., 1997. *Phys. Rev. Lett.* **78**, 1311.
- Ng, K.K., Zhang, F.C., Anisimov, V.I., Rice, T.M., 1999. *Phys. Rev. B* **59**, 5398.
- Notten, P.H.L., Kremers, M., Griessen, R., 1996. *J. Electrochem. Soc.* **143**, 3348.
- Osterwalder, J., 1985. *Z. Phys. B* **61**, 113.
- Ouwkerk, M., 1998. *Solid State Ionics* **113–115**, 431.
- Parkhutik, V., Matveeva, E.S., 2002. *Thin Solid Films* **403–404**, 480.
- Peterman, D.J., Harmon, B.N., Marchiando, J., Weaver, J.H., 1979. *Phys. Rev. B* **19**, 4867.
- Pick, M.A., Davenport, J.W., Strongin, M., Dienes, G.J., 1979. *Phys. Rev. Lett.* **43**, 286.
- Preuss, W.H., Flannery, B.P., Teukolsky, S.A., Vetterling, W.T., 1989. *Numerical Recipes*. Cambridge Univ. Press, Cambridge, UK, p. 523.
- Pundt, A., Getzlaff, M., Bode, M., Kirchheim, R., Wiesendanger, R., 2000. *Phys. Rev. B* **61**, 9964.
- Rahman Khan, M.S., 1981. *Ind. J. Phys. A* **55**, 23.
- Rahman Khan, M.S., 1984. *Appl. Phys. A* **35**, 263.
- Rahman Khan, M.S., 1987. *Bull. Mater. Sci.* **9**, 181.
- Remhof, A., Song, G., Theis-Bröhl, K., Zabel, H., 1997. *Phys. Rev. B* **56**, R2897.
- Remhof, A., Song, G., Sutter, Ch., Labergerie, D., Schreyer, A., Guthoff, F., Windgasse, J., Zabel, H., 1999. *Phys. Rev. B* **59**, 6689.
- Remhof, A., Kerssemakers, J.W.J., van der Molen, S.J., Griessen, R., Kooij, E.S., 2002a. *Phys. Rev. B* **65**, 054110.
- Remhof, A., van der Molen, S.J., Antosik, A., Dobrowolska, A., Koeman, N.J., Griessen, R., 2002b. *Phys. Rev. B* **66**, 020101(R).
- Remhof, A., Wijngaarden, R.J., Griessen, R., 2003a. *Phys. Rev. Lett.* **90**, 145502.
- Remhof, A., Wijngaarden, R.J., Griessen, R., 2003b. *J. Alloys Compd.* **356–357**, 300.
- Richardson, T.J., Slack, J.L., Armitage, R.D., Kostecki, R., Farangis, B., Rubin, M.D., 2001. *Appl. Phys. Lett.* **78**, 3047.
- Richardson, T.J., Slack, J.L., Farangis, B., Rubin, M.D., 2002. *Appl. Phys. Lett.* **80**, 1349.
- Rode, M., Borgschulte, A., Jacob, A., Stellmach, C., Barkow, U., Scheones, J., 2001. *Phys. Rev. Lett.* **87**, 235502.
- Roesnbaum, T.F., Hoekstra, A.F.T., 2002. *Adv. Mater.* **14**, 247.
- Roy, A.S., Hoekstra, A.F.T., Rosenbaum, T.F., Griessen, R., 2002. *Phys. Rev. Lett.* **89**, 276402.
- Rush, J.J., Flowtow, H.E., Connor, D.W., Thaper, C.L., 1966. *J. Chem. Phys.* **45**, 3817.
- Rushton, P.P., Tozer, D.J., Clark, S.J., 2002. *Phys. Rev. B* **65**, 235203.
- Schlapbach, L., 1992. Surface properties and activation. In: Schlapbach, L. (Ed.), *Hydrogen in Intermetallic Compounds II, Topics in Applied Physics*, vol. **67**. Springer, Berlin (chapter 2).
- Schneider, W., Molodtsov, S.L., Richter, M., Ganz, Th., Engelmann, P., Laubschat, C., 1998. *Phys. Rev. B* **57**, 14930.
- Schoenes, J., Borgschulte, A., Carsteanu, A.-M., Kierey, H., Rode, M., 2003. *J. Alloys Compd.* **356–357**, 211.
- Shinar, J., Dehner, B., Beaudry, B.J., Peterson, D.T., 1988. *Phys. Rev. B* **37**, 2066.
- Shinar, J., Dehner, B., Beaudry, B.J., 1989. *Z. Phys. Chem. NF* **163**, 591.
- Shinar, J., Dehner, B., Barnes, R.G., Beaudry, B.J., 1990. *Phys. Rev. Lett.* **64**, 563.
- Stepanov, A.L., Bour, G., Gartz, M., Osin, Yu.N., Reinholdt, A., Kreibig, U., 2002a. *Vacuum* **64**, 9.
- Stepanov, A.L., Bour, G., Reinholdt, A., Kreibig, U., 2002b. *Tech. Phys. Lett.* **28**, 642.
- Switendick, A.C., 1970. *Solid State Commun.* **8**, 1463.
- Switendick, A.C., 1971. *Int. J. Quantum Chem.* **5**, 459.
- Talik, E., Neumann, M., Mydlarz, T., 1998. *J. Magn. Magn. Mater.* **189**, 183.
- Toy, S.M., Phillips, A. (1973). Rare earth hydrogen detector, US patent **3**, 732076.
- Udovic, T.J., Huang, Q., Rush, J.J., 1996. *J. Phys. Chem. Solids* **57**, 423.
- Udovic, T.J., Huang, Q., Rush, J.J., 1997a. *Phys. Rev. Lett.* **79**, 2920.
- Udovic, T.J., Rush, J.J., Hung, Q., Anderson, I.S., 1997b. *J. Alloys Compd.* **253–254**, 241.
- Udovic, T.J., Huang, Q., Rush, J.J., 1998. In: Nickel, N.N., Jackson, W.B., Bowman, R.C., Leisure, R.G. (Eds.), *Hydrogen in Semiconductors and Metals, Materials Research Symposium Proceedings*, vol. **513**. MRS, Pittsburg, p. 197.
- Udovic, T.J., Huang, Q., Erwin, R.W., Hjärvarsson, B., Ward, R.C.C., 2000. *Phys. Rev. B* **61**, 12701.

- Vajda, P., Daou, J.N., 1993. The rare-earth-hydrogen systems. In: Aladjem, A., Lewis, F.A. (Eds.), *Metal-Hydrogen Systems*, vol. 1. VCH, Weinheim (chapter 3a).
- Vajda, P., 1995. Hydrogen in rare-earth metals, including RH_{2+x} phases. In: Gschneidner Jr., K.A., Eyring, L. (Eds.), *Handbook on the Physics and Chemistry of Rare Earths*, vol. 20. North-Holland, Amsterdam (chapter 137).
- van der Molen, S.J., Kerssemakers, J.W.J., Rector, J.H., Koeman, N.J., Dam, B., Griessen, R., 1999. *J. Appl. Phys.* **86**, 6107.
- van der Molen, S.J., Welling, M.S., Griessen, R., 2000. *Phys. Rev. Lett.* **85**, 3882.
- van der Molen, S.J., Nagengast, D.G., van Gogh, A.T.M., Kalkman, J., Kooij, E.S., Rector, J.H., Griessen, R., 2001. *Phys. Rev. B* **63**, 235116.
- van der Molen, S.J., Welling, M.S., Griessen, R., 2002a. *J. Alloys Compd.* **330–332**, 426.
- van der Molen, S.J., Huisman, W.H., Griessen, R., 2002b. *J. Alloys Compd.* **330–332**, 430.
- van der Sluis, P., Ouwerkerk, M., Duine, P.A., 1997. *Appl. Phys. Lett.* **70**, 3356.
- van der Sluis, P., 1998. *Appl. Phys. Lett.* **73**, 1826.
- van der Sluis, P., 1999. *Electrochim. Acta* **44**, 3063.
- van der Sluis, P., Mercier, V.M.M., 2001. *Electrochim. Acta* **46**, 2167.
- van Gelderen, P., Bobbert, P.A., Kelly, P.J., Brocks, G., 2000. *Phys. Rev. Lett.* **85**, 2989.
- van Gelderen, P., Kelly, P.J., Brocks, G., 2001. *Phys. Rev. B* **63**, 100301.
- van Gelderen, P., Bobbert, P.A., Kelly, P.J., Brocks, G., Tolboom, R., 2002. *Phys. Rev. B* **66**, 075104.
- van Gelderen, P., Kelly, P.J., Brocks, G., 2003a. *Phys. Rev. B* **64**, 094302.
- van Gelderen, P., Bobbert, P.A., Kelly, P.J., Brocks, G., 2003b. *Phys. Rev. B* **85**, 2989.
- van Gogh, A.T.M., Kooij, E.S., Griessen, R., 1999. *Phys. Rev. Lett.* **83**, 4614.
- van Gogh, A.T.M., van der Molen, S.J., Kerssemakers, J.W.J., Koeman, N.J., Griessen, R., 2000a. *Appl. Phys. Lett.* **77**, 815.
- van Gogh, A.T.M., Nagengast, D.G., Kooij, E.S., Koeman, N.J., Griessen, R., 2000b. *Phys. Rev. Lett.* **85**, 2156.
- van Gogh, A.T.M., Nagengast, D.G., Kooij, E.S., Koeman, N.J., Rector, J.H., Griessen, R., Flipse, C.F.J., Smeets, R.J.J.G.A.M., 2001. *Phys. Rev. B* **63**, 195105.
- van Mechelen, J.L.M., Noheda, B., Lohstroh, W., Westervaal, R.J., Rector, J.H., Dam, B., Griessen, R., 2004. *Appl. Phys. Lett.* **84**, 3651.
- von Rottkay, K., Rubin, M., Michalak, F., Armitage, R., Richardson, T., Slack, J., Duine, P.A., 1999a. *Electrochim. Acta* **44**, 3093.
- von Rottkay, K., Rubin, M., Duine, P.A., 1999b. *J. Appl. Phys.* **85**, 408.
- Voss, D., 2001. *Science* **292**, 1987.
- Wang, Y., Chou, M.Y., 1993. *Phys. Rev. Lett.* **71**, 1226.
- Wang, Y., Chou, M.Y., 1994. *Phys. Rev. B* **49**, 13357.
- Wang, Y., Chou, M.Y., 1995. *Phys. Rev. B* **51**, 7500.
- Weaver, J.H., Rosie, R., Peterson, D.T., 1978. *Solid State Commun.* **25**, 201.
- Weaver, J.H., Rosie, R., Peterson, D.T., 1979a. *Phys. Rev. B* **19**, 4855.
- Weaver, J.H., Peterson, D.T., Benbow, R.L., 1979b. *Phys. Rev. B* **20**, 5301.
- Wiesinger, G., Hilscher, G., 1991. Magnetism of hydrides. In: Buschow, K.H.J. (Ed.), *Handbook of Magnetic Materials*, vol. 6. North-Holland, Amsterdam (chapter 6).
- Wildes, A.R., Ward, R.C.C., Wells, M.R., Hjörvarsson, B., 1996. *J. Alloys Compd.* **242**, 49.
- Winkler, C., 1891. *Ber. Dtsch. Chem. Ges.* **24**, 873.
- Wolf, W., Herzig, P., 2002. *Phys. Rev. B* **66**, 224112.
- Wolf, W., Herzig, P., 2003. *J. Alloys Compd.* **356–357**, 73.
- Wu, Z., Cohen, R.E., Singh, N.J., Gupta, R., Gupta, M., 2004. *Phys. Rev. B* **69**, 085104.
- Yannopoulos, L.N., Edwards, R.K., Wahlbeck, P.G., 1965. *J. Phys. Chem.* **69**, 2510.
- Yoshimura, K., Yamada, Y., Okada, M., 2002. *Appl. Phys. Lett.* **81**, 4709.

Chapter 229

APPLICATIONS OF TETRAVALENT CERIUM COMPOUNDS

Koen BINNEMANS

*Katholieke Universiteit Leuven, Department of Chemistry, Celestijnenlaan 200F,
B-3001 Leuven, Belgium*

E-mail: koen.binnemans@chem.kuleuven.be

Contents

Abbreviations	282	5.14. Bis[trinitratocerium(IV)] chromate	
1. Introduction	283	and dinitratocerium(IV) chromate di-	
2. Redox properties of cerium(IV)	284	hydrate	311
3. Oxidimetry (cerimetry)	286	5.15. Cerium(IV) alkoxides	311
3.1. Principles	286	5.16. Cerium(IV) fluoride	312
3.2. Standard solutions	287	5.17. Cerium dioxide	312
3.3. End-point determination and redox indicators	288	5.18. Supported cerium(IV) reagents	313
3.4. Applications	289	5.19. Other cerium(IV) compounds	314
4. Cerium-catalyzed Belousov–Zhabotinsky reactions	291	6. Stoichiometric cerium(IV)-mediated reactions	314
4.1. Historical background	291	6.1. Oxidation of hydrocarbons	314
4.2. Mechanism	292	6.2. Oxidation of alcohols and phenols	319
4.3. Demonstration experiments	298	6.3. Oxidation of hydroquinones and catechols	322
5. Cerium(IV) reagents	299	6.4. Oxidation of carbonyl compounds	323
5.1. Ammonium hexanitratocerate(IV) (CAN)	299	6.5. Ethers and epoxides	325
5.2. Ammonium cerium(IV) sulfate (CAS)	302	6.6. Sulfur-containing compounds	325
5.3. Cerium(IV) sulfate tetrahydrate	304	6.7. Halogenation reactions	326
5.4. Cerium(IV) acetate	304	6.8. Esterification reactions	334
5.5. Cerium(IV) trifluoroacetate	306	6.9. Nitration	334
5.6. Cerium(IV) perchlorate	306	6.10. Functionalization of alkenes	338
5.7. Cerium(IV) methanesulfonate	307	6.11. Removal of protecting groups	343
5.8. Cerium(IV) triflate	307	6.12. Splitting of organometallic compounds	343
5.9. Hydrophobic cerium(IV) reagents	308	7. Indirect and catalytic reactions with cerium(IV) ions	344
5.10. Pyridinium hexachlorocerate(IV) (CPC)	309	7.1. Oxidations by bromate ions	344
5.11. Cerium(IV) trihydroxy hydroperoxide (CTH)	310	7.2. Oxidations by peroxides	345
5.12. Cerium(IV) periodate	310	7.3. Oxidations by molecular oxygen	346
5.13. Tris[trinitratocerium(IV)] paraperiodate (TTCPP)	310	8. Cerium-mediated electrosynthesis	350
		9. Initiation of radical polymerization reactions	354
		10. Miscellaneous reactions	364
		10.1. Generation of nitrate free radicals	364
		10.2. Decomposition of water	365

10.3. Hydrolysis of phosphodiester and DNA	366	11.4. Ceric-cerous sulfate dosimeter	372
10.4. Hydrolysis of peptides	371	11.5. CerOx™ process	373
11. Various applications	371	11.6. Model for tetravalent plutonium	374
11.1. TLC stains	371	12. Conclusions and outlook	376
11.2. Test reagents	372	Acknowledgements	377
11.3. CAN as etchant	372	References	377

Abbreviations

atm	atmosphere	HOPO	hydroxypyridonate
BNPP	bis-(<i>p</i> -nitrophenyl)phosphate	HTPA	1,3-amino-2-hydroxypropane- <i>N,N,N',N''</i> -tetraacetic acid
bpy	2,2'-bipyridine	HTXA	5-methyl-2-hydroxy-1,3-xylene- α,α -diamine- <i>N,N,N',N''</i> -tetraacetic acid
bpyO ₂	2,2'-bipyridine <i>N,N'</i> -oxide	<i>i</i> -PrOH	<i>iso</i> -propanol
Bu	butyl	Me	methyl
BZ	Belousov-Zhabotinsky	MMTr	monomethoxytrityl
CAN	ammonium hexanitratocerate(IV)	NBS	<i>N</i> -bromosuccinimide
CAS	ammonium cerium(IV) sulfate	NHPI	<i>N</i> -hydroxy phthalimide
CPC	pyridinium hexachlorocerate(IV)	PCB	polychlorobenzene
CPN	pyridinium hexanitratocerate(IV)	Phe	phenyl
CTAN	tetra- <i>n</i> -butylammonium hexanitratocerate(IV)	phen	1,10-phenanthroline, <i>o</i> -phenanthroline
CTEAN	triethylammonium hexanitratocerate(IV)	RT	room temperature
CTH	cerium(IV) trihydroxy hydroperoxide	SAP	superabsorbent polymer
DCM	dichloromethane	SDS	sodium dodecylsulfate
DMF	<i>N,N</i> -dimethylformamide	TBHP	<i>tert</i> -butyl hydroperoxide
DMP	dimethyl phosphate	TBMS	<i>tert</i> -butyldimethylsilyl
dmso	dimethylsulfoxide (as ligand)	<i>t</i> -Boc	<i>tert</i> -butoxycarbonyl
DMSO	dimethylsulfoxide (as solvent)	tdpo	tris(dimethylamido)phosphine oxide
Et	ethyl	TEMPO	2,2,6,6-tetramethylpiperidiny-1-oxyl
EXAFS	extended X-ray absorption fine structure	TFA	trifluoroacetic acid
FKM	Field, Köros, and Noyes	THF	tetrahydrofuran
Gy	gray (unit of absorbed dose)	THP	tetrahydropyran
HEPES	<i>N'</i> -(2-hydroxyethyl)piperazine- <i>N</i> -ethanesulfonic acid	tppo	triphenylphosphine oxide
H ₂ ETAM	<i>N,N'</i> -diethyl-2,3-dihydroxyterephthalamide	TRIS	tris(hydroxymethyl)methylamine
HNPP	2-hydroxypropyl (<i>p</i> -nitrophenyl) phosphate	TTCPP	tris[trinitratocerium(IV)] paraperiodate
		XANES	X-ray absorption near-edge structure

1. Introduction

Cerium is the most abundant element of the rare earths. On average the Earth's crust contains 66 ppm of cerium (=66 g per ton), a value that is very comparable with the abundance of copper (68 ppm) (Emsley, 1991). Few people know that there are on Earth larger resources of cerium than of other more popular elements like cobalt (29 ppm), lead (13 ppm), tin (2.1 ppm), silver (0.08 ppm) or gold (0.004 ppm). A special property of cerium is that it has a stable tetravalent oxidation state besides the trivalent state which is so common for the rare earths. Although the tetravalent oxidation state is also known for solid state compounds of praseodymium and terbium, cerium is the only rare-earth element that has a stable tetravalent oxidation state in solution. Many of the applications of cerium are based on the one-electron $\text{Ce}^{4+}/\text{Ce}^{3+}$ redox couple.

The aim of this chapter is to give an overview of the applications of tetravalent cerium compounds in solution; not only their well-known use as reagents in organic synthesis and as oxidizing agents for redox titrations (cerimetry), but also their role in oscillating reactions, their application in biochemical research will be covered, as well as more exotic applications. The message is that cerium(IV) reagents are not restricted to ammonium hexanitratocerate(IV), which is better known as ceric ammonium nitrate or as CAN for short. When reading the literature, one could get the impression that there are no other cerium(IV)-containing reagents besides CAN (Ho, 1973; Nair et al., 1997, 2004; Hwu and King, 2001). For this reason, this chapter gives a detailed description of the cerium(IV) salts that are used in organic reactions. However all organic reactions that can be mediated by cerium(IV) salts will not be described here. This would take up too much space, given that CAN is very often used as an oxidizing reagent. The interested reader will be given a feeling of what is possible with cerium(IV) reagents in organic synthesis. More examples can be found in earlier reviews (Ho, 1973; Kagan and Namy, 1986; Molander, 1992; Imamoto, 1994; Nair et al., 1997, 2004; Hwu and King, 2001). This review will not focus on applications of cerium dioxide (ceria), because its applications in heterogeneous catalysis have been reviewed elsewhere (Trovarelli, 2002). For an overview of applications of cerium in chemical technology, the reader is referred to a booklet written by Kilbourn (Kilbourn, 1992). Several chapters in this handbook have been devoted to different aspects of cerium. These include chapter 20 on valence changes (Jayaraman, 1979), chapter 43 on catalysis (Netzer and Bertel, 1982), chapter 57 on reagents for organic synthesis (Long, 1986), chapter 66 on photoemission (Lynch and Weaver, 1988), chapter 98 on low-temperature behavior of cerium compounds (Sereni, 1991), chapters 102 and 122 on redox reactions (Nash and Sullivan, 1991; Morss, 1994), chapters 103 and 127 on hydrolysis (Rizkalla and Choppin, 1991, 1994), chapter 105 on valence fluctuations (Loewenhaupt and Fischer, 1993), chapter 125 on oxides (Haire and Eyring, 1994), chapter 184 on ceria-containing three-way catalysts (Kašpar et al., 2000), and chapter 222 on DNA and RNA hydrolysis (Komiyama, 2005). The terms "*cerous*" and "*ceric*" are often used, respectively, for the cerium ion in its lower oxidation state (+3) and in its higher oxidation state (+4). The terms *cerium(III)* instead of *cerous*, and *cerium(IV)* instead of *ceric* will be consistently used in this review.

2. Redox properties of cerium(IV)

The characteristic oxidation state for the rare earth elements is +3 (Nash and Sullivan, 1991). The chemistry of the rare earths is largely determined by this oxidation state. There are only few examples of stable rare-earth ions in other oxidation states. One example is tetravalent cerium, cerium(IV). The stability of the +4 oxidation state can be attributed to the empty 4f-shell in the $[\text{Xe}]4f^0$ electronic configuration of Ce^{4+} .

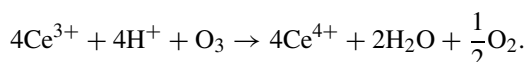
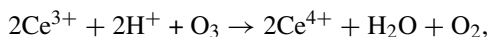
In acidic medium, cerium(IV) is a very strong one-electron oxidant and its oxidizing power is comparable to that of lead(IV) oxide or that of manganese(III) salts. The first detailed study of the redox potential of the $\text{Ce}^{4+}/\text{Ce}^{3+}$ couple under carefully controlled conditions in sulfuric acid was published by Kunz (1931). Noyes and Garner (1936) studied the redox potential of the same redox couple in nitric acid. The redox potential of the $\text{Ce}^{4+}/\text{Ce}^{3+}$ couple depends very much on the nature and the concentration of the acid. For instance, the redox potential is +1.28 V in 1 M HCl, +1.44 V in 1 M H_2SO_4 , +1.61 V in 1 M HNO_3 , +1.70 V in 1 M HClO_4 , and it is as high as +1.87 V in 8 M HClO_4 (Smith and Getz, 1938; Wadsworth et al., 1957). The redox potential thus increases in the order hydrochloric acid < sulfuric acid < nitric acid < perchloric acid. Whereas the redox potential increases with increasing concentrations of perchloric acid, it decreases with increasing concentrations of nitric acid and sulfuric acid (Smith and Getz, 1938).

Fluoride ions forms very stable complexes with cerium(IV) and lowers the redox potential considerably. A cerium(IV) sulfate solution is not able to oxidize iodide to iodine when appreciable amounts of fluoride ions are present. The most important fluoro complex is hexafluorocerate(IV), $[\text{CeF}_6]^{2-}$, which can be formed by addition of ammonium fluoride to a solution of cerium(IV). The behavior of cerium(IV) in presence of fluoride ions is markedly different from that of cerium(III). Addition of an ammonium fluoride solution to a solution containing cerium(III) results in the precipitation of gelatinous cerium(III) fluoride, CeF_3 , which becomes powdery upon standing (Svehla, 1979). The use of cerium(IV) fluoride as a fluorinating agent is discussed in sections 5.16 and 6.7.

Cerium(III) can be oxidized to cerium(IV) electrolytically or by the use of strong oxidizing agents. Upon addition of a small excess of silver(II) oxide, AgO , to a cold solution of cerium(III) in a 3 to 5 M nitric acid solution, rapid oxidation of cerium(III) to cerium(IV) takes place. By simply diluting and warming the solution for a few minutes the excess of silver(II) is completely reduced by water (Lingane and Davis, 1956). The problem of oxidizing cerium(III) by metal-containing oxidizing agents is that the cerium solution gets contaminated by other metal ions. For some applications this is not a problem, but for other applications it is. A useful oxidizing agent for oxidation of cerium(III) in sulfuric acid medium is lead(IV) oxide (Gordon and Feibush, 1955). Neither PbO_2 nor PbSO_4 , that are formed during the reaction, are soluble in sulfuric acid, so that both compounds can easily be removed by filtration. The oxidation of cerium(III) to cerium(IV) by persulfate is catalyzed by small amounts of silver(I) salts (Skarzewski, 1984). Milyukova et al. used a mixture of silver nitrate and ammonium persulfate to oxidize cerium(III) and berkelium(III) (Milyukova et al., 1977). The persulfate method is the most popular method for the chemical oxidation of cerium(III) to

cerium(IV). Potassium persulfate, $K_2S_2O_8$, or ammonium persulfate, $(NH_4)_2S_2O_8$, can be used as oxidizing reagents.

Nikitina and coworkers have studied the kinetics of the oxidation of cerium(III) by ozone in nitric acid solutions (Nikitina et al., 1980). It was observed that the oxidation of cerium(III) by ozone in 4 M HNO_3 at 25 °C required substantially more than two moles of cerium(III) per ozone molecule consumed. The kinetic data could only be explained by considering that the oxidation takes place by two different reactions, that occur simultaneously and that are of overall second order. The stoichiometry of the reaction of cerium(III) with ozone can be described by the following equations:



In general, cerium(III) cannot be oxidized to cerium(IV) by molecular oxygen. An exception is the oxidation of cerium β -diketonate complexes by O_2 (Christoffers and Werner, 2002; Christoffers et al., 2003a, 2003b; Rössle et al., 2005). Complex formation shifts the redox potential of the Ce^{4+}/Ce^{3+} couple to less positive values. As discussed in section 10.2, aqueous solutions of cerium(IV) are metastable with respect to oxidation of water to oxygen gas. Under normal conditions this reaction will not occur due to the presence of a high kinetic barrier, and acidic solutions of cerium(IV) can be stored for quite a long time. However, cerium(IV) ions can decompose water in presence of a catalyst like platinum or ruthenium(IV) oxide.

Because of the high redox potential of the Ce^{4+}/Ce^{3+} redox couple, the choice of the electrode is important, especially in electroanalytical studies. The kinetics of the Ce^{4+}/Ce^{3+} redox reaction have been investigated using different types of electrodes: a stationary platinum disc electrode (Randle and Kuhn, 1983; Kuhn and Randle, 1985), a rotating platinum disc electrode (Greef and Aulich, 1968; Randle and Kuhn, 1986), a bubbling platinum electrode (Desideri, 1961), a platinized titanium electrode (Tzedakis and Savall, 1997), a gold electrode (Ferro and De Battisti, 2002), a glassy carbon electrode (Pletcher and Valdes, 1988a; Maeda et al., 1999; Vijayarathi et al., 2001), a conductive diamond electrode (Ferro and De Battisti, 2002), and a pyrolytic graphite electrode (Miller and Zittel, 1964). The bubbling platinum electrode is a thin platinum ring electrode renewed at regular intervals by gas bubbles, and can be used as an alternative for the dropping mercury electrode for polarographic systems with a high redox potential (Cozzi and Desideri, 1960).

The assignment of oxidation states in cerium compounds is not always an easy task. A well-known case is that of *cerocene*, bis(cyclooctatetraene)cerium, $Ce(\eta^8-C_8H_8)_2$. This complex was originally formulated as a cerium(IV) compound with two $(\eta^8-C_8H_8)_2^{2-}$ anions (Greco et al., 1976). Later calculations indicated that the stoichiometry of cerocene is better described as $[Ce^{3+}\{(\eta^8-C_8H_8)_2\}^{3-}]$ (Neumann and Fulde, 1989). *Ab initio* calculations showed that cerocene is in fact a mixed valent compound, with a ground state consisting of 83% $4f_{e2u}^1\pi_{e2u}^3$ (i.e. Ce^{3+}) and 17% $4f_{e2u}^0\pi_{e2u}^4$ (i.e. Ce^{4+}) (Dolg et al., 1991, 1995). X-ray absorption near-edge structure (XANES) data gave evidence that the ground state of cerocene was primarily Ce^{3+} (Edelstein et al., 1996). The layered cerium iodate $Ce_2(IO_3)_6(OH_{0.44})$ that can be prepared

by reaction of $(\text{NH}_4)_2[\text{Ce}(\text{NO}_3)_6]$ with I_2O_5 at 180°C in aqueous medium in an autoclave is another example of a mixed valent cerium compound (Sykora et al., 2004). The best method to determine the oxidation state of cerium is by XANES, because this is a direct spectroscopic probe for the cerium oxidation state (Antonio et al., 1999). Both K-edge and L-edge Ce XANES has been used for solving problems about the valence of cerium (Antonio and Soderholm, 1994; Antonio et al., 1988, 1996, 1999; Edelstein et al., 1996; Bidoglio et al., 1992; Sham, 1983; Skanthakumar and Soderholm, 1996; Reidy and Swider, 1995; Sunstrom et al., 1993; Overbury et al., 1998; Beck et al., 1989). Other experimental methods like EPR, magnetic measurements, UV–VIS spectroscopy or cyclic voltammetry give less conclusive results.

Because the anionic ligands that are typically used for the synthesis of organolanthanide complexes, e.g. C_5H_5^- , $\text{C}_8\text{H}_8^{2-}$ or R^- , are strongly reducing, it remains a challenge to obtain organometallic cerium(IV) complexes. One of the few examples of such compounds is the cerium(IV) cyclopentadienyl *tert*-butoxide complex $(\text{C}_5\text{H}_5)_3\text{Ce}(\text{OCMe}_3)$ reported by Evans and coworkers (Evans et al., 1989b).

3. Oxidimetry (cerimetry)

3.1. Principles

Solutions of cerium(IV) have been often used as oxidizing titrants for redox titrations, because the reduction of Ce^{4+} to Ce^{3+} proceeds cleanly in acidic solutions. The titrimetric methods based on cerium(IV) are also known as *cerimetry* or *cerate oxidimetry*. The use of cerium(IV) salts as reagents for volumetric analysis was first proposed by Lange in the middle of the 19th century (Lange, 1861), but systematic studies started only about 70 years later (Willard and Young, 1928a, 1928b, 1928c, 1928d, 1928e, 1929a, 1929b). Potentiometric methods based on cerium(IV) sulfate as titrant were developed at the same time by Furman (Furman, 1928a, 1928b; Furman and Evans, 1929; Furman and Wallace Jr., 1930a, 1930b) and by Atanasiu (Atanasiu, 1927; Atanasiu and Stefanescu, 1928). A review on the earlier work of oxidimetry with cerium(IV) salts was written by Young (Young, 1952). The classic work of Kolthoff on volumetric analysis (Kolthoff et al., 1957) contains descriptions of detailed procedures for cerimetry. Several examples of cerimetry are described also in the well-known *Vogel's textbook of quantitative inorganic analysis* (Bassett et al., 1981). Standard solutions can be prepared from different cerium(IV) salts (see section 3.2), but most often cerium(IV) sulfate is chosen. Solutions of cerium(IV) sulfate can be used only in acidic medium (0.5 M H_3O^+ or higher concentrations), because at neutral or high pH values, cerium(IV) hydroxide (hydrated CeO_2) or other basic salts precipitate. Although the most popular reagent for oxidimetry is without doubt potassium permanganate, KMnO_4 , solutions of cerium(IV) sulfate offer several advantages. Firstly, cerium(IV) sulfate solutions are very stable over long periods of time. It is not necessary to take precautions to protect the standard solutions from light, and the solutions may be boiled without noticeable change in concentration. Acidic solutions of cerium(IV) sulfate are therefore more stable than permanganate solutions. Secondly, cerium(IV) is a one-electron acceptor, and a simple valence change takes place upon

reduction: $\text{Ce}^{4+} + \text{e}^- \rightleftharpoons \text{Ce}^{3+}$. The equivalent weight is therefore equal to the molecular weight. With potassium permanganate, a number of intermediate unstable oxidation states can be formed depending on the experimental conditions. Thirdly, cerium(IV) sulfate may be used as an oxidizing titrant in presence of high concentrations of hydrochloric acid, provided that the solutions are not boiled. In contrast, potassium permanganate cannot be used for titrations of the reducing agent in a hydrochloric acid solution, because chlorine gas is liberated. However, solutions of cerium(IV) in hydrochloric acid do not have a long-term stability (see below). Fourthly, cerium(IV) solutions at the commonly used concentration of 0.1 M are not too highly colored, so that there are no problems when reading the meniscus in burettes. Fifthly, the $\text{Ce}^{4+}/\text{Ce}^{3+}$ couple has a highly positive standard redox potential, so that cerium(IV) acts as an oxidant towards many reducing agents. Notice that a unique property of cerium(IV) salts is that they are together with silver(II) and cobalt(III) salts among the few stable oxidizing agents that have the cation as the primary active component (Furman and Evans, 1929). In most other strongly oxidizing agents, like perchlorate, bromate, periodate, bismuthate, persulfate, permanganate and dichromate, the active component is an anion. As mentioned in section 2, the redox potential of the $\text{Ce}^{4+}/\text{Ce}^{3+}$ couple is strongly dependent on the acidity of the solution and on the nature of the counter ion.

3.2. Standard solutions

An overview of the compounds used for the preparation of standard solutions of cerium(IV) is given in table 1. Ammonium hexanitratocerate(IV) is commercially available in primary-standard grade and can be used to prepare standard solutions of cerium(IV) by weight (Smith and Fly, 1949). The weighted amount of ammonium hexanitratocerate(IV) is dissolved in 1 M H_2SO_4 and used directly (Smith et al., 1936). It is recommended to dry primary-standard grade ammonium hexanitratocerate(IV) at 85 °C before use. Cerium(IV) dissolved in sulfuric acid is indefinitely stable. Solutions of cerium(IV) in nitric acid or in perchloric acid undergo slow photochemical decomposition. Solutions of cerium(IV) in hydrochloric acid are slowly oxidized. When the less expensive ammonium hexanitratocerate(IV) of reagent-grade or another cerium(IV) compound is used to prepare the cerium(IV) solution, the resulting solutions have to be standardized with a primary standard.

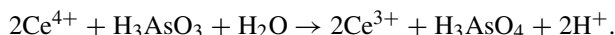
When a cerium(IV) solution is prepared by dissolving ammonium hexanitratocerate(IV) in sulfuric acid, both sulfate and nitrate ions are present. In many cases, the nitrate ions do not interfere in the analysis. When the presence of nitrate ions is undesirable, the ammonium

Table 1
Cerium(IV) compounds used for the preparation of standard solutions

Name	Formula	Formula weight (g/mol)
Ammonium hexanitratocerate(IV)	$(\text{NH}_4)_2[\text{Ce}(\text{NO}_3)_6]$	548.23
Ammonium cerium(IV) sulfate	$(\text{NH}_4)_4\text{Ce}(\text{SO}_4)_4 \cdot 2\text{H}_2\text{O}$	632.56
Cerium(IV) sulfate	$\text{Ce}(\text{SO}_4)_2$	333.25
Cerium(IV) hydrogen sulfate	$\text{Ce}(\text{HSO}_4)_4$	502.13
Cerium(IV) hydroxide	$\text{Ce}(\text{OH})_4$	208.15

hexanitratocerate(IV) solution is evaporated almost to dryness with an excess of concentrated sulfuric acid. The resulting cerium(IV) sulfate is redissolved in a molar sulfuric acid solution. Alternatively, cerium(IV) is precipitated from the ammonium hexanitratocerate(IV) solution by addition of an aqueous ammonia solution, and after washing with water to remove the adsorbed nitrate ions the precipitate is redissolved in sulfuric acid. A standard cerium(IV) solution can be prepared also from $\text{Ce}(\text{HSO}_4)_4$ as the starting material (Zielen, 1969). For titrations in nitric acid or in hydrochloric acid solution, ammonium hexanitratocerate(IV) is chosen as the titrant (Rao et al., 1962). For redox titrations in non-aqueous media, the use of a solution of ammonium hexanitratocerate(IV) in glacial acetic acid has been suggested (Hinsvark and Stone, 1956). The authors preferred acetic acid because it is readily available in pure form and because it dissolves most oxygen-containing organic compounds. However, the solution has only a moderate stability and should be standardized every day. The oxidations have to be carried out in presence of perchloric acid, because otherwise they are too slow. Studies have shown that the solvent also participates in the reaction.

Arsenic(III) oxide, As_2O_3 , is the preferred reagent for the standardization of cerium(IV) solutions (Bassett et al., 1981). Because the reaction is very slow at ambient temperatures, it must be catalyzed by addition of small amounts of osmium tetroxide, OsO_4 , ruthenium tetroxide, RuO_4 , or less preferably iodine monochloride, ICl . Ruthenium tetroxide is less toxic and less expensive than osmium tetroxide (Keattch, 1961). Arsenic(III) oxide is dissolved in a sodium hydroxide solution, and the solution is acidified with a dilute sulfuric acid solution. After adding the catalyst and the redox indicator, the solution is titrated with the cerium(IV) solution to the first sharp color change from orange-red to very pale blue. The relevant reaction is:



Other primary standards for the standardization of cerium(IV) solutions are pure iron or sodium oxalate. For the standardization of cerium(IV) against sodium oxalate, a hot solution of hydrochloric or sulfuric acid is used.

In coulometric titrations, cerium(IV) is generated *in situ* by electrolysis. Pastor et al. (1982) studied the anodic generation of cerium(IV). The formal redox potential of the $\text{Ce}^{4+}/\text{Ce}^{3+}$ system decreases as concentration of potassium acetate in the solution increases.

3.3. End-point determination and redox indicators

The end-point of titrations with cerium(IV) solutions can be detected visually (without or with use of a redox indicator) or potentiometrically. Whereas the intense purple color of a permanganate solution allows an easy visual detection of the end point, the yellow-orange color of cerium(IV) solutions is often not intense enough to act as an indicator. Only in a limited number of cases, for instance when oxalic acid or hydrogen peroxide is the analyte, can the titration be made without a redox indicator, provided that the concentrations of the analyte are not too low and that an appropriate blank correction is made. It is easier to detect the end point in hot solutions than in cold solutions, because of an intensification of the yellow color of the cerium(IV) ion with a rise in temperature. A large blank correction is required

when the titrant serves as its own indicator. On the other hand, end points can readily be determined potentiometrically by measuring the potential of the cell containing the analyte solution during the titration.

The preferred redox indicator for titrations with cerium(IV) is *ferroin*, which is in fact the tris(1,10-phenanthroline)iron(II) complex, $[\text{Fe}(\text{phen})_3]^{2+}$ (Walden et al., 1931, 1933). Ferroin itself has a deep red color, whereas its oxidized form (*ferrin*), $[\text{Fe}(\text{phen})_3]^{3+}$, is pale blue to colorless. The transition potential is +1.10 V in 1 M sulfuric acid. Ferroin is a very good redox indicator, because its reaction is rapid and reversible, because the color change is very pronounced, and because ferroin solutions are easy to prepare and stable up to 60 °C. Several redox indicators based on 1,10-phenanthroline derivatives have been reported. Walden and coworkers (Walden et al., 1934) prepared the iron(II) complex of 5-nitro-1,10-phenanthroline (*nitroferroin*), which has a transition potential of +1.25 V. Nitroferroin is more stable than ferroin, but is not very useful for oxidations with cerium(IV) sulfate in sulfuric acid solution, because a significant excess of the titrant is required to oxidize the indicator. However, nitroferroin is useful for titrations with cerium(IV) ions in perchloric acid or in nitric acid solution, where the oxidation potential of the $\text{Ce}^{4+}/\text{Ce}^{3+}$ redox couple is higher. The oxidation potential of iron(II) phenanthroline complexes can be systematically varied between +0.84 V and +1.10 V by the number and position of methyl substituents on the 1,10-phenanthroline core (Brandt and Smith, 1949). The kinetics of the oxidation of ferroin by cerium(IV) have been studied by Dulz and Sutin (1963). The rate constant of the oxidation reaction increased with increasing sulfuric acid concentrations. Iron(II) complexes of 2,2'-bipyridine are less suitable as redox indicator than those of 1,10-phenanthroline, because of the poor stability of the complexes of 2,2'-bipyridine in acidic medium (Walden et al., 1931, 1933). However, tris(2,2'-bipyridine)ruthenium(II) dichloride can be applied as indicator for titrations with cerium(IV) in perchloric or nitric acid solution, because of the high transition potential (+1.25 V) and because the ruthenium(II) complex is more stable than the corresponding iron(II) complex (Steigman et al., 1942). A useful alternative indicator for ferroin in sulfuric acid solution is *N*-phenylanthranilic acid (*o*-diphenylaminocarboxylic acid) (Syrokomsii and Stiepin, 1936). This indicator is pink in the oxidized form and colorless in the reduced form. Bányai et al. (1965) proposed eriochrome blue as a redox indicator for cerimetry. Chlorpromazine hydrochloride was introduced as an indicator for microtitrations with 0.0005–0.001 N cerium(IV) solutions (Kum-Tatt and Tong, 1962).

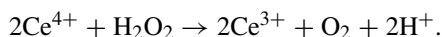
3.4. Applications

Most of the procedures for oxidimetry with potassium permanganate work also with cerium(IV) solutions (Kolthoff et al., 1957). As mentioned in section 3.1, the latter have some advantages over permanganate solutions. For instance, cerium(IV) can be used for the titration of iron(II) ions in presence of chloride, contrary to permanganate. Methods have been developed for the titration of many metals and metalloids: antimony (Willard and Young, 1933; Furman, 1932), arsenic (Furman, 1932; Gleu, 1933; Smith and Fritz, 1948), mercury (Willard and Young, 1930d), thallium (Willard and Young, 1930a), rhenium (Geilmann and Wrigge, 1935), tellurium (Willard and Young, 1930c), tin (Bassett and Stumpf, 1934), vanadium (Willard and Young, 1929a), iron (Willard and Young, 1928b), copper (Birnbaum

and Edmonds, 1940; Baker and Gibbs, 1943, 1946), molybdenum (Furman and Murray, 1936), titanium (Claassen and Visser, 1941) and uranium (Birnbbaum and Edmonds, 1940; Fritz et al., 1954; Furman and Schoonover, 1931; Ewing and Wilson, 1931). It is evident from the publication year of the references that all these procedures are quite old. They have been published in a time when instrumental analysis methods were not widely available. Many of the older titration methods have been replaced by more modern analytical methods, although the procedures themselves remain useful.

In some applications, the oxidation of the analyte by cerium(IV) is very slow. In this case, an alkali iodide can be added as a catalyst. Ce^{4+} is able to oxidize I^- very fast to I_2 , and iodine acts as the redox active species in the titration reaction. The iodide ions that are formed are regenerated by oxidation by Ce^{4+} . A typical example is the iodide-catalyzed oxidation of arsenic(III) by cerium(IV) (Yates and Thomas, 1956).

An analytical application of cerimetry that is still in use is the determination of *hydrogen peroxide* by titration with a 0.1 M cerium(IV) sulfate solution to the pale blue end point of a ferroin indicator (Hurdis and Romeyn, 1954). The reaction is:



The method is applicable to solutions that contain 1 to 30 wt.% H_2O_2 . Samples with a higher concentration should be diluted prior to analysis. Other peroxides in the solution do not interfere. Takahashi and Sakurai (1962) determined H_2O_2 coulometrically with electro-generated cerium(IV).

Cerium(IV) solutions have been used intensively in the past for the determination of organic compounds. A review of these methods has been written by Ashworth (1964, 1965). Cerium(IV) oxidizes most organic compounds to carbon dioxide and water, although the oxidation is sometimes stopped at an intermediate stage. For instance, formic acid is the stable end product of different polycarboxylic acids and hydroxycarboxylic acids under certain conditions. The organic compounds can be titrated in an acidic aqueous solution, although ethanol or acetic acid can be added for solubilizing purposes. Acetonitrile has also been used as a solvent for titrations with cerium(IV). Maleic, fumaric, benzoic, phthalic and salicylic acid are completely oxidized to carbon dioxide and water by cerium(IV) sulfate, so that these acids can be titrated by cerium(IV) sulfate (Sharma and Mehrotra, 1954b). On the other hand, acetic and succinic acid are not oxidized by cerium(IV) sulfate, even not in solutions with a high sulfuric acid concentration. By choosing an appropriate sample treatment, it is also possible to oxidize formic, glycolic, malic, malonic and tartaric acid by cerium(IV) sulfate (Sharma and Mehrotra, 1954a). Oxidation of formic acid by pure cerium(IV) sulfate is negligible (Willard and Young, 1930b), but by using chromium(III) sulfate as a catalyst, formic acid can be quantitatively oxidized (Sharma and Mehrotra, 1955). Koch and Strong (1969) described a procedure for the determination of oxalate in urine by cerimetry.

4. Cerium-catalyzed Belousov–Zhabotinsky reactions

4.1. Historical background

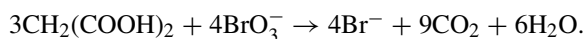
Most chemical reactions proceed continuously from a starting point to an end point. However, *oscillating reactions* change their state in a rhythmic way, when they are proceeding to their end point (Franck, 1978). This type of reactions is characterized for instance by a periodic color change. The Russian biophysicist *Boris Pavlovich Belousov* (1883–1970) has attempted to model catalysis in the Krebs cycle by using cerium(IV) as the catalyst instead of metalloenzymes, when, purely by accident, he observed in 1951 that the color of a solution of citric acid, bromate, and of a cerium(IV) salt in diluted sulfuric acid oscillated between yellow and colorless. However, due to resistance among the chemistry community he encountered difficulties during several years problems for publishing his work. Finally, it appeared in an obscure journal (Belousov, 1959). An English translation of Belousov's seminal paper can be found in a book authored by Field and Burger (1985). The resistance of the chemical community to accept chemical oscillations can be explained by the fact that it was commonly thought that it would be contrary to the second law of thermodynamics for a chemical reaction to oscillate. Chemical reactions should approach the thermodynamic equilibrium monotonically. It was thought that Belousov's observations were caused by an insufficient stirring of the solution. Belousov used the redox indicator ferroin to intensify the color change during oscillations. As mentioned in section 3.3, ferroin is red in reduced solution and blue in oxidized form, providing a more easily visible variation than the pale yellow to colorless change of the cerium(IV)/cerium(III) system. Another Russian biophysicist, *Anatol Markovich Zhabotinsky* (1938–) refined Belousov's reaction, replacing citric acid by malonic acid and discovering that when a thin, homogenous layer of the solution is left undisturbed, fascinating geometric patterns such as concentric circles and Archimedean spirals propagate across the medium. Therefore, the reaction oscillates both in space and time; it is a so-called *spatio-temporal oscillator*. Despite initial problems to convince referees and journal editors, Zhabotinsky was ultimately able to publish several papers concerning what would become known as the *Belousov–Zhabotinsky reaction* (Zhabotinsky, 1964a, 1964b; Zaikin and Zhabotinsky, 1970). The *Belousov–Zhabotinsky reaction* is also spelled as the *Belousov–Zhabotinskii reaction*, or written as BZ reaction for short. In 1980, twenty years after Belousov's death, the Lenin Prize was awarded to Belousov (posthumously), Zhabotinsky, Krinsky and Ivantinsky for their work on oscillating reactions. The discovery of the oscillating reaction by Belousov has been described by Winfree (1984). The acceptance of oscillating reactions by the chemical community was made possible not only by the research of Zhabotinsky, but also by the work of Prigogine on the thermodynamics of systems far from the state of thermodynamics equilibrium (Prigogine, 1962; Nicolis and Prigogine, 1977). The Belousov–Zhabotinsky reaction is widely used as a model system for the study of non-linear phenomena in chemical kinetics. The theory that deals with such non-linear phenomena is known as “*catastrophe theory*” (Okninski, 1992).

The Belousov–Zhabotinsky reaction is an example of a class of processes, in which the chemical compositions exhibit regular periodic variations in time or space. These periodic

variations can be made visible by a sequence of color changes. Many chemical oscillators (including the BZ reaction) contain the bromate ions as an essential component, and are also referred to as *bromate-driven oscillators* (Ruoff et al., 1988). The reactions related to a bromate-driven oscillator involve bromination and oxidation of an organic compound by bromate in acidic solution. In some systems a catalyst is used, although also uncatalyzed bromate oscillators have been described (Kuhnert and Linde, 1977). Bromate-driven oscillators where a metal ion or a metal complex is present as a catalyst are known as “*classical systems*” (Noyes, 1980). The term *Belousov–Zhabotinsky reaction* is today not restricted to the original chemical system, but is used for any metal-ion-catalyzed, bromate-driven oscillating system. The Belousov–Zhabotinsky reaction is a homogenous chemical oscillator, because the reaction products are all dissolved in one liquid phase.

4.2. Mechanism

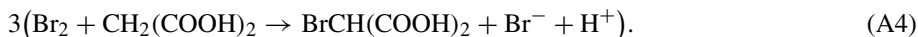
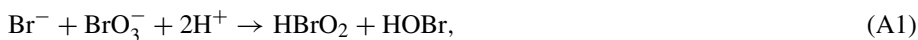
Most studies of the Belousov–Zhabotinsky reaction use malonic acid as the organic acid. The BZ reaction is based on an autocatalytic system, with reaction steps coupled in such a way that the products formed by one reaction slow down another reaction or make another reaction possible. In this way, reactions can experience positive or negative feed-back. The oscillations can only take place because the system is far away from equilibrium; otherwise equilibrium would be established very quickly. Oscillating chemical reactions are always very complex and involve a large number of chemical species, which can be classified as reactants, products or intermediates. In a classic chemical reaction, the concentration of the reactants steadily decreases and the concentration of the products steadily increases, while the intermediates are present at a low, relatively constant concentration. In an oscillating reaction, the concentration of the reactants also steadily decreases, but the concentrations of the intermediates shows oscillatory behavior. The oscillations in concentration can be very large. For instance, in the BZ reaction, the bromide ion concentration varies between 10^{-11} M and 10^{-6} M (Field and Schneider, 1989). The color changes are due to differences in the ratio of the concentrations of the oxidized and reduced forms of the cerium catalyst and of the redox indicator. Field, Körös and Noyes (Field et al., 1972; Noyes et al., 1972) proposed a detailed mechanistic model for the oscillating behavior of the Belousov–Zhabotinsky reaction (*FKN model*). The overall reaction occurring is the cerium-catalyzed oxidation of malonic acid by bromate ions in dilute sulfuric acid. The bromate ions are reduced to bromide ions, while the malonic acid is oxidized to carbon dioxide and water. In the course of the reaction, bromide ions and malonic acids are slowly consumed and their concentrations monotonically decrease. The overall reaction can be written as:



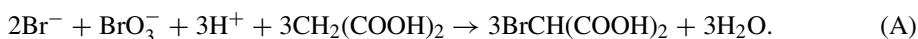
This equation cannot explain the most striking feature of the BZ reaction, namely the periodic changes in the color of the solution when the reaction proceeds. The equation does not explain the role played by the cerium catalyst or by the bromide ions that are added before the start of the reaction. A careful examination of the reaction mechanism is therefore necessary. Three processes are of importance: Process A: consumption of bromide ions; Process B: formation

of cerium(IV) ions; Process C: formation of bromide ions upon consumption of cerium(IV) ions. In these processes, the following reactions take place (Ruoff et al., 1988; Jacobs and Epstein, 1976):

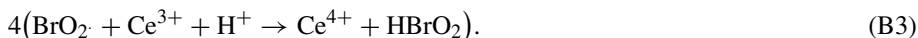
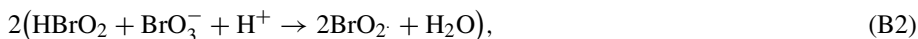
Process A:



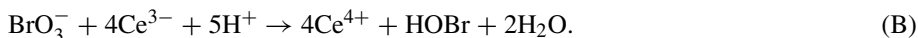
The overall reaction for process A is:



Process B:



The overall reaction for process B is:



Process C:

Process C is the reaction of bromomalonic acid with cerium(IV). The detailed mechanism of this process is not known yet. Zhabotinsky (1964a, 1964b) made the first suggestion for the overall reaction in process C:



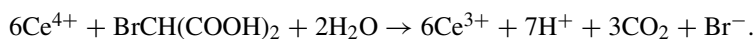
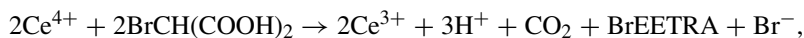
In the FKN model, process C is usually written in the following form:



Processes A and B are fundamentally different. Process A involves ions, and the steps are two-electron transfers (oxygen-atom transfer). The dominant reaction is the reaction between bromide (Br^-) and bromate (BrO_3^-) ions, followed by the bromination of malonic acid. Intermediates are hypobromous acid (HOBr) and bromous acid (HBrO_2). Process B involves radicals and one-electron transfers, whereby cerium(III) is oxidized to cerium(IV). The bromide ion concentration determines which process is dominant at a particular time. Process A occurs when the bromide concentration rises above a certain critical concentration, while

process B takes place when the bromide concentration is lower than the critical concentration. The oscillations occur because process A consumes bromide ions and leads to conditions at which process B becomes favorable. On the other hand, process B indirectly generates bromide ions, so that the system returns to the condition where it is controlled by process A. The critical bromide ion concentration is $[\text{Br}^-]_{\text{crit}} = 5 \times 10^{-6} [\text{BrO}_3^-]$ (Noyes et al., 1972; Gyenge et al., 1977, 1978). During process A, the system is said to be in its *reduced state*, while during process B the system is considered to be in its *oxidized state*. Process B is an example of an *autocatalytic process*, because HBrO_2 formed in reaction B3 is a reactant in reactions B1 and B2. It should be noticed that although the FKN model explains the basic mechanism of the Belousov–Zhabotinsky reaction, many of the details of the reaction still remain unclear. For instance, there is still no agreement about the exact stoichiometry and the reaction mechanism of process C. Edelson, Field and Noyes (Edelson et al., 1975, 1979) published a more detailed description of Belousov–Zhabotinsky reaction than the original FKN model, with over 20 steps. Calculations based on this model can account for the long induction time before the oscillations begin.

Originally, it was assumed that the other products in process C included formic acid (Field et al., 1972), but this assumption was later abandoned (Field, 1975). Oslonovitch et al. (1998) investigated the reaction of bromomalonic acid with cerium(IV) (process C). They detected bromethenetetracarboxylic acid (BrEETRA), $(\text{HOOC})_2\text{C}=\text{CBrCOOH}$, as a reaction product, and proposed the following stoichiometries for process C:



The first reaction dominates at low cerium(IV) concentrations, i.e. as in the cerium-catalyzed BZ reaction. The second reaction dominates when cerium(IV) is present in large excess. Nagygyory et al. (1999) postulated the occurrence of carbene intermediates in the reactions between cerium(IV) and malonic acid or bromomalonic acid. These authors also consider two different reactions, depending on the concentration of cerium(IV). Process C has two functions (Field and Boyd, 1985). The first function is the transformation of some reaction products of process B into a species which inhibits process B, by competing with reaction B1 for HBrO_2 . The second function is to reinitialize the system by reducing cerium(IV) to cerium(III) after process B has stopped.

The formation of peroxy malonyl radicals in the reaction of cerium with malonic acid in acidic medium was experimentally established by Neumann et al. (1995). Malonyl radicals were observed in the reaction mixture (Brusa et al., 1985; Försterling and Noszticzius, 1989; Försterling et al., 1990). The presence of malonyl radicals is evident from the detection of ethanetetracarboxylic acid (recombination product of two alkyl malonyl radicals) and malonyl malonate (recombination product of an alkyl and a carboxylato malonyl radical) (Gao et al., 1994; Sirimungkala et al., 1996). Försterling et al. (1990) proposed that the oscillations are controlled by malonyl radicals instead of bromide ions. Noszticzius et al. (1984) suggested control of the oscillations by Br_2 . Field and Försterling (1986) published a revised set of rate constants for the reactions involved in the FKN mechanism. One conclusion was that HBrO_2

is considerably more stable than previously thought. There has been debate about how bromide ions are produced in the reaction (Ruoff et al., 1988). According to the FKN mechanism, bromide ions are generated by reaction between cerium(IV) and bromomalonic acid. This assumption was supported by the fact that the oscillations start only after the concentration of bromomalonic acid is above a certain critical value. There is however evidence for the production of bromide ions from other sources than bromomalonic acid. Varga et al. (1985) have demonstrated by isotope tracer experiments with ^{82}Br -labeled bromomalonic acid that a large fraction of the bromide ions produced in process C comes from reduction products of BrO_3^- , like HOBr, and not from bromomalonic acid. High performance liquid chromatography is a valuable experimental tool for the study of the Belousov–Zhabotinsky reaction (Hegedus et al., 2001). At different moments during the reaction, samples can be withdrawn from the reaction mixture and analyzed. This allows the characterization of different intermediates and measurements of their concentrations. It is difficult to measure the concentration of bromine in solution, because Br_2 rapidly reacts with malonic acid to form bromomalonic acid. The reaction occurs via the enol form of malonic acid, rather than via the diacid form (Sirimungkala et al., 1999).

The important role of the bromide ion in the metal-catalyzed BZ reaction is emphasized in the *Oregonator* model, which is a simplified version of the FKN model (Field and Noyes, 1974; Ruoff et al., 1988; Field and Schneider, 1989). The Oregonator is so-called because Noyes's group works at the University of Oregon. This oscillator is characterized by five steps:



here, X stands for HBrO_2 , Y for Br^- , Z for 2Ce^{4+} , A for BrO_3^- and P for HOBr. The concentration of A is often kept constant in the model, so that X, Y and Z are the only kinetically active species. These dynamic variables correspond to reaction intermediates. In Eq (O5), f is an expendable stoichiometric factor. Oscillations occur only for $0.5 \leq f \leq 1 + 2^{1/2}$. It is a good assumption that f is close to 1 (Noyes and Jwo, 1975). The Oregonator was developed because the equations in the initial FKN model were too complex for numerical analysis by the computers of that time. The Oregonator can be written in the form of a set of differential equations with only three variables. The individual steps in the Oregonator are not balanced chemical equations, but they summarize well what is happening in the system.

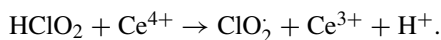
The oscillations in the Belousov–Zhabotinsky reaction occur over a wide range of initial concentrations of the reagents (table 2). Citric acid or malonic acid are not the only possible choices for the organic compounds. The only condition seems to be that the compound should contain one or more active methylene (CH_2) groups, that can be brominated or that active methylene groups can be formed easily by an oxidation reaction (Zhabotinsky,

Table 2
Ranges of initial concentrations in the Belousov–Zhabotinsky reaction

Reagent	Concentration range (mol/L)	Typical concentration (mol/L)
malonic acid	0.125–0.50	0.275
sodium bromate	0.03–0.625	0.625
sulfuric acid	0.5–2.5	1.5
(NH ₄) ₂ [Ce(NO ₃) ₆]	0.0001–0.01	0.002
ferroin	0.0006	0.0006

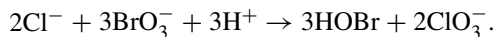
1964a). This condition is important, because the organic substrate should be easily brominated. Examples of such organic compounds include methylmalonic acid, ethylmalonic acid, benzylmalonic acid, maleic acid, malic acid, gallic acid, acetone, acetylacetone, acetyl acid and acetone dicarboxylic acid. No oscillatory reaction is observed for oxalic acid, tartronic acid, 3-hydroxypropionic acid, succinic acid and pyruvic acid (Kasperek and Bruice, 1971). Instead of ammonium hexanitratocerate(IV), (NH₄)₂[Ce(NO₃)₆], also ammonium tetrasulfatocerate(IV), (NH₄)₄[Ce(SO₄)₄], can be used as the cerium(IV) salt. The Ce⁴⁺/Ce³⁺ redox couple in the catalytic cycle can be replaced for instance by the Mn³⁺/Mn²⁺, the [Fe(phen)₃]³⁺/[Fe(phen)₃]²⁺ (ferriin/ferroin), the [Ru(bpy)₃]³⁺/[Ru(bpy)₃]²⁺, or the [Ru(phen)₃]³⁺/[Ru(phen)₃]²⁺ redox couples. A common feature of the catalytic system is that they are all one-electron redox systems with a redox potential between +1.0 V and +1.5 V. The actual choice of the reagent and concentration conditions has an influence on the oscillation characteristics: the induction period, the oscillation period, the peak potential and the total oscillation time. Generally, the induction period increases with increasing concentrations of bromate and malonic acid, whereas the oscillation period decreases with increasing concentrations of these reagents (Than et al., 2001). Typical periods are between 20 seconds and 2 minutes, but the period can be as long as 15 to 20 minutes (Shkhashiri, 1985). The oscillation period is not constant during the reaction and gradually increases toward the end of the reaction. BZ reactions with short oscillation periods can last for about 20 minutes before the oscillations stop, but BZ reactions with long oscillation periods can repeat their cycles for more than 8 hours.

Zhabotinsky (1964b) noticed that the oscillating reaction is completely inhibited by traces of chloride ions. This inhibition was also observed by Janjic et al. (1974) for systems where the dicarboxylic acid is replaced by acetylacetone. Jacobs and Epstein (1976) reported that the inhibition of the concentration oscillation by trace amounts of chloride ions is only of temporary duration, provided that the initial chloride concentration is below a threshold value. High concentrations of chloride ions suppress the oscillations completely. The inhibition is caused by the oxidation of chloride ions to chlorous acid, which then reduces cerium(IV) to cerium(III).



This reduction prevents the oscillations. When chlorous acid has been completely oxidized to chlorate, oscillations resume. The ultimate fate of any chloride in the system is thus oxidation

to chlorate, which has no effect on the oscillations. The overall reaction of chloride oxidation is:



Addition of iodide and the pseudohalide azide (N_3^-) had a similar effect as addition of chloride, whereas addition of nitrate, sulfate or perchlorate ions had no effect. The oscillation period after the initial state was found to be identical with that of the unperturbed system. When the amount of chloride added is less than the amount of cerium(IV) present initially, no observable inhibition is expected. This system is more sensitive to addition of chloride after the oscillating reaction has started than to initial addition of chloride ions; smaller amounts of chloride ions are required to induce inhibition or to suppress the oscillations completely. Because of this inhibitory effect, the glass vessels used to prepare the solutions for a Belousov–Zhabotinsky experiment should be clean and free of chloride ions. Moreover, in the preparation of the ferroin indicator solution 1,10-phenanthroline must be used in its free base form and not in the form of the hydrochloride salt. If one wants to monitor the periodic changes in the chemical potential of the solution, one must use a reference electrode that does not leak chloride ions. Conventional calomel electrodes or silver/silver chloride electrodes are not suitable, but double-junction version of these electrodes are adequate.

The effect of oxygen on the BZ reaction has been investigated by several authors (Barkin et al., 1978; Bar-Eli and Haddad, 1979; Treindl and Fabian, 1980; Ruoff, 1982; Ganapathisubramanian and Noyes, 1982; Menzinger and Jankowski, 1986; Li and Li, 1988; Ruoff and Noyes, 1989; Jwo and Noyes, 1975; Sevcik and Adamacikova, 1988; Wang et al., 1996; Petrascu et al., 1999). The rate of the reduction of cerium(IV) by malonic acid is increased in presence of molecular oxygen (Barkin et al., 1978). Oxygen accelerates the release of bromide during oxidation of a mixture of bromomalonic acid and malonic acid by cerium(IV) (Jwo and Noyes, 1975). Introduction of oxygen in the reaction mixture increases the complexity of the oscillations and reduces their duration (Wang et al., 1996). The same authors attributed the influence of the stirring rate on the reaction to differences in dissolved oxygen. At low cerium concentrations, the effect of oxygen is an abrupt drop of the cerium(IV) concentration (Petrascu et al., 1999). The nature of the organic substrate influences the effect of oxygen, and this effect is most pronounced in the autocatalytic oxidation of cerium(III) by bromate ions (Treindl et al., 1997). This can be attributed to the scavenging of BrO_2 radicals by malonyl and peroxy malonyl radicals.

Whereas the Belousov–Zhabotinsky reaction with methylmalonic and with ethylmalonic acid shows oscillatory behavior under the conditions that gives oscillatory behavior for malonic acid, no oscillations are observed for benzylmalonic acid under the same conditions (Cavasino et al., 1999). Interestingly, oscillatory behavior was observed for the benzylmalonic acid system after addition of the cationic surfactant cetyltrimethylammonium nitrate. Addition of the surfactant also shortened the induction period for the reactions with methylmalonic and ethylmalonic acid. The oscillation period was affected as well by the surfactant. Pojman et al. (1992) reported that upon addition of acrylonitrile monomer to the reaction mixture of the Belousov–Zhabotinsky reaction, polymerization did not occur continuously, but in a step-wise manner, in phase with the oscillations in the cerium(IV) concentration. The addition of

other types of monomers like styrene or methacrylate has an inhibiting effect on the oscillations. Temperature has a pronounced effect on the BZ reaction. An increase in temperature generally leads to an increase in the frequency of the oscillations (Nagy et al., 1996).

Belousov originally studied only temporal oscillations in a well-stirred solution, but the formation of spatial patterns in an unstirred solution is also very interesting. If the reaction begins at a given point, the concentration of intermediates will propagate outward by diffusion and this diffusion process will initiate the reaction in the adjacent regions. The propagation of the spatial patterns is known as a *trigger wave*. Periodically, the reaction will reinitiate at the nucleation point. This results in successive bands (in a test tube) or in concentric rings (in a Petri dish). Nagy-Ungvarai and coworkers (Nagy-Ungvarai et al., 1989a, 1989b) investigated the wave profiles of the cerium-catalyzed BZ reaction in detail. The shape of the wave profiles – from very sharp to very broad wave fronts – depends on the initial composition of the system. The cerium waves are slower than the waves in the ferroin- or ruthenium-catalyzed systems, and the velocity depends on the catalyst concentration. The chemical waves are accompanied by changes in the local refractive index and density of the solution (Kasuya et al., 2005). Rotating spiral waves have been the subject of several theoretical and experimental studies (Winfrey, 1973; Keener and Tyson, 1986; Mikhailov and Krinskii, 1983; Müller et al., 1987; Agladze and Krinskii, 1982; Jahnke et al., 1989; Nagy-Ungvarai et al., 1990). Gao et al. (1996) studied the cerium-catalyzed BZ reaction by magnetic resonance imaging (MRI). The imaging process is based on the fact that the proton relaxation times T_1 and T_2 for paramagnetic cerium(III) are shorter than for diamagnetic cerium(IV). The MRI contrast is determined by the ratio of relaxation times of cerium(III) and cerium(IV). For cerium, contrast produced by T_1 weighting is comparable to that produced by T_2 weighting. In the MRI images, a bright background is related to an excess of cerium(III), whereas a dark background is related to an excess of cerium(IV). The authors noticed that the cerium-catalyzed Belousov–Zhabotinsky reaction is much more difficult to visualize by MRI than the manganese- or ruthenium-catalyzed reactions. Ruoff (1994) showed that oscillatory photoluminescence due to oscillations in the cerium(III) concentration could be detected in the cerium-catalyzed BZ reaction. No chemiluminescence was observed. Monolayers of the dioctadecylester of luminescent $[\text{Ru}(\text{bpy})_3]^{2+}$ spread on the surface of a Belousov–Zhabotinsky reaction mixture have been used as a photosensitive redox indicator for the organization of the spatio-temporal structures in the subphase (Yoneyama et al., 1994a, 1994b; Yoneyama, 1995). The quality of the monolayer depends very much on the anions that are present in the aqueous subphase. Perchlorate ions have been found to give the most rigid packing in the monolayer, with the formation of crystalline microdomains. The presence of perchlorate ions in the subphase also lead to a higher luminescence intensity of the monolayer. The reaction has also been studied calorimetrically (Körös et al., 1979; Roelofs, 1988; Lamprecht, 1992; Fujieda and Zhang, 1995).

4.3. *Demonstration experiments*

The Belousov–Zhabotinsky reaction and other oscillating reactions can be used for very fascinating chemical demonstrations. Detailed experimental descriptions of several oscillat-

ing reactions, including the classic Belousov–Zhabotinsky reaction and modified Belousov–Zhabotinsky reactions are given by Shkhashiri (1985). Jahnke and Winfree (1991) compared the different recipes for the BZ reaction. In the classic reaction, a clear colorless solution (containing potassium bromate) and a pale yellow solution (containing malonic acid and potassium bromide) are mixed producing an amber solution, which becomes colorless after about one minute. Then a yellow solution (containing ammonium hexanitratocerate(IV)) is added, followed by a small amount of a red solution (containing ferroin), producing a green solution. The color of the solution gradually changes over a period of one minute from green to blue, then to violet and finally to red. The color then suddenly returns to green, and the cycle is repeated more than twenty times. The color changes are more complex than the simple red-to-blue color change of the ferroin redox indicator. There are also the color changes related to the cerium ions: cerium(III) is colorless, while cerium(IV) is yellow. The color changes can be monitored spectrophotometrically. After some time the oscillations disappear and the stationary state (equilibrium) is reached.

The oscillations in most demonstration experiments produce periodic color changes. However, other properties of the solution, like the electrical potential, oscillate as well. This is due to changes in the concentrations of the redox active species. The electrical potential changes can be observed by measuring the potential of a platinum electrode versus a reference electrode. The voltage oscillates in phase with the color changes. The range of oscillations in the classic Belousov–Zhabotinsky reaction is about 200 mV. If the solution is poured in a petri dish and left unstirred, mosaic patterns appear as spatial oscillations.

5. Cerium(IV) reagents

5.1. Ammonium hexanitratocerate(IV) (CAN)

Ammonium hexanitratocerate(IV) is undoubtedly the most important cerium(IV) reagent for organic synthesis. A search in Chemical Abstracts (January 2006) resulted in more than 51 000 organic reactions in which ammonium hexanitratocerate(IV) was used as a reagent! The compound is commercially available from several chemical suppliers. Besides ammonium hexanitratocerate(IV), many other names are used for this reagent. Examples include ceric ammonium nitrate, ammonium ceric nitrate, cerium ammonium nitrate, cerium diammonium hexanitate, cerium(IV) ammonium nitrate, diammonium cerium hexanitate, diammonium hexanitratocerate and nitric acid ammonium cerium(+4) salt. However, most organic chemists know this compound as ceric ammonium nitrate or CAN for short. Likewise, the formula of CAN is written as $(\text{NH}_4)_2[\text{Ce}(\text{NO}_3)_6]$, $\text{Ce}(\text{NH}_4)_2(\text{NO}_3)_6$ or $(\text{NH}_4)_2\text{Ce}(\text{NO}_3)_6$, $\text{Ce}(\text{NO}_3)_4 \cdot 2\text{NH}_4\text{NO}_3$ or $[\text{Ce}(\text{NH}_4)_2](\text{NO}_3)_6$. The first form is the most correct one, because it reflects that the cerium(IV) ion is surrounded by six nitrate groups and that the ammonium ions are counter ions to compensate for the negative charge of the hexanitratocerate(IV) unit.

The compound can be prepared by dissolving cerium(IV) oxide or cerium(IV) hydroxide in concentrated nitric acid (Smith et al., 1936). The resulting solution is evaporated close to dryness, and ammonium nitrate is added. Nitric acid is added to the solution, and this solution

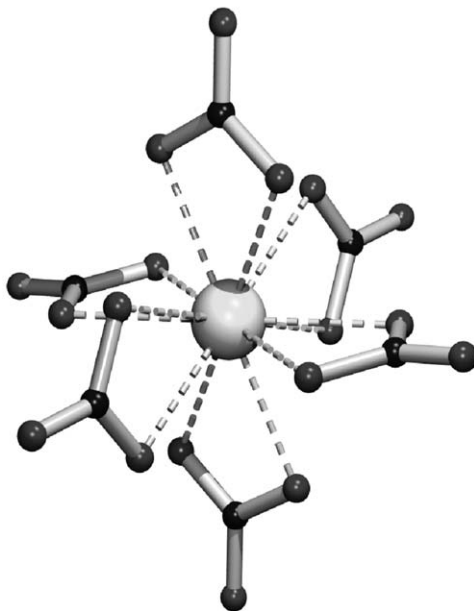


Fig. 1. First coordination sphere of cerium(IV) in ammonium hexanitratocerate(IV). The coordination number of cerium is twelve. The average Ce–O distance is 2.508 ± 0.007 Å (Beineke and Delgaudio, 1968).

is evaporated until crystals start to appear. Ammonium hexanitratocerate(IV) will crystallize from this concentrated solution. Although in some works the addition of a stoichiometric amount of ammonium is suggested (Smith et al., 1936), other papers advise to add a slight excess of ammonium nitrate (Smith, 1967). The complex can be precipitated from an aqueous solution by addition of concentrated nitric acid. The compound can be recrystallized from a dilute aqueous nitric acid solution. Crystals free of nitric acid can be obtained by drying at 100°C (Smith et al., 1936).

Ammonium hexanitratocerate(IV) occurs as small, orange-red, monoclinic crystals. Its crystal structure has been determined by Beineke and Delgaudio (1968) (figs. 1 and 2). The structure is composed of discrete ammonium cations and hexanitratocerate(IV) anions. In the hexanitratocerate(IV) cations, six bidentate nitrate groups bind to the cerium(IV) ion. The approximate symmetry of the complex is T_h . The hexanitratocerate(IV) anion is one of the few examples of a complex with coordination number twelve. The structure is held together by a three-dimensional network of hydrogen bonds. Each hexanitratocerate(IV) ion is involved in twelve hydrogen bonds. The hexanitratocerate(IV) ion is a relatively stable entity in solution (Larsen and Brown, 1964; Miller and Irish, 1967; Karraker, 1968), where it exists mainly as free ammonium ions and hexanitrated cerium(IV) species. The structure of the latter in solution is similar to that in the solid state. This is also evident from the lack of hydrolysis of the salt to insoluble cerium(IV) compounds; this is

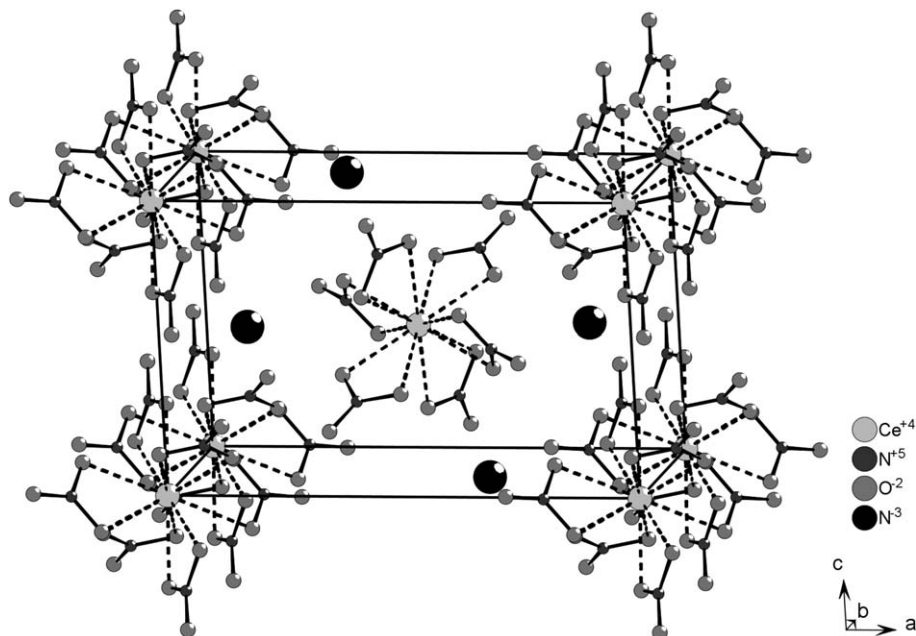


Fig. 2. Crystal structure of ammonium hexanitratocerate(IV). The atomic coordinates are those reported by Beineke and Delgaudio (1968).

in contrast to the behavior of ammonium cerium(IV) nitrate. $(\text{NH}_4)_2[\text{Ce}(\text{NO}_3)_6]$ is the only compound that precipitates out a saturated solution in the ternary $(\text{NH}_4)_2[\text{Ce}(\text{NO}_3)_6] - \text{HNO}_3 - \text{H}_2\text{O}$ system. Blaustein and Gryder (1957) report that the $[\text{Ce}(\text{NO}_3)_6]^{2-}$ ion forms dimers or polymers in 5 M nitric acid.

Ammonium hexanitratocerate(IV) is very well soluble in water; its solubility is 141 g per 100 mL at 25 °C. Meyer and Jacoby (1901) mention that a saturated aqueous solution of ammonium hexanitratocerate(IV) contains at 0 °C, 25 °C and 50 °C respectively 55.74, 59.51 and 65.55 wt.% of $(\text{NH}_4)_2[\text{Ce}(\text{NO}_3)_6]$. The reagent is also soluble in polar organic solvents like methanol, ethanol, acetonitrile, and DMF. Often these solvents are mixed with water, in order to increase the solubility of the reagent. Acetic acid is a useful solvent for performing reactions with CAN, but the solubility of CAN in acetic acid is only 8×10^{-3} M at room temperature (Baciocchi et al., 1977). Ammonium hexanitratocerate(IV) is only very sparingly soluble in apolar solvents.

To overcome the solubility problems in apolar solvents, some authors added surfactants or phase transfer reagents to the aqueous reaction medium in which the cerium(IV) salt is dissolved, so that organic substrate could be solubilized inside micelles or that the surfactant acts as a phase transfer agent (Skarzewski, 1980; Skarzewski and Młochowski, 1985; Skarzewski and Cichacz, 1984; Pletcher and Valdes, 1987; Dehmlow and Makrandi, 1986; Baciocchi et al., 1988a). The yields of the reactions depend very much on the type of surfac-

tant used (Skarzewski and Cichacz, 1984), the best results being obtained with the anionic surfactant sodium dodecylsulfate (SDS). Pletcher and Valdes (1987) used tetrabutylammonium nitrate or tributylphosphate to transfer CAN to the organic phase in a biphasic system consisting of aqueous nitric acid and 1,2-chloroethane. The yields depended very much on the organic substrate and on the phase transfer agent. For instance tributylphosphate worked better for the oxidation of anthracene to anthraquinone, while tetrabutylammonium nitrate gave better yields for the oxidation of naphthalene to naphthoquinone. An uncommon phase transfer reagent is the lipophilic 4,4'-dialkoxy-2,2'-bipyridine 1,1'-dioxide (Skarzewski, 1980), but the reaction yields observed for this reagent are poor. Baciocchi et al. (1988a) added tetrabutylammonium bromide to the biphasic water/dichloromethane system to transfer CAN from the aqueous phase to the organic phase.

Different solvents can be used for reactions with ammonium hexanitratocerate(IV) as reagent. The most popular solvents are (in decreasing order of importance) water, acetonitrile, dichloromethane, THF and methanol. Often mixtures of these solvents are used. Solvents of less importance are DMF, toluene, diethyl ether, ethanol, pyridine, acetone, benzene, ethyl acetate, hexane, acetic acid, chloroform, dioxane, DMSO, carbon tetrachloride and 1,2-dichloroethane. Other solvents have found only marginal use for this type of reactions. One report describes CAN-mediated oxidation reactions in a mixture of dichloromethane and an imidazolium ionic liquid (Bar et al., 2003). Methanol is a better solvent than ethanol for CAN (Cho and Romero, 1995); whereas methanol reacts only very slowly with CAN, the reaction between ethanol and CAN is fast. It should be mentioned that in many reactions in apolar solvents, CAN is used as a suspension; thus under heterogeneous reaction conditions. Also reactions of CAN in acetic acid are often done under heterogeneous conditions. It was observed that for heterogeneous reactions of CAN in acetic acid, the nitrate/acetate ratio in the reactions mixture depends on the amount of solid CAN dispersed in acetic acid; as the amount of undissolved CAN increases, the nitrate/acetate ratio increases significantly (Baciocchi et al., 1977).

Ammonium hexanitratocerate(IV) is a very versatile reagent and can be used for many types of organic reactions (see further). However, it is not an ideal reagent. Disadvantages are the poor solubility in apolar solvents and the fact that many reactions are not specific. Side products are often formed.

5.2. Ammonium cerium(IV) sulfate (CAS)

Given the popularity of ammonium cerium(IV) sulfate for preparing standard solutions for redox titrations (cerimetry), it is surprising that it has been used only in very few cases as an oxidizing reagent in organic synthesis. This can partially be explained by the lower solubility of the ammonium sulfate cerium(IV) in polar organic solvents. This reagent is commercially available as a dihydrate, $(\text{NH}_4)_4\text{Ce}(\text{SO}_4)_4 \cdot 2\text{H}_2\text{O}$. Is also known under the names ammonium tetrasulfatocerate(IV) and ceric ammonium sulfate (CAS). There is a major difference between CAS and ammonium hexanitratocerate(IV) (CAN). Whereas CAN is a complex salt with anionic hexanitratocerate(IV) complexes, dimeric units with bridging sulfate groups are present in CAS. The crystal structure of $(\text{NH}_4)_4\text{Ce}(\text{SO}_4)_4 \cdot 2\text{H}_2\text{O}$ has been reported by Shan and Huang (figs. 3 and 4) (Shan and Huang, 1998). $(\text{NH}_4)_4\text{Ce}(\text{SO}_4)_4 \cdot 2\text{H}_2\text{O}$ is not the

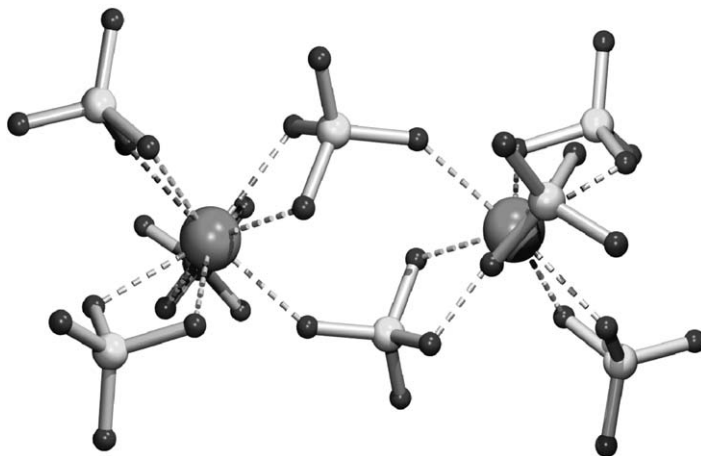


Fig. 3. Coordination sphere of cerium(IV) ammonium sulfate (Shan and Huang, 1998).

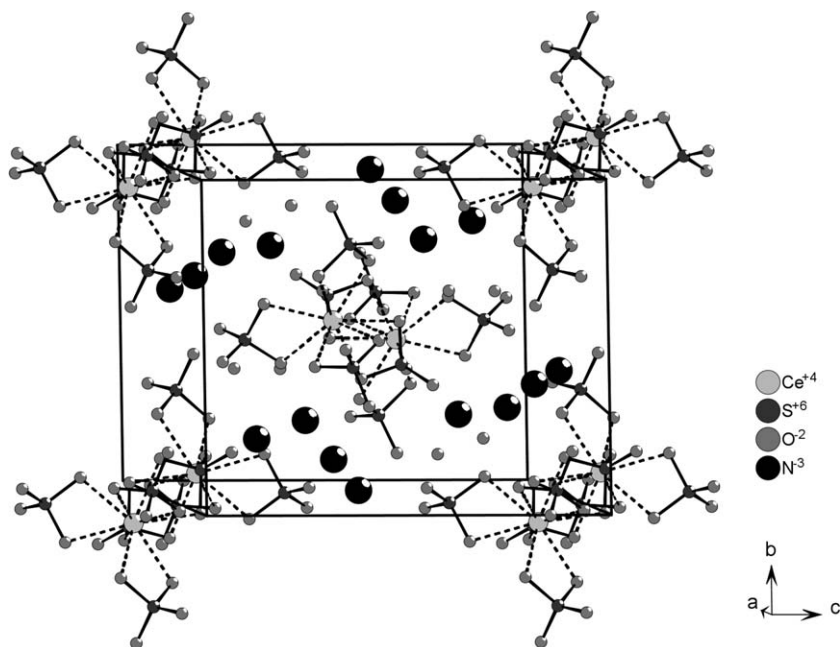


Fig. 4. Crystal structure cerium(IV) ammonium sulfate. The atomic coordinates are those of Shan and Huang (1998).

only compound in the ternary system $\text{NH}_4(\text{SO}_4)_2\text{-Ce}(\text{SO}_4)_2\text{-H}_2\text{O}$. Other compounds include $(\text{NH}_4)_4\text{Ce}(\text{SO}_4)_4$, $(\text{NH}_4)_2\text{Ce}(\text{SO}_4)_3 \cdot 2\text{H}_2\text{O}$, $(\text{NH}_4)_2\text{Ce}(\text{SO}_4)_3 \cdot 3\text{H}_2\text{O}$, $(\text{NH}_4)_6\text{Ce}(\text{SO}_4)_5 \cdot 3\text{H}_2\text{O}$, $(\text{NH}_4)_8\text{Ce}(\text{SO}_4)_6 \cdot 3\text{H}_2\text{O}$, $(\text{NH}_4)_8\text{Ce}(\text{SO}_4)_6 \cdot 5\text{H}_2\text{O}$ and $(\text{NH}_4)_{10}\text{Ce}(\text{SO}_4)_7 \cdot 3\text{H}_2\text{O}$ (Golovnya and Pospelova, 1961; Golovnya et al., 1960).

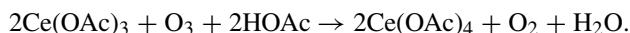
Mehta et al. (1976) reported on the use of this reagent for the Baeyer–Villiger oxidation of polycyclic ketones like 1,3-bishomocubanone and 1,4-bishomocubanone into lactones. Ammonium tetrasulfatocerate(IV) dissolved in a mixture of dilute sulfuric acid and acetonitrile was applied as a reagent to transform polycyclic aromatic compounds into quinones (Periasamy and Bhatt, 1977a, 1977b). Skarzewski (1984) oxidized polycyclic aromatics with this reagent in a two-phase system with sodium dodecyl sulfate as a surfactant. CAS could be used in catalytic amounts if an excess of ammonium persulfate was present to steadily reconvert cerium(III) in cerium(IV).

5.3. Cerium(IV) sulfate tetrahydrate

The reactivity of cerium(IV) sulfate tetrahydrate, $\text{Ce}(\text{SO}_4)_2 \cdot 4\text{H}_2\text{O}$, is comparable to that of ammonium tetrasulfatocerate(IV), but the former compound has a lower solubility in water. It has been suggested that cerium(IV) sulfate exists in sulfuric acid solutions either as $\text{H}_4[\text{Ce}(\text{SO}_4)_4]$ or as the hydrolysis products $\text{H}_4[\text{CeO}_x(\text{SO}_4)_{4-x}]$ (Jones and Soper, 1935). When the sulfuric acid concentration is below 0.5 M basic sulfates can precipitate. At this concentration cerium(IV) exists predominantly in solution as $\text{H}_3[\text{Ce}(\text{OH})(\text{SO}_4)_3]$. Further decrease of the sulfuric acid concentration leads to transformation of $\text{H}_3[\text{Ce}(\text{OH})(\text{SO}_4)_3]$ into $\text{H}_2[\text{Ce}(\text{OH})_2(\text{SO}_4)_2]$ and finally into $\text{H}[\text{Ce}(\text{OH})_3(\text{SO}_4)]$. Hardwick and Robertson (1951) suggested that in 1 M sulfuric acid solutions the cerium(IV) ion associates with sulfate ions to form successively $[\text{Ce}(\text{SO}_4)_4]^{2+}$, $[\text{Ce}(\text{SO}_4)_2]$ and $[\text{Ce}(\text{SO}_4)_3]^{2-}$. The most abundant species in solution is $[\text{Ce}(\text{SO}_4)_3]^{2-}$. The findings of these authors are in disagreement with those of Jones and Soper (Jones and Soper, 1935), who found no evidence of binding of protons or hydroxyl groups to the cerium complexes. The solubility of cerium(IV) sulfate in sulfuric acid has been studied by Paulenova and coworkers (Paulenova et al., 2002). The crystal structure of cerium(IV) sulfate tetrahydrate has been reported by Lindgren (fig. 5) (Lindgren, 1977) and that of anhydrous cerium(IV) sulfate by Rogachev and coworkers (fig. 6) (Rogachev et al., 1974). From the figures, it is evident that the cerium ion is part of a 3D polymeric network. This explains the lower solubility of these cerium(IV) sulfate salts in water. Brockhaus used cerium(IV) sulfate for the oxidation of catechol to *ortho*-benzoquinone (Brockhaus, 1968). Weinstock et al. (1988) generated malonyl radicals from dimethylmalonate with cerium(IV) sulfate and let this reactive species react with thiophene and furans. These heterocycles undergo reaction at the C₂ position with malonyl radicals. Finally, cerium(IV) sulfate in presence of iodine cleaves 2-alkylcycloalkanones to keto esters (He et al., 1999).

5.4. Cerium(IV) acetate

Cerium(IV) acetate, $\text{Ce}(\text{CH}_3\text{COO})_4$ or $\text{Ce}(\text{OAc})_4$, has been synthesized by oxidation of cerium(III) acetate by ozone in presence of nitrate ions (Hay and Kochi, 1968):



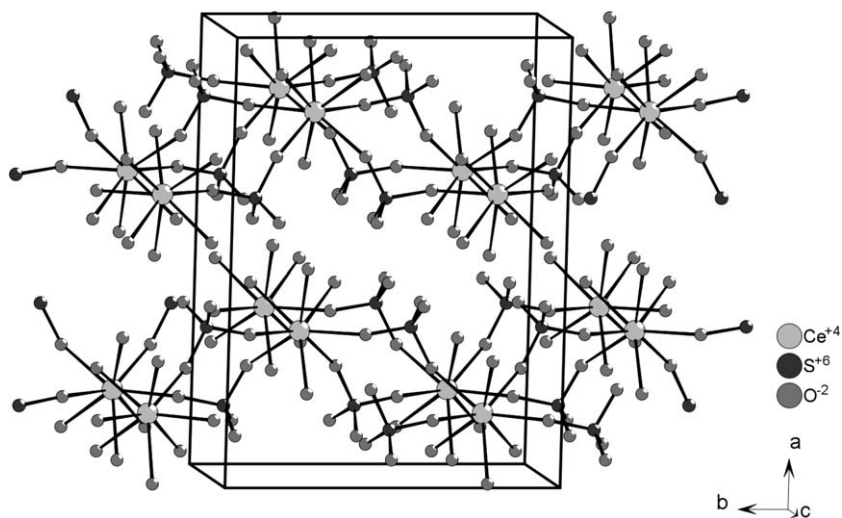


Fig. 5. Crystal structure of cerium(IV) sulfate tetrahydrate. The atomic coordinates are those given by Lindgren (1977).

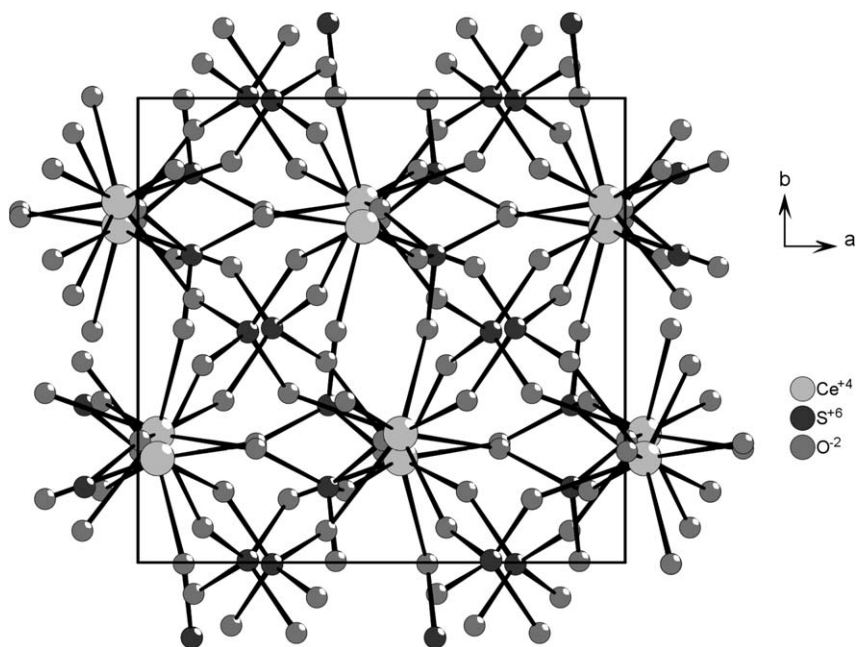


Fig. 6. Crystal structure of anhydrous cerium(IV) sulfate. The atomic coordinates are those reported by Rogachev et al. (1974).

The role of the nitrate ions is to prevent polymerization of cerium(III) acetate in glacial acetic acid/acetic anhydride solution, and to enhance the solubility of cerium(III) acetate in this medium. The yield of cerium(IV) acetate depended on the amount of nitrate ions present; the best results were obtained when 3.5 mol% of cerium(III) nitrate was added to cerium(III) acetate. Cerium(IV) acetate is soluble in aqueous solutions of strong acids, but is only slightly soluble in acetic acid and in benzene. A mixture of acetic acid and acetic anhydride can be used as a recrystallization solvent. The compound is hygroscopic and is also reported to be light sensitive. A solvate of cerium(IV) acetate with acetic acid is more soluble in organic solvents than the pure cerium(IV) acetate. When dissolved in glacial acetic acid that contains 10% potassium acetate, it can be used for the transformation of alkenes into lactones (Heiba and Dessau, 1971). Cerium(IV) acetate was used as a reagent for free-radical aromatic nitromethylations (Kurz and Ngoviwatchai, 1981).

5.5. *Cerium(IV) trifluoroacetate*

Cerium(IV) trifluoroacetate, $\text{Ce}(\text{CF}_3\text{COO})_4$, can be prepared by reaction of cerium(IV) hydroxide with trifluoroacetic acid (TFA). First a basic salt with composition $\text{Ce}(\text{OH})_2(\text{CF}_3\text{COO})_2$ or $\text{CeO}(\text{CF}_3\text{COO})_2 \cdot \text{H}_2\text{O}$ is formed, which can be transformed into the desired product by further treatment with trifluoroacetic acid and the corresponding anhydride (Norman et al., 1973). This reagent is moisture sensitive and undergoes hydrolysis upon exposure to humid air. It can be dissolved in trifluoroacetic acid in presence of lithium trifluoroacetate. It is assumed that the cerium(IV) ion is present in these solutions under the form of an anionic complex. The solutions are stable in the absence of light. The presence of lithium trifluoroacetate has the advantage that it allows dissolution of larger quantities of aromatic compounds. Cerium(IV) trifluoroacetate is insoluble in chloroform, dichloromethane and benzene, but it can be solubilized in coordinating solvents like acetone, 1,2-dimethoxyethane, DMSO and acetonitrile. It has been used for the oxidation of electron rich hydrocarbons like mesitylene. Marrocco and Brilmyer (1983) describe the use of cerium(IV) trifluoroacetate for the oxidation of *m*-phenoxyltoluene to *m*-phenyloxybenzaldehyde.

5.6. *Cerium(IV) perchlorate*

Although the redox potential of the $\text{Ce}^{4+}/\text{Ce}^{3+}$ couple reaches the high value of +1.87 V in 8 M HClO_4 (Smith and Getz, 1938; Wadsworth et al., 1957), cerium(IV) perchlorate has not been often used as a reagent for organic reactions. When it is used, this is mostly under the form of an aqueous perchloric acid solution. The lack of interest in cerium(IV) perchlorate in comparison to ammonium hexanitratocerate(IV) can partially be explained by the fact that the former is more difficult to handle than other cerium(IV) salts. Perchlorates can be hazardous chemicals (for instance grinding of the solid compound can lead to an explosion) and this is also true for cerium(IV) perchlorate. Metal perchlorates are often very hygroscopic, because the perchlorate anion is a weakly coordinating anion. In aqueous solutions, perchlorate ions are not coordinated to the cerium(IV) ion. This lack of complex formation, causes hydrolysis of cerium(IV), even in strongly acidic solutions. In an aqueous perchloric acid solution of cerium(IV) perchlorate, different species are present. They include hydrated Ce^{4+} ,

the hydrolyzed species $[\text{Ce}(\text{OH})]^{3+}$ and $[\text{Ce}(\text{OH})_2]^{2+}$, and the dimeric species $[\text{Ce}-\text{O}-\text{Ce}]^{6+}$ (Sherrill et al., 1943; Heidt and Smith, 1948; Baker et al., 1960). The tendency to form dimers increases at increasing cerium(IV) concentrations. Although there is agreement that hydrolysis products and dimeric species co-exist in solution, there is still discussion about which hydrolyzed species are actually present and about the exact values of the equilibrium constants.

Standardized solutions of cerium(IV) perchlorate can be prepared starting from ammonium hexanitratocerate(IV) (Daugherty and Taylor, 1972). Under this firm, cerium(IV) is reduced to cerium(III) by hydrogen peroxide, and cerium(III) is precipitated by oxalic acid. Cerium(III) oxalate is ignited to form cerium dioxide, which is subsequently dissolved in hydrogen peroxide, and the latter is destroyed by boiling. Finally, cerium(III) is electrolytically oxidized to cerium(IV).

5.7. *Cerium(IV) methanesulfonate*

Solutions of cerium(IV) methanesulfonate, $\text{Ce}(\text{CH}_3\text{SO}_3)_4$, in aqueous methanesulfonic acid are most conveniently obtained by electrochemical oxidation of the corresponding cerium(III) methanesulfonate solution (Kreh et al., 1987, 1989; Kreh, 1988). A solution of cerium(III) in aqueous methanesulfonic acid can be prepared by adding the acid to a stirred suspension of cerium(III) carbonate in water. The behavior of solutions of cerium(III) and cerium(IV) methanesulfonate have been discussed in section 8. Because cerium(IV) has a lower solubility than cerium(III) in methanesulfonic acid, a solid cerium(IV) compound precipitates from concentrated cerium(III) methanesulfonate solution in dilute methanesulfonic acid during electrochemical oxidation. The stoichiometry of this solid compound is $\text{Ce}(\text{CH}_3\text{SO}_3)_2(\text{OH})_2 \cdot \text{H}_2\text{O}$ and its solubility in water is high, up to 1.7 M. The salt can be used for preparing solutions of cerium(IV) methanesulfonate in aqueous methanesulfonic acid. $\text{Ce}(\text{CH}_3\text{SO}_3)_2(\text{OH})_2 \cdot \text{H}_2\text{O}$ can be used for oxidation reactions as a solution in water or as a suspension in aqueous methanesulfonic acid. Both methods give similar results in most cases, although sometimes the suspension method works better. The use of slurries of this solid oxidant generates the more soluble cerium(III) methanesulfonate upon reduction. Other names that are used for cerium(IV) methanesulfonate are ceric mesylate and ceric methanesulfonate.

5.8. *Cerium(IV) triflate*

The rare-earth salts of trifluoromethanesulfonic acid (triflic acid) are popular reagents for lanthanide-mediated organic reactions. Especially scandium(III) triflate, $\text{Sc}(\text{CF}_3\text{SO}_3)_3$, and ytterbium(III) triflate, $\text{Yb}(\text{CF}_3\text{SO}_3)_3$, are often used as mild Lewis acids for reactions in water (Kobayashi et al., 2002). It is therefore surprising that only very few studies of cerium(IV)-mediated reactions describe the use of cerium(IV) triflate, $\text{Ce}(\text{CF}_3\text{SO}_3)_4$ or $\text{Ce}(\text{OTf})_4$, as a reagent. This salt was first reported by Kreh et al. (1987), who prepared a solution of cerium(IV) in aqueous triflic acid by electrochemical oxidation of a cerium(III) triflate solution. They illustrated the use of this reagent for oxidation of alkylaromatic and polycyclic aromatic compounds. Imamoto et al. (1990) prepared cerium(IV) triflate by reaction

of cerium(IV) carbonate with triflic acid. These authors noticed that “wet” cerium(IV) carbonate has to be used; dry cerium(IV) carbonate did not react. Cerium(IV) carbonate can be prepared by mixing aqueous solutions of potassium carbonate and ammonium hexanitratocerate(VI). Attempts to prepare cerium(IV) triflate by reaction of cerium(IV) hydroxide or cerium(IV) oxide were unsuccessful. The compound could be obtained as a bright yellow hygroscopic solid with composition $\text{Ce}(\text{CF}_3\text{SO}_3)_4 \cdot 1.5\text{H}_2\text{O}$, which decomposes above 120°C into cerium(III) triflate. It is soluble in water, ethanol, tetrahydrofuran, 1,2-dimethoxyethane and 1,4-dioxane. Commercial cerium(IV) triflate hydrate, $\text{Ce}(\text{CF}_3\text{SO}_3)_4 \cdot n\text{H}_2\text{O}$, contains 2 to 5 moles of water (available from Aldrich). By using triflic anhydride (TfOTf) as a dehydrating agent, it is possible to obtain anhydrous cerium(IV) triflate in the form of a pale yellow powder (Berthet et al., 2000):



The reaction can be carried out at room temperature. In contrast to the hydrated form, the anhydrous form is stable against reduction: no decomposition was observed after 15 hours of heating at 100°C . Cerium(IV) triflate is soluble in coordinating solvents like pyridine, tetrahydrofuran and diethyl ether; stable Lewis base adducts are formed. Although no crystal structure of anhydrous cerium(IV) triflate has been determined yet, it is assumed that this compound forms a polymeric structure with bridging triflate groups.

Cerium(IV) triflate has been used for epoxide ring opening (Iranpoor et al., 1998, 2002, 2003), benzylic oxidations of aromatics (Laali et al., 2001), oxidation of α -methylpyrrole (Thyran and Lightner, 1996), esterification (Iranpoor and Shekarriz, 1999a), iodofunctionalization of alkenes (Iranpoor and Shekarriz, 2000), the synthesis of biaryls (Iranpoor and Shekarriz, 1999b), and the deprotection of trityl ethers (Khalafi-Nezhad and Alamdari, 2001) and *tert*-butyldimethylsilyl ethers (Bartoli et al., 2002). Studies on the oxidation of benzylic compounds by cerium(IV) triflate (Laali et al., 2001), showed that the water content has a marked influence on the oxidation ability; the optimal water content is between 14 and 22 wt.% water. Commercial samples were found to have a lower oxidation power than freshly prepared samples. This behavior could be traced back to a lower water content in the commercial samples (11 to 13 wt.%). However, rehydration of the commercial samples did not lead to an activity as high as that of the initial samples. These studies show that the performance of cerium(IV) triflate as an oxidizing reagent depends very much on the preparation method. On the other hand, less unwanted side products are obtained than with ammonium hexanitratocerate(IV).

5.9. Hydrophobic cerium(IV) reagents

Although ammonium hexanitratocerate(IV) is a good reagent for many organic transformations in aqueous solutions or in polar organic solvents, it is much less suitable for use in non-polar organic solvents due to its poor solubility in these solvents. Several authors have tried to overcome these solubility problems by replacing the ammonium group by tertiary or quaternary ammonium ions. These ions are more hydrophobic (more lipophilic) than the ammonium ion, and it can be expected that the resulting cerium(IV) reagents dissolve as ion-pairs in apolar solvents.

Dehmlow and Makrandi (1986) prepared tetra-*n*-butylammonium hexanitratocerate(IV), $[(n\text{-Bu})_4\text{N}]_2[\text{Ce}(\text{NO}_3)_6]$, for use as an oxidant in solvents like dichloromethane. Here tetra-*n*-butylammonium acted as a phase reagent to transfer the hexanitratocerate(IV) anion into the organic phase. This reagent has been explored further by other authors for direct use in dichloromethane (Muathen, 1991; Chen and Mariano, 2000; Zhang et al., 2003a, 2003b, 2004; Zhang and Flowers II, 2004) and it is known as CTAN. Mishra et al. (2001) developed cetyltrimethylammonium hexanitratocerate(IV), $[(\text{C}_{16}\text{H}_{33})\text{N}(\text{CH}_3)_3]_2[\text{Ce}(\text{NO}_3)_6]$, which is soluble in both polar and apolar solvents due to its amphiphilic nature. It has been reported to be soluble in water, methanol, ethanol, chloroform, dioxane, benzene, tetrahydrofuran, acetic acid, acetonitrile, ethylacetate, DMF, DMSO, 1-octanol and *iso*-octanol. An example of a cerium(IV) reagent with a tertiary ammonium counter ion is triethylammonium hexanitratocerate(IV), $[\text{Et}_3\text{NH}]_2[\text{Ce}(\text{NO}_3)_6]$ (Firouzabadi and Iranpoor, 1983). These authors report the formula of this compound as $[\text{Ce}(\text{Et}_3\text{NH})_2](\text{NO}_3)_6$, which is misleading. The reagent is soluble in dichloromethane, alcohols, acetone, acetonitrile and water. It is also known as CTEAN, after ceric triethylammonium nitrate. A closely related reagent, that has not been studied in detail yet, is pyridinium hexanitratocerate(IV) (referred to as CPN) (Iranpoor and Owji, 1991).

5.10. Pyridinium hexachlorocerate(IV) (CPC)

Pyridinium hexachlorocerate(IV), $(\text{C}_5\text{H}_6\text{N})_2[\text{CeCl}_6]$, has been known for a long time (Grant and James, 1915), but Bradley and coworkers described a reliable method for the synthesis of this compound in 1956 (Bradley et al., 1956a). For the preparation, cerium(IV) hydroxide is freshly synthesized by addition of an excess of an aqueous sodium hydroxide solution (containing some bromine) to a solution of cerium(IV) ammonium sulfate. The carefully washed cerium(IV) hydroxide precipitate is then suspended in absolute ethanol, and dry hydrogen chloride is bubbled through the solution. The solution is filtrated, and pyridine is added to the filtrate. After further treatment of the solution with hydrogen chloride, the bright yellow $(\text{C}_5\text{H}_6\text{N})_2[\text{CeCl}_6]$ complex can be obtained by crystallization from the solution. Pyridinium hexachlorocerate(IV) is also known as dipyridinium hexachloride or cerium(IV) pyridinium chloride, and is referred to as CPC. The compound is stable in boiling ethanol, but not in boiling methanol (Maini et al., 1978). In boiling acetonitrile, the formation of chlorine gas is observed (Maini et al., 1978). CPC was originally used as a starting material for the synthesis of cerium(IV) alkoxides (Bradley et al., 1956a), and it is a reagent for the side-chain oxidation of highly substituted methylbenzenes (Maini et al., 1978). The pyridinium ions can be replaced by quaternary ammonium ions. Such compounds have not been reported as cerium(IV) reagents, although the synthesis of tetraethylammonium hexachlorocerate(IV), $(\text{NEt}_4)_2[\text{CeCl}_6]$ has been described (Barry et al., 1981). It is prepared by refluxing a solution of $\text{CeCl}_3 \cdot 7\text{H}_2\text{O}$ and tetraethylammonium chloride in thionyl chloride, which acts as an anhydrous oxidative chlorinating medium. The authors claim that this is a general method for the preparation of hexachlorocerate(IV) complexes with different counter ions, such as quaternary ammonium ions, but also quaternary phosphonium ions.

Notice that chloro complexes of cerium(IV) are much less stable than the corresponding nitrate or sulfato complexes, due to the oxidation of the chlorides to molecular chlorine by cerium(IV). For instance, cerium(IV) chloride, CeCl_4 , is an unstable compound.

However, hexachlorocerate(IV) salts have a much higher stability, as is illustrated by pyridinium hexachlorocerate(IV). This complex can be dried without decomposition at 120 °C in vacuo (Bradley et al., 1956a). The CeCl₄ moiety can also be stabilized by adduct formation with neutral ligands. Examples include [CeCl₄(dmsO)₃] (Brezina, 1971), [CeCl₄(tppo)₂] (Brezina, 1971), [CeCl₄(bpyO₂)₂] (Brezina, 1973) and [CeCl₄(tdpo)₂] (du Preez et al., 1978; Barry et al., 1978), where dmsO = dimethylsulfoxide, tppo = triphenylphosphine oxide, bpyO₂ = 2,2'-bipyridine-*N,N'*-dioxide and tdpo = tris(dimethylamino)phosphine oxide.

5.11. Cerium(IV) trihydroxy hydroperoxide (CTH)

Cerium(IV) trihydroxy hydroperoxide (CTH), Ce(OH)₃O₂H, was developed as a mild oxidation agent (Firouzabadi and Iranpoor, 1984). It can be synthesized by addition of a concentrated ammonia solution to a concentrated solution of cerium(III) chloride in water, followed by addition of hydrogen peroxide (30%). Other names for this orange-red reagent are ceric trihydroxy hydroperoxide and cerium(IV) hydroxide peroxide. The interesting feature of this reagent is that it can simply be regenerated after reaction by treatment of the solid with a concentrated solution of hydrogen peroxide (30%). The reagent has been tested for the oxidation of organic compounds in dry benzene. Since the reagent does not dissolve in benzene, reactions are heterogeneous. CTH is very efficient for the oxidation of benzyl alcohol to benzaldehyde. Benzhydrol is qualitatively oxidized to benzophenone. Hydroquinone and catechol are easily oxidized to the corresponding quinones. Aromatic thiols are converted to disulfides. For most reactions, two to three equivalents of CTH are used with respect to the organic substrate.

Other compounds that contain cerium(IV) and the peroxide group have been reported in the past, but these compounds have not found use as reagent for organic reactions. In 1885, a hydrated cerium(IV) peroxide was prepared by Cleve (Cleve, 1885). Job (1899a, 1899b) and Meloche (1915a, 1915b) reported procedures for the preparation of cerium(IV) peroxy carbonates. Warren (1964) investigated cerium(IV) peroxy acetate, Ce₂(O₂)₃(CH₃COO)₂. This compound precipitates as an amorphous solid from an aqueous solution containing acetic acid, sodium acetate, cerium(III) nitrate, and hydrogen peroxide. However, cerium(IV) peroxy acetate is unstable and loses oxygen and acetic acid on standing at room temperature.

5.12. Cerium(IV) periodate

Hydrated cerium(IV) periodate, CeHIO₆·4H₂O, was obtained as a yellow solid by reaction between (NH₄)₂[Ce(NO₃)₆] and H₅IO₆ in aqueous solutions at low pH (Levason and Ouldroyd, 1996). This compound, which is insoluble in water, is able to oxidize benzyl alcohol to benzaldehyde in dichloromethane with tetramethylammonium periodate as co-oxidant, but the yields are only moderate (Griffith et al., 1996).

5.13. Tris[trinitratocerium(IV)] paraperiodate (TTCPP)

Tris[trinitratocerium(IV)] paraperiodate, [Ce(NO₃)₃]₃·H₂IO₆ (TTCPP for short) was developed as a reagent for oxidation reactions in aprotic organic solvents under neutral conditions (Firouzabadi et al., 1984d). TTCPP is sometimes also formulated as [Ce(NO₃)₃]₃·HIO₆

(Heravi et al., 1999). Heterogeneous reaction conditions are chosen for this compound. The reagent was prepared by addition of a solution of ammonium hexanitratocerate(IV) to a solution of potassium periodate, KIO_4 , in water. TTCPP is a very efficient oxidant for the cleavage of 1,2-diols to aldehydes. It also works well for the common oxidation reactions for which tetravalent cerium is used, like oxidation of benzyl alcohol to benzaldehyde and the oxidation of thiols to disulfides. Whereas triphenylphosphine is resistant towards oxidation by CAN, it is quantitatively converted to triphenylphosphine oxide by TTCPP. Other applications of tris[trinitratocerium(IV)] paraperiodate include the regioselective and stereoselective ring opening of epoxides (Iranpoor and Zardaloo, 1994), the tetrahydropyranlation of alcohols (Oskooie et al., 1998), and the oxidative deprotection of trimethylsilyl ethers to the corresponding carbonyl compounds (Firouzabadi and Shiriny, 1996a).

5.14. Bis[trinitratocerium(IV)] chromate and dinitratocerium(IV) chromate dihydrate

Bis[trinitratocerium(IV)] chromate, $[\text{Ce}(\text{NO}_3)_3]_2\text{CrO}_4$, was introduced as a mild oxidizing agent by Firouzabadi et al. (1984a). It is obtained as an orange-yellow compound by mixing a solution of potassium dichromate and ammonium hexanitratocerate(IV) in water. The compound is quite stable up to 190 °C. The reagent was developed for oxidation reactions in aprotic organic solvents. Bis[trinitratocerium(IV)] chromate worked well for oxidizing organic compounds in refluxing benzene, but not in refluxing dichloromethane. In contrast to tris[trinitratocerium(IV)] paraperiodate, bis[trinitratocerium(IV)] chromate cannot oxidize triphenylphosphine. The reagent has been used for the oxidation of thiols to disulfides (Firouzabadi et al., 1984b), the tetrahydropyranlation of alcohols (Oskooie et al., 1998), and oxidation of trimethylsilyl ethers to the corresponding carbonyl compounds (Firouzabadi and Shiriny, 1996b).

Dinitratocerium(IV) chromate dihydrate, $[\text{Ce}(\text{NO}_3)_3]_2\text{CrO}_4 \cdot 2\text{H}_2\text{O}$, was presented as a more economical alternative to bis[trinitratocerium(IV)] chromate because of the smaller cerium(IV)/chromium(VI) ratio (Firouzabadi et al., 1984c). It has been tested for the oxidation of different organic compounds like benzyl alcohols, secondary alcohols, and thiols in benzene, but in general the yields are lower than for bis[trinitratocerium(IV)] chromate. Later it was reported that this reagent gave unsatisfying results for the oxidative deprotection of trimethylsilyl ethers (Firouzabadi and Shiriny, 1996a, 1996b).

5.15. Cerium(IV) alkoxides

The first detailed accounts on the synthesis of cerium(IV) alkoxides have been published by Bradley and coworkers (Bradley et al., 1956a, 1956b, 1957). The cerium(IV) alkoxides of methanol, ethanol, *n*-propanol, *n*-butanol, *n*-pentanol, *iso*-butanol and *neo*-pentanol were prepared by passing ammonia gas through a solution of pyridinium hexachloroerate(IV) and the corresponding alcohol in benzene (Bradley et al., 1956a). With *iso*-propanol, not the pure cerium(IV) isopropoxide was obtained, but an *iso*-propanol solvate. This compound was used to prepare other cerium(IV) alkoxides by alcohol interchange. Most of the cerium(IV) alkoxides are bright yellow solids that are extremely sensitive to hydrolysis. Upon heating the compounds melt without decomposition. However, the cerium(IV) *neo*-pentoxide is volatile so

that it could be sublimed. Later, cerium(IV) *iso*-propoxide (Bradley et al., 1956b) and the cerium(IV) alkoxides of several tertiary alcohols (Bradley et al., 1957) were also found to be volatile. The non-volatile cerium(IV) alkoxides are assumed to have a oligomeric or polymeric structure. Cerium(IV) methoxide and cerium(IV) ethoxide are insoluble in benzene or toluene. Gradeff and coworkers (Gradeff et al., 1985, 1986) reported procedures for the synthesis of cerium(IV) alkoxides from the readily available ammonium hexanitratocerate(IV), rather than from pyridinium hexachlorocerate(IV) (that has to be synthesized separately). Evans et al. (1989a) prepared a series of cerium(IV) *tert*-butoxides and cerium(IV) *tert*-butoxides by reaction between ammonium hexanitratocerate(IV) and sodium *iso*-butoxide. The stoichiometry of the complexes depended on the reaction conditions (solvent, molar ratio between reagents). The bulky *tert*-butoxide ligand allows stabilization of the complexes and causes an increase in solubility. Due to their susceptibility to hydrolysis, the cerium(IV) alkoxides are not used as reagents in organic synthesis, but they are very useful starting materials for the synthesis of cerium(IV) coordination compounds and organocerium(IV) compounds.

5.16. Cerium(IV) fluoride

Cerium(IV) fluoride or cerium tetrafluoride, CeF_4 , can be prepared by reaction of cerium(III) fluoride with elemental fluorine at 450 to 500 °C (Cunningham et al., 1954; Wartenburg, 1940; Kim et al., 2003). It is also formed by reaction of xenon tetrafluoride, XeF_4 , with cerium(III) fluoride at 200–400 °C (Spitsyn et al., 1974) or by stepwise reaction of xenon difluoride, XeF_2 , with cerium(III) fluoride at 177 °C, 236 °C and 295 °C (Kiselev et al., 1985). Interestingly, reaction of CeO_2 with elemental fluorine does not yield CeF_4 , but CeF_3 (Takashima et al., 1992). CeF_4 has a higher thermal stability than fluorides of other tetravalent lanthanides and actinides, but will eventually decompose with the release of gaseous fluorine (Kaiser et al., 1972; Gibson and Haire, 1988a, 1988b; Rau et al., 2001). Lanza and Fragala (1998) published a theoretical study on the molecular geometry, vibrational frequencies and bond dissociation energies of CeF_4 . Cerium(IV) fluoride is a solid fluorinating agent, which has been used for the fluorination of benzene (Hudson et al., 1969) and benzotrifluoride (Hudson and Pedler, 1970) (see section 6.7). It was found that cerium(IV) fluoride could be regenerated in situ in the fluorination reactor by passing fluorine gas over the cerium(III) fluoride that was formed upon fluorination of benzene. It is also able to fluorinate ethylene (Asovich et al., 1994).

5.17. Cerium dioxide

Cerium dioxide (ceria) is a well-known heterogeneous catalyst. It is a key component in important industrial processes like fluid catalytic cracking and in the three-way catalyst in automobile exhaust systems. CeO_2 is also applied for the oxidative destruction of organic compounds in waste water and for removal of soot particles in diesel engine exhaust gases. The interested reader is referred to a book edited by Trovarelli (Trovarelli, 2002). In section 10.2 the use of cerium dioxide as photocatalyst for the decomposition of water is described. CeO_2 nanoparticles are catalyst for the photooxidation of toluene (Hernandez-Alonso et al., 2004). It can be expected that cerium dioxide, especially in the form of nanoparticles, has potential for application as reagents for organic transformations.

5.18. Supported cerium(IV) reagents

Supported reagents and catalysts offer the advantage of easy separation of excess reagent or catalyst from the products by simple filtration. Fischer and Henderson (1985) introduced ammonium hexanitratocerate(IV) coated on silica gel as a reagent for convenient oxidation of hydroquinones to quinones. The cerium(IV)/SiO₂ oxidizing agents with 10% to 20% ammonium hexanitratocerate(IV) was prepared by addition of dichloromethane, followed by silica gel to an efficiently stirred solution of ammonium hexanitratocerate(IV) in methanol. Evaporation of the solvents gave a free-flowing yellow powder. This supported reagent has been used for the deprotection of benzaldehyde diacetates to benzaldehydes (Cotelle and Catteau, 1992), for the removal of trityl and silyl protecting groups (Hwu et al., 2000), and for the removal of the *tert*-butoxycarbonyl (*t*-Boc) group (Hwu et al., 2002). Chawla and Mittal (1985) used silica gel-supported ammonium hexanitratocerate(IV) for the oxidative nitration of naphthalene, anthracene and phenanthrene. The adsorption of the cerium(IV) salt on silica gel reduced its oxidizing power so that mononitro derivatives could be obtained as the main product, whereas solutions of ammonium hexanitratocerate(IV) yield considerable amounts of dinitro derivatives or of the corresponding quinones. The authors use a quite uncommon reaction technique. They adsorb the polycyclic aromatic compound and the cerium(IV) salt separately on silica gel in an acetonitrile solution. The solvent is evaporated and the silica gel is dried. The dried powders are thoroughly mixed, added on top of a column packed with silica gel and eluted by a petroleum/benzene mixture. The mixture reacts in the column and the reaction product is collected in the eluate. Sulfides could be oxidized fast and in excellent yields to the corresponding sulfoxides by ammonium hexanitratocerate(IV) supported on hydrated silica gel in dichloromethane (Ali et al., 1998). Ammonium hexanitratocerate(IV) supported on silica gel in refluxing carbon tetrachloride or tetrachloroethylene have a low activity for the oxidation of cyclododecanol to cyclododecanone (Nishiguchi and Asano, 1989). Cerium(IV) sulfate supported on silica gel is an efficient catalyst for the acylation of alcohols by esters (Nishiguchi and Taya, 1990), such as ethyl formate or ethyl acetate which were used both as reagents and solvents. Microwave irradiation accelerates the oxidation of benzyl alcohols by ammonium hexanitratocerate(IV) supported on silica gel (Heravi et al., 2004).

Clay supported bis[trinitratocerium(IV)] chromate and tris[trinitratocerium(IV)] paraperiodate (on montmorillonite K-10 clay) have been used for the oxidative deprotection of tetrahydropyranyl ethers to the corresponding carbonyl compounds in dichloromethane (Heravi et al., 1999). The authors mention as advantages of the methodology the mild conditions, quite fast reaction times and good to high yields. Aghapoor et al. (2002) reported that for the cleavage of semicarbazones to the corresponding carbonyl compounds under solventless conditions (and with microwave irradiation) ammonium hexanitratocerate(IV) supported on wet alumina is a superior reagent in comparison with the same salt supported on montmorillonite K-10 clay or on silica gel.

There are only very few examples of polymer-supported cerium(IV) salts. Kanemoto et al. (1984) used ammonium hexanitratocerate(IV) impregnated in Nafion[®] as a catalyst for the oxidation of alcohols with *tert*-butylhydroxyperoxide. Nafion[®] is Dupont's brand name for a perfluorinated copolymer with sulfonate groups. This supported catalyst is also active for the oxidation of alcohols (Yamato and Shinoda, 2002) and of polyaromatic compounds (Yamato et

al., 2000) by sodium bromate. Poly(vinylpyridine) supported cerium(IV) nitrate has been used for the catalytic ring opening of epoxides (Tamani et al., 1993). This reagent can be considered as the solid analogue of pyridinium hexanitratocerate(IV). The pyridine group of the polymer becomes protonated under the reaction conditions used for the preparation of the reagent.

Hatanaka and coworkers prepared a CAN catalyst supported on activated charcoal (Hatanaka et al., 1983). The catalyst can be prepared by adding activated charcoal (3.0 g) to a solution of ammonium hexanitratocerate(IV) (0.82 g) in water (100 mL) with stirring. After 10 minutes, the solid compound is collected by filtration and dried in vacuo. The CAN-charcoal catalyst is effective for the oxidation of benzyl alcohols and acyloins to the corresponding carbonyl compounds.

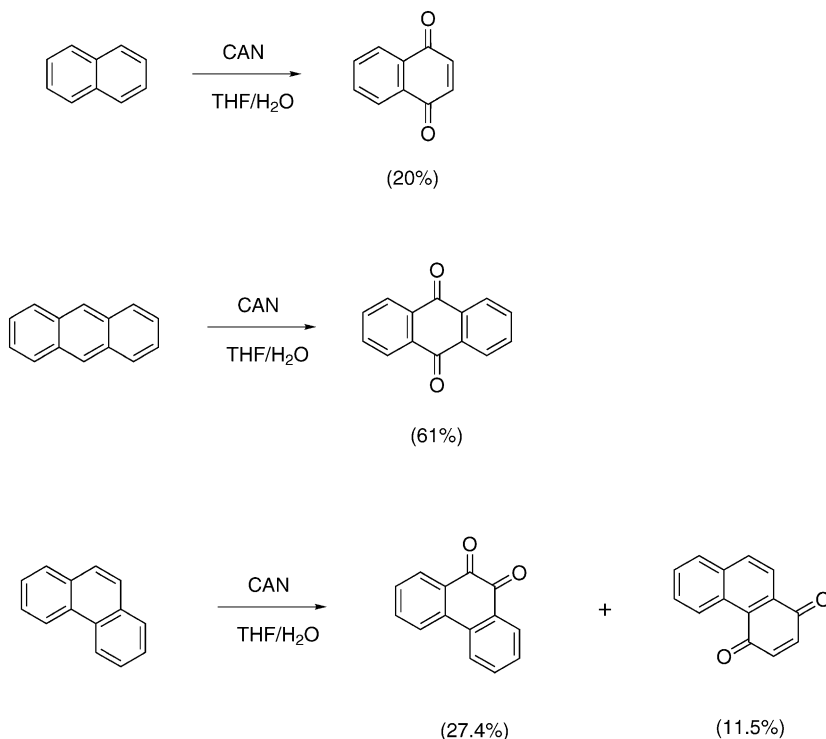
5.19. Other cerium(IV) compounds

Weakley-type polyoxometalate $\text{Na}_6\text{H}_2[\text{CeW}_{10}\text{O}_{36}]$ can be solubilized in apolar organic solvents by exchanging the counter ions for *N*-hexadecylpyridinium ions (Shiozaki et al., 1996). However, the corresponding compounds with tetraalkylammonium cations could not be obtained in acceptable purity. The reagent has been used for the oxidation of benzyl alcohols and secondary alcohols with hydrogen peroxide as oxidant. Ammonium decatungstocerate(IV), $(\text{NH}_4)_8[\text{CeW}_{10}\text{O}_{36}] \cdot 20\text{H}_2\text{O}$ can convert oxiranes into the corresponding thiiranes in the presence of ammonium thiocyanate and thiourea (Mirkhani et al., 2002). Cerium(IV) nitrates are not used as such, but cerium(III) nitrate hexahydrate, $\text{Ce}(\text{NO}_3)_3 \cdot 6\text{H}_2\text{O}$, is a precursor for electrochemically generated cerium(IV) at a rather low anodic potential (1.4 V) (Cho and Romero, 1995). Therefore it can be used for organic electrosynthesis in solvents like acetonitrile. Cerium(III) nitrate is also used for the generation of the active cerium(IV) species in the CerOx process (see section 11.5). Tetranitratobis(triphenylphosphine oxide)cerium(IV) can be synthesized by mixing a solution of ammonium hexanitratocerate(IV) in acetone with a solution of triphenylphosphine oxide in acetone (Mazhar-ul-Haque et al., 1971). Ammonium nitrate will precipitate in acetone, and the cerium(IV) complex can be recovered by removal of the solvent. Tetravalent cerium forms stable tetrakis complexes with β -diketonate ligands (Allard, 1976; Baxter et al., 1998; Binnemans, 2005), but these compounds have not yet found use as reagents in cerium-mediated organic reactions.

6. Stoichiometric cerium(IV)-mediated reactions

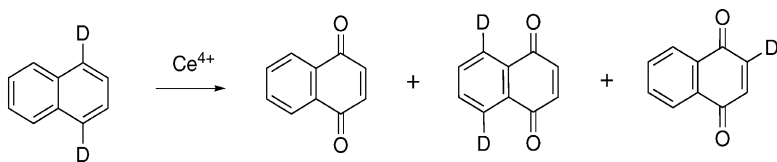
6.1. Oxidation of hydrocarbons

Polynuclear aromatic systems are oxidized to the corresponding quinones by ammonium hexanitratocerate(IV) in aqueous THF under mild conditions (25–60 °C) (scheme 1) (Ho et al., 1973). Water is the source of oxygen in the oxidation process. The yields are reasonable, but not very high, and the reaction is only useful for symmetric molecules like naphthalene and anthracene. Substituted and asymmetric substrates give often an intractable mixture of oxidation products (Balanikas et al., 1988). A problem associated with the use of ammonium hexanitratocerate(IV) is that nitration of the aromatic ring can also occur. Cerium(IV) ammonium

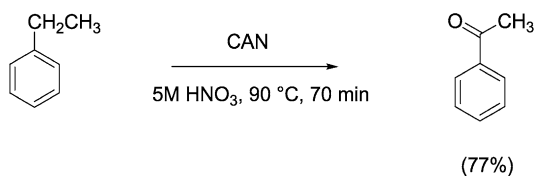
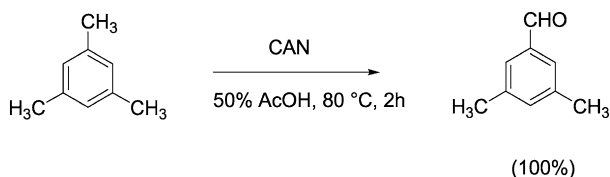


Scheme 1.

sulfate dissolved in a mixture of acetonitrile and 4 M aqueous sulfuric acid has been used as an alternative reaction medium for this reaction, leading to higher yields than with CAN in aqueous THF (Periasamy and Bhatt, 1977a). For instance, naphthoquinone could be obtained in 90 to 95% yield by this method. Six moles of cerium(IV) ammonium sulfate are required for the oxidation of one mole of naphthalene to 1,4-naphthoquinone. Kinetic experiments have shown that the initial step in the reaction is the formation of a 1 : 1 complex between cerium(IV) and naphthalene (Bhatt and Periasamy, 1993). This complex slowly decomposes to afford the naphthalene radical cation that is converted by fast further reaction steps into the 1,4-naphthoquinone. Periasamy and Bhatt observed a 1,2-shift in the oxidation of naphthalene and its derivatives (Periasamy and Bhatt, 1977b). For instance, the oxidation of deuterium-labeled naphthalene gave a mixture of three products (scheme 2). These results show that deuterium migrates to some extent from the 1- to the 2-position. Similar migration has been observed for phenyl or bromine substituents in oxidation of substituted naphthalenes. Later work has shown that this shift can arise from involvement of radical cations (Bhat et al., 1979; Bhatt and Periasamy, 1994). Rindone and Scolastico (1971) studied the reaction mechanism of the oxidation of anthracene by CAN in acetonitrile, methanol and acetic acid. The oxidation reaction occurs via an initial anthracene radical cation. The trinuclear aromatic compounds anthrone,



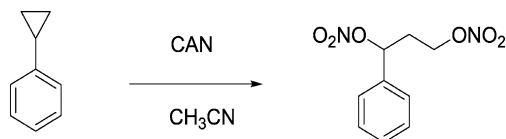
Scheme 2.



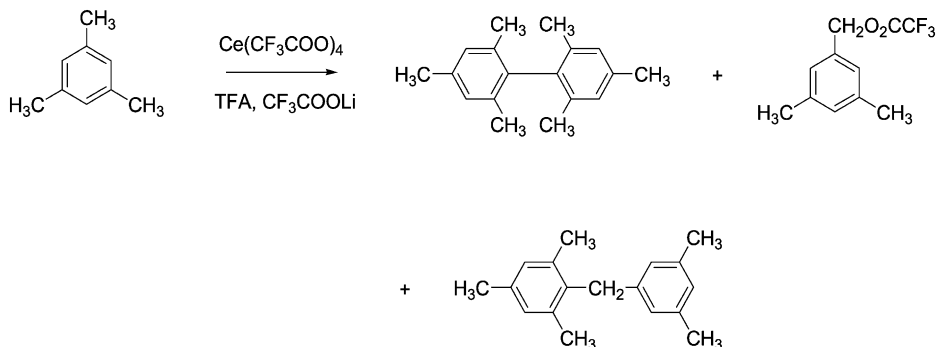
Scheme 3.

xanthen and thioxanthen were oxidized by CAN in methanol to anthraquinone, xanthone and thioxanthone, respectively (Rindone and Scolastico, 1975). Phenazine is oxidized in methanol to the corresponding mono-*N*-oxide. No reaction was observed for phenazine in acetic acid.

In an aqueous acidic medium (perchloric, nitric or acetic acid), ammonium hexanitratocerate(IV) readily oxidizes a single aromatic methyl group to an aldehyde group in very high yields (scheme 3) (Syper, 1966; Laing, 1968). Toluene is first oxidized to benzyl alcohol, and benzyl alcohol is further oxidized to benzaldehyde (Young and Trahanovsky, 1967). Dust and Gill (1970) report that the major primary reaction product of the oxidation of methylbenzenes by CAN in dilute nitric acid solution is a benzyl nitrate ester, which is subsequently hydrolyzed to the corresponding benzyl alcohol. Finally the benzyl alcohol is oxidized to the aldehyde. Reaction temperatures higher than 60 °C have to be avoided, because otherwise further oxidation of the aldehyde into the carboxylic acid occurs. The presence of electron-withdrawing groups (e.g. nitro or chloro groups) on the aromatic ring diminishes the yields. However, a second methyl group can be oxidized only under much more drastic reaction conditions. The benzylic CH₂ group of alkyl-substituted benzenes is oxidized to a ketone function (Syper, 1966). Methylbenzenes with a strongly electron-donating group like a methoxy, amino or hydroxy group tend to polymerize (Young and Trahanovsky, 1967). Tzedakis and Savall (1992) investigated the kinetics of the oxidation of 4-methoxytoluene to 4-methoxybenzaldehyde by cerium(IV) sulfate in aqueous sulfuric



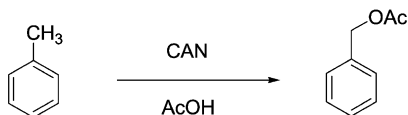
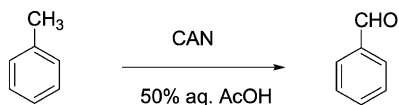
Scheme 4.



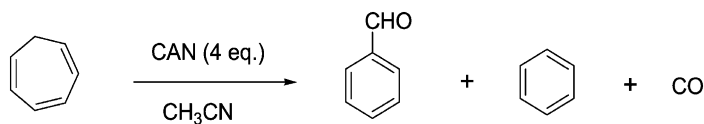
Scheme 5.

acid. Naphthalenes with a methyl group in the 1-position are oxidized to the corresponding naphthaldehydes by CAN in aqueous acetic acid at 80 °C (Sydnes et al., 1985). Arylcyclopropanes are cleaved by CAN to dinitrates in acetonitrile and to a mixture of dinitrates and nitrate acetates in acetic acid as solvent (Young, 1968). The major product of the reaction of cyclopropylbenzene with CAN in acetonitrile or in acetonitrile/methanol mixed solvents is 1-phenylpropane-1,3-diylnitrate (scheme 4) (Wang and Tanko, 1998). Cerium(IV) trifluoroacetate dissolved in trifluoroacetic acid containing lithium trifluoroacetate oxidizes mesitylene to a mixture of products (scheme 5) (Norman et al., 1973). Also other electron-rich aromatic hydrocarbons react under these conditions, but benzene is unreactive. Cerium(IV) triflate has been proposed as an alternative to ammonium hexanitratocerate(IV) for the oxidation of alkylbenzenes under very mild conditions (Imamoto et al., 1990). The choice of the solvent is an important parameter controlling the reactivity of alkylbenzenes in presence of cerium(IV) salts (scheme 6). In general, carbonyl compounds are obtained in acidic aqueous medium. However, benzylic acetates are formed in glacial acetic acid (Bacocchi et al., 1986; Trahanovsky and Young, 1966), and ethers in alcoholic solvents (Della Cort et al., 1983). Nitrates are formed by reaction of methylbenzenes with CAN in acetonitrile under photolytic conditions (Bacocchi et al., 1984a). In the absence of solvent, toluene is oxidized by CAN to benzaldehyde, but *ortho*-xylene gives 2-methylbenzyl nitrate.

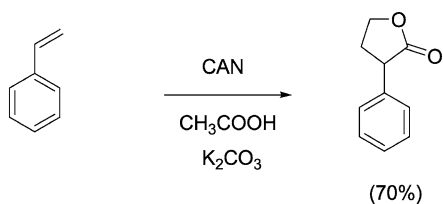
1,3,5-Cycloheptatriene is rapidly oxidized at 90 °C by 4 equivalents of ammonium hexanitratocerate(IV) in aqueous acetic acid to a mixture of benzaldehyde, benzene and carbon monoxide (scheme 7) (Trahanovsky et al., 1969d). The reaction works also in other solvents like acetonitrile and water. There is evidence that the tropylium ion is an intermediate in this



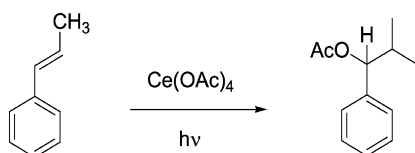
Scheme 6.



Scheme 7.



Scheme 8.



Scheme 9.

reaction. In anhydrous acetonitrile, the oxygen of the benzaldehyde produced comes from the nitrate ion of ammonium hexanitratocerate(IV).

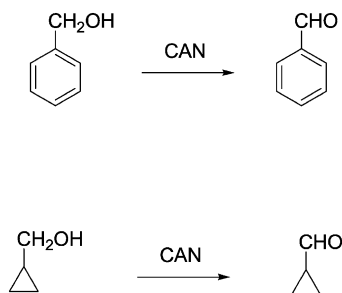
The reaction of styrene with cerium(IV) acetate in glacial acetic acid containing 10% potassium acetate at 110 °C for 20 hours gives a lactone (scheme 8) (Heiba and Dessau, 1971). The reaction works with ammonium hexanitratocerate(IV) as well. The photochemical reaction of *trans*- β -methylstyrene gives an ester as the major product (scheme 9).

6.2. Oxidation of alcohols and phenols

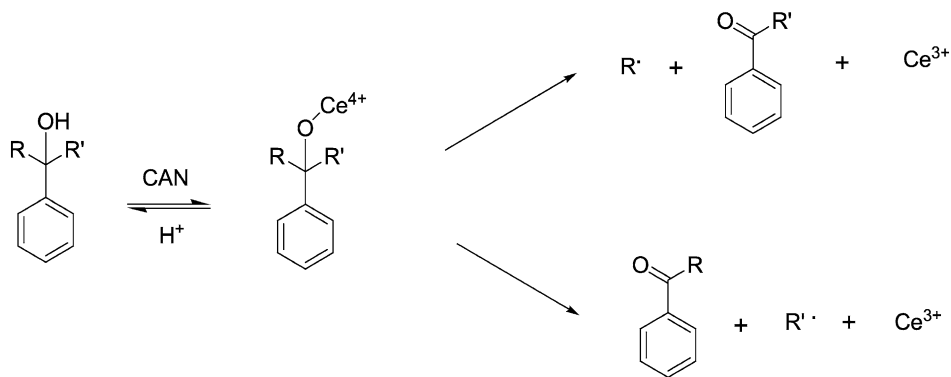
Depending on the structure of the alcohol, different types of reaction products can be formed by the reaction between an alcohol and a cerium(IV) salt (Ho, 1973; Trahanovsky, 1973). The alcohol can undergo direct oxidation, fragmentation or a combination of both processes. Benzyl alcohols and hydroxymethylcyclopropanol are oxidized in high yields to the corresponding aldehydes (scheme 10) (Trahanovsky et al., 1967; Young and Trahanovsky, 1969). These reactions are good synthetic routes for the preparation of these aldehydes, because the aldehydes are less easily oxidized by cerium(IV) than the alcohols. The fact that benzyl alcohols and hydroxymethylpropanol do not undergo oxidative cleavage can be rationalized by the low stability of the phenyl and cyclopropyl radicals. The presence of stable carbon radicals is indeed a condition for oxidative cleavage to occur.

Oxidation of benzyl alcohols is generally performed with ammonium hexanitratocerate(IV) (2.1. equivalents) in water or in aqueous acetic acid. Primary alcohols are in general resistant to oxidation by cerium(IV) reagents, although cyclic ethers can be formed (see below). Ethanol can be oxidized to acetaldehyde and acetic acid (Briois et al., 2005). Secondary alcohols are oxidized to the corresponding ketones (although slower than benzylic alcohols). Tertiary alcohols are fragmented by oxidative cleavage to give ketones with the formation of radicals (scheme 11) (Trahanovsky and Macaulay, 1973). Vicinal diols (1,2-diols) undergo oxidative cleavage (Trahanovsky et al., 1969c; Hintz and Johnson, 1967). Duke and coworkers showed that this oxidation takes place via the disproportionation of a coordination complex formed between the 1,2-diol and cerium(IV) (Duke and Forist, 1949; Duke and Bremer, 1951). The mechanism involves probably the formation of a monodentate cerium(IV) complex, followed by a one electron-cleavage to form an intermediate radical (Trahanovsky et al., 1973) which can be trapped by addition of acrylamide (Trahanovsky et al., 1969c). Mino and coworkers studied the oxidation of 2,3-dimethylbutane-2,3-diol (pinacol) to acetone by cerium(IV) sulfate in water (Mino et al., 1959).

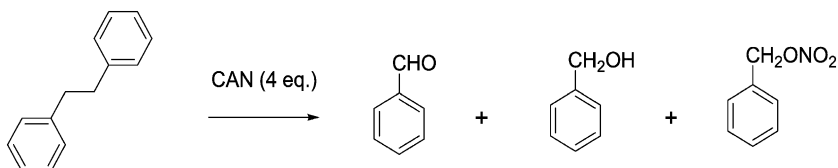
1,2-Diarylethanols give only products of oxidative cleavage (Nave and Trahanovsky, 1968, 1971; Trahanovsky and Brixius, 1973). For instance, 1,2-diphenylethanol is oxidized by 4 equivalents of CAN to a mixture of benzylaldehyde, benzyl alcohol and benzyl nitrate (scheme 12) (Trahanovsky and Brixius, 1973). A radical cation intermediate is involved.



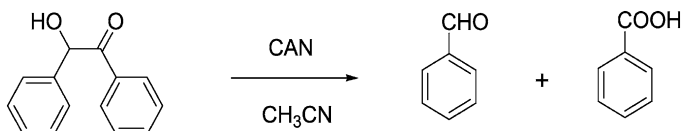
Scheme 10.



Scheme 11.



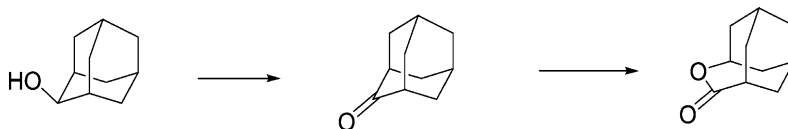
Scheme 12.



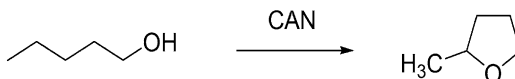
Scheme 13.

Phenylarylmethanols are transformed by cerium(IV) into a mixture of benzaldehyde and an alkyl phenyl ketone (Trahanovsky and Cramer, 1971). The ratio of the yield of benzaldehyde to the yield of ketone depends largely on the alkyl group. Ketone formation is predominant for methylphenylmethanol, whereas *iso*-propylmethanol and *tert*-butylmethanol undergo mainly oxidative cleavage. For ethylphenylketone, oxidative cleavage and ketone formation are of equal importance. These results can be explained by the high stability of the *iso*-propyl and *tert*-butyl free radicals. Benzoin is split by ammonium hexanitratocerate(IV) into an aryl aldehyde and an aryl radical. The radical is oxidized further to an arenecarboxylic acid (Ho, 1972). For instance benzoin itself is split into benzaldehyde and benzoic acid (scheme 13).

Cyclopropanol (Schaafsma et al., 1966) and cyclobutanol (Meyer and Roček, 1972) undergo rapid oxidative cleavage, due to the release of the strain energy of the aliphatic ring. Chain opening is a typical reaction of strained cycloalkanols in presence of one-electron oxidants. A mixture of reaction products is formed, and the actual composition of the reaction



Scheme 14.

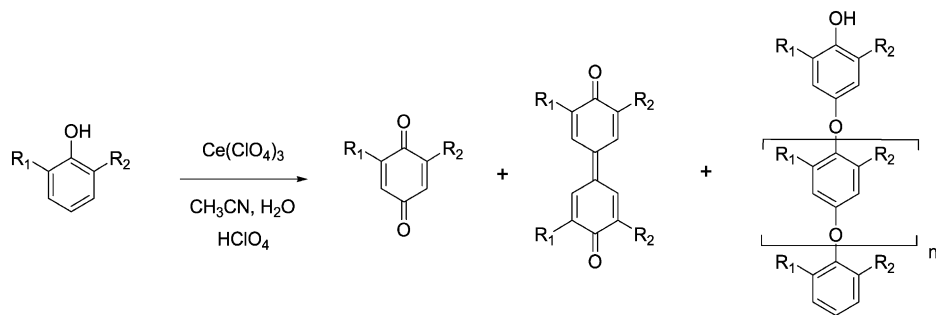


Scheme 15.

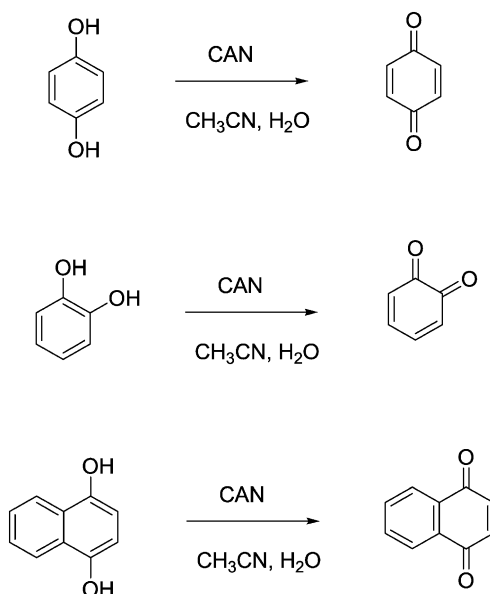
mixture depends on the reaction conditions, which can be optimized in order to obtain one major component. For instance, succinaldehyde is the only product observed upon oxidation of cyclobutanol with ammonium hexanitratocerate(IV) in acetonitrile in presence of molecular oxygen (Meyer and Roček, 1972). Cyclopentanol and cyclohexanol are oxidized by cerium(IV) sulfate to cyclopentanone, resp. cyclohexanone (Hintz and Johnson, 1967). Although adamantan-2-ol is initially oxidized by ammonium hexanitratocerate(IV) to adamantanone, it is subsequently transformed into a lactone by a Baeyer–Villiger oxidation reaction (scheme 14) (Soucy et al., 1972). The main reaction for bicyclic alcohols like bicyclo[2.2.1]-2-heptanol and bicyclo[2.2.2]-2-octanol is oxidative cleavage (Trahanovsky et al., 1969b).

Certain primary alcohols that possess a δ -hydrogen undergo an intramolecular cyclization into a tetrahydrofuran derivative via alkoxy δ -hydrogen abstraction and subsequent ring closure. For instance, *n*-pentanol reacts with ammonium hexanitratocerate(IV) to afford 2-methyltetrahydrofuran (scheme 15) (Trahanovsky et al., 1969a). This reaction has been further investigated by Doyle and coworkers (Doyle et al., 1975), who were also able to oxidize 5-phenyl-1-pentanol and 4-phenyl-1-butanol into 2-benzyltetrahydrofuran and 2-phenyltetrahydrofuran, respectively.

Simple phenols undergo oxidation and oxidative coupling reactions in presence of cerium(IV) salts (scheme 16). 2,6-dimethylphenols are oxidized to 4,4'-diphenoquinone and 1,4-benzoquinone derivatives by cerium(IV) perchlorate in aqueous or aqueous-acetonitrile solutions of perchloric acid at room temperature (Ignaczak and Dziegieć, 1992). The oxidation of 2,6-diisopropylphenol, 2-*tert*-butyl-6-methylphenol, 2,6-diphenylphenol and 2,6-dichlorophenol proceeds under the same experimental conditions to the corresponding 4,4'-diphenoquinones and oligomeric poly(1,4-phenylene) oxides (Domagała et al., 1998). 2,6-difluorophenol and 2,3,5,6-tetrafluorophenol give a high yield of the poly(1,4-phenylene) oxides (Prawicki and Dziegieć, 1996; Grzejdzia and Dziegieć, 1997), whereas 2,6-di-*tert*-butylphenol gives a high yield of the 4,4'-diphenoquinone (Ignaczak and Dziegieć, 1992). These differences in reactivity can be attributed to the stabilization of cation radicals in acidic phenols (those with fluoro or chloro substituents) or radicals (in phenols with branched alkyl groups).



Scheme 16.



Scheme 17.

6.3. Oxidation of hydroquinones and catechols

Hydroquinones (1,4-dihydroxybenzenes) and catechols (1,2-dihydroxybenzenes) are easily oxidized by ammonium hexanitratocerate(IV) to quinones (scheme 17) (Ho et al., 1972; Ho, 1973). However, the reaction conditions are critical, since it is not easy to avoid over-oxidation and the formation of side-products. The reactivity of ammonium hexanitratocerate(IV) can be reduced by coating the salt on silica gel (Fischer and Henderson, 1985), or by using the dual oxidant system CAN-NaBrO₃ (Ho, 1979). Brockhaus (1968) reported on the oxidation of catechol to *ortho*-benzoquinone by cerium(IV) sulfate in a chloroform/sulfuric acid biphasic

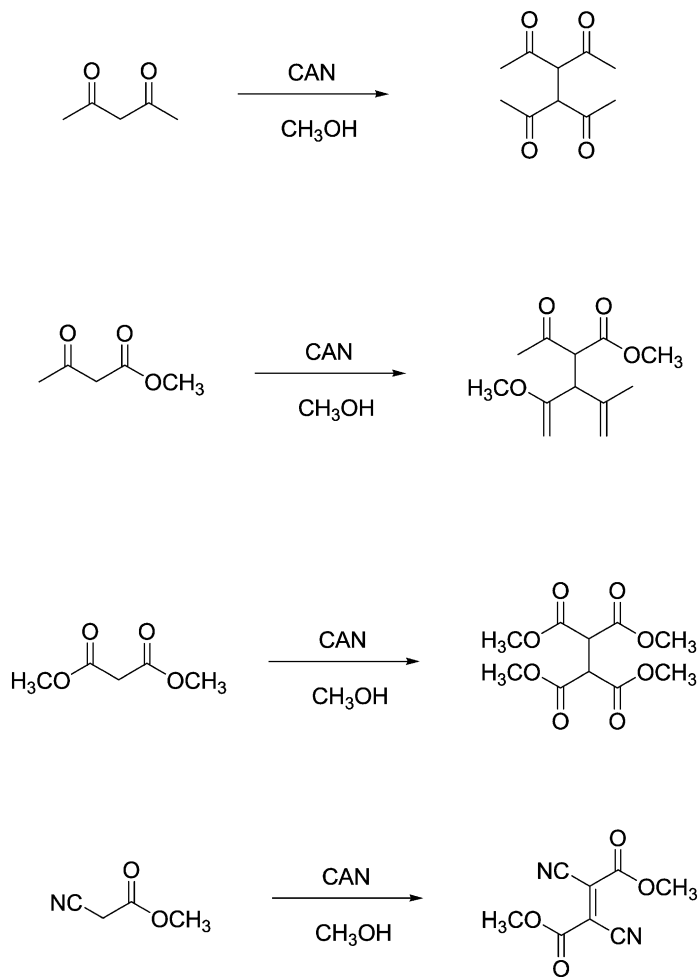
system. The oxidation of hydroquinones by ammonium hexanitratocerate(IV) can also be carried out in the solid state by grinding the substrate and cerium(IV) salt together with pestle and mortar, followed by keeping the mixture for several days in a closed vial (Morey and Saá, 1993). The oxidation reaction was found to be not very dependent on temperature, but it could be appreciably accelerated by ultrasonic irradiation or by shaking the reaction mixture. Brown-red vapors of nitrogen dioxide gas are formed during the reaction, which acts as a gaseous oxidant. Therefore, the best results for the oxidation of hydroquinones to quinones were obtained by keeping the reaction mixture in closed vials. In open vessels, or when the solid reaction mixture was flushed with a gentle stream of argon to remove nitrogen dioxide, only low reaction yields were obtained, even in presence of an excess of CAN. Catalytic amounts of CAN were sufficient when potassium bromate was used as a second solid oxidant. No reaction was observed with potassium chlorate or potassium iodate as the second oxidant, and potassium bromate alone cannot oxidize the hydroquinones.

6.4. Oxidation of carbonyl compounds

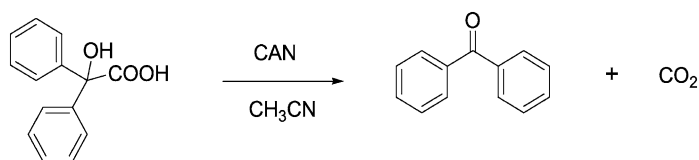
Polycyclic ketones undergo Baeyer–Villiger oxidation with ammonium hexanitratocerate(IV) or cerium(IV) ammonium sulfate to afford lactones (Soucy et al., 1972; Mehta et al., 1976). The Baeyer–Villiger oxidation of adamantanone to the corresponding lactone is shown above in scheme 14. Camphorquinone is oxidized to a complex mixture of oxidation products (Danieli and Palmisano, 1976). Simple aliphatic ketones are not oxidized by cerium(IV) in the absence of a catalyst. In presence of ruthenium(III) chloride, cerium(IV) sulfate oxidizes 2-butanone to acetic acid and formic acid, and 3-pentanone to a mixture of propionic acid, acetic acid and formic acid (Singh et al., 1980).

β -dicarbonyl and β -cyanocarbonyl compounds undergo oxidative dimerization in presence of ammonium hexanitratocerate(IV) (scheme 18) (Cho and Romero, 1995). For instance, 2,4-pentanedione is dimerized in methanol into 1,1,2,2-ethane tetraacetyl. The reaction can also be carried out by cerium(IV)-mediated electrosynthesis.

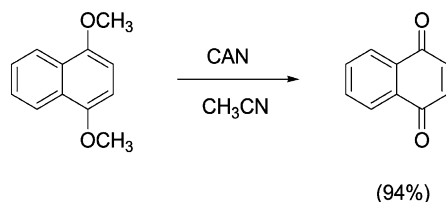
Oxalic and malonic acids, as well as α -hydroxy acids, easily react with cerium(IV) salts (Sheldon and Kochi, 1968). Simple alkanolic acids are much more resistant to attack by cerium(IV) salts. However, silver(I) salts catalyze the thermal decarboxylation of alkanolic acids by ammonium hexanitratocerate(IV) (Nagori et al., 1981). Cerium(IV) carboxylates can be decomposed by either a thermal or a photochemical reaction (Sheldon and Kochi, 1968). Alkyl radicals are released by the decarboxylation reaction, which yields alkanes, alkenes, esters and carbon dioxide. The oxidation of substituted benzoic acids by cerium(IV) salts affords the corresponding benzoic acids in quantitative yield (scheme 19) (Hanna and Sarac, 1977). Trahanovsky and coworkers reported that phenylacetic acid is decarboxylated by reaction with ammonium hexanitratocerate(IV) in aqueous acetonitrile containing nitric acid (Trahanovsky et al., 1974). The reaction products are benzyl alcohol, benzaldehyde, benzyl nitrate and carbon dioxide. The reaction is also applicable to substituted phenylacetic acids. The decarboxylation is a one-electron process and radicals are formed as intermediates. The rate-determining step is the decomposition of the phenylacetic acid/cerium(IV) complex into a benzyl radical and carbon dioxide.



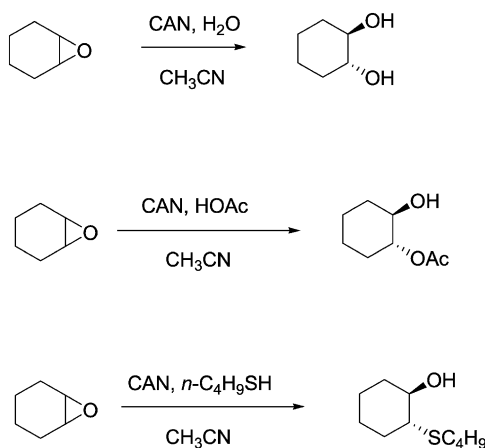
Scheme 18.



Scheme 19.



Scheme 20.



Scheme 21.

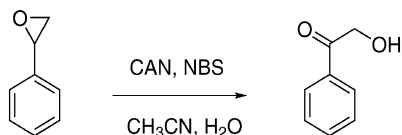
6.5. Ethers and epoxides

Hydroquinones dimethyl ethers undergo oxidative demethylation with ammonium hexanitratocerate(IV) to afford quinones (scheme 20) (Jacob et al., 1976). The reaction is fast in acetonitrile, even at room temperature. However, dimerization is a competitive side reaction for some substrates.

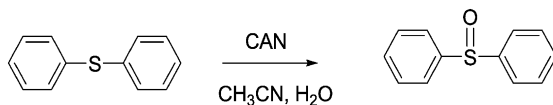
Ammonium hexanitratocerate(IV) can be used as a catalyst for the ring opening of epoxides in presence of water, thiols or acetic acid (scheme 21) (Iranpoor et al., 1991). Epoxides react in presence of an excess of nitrate ions and a catalytic amount of ammonium hexanitratocerate(IV) in acetonitrile to β -nitrate alcohols (Iranpoor and Salehi, 1995). A combination of ammonium hexanitratocerate(IV) and *N*-bromosuccinimide (NBS) transforms epoxides into α -hydroxy ketones (scheme 22) (Surendra et al., 2005). Aziridines give α -aminoketones under the same conditions.

6.6. Sulfur-containing compounds

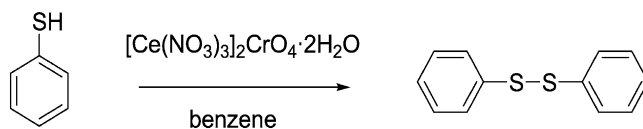
Diarylsulfides are oxidized in high yield by ammonium hexanitratocerate(IV) to the corresponding sulfoxides, without over-oxidation to sulfones (scheme 23) (Ho and Wong, 1972).



Scheme 22.



Scheme 23.

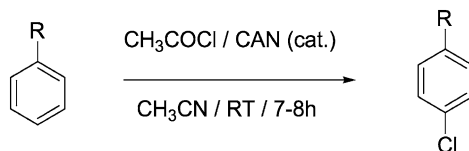


Scheme 24.

The reaction is generally carried out in aqueous acetonitrile at room temperature, and is complete within a few minutes. However, the synthetic method is not suitable for the oxidation of dialkyl sulfides containing α -hydrogen atoms, probably due to a Pummerer-type rearrangement of the resulting sulfoxides. Dialkylsulfides can be oxidized to the sulfoxides by CAN under phase transfer conditions (Bacocchi et al., 1988a). Thiols can be selectively oxidized to disulfides by dinitratocerium(IV) chromate dihydrate, $[\text{Ce}(\text{NO}_3)_3]_2\text{CrO}_4 \cdot 2\text{H}_2\text{O}$, in benzene (scheme 24) (Firouzabadi et al., 1984c). Aldehydes react with one equivalent of ethanedithiol and a catalytic amount of CAN in chloroform to 1,3-dithiolanes (Mandal and Roy, 1995). This thioacetalization can be used to protect an aldehyde function.

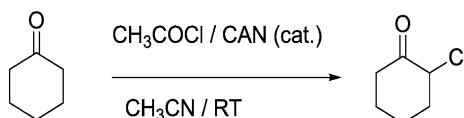
6.7. Halogenation reactions

Cerium(IV) fluoride is suitable for the fluorination of benzene (Hudson et al., 1969). The reaction was carried out by passing benzene vapor over heated cerium(IV) fluoride at temperatures between 250 °C and 480 °C. Below 400 °C little fluorination takes place, but above 410 °C the reaction rate increases rapidly. The reaction leads to a mixture of fluorinated compounds. For instance, the following products were isolated from the reaction mixture after fluorination at 480 °C: fluorobenzene, 1,3-difluorobenzene, 1,4-difluorobenzene, 1,2,4-trifluorobenzene, 1,2,4,5-tetrafluorobenzene, 1,2,3,4-tetrafluorobenzene and different fluorinated cyclohexenes and cyclohexadienes. Benzotrifluoride (trifluoromethylbenzene) was also fluorinated by the same procedure (Hudson and Pedler, 1970). Asovich et al. (1994) describe the use of cerium(IV) fluoride for the fluorination of ethylene. The extent of fluorination depends on the temperature; the higher the temperature, the more fluorine atoms are bound to the ethylene molecule. The composition of the mixture formed by reaction between ethylene



R = activating group

Scheme 25.



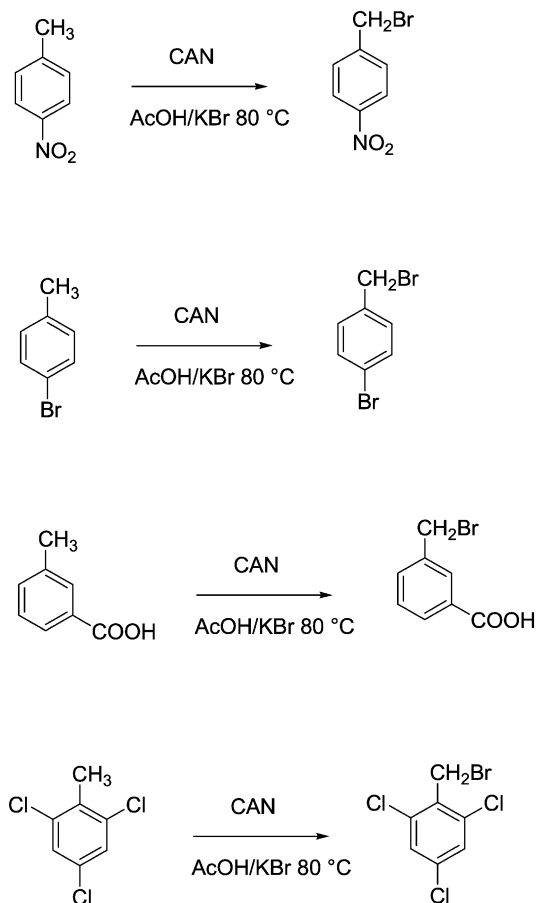
Scheme 26.

and CeF_4 at 370°C is $\text{CF}_2\text{HCH}_2\text{F}$ (1%), $\text{CF}_3\text{CH}_2\text{F}$ (9%), CF_2HCF_3 (1%) and $\text{CF}_2\text{HCF}_2\text{H}$ (89%). No formation of hexafluoroethane was observed.

Acetyl chloride in presence of a catalytic amount of ammonium hexanitratocerate(IV) efficiently chlorinates activated aromatic compounds at room temperature (scheme 25) (Roy et al., 2003a), while deactivated aromatic compounds do not react. The same reagent can be used for the α -chlorination of ketones (scheme 26) (Roy et al., 2003b), but only monochlorination takes place, even in presence of a large excess of acetyl chloride.

Treatment of methylbenzenes containing electron-withdrawing substituents (COOH , NO_2 , Br) with ammonium hexanitratocerate(IV) in a mixture of acetic acid and potassium bromide at 80°C allows bromination of the methyl group (Bacocchi et al., 1984b) (scheme 27). Benzyl bromides were also prepared by reaction of *para*-substituted toluenes with ammonium hexanitratocerate(IV) in aqueous solutions containing trifluoroacetic acid and sodium bromide (Maknon'kov et al., 1986).

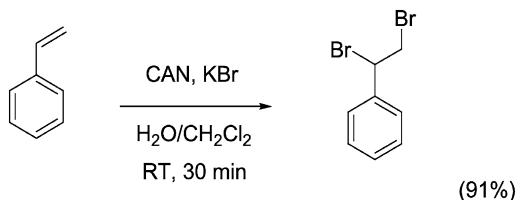
Nair et al. (2001) describe the bromination of alkenes using a mixture of ammonium hexanitratocerate(IV) and potassium bromide in a two-phase system consisting of water and dichloromethane. For instance, styrene is transformed by this reaction system in excellent yield at room temperature into 1,2-dibromo-phenyl ethane (scheme 28). It is assumed that the bromide ion is first oxidized by CAN to the bromine radical, which subsequently undergoes addition to the double bond to produce a benzylic radical. Trapping of another bromine radical results in the formation of the 1,2-dibromide. The method is not only applicable to substituted styrenes, but also to alkenes and α,β -unsubstituted carbonyl compounds. However, the choice of the solvent is of prime importance: the reaction only occurs in the water/dichloromethane two-phase system. In other solvents, like aqueous solutions of methanol or acetonitrile, a variety of products such as phenacyl bromides and nitratobromides are formed (scheme 29). The nitro bromides are formed exclusively when the reaction is carried out in a deoxygenated atmosphere. In the two-phase system water/dichloromethane, side reactions are avoided be-



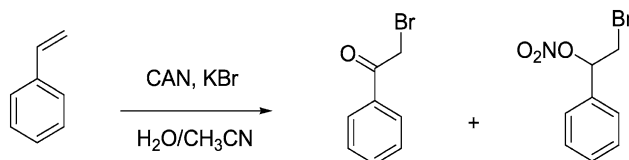
Scheme 27.

cause the bromine radicals and the alkene are mainly in the organic phase, whereas the cerium(IV) salt remains in the aqueous phase. 1,3-Dibromides can be synthesized by the reaction of cyclopropanes with ammonium hexanitratocerate(IV) and potassium bromide in the water/dichloromethane two-phase system (Nair et al., 2003).

The aromatic ring of electron-rich aromatics can be brominated by a system composed of lithium bromide as the bromine source and ammonium(IV) hexanitratocerate as the oxidant, and with acetonitrile as solvent (scheme 30) (Roy et al., 2001a). The electrophilic Br^+ is generated *in situ* by reaction between lithium bromide and CAN. The reaction is regioselective in the sense that the *para*-isomer is preferentially formed. Aromatic amines like aniline and *para*-toluidine did not show reaction under the given conditions. Naphthalene could be transformed in very high yield to 1-bromo-naphthalene. Roy and coworkers reported that *trans*- α,β -unsaturated aromatic acids undergo oxidative halodecarboxylation in presence of a



Scheme 28.



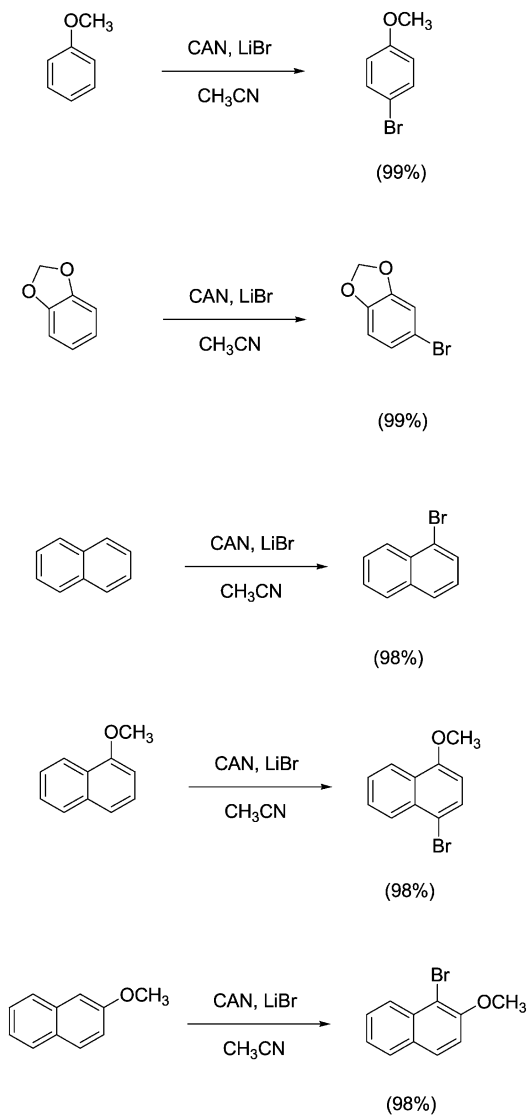
Scheme 29.

mixture of lithium bromide (or lithium chloride) and ammonium hexanitratocerate(IV) (Roy et al., 2001b). In aqueous acetonitrile, the reaction transforms *trans*- α,β -unsaturated aromatic acids into *trans*- β -halo styrenes (vinyl halides) (scheme 31). The solvent was an aqueous acetonitrile solution. The reaction yield increases with increasing water content, the maximum yield being obtained for a 10 : 1 acetonitrile:water mixture.

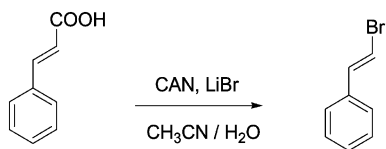
Sugiyama (1981) suggested ammonium hexanitratocerate(IV) as a reagent for the iodination of polymethylbenzenes, polymethoxybenzenes and naphthalene with tetrabutylammonium iodide, alkali iodides (LiI, NaI, KI) and molecular iodine as iodinating reagents (schemes 32 and 33). Ammonium hexanitratocerate(IV) was needed in stoichiometric amounts for the iodination with tetrabutylammonium iodide or alkali iodides, whereas catalytic amounts were sufficient in the case of iodination with molecular iodine.

The regioselective synthesis of α -iodo ketones is achieved in good yields by CAN in presence of iodine. The more highly substituted α -iodo ketones are preferentially formed (scheme 34) (Horiuchi and Kiji, 1988). In a study of the iodination of 1,3,5-trimethylbenzene (mesitylene) and 1,2,3,4,5-tetramethylbenzene (durene) by CAN/I₂, it was shown that the reactive intermediate is most likely the I⁺ ion and that the reaction can be considered as an electrophilic aromatic substitution reaction (Galli, 1991).

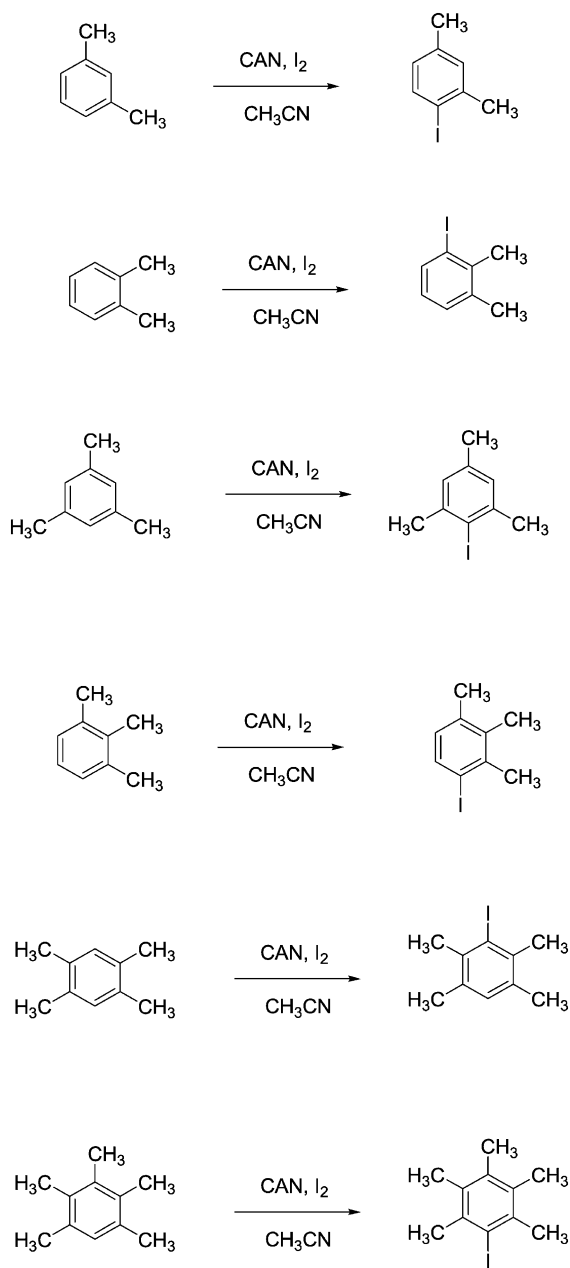
Asakura and Robins described a mild procedure for the regioselective halogenation of uracil derivatives at the C-5 position with ammonium hexanitratocerate(IV) and elemental iodine, lithium halides or hydrochloric acid (scheme 35) (Asakura and Robins, 1988, 1990). The solvent for this type of reactions is methanol or acetonitrile. The reaction is very useful for the conversion of (protected) uracil nucleosides into (protected) 5-halouracil nucleosides. 4-Iodopyrazoles can be prepared by iodination of *N*-H and *N*-benzylpyrazoles with elemental iodine in presence of ammonium hexanitratocerate(IV) (scheme 36) (Rodriguez-Franco et al., 2001). The reaction works well, even with electron-withdrawing groups. Firouzabadi and coworkers reported that micellar solutions of sodium dodecyl sulfate catalyze the regio-



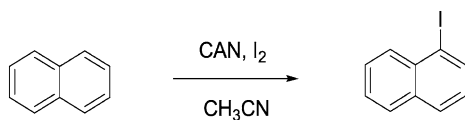
Scheme 30.



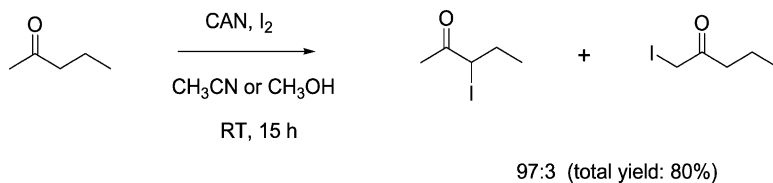
Scheme 31.



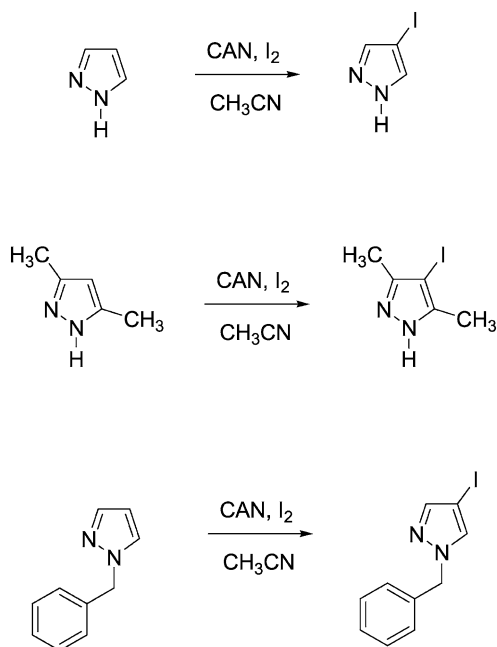
Scheme 32.



Scheme 33.

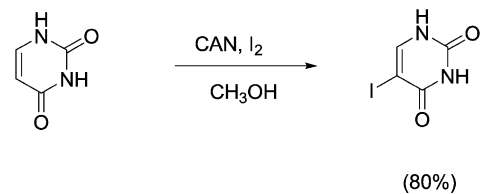
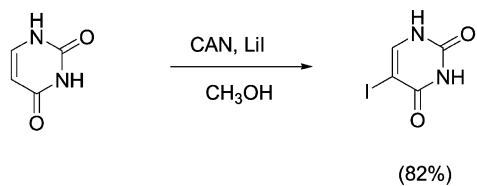
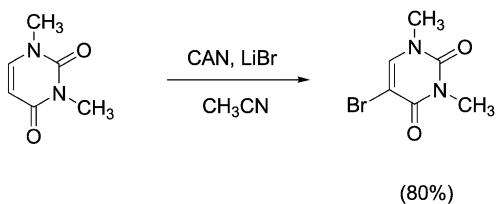
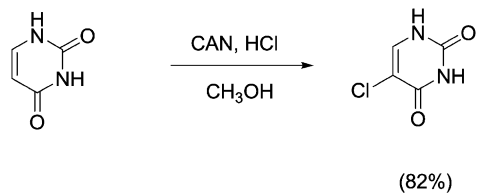
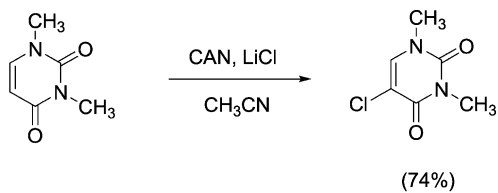


Scheme 34.

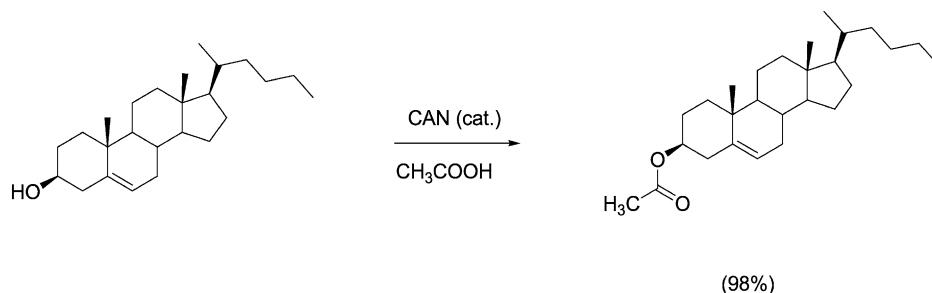


Scheme 35.

elective iodination of aromatic compounds with sodium iodide in presence of cerium(IV) trihydroxy hydroperoxide at room temperature (Firouzabadi et al., 2005). For instance, anisole could be transformed into 4-iodoanisole in 97% yield. In general, monosubstituted benzenes, 1,2-disubstituted benzenes and 1,3-disubstituted benzenes are regioselectively iodinated in the 4-position. Naphthalene was transformed into 1-iodonaphthalene. The presence of the mi-



Scheme 36.



Scheme 37.

celles is essential as shown by very low yields in acetonitrile or in dichloromethane only. It is proposed that within the micelles the reactants are in closer contact than in the bulk solvent phase.

Benzene and monosubstituted benzene derivatives could be radiolabeled with iodide-131 by reaction of the substrate with iodine-131 in presence of cerium(IV) triflate (Mennicke et al., 2000). The reaction was carried out in trifluoroacetic acid as solvent. Cerium(IV) is however not soluble in this solvent.

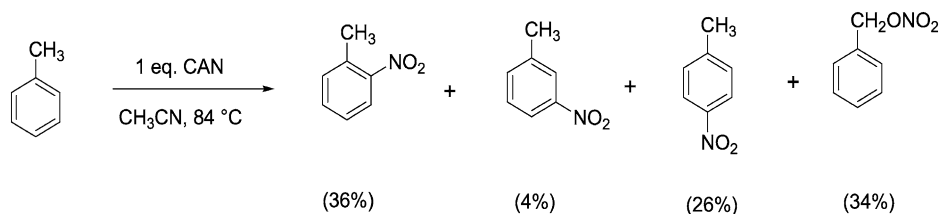
6.8. Esterification reactions

Ammonium hexanitratocerate(IV) is an efficient catalyst for fast esterification of carboxylic acids and alcohols under mild conditions (Goswami and Chowdhury, 2000). The reaction can be carried out under solventless conditions, or in chloroform. The reaction works with primary and secondary alcohols, and with aliphatic carboxylic acids. No reaction was observed for tertiary alcohols or for aromatic acids. The method is of interest because it is also applicable to the esterification of alcohols based on steroids and on other natural products (scheme 37). Pan and coworkers described the esterification of phenylacetic acids and *cis*-oleic acid with simple primary and secondary alcohols in presence of an excess of CAN at room temperature (Pan et al., 2003). The alcohol acted as solvent. Ammonium hexanitratocerate(IV) does catalyze not only the esterification of carboxylic acid, but also the transesterification with another alcohol (Stefane et al., 2002).

6.9. Nitration

Aromatic nitration or nitration in the benzylic position are often side reactions of oxidation reactions with ammonium hexanitratocerate(IV). In fact these unwanted reactions are one of the main drives to develop cerium(IV) reagents other than ammonium hexanitratocerate(IV). However, in some cases ammonium hexanitratocerate(IV) can be turned into a useful nitration reagent. A major parameter that governs the chemoselectivity of CAN is the solvent.

Benzene, alkylbenzenes and phenolic ethers react with CAN in acetonitrile to give nitration of the aromatic ring and, if α -hydrogen atoms are present, also products of side-chain substitution (Dinçtürk and Ridd, 1982a, 1982b). With many substrates, for instance with toluene,

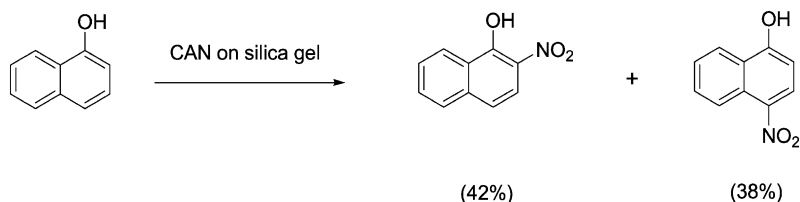


Scheme 38.

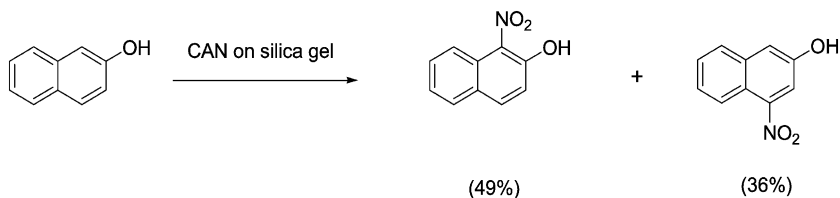
benzyl nitrates are formed by the side-chain reaction, while in other cases, for instance with ethylbenzene, an amide is formed (Dinçtürk and Ridd, 1982a). The side-chain substitution seems to occur through the intermediate formation of an aromatic radical cation, while the nitronium ion is involved in the nitration of the aromatic ring. Addition of water to acetonitrile suppresses the nitration of the aromatic ring, but not the side-chain substitution (Dinçtürk and Ridd, 1982b). No nitration of the aromatic ring occurs when the solvent is acetic acid. The product distribution of the reaction of toluene with CAN in acetonitrile is shown in scheme 38. Whereas the reactivities relative to benzene for nitration by ammonium hexanitratocerate(IV) in acetonitrile are very similar to those for nitration by nitric acid in acetonitrile, a large discrepancy is observed for anisole. Anisole reacts 298 times faster than benzene with HNO_3 , but it reacts 4899 times faster than benzene with CAN. Another difference is the product composition: with CAN 36.5% of the *ortho*-isomer and 63.5% of the *para*-isomer is formed, whereas with HNO_3 65.9% of the product mixture consists of the *ortho*-isomer and 34.1% of the *para*-isomer. It was assumed that these differences arose from the fact that anisole interacts more strongly with CAN at the time that the nitronium ion is formed. However, the detailed mechanism is not known yet. Benzyl nitrates are obtained in high yield by the photochemical reaction between CAN and methylbenzenes in acetonitrile (Baciocchi et al., 1984a).

Mononitration of 1-hydroxynaphthalene could be obtained by use of ammonium hexanitratocerate(IV) supported on silica gel in acetonitrile (Chawla and Mittal, 1985) (scheme 39). The same reaction with CAN in acetic acid give the 2,4- and 4,6-dinitro derivatives. By the same method, 2-hydroxynaphthalene is converted into 1-nitro-2-hydroxynaphthalene and 4-nitro-2-hydroxynaphthalene (scheme 40). The 1-alkoxynaphthalenes can be mononitrated regioselectively in the 4-position (scheme 41). The lower reactivity of CAN supported on silica gel is also evident from the fact that naphthalene derivatives are not oxidized into 1,4-naphthoquinones. The authors noticed that no reaction could be observed when ammonium hexanitratocerate(IV) was replaced by a mixture of ammonium nitrate and ammonium cerium(IV) nitrate. Silica supported CAN has also been used for the nitration of methoxybenzenes (Grenier et al., 1999) and less electron rich aromatic compounds like benzene, toluene, chlorobenzene and bromobenzene (Mellor et al., 2000) (scheme 42). For the less electron rich aromatics, dichloromethane is used as solvent instead of acetonitrile. In most cases, the yields are good to excellent.

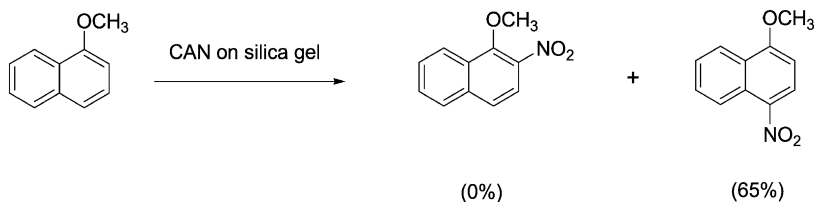
Mellor et al. (1997, 2000) found that when well-dried CAN supported on silica gel, sulfuric acid supported on silica gel, and naphthalene were stirred at room temperature in dichloromethane in presence of tetrabutylammonium nitrite, 1-nitronaphthalene was rapidly



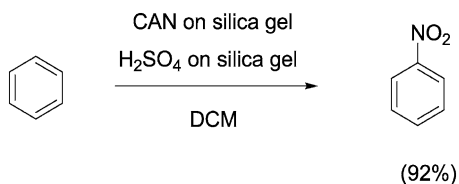
Scheme 39.



Scheme 40.

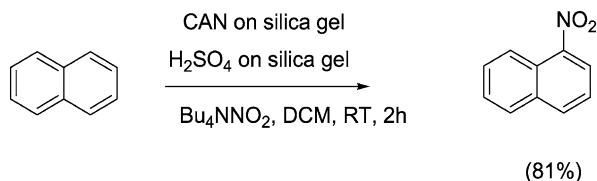


Scheme 41.

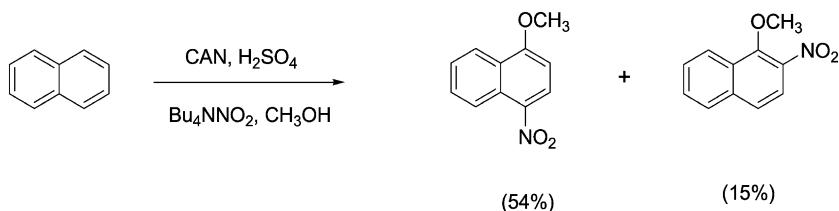


Scheme 42.

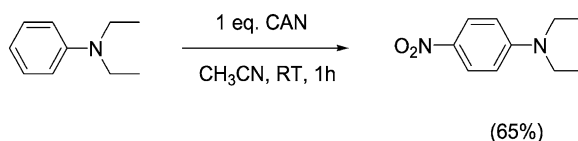
formed and could be isolated in good yield (scheme 43). The authors discovered that when naphthalene is treated with CAN, sulfuric acid and tetrabutylammonium nitrite in methanol, 1-methoxy-4-nitronaphthalene and 1-methoxy-2-nitronaphthalene could be obtained (scheme 44). When CAN is replaced by other nitrates like potassium nitrate or tetrabutylammonium nitrate, no nitration was observed.



Scheme 43.



Scheme 44.

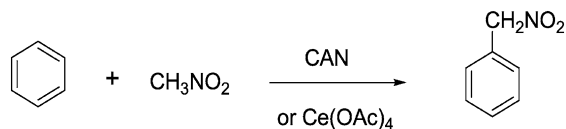


Scheme 45.

Ammonium hexanitratocerate(IV) can be used for the nitration of *N,N*-dialkylanilines in acetonitrile at room temperature to give *N,N*-dialkyl-4-nitroanilines in moderate yields, but with a good regioselectivity (Yang et al., 2005) (scheme 45).

A careful choice of the reaction conditions are of importance. The highest yields were observed when 1 equivalent of CAN was used, while no reaction was observed when the substrate was treated with 2 equivalents of CAN. The reaction only proceeds in aprotic solvents like acetonitrile in which CAN can be solubilized. No reaction was observed in dichloromethane, carbon tetrachloride or tetrahydrofuran, whereas the use of water, methanol or even mixtures of these solvents with acetonitrile yielded *N,N,N',N'*-tetraalkylbenzidines as the result of a coupling reaction. In fact the coupling of *N,N*-dialkylanilines by CAN (2 eq. for 1 eq. of substrate) in water is an efficient method for the synthesis of *N,N,N',N'*-tetraalkylbenzidines (Xi et al., 2005). The yields of the nitration reactions were low when a chlorine substituent was present on the phenyl ring; at the same time partial dealkylation of the amine group was observed. The reaction did not proceed when the aromatic ring contained two methyl groups in *meta*-position.

Free-radical aromatic nitromethylation is promoted by different cerium(IV) salts (Kurz and Ngoviwatchai, 1981). The reaction is carried out by refluxing a mixture of an aromatic compound, nitromethane, and a cerium(IV) salt in acetic acid (scheme 46). The mechanism in-



Scheme 46.

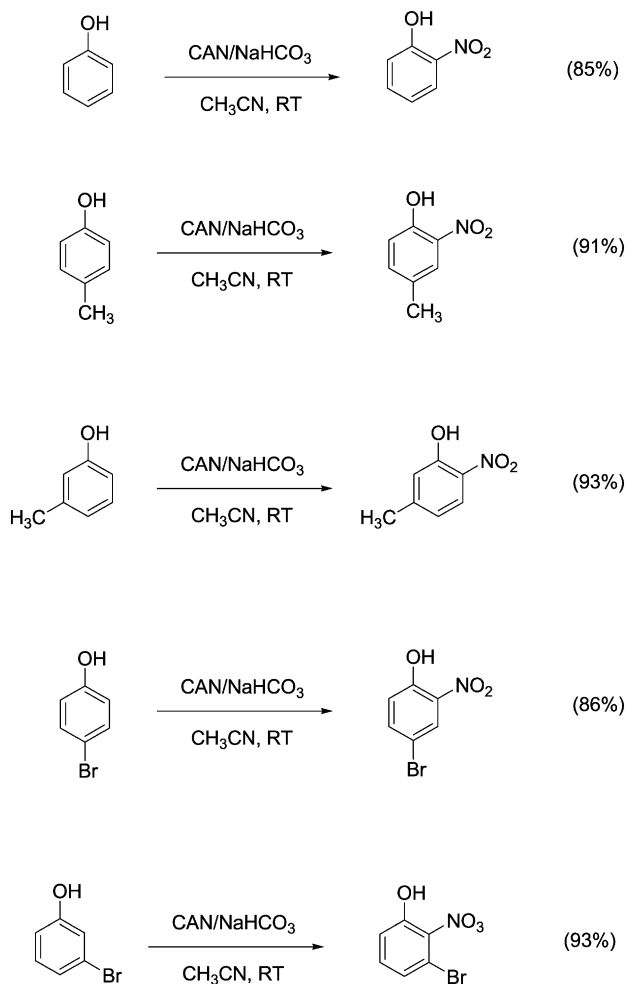
volves the generation of nitromethyl radicals by the oxidative deprotonation of nitromethane, and their subsequent substitution on the aromatic compound. The best cerium(IV) reagents for this reaction are ammonium hexanitratocerate(IV) and cerium(IV) acetate. However, both reagents have their advantages and disadvantages. The advantages of CAN are its commercial availability at a reasonable price and the good reaction yield (based on the conversion of the substrate). A disadvantage is that different byproducts are formed. For instance, nitromethylation of benzene not only gave the desired nitromethylated product, but also large amounts of benzaldehyde and benzyl acetate. Nitromethylation of toluene resulted in the formation of benzaldehyde, isomeric nitrotoluenes and toluenealdehydes, and methylbenzyl acetate as byproducts. Advantages of cerium(IV) acetate are the short reaction times, the color change occurring upon cerium(IV) reduction, which allows convenient monitoring of the reaction, and the lack of byproduct formation. Disadvantages are the fact that this salt is not commercially available and that it is rather light-sensitive. However, these disadvantages can be circumvented by preparing cerium(IV) acetate prior to its use and using it immediately without isolation.

Phenols that possess at least one unsubstituted *ortho*-position undergo fast, regioselective *ortho*-nitration with ammonium hexanitratocerate(IV) in presence of NaHCO_3 at room temperature to yield *ortho*-nitro phenols in high yield (schemes 47 and 48) (Sathunuru et al., 2003). Phenols with ring activating groups (OCH_3 , CH_3) and moderately ring deactivating groups (Cl , Br , CHO , CO_2Me) undergo nitration. However, phenols with strongly deactivating groups (CN , NO_2) or 2,6-disubstituted phenols could not be nitrated by $\text{CAN}/\text{NaHCO}_3$ in acetonitrile. The reaction has been extended to the nitration of hydroxy heterocycles (Sathunuru and Biehl, 2004) (scheme 49).

6.10. Functionalization of alkenes

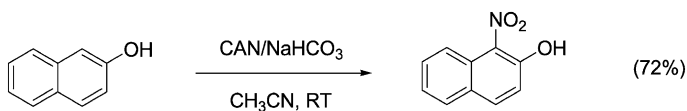
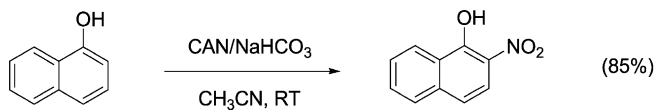
Cerium(IV) salts are very useful reagents for the functionalization of alkenes. In this section, only a few representative examples are shown. More examples can be found in reviews written by Nair and coworkers (Nair et al., 2002, 2004). The halogenation of alkenes with CAN has been described in section 6.7. Alkenes react with carboxylic acids in presence of cerium(IV) sulfate to yield carboxylic esters (scheme 50) (Horiuchi et al., 2003). The addition reaction follows Markovnikov's rule. The carboxylic acid also acts as solvent. This reaction provides a simple method for the preparation of carboxylic esters from alkenes.

Styrenes react with CAN and ammonium thiocyanate in methanol (Nair et al., 2000a). In presence of air (oxygen) phenacyl thiocyanates are formed, whereas in argon atmosphere bis(thiocyanates) are obtained (scheme 51). A similar reaction with potassium selenocyanate in methanol affords phenacyl selenocyanates and bis(selenocyanates) (scheme 52) (Nair et

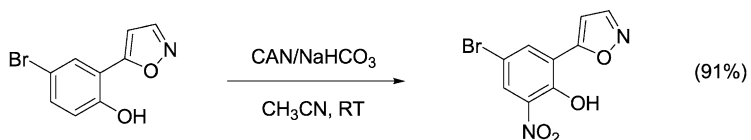
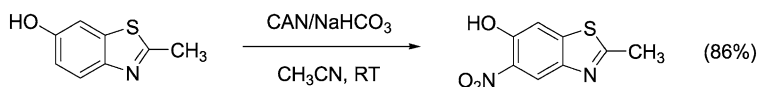
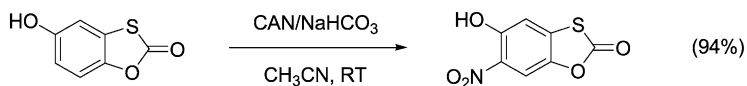
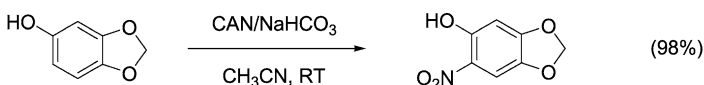


Scheme 47.

al., 2002). The reactions also work with indoles as substrates. Reaction of styrenes with CAN and sodium azide in methanol under oxygen atmosphere gives phenacyl azides (scheme 53) (Nair et al., 2000a). When sodium iodide is present besides sodium azide, azidoiodides are formed (Nair et al., 2000b). Replacement of methanol as solvent by acetonitrile, will result in the formation of other products: an alkene in presence of CAN and sodium azide will then be transformed into α -azido- β -nitroalkanes (scheme 54) (Trahanovsky and Robbins, 1971). It should be noticed that in absence of an alkene, the azide ion is very fast oxidized into nitrogen gas by CAN.

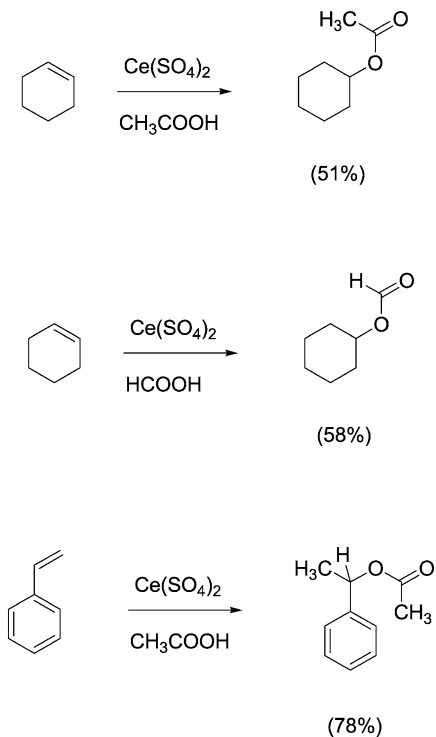


Scheme 48.

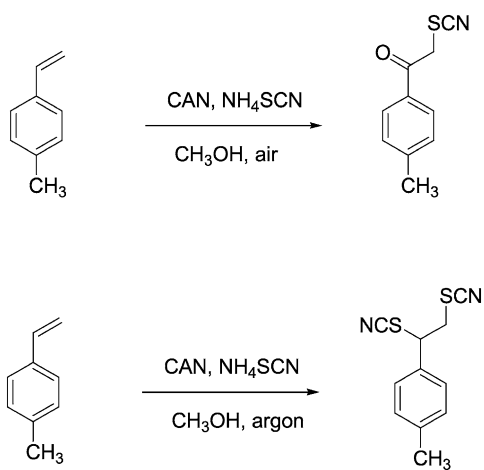


Scheme 49.

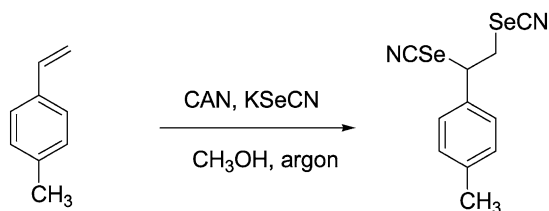
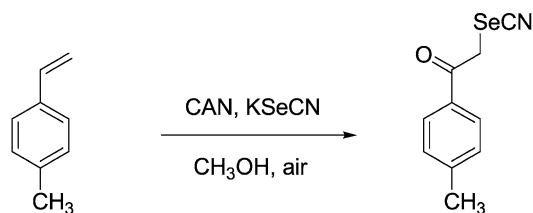
Depending on the solvent, different reaction products form when alkenes react with iodine in presence of cerium(IV) triflate: 1,2-hydroxy iodides in water, 1,2-alkoxy iodides in alcohols and 1,2-acetoxy iodides in acetic acid (Iranpoor and Shekarriz, 2000). Treatment of a mixture of styrene and sodium *p*-toluene sulfinate in anhydrous acetonitrile with CAN af-



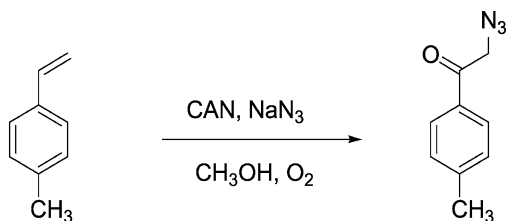
Scheme 50.



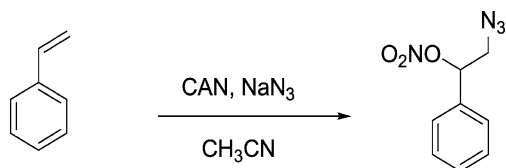
Scheme 51.



Scheme 52.



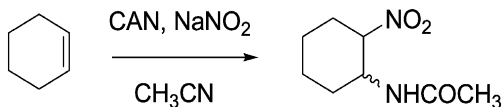
Scheme 53.



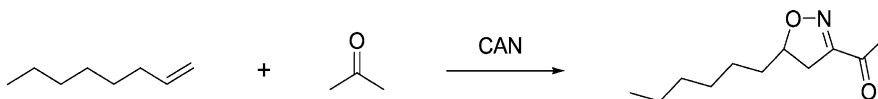
Scheme 54.

fords α -sulfonyl- β -nitrate compounds (Nair et al., 2003). Nitroacetamidation of alkenes led to a mixture of ammonium hexanitratocerate(IV) and sodium nitrite in acetonitrile (scheme 55) (Reddy et al., 1995). Acetonitrile is not just a solvent, but also a reagent in this reaction.

Cerium-mediated reactions are also useful for the synthesis of heterocyclic compounds. 3-Acetylisoxazole derivatives are formed by reaction between alkenes and acetone in presence of CAN (scheme 56) (Itoh et al., 2002; Itoh and Horiuchi, 2004). When acetone is replaced



Scheme 55.



Scheme 56.

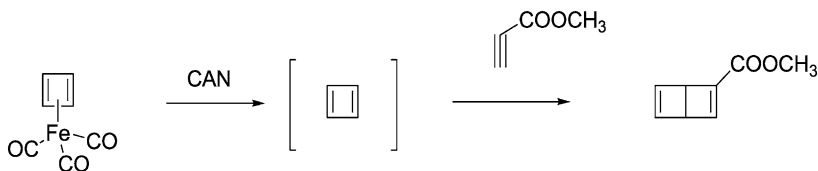
by acetophenone, 3-benzoylisoxazole derivatives are obtained. The reaction also works with alkynes. [Baciocchi and Ruzziconi \(1986\)](#) investigated the addition of different ketones as well as ethyl acetoacetate to 1,3-butadiene in presence of CAN. A mixture of 1,2- and 1,4-adducts was obtained.

6.11. Removal of protecting groups

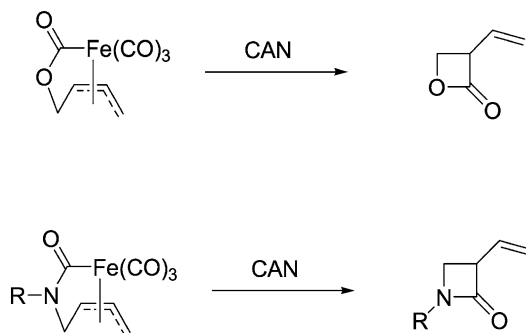
Ammonium hexanitratocerate(IV) is becoming more and more popular for the removal of protecting groups, especially on amino acids and nucleic acids ([Hwu and King, 2001](#)). The *tert*-butoxycarbonyl group (*t*-Boc) is often used for the protection of primary amines of amino acids in peptide synthesis. This group can also protect alcohols and thiols. CAN is able to remove this protecting group under neutral conditions, by heating the protected compounds with 0.2 equivalents of CAN in acetonitrile ([Hwu et al., 1996a](#)). This deprotection methodology is applicable to substrates with acid sensitive groups. Other protecting groups that can be removed by CAN include the triphenylmethyl (trityl) and the monomethoxytrityl (MMTr) protecting groups ([Hwu et al., 1996b](#)), as well as the *tert*-butyldimethylsilyl (TBDMS) group ([Hwu and King, 2001](#)). CAN impregnated on silica gel is effective for the removal of triisopropylsilyl protecting groups ([Hwu and King, 2001](#)). Bull and coworkers described the debenzoylation of *N*-benzyl tertiary amines with ammonium hexanitratocerate(IV) ([Bull et al., 2000](#)). Deprotection of tetrahydropyranyl (THP) and tetrahydrofuranyl (THF) ethers to the corresponding alcohols could be carried out by a catalytic amount of CAN (3 mol%) in a acetonitrile/borate buffer at pH 8 ([Marko et al., 1999](#)).

6.12. Splitting of organometallic compounds

Although cyclobutadiene itself is unknown, it can be liberated as an intermediate by oxidative degradation of the organometallic compound cyclobutadiene tricarbonyliron by ammonium hexanitratocerate(IV) ([Watts et al., 1965](#); [Paquette and Kelly, 1969](#)). The transient intermediate can be trapped by a dienophile (scheme 57). When the oxidation is carried out in presence of a CAN solution saturated with lithium chloride, *trans*-3,4,-dichloro-cyclobutene is formed ([Emerson et al., 1965](#)). Because tricarbonyliron complexes are often used as reagents or intermediates in organic synthesis, the possibility to remove the Fe(CO)₃ group by decomplexation



Scheme 57.



Scheme 58.

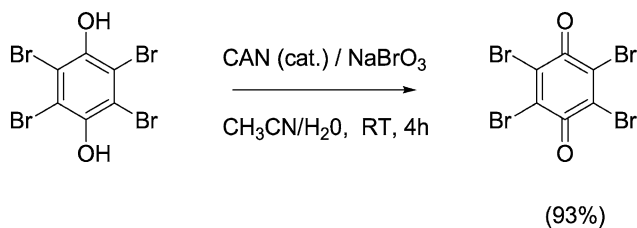
with ammonium hexanitratocerate(IV) is a very useful synthetic methodology (Levy, 1994). π -allyltricarbonyliron lactones and lactams can be obtained from a variety of precursors and they allow the regioselective synthesis of lactones and lactams (scheme 58). The stereochemistry of the organometallic compounds controls the stereochemistry of the product.

7. Indirect and catalytic reactions with cerium(IV) ions

7.1. Oxidations by bromate ions

Inspired by the Belousov–Zhabotinskii reaction, where cerium(III) is reoxidized by bromate ions, Ho developed a dual oxidant system consisting of ammonium hexanitratocerate(IV) and sodium bromate for the oxidation of arylmethanols (benzylic alcohols) to the corresponding aldehydes (Ho, 1978). The method has also been successfully used for the oxidation of hydroquinones to quinones (scheme 59) and for the oxidation of sulfides to sulfoxides (Ho, 1979).

Sodium bromate in presence of CAN or CAS is an effective reagent for the oxidation of secondary alcohols into the corresponding ketones (Tomioka et al., 1982; Kanemoto et al., 1986). For instance cyclododecanol is oxidized in 98% yield to cyclododecanone, and borneol is oxidized in 77% yield into camphor. Primary alcohols are not affected, so that this is a useful methodology for the oxidation of secondary alcohols in presence of primary ones. The presence of a double bond in the substrate, even at a position far way from the sec-



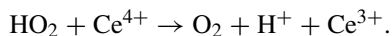
Scheme 59.

ondary alcohol group inhibits the reaction. Primary 1,4-diols react to yield γ -lactones. Sodium bromate does not dissolve in aqueous acetonitrile, so that the reaction mixture is a heterogeneous system. Ammonium hexanitratocerate(IV) and cerium(IV) ammonium sulfate are equally active as catalyst. Cerium(IV) impregnated on a perfluorinated sulfonic acid (Nafion) has been used as a supported catalyst for the oxidation of alcohols (Kanemoto et al., 1989; Yamato and Shinoda, 2002) and of polyaromatic compounds (Yamato et al., 2000) by sodium bromate.

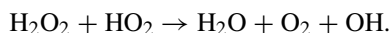
Alkyl and silyl ethers undergo oxidative cleavage to form the corresponding carbonyl compound by reaction with a molar equivalent of sodium bromate in presence of a catalytic amount of ammonium hexanitratocerate(IV) (Olah et al., 1980). For instance cyclohexyl methyl ether is transformed into cyclohexanone. Primary alkyl ethers were found to react slower than secondary alkyl ethers under similar reaction conditions. Ganin and Amer investigated the CAN-catalyzed oxidation of alkylbenzenes with potassium bromate (Ganin and Amer, 1995), whereas Shi and coworkers reported on the CeO_2 -catalyzed oxidation of alkylbenzenes with sodium bromate into aldehydes and ketones (Shi et al., 1999). α -Methylpyrroles can be converted to α -formyl pyrroles by sodium bromate in aqueous methanol, in presence of a catalytic quantity (1%) of CAN (Bobal and Lightner, 2001).

7.2. Oxidations by peroxides

Hydrogen peroxide is often used as an environmentally friendly oxidant (Sanderson, 2000). Although hydrogen peroxide can be decomposed catalytically by different redox active transition metal ions and complexes, the decomposition of hydrogen peroxide by cerium(IV) is not a catalytic process. It occurs spontaneously in the pH range from 0 to 1.4 if an excess of hydrogen peroxide is avoided. Hydrogen peroxide is oxidized to oxygen and Ce^{4+} is reduced to Ce^{3+} . Unlike $\text{Fe}^{3+}/\text{Fe}^{2+}$, the $\text{Ce}^{4+}/\text{Ce}^{3+}$ redox couple is not able to decompose hydrogen peroxide catalytically. The relevant reactions are (Baer and Stein, 1953):



The following reaction does not seem to take place, even in presence of a large excess of hydrogen peroxide:



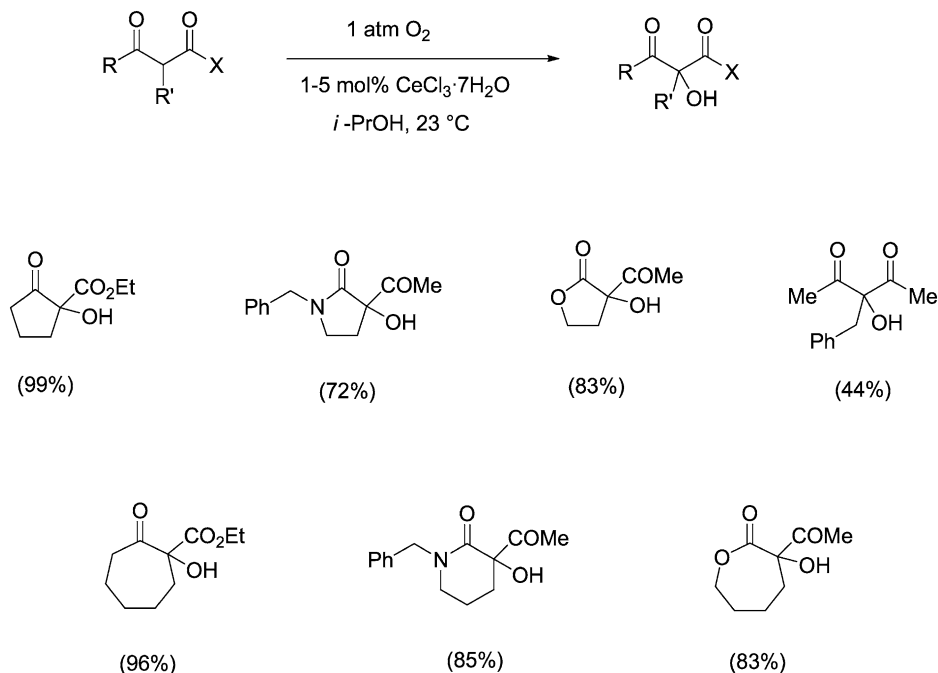
The fast reaction between cerium(IV) sulfate and hydrogen peroxide is useful to determine the concentration of hydrogen peroxide in solution by cerimetric titrations (see section 3). However, the decomposition of hydrogen peroxide by cerium(IV) in perchloric acid solution is slow at pH values above 0.7 (Baer and Stein, 1953; Ardon and Stein, 1956), at which colloid polymeric cerium(IV) complexes are formed. These are able to interact with hydrogen peroxide to afford colored complexes that are only slowly decomposed. At very low pH values, the polymeric complexes are not formed and decomposition of hydrogen peroxide is fast.

Auty and coworkers showed that 4-*tert*-butyltoluene can be oxidized in acetic acid into 4-*tert*-butylbenzaldehyde by 35% aqueous hydrogen peroxide in a process catalyzed by cerium(III) and bromide ions (Auty et al., 1997). The different reaction steps are benzylic bromination, hydrolysis of the bromide to the benzylic alcohol and the fast oxidation of the benzylic alcohol to the aldehyde by bromine. The role of cerium(III) is not clear yet. It is assumed that cerium(IV) is formed during the first step; experimental evidence for the occurrence of cerium(IV) was given by the absorption spectrum of the reaction mixture. The reaction does not work when sodium bromide is replaced by sodium chloride or sodium iodide. The polyoxometalate $[\text{CeW}_{10}\text{O}_{36}]^{8-}$ with hydrogen peroxide as co-oxidant is able to oxidize benzyl alcohol to benzaldehyde and secondary alcohols into ketones, but it seems that the active catalytic species is $[\text{W}_2\text{O}_3(\text{O}_2)_4(\text{H}_2\text{O})_2]^{2-}$ and not a cerium(IV) compound (Griffith et al., 1996). $[\text{CeW}_{10}\text{O}_{36}]^{8-}$ with *N*-hexadecylpyridinium counter ions was used for the oxidation of benzyl and secondary alcohols by hydrogen peroxide under biphasic reaction conditions with chloroform as the organic solvent (Shiozaki et al., 1996). No reaction mechanism has been reported. Hydrogen peroxide can be used to control the oxidizing capability of cerium(IV) salts, so that over-oxidation can be avoided (Chawla and Sharma, 1990; Chakrabarty et al., 1993). The control of the oxophilicity can be attributed to the formation of cerium(IV) peroxo complexes, which are less oxidizing than for instance ammonium hexanitratocerate(IV). Differences in product distribution were observed when oxidative couplings of phenol by CAN were carried out in presence and absence of hydrogen peroxide.

Krohn and Vitz (2000) used *tert*-butyl hydroperoxide (TBHP) with catalytic amounts of CAN for the oxidation of hydroquinones and hydroquinone monomethyl ethers to quinones. TBHP is a cheap and convenient oxygen source (Sherrington, 1988). It will not oxidize organic substrates in the absence of a catalyst. High regioselectivity can be obtained by a careful choice of a catalyst. Cerium(IV) impregnated on Nafion[®] is an example of a supported catalyst for the oxidation of alcohols by *tert*-butyl hydroperoxide (Kanemoto et al., 1984, 1989).

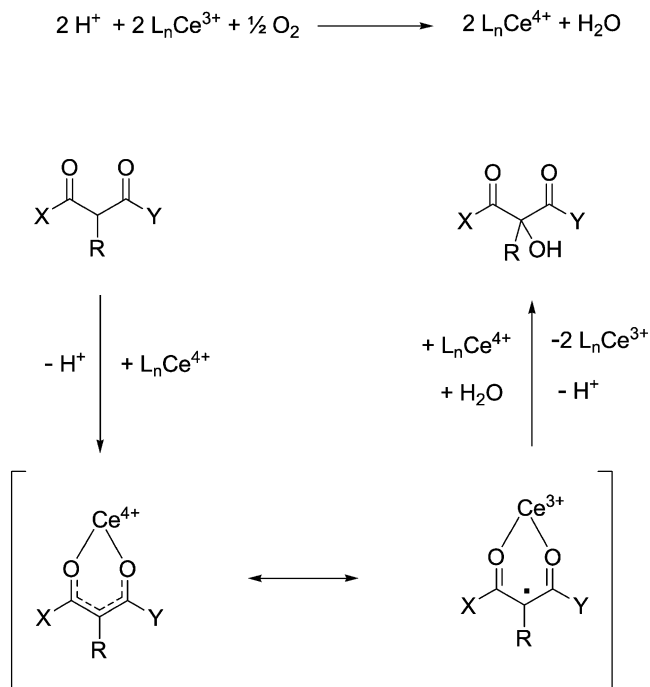
7.3. Oxidations by molecular oxygen

Cerium(III) chloride heptahydrate has been used by Christoffers and coworkers as a catalyst for the α -hydroxylation of β -dicarbonyl compounds by molecular oxygen (Christoffers and Werner, 2002; Christoffers et al., 2003a). The reaction is useful for the hydroxylation of cyclic β -dicarbonyl compounds, but many side reactions occur with acyclic β -dicarbonyl (scheme 60). The byproducts include α -chlorinated β -dicarbonyl compounds. In the proposed reaction mechanism, cerium(III) coordinates to a β -dicarbonyl ligand (scheme 61). The coordinated cerium(III) (L_nCe^{3+} in scheme 61) is oxidized by molecular oxygen to cerium(IV).



Scheme 60.

By an intramolecular electron transfer (ligand-to-metal charge transfer), cerium(IV) is transformed back into cerium(III), while at the same time an unpaired electron is generated on the β -dicarbonyl ligand. This radical species is further oxidized by a second cerium(IV) ion and hydrated. During the reaction, two moles of protons are released, so that the reaction mixtures becomes more and more acidic when the reaction proceeds. The reaction can be considered as a form of water activation. It is assumed that molecular oxygen is able to oxidize cerium(III) to cerium(IV), because coordination of β -dicarbonyl compounds to cerium(III) reduces the redox potential of the $\text{Ce}^{4+}/\text{Ce}^{3+}$ redox couple. The solvent plays an important role in the reaction, because the solubility of molecular oxygen in the solvent is crucial. The optimal solvents were found to be DMF or *iso*-propanol. The reaction can be run at room temperature. For some substrates, the reaction can be run with air, but in most cases pure oxygen gas (1 atm) gave superior results. Oxygen has to be bubbled through the reaction solution; a static oxygen atmosphere gave irreproducible results, probably due to lowering of the partial oxygen pressure about the liquid phase by partial evaporation of the solvent. $\text{CeCl}_3 \cdot 7\text{H}_2\text{O}$ was chosen as the source of cerium, because it is one of the cheapest cerium salts. However, it has been replaced in some experiments by $(\text{NH}_4)_2[\text{Ce}(\text{NO}_3)_6]$ or $\text{Ce}(\text{OAc})_3 \cdot \text{H}_2\text{O}$. The cerium salts were used in catalytic amounts (less than 5 mol%) and after the reaction they were removed by filtration through SiO_2 .

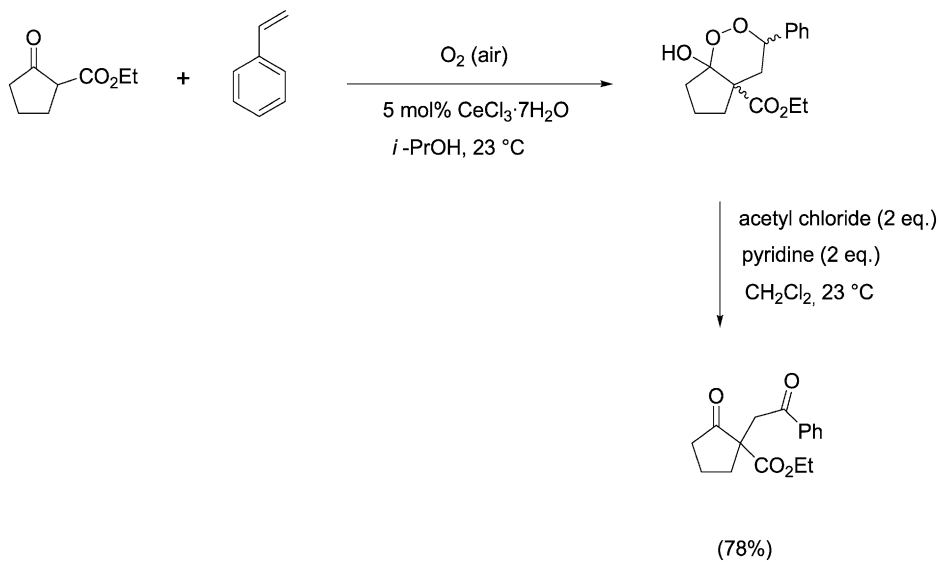


Scheme 61.

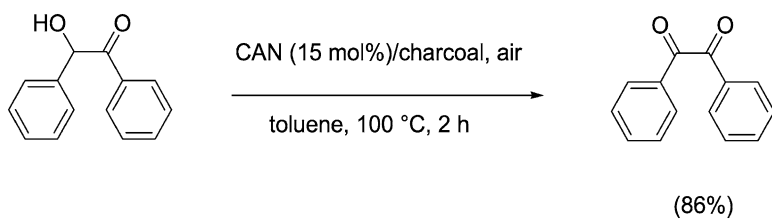
The methodology has been extended to C–C coupling reactions of alkenes and β -dicarbonyl compounds with air as the oxidant and with $\text{CeCl}_3 \cdot 7\text{H}_2\text{O}$ as the catalyst (Christoffers et al., 2003b; Rössle et al., 2005). The reactions yield diastereoisomeric mixtures of hydroxyperoxides, which disproportionate in presence of acetyl chloride/pyridine by Kornblum–DeLaMare fragmentation into dioxo esters (scheme 62). These dioxo derivatives have a 1,4-dicarbonyl structural motif. This reaction has been explored with styrene and substituted alkenes as the alkene substrate.

Yamada and coworkers (Yamada et al., 1993) reported on the cyclization reaction of mono-substituted alkenes with β -ketoesters, in presence of molecular oxygen and catalytic amounts of CAN. The reaction yielded substituted 1,2-dioxan-3-ols. CAN supported on charcoal (CAN-charcoal) is a catalyst for the air oxidation of benzyl alcohols to benzaldehydes and α -hydroxyketones (acyloins) into α -diketones (Hatanaka et al., 1983) (scheme 63).

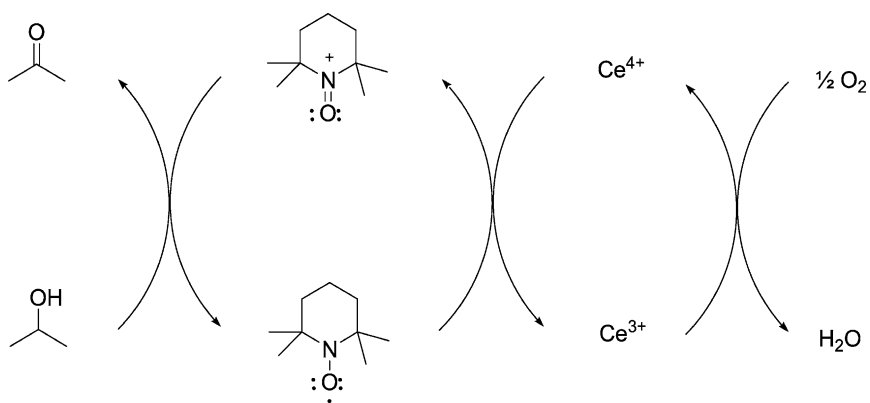
Kim and Jung (2003) oxidized benzylic and allylic alcohols by molecular oxygen in presence of catalytic amounts of 2,2,6,6-tetramethylpiperidinyl-1-oxyl (TEMPO) and CAN (scheme 64). Molecular oxygen is reduced to water by oxidation of Ce^{3+} to Ce^{4+} . The nitroxyl radical of TEMPO is oxidized to the *N*-oxoammonium cation by Ce^{4+} . The *N*-oxoammonium cation then oxidizes the alcohol to a carbonyl compound. The reactions were carried out in refluxing acetonitrile and molecular oxygen was bubbled through the reaction mixture. The amount of CAN varied between 10 and 20 mol%, and the amount of TEMPO



Scheme 62.



Scheme 63.



Scheme 64.

was 10 mol%. Both primary and secondary benzyl alcohol gave good reaction yields, but the latter reacted much faster than the primary ones. Allylic alcohols gave good yields after prolonged reaction periods, but the presence of sterically demanding groups reduced the yields. Aliphatic alcohols like cyclohexanol showed no reactivity. The reactions are slow at room temperature. TEMPO can be replaced by *N*-hydroxy phthalimide (NHPI) (Kim and Rajagopal, 2004). Both diarylsulfides and dialkylsulfides can be oxidized to the corresponding sulfoxides by molecular oxygen in presence of catalytic amounts of CAN (Riley and Correa, 1986).

8. Cerium-mediated electrosynthesis

Electrochemical synthesis (electrosynthesis) is being used for a long time by the chemical industry for the manufacture of inorganic chemicals like chlorine, sodium hydroxide, sodium hypochlorite, fluorine, potassium peroxydisulfate, potassium permanganate, and perchloric acid. Electrosynthesis could be a method for the environmentally benign manufacture of organic compounds on an industrial scale, establishing a “green” alternative to conventional processing methods (Scott, 1995). There are many advantages associated with electrochemical synthesis methods. They are applicable to a wide range of substrates and are often highly selective, only a limited amount of side products being formed. Moreover, toxic reagents can be avoided. As a result, much less waste is generated by electrochemical processes than by conventional chemical processes. Electrons are relatively cheap reagents; they are much cheaper than commonly used redox agents like chromate and peroxide (but not cheaper than air or nitric acid). The conditions in electrochemical processes are close to ambient temperature and pressure. Finally, electrochemical technology is well developed. Electrolytic cells are readily available for both batch and continuous processes. They can be integrated with other production units in a complex production process. However, there are still some limitations in electrochemical technology that hampers the widespread use of electrochemical synthesis of organic compounds on an industrial scale. In *direct electrosynthesis*, the maximum rate of chemical change per unit area of electrode (the current density) is proportional to the concentration of the reactant in solution. An electrochemical process can become economically feasible only if the current density of the process is high, and this requires a high concentration of the reactants in the electrolyte solution. The preferred medium in commercial electrolysis processes is an aqueous electrolyte, because of the less complex electrochemistry than in non-aqueous media, the easier pH control, the cost-effectiveness and less problems due to solvent loss. Unfortunately, many organic compounds have a very low solubility in aqueous media. A strategy to overcome this difficulty is *indirect electrosynthesis*, where a *redox mediator* (a redox couple soluble in water) is used to transfer the electrons between the electrode and the reactant (Clarke et al., 1975). The redox mediator is continuously generated in its active oxidation state at the electrode and allowed to react with the organic substrate away from the electrode, either in-cell or ex-cell. In an *in-cell method*, the electrochemical reaction between the redox mediator and the organic substrate takes place in the electrolytic cell, where also the used redox mediator is regenerated. In an *ex-cell method*, the reaction occurs in a chemical reactor that is separated from the electrolytic cell. Following the reaction,

the electrolyte containing the used redox mediator is separated from the product phase, and the electrolyte solution is returned to the electrolytic cell for regeneration of the redox mediator. An advantage of the ex-cell method is that direct contact between the organic phase and the electrode is avoided, so that deactivation of the electrode (for instance by product deposition or by side reactions) is limited. Many indirect redox processes use multiphase conditions. The redox mediator can be transferred to the organic phase by a phase-transfer catalyst. Because the redox species are recycled, only small amounts of the redox reagents have to be used and there is no stoichiometric by-product stream from the redox reagent. Examples of popular redox mediators are Co^{3+} , Mn^{3+} and also Ce^{4+} . The interest of the chemical industry in cerium(IV)-mediated organic electrosynthesis can be explained by the need for fast and selective oxidation of toluene or xylenes to benzaldehydes and of (poly)aromatic compounds to quinones. Naphthoquinones are well-known intermediates for organic dyes. Aldehydes are used in perfumes or as intermediates for pharmaceuticals.

Several authors have explored the use of Ce^{4+} as a redox mediator in organic electrosynthesis, but they have been facing different types of problems. The main difficulty was to create a cerium solution that is concentrated enough to make the electrochemical regeneration process efficient. Oehr investigated cerium sulfate in dilute sulfuric acid for the electrooxidation of naphthalene to 1,4-naphthoquinone (Oehr, 1982a, 1982b). Unfortunately, both cerium(III) and cerium(IV) sulfates have a low solubility in dilute sulfuric acid. This leads to large volumes of solution for oxidizing small amounts of organic substrate. As a result the current efficiencies are low and the reaction vessels need to be prohibitively large to accommodate the large volumes of electrolyte. Oehr also used a cerium sulfate slurry to overcome the low solubility, but this is impractical in process technology. Rennie (1972) overcame the solubility problems of the cerium salts by working in nitric acid, but in this case significant quantities of nitrated by-products were formed. Ibl and coworkers (Ibl et al., 1979; Kramer et al., 1980) used cerium salts in perchloric acid for the electrosynthesis of substituted benzaldehydes. Although the process was very interesting from an economical point of view, explosion hazards related to the mixing of perchloric acid and organic compounds have probably limited further developments. Other authors (Torii et al., 1982) turned to the use of non-aqueous solvents for the oxidation reaction and electrochemical regeneration of ammonium hexanitratocerate(IV). Methanol turned out to be a suitable solvent for the oxidation of *p*-methoxytoluene to *p*-methoxybenzaldehyde, but cerium(IV) is not very stable in methanol. Cho and Romero (1995) proposed to use cerium(III) nitrate hexahydrate as a precursor for electrochemically generated cerium(IV). The advantage of this salt is that it has a lower redox potential than other cerium salts, so that an anodic potential of 1.4 V is sufficient to oxidize cerium(III) into cerium(IV). This low potential also allows the use of acetonitrile as solvent. Research has been conducted for increasing the solubility of cerium salts in the systems used for oxidation of organic compounds. Higher cerium concentrations have the advantage that the solution containing the redox mediator can oxidize a larger amount of organic substrate before regeneration is necessary.

Kreh et al. discovered that cerium(III) and cerium(IV) have a high solubility in aqueous methanesulfonic acid (Kreh and Spotnitz, 1987a, 1987c; Kreh et al., 1989; Spotnitz et al., 1990). When the concentration of methanesulfonic acid is between 1.5 and 9 molar the sol-

ubility of the cerium salt is at least 0.2 mol/L. For instance, in 2 M methanesulfonic acid, the solubility of cerium(III) is about 2.3 mol/L. The solubility of cerium(IV) decreases with increasing methanesulfonic acid concentration. The solubility of cerium(IV) in aqueous methanesulfonic acid is lower than the solubility of cerium(III), but the solubility of cerium(IV) depends very much on the concentration of methanesulfonic acid. At low concentrations of methanesulfonic acid, the solubility of cerium(IV) is limited (only about 0.1 mol/L cerium(IV) dissolves in 1 M methanesulfonic acid), but increases sharply with increasing acid concentration (about 1 mol/L cerium(IV) dissolves in 4 M methanesulfonic acid). Notice this major difference: the solubility of cerium(IV) increases with increasing methanesulfonic acid concentration, whereas the solubility of cerium(III) decreases (Spotnitz et al., 1990). The lower solubility of cerium(IV) in comparison to cerium(III) can result in precipitation of a cerium(IV) salt upon oxidation of cerium(III) to cerium(IV). The precipitated cerium(IV) salt is still effective for oxidizing organic substrates, although slurries are more difficult to handle than homogenous solutions. Advantages reported for methanesulfonic acid include low cost, safety, low nucleophilicity, stability to anodic oxidation and oxidation by cerium(IV), and a high solubility of cerium(III) and cerium(IV) (Kreh et al., 1989). The latter feature enables the use of high current density for fast anodic regeneration of cerium(IV) and allows faster reactions with the organic substrates. Regeneration of cerium(IV) takes place at current densities as high as 4000 A m^{-2} , with a current efficiency higher than 90%. It should be noticed that while Ce^{3+} is oxidized to Ce^{4+} at the anode, protons are reduced to hydrogen gas at the cathode. Therefore, the acidity of the solution decreases as the regeneration process proceeds. Cerium(IV) methanesulfonate that is electrochemically generated from cerium(III) methanesulfonate has been used as a redox mediator for the oxidizing of several types of organic compounds. Examples of substrates include toluene, xylenes, chlorotoluenes, ethylbenzene, styrene, naphthalene and anthracene. These oxidation reactions have been discussed more in detail in section 6. Pilot plant projects based on this method have been constructed for the synthesis of anthraquinone, aminoanthraquinone and *p*-tolualdehyde. It is also possible to replace methanesulfonic acid by trifluoromethanesulfonic acid (triflic acid), but the latter acid is more expensive (Kreh and Spotnitz, 1987b).

Although the process described by Kreh et al. was a major improvement in comparison with earlier processes, it is still not energy efficient enough to be of economical interest. Harrison (1993) developed an integrated process to improve the speed and efficiency of the indirect cerium-mediated electrosynthesis of oxidized aromatic compounds like 1,4-naphthoquinone in aqueous methanesulfonic acid. Naphthalene is dissolved in a water immiscible solvent like benzene, chlorobenzene, 1,2-dichloroethane or dichloromethane. The reaction rate depends on the degree of mixing of the two phases. Turbulence in the reaction mixture can be created by a static mixer. However, too fast mixing of the two immiscible solvents can lead to formation of emulsions. Following the reaction, Ce^{3+} is reoxidized to Ce^{4+} in an electrolytic cell under turbulent flow conditions, where the cerium solution is allowed to flow at large velocities past the anode. The cell was designed so that the anode area is greatly reduced, and that the anode and cathode compartments need not to be separated by an ion exchange membrane. The reaction conditions were improved to such an extent that the process could be run continuously. The electrosynthesis of naphthoquinone and tetrahydroanthraquinone

was scaled up to a 100 ton per year pilot-plant (Harrison and Théorêt, 1999). Mahdavi et al. (2002) described a method for the purification of a solution of the spent redox mediator before electroregeneration.

As mentioned above, hydrogen gas is produced at the cathode during the regeneration process. It would be desirable to produce simultaneously with the regeneration of the redox mediator in the oxidized form another redox mediator in the reduced form. This reduced mediator could then perform a reductive electrochemical reaction. Harrison (1997) describes a setup for simultaneously generating Ce^{4+} at the anode and Ti^{3+} at the cathode. The trivalent titanium was subsequently used for reactions such as the reduction of a nitro group into an amino group.

In addition to the interest in cerium-mediated electrosynthesis on an industrial scale, more fundamental studies have been performed. Morita et al. (1993) compared cerium sulfate and cerium perchlorate salt as redox mediators for the oxidation of alkylbenzenes to aromatic aldehydes. Cerium(IV) perchlorate has a higher oxidizing power than cerium(IV) sulfate. Therefore, cerium sulfate could be used to oxidize the easily oxidizable *p*-methylanisole, but not *p*-xylene. On the other hand, the redox mediator should be not too powerful. Therefore cerium(IV) sulfate is more suitable for the oxidation of *p*-methylanisole than cerium(IV) perchlorate. Cerium(IV) *p*-toluenesulfonate is slightly more reactive than cerium *p*-methoxybenzenesulfonate as redox mediator for the oxidation of alcohols, diols and alkylarenes (Purgato et al., 2000; Purgato and Romero, 2002). Cerium(IV) *p*-hydroxybenzenesulfonate is unsuitable as redox mediator, because of electrochemical oxidation of the ligand (Purgato et al., 2000). Cho and coworkers found that the behavior of β -dicarbonyl compounds in electrochemical oxidation reaction with Ce^{4+} depends on the nature of the cerium salt (Cho and Romero, 1988; Cho et al., 1999; Aleixo et al., 2000). When cerium nitrate was used, dimers were formed, whereas upon use of cerium methanesulfonate fragmentation products were obtained. With cerium methanesulfonate as the redox mediator, 2,4-pentanedione is transformed into acetic acid, 1,3-diphenyl-1,3-pentanedione into benzoic acid, 1,3-cyclohexanedione into glutaric acid, methyl acetoacetate into acetic acid and methanol, and dimethyl malonate yields methanol (Cho and Romero, 1988). Because of the low current densities, the reactions were slow. For instance, it took 48 hours to convert 2 mmol of 1,3-diphenyl-1,3-pentanedione into benzoic acid (initial current: 58 mA). No reaction was observed for methyl cyanoacetate and malononitrile. Indian researchers optimized the electrochemical oxidation of anthracene, naphthalene, benzene (Vijayabarathi et al., 1999) and *p*-xylene (Jayaraman et al., 1998) in methanesulfonic acid. Studies of the $\text{Ce}^{4+}/\text{Ce}^{3+}$ redox couple in methanesulfonic acid by cyclic voltammetry showed that the redox mediator Ce^{4+} can be employed in solutions of widely different acid strength, cerium concentrations and temperatures (Devadoss et al., 2003). In this respect the $\text{Ce}^{4+}/\text{Ce}^{3+}$ redox couple is superior to the $\text{Mn}^{3+}/\text{Mn}^{2+}$ and $\text{Co}^{3+}/\text{Co}^{2+}$ redox couples. Ag^+ ions catalyze the oxidation of toluene to benzaldehyde by the redox mediator Ce^{4+} (Jow and Chou, 1988). Because of the formation of silver(II) oxide on the surface of the anode, the current efficiency for regeneration of Ce^{4+} increases. Ag^+ ions have thus also a catalytic effect on the regeneration of the redox mediator.

Because organic electrosynthesis with a redox mediator is often performed in multiphase systems (see above), knowledge about the extractability of the Ce^{4+} redox mediator from

the aqueous to the organic phase is very important. Pletcher and Valdes (1988a) showed that Ce^{4+} , but not Ce^{3+} , can be transferred from aqueous acid solutions to organic solvents by tetrabutylammonium or tributylphosphate as phase transfer catalysts. Extraction of Ce^{4+} to organic solvents is efficient from a nitric acid solution, but extraction is much less efficient from sulfuric acid and from perchloric acid solutions. Dichloromethane was found to be the only suitable organic solvent for extractions with tetrabutylammonium salts. With tributylphosphate as extractant, *n*-hexane is a better solvent than dichloromethane. However, extraction with tributylphosphate is less efficient than extraction with tetrabutylammonium. The electrochemical oxidation of cerium(III) to cerium(IV) in emulsions of aqueous nitric acid and water-immiscible organic solvents have been studied (Pletcher and Valdes, 1988b). A problem associated with the anodic oxidation of cerium in an undivided cell is the cathodic reduction of cerium(IV) to cerium(III). The problem can be solved by a proper choice of the phase catalyst and the organic phase, because in this case cerium(IV) is transferred immediately after its formation from the aqueous phase to the organic phase and is thus protected from cathodic reduction. The authors conclude that the best choice for the organic phase for oxidations with emulsions in an undivided cell is hexane/tributylphosphate or heptane/tributylphosphate. The oxidation of anthracene and naphthalene to the corresponding quinones was fast and good yields were obtained. The oxidation of toluenes to benzaldehydes in emulsions was less successful and the results largely depended on the substituents on the toluenes. Not only was the yield low, but many side products were formed as well. Better results were obtained for the oxidation of xylenes. These data illustrate that cerium(IV)-mediated electrochemical oxidations in organic/aqueous emulsions only work well under precise conditions, and that the choice of the reaction medium is of prime importance. For the direct anodic oxidation of cerium(III) to cerium(IV) in an aqueous solution, a divided cell has to be used to avoid reduction of the electrogenerated cerium(IV) at the cathode. This study also illustrated that divided cells are often much more convenient to work with.

The maximum rate of electrochemical regeneration of cerium(IV) is obtained with the concentration of cerium(III) at saturation level. When the cerium(III) ion does not interfere with the cerium(IV)-mediated reaction, it is advisable to add more cerium(III) salts to the reaction mixture than the amount that can be oxidized to cerium(IV). The concentration of cerium(IV) that can be reached is limited by the solubility of cerium(IV) in the reaction solvent, and the cerium(IV) solubility is often lower than the cerium(III) solubility. Tzedakis and Savall (1992) showed that the concentration of cerium(III) has no significant influence on the oxidation of 4-methoxytoluene to 4-methoxybenzaldehyde.

9. Initiation of radical polymerization reactions

Cerium(IV) ions are widely used as initiators for *radical polymerizations* of vinyl monomers (acrylamide, acrylonitrile, methyl methacrylate, vinyl acetate, ...). In order to act as an initiator, a reductant has to be added to the solutions containing the monomer and a cerium(IV) salt. Free radicals are produced by the oxidation of the reductant by cerium(IV) and these free radicals can initiate the polymerization reaction. Table 3 gives an overview of the different

Table 3
Overview of radical polymerization reactions initiated by cerium(IV)

Monomer	Reductant	Reference
acrylamide	acetoacetanilide	(Dong et al., 1994)
acrylamide	amino tri(methylene phosphonic acid)	(Öz and Akar, 2000)
acrylamide	4,4'-azobis(4-cyano pentanol)	(Tunca et al., 1989; Erim et al., 1992)
acrylamide	2-chloroethanol	(Gupta and Behari, 1986)
acrylamide	ethylenediamine tetraacetic acid	(Hsu et al., 1992)
acrylamide	lactic acid	(Misra and Khatib, 1982)
acrylamide	methionine	(Dinçer et al., 1997)
acrylic acid	amino tri(methylene phosphonic acid)	(Öz and Akar, 2000)
acrylonitrile	2-amino ethanethiol	(Lenka and Nayak, 1982)
acrylonitrile	amino tri(methylene phosphonic acid)	(Öz and Akar, 2000)
acrylonitrile	cysteine	(Lenka and Nayak, 1982)
acrylonitrile	glucose	(Padhi and Singh, 1983; Panda and Singh, 1995)
acrylonitrile	<i>N</i> -acetylglycine	(Patra and Singh, 1994a, 1994b)
acrylonitrile	propane-1,2-diol	(Mohanty et al., 1979)
acrylonitrile	sorbitol	(Mohanty et al., 1980)
acrylonitrile	thioacetamide	(Lenka and Nayak, 1982)
acrylonitrile	thioglycolic acid	(Lenka and Nayak, 1982)
acrylonitrile	thiourea	(Rout et al., 1977; Lenka and Nayak, 1982)
alkylcyanoacrylates	dextran	(Chauvierre et al., 2003)
ethyl acrylate	ethanol	(Reddy et al., 2006)
ethyl acrylate	methyl ethyl ketone	(Reddy et al., 2005)
ethyl acrylate	<i>n</i> -propanol	(Reddy et al., 2006)
methyl methacrylate	cellobiose	(Fernández and Guzmán, 1991)
methyl methacrylate	diethanol amine	(Pramanick, 1979)
methyl methacrylate	diethylamine	(Pramanick, 1979)
methyl methacrylate	ethanol amine	(Pramanick, 1979)
methyl methacrylate	ethylene diamine	(Pramanick, 1979)
methyl methacrylate	isobutanol	(Fernández and Guzmán, 1989a)
methyl methacrylate	isopropanol	Fernández and Guzmán, 1989a, 1989b; Fernández et al., 1989)
methyl methacrylate	maltose	(Fernández and Guzmán, 1991)
methyl methacrylate	methanol	(Coutinho et al., 1986)
methyl methacrylate	triethanol amine	(Pramanick, 1979)
methyl methacrylate	triethylamine	(Pramanick, 1979)
methyl methacrylate	water	(Pramanick and Sarkar, 1976)
methyl methacrylate	thiourea	(Pramanick and Chatterjee, 1981)
<i>N,N'</i> -methylenebis(acrylamide)	thiourea	(Paulrajan et al., 1983)
styrene	ethanol	(Kaeriyama, 1969)
styrene	cyclohexanone	(Kaeriyama, 1969)
styrene	dodecyl poly(ethylene oxide)	(Coutinho and Martins, 1991, 1992; Coutinho and Furtado, 1992)
vinyl acetate	amino tri(methylene phosphonic acid)	(Öz and Akar, 2000)

monomers that can be polymerized by radical polymerization by cerium(IV) ions, as well as an overview of the reductants used to generate the radicals.

When the reductant in the system is a polymer itself, the cerium(IV) mediated polymerization reactions allows one to graft another polymer onto the redox active polymer. A *graft copolymer* is a polymer in which a polymer chain of one polymer is chemically bonded to a polymer molecule of another monomer. The two components are known as the *backbone polymer* (or *substrate polymer*) and the *side-chain polymer* (or *rib polymer*). A graft copolymer differs from a block copolymer, because in the latter the addition takes place at one end of the substrate polymer, whereas this is not the case for a graft copolymer. In both cases the final product cannot be considered as a true copolymer because there is no random distribution of the monomers. The final polymeric products of both block and graft copolymerization look as if two polymers have been linked together. The experimental conditions of graft polymerization can be tuned so that a smaller or larger portion of the polymer that is intended to become the side chain is actually bonded to the polymer backbone. This ungrafted fraction of the side-chain polymer is called *homopolymer*. The term *homopolymer* is often used for the fraction of the side-chain polymer that can be extracted by a suitable solvent. Graft polymerization can be used to modify the substrate polymer and improve its properties. No phase separation of the two polymers is possible by the grafting process, because by grafting the polymer side chain is covalently linked to the backbone. Phase separation is a problem that often occurs in the case of physical blending. The grafting process can be influenced by the choice of the experimental conditions (Bhattacharyya and Maldas, 1984). The temperature has a large effect on the extent of grafting. In general the grafting yield increases with increasing temperature until a limiting value is reached. Further increase of the temperature beyond this limit causes an increased extent of radical termination and thus leads to a reduction of the grafting yield. The extent of grafting also increases with an increase of the Ce^{4+} concentration up to a certain limit; beyond the limit it levels off and even decreases with a further increase of the concentration of the initiator. The grafting yield increases with time, but tends to level off after some time. The influence of the monomer concentration on the yield is less obvious. In some cases an increase in monomer concentration has a positive effect, while it has a negative effect in other cases. It is often observed that more homopolymer is formed at high monomer concentrations.

Very often the redox active polymers that are used as backbone polymer are biopolymers like cellulose, which contains many oxidizable hydroxyl groups (Mino and Kaizerman, 1958; McDowall et al., 1984). Table 4 summarizes the different biopolymers and vinyl monomers used for graft polymerization. The graft polymerization process is a very complex chemical process, and all details are not understood yet. The formation of free radicals on these biopolymers can be demonstrated by electron spin resonance (Deshmukh and Singh, 1987). It is believed that the mechanism by which cerium(IV) generates the free radicals involves the formation of a complex between the cerium(IV) salt and the hydroxyl groups of the biopolymer. This complex subsequently disproportionates, with formation of a cerium(III) ion, a proton, and a free radical on the biopolymer chain. The presence of 1,2-diols in the substrate are of great importance for the graft polymerization with cerium(IV) salts (Hintz, 1966). A problem associated with this process is that the grafting yield is rather low. Okieimen and Ebhoaye

Table 4
Overview of studies of graft copolymerization initiated by ceric(IV) ions

Substrate	Monomer	Reference
agar	methacrylamide	(Athawale and Padwaldesai, 1999)
alginate acid	glycidyl methacrylate	(Vijayakumar et al., 1985)
amylopectin	acrylamide	(Rath and Singh, 1998)
amylopectin	hydroxyethyl methacrylate/methyl methacrylate	(Gurruchaga et al., 1992a, 1992b)
amylopectin	hydroxypropyl methacrylate/methyl methacrylate	(Gurruchaga et al., 1992a, 1992b)
amylopectin	hydroxyethyl methacrylate/ethyl methacrylate	(Gurruchaga et al., 1992a, 1992b)
amylopectin	hydroxypropyl methacrylate/ethyl methacrylate	(Gurruchaga et al., 1992a, 1992b)
amylose	acrylamide	(Karmakar and Singh, 1998)
amylose	butyl acrylate	(Vázquez et al., 1987a, 1987b)
amylose	butyl methacrylate	(Goñi et al., 1992)
amylose	ethyl acrylate	(Goñi et al., 1992)
amylose	ethyl methacrylate	(Goñi et al., 1992)
amylose	2-hydroxypropyl methacrylate/butyl acrylate	(Pascual et al., 1996)
amylose	2-hydroxypropyl methacrylate/ethyl acrylate	(Pascual et al., 1996)
amylose	2-hydroxypropyl methacrylate/methyl acrylate	(Pascual et al., 1996)
amylose	methyl acrylate	(Goñi et al., 1992)
carboxymethyl cellulose	acrylamide	(Biswal and Singh, 2004)
carboxymethyl cellulose	acrylonitrile	(Okieimen, 1998)
carboxymethyl cellulose	ethyl acrylate	(Okieimen, 1998; Okieimen and Ogbeifun, 1996)
carboxymethyl cellulose	methyl acrylate	(Okieimen, 1998; Okieimen and Ogbeifun, 1996)
carboxymethyl cellulose	ethyl methacrylate	(Okieimen, 1998; Okieimen and Ogbeifun, 1996)
carboxymethyl cellulose	methyl methacrylate	(Okieimen, 1998)
carboxymethyl starch	acrylamide	(Cao et al., 2002)
cassava starch	acrylonitrile	(Vera-Pacheco et al., 1993)
<i>cassia tora</i> gum	acrylonitrile	(Sharma et al., 2003)
α -cellulose	methyl methacrylate	(Saikia and Ali, 1999)
cellulose	acrylamide	(Gupta and Khandekar, 2006)
cellulose	acrylamide/methyl methacrylate comonomer	(Gupta and Khandekar, 2002)

continued on next page

Table 4, *continued*

Substrate	Monomer	Reference
cellulose	acrylic acid	(Casinos, 1994; Okieimen, 1987; Vitta et al., 1986; Vitta et al., 1989; Okieimen and Ebhoaye, 1986)
cellulose	acrylonitrile	(Gupta and Sahoo, 2001a; Gupta and Sahoo, 2001b; Rao and Kapur, 1969; Fanta et al., 1969; Hebeish and Mehta, 1968; Okieimen and Ebhoaye, 1986)
cellulose	ethyl acrylate	(Gupta et al., 2002)
cellulose	ethyl methacrylate	(Gupta and Sahoo, 2001a)
cellulose	glycidyl methacrylate	(Navarro et al., 1999; Shukla and Athalye, 1994)
cellulose	hydroxyethyl methacrylate	(Shukla et al., 1991)
cellulose	methyl acrylate	(Fernández et al., 1990b, 1992; Graczyk, 1986; Vitta et al., 1989; Misra et al., 1993)
cellulose	methyl methacrylate	(Ogiwara et al., 1970; Ogiwara and Kubota, 1970)
cellulose	<i>N</i> -acryloyl-6-caproic acid	(Barbucci et al., 1989)
cellulose	<i>N</i> -acryloyl glycine	(Barbucci et al., 1989)
cellulose	<i>N</i> -isopropylacrylamide	(Gupta and Khandekar, 2003)
cellulose	styrene	(Huang and Chandramouli, 1968; Shukla et al., 1993)
cellulose	vinyl acetate	(Fernández et al., 1990b, 1992)
cellulose	vinyl acetate/methyl acrylate	(Fernández et al., 1990a, 1990c, 1991)
cellulose	vinyl chloride	(Guthrie, 1962)
cellulose (delignified)	acrylonitrile	(Farag and Al-Afaeq, 2002)
cellulose (regenerate film)	methyl methacrylate	(Kondo et al., 1989; Gupta and Sahoo, 2001b)
cellulose-thiocarbamate	acrylonitrile	(Nagieb and El-Gammal, 1986)
cellulose-thiocarbamate	ethyl acrylate	(Nagieb and El-Gammal, 1986)
β -chitin	methyl methacrylate	(Ren and Tokura, 1994)
chitin	methyl methacrylate	(Ren et al., 1993)
chitin	vinyl acetate	(Don et al., 2002)
chitosan	ethyl methacrylate	(Fares and Al-Ta'ani, 2003)

continued on next page

Table 4, *continued*

Substrate	Monomer	Reference
chitosan	eugenol	(Jung et al., 2006)
chitosan	<i>N,N</i> -dimethyl- <i>N</i> -methacryloxyethyl- <i>N</i> -(3-sulfopropyl) ammonium	(Zhang et al., 2003b)
chitosan	4-vinylpyridine	(Yilmaz et al., 1998)
collagen	methyl acrylate	(Brauer and Termini, 1973)
collagen	methyl methacrylate	(Brauer and Termini, 1973)
corn starch	methyl acrylate	(Ge et al., 2005)
cotton	styrene	(Thejappa and Pandey, 1982)
cotton yarn	methacrylamide	(Mostafa, 2005)
cianoethylated cotton	acrylonitrile	(Kantouch et al., 1971)
cianoethylated cotton	methyl methacrylate	(Kantouch et al., 1971)
dextran	acrylamide/ <i>N</i> -(1,1-dimethyl-3-oxybutyl)acrylamide	(McCormick and Park, 1985)
dextran	<i>N</i> -isopropylacrylamide	(Wang et al., 2002)
dextran	methyl methacrylate	(Onishi et al., 1978; Onishi, 1980)
dextrin	methyl acrylate	(Okieimen and Egharevba, 1992)
gelatin	butyl acrylate	(Li et al., 1989)
gelatin	2-hydroxyethyl methacrylate/butyl acrylate	(Vázquez et al., 1995)
gelatin	methyl methacrylate	(Kumaraswamy et al., 1980)
gelatinized wheat starch	acrylonitrile	(Fanta et al., 1982, 2003)
guar gum	acrylonitrile	(Thimma et al., 2003)
guar gum	methyl methacrylate	(Chowdhury et al., 2001)
hemicellulose	acrylonitrile	(El-Shinnawy and El-Kalyoubi, 1985; Fanta et al., 1982)
hemicellulose	methyl acrylate	(Fanta et al., 1982)
holocellulose	methyl methacrylate	(Okieimen et al., 1987)
holocellulose (bleached)	acrylonitrile	(Okieimen and Idehen, 1987)
holocellulose (bleached)	methyl methacrylate	(Okieimen and Idehen, 1987)
holocellulose (thiolated)	acrylonitrile	(Okieimen and Idehen, 1987)
holocellulose (thiolated)	methyl methacrylate	(Okieimen and Idehen, 1987)
hydroxypropyl guar gum	acrylamide	(Nayak and Singh, 2001)
jute fiber	acrylonitrile	(Das et al., 1990; Nayak et al., 1991; Patra and Singh, 1994a, 1994b)

continued on next page

Table 4, *continued*

Substrate	Monomer	Reference
jute fiber	methyl methacrylate	(Chauhan et al., 2000; Patra and Singh, 1994a, 1994b)
kenaf fibers	acrylonitrile	(Eromosele and Agbo, 1999)
Kundoor mucilage	acrylamide	(Mishra and Bajpai, 2005)
lignin	acrylamide	(Meister et al., 1984)
maize starch	acrylic acid	(Athawale and Lele, 1998)
maize starch	methacrylonitrile	(Athawale and Lele, 2000)
mercaptochitin	methyl methacrylate	(Kurita et al., 2002)
methylcellulose	acrylic acid	(Eromosele et al., 2002)
mucilage (from <i>Plantago psyllium</i>)	acrylonitrile	(Mishra et al., 2002, 2003)
nitrocellulose	methyl methacrylate	(Sudhakar et al., 1979)
ovalbumin	acrylamide	(Imai and Iwakura, 1967)
ovalbumin	methyl methacrylate	(Imai and Iwakura, 1967)
paper	glycidyl acrylate	(Riande et al., 1970)
paper	methyl acrylate	(Riande et al., 1970)
pineapple leaf fiber	acrylonitrile	(Samal and Bhuyan, 1994)
pine lignin	acrylamide	(Meister and Patil, 1985)
poly(ether urethane)	acrylamide	(Feng et al., 1985)
poly(ethylene terephthalate) fiber	acrylic acid	(Chansook and Kiatkamjornwong, 2003)
poly(urethane) (segmented)	2-(methacryloyloxy)ethyl phosphorylcholine	(Korematsu et al., 2002)
poly(urethane) (segmented)	2-(methacryloyloxy)ethyl-2-(trimethylammonium)ethyl phosphate	(Tomita et al., 1999)
poly(vinyl alcohol)	acrylic acid	(Fang et al., 1992)
poly(vinyl alcohol)	acrylonitrile	(Jana et al., 2000; Jin and Huang, 1988)
poly(vinyl alcohol)	hydroxyethyl methacrylate	(Jin and Huang, 1988)
poly(vinyl alcohol)	methyl acrylate	(Chowdhury and Pal, 1999)
poly(vinyl alcohol)	methylacrylic acid	(Beliakova et al., 2004)
poly(vinyl alcohol)	methacryloxyethyl trimethylammonium chloride	(Zheng et al., 2005)
poly(vinyl alcohol)	methyl methacrylate	(Chowdhury and Banerjee, 1998)
sago starch	acrylonitrile	(Lutfor et al., 2001)
sago starch	glycidyl methacrylate	(Han et al., 2004)
sago starch	methyl acrylate	(Rahman et al., 2000)
sago starch	methyl methacrylate	(Fakhru'l-razi et al., 2001)

continued on next page

Table 4, *continued*

Substrate	Monomer	Reference
sago starch	styrene	(Janarthanan et al., 2003)
sericin	acrylonitrile	(Cho and Ahn, 1976b)
silk	acrylamide	(Cho and Ahn, 1976a)
silk	acrylonitrile	(Cho and Ahn, 1976a)
silk	methacrylamide	(Shim and Kim, 1969)
silk	methyl methacrylate	(Mohanty et al., 1983)
silk	tetrahydrofurfuryl acrylate	(El-Molla et al., 2001)
sisal	ethyl acrylate	(Barkakaty and Robson, 1979)
sisal	methyl acrylate	(Barkakaty and Robson, 1979)
sisal	methyl methacrylate	(Barkakaty and Robson, 1979)
sodium alginate	acrylamide	(Tripathy et al., 1999)
sodium alginate	methyl acrylate	(Shah et al., 1995)
sodium alginate	methyl methacrylate	(Shah et al., 1995)
sodium alginate (partially carboxymethylated)	methyl acrylate	(Patel et al., 1999)
starch	acrylamide	(Athawale and Mumbai, 1998; Willett and Finkenstadt, 2006)
starch	acrylic acid	(Okieimen et al., 1989)
starch	acrylonitrile	(Reyes et al., 1973; Pourjavadi and Zohuriaan-Mehr, 2002; Bazuaye et al., 1988; Nagaty et al., 1980)
starch	2-butenyl acrylate	(Abbott and James, 1981)
starch	butyl methacrylate	(Athawale and Rathi, 1997)
starch	ethyl acrylate	(Okieimen and Egharevba, 1989)
starch	ethyl methacrylate	(Athawale and Rathi, 1997)
starch	2-hydroxy-3-methacryloyloxypropyltrimethyl-ammonium chloride	(Fanta et al., 1970)
starch	methylacrylic acid	(Beliakova et al., 2004)
starch	methyl acrylate	(Patil and Fanta, 1993; Liu et al., 1993)
starch	methyl methacrylate	(Athawale and Rathi, 1997)
starch	<i>N</i> -tert-butylacrylamide	(Fares et al., 2003)
starch-coated polyethylene film	acrylonitrile	(Fanta et al., 2003)
styrene-maleic acid copolymer	acrylonitrile	(Vora et al., 1995)

continued on next page

Table 4, *continued*

Substrate	Monomer	Reference
wood pulp	acrylonitrile	(Lepoutre and Hui, 1975)
wood pulp	methyl methacrylate	(Hecker De Carvalho and Rudin, 1984)
wool fiber	acrylic acid	(Misra et al., 1980)
wool fiber	allyl methacrylate	(Abdel-Hay et al., 1982)
wool fiber	methyl methacrylate	(Kantouch et al., 1971; Misra et al., 1980; Shukla and Sharma, 1987)
wool fiber	vinyl acetate	(Misra et al., 1979)
wool (reduced)	acrylic acid	(Misra et al., 1981)
wool (reduced)	ethylacrylate	(Misra et al., 1980)

(1986) reported that on average less than five molecules of the side chain polymer are grafted onto one cellulose molecule. Another problem is that large quantities of the homopolymer are often formed. According to Okieimen (1998) the graft polymer formation on carboxymethyl-cellulose occurs preferentially by combination of the growing homopolymer chains with radicals formed on the backbone polymer rather than by the addition of monomer to the radicals formed on the backbone polymer. The extent of grafting depends on the physical state of the cellulose: the grafting mainly takes place in the amorphous region of the cellulose. The grafting of vinyl monomers on cellulose is usually carried out in aqueous medium, which is acidified to prevent hydrolysis of the cerium(IV) salt. Radical polymerizations are generally performed under an inert atmosphere, because oxygen has an inhibitory role on the reaction (oxygen is a radical scavenger).

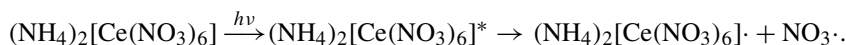
The graft copolymerization of acrylonitrile, acrylamide or acrylic acid on starch or related biopolymers is of great importance for the preparation of superabsorbent polymers (Po, 1994). *Superabsorbent polymers* (SAPs) are a group of materials that can absorb over one hundred times their weight in liquids and do not easily release the absorbed fluids under pressure. The possibility of SAPs to retain water relies on the formation of a hydrogel. The superabsorbent polymers have been discovered by researchers at the National Center for Agricultural Utilization Research of the United States Department of Agriculture in 1973. Applications for these polymers were originally focused in the agriculture/horticulture markets where they were used as hydrogels to retain moisture in the surrounding soil during growing and transportation. These applications are still of prime importance. However, the popularity of superabsorbent polymers increased dramatically since they are being used as active material in disposable diapers. Other related applications include adult incontinence products and feminine hygiene products. In industry, SAPs are being used in packaging materials and for disposal of liquid waste. The original superabsorbent polymers were saponified starch-graft polyacrylonitrile copolymers, and they became known under the trivial name “*Super Slurper*”. Ammonium hexanitratocerate(IV) has been used as an initiator with 0.1 mole of cerium(IV) ions in 1 N nitric acid. Optimal results are obtained when starch was gelatinized by heating in water at 80 °C for an hour prior to the reaction. The graft polymerization occurs at around 30 °C and atmospheric pressure. The starch chains are broken down by the gelatinization. This gives and increased reactivity with acrylonitrile monomers and a higher molecular weight product. After graft polymerization, the cyano groups have to be saponified to carboxylate or amide groups. The saponification reaction takes place at 95 °C and atmospheric pressure with a ratio of alkali to acrylonitrile of 0.6–0.8 to 1. Washing with water removes excess salts produced during saponification. Although acrylonitrile was used initially, acrylic acid is presently often the preferred monomer, because it is non-toxic. Several starch sources can be used. Examples include corn, potato, and rice starches. The final product looks like flakes of dried, colorless gelatin.

Ceric(IV)-mediated graft polymerization can also be used to prepare inorganic–organic hybrid materials. Rao et al. (1981) grafted methyl methacrylate and acrylonitrile on mica. Murugan and Ramakrishna (2004) grafted glycidylmethacrylate on a demineralized bone matrix, while Wang et al. (2005) grafted *N*-isopropylacrylamide on hydroxylated glass coated with 3-aminopropyltriethoxysilane.

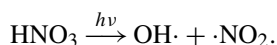
10. Miscellaneous reactions

10.1. Generation of nitrate free radicals

Martin and coworkers showed that nitrate free radicals can be generated efficiently at room temperature by flash photolysis of a solution of ammonium hexanitratocerate(IV) in a 6 M aqueous nitric acid solution, upon irradiation with light quanta between 280 and 400 nm (Martin et al., 1963, 1964). Although there was the opinion that these nitrate free radicals arose from the direct photolysis of undissociated nitric acid solvent molecules (Hayon and Saito, 1965), Martin and Glass (Glass and Martin, 1970; Martin and Glass, 1970) were convinced that the cerium(IV) ion was directly involved in the generation of the radicals. It has been suggested that the $\text{NO}_3\cdot$ radicals are formed by an intramolecular electron-transfer process in the excited cerium(IV) complex (Wine et al., 1988; Glass and Martin, 1970):

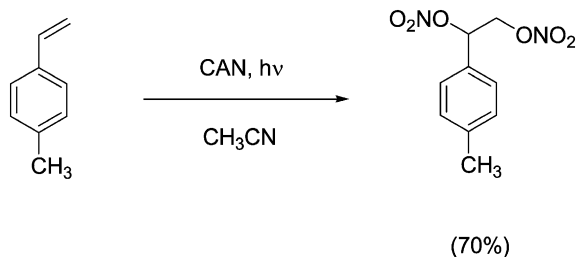


It has been shown later that under the same experimental conditions as those used for the photolysis of ammonium hexanitratocerate(IV), nitric acid is decomposed in hydroxyl radicals and nitrogen dioxide (Vione et al., 2001):



The quantum yield for the generation of the nitrate free radical by photolysis of CAN in presence of nitric acid is quite high at 360 nm. It ranges from 51% for 0.1 M HNO_3 to 88% for 1 M HNO_3 (Herrmann et al., 1991). The nitration of naphthalene with photochemically generated nitrate free radicals in an aqueous nitric acid solution has been investigated as part of an environmental study on the reactivity of polyaromatic compounds in the hydrosphere (Vione et al., 2005). The main product was 1-nitronaphthalene, with 2-nitronaphthalene being a byproduct. However, it was found that the formation rate of both 1-nitronaphthalene and 2-nitronaphthalene are higher in the dark than under UV irradiation, which suggests that the nitrate free radical mediated nitration is an unimportant pathway for naphthalene nitration in aqueous solutions. No nitronaphthalenes were formed in the dark in presence of nitric acid alone.

The $\text{NO}_3\cdot$ radicals can also be generated by flash photolysis of CAN in acetonitrile (Del Giacco et al., 1993). These photochemically produced nitrate free radicals have been used to study the one-electron oxidation of methylbenzenes. Depending on the oxidation potential of the substrate, radical cations or benzyl-type neutral radicals were formed. Formation of radical cations was observed for most of the methylbenzene derivatives that were studied, whereas formation of the benzyl radical was observed with toluene and with *ortho*- and *meta*-xylene. This reaction is not useful for synthetic applications. The reactivity of propellane C–C bonds towards free nitrate radicals photochemically generated from ammonium hexanitratocerate(IV) in acetonitrile was studied from both theoretical and experimental points of view (Fokin et al., 2000). Baciocchi and coworkers reported that the photochemical reaction of CAN in acetonitrile with cyclohexene, 1-octene and styrene derivatives leads to the formation of 1,2-dinitrate adducts in high yields (scheme 65) (Baciocchi et al., 1988b).



Scheme 65.

10.2. Decomposition of water

Because of the strongly oxidizing power of cerium(IV) ions, aqueous solutions of cerium(IV) are metastable with regard to the oxidation of water to oxygen gas. However, the kinetics of this reaction is very slow so that acidic aqueous solution of cerium(IV) can be stored for a long time without appreciable reduction of cerium(IV) to cerium(III). The reaction is only observed in presence of a catalyst, although it should be noticed that the wall of a glass vessel can show catalytic activity. The slowness of the reaction in the absence of a catalyst can be explained by the fact the oxidation of water to oxygen ($2\text{H}_2\text{O} \rightarrow 4\text{H}^+ + \text{O}_2 + 4\text{e}^-$) is a four-electron process. Because it is very difficult to get the four electrons at the same place at the same time, this reaction has a high overpotential (although the E_0 value is not higher than +1.23 V) (Mills, 1989).

Grant and Payne (1961) report that the decomposition of water by cerium(IV) is catalyzed heterogeneously at the surface of a glass vessel and by precipitated material in the solution. Grant (1964) also observed reduction of cerium(IV) by water upon heating a solution of cerium(IV) sulfate in sulfuric acid. Cerium(IV) containing solids and added silver(I) and mercury(II) ions were found to catalyze the redox reaction. However added copper(II) retarded the reaction. The silver(I) catalyzed oxidation of water with cerium(IV) in aqueous perchloric solutions was studied in detail by Indrayan and coworkers (Indrayan et al., 1982). Bruce and coworkers (King et al., 2005) showed that RuO_2 nanoparticles supported on mesoporous silica are very active in catalyzing the oxidation of water by cerium(IV) in sulfuric acid solution.

Cerium(IV) undergoes photochemical reduction in water, whereby water is oxidized to oxygen gas (Baur, 1908; Weiss and Porret, 1937; Heidt and Smith, 1948; Sworski, 1957). On the other hand, cerium(III) ions undergo photochemical oxidation, resulting in the formation of hydrogen gas (Heidt and McMillan, 1954). Because cerium(IV) can oxidize water in the dark, and cerium(III) can reduce water only in light, an experimental set-up can be designed in such a way that an aqueous solution of cerium(IV) and cerium(III) can produce pure oxygen in the dark and almost pure hydrogen or a mixture of oxygen and hydrogen in light (Heidt and McMillan, 1953). Because cerium(III) can only absorb UV light, the efficiency of the photoreduction of water is low. As mentioned above, the oxidation of water by cerium(IV) can be mediated by different catalysts. Cerium dioxide is a promising photocatalyst for the splitting of water into oxygen (Bamwenda and Arakawa, 2000, 2001; Bamwenda

et al., 2001). The oxygen is formed when a suspension of CeO_2 in an aqueous Ce^{4+} solution is illuminated by UV irradiation. When the energy of the absorbed radiation is larger than the band-gap of cerium dioxide, an electron-hole pair is created in the material. Electrons can be removed from the cerium oxide by surface-adsorbed Ce^{4+} ions, reducing them to Ce^{3+} . Simultaneously, surface-adsorbed water molecules are oxidized by the holes to oxygen in a four-electron exchange process. The role of Ce^{4+} is thus to act as an electron acceptor to remove the photogenerated electrons from the conduction band. The Ce^{3+} ions can be oxidized to Ce^{4+} in a photochemical process that involves the direct photoexcitation of the Ce^{3+} ion, which is followed by the reduction of protons or water to hydrogen gas. Alternatively, Ce^{4+} can be regenerated by reaction of Ce^{3+} on the surface with holes. Other semiconductor materials like WO_3 or TiO_2 show photocatalytic behavior as well. Research efforts are made towards the use of cerium dioxide for the overall splitting of water into oxygen and hydrogen, because this could be a means of solar energy conversion.

10.3. Hydrolysis of phosphodiester and DNA

Cerium(IV) complexes are used as very efficient non-enzymatic reagents for the hydrolysis of phosphodiester and the phosphodiester backbone of DNA (Ott and Krämer, 1999; Franklin, 2001; Mancin et al., 2005; Komiyama et al., 1999; Komiyama, 2005; Sreedhara Cowan, 2001). DNA is very resistant to spontaneous (uncatalyzed) hydrolysis. It has been estimated that the half-life of a single phosphodiester P-O bond at pH 7 and 25 °C is about 200 million years (Kim and Chin, 1992; Williams et al., 1999)! Although such hydrolytic inertness is a great advantage for the preservation of the genetic code, it makes DNA manipulation (expression, duplication, repair of damage) difficult. Nature solves this problem by the use of a variety of hydrolytic enzymes, like the nucleases. Many of these enzymes are metalloenzymes that contain a calcium(II), magnesium(II) or zinc(II) ion in the active site. Other studies have shown that transition metal ions, and especially the rare-earth ions, effectively accelerate the hydrolysis of phosphate esters (Takasaki and Chin, 1994; Komiyama et al., 1994a, 1995; Komiyama, 2005; Roigk et al., 1998).

The extremely high resistance of DNA towards hydrolysis makes it very difficult to study the mechanism of the hydrolysis reaction. Therefore, DNA is replaced in many studies by more reactive compounds with a phosphodiester bond (chart 1). Bis-(*p*-nitrophenyl)phosphate (BNPP) is a very popular model compound for the study of the hydrolytic cleavage by nucleases. Hydrolysis of the diphosphate ester yields two equivalents of a yellow nitrophenolate product, the formation of which can be monitored by spectrophotometry ($\lambda_{\text{max}} =$

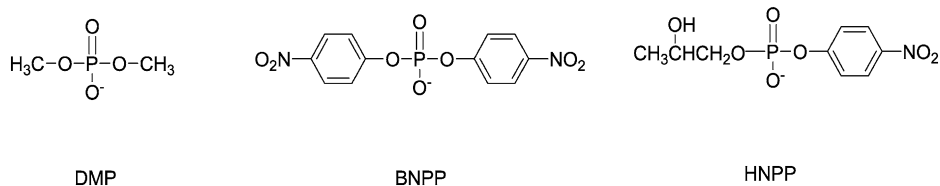
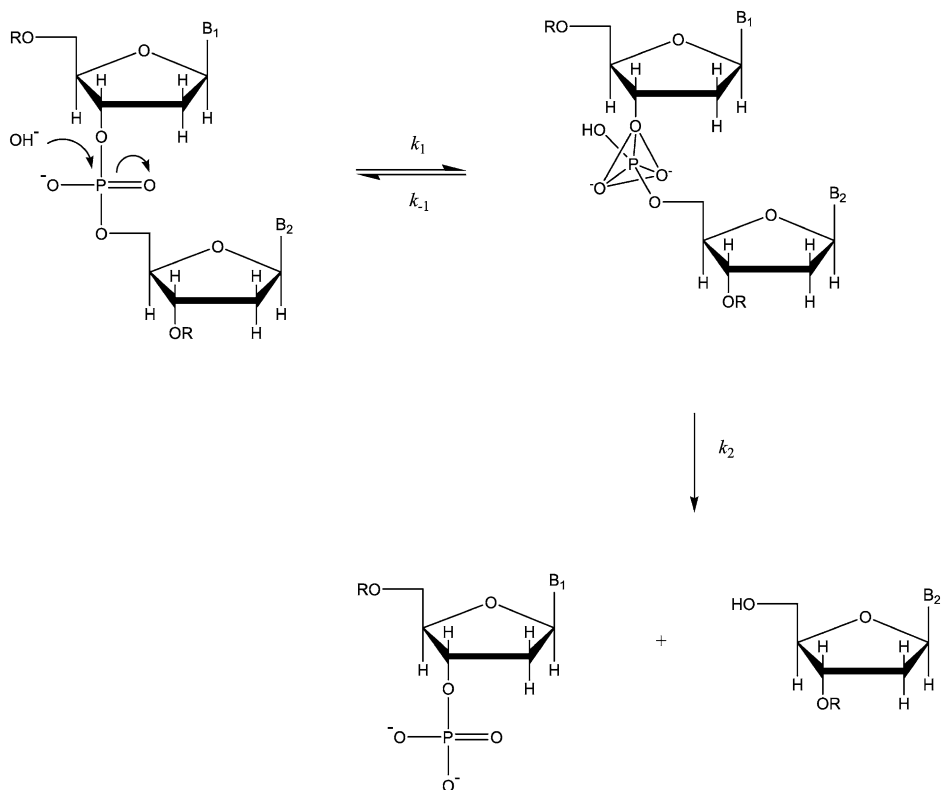


Chart 1. Model compounds for the study of phosphodiester hydrolysis.



400 nm). Other model compounds are dimethyl phosphate (DMP), and 2-hydroxypropyl (*p*-nitrophenyl) phosphate (HNPP) (chart 1). Supercoiled DNA is a more reactive form of DNA that can also be used in the study of hydrolytic cleavage, because it is activated by strain and other factors.

The presently accepted mechanism for the hydrolysis of the phosphodiester backbone of DNA involves the nucleophilic attack of the phosphorus atom by the oxygen atom of water or a hydroxide ion to give a five-coordinate phosphate intermediate (Hegg and Burstyn, 1998; Komiyama and Sumaoka, 1998; Komiyama et al., 1999) (scheme 66). This attack is followed by cleavage, leaving ROH and ROPO₃(H₂) termini. In metal-assisted hydrolysis, the metal activates, as a Lewis acid, the phosphate group for attack by the nucleophile, increases the leaving group ability of the alcohol, or activates a metal-coordinated water molecule as a nucleophile (Mancin et al., 2005). Multinuclear complexes are often more active than mononuclear complexes. This is in agreement with the finding that many natural metallonucleases make use of the cooperative action of two or more metal ions. A high charge-to-ionic size diameter seems to be necessary for efficient catalysis of phosphodiester hydrolysis.

The Ce^{4+} ion has been found to enhance the rate of BNPP hydrolysis by a factor of more than 10^{10} and the rate of DNA hydrolysis by a factor of more than 10^{11} (Rammo et al., 1996; Komiyama, 1999; Moss and Ragnathan, 1998; Sumaoka et al., 1998a)! These rates are 20 to 1000 times faster than the rates of hydrolysis catalyzed by trivalent lanthanide ions. In fact, the Ce^{4+} ion is of all metal ions the best catalyst for DNA hydrolysis. It should be noticed that the trivalent lanthanide ions are better catalysts for the hydrolysis of RNA than Ce^{4+} (Komiyama et al., 2005). The rate of DNA hydrolysis is almost constant in the pH range from 2.5 to pH 8.5. The nature of the nucleic acid bases does not influence the hydrolysis rate. At pH 7 and 50°C , the half-life of the phosphodiester of DNA is reduced to a few hours (Komiyama et al., 1994a, 1995). Some other substrates are hydrolyzed very fast: at pH 7 and 30°C , the half-lives of the 3,5-cyclic monophosphates of adenosine and guanosine in presence of 0.1 M ammonium hexanitratocerate(IV) are as short as 7 and 16 seconds, respectively (Sumaoka et al., 1994). Cerium(III) becomes a more efficient catalyst for phosphodiester hydrolysis in presence of molecular oxygen, due to the oxidation of cerium(III) to cerium(IV) (Komiyama et al., 1995). The activity of cerium(IV) is independent of the presence of molecular oxygen. Despite the redox activity of cerium(IV), the hydrolysis of phosphodiester by cerium(IV) takes place through a purely hydrolytic pathway, rather than through an oxidative pathway (Moss and Ragnathan, 1998). No oxidative cleavage of the deoxyribose units occurs. In a study to determine whether the P–O or the C–O bond is cleaved during phosphodiester hydrolysis, it was found that dimethylphosphate is cleaved by cerium(IV) with 91% P–O scission (Moss and Morales-Rojas, 1999). Phosphomonoesters are faster hydrolyzed by cerium(IV) than phosphodiester (Miyama et al., 1997). The selectivity of cerium(IV) for hydrolysis of phosphomonoesters over phosphodiester can be increased by using concentrated buffer solutions of tris(hydroxymethyl)methylamine (TRIS) or *N'*-(2-hydroxyethyl)piperazine-*N*-ethanesulfonic acid (HEPES). This selectivity is useful for selective removal of the terminal monophosphate from a dinucleotide.

Core-level photoelectron spectra of the $2p$ orbitals of the phosphorus atom in diphenyl phosphate (DPP) show that the binding energy of the orbitals is much greater in the cerium(IV)-DPP complexes than in the complexes formed with the trivalent lanthanide ions (Shigekawa et al., 1996). This indicates that cerium(IV) is more effective in electron-withdrawal from the phosphate than the trivalent lanthanide ions. The electron-withdrawing effect results in a higher electrophilicity of the phosphodiester linkage. The active role of the cerium $4f$ orbitals in the hydrolysis of phosphodiester was investigated by EXAFS and XANES (Shigekawa et al., 1999). It was observed that upon complex formation of cerium(IV) with DPP, 0.67 electrons are present in the $4f$ orbitals. Because one expects empty $4f$ orbitals for cerium(IV) (Ce^{4+} has no $4f$ electrons), these results show that electron density was transferred from the environment to cerium(IV). Most trivalent lanthanide ions cannot accept electrons (their divalent state is too unstable). There is evidence that the orbitals of the phosphodiester linkage mix with the $4f$ orbitals of cerium(IV) to form new hybrid orbitals (Komiyama et al., 1999). This mixing is possible because the $4f$ orbitals of cerium(IV) are lower in energy than the $4f$ orbitals of the lanthanide(III) ions. These two factors, electron-withdrawal from the phosphate by cerium(IV) and the formation of hybrid orbitals, activate the phosphodiester linkage greatly for nucleophilic attack. The phosphate

group is actually attacked by a hydroxide ion coordinated to one or two cerium(IV) ions. The most active catalytic species is $[\text{Ce}_2(\text{OH})_4]^{4+}$. The phosphodiester is thus coordinated by two cerium(IV) in a bimetallic complex. The cerium(IV) hydroxo cluster stabilizes the negatively charged transition state of DNA hydrolysis, and the pentacoordinate intermediate is efficiently formed. The water bound to cerium(IV) acts as an acid catalyst in the breakdown of this pentacoordinate intermediate, which is the rate-limiting step in the catalytic process. A comparison of the catalytic activity of different cerium(IV) hydroxo species in aqueous acetonitrile solutions was made by Maldonado and Yatsimirsky (2005). The catalytic activity was found to increase with increasing positive charge of the hydroxo species: $[\text{Ce}_4(\text{OH})_{15}]^+ < [\text{Ce}_4(\text{OH})_{14}]^{2+} < [\text{Ce}_4(\text{OH})_{13}]^{3+}$. The $[\text{Ce}_4(\text{OH})_{15}]^+$ complex occurs at $\text{pH} > 7$, $[\text{Ce}_4(\text{OH})_{13}]^{3+}$ below $\text{pH} 5$ and $[\text{Ce}_4(\text{OH})_{14}]^{2+}$ at intermediate pH values.

The activity of cerium for DNA hydrolysis can be enhanced further by one order of magnitude by addition of a praseodymium(III) salt ($\text{Ce}^{4+} : \text{Pr}^{3+}$ ratio is 2) (Tikeda et al., 1996). The two metal ions form a mixed hydroxo cluster, which is the active catalytic species. The function of praseodymium(III) is to provide metal-bound water to act as the acid catalyst in the cleavage of the intermediate (Komiya et al., 1999). Cooperative effects were also observed for the ternary system cerium(IV)–lanthanide(III)–dextran (Sumaoka et al., 1994, 1997, 1998b).

Most of the studies of the cerium(IV) catalyzed hydrolysis of phosphodiester are performed under acidic conditions. For instance, Moss and Ragunathan (1998) investigated the hydrolysis of dimethyl phosphate by ammonium hexanitratocerate(IV) at $\text{pH} 1.8$. Above $\text{pH} 4$, the formation and precipitation of cerium(IV) hydroxide gels hinders kinetic studies under physiological conditions. Complexation of the cerium(IV) ions could solve this problem. However stable cerium(IV) have a much lower activity than the free ion, probably because of the reduction of the overall charge of the complex and because of the saturation of the coordination sphere. An exception is the cerium(IV)-EDTA complex, that has a high activity for hydrolysis of DNA (Igawa et al., 2000). The catalytic activity of the cerium(IV)-EDTA complex is increased in presence of amines like ethylenediamine and spermine (Sumaoka et al., 2001). The degree of polymerization of DNA is crucial for the catalytic activity: the cerium(IV)-EDTA complex hydrolyzes oligonucleotides longer than tetranucleotides under physiological conditions, but not dinucleotides or trinucleotides (Igawa et al., 2000). The cerium(IV) EDTA complex hydrolyses single-stranded DNA far more efficiently than double-stranded DNA (Kitamura et al., 2003). By using this selectivity, gap-sites in DNA are preferentially hydrolyzed (Kitamura and Komiya, 2002). Unfortunately, this gap-site selective DNA hydrolysis is rather slow. Co-catalysts were designed to accelerate the selective hydrolysis at the gap site. Examples are oligoamine–acridine conjugates (Yamamoto et al., 2003). Kimiyama and coworkers tried to overcome the cerium hydroxo gel formation at physiological pH by forming a weak complex of cerium(IV) and γ -cyclodextrin (Sumaoka et al., 1994). Yan and coworkers investigated the catalytic activity of a cerium(IV) complex of ligands that can be considered as EDTA-bridged β -dimers (Yan et al., 2002). Cyclodextrins are able to bind a variety of hydrophobic substrates. The hydrophobic binding sites strongly contribute to the catalytic activity towards hydrolysis of BNPP. It was estimated that the cyclodextrin accelerates the reaction by a factor of 520 in comparison to the rate observed for the cerium(IV)

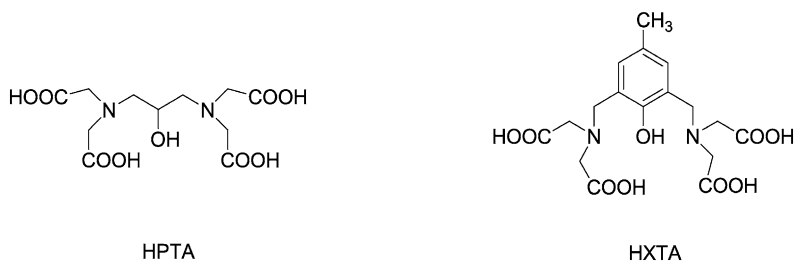


Chart 2. Aminopolycarboxylate ligands for cerium(IV).

complex of the dimethyl ester of EDTA. A remarkably fast cleavage of BNPP was observed by cerium(IV) complexes in an aqueous micellar solution (Bracken et al., 1997). The micelles were formed by the nonionic surfactant Brij-35 (a polyoxyethylene monolauryl ether). Ligands were palmitic acid, *N*-octanoyl-*N*-methyl-D-glucamine and 4-(1-hexadecynyl)-2,6-pyridinedicarboxylic acid. A complex composed of algae polysaccharides and cerium(IV) was found to be able to split supercoiled DNA into its linear form (Wang et al., 2005).

Cerium(IV)-containing systems that are able to catalyze sequence-specific hydrolysis of DNA are prototypes of artificial restriction enzymes. Site-selective DNA hydrolysis was achieved by attaching cerium(IV) complexes to sequence-recognizing antisense deoxy-oligonucleotides (Komiyama et al., 1994b; Komiyama, 1995). Komiyama used a system consisting of a ligand with an iminodiacetate group for cerium(IV) binding appended to a 19-mer DNA oligonucleotide for DNA recognition. A single strand 40-residue DNA was selectively cleaved at the linkage between residue 30 and residue 31 (Komiyama, 1995). There is no evidence for the self-digestion of the cerium(IV)-oligomer conjugate. Taking into account the fact that DNA is preferentially hydrolyzed at gap structures (see above), selective DNA hydrolysis can be obtained by forming gap structures in predetermined positions in substrate DNA (Chen et al., 2004). This gap formation can be obtained either by using two oligonucleotide additives that bear a monophosphate group at the termini through various linkers (Chen et al., 2004), by two oligonucleotides bearing ethylenediamine-*N,N,N',N'*-triacetate groups (Komiyama et al., 2005), or by one oligonucleotide additive bearing two monophosphate groups (Chen and Komiyama, 2005). The one-additive system is simpler and more convenient. Moreover, it has a higher stability so that it can be used at higher reaction temperatures.

The dicerium(IV) complex of 1,3-amino-2-hydroxypropane-*N,N,N',N'*-tetraacetate (HPTA) is capable of double-strand cleavage of plasmid DNA (chart 2) (Branum and Que, 1999). This is in contrast with the behavior of cerium(IV)-EDTA which favors single-strand cleavage of DNA. Another complex able of double-strand hydrolysis is the dicerium(IV) complex of 5-methyl-2-hydroxy-1,3-xylene- α,α' -diamine-*N,N,N',N'*-tetraacetic acid (HXTA) (chart 2) (Branum et al., 2001). Progress to site-selective two-strand hydrolysis of double-stranded DNA was made by Komiyama and coworkers (Yamamoto et al., 2004). They formed gap-like structures at predesigned sites in double-stranded DNA by using invasion of two

pseudo-complementary peptide nucleic acid additives. The cerium(IV)-EDTA complex divides the double-stranded DNA into the desired two fragments.

The hydrolysis of phosphonic acid esters in Brij-35 micelles by cerium(IV) was investigated by Moss and Ragunathan (1999). The phosphonic esters differ from the phosphodiester by the presence of only one ester bond and by a direct bond between phosphorus and the carbon atom of an alkyl or aryl group. Cerium(IV) ions also accelerate the hydrolysis of these diesters (Moss and Morales-Rojas, 2001; Moss et al., 2004). The phosphonoformate diesters show structural similarities with the phosphodiester. Whereas zirconium(IV) and hafnium(IV) hydrolyze mainly the P-OR bond, cerium(IV) and thorium(IV) hydrolyze principally the C-OR bond in the phosphonoformate diesters. This chemoselective ester hydrolysis was not observed for the phosphodiester compounds.

10.4. Hydrolysis of peptides

The Ce^{4+} ion is one of the most active catalysts for peptide hydrolysis. Its activity is much higher than that of the trivalent lanthanide ions and other transition metal ions. In particular, Ce^{4+} is far superior to other tetravalent ions like Zr^{4+} or Hf^{4+} . Yashiro et al. (1994) reported that dipeptides and tripeptides were efficiently hydrolyzed under neutral conditions by the γ -cyclodextrin complex of cerium(IV). Komiyama and coworkers (Takarada et al., 2000) studied the catalytic hydrolysis of oligopeptides by cerium(IV) salts. The hydrolysis is fast, especially when the oligopeptides contain no metal-coordinating side-chains. The hydrolysis rates of the dipeptides, tripeptides and tetrapeptides is similar. The hydrolysis reaction was performed at pH 7 and 50 °C and under these conditions, the half-life of the amide bond was only a few hours. The authors found that ammonium hexanitratocerate(IV) is more active than other cerium(IV) compounds like ammonium cerium(IV) sulfate, cerium(IV) sulfate and cerium(IV) hydroxide. The lower reactivity of ammonium cerium(IV) sulfate is ascribed to the competitive inhibition by sulfate ions, while the low reactivity of cerium(IV) sulfate and cerium(IV) hydroxide can be explained by their poor solubility in water. However, in the reaction mixtures at the given reaction conditions, most of the cerium(IV) consists in a gel of cerium(IV) hydroxides. No oxidative cleavage has been observed.

11. Various applications

11.1. TLC stains

The most typical way of visualizing a developed TLC (Thin Layer Chromatography) plate is by examining it under UV light to observe the quenching of the luminescence of the phosphor in the alumina or silica gel layer by chromophoric groups of the organic compound. Unfortunately, many compounds do not have chromophoric groups. In this case, the spots on a TLC plate must be visualized by other means, typically by treating with a vapor or solution which reacts with residues on the plate to produce an image. Various staining solutions are based on cerium(IV) salts (Stahl, 1965; Touchstone, 1982; Touchstone and Dobbins, 1978). Cerium molybdate is prepared by dissolving cerium(IV)

sulfate and ammonium heptamolybdate in dilute sulfuric acid. Ammonium hexanitratocerate(IV) can be used instead of cerium(IV) sulfate. Cerium molybdate reagent is also known as “*Hanessian's Stain*” or “*Blue stain*”. It is a general purpose stain, but it is very good for visualizing hydroxy groups. The stain requires heating to make the spots visible on the TLC plate. A stain prepared by dissolving cerium(IV) sulfate in dilute sulfuric acid is useful for alkaloids.

11.2. *Test reagents*

An application that has now become obsolete, but which is worth to be mentioned, is the use of cerium(IV) solutions as a test reagent for alcohols (Duke and Smith, 1940; Feigl, 1954), which form red 1 : 1 complexes upon coordination to cerium(IV) (Young and Trahanovsky, 1969). The reagent is either a solution of 400 g of $(\text{NH}_4)_2[\text{Ce}(\text{NO}_3)_6]$ in 1 liter of 2 M HNO_3 , or a solution of 0.5 M $\text{Ce}(\text{ClO}_4)_4$ in 2 M HClO_4 . One ml of this test solution is diluted with 2 ml water or dioxane. The unknown material is dissolved in as little water or dioxane as possible, and one drop of this solution is added to the diluted test solution. A color change from yellow to red indicates the presence of primary, secondary or tertiary alcohols. Aldehydes, ketones, acids, esters and hydrocarbons do not interfere. Aliphatic amines could induce a raise in pH, leading to precipitation of cerium(IV) hydroxides. Aromatic phenols and amines interfere by the formation of colored complexes. Compounds that are easily oxidized may reduce the test reagent. The formation constant of cerium(IV) with different types of alcohols have been determined in aqueous acetonitrile containing 0.5 M nitric acid (Young and Trahanovsky, 1969). When ammonium hexanitratocerate(IV) is used as the source of cerium(IV) it is found that the nitrate ions are competing with the alcohol molecules for coordination to cerium(IV).

11.3. *CAN as etchant*

Solutions of ammonium hexanitratocerate(IV) in dilute perchloric acid or in dilute nitric acid are being widely used as etchants for the preparation of printed circuit boards, and in the semiconductor and microelectronics industry (Basceri et al., 2004). They are also used for cleaning surfaces prior to soldering (GFS Chemicals product catalog). They are particularly useful for etching nichrome, monel, stainless steel and many other ferrous and non-ferrous alloys (Acocella and David, 1988).

11.4. *Ceric-cerous sulfate dosimeter*

The *ceric-cerous sulfate dosimeter* is a chemical dosimeter acting either as a routine dosimeter or as a reference standard dosimeter for the measurement of high dose levels (Matthews, 1982). A routine dosimeter is used in radiation processing facilities for dose mapping. A reference standard dosimeter is used to calibrate radiation fields and routine dosimeters. The dosimeter is based on the reduction of cerium(IV) to cerium(III) in an aqueous solution by radiation (Matthews, 1971). Doses in the range 0.5 to 50 kGy can be determined by conventional spectrophotometric analysis in the ultraviolet region, or by measuring the difference in the electrochemical potential between the irradiated and non-irradiated solutions in an electrochemical potentiometer (Matthews, 1972; Church et al., 1976). As most dosimeters, the

ceric-cerous sulfate dosimeter does not exhibit a strict linear relationship between readout signal and absorbed dose. This means that it is not possible to define a single calibration factor for this type of dosimeter, and a curved calibration function has to be used instead. A new method to read out the dosimeter is via measurement of the NMR relaxation rate (Bäck et al., 2002). Applications of this type of dosimeters are found in the fields of food irradiation or radiation sterilization of medical devices to measure the amount of γ -radiation that the product has received in the irradiation facility.

11.5. *CerOxTM* process

The *CerOxTM* is a cerium-catalyzed electrochemical oxidation process for the destruction of organic hazardous wastes (Nelson, 2002; Surma et al., 1998, 1999; Steward, 1998). Applications of the process include the destruction of polychlorobenzenes (PCBs), dioxins, tetrachloroethylene, and a variety of chlorinated pesticides and herbicides. Non-chlorinated organic waste compounds like amines and phenols can also be destroyed by this technique. The *CerOxTM* process was originally developed by the Pacific Northwest National Laboratory and has been commercialized by *CerOx Corporation* (www.cerox.com). The oxidation reactions convert the organic material primarily into carbon dioxide and water, whereas carbon bound chlorine is converted to chlorine gas. Other heteroatoms such as nitrogen, phosphorus and sulfur are oxidized to respectively nitric, phosphoric and sulfuric acid. The chlorine gas that is formed by the oxidation of the chlorinated organic compounds is removed from the exhaust gas stream before venting. The *CerOxTM* process is performed in a series of enclosed tanks and pipes to avoid contamination of the environment. The electrolyte in the cathodic part is 4 M nitric acid. The organic waste materials are injected into the oxidizing electrolyte through an ultrasonic mixer (sonicator) that emulsifies the organic phase into the aqueous phase. The oxidative destruction of the organic waste by cerium(IV) takes place at 90 to 95 °C. The active cerium(IV) oxidant is regenerated from the reduced cerium(III) by reoxidation at the anode in the electrochemical cell. At the same time, nitrous acid, HNO₂, is formed by reduction of nitric acid at the cathode. However nitrous acid disproportionates in solution to produce nitric acid and nitric oxide, NO. The gaseous NO is oxidized with atmospheric oxygen to NO₂, which is redissolved in water to produce nitric acid. In this way much of the nitric acid consumed by the cathode reaction can be recycled. A schematic presentation of the liquid phase treatment in the *CerOxTM* process is shown in fig. 7. From time to time the cerium-containing electrolyte has to be replaced because of accumulation of inorganic salts in the electrolyte. In large systems, the removal process is done continuously. The anodic processes (waste destruction) are separated from the cathodic processes by a Nafion[®] membrane. The membrane allows the free passage of protons between the two cell compartments, but it is impermeable to anions. The electrodes are made of titanium, but the anode surface is covered with a layer of electroplated platinum metal. The electrolyte in the anodic part of the electrochemical cell is cerium nitrate (1.5 M) in 3.5 M nitric acid solution. Typically 2/3 of the cerium is present in the form of cerium(IV) and 1/3 in the form of cerium(III). This ratio provides a high enough cerium(IV) concentration for oxidation of the organic compounds, but makes the concentration potential for the anodic oxidation of cerium(III) not too high. The technology presented

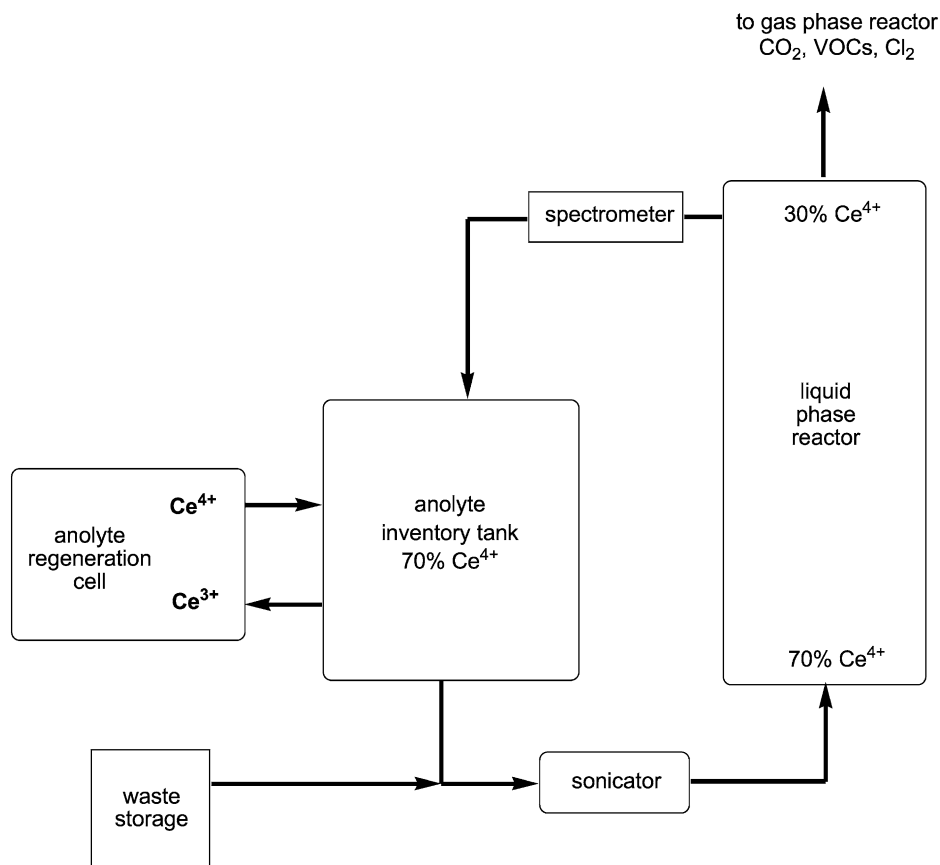


Figure 7. Liquid phase treatment in the *CerOx*TM process.

here is in many ways similar to the cerium-mediated electrosynthesis process discussed in section 8, but with the main difference that in the present case the process is intended for the destruction of organic compounds, not for their synthesis.

11.6. Model for tetravalent plutonium

The coordination chemistry of tetravalent cerium is in many aspects very similar to the coordination chemistry of tetravalent plutonium. The ionic radius of Ce^{4+} (0.94 Å) is within the experimental error identical to the ionic radius of Pu^{4+} (Shannon and Prewitt, 1969). Due to the similarity in the charge-to-ionic size ratio, the complex formation constants of tetravalent cerium are essentially the same as those of tetravalent plutonium. Complex formation causes for the two metal systems the same shift of the $\text{M}^{4+}/\text{M}^{3+}$ redox potential. Cerium(IV) complexes are therefore good models for predicting the coordination chemistry

of plutonium(IV) (Gorden et al., 2003). Working with plutonium(IV) itself is difficult and expensive, because of the safety precautions that are necessary when handling this highly radioactive and chemotoxic material and because of the limited availability of plutonium in comparison with cerium. A good knowledge of the coordination chemistry of plutonium is however necessary to develop sequestering agents that are specific for the removal of plutonium(IV). Such sequestering agents are useful for environmental remediation and for chelation therapy (removal of plutonium from the human body after accidental uptake). The knowledge of plutonium chemistry is also of interest for the development of selective extraction agents. However, due to the very similar aqueous coordination chemistry of cerium(IV) and plutonium(IV) it is very difficult to separate cerium from plutonium. This is an important issue, because fission products in spent nuclear fuel rods contain often large quantities of rare earths. Pioneering work in the field of actinide specific sequestering agents has been done by Raymond and coworkers (Raymond and Smith, 1981; Raymond et al., 1984; Zhu et al., 1988; Gorden et al., 2003). An overview of ligands that form very stable complexes with cerium(IV) and that have been used as model compounds for plutonium(IV) is shown in chart 3.

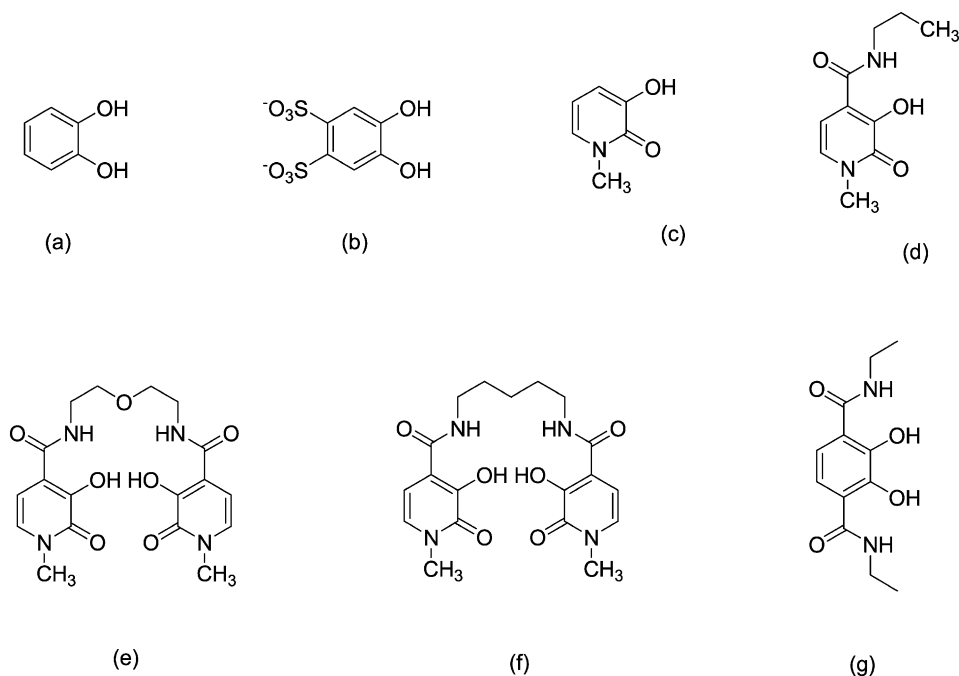


Chart 3. Ligands used for complex formation with cerium(IV) in model studies of plutonium(IV) coordination chemistry: (a) 1,2-dihydroxybenzene (catechol); (b) 3,5-disulfonate-1,2-dihydroxybenzene (tiron); (c) 1-methyl-3-hydroxy-2(1H)-pyridinone (Me-3,2-HOPO); (d) PR-Me-3,2-HOPO; (e) 5LO-Me-3,2-HOPO; (f) 5LI-Me-3,2-HOPO (g) *N,N'*-diethyl-2,3-dihydroxyterephthalamide (H_2ETAM). The nomenclature of the HOPO ligands is that of Raymond and coworkers (Xu et al., 2000).

The first model compound studied was the cerium(IV) tetrakis(catecholate) complex, $\text{Na}_4[\text{Ce}(\text{O}_2\text{C}_6\text{H}_4)_4] \cdot 2\text{H}_2\text{O}$. A crystallographic study revealed that this diamagnetic bright red compound is indeed cerium(IV) tetrakis(catecholate), and not cerium(IV) tris(catecholate)-(semiquinone) complex (Sofen et al., 1978, 1979). The cerium(IV) ion is eight coordinate and the coordination polyhedron is very close to an ideal trigonal-faced dodecahedron. Electrochemical studies revealed that the formation constant of the cerium(IV) tetrakis(catecholate) complex is 10^{36} -fold larger than the formation constant of the corresponding cerium(III) complex! In general, catecholate and its derivatives form very stable complexes with metal ions in their high oxidation states, provided that the pH is high enough to fully deprotonate the ligand. Ligands such as catechol which form stable complexes with cerium(IV) lower the redox potential of the $\text{Ce}^{4+}/\text{Ce}^{3+}$ significantly. A model compound related to the cerium(IV) catecholate complex is the tetrakis(tironato)cerate(IV) complex (Haddad and Raymond, 1986). Tironate is 3,5-disulfonatecatecholate. In the crystal structure of $\text{Na}_{12}[\text{Ce}(\text{C}_6\text{H}_2\text{O}_2(\text{SO}_3)_2)_4] \cdot 9\text{H}_2\text{O} \cdot 6\text{C}_3\text{H}_7\text{NO}$, the coordination polyhedron of cerium(IV) is a highly distorted dodecahedron ($\text{C}_3\text{H}_7\text{NO}$ stands for dimethylformamide). The complex lacks any symmetry.

Several cerium(IV) complexes of various bidentate and tetradentate hydroxypyridinonate (HOPO) complexes have been studied as model compounds for plutonium(IV) complexes (Xu et al., 2000). Bidentate HOPO monoanions are isoelectronic with catecholate dianions and they display a similar complex formation behavior towards cerium(IV) ions. However, HOPO ligands are more acidic and form stable complexes with cerium(IV) at lower pH values than catechol. The tetradentate ligands form more stable complexes than the corresponding bidentate ligands. New types of chelators for cerium(IV) and plutonium(IV) are the 2,3-dihydroxyterephthalamides (Gramer and Raymond, 2004; Xu et al., 2004). Some authors have made comparisons between the coordination chemistry and the redox behavior of cerium and berkelium (Lebedev et al., 1975; Milyukova et al., 1980; Yakovlev et al., 1982).

12. Conclusions and outlook

It is evident that cerium(IV) salts are very versatile reagents for a myriad of organic reactions. The unique reactivity is mainly based on the fact that Ce^{4+} is a strong one-electron oxidant and it is thus able to generate radicals and radical cations, promoting radical reactions. Some cerium(IV)-mediated organic reactions are difficult to achieve with other reagents, although manganese(III) can often replace cerium(IV) in oxidation reactions. Of special usefulness is the ability of cerium(IV) salts to initiate radical polymerization of vinylic monomers. This has been exploited in different applications related to the modification of biopolymers. A major disadvantage of cerium(IV) salts for use as a stoichiometric reagents in organic reactions is their high molecular weight. For instance, the molecular weight of ammonium hexanitratocerate(IV) is 548.23 g/mol. Moreover, since the $\text{Ce}^{4+}/\text{Ce}^{3+}$ redox couple is a one-electron redox system, large amounts of cerium(IV) reagents are required to transform one mole of substrate into the desired product. There is thus a need to develop synthetic procedures that are based

on cheap, widely available low-molecular weight oxidants (air, molecular oxygen, hydrogen peroxide, *tert*-butylhydroperoxide, etc.) and that make use of catalytic amounts of cerium(IV) salts. The electrochemical regeneration of cerium(IV) offers interesting perspectives when stoichiometric amounts of cerium(IV) are still needed.

The dominance of ammonium hexanitratocerate(IV) among cerium(IV) reagent is evident. Although this reagent is a very useful one and gives access to synthetic transformations that cannot be made with other cerium(IV) compounds, it should be realized that this reagent has its limitations. For instance, unwanted side reactions may occur. It is surprising that all the other cerium(IV) salts remain underdeveloped. The exploration of the applicability of the whole variety of cerium(IV) salts to organic reactions remains a challenge, but very interesting results are to be expected. It is also desirable that further studies focus on reaction mechanisms and optimization of the experimental conditions, rather than on a simple screening of a large variety of substrates. A better understanding of the reasons why side reactions occur could lead to much higher yields. Because relatively few crystal structures of cerium(IV) compounds have been investigated, the coordination chemistry of cerium(IV) still offers a playground for coordination chemists and inorganic chemists.

This review shows that cerium(IV) salts can be used for applications other than reagents in organic synthesis. Whereas some applications like cerium(IV) salts as oxidizing agents in redox titrations (cerimetry) are one of the oldest applications of rare earths and are now of less importance, other applications still need to be further developed. From an industrial point of view, cerium-mediated electrosynthesis of fine chemicals offers great opportunities. Closely related to this application is the treatment of industrial organic waste streams by electrochemically generated cerium(IV). The ability of cerium to decompose water into oxygen and hydrogen could solve partially the energy problem in the future. An artificial photosynthetic system based on the $\text{Ce}^{4+}/\text{Ce}^{3+}$ redox couple provides a means for solar energy conversion. However, there is still a long way to go before the yields of the water splitting reaction will reach acceptable values.

Acknowledgements

I would like to thank Dr. Peter Nockemann for his help in preparing the crystal structures shown in this review.

References

- Abbott, T.P., James, C., 1981. *J. Appl. Polym. Sci.* **26**, 207.
- Abdel-Hay, F.I., Khalil, M.I., Hebeish, A., 1982. *J. Appl. Polym. Sci.* **27**, 1249.
- Acocella, J., David, L.D., 1988. US Patent 4,747,907.
- Aghapoor, K., Heravi, M.M., Nooshabadi, M.A., Ghassemzadeh, M., 2002. *Monatsh. Chem.* **133**, 107.
- Agladze, K.I., Krinskii, V.I., 1982. *Nature* **296**, 424.
- Aleixo, P.C., Cho, L.Y., Romero, J.R., 2000. *J. Catal.* **192**, 284.
- Ali, M.H., Leach, D.R., Schmitz, C.E., 1998. *Synth. Commun.* **28**, 2969.
- Allard, B., 1976. *J. Inorg. Nucl. Chem.* **38**, 2109.

- Antonio, M.R., Soderholm, L., 1994. *Inorg. Chem.* **33**, 5988.
- Antonio, M.R., Brazdil, J.F., Glaeser, L.C., Mehicic, M., Teller, R.G., 1988. *J. Phys. Chem.* **92**, 2338.
- Antonio, M.R., Soderholm, L., Williams, C.W., Ullah, N., Francesconi, L.C., 1999. *J. Chem. Soc., Dalton Trans.*, 3825.
- Antonio, M.R., Staub, U., Xue, J.S., Soderholm, L., 1996. *Chem. Mater.* **8**, 2673.
- Ardon, M., Stein, G., 1956. *J. Chem. Soc.*, 104.
- Asakura, J., Robins, M.J., 1988. *Tetrahedron Lett.* **29**, 2855.
- Asakura, J., Robins, M.J., 1990. *J. Org. Chem.* **55**, 4928.
- Ashworth, M.R.F., 1964. *Titrimetric Organic Analysis, Part I: Direct Methods*. Interscience, New York.
- Ashworth, M.R.F., 1965. *Titrimetric Organic Analysis, Part II: Indirect Methods*. Interscience, New York.
- Asovich, V.S., Kornilov, V.V., Maksimov, B.N., 1994. *Russ. J. Appl. Chem.* **67**, 97.
- Atanasiu, J.A., 1927. *Bull. Chim. Soc. Române Chim.* **30**, 73.
- Atanasiu, J.A., Stefanescu, V., 1928. *Ber.* **61**, 1343.
- Athawale, V.D., Lele, V., 2000. *Carbohydr. Polym.* **41**, 407.
- Athawale, V.D., Rathi, S.C., 1997. *Eur. Polym. J.* **33**, 1067.
- Athawale, V.D., Lele, V., 1998. *Carbohydr. Polym.* **35**, 21.
- Athawale, V.D., Padwaldesai, M.P., 1999. *Eur. Polym. J.* **35**, 1237.
- Athawale, V.D., Mumbai, V., 1998. *Starch* **50**, 426.
- Auty, K., Gilbert, B.C., Thomas, C.B., Brown, S.W., Jones, C.W., Sanderson, W.R., 1997. *J. Mol. Catal. A* **117**, 279.
- Baclocchi, E., Della Cort, A., Ebersson, L., Mandolini, L., Rol, C., 1986. *J. Org. Chem.* **51**, 4544.
- Baclocchi, E., Piermattei, A., Ruzziconi, R., 1988a. *Synth. Commun.* **18**, 2167.
- Baclocchi, E., Ruzziconi, R., 1986. *J. Org. Chem.* **51**, 1645.
- Baclocchi, E., Rol, C., Mandolini, L., 1977. *J. Org. Chem.* **42**, 3682.
- Baclocchi, E., Rol, C., Sebastiani, G.V., Serena, B., 1984a. *Tetrahedron Lett.* **25**, 1945.
- Baclocchi, E., Rol, C., Sebastiani, G.V., Serena, B., 1984b. *J. Chem. Res. (S)*, 24.
- Baclocchi, E., Del Giacco, T., Murgia, S.M., Sebastiani, G.V., 1988b. *Tetrahedron* **44**, 6651.
- Bäck, S.Å.J., Lepage, M., Baldock, C., 2002. *Appl. Radiat. Isot.* **56**, 895.
- Baer, S., Stein, G., 1953. *J. Chem. Soc.*, 3176.
- Baker, F.B., Newton, T.W., Kahn, M., 1960. *J. Phys. Chem.* **64**, 109.
- Baker, I., Gibbs, R.S., 1943. *Ind. Eng. Chem., Anal. Ed.* **15**, 505.
- Baker, I., Gibbs, R.S., 1946. *Ind. Eng. Chem., Anal. Ed.* **18**, 124.
- Balanikas, G., Hussain, N., Amin, S., Hecht, S.S., 1988. *J. Org. Chem.* **53**, 1007.
- Bamwenda, G.R., Arakawa, H., 2000. *J. Mol. Catal. A* **161**, 105.
- Bamwenda, G.R., Arakawa, H., 2001. *Sol. Energy Mater. Sol. Cells* **70**, 1.
- Bamwenda, G.R., Uesigi, T., Abe, Y., Sayama, K., Arakawa, H., 2001. *Appl. Catal. A* **205**, 117.
- Bányai, É., Erdey, L., Kolos, E., 1965. *Talanta* **12**, 21.
- Bar, G., Bini, F., Parsons, A.F., 2003. *Synth. Commun.* **33**, 213.
- Barbucci, R., Casolaro, M., Magnani, A., Roncolini, C., Ferruti, P., 1989. *Polymer* **30**, 1751.
- Bar-Eli, K., Haddad, S., 1979. *J. Phys. Chem.* **83**, 2952.
- Barkakaty, B.C., Robson, A., 1979. *J. Appl. Polym. Sci.* **24**, 269.
- Barkin, S., Bixon, M., Noyes, R.M., Bar-Eli, K., 1978. *Int. J. Chem. Kinet.* **10**, 619.
- Barry, J., du Preez, J.G.H., Els, E., Rohwer, H.E., Wright, P.J., 1981. *Inorg. Chim. Acta* **53**, L17.
- Bartoli, C., Cupone, G., Dalpozzo, R., De Nino, A., Maiuolo, L., Procopio, A., Sambri, L., Tagarelli, A., 2002. *Tetrahedron Lett.* **43**, 5945.
- Basceri, C., Visokay, M., Graettinger, T.M., Cummings, C.M., 2004. US Patent 6,812,112.
- Bassett, J., Denney, R.C., Jeffery, G.H., Mendham, J., 1981. *Vogel's Textbook of Quantitative Inorganic Analysis*. Longman, London.
- Bassett, L.G., Stumpf, L.F., 1934. *Ind. Eng. Chem., Anal. Ed.* **6**, 477.
- Baur, E., 1908. *Z. Phys.* **63**, 683.
- Baxter, I., Darr, J.A., Hursthouse, M.B., Malik, K.M.A., Mingos, D.M.P., Plakatouras, J.C., 1998. *J. Chem. Crystallogr.* **28**, 267.
- Bazuaye, A., Okieimen, E.F., Said, O.B., 1988. *Eur. Polym. J.* **24**, 811.
- Beck, D.D., Capehart, T.W., Hoffmann, R.W., 1989. *Chem. Phys. Lett.* **159**, 207.
- Beineke, T.A., Delgaudio, J., 1968. *Inorg. Chem.* **7**, 715.
- Beliakova, M.K., Aly, A.A., Abdel-Mohdy, F.A., 2004. *Starch* **56**, 407.
- Belousov, B.P., 1959. *Sb. Ref. Radiat. Med.*, 145.
- Berthet, J.C., Lance, M., Nierlich, M., Ephritikhine, M., 2000. *Eur. J. Inorg. Chem.*, 1969.
- Bhat, G.A., Periasamy, M., Bhatt, M.V., 1979. *Tetrahedron Lett.* **20**, 3097.

- Bhatt, M.V., Periasamy, M., 1993. *J. Chem. Soc., Perkin Trans. II*, 1811.
- Bhatt, M.V., Periasamy, M., 1994. *Tetrahedron* **50**, 3575.
- Bhattacharyya, S.N., Maldas, D., 1984. *Prog. Polym. Sci.* **10**, 171.
- Bidoglio, G., Gibson, P.N., Haltier, E., Omenetoo, N., Lipponen, M., 1992. *Radiochim. Acta* **58-69**, 181.
- Binnemans, K., 2005. Rare-earth beta-diketonates. In: Gschneidner Jr., K.A., Bünzli, J.-C.G., Pecharsky, V.K. (Eds.), *Handbook on the Physics and Chemistry of Rare Earths*, vol. **35**. Elsevier, Amsterdam, pp. 107-272 (chapter 225).
- Birnbaum, N., Edmonds, S.M., 1940. *Ind. Eng. Chem., Anal. Ed.* **12**, 156.
- Biswal, D.R., Singh, R.P., 2004. *Carbohydr. Polym.* **57**, 379.
- Blaustein, B.D., Gryder, J.W., 1957. *J. Am. Chem. Soc.* **79**, 540.
- Bobal, P., Lightner, D.A., 2001. *J. Heterocycl. Chem.* **38**, 1219.
- Bracken, K., Moss, R.A., Ragnathan, K.G., 1997. *J. Am. Chem. Soc.* **119**, 9323.
- Bradley, D.C., Chatterjee, A.K., Wardlaw, W., 1956a. *J. Chem. Soc.*, 2261.
- Bradley, D.C., Chatterjee, A.K., Wardlaw, W., 1956b. *J. Chem. Soc.*, 3469.
- Bradley, D.C., Chatterjee, A.K., Wardlaw, W., 1957. *J. Chem. Soc.*, 2600.
- Brandt, W.W., Smith, G.F., 1949. *Anal. Chem.* **21**, 1313.
- Branum, M.E., Tipton, A.K., Zhu, S., Que Jr., L., 2001. *J. Am. Chem. Soc.* **123**, 1898.
- Branum, M.E., Que Jr., L., 1999. *J. Biol. Inorg. Chem.* **4**, 593.
- Brauer, G.M., Termini, D.J., 1973. *J. Appl. Polym. Sci.* **17**, 2557.
- Brezina, F., 1971. *Collect. Czech. Chem. Commun.* **36**, 2889.
- Brezina, F., 1973. *Collect. Czech. Chem. Commun.* **39**, 2162.
- Briois, V., Lützenkirchen-Hecht, D., Villain, F., Fonda, E., Belin, S., Griesebock, B., Frahm, R., 2005. *J. Phys. Chem. A* **109**, 320.
- Brockhaus, R., 1968. *Liebigs Ann. Chem.* **712**, 214.
- Brusa, M.A., Perissinotti, L.J., Colussi, A.J., 1985. *J. Phys. Chem.* **89**, 1572.
- Bull, S.D., Davies, S.G., Fenton, G., Mulvaney, A.W., Prasad, R.S., Smith, A.D., 2000. *J. Chem. Soc., Perkin Trans. I*, 3765.
- Cao, Y.M., Qing, X.S., Sun, J., Zhou, F.M., Lin, S.G., 2002. *Eur. Polym. J.* **38**, 1921.
- Casinos, I., 1994. *Polymer* **35**, 606.
- Cavasio, F.P., Cervellati, R., Lombardo, R., Liveri, M.L.T., 1999. *J. Phys. Chem. B* **103**, 4285.
- Chakrabarty, K., Chawla, H.M., Suresh, V.V., 1993. *Indian J. Chem. B* **32**, 266.
- Chansook, N., Kiattkamjornwong, S., 2003. *J. Appl. Polym. Sci.* **89**, 1952.
- Chauhan, G.S., Bhatt, S.S., Kaur, I., Singha, A.S., Kaith, B.S., 2000. *Polym. Degrad. Stab.* **69**, 261.
- Chauvierre, C., Labarre, D., Couvreur, P., Vauthier, C., 2003. *Macromolecules* **36**, 6018.
- Chawla, H.M., Sharma, S.K., 1990. *Bull. Soc. Chim. Fr.* **127**, 656.
- Chawla, H.M., Mittal, R.S., 1985. *Synthesis*, 70.
- Chen, C., Mariano, P.S., 2000. *J. Org. Chem.* **65**, 3252.
- Chen, W., Komiya, M., 2005. *ChemBioChem* **6**, 1825.
- Chen, W., Kitamura, Y., Zhou, J.M., Sumaoka, J., Komiya, M., 2004. *J. Am. Chem. Soc.* **33**, 10285.
- Cho, I., Ahn, K.D., 1976a. *J. Korean Chem. Soc.* **20**, 299.
- Cho, I., Ahn, K.D., 1976b. *J. Korean Chem. Soc.* **20**, 309.
- Cho, L.Y., Romero, J.R., 1988. *Quim. Nova* **21**, 144.
- Cho, L.Y., Romero, J.R., 1995. *Tetrahedron Lett.* **36**, 8757.
- Cho, L.Y., Madurro, J.M., Romero, J.R., 1999. *J. Catal.* **186**, 31.
- Chowdhury, P., Pal, C.M., 1999. *Eur. Polym. J.* **35**, 2207.
- Chowdhury, P., Banerjee, M., 1998. *J. Appl. Polym. Sci.* **70**, 523.
- Chowdhury, P., Samui, S., Kundu, T., Nandi, M.M., 2001. *J. Appl. Polym. Sci.* **82**, 3520.
- Christoffers, J., Werner, T., 2002. *Synlett*, 119.
- Christoffers, J., Werner, T., Unger, S., Frey, W., 2003a. *Eur. J. Org. Chem.*, 425.
- Christoffers, J., Werner, T., Frey, W., Baro, A., 2003b. *Eur. J. Org. Chem.*, 4879.
- Church, V.E., Fraser, H.J., Matthews, R.W., 1976. *J. Phys. E: Sci. Instrum.* **9**, 182.
- Claassen, A., Visser, J., 1941. *Recl. Trav. Chim.* **60**, 213.
- Clarke, R., Kuhn, A., Okoh, E., 1975. *Chem. Br.* **11**, 59.
- Cleve, P.T., 1885. *Bull. Soc. Chim.* **2**, 43, 53.
- Cotelle, P., Catteau, J.P., 1992. *Tetrahedron Lett.* **33**, 3855.
- Coutinho, F.M.B., Martins, J.C.A., 1991. *Eur. Polym. J.* **27**, 1161.
- Coutinho, F.M.B., Martins, J.C.A., 1992. *Eur. Polym. J.* **28**, 19.
- Coutinho, F.M.B., Guimarães, M.J.O.C., Gomes, A.S., 1986. *J. Polym. Sci. A* **24**, 2131.
- Coutinho, F.M.B., Furtado, C.R.G., 1992. *Eur. Polym. J.* **28**, 1111.
- Cozzi, D., Desideri, P.G., 1960. *J. Electroanal. Chem.* **1**, 301.

- Cunningham, B.B., Feay, D.C., Rollier, M.A., 1954. *J. Am. Chem. Soc.* **76**, 3361.
- Danieli, B., Palmisano, G., 1976. *Chem. Ind.*, 565.
- Das, N.R., Nayak, N.C., Das, H.K., Mishra, S.N., Singh, B.C., 1990. *J. Appl. Polym. Sci.* **39**, 1079.
- Daugherty, N.A., Taylor, R.L., 1972. *J. Inorg. Nucl. Chem.* **34**, 1756.
- Dehmlow, E.V., Makrandi, J.K., 1986. *J. Chem. Res. (S)*, 32.
- Del Giacco, T., Baciocchi, E., Steenken, S., 1993. *J. Phys. Chem.* **97**, 5451.
- Della Cort, A., Barbera, A.L., Mandolini, L., 1983. *J. Chem. Res. (S)*, 44.
- Deshmukh, S.R., Singh, R.P., 1987. *J. Appl. Polym. Sci.* **33**, 1963.
- Desideri, P.G., 1961. *J. Electroanal. Chem.* **2**, 39.
- Devadoss, V., Noel, M., Jayaraman, K., Basha, C.A., 2003. *J. Appl. Electrochem.* **33**, 319.
- Diñçer, B., Bayülken, S., Saraç, A.S., 1997. *J. Appl. Polym. Sci.* **63**, 1643.
- Diñçtürk, S., Ridd, J.H., 1982a. *J. Chem. Soc., Perkin Trans. II*, 961.
- Diñçtürk, S., Ridd, J.H., 1982b. *J. Chem. Soc., Perkin Trans. II*, 965.
- Dolg, M., Fulde, P., Stoll, H., Preuss, H., Chang, A., Pitzer, R.M., 1995. *Chem. Phys.* **195**, 71.
- Dolg, M., Fulde, P., Küchle, W., Neumann, C.S., Stoll, H., 1991. *J. Chem. Phys.* **94**, 3011.
- Domagała, S., Steglińska, V., Dziegieć, J., 1998. *Monatsh. Chem.* **129**, 761.
- Don, T.M., Chen, Y.R., Chiu, W.Y., 2002. *J. Polym. Res.* **9**, 257.
- Dong, J.H., Qiu, K.Y., Feng, X.D., 1994. *Macromol. Chem. Phys.* **195**, 823.
- Doyle, M.P., Zuidema, L.J., Bade, T.R., 1975. *J. Org. Chem.* **40**, 1454.
- du Preez, J.G.H., Rohrer, H.E., de Wet, J.F., Cairns, M.R., 1978. *Inorg. Chim. Acta* **26**, L59.
- Duke, F.R., Forist, A.A., 1949. *J. Am. Chem. Soc.* **71**, 2790.
- Duke, F.R., Smith, G.F., 1940. *Ind. Eng. Chem., Anal. Ed.* **12**, 201.
- Duke, F.R., Bremer, R.F., 1951. *J. Am. Chem. Soc.* **73**, 5179.
- Dulz, G., Sutin, N., 1963. *Inorg. Chem.* **2**, 917.
- Dust, L.A., Gill, E.W., 1970. *J. Chem. Soc. C*, 1630.
- Edelson, D., Field, R.J., Noyes, R.M., 1975. *Int. J. React. Kinet.* **7**, 417.
- Edelson, D., Noyes, R.M., Field, R.J., 1979. *Int. J. React. Kinet.* **11**, 155.
- Edelstein, N.M., Allen, P.G., Bucher, J.J., Shuh, D.K., Sofield, C.D., Kaltsoyannis, N., Maunder, G.H., Russo, M.R., Sella, A., 1996. *J. Am. Chem. Soc.* **118**, 13115.
- El-Molla, M.M., El-Halwagy, A.A., El-Sayad, H.S., 2001. *Adv. Polym. Technol.* **20**, 296.
- El-Shinnawy, N.A., El-Kalyoubi, S.F., 1985. *J. Appl. Polym. Sci.* **30**, 2171.
- Emerson, G.F., Watts, L., Pettit, R., 1965. *J. Am. Chem. Soc.* **87**, 133.
- Emsley, J., 1991. *The Elements*. Oxford Univ. Press, Oxford.
- Erim, M., Erciyas, A.T., Serhatli, I.E., 1992. *Polym. Bull.* **27**, 361.
- Eromosele, I.C., Agbo, A., 1999. *J. Appl. Polym. Sci.* **73**, 1751.
- Eromosele, I.C., Eromosele, C.O., Zanna, H.K., 2002. *J. Appl. Polym. Sci.* **84**, 500.
- Evans, W.J., Deming, T.J., Ziller, J.W., 1989b. *Organometallics* **8**, 1581.
- Evans, W.J., Deming, T.J., Olofson, J.M., Ziller, J.W., 1989a. *Inorg. Chem.* **28**, 4027.
- Ewing, D.T., Wilson, M., 1931. *J. Am. Chem. Soc.* **53**, 2105.
- Fakhru'l-Razi, A., Qudsieh, I.Y.M., Yunus, W.M.Z.W., Ahmad, M.B., Rahman, M.K.A., 2001. *J. Appl. Polym. Sci.* **82**, 1375.
- Fang, T.R., Ji, L.C., Yu, J.G., Wang, L.Y., Xu, S.X., 1992. *Polym. Bull.* **29**, 71.
- Fanta, G.F., Burr, R.C., Doane, W.M., 1982. *J. Appl. Polym. Sci.* **27**, 4239.
- Fanta, G.F., Felker, F.C., Salch, J.H., 2003. *J. Appl. Polym. Sci.* **89**, 3323.
- Fanta, G.F., Burr, R.C., Russell, C.R., Rist, C.E., 1969. *J. Appl. Polym. Sci.* **13**, 133.
- Fanta, G.F., Burr, R.C., Russell, C.R., Rist, C.E., 1970. *J. Appl. Polym. Sci.* **14**, 2601.
- Farag, S., Al-Afaeq, E.I., 2002. *Carbohydr. Polym.* **48**, 1.
- Fares, M.M., El-faqeh, A.S., Osman, M.E., 2003. *J. Polym. Res.* **10**, 119.
- Fares, M.M., Al-Ta'ani, B., 2003. *Acta Chim. Slov.* **50**, 275.
- Feigl, F., 1954. *Spot Tests, Volume II: Organic Applications*. Elsevier, Amsterdam.
- Feng, X.D., Sun, Y.H., Qiu, K.Y., 1985. *Macromolecules* **18**, 2105.
- Fernández, M.D., Guzmán, G.M., 1991. *Eur. Polym. J.* **26**, 301.
- Fernández, M.D., Guzmán, G.M., 1989a. *J. Polym. Sci. A* **27**, 2427.
- Fernández, M.D., Guzmán, G.M., 1989b. *J. Polym. Sci. A* **27**, 3703.

- Fernández, M.D., Fernández, M.J., Guzmán, G.M., 1989. *J. Polym. Sci. A* **27**, 3439.
- Fernández, M.J., Fernández, M.D., Guzmán, G.M., Montiel, R., Castaño, V.M., 1992. *Eur. Polym. J.* **28**, 969.
- Fernández, M.J., Casinos, I., Guzmán, G.M., 1990a. *J. Appl. Polym. Sci.* **41**, 2221.
- Fernández, M.J., Casinos, I., Guzmán, G.M., 1990c. *J. Polym. Sci. A* **28**, 2275.
- Fernández, M.J., Casinos, I., Guzmán, G.M., 1991. *J. Appl. Polym. Sci.* **42**, 767.
- Fernández, M.J., Fernández, M.D., Casinos, I., Guzmán, G.M., 1990b. *J. Appl. Polym. Sci.* **39**, 2219.
- Ferro, S., De Battisti, A., 2002. *Phys. Chem. Chem. Phys.* **4**, 1915.
- Field, R.J., 1975. *J. Chem. Phys.* **63**, 2289.
- Field, R.J., Schneider, F.W., 1989. *J. Chem. Educ.* **66**, 195.
- Field, R.J., Burger, M., 1985. *Oscillations and Traveling Waves in Chemical Systems*. Wiley, New York.
- Field, R.J., Boyd, P.M., 1985. *J. Phys. Chem.* **89**, 3707.
- Field, R.J., Noyes, R.M., 1974. *J. Chem. Phys.* **60**, 1877.
- Field, R.J., Körös, E., Noyes, R.M., 1972. *J. Am. Chem. Soc.* **94**, 8649.
- Field, R.M., Försterling, H.D., 1986. *J. Phys. Chem.* **90**, 5400.
- Firouzabadi, H., Shiriny, F., 1996a. *Synth. Commun.* **26**, 423.
- Firouzabadi, H., Shiriny, F., 1996b. *Synth. Commun.* **26**, 649.
- Firouzabadi, H., Iranpoor, N., 1983. *Synth. Commun.* **13**, 143.
- Firouzabadi, H., Iranpoor, N., 1984. *Synth. Commun.* **14**, 875.
- Firouzabadi, H., Iranpoor, N., Garzan, A., 2005. *Adv. Funct. Catal.* **347**, 1925.
- Firouzabadi, H., Iranpoor, N., Kiaeezadeh, F., Toofan, J., 1984c. *Synth. Commun.* **14**, 973.
- Firouzabadi, H., Iranpoor, N., Hajipour, G., Toofan, J., 1984d. *Synth. Commun.* **14**, 1033.
- Firouzabadi, H., Iranpoor, N., Parham, H., Tootan, J., 1984a. *Synth. Commun.* **14**, 631.
- Firouzabadi, H., Iranpoor, N., Parham, H., Sardarian, A., Toofan, J., 1984b. *Synth. Commun.* **14**, 717.
- Fischer, A., Henderson, G.N., 1985. *Synthesis*, 641.
- Fokin, A.A., Peleshanko, S.A., Gunchenko, P.A., Gusev, D.V., Schreiner, P.R., 2000. *Eur. J. Org. Chem.*, 3357.
- Försterling, H.D., Noszticzius, Z., 1989. *J. Phys. Chem.* **93**, 2740.
- Försterling, H.D., Muranyi, S., Noszticzius, Z., 1990. *J. Phys. Chem.* **94**, 2915.
- Franck, U.F., 1978. *Angew. Chem., Int. Ed.* **17**, 1.
- Franklin, S.J., 2001. *Curr. Opin. Chem. Biol.* **5**, 201.
- Fritz, J.S., Fulda, M.O., Margerum, S.L., Lane, E.I., 1954. *Inorg. Chim. Acta* **10**, 513.
- Fujieda, S., Zhang, W., 1995. *Thermochim. Acta* **267**, 95.
- Furman, N.H., 1928a. *J. Am. Chem. Soc.* **50**, 755.
- Furman, N.H., 1928b. *J. Am. Chem. Soc.* **50**, 1675.
- Furman, N.H., 1932. *J. Am. Chem. Soc.* **54**, 4235.
- Furman, N.H., Schoonover, C., 1931. *J. Am. Chem. Soc.* **53**, 2561.
- Furman, N.H., Wallace Jr., J.M., 1930a. *J. Am. Chem. Soc.* **52**, 1443.
- Furman, N.H., Wallace Jr., J.M., 1930b. *J. Am. Chem. Soc.* **52**, 2346.
- Furman, N.H., Evans, O.M., 1929. *J. Am. Chem. Soc.* **51**, 1128.
- Furman, N.H., Murray, W.M., 1936. *J. Am. Chem. Soc.* **58**, 1689.
- Galli, C., 1991. *J. Org. Chem.* **56**, 3238.
- Ganapathisubramanian, N., Noyes, R.M., 1982. *J. Phys. Chem.* **86**, 5158.
- Ganin, E., Amer, I., 1995. *Synth. Commun.* **25**, 3149.
- Gao, Y., Cross, A.R., Armstrong, R.L., 1996. *J. Phys. Chem.* **100**, 10159.
- Gao, Y., Försterling, H.D., Noszticzius, Z., 1994. *J. Phys. Chem.* **98**, 8377.
- Ge, X.C., Xu, Y., Meng, Y.Z., Li, R.K.Y., 2005. *Compos. Sci. Technol.* **65**, 2219.
- Geilmann, W., Wrigge, F.W., 1935. *Z. Anorg. Allg. Chem.* **222**, 56.
- Gibson, J.K., Haire, R.G., 1988b. *Thermochim. Acta* **133**, 241.
- Gibson, J.K., Haire, R.G., 1988a. *J. Less-Common Met.* **144**, 123.
- Glass, R.W., Martin, T.W., 1970. *J. Am. Chem. Soc.* **92**, 5084.
- Gleu, K., 1933. *Z. Anal. Chem.* **95**, 305.
- Golovnya, V.A., Pospelova, L.A., 1961. *Russ. J. Inorg. Chem.* **6**, 324.
- Golovnya, V.A., Pospelova, L.A., Bolotova, G.T., 1960. *Russ. J. Inorg. Chem.* **5**, 2204.
- Goñi, I., Gurruchaga, M., Vazquez, B., Valero, M., Guzman, G.M., 1992. *Eur. Polym. J.* **28**, 975.
- Gorden, A.E.V., Xu, J.D., Raymond, K.N., Durbin, P., 2003. *Chem. Rev.* **103**, 4207.
- Gordon, L., Feibush, A.M., 1955. *Anal. Chem.* **27**, 1050.
- Goswami, P., Chowdhury, P., 2000. *New J. Chem.* **24**, 955.
- Graczyk, T., 1986. *J. Appl. Polym. Sci.* **31**, 1069.
- Gradeff, P.S., Schreiber, F.G., Mauermann, H., 1986. *J. Less-Common Met.* **126**, 335.

- Gradef, P.S., Schreiber, F.G., Brooks, K.C., Sievers, R.E., 1985. *Inorg. Chem.* **24**, 1110.
- Gramer, C.J., Raymond, K.N., 2004. *Inorg. Chem.* **43**, 6397.
- Grant, A.J., James, C., 1915. *J. Am. Chem. Soc.* **37**, 2652.
- Grant, D., 1964. *J. Inorg. Nucl. Chem.* **26**, 337.
- Grant, D., Payne, D.S., 1961. *Anal. Chim. Acta* **25**, 422.
- Greco, A., Cesca, S., Bertolini, G., 1976. *J. Organomet. Chem.* **113**, 321.
- Greef, R., Aulich, H., 1968. *J. Electroanal. Chem.* **18**, 295.
- Grenier, J.C., Catteau, J.P., Cotelle, P., 1999. *Synth. Commun.* **29**, 1201.
- Griffith, W.P., Moreea, R.G.H., Nogueira, H.I.S., 1996. *Polyhedron* **15**, 3493.
- Grzejdziak, A., Dziegieć, J., 1997. *Zh. Obshchei Khim.* **67**, 121.
- Gupta, K.C., Behari, K., 1986. *J. Polym. Sci. A* **24**, 767.
- Gupta, K.C., Khandekar, K., 2002. *J. Appl. Polym. Sci.* **86**, 2631.
- Gupta, K.C., Khandekar, K., 2003. *Biomacromolecules* **4**, 758.
- Gupta, K.C., Khandekar, K., 2006. *Polym. Int.* **55**, 139.
- Gupta, K.C., Sahoo, S., 2001a. *Biomacromolecules* **2**, 239.
- Gupta, K.C., Sahoo, S., 2001b. *J. Appl. Polym. Sci.* **79**, 767.
- Gupta, K.C., Sahoo, S., Khandekar, K., 2002. *Biomacromolecules* **3**, 1087.
- Gurruchaga, M., Goñi, I., Valero, M., Guzmán, G.M., 1992a. *Polymer* **33**, 2860.
- Gurruchaga, M., Goñi, I., Valero, M., Guzmán, G.M., 1992b. *Polymer* **33**, 3274.
- Guthrie, F.K., 1962. PhD thesis, The Institute of Paper Chemistry, Appleton, WI, USA.
- Gyenge, R., Körös, E., Toth, K., Pungor, E., 1978. *Anal. Chim. Acta* **98**, 385.
- Gyenge, R., Toth, K., Pungor, E., Körös, E., 1977. *Anal. Chim. Acta* **94**, 111.
- Haddad, S.F., Raymond, K.N., 1986. *Inorg. Chim. Acta* **122**, 111.
- Haire, R.G., Eyring, L., 1994. Lanthanides and actinides hydration and hydrolysis. In: Gschneidner Jr., K.A., Eyring, L.A., Choppin, G.R., Lander, L.H. (Eds.), *Handbook on the Physics and Chemistry of Rare Earths*, vol. **18**. Elsevier, Amsterdam, p. 413 (chapter 125).
- Han, T.L., Kumar, R.N., Rozman, H.D., Noor, M.A.M., 2004. *Carbohydr. Polym.* **54**, 509.
- Hanna, S.B., Sarac, S.A., 1977. *J. Org. Chem.* **42**, 2069.
- Hardwick, T.J., Robertson, E., 1951. *Can. J. Chem.* **29**, 818.
- Harrison, S., 1993. World Patent 93/18208.
- Harrison, S., 1997. US Patent 5,679,235.
- Harrison, S., Théorêt, A., 1999. *J. New Mater. Electrochem. Syst.* **2**, 1.
- Hatanaka, Y., Imamoto, T., Yokoyama, M., 1983. *Tetrahedron Lett.* **24**, 2399.
- Hay, N., Kochi, J.K., 1968. *J. Inorg. Nucl. Chem.* **30**, 884.
- Hayon, E., Saito, E., 1965. *J. Chem. Phys.* **43**, 4314.
- He, L., Kanamori, M., Horiuchi, C.A., 1999. *J. Chem. Res. (S)*, 122.
- Hebeish, A., Mehta, P.C., 1968. *J. Appl. Polym. Sci.* **12**, 1625.
- Hecker De Carvalho, L., Rudin, A., 1984. *J. Appl. Polym. Sci.* **29**, 2921.
- Hegedus, L., Wittmann, M., Noszticzus, Z., Yan, S.H., Sirimungkala, A., Försterling, H.D., Field, R.J., 2001. *Faraday Discuss.* **120**, 21.
- Hegg, E.L., Burstyn, J.N., 1998. *Coord. Chem. Rev.* **173**, 133.
- Heiba, E.I., Dessau, R.M., 1971. *J. Am. Chem. Soc.* **93**, 995.
- Heidt, L.J., McMillan, A.F., 1953. *Science* **117**, 75.
- Heidt, L.J., McMillan, A.F., 1954. *J. Am. Chem. Soc.* **76**, 2135.
- Heidt, L.J., Smith, M.E., 1948. *J. Am. Chem. Soc.* **70**, 2476.
- Heravi, M.M., Oskooie, H.A., Ghassemzadeh, M., Zameni, F.F., 1999. *Monatsh. Chem.* **130**, 1253.
- Heravi, M.M., Oskooie, H.A., Kazemian, P., Drikvand, F., Ghassemzadeh, M., 2004. *Phosphorus Sulfur Silicon* **179**, 2341.
- Hernandez-Alonso, M.D., Hungria, A.B., Martinez-Arias, A., Fernandez-Garcia, M., Coronado, J.M., Conesa, J.C., Soria, J., 2004. *Appl. Catal. B* **50**, 167.
- Herrmann, H., Exner, M., Zellner, R., 1991. *Ber. Bunsen-Ges. Phys. Chem.* **95**, 598.
- Hinsvark, O.N., Stone, K.G., 1956. *Anal. Chem.* **28**, 334.
- Hintz, H.L., 1966. PhD thesis, The Institute of Paper Chemistry, Appleton, WI, USA.
- Hintz, H.L., Johnson, D.C., 1967. *J. Org. Chem.* **32**, 556.
- Ho, T.L., 1972. *Synthesis*, 560.
- Ho, T.L., 1973. *Synthesis*, 347.
- Ho, T.L., 1978. *Synthesis*, 936.
- Ho, T.L., 1979. *Synth. Commun.*, 237.
- Ho, T.L., Wong, C.M., 1972. *Synthesis*, 561.
- Ho, T.L., Hall, T.W., Wong, C.M., 1972. *Chem. Ind.*, 729.
- Ho, T.L., Hall, T.W., Wong, C.M., 1973. *Synthesis*, 206.

- Horiuchi, C.A., Fukushima, T., Furuta, N., Chai, W., Ji, S.J., Saito, Y., Hashimoto, C., Takahashi, T.T., Sugiyama, T., Muto, A., Sakata, Y., Nozaki, S., 2003. *J. Chem. Res. (S)*, 270.
- Horiuchi, C.A., Kiji, S., 1988. *Chem. Lett.*, 31.
- Hsu, W.C., Kuo, J.F., Chen, C.Y., 1992. *J. Polym. Sci. A* **30**, 2459.
- Huang, R.Y.M., Chandramouli, P., 1968. *J. Appl. Polym. Sci.* **12**, 2549.
- Hudson, A.G., Pedler, A.E., Tatlow, J.C., 1969. *Tetrahedron* **25**, 4371.
- Hudson, A.G., Pedler, A.E., 1970. *Tetrahedron* **26**, 3435.
- Hurdis, E.C., Romeyn Jr., H., 1954. *Anal. Chem.* **26**, 320.
- Hwu, J.R., King, K.Y., 2001. *Current Sci.* **81**, 1043.
- Hwu, J.R., Jain, M.L., Tsai, F.Y., Tsay, S.C., Balakumar, A., Hakimelahi, G.H., 2000. *J. Org. Chem.* **65**, 5077.
- Hwu, J.R., Jain, M.L., Tsay, S.C., Hakimelahi, G.H., 1996a. *Tetrahedron Lett.* **37**, 2035.
- Hwu, J.R., Jain, M.L., Tsay, S.C., Hakimelahi, G.H., 1996b. *J. Chem. Soc., Chem. Commun.*, 545.
- Hwu, J.R., Jain, M.T., Tsai, F.Y., Balakumar, A., Hakimelahi, G.H., Tsay, S.C., 2002. *Arkivoc* **IX**, 28.
- Ibl, N., Kramer, K., Ponto, L., Robertson, P., 1979. *AICHe Symp. Ser.* **75**, 45.
- Igawa, T., Sumaoka, J., Komiyama, M., 2000. *Chem. Lett.*, 356.
- Ignaczak, M., Dziegieć, J., 1992. *Polish J. Appl. Chem.* **36**, 183.
- Imai, Y., Iwakura, Y., 1967. *J. Appl. Polym. Sci.* **11**, 1529.
- Imamoto, T., 1994. *Lanthanides in Organic Synthesis*. Academic Press, London.
- Imamoto, T., Koide, Y., Hiyama, S., 1990. *Chem. Lett.*, 1445.
- Indrayan, A.K., Mishra, S.K., Gupta, Y.K., 1982. *J. Chem. Soc., Dalton Trans.*, 549.
- Iranpoor, N., Zardaloo, F.Z., 1994. *Synth. Commun.* **24**, 1959.
- Iranpoor, N., Owji, J., 1991. *Tetrahedron* **47**, 149.
- Iranpoor, N., Shekarriz, M., 1999a. *Bull. Chem. Soc. Jpn.* **72**, 455.
- Iranpoor, N., Shekarriz, M., 1999b. *J. Chem. Res. (S)*, 442.
- Iranpoor, N., Shekarriz, M., 2000. *Tetrahedron* **56**, 5209.
- Iranpoor, N., Salehi, P., 1995. *Tetrahedron* **51**, 909.
- Iranpoor, N., Firouzabadi, H., Safavi, A., Shekarriz, M., 2002. *Synth. Commun.* **32**, 2287.
- Iranpoor, N., Firouzabadi, H., Shekarize, M., 2003. *Org. Biomol. Chem.* **1**, 724.
- Iranpoor, N., Baltork, I.M., Zardaloo, F.S., 1991. *Tetrahedron* **47**, 9861.
- Iranpoor, N., Shekarriz, M., Shiriny, F., 1998. *Synth. Commun.* **28**, 347.
- Itoh, K.I., Horiuchi, C.A., 2004. *Tetrahedron* **60**, 1671.
- Itoh, K.I., Takahashi, S., Ueki, T., Sugiyama, T., Takahashi, T.T., Horiuchi, C.A., 2002. *Tetrahedron Lett.* **43**, 7035.
- Jacob III, P., Callery, P.C., Shulgin, A.T., Castagnoli Jr., N., 1976. *J. Org. Chem.* **41**, 3627.
- Jacobs, S.S., Epstein, I.R., 1976. *J. Am. Chem. Soc.* **98**, 1721.
- Jahnke, W., Winfree, A.T., 1991. *J. Chem. Educ.* **68**, 320.
- Jahnke, W., Skaggs, W.E., Winfree, A.T., 1989. *J. Phys. Chem.* **93**, 740.
- Jana, S.C., Maiti, S., Biswas, S., 2000. *J. Appl. Polym. Sci.* **78**, 1586.
- Janarthanan, J., Yunus, W.M.Z.W., Ahmad, M.B., 2003. *J. Appl. Polym. Sci.* **90**, 2053.
- Janjic, D., Stroot, P., Burger, U., 1974. *Helv. Chim. Acta* **57**, 266.
- Jayaraman, A., 1979. Valence changes in compounds. In: Gschneidner Jr., K.A., Eyring, L.A. (Eds.), *Handbook on the Physics and Chemistry of Rare Earths*, vol. 2. Elsevier, Amsterdam, p. 575 (chapter 20).
- Jayaraman, K., Krishnamoorthy, S., Devadoss, V., Srinivasan, R.K., Chidambaram, S., 1998. *Bull. Electrochem.* **14**, 326.
- Jin, Y., Huang, R.Y.M., 1988. *Eur. Polym. J.* **24**, 471.
- Job, A., 1899a. *C. R. Acad. Sci. Paris* **128**, 178.
- Job, A., 1899b. *C. R. Acad. Sci. Paris* **128**, 1098.
- Jones, E.G., Soper, F.G., 1935. *J. Chem. Soc.*, 802.
- Jow, J.J., Chou, T.C., 1988. *J. Appl. Electrochem.* **18**, 298.
- Jung, B.O., Chung, S.J., Lee, S.B., 2006. *J. Appl. Polym. Sci.* **99**, 3500.
- Jwo, J.J., Noyes, R.M., 1975. *J. Am. Chem. Soc.* **97**, 5422.
- Kaeriyama, K., 1969. *Polymer* **10**, 11.
- Kagan, H.B., Namy, J.L., 1986. *Tetrahedron* **42**, 6573.
- Kaiser, E.W., Sunder, W.A., Falconer, W.E., 1972. *J. Less-Common Met.* **27**, 383.
- Kanemoto, S., Saimoto, H., Oshima, K., Nozaki, H., 1984. *Tetrahedron Lett.* **25**, 3317.
- Kanemoto, S., Saimoto, H., Oshima, K., Utimoto, K., Nozaki, H., 1989. *Bull. Chem. Soc. Jpn.* **62**, 519.
- Kanemoto, S., Tomioka, H., Oshima, K., Nozaki, H., 1986. *Bull. Chem. Soc. Jpn.* **59**, 105.
- Kantouch, A., Hebeish, A., El-Rafie, M.H., 1971. *J. Appl. Polym. Sci.* **15**, 1007.
- Karmakar, G.P., Singh, R.P., 1998. *Colloids Surf. A* **133**, 119.
- Karraker, D.G., 1968. *J. Inorg. Nucl. Chem. Lett.* **4**, 309.

- Kašpar, J., Graziani, M., Fornasiero, P., 2000. Ceria-containing three-way catalysts. In: Gschneidner Jr., K.A., Eyring, L.A., Bernal Mquez, S. (Eds.), *Handbook on the Physics and Chemistry of Rare Earths*, vol. **29**. Elsevier, Amsterdam, p. 159 (chapter 184).
- Kasperek, G.J., Bruce, T.C., 1971. *Inorg. Chem.* **10**, 382.
- Kasuya, M., Hatanaka, K., Hobley, J., Fukumura, H., Sevcikova, H., 2005. *J. Phys. Chem. A* **109**, 1405.
- Keatch, C.J., 1961. *Talanta* **8**, 620.
- Keener, J.P., Tyson, J.J., 1986. *Physica D* **21**, 307.
- Khalafi-Nezhad, A., Alamdari, R.F., 2001. *Tetrahedron* **57**, 6805.
- Kilbourn, T., 1992. *Cerium: A guide to its role in chemical technology*. Molycorp, Whiteplains, NY. Available free of charge on the Molycorp website: http://www.molycorp.com/cerium_book.pdf.
- Kim, J.H., Chin, J., 1992. *J. Am. Chem. Soc.* **114**, 9792.
- Kim, J.H., Yonezawa, S., Takashima, M., 2003. *J. Fluorine Chem.* **120**, 111.
- Kim, S.S., Rajagopal, G., 2004. *Synth. Commun.* **34**, 2237.
- Kim, S.S., Jung, H.C., 2003. *Synthesis* **14**, 2135.
- King, N.C., Dickinson, C., Zhou, W.Z., Bruce, D.W., 2005. *Dalton Trans.*, 1027.
- Kiselev, Yu.M., Goryachenkov, S.A., Ii'inskii, A.L., 1985. *Zh. Neorg. Khim.* **30**, 835.
- Kitamura, Y., Komiyama, M., 2002. *Nucleic Acids Res.* **30**, e102.
- Kitamura, Y., Sumaoka, J., Komiyama, M., 2003. *Tetrahedron* **59**, 10403.
- Kobayashi, S., Sugiura, M., Kitagawa, H., Lam, W.W.L., 2002. *Chem. Rev.* **102**, 2227.
- Koch, G.H., Strong, F.M., 1969. *Anal. Biochem.* **27**, 162.
- Kolthoff, I.M., Belcher, R., Stenger, V.A., Matsuyama, G., 1957. *Volumetric Analysis, Volume III, Titration Methods: Oxidation-Reduction Reactions*. Interscience, New York.
- Komiyama, M., 1995. *J. Biochem.* **118**, 665.
- Komiyama, M., 2005. Cutting DNA and RNA. In: Gschneidner Jr., K.A., Bnzli, J.-C.G., Pecharsky, V.K. (Eds.), *Handbook on the Physics and Chemistry of Rare Earths*, vol. **34**. Elsevier, Amsterdam, p. 405 (chapter 222).
- Komiyama, M., Sumaoka, J., 1998. *Curr. Opin. Chem. Biol.* **2**, 751.
- Komiyama, M., Arishima, H., Yokoyama, M., Kitamura, Y., Yamamoto, Y., 2005. *ChemBioChem* **6**, 192.
- Komiyama, M., Takeda, N., Shigekawa, H., 1999. *Chem. Commun.*, 1443.
- Komiyama, M., Takeda, N., Takahashi, Y., Uchida, H., Shiiba, T., Kodama, T., Yashiro, M., 1995. *J. Chem. Soc., Perkin Trans. II*, 269.
- Komiyama, M., Shiiba, T., Kodama, T., Takeda, N., Sumaoka, J., Yashiro, M., 1994a. *Chem. Lett.* **23**, 1025.
- Komiyama, M., Shiiba, T., Takahashi, Y., Takeda, N., Matsumura, K., Kodama, T., 1994b. *Supramol. Chem.* **4**, 31.
- Komiyama, M., 1999. *Chem. Commun.*, 1443.
- Kondo, T., Kubota, H., Katakai, R., 1989. *J. Appl. Sci.* **71**, 251.
- Korematsu, A., Takemoto, Y., Nakaya, T., Inoue, H., 2002. *Biomaterials* **23**, 263.
- Krs, E., Orban, M., Nazy, Zs., 1979. *Acta Chim. Acad. Sci. Hung.* **100**, 449.
- Kramer, K., Robertson, P.M., Ibl, N., 1980. *J. Appl. Electrochem.* **10**, 29.
- Kreh, R.P., 1988. US Patent 4,794,172.
- Kreh, R.P., Spotnitz, R.M., 1987a. US Patent 4,639,298.
- Kreh, R.P., Spotnitz, R.M., 1987b. US Patent 4,647,349.
- Kreh, R.P., Spotnitz, R.M., 1987c. US Patent 4,670,108.
- Kreh, R.P., Spotnitz, R.M., Lundquist, J.T., 1987. *Tetrahedron Lett.* **28**, 1067.
- Kreh, R.P., Spotnitz, R.M., Lundquist, J.T., 1989. *J. Org. Chem.* **54**, 1526.
- Krohn, K., Vitz, J., 2000. *J. Prakt. Chem.* **342**, 825.
- Kuhn, A.T., Randle, T.H., 1985. *J. Chem. Soc., Faraday Trans. I* **81**, 403.
- Kuhnert, L., Linde, H., 1977. *Z. Phys.* **17**, 19.
- Kumaraswamy, M.D.K., Rao, K.P., Joseph, K.T., 1980. *Eur. Polym. J.* **14**, 353.
- Kum-Tatt, L., Tong, H.K., 1962. *Anal. Chim. Acta* **26**, 583.
- Kunz, A.H., 1931. *J. Am. Chem. Soc.* **53**, 98.
- Kurita, K., Inoue, M., Harata, M., 2002. *Biomacromolecules* **3**, 147.
- Kurz, M.R., Ngoviwatchai, P., 1981. *J. Org. Chem.* **46**, 4672.
- Laali, K.K., Herbert, M., Cushnyr, B., Bhatt, A., Terrano, D., 2001. *J. Chem. Soc., Perkin Trans. I*, 578.
- Laing, S.B., 1968. *J. Chem. Soc. C*, 2915.
- Lamprecht, I., 1992. *Indian J. Technol.* **30**, 578.
- Lange, L.T., 1861. *J. Prakt. Chem.* **82**, 129.
- Lanza, G., Fragala, I.L., 1998. *J. Phys. Chem. A* **102**, 7990.
- Larsen, R.D., Brown, G.H., 1964. *J. Phys. Chem.* **68**, 360.
- Lebedev, I.A., Chepovoy, V.I., Myasoedov, B.F., 1975. *Radiochem. Radioanal. Lett.* **22**, 239.
- Lenka, S., Nayak, P.L., 1982. *Colloid Polym. Sci.* **260**, 1114.
- Lepoutre, P., Hui, S.H., 1975. *J. Appl. Polym. Sci.* **19**, 1257.

- Levason, W., Oldroyd, R.D., 1996. *Polyhedron* **15**, 409.
- Levy, S.V., 1994. *Pure Appl. Chem.* **66**, 1415.
- Li, R., Li, J., 1988. *Chem. Phys. Lett.* **144**, 96.
- Li, Z.C., Fu, Z.F., Huang, M.Z., Miao, J.K., Lian, N., 1989. *J. Appl. Polym. Sci.* **38**, 2171.
- Lindgren, O., 1977. *Acta Chem. Scand. Ser. A* **31**, 453.
- Lingane, J.J., Davis, D.G., 1956. *Anal. Chim. Acta* **15**, 201.
- Liu, M.Z., Cheng, R.S., Wu, J.J., Ma, C., 1993. *J. Polym. Sci. A* **31**, 3181.
- Loewenhaupt, M., Fischer, K.H., 1993. Valence-fluctuations and heavy-fermion 4f systems. In: Gschneidner Jr., K.A., Eyring, L.A. (Eds.), *Handbook on the Physics and Chemistry of Rare Earths*, vol. **16**. Elsevier, Amsterdam, p. 1 (chapter 105).
- Long, J.R., 1986. Implications in organic synthesis. In: Gschneidner Jr., K.A., Eyring, L.A. (Eds.), *Handbook on the Physics and Chemistry of Rare Earths*, vol. **8**. Elsevier, Amsterdam, p. 335 (chapter 57).
- Lutfor, M.R., Rahman, M.Z.A., Sidik, S., Mansor, A., Haron, J., Yunus, W.M.Z.W., 2001. *Designed Monomers Polymers* **4**, 252.
- Lynch, D.W., Weaver, J.H., 1988. Photoemission of Ce and its compounds. In: Gschneidner Jr., K.A., Eyring, L.A. (Eds.), *Handbook on the Physics and Chemistry of Rare Earths*, vol. **10**. Elsevier, Amsterdam, p. 231 (chapter 66).
- Maeda, Y., Sato, K., Ramaraj, R., Rao, T.N., Tryk, D.A., Fujishima, A., 1999. *Electrochim. Acta* **44**, 3441.
- Mahdavi, B., Harrison, S., Amouzegar, K., 2002. *World Patent WO 02/066690 A2*.
- Maini, S., Mandolini, L., Rol, C., 1978. *J. Org. Chem.* **43**, 3236.
- Maknon'kov, D.I., Cheprakov, A.V., Rodkin, M.A., Mil'chenko, A.Y., Beletskaya, I.P., 1986. *Zh. Org. Khim.* **22**, 30.
- Maldonado, A.L., Yatsimirsky, A.K., 2005. *Org. Biomol. Chem.* **3**, 2859.
- Mancin, F., Scrimin, P., Tecilla, P., Tonellato, U., 2005. *Chem. Commun.*, 2540.
- Mandal, P.K., Roy, S.C., 1995. *Tetrahedron* **51**, 7823.
- Marko, I.E., Ates, A., Augustyns, B., Gautier, A., Quesnel, Y., Turet, L., Wiaux, M., 1999. *Tetrahedron Lett.* **40**, 5613.
- Marocco, M., Brilmyer, G., 1983. *J. Org. Chem.* **48**, 1487.
- Martin, T.W., Henshall, A., Gross, R.C., 1963. *J. Am. Chem. Soc.* **85**, 113.
- Martin, T.W., Glass, R.W., 1970. *J. Am. Chem. Soc.* **92**, 5075.
- Martin, T.W., Rummel, R.E., Gross, R.C., 1964. *J. Am. Chem. Soc.* **86**, 2595.
- Matthews, R.W., 1971. *Int. J. Appl. Radiat. Isot.* **22**, 199.
- Matthews, R.W., 1972. *Int. J. Appl. Radiat. Isot.* **23**, 179.
- Matthews, R.W., 1982. *Int. J. Appl. Radiat. Isot.* **33**, 1159.
- Mazhar-ul-Haque, Caughlan, C.N., Hart, F.A., VanNice, R., 1971. *Inorg. Chem.* **10**, 115.
- McCormick, C.L., Park, L.S., 1985. *J. Appl. Polym. Sci.* **30**, 45.
- McDowall, D.J., Gupta, B.S., Stannett, V.T., 1984. *Prog. Polym. Sci.* **10**, 1.
- Mehta, G., Pandey, P.N., Ho, T.L., 1976. *J. Org. Chem.* **41**, 953.
- Meister, J.J., Patil, D.R., Channell, H., 1984. *J. Appl. Polym. Sci.* **29**, 3457.
- Meister, J.J., Patil, D.R., 1985. *Macromolecules* **18**, 1559.
- Mellor, J.M., Parkes, R., Millar, R.W., 1997. *Tetrahedron Lett.* **38**, 8739.
- Mellor, J.M., Mittoo, S., Parkes, R., Millar, R.W., 2000. *Tetrahedron* **56**, 8019.
- Meloche, C.G., 1915a. *J. Am. Chem. Soc.* **37**, 2339.
- Meloche, C.G., 1915b. *J. Am. Chem. Soc.* **37**, 2645.
- Mennicke, E., Holschbach, M.H., Coenen, H.H., 2000. *Radiochim. Acta* **88**, 221.
- Menzinger, M., Jankowski, P., 1986. *J. Phys. Chem.* **90**, 1217.
- Meyer, K., Roček, J., 1972. *J. Am. Chem. Soc.* **94**, 1209.
- Meyer, R.J., Jacoby, R., 1901. *Z. Anorg. Allg. Chem.* **27**, 359.
- Mikhailov, A.S., Krinskii, V.I., 1983. *Physica D* **9**, 356.
- Miller, F.J., Zittel, H.E., 1964. *J. Electroanal. Chem.* **7**, 116.
- Miller, J.T., Irish, D.E., 1967. *Can. J. Chem.* **45**, 147.
- Mills, A., 1989. *Chem. Soc. Rev.* **18**, 285.
- Milyukova, M.S., Malikov, D.A., Myasoedov, B.F., 1977. *Radiochem. Radioanal. Lett.* **29**, 93.
- Milyukova, M.S., Malikov, D.A., Myasoedov, B.F., 1980. *Sov. Radiochem.* **22**, 267.
- Mino, G., Kaizerman, S., 1958. *J. Polym. Sci.* **31**, 242.
- Mino, G., Kaizerman, S., Ramussen, E., 1959. *J. Am. Chem. Soc.* **81**, 1494.
- Mirkhani, V., Tangestaninejad, S., Alipanah, L., 2002. *Synth. Commun.* **32**, 621.
- Mishra, A., Bajpai, M., 2005. *J. Appl. Polym. Sci.* **98**, 1186.
- Mishra, A., Srinivasan, R., Gupta, R., 2003. *Colloid Polym. Sci.* **281**, 187.
- Mishra, A., Rajani, S., Agarwal, M., Dubey, R., 2002. *Polym. Bull.* **48**, 439.
- Mishra, B.K., Kuanar, M., Sharma, A., Nayak, B.B., 2001. *Indian J. Chem.* **40B**, 724.

- Misra, B.N., Kaur, I., Dogra, R., 1979. *J. Appl. Polym. Sci.* **24**, 1595.
- Misra, B.N., Kaur, I., Sharma, R.K., 1981. *Polym. Bull.* **4**, 636.
- Misra, B.N., Mehta, I.K., Dogra, R., 1980. *J. Appl. Polym. Sci.* **25**, 235.
- Misra, B.N., Mehta, I.K., Rathore, M.P.S., Lakhanpal, S., 1993. *J. Appl. Polym. Sci.* **49**, 1979.
- Misra, G.S., Khatib, J.I., 1982. *Colloid Polym. Sci.* **261**, 188.
- Miyama, S., Asanuma, H., Komiyama, M., 1997. *J. Chem. Soc., Perkin Trans. II*, 1685.
- Mohanty, N., Pradhan, B., Mohanta, M.C., Das, H.K., 1983. *Eur. Polym. J.* **19**, 415.
- Mohanty, N., Pradhan, B., Mohanta, M.C., 1979. *Eur. Polym. J.* **15**, 743.
- Mohanty, N., Pradhan, B., Mahanta, M.C., 1980. *Eur. Polym. J.* **16**, 451.
- Molander, G., 1992. *Chem. Rev.* **92**, 29.
- Morey, J., Saá, J.M., 1993. *Tetrahedron* **49**, 105.
- Morita, M., Masatani, T., Matsuda, Y., 1993. *Bull. Chem. Soc. Jpn.* **66**, 2747.
- Morss, L.R., 1994. Comparative thermochemical and oxidation – reduction properties of lanthanides and actinides. In: Gschneidner Jr., K.A., Eyring, L., Bernal Marquez, S. (Eds.), *Handbook on the Physics and Chemistry of Rare Earths*, vol. **18**. Elsevier, Amsterdam, pp. 239–291 (chapter 122).
- Moss, R.A., Morales-Rojas, H., 1999. *Org. Lett.* **1**, 1791.
- Moss, R.A., Morales-Rojas, H., 2001. *J. Am. Chem. Soc.* **123**, 7457.
- Moss, R.A., Ragunathan, K.G., 1998. *Chem. Commun.*, 1871.
- Moss, R.A., Ragunathan, K.G., 1999. *Langmuir* **15**, 107.
- Moss, R.A., Morales-Rojas, H., Vijayaraghavan, S., Tian, J.Z., 2004. *J. Am. Chem. Soc.* **126**, 10923.
- Mostafa, K.M., 2005. *J. App. Sci.* **5**, 341.
- Muathen, H.A., 1991. *Indian J. Chem. B* **30**, 522.
- Müller, S.C., Plessner, T., Hess, B., 1987. *Physica D* **24**, 71.
- Murugan, R., Ramakrishna, S., 2004. *Colloid Polym. Sci.* **282**, 1316.
- Nagaty, A., Abd-Et-Mouti, F., Mansour, O.Y., 1980. *Eur. Polym. J.* **16**, 343.
- Nagieb, Z.A., El-Gammal, A.A., 1986. *J. Appl. Polym. Sci.* **31**, 179.
- Nagori, R.R., Mehta, M., Mehrotra, R.N., 1981. *J. Inorg. Nucl. Chem.* **43**, 2899.
- Nagy, G., Körös, E., Oftedal, N., Tjellflaat, K., Ruoff, P., 1996. *Chem. Phys. Lett.* **250**, 255.
- Nagygyory, S., Wittmann, M., Pinter, S., Visegrady, A., Dancso, A., Thuy, N.B., Noszticzius, Z., Hegedus, L., Försterling, H.D., 1999. *J. Phys. Chem. A* **103**, 4885.
- Nagy-Ungvarai, Z., Tyson, J.J., Hess, B., 1989a. *J. Phys. Chem.* **93**, 707.
- Nagy-Ungvarai, Z., Tyson, J.J., Müller, S.C., Watson, L.T., Hess, B., 1990. *J. Phys. Chem.* **94**, 8677.
- Nagy-Ungvarai, Z., Müller, S.C., Tyson, J.J., Hess, B., 1989b. *J. Phys. Chem.* **93**, 2760.
- Nair, V., Augustine, A., George, T.G., 2002. *Eur. J. Org. Chem.*, 2363.
- Nair, V., Augustine, A., Panicker, S.B., Suja, T.D., Mathai, S., 2003. *Res. Chem. Intermed.* **29**, 213.
- Nair, V., Mathews, J., Prabhakaran, J., 1997. *Chem. Soc. Rev.*, 127.
- Nair, V., Balagopal, L., Rajan, R., Mathew, J., 2004. *Acc. Chem. Res.* **37**, 21.
- Nair, V., Nair, L.G., George, T.G., Augustine, A., 2000a. *Tetrahedron* **56**, 7607.
- Nair, V., Panicker, S.B., Mathai, S., 2003. *Res. Chem. Intermed.* **29**, 227.
- Nair, V., Panicker, S.B., Augustine, A., George, T.G., Thomas, S., Vairamani, M., 2001. *Tetrahedron* **57**, 7417.
- Nair, V., George, T.G., Sheeba, V., Augustine, A., Balagopal, L., Nair, L.G., 2000b. *Synlett*, 1597.
- Nash, K.L., Sullivan, J.C., 1991. Kinetics of complexation and redox reactions of the lanthanides in aqueous solution. In: Gschneidner Jr., K.A., Eyring, L.A. (Eds.), *Handbook on the Physics and Chemistry of Rare Earths*, vol. **15**. Elsevier, Amsterdam, p. 347 (chapter 102).
- Navarro, R.R., Sumi, K., Matsumura, M., 1999. *Water Res.* **33**, 2037.
- Nave, P.M., Trahanovsky, W.S., 1968. *J. Am. Chem. Soc.* **90**, 4755.
- Nave, P.M., Trahanovsky, W.S., 1971. *J. Am. Chem. Soc.* **93**, 4536.
- Nayak, B.R., Singh, R.P., 2001. *Eur. Polym. J.* **37**, 1655.
- Nayak, N.C., Das, H.K., Singh, B.C., 1991. *J. Appl. Polym. Sci.* **42**, 2391.
- Nelson, N., 2002. *Platinum Metals Rev.* **46**, 18.
- Netzer, F.P., Bertel, E., 1982. Adsorption and catalysis on rare earth surfaces. In: Gschneidner Jr., K.A., Eyring, L.A. (Eds.), *Handbook on the Physics and Chemistry of Rare Earths*, vol. **5**. Elsevier, Amsterdam, p. 217 (chapter 43).
- Neumann, B., Müller, S.C., Hauser, M.J.B., Steinbock, O., Simoyi, R.H., Dalal, N.S., 1995. *J. Am. Chem. Soc.* **117**, 6372.
- Neumann, C.S., Fulde, P., 1989. *Z. Phys. B* **74**, 277.

- Nicolis, G., Prigogine, I., 1977. Self-Organization in Nonequilibrium Systems: From Dissipative Structures to Order through Fluctuations. Wiley, New York.
- Nikitina, G.P., Egorova, V.P., Miftakhudinova, I.K., 1980. *Sov. Radiochem.* **22**, 528.
- Nishiguchi, T., Asano, F., 1989. *J. Org. Chem.* **54**, 1531.
- Nishiguchi, T., Taya, H., 1990. *J. Chem. Soc., Perkin Trans. I*, 172.
- Norman, R.O.C., Thomas, C.B., Ward, P.J., 1973. *J. Chem. Soc., Perkin Trans. I*, 2914.
- Noszticzus, Z., Farkas, H., Schelly, Z., 1984. *J. Chem. Phys.* **80**, 6062.
- Noyes, A.A., Garner, C.S., 1936. *J. Am. Chem. Soc.* **58**, 1265.
- Noyes, R.M., Jwo, J.J., 1975. *J. Am. Chem. Soc.* **97**, 5431.
- Noyes, R.M., 1980. *J. Am. Chem. Soc.* **102**, 4644.
- Noyes, R.M., Field, R.J., Körös, E., 1972. *J. Am. Chem. Soc.* **94**, 1394.
- Oehr, K., 1982a. US Patent 4,313,804.
- Oehr, K., 1982b. Canadian Patent 1,132,996.
- Ogiwara, Y., Kubota, H., 1970. *J. Appl. Polym. Sci.* **14**, 2611.
- Ogiwara, Y., Kubota, H., Arai, K., 1970. *J. Appl. Polym. Sci.* **14**, 1049.
- Okieimen, E.F., 1987. *Eur. Polym. J.* **23**, 319.
- Okieimen, E.F., Ebhoaye, J.E., 1986. *J. Appl. Polym. Sci.* **31**, 1275.
- Okieimen, E.F., Idehen, K.I., 1987. *Eur. Polym. J.* **23**, 867.
- Okieimen, E.F., Idehen, K.I., Ahiedu, H., 1987. *J. Appl. Polym. Sci.* **34**, 737.
- Okieimen, F.E., Ogbeifun, D.E., 1996. *Eur. Polym. J.* **32**, 311.
- Okieimen, F.E., 1998. *Angew. Macromol. Chem.* **260**, 5.
- Okieimen, F.E., Egharevba, F., 1989. *Eur. Polym. J.* **25**, 99.
- Okieimen, F.E., Nkumah, J.E., Egharevba, F., 1989. *Eur. Polym. J.* **25**, 423.
- Okieimen, F.E., Egharevba, F., 1992. *Eur. Polym. J.* **28**, 415.
- Okiniski, A., 1992. In: Compton, R.G. (Ed.), *Chemical Kinetics. Catastrophe Theory*, vol. **33**. Elsevier, Amsterdam.
- Olah, G.A., Gupta, B.G.B., Fung, A.P., 1980. *Synthesis*, 897.
- Onishi, Y., 1980. *Polymer* **21**, 819.
- Onishi, Y., Maruno, S., Kamiya, S., Hokkoku, S., Hasegawa, M., 1978. *Polymer* **19**, 1325.
- Oskooie, H.A., Abaszadeh, M.R., Zamani, F.F., Heravi, M.M., 1998. *Synth. Commun.* **28**, 2281.
- Oslovitch, J., Försterling, H.D., Wittmann, M., Noszticzus, Z., 1998. *J. Phys. Chem. A* **102**, 922.
- Ott, R., Krämer, R., 1999. *Appl. Microbiol. Biotechnol.* **52**, 761.
- Overbury, S.H., Huntley, D.R., Mullins, D.R., Glavee, G.N., 1998. *Catal. Lett.* **51**, 133.
- Öz, N., Akar, A., 2000. *Eur. Polym. J.* **36**, 193.
- Ruoff, P., 1982. *Chem. Phys. Lett.* **92**, 239.
- Padhi, N.P., Singh, B.C., 1983. *Colloid Polym. Sci.* **261**, 390.
- Pan, W.B., Chang, F.R., Wei, L.M., Wu, M.J., Wu, Y.C., 2003. *Tetrahedron Lett.* **44**, 331.
- Panda, A., Singh, B.C., 1995. *J. Appl. Polym. Sci.* **58**, 1999.
- Paquette, L.A., Kelly, J.F., 1969. *Tetrahedron Lett.* **10**, 4509.
- Pascual, B., Castellano, I., Vazquez, B., Gurruchaga, M., Goñi, I., 1996. *Polymer* **37**, 1005.
- Pastor, T.J., Vajgand, V.J., Cyric, I., 1982. *Anal. Chim. Acta* **138**, 87.
- Patel, G.M., Patel, C.P., Trivedi, H.C., 1999. *Eur. Polym. J.* **35**, 201.
- Patil, D.R., Fanta, G.F., 1993. *J. Appl. Polym. Sci.* **47**, 1765.
- Patra, C.M., Singh, B.C., 1994b. *J. Appl. Polym. Sci.* **52**, 1557.
- Patra, C.M., Singh, B.C., 1994a. *J. Appl. Polym. Sci.* **52**, 1549.
- Paulenova, A., Creager, S.E., Navratil, J.D., Wei, Y., 2002. *J. Power Sources* **109**, 431.
- Paulrajan, S., Gopalan, A., Subbaratnam, N.R., Venkatarao, K., 1983. *Polymer* **24**, 906.
- Periasamy, M., Bhatt, M.V., 1977a. *Synthesis*, 330.
- Periasamy, M., Bhatt, M.V., 1977b. *Tetrahedron Lett.* **18**, 2357.
- Petrascu, A.M., Koch, M.H.J., Försterling, H.D., 1999. *J. Phys. Chem. A* **103**, 6757.
- Pletcher, D., Valdes, E.M., 1988a. *Electrochim. Acta* **33**, 499.
- Pletcher, D., Valdes, E.M., 1988b. *Electrochim. Acta* **33**, 509.
- Pletcher, D., Valdes, E.M., 1987. *J. Chem. Res. (S)*, 386.
- Po, R., 1994. *J. Macromol. Sci. Rev. Macromol. Chem. Phys. C* **34**, 607.
- Pojman, J.A., Leard, D.C., West, W., 1992. *J. Am. Chem. Soc.* **114**, 8298.
- Pourjavadi, A., Zohuriaan-Mehr, M.J., 2002. *Starch* **54**, 140.
- Pramanick, D., 1979. *Colloid Polym. Sci.* **257**, 41.
- Pramanick, D., Chatterjee, A.K., 1981. *Eur. Polym. J.* **17**, 239.

- Pramanick, D., Sarkar, S.K., 1976. *Colloid Polym. Sci.* **254**, 989.
- Prawicki, K., Dziegieć, J., 1996. *Zh. Obsch. Khim.* **66**, 2003.
- Prigogine, I., 1962. *Introduction to Thermodynamics of Irreversible Processes*. Wiley, New York.
- Purgato, F.L.S., Romero, J.R., 2002. *J. Catal.* **209**, 394.
- Purgato, F.L.S., Ferreira, M.I.C., Romero, J.R., 2000. *J. Mol. Catal. A* **161**, 99.
- Rahman, L., Silong, S., Zin, W., Rahman, M.Z.A., Ahmad, M., Haron, J., 2000. *J. Appl. Polym. Sci.* **76**, 516.
- Rammo, J., Hettich, R., Roigk, A., Schneider, H.J., 1996. *Chem. Commun.*, 105.
- Randle, T.H., Kuhn, A.T., 1983. *J. Chem. Soc. Faraday Trans. I* **79**, 1741.
- Randle, T.H., Kuhn, A.T., 1986. *Electrochim. Acta* **31**, 739.
- Rao, G.G., Rao, P.V.K., Murty, K.S., 1962. *Talanta* **9**, 835.
- Rao, K.P., Kannappan, E.P., Jayaraman, K.S., Joseph, K.T., Nayudamma, Y., 1981. *J. Appl. Polym. Sci.* **26**, 3343.
- Rao, S.R., Kapur, S.L., 1969. *J. Appl. Polym. Sci.* **13**, 2649.
- Rath, S.K., Singh, R.P., 1998. *Colloids Surf., A* **139**, 129.
- Rau, J.V., Chilingarov, N.S., Leskiv, M.S., Sukhoverkhov, V.F., Albertini, V.R., Sidorov, L.N., 2001. *J. Phys. IV (France)* **11**, 109.
- Raymond, K.N., Smith, W.L., 1981. *Struct. Bond.* **43**, 159.
- Raymond, K.N., Freeman, G.E., Kappel, M.J., 1984. *Inorg. Chim. Acta* **94**, 193.
- Reddy, G.V.R., Selvakumar, S., Francisca, L.J., 2005. *Colloid Polym. Sci.* **283**, 1085.
- Reddy, G.V.R., Arun, J., Panda, J., 2006. *J. Appl. Polym. Sci.* **99**, 218.
- Reddy, M.V.K., Mehrotra, B., Vankar, Y.D., 1995. *Tetrahedron Lett.* **36**, 4861.
- Reidy, R.F., Swider, K.E., 1995. *J. Am. Ceram. Soc.* **78**, 1121.
- Ren, L., Tokura, S., 1994. *Carbohydr. Polymers* **23**, 19.
- Ren, L., Miura, Y., Nishi, N., Tokura, S., 1993. *Carbohydr. Polymers* **21**, 23.
- Rennie, R.A.C., 1972. Canadian Patent 899,856.
- Reyes, Z., Clark, C.F., Dreier, F., Phillips, R.C., Russell, C.R., Rist, C.E., 1973. *Ind. Eng. Chem. Proc. Des. Dev.* **12**, 62.
- Riande, E., Mateos, A.M., Guzmán, G.M., 1970. *Eur. Polym. J.* **6**, 437.
- Riley, D.P., Correa, P.E., 1986. *J. Chem. Soc., Chem. Commun.*, 1097.
- Rindone, B., Scolastico, C., 1971. *J. Chem. Soc. B*, 2238.
- Rindone, B., Scolastico, C., 1975. *J. Chem. Soc., Perkin Trans. I*, 1398.
- Rizkalla, E.N., Choppin, G.R., 1991. Hydration and hydrolysis of lanthanides. In: Gschneidner Jr., K.A., Eyring, L.A. (Eds.), *Handbook on the Physics and Chemistry of Rare Earths*, vol. **15**. Elsevier, Amsterdam, p. 393 (chapter 103).
- Rizkalla, E.N., Choppin, G.R., 1994. Lanthanides and actinides hydration and hydrolysis. In: Gschneidner Jr., K.A., Eyring, L.A., Choppin, G.R., Lander, L.H. (Eds.), *Handbook on the Physics and Chemistry of Rare Earths*, vol. **18**. Elsevier, Amsterdam, p. 529 (chapter 127).
- Rodriguez-Franco, M.I., Dorransoro, I., Hernandez-Higuera, A.I., Antequera, G., 2001. *Tetrahedron Lett.* **42**, 863.
- Roelofs, M.G., 1988. *J. Chem. Phys.* **88**, 5516.
- Rogachev, D.L., Porai-Koshits, M.A., Kuznetsov, V.Y., Dikareva, L.M., 1974. *Zh. Strukt. Khim.* **15**, 465.
- Roigk, A., Hettich, R., Schneider, H.J., 1998. *Inorg. Chem.* **37**, 751.
- Rössle, M., Werner, T., Frey, W., Christoffers, J., 2005. *Eur. J. Org. Chem.*, 5031.
- Rout, A., Rout, S.P., Singh, B.C., Santappa, M., 1977. *Eur. Polym. J.* **13**, 497.
- Roy, S.C., Guin, C., Maiti, G., 2001b. *Tetrahedron Lett.* **42**, 9253.
- Roy, S.C., Guin, C., Rana, K.K., Maiti, G., 2001a. *Tetrahedron Lett.* **42**, 6941.
- Roy, S.C., Rana, K.K., Guin, C., Banerjee, B., 2003a. *Synlett*, 221.
- Roy, S.C., Rana, K.K., Guin, C., Banerjee, B., 2003b. *Arkivoc* (ix), 34.
- Ruoff, P., 1994. *Chem. Phys. Lett.* **226**, 295.
- Ruoff, P., Noyes, R.M., 1989. *J. Phys. Chem.* **93**, 7394.
- Ruoff, P., Varga, M., Körös, E., 1988. *Acc. Chem. Res.* **21**, 326.
- Saikia, C.N., Ali, F., 1999. *Bioresour. Technol.* **68**, 165.
- Samal, R.K., Bhuyan, B.L., 1994. *J. Appl. Polym. Sci.* **52**, 1675.
- Sanderson, W.R., 2000. *Pure Appl. Chem.* **72**, 1289.
- Sathunuru, R., Biehl, E., 2004. *Arkivoc* (xiv), 89.
- Sathunuru, R., Rao, U.N., Biehl, E., 2003. *Arkivoc* (iv), 124.
- Schaafsma, S.E., Steinberg, H., de Boer, T.J., 1966. *Recl. Trav. Chim. Pays-Bas* **85**, 73.
- Scott, K., 1995. *Electrochemical Process for Clean Technology*. Royal Society of Chemistry, Cambridge.

- Sereni, J.G., 1991. Low-temperature behaviour of cerium compounds. In: Gschneidner Jr., K.A., Eyring, L.A. (Eds.), *Handbook on the Physics and Chemistry of Rare Earths*, vol. **15**. Elsevier, Amsterdam, p. 1 (chapter 98).
- Sevcik, P., Adamacikova, I., 1988. *Chem. Phys. Lett.* **146**, 419.
- Shah, S.B., Patel, C.P., Trivedi, H.C., 1995. *Carbohydr. Polym.* **26**, 61.
- Shakhashiri, B.Z., 1985. *Chemical Demonstrations: A Handbook for Teachers of Chemistry*, vol. II. The University of Wisconsin Press, Madison, pp. 232–307 (chapter 7).
- Sham, T.K., 1983. *J. Chem. Phys.* **79**, 1116.
- Shan, Y., Huang, S.D., 1998. *Acta Cryst. C* **54**, 1744.
- Shannon, R.D., Prewitt, C.T., 1969. *Acta Cryst. B* **25**, 925.
- Sharma, B.R., Kumar, V., Soni, P.L., 2003. *J. Appl. Polym. Sci.* **90**, 129.
- Sharma, N.N., Mehrotra, R.C., 1954a. *Anal. Chim. Acta* **11**, 417.
- Sharma, N.N., Mehrotra, R.C., 1954b. *Anal. Chim. Acta* **11**, 507.
- Sharma, N.N., Mehrotra, R.C., 1955. *Anal. Chim. Acta* **13**, 419.
- Sheldon, R.A., Kochi, J.K., 1968. *J. Am. Chem. Soc.* **90**, 6688.
- Sherrill, M.S., King, C.B., Spooner, R.C., 1943. *J. Am. Chem. Soc.* **65**, 170.
- Sherrington, D.C., 1988. *Pure Appl. Chem.* **60**, 401.
- Shi, Q.Z., Wang, J.G., Cai, K., 1999. *Synth. Commun.* **29**, 1177.
- Shigekawa, H., Ikawa, H., Yoshizaki, R., Ijima, Y., Sumaoka, J., Komiyama, M., 1996. *Appl. Phys. Lett.* **68**, 1433.
- Shigekawa, H., Ishida, M., Miyake, K., 1999. *Appl. Phys. Lett.* **74**, 460.
- Shim, S.J., Kim, Y.D., 1969. *J. Korean Chem. Soc.* **13**, 365.
- Shiozaki, R., Kominami, H., Kero, Y., 1996. *Synth. Commun.* **26**, 1663.
- Shukla, J.S., Sharma, G.K., 1987. *J. Polym. Sci. A* **25**, 595.
- Shukla, S.R., Athalye, A.R., 1994. *J. Appl. Polym. Sci.* **54**, 279.
- Shukla, S.R., Rao, G.V.G., Athalye, A.R., 1991. *J. Appl. Polym. Sci.* **42**, 2163.
- Shukla, S.R., Rao, G.V.G., Athalye, A.R., 1993. *J. Appl. Polym. Sci.* **49**, 1423.
- Singh, M.P., Singh, H.S., Verma, M.K., 1980. *J. Phys. Chem.* **84**, 256.
- Sirimungkala, A., Försterling, H.D., Noszticzius, Z., 1996. *J. Phys. Chem.* **100**, 3051.
- Sirimungkala, A., Försterling, H.D., Dlask, V., Field, R.J., 1999. *J. Phys. Chem. A* **103**, 1038.
- Skanthakumar, S., Soderholm, L., 1996. *Phys. Rev. B* **53**, 920.
- Skarzewski, J., 1984. *Tetrahedron* **40**, 4997.
- Skarzewski, J., Mlochowski, J., 1985. *J. Prakt. Chem.* **327**, 963.
- Skarzewski, J., 1980. *J. Chem. Res. (S)*, 410.
- Skarzewski, J., Cichacz, E., 1984. *Bull. Chem. Soc. Jpn.* **57**, 271.
- Smith, G.F., Fritz, J.S., 1948. *Anal. Chem.* **20**, 874.
- Smith, G.F., 1967. *Talanta* **14**, 1131.
- Smith, G.F., Getz, C.A., 1938. *Ind. Eng. Chem., Anal. Ed.* **10**, 191.
- Smith, G.F., Fly, W.H., 1949. *Anal. Chem.* **21**, 1233.
- Smith, G.F., Sullivan, V.R., Frank, G., 1936. *Ind. Eng. Chem., Anal. Ed.* **8**, 449.
- Sofen, S.R., Abu-Dari, K., Freyberg, D.P., Raymond, K.N., 1978. *J. Am. Chem. Soc.* **100**, 7882.
- Sofen, S.R., Cooper, S.R., Raymond, K.N., 1979. *Inorg. Chem.* **18**, 1611.
- Soucy, P., Ho, T.L., Deslongchamps, P., 1972. *Can. J. Chem.* **50**, 2047.
- Spitsyn, V.I., Kiselev, Yu.M., Martynenko, L.I., 1974. *Zh. Neorg. Khim.* **19**, 3194.
- Spotnitz, R.M., Kreh, R.P., Lundquist, J.T., Press, P.J., 1990. *J. Appl. Electrochem.* **20**, 209.
- Sreedhara, A., Cowan, J.A., 2001. *J. Biol. Inorg. Chem.* **6**, 337.
- Stahl, E., 1965. *Thin-Layer Chromatography; A Laboratory Handbook*. Springer-Verlag, Berlin.
- Stefane, B., Kocevar, M., Polanc, S., 2002. *Synth. Commun.* **32**, 1703.
- Steigman, J., Birnbaum, N., Edmonds, S.M., 1942. *Ind. Eng. Chem., Anal. Ed.* **14**, 30.
- Steward, G.A., 1998. US Patent 5,756,874.
- Sudhakar, D., Srinivasan, K.S.V., Joseph, K.T., Santappa, M., 1979. *J. Appl. Polym. Sci.* **23**, 2923.
- Sugiyama, T., 1981. *Bull. Chem. Soc. Jpn.* **54**, 2847.
- Sumaoka, J., Kajimura, A., Ohno, H., Komiyama, M., 1997. *Chem. Lett.*, 507.
- Sumaoka, J., Kajimura, A., Imai, T., Ohno, M., Komiyama, M., 1998b. *Nucleosides Nucleotides* **17**, 613.
- Sumaoka, J., Miyama, S., Komiyama, M., 1994. *Chem. Commun.*, 1755.
- Sumaoka, J., Igawa, T., Yagi, T., Komiyama, M., 2001. *Chem. Lett.*, 20.
- Sumaoka, J., Azuma, Y., Komiyama, M., 1998a. *Chem. Eur. J.* **4**, 205.

- Sunstrom, J.E., Kauzlarich, S.M., Antonio, M.R., 1993. *Chem. Mater.* **5**, 182.
- Surendra, K., Krishnaveni, N.K., Rao, K.R., 2005. *Tetrahedron Lett.* **46**, 4111.
- Surma, J.E., Bryan, G.H., Greeting, J.G.H., Butner, R.S., 1998. US Patent 5,756,874.
- Surma, J.E., Nelson, N., Steward, G.A., Bryan, G.H., 1999. US Patent 5,968,337.
- Svehla, G., 1979. *Vogel's Textbook of Macro and Semimicro Qualitative Inorganic Analysis*. Longman, London.
- Sworski, T.J., 1957. *J. Am. Chem. Soc.* **79**, 3655.
- Sydnese, L.K., Burkov, I.C., Hansen, S.H., 1985. *Tetrahedron* **41**, 5703.
- Sykora, R.E., Deakin, L., Mar, A., Skanthakumar, S., Soderholm, L., Albrecht-Schmitt, T.E., 2004. *Chem. Mater.* **16**, 1343.
- Syper, L., 1966. *Tetrahedron Lett.* **7**, 4493.
- Syrokomskaa, V.S., Stiepin, V.V., 1936. *J. Am. Chem. Soc.* **58**, 928.
- Takahashi, T., Sakurai, H., 1962. *Talanta* **9**, 189.
- Takarada, T., Yashiro, M., Komiya, M., 2000. *Chem. Eur. J.* **6**, 3906.
- Takasaki, B.K., Chin, J., 1994. *J. Am. Chem. Soc.* **116**, 1121.
- Takashima, M., Fukami, S., Nosaka, Y., Unishi, T., 1992. *J. Fluorine Chem.* **57**, 131.
- Tamani, B., Iranpoor, N., Karimi Zarchi, M.A.K., 1993. *Polymer* **34**, 2011.
- Than, M.M., Aye, M.M., Win, D.T., 2001. *AU J. Technol.*, October 2001, article 5, <http://www.journal.au.edu/au techno/2001/oct2001/article5.pdf>.
- Thejappa, N., Pandey, S.N., 1982. *J. Appl. Polym. Sci.* **27**, 2307.
- Thimma, R.T., Reddy, N.S., Tammishetti, S., 2003. *Polym. Adv. Technol.* **14**, 663.
- Thyran, T., Lightner, D.A., 1996. *Tetrahedron Lett.* **37**, 315.
- Tikeda, N., Imai, T., Irisawa, M., Sumaoka, J., Yashiro, M., Shigekawa, H., Komiya, M., 1996. *Chem. Lett.*, 599.
- Tomioka, H., Oshima, K., Nozaki, H., 1982. *Tetrahedron Lett.* **23**, 539.
- Tomita, T., Li, Y.J., Nakaya, T., 1999. *Chem. Mater.* **11**, 2155.
- Torii, S., Tanaka, H., Inokuchi, T., Nakane, S., Akada, M., Saito, N., Sirakawa, T., 1982. *J. Org. Chem.* **47**, 1647.
- Touchstone, J., 1982. *Advances in Thin-Layer Chromatography*. Wiley, New York.
- Touchstone, J., Dobbins, M., 1978. *Practice of Thin-Layer Chromatography*. Wiley, New York.
- Trahanovsky, W.S., Gilmore, J.R., Heaton, P.C., 1973. *J. Org. Chem.* **38**, 760.
- Trahanovsky, W.S., Young, L.B., Brown, G.L., 1967. *J. Org. Chem.* **32**, 3865.
- Trahanovsky, W.S., 1973. In: Huysen, E.S. (Ed.), *Methods in Free-Radical Chemistry*, vol. **4**. Marcel Dekker, New York, pp. 133–169.
- Trahanovsky, W.S., Macaulay, D.B., 1973. *J. Org. Chem.* **38**, 1497.
- Trahanovsky, W.S., Brixius, D.W., 1973. *J. Am. Chem. Soc.* **95**, 6778.
- Trahanovsky, W.S., Cramer, J., 1971. *J. Org. Chem.* **36**, 1890.
- Trahanovsky, W.S., Young, L.B., 1966. *J. Org. Chem.* **31**, 2033.
- Trahanovsky, W.S., Robbins, M.D., 1971. *J. Am. Chem. Soc.* **93**, 5256.
- Trahanovsky, W.S., Cramer, J., Brixius, D.W., 1974. *J. Am. Chem.* **96**, 1077.
- Trahanovsky, W.S., Brewster, L.B., Robbins, M.D., 1969d. *J. Am. Chem. Soc.* **91**, 7084.
- Trahanovsky, W.S., Young, L.H., Bierman, M.H., 1969c. *J. Org. Chem.* **34**, 869.
- Trahanovsky, W.S., Young, M.G., Nave, P.M., 1969a. *Tetrahedron Lett.* **30**, 2501.
- Trahanovsky, W.S., Flash, P.J., Smith, L.M., 1969b. *J. Am. Chem. Soc.* **91**, 5068.
- Treindl, L., Fabian, P., 1980. *Collect. Czech. Chem. Commun.* **45**, 1168.
- Treindl, L., Ruoff, P., Kvernberg, P.O., 1997. *J. Phys. Chem. A* **101**, 4606.
- Tripathy, T., Pandey, S.R., Karmakar, N.C., Bhagat, R.P., Singh, R.P., 1999. *Eur. Polym. J.* **35**, 2057.
- Trovarelli, A. (Ed.), 2002. *Catalysis by Ceria and Related Materials*. Imperial College Press, London.
- Tunca, U., Serhatli, I.E., Yağci, Y., 1989. *Polym. Bull.* **22**, 483.
- Tzedakis, T., Savall, A.J., 1992. *Ind. Eng. Chem. Res.* **31**, 2475.
- Tzedakis, T., Savall, A., 1997. *J. Appl. Electrochem.* **27**, 589.
- Varga, M., Györgyi, L., Körös, E., 1985. *J. Am. Chem. Soc.* **107**, 4780.
- Vázquez, B., Gurruchaga, M., Goñi, I., 1995. *Polymer* **36**, 2311.
- Vázquez, M.B., Goñi, I., Gurruchaga, M., Valero, M., Guzmán, G.M., 1987a. *J. Polym. Sci. A* **25**, 719.
- Vázquez, M.B., Goñi, I., Gurruchaga, M., Valero, M., Guzmán, G.M., 1987b. *J. Polym. Sci. A* **25**, 1309.
- Vera-Pacheco, M., Vázquez-Torres, H., Canché-Escamilla, G., 1993. *J. Appl. Polym. Sci.* **47**, 53.

- Vijayarathi, T., Velayutham, D., Noel, M., 2001. *J. Appl. Electrochem.* **31**, 979.
- Vijayarathi, T., Srinivasan, R.K., Noel, M., 1999. *Bull. Electrochem.* **15**, 293.
- Vijayakumar, M.T., Reddy, C.R., Joseph, K.T., 1985. *Eur. Polym. J.* **21**, 415.
- Vione, D., Maurino, V., Minero, C., Pelizzetti, E., 2005. *Environ. Sci. Technol.* **39**, 1101.
- Vione, D., Maurino, V., Minero, C., Vincenti, M., Pelizzetti, E., 2001. *Chemosphere* **44**, 237.
- Vitta, S.B., Stahel, E.P., Stannett, V.T., 1986. *J. Appl. Polym. Sci.* **32**, 5799.
- Vitta, S.B., Stahel, E.P., Stannett, V.T., 1989. *J. Appl. Polym. Sci.* **38**, 503.
- Vora, R.A., Trivedi, H.C., Patel, C.P., Trivedi, M.C., 1995. *J. Appl. Polym. Sci.* **58**, 1543.
- Wadsworth, E., Duke, F.R., Goetz, O.A., 1957. *Anal. Chem.* **29**, 1824.
- Walden, G.H., Hammett, L.P., Chapman, R.P., 1931. *J. Am. Chem. Soc.* **53**, 3908.
- Walden, G.H., Hammett, L.P., Chapman, R.P., 1933. *J. Am. Chem. Soc.* **55**, 2649.
- Walden, G.H., Hammett, L.P., Chapman, R.P., 1934. *J. Am. Chem. Soc.* **56**, 1092.
- Wang, D.F., Luo, Y., Sun, J.P., Du, D.H., Wang, C.H., Zhou, X.L., Xue, C.H., 2005. *Carbohydr. Polym.* **62**, 1.
- Wang, J.C., Hynne, F., Sørensen, P.G., Nielsen, K., 1996. *J. Phys. Chem.* **100**, 17593.
- Wang, L.Q., Tu, K.H., Li, Y.P., Zhang, J., Jiang, L.M., Zhang, Z.H., 2002. *React. Funct. Polym.* **53**, 19.
- Wang, Y.H., Tanko, J.M., 1998. *J. Chem. Soc., Perkin Trans. II*, 2705.
- Wang, Y.P., Yuan, K., Li, Q.L., Wang, L.P., Gu, S.J., Pei, X.W., 2005. *Mater. Lett.* **59**, 1736.
- Warren, C.G., 1964. *J. Inorg. Nucl. Chem.* **26**, 1391.
- Wartenburg, H., 1940. *Z. Anorg. Allgem. Chem.* **244**, 237.
- Watts, L., Fitzpatrick, J.D., Pettit, R., 1965. *J. Am. Chem. Soc.* **87**, 3253.
- Weinstock, L.M., Corley, E., Abramson, N.L., Karady, S., 1988. *Heterocycles* **27**, 2627.
- Weiss, J., Porret, D., 1937. *Nature* **139**, 1019.
- Willard, H.H., Young, P., 1928a. *J. Am. Chem. Soc.* **50**, 1322.
- Willard, H.H., Young, P., 1928b. *J. Am. Chem. Soc.* **50**, 1334.
- Willard, H.H., Young, P., 1928c. *J. Am. Chem. Soc.* **50**, 1368.
- Willard, H.H., Young, P., 1928d. *J. Am. Chem. Soc.* **50**, 1372.
- Willard, H.H., Young, P., 1928e. *J. Am. Chem. Soc.* **50**, 1379.
- Willard, H.H., Young, P., 1929a. *J. Am. Chem. Soc.* **51**, 139.
- Willard, H.H., Young, P., 1929b. *J. Am. Chem. Soc.* **51**, 149.
- Willard, H.H., Young, P., 1930a. *J. Am. Chem. Soc.* **52**, 557.
- Willard, H.H., Young, P., 1930b. *J. Am. Chem. Soc.* **52**, 132.
- Willard, H.H., Young, P., 1930c. *J. Am. Chem. Soc.* **52**, 553.
- Willard, H.H., Young, P., 1930d. *J. Am. Chem. Soc.* **52**, 557.
- Willard, H.H., Young, P., 1933. *J. Am. Chem. Soc.* **55**, 3260.
- Willett, J.L., Finkenstadt, V.L., 2006. *J. Appl. Polym. Sci.* **99**, 52.
- Williams, N.H., Takasaki, B., Wall, M., Chin, J., 1999. *Acc. Chem. Res.* **32**, 485.
- Wine, P.H., Mauldin III, R.L., Thorn, R.P., 1988. *J. Phys. Chem.* **92**, 1156.
- Winfree, A.T., 1973. *Science* **175**, 634.
- Winfree, A.T., 1984. *J. Chem. Educ.* **61**, 661.
- Xi, C.J., Jiang, Y.F., Yang, X.H., 2005. *Tetrahedron Lett.* **46**, 3909.
- Xu, J.D., Gorden, A.E., Raymond, K.N., 2004. *Eur. J. Org. Chem.*, 3244.
- Xu, J.D., Radkov, E., Ziegler, M., Raymond, K.N., 2000. *Inorg. Chem.* **39**, 4256.
- Yakovlev, N.G., Kosyakov, V.N., Kazakova, G.M., 1982. *J. Radioanal. Chem.* **75**, 7.
- Yamada, T., Iwahara, Y., Nishino, H., Kurosawa, K., 1993. *J. Chem. Soc., Perkin Trans. I*, 609.
- Yamamoto, Y., Uehara, A., Tomita, T., Komiyama, M., 2004. *Nucleic Acids Res.* **32**, e153.
- Yamamoto, Y., Tsuboi, W., Komiyama, M., 2003. *Nucleic Acids Res.* **31**, 4497.
- Yamato, T., Shinoda, N., 2002. *J. Chem. Res. (S)*, 400.
- Yamato, T., Shinoda, N., Kanakogi, T., 2000. *J. Chem. Res. (S)*, 522.
- Yan, J.M., Atsumi, M., Yuan, D.Q., Fujita, K., 2002. *Helv. Chim. Acta* **85**, 1496.
- Yang, X.H., Xi, C.J., Jiang, Y.F., 2005. *Tetrahedron Lett.* **46**, 8781.
- Yashiro, M., Takarada, T., Miyami, S., Komiyama, M., 1994. *J. Chem. Soc., Chem. Commun.*, 1757.
- Yates, J.S., Thomas, H.C., 1956. *J. Am. Chem. Soc.* **78**, 3950.
- Yilmaz, E., Caner, H., Hasipoglu, H., Yilmaz, O., 1998. *Eur. Polym. J.* **34**, 493.
- Yoneyama, M., 1995. *Colloids Surf., A* **102**, 39.

- Yoneyama, M., Fujii, A., Maeda, S., 1994a. *J. Am. Chem. Soc.* **116**, 7294.
- Yoneyama, M., Fujii, A., Maeda, S., 1994b. *Adv. Mater.* **6**, 869.
- Young, L.B., 1968. *Tetrahedron Lett.* **9**, 5105.
- Young, L.B., Trahanovsky, W.S., 1967. *J. Org. Chem.* **32**, 2349.
- Young, L.B., Trahanovsky, W.S., 1969. *J. Am. Chem. Soc.* **91**, 5060.
- Young, P., 1952. *Anal. Chem.* **24**, 152.
- Zaikin, A.N., Zhabotinsky, A.M., 1970. *Nature* **225**, 535.
- Zhabotinsky, A.M., 1964a. *Dokl. Akad. Nauk SSSR* **157**, 392.
- Zhabotinsky, A.M., 1964b. *Biofizika* **9**, 306.
- Zhang, J., Yuan, Y.L., Shen, J., Lin, S.C., 2003a. *Eur. Polym. J.* **39**, 847.
- Zhang, Y., Raines, A.J., Flowers II, R.A., 2003b. *Org. Lett.* **5**, 2363.
- Zhang, Y., Raines, A.J., Flowers II, R.A., 2004. *J. Org. Chem.* **69**, 6267.
- Zhang, Y., Flowers II, R.A., 2004. *J. Org. Chem.* **68**, 4560.
- Zheng, S.Y., Chen, Z.C., Lu, D.S., Wu, Q., Lin, X.F., 2005. *J. Appl. Polym. Sci.* **97**, 2186.
- Zhu, D.H., Kappel, M.J., Raymond, K.N., 1988. *Inorg. Chim. Acta* **147**, 115.
- Zielen, A.J., 1969. *Anal. Chem.* **41**, 1905.

Chapter 230

SAMARIUM (II) BASED REDUCTANTS

Robert A. FLOWERS II and Edamana PRASAD

Department of Chemistry, Lehigh University, Bethlehem, PA 18015, USA

E-mail: rof2@lehigh.edu

Contents

List of symbols	394	2.4.1. Sequential radical reactions	405
1. Introduction and scope of the review	395	2.4.2. Sequential radical/anionic reactions	406
2. Samarium (II) halides	395	2.4.3. Sequential anionic/radical reactions	407
2.1. Samarium (II) iodide	395	2.4.4. Sequential anionic/anionic reactions	407
2.1.1. Preparation of samarium diiodide	396	2.4.5. Domino epoxide ring opening/ketyl olefin coupling reactions	408
2.2. Functional group transformations	396	2.4.6. Ring expansion by Grob fragmentation	408
2.2.1. Reduction of unsaturated systems	396	2.5. Role of proton donors and additives in SmI ₂ -mediated reactions	409
2.2.2. Reduction of carbonyl substrates	397	2.5.1. Proton sources	410
2.2.3. Reduction of α,β -unsaturated systems	398	2.5.2. Role of additives in SmI ₂ -mediated reactions	416
2.2.4. Reduction of organic halides	398	2.5.3. Use of lithium salts as additives in SmI ₂ mediated reductive coupling reactions	418
2.2.5. Reduction of α -heterosubstituted ketones	399	2.6. The role of solvation in reactions of SmI ₂	423
2.2.6. Deoxygenation reactions	399	2.7. Samarium (II) chloride and samarium (II) bromide	429
2.2.7. Reduction of other functional groups	400	3. Sm(II) cyclopentadienyl-based complexes	431
2.3. Carbon-carbon bond forming reactions	401	3.1. Samarium (II)Cp ₂	431
2.3.1. Barbier-type and Grignard-type reactions	401	3.1.1. Synthesis of Sm(II)Cp ₂	431
2.3.2. Reformatsky-type coupling reactions	402	3.2. Reactions of Sm(II)Cp ₂	432
2.3.3. Nucleophilic acyl substitution reactions	402	3.3. Synthesis of SmCp* ₂	433
2.3.4. Pinacol coupling reactions	402	3.4. Reactions of Sm(Cp* ₂)(THF) ₂ and Sm(Cp* ₂)	435
2.3.5. Ketone-olefin coupling reactions	403	3.5. Reactions of SmCp* ₂ and Sm(Cp* ₂)-(THF) ₂ with small inorganic molecules (N ₂ , CO, CO ₂) and related compounds	435
2.3.6. Halide-olefin coupling reactions	403	3.5.1. Reaction of SmCp* ₂ with N ₂	435
2.3.7. Insertion of isocyanides into organic halides: Synthesis of α -hydroxyketones	404		
2.3.8. Coupling of organic halides	404		
2.3.9. Miscellaneous coupling reactions	404		
2.4. 'Sequential' (or 'tandem') reactions mediated by SmI ₂	405		

3.5.2. Reaction of $\text{Sm}(\text{Cp}^*)_2(\text{THF})_2$ with CO	436	3.13.1. Reactions of SmCp^*_2 and $\text{Sm}(\text{Cp}^*)_2(\text{THF})_2$ with cyclopentadiene	448
3.5.3. Reaction of $\text{Sm}(\text{Cp}^*)_2(\text{THF})_2$ with CO_2 and COS	437	3.13.2. Reactions of SmCp^*_2 and $\text{Sm}(\text{Cp}^*)_2(\text{THF})_2$ with aryl-substituted alkenes	449
3.5.4. Reactions of $\text{Sm}(\text{Cp}^*)_2(\text{THF})_2$ with NO, epoxides, and related compounds	437	3.13.3. Reactions of SmCp^*_2 and $\text{Sm}(\text{Cp}^*)_2(\text{THF})_2$ with short chain alkenes and dienes	450
3.6. Reactions of SmCp^*_2 and $\text{Sm}(\text{Cp}^*)_2(\text{THF})_2$ with inorganic and organometallic substrates	438	3.13.4. Reactions of $\text{Sm}(\text{Cp}^*)_2(\text{THF})_2$ with heteroatom containing double bonds unsaturated heterocycles	452
3.6.1. Reactions of $\text{Sm}(\text{Cp}^*)_2(\text{THF})_2$ and SmCp^*_2 with trialkylaluminum	438	3.13.5. Reactions of $\text{Sm}(\text{Cp}^*)_2(\text{THF})_2$ with triple bonds	455
3.7. Reactions of $\text{Sm}(\text{Cp}^*)_2(\text{THF})_2$ and SmCp^*_2 with group 15 organometallic compounds	440	4. Sm(II) alkoxide and amide reductants	456
3.8. Reactions of $\text{Sm}(\text{Cp}^*)_2(\text{THF})_2$ with group 16 metals and organometallics	441	4.1. Synthesis of $[(\text{Me}_3\text{Si})_2\text{N}]_2\text{Sm}(\text{THF})_2$ and $[\text{Sm}(\text{OC}_6\text{H}_2\text{-2,6-di-}^i\text{butyl-4-methyl})_2(\text{THF})_3]$	456
3.9. Reactions of $\text{Sm}(\text{Cp}^*)_2(\text{THF})_2$ with tetrathio-tungstate and -molybdate	443	4.2. Reactions of $[(\text{Me}_3\text{Si})_2\text{N}]_2\text{Sm}(\text{THF})_2$	458
3.10. Reactions of $\text{Sm}(\text{Cp}^*)_2(\text{THF})_2$ and $\text{Sm}(\text{Cp}^*)_2$ with AgBPh_4	444	4.3. Reactions of $[\text{Sm}(\text{OC}_6\text{H}_2\text{-2,6-di-}^i\text{butyl-4-methyl})_2(\text{THF})_3]$	463
3.11. Reactions of $\text{Sm}(\text{Cp}^*)_2(\text{THF})_2$ and $\text{Sm}(\text{Cp}^*)_2$ with organomercury reagents	445	5. Sm(II) pyrazolyborate reductants	466
3.12. Reaction of $\text{Sm}(\text{Cp}^*)_2(\text{THF})_2$ with monodentate anionic ligands	446	5.1. Synthesis of $\text{Sm}(\text{Tp}^{\text{Me}_2})_2$	466
3.13. Reactions of SmCp^*_2 and $\text{Sm}(\text{Cp}^*)_2(\text{THF})_2$ with alkenes, alkynes, and related unsaturated compounds	448	5.2. Reactions of $\text{Sm}(\text{Tp}^{\text{Me}_2})_2$	467
		6. Conclusions and outlook	469
		Acknowledgements	470
		References	470

List of symbols

acac	acetylacetonate	ITC	isothermal titration calorimetry
Cp	cyclopentadienyl	Ln	lanthanide
Cp^*	pentamethylcyclopentadienyl	PMDTA	<i>N, N, N', N'', N'''</i> -pentamethyldiethylene-triamine
CV	cyclic voltammetry	SET	single electron transfer
de	diastereoselectivity	SCE	saturated calomel electrode
DBM	dibenzoylmethane	^t BuOH	tertiary butanol
DBU	1,8-diazabicyclo[5.4.0] undec-7-ene	^t Et ₃ N	triethylamine
DET	dimethyl tartrate	TFA	trifluoroacetic acid
DMA	<i>N,N</i> -dimethyl acetamide	THF	tetrahydrofuran
DME	dimethoxyethane	THP	tetrahydropyran
DMEA	<i>N,N</i> -dimethyl acetamide	TMEDA	tetramethylethylenediamine
DMF	dimethyl formamide	TMG	tetramethylguanidine
DMPU	1,3-dimethyl-3,4,5,6-tetrahydro-2(1H)-pyrimidinone	<i>p</i> -TSA	<i>p</i> -toluenesulfonic acid
ER	alkoxide or amide ligand	VPO	vapor pressure osmometry
HMPA	hexamethyl phosphoramide	Xy	xylene

1. Introduction and scope of the review

Although the +3 oxidation state is the most stable, many of the lanthanides have stable (or accessible) +2 oxidation (divalent) states. The unique reactivity of divalent lanthanides makes them important reducing reagents for highly selective transformations. Although divalent ions of almost all of the lanthanides have been generated (McClure and Kiss, 1963; Kiss and Yocum, 1964; Mikheev, 1984), only three, europium, ytterbium, and samarium are easily accessible under standard laboratory conditions (Evans, 2000, 1987a). More recently divalent thulium, dysprosium, and neodymium have been generated as well (Evans and Allen, 2000a; Evans et al., 2000b; Bochkarev et al., 2001). Morss (1976) reported the aqueous redox potentials for the $\text{Ln}^{3+}/\text{Ln}^{2+}$ redox couples as -0.35 V for Eu, -1.1 V for Yb, and -1.5 V for Sm vs. NHE. More recent estimates of redox potentials for the $\text{Ln}^{3+}/\text{Ln}^{2+}$ redox couples for Tm, Dy, and Nd are provided by Cotton (1991) as -2.3 V, -2.5 V, and -2.6 V, respectively. While the latter three lanthanides are powerful reductants and have potential for use in organic synthesis (Evans, 2002), their preparation is somewhat more difficult from the viewpoint of an organic chemist. Among the former three Ln^{2+} ions that are relatively straightforward to prepare, Eu^{2+} is a weak reductant, with Yb^{2+} intermediate in its reducing ability and Sm^{2+} being the most powerful. Because of their ease of preparation and relative stability in a range of organic solvents, reductants based on Sm^{2+} have found enormous use in organic synthesis and polymer chemistry (Girard et al., 1980; Molander, 1992; Evans et al., 1998a, 1998b, 1998c).

This chapter will focus on the synthesis of Sm(II)-based reductants and their use in organic and inorganic synthesis. The predominant emphasis of this contribution is on the synthesis and utility of homoleptic Sm(II) reductants containing halide (I, Br, Cl) and cyclopentadienyl (Cp and Cp*) ligands with a brief section on amide ($-\text{N}(\text{SiMe}_3)_2$), and alkoxide ligands and a brief section on pyrazolylborate ligands. Each section will describe the synthesis of the individual Sm(II) complex followed by a discussion of reactivity. Since a great deal of scientific effort has been directed towards understanding the reactivity and behavior of Sm(II) reductants containing iodide and pentamethylcyclopentadienyl ligands, the majority of this chapter will concentrate on these two classes of Sm(II)-based reductants.

2. Samarium (II) halides

2.1. Samarium (II) iodide

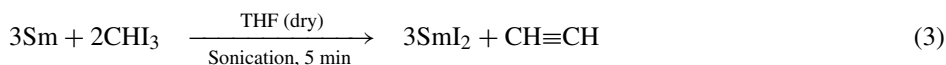
Samarium diiodide is an extremely mild, selective reductant that is commonly utilized in organic synthesis. It is a versatile, single electron reducing agent regularly utilized in several reduction, carbon-carbon bond formation, and sequential reactions and is indeed, the reagent of choice for several organic reactions (Molander, 1992). The preparation and application of SmI_2 was first reported by Kagan (Girard et al., 1980). These reactions are generally divided into three classes, (a) reduction reactions of functional groups, (b) carbon-carbon bond form-

ing reactions, and (c) sequential reactions. The aim of this portion of the chapter is to discuss the preparation and utility of samarium diiodide in organic synthesis and provide a brief introduction to the variety of reactions mediated by it. This section of the chapter will also offer insights into mechanistic details of this reagent (including the role of additives) and its mode of action in various reactions.

2.1.1. Preparation of samarium diiodide

Samarium diiodide has been developed as a mild, cyclic ether-soluble, single electron reducing agent with applications in diverse organic transformations (Molander, 1992; Steel, 2001; Kagan and Namy, 1986). Tetrahydrofuran (THF) is the solvent of choice for SmI_2 though other solvents such as dimethoxyethane (DME) (Evans et al., 1998a), acetonitrile (Ruder, 1992), tetrahydropyran (THP) (Namy et al., 1994), and benzene (Kunishima et al., 1992), have also been utilized. It was first prepared by Kagan from the reaction of samarium metal with diiodoethane in THF at ambient temperatures (Girard et al., 1980).

Samarium diiodide can also be prepared by reacting Sm metal directly with molecular iodine (I_2) (Totleben et al., 1992). Recently, it has been reported that sonication in the presence of triodomethane instead of iodine accelerates this reaction significantly and leads to completion in minutes rather than hours (Concellon et al., 2003).

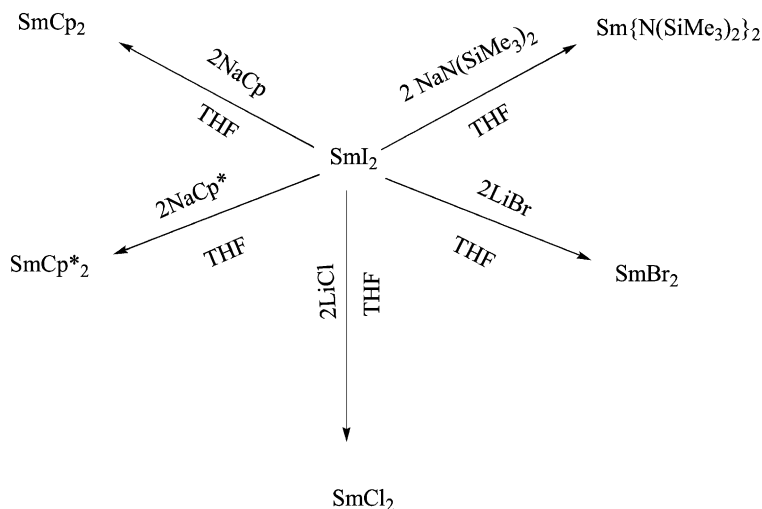


Under all these conditions, a dark blue solution of samarium diiodide in THF is formed. The limiting concentration of samarium diiodide in THF is approximately 0.1 M. It is a stable solution and can be stored for a long period of time under an inert atmosphere. One of the key features of SmI_2 is that it can be used as an intermediate to other Sm(II)-based reductants. Scheme 1 shows a schematic representation of different approaches to prepare several Sm(II) based reductants from SmI_2 .

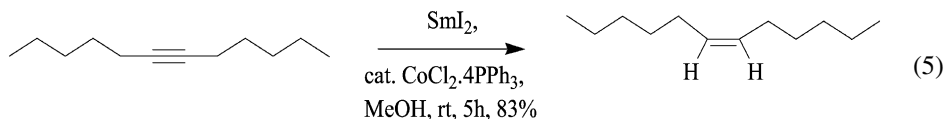
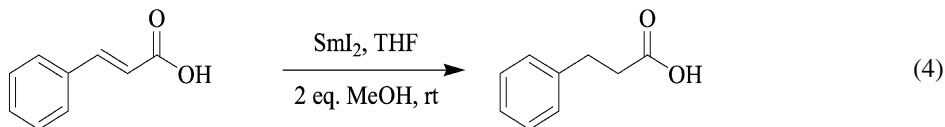
2.2. Functional group transformations

2.2.1. Reduction of unsaturated systems

Samarium diiodide serves as an effective reductant for a variety of functional groups. Conjugated double bonds are readily reduced by SmI_2 in the presence of proton donors such as methanol (Kagan and Namy, 1986). Inanaga (1990) has shown that alkynes are reduced efficiently to alkenes by samarium diiodide in the presence of catalytic amounts of cobalt (Co) complexes. Selective synthesis of (*Z*)-alkenes is possible due to the chemoselective nature of

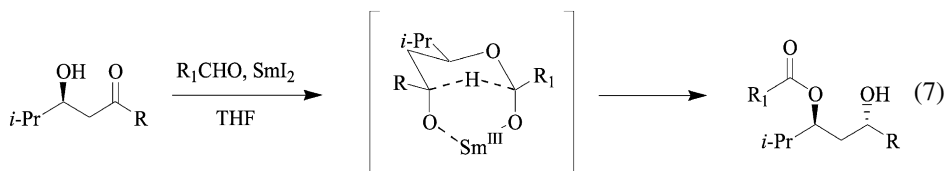
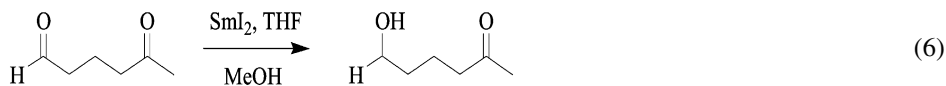
Scheme 1. Methods of preparation of different Sm(II) complexes from SmI₂.

samarium diiodide. The presence of additives is characteristic of many SmI₂ mediated reactions (eqs. (4), (5)).



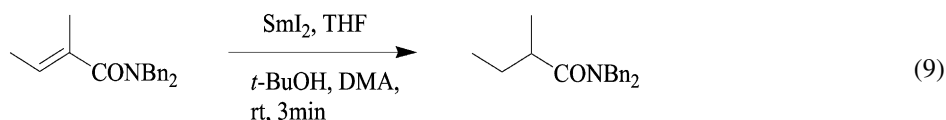
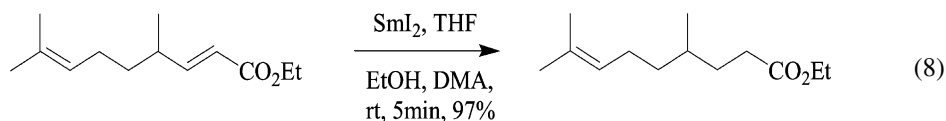
2.2.2. Reduction of carbonyl substrates

Samarium diiodide provides a useful alternative to the [Luche \(1978\)](#) protocol utilizing NaBH₄/CeCl₃ in the reduction of carbonyl substrates. It provides excellent chemoselectivity in reactions with various carbonyl substrates. Aldehydes react very rapidly and efficiently with samarium diiodide to form primary alcohols. Ketones react with SmI₂ much slowly and selective reduction of aldehydes in the presence of ketones is therefore readily achieved ([Girard et al., 1980](#)). The reduction of ketones requires the presence of HMPA. Reduction of chiral aldehydes and ketones with moderate stereochemical control has also been reported ([Yamamoto et al., 1988](#); [Ohgo, 1988](#)). Carboxylic acids and esters are not reduced by SmI₂ alone, though SmI₂-H₂O mixtures have been reported to reduce carboxylic acids to alcohols ([Kamochi and Kindo, 1993](#)). Tischenko-type redox reactions utilizing SmI₂ have been reported by [Evans and Hoveyda \(1990a\)](#). This methodology enables the synthesis of *anti*-1,3-diol monoesters from β -hydroxyketones as shown in eqs. (6), (7).



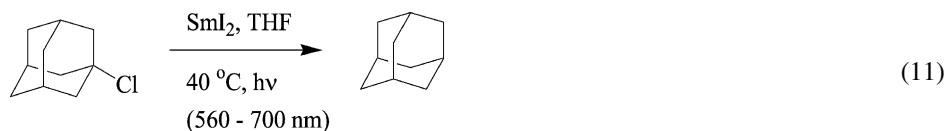
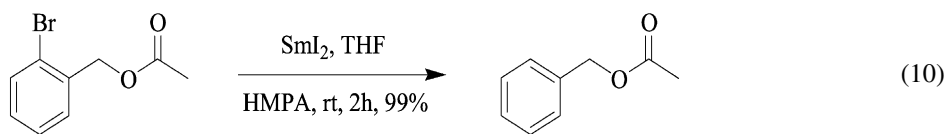
2.2.3. Reduction of α,β -unsaturated systems

α,β -unsaturated carboxylic acids, esters, and amides are reduced easily to saturated derivatives by treating them with SmI_2 in the presence of a proton source (Girard et al., 1980). The use of dimethylformamide (DMF) or *N,N*-dimethyl acetamide (DMA) as a cosolvent with THF enhances the rates of reaction and improves yields considerably as shown in eqs. (8), (9) (Inanaga, 1990).



2.2.4. Reduction of organic halides

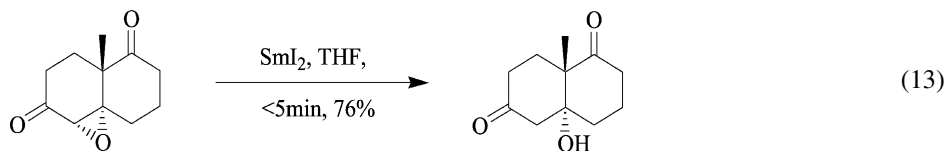
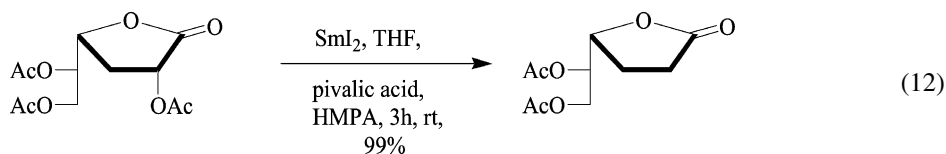
Alkyl iodides and bromides are reduced to their corresponding hydrocarbons by treating them with SmI_2 in the presence of a proton source such as water, methanol, 2-propanol, or tert-butanol (Inanaga et al., 1987). The reactivity and ease of reduction in the reactions follows the order, $\text{I} > \text{Br} > \text{Cl} > \text{F}$ with alkyl fluorides being inert to SmI_2 . Addition of HMPA as a cosolvent enables efficient reduction of primary, secondary, and tertiary alkyl halides as well as aryl or alkenyl halides. Irradiation of SmI_2 with visible light has been reported to accelerate the reduction of alkyl chlorides as shown in eq. (11) (Ogawa et al., 1997).



This methodology is commonly utilized in the deprotection of amines by cleavage of the 2-chloroethyl carbamate (protecting group) functionality (Anathanarayan et al., 1983) and reductive cleavage of (2,2,2-trichloroethoxy) methoxy ether protecting group to provide the corresponding alcohol products (Evans and Hoveyda, 1990a).

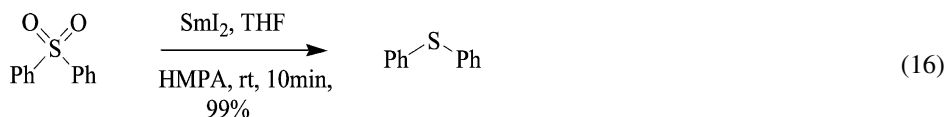
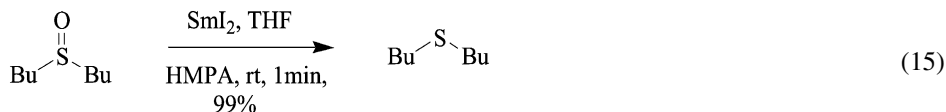
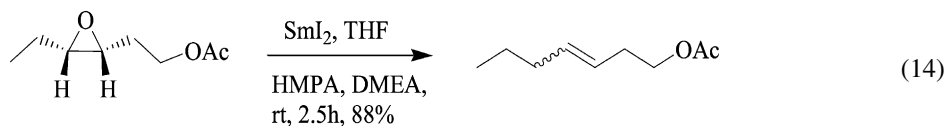
2.2.5. Reduction of α -heterosubstituted ketones

A variety of α -heterosubstituted ketones and similar substrates are reduced by SmI_2 under mild conditions, to form unsubstituted ketones. The heteroatom functionalities that can be reductively cleaved include halides ($-\text{I}$, $-\text{Br}$, $-\text{Cl}$), $-\text{SR}$, $-\text{S}(\text{O})\text{R}$, $-\text{SO}_2\text{R}$, and $-\text{OR}$ (Molander and Hahn, 1986b; Smith et al., 1988). Reductive cleavage of some of these heteroatom substituents requires the presence of HMPA as cosolvent for greater efficiency (Kusuda et al., 1989). α,β -epoxy ketones are also reduced to β -hydroxy carbonyl compounds as shown in eq. (13) (Otsubo et al., 1987a). This is an important pathway for the synthesis of chiral β -hydroxy carbonyl compounds as the chiral substrates are easily synthesized by the sharpless epoxidation reactions. α,β -epoxy esters require more vigorous conditions and the presence of HMPA for efficient reduction.



2.2.6. Deoxygenation reactions

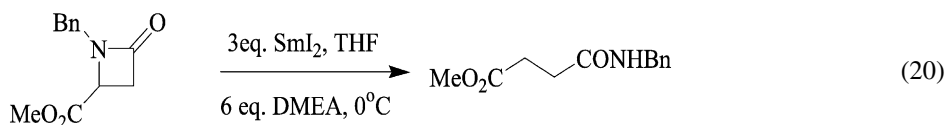
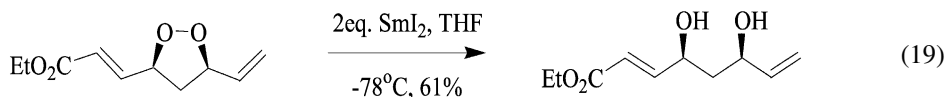
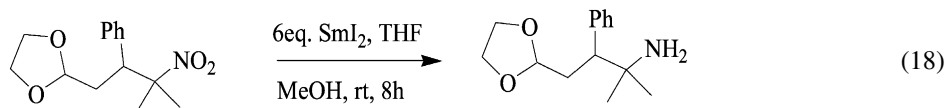
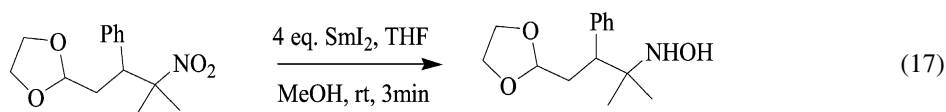
Samarium diiodide has been utilized for deoxygenation of diverse functional groups. These include the conversion of epoxides to olefins (Matsukawa et al., 1987), sulfoxides to sulfides, and aryl sulfones to sulfides (Honda et al., 1989). Examples are shown in eqs. (14)–(16).



Conversion of aliphatic and aromatic amine N-oxides to corresponding amines, phosphine oxides to phosphines and triaryl arsine oxides to triaryl arsines have also been achieved. These reactions require the presence of HMPA as cosolvent (Zhang and Lin, 1987).

2.2.7. Reduction of other functional groups

Nitro-compounds are selectively reduced to either hydroxyl amines or amines by treating them with 4 or 6 equivalents of SmI_2 respectively (Soupe et al., 1983; Kende and Mendoza, 1991). Cyclic peroxy compounds have also been reduced by SmI_2 to corresponding diols (Johnson and Senanayake, 1989; Feldman and Simpson, 1989). Reduction reactions of nitrones (McAuley et al., 2000; Myers et al., 2000), ring fragmentations of acylaziridines and acetidinones (Molander and Stengel, 1997) in the presence of *N,N*-dimethylethanolamine, DMEA, conversions of aliphatic or aromatic acetals to the corresponding ether in the presence of TFA, water or AlCl_3 (Studer and Curran, 1996) are mediated by SmI_2 as shown in eqs. (17)–(20).

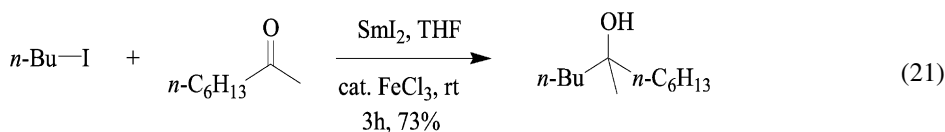


Thus, SmI_2 is capable of reducing or reductively cleaving a broad spectrum of functional groups. These reactions require the presence of proton donors, which may be alcohols such as methanol and DMEA, or carboxylic acids such as pivalic acid, or simply, water. The reductive ability of SmI_2 is also altered by the addition of electron donating solvents such as HMPA DMF, and DMA. Metal salts such as CoCl_2 , FeX_3 (Molander and McKie, 1992b) and NiI_2 (Machrouhi and Namy, 1999) are also commonly utilized to alter the $\text{Sm}^{+3}/\text{Sm}^{+2}$ redox potential or increase the efficiency of the $\text{Sm}(\text{II})$ reductant. Thus, it is essential to understand clearly to role of proton donors in SmI_2 mediated reactions. It is equally important to understand the role of other electron donor additives and metal donors since they are capable of changing the nature of the $\text{Sm}(\text{II})$ reductant. This study will enable chemists to manipulate reaction conditions for maximum efficiency.

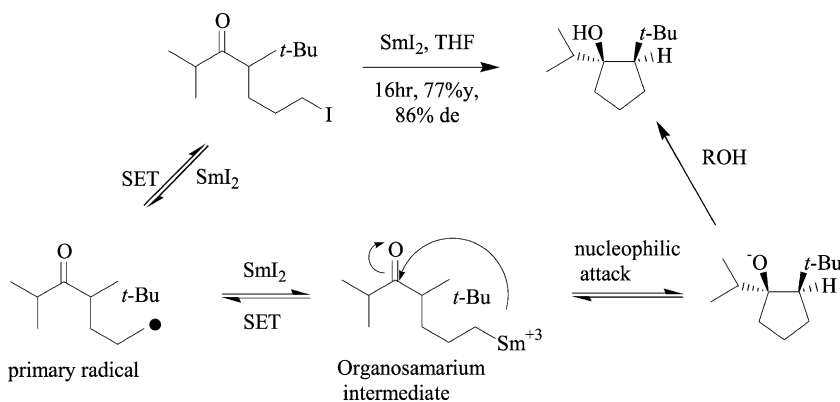
2.3. Carbon-carbon bond forming reactions

2.3.1. Barbier-type and Grignard-type reactions

SmI_2 mediates a variety of carbon-carbon bond forming reactions that are efficient alternatives to traditional approaches. The reactions are generally characterized by high yields and excellent stereochemical control. Barbier-type and Grignard reactions involve carbon-carbon bond formation between an organic halide and aldehyde or ketone analogous to the Mg-mediated Grignard reaction. The difference between these two methodologies is in the order of addition of reagents. In the Barbier-type protocol, SmI_2 is added to a mixture of the halide and electrophile (ketone or aldehyde), whereas in the Grignard protocol, SmI_2 is added to the organic halide to form an organosamarium species, followed by the addition of the electrophile. SmI_2 is extremely efficient in promoting these reactions (eq. (21)). The reactivity of halides follows the order, $\text{I} > \text{Br} > \text{Cl}$. Organic chlorides require vigorous reaction conditions. Addition of catalytic quantities of Fe(III) salts (Girard et al., 1980) or HMPA as a cosolvent (Otsubo et al., 1987b) or irradiation of the reaction mixture (Ogawa et al., 1997) increases reactivity drastically.



This reaction involves the reduction of the C-X bond to carbon radical followed by another single electron transfer (SET) from a second mole of SmI_2 , forming an organosamarium intermediate that undergoes nucleophilic attack onto the carbonyl functionality as shown in scheme 2. Intramolecular Barbier reactions mediated by SmI_2 have been shown to proceed through high diastereoselectivity and yields (Molander and Etter, 1987a). This methodology has also been utilized in the synthesis of bridged structures and spiro-systems with high stereochemical control (Molander et al., 1987c). SmI_2 is especially useful in the reactions between

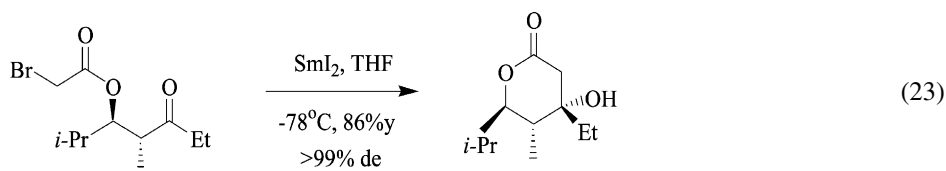
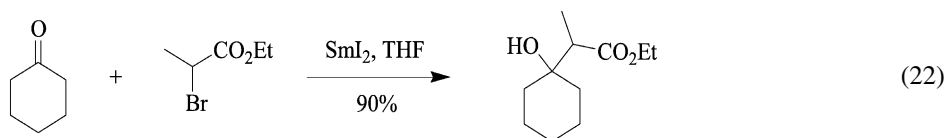


Scheme 2. Inter- and intramolecular examples of the Barbier-type and Grignard-type reactions.

aldehydes and reactive organic halides such as allylic or benzylic halides (Girard et al., 1980; Souppe et al., 1982). Iodomethylation of aldehydes and ketones is readily achieved by utilizing SmI_2 and diiodomethane (Imamoto et al., 1986; Tabuchi et al., 1986).

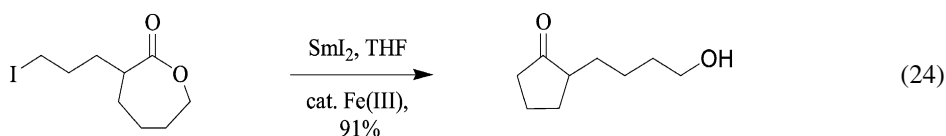
2.3.2. Reformatsky-type coupling reactions

SmI_2 provides an excellent alternative to the traditional Zn-promoted Reformatsky reactions by mediating carbon-carbon bond formation between α -halo esters or α -halo ketones and carbonyl substrates as electrophiles. This reaction proceeds through the formation of a nucleophilic organosamarium species (equivalent to a Grignard reagent), followed by attack on the electrophile carbonyl functionality. Both intra- and intermolecular (Kagan et al., 1981; Molander and Etter, 1987b) versions of this reaction have been reported (eqs. (22), (23)).



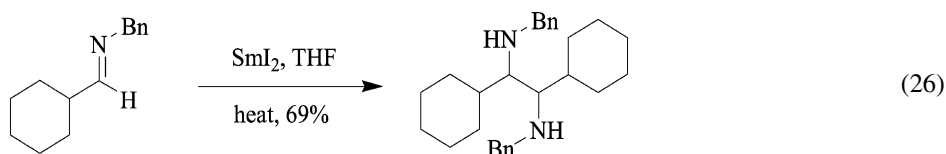
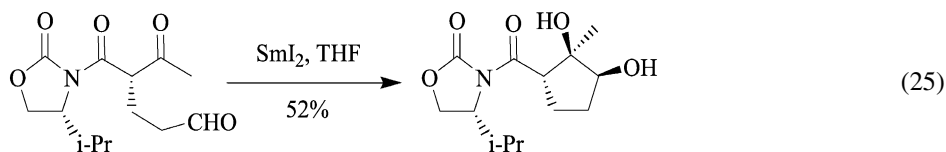
2.3.3. Nucleophilic acyl substitution reactions

Esters are generally unreactive under Barbier-type reaction conditions. However, SmI_2 mediated nucleophilic acyl substitutions are readily accomplished utilizing esters (Molander and McKie, 1992b).



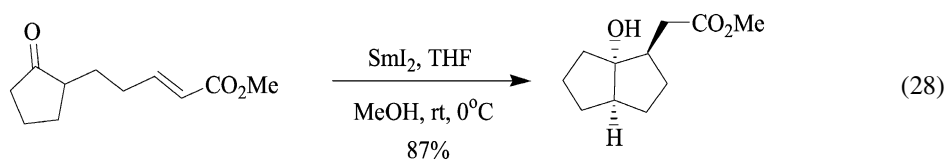
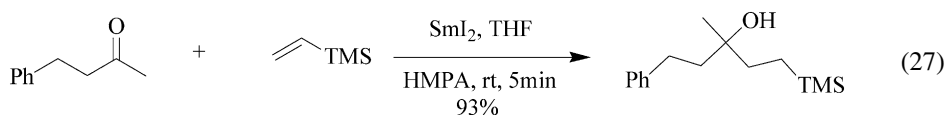
2.3.4. Pinacol coupling reactions

Aldehydes and ketones undergo coupling upon treatment with SmI_2 in the absence of proton donors. This reaction proceeds extremely well with high yields in most cases to form vicinal diols (Namy et al., 1983; Furstner et al., 1988). It involves reduction of the aldehyde and ketone through single electron transfer to form ketyl radical anion intermediates. These intermediates undergo coupling to form a new carbon-carbon bond. Similar reactions involving coupling between aldimines to form vicinal diamines (Enholm et al., 1990; Imamoto and Nishimura, 1990). Cross coupling between aldimines and aldehydes has also been reported (Tanaka et al., 2002).



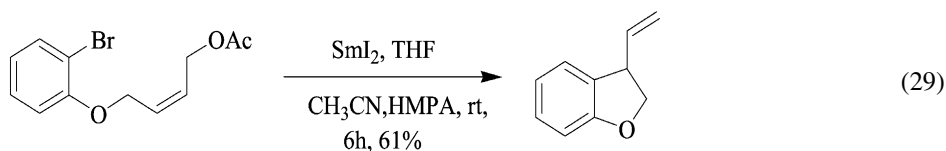
2.3.5. Ketone–olefin coupling reactions

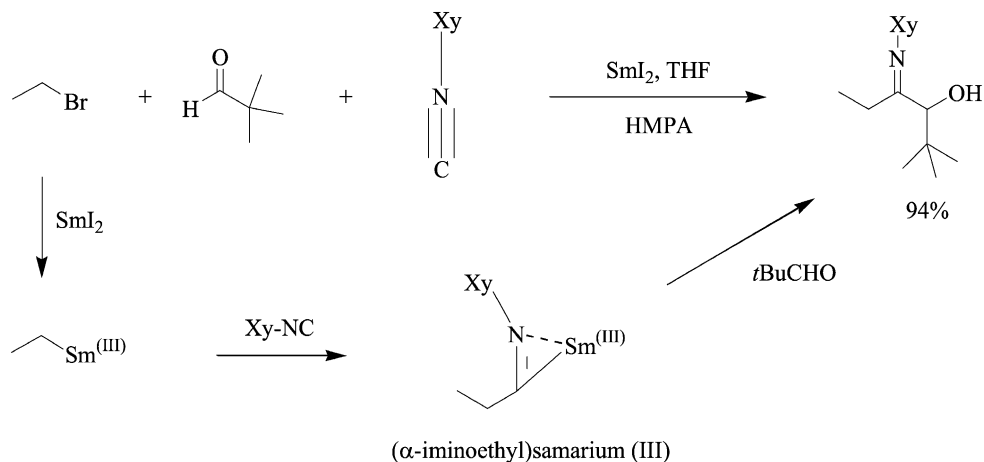
Radical addition reactions involving carbon–carbon bond formation between ketone/aldehydes and alkenes/alkynes mediated by SmI_2 are common (Molander and McKie, 1992b). These reactions involve a SET from SmI_2 to the aldehyde/ketone to form a ketyl radical intermediate, which then couples to an olefinic bond. Both inter- and intra-molecular ketone–olefin coupling reactions have been reported, though intermolecular reactions require an activated olefin such as α,β -unsaturated substrates, conjugated olefins, and vinyl silanes (Fukuzawa et al., 1986, 1988). A high degree of stereochemical control has been demonstrated in these coupling reactions. Examples are shown in eqs. (27), (28).



2.3.6. Halide–olefin coupling reactions

SmI_2 mediated coupling reactions between organic halides and olefins have several advantages over traditional methodologies that typically utilize tin reagents. The ease of purification, better yields and high stereochemical control has made SmI_2 the reagent of choice compared to tin reagents. SmI_2 is especially suited in the coupling of aryl halides, since the aryl radicals formed by SET are not readily reduced to aryl anions (Inanaga et al., 1991a).





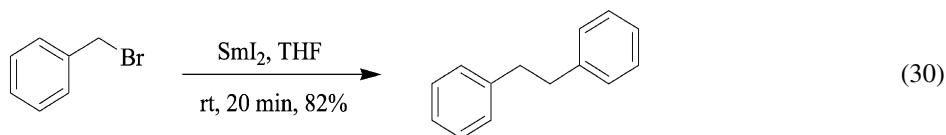
Scheme 3. Samarium iodide mediated coupling reaction between halides, isocyanides and carbonyl substrates to form α-hydroxyketones.

2.3.7. Insertion of isocyanides into organic halides: Synthesis of α-hydroxyketones

A novel, three component coupling reaction involving organic halides, 2,6-xylyl isocyanide (Xy-CN), and carbonyl compounds to form α-hydroxyketones in excellent to moderate yields is readily achieved by SmI₂ (Murakami et al., 1990, 1993). This reaction proceeds through α-addition of an organosamarium intermediate to the isocyanide resulting in an (α-iminoalkyl) samarium complex which can act as an acyl anion equivalent. The (α-iminoalkyl) samarium complex then adds to the carbonyl substrates to form α-hydroxyimines that can be easily hydrolyzed to α-hydroxyketones as shown in scheme 3.

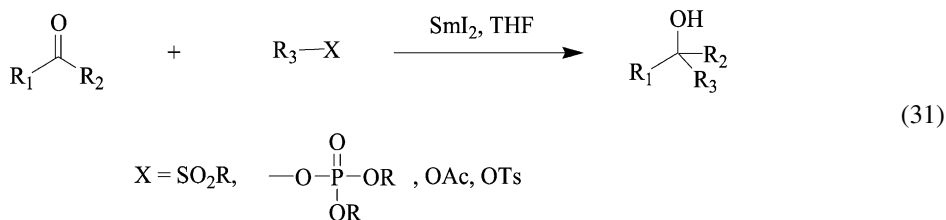
2.3.8. Coupling of organic halides

Coupling of organic halides is isolated to benzylic iodides or bromides with SmI₂ in the absence of proton donors (Girard et al., 1980). The mechanism of the reaction likely proceeds through either radical coupling, or the formation of an organosamarium that displaces the halide from unreacted substrate.



2.3.9. Miscellaneous coupling reactions

SmI₂ can reductively cleave several C-X bonds (X = -SO₂R, -OP(O)(OR)₂, -OAc, -OTs) by single electron transfer (Kagan and Namy, 1986). The resultant radicals formed are further reduced to organosamarium intermediates. These intermediates can couple easily to carbonyl substrates.



It is clear from the preceding discussion that SmI₂ mediates carbon–carbon bond formation reactions in a variety of functional groups. It is an excellent alternative to several traditional carbon–carbon bond formation reactions utilizing transition metals, namely the Zn-mediated Reformatsky reactions, Mg-mediated Grignard and Barbier reactions and Sn-mediated halide–olefin coupling reactions that are efficient for selective functionalities. The major advantage of SmI₂ is the ability to fine-tune its reactivity by utilizing cosolvents and other additives depending on the substrates. Similar to the reduction reactions discussed in sections 2.2.1 to 2.3.9, electron donor cosolvents such as HMPA, metal salts such as FeX₃, and proton donors such as methanol are commonly utilized and they have a profound effect on the reaction outcomes.

2.4. ‘Sequential’ (or ‘tandem’) reactions mediated by SmI₂

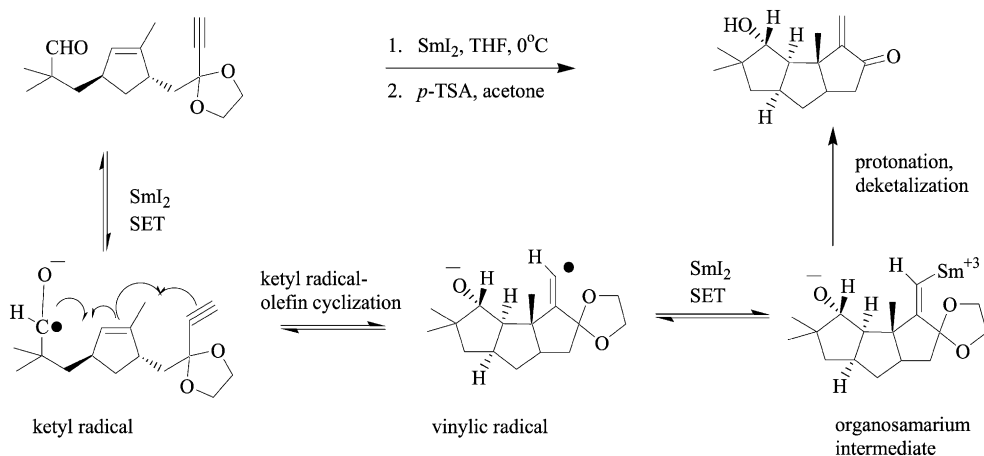
Sequential reactions also termed tandem reactions, involve the formation of multiple carbon–carbon or carbon–heteroatom bonds in a specific sequence without purification or separation of any intermediate products. Thus, sequential reactions can potentially provide complex, multifunctional products in a single step. However, for sequential reaction to be useful, they should be extremely efficient and specific to minimize formation of unwanted products. The reactions should also proceed with high yields.

Sequential reactions can be divided into four main types, depending on the type of reactions involved in the sequence. These sequences are (a) radical/radical, (b) radical/anionic, (c) anionic/radical, and (d) anionic/anionic. Though methodologies utilizing tin and silicon hydrides have dominated these reactions, SmI₂ is proving to be an excellent alternative and in some cases, the reagent of choice.

2.4.1. Sequential radical reactions

These types of tandem reactions involve multiple radical reactions or cyclizations. Curran and coworkers reported an excellent example of sequential radical reaction mediated by SmI₂ as a critical step in the synthesis of (±)-hynophilin (scheme 4) (Fevig et al., 1988).

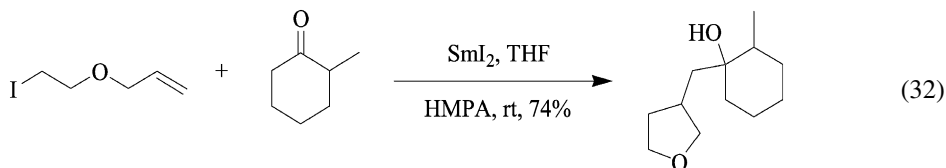
This reaction proceeds through SET to the aldehyde functionality to form the ketyl radical, followed by ketyl radical–olefin coupling resulting in 5-exo-trig (the terminology is from Baldwin rules for ring closure, Smith and March (2001)) cyclization between the carbonyl carbon and olefin carbon. The relatively stable tertiary radical formed as a result of the cyclization undergoes 5-exo-dig cyclization (Smith and March, 2001) to form the tricyclic system. The terminal radical abstracts a hydrogen atom from solvent to terminate the sequence. Thus, radical/radical sequential reactions are favored in the presence of stable radicals that

Scheme 4. Radical/radical sequential reaction mediated by SmI_2 .

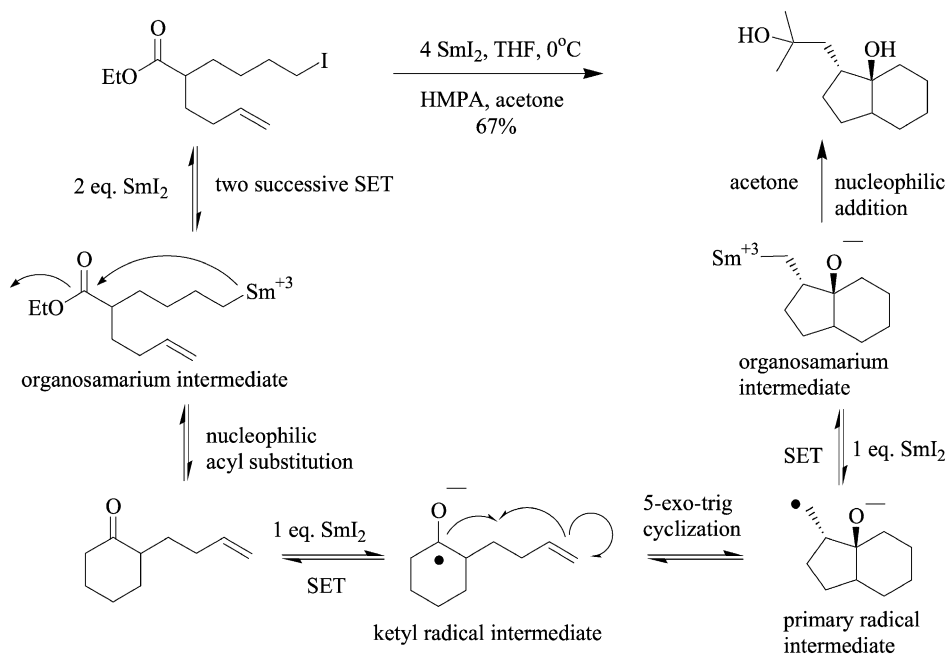
are relatively inert to reduction by SmI_2 to the anion. These include tertiary, aryl and allylic radicals.

2.4.2. Sequential radical/anionic reactions

These reactions involve a radical process followed by an anionic reaction. Radical/anionic sequential reactions are the most common sequential reactions mediated by SmI_2 (Molander and Kenny, 1991). An example is shown in eq. (32).



The first step involves SET to the carbon-iodide bond to form a primary radical, followed by halide-olefin coupling resulting in 5-exo-trig cyclization between the primary radical and olefin carbon. The resultant primary radical is reduced by a second SET to form an organosamarium species that undergoes nucleophilic attack on the carbonyl functionality of the ketone. Ketyl-olefin radical coupling followed by SET and nucleophilic attack are another type of sequential radical/anionic reactions. Radicals that undergo rapid cyclization rather than reduction to anionic species favor this sequence and often result in high yields. Aryl radicals are resistant to reduction to anions by SmI_2 and also favor radical/anionic reactions (Curran and Totleben, 1992). A variety of electrophiles other than carbonyl substrates have been utilized in this sequence, namely, iodine (I_2), diselenium compounds (RSe-SeR), tin reagents (R_3SnI), disulfur compounds (RS-SR), isocyanates (R-NCO), iminium salts ($\text{R}_2\text{N}^+=\text{CR}_2$), etc.

Scheme 5. Anionic/radical sequential reaction mediated by SmI_2 .

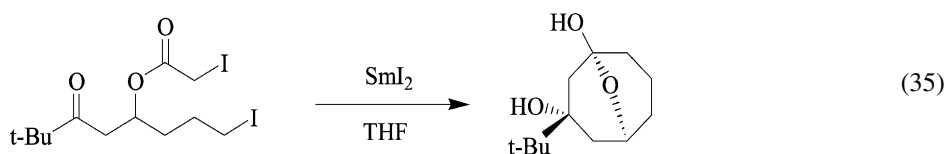
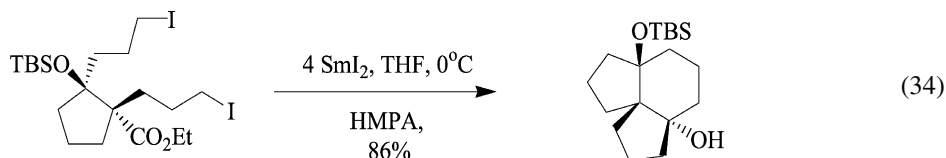
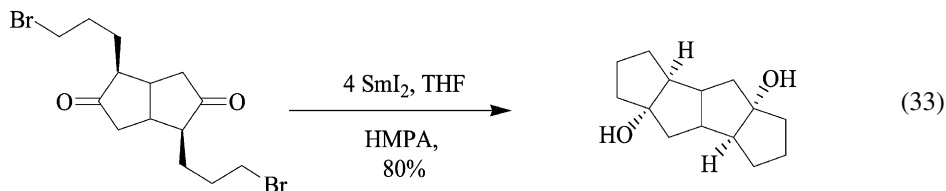
2.4.3. Sequential anionic/radical reactions

This type of sequence generally involves nucleophilic acyl substitution followed by ketone-olefin coupling. Molander and Harris (1997) reported several efficient examples of anionic/radical sequential reactions. The proposed mechanism of this reaction involves reduction of the carbon-iodide bond by two SET to form the organosamarium species, which undergoes nucleophilic acyl substitution to form a ketone. The ketone is then reduced by one SET reactions to form a ketyl radical that undergoes 5-exo-trig ketyl-olefin cyclization to form a primary radical. This radical is reduced by another SET from SmI_2 and the organosamarium species then attacks the electrophilic acetone to form the final product. The likely general mechanism is shown in scheme 5.

2.4.4. Sequential anionic/anionic reactions

SmI_2 mediates several types of tandem anionic reactions. These include two intramolecular Barbier-type reactions in one-pot (Lannoye and Cook, 1988a; Lannoye et al., 1988b), nucleophilic acyl substitution followed by Barbier-type reaction (Molander and McKie, 1993) and Barbier-type reaction followed by nucleophilic acyl substitution (Molander and Harris, 1995). The substrates are designed specifically to favor any of the above three types of pathways. Similar to other sequential reactions, these reactions result in high yields and high stereoselectivity. A variety of strained, multicyclic, and spirocyclic systems are synthesized by the use

of these methodologies. Examples of sequential anionic/anionic reactions are shown in eqs. (33)–(35).



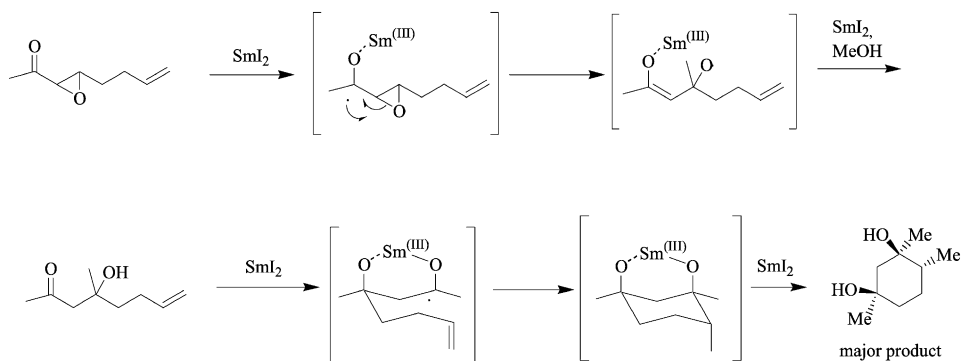
Another example of anionic/anionic reaction mediated by SmI_2 is the Reformatsky/nucleophilic acyl substitution reaction (Molander et al., 2002). SmI_2 mediates the Reformatsky/nucleophilic acyl substitution resulting in the formation of bridged large rings. Eight and nine membered rings are easily synthesized by utilizing this methodology. This reaction proceeds through reduction of the α -substituted C–X bond to an organosamarium species, followed by nucleophilic attack onto the ketone (equivalent to the Reformatsky reaction). The other C–X bond is then reduced to an organosamarium species which undergoes nucleophilic attack on the ester functionality (equivalent to nucleophilic acyl substitution reaction).

2.4.5. Domino epoxide ring opening/ketyl olefin coupling reactions

This reaction is a different type of sequential reaction that involves multiple SET reductions and ketyl olefin couplings (Molander and Losada, 1997). The first step of the proposed mechanism involves SET to the ketone functionality to form a ketyl radical anion. The ketyl radical anion brings about ring opening of the epoxide to form oxygen radical. This oxygen radical is reduced by a second SET to form an oxygen anion that abstracts a proton from the proton donor (alcohol). The resultant β -hydroxyketone is reduced further to a ketyl radical that undergoes ketyl olefin coupling. The primary radical formed as the result of the coupling is reduced to an organosamarium species that finally abstracts another proton to form a cyclic diol in excellent yields and stereochemical control. The detailed mechanism is shown in scheme 6.

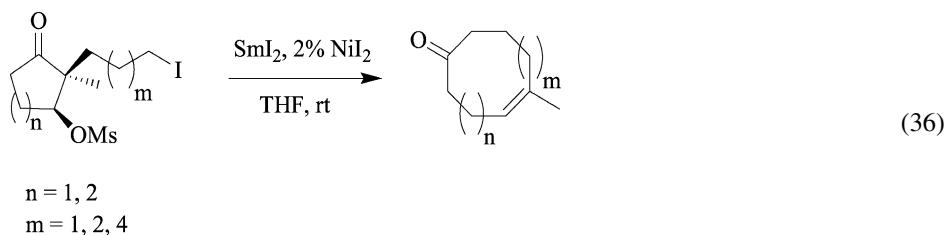
2.4.6. Ring expansion by Grob fragmentation

SmI_2 is capable of mediating ring expansion by Grob fragmentation. Molander and coworkers (Molander et al., 2001) have reported SmI_2 mediated Grob fragmentation that results in the



Scheme 6. Domino epoxide ring opening/ketyl olefin coupling reactions mediated by SmI_2 .

synthesis of several large rings. Products as large as 12-membered rings have been synthesized in moderate to good yields. *Cis* and *trans* cyclic olefins can be synthesized in a selective manner.



2.5. Role of proton donors and additives in SmI_2 -mediated reactions

The aim of the discussion to this point is to impress upon the reader the prevalent use of SmI_2 in organic synthesis. Though SmI_2 has been found to have numerous applications in organic synthesis, little is known about its mechanism of action. As is evident from reactions discussed in earlier sections, SmI_2 does not work alone, rather in concert with a variety of reagents. Some reagents such as HMPA, enhance the reactivity of SmI_2 while others such as alcohols and water, act as proton donors. Several other cosolvents such as TMG, DBU, DMF, and DMPU are sometimes used in place of HMPA. Metal salts such as Fe(III) , Co(II) , and Ni(II) , are utilized as well. The role of additives and other manipulations is only recently being explored and understood. Some of the most important questions related to SmI_2 chemistry and its mode of action with proton donors, cosolvents, additives and solvent are outlined below.

Proton donors: What is the exact role of alcohols and water commonly utilized in these reactions? How does change in structure and acidity of alcohols affect the mechanism of reaction? Since Sm^{+2} is oxophilic, do alcohols and water coordinate to SmI_2 ? If yes, does coordination to SmI_2 change the nature of the actual reducing species?

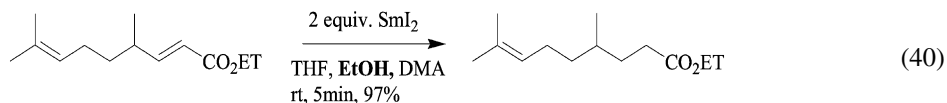
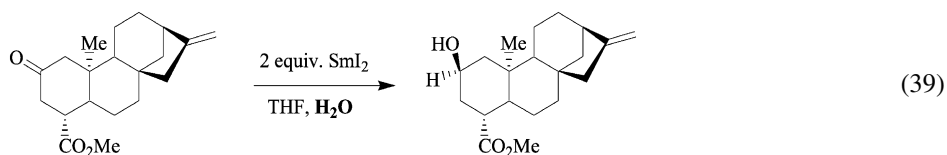
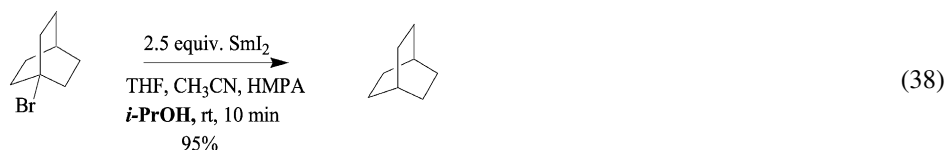
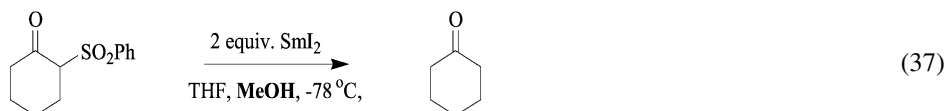
Cosolvents and additives: HMPA is the most commonly utilized cosolvent that coordinates strongly to SmI_2 . How does HMPA enhance the reactivity of SmI_2 ? Does addition of bulky HMPA inhibit coordination and chelation of SmI_2 to oxygen rich substrates?

Solvent: THF is the common solvent for SmI_2 reactions. However, acetonitrile, dimethoxyethane (DME), tetrahydropyran (THP), benzene and even water have been utilized as solvents for SmI_2 . Since it is known that THF is a reasonable ligand for SmI_2 , do other solvents also coordinate to SmI_2 ? Is the reducing ability of SmI_2 dependent on the solvent? Does the mode of action and the mechanism of reduction vary depending on the solvent utilized? How do common additives, especially alcohols and water, behave in different solvents?

While all of the questions posed in the preceding paragraphs cannot be fully answered because of the absence of solid mechanistic data in some instances, the following sections will provide literature background on the influence of proton sources, additives, and solvents on reaction outcomes of SmI_2 mediated reactions. Mechanistic data is discussed in cases where it is available.


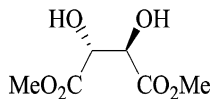
2.5.1. Proton sources

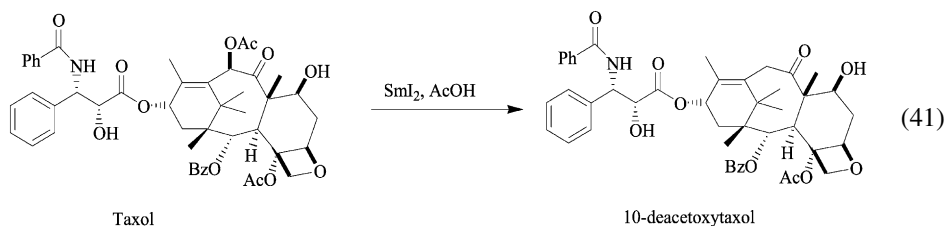
As shown previously, a variety of functional groups are reduced by SmI_2 . Many reactions mediated by SmI_2 require the presence of proton donors. The most commonly utilized proton donors are alcohols and water (Singh et al., 1987). A few examples involving the use of these proton donors are shown in eqs. (37)–(40). Several carboxylic acids



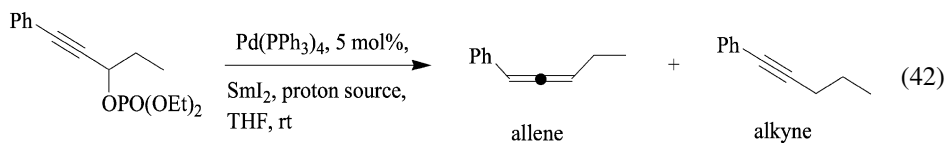
such as acetic acid and pivalic acid are also utilized as proton donors (Inanaga, 1990). Use of glycols and diols as proton donors has also been reported (Dahlen and Hilmersson, 2001). One important example is the deacylation of Taxol (Kagan and Namy, 1986) in the presence of acetic acid shown in eq. (41).

Table 1
Effect of proton source on regioselectivity in the SmI₂ mediated reduction
of propargylic phosphates

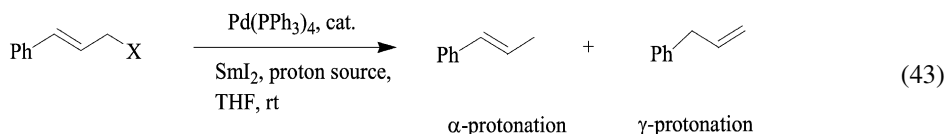
proton source	% yield	allene/alkyne
<i>t</i> -BuOH	80	>99 : 1
H ₂ O	70	56 : 44
	86	90 : 10
	81	15 : 85



Proton donors are known to exert considerable influence on the regiochemical and stereochemical outcome of several SmI₂-mediated reactions. Yoshida and Mikami (1997) have reported the effect of proton source in the reduction of propargylic phosphates by Palladium(0)/SmI₂/proton source system (eq. (42), table 1). The use of 2-methyl-2-propanol as the proton source results in the exclusive formation of allenes, while the diol, dimethyl tartrate ((+)-DMT) gave the alkyne as the major product.



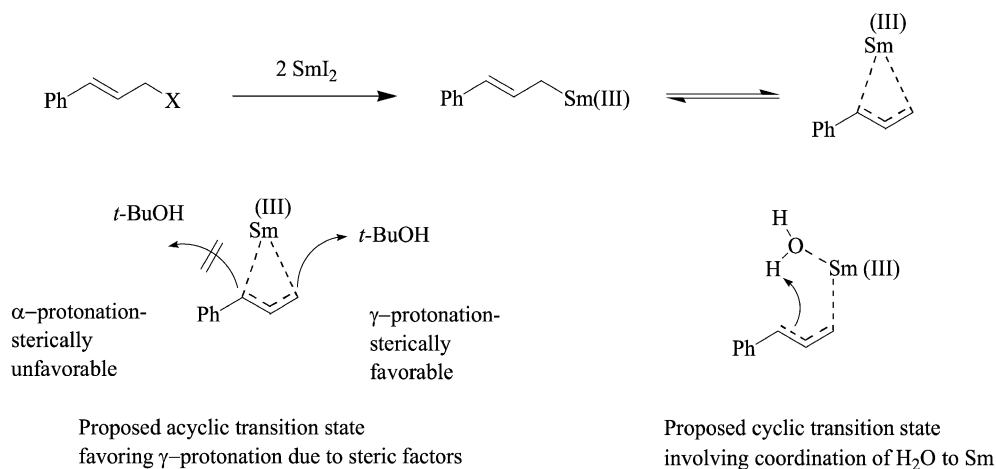
Yoshida et al. (1998) have also reported the effect of proton donors on the regioselectivity in the reduction of cinnamyl esters utilizing Pd(0)/SmI₂/proton source system. Similar to the propargylic phosphates discussed above, fine tuning the proton source resulted in the selective synthesis of different products (eq. (43), table 2).



The use of water as the proton donor resulted in γ -protonation selectively and *tert*-butanol selectively gave the α -protonation product. This reaction outcome and the regioselectivity

Table 2
Effect of proton source on regioselectivity in reduction of cinnamyl esters

X	proton source	reaction time	ratio (α : γ)
OP(O)(OHEt) ₂	<i>t</i> -BuOH	20 min	7 : 93
OP(O)(OHEt) ₂	H ₂ O	2.5 h	81 : 19
OC(O)OMe	<i>t</i> -BuOR	1 h	72 : 28
OC(O)OMe	H ₂ O	1 h	11 : 89
OAc	<i>t</i> -BuOH	2 h	81 : 19
OAc	H ₂ O	2 h	5 : 95



Scheme 7. Proposed transition states for rationalizing regioselectivity in the reduction of cinnamyl esters.

associated with the type of proton source utilized are explained with cyclic versus acyclic transition states. The authors proposed the coordination of water to the Sm(III) cation followed by proton transfer through a six-membered ring resulting in selective α -protonation. In the case of *t*-butanol, steric factors favor γ -protonation (scheme 7).

Proton sources have also been shown to influence the stereochemical outcome of several SmI₂ mediated reactions. Keck et al. (1999) has reported the stereoselective reduction of β -hydroxyketones to 1,3-diols utilizing SmI₂ in the presence of various proton donors. Interestingly, they observed that the reaction outcome was not only influenced by the nature of the proton source but also its concentration (eq. (44), table 3). The use of *t*-BuOH as the proton donor gave no reaction. Methanol and water are

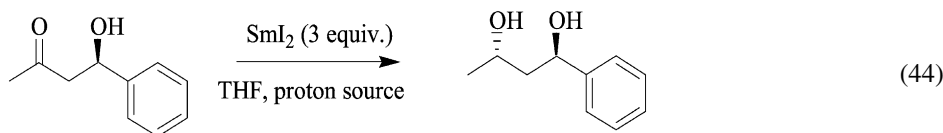
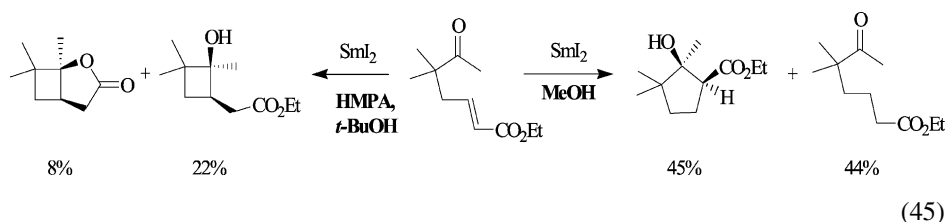


Table 3
Effect of proton source on stereoselectivity in the SmI₂-mediated reduction of β -hydroxyketones

proton source	concentration of proton donor	% yield	ds (<i>anti</i> : <i>syn</i>)
<i>t</i> -BuOH	10 equiv.	no rxn	–
H ₂ O	2 equiv.	96%	83 : 17
H ₂ O	10 equiv.	88%	50 : 50
MeOH	10 equiv.	99%	>99 : 1

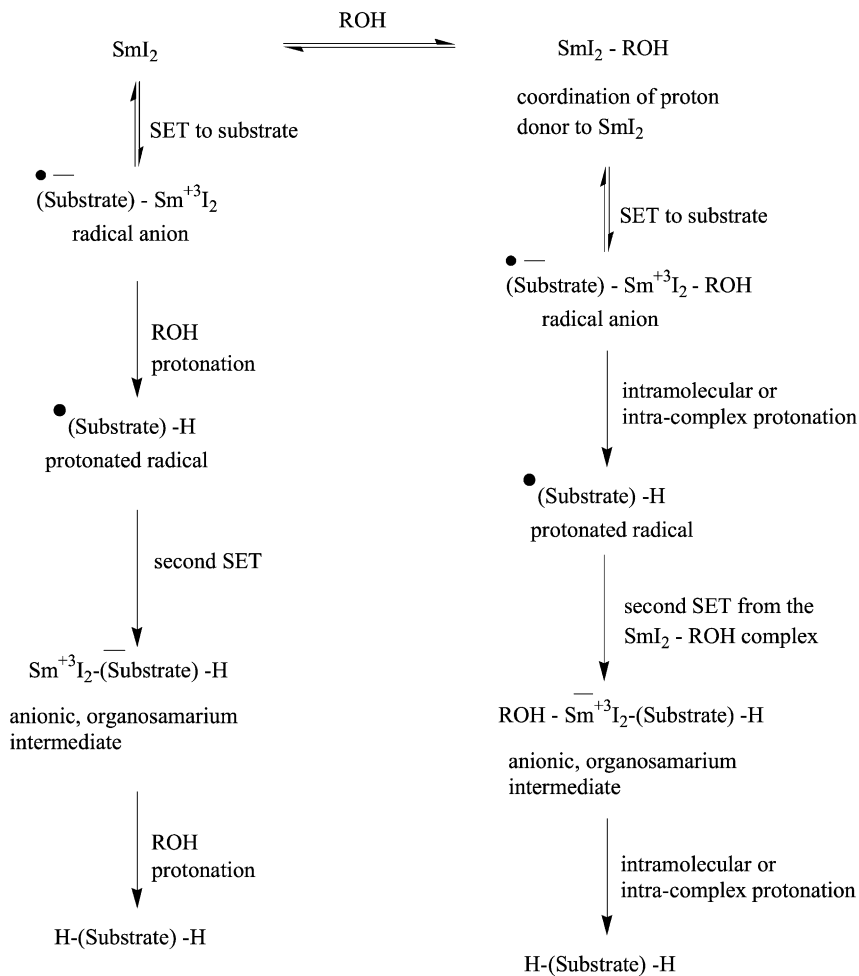
suitable proton donors and result in high yields. Excellent diastereoselectivity was obtained with 10 equivalents of methanol and 2 equivalents of water, with the *anti* 1,3-diol being the major product. The increase in concentration from 2 equivalents to 10 equivalents of water resulted in complete loss of stereoselectivity. Though the authors did not provide an explanation for these results, it is quite clear that proton donors exert a substantial influence on the stereoselectivity of reaction products.

Another important example of the effect of proton donors on the reaction outcome was reported by Procter (Hutton et al., 2002). The reduction of γ,δ -unsaturated methyl ketones by SmI₂ resulted in the formation of cyclobutanol or cyclopentanol derivatives depending on the proton donor utilized in the reaction (eq. (45)).



The predominant function of alcohols and water in SmI₂ mediated reactions is the donation of a proton through heterolytic cleavage of the O–H bond. However, coordination of alcohols to Sm(II) has also been reported. The seminal work by Hoz et al. (1996) has demonstrated the ability of methanol to coordinate to SmI₂ utilizing UV–visible spectroscopy. They observed a merging of the $f \rightarrow d$ transition peaks in the UV–vis spectrum of SmI₂ on addition of increasing amounts of methanol (λ_{max} for SmI₂ – 616 and 552 nm, λ_{max} for SmI₂–MeOH mixture at 4.115 M concentration of methanol – 584 nm). They studied the effect of proton donor concentration on the competitive reduction of a mixture of two conjugated alkenes. Two distinct pathways for reduction reactions mediated by SmI₂ were proposed as a result of this study, as shown in scheme 8.

One pathway involves the reaction of free SmI₂ with the substrate prior to the reaction with the alcohol. The second pathway involves coordination of SmI₂ to ROH resulting in the formation of a unique reducing species, the SmI₂–ROH complex. This complex reduces the substrate by SET to form a radical–anion intermediate that on “intra-complex” protonation forms a radical intermediate. This radical is further reduced by another mole of SmI₂–ROH complex to form an anionic, basic, organosamarium intermediate.



Scheme 8. Two distinct pathways for reduction of substrates either by SmI_2 or a $\text{SmI}_2\text{-ROH}$ complex.

Dahlen and Hilmersson (2001) have shown that proton donors capable of coordinating or chelating to SmI_2 accelerate the rate of reduction of 3-heptanone. The results are shown in table 4. Comparison of entries 1, 2, and 3, in table 4 clearly indicates that chelating proton donors accelerate the rate of reduction of 3-heptanone. The same trend is observed for the diols in entries 4 and 5.

The reports by Hoz and Hilmersson underscore the significance of alcohol coordination to Sm(II) . Clearly the interplay between coordination and proton donor ability of various alcohols and water will have an impact on the mechanistic pathway of SmI_2 -based reductions which utilize proton donors. To address this issue, Flowers et al. (Chopade et al., 2004b) stud-

Table 4
Effect of coordinating and chelating proton donors on the rate constant of reduction of 3-heptanone to 3-heptanol

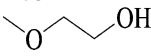
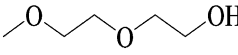
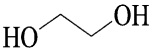
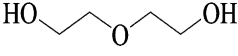
#	proton donor	$10^4 k$ (Mh ⁻¹)
1	MeOH	1.4
2		2.7
3		4.4
4		16
5		97

Table 5
Observed rate constant, reaction order, and k_H/k_D for the reduction of acetophenone by SmI₂ and proton donors

proton donor	k_{obs} (s ⁻¹) ^a	proton donor order	k_H/k_D
none	0.25 ± 0.02		
H ₂ O	7.6 ± 0.2	1.4 ± 0.1	1.8
CH ₃ OH	1.0 ± 0.1	0.9 ± 0.1	1.9
CH ₃ CH ₂ OH	0.9 ± 0.1	0.8 ± 0.1	1.8
(CH ₃) ₂ CHOH	0.33 ± 0.01	0	1.0
(CH ₃) ₃ COH	0.23 ± 0.01	0	1.0
CF ₃ CH ₂ OH	1.4 ± 0.1	0.9 ± 0.1	2.0
C ₆ H ₅ OH	1.7 ± 0.1	0.8 ± 0.1	1.9

^aExperimental conditions: [SmI₂] = 0.0025 M; [acetophenone] = 0.025 M; [proton donor] = 0.0625 M.

ied the influence of a series of alcohols and water on the rate of reduction of acetophenone by SmI₂. Table 5 contains the observed rate constants and reaction orders for each of the proton sources examined. Both 2-propanol and 2-methyl-2-propanol had no effect on k_{obs} and subsequent studies designed to determine their reaction order showed no influence even at high concentrations. Conversely, methanol, ethanol, 2,2,2-trifluoroethanol, and phenol significantly accelerated the rate of reduction and all four proton donors displayed a rate order of one (within experimental error). Water provided the highest rate enhancement and its reaction order was found to be 1.4. Further studies of reactions showing rate enhancements with added proton donor displayed a kinetic isotope effect of approximately 2, consistent with proton transfer in the rate-limiting step of the reduction.

Application of a steady-state approximation to the concentration of the intermediate acetophenone ketyl provided a rate equation that predicted first order dependence on [SmI₂], [acetophenone], and [proton donor] for a traditional House mechanism for the reduction of a ketone (House, 1972). The presence of methanol, ethanol, 2,2,2-trifluoroethanol, and phenol fit this mechanism and in fact a plot of pK_a vs. k_{obs} provided a linear correlation coefficient of 0.996 consistent with the acidity of the proton donor dictating the rate of reduction. Since

2-propanol, and 2-methyl-2-propanol have higher pK_a 's they were not acidic enough to protonate the ketyl radical intermediate, and as a result, did not enhance the rate of reduction.

While the mechanistic analysis was consistent with results obtained with alcohols, it did not explain the findings obtained for water. Water accelerates the reduction at a much faster rate than predicted based upon its acidity (pK_a), and its rate order in the reaction was 1.4. To study the system in more detail, UV-vis spectra of SmI_2 in the presence of increasing amounts of water were obtained. Clear differences in the spectra were observed after the addition of as little as 10 equivalents of water and consistent with coordination of water. Follow-up rate studies at low concentration of water (less than 9 equivalents, based on SmI_2) showed that water behaved the same as alcohols and had a rate order of 1. At higher concentrations carried out at the onset of coordination to SmI_2 , the rates were further enhanced and the rate order was larger than 1. At very high concentrations of water (above 80 equivalents) the rate order was 2. Similar experiments at high concentrations of alcohols were carried out. Addition of methanol at concentrations of 1 M showed evidence of coordination by UV-vis and began to show a rate enhancement greater than expected upon the onset of coordination. Ethanol, 2,2,2-trifluoroethanol, and phenol showed no evidence of coordination even at concentrations above 4 M and as a result were first order through the whole concentration range.

While it is clear that more experiments need to be done to examine the role of proton donors in SmI_2 mediated reactions in detail, the experiments described above show the following: (1) There is a linear correlation between the acidity of proton donors and the rate of ketone (acetophenone) reduction. (2) The proton source must have sufficient acidity to protonate the ketyl intermediate formed upon reduction of a ketone by SmI_2 . (3) Water has a much higher affinity for SmI_2 in THF than alcohols. (4) Complexation between a proton donor and SmI_2 produces a unique reductant that reacts with ketones through a mechanistically distinct pathway. This facet of SmI_2 chemistry should be recognized when utilizing proton donor sources in reductions and reductive coupling reactions.

2.5.2. Role of additives in SmI_2 -mediated reactions

The unique character of SmI_2 that has resulted in its broad applicability is that its reducing power can be controlled by the addition of cosolvents and additives. Even the seminal paper by Kagan describes the use of catalytic amounts of ferric chloride to accelerate several coupling reactions (eq. (46), table 6).

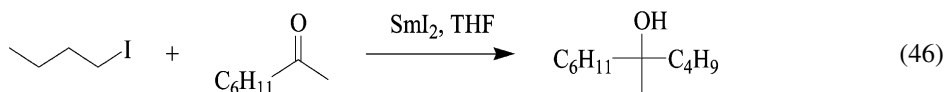


Table 6
Use of ferric chloride as catalyst in SmI_2 mediated coupling reactions

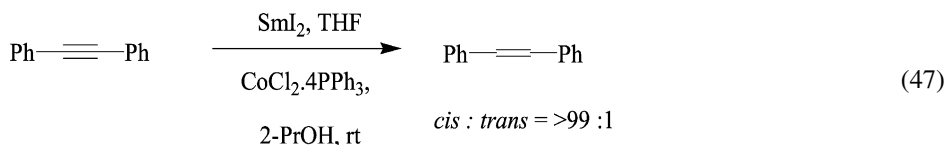
additive	rxn time	yield %
no additive	8 h	76
0.5 mol% FeCl_3	3 h	73

Table 7
Use of [Fe(DBM)₃] as catalyst in SmI₂ mediated coupling reaction

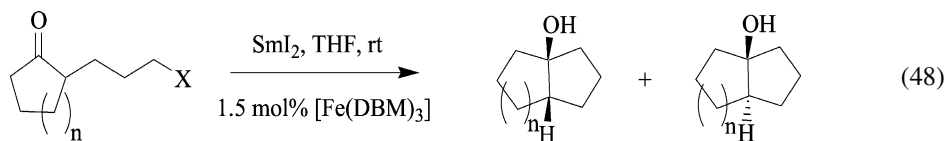
<i>n</i>	% yields	<i>syn</i> : <i>anti</i>
1	90	>99 : 1
2	100	1.3 : 1
3	85	2 : 1

The additives commonly utilized to alter the reducing power of SmI₂ are classified into two major types: (a) basic cosolvents such as HMPA and DMPU, (b) inorganic salts such as LiX, NiX₂, and FeX₃. This section will provide a brief introduction to the application of various additives utilized in SmI₂ mediated reactions.

Inanaga and coworkers (Inanaga et al., 1991b) reported the use of several first-row transition metals as catalysts in SmI₂ mediated reduction of alkynes to alkenes. FeCl₃.4PPh₃, CoCl₂.(H₂O)_X, CoCl₂.4PPh₃, NiCl₂.(H₂O)_X, NiCl₂.4PPh₃ catalyze these reactions with cobalt salts providing the best results. The reduction can be limited to the formation of alkenes. Further reduction to alkanes is suppressed by controlling the equivalents of SmI₂ (eq. (47)).



Molander and Etter (1986a) reported the reductive coupling of 2-(ω -iodoalkyl) cycloalkenones by SmI₂ in THF in the presence of catalytic amounts of iron tris-(dibenzoylmethane), [Fe(DBM)₃]. These reactions gave excellent yields of bicyclic alcohols. This methodology is especially useful in the synthesis of 6-membered rings (eq. (48), table 7).



The application of bases such as lithium amide (LiNH₂), lithium methoxide (LiOMe) and potassium hydroxide (KOH) as additives in SmI₂ mediated reactions is also known. Kamochi and Kudo (1991) reported the use of these bases in reductions of esters, carboxylic acids, anhydrides, and amides to the corresponding alcohols. These substrates are not reduced by SmI₂ alone (eqs. (49)–(51)).

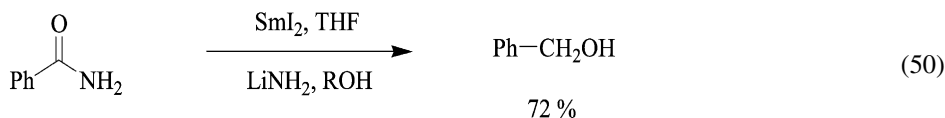
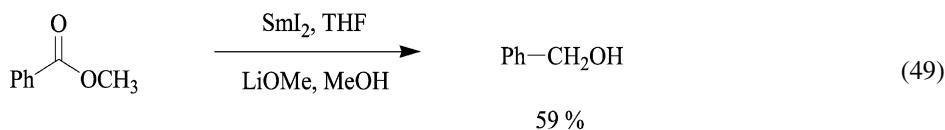
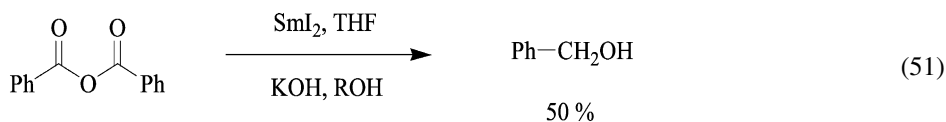
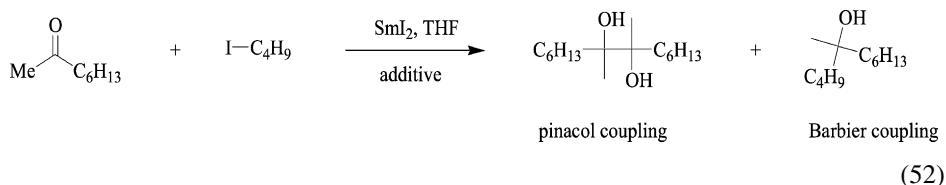


Table 8
Use of lithium salts as additives in SmI₂ mediated reductive coupling reactions

additive	equiv/SmI ₂	pinacol %	Barbier %	starting material %
no additive		23	59	18
HMPA	8	<1	91	8
LiCl	8	64	21	15
LiBr	8	98	<1	<1



Lithium bromide and lithium chloride can also enhance the reactivity of SmI₂ in THF (Fuchs et al., 1997; Miller et al., 2000). Addition of anhydrous LiCl and LiBr to SmI₂ resulted in rate enhancement and better yields in pinacol coupling of cyclohexanone. In the Barbier type reaction of 1-iodobutane with 2-octanone, the presence of LiBr and LiCl resulted in the formation of pinacol coupling product (diol from 2 moles of 2-octanone) as the major product rather than the nucleophilic addition of halide to ketone (eq. (52), table 8).



2.5.3. Use of lithium salts as additives in SmI₂ mediated reductive coupling reactions

Examination of the UV-vis spectra of SmI₂-LiBr and SmI₂-LiCl mixtures are identical to those of SmBr₂ and SmCl₂. Thus, addition of anhydrous LiBr and LiCl to a THF solution of SmI₂ results in the formation of SmBr₂ and SmCl₂, both of which are stronger reductants than SmI₂. They are capable of preferentially reducing a ketone in the presence of a more easily reducible alkyl iodide due to their ability to coordinate to the carbonyl oxygen.

The examples described above clearly show that a variety of inorganic salts are commonly utilized in SmI₂ mediated reactions. They are capable of altering the Sm(II) reductant in situ leading to different reaction outcomes. The most commonly utilized additive in reactions of SmI₂ is HMPA. The pioneering work by Inanaga et al. (1987) is the first example of the use basic cosolvents such as HMPA in SmI₂ mediated reactions. They observed remarkable acceleration and better yields in reduction of organic halides by SmI₂ in presence of HMPA. Primary-, secondary-, tertiary-alkyl, vinyl and aryl iodides, bromides, and even chlorides are reduced by SmI₂-HMPA mixture. Reduction reactions utilizing SmI₂-HMPA are usually completed in minutes rather than hours (eq. (53), table 9).

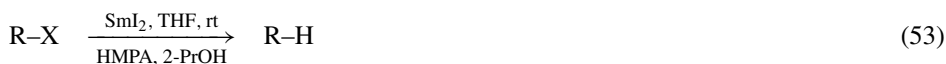


Table 9
Use of HMPA as cosolvent in SmI_2 mediated reduction reactions

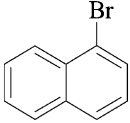
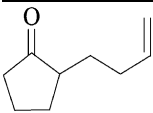
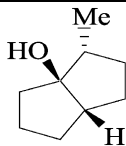
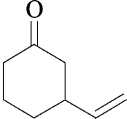
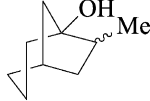
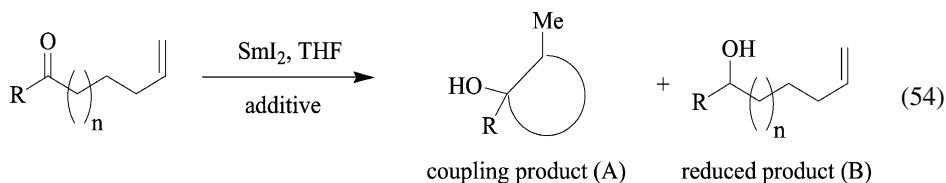
R-X	rxn time	yield %
$n\text{-C}_{10}\text{H}_{21}\text{I}$	5 min	>95
$n\text{-C}_{10}\text{H}_{21}\text{Br}$	10 min	>95
	5 min	98
cholesteryl chloride	3 h	99

Table 10
Use of HMPA as additive in SmI_2 mediated reduction and reductive coupling reactions

substrate	product	HMPA	time	yield (A : B)	% de
		8 eq.	<15 min	100 : 0	>99%
		0 eq.	36 h	62 : 5	92%
		8 eq.	30 min	100 : 0	88%
		0 eq.	48 h	4 : 96	0%

In spite of the utility of metal salts, HMPA remains the additive of choice in SmI_2 mediated reduction reactions. Since [Inanaga et al.'s \(1987\)](#) discovery of the use of HMPA, numerous reports describing novel applications and mechanistic insights of SmI_2 -HMPA mixture have appeared ([Hou and Wakatsuki, 1994](#); [Hou et al., 1997](#)). [Molander and McKie \(1992b\)](#) studied the effects of HMPA on a series of ketyl-olefin cyclization reactions. They observed an increase in reaction rates, better yields and higher diastereoselectivity upon addition of HMPA (eq. (54), table 10).



Early proposals suggested that addition of HMPA produces a sterically encumbered reductant that not only dictates the diastereoselectivity of the reactions, but also stabilizes reactive intermediates (ketyls, radicals) in close proximity to the Sm -HMPA complex, thereby

preventing competing reaction processes. Two possible mechanistic rationalizations were proposed for the enhanced reaction rates of the SmI_2 -HMPA mixture compared to SmI_2 : (1) HMPA may cause the dissociation of SmI_2 aggregates in THF, making the reductant more reactive; (2) HMPA is a strong donor ligand and may perturb the f-orbital (or other electron-donating homo orbital) due to ligand field effects. This may result in an increase in the energy of homo- (electron-donating) orbital and an increase in the Sm(II)/Sm(III) cell emf making it a more powerful reductant.

Studies by Flowers and coworkers (Shotwell et al., 1999) provide evidence that deaggregation is unimportant. Vapor pressure osmometry (VPO) experiments show that SmI_2 exists as a monomer in THF and other solvents. Addition of HMPA causes changes in the UV-visible spectrum of SmI_2 suggesting coordination of HMPA. Cyclic voltammetry (CV) was utilized to examine the influence of HMPA on the reducing power of SmI_2 . The standard potential (vs. SCE in THF) for SmI_2 was determined to be -0.98 ± 0.04 V and for SmI_2 -1.75 ± 0.06 V. Thus, addition of a minimum of four equivalents of HMPA increases the reducing ability of the reductant by 0.8 V (18 kcal/mol).

Crystallographic data reported by Evans et al. (1995c) provides evidence that the solvated structure of SmI_2 in THF is $[\text{SmI}_2(\text{THF})_5]$. Initial insight into the structural details of SmI_2 -HMPA were provided by Hou et al. (1997). Solutions containing four equivalents of HMPA produced crystals of $[\text{SmI}_2(\text{HMPA})_4]$, with the iodide ligands in the inner sphere, but solutions containing ten or more equivalents of HMPA produced crystals of octahedral $[\text{Sm}(\text{HMPA})_6]\text{I}_2$, with the iodide ligands in the outer sphere and HMPA ligands bound to Sm. Elegant followup studies of Skrystrup, and Daasbjerg (Enemark et al., 2000) provides evidence that the addition of four equivalents of HMPA to SmI_2 in THF results in the formation of $[\text{Sm}(\text{THF})_2(\text{HMPA})_4]\text{I}_2$, while the addition of 10 or more equivalents produces $[\text{Sm}(\text{HMPA})_6]\text{I}_2$. Clearly SmI_2 and SmI_2 -HMPA mixture in THF are completely distinct species. An obvious question then arises is, how does the difference in structures of SmI_2 and SmI_2 -HMPA affect their reactivity? Does it cause a change in mechanism of reduction? Furthermore, does a sufficiently detailed mechanistic understanding of the role of HMPA in SmI_2 reductions provide the insight necessary to design alternative methods that do not require HMPA, but mimic its useful features? Again, while not all of these questions can be answered sufficiently, some mechanistic data is beginning to emerge that provides insight into the role of HMPA in reductions of SmI_2 .

Alkyl halides and ketones are known to be reduced faster by SmI_2 in the presence of HMPA. Furthermore, SmI_2 -mediated Grignard or Barbier type couplings of alkyl halides and ketones are known to be facilitated upon the addition of HMPA and since both substrates can be reduced by SmI_2 -HMPA, there are a number of potential mechanistic pathways the reduction can proceed through. Curran and Totleben (1992) found that primary and secondary alkyl halides can be reduced by SmI_2 -HMPA in THF to form alkylsamarium reagents. These reagents can be quenched by a number of electrophiles including aldehydes and ketones and results were consistent with organosamarium species being the reactive intermediates in SmI_2 -HMPA reductive couplings of alkyl iodides and ketones.

Rates of reduction of a series of ketone and alkyl iodide substrates by SmI_2 , $[\text{Sm}(\text{THF})_2(\text{HMPA})_4]\text{I}_2$, and $[\text{Sm}(\text{HMPA})_6]\text{I}_2$ were reported by Flowers and coworkers (Prasad and

Flowers, 2002a). While the addition of HMPA increased the rate of ketone reduction, there was no difference in the rate and activation parameters for ketone reduction when the reductant was changed from $[\text{Sm}(\text{THF})_2(\text{HMPA})_4]\text{I}_2$ to $[\text{Sm}(\text{HMPA})_6]\text{I}_2$. Examination of the crystal structure of $[\text{Sm}(\text{HMPA})_6]\text{I}_2$ shows that the complex is sterically hindered and while displacement of THF from $[\text{Sm}(\text{THF})_2(\text{HMPA})_4]\text{I}_2$ by a ketone during reduction is reasonable, it should be more difficult for a ketone to access the metal center of the sterically encumbered octahedral Sm–HMPA complex. The similarities of the rate and activation parameters for reduction of ketones by both Sm–HMPA complexes suggest that the transition states for ketone reduction by either complex are comparable.

In contrast to ketones, the rate of reduction of primary and secondary alkyl iodides was found to be dependent on the concentration of HMPA. Rate experiments in the presence of increasing amounts of HMPA showed that while increasing medium polarity influences the rate of alkyl iodide reduction, it has a minimal influence on ketone reduction. Since oxygen is a relatively hard atom, a ketone should have a high affinity for Sm(II) whereas the softer iodide is expected to have a lower affinity for the metal. The combination of these results were interpreted to be consistent with reduction of alkyl iodides by SmI_2 –HMPA complexes having a stronger outer-sphere component (where solvent polarity is important) and reduction of ketones having a stronger inner-sphere component. As a result, in the presence of HMPA, alkyl iodides are reduced at a faster rate than ketones leading to organosamarium intermediates that react with a ketone leading to C–C bond formation.

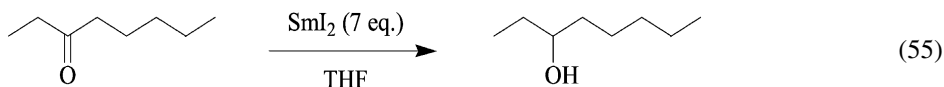
The use of HMPA is extremely common in SmI_2 -mediated reactions due to its convenience and its ability to optimize reaction outcomes. However, one serious drawback is that HMPA is a suspected human carcinogen. Therefore the search for potential alternatives is an ongoing process. Cabri et al. (1995) have reported the use of non-toxic ligands in SmI_2 -mediated cyclization reactions. These include among others, DBU, Et_3N , TMG, and DMPU. Though these ligands have proven useful in a limited number of reactions, HMPA continues to be preferred due to its broad applicability in a variety of reductions and reductive coupling reactions.

A mechanistic understanding of the unique features of SmI_2 –HMPA may provide a means to developing methods that mimic its useful features. Upon the addition of HMPA to SmI_2 in THF, strong evidence suggests that the iodides are displaced to the outer-sphere (Enemark et al., 2000). Concurrent with this addition, the Sm(II) becomes a stronger reductant based on its measured ease of oxidation (by cyclic voltammetry). This suggests that iodide (or other ligand) displacement may be important. To study this in detail, Flowers et al. studied the impact of HMPA addition to SmI_2 and $\text{Sm}\{\text{N}(\text{SiMe}_3)_2\}_2$ (with $-\text{N}(\text{SiMe}_3)_2$ being a less labile ligand) and compared the rates of reactions (Prasad et al., 2004). VPO and ITC studies were consistent with the addition of two equivalents of HMPA to $\text{Sm}\{\text{N}(\text{SiMe}_3)_2\}_2$ in THF and while a strong reductant was formed as measured by cyclic voltammetry, the $\text{Sm}\{\text{N}(\text{SiMe}_3)_2\}_2$ –HMPA combination reduced alkyl iodides and dialkyl ketones at a slower rate than $\text{Sm}\{\text{N}(\text{SiMe}_3)_2\}_2$ alone. Comparison of activation parameters of $\text{Sm}\{\text{N}(\text{SiMe}_3)_2\}_2$ –HMPA and SmI_2 –HMPA in ketone and alkyl iodide reduction showed that a less ordered transition state was attained in the former case. This work shows that providing a more powerful reductant through HMPA addition is not sufficient to produce a more reactive species. Substrate access to the metal center though ligand exchange is of paramount importance as well.

Table 11
Reduction of 3-heptanone to 3-heptanol in the presence of Et₃N and proton donors

proton donor (eq.)	cosolvent (eq.)	% yield after 1 min	relative rate
–	–	0.007	1
H ₂ O (7)	–	0.018	2.6
–	Et ₃ N (7)	0.006	0.9
MeOH (14)	Et ₃ N (7)	0.7	100
H ₂ O (7)	Et ₃ N (7)	>99	>100000

In this regard, the work reported by Hilmersson et al. (Dahlen and Hilmersson, 2002) is of considerable significance. They have reported the use of SmI₂/H₂O/Et₃N mixture in the reduction of ketones. These reactions are instantaneous (completed within 10 seconds of addition) based on the color change from blue to white, and provide excellent yields of reduced products (eq. (55), table 11).



Initial studies have shown that water and Et₃N do not accelerate the reactions separately. The acceleration is an effect of the Et₃N–H₂O mixture. Other amines such as TMEDA and PMDTA have identical effects as Et₃N. Further experiments suggested that addition of 2.5 equivalents of SmI₂, 5 equivalents of amine, and 6.25 equivalents of H₂O for every 1 equivalent of ketone provided optimum reaction outcome.

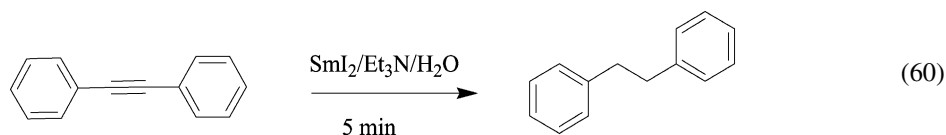
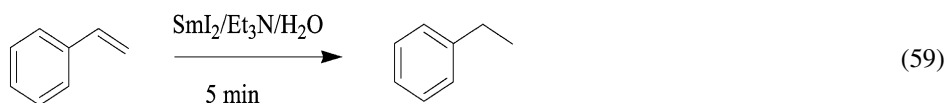
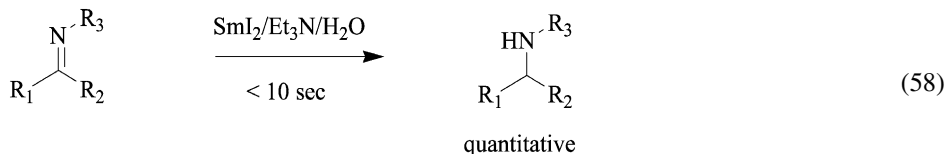
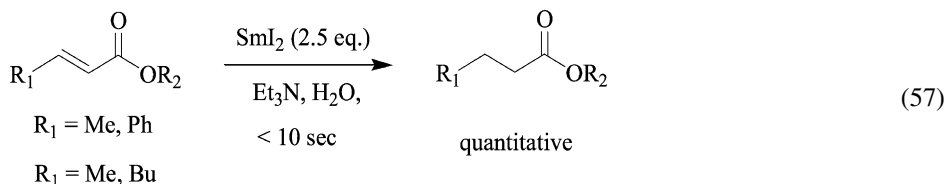
The first step in the mechanism involving SET from SmI₂ to ketone is likely a fast equilibrium that lies to the left. Therefore, this reaction can be accelerated by driving the equilibrium forward by means of precipitation of byproducts, the Sm⁺³ and I[–] ions. It is proposed that the presence of water and amine promotes the rapid precipitation of insoluble salts such as Sm(OH)₃ and R₃NHI. A clear colorless solution and white precipitate containing Sm and amine salts is obtained in these reactions. The reduction of ketones utilizing SmI₂/Et₃N/H₂O is therefore represented as:



Thus, rapid precipitation of Sm(OH)₃ and an ammonium salt, R₃NHI increases reaction rates. Although extensive mechanistic studies have not been carried out on the SmI₂/H₂O/amine reducing system, there are two important features of this combination worth mentioning. First, it is believed that displacement of iodide through precipitation of ammonium iodide provides the driving force for the reaction. Second, the redox potential of SmI₂/H₂O/Et₃N in THF is nearly identical to SmI₂ in THF alone (Dahlen and Hilmersson, 2003a). Thus coordination of a strong electron donor ligand such as HMPA and production of a more powerful ground state reductant is not a precondition for accelerating reactions of SmI₂.

A comparison of the Et₃N/H₂O method and HMPA/alcohol method in reduction of ketones indicates Et₃N/H₂O is approximately 100 times faster. This methodology has also been applied in the reduction of α,β -unsaturated esters, imines and conjugated olefins with excellent

results (Dahlen and Hilmersson, 2003a, 2003b) (eqs. (57)–(60)).



These examples clearly show the utility of SmI₂/amine/H₂O mixtures in reduction of several functional groups. Moreover, they provide better yields and require much less time than the HMPA/alcohol systems. The workup and subsequent purification of products is simplified because most byproducts are precipitated in the course of the reaction. Therefore, amine/H₂O mixtures are excellent alternatives to HMPA cosolvent. Recently, this combination has been shown to give very high yields and diastereoselectivities in the reduction of β-hydroxyketones (Davis et al., 2005). Further work in this area may lead to safer and more efficient protocols and provide an ideal replacement for SmI₂-HMPA.

2.6. The role of solvation in reactions of SmI₂

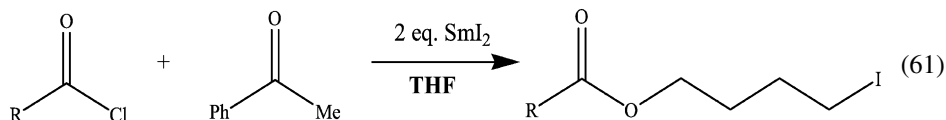
The first synthetically useful preparation of SmI₂ was performed in tetrahydrofuran (THF) by the reaction of samarium powder and diiodoethane under inert conditions and this combination of solvent and reductant has proven quite useful in organic synthesis. Nonetheless, there are important limitations for the use of SmI₂ in THF since it is a good hydrogen atom donor capable of terminating some of the radical reactions discussed previously.

As an example, Ruder (1992) has reported studies on reactions involving SmI₂ mediated reductive coupling reactions of acid halides. The use of SmI₂ in THF as the reducing species did not result in the formation of α-hydroxy ketones. Instead only formation of iodoester was

Table 12
Use of acetonitrile as solvent in SmI_2 mediated reactions

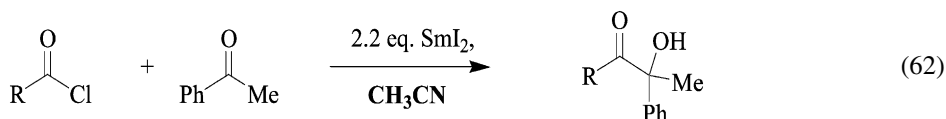
R	yield %
Ph	78
Me	80
<i>t</i> -Bu	83
PhOCH ₂	62
C ₈ H ₁₇	60

observed from the attack of the solvent THF on the acid halide as shown in eq. (61).



This example shows that THF can sometimes react with intermediates leading to unwanted or unexpected side products. To avoid this problem a number of groups have utilized solvents other than THF in the preparation of SmI_2 . A brief introduction to these SmI_2 -solvates and their utility in organic reactions is provided in this section.

To avoid the problem noted above, Ruder and coworkers utilized acetonitrile as the solvent milieu for the SmI_2 mediated coupling of acid halides with ketones. The reductant was prepared in acetonitrile by the reaction of samarium metal and diiodoethane. The resultant solution was green in color. While the reaction of acid halides and ketones was shown to result in the formation of iodoesters (eq. (61)) using THF, in acetonitrile, this side reaction is suppressed and higher yields of α -hydroxy ketones were obtained (table 12).



Ishii and coworkers have reported a different methodology for the preparation of SmI_2 in acetonitrile (Akane et al., 1994). In their work, chlorotrimethylsilane was added to a solution of NaI in acetonitrile followed by samarium grains under nitrogen at room temperature. The mixture was stirred for 3 hours during which the color of the solution changes to dark green, the characteristic color of SmI_2 in acetonitrile. Identical results were obtained by utilizing Sm metal and trimethylsilyl iodide in place of $\text{Me}_3\text{SiCl}/\text{NaI}$ mixture. This $\text{Me}_3\text{SiCl}/\text{NaI}/\text{Sm}$ system has been successfully applied in the reductive coupling of acetophenone (eq. (63)).

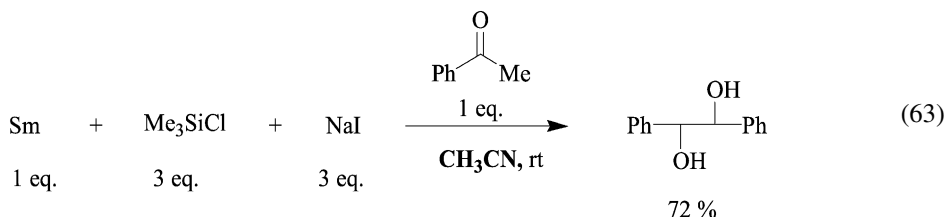
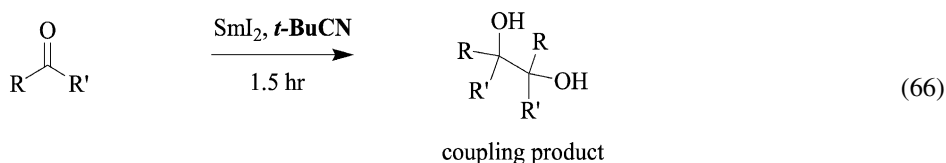
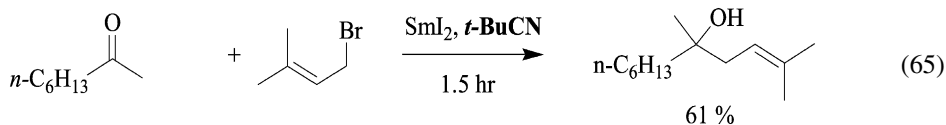
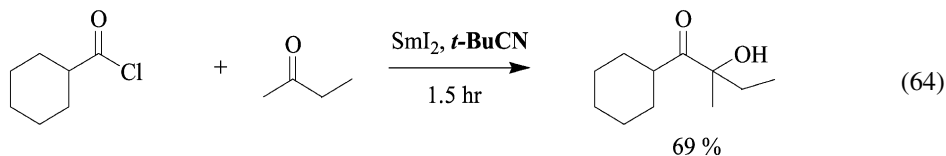


Table 13
Use of SmI₂ in pivalonitrile as solvent in SmI₂ mediated coupling reactions

ketone	yield %
2-octanone	80
cyclohexanone	90
acetophenone	94

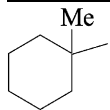
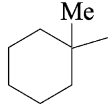
Acetonitrile is not the only nitrile utilized as a solvent for the preparation of SmI₂. Kagan and coworkers (Hamann et al., 1996) have reported the preparation of SmI₂ in other nitriles such as pivalonitrile, propanenitrile, and octanenitrile, by the reaction of metallic samarium and 1,2-diiodoethane under an inert atmosphere. The SmI₂ solution in pivalonitrile is dark green in color. This solution was utilized in the reductive coupling of acid chlorides and ketones to form α -hydroxyketones, the Barbier reactions of organic halides with 2-octanone, and pinacolization of ketones. The results are shown in eqs. (64)–(66) and in table 13.

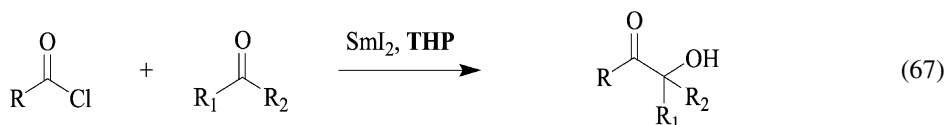


Reactions mediated by SmI₂-*t*-BuCN were slower compared to SmI₂-THF. Addition of metal salts such as NiI₂, NiBr₂, Fe(acac)₃ accelerated the reaction rates considerably. The reactions of SmI₂ in pivalonitrile were found to be cleaner compared to SmI₂ in acetonitrile due to the absence of acidic hydrogen atoms in pivalonitrile. In acetonitrile, several by-products are formed due to the acidic nature of the methyl hydrogen atoms. SmI₂-pivalonitrile provides more regioselectivity compared to SmI₂ in CH₃CN.

Tetrahydropyran (THP) has also been utilized as solvent in the preparation of SmI₂ (Namy et al., 1994). The major benefit of utilizing THP in place of THF is the complete absence of by-products arising from ring opening of the solvent (table 14). A solution of SmI₂ in THP is readily prepared by the reaction of samarium metal and 1,2-diiodoethane. Its application in the coupling of acid chlorides with carbonyl substrates has been reported (eq. (67)).

Table 14
Use of tetrahydropyran (THP) as solvent in SmI_2 mediated coupling of acid chlorides with carbonyl substrates

R	R ₁	R ₂	temp (°C)	yield %
	H	Et	-18 °C	>95
	H	Et	25 °C	55
1-adamantyl	Me	Et	-18 °C	>95



Benzene can also be used as a solvent in reactions of SmI_2 . Tani and coworkers have reported the preparation of SmI_2 in benzene-HMPA mixture and its use in the generation of alkylidenecarbenes from 1,1-dibromo-alk-1-enes. One drawback is that the preparation of SmI_2 in benzene is tedious compared to other solvents. It involves the addition of a solution of diiodoethane in benzene and HMPA (approximately 9 : 1 mixture by volume) to samarium powder under nitrogen. This mixture is heated gently to initiate the reaction and stirred for 5 days at ambient temperatures. The resultant purple-colored SmI_2 solution was treated with 1,1-dibromoalk-1-enes to form alkynes. These reaction conditions provided slightly better yields compared to SmI_2 in THF (eqs. (68)–(70), table 15). Benzene is an excellent solvent for reagents involving formation of radicals since it is a poor hydrogen atom donor. However, the tedious preparation of SmI_2 in benzene has limited its utility.

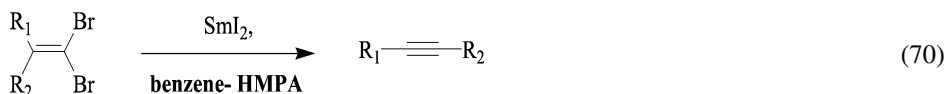
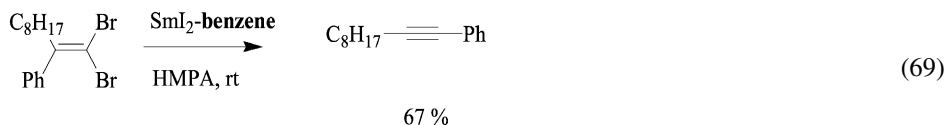
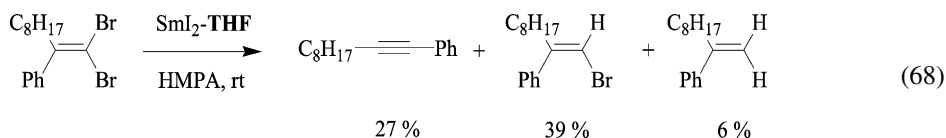


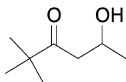
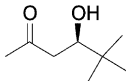
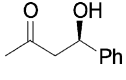
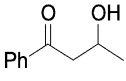
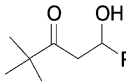
Table 15
Use of SmI₂ in benzene–HMPA mixture in reduction reactions of vicinal dibromoalkenes

R ₁	R ₂	yield %
C ₆ H ₁₃	H	90
<i>cyclo</i> -C ₆ H ₁₃	H	86
C ₈ H ₁₇	H	74

The examples above clearly show that there are advantages to using solvents other than THF in SmI₂ mediated reactions. Since solvent is likely to interact intimately with the Sm(II) ion, it is possible that solvent affects the nature of the Sm(II) reductant. Studies of these SmI₂-solvates are essential to understand the difference in their reactivity. The most common approach to examining SmI₂ solvates has been the use of X-ray crystallography. Sen and coworkers have studied the coordination chemistry of Sm(II) reagents in nitriles (Chebolu et al., 1985). The X-ray crystallographic data for SmI₂ in pivalonitrile reveals a distorted octahedral geometry. Each Sm atom is surrounded by two nitrogen atoms and four iodide ions. All the iodide ions are bridging resulting in an infinite chain of the repeating unit, SmI₂(NCMe₃)₂. The X-ray structure of SmI₂ in DME was reported by Evans et al. (1995c) that provides evidence for two distinct eight-coordinate molecular geometries and two very different I–Sm–I angles within the same unit. The Sm atom is surrounded by two iodide and three chelating DME ligands, but the arrangement of the ligands is either bent or linear with distorted hexagonal bipyramidal geometry. Evans has also reported the X-ray crystal structure of the SmI₂–THF solvate. SmI₂ is conveniently obtained as a dry powder by the removal of THF under vacuum. This solid has the molecular formula, SmI₂(THF)₂. However, a simple, four-coordinate structure is highly unlikely for a large Sm⁺² ion, which is known to have high coordination numbers (up to 10) (Shannon, 1976), though eight-coordinate structures are most common (Evans and Foster, 1992). Therefore, the SmI₂(THF)₂ powder obtained by removal of THF is most likely oligomeric in the solid state. The crystals of SmI₂ in excess of THF were then obtained. These crystals were extremely unstable and dissolved rapidly when warmed to ambient temperatures. Therefore, these crystals were grown at –35 °C and studied under cold nitrogen. The crystallographic data reveals that five THF molecules solvate the SmI₂ moiety to form the seven coordinate complex, SmI₂(THF)₅.

These X-ray crystallography studies provide significant information concerning the structure of SmI₂-solvates. There are however, inherent disadvantages in the use of this technique: (a) the preparation of high-quality, stable crystals can be a time consuming process, and (b) the crystals are usually obtained by slow removal of solvent or slow exchange with a different solvent with reduced solubility of the complex. The structure of crystals obtained by these processes may not always resemble the actual structure in solvent. While care should be taken in evaluation of crystallographic data in relation to solution structure and chemistry, the diversity of SmI₂-solvates and the likely variable affinity of different solvents for Sm(II) leads to the supposition that the solvent milieu will have an impact on the reactivity of SmI₂ and potentially alter product distributions.

Table 16
Reduction of β -hydroxyketones by SmI_2 in THF, CH_3CN , and DME

entry	substrate	<i>syn</i> : <i>anti</i>		
		THF (yield, %) ^{a,b}	equiv. MeOH ^c - CH_3CN (yield, %) ^a	DME (yield, %) ^{a,b}
1		3 : 1 (q)	2-1 : 5 (68) 5-1 : 5 (75) 10-1 : 3 (79) 15-1 : 3 (82) 25-1 : 3 (78)	15 : 1 (q)
2		9 : 1 (q)	10-1 : 3 (72) 25-1 : 2 (75)	>99 : 1 (q)
3		>1 : 99 (q)	10-1 : 5 (89) 25-1 : 2 (76)	>1 : 99 (q)
4		3 : 1 (q)	10-1 : 10 (75) 25-1 : 5 (84)	>99 : 1 (q)
5		55 : 45 (q)	10-1 : 3 (75) 25-1 : 2 (84)	50 : 50 (q)

^aGC yields.

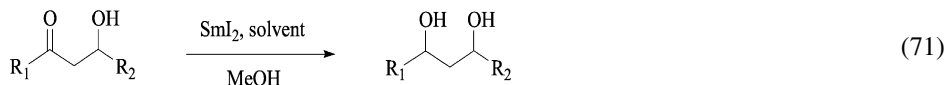
^b25 equivalents of MeOH (based on $[\text{SmI}_2]$ was used in the THF and DME studies).

^cVariable concentrations of MeOH were used in the acetonitrile studies.

The hypothesis described above has recently been examined by Flowers and coworkers (Chopade et al., 2004a). SmI_2 was prepared and characterized by UV-vis, VPO, and cyclic voltammetry in THF, dimethoxyethane (DME) and acetonitrile. The characterization of SmI_2 in THF, CH_3CN , and DME was found to be consistent with the following: (1) SmI_2 is monomeric in all three solvents; (2) dissolution of SmI_2 in each solvent provides unique UV-vis spectra; and (3) the redox ($E_{1/2}$) values are nearly the same within experimental error. The affinity of solvent for SmI_2 and the ability of various functional groups to displace solvent (or I^-) and interact with Sm(II) through chelation can potentially alter the *energies* of intermediates and activated complexes along the reaction coordinate resulting in different product distributions.

To address this issue, the reduction of a series of β -hydroxyketones was examined in all three solvents. The results are shown in table 16. Examination of the data shows some very interesting trends. In global terms, reductions in THF and DME show the same trends, while reductions in CH_3CN always provide the anti-1,3-diol as the major diastereomer. Quantitative reductions were obtained in THF and DME, while good yields (70–80%) were obtained in CH_3CN . Use of greater amounts of SmI_2 in CH_3CN did not provide significantly better yields in the reductions.

In comparison to SmI_2 in THF, reduction of β -hydroxyketones (entries 1, 2, and 4, table 16) by SmI_2 in DME provided significantly higher diastereoselectivities. The eight coordinate solvate provided by the bidentate DME could potentially increase the steric demands of the reductant enough to provide the observed increase in diastereoselectivity.



Although reduction of all substrates by SmI_2 in CH_3CN provided anti-diastereoselectivity, the selectivity was modest using 25 equivalents of MeOH. The different stereochemical outcome for reductions in CH_3CN indicated the possibility of an alternate mechanistic pathway for the SmI_2 -mediated conversion in this solvent. Another factor that could potentially have mechanistic implications is the presence of the proton source, MeOH. Proton sources (as mentioned previously) are known to have an impact on the stereochemical outcome of numerous SmI_2 -based reactions and recent mechanistic studies have shown that proton donor concentration can have an impact on the mechanistic pathway of the reduction.

To examine the interplay between the proton donor, MeOH and solvent on SmI_2 , UV-vis spectra of the reductant in each solvent was monitored in the presence of increasing amounts of MeOH. In THF and DME, no changes were visible in the spectra upon addition of up to 200 equivalents of MeOH. Conversely, addition of MeOH to SmI_2 in CH_3CN showed changes with as little as 2 equivalents of the proton donor suggesting coordination of the alcohol to Sm. These findings showed that MeOH has a much higher affinity for the oxophilic Sm in CH_3CN . In THF and DME, higher concentrations of MeOH are required to displace bulk solvent from the inner sphere of Sm.

Since coordination of MeOH to SmI_2 could disrupt chelation of β -hydroxyketones, a number of reductions were run at lower concentration of the proton donor in CH_3CN . In all cases it was found that 10 or fewer equivalents of MeOH provided higher diastereoselectivities in CH_3CN than the original experiments conducted with 25 equivalents (table 16). Although the diastereoselectivities in CH_3CN were modest, reduction of 3-hydroxy-1-phenylbutane-1-one (entry 4, table 16) to the corresponding diol provides a *syn* : *anti* ratio of 1 : 10.

The study described above shows that the affinity of solvent for SmI_2 likely plays a direct role in the ability of various substrates or additives (alcohols) to displace solvent from the metal and interact with it through direct coordination to the inner sphere. If this supposition is correct, different combinations of solvent, additive, and substrate could have an impact on the outcome of SmI_2 -mediated reactions. Further mechanistic studies will shed light on the roles of solvent, cosolvent, additives, and proton donors and their interdependence on the outcome of SmI_2 -mediated reactions. The utility of SmI_2 in organic synthesis and reactions still being discovered make this a ripe area of investigation for the foreseeable future.

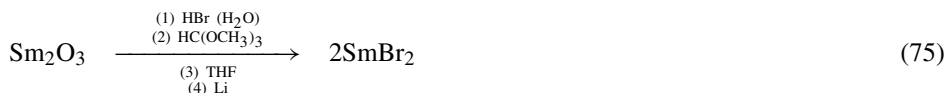
2.7. Samarium (II) chloride and samarium (II) bromide

While it is recognized that samarium diiodide (SmI_2) is by far the most utilized reductant among Sm(II) halides, samarium dichloride (SmCl_2) and samarium dibromide (SmBr_2) have been used in a number of applications. The main limitation of these two reductants is their

limited solubility in common organic solvents. A convenient reported synthesis of SmCl_2 was carried out by reduction of SmCl_3 by Li and naphthalene in THF (Rossmanith, 1979). Preparation of SmCl_2 can also be carried out by reaction SmI_2 with LiCl in THF (Fuchs et al., 1997; Miller et al., 2000). More recently (and surprisingly), SmCl_2 has been prepared in water using the combination of Sm metal and SmCl_3 (Matsukawa and Hinakubo, 2003).

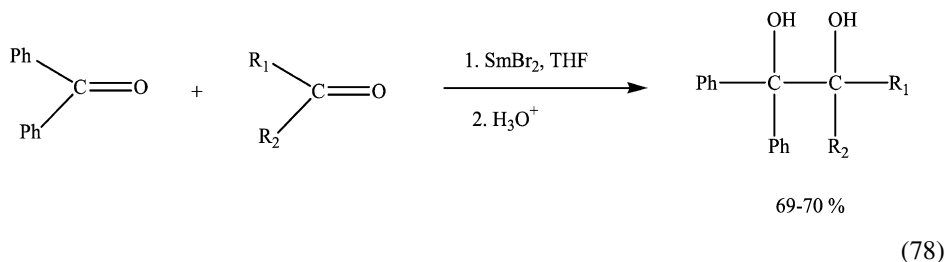


A straightforward preparation of SmBr_2 was carried out via conversion of Sm_2O_3 to an SmBr_3 hydrate followed by drying and reduction with metallic lithium (Lebrun et al., 1993). Reaction of SmI_2 with LiBr in THF produces in SmBr_2 *in situ* (Fuchs et al., 1997; Miller et al., 2000). The most straightforward (and direct) preparation of SmBr_2 is the reaction of excess Sm metal with 1,1,2,2-tetrabromoethane in THF (Héliion et al., 2003).



Both SmBr_2 and SmCl_2 are powerful reductants. Work of Flowers has shown that SmCl_2 is the strongest reductant of the two with an $E_{1/2}$ of -1.8 ± 0.1 V (vs. SCE) whereas the potential of SmBr_2 is -1.55 ± 0.07 V (Miller et al., 2000). Work by Kagan comparing the reactivity of SmBr_2 and SmCl_2 with SmI_2 shows some interesting trends as well (Kagan et al., 1993). For instance, SmCl_2 was found to reduce alkyl halides and deoxygenate sulphoxides in a manner similar to SmI_2 .

The use of SmBr_2 has been predominantly directed towards pinacol coupling reactions. Kagan et al. found that SmBr_2 was quite effective in mediating pinacol couplings. Most attempts to cross couple ketones lead to a statistical distribution of diol mixtures. Cross couplings of benzophenone with dialkyl ketones, camphor and menthone lead to good yields of diols (Lebrun et al., 1993). More recently, Namy et al. (Héliion et al., 2003) have



developed a procedure that utilizes mischmetal as a coreductant with SmBr_2 in pinacol coupling reactions. Not surprisingly, addition of HMPA to SmBr_2 enhances the reducing power to a great extent producing a reductant capable of reducing imines to amines and alkyl chlorides to the corresponding hydrocarbons (Knettle and Flowers, 2001).

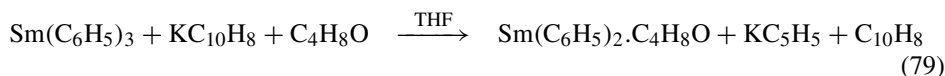
3. Sm(II) cyclopentadienyl-based complexes

The formulation of ligands plays an important role in lanthanide chemistry. In the lanthanide series, ligands were typically produced to prevent oligomerization or polymerization of lanthanides whose coordination sphere was unsaturated with the goal of producing monomeric species (Evans, 1995a). Ligands based on the cyclopentadienyl unit played an important role in this regard and were critical in the early development of organolanthanide chemistry (Schumann et al., 1995). Cyclopentadienyl ligands are considered to be ancillary ligands and hence in general do not take part in reactions (although there are exceptions). While there are a number of cyclopentadienyl-based ligands, this section will focus on two, C_5H_5 (Cp), and C_5Me_5 (Cp*) and their role in Sm(II) chemistry.

3.1. Samarium (II)Cp₂

3.1.1. Synthesis of Sm(II)Cp₂

The synthesis of SmCp_2 was first reported by Watt and Gillow (1969) and the synthesis was carried out by reduction of SmCp_3 by potassium naphthalene in THF.



The product was isolated as an insoluble, purple powder (eq. (79)). An alternative synthesis of SmCp_2 was reported by Kagan and coworkers (Namy et al., 1981) and was carried out by reaction of SmI_2 with NaCp in THF.



More recently, Swamy (2002) reported a synthesis of SmCp_2 from the reaction of SmX_2 ($\text{X} = \text{Cl}^-$, I^-) with a stoichiometric amount of *t*-butyllithium at -40°C in THF followed by

addition of NaCp. After concentration of the solution and storage at -25°C , crystals of

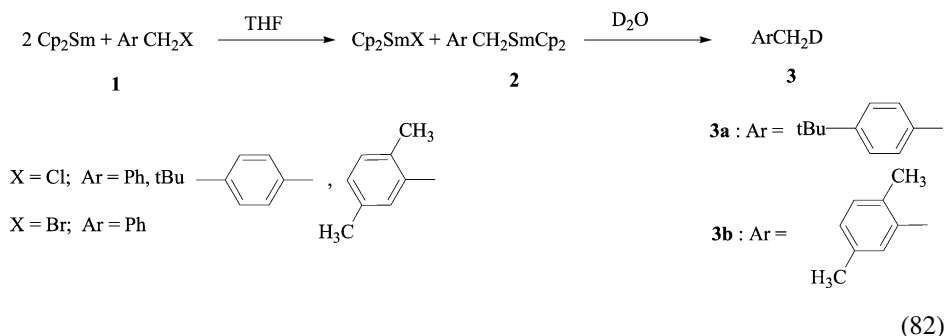


$[\text{Sm}(\text{Cp})_2(\text{THF})_2]$ were obtained (eq. (81)). While the structure is similar to that obtained for $[\text{Sm}(\text{Cp}^*)_2(\text{THF})_2]$ (Evans et al., 1981) there are some minor differences. The most apparent difference is the Cp–Sm–Cp angle of $129.8(1)^{\circ}$ compared to the angle in other Cp* complexes with bond angles in the range of 136.7° – 140° . The smaller angle in the $[\text{Sm}(\text{Cp})_2(\text{THF})_2]$ complex was attributed to the lower degree of steric interaction of the Cp ligand compared to Cp*. All reports on the synthesis of SmCp_2 describe it as a very pyrophoric material requiring handling under an anhydrous oxygen-free environment.

Because of its insolubility, redox potentials of SmCp_2 are difficult to obtain. However, electrochemical reduction of $(\text{C}_5\text{H}_5)_3\text{Sm}$ in THF at mercury, gold and platinum electrodes have been used to estimate the redox potential (Bond et al., 1986). The $E_{1/2}$ value was found to be -2.66 V vs. ferrocene/ferrocenium redox couple. The redox potential is considerably more negative than for the reduction of Sm(III) in water (Morss, 1976) indicating the impact of the Cp ligand on Sm(II) redox chemistry.

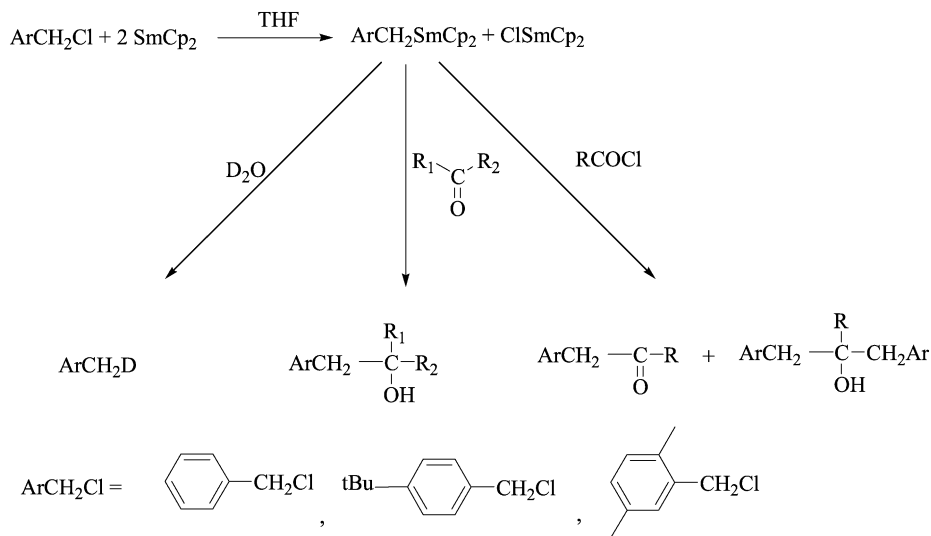
3.2. Reactions of $\text{Sm}(\text{II})\text{Cp}_2$

Although the insolubility of SmCp_2 limits its synthetic utility, a number of reactions utilizing this reagent have been reported in the literature. The addition of benzylic halides to a suspension of SmCp_2 in THF resulted in the formation of a solution in which the precipitate disappeared (Collin et al., 1987). Formation of an organometallic species was ascertained through the addition of D_2O which resulted in the formation of monodeuterated toluene derivatives. The intermediate benzylsamarium complex was



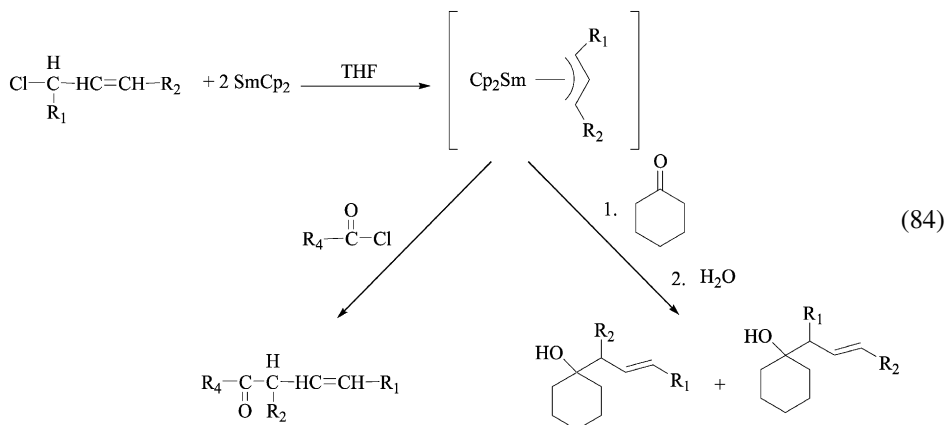
found to be stable up to 24 h at room temperature without any evidence of decomposition.

Benzylsamarium complexes display a range of reactivity with various functional groups. Reaction with benzyl halides produces 1,2-diphenylethanes in good yields. Addition of benzylsamariums to a wide variety of ketones and aldehydes leads to good yields of alcohols. Reactions of benzylsamarium derived from SmCp_2 react with acid chlorides to produce a mixture of alcohols and ketones (Kagan et al., 1993).



(83)

In related studies it was found that allyl chlorides react with SmCp_2 to give allylsamarium intermediates. The allylsamarium intermediates are proposed to have a η^3 structure based upon the reactivity of the intermediate with ketones. These reagents can



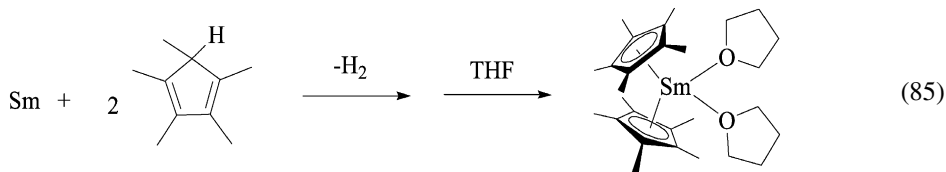
(84)

also be reacted with acid chlorides to provide β,γ -unsaturated ketones (Collin et al., 1991; Bied et al., 1992).

3.3. Synthesis of SmCp^*_2

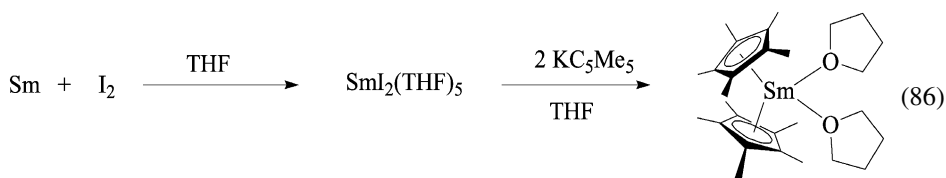
Although there are some advantages to utilizing SmCp_2 , the main limitation of this reagent is its poor solubility. In 1981, Evans and coworkers reported the synthesis of SmCp^*_2 (Evans et al., 1981). This synthesis and the work that followed from this seminal report has had

a profound impact on the use of Sm(II) reductants in a number of diverse areas including but not limited to, organic and inorganic synthesis, catalysis, and polymerization reactions. The original synthesis was carried out utilizing metal vaporization techniques to generate the complex (eq. (85)). The $[\text{Sm}(\text{Cp}^*)_2(\text{THF})_2]$ complex was soluble in a wide

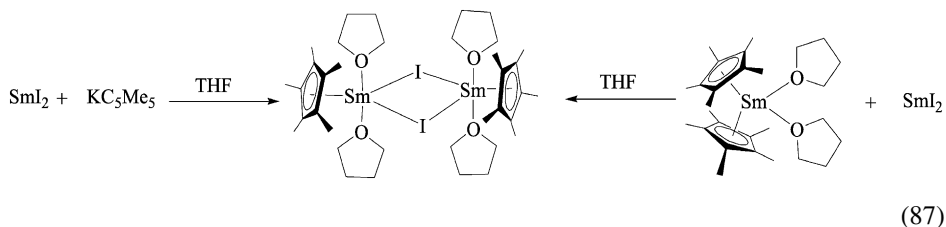


range of solvents enabling the chemistry of Sm(II) to be examined over a broad range of conditions. Low temperature recrystallization of SmCp^*_2 from THF provided access to high quality crystals which enabled structural characterization of the first divalent organosamarium system. The average $\text{Sm}-\text{C}(\eta^5)$ bond length was 2.86(3) Å while the average $\text{Sm}-\text{O}$ bond length between the metal center and the oxygen of THF was 2.63(1) Å (Evans et al., 1985c). These bond lengths are comparable to structurally similar Yb(II) complex (when taking into account the differences in ionic radii of Sm(II) and Yb(II)) (Tilley et al., 1980).

While the solubility of $[\text{SmCp}^*_2(\text{THF})_2]$ provided a conduit to examine the solution chemistry of Sm(II) in great detail, the fact that a specialized rotary metal vaporization reactor was required in the synthesis limited access to this reagent. The convenient preparation of SmI_2 developed by Kagan (Girard et al., 1980) and coworkers negated the need for specialized equipment and provided a straightforward solution synthesis of $[\text{SmCp}^*_2(\text{THF})_2]$ via the reaction of SmI_2 with 2 equivalents of KC_5Me_5 (eq. (86)).

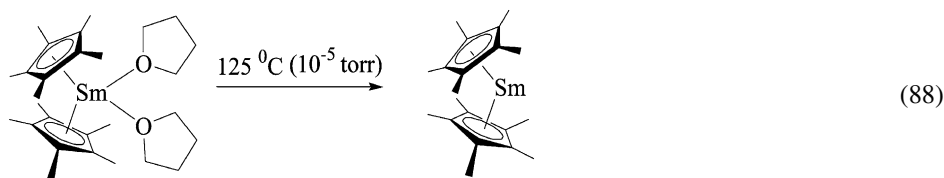


When the stoichiometry of KC_5Me_5 is changed from 2 to 1 or when one equivalent of SmI_2 is reacted with one equivalent of SmCp^*_2 in THF a heteroleptic dimer $[\text{C}_5\text{Me}_5\text{Sm}(\mu\text{-I})(\text{THF})_2]_2$ containing two bridging iodides (Evans et al., 1988c) is obtained in the solid state (eq. (87)). While the species is a discrete dimer in the solid state, solution NMR studies are



consistent with more than one species in solution.

Lanthanides are usually coordinatively saturated and when sterically demanding ligands (like Cp*) are used, they are monomeric, but typically, when smaller ligands are utilized, they tend to occur as oligomers in the solid state. In 1984, an unusual discovery was made that was contrary to this trend. Evans et al. (1984) found that upon heating $[\text{Sm}(\text{Cp}^*)_2(\text{THF})_2]$ under vacuum at 125°C produced the unsolvated, monomeric SmCp^*_2 (eq. (88)). The structure of the complex was unusual because the Cp* rings were



not parallel (as in FeCp^*_2), but had a bent metallocene structure that more closely resembled the THF solvate from which it was derived. As expected, the loss of two THF molecules from the structure, led to a decrease in the Sm–C bond length and an increase in the Cp* centroid–Sm–Cp* centroid bond angle as a result of a decrease in ligand crowding. As expected, the high degree of coordinative unsaturation of SmCp^*_2 makes it highly reactive. Much of the important work in this area in the last 20 years was initiated as a result of this seminal work with many researchers redoubling their efforts to examine and understand the reactivity of Sm(II) both from an organic and organometallic perspective.

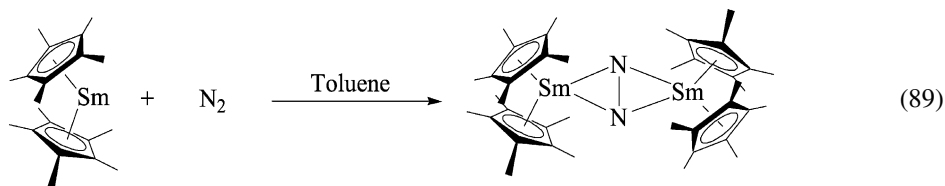
3.4. Reactions of $\text{Sm}(\text{Cp}^*)_2(\text{THF})_2$ and $\text{Sm}(\text{Cp}^*)_2$

The unusual geometry of the $\text{Sm}(\text{Cp}^*)_2(\text{THF})_2$ and $\text{Sm}(\text{Cp}^*)_2$ complexes coupled with their high reactivity and reducing power lead to the supposition that they should possess a rich chemistry in a wide variety of organic and inorganic reactions. The following sections are devoted to describing this chemistry. The sections are not meant to be an exhaustive review of the chemistry of $\text{Sm}(\text{Cp}^*)_2(\text{THF})_2$ and SmCp^*_2 in their reactions with substrates, but an overview of the wide variety of reactions they are capable of initiating. The sections are separated into reactions of $\text{Sm}(\text{Cp}^*)_2(\text{THF})_2$ and SmCp^*_2 with different classes of inorganic and organic substrates or different functional groups.

3.5. Reactions of SmCp^*_2 and $\text{Sm}(\text{Cp}^*)_2(\text{THF})_2$ with small inorganic molecules (N_2 , CO , CO_2) and related compounds

3.5.1. Reaction of SmCp^*_2 with N_2

Initial studies on the stability and reactivity of $\text{Sm}(\text{Cp}^*)_2$ provided some evidence that the complex reacted with nitrogen (Evans et al., 1985a), and in 1988, Evans and coworkers isolated $[(\text{Cp}^*)_2\text{Sm}]_2(\mu\text{-}\eta^2\text{:}\eta^2\text{-N}_2)$ from the reactions of SmCp^*_2 with N_2 in toluene (eq. (89)) (Evans et al., 1988c).

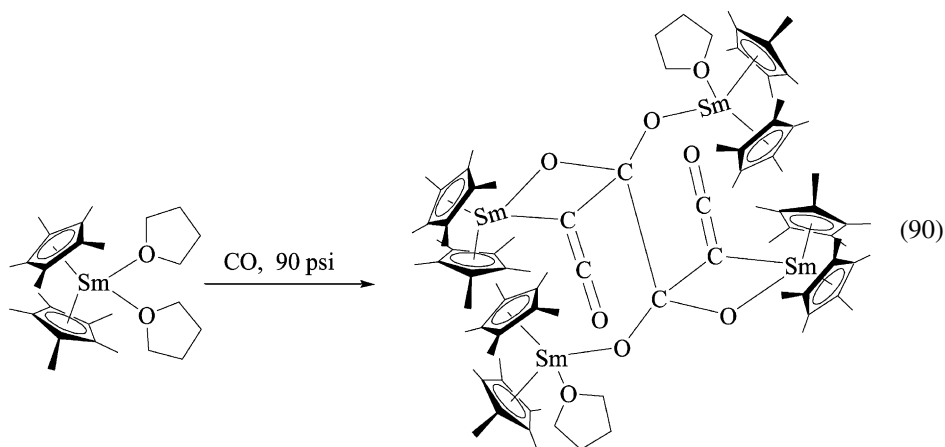


The two Sm atoms and the N_2 unit are in the same plane and the four Cp* rings produce a tetrahedral arrangement around each Sm. The N–N bond distance was shorter than expected based on the close proximity of the $SmCp^*_2$ suggesting potentially unusual chemistry.

Surprisingly, dissolution of $[(Cp^*)_2Sm]_2(\mu-\eta^2:\eta^2-N_2)$ in toluene lead to the evolution of N_2 gas suggesting that formation of the dinitrogen complex is reversible. Solid state $Sm(Cp^*)_2$ was found to react with N_2 and placement of the resulting $[(Cp^*)_2Sm]_2(\mu-\eta^2:\eta^2-N_2)$ under vacuum lead to the recovery of N_2 . In solution, NMR experiments showed that $[(Cp^*)_2Sm]_2(\mu-\eta^2:\eta^2-N_2)$ is in equilibrium with $Sm(Cp^*)_2$ and N_2 in toluene. Decreasing the temperature lead to an increase in the concentration of $[(Cp^*)_2Sm]_2(\mu-\eta^2:\eta^2-N_2)$, however complete conversion to the dinitrogen complex could not be achieved.

3.5.2. Reaction of $Sm(Cp^*)_2(THF)_2$ with CO

Reaction of CO at atmospheric pressure with $Sm(Cp^*)_2(THF)_2$ leads to a complex mixture of products. When the reaction is carried out under a CO atmosphere at 90 psi, a mixture is still obtained, but one product can be separated (in a 20% yield) and crystallized. The product was identified as $[(Cp^*)_2Sm_2(O_2CCCO)(THF)_2]$ (eq. (90)) (Evans et al., 1985d).



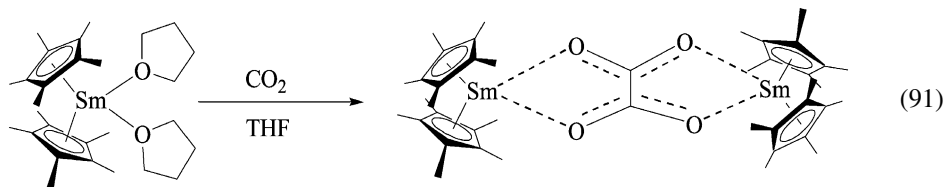
The unusual ketenecarboxylate (O_2CCCO) moiety is likely derived from three CO molecules and two molecules of $Sm(Cp^*)_2(THF)_2$.

While single electron reduction of CO offers an alternative strategy to traditional hydride reduction approaches, the unusual feature of this reaction is the orientation of the atoms in the product ketenecarboxylate. While the three consecutive carbons are consistent with the

coupling of three CO units, the discontinuous placement of oxygens in the ketenecarboxylate indicates a rearrangement has occurred through cleavage of a C–O bond.

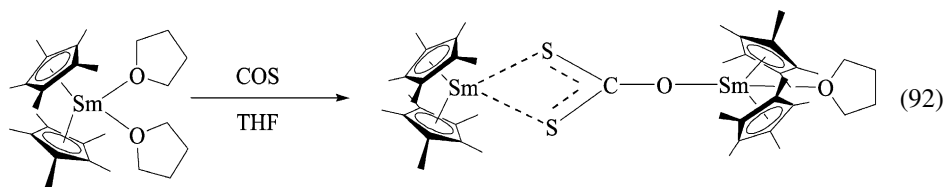
3.5.3. Reaction of $\text{Sm}(\text{Cp}^*)_2(\text{THF})_2$ with CO_2 and COS

Reaction of CO_2 with $\text{Sm}(\text{Cp}^*)_2(\text{THF})_2$ in THF at room temperature provides a high yield (>90%) of $[(\text{Cp}^*)_2\text{Sm}]_2(\mu-\eta^2:\eta^2-\text{O}_2\text{CCO}_2)$ (Evans et al., 1998b) (eq. (91)).



Surprisingly, when the reaction was carried out at -78°C in hexanes or toluene, complex product mixtures were obtained. Although the quality of the X-ray data was insufficient to provide a detailed description of bond angles and distances, a number of features of the complex can be qualitatively described. The oxygens on adjacent carbon atoms in the oxalate moiety coordinate with $\text{Sm}(\text{Cp}^*)_2$ to form two fused five-membered rings. The fused rings appear to be roughly planar with the Cp^* ligands producing a tetrahedral geometry around each Sm atom in a similar fashion displayed by the $[(\text{Cp}^*)_2\text{Sm}]_2(\mu-\eta^2:\eta^2-\text{N}_2)$ complex. Solution ^1H and ^{13}C NMR studies were consistent with the solid state structure.

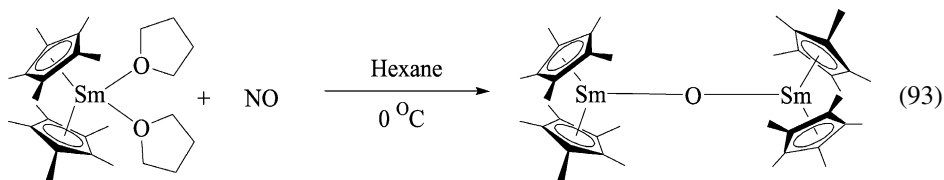
Reaction of $\text{Sm}(\text{Cp}^*)_2(\text{THF})_2$ with COS provides an unusual dithiocarbonate product, resulting from disproportionation of the reacting species (eq. (92)). Although a



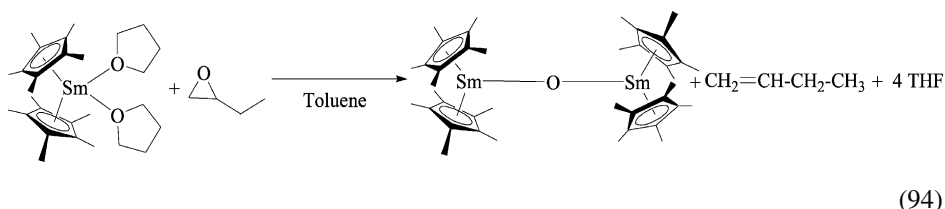
second organosamarium product is formed in the reaction, it was not identified. When the reaction was carried out using high concentrations of $\text{Sm}(\text{Cp}^*)_2(\text{THF})_2$, a high yield of the disproportionation product was obtained. NMR studies clearly showed the presence of two unique Cp^* ligands, a finding consistent with the X-ray structure. While this reactivity appears unique in comparison to reaction with CO_2 , disproportionation products are common for COS (Pandey, 1995).

3.5.4. Reactions of $\text{Sm}(\text{Cp}^*)_2(\text{THF})_2$ with NO , epoxides, and related compounds

In a survey of the chemistry of $\text{Sm}(\text{Cp}^*)_2(\text{THF})_2$, reactions with NO were examined. While a distribution of products was obtained, a toluene soluble product was obtained which after crystallization was shown to be an oxo-bridged bimetallic Sm complex $[(\text{Cp}^*)_2\text{Sm}]_2(\mu-\text{O})$ (Evans et al., 1985b) (eq. (93)). Reaction of N_2O with $\text{Sm}(\text{Cp}^*)_2(\text{THF})_2$ also produced



the oxo-bridged complex. In fact, any trace of substrates containing a reactive oxygen site produced the complex. Since the bimetallic bridged oxo-complex was thought to have potential as a starting material for examining organometallic oxide chemistry, more efficient routes were identified. Replacement of NO with pyridine N-oxide in reactions with $\text{Sm}(\text{Cp}^*)_2(\text{THF})_2$ produces the oxo bridged dimer in an overall yield of 47%, whereas reaction with 1,2-epoxybutane (eq. (94)) produces the bimetallic species in an



overall yield of 55% with 1-butene identified as a side product.

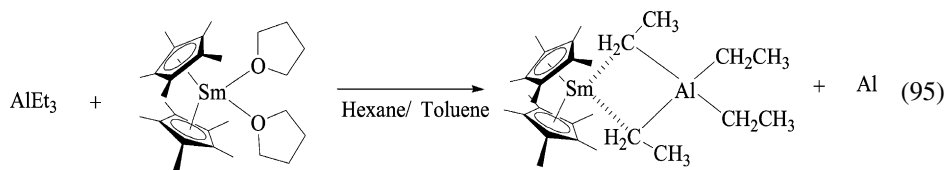
The structure of the complex is somewhat unusual and merits brief discussion. The Sm–O–Sm bond angle is 180° with the four Cp* ligands arranged in a tetrahedral fashion around the Sm_2O core. Typically, etheral types of oxygens (where oxygen contains two single bonds) are bent (Cotton, 1991). Furthermore, comparison with other metal oxide bridged dimers showed that $[(\text{Cp}^*)_2\text{Sm}]_2(\mu\text{-O})$ has a low value for the oxide radius compared to transition metal analogs. These structural features are compatible with the high oxophilicity of Sm and the steric requirements of the $\text{Sm}(\text{Cp}^*)_2$ units. The short Sm–O bond distance is also consistent with π interactions between the bridging oxygen and both $\text{Sm}(\text{Cp}^*)_2$ units.

3.6. Reactions of SmCp^*_2 and $\text{Sm}(\text{Cp}^*)_2(\text{THF})_2$ with inorganic and organometallic substrates

Reactions of SmCp^*_2 and $\text{Sm}(\text{Cp}^*)_2(\text{THF})_2$ with organometallic substrates are generally used as a route to produce bimetallic complexes or novel Sm(III)-based complexes. Bimetallic complexes in particular are potentially attractive targets as novel catalysts (Ma and Cahard, 2004). This section will describe some of the basic reactions of SmCp^*_2 and $\text{Sm}(\text{Cp}^*)_2(\text{THF})_2$ with inorganic and organometallic substrates. The reactivity of the product of these reactions is briefly described in notable cases.

3.6.1. Reactions of $\text{Sm}(\text{Cp}^*)_2(\text{THF})_2$ and SmCp^*_2 with trialkylaluminum

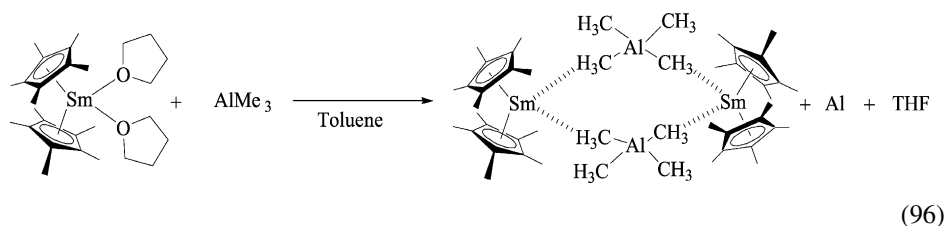
Addition of triethylaluminum in hexane with a solution of SmCp^*_2 in toluene reacts over a three hour period to produce $\text{Cp}^*_2\text{SmAlEt}_4$ (Evans et al., 1987b) (eq. (95)).



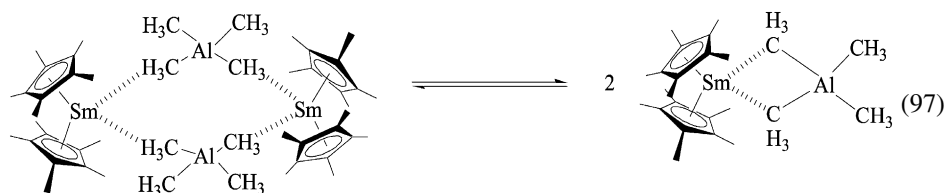
Spectroscopic examination by ^1H NMR revealed broad peaks in the range of 0 to -4 ppm whose width was found to be temperature dependent, a finding consistent with a Schlenk type equilibrium in solution.

Crystallization and subsequent analysis revealed an unusual ethyl bridged structure with the Cp^*_2Sm unit coordinated to the $\text{Et}_2\text{Al}(\mu\text{-Et})_2$ through two methylene bridging carbon atoms. The $\text{Sm}-\text{C}$ distance were clearly found to be within bonding range indicating that the structure is clearly not a $[\text{Cp}^*_2\text{Sm}]^- [\text{AlEt}_4]^-$ ion pair.

To examine this chemistry in more detail, [Evans and coworkers \(1988a\)](#) followed up this work by examining the reactivity of $\text{Sm}(\text{Cp}^*)_2(\text{THF})_2$ with trimethylaluminum. Reaction in of excess AlMe_3 with $\text{Sm}(\text{Cp}^*)_2(\text{THF})_2$ in toluene produced $\text{Cp}^*_2\text{Sm}[(\mu\text{-Me})\text{AlMe}_2(\mu\text{-Me})_2]\text{SmCp}^*_2$ in an 80% yield (eq. (96)). Each of the Sm atoms are eight-

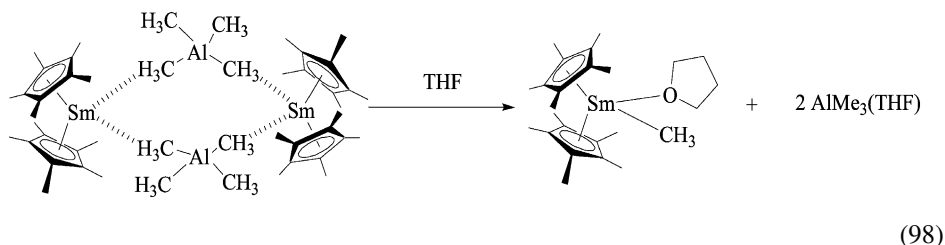


coordinate and the geometry around aluminum is consistent with an AlMe_4^- species. Examination of the ^1H NMR spectrum of the methyl bridged dimer showed a spectrum more complex than predicted by the solid-state structure. The spectrum was found to be temperature dependent and consistent with a monomer–dimer equilibrium (eq. (97)).



Studies of the observed equilibrium constants over a 70 degree temperature range provided ΔH° and ΔS° values of 8.7 ± 0.5 kcal/mol and 24 ± 2 e.u.'s respectively.

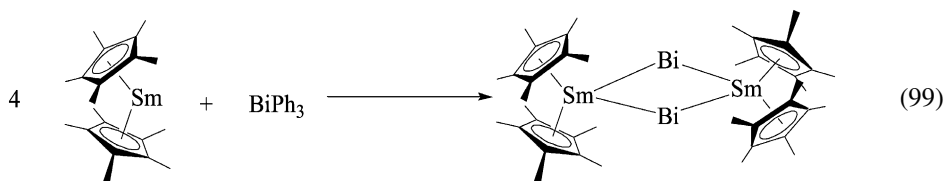
Dissolution of $\text{Cp}^*_2\text{Sm}[(\mu\text{-Me})\text{AlMe}_2(\mu\text{-Me})_2]\text{SmCp}^*_2$ in THF followed by cooling produced $\text{Cp}^*_2\text{Sm}(\text{Me})(\text{THF})$ through the pathway shown below (eq. (98)). The



compound is stable at room temperature, but decomposes at higher temperatures in both solution and the solid-state. Solvents other than THF (including C_6D_6 and toluene) react with $Cp^*_2Sm(Me)(THF)$ at room temperature. This complex also reacts with H_2 to produce $[Cp^*_2Sm(\mu-H)]_2$, an important catalyst for a wide variety of organic transformations (Kawaoka and Marks, 2004).

3.7. Reactions of $Sm(Cp^*)_2(THF)_2$ and $SmCp^*_2$ with group 15 organometallic compounds

A survey of reactions of $SmCp^*_2$ and $SmCp^*_2(THF)_2$ with triphenyl derivatives of group 15 compounds was carried out by Evans et al. (1991, 1996). The results of these studies are shown in table 17. As expected, $SmCp^*_2$ was found to be somewhat more reactive than the THF solvated derivative. While $SmCp^*_2$ formed a 1 : 1 coordination complex with PPh_3 , the phosphine was incapable of displacing THF from $SmCp^*_2(THF)_2$. Combination of $SmCp^*_2$ with $SbPh_3$ or $BiPh_3$ in benzene lead to cleavage of the metal–carbon bond whereas $SmCp^*_2(THF)_2$ only reacted with $BiPh_3$. Careful analysis of the reaction of $SmCp^*_2$ with $BiPh_3$ in a 4 : 1 ratio produced $[Cp^*_2Sm]_2(\mu-\eta^2 : \eta^2-Bi_2)$ and Cp^*_2SmPh (eq. (99)). The dibismuth complex is unusual in

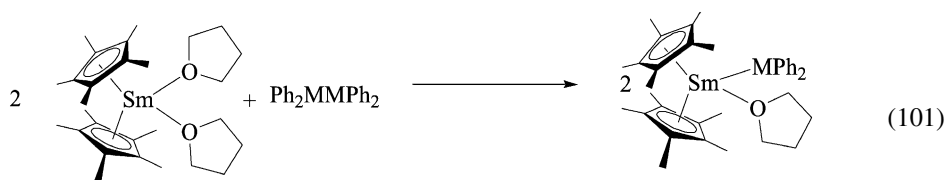
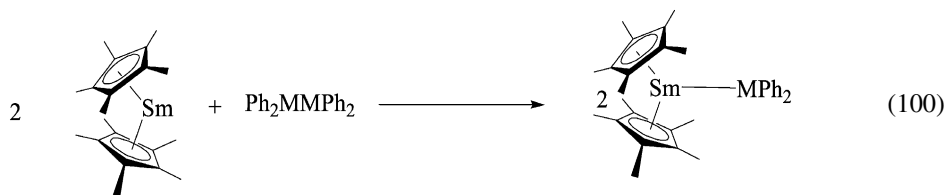


that the Bi_2 unit coordinates to the two Sm in a side on mode in a manner similar to that observed for the $[(Cp^*)_2Sm]_2(\mu-\eta^2 : \eta^2-N_2)$ complex except that in the dibismuth complex, the four Cp^* units form a square plane, whereas the dinitrogen complex has the four Cp^* units are arranged in a tetrahedron.

Table 17
Reactivity of $SmCp^*_2$ and $SmCp^*_2(THF)_2$ with MPh_3 ($M = P, As, Sb, Bi$)

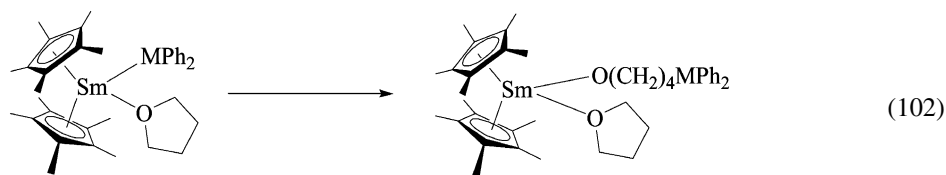
reductant	PPh_3	$AsPh_3$	$SbPh_3$	$BiPh_3$
$SmCp^*_2$	coordination	no rxn	M–C cleavage	M–C cleavage
$SmCp^*_2(THF)_2$	no rxn	no rxn	no rxn	M–C cleavage

Both SmCp^*_2 and $\text{SmCp}^*_2(\text{THF})_2$ were found to react with Ph_2MMPH_2 (where $\text{M} = \text{P}$ or As) to produce $\text{Cp}^*_2\text{Sm}(\text{MPh}_2)$ or $\text{Cp}^*_2\text{Sm}(\text{MPh}_2)(\text{THF})$ respectively (eqs. (100), (101)).



$\text{M} = \text{P}$ or As

The unsolvated species was found to be quite stable in solution while the THF solvated species was found to undergo ring opening of the coordinated THF resulting in a butoxide complex (eq. (102)). Ring opening of the THF solvate also occurred when

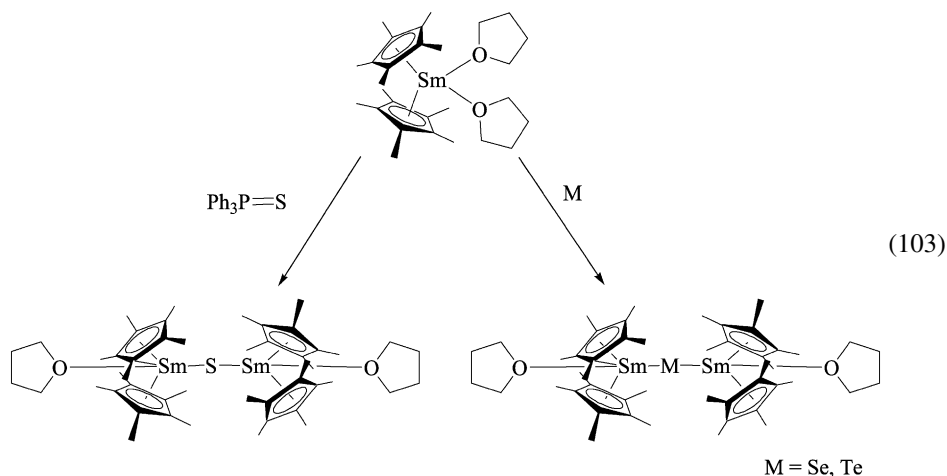


$\text{M} = \text{P}$ or As

$\text{Cp}^*_2\text{Sm}(\text{MPh}_2)(\text{THF})$ was heated under vacuum leading to the supposition that the rearrangement was the result of intramolecular nucleophilic attack on THF by the neighboring MPh_2 ligand.

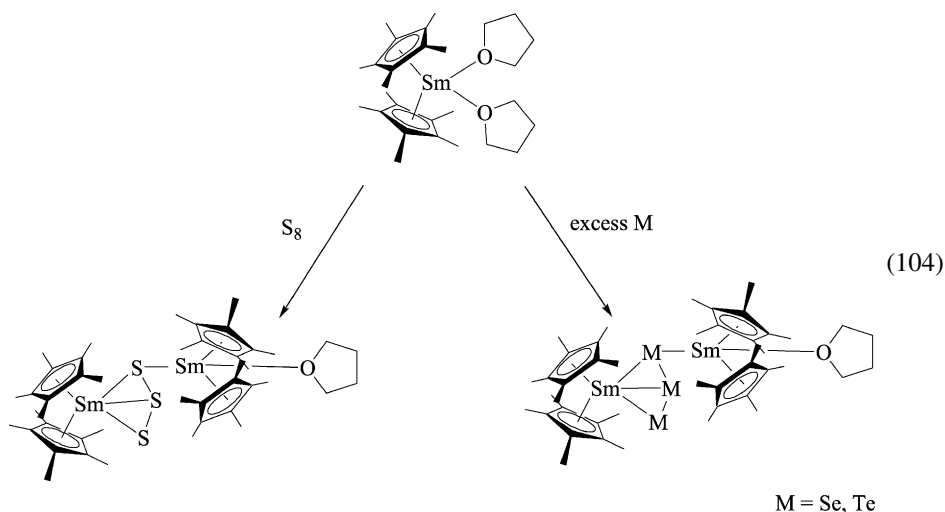
3.8. Reactions of $\text{Sm}(\text{Cp}^*)_2(\text{THF})_2$ with group 16 metals and organometallics

Reaction of $\text{Sm}(\text{Cp}^*)_2(\text{THF})_2$ with elemental Se and Te in a 2 : 1 ratio provides $[\text{Sm}(\text{Cp}^*)_2(\text{THF})_2(\mu\text{-Se})]$ and $[\text{Sm}(\text{Cp}^*)_2(\text{THF})_2(\mu\text{-Te})]$, respectively in a 65–85% yield whereas synthesis of $[\text{Sm}(\text{Cp}^*)_2(\text{THF})_2(\mu\text{-S})]$ occurs via reaction of $\text{Sm}(\text{Cp}^*)_2(\text{THF})_2$ with $\text{Ph}_3\text{P}=\text{S}$ (Evans et al., 1994) (eq. (103)). Characterization of the monochalcogenide complexes by NMR,



IR, and X-ray shows that the complexes are essentially isostructural. The ^1H NMR data for the complexes are nearly identical to that obtained for the oxygen analog $[\text{Sm}(\text{Cp}^*)_2(\text{THF})]_2(\mu\text{-O})$ suggesting similar bonding arrangements among the group 16 elements with Sm. One notable difference was that color of the complexes with the Te analog displaying a red color, the Se displaying an orange color and the S and O displaying a yellow color. Evans ascribed the red color to the possible presence of charge transfer between the Te and Sm metal center.

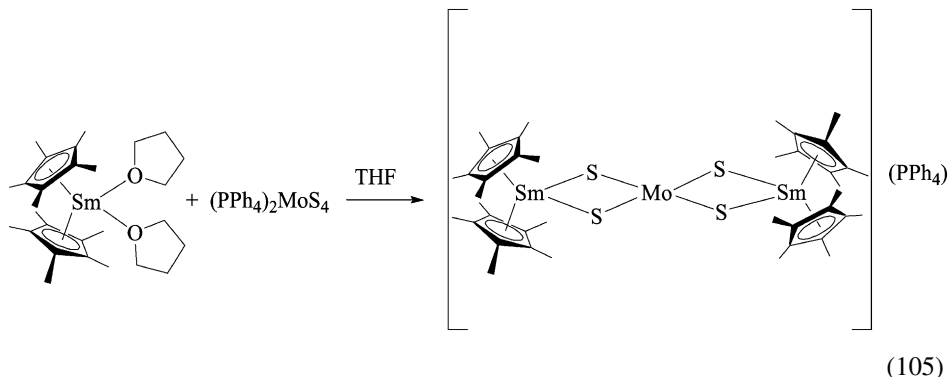
Altering the stoichiometry of the reactions changes the products. Reaction of $\text{Sm}(\text{Cp}^*)_2(\text{THF})_2$ with excess Se or Te in THF produced $[\text{Sm}(\text{Cp}^*)_2(\text{THF})]_2(\text{Se}_3)(\text{THF})$ and $[\text{Sm}(\text{Cp}^*)_2(\text{THF})]_2(\text{Te}_3)(\text{THF})$ respectively. Reaction of $\text{Sm}(\text{Cp}^*)_2(\text{THF})_2$ with S_8 in a 2 : 3 ratio was required to produce the analogous S_3 analog (eq. (104)). The Se_3 analog was



identified by X-ray crystallography as $[\text{Sm}(\text{Cp}^*)_2(\text{THF})_2(\mu\text{-}\eta^1\text{:}\eta^3\text{-Se}_3)(\text{THF})]$. Examination of the X-ray structure of the Se_3 analog was consistent with the asymmetry displayed in eq. (102) above. However, the solid-state asymmetry was not apparent in solution when the complexes were examined by ^1H and ^{13}C NMR.

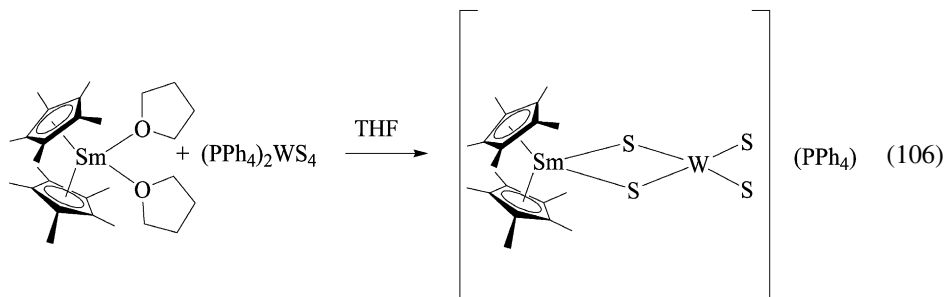
3.9. Reactions of $\text{Sm}(\text{Cp}^*)_2(\text{THF})_2$ with tetrathio-tungstate and -molybdate

Tetrathiometallates provide a bidentate ligand arrangement with the ability to lead to mixed metal species. Evans et al. (1995b) examined the reactivity of $\text{Sm}(\text{Cp}^*)_2(\text{THF})_2$ with $(\text{MoS}_4)^{2-}$ and $(\text{MWS}_4)^{2-}$ to study the reactivity of these ligands with $\text{Sm}(\text{II})$. Reaction of $\text{Sm}(\text{Cp}^*)_2(\text{THF})_2$ with $(\text{PPh}_4)_2\text{MoS}_4$ in THF provides $\{[(\text{Cp}^*)_2\text{Sm}]_2\text{Mo}(\mu\text{-S})_4\}(\text{PPh}_4)$ (eq. (105)). Solution NMR studies were consistent with the



presence of $\text{Sm}(\text{III})$ and a single Cp^* ligand environment. The presence of $(\text{PPh}_4)^+$ shows that reduction of the metal center of the tetrathiometallate occurs during the reaction producing an $\text{Mo}(\text{V})$ species.

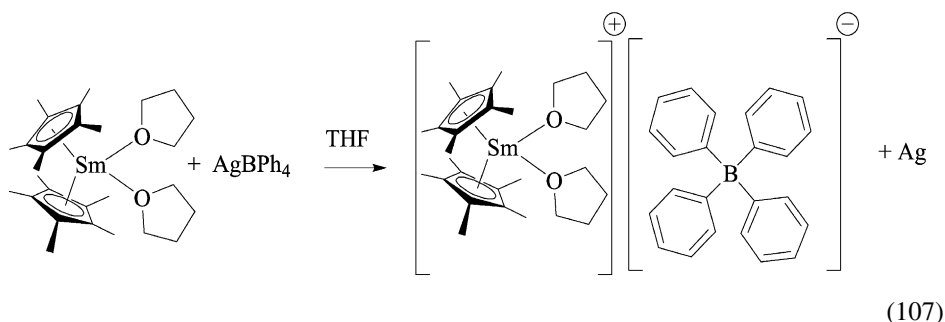
Surprisingly, reaction of $\text{Sm}(\text{Cp}^*)_2(\text{THF})_2$ with $(\text{PPh}_4)_2\text{WS}_4$ under the same conditions did not provide the analog shown in (105), but instead provided $[(\text{Cp}^*)_2\text{Sm}(\mu\text{-S}_2)\text{WS}_2](\text{PPh}_4)$ (eq. (106)). Another contrast between the Mo and W tetrathiometallate analogs



is the lack of reduction of the tungstate metal center. Clearly, the identity of the metal in tetrathiometallates controls their reactivity and product distributions in reactions with $\text{Sm}(\text{Cp}^*)_2(\text{THF})_2$.

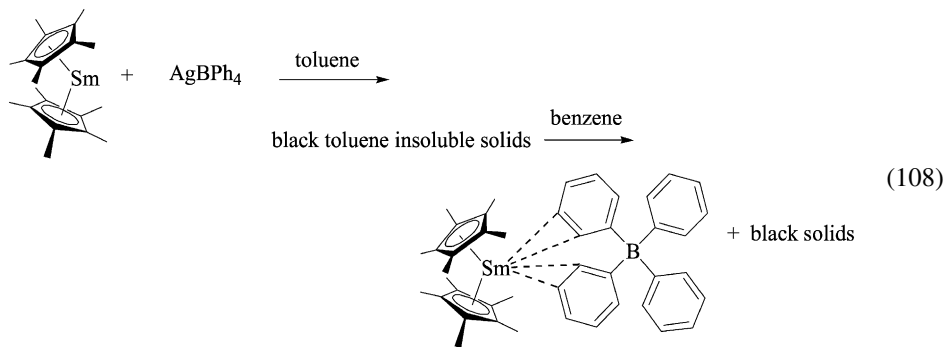
3.10. Reactions of $\text{Sm}(\text{Cp}^*)_2(\text{THF})_2$ and $\text{Sm}(\text{Cp}^*)_2$ with AgBPh_4

Oxidation of $\text{Sm}(\text{Cp}^*)_2(\text{THF})_2$ with AgBPh_4 in THF produced the samarocene cation (eq. (107)). While the samarocene cation is expected to be more reactive than the



divalent precursor, the enhanced electrophilicity of the oxophilic $\text{Sm}(\text{III})$ cation leads to tight coordination of the THF ligands making them difficult to displace even in refluxing pyridine. Although the THF solvate of the samarocene cation is relatively unreactive, its stability indicates that the unsolvated species should be quite reactive (Evans et al., 1990b).

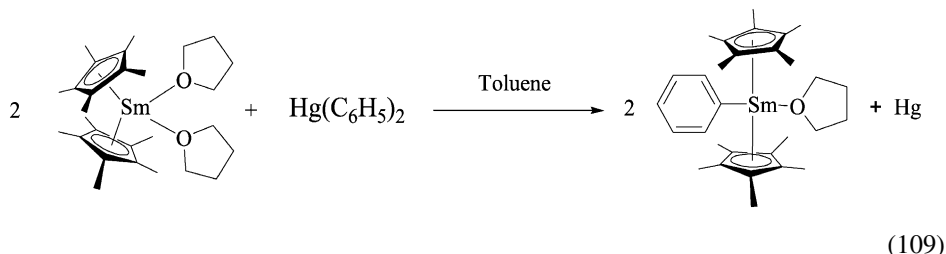
While initial attempts to produce the unsolvated species from $\text{Sm}(\text{Cp}^*)_2$ were unsuccessful, it was found that addition of $\text{Sm}(\text{Cp}^*)_2$ to AgBPh_4 in toluene and stirring over a 12 hour period produced black toluene insoluble solids that could be extracted with benzene to produce a crimson red solution which upon evaporation provided reasonable yields of (60–65%) of $[(\text{Cp}^*)_2\text{Sm}][\text{BPh}_4]$ (Evans et al., 1998c) (eq. (108)). The extreme electrophilicity



of the unsolvated samarocene necessitated rigorous exclusion of ligating solvents. While the reactivity of $[(\text{Cp}^*)_2\text{Sm}][\text{BPh}_4]$ is similar to $[(\text{Cp}^*)_2\text{Sm}(\text{THF})_2][\text{BPh}_4]$ in reactions with Na and $\text{LiCH}(\text{SiMe}_3)_2$, the unsolvated samarocene with KCp^* provides excellent yields of $\text{Sm}(\text{Cp}^*)_3$ thus providing the first access to sterically crowded $\text{Ln}(\text{Cp}^*)_3$ complexes not requiring a divalent precursor.

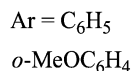
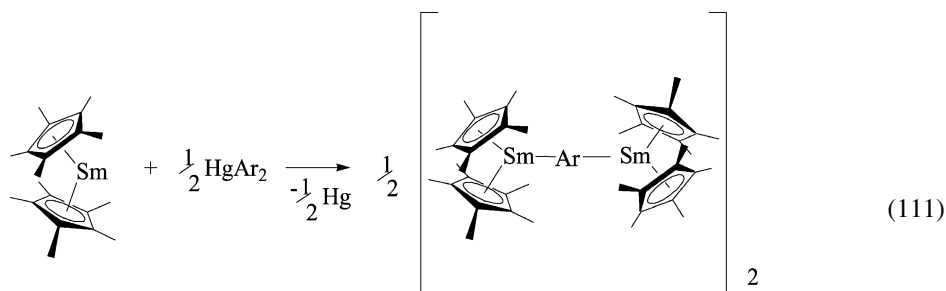
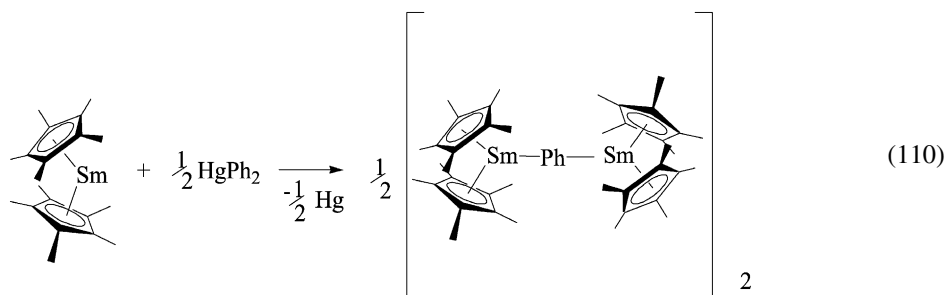
3.11. Reactions of $\text{Sm}(\text{Cp}^*)_2(\text{THF})_2$ and $\text{Sm}(\text{Cp}^*)_2$ with organomercury reagents

Addition of 1 equivalent of HgPh_2 to 2 equivalents of $\text{Sm}(\text{Cp}^*)_2(\text{THF})_2$ in toluene followed by evaporation of solvent produced $(\text{Cp}^*)_2\text{Sm}(\text{Ph})(\text{THF})$ and Hg providing (eq. (109))

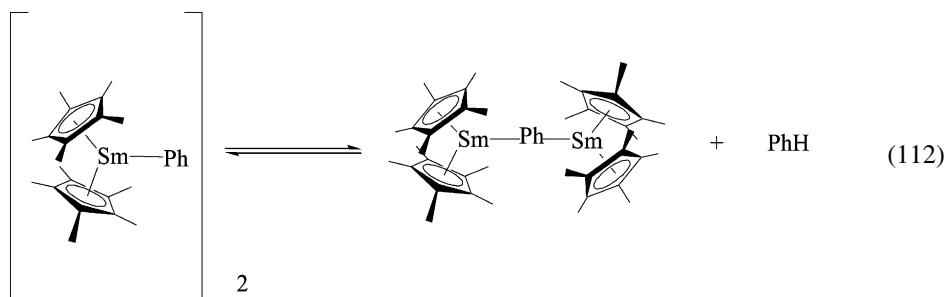


a halide free route to the synthesis of organosamarium(III) complexes containing $\text{Sm}-\text{C}$ bonds (Evans et al., 1985a). Crystallographic analysis of the product, $(\text{Cp}^*)_2\text{Sm}(\text{Ph})(\text{THF})$ shows that it has the typical bent metallocene structure.

More recently, Tilley (Castillo and Tilley, 2001), examined the reaction of $\text{Sm}(\text{Cp}^*)_2$ with diaryl mercury reagents in inert solvents (eqs. (110), (111)). The perfluorophenyl and *o*-methoxy containing $\text{Sm}(\text{III})$



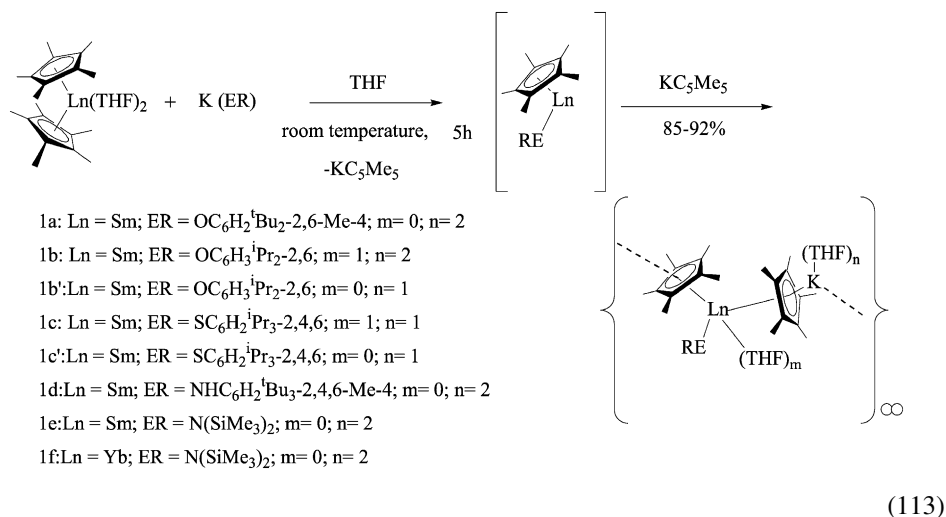
complexes are quite stable, whereas the phenyl containing dimer decomposed to provide the $(Cp^*)_2Sm(\mu-C_6H_4)SmCp^*_2$ complex and benzene (eq. (112)). Careful mechanistic studies



were found to be consistent with competing first and second order pathways suggesting that deaggregation of $[(Cp^*)_2SmPh]_2$ produces an equilibrium amount of monomeric $(Cp^*)_2SmPh$ that was more reactive to σ -bond metathesis leading to decomposition pathway responsible for the formation of $(Cp^*)_2Sm(\mu-C_6H_4)SmCp^*_2$.

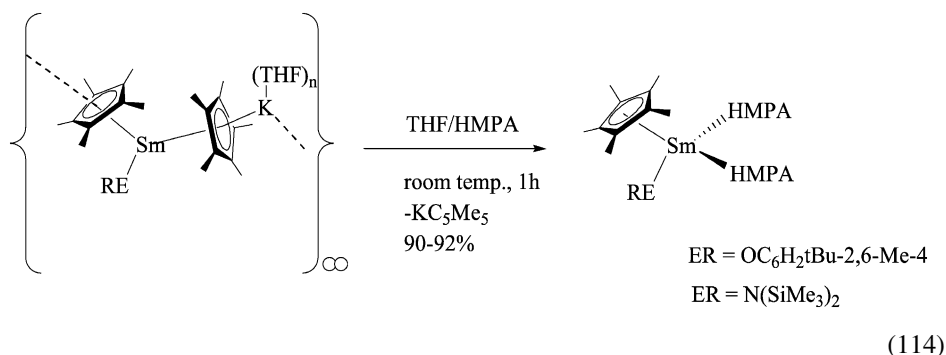
3.12. Reaction of $Sm(Cp^*)_2(THF)_2$ with monodentate anionic ligands

During studies designed to tune the steric environment of divalent Sm complexes, Hou et al. (2000) have shown that reaction of $Sm(Cp^*)_2(THF)_2$ with a series of monodentate anionic ligands (ER) bearing a negative charge on oxygen, sulfur, or nitrogen produced divalent heteroleptic complexes of the general structure $[(Cp^*)_2Sm(THF)_m(ER)(\mu-Cp^*)K(THF)_n]$ (eq. (113)). Surprisingly it was discovered that the $(Cp^*)K(THF)$ unit behaves



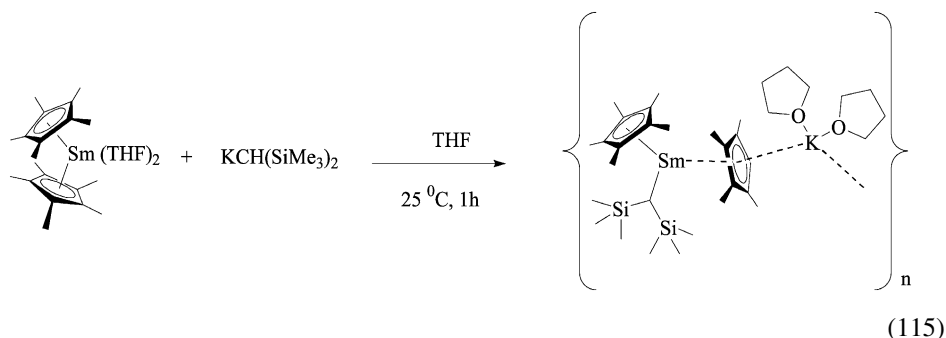
as a neutral coordination ligand with bonding to Sm occurring through the Cp^* moiety. While all structures were similar, the steric bulk of ER dictated the number of THF ligands

bound to the divalent Sm. Reaction of the polymeric complexes (where ER = OC₆H₂^tBu₂-2,6-Me-4 or N(SiMe₃)₂) with 2 equivalents of HMPA (per Sm) yielded the monomeric complex(Cp*)Sm(ER)(HMPA)₂ showing that the Cp*K ligand could be displaced (eq. (114)).

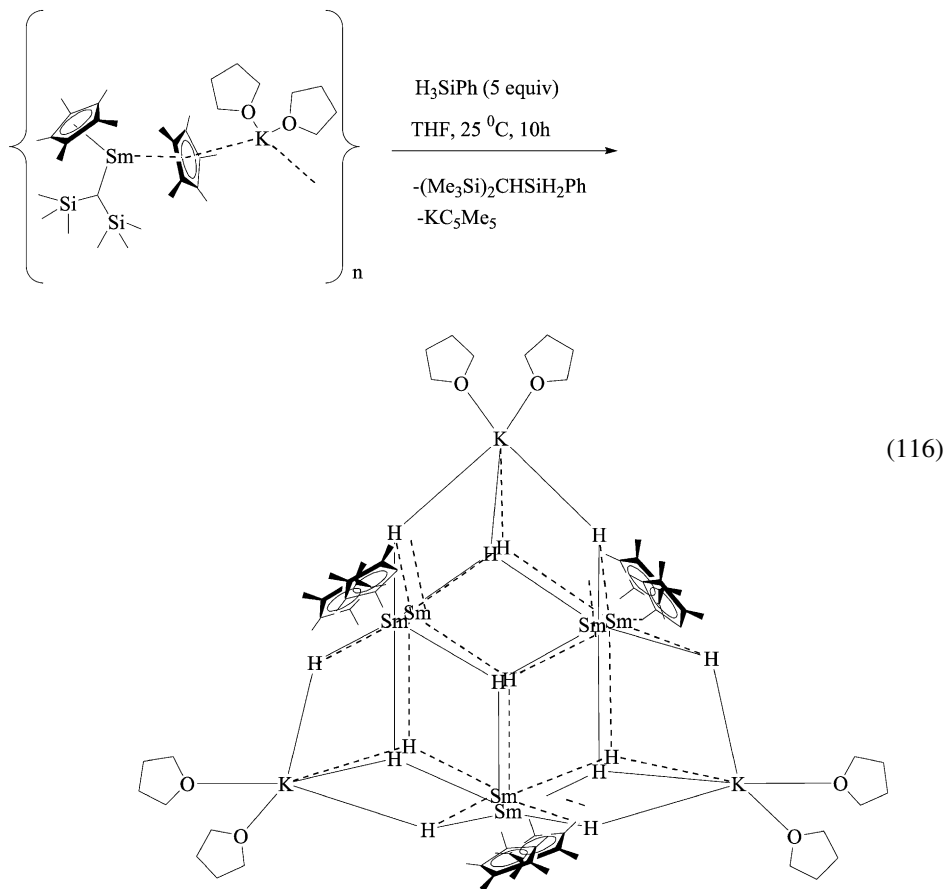


The polymeric Cp*/ER divalent Sm complexes were found to be effective as polymerization catalysts for ethylene and styrene. Mechanistic studies showed that the polymerization likely occurs through dissociation of the Cp*K ligand followed by reduction of the monomer by the Sm(II) complex. Another interesting feature of these reactions is the fact that the polymeric Sm complexes showed reactivity towards ethylene and styrene that was dependent upon the ER ligand. For instance when ER = SC₆H₂^tPr₃-2,4,6 the complex was found to be quite effective for the block copolymerization of styrene and ethylene whereas when ER = OC₆H₂^tBu₂-2,6-Me-4 or N(SiMe₃)₂, the complexes were more effective at polymerizing ethylene and styrene, respectively. These studies clearly showed that changing the ER ligand of the Sm(II) complex had a profound influence on stability and reactivity of these complexes, presumably through a combination of steric and electronic factors.

Follow up work by Hou et al. (2001) has shown that reaction of Sm(Cp*)₂(THF)₂ with KCH(SiMe₃)₂ in THF produces a polymeric structure similar to that obtained with ER ligands in previous studies where the (Cp*)K(THF)₂ moiety acts as a neutral stabilization ligand (eq. (115)). This complex reacts with H₃SiPH in THF at room



temperature to provide a polyhydrido Sm(III)K complex consisting of six $(Cp^*)_2SmH_2$ and three $KH(THF)_2$ units with a D_{3h} symmetry in an overall 42% yield (eq. (116)). This



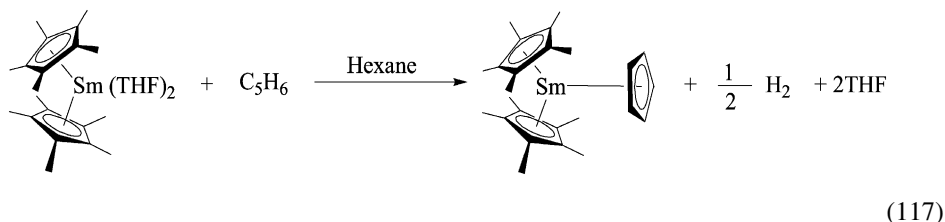
product represented the first example of a structurally characterized dihydrido lanthanide complex. As a result of this finding, the catalytic activity of $[(Cp^*)_2Sm(CH(SiMe_3)_2)(Cp^*)_K(THF)_2]_n$ was examined in hydrosilylation reactions of H_3SiPh and several types of olefins. In all cases good yield were obtained with as little as 2 mol% catalyst.

3.13. Reactions of $SmCp^*_2$ and $Sm(Cp^*)_2(THF)_2$ with alkenes, alkynes, and related unsaturated compounds

3.13.1. Reactions of $SmCp^*_2$ and $Sm(Cp^*)_2(THF)_2$ with cyclopentadiene

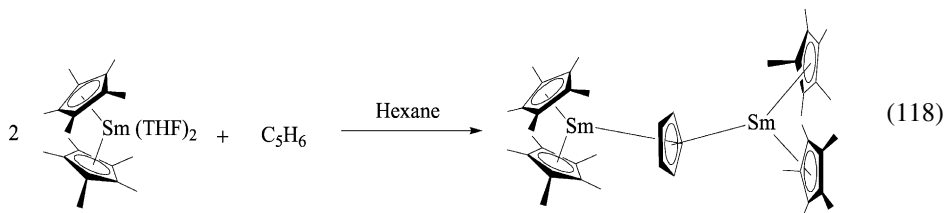
During early studies on the reactivity of $Sm(Cp^*)_2(THF)_2$ and $SmCp^*_2$, with organic substrates, Evans and Ulibarri (1987c) found that addition of a slight stoichiometric excess

of freshly cracked cyclopentadiene to a slurry of $\text{Sm}(\text{Cp}^*)_2(\text{THF})_2$ in hexane produced $\text{Sm}(\text{Cp}^*)_2(\text{Cp})$ in a nearly quantitative (98%) yield (eq. (117)). Not surprisingly, the same



reaction utilizing SmCp^*_2 also produced $\text{Sm}(\text{Cp}^*)_2(\text{Cp})$ albeit at a faster rate. This protocol provided a more efficient route to $\text{Sm}(\text{Cp}^*)_2(\text{Cp})$ which previously had been synthesized by the reaction of $\text{Sm}(\text{Cp}^*)_2\text{Cl}$ compounds with sodium cyclopentadienide (Evans et al., 1986c).

In ancillary studies it was discovered that reaction of SmCp^*_2 with a half molar equivalent amount of cyclopentadiene in hexane produced the mixed valent $(\text{Cp}^*)_2\text{Sm}^{\text{III}}(\mu\text{-Cp})\text{Sm}^{\text{II}}(\text{Cp}^*)_2$ (eq. (118)). Success in isolation of this complex was dependent

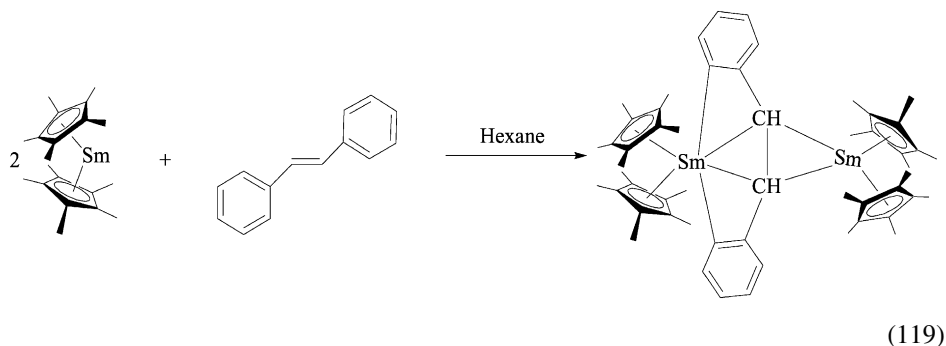


on a number of factors including concentration and crystallization procedures. Typically recrystallization in hexane by slow concentration at 30 °C provided good yields of $(\text{Cp}^*)_2\text{Sm}^{\text{III}}(\mu\text{-Cp})\text{Sm}^{\text{II}}(\text{Cp}^*)_2$. Dissolution of the complex in THF dissociated it into $\text{Sm}(\text{Cp}^*)_2(\text{THF})_2$ and $\text{Sm}(\text{Cp}^*)_2(\text{Cp})$.

3.13.2. Reactions of SmCp^*_2 and $\text{Sm}(\text{Cp}^*)_2(\text{THF})_2$ with aryl-substituted alkenes

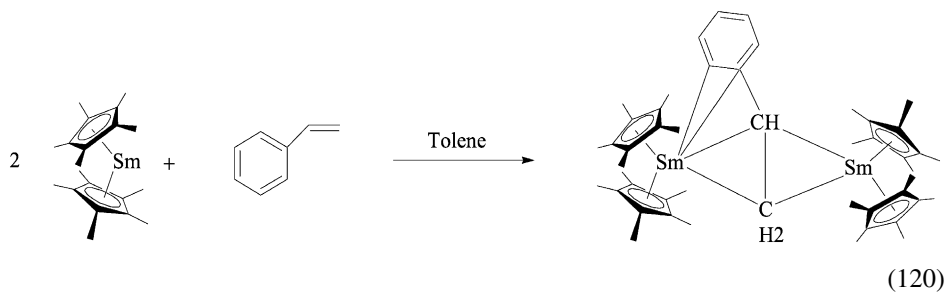
Both $\text{Sm}(\text{Cp}^*)_2(\text{THF})_2$ and SmCp^*_2 were subjected to reaction with *cis*-stilbene to study the interaction of unsaturated hydrocarbons with these metallocene complexes. Reactions of substoichiometric amounts of $\text{Sm}(\text{Cp}^*)_2(\text{THF})_2$ were exposed to *cis*-stilbene in benzene- d_6 . Surprisingly, the solution maintained the color of the Sm(II) complex. Examination of the solution by NMR showed peaks consistent with $\text{Sm}(\text{Cp}^*)_2(\text{THF})_2$ and free *cis*- and *trans*-stilbene indicating that no complex was formed (Evans et al., 1990c). Complete conversion to the thermodynamically more stable *trans*-stilbene occurred over a two hour period. Although reductive isomerization of stilbene is well-known, this was the first case where the reaction had been carried out with an f-element. Since the Sm-THF solvate worked effectively, the more highly electrophilic solvent free SmCp^*_2 was subjected to similar conditions and found to be more reactive converting approximately 70 equivalents of *cis*-stilbene to *trans*-stilbene in 5 minutes. To obtain more information on the nature of the reactive intermediate in the process, SmCp^*_2 was reacted with *cis*-stilbene in hexane. A complex was isolated that was consistent

with the formation of $[\text{SmCp}^*_2]_2(\text{PhCHCHPh})$ (eq. (119)). While high quality crystal data could not be obtained,



the data was of sufficient quality to verify the connectivity of the atoms. Reaction of $[\text{SmCp}^*_2]_2(\text{PhCHCHPh})$ with THF led to dissociation of the complex and formation of $\text{Sm}(\text{Cp}^*)_2(\text{THF})_2$ and *trans*-stilbene.

To further study the reaction, SmCp^*_2 was reacted with styrene in toluene. Extraction with hexane produced $[\text{SmCp}^*_2]_2(\mu\text{-}\eta^2\text{:}\eta^4\text{-CH}_2\text{CHPh})$ in excellent yield (eq. (120)).

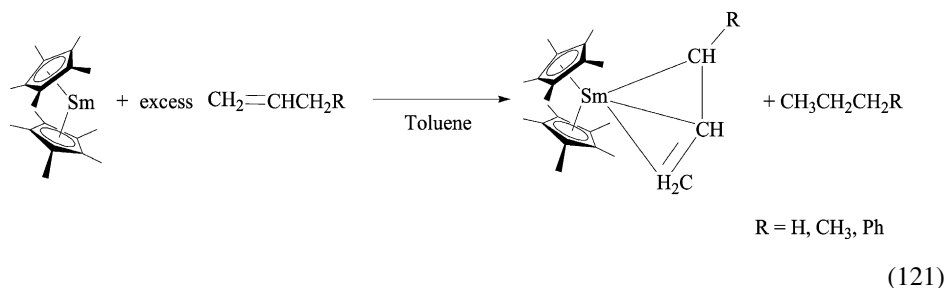


Similar to the previous example, reaction of THF with $[\text{SmCp}^*_2]_2(\mu\text{-}\eta^2\text{:}\eta^4\text{-CH}_2\text{CHPh})$ produced $\text{Sm}(\text{Cp}^*)_2(\text{THF})_2$ and styrene. Analysis by X-ray crystallography showed that the phenyl ring of the styrene was distorted towards one of the Sm centers in the complex. The results of this work clearly showed that lanthanides could have relatively strong interactions with unsaturated hydrocarbons.

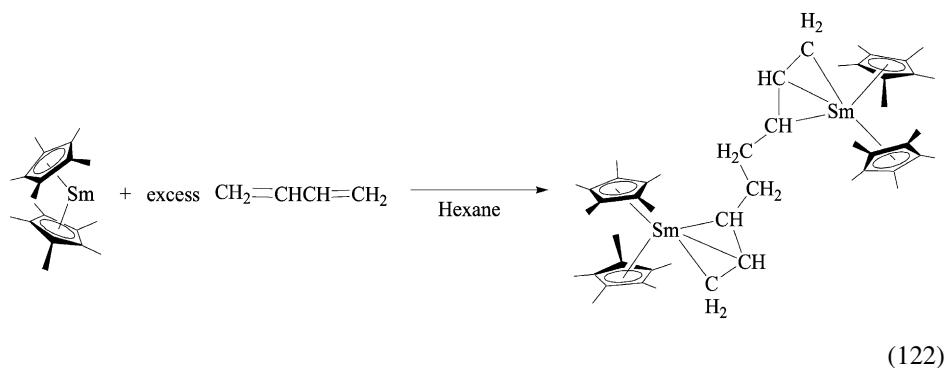
3.13.3. Reactions of SmCp^*_2 and $\text{Sm}(\text{Cp}^*)_2(\text{THF})_2$ with short chain alkenes and dienes

In further studies comparing the reactivity of SmCp^*_2 and $\text{Sm}(\text{Cp}^*)_2(\text{THF})_2$ with alkenes both complexes were subjected to reaction with ethene, propene, *cis*- and *trans*-2-butene, and allylbenzene (Evans et al., 1990d). Both reductants polymerize ethene to give polyethylene.

Reaction of SmCp^*_2 with propene, 2-butene, and allylbenzene in toluene provides allyl type complexes in high yields with alkanes as byproducts (eq. (121)).

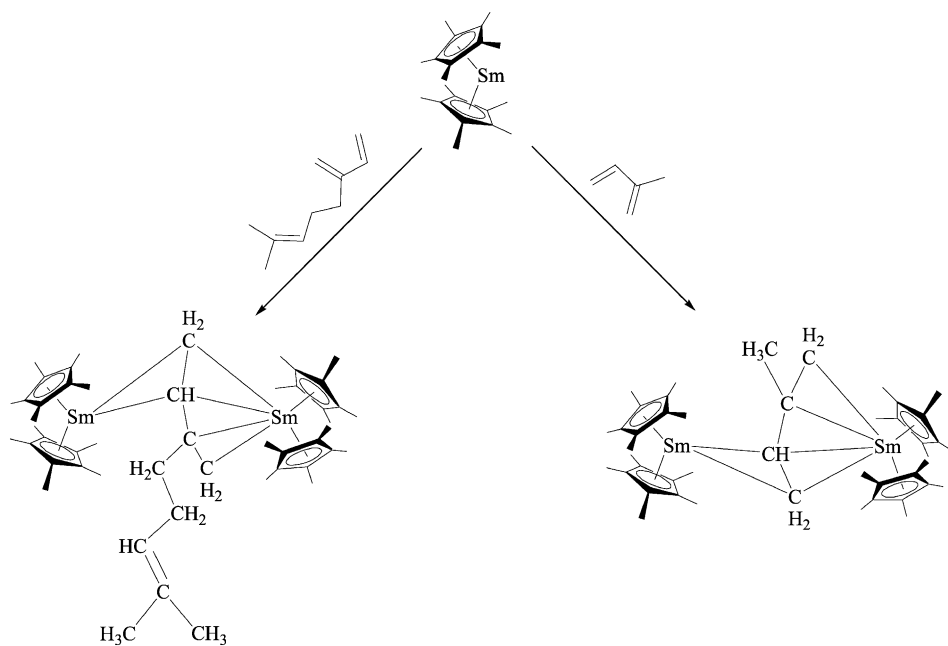


While $\text{Sm}(\text{Cp}^*)_2(\text{THF})_2$ reacts with allylbenzene to produce the corresponding allyl complex under similar conditions, it does not react with propene and forms complex mixtures with butene. In studies of reactions of the reductants with dienes, both were found to react with the conjugated 1,3-butadiene to form bis-allyl complexes resulting from dimerization of the diene (eq. (122)) but only SmCp^*_2 reacted with the non-conjugated 1,5-hexadiene to form a bis-allyl complex. The difference in reactivity of the



complexes with alkenes and dienes is likely due to a combination of factors including the increased electrophilicity of SmCp^*_2 compared to the THF solvate and the ability of the alkene substrate to displace THF from $\text{Sm}(\text{Cp}^*)_2(\text{THF})_2$. Clearly, this work demonstrates that coordinating solvents (such as THF), can potentially play an important role in moderating the reactivity of $\text{Sm}(\text{II})$ -based reductants.

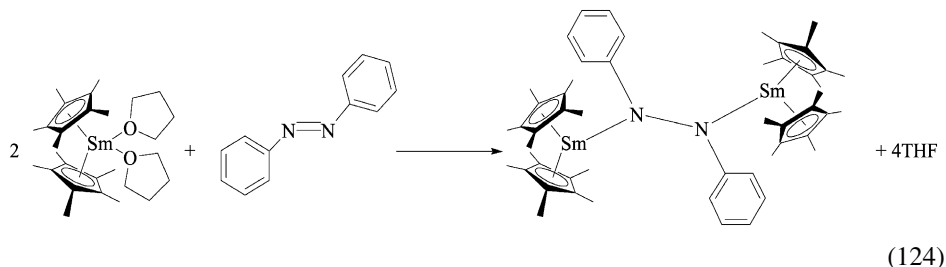
To further examine the interaction of SmCp^*_2 with more highly substituted dienes, reactions of the unsolvated reductant with isoprene and myrcene were examined (Evans et al., 2001). Addition of isoprene or myrcene to a toluene solution of SmCp^*_2 at -36°C generated single products whose crystal structures were consistent with $[(\text{Cp}^*)_2\text{Sm}]_2[\mu-\eta^2:\eta^4\text{-CH}_2\text{CHC}(\text{CH}_3)\text{CH}_2]$ and $[(\text{Cp}^*)_2\text{Sm}]_2[\mu-\eta^2:\eta^4\text{-CH}_2\text{CHC}(\text{CH}_2)\text{-CH}_2\text{CH}_2\text{CHC}(\text{CH}_3)_2]$ respectively (eq. (123)). Attempts to run the reactions at room



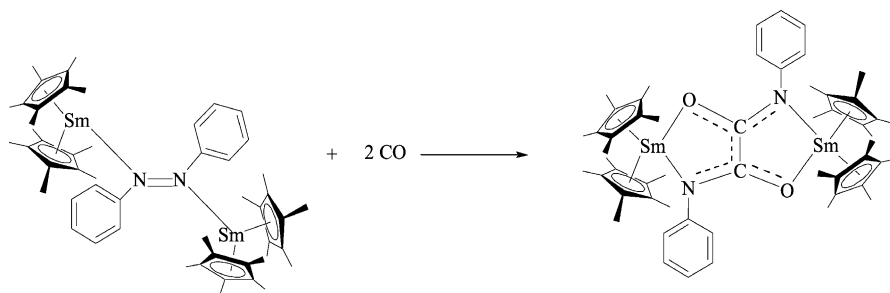
temperature failed and led to complex mixtures of products. Reaction of both these products with THF regenerated the diene starting materials and $\text{Sm}(\text{Cp}^*)_2(\text{THF})_2$ in a fashion analogous to that observed for the $\text{Sm}(\text{Cp}^*)_2$ -styrene complex. Surprisingly, substitution of the diene hinders dimerization compared to the unsubstituted butadiene showing that small structural changes in conjugated diene substrates can have a relatively large impact on reactions with $\text{Sm}(\text{Cp}^*)_2$.

3.13.4. Reactions of $\text{Sm}(\text{Cp}^*)_2(\text{THF})_2$ with heteroatom containing double bonds unsaturated heterocycles

In early studies designed to explore the chemistry of samarium pentamethylcyclopentadienide complexes, azobenzene was added to two equivalents of $\text{Sm}(\text{Cp}^*)_2(\text{THF})_2$ in toluene. After reaction for six hours, $[(\text{Cp}^*)_2\text{Sm}]_2\text{N}_2(\text{C}_6\text{H}_5)_2$ was isolated in a 90% yield (124) (Evans et al., 1986b). Examination of the crystal structure

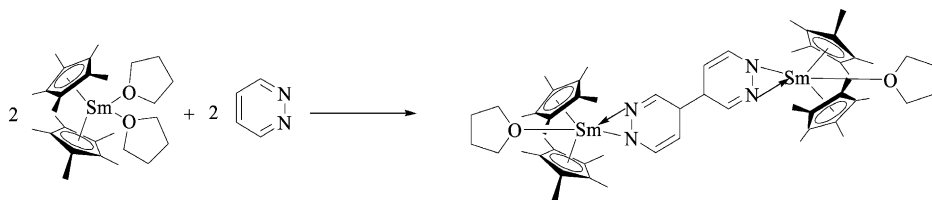


showed that azobenzene was reduced and THF was displaced from Sm by the lone pairs of the resulting azo dianion. Another interesting feature of the product complex was the asymmetry of the phenyl rings. In the complex one of the phenyl rings was distorted towards both $\text{Sm}(\text{Cp}^*)_2$ units placing the ortho hydrogens within the distance expected for a bridging Sm-H bond. This suggests that $[(\text{Cp}^*)_2\text{Sm}]_2\text{N}_2(\text{C}_6\text{H}_5)_2$ should be quite reactive and in follow up studies, 2 equivalents of carbon monoxide were found to insert into the N-N of the complex (eq. (125)) (Evans and Drummond, 1986a).



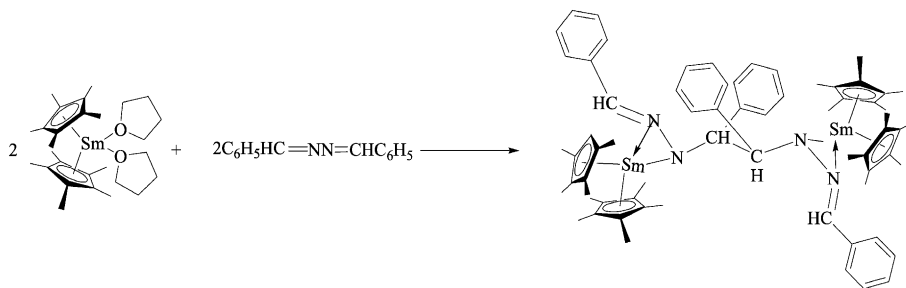
(125)

Many of the reactions of SmCp^*_2 and $\text{Sm}(\text{Cp}^*)_2(\text{THF})_2$ with olefins and other unsaturated substrates had no precedents in organometallic chemistry indicating that these reductants could reduce unsaturated systems in nonstandard ways. To explore this issue further, Evans (Evans and Drummond, 1989) examined reactions of $\text{Sm}(\text{Cp}^*)_2(\text{THF})_2$ pyridazine and benzaldehyde azine. Addition of 1 equivalent of pyridazine to a solution of $\text{Sm}(\text{Cp}^*)_2(\text{THF})_2$ in toluene produces $[(\text{Cp}^*)_2(\text{THF})\text{Sm}]_2[\mu, \eta^4\text{-(pyraz)}_2]$ in a 98% yield (eq. (126)). The reduction leading to coupling of the pyridazine



(126)

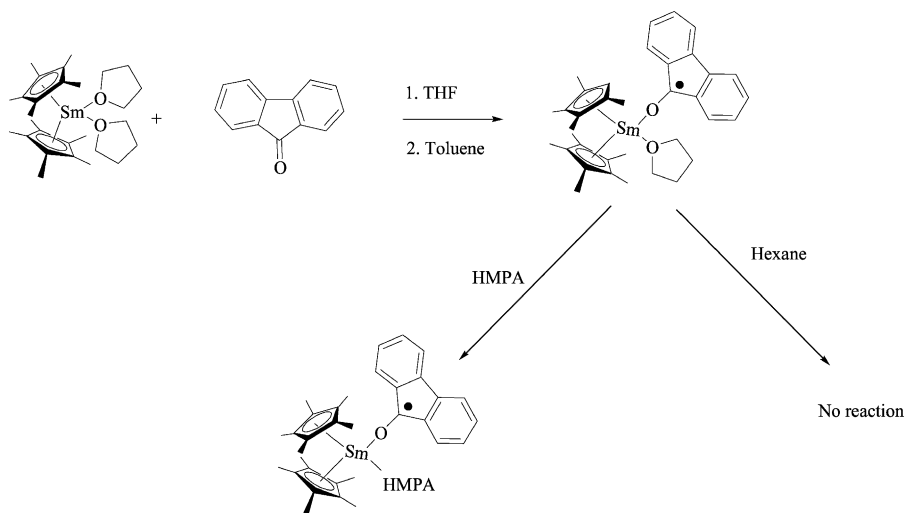
likely proceeds through radical intermediates. The $\text{Sm}(\text{Cp}^*)_2$ moiety coordinates to the adjacent nitrogens in the ring and crystallographic data is consistent with reduction of the $\text{N}=\text{N}$ double bond to a single bond. Similarly, reaction of equimolar amounts of benzaldehyde azine with $\text{Sm}(\text{Cp}^*)_2(\text{THF})_2$ in toluene lead to a bimetallic complex resulting from dimerization of the azine (eq. (127)). The dimerization occurred through the benzylic carbon of the azine moiety and the SmCp^*_2 unit is coordinated to adjacent



(127)

nitrogen atoms. Presumably, reduction of the carbon nitrogen double bond leads to a radical anion. Coordination of the cationic SmCp^*_2 to the nitranion coupled with the stability of the benzylic-like radical likely provides a sufficiently high concentration of the intermediate leading to homocoupling. Similar homocoupling processes are well-known in SmI_2 chemistry (Evans and Drummond, 1989).

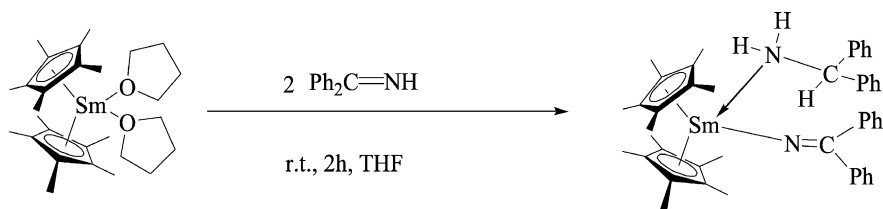
The reduction of ketones with Sm(II) reductants to ketyls constitutes the first step in a number of important reactions including reductions, pinacol couplings and ketyl-olefin couplings. In spite of this, little was known about the nature of the intermediates in these reactions. To study these systems in detail, Hou et al. exposed $\text{Sm(Cp}^*_2\text{)(THF)}_2$ in THF to an equimolar amount of fluorenone in an attempt to isolate the ketyl intermediate (Hou et al., 1998). Evaporation of the solvent provided a crystalline product that was dissolved in toluene, which after concentration of the solvent produced $(\text{Cp}^*)_2\text{Sm}(\text{biphenyl-2,2'-diyl ketyl})(\text{THF})$ in an overall 87% yield (eq. (128)).



(128)

The product ketyl had a pseudotetrahedral geometry. While addition of hexane did not cause any further reaction, addition of HMPA, displaced the THF producing the sterically encumbered $(Cp^*)_2Sm(\text{biphenyl-2,2'-diyl ketyl})(\text{HMPA})$. Comparisons of the reactivity of $SmCp^*_2$ complexes with styrene, isoprene and myrcene show some major differences from the present case. Addition of the electron donor solvent THF leads to dissolution of the $SmCp^*_2$ -alkene complexes into starting material but surprisingly even the strong donor ligand HMPA is incapable of disrupting the $SmCp^*_2$ -ketyl complex suggesting that the latter is a relatively stable complex under inert atmosphere conditions.

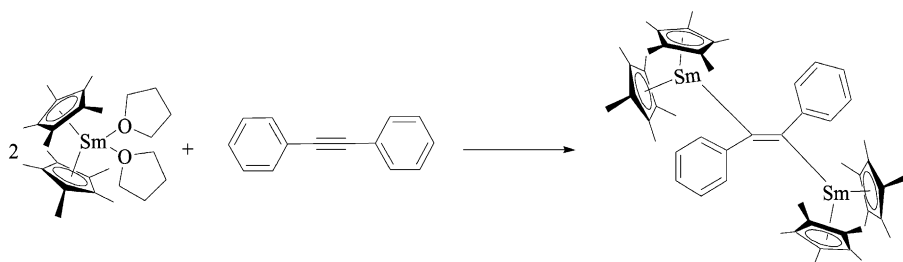
In related studies, Hou et al. examined the reduction of benzophenone imine ($Ph_2C=NH$) in an attempt to isolate the corresponding lanthanide imine radical anion species (Hou et al., 2003). Reaction of 1 equivalent of benzophenone imine with $Sm(Cp^*)_2(THF)_2$ in THF provided a 20% yield of the complex $(Cp^*)_2Sm(N=CPh_2)(NH_2CHPh_2)$ (eq. (129)). Addition of 2 equivalents of the benzophenone imine increased the yield of the resulting complex to 58%. Examination of the complex by 1H NMR and X-ray crystallography confirmed the structure of the complex. Mechanistic studies with THF- d_8 were consistent with hydrogen atom abstraction from THF and intramolecular hydrogen atom transfer from the N-H of the amine of the initially formed iminyl radical occurred resulting in the inability to isolate the intermediate iminyl radical.



(129)

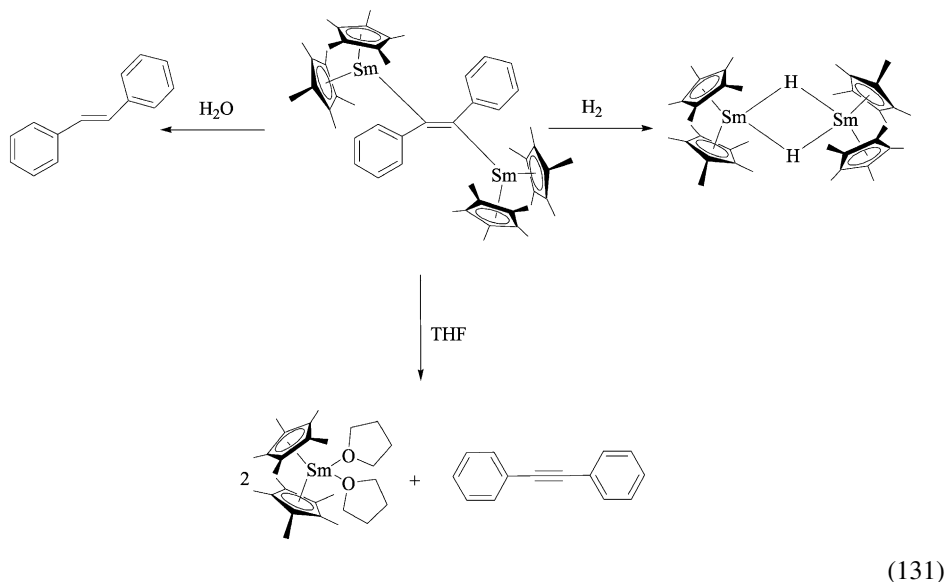
3.13.5. Reactions of $Sm(Cp^*)_2(THF)_2$ with triple bonds

Combination of equimolar amounts of $Sm(Cp^*)_2(THF)_2$ and diphenylacetylene in pentane produces a black solution which upon removal of solvent provides a glassy material (Evans et al., 1983). Elemental analysis and 1H NMR and IR spectra were found to be consistent with the enediyl structure $[(Cp^*)_2Sm](C_6H_5)C=C(C_6H_5)[Sm(Cp^*)_2]$ (eq. (130)). The steric bulk of the $SmCp^*_2$ unit likely dictates a *trans*-configuration around the



(130)

double bond. Interestingly, the product reacts with THF to produce starting materials while hydrolysis produces *trans*-stilbene. Reaction of $[(Cp^*)_2Sm](C_6H_5)C=C(C_6H_5)[Sm(Cp^*)_2]$ with H_2 produces $[(Cp^*)_2SmH]_2$ (eq. (131)). This product has been found to be a useful catalysts for a number of important



hydrogenations, polymerizations, and bond-forming reactions (Radu et al., 1996).

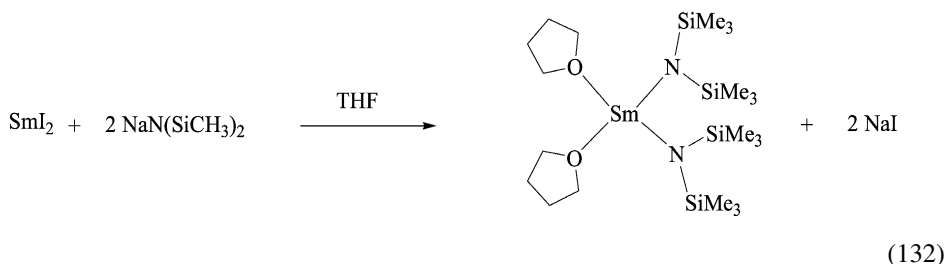
4. Sm(II) alkoxide and amide reductants

Cyclopentadienyl (Cp and Cp*) ligands have played a crucial role in organolanthanide chemistry because they provide the steric bulk necessary to prevent aggregation and are lipophilic enough to produce complexes that are soluble in organic solvents. While these ligands have played an important role in the development of Sm(II) chemistry, monoanionic nitrogen and oxygen based ligands have also been explored. Among nitrogen based ligands, the *bis*-(trimethylsilyl)amide ligand has been the most exploited nitrane as a ligand to promote monomeric Sm(II) reductants that have been utilized in a number of organic and inorganic reactions. Among alkoxides, the 2,6-di-*t*-butyl-4-methylphenoxide ligand provides the steric and electronic requirements necessary to form stable Sm(II) complexes although these reductants have been less utilized in synthesis. The synthesis of these alkoxide and amide complexes and their reactions will be discussed in this section.

4.1. Synthesis of $[(Me_3Si)_2N]_2Sm(THF)_2$ and $[Sm(OC_6H_2-2,6-di-*t*-butyl-4-methyl)_2(THF)_3]$

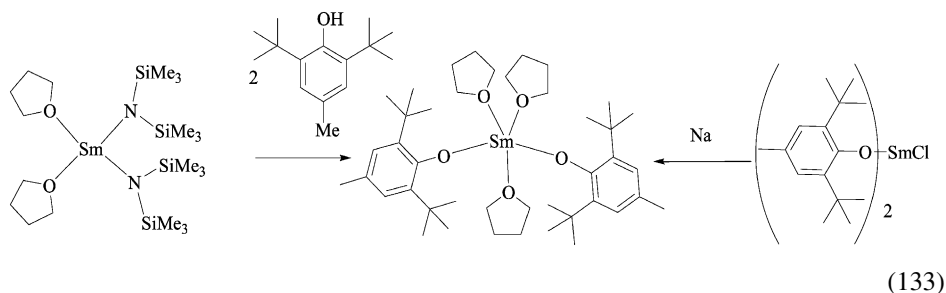
The synthesis of $[(Me_3Si)_2N]_2Sm(THF)_2$ was first described by Evans and coworkers in 1988 (Evans et al., 1988b) and was carried out by the addition of two equivalents of sodium

bis(trimethylsilyl)amide with one equivalent of SmI_2 in THF (eq. (132)). Rotary evaporation of the solvent followed dissolution in hexane precipitated NaI. Concentration of the hexane solution at -34°C provided crystals suitable for X-ray analysis. Inspection of the crystal structure of $[(\text{Me}_3\text{Si})_2\text{N}]_2\text{Sm}(\text{THF})_2$ reveals some interesting features and differences from those published for $[\text{SmI}_2(\text{THF})_5]$ (Evans et al., 1995c), $[\text{SmI}_2\text{HMPA}_4]$ (Hou and Wakatsuki, 1994), and $[\text{Sm}(\text{HMPA})_6]\text{I}_2$ (Hou et al., 1997).



In particular, the two nitrogen donor atoms from the hexamethyldisilazide ligands and the two oxygen donor atoms (from THF) form a pseudo tetrahedral geometry around the samarium atom. Furthermore, one methyl on each of the silicon atoms is oriented towards the samarium atom as well and each of the Sm–C bond distances for the distorted methyl group is smaller than the sum of their van der Waals radii. The bent structure of this molecule is more reminiscent of SmCp^*_2 than SmI_2 and its associated HMPA complexes. The uncharacteristic bent shape of $[(\text{Me}_3\text{Si})_2\text{N}]_2\text{Sm}(\text{THF})_2$ provides an increased probability for interaction between the metal center and organic substrates assuming THF is easily displaced during the course of the reaction. Furthermore, similar to SmCp^*_2 , the $[(\text{Me}_3\text{Si})_2\text{N}]_2\text{Sm}(\text{THF})_2$ complex is soluble in a range of solvents from THF to hexane.

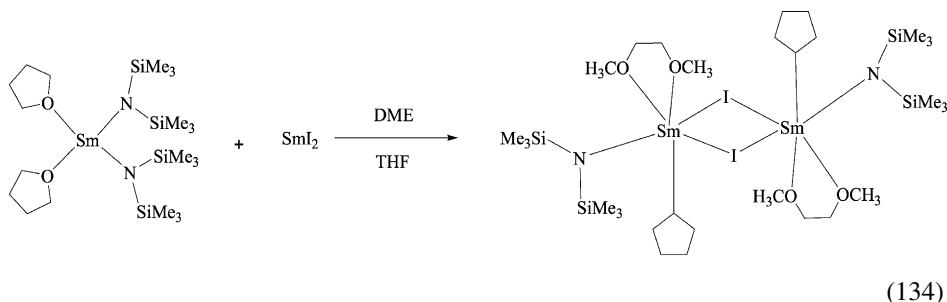
The synthesis and the crystal structure of $[\text{Sm}(\text{OC}_6\text{H}_2\text{-2,6-di-}^i\text{butyl-4-methyl})_2(\text{THF})_3]$ was reported by Shen and coworkers in 1994 (Qi et al., 1994) with an alternative synthesis published by Hou and coworkers in 1995 (Hou et al., 1995). The first preparation was carried out by reducing a Sm(III)monochloride precursor with sodium metal in THF whereas the latter synthesis was carried out by adding two equivalents of the conjugate acid of the phenoxide to $[(\text{Me}_3\text{Si})_2\text{N}]_2\text{Sm}(\text{THF})_2$ (eq. (133)).



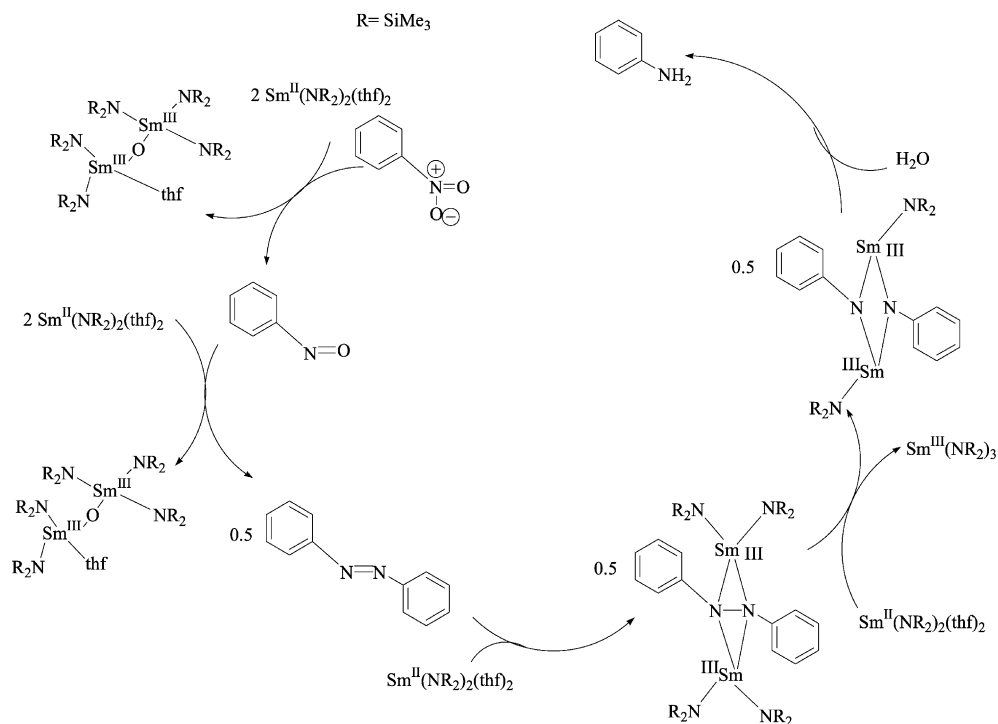
In both instances, high yields of product were obtained. The crystal structure of $[\text{Sm}(\text{OC}_6\text{H}_2\text{-}2,6\text{-di-}i\text{-butyl-4-methyl})_2(\text{THF})_3]$ shows the complex is a distorted trigonal bipyramid. The O–Sm–O bond angle for the two phenoxide ligands is 156.7° exhibiting the bent structure similar to that in samarium Cp, Cp*, and hexamethyldisilazide ligands.

4.2. Reactions of $[(\text{Me}_3\text{Si})_2\text{N}]_2\text{Sm}(\text{THF})_2$

The seminal report of Evans on the THF solvate of $[\text{Sm}\{\text{N}(\text{SiMe}_3)_2\}_2]$ also describes the structure and synthesis of $\{[(\text{Me}_3\text{Si})_2\text{N}]\text{Sm}(\mu\text{-I})(\text{DME})(\text{THF})_2\}_2$ (Evans et al., 1988b). The synthesis of this complex was carried out by the combination of an equivalent amount of $\text{SmI}_2(\text{THF})_2$ and $[\text{Sm}\{\text{N}(\text{SiMe}_3)_2\}_2]$ in THF/DME followed by removal of solvent (eq. (134)). More recent studies on the solution chemistry of $[(\text{Me}_3\text{Si})_2\text{N}]_2\text{Sm}(\text{THF})_2$ have shown that although the mixed complex is clearly stable in the solid state, analysis of UV–vis spectra were consistent with SmI_2 and $[\text{Sm}\{\text{N}(\text{SiMe}_3)_2\}_2]$, exclusively in solution. No evidence was observed in THF for the mixed Sm(II) species (Prasad et al., 2002b).



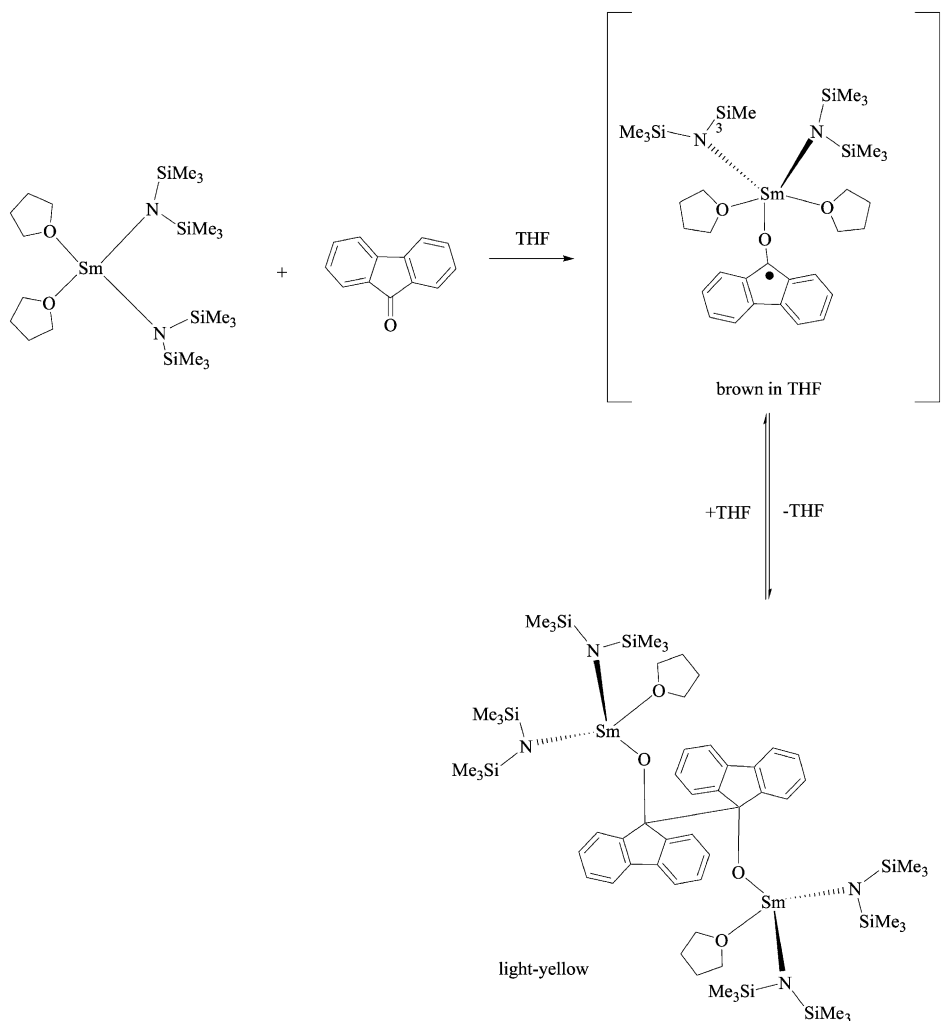
A great deal of the reaction chemistry of $[(\text{Me}_3\text{Si})_2\text{N}]_2\text{Sm}(\text{THF})_2$ has been used as a conduit to understand the mechanistic nuances of SmI_2 and related Sm(II) chemistry. This Sm(II) species is not as reactive as SmCp^*_2 . Furthermore, the increased lipophilicity of $\text{N}(\text{Me}_3\text{Si})_2$ enables the chemistry of Sm(II) to be studied in non-complexing solvents and also provides ^1H NMR signatures not possible with SmI_2 allowing the delineation of various reaction intermediates in solution. One case where these attributes are important is the Sm(II) mediated reduction of nitro groups to amines. Since there are a number of possible intermediates in the conversion that can be isolated and characterized, Keogh and coworkers utilized ^1H NMR and X-ray crystallography to study each of the intermediates in the reduction at each key step of the reaction to elucidate the mechanism of this important conversion shown in scheme 9 below (Brady et al., 2002). Under anhydrous conditions, treatment of nitrobenzene with 6 equivalents of $[(\text{Me}_3\text{Si})_2\text{N}]_2\text{Sm}(\text{THF})_2$ in toluene allowed for the isolation of aniline. Reducing the number of equivalents of Sm(II) to two allowed for the isolation of nitrosobenzene and the oxo-bridged dimer $\{[\text{Sm}\{\text{N}(\text{SiMe}_3)_2\}_2(\text{THF})_2\}_2(\mu_2\text{-O})$. Reaction of the intermediate nitrosobenzene with 2 equivalents of $[(\text{Me}_3\text{Si})_2\text{N}]_2\text{Sm}(\text{THF})_2$, again provided the oxo-bridged dimer and a half equivalent of azobenzene. Reduction



Scheme 9. Intermediates in the reduction of nitrobenzene by $[(\text{Me}_3\text{Si})_2\text{N}]_2\text{Sm}(\text{THF})_2$.

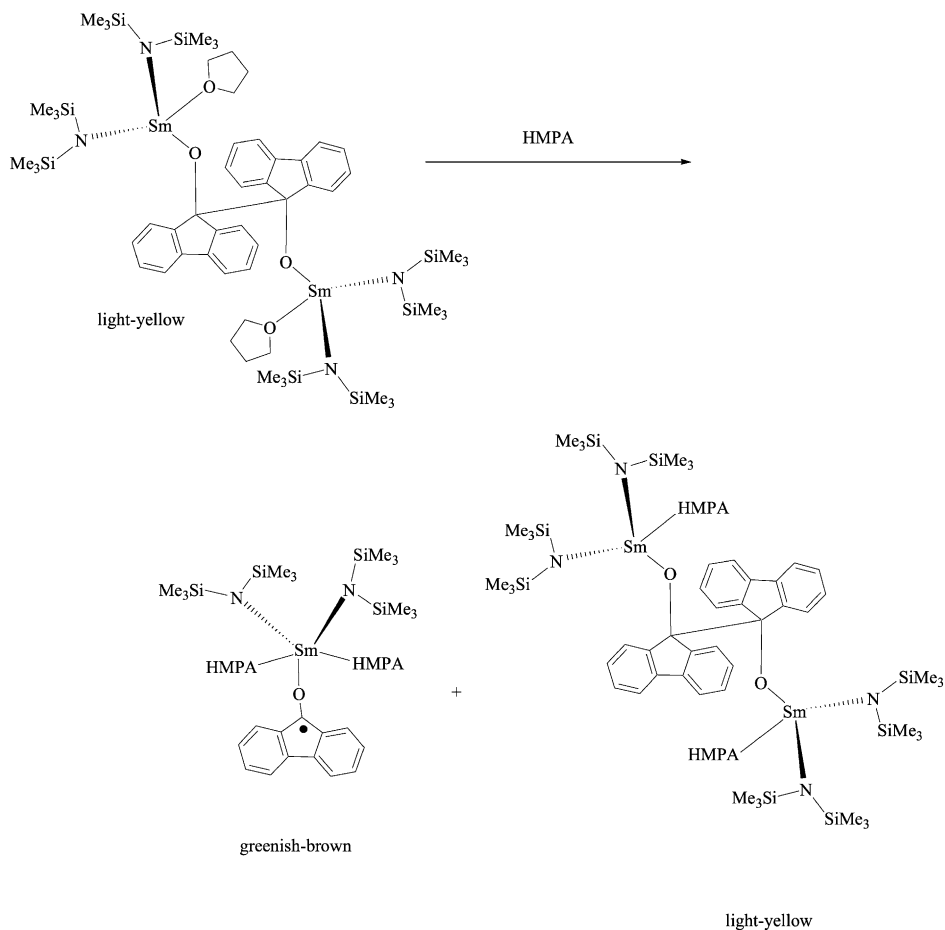
of azobenzene by $[(\text{Me}_3\text{Si})_2\text{N}]_2\text{Sm}(\text{THF})_2$ lead to the azo bridged samarium complex $[(\text{Me}_3\text{Si})_2\text{N}]_2\text{Sm}(\text{THF})(\mu\text{-PhNNPh})\text{Sm}[\text{N}(\text{SiMe}_3)_2]_2$ and subsequent reaction with another equivalent of $[(\text{Me}_3\text{Si})_2\text{N}]_2\text{Sm}(\text{THF})_2$ lead to cleavage of the N–N single bond of the azo-bridged complex. Subsequent hydrolysis leads to aniline. Isolation of most intermediates and examination by ^1H NMR and X-ray established the identity of all organic and organosamarium intermediates providing great detail into the stepwise conversion of nitrobenzene into aniline.

Studies by Hou and coworkers were initiated to compare and contrast the ability of different ligands to stabilize ketyl intermediates and showed that the $(-\text{N}(\text{SiMe}_3)_2)$ ligand behaved somewhat different than the Cp^* ligand upon the reduction of a ketone (Hou et al., 1998). The reaction of $[(\text{Me}_3\text{Si})_2\text{N}]_2\text{Sm}(\text{THF})_2$ with one equivalent of fluorenone in THF produced a brown solution with a UV–vis spectrum consistent with the formation of a ketyl radical. Upon removal of solvent however the pinacolate was isolated as the major product in 79% yield (eq. (135)). This finding is in contrast to the



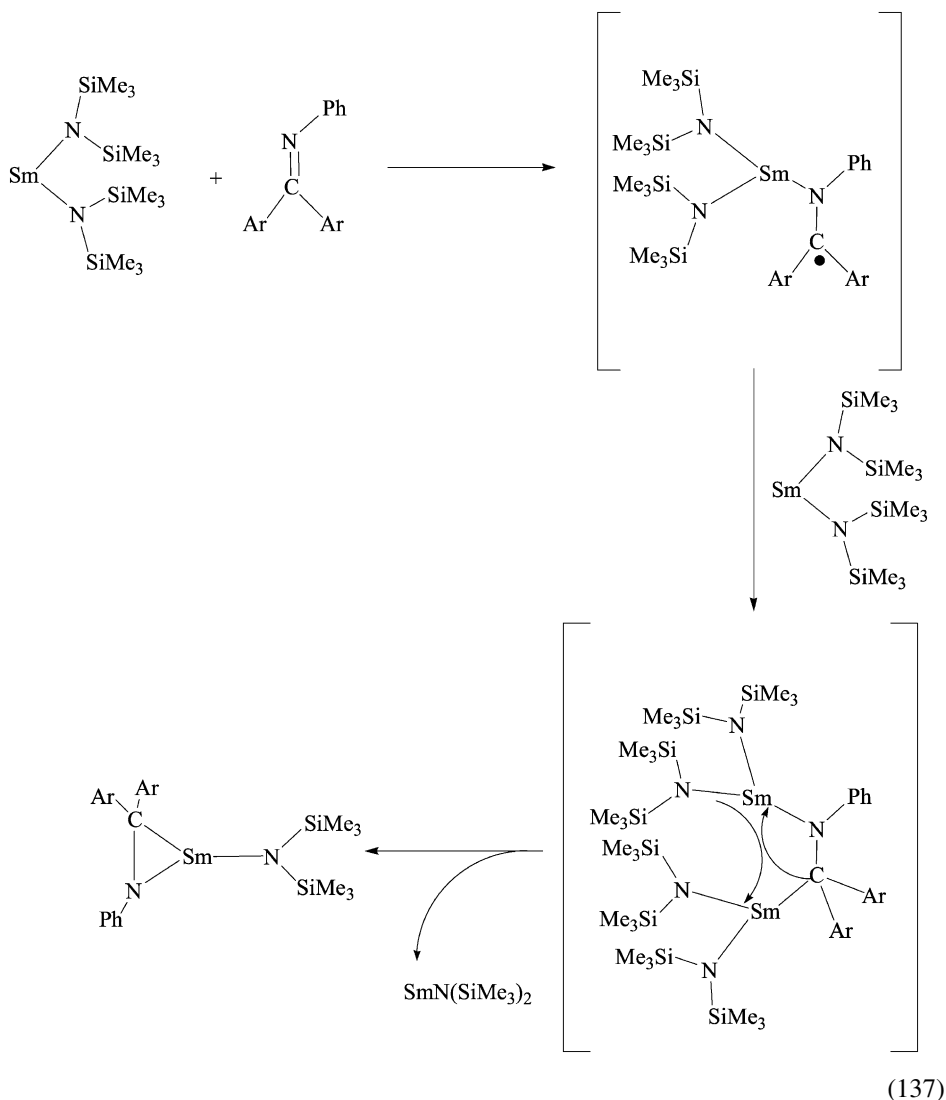
(135)

reaction of $\text{Sm}(\text{Cp}^*)_2(\text{THF})_2$ with fluorenone described previously and indicates that the $-\text{N}(\text{SiMe}_3)_2$ ligand is not sterically bulky enough to prevent colligation of the ketyl radicals. Dissolution of the pinacolate in THF produces regenerates the Sm-ketyl complex suggesting the C–C bond of the pinacolate is relatively weak. Addition of HMPA leads to two products, one consistent with homolytic cleavage of the central C–C bond producing a ketyl-Sm complex and one leaving the pinacolate intact with only replacement of the THF solvent (eq. (136)). This study shows that alteration of the ligand environment around Sm(II) leads to different reactivity patterns with organic substrates.



(136)

In related studies, reaction of 2 equivalents of $[(\text{Me}_3\text{Si})_2\text{N}]_2\text{Sm}(\text{THF})_2$ with the N-phenyl imines of benzophenone and fluorenone were carried out in THF to determine if an iminyl radical could be isolated (Hou et al., 2003). These reactions lead to the tris(silylamido)Sm(III) complex and the η^2 complexes $\text{Sm}(\eta^2\text{-Ph}_2\text{CNPh})\{\text{N}(\text{SiMe}_3)_2\}(\text{THF})_3$ and $\text{Sm}(\eta^2\text{-C}_{12}\text{H}_8\text{-CNPh})\{\text{N}(\text{SiMe}_3)_2\}(\text{THF})_3$, respectively. Hou and coworkers proposed that after the initial reduction to the iminyl radical, further reduction by another equivalent of Sm(II) produces a disamarium-imine dianion. Subsequent ligand redistribution provides the η^2 complexes (eq. (137)). The η^2 complexes are formed even when one equivalent of $[(\text{Me}_3\text{Si})_2\text{N}]_2\text{Sm}(\text{THF})_2$ is used (albeit in reduced yield) suggesting that the intermediate iminyl radical is more easily reduced than its neutral imine precursor.



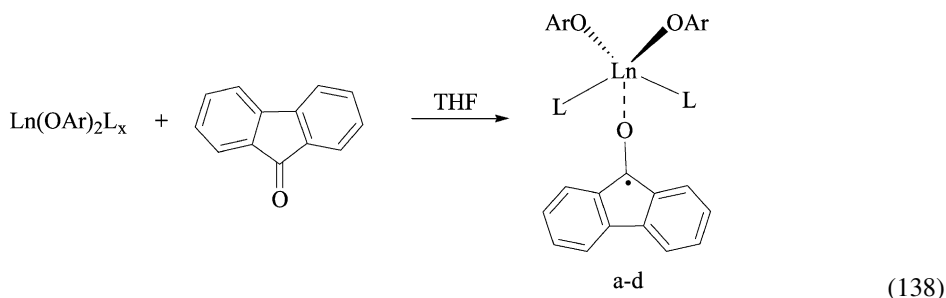
Prasad and Flowers have recently carried out a comparison of the reactivity of $\text{Sm}[\text{N}(\text{SiMe}_3)_2]_2$, SmI_2 , and $[\text{Sm}(\text{HMPA})_6]_2$ with 2-butanone and 1-iodobutane in THF to further explore the effect of ligands on the reactivity of Sm(II) reductants (Prasad and Flowers, 2002a). Cyclic voltammetry experiments were consistent with $\text{Sm}[\text{N}(\text{SiMe}_3)_2]_2$ being intermediate in thermodynamic reducing power between SmI_2 and $[\text{Sm}(\text{HMPA})_6]_2$. Surprisingly, $\text{Sm}[\text{N}(\text{SiMe}_3)_2]_2$ reduced 1-iodobutane 7 times faster and 2-butanone 4 orders of magnitude faster than the thermodynamically stronger reductant $[\text{Sm}(\text{HMPA})_6]_2$. Activation data for the reduction of 1-iodobutane and 2-butanone by $\text{Sm}[\text{N}(\text{SiMe}_3)_2]_2$ were consistent with highly

ordered transition states having low activation barriers. While the rate and mechanistic data in this study showed that $\text{Sm}[\text{N}(\text{SiMe}_3)_2]_2$ was an effective reductant, the data suggests that thermodynamic reducing power (as measured by redox potential) is not a good indicator of rates. The ability of the Sm(II) reductant to interact with substrates through close contact (inner sphere) interactions, plays an important role in the mechanism of reduction of organic substrates.

Although relatively little synthetic chemistry has been explored using $[(\text{Me}_3\text{Si})_2\text{N}]_2\text{Sm}(\text{THF})_2$, Kim and coworkers recently reported that this reductant is useful in the reduction and reductive coupling of aldimines and ketimines derived from benzaldehyde and acetophenone (Kim et al., 2003). In particular, reduction of the N-butyl and N-benzyl imine of benzaldehyde by $[(\text{Me}_3\text{Si})_2\text{N}]_2\text{Sm}(\text{THF})_2$ provided the coupled diamine with good *anti*-selectivity whereas SmBr_2 and the Hilmersson reducing system, $(\text{SmI}_2/\text{Et}_3\text{N}/\text{H}_2\text{O})$ provided little diastereoselectivity in the reductive coupling reaction. Reduction of ketimines by $[(\text{Me}_3\text{Si})_2\text{N}]_2\text{Sm}(\text{THF})_2$ lead to formation of the corresponding amine with no apparent reductive coupling.

4.3. Reactions of $[\text{Sm}(\text{OC}_6\text{H}_2\text{-2,6-di-}^t\text{Bu-4-Me})_2(\text{THF})_3]$

Reaction of $[\text{Sm}(\text{OC}_6\text{H}_2\text{-2,6-di-}^t\text{Bu-4-Me})_2(\text{THF})_3]$ with one of benzophenone provided a product consistent with formation of a ketyl radical. Unfortunately, the complex could not be isolated and removal of solvent, or allowing the complex to stand at room temperature lead to the formation of the corresponding alcohol (Hou et al., 1998). To prevent hydrogen abstraction, the Sm(II) complex was reacted with one equivalent of fluorenone in THF at room temperature leading to successful isolation of the Sm-coordinated ketyl complex (138). The complex is a distorted trigonal



a: Ln = Sm, L = THF, x = 3

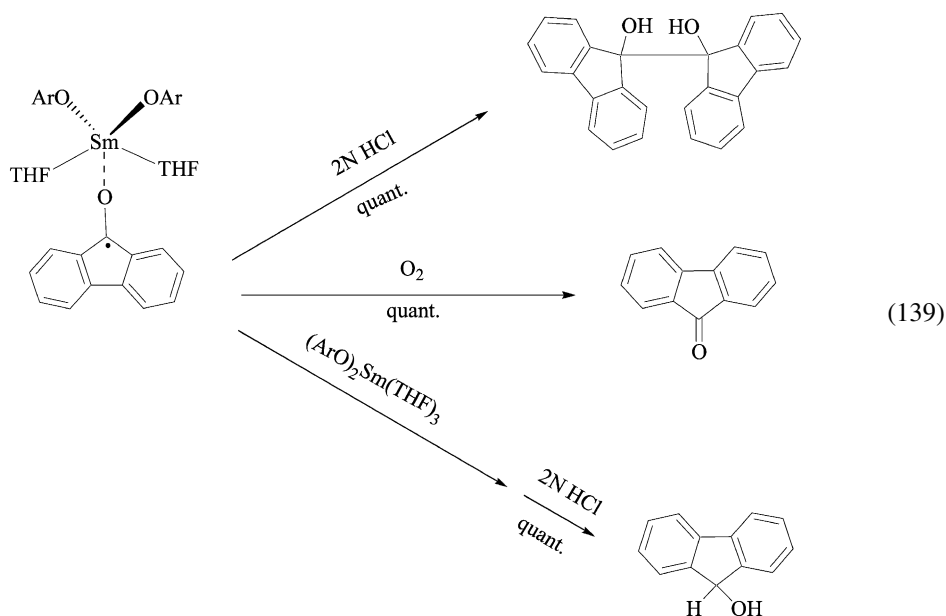
b: Ln = Yb, L = THF, x = 3

c: Ln = Sm, L = HMPA, x = 2

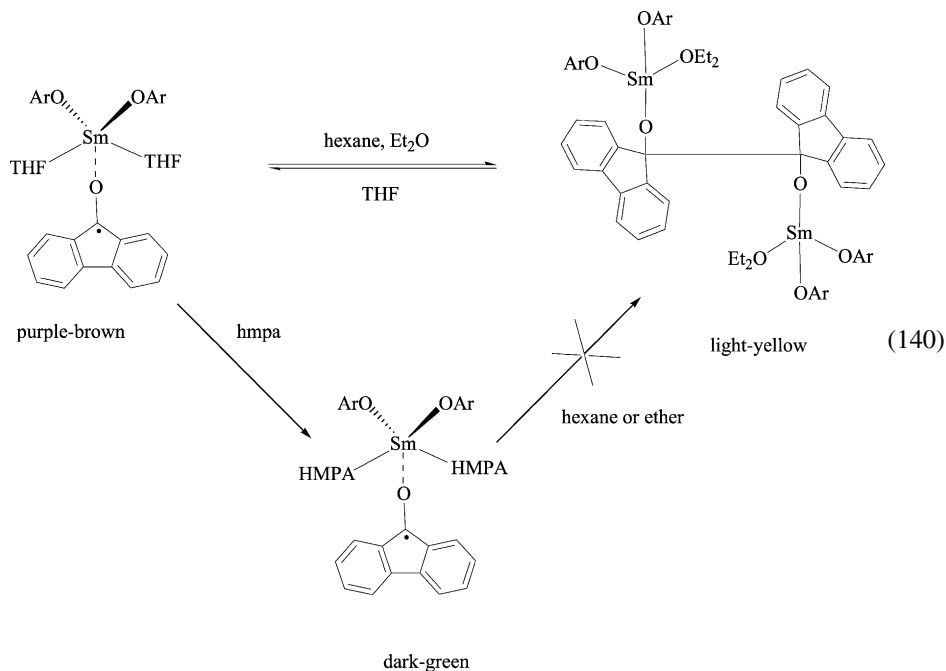
d: Ln = Yb, L = HMPA, x = 2

Ar: $\text{C}_6\text{H}_2^t\text{Bu-2, 6-Me-4}$

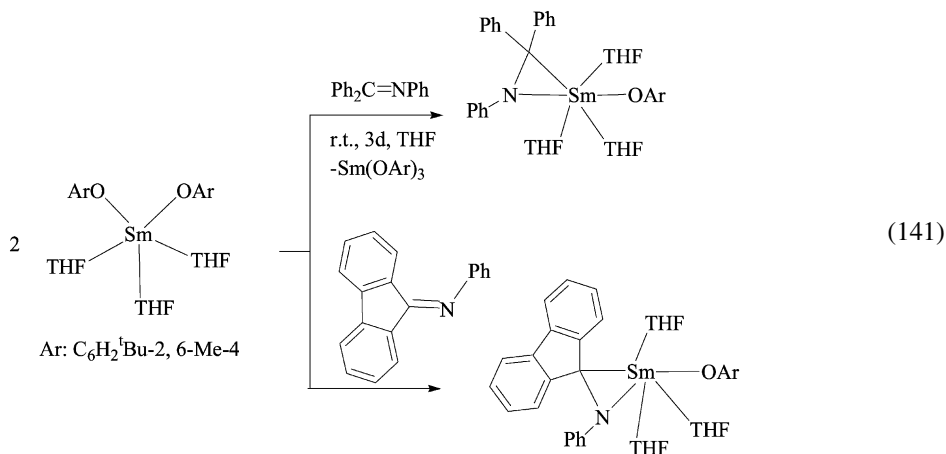
bipyramid with the ketyl and two alkoxide ligands in the equatorial positions and the two THF ligands in the apical positions. It is likely that the ketyl intermediate described in equation (eq. (135)) (formed from reaction between $[(\text{Me}_3\text{Si})_2\text{N}]_2\text{Sm}(\text{THF})_2$ and fluorenone) has a similar structure. The Sm-ketyl intermediate displays typical behavior in that hydrolysis leads to the corresponding pinacol and reaction with oxygen provides fluorenone almost quantitatively. Surprisingly, reaction of the ketyl with another equivalent of $[\text{Sm}(\text{OC}_6\text{H}_2\text{-2,6-di-}^t\text{butyl-4-methyl})_2(\text{THF})_3]$ followed by hydrolysis lead to fluorenol indicating that a dianion is probably formed as an intermediate (eq. (139)).



Dissolution of the Sm-ketyl in hexane leads to a loss of color and removal of the solvent followed by recrystallization from hexane containing a small amount of Et₂O provided a binuclear Sm(III)-pinacolonate complex where the two THF ligands on each ketyl were replaced with one Et₂O ligand. Dissolution of the pinacolonate in THF provided the Sm-ketyl quantitatively. Addition of HMPA to the ketyl lead to replacement of the THF ligands (eq. (140)). The HMPA coordinated ketyl complex was quite stable and no change occurred when it was dissolved in hexane. Apparently the increased steric bulk of HMPA compared to THF inhibits colligation of the ketyl.



In related studies Hou et al. examined the reaction of $[\text{Sm}(\text{OC}_6\text{H}_2\text{-}2,6\text{-di-}^t\text{butyl-4-methyl})_2(\text{THF})_3]$ with the N-phenyl imines of benzophenone and fluorenone to determine if an iminyl radical could be isolated (Hou et al., 2003). The Sm(II)-alkoxide complex reacted with both imines in a similar fashion to $[(\text{Me}_3\text{Si})_2\text{N}]_2\text{Sm}(\text{THF})_2$ providing $\text{Sm}(\eta^2\text{-Ph}_2\text{CNPh})(\text{OC}_6\text{H}_2\text{-}2,6\text{-di-}^t\text{butyl-4-methyl})(\text{THF})_3$ and $\text{Sm}(\eta^2\text{-C}_{12}\text{H}_8\text{CNPh})(\text{OC}_6\text{H}_2\text{-}2,6\text{-di-}^t\text{butyl-4-methyl})(\text{THF})_3$, respectively (eq. (141)). The mechanism of formation of the products likely occurs through the process shown in equation (eq. (137)).



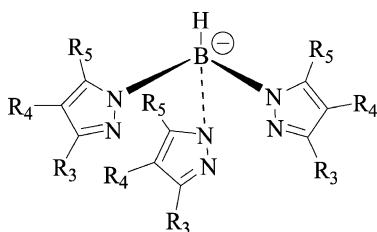
5. Sm(II) pyrazolylborate reductants

Saturation of the coordination sphere of lanthanides is critical in producing monomeric species. As shown in previous sections, sterically encumbered ligands such as Cp* and bulky alkoxides and silyl amides have provided a means to study and tune the reactivity of divalent samarium. While these studies have provided great insight into the reactivity of Sm(II)-based reductants, the search for alternative ligands is ongoing. One ligand group that has been used in lanthanide chemistry more recently is the hydrotris(pyrazolyl)borate family of ligands ([chart 1](#)). The steric demand of these ligands can be readily tuned and they have been used with a wide range of lanthanides ([Marques et al., 2002](#)). In regard to the chemistry of divalent samarium, the most utilized ligand of this family is hydrotris(3,5-dimethylpyrazolyl)borate (henceforth referred to as Tp^{Me_2}). Although $\text{Sm}(\text{Tp}^{\text{Me}_2})_2$ is insoluble in most organic solvents, it has a number of interesting applications since its chemistry is unique compared to the reductants discussed previously in this contribution. This section will focus on the synthesis of $\text{Sm}(\text{Tp}^{\text{Me}_2})_2$ and a few of the unique reactions it initiates.

5.1. Synthesis of $\text{Sm}(\text{Tp}^{\text{Me}_2})_2$

The original synthesis of $\text{Sm}(\text{Tp}^{\text{Me}_2})_2$ was communicated in 1993. The preparation utilized SmI_2 in THF and two equivalents of the potassium salt of Tp^{Me_2} ([Moss et al., 1993](#)). This initial communication drew attention to the insolubility of the $\text{Sm}(\text{Tp}^{\text{Me}_2})_2$ complex and different reactivity patterns compared to $\text{Sm}(\text{Cp}^*)_2$. The structure of $\text{Sm}(\text{Tp}^{\text{Me}_2})_2$ is very different from that of $\text{Sm}(\text{Cp}^*)_2$. The two Tp^{Me_2} ligands lie in a staggered arrangement around the metal center with the methyl groups sitting of one ligand sitting in the cleft created by the other with the boron atoms lying on the C3–S6 axis ([chart 2](#)). This unusual arrangement accounts for the lack of coordinated solvent and likely shields the metal from access to substrates.

Work by Takats and coworkers ([Hillier et al., 2001](#)) showed that the use of the sodium salt of Tp^{Me_2} provided a more convenient route to $\text{Sm}(\text{Tp}^{\text{Me}_2})_2$ in THF since the relatively soluble NaI byproduct could be easily removed from the insoluble $\text{Sm}(\text{Tp}^{\text{Me}_2})_2$ (eq. (142)). Unlike $\text{Sm}(\text{Cp}^*)_2$, $\text{Sm}(\text{Tp}^{\text{Me}_2})_2$ is isolated from THF as a solvent-free complex, suggesting



$\text{R}_3, \text{R}_4, \text{R}_5 = \text{H}$ or alkyl

Chart 1.

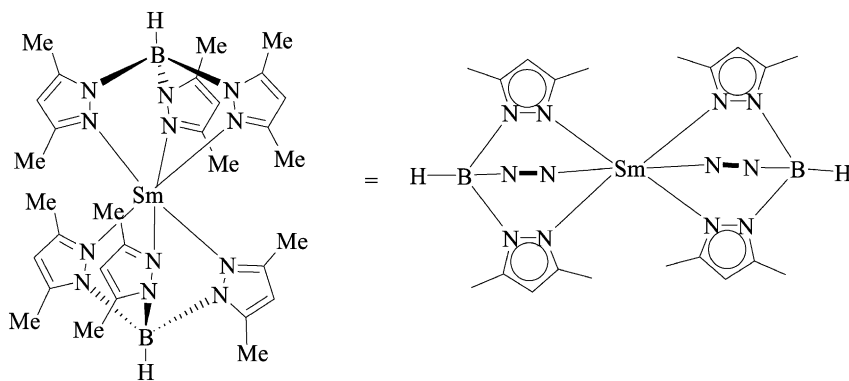
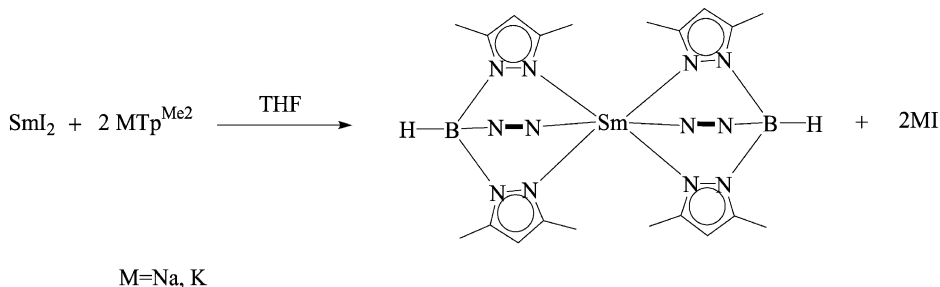


Chart 2.

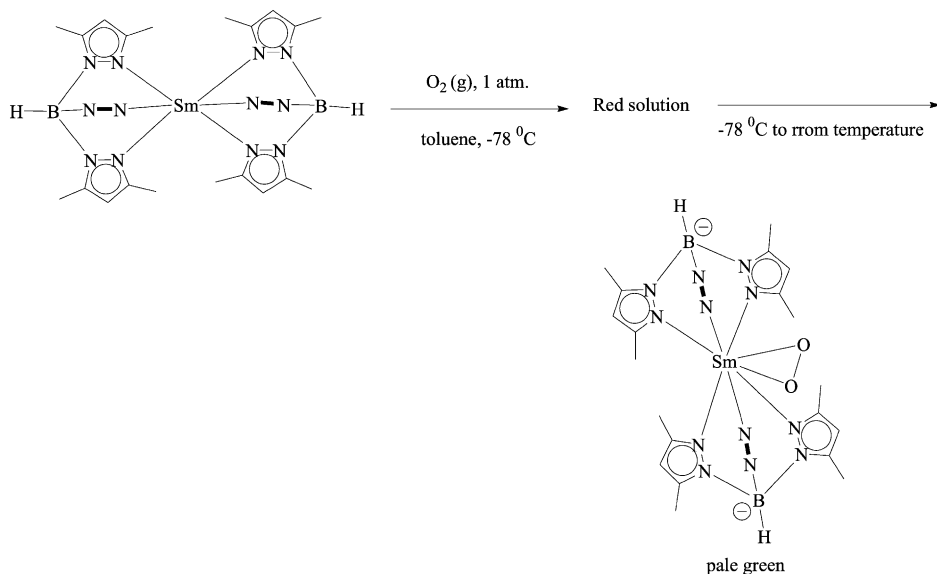
that the more sterically congested nature of the latter is likely responsible for the different reactivity.



(142)

5.2. Reactions of $\text{Sm}(\text{Tp}^{\text{Me}_2})_2$

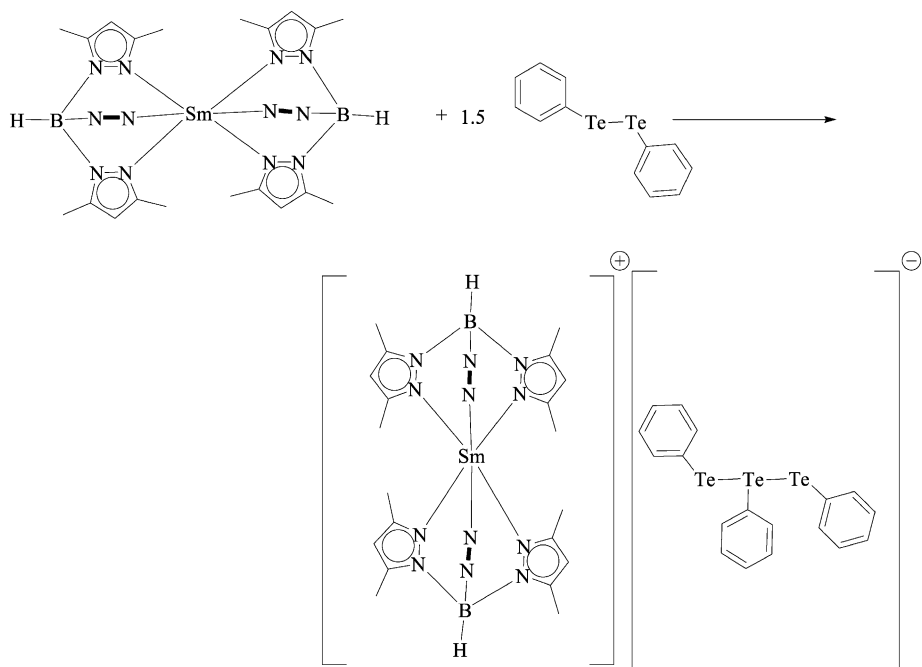
Although $\text{Sm}(\text{Tp}^{\text{Me}_2})_2$ initiates a number of standard reactions previously described for other Sm(II)-based reductants (Marques et al., 2002), there are a number of unique reactions it undergoes that make it a useful alternative for the synthesis of novel Sm(III) complexes and the production of unique reaction products. The most notable reaction is with molecular oxygen. Addition of one atmosphere of oxygen to a slurry of $\text{Sm}(\text{Tp}^{\text{Me}_2})_2$ in toluene at -78°C lead to the dissolution of insoluble complex concomitant with the appearance of a red color. Removal of excess oxygen and slow warming of the solution to room temperature provided a pale green solution. Raman spectroscopy provided strong evidence for the presence of a superoxo ligand and coupled with NMR studies provided evidence that the structure was likely $[\text{Sm}(\text{Tp}^{\text{Me}_2})_2(\eta^2\text{-O}_2)]$ (eq. (143)) (Zhang et al., 1995). Although



(143)

initial attempts to crystallize the product were unsuccessful it was found that slow crystallization of from a 1 : 1 mixture of hexane/DME solution at -40°C provided a sample suitable for analysis. Analysis of the structure showed that the two Tp^{Me_2} ligands provided a cleft that shielded the O_2^- ligand. The lack of O_2^- displacement by donor solvents including THF and CH_3CN were indicative of strong binding by the ligand as well. This elegant study provided the first example of a lanthanide superoxo complex and lead to increased activity in the area as other groups began to fully explore the unique reactivity of related complexes.

One of the main differences between the reactivity of $\text{Sm}(\text{Cp}^*)_2$ and $\text{Sm}(\text{Tp}^{\text{Me}_2})_2$ with similar substrates is the former tends to form binuclear complexes while the latter forms mononuclear Sm complexes. An interesting example of the different reactivity is in the reaction of $\text{Sm}(\text{Tp}^{\text{Me}_2})_2$ with diphenylditelluride (Hillier et al., 1999). Reaction of diphenylditelluride with two equivalents of $\text{Sm}(\text{Tp}^{\text{Me}_2})_2$ as a slurry in toluene produced $[\text{Sm}(\text{Tp}^{\text{Me}_2})(\text{TePh})]$. Examination of the product by ^1H NMR showed that the *ortho* hydrogens of the phenyl group were deshielded indicative of a close interaction between the TePh moiety and the $\text{Sm}(\text{Tp}^{\text{Me}_2})_2^+$ cation. Surprisingly, addition of 1.5 equivalents of diphenylditelluride with $\text{Sm}(\text{Tp}^{\text{Me}_2})_2$ under identical conditions provided a product consistent with the structure $[\text{Sm}(\text{Tp}^{\text{Me}_2})_2(\text{TePh})_3]$ (eq. (144)). Analysis by ^1H NMR showed that the spectrum was similar



to the previous one except that there was no deshielding of the phenyl protons. Crystallization of the product from toluene revealed a unique structure with a separated $[\text{Te}_3\text{Ph}_3]^-$ counteranion coupled with the $\text{Sm}(\text{Tp}^{\text{Me}_2})_2^+$ cation. The $[\text{Te}_3\text{Ph}_3]^-$ in the product is slightly bent with a $(\text{Te}-\text{Te}-\text{Te})$ bond angle of $172.92(3)^\circ$. The anion is asymmetric and consistent with a phenyltelluroate anion bound to a neutral diphenylditelluride. Since the $[\text{Te}_3\text{Ph}_3]^-$ anion had not been reported previously via reduction of diphenylditelluride with alkali metals, this study suggests that the stabilization may be due to the presence of the sterically encumbered $\text{Sm}(\text{Tp}^{\text{Me}_2})_2^+$ cation.

The few studies on $\text{Sm}(\text{Tp}^{\text{Me}_2})_2$ presented herein show that unique structure of this reductant is likely responsible for its unusual reactivity and subsequent isolation of unique reaction products. Further studies of this and similar reductants utilizing pyrazolylborate ligands will likely lead to novel reactions and greatly extend the chemistry of $\text{Sm}(\text{II})$.

6. Conclusions and outlook

The use and applications of divalent samarium as reagents in the synthesis of organic and inorganic substrates have grown substantially during the past 25 years. Although their use in the synthesis of catalysts and precatalysts is a relatively mature area, advances have been made recently in the use of heteroleptic $\text{Sm}(\text{II})$ -based reductants for these purposes (Hou and

Wakatsuki, 2002). The use of these reagents as stoichiometric reductants is continuing to grow as well with over 100 publications a year using Sm(II)-based reductants (predominantly SmI₂) as an integral part of multi-step syntheses or in the development of novel methodologies. Although these applications are quite useful in organic synthesis, scale-up is problematic and many of the additives used in reactions are non-ideal in regard to environmental and safety issues. Nonetheless, as more is learned about the mechanism of these reductants, many of these problems can be overcome. For instance, recent work using coreductants have allowed the use of substoichiometric amounts of Sm in certain classes of reactions (Aspinall et al., 2005; Hé lion and Namy, 1999; Namura et al., 1996). Furthermore, novel approaches to enhancing the reactivity Sm(II)-based reductants (such as those developed by Hilmersson) (Dahlen and Hilmersson 2003a, 2003b) will lead to protocols that mimic the beneficial behavior of additives such as HMPA, but provide safer alternatives. As these advances are exploited and others are developed, the use of Sm(II) reagents are likely to continue and grow for the foreseeable future.

Acknowledgements

The authors thank Drs. Rebecca Miller and Pramod Chopade for their assistance during the preparation of the manuscript.

References

- Akane, N., Hatano, T., Kusui, H., Nishiyama, Y., Ishii, Y., 1994. *J. Org. Chem.* **59**, 7902.
- Anathanarayan, T.P., Gallagher, T., Magus, P., 1983. *J. Chem. Soc., Chem. Commun.*, 709.
- Aspinall, H.C., Greeves, N., Valla, C., 2005. *Org. Lett.* **7**, 1919.
- Bied, C., Collin, J., Kagan, H.B., 1992. *Tetrahedron* **48**, 3877.
- Bochkarev, M.N., Fedushkin, I.L., Dechert, S., Fagin, A.A., Schumann, H., 2001. *Angew. Chem., Int. Ed. Engl.* **40**, 3176.
- Bond, A.M., Deacon, G.B., Newham, R.H., 1986. *Organometallics* **5**, 2312.
- Brady, E.K., Clark, D.L., Keogh, D.W., Scott, B.L., Watkin, J.G., 2002. *J. Am. Chem. Soc.* **124**, 7007.
- Cabri, W., Candiani, I., Colombo, M., Franzoi, L., Bedeschi, A., 1995. *Tetrahedron Lett.* **36**, 949.
- Castillo, I., Tilley, T.D., 2001. *J. Am. Chem. Soc.* **123**, 10526.
- Chebolu, V., Whittle, R.R., Sen, A., 1985. *Inorg. Chem.* **24**, 3082.
- Chopade, P.R., Davis, T.A., Prasad, E., Flowers II, R.A., 2004a. *Org. Lett.* **6**, 2685.
- Chopade, P.R., Prasad, E., Flowers II, R.A., 2004b. *J. Am. Chem. Soc.* **126**, 44.
- Collin, J., Bied, C., Kagan, H.B., 1991. *Tetrahedron Lett.* **32**, 629.
- Collin, J., Namy, J.L., Bied, C., Kagan, H.B., 1987. *Inorg. Chim. Acta* **140**, 29.
- Concellon, J.M., Rodriguez-Solla, H., Bardales, E., Huerta, M., 2003. *Eur. J. Org. Chem.*, 1775.
- Cotton, S.A., 1991. *Lanthanides & Actinides*. Oxford Univ. Press, New York, p. 26.
- Curran, D.P., Tottleben, M.J., 1992. *J. Am. Chem. Soc.* **114**, 6050.
- Dahlen, A., Hilmersson, G., 2001. *Tetrahedron Lett.* **42**, 5565.
- Dahlen, A., Hilmersson, G., 2002. *Tetrahedron Lett.* **43**, 7197.
- Dahlen, A., Hilmersson, G., 2003a. *Chem. Eur. J.* **9**, 1123.
- Dahlen, A., Hilmersson, G., 2003b. *Tetrahedron Lett.* **44**, 2661.
- Davis, T.A., Chopade, P.R., Hilmersson, G., Flowers II, R.A., 2005. *Org. Lett.* **7**, 119.

- Enemark, R.J., Hertz, T., Skrydstrup, T., Daasbjerg, K., 2000. *Chem. Eur. J.* **6**, 3747.
- Enholm, E.J., Forbes, D.C., Holub, D.P., 1990. *Synth. Commun.* **20**, 981.
- Evans, W.J., 2000. *Coord. Chem. Rev.* **206**, 263.
- Evans, W.J., 1987a. *Polyhedron* **6**, 803.
- Evans, W.J., 1995a. *New J. Chem.* **19**, 525.
- Evans, W.J., 2002. *J. Organomet. Chem.* **652**, 61.
- Evans, W.J., Allen, N.T., 2000a. *J. Am. Chem. Soc.* **122**, 2118.
- Evans, W.J., Allen, N.T., Ziller, J.W., 2000b. *J. Am. Chem. Soc.* **122**, 11749.
- Evans, W.J., Ansari, M.A., Ziller, J.W., Khan, S.I., 1995b. *Organometallics* **14**, 3.
- Evans, W.J., Bloom, I., Hunter, W.E., Atwood, J.L., 1981. *J. Am. Chem. Soc.* **103**, 6507.
- Evans, W.J., Bloom, I., Hunter, W.E., Atwood, J.L., 1983. *J. Am. Chem. Soc.* **105**, 1401.
- Evans, W.J., Bloom, I., Hunter, W.E., Atwood, J.L., 1985a. *Organometallics* **4**, 112.
- Evans, W.J., Broomhall-Dillard, R.N.R., Ziller, J.W., 1998a. *Polyhedron* **17**, 3361.
- Evans, W.J., Chamberlain, L.R., Ziller, J.W., 1987b. *J. Am. Chem. Soc.* **109**, 7209.
- Evans, W.J., Chamberlain, L.R., Ulibarri, T.A., Ziller, J.W., 1988a. *J. Am. Chem. Soc.* **110**, 6423.
- Evans, W.J., Drummond, D.K., 1989. *J. Am. Chem. Soc.* **111**, 3329.
- Evans, W.J., Drummond, D.K., 1986a. *J. Am. Chem. Soc.* **108**, 7440.
- Evans, W.J., Drummond, D.K., Bott, S.G., Atwood, J.L., 1986b. *Organometallics* **5**, 2389.
- Evans, W.J., Drummond, D.K., Zhang, H., Atwood, J.L., 1988b. *Inorg. Chem.* **27**, 575.
- Evans, W.J., Foster, S.E., 1992. *J. Organomet. Chem.* **433**, 79.
- Evans, W.J., Giarikos, D.G., Robledo, C.B., Leong, V.S., Ziller, J.W., 2001. *Organometallics* **20**, 5648.
- Evans, W.J., Gonzales, S.L., Ziller, J.W., 1991. *J. Am. Chem. Soc.* **113**, 9880.
- Evans, W.J., Grate, J.W., Bloom, I., Hunter, W.E., Atwood, J.L., 1985b. *J. Am. Chem. Soc.* **107**, 405.
- Evans, W.J., Grate, J.W., Choi, H.W., Bloom, I., Hunter, W.E., Atwood, J.L., 1985c. *J. Am. Chem. Soc.* **107**, 941.
- Evans, W.J., Grate, J.W., Hughes, L.A., Zhang, H., Atwood, J.L., 1985d. *J. Am. Chem. Soc.* **107**, 3728.
- Evans, W.J., Grate, J.W., Levan, K.R., Bloom, I., Peterson, T.T., Doedens, R.J., Zhang, H., Atwood, J.L., 1986c. *Inorg. Chem.* **25**, 3614.
- Evans, W.J., Gummersheimer, T.S., Ziller, J.W., 1995c. *J. Am. Chem. Soc.* **117**, 8999.
- Evans, D.A., Hoveyda, A.H., 1990a. *J. Am. Chem. Soc.* **112**, 6447.
- Evans, W.J., Hughes, L.A., Hanusa, T.P., 1984. *J. Am. Chem. Soc.* **106**, 4270.
- Evans, W.J., Leman, J.T., Ziller, J.W., Khan, S.I., 1996. *Inorg. Chem.* **35**, 4283.
- Evans, W.J., Rabe, G.W., Ziller, J.W., Doedens, R.J., 1994. *Inorg. Chem.* **33**, 2719.
- Evans, W.J., Sibel, C.A., Ziller, J.W., 1998b. *Inorg. Chem.* **37**, 770.
- Evans, W.J., Seibel, C.A., Ziller, J.W., 1998c. *J. Am. Chem. Soc.* **120**, 6745.
- Evans, W.J., Ulibarri, T.A., 1987c. *J. Am. Chem. Soc.* **109**, 4292.
- Evans, W.J., Ulibarri, T.A., Chamberlain, L.R., Ziller, J.W., Alvarez Jr., D., 1990b. *Organometallics* **9**, 2124.
- Evans, W.J., Ulibarri, T.A., Ziller, J.W., 1988c. *J. Am. Chem. Soc.* **110**, 6877.
- Evans, W.J., Ulibarri, T.A., Ziller, J.W., 1990c. *J. Am. Chem. Soc.* **112**, 219.
- Evans, W.J., Ulibarri, T.A., Ziller, J.W., 1990d. *J. Am. Chem. Soc.* **112**, 2314.
- Feldman, K.S., Simpson, R.E., 1989. *Tetrahedron Lett.* **30**, 6985.
- Fevig, T.L., Elliot, R.L., Curran, D.P., 1988. *J. Am. Chem. Soc.* **110**, 5064.
- Fuchs, J.R., Mitchell, M.L., Shabangi, M., Flowers II, R.A., 1997. *Tetrahedron Lett.* **38**, 8157.
- Fukuzawa, S., Nakanishi, A., Fuginami, T., Sakai, S., 1986. *J. Chem. Soc. Chem. Commun.* **1**, 624.
- Fukuzawa, S., Nakanishi, A., Fuginami, T., Sakai, S., 1988. *J. Chem. Soc. Perkin Trans.* **1**, 1669.
- Furstner, A., Csuk, R., Rohrer, C., Weidmann, H., 1988. *J. Chem. Soc. Perkin Trans.* **1**, 1729.
- Girard, P., Namy, J.L., Kagan, H.B., 1980. *J. Am. Chem. Soc.* **102**, 2693.
- Héliion, F., Lannou, M.I., Namy, J.L., 2003. *Tetrahedron Lett.* **44**, 5507.
- Héliion, F., Namy, J.-L., 1999. *J. Org. Chem.* **64**, 2944.
- Hamann, B., Namy, J.L., Kagan, H.B., 1996. *Tetrahedron* **52**, 14225.
- Hillier, A.C., Liu, S.-Y., Sella, A., Elsegood, M.R.J., 1999. *Angew. Chem., Int. Ed. Engl.* **38**, 2745.
- Hillier, A.C., Zhang, X.W., Maunder, G.H., Liu, S.Y., Eberspacher, T.A., Metz, M.V., McDonald, R., Domingos, A., Marques, N., Day, V.W., Sella, A., Takats, J., 2001. *Inorg. Chem.* **40**, 5106.
- Honda, Y., Inanaga, J., Yamaguchi, M., 1989. *J. Chem. Soc. Chem. Commun.*, 298.
- Hou, Z., Fujita, A., Zhang, Y., Miyano, T., Yamazaki, H., Wakatsuki, Y., 1998. *J. Am. Chem. Soc.* **120**, 754.

- Hou, Z., Miyano, T., Yamazaki, H., Wakatsuki, Y., 1995. *J. Am. Chem. Soc.* **117**, 4421.
- Hou, Z., Wakatsuki, Y., 1994. *J. Chem. Soc. Chem. Commun.*, 1205.
- Hou, Z., Wakatsuki, Y., 2002. *J. Organomet. Chem.* **647**, 61.
- Hou, Z., Yoda, C., Koisumi, T.-A., Nishiura, M., Wakatsuki, Y., Fukuzawa, S.-I., Takats, J., 2003. *Organometallics* **22**, 3586.
- Hou, Z., Zhang, Y., Tezuka, H., Xie, P., Tardif, O., Koizumi, T.-A., Yamazaki, H., Wakatsuki, Y., 2000. *J. Am. Chem. Soc.* **122**, 10533.
- Hou, Z., Zhang, Y., Tardif, O., Wakatsuki, Y., 2001. *J. Am. Chem. Soc.* **123**, 9216.
- Hou, Z., Zhang, Y., Wakatsuki, Y., 1997. *Bull. Chem. Soc. Jpn.* **70**, 149.
- House, H.O., 1972. *Modern Synthetic Reactions*, second ed. Benjamin, Menlo Park, CA.
- Hoz, S., Yacovan, A., Bilkis, I., 1996. *J. Am. Chem. Soc.* **118**, 261.
- Hutton, T.K., Muir, K., Procter, D.J., 2002. *Org. Lett.* **4**, 2345.
- Imamoto, T., Nishimura, S., 1990. *Chem. Lett.*, 1141.
- Imamoto, T., Takeyama, T., Koto, H., 1986. *Tetrahedron Lett.* **27**, 3243.
- Inanaga, J., 1990. *Rev. Heteroat. Chem.* **3**, 75.
- Inanaga, J., Ishikawa, M., Yamaguchi, M., 1987. *Chem. Lett.*, 1485.
- Inanaga, J., Ujikawa, O., Yamaguchi, M., 1991a. *Tetrahedron Lett.* **32**, 1737.
- Inanaga, J., Yokoyama, Y., Baba, Y., Yamaguchi, M., 1991b. *Tetrahedron Lett.* **32**, 5559.
- Johnson, C.R., Senanayake, C.H., 1989. *J. Org. Chem.* **54**, 735.
- Kagan, H.B., Collin, J., Namy, J.L., Bied, C., Dallemer, F., Lebrun, A., 1993. *J. Alloys Compd.* **192**, 191.
- Kagan, H.B., Namy, J.L., 1986. *Tetrahedron* **42**, 6573.
- Kagan, H.B., Namy, J.L., Girard, P., 1981. *Tetrahedron* **37** (Suppl. 1), 175.
- Kamochi, Y., Kindo, T., 1993. *Chem. Lett.* **9**, 1495.
- Kamochi, Y., Kudo, T., 1991. *Tetrahedron Lett.* **32**, 3511.
- Kawaoka, A.M., Marks, T.J., 2004. *J. Am. Chem. Soc.* **126**, 12764.
- Keck, G.E., Wager, C.A., Sell, T., Wager, T.T., 1999. *J. Org. Chem.* **64**, 2172.
- Kende, A.S., Mendoza, J.S., 1991. *Tetrahedron Lett.* **32**, 1699.
- Kim, M., Knettle, B.W., Dahlén, A., Hilmersson, G., Flowers II, R.A., 2003. *Tetrahedron* **59**, 10397.
- Kiss, Z., Yocum, P.N., 1964. *J. Chem. Phys.* **41**, 1511.
- Knettle, B.W., Flowers II, R.A., 2001. *Org. Lett.* **3**, 2321.
- Kunishima, M., Hioki, K., Ohara, T., Tani, S., 1992. *J. Chem. Soc. Chem. Commun.*, 219.
- Kusuda, K., Inanaga, J., Yamaguchi, M., 1989. *Tetrahedron Lett.* **30**, 2945.
- Lannoye, G., Cook, J.M., 1988a. *Tetrahedron Lett.* **29**, 171.
- Lannoye, G., Sambasivarao, K.W.S., Cook, J.M., 1988b. *J. Org. Chem.* **53**, 2327.
- Lebrun, A., Namy, J.L., Kagan, H.B., 1993. *Tetrahedron Lett.* **34**, 2311.
- Luche, J.L., 1978. *J. Am. Chem. Soc.* **100**, 2226.
- Ma, J.-A., Cahard, D., 2004. *Angew. Chem., Int. Ed. Engl.* **43**, 4566.
- Machrouhi, F., Namy, J.L., 1999. *Tetrahedron Lett.* **40**, 1315.
- Marques, N., Sella, A., Takats, J., 2002. *Chem. Rev.* **102**, 2137.
- Matsukawa, M., Tabuchi, T., Inanaga, J., Yamaguchi, M., 1987. *Chem. Lett.*, 2101.
- Matsukawa, S., Hinakubo, Y., 2003. *Org. Lett.* **5**, 1221.
- McAuley, B.J., Nieuwenhuyzen, M., Sheldrake, G.N., 2000. *Org. Lett.* **2**, 1457.
- McClure, D.S., Kiss, Z., 1963. *J. Chem. Phys.* **39**, 3251.
- Mikheev, N.B., 1984. *Inorg. Chim. Acta* **94**, 241.
- Miller, R.S., Sealy, J.M., Shabangi, M., Kuhlman, M.L., Fuchs, J.R., Flowers II, R.A., 2000. *J. Am. Chem. Soc.* **122**, 7718.
- Molander, G.A., 1992. *Chem. Rev.* **92**, 29.
- Molander, G.A., Brown, G.A., Storch, D.G., 2002. *J. Org. Chem.* **67**, 3459.
- Molander, G.A., Etter, J.B., 1986a. *J. Org. Chem.* **51**, 1778.
- Molander, G.A., Etter, J.B., 1987a. *Synth. Commun.* **17**, 901.
- Molander, G.A., Etter, J.B., 1987b. *J. Am. Chem. Soc.* **109**, 6556.
- Molander, G.A., Etter, J.B., Zinke, P.W., 1987c. *J. Am. Chem. Soc.* **109**, 453.
- Molander, G.A., Hahn, G., 1986b. *J. Org. Chem.* **51**, 1135.
- Molander, G.A., Harris, C.R., 1995. *J. Am. Chem. Soc.* **117**, 3705.
- Molander, G.A., Harris, C.R., 1997. *J. Org. Chem.* **62**, 2944.
- Molander, G.A., Kenny, C., 1991. *J. Org. Chem.* **56**, 1439.
- Molander, G.A., Le, H., Brown, G.A., 2001. *J. Org. Chem.* **66**, 4511.
- Molander, G.A., Losada, C.P., 1997. *J. Org. Chem.* **62**, 2935.
- Molander, G.A., McKie, J.A., 1992b. *J. Org. Chem.* **57**, 3132.

- Molander, G.A., McKie, J.A., 1993. *J. Org. Chem.* **58**, 7216.
- Molander, G.A., Stengel, P.J., 1997. *Tetrahedron* **53**, 8887.
- Morss, L.R., 1976. *Chem. Rev.* **76**, 827.
- Moss, M.A.J., Kresinski, R.A., Jones, C.J., Evans, W.J., 1993. *Polyhedron* **12**, 1953.
- Murakami, M., Kawano, T., Ito, Y., 1990. *J. Am. Chem. Soc.* **112**, 2437.
- Murakami, M., Kawano, T., Ito, H., Ito, Y., 1993. *J. Org. Chem.* **58**, 1458.
- Myers, R.M., Langston, S.P., Conway, S.P., Abell, C., 2000. *Org. Lett.* **2**, 1349.
- Namura, R., Matsuno, T., Endo, T., 1996. *J. Am. Chem. Soc.* **118**, 11666.
- Namy, J.L., Colomb, M., Kagan, H.B., 1994. *Tetrahedron Lett.* **35**, 1723.
- Namy, J.L., Girard, P., Kagan, H.B., Caro, P.E., 1981. *Nou. J. Chim.* **5**, 479.
- Namy, J.L., Soupe, J., Kagan, H.B., 1983. *Tetrahedron Lett.* **24**, 765.
- Ogawa, A., Sumino, Y., Nanke, T., Ohya, S., Sonada, N., Hitao, T., 1997. *J. Am. Chem. Soc.* **119**, 2745.
- Ohgo, Y., 1988. *Chem. Lett.*, 403.
- Otsubo, K., Inanaga, J., Yamaguchi, M., 1987a. *Tetrahedron Lett.* **28**, 4437.
- Otsubo, K., Inanaga, J., Yamaguchi, M., 1987b. *Chem. Lett.* **28**, 1487.
- Pandey, K., 1995. *Coord. Chem. Rev.* **140**, 37.
- Prasad, E., Flowers II, R.A., 2002a. *J. Am. Chem. Soc.* **124**, 6895.
- Prasad, E., Knettle, B.W., Flowers II, R.A., 2004. *J. Am. Chem. Soc.* **126**, 6891.
- Prasad, E., Knettle, B.W., Flowers II, R.A., 2002b. *J. Am. Chem. Soc.* **124**, 14663.
- Qi, G.-Z., Shen, Q., Lin, Y.-H., 1994. *Acta Crystallogr., Sect. C* **50**, 1456.
- Radu, N.S., Buchwald, S.L., Scott, B., Burns, C.J., 1996. *Organometallics* **15**, 3913.
- Rossmann, K., 1979. *Monatsh. Chem.* **110**, 109.
- Ruder, S.M., 1992. *Tetrahedron Lett.* **33**, 2621.
- Schumann, H., Meese-Markscheffel, J.A., Esser, L., 1995. *Chem. Rev.* **95**, 865.
- Shannon, R.D., 1976. *Acta Crystallogr.* **A32**, 751.
- Shotwell, J.B., Sealy, J.M., Flowers II, R.A., 1999. *J. Org. Chem.* **64**, 5251.
- Singh, A.K., Bakshi, R.K., Corey, E.J., 1987. *J. Am. Chem. Soc.* **109**, 6187.
- Smith III, A.B., Dunlap, N.K., Sulikowski, G.A., 1988. *Tetrahedron Lett.* **29**, 439.
- Smith, A.B., March, J., 2001. *March's Advanced Organic Chemistry Reactions, Mechanisms and Structure*, fifth ed. John Wiley & Sons, New York, p. 282.
- Soupe, J., Danon, L., Namy, J.L., Kagan, H.B., 1983. *J. Organomet. Chem.* **250**, 227.
- Soupe, J., Namy, J.L., Kagan, H.B., 1982. *Tetrahedron Lett.* **23**, 3497.
- Steel, P.G., 2001. *J. Chem. Soc., Perkin Trans. I*, 2727.
- Studer, A., Curran, D.P., 1996. *Synlett*, 255.
- Swamy, S.J., 2002. *Indian J. Chem. Sect. A* **41**, 1850.
- Tabuchi, T., Inanaga, J., Yamaguchi, M., 1986. *Tetrahedron Lett.* **27**, 3891.
- Tanaka, Y., Taniguchi, N., Kimura, T., Uemura, M., 2002. *J. Org. Chem.* **67**, 9227.
- Tilley, D.T., Anderson, R.A., Spender, B., Ruben, H., Zalkin, A., Templeton, D.H., 1980. *Inorg. Chem.* **19**, 2999.
- Totleben, M.J., Curran, D.P., Wipf, P., 1992. *J. Org. Chem.* **57**, 1740.
- Watt, G.W., Gillow, E.W., 1969. *J. Am. Chem. Soc.* **91**, 775.
- Yamamoto, Y., Matsuoka, K., Nemoto, H., 1988. *J. Am. Chem. Soc.* **110**, 4475.
- Yoshida, A., Hanamoto, T., Inanaga, J., Mikami, K., 1998. *Tetrahedron Lett.* **39**, 1777.
- Yoshida, A., Mikami, K., 1997. *Synlett*, 1375.
- Zhang, Y., Lin, R., 1987. *Synth. Commun.* **17**, 329.
- Zhang, X., Loppnow, G.R., McDonald, R., Takats, J., 1995. *J. Am. Chem. Soc.* **117**, 7828.

AUTHOR INDEX

- Abaszadeh, M.R., see Oskooie, H.A. 311
Abbott, T.P. 361
Abd-El-Mouti, F., see Nagaty, A. 361
Abdel-Hay, F.I. 362
Abdel-Mohdy, F.A., see Beliakova, M.K. 360, 361
Abdusalyamova, M.N. 4, 9, 10
Abe, S., see Suzuki, H. 47
Abe, Y., see Bamwenda, G.R. 365
Abell, C., see Myers, R.M. 400
Abilov, Ch.I., see Rustamov, P.G. 73
Abilov, Ch.I., see Sadygov, F.M. 71, 72
Abraham, B.M., see Flotow, H.E. 88, 117, 183
Abramson, N.L., see Weinstock, L.M. 304
Abu-Dari, K., see Sofen, S.R. 376
Abulkhaev, V.D. 4, 9, 10
Acocella, J. 372
Adamacikova, I., see Sevcik, P. 297
Aebi, P., see Hayoz, J. 91, 146, 151, 160, 161, 194, 201–204, 215
Aeppli, G., see Thompson, J.D. 47
Agarwal, M., see Mishra, A. 360
Agbo, A., see Eromosele, I.C. 360
Aghapoor, K. 313
Agladze, K.I. 298
Aguí, A., see Hjärvarsson, B. 206
Ahiedu, H., see Okieimen, E.F. 359
Ahmad, M., see Rahman, L. 360
Ahmad, M.B., see Fakhru'l-Razi, A. 360
Ahmad, M.B., see Janarthanan, J. 361
Ahn, K.D., see Cho, I. 361
Ahuja, R. 231
Ahuja, R., see Hjärvarsson, B. 206
Akada, M., see Torii, S. 351
Akane, N. 424
Akar, A., see Öz, N. 355
Aktaş, B., see Güner, S. 46
Al-Afaleq, E.I., see Farag, S. 358
Al-Ta'ani, B., see Fares, M.M. 358
Alamdari, R.F., see Khalafi-Nezhad, A. 308
Albendov, A.A., see Garibov, F.A. 63, 68, 69
Albering, J., see Prill, M. 10, 13
Albertini, V.R., see Rau, J.V. 312
Albrecht-Schmitt, T.E., see Sykora, R.E. 286
Alefeld, G. 88
Aleixo, P.C. 353
Alexander, M.G., see Gordon, R.A. 39, 42
Alford, J.A. 221–223
Ali, F., see Saikia, C.N. 357
Ali, M.H. 313
Ali-Zade, M.Z., see Rustamov, P.G. 72, 73
Alidzhanov, M.A., see Rustamov, P.G. 72, 73
Aliev, F.G., see Garibov, F.A. 63, 64, 68, 69
Aliev, F.G., see LeBras, G. 39, 41
Aliev, I.G., see Tanryverdiev, V.S. 63, 64, 68
Aliev, I.I., see Rustamov, P.G. 72, 73
Aliev, I.I., see Sadygov, F.M. 63, 64, 68, 69, 72, 73
Aliev, O.M. 63, 64, 69–73
Aliev, O.M., see Asadov, M.M. 72, 73
Aliev, O.M., see Garibov, F.A. 63, 64, 68, 69
Aliev, O.M., see Godzhaev, E.M. 63, 70, 71, 73
Aliev, O.M., see Maksudova, T.F. 5, 9, 10, 73
Aliev, O.M., see Rustamov, P.G. 63, 64, 70
Aliev, O.M., see Sadygov, F.M. 63, 64, 68, 69, 73
Aliev, O.M., see Tanryverdiev, V.S. 63, 64, 68
Alieva, O.A., see Maksudova, T.F. 73
Alipanah, L., see Mirkhani, V. 314
Aliyev, O.M., see Sadigov, F.M. 4, 8
Allard, B. 314
Allemand, J. 23
Allen, N.T., see Evans, W.J. 395
Allen, P.G., see Edelstein, N.M. 285, 286
Alonso, J.A. 7
Alvarez Jr., D., see Evans, W.J. 444
Aly, A.A., see Beliakova, M.K. 360, 361
Amato, A. 47
Amer, I., see Ganin, E. 345
Amin, S., see Balanikas, G. 314
Amouzegar, K., see Mahdavi, B. 353
Anathanarayan, T.P. 399
Anderson, I.S. 113
Anderson, I.S., see Udovic, T.J. 113
Anderson, R.A., see Tilley, D.T. 434
Andersson, G., see Hjärvarsson, B. 206
Andersson, M., see Miniotas, A. 271, 273
Andraka, B., see Kaczorowski, D. 39, 41, 49–51

- Andraka, B., see Pietri, R. 41
 André, G., see LeBras, G. 39, 41
 Anisimov, V.I., see Ng, K.K. 107, 126, 127, 136,
 191, 192, 198, 199, 202, 206, 212–214, 219, 222,
 231
 Ansari, M.A., see Evans, W.J. 443
 Antequera, G., see Rodriguez-Franco, M.I. 329
 Antonio, M.R. 286
 Antonio, M.R., see Sunstrom, J.E. 286
 Antonov, V.N., see Oppeneer, P.M. 47
 Antosik, A., see Remhof, A. 103, 270, 271
 Aoki, H. 60, 61
 Arai, K., see Ogiwara, Y. 358
 Arakawa, H., see Bamwenda, G.R. 365
 Ardon, M. 346
 Arishima, H., see Komiyama, M. 368, 370
 Armitage, R. 97, 233, 267, 268
 Armitage, R., see von Rottkay, K. 90–93, 97,
 128–130, 239, 241, 243, 245, 246, 250, 267
 Armitage, R.D., see Richardson, T.J. 90
 Arms, D., see Movshovich, R. 47
 Armstrong, R.L., see Gao, Y. 298
 Arons, R.R. 87
 Arun, J., see Reddy, G.V.R. 355
 Aruna, I. 90, 91, 93, 98, 175, 178, 180, 181, 255,
 257, 260–266
 Aryasetiawan, R., see Miyake, T. 215–217, 222,
 226, 231
 Asada, S., see Suzuki, H. 47
 Asadov, M.M. 72, 73
 Asakura, J. 329
 Asano, F., see Nishiguchi, T. 313
 Asanuma, H., see Miyama, S. 368
 Ashworth, M.R.F. 290
 Asovich, V.S. 312, 326
 Aspinall, H.C. 470
 Atanasiu, J.A. 286
 Ates, A., see Marko, I.E. 343
 Athalye, A.R., see Shukla, S.R. 358
 Athawale, V.D. 357, 360, 361
 Atsumi, M., see Yan, J.M. 369
 Atwood, J.L., see Evans, W.J. 432–437, 445, 449,
 452, 455, 456, 458
 Augustine, A., see Nair, V. 327, 328, 338, 339
 Augustyns, B., see Marko, I.E. 343
 Aulich, H., see Greef, R. 285
 Auty, K. 346
 Avasthi, D.K., see Aruna, I. 98, 255, 260–266
 Averous, M., see El Kholdi, M. 74
 Averous, M., see Gratens, X. 71
 Aye, M.M., see Than, M.M. 296
 Azofeifa, D.E. 89, 98, 130, 138, 145–147
 Azuma, Y., see Sumaoka, J. 368
 Baba, Y., see Inanaga, J. 417
 Babaev, Ya.N., see Dzhafarova, E.K. 70, 71
 Babaeva, I.G., see Asadov, M.M. 72, 73
 Babanly, M.B., see Dzhafarova, E.K. 70, 71
 Babanly, M.B., see Mamedova, S.G. 69, 71
 Babanly, M.B., see Sadygov, F.M. 70, 71
 Baciocchi, E. 301, 302, 317, 326, 327, 335, 343,
 364
 Baciocchi, E., see Del Giacco, T. 364
 Bäck, S.Å.J. 373
 Bade, T.R., see Doyle, M.P. 321
 Baer, S. 345, 346
 Bajpai, M., see Mishra, A. 360
 Baker, F.B. 307
 Baker, I. 290
 Bakhtiyarov, I.B., see Sadygov, F.M. 71
 Bakshi, R.K., see Singh, A.K. 410
 Balagopal, L., see Nair, V. 283, 338, 339
 Balakumar, A., see Hwu, J.R. 313
 Balanikas, G. 314
 Baldock, C., see Bäck, S.Å.J. 373
 Balducci, G., see Parodi, N. 4
 Baltork, I.M., see Iranpoor, N. 325
 Bamwenda, G.R. 365
 Bando, Y., see Jung, M.H. 43, 46
 Bando, Y., see Kim, M.-S. 43, 45, 47
 Banerjee, B., see Roy, S.C. 327
 Banerjee, M., see Chowdhury, P. 360
 Bányai, É. 289
 Bar, G. 302
 Bar-Eli, K. 297
 Bar-Eli, K., see Barkin, S. 297, 310
 Barbera, A.L., see Della Cort, A. 317
 Barberis, G.E., see Martins, G.B. 46
 Barbucci, R. 358
 Bardales, E., see Concellon, J.M. 396
 Barkakaty, B.C. 361
 Barkin, S. 297, 310
 Barkow, U., see Rode, M. 116, 206–209, 215, 247
 Barnes, R.G., see Shinar, J. 87, 207, 214
 Baro, A., see Christoffers, J. 285, 348
 Barry, J. 309
 Bartholin, H. 74
 Bartholin, H., see Rossat-Mignod, J. 6
 Bartholin, H., see Sera, M. 74
 Bartoli, C. 308
 Basceri, C. 372
 Basha, C.A., see Devadoss, V. 353

- Bassett, J. 286, 288
 Bassett, L.G. 289
 Baur, E. 365
 Baxter, I. 314
 Bayanov, A.P., see Degtyar, V.A. 57
 Bayülken, S., see Dinçer, B. 355
 Bazuaye, A. 361
 Beaudry, B.J., see Shinar, J. 87, 207, 214
 Beck, D.D. 286
 Bedeschi, A., see Cabri, W. 421
 Behari, K., see Gupta, K.C. 355
 Behrens, H. 117
 Beineke, T.A. 300, 301
 Belcher, R., see Kolthoff, I.M. 286, 289
 Beletskaya, I.P., see Maknon'kov, D.I. 327
 Beliakova, M.K. 360, 361
 Belin, S., see Briois, V. 319
 Belousov, B.P. 291
 Benbow, R.L., see Weaver, J.H. 87, 105, 191
 Benz, R. 61, 62
 Bertel, E., see Netzer, F.P. 283
 Berthet, J.C. 308
 Bertolini, G., see Greco, A. 285
 Besnus, M.J., see LeBras, G. 39, 41
 Beyermann, W.P., see Canfield, P.C. 43, 44, 46, 47
 Beyermann, W.P., see Fisk, Z. 47
 Beyermann, W.P., see Kwei, G.H. 44
 Beyermann, W.P., see Robinson, R.A. 47
 Bhagat, R.P., see Tripathy, T. 361
 Bhat, G.A. 315
 Bhatt, A., see Laali, K.K. 308
 Bhatt, M.V. 315
 Bhatt, M.V., see Bhat, G.A. 315
 Bhatt, M.V., see Periasamy, M. 304, 315
 Bhatt, S.S., see Chauhan, G.S. 360
 Bhattacharyya, D., see Mor, G.K. 92, 122, 125–128, 136, 163, 175, 176
 Bhattacharyya, S.N. 356
 Bhuyan, B.L., see Samal, R.K. 360
 Bidoglio, G. 286
 Bied, C. 433
 Bied, C., see Collin, J. 432, 433
 Bied, C., see Kagan, H.B. 430, 432
 Biehl, E., see Sathunuru, R. 338
 Bierman, M.H., see Trahanovsky, W.S. 319
 Bilc, D., see Kim, S.-J. 54, 56
 Bilkis, I., see Hoz, S. 413
 Bini, F., see Bar, G. 302
 Binnemans, K. 314
 Birgeneau, R.J., see Turberfield, K.C. 7
 Birnbaum, N. 289, 290
 Birnbaum, N., see Steigman, J. 289
 Biswal, D.R. 357
 Biswas, S., see Jana, S.C. 360
 Bixon, M., see Barkin, S. 297, 310
 Blackledge, J.P., see Mueller, W.M. 87, 117, 133, 138, 139, 183, 186, 188
 Blaustein, B.D. 301
 Block, H., see Haase, M.G. 28–30, 32, 36, 38–40, 43, 44
 Bloom, I., see Evans, W.J. 432–435, 437, 445, 449, 455
 Bobal, P. 345
 Bobbert, P.A., see van Gelderen, P. 193, 211, 217–220, 224, 226, 231
 Bochkarev, M.N. 395
 Bodak, O. 21, 22
 Bodak, O.I., see Stetskiy, A.O. 59
 Bode, M., see Pundt, A. 147
 Bolotaev, A.G. 17, 19, 20
 Bolotova, G.T., see Golovnyia, V.A. 304
 Bond, A.M. 432
 Bonville, P., see LeBras, G. 39, 41
 Borgschulte, A. 91–93, 103, 151, 161–163, 166, 168, 170–173, 175–179
 Borgschulte, A., see Jacob, A. 91, 147
 Borgschulte, A., see Kierey, H. 211
 Borgschulte, A., see Rode, M. 116, 206–209, 215, 247
 Borgschulte, A., see Schoenes, J. 103, 116
 Boring, A.M., see Eriksson, O. 47
 Borisov, S.V. 69
 Borsa, D., see Dam, B. 90, 195
 Borstel, G., see Chelkowska, G. 57
 Borstel, G., see Ufer, H. 57
 Borzone, G. 4
 Borzone, G., see Parodi, N. 4
 Boschung, E., see Hayoz, J. 91, 146, 151, 160, 202
 Bott, S.G., see Evans, W.J. 452
 Böttcher, P., see Jemetio, J.-P. 35
 Boucherle, J.X., see Alonso, J.A. 7
 Bour, G. 90, 91, 255, 257–259, 266
 Bour, G., see Stepanov, A.L. 255–257, 260
 Bovet, M., see Hayoz, J. 194, 201, 215
 Boyd, P.M., see Field, R.J. 294
 Bracconi, P. 91
 Bracken, K. 370
 Bradley, D.C. 309–312
 Brady, E.K. 458
 Brandt, W.W. 289
 Branum, M.E. 370
 Brauer, G.M. 359

- Brazdil, J.F., see Antonio, M.R. 286
 Brechtel, E. 54
 Bremer, R.F., see Duke, F.R. 319
 Brewster, L.B., see Trahanovsky, W.S. 317
 Brezina, F. 310
 Brilmyer, G., see Marrocco, M. 306
 Briois, V. 319
 Brixius, D.W., see Trahanovsky, W.S. 319, 323
 Brockhaus, R. 304, 322
 Brocks, G., see van Gelderen, P. 193, 210, 211, 217–220, 224, 226, 231
 Brooks, K.C., see Gradeff, P.S. 312
 Broomhall-Dillard, R.N.R., see Evans, W.J. 395, 396
 Brown, G.A., see Molander, G.A. 408
 Brown, G.H., see Larsen, R.D. 300
 Brown, G.L., see Trahanovsky, W.S. 319
 Brown, S.W., see Auty, K. 346
 Bruce, D.W., see King, N.C. 365
 Bruggeman, D.A.G. 235
 Bruice, T.C., see Kasperek, G.J. 296
 Brun, G., see El Kholdi, M. 74
 Brusa, M.A. 294
 Brutti, S., see Parodi, N. 4
 Bryan, G.H., see Surma, J.E. 373
 Bucher, E., see Turberfield, K.C. 7
 Bucher, J.J., see Edelstein, N.M. 285, 286
 Buchwald, S.L., see Radu, N.S. 456
 Bud'ko, S.L., see Petrovic, C. 4, 52, 53
 Bull, S.D. 343
 Burger, M., see Field, R.J. 291
 Burger, U., see Janjic, D. 296
 Burkov, I.C., see Sydnes, L.K. 317
 Burlet, P., see Rossat-Mignod, J. 6
 Burnashova, V.V., see Krypyakevich, P.I. 19
 Burns, C.J., see Radu, N.S. 456
 Burr, R.C., see Fanta, G.F. 358, 359, 361
 Burstyn, J.N., see Hegg, E.L. 367
 Butner, R.S., see Surma, J.E. 373
 Butori, S.M., see Hjörvarsson, B. 206
 Bykov, V.N., see Miron, N.F. 210

 Cabri, W. 421
 Cahard, D., see Ma, J.-A. 438
 Cai, K., see Shi, Q.Z. 345
 Caira, M.R., see du Preez, J.G.H. 310
 Calderwood, F.W., see Gschneidner Jr., K.A. 188
 Callery, P.C., see Jacob III, P. 325
 Calvert, J.D., see Yoshihara, K. 3, 4, 6–9
 Calvert, L.D., see Wang, Y. 4, 6, 24
 Canché-Escamilla, G., see Vera-Pacheco, M. 357
 Candiani, I., see Cabri, W. 421
 Caner, H., see Yilmaz, E. 359
 Canfield, P.C. 43, 44, 46, 47
 Canfield, P.C., see Amato, A. 47
 Canfield, P.C., see Fisk, Z. 47
 Canfield, P.C., see Hundley, M.F. 43, 44, 48
 Canfield, P.C., see Kwei, G.H. 44
 Canfield, P.C., see Morelli, D.T. 47
 Canfield, P.C., see Movshovich, R. 47
 Canfield, P.C., see Petrovic, C. 4, 52, 53
 Canfield, P.C., see Robinson, R.A. 43, 45, 47
 Canfield, P.C., see Severing, A. 43, 44
 Canfield, P.C., see Thompson, J.D. 47
 Cao, Y.M. 357
 Capehart, T.W., see Beck, D.D. 286
 Caro, P.E., see Namy, J.L. 431
 Carré, D., see Lemoine, P. 63, 64, 66, 67
 Carsteanu, A.-M., see Schoenes, J. 103, 116
 Casinos, I. 358
 Casinos, I., see Fernández, M.J. 358
 Casolaro, M., see Barbucci, R. 358
 Castagnoli Jr., N., see Jacob III, P. 325
 Castaño, V.M., see Fernández, M.J. 358
 Castellano, I., see Pascual, B. 357
 Castillo, I. 445
 Catteau, J.P., see Cotelte, P. 313
 Catteau, J.P., see Grenier, J.C. 335
 Caughlan, C.N., see Mazhar-ul-Haque, 314
 Cavasino, F.P. 297
 Céolin, R. 63–65
 Cervellati, R., see Cavasino, F.P. 297
 Cesca, S., see Greco, A. 285
 Chai, W., see Horiuchi, C.A. 338
 Chakrabarty, K. 346
 Chamberlain, L.R., see Evans, W.J. 438, 439, 444
 Chan, J.Y. 17, 18, 58
 Chan, W.Y., see Morgan, M.G. 57
 Chandhok, V.K., see Saha, S. 21
 Chandramouli, P., see Huang, R.Y.M. 358
 Chang, A., see Dolg, M. 285
 Chang, F.R., see Pan, W.B. 334
 Chang, J.T., see Wang, M.E. 4, 8
 Chang, K.E. 220, 221
 Chang, K.E., see Alford, J.A. 221–223
 Channell, H., see Meister, J.J. 360
 Chansook, N. 360
 Chapman, R.P., see Walden, G.H. 289
 Charar, S., see El Kholdi, M. 74
 Charar, S., see Gratens, X. 71
 Chatterjee, A.K., see Bradley, D.C. 309–312
 Chatterjee, A.K., see Pramanick, D. 355

- Chauhan, G.S. 360
 Chauvierre, C. 355
 Chawla, H.M. 313, 335, 346
 Chawla, H.M., see Chakrabarty, K. 346
 Chebolu, V. 427
 Chechernikov, V.I. 61
 Chełkowska, G. 57
 Chełkowska, G., see Ufer, H. 57
 Chełkowski, A., see Chełkowska, G. 57
 Chełkowski, A., see Jarosz, J. 57
 Chen, C. 309
 Chen, C.Y., see Hsu, W.C. 355
 Chen, H.-H., see Lu, Y.-M. 32, 34, 35
 Chen, H.H., see Lu, Y.M. 48, 49
 Chen, L. 20, 72, 73
 Chen, W. 370
 Chen, Y., see Armitage, R. 97, 233, 267, 268
 Chen, Y.R., see Don, T.M. 358
 Chen, Z.C., see Zheng, S.Y. 360
 Cheng, R.S., see Liu, M.Z. 361
 Cheng, Y.T., see Li, Y. 119
 Chepovoy, V.I., see Lebedev, I.A. 376
 Cheprakov, A.V., see Maknon'kov, D.I. 327
 Chernikov, M., see Thompson, J.D. 47
 Cherstvova, V.B., see Rustamov, P.G. 71, 72
 Cherstvova, V.B., see Sadygov, F.M. 71, 72
 Chidambaram, S., see Jayaraman, K. 353
 Chilingarov, N.S., see Rau, J.V. 312
 Chin, J., see Kim, J.H. 366
 Chin, J., see Takasaki, B.K. 366
 Chin, J., see Williams, N.H. 366
 Chiu, W.Y., see Don, T.M. 358
 Cho, B.K. 42
 Cho, I. 361
 Cho, L.Y. 302, 314, 323, 351, 353
 Cho, L.Y., see Aleixo, P.C. 353
 Cho, Y.S., see Huiberts, J.H. 88, 90–92, 98–100,
 103, 104, 107, 112, 113, 116–118, 123, 133, 136,
 163, 167, 183, 214, 224
 Choi, H.W., see Evans, W.J. 434
 Chopade, P.R. 414, 428
 Chopade, P.R., see Davis, T.A. 423
 Choppin, G.R., see Rizkalla, E.N. 283
 Chou, M.Y., see Alford, J.A. 221–223
 Chou, M.Y., see Wang, Y. 208, 224, 226
 Chou, T.C., see Jow, J.J. 353
 Chowdhury, P. 359, 360
 Chowdhury, P., see Goswami, P. 334
 Christianson, A., see Robinson, R.A. 47
 Christoffers, J. 285, 346, 348
 Christoffers, J., see Rössle, M. 285, 348
 Chuiko, A.G., see Abdusalyamova, M.N. 4, 10
 Chung, S.J., see Jung, B.O. 359
 Church, V.E. 372
 Chykhrij, S., see Kuz'ma, Y. 3
 Ciccioli, A., see Parodi, N. 4
 Cichacz, E., see Skarzewski, J. 301, 302
 Cichorek, T., see Kaczorowski, D. 39, 41, 49–51
 Claassen, A. 290
 Clark, C.F., see Reyes, Z. 361
 Clark, D.L., see Brady, E.K. 458
 Clark, N., see Azofeifa, D.E. 89, 98, 130, 138,
 145–147
 Clark, S.J., see Rushton, P.P. 224
 Clarke, R. 350
 Cleve, P.T. 310
 Coenen, H.H., see Mennicke, E. 334
 Coey, J.M.D. 21–23
 Cohen, R.E., see Wu, Z. 224, 226, 227
 Collin, J. 432, 433
 Collin, J., see Bied, C. 433
 Collin, J., see Kagan, H.B. 430, 432
 Colomb, M., see Namy, J.L. 396, 425
 Colombo, M., see Cabri, W. 421
 Colussi, A.J., see Brusa, M.A. 294
 Comnor, D.W., see Rush, J.J. 113
 Concellon, J.M. 396
 Conesa, J.C., see Hernandez-Alonso, M.D. 312
 Conway, S.P., see Myers, R.M. 400
 Cook, J.M., see Lannoye, G. 407
 Cooper, S.R., see Sofen, S.R. 376
 Corbett, J.D. 11
 Corbett, J.D., see Chen, L. 20, 72, 73
 Corbett, J.D., see Guloy, A.M. 59
 Corbett, J.D., see Hung, W.-M. 11, 75
 Corbett, J.D., see Jensen, E.A. 74, 75
 Corbett, J.D., see Kwon, Y.-U. 19
 Corbett, J.D., see Leon-Escamilla, E. 10, 11
 Corbett, J.D., see Leon-Escamilla, E.A. 4, 8, 10
 Cordier, G. 59
 Cordier, G., see Brechtel, E. 54
 Corey, E.J., see Singh, A.K. 410
 Corley, E., see Weinstock, L.M. 304
 Coronado, J.M., see Hernandez-Alonso, M.D. 312
 Correa, P.E., see Riley, D.P. 350
 Cotellet, P. 313
 Cotellet, P., see Grenier, J.C. 335
 Cotton, S.A. 395, 438
 Coutinho, F.M.B. 355
 Couvreur, P., see Chauvierre, C. 355
 Cowan, J.A., see Sreedhara, A. 366
 Cozzi, D. 285

- Cramer, J., see Trahanovsky, W.S. 320, 323
 Creager, S.E., see Paulenova, A. 304
 Cross, A.R., see Gao, Y. 298
 Csuk, R., see Furstner, A. 402
 Cummings, C.M., see Basceri, C. 372
 Cunningham, B.B. 312
 Cupone, G., see Bartoli, C. 308
 Curran, D.P. 406, 420
 Curran, D.P., see Fevig, T.L. 405
 Curran, D.P., see Studer, A. 400
 Curran, D.P., see Totleben, M.J. 396
 Curzon, A.E. 90, 91
 Cushnyr, B., see Laali, K.K. 308
 Cyric, I., see Pastor, T.J. 288
- Daasbjerg, K., see Enemarke, R.J. 420, 421
 Dahlen, A. 410, 413, 414, 422, 423, 470
 Dahlén, A., see Kim, M. 463
 Dai, C., see Dai, D. 21
 Dai, C., see Fang, R. 21
 Dai, D. 21
 Dai, D., see Fang, Q. 21
 Dai, D., see Fang, R. 21
 Dalal, N.S., see Neumann, B. 294
 Dallemer, F., see Kagan, H.B. 430, 432
 Dalpozzo, R., see Bartoli, C. 308
 Dam, B. 90, 195
 Dam, B., see Borgschulze, A. 92, 93, 103, 163, 166, 175, 176, 178
 Dam, B., see den Broeder, F.J.A. 103, 120, 141, 167, 197–199, 215, 266
 Dam, B., see Huiberts, J.H. 88, 90–92, 98–100, 103, 104, 107, 112, 113, 116–118, 123, 133, 136, 163, 167, 183, 214, 224
 Dam, B., see Kerssemakers, J.W.J. 147–152, 160, 266
 Dam, B., see Kooi, B.J. 151, 154, 157–159
 Dam, B., see Kooij, E.S. 154–157
 Dam, B., see Lokhorst, A.C. 195, 196, 260
 Dam, B., see Nagengast, D.G. 89, 91, 147, 148, 150, 151, 153, 154, 228–230, 232, 246, 266
 Dam, B., see van der Molen, S.J. 91, 92, 103, 119, 163–169, 175, 177
 Dam, B., see van Mechelen, J.L.M. 90
 Dancso, A., see Nagygyory, S. 294
 Danieli, B. 323
 Danon, L., see Soupe, J. 400
 Daou, J.N., see Vajda, P. 87
 Darr, J.A., see Baxter, I. 314
 Das, H.K., see Das, N.R. 359
 Das, H.K., see Mohanty, N. 361
 Das, H.K., see Nayak, N.C. 359
 Das, N.R. 359
 Daugherty, N.A. 307
 Davenport, J.W., see Pick, M.A. 91
 David, L.D., see Acocella, J. 372
 Davies, S.G., see Bull, S.D. 343
 Davis, D.G., see Lingane, J.J. 284
 Davis, T.A. 423
 Davis, T.A., see Chopade, P.R. 428
 Day, V.W., see Hillier, A.C. 466
 De Battisti, A., see Ferro, S. 285
 de Boer, T.J., see Schaafsma, S.E. 320
 de Groot, D.G., see Huiberts, J.H. 88–92, 96, 98–101, 103, 104, 107, 112, 113, 116–118, 120–123, 133, 136, 163, 166, 167, 183, 208, 214, 224
 De Hosson, J.Th.M., see Kooi, B.J. 151, 154, 157–159
 De Nino, A., see Bartoli, C. 308
 de Wet, J.F., see du Preez, J.G.H. 310
 Deacon, G.B., see Bond, A.M. 432
 Deakin, L., see Mills, A.M. 75
 Deakin, L., see Sykora, R.E. 286
 Dechert, S., see Bochkarev, M.N. 395
 Degtyar, V.A. 57
 Dehmow, E.V. 301, 308, 309
 Dehner, B., see Shinar, J. 87, 207, 214
 Dekker, J.P. 208, 221
 Dekker, J.P., see Griessen, R. 98, 103, 116, 117, 120, 224
 Dekker, J.P., see Huiberts, J.H. 88, 89, 91, 96, 101, 103, 107, 113, 120–122, 133, 136, 166, 208, 214, 224
 Dekker, J.P., see Kelly, P.J. 202, 203, 206, 209–211, 222, 224
 Del Giacco, T. 364
 Del Giacco, T., see Baciocchi, E. 364
 Delacote, D., see Rossat-Mignod, J. 6
 Delgaudio, J., see Beineke, T.A. 300, 301
 Della Cort, A. 317
 Della Cort, A., see Baciocchi, E. 317
 Deming, T.J., see Evans, W.J. 286, 312
 den Broeder, F.J.A. 103, 120, 141, 167, 197–199, 215, 266
 Deniszczyk, J., see Drzyzga, M. 4
 Denney, R.C., see Bassett, J. 286, 288
 Deportes, J., see El Kholdi, M. 74
 Désévéday, F. 58
 Deshmukh, S.R. 356
 Desideri, P.G. 285
 Desideri, P.G., see Cozzi, D. 285

- Deslongchamps, P., see Soucy, P. 321, 323
 Despault, J.G., see Yoshihara, K. 3, 4, 6–9
 Dessau, R.M., see Heiba, E.I. 306, 318
 Devadoss, V. 353
 Devadoss, V., see Jayaraman, K. 353
 Dhar, S.K. 39, 41
 Dhar, S.K., see LeBras, G. 39, 41
 Di Vece, M. 91, 97, 98, 103, 119–121, 139, 140, 142, 244–249
 Di Vece, M., see Giebels, I.A.M.E. 90, 91, 98, 103, 235, 236
 Di Vece, M., see Isidorsson, J. 90
 Dickinson, C., see King, N.C. 365
 Dienes, G.J., see Pick, M.A. 91
 Dikareva, L.M., see Rogachev, D.L. 304, 305
 Dinçer, B. 355
 Dinçtürk, S. 334, 335
 DiSalvo, F.J., see Cho, B.K. 42
 DiSalvo, F.J., see Gordon, R.A. 39, 42
 Dlask, V., see Sirimungkala, A. 295
 Doane, W.M., see Fanta, G.F. 359
 Dobbins, M., see Touchstone, J. 371
 Dobrowolska, A., see Remhof, A. 103, 270, 271
 Doedens, R.J., see Evans, W.J. 441, 449
 Doert, Th., see Jemetio, J.-P. 35
 Dogra, R., see Misra, B.N. 362
 Dolg, M. 285
 Domagała, S. 321
 Domingos, A., see Hillier, A.C. 466
 Don, T.M. 358
 Dong, J.H. 355
 Dornheim, M. 103, 119
 Dorransoro, I., see Rodriguez-Franco, M.I. 329
 Doyle, M.P. 321
 Dreier, F., see Reyes, Z. 361
 Drikvand, F., see Heravi, M.M. 313
 Drummond, D.K., see Evans, W.J. 452–454, 456, 458
 Drymiotis, P., see Morelli, D.T. 47
 Drzyzga, M. 4, 8, 9
 Du, D.H., see Wang, D.F. 363
 du Preez, J.G.H. 310
 du Preez, J.G.H., see Barry, J. 309
 Dubey, R., see Mishra, A. 360
 Duine, P.A., see den Broeder, F.J.A. 103, 120, 141, 167, 197–199, 215, 266
 Duine, P.A., see Kremers, M. 92, 97–99, 103–105, 163, 175
 Duine, P.A., see van der Sluis, P. 89–91, 227, 233, 242, 244
 Duine, P.A., see von Rottkay, K. 90–93, 97, 128–130, 136, 239–241, 243–246, 249, 250, 267
 Duke, F.R. 319, 372
 Duke, F.R., see Wadsworth, E. 284, 306
 Dulz, G. 289
 Dunlap, N.K., see Smith III, A.B. 399
 Durbin, P., see Gorden, A.E.V. 375
 Duro, R.J., see Martins, G.B. 46
 Dust, L.A. 316
 Dwight, A.E. 32, 36, 40, 43–45
 Dzhafarova, E.K. 70, 71
 Dzhafarova, E.K., see Sadygov, F.M. 70, 71
 Dziegieć, J., see Domagała, S. 321
 Dziegieć, J., see Grzejdziaak, A. 321
 Dziegieć, J., see Ignaczak, M. 321
 Dziegieć, J., see Prawicki, K. 321
 Ebel, G., see Behrens, H. 117
 Ebel, T., see Prill, M. 10, 13
 Ebersohn, L., see Baciocchi, E. 317
 Eberspacher, T.A., see Hillier, A.C. 466
 Ebhoaye, J.E., see Okieimen, E.F. 356, 358, 363
 Eckert, D., see Wosnitza, J. 46
 Ecrepont, C. 63, 64, 68, 69
 Edelson, D. 294
 Edelstein, N.M. 285, 286
 Eder, R. 107, 198, 199, 212–214, 216, 222, 231
 Edmonds, S.M., see Birnbaum, N. 289, 290
 Edmonds, S.M., see Steigman, J. 289
 Edwards, J.W., see Milner, G.W.C. 15
 Edwards, R.K., see Yannopoulos, L.N. 88, 116, 117, 183
 Effantin, J.M., see Rossat-Mignod, J. 6
 Egharevba, F., see Okieimen, E.F. 359, 361
 Egorova, V.P., see Nikitina, G.P. 285
 Eisenmann, B., see Cordier, G. 59
 El Kholdi, M. 74
 El-faqeeh, A.S., see Fares, M.M. 361
 El-Gammal, A.A., see Nagieb, Z.A. 358
 El-Halwagy, A.A., see El-Molla, M.M. 361
 El-Kalyoubi, S.F., see El-Shinnawy, N.A. 359
 El-Molla, M.M. 361
 El-Rafie, M.H., see Kantouch, A. 359, 362
 El-Sayad, H.S., see El-Molla, M.M. 361
 El-Shinnawy, N.A. 359
 Elliot, R.L., see Fevig, T.L. 405
 Els, E., see Barry, J. 309
 Elsgood, M.R.J., see Hillier, A.C. 468
 Emerson, G.F. 343
 Emsley, J. 283
 Enache, S. 90
 Endo, T., see Namura, R. 470

- Enemark, R.J. 420, 421
 Engelmann, P., see Schneider, W. 170
 Enholm, E.J. 402
 Ephritikhine, M., see Berthet, J.C. 308
 Epstein, I.R., see Jacobs, S.S. 293, 296
 Erciyes, A.T., see Erim, M. 355
 Erdely, L., see Bányai, É. 289
 Eriksson, O. 47
 Eriksson, O., see Ahuja, R. 231
 Eriksson, O., see Hjörvarsson, B. 206
 Erim, M. 355
 Eromosele, I.C. 360
 Eromosele, C.O., see Eromosele, I.C. 360
 Erwin, R., see Robinson, R.A. 43, 45, 47
 Erwin, R.W., see Udovic, T.J. 222
 Eschrig, H., see Oppeneer, P.M. 47
 Esser, L., see Schumann, H. 431
 Etter, J.B., see Molander, G.A. 401, 402, 417
 Evans, D.A. 397, 399
 Evans, O.M., see Furman, N.H. 286, 287
 Evans, W.J. 286, 312, 395, 396, 420, 427, 431–441, 443–445, 448–458
 Evans, W.J., see Moss, M.A.J. 466
 Ewing, D.T. 290
 Exner, M., see Herrmann, H. 364
 Eyring, L., see Haire, R.G. 283
- Fabian, P., see Treindl, L. 297
 Fagin, A.A., see Bochkarev, M.N. 395
 Fakhru'l-Razi, A. 360
 Falconer, W.E., see Kaiser, E.W. 312
 Fang, Q. 21
 Fang, Q., see Fang, R. 21
 Fang, R. 21
 Fang, R., see Dai, D. 21
 Fang, R., see Fang, Q. 21
 Fang, T.R. 360
 Fanta, G.F. 358, 359, 361
 Fanta, G.F., see Patil, D.R. 361
 Farag, S. 358
 Farangis, B., see Richardson, T.J. 90
 Fares, M.M. 358, 361
 Farkas, H., see Noszticzus, Z. 294
 Fau, C., see El Kholdi, M. 74
 Fau, C., see Gratens, X. 71
 Feay, D.C., see Cunningham, B.B. 312
 Fedushkin, I.L., see Bochkarev, M.N. 395
 Feibush, A.M., see Gordon, L. 284
 Feigl, F. 372
 Felder, E., see Fisk, Z. 47
 Felder, E., see Thompson, J.D. 47
- Feldman, K.S. 400
 Felker, F.C., see Fanta, G.F. 359, 361
 Feng, X.D. 360
 Feng, X.D., see Dong, J.H. 355
 Fenton, G., see Bull, S.D. 343
 Ferguson, M.J. 18
 Ferguson, M.J., see Mills, A.M. 75
 Ferhat, M., see Gratens, X. 71
 Fernández, M.D. 355
 Fernández, M.D., see Fernández, M.J. 358
 Fernández, M.J. 358
 Fernández, M.J., see Fernández, M.D. 355
 Fernandez-Garcia, M., see Hernandez-Alonso, M.D. 312
 Ferreira, M.I.C., see Purgato, F.L.S. 353
 Ferrer Jiménez, C., see Matveeva, E.S. 93, 97, 103, 267
 Ferris, L.M., see Smith, F.J. 32, 38
 Ferro, R., see Borzone, G. 4
 Ferro, R., see Marazza, R. 32, 36, 38, 40, 43, 44
 Ferro, R., see Riani, P. 38–41
 Ferro, S. 285
 Ferruti, P., see Barbucci, R. 358
 Fevig, T.L. 405
 Feyerherm, R., see Amato, A. 47
 Field, R.J. 291, 292, 294, 295
 Field, R.J., see Edelson, D. 294
 Field, R.J., see Hegedus, L. 295
 Field, R.J., see Noyes, R.M. 292, 294
 Field, R.J., see Sirimungkala, A. 295
 Field, R.M. 294
 Finkel'shtein, L.D., see Aliev, O.M. 63, 64, 69–73
 Finkenstadt, V.L., see Willett, J.L. 361
 Firouzabadi, H. 309–311, 326, 332
 Firouzabadi, H., see Iranpoor, N. 308
 Fischer, A. 313, 322
 Fischer, K.H., see Loewenhaupt, M. 283
 Fisher, P. 9
 Fisk, Z. 47
 Fisk, Z., see Amato, A. 47
 Fisk, Z., see Canfield, P.C. 43, 44, 46, 47
 Fisk, Z., see Hundley, M.F. 43, 44, 48
 Fisk, Z., see Kwei, G.H. 44
 Fisk, Z., see Martins, G.B. 46
 Fisk, Z., see Movshovich, R. 47
 Fisk, Z., see Pagliuso, P.G. 46
 Fisk, Z., see Robinson, R.A. 47
 Fisk, Z., see Severing, A. 43, 44
 Fisk, Z., see Thompson, J.D. 47
 Fitzpatrick, J.D., see Watts, L. 343
 Flahaut, J., see Ecrepont, C. 63, 64, 68, 69

- Flendorfer, H. 32, 34, 48, 49
 Flendorfer, H., see Kaczorowski, D. 39, 41, 49–51
 Flannery, B.P., see Preuss, W.H. 243
 Flash, P.J., see Trahanovsky, W.S. 321
 Flipse, C.F.J., see van Gogh, A.T.M. 89, 97, 98,
 116, 120–122, 186–195, 217, 224, 226
 Flotow, H.E. 88, 117, 183
 Flowers II, R.A., see Chopade, P.R. 414, 428
 Flowers II, R.A., see Davis, T.A. 423
 Flowers II, R.A., see Fuchs, J.R. 418, 430
 Flowers II, R.A., see Kim, M. 463
 Flowers II, R.A., see Knettle, B.W. 431
 Flowers II, R.A., see Miller, R.S. 418, 430
 Flowers II, R.A., see Prasad, E. 420, 421, 458, 462
 Flowers II, R.A., see Shotwell, J.B. 420
 Flowers II, R.A., see Zhang, Y. 309, 359
 Flowtow, H.E., see Rush, J.J. 113
 Fly, W.H., see Smith, G.F. 287
 Fokin, A.A. 364
 Fonda, E., see Briois, V. 319
 Forbes, D.C., see Enholm, E.J. 402
 Forist, A.A., see Duke, F.R. 319
 Fornasiero, P., see Kašpar, J. 283
 Fornasini, M.L., see Merlo, F. 49–51
 Försterling, H.D. 294
 Försterling, H.D., see Field, R.M. 294
 Försterling, H.D., see Gao, Y. 294
 Försterling, H.D., see Hegedus, L. 295
 Försterling, H.D., see Nagygyory, S. 294
 Försterling, H.D., see Oslonovitch, J. 294
 Försterling, H.D., see Petruscu, A.M. 297
 Försterling, H.D., see Sirimungkala, A. 294, 295
 Foster, S.E., see Evans, W.J. 427
 Fragala, I.L., see Lanza, G. 312
 Frahm, R., see Briois, V. 319
 Francesconi, L.C., see Antonio, M.R. 286
 Francisca, L.J., see Reddy, G.V.R. 355
 Franck, U.F. 291
 Frank, G., see Smith, G.F. 287, 299, 300
 Franklin, S.J. 366
 Franzen, H.F., see Mozharivskyj, Y. 31, 33, 37, 39,
 41, 43, 44, 48
 Franzen, H.F., see Zeng, L. 32, 34, 35
 Franzoi, L., see Cabri, W. 421
 Fraser, H.J., see Church, V.E. 372
 Freeman, G.E., see Raymond, K.N. 375
 Frey, W., see Christoffers, J. 285, 346, 348
 Frey, W., see Rössle, M. 285, 348
 Freyberg, D.P., see Sofen, S.R. 376
 Fritz, J.S. 290
 Fritz, J.S., see Smith, G.F. 289
 Fromhold Jr., A.T. 174
 Fu, Z.F., see Li, Z.C. 359
 Fuchs, J.R. 418, 430
 Fuchs, J.R., see Miller, R.S. 418, 430
 Fuginami, T., see Fukuzawa, S. 403
 Fujieda, S. 298
 Fujii, A., see Yoneyama, M. 298
 Fujimori, A., see Oh, S.-J. 74
 Fujishima, A., see Maeda, Y. 285
 Fujita, A., see Hou, Z. 454, 459, 463
 Fujita, K., see Yan, J.M. 369
 Fukami, S., see Takashima, M. 312
 Fukumura, H., see Kasuya, M. 298
 Fukushima, T., see Horiuchi, C.A. 338
 Fukuzawa, S. 403
 Fukuzawa, S.-I., see Hou, Z. 455, 461, 465
 Fulda, M.O., see Fritz, J.S. 290
 Fulde, P., see Dolg, M. 285
 Fulde, P., see Neumann, C.S. 285
 Fung, A.P., see Olah, G.A. 345
 Furman, N.H. 286, 287, 289, 290
 Furstner, A. 402
 Furtado, C.R.G., see Coutinho, F.M.B. 355
 Furuta, N., see Horiuchi, C.A. 338
 Gabe, E.J., see Wang, Y. 4, 6, 24
 Galatanu, A., see Thamizhavel, A. 34, 36, 48
 Galdecka, E., see Bodak, O. 21, 22
 Gallagher, T., see Anathanarayan, T.P. 399
 Galli, C. 329
 Gambino, R.J. 6–9, 14
 Ganapathisubramanian, N. 297
 Ganiev, I.N., see Abulkhaev, V.D. 4, 10
 Ganin, E. 345
 Ganz, Th., see Schneider, W. 170
 Gao, Y. 294, 298
 Garibov, F.A. 63, 64, 68, 69
 Garner, C.S., see Noyes, A.A. 284
 Gartz, M. 255
 Gartz, M., see Stepanov, A.L. 255–257
 Garzan, A., see Firouzabadi, H. 332
 Gasymov, V.A., see Mamedova, S.G. 69, 71
 Gautier, A., see Marko, I.E. 343
 Ge, X.C. 359
 Geidarova, E.A., see Sadygov, F.M. 71–73
 Geilmann, W. 289
 Gelato, L.M. 3
 Gelato, L.M., see Parthé, E. 3
 George, T.G., see Nair, V. 327, 338, 339
 Gerboc, J., see Washko, S. 28
 Getz, C.A., see Smith, G.F. 284, 306

- Getzlaff, M., see Pundt, A. 147
 Geyer, U., see Dornheim, M. 103, 119
 Ghassemzadeh, M., see Aghapoor, K. 313
 Ghassemzadeh, M., see Heravi, M.M. 311, 313
 Ghoumari-Bouanani, H., see El Kholdi, M. 74
 Giarikos, D.G., see Evans, W.J. 451
 Gibbs, R.S., see Baker, I. 290
 Gibson, J.K. 312
 Gibson, P.N., see Bidoglio, G. 286
 Giebels, I.A.M.E. 90, 91, 98, 103, 234–236, 243, 250–253
 Giebels, I.A.M.E., see Isidorsson, J. 90, 91, 233, 235, 237–239
 Giebels, I.A.M.E., see Lokhorst, A.C. 195, 196, 260
 Gigli, G., see Parodi, N. 4
 Gilbert, B.C., see Auty, K. 346
 Gileadi, E. 134
 Gill, E.W., see Dust, L.A. 316
 Gillow, E.W., see Watt, G.W. 431
 Gilmore, J.R., see Trahanovsky, W.S. 319
 Girard, P. 395–398, 401, 402, 404, 434
 Girard, P., see Kagan, H.B. 402
 Girard, P., see Namy, J.L. 431
 Glaeser, L.C., see Antonio, M.R. 286
 Glass, R.W. 364
 Glass, R.W., see Martin, T.W. 364
 Glavee, G.N., see Overbury, S.H. 286
 Gleu, K. 289
 Godart, C., see Flandorfer, H. 32, 34, 48, 49
 Godzhaev, E.M. 63, 70, 71, 73
 Godzhaev, E.M., see Rustamov, P.G. 63, 64, 70
 Goetz, O.A., see Wadsworth, E. 284, 306
 Gofryk, K., see Kaczorowski, D. 41
 Golacki, Z., see Gratens, X. 71
 Goldstone, J.A., see Kwei, G.H. 44
 Goll, G. 45, 46
 Goll, G., see Wosnitza, J. 46
 Golovnya, V.A. 304
 Gomes, A.S., see Coutinho, F.M.B. 355
 Goñi, I. 357
 Goñi, I., see Gurruchaga, M. 357
 Goñi, I., see Pascual, B. 357
 Goñi, I., see Vázquez, B. 359
 Goñi, I., see Vázquez, M.B. 357
 Gonzales, S.L., see Evans, W.J. 440
 Gopalan, A., see Paulrajan, S. 355
 Gorden, A.E., see Xu, J.D. 376
 Gorden, A.E.V. 375
 Gordon, L. 284
 Gordon, R.A. 39, 42
 Gordon, R.A., see Cho, B.K. 42
 Goryachenkov, S.A., see Kiselev, Yu.M. 312
 Goswami, P. 334
 Goto, T., see Kim, M.-S. 43, 45, 47
 Goto, T., see Suzuki, H. 43, 46
 Gracheva, N.V., see Chechernikov, V.I. 61
 Graczyk, T. 358
 Gradeff, P.S. 312
 Graettinger, T.M., see Basceri, C. 372
 Gramer, C.J. 376
 Grant, A.J. 309
 Grant, D. 365
 Grate, J.W., see Evans, W.J. 434, 436, 437, 449
 Gratens, X. 71
 Graziani, M., see Kašpar, J. 283
 Greco, A. 285
 Greef, R. 285
 Greeting, J.G.H., see Surma, J.E. 373
 Greeves, N., see Aspinall, H.C. 470
 Grenier, J.C. 335
 Grier, E.R. 147
 Griesebock, B., see Briois, V. 319
 Griessen, R. 88, 89, 98, 103, 116, 117, 120, 224
 Griessen, R., see Borgschulte, A. 92, 93, 103, 163, 166, 175, 176, 178
 Griessen, R., see den Broeder, F.J.A. 103, 120, 141, 167, 197–199, 215, 266
 Griessen, R., see Dornheim, M. 103, 119
 Griessen, R., see Enache, S. 90
 Griessen, R., see Giebels, I.A.M.E. 90, 91, 98, 103, 234–236, 243, 250–253
 Griessen, R., see Hoekstra, A.F.Th. 103, 108, 110–112, 215, 266
 Griessen, R., see Huiberts, J.H. 88–92, 96, 98–101, 103, 104, 107–109, 112, 113, 116–118, 120–123, 133, 136, 163, 166, 167, 183, 208, 214, 224
 Griessen, R., see Isidorsson, J. 90, 91, 233, 235, 237–239
 Griessen, R., see Kerssemakers, J.W.J. 147–152, 157, 160, 266
 Griessen, R., see Kooij, E.S. 93–98, 101, 103, 105, 106, 111, 116–118, 126, 127, 133, 136, 137, 148–150, 154–157, 180, 182, 183, 185, 186, 204
 Griessen, R., see Kremers, M. 92, 97–99, 103–105, 163, 175
 Griessen, R., see Nagengast, D.G. 89, 91, 147, 148, 150, 151, 153, 154, 228–230, 232, 246, 266
 Griessen, R., see Notten, P.H.L. 93, 94, 97, 103, 104, 133
 Griessen, R., see Remhof, A. 103, 118, 185, 186, 270–272

- Griessen, R., see Roy, A.S. 108, 215, 266
 Griessen, R., see van der Molen, S.J. 91, 92, 103, 119, 163–169, 175, 177, 197–202, 211, 215, 228, 229, 231–233, 246, 266
 Griessen, R., see van Gogh, A.T.M. 89, 92, 93, 97, 98, 103, 116, 118, 120–122, 163, 173–175, 184–195, 203–206, 211, 217, 224, 226
 Griessen, R., see van Mechelen, J.L.M. 90
 Griffith, W.P. 310, 346
 Grin, Yu.N., see Sichevich, O.M. 23
 Grin, Yu., see Kaczorowski, D. 41
 Gross, R.C., see Martin, T.W. 364
 Grund, I. 10, 11, 13
 Gryder, J.W., see Blaustein, B.D. 301
 Grzejdziaik, A. 321
 Gschneidner Jr., K.A. 188
 Gschneidner Jr., K.A., see Niu, X.J. 60, 61
 Gschneidner Jr., K.A., see Pecharsky, A.O. 15, 17
 Gu, S.J., see Wang, Y.P. 370
 Guimarães, M.J.O.C., see Coutinho, F.M.B. 355
 Guin, C., see Roy, S.C. 327–329
 Guittard, M., see Ecrepont, C. 63, 64, 68, 69
 Guittard, M., see Lemoine, P. 63, 64, 66, 67
 Guloy, A.M. 59
 Gummersheimer, T.S., see Evans, W.J. 420, 427, 457
 Gunchenko, P.A., see Fokin, A.A. 364
 Güner, S. 46
 Gunther, R., see Kerssemakers, J.W.J. 147–152, 157, 160, 266
 Guo, J.-H., see Hjörvarsson, B. 206
 Gupta, B.G.B., see Olah, G.A. 345
 Gupta, B.S., see McDowall, D.J. 356
 Gupta, K.C. 355, 357, 358
 Gupta, M., see Wu, Z. 224, 226, 227
 Gupta, R., see Mishra, A. 360
 Gupta, R., see Wu, Z. 224, 226, 227
 Gupta, Y.K., see Indrayan, A.K. 365
 Gurruchaga, M. 357
 Gurruchaga, M., see Goñi, I. 357
 Gurruchaga, M., see Pascual, B. 357
 Gurruchaga, M., see Vázquez, B. 359
 Gurruchaga, M., see Vázquez, M.B. 357
 Guseinov, M.S., see Godzhaev, E.M. 63, 70, 71, 73
 Guseinov, M.S., see Rustamov, P.G. 63, 64, 70
 Gusev, D.V., see Fokin, A.A. 364
 Guthoff, F., see Remhof, A. 117, 146, 151, 210
 Guthrie, F.K. 358
 Guthrie, St., see Hayoz, J. 194, 201
 Guzmán, G.M., see Fernández, M.D. 355
 Guzmán, G.M., see Fernández, M.J. 358
 Guzman, G.M., see Goñi, I. 357
 Guzmán, G.M., see Gurruchaga, M. 357
 Guzmán, G.M., see Riande, E. 360
 Guzmán, G.M., see Vázquez, M.B. 357
 Gyenge, R. 294
 Gygax, F.N., see Amato, A. 47
 Györgyi, L., see Varga, M. 295
 Haaksma, M., see den Broeder, F.J.A. 103, 120, 141, 167, 197–199, 215, 266
 Haase, M.G. 28–30, 32, 36, 38–40, 43, 44
 Haddad, S., see Bar-Eli, K. 297
 Haddad, S.F. 376
 Haen, P., see Bartholin, H. 74
 Haen, P., see Sera, M. 74
 Haga, Y., see Kasuya, T. 14
 Hagel, J., see Goll, G. 45, 46
 Hagel, J., see Wosnitzka, J. 46
 Hahn, G., see Molander, G.A. 399
 Haire, R.G. 283
 Haire, R.G., see Gibson, J.K. 312
 Hajipour, G., see Firozabadi, H. 310
 Hakimelahi, G.H., see Hwu, J.R. 313, 343
 Hålg, W., see Fisher, P. 9
 Hall, T.W., see Ho, T.L. 314, 322
 Haltier, E., see Bidoglio, G. 286
 Hamann, B. 425
 Hammann, J., see LeBras, G. 39, 41
 Hammer, B. 171
 Hammett, L.P., see Walden, G.H. 289
 Han, T.L. 360
 Hanamoto, T., see Yoshida, A. 411
 Hanna, S.B. 323
 Hansen, P. 23
 Hansen, S.H., see Sydnes, L.K. 317
 Hanusa, T.P., see Evans, W.J. 435
 Hanzen, R.M.N., see den Broeder, F.J.A. 103, 120, 141, 167, 197–199, 215, 266
 Harata, M., see Kurita, K. 360
 Hardwick, T.J. 304
 Harmon, B.N., see Peterman, D.J. 105, 191, 205
 Harms, H., see Dornheim, M. 103, 119
 Haron, J., see Lutfor, M.R. 360
 Haron, J., see Rahman, L. 360
 Harris, C.R., see Molander, G.A. 407
 Harrison, S. 352, 353
 Harrison, S., see Mahdavi, B. 353
 Hart, F.A., see Mazhar-ul-Haque, 314
 Hartmann, M. 23
 Hartmann, M., see McGuire, T.R. 23
 Hasegawa, M., see Onishi, Y. 359

- Hashimoto, C., see Horiuchi, C.A. 338
 Hasipoglu, H., see Yilmaz, E. 359
 Hatanaka, K., see Kasuya, M. 298
 Hatanaka, Y. 314, 348
 Hatano, T., see Akane, N. 424
 Hauser, M.J.B., see Neumann, B. 294
 Hay, N. 304
 Hayakawa, H., see Nomura, K. 4, 6
 Hayon, E. 364
 Hayoz, J. 91, 146, 151, 160, 161, 194, 201–204, 215
 He, L. 304
 Heaton, P.C., see Trahanovsky, W.S. 319
 Hebeish, A. 358
 Hebeish, A., see Abdel-Hay, F.I. 362
 Hebeish, A., see Kantouch, A. 359, 362
 Hecht, S.S., see Balanikas, G. 314
 Hecker De Carvalho, L. 362
 Heckman, R.C. 107, 112
 Heffner, R.H., see Amato, A. 47
 Heffner, R.H., see Canfield, P.C. 47
 Hegedus, L. 295
 Hegedus, L., see Nagygyory, S. 294
 Hegg, E.L. 367
 Heiba, E.I. 306, 318
 Heidt, L.J. 307, 365
 Heijna, M.C.R., see Dam, B. 90, 195
 Heijna, M.C.R., see Lokhorst, A.C. 195, 196, 260
 Heitmann, H. 23
 Hélion, F. 430, 470
 Henderson, G.N., see Fischer, A. 313, 322
 Henshall, A., see Martin, T.W. 364
 Heravi, M.M. 311, 313
 Heravi, M.M., see Aghapoor, K. 313
 Heravi, M.M., see Oskooie, H.A. 311
 Herbert, M., see Laali, K.K. 308
 Hernandez-Alonso, M.D. 312
 Hernandez-Higueras, A.I., see Rodriguez-Franco, M.I. 329
 Herrmann, H. 364
 Hertz, T., see Enemark, R.J. 420, 421
 Herzig, P., see Wolf, W. 222, 224, 225
 Hess, B., see Müller, S.C. 298
 Hess, B., see Nagy-Ungvarai, Z. 298
 Hettich, R., see Rammo, J. 368
 Hettich, R., see Roigk, A. 366
 Hiebl, K., see Flandorfer, H. 32, 34, 48, 49
 Hiebl, K., see Weitzer, F. 21, 22, 25, 26
 Hill, F.B., see Katz, H.M. 13
 Hillier, A.C. 466, 468
 Hilmersson, G., see Dahlen, A. 410, 413, 414, 422, 423, 470
 Hilmersson, G., see Davis, T.A. 423
 Hilmersson, G., see Kim, M. 463
 Hilscher, G., see Wiesinger, G. 87
 Hinakubo, Y., see Matsukawa, S. 430
 Hinsvark, O.N. 288
 Hintz, H.L. 319, 321, 356
 Hioki, K., see Kunishima, M. 396
 Hitao, T., see Ogawa, A. 398, 401
 Hiyama, S., see Imamoto, T. 307, 317
 Hjörvarsson, B. 206
 Hjörvarsson, B., see Grier, E.R. 147
 Hjörvarsson, B., see Huiberts, J.H. 88, 90–92, 98–100, 103, 104, 107, 112, 113, 116–118, 123, 133, 136, 163, 167, 183, 214, 224
 Hjörvarsson, B., see Miniotas, A. 271, 273
 Hjörvarsson, B., see Udovic, T.J. 222
 Hjörvarsson, B., see Wildes, A.R. 90, 91, 146
 Ho, T.L. 283, 314, 319, 320, 322, 325, 344
 Ho, T.L., see Mehta, G. 304, 323
 Ho, T.L., see Soucy, P. 321, 323
 Hobley, J., see Kasuya, M. 298
 Hodges, J.A., see LeBras, G. 39, 41
 Hoekstra, A.F.T., see Roesbaum, T.F. 108, 266
 Hoekstra, A.F.Th. 103, 108, 110–112, 215, 266
 Hoekstra, A.F.Th., see Roy, A.S. 108, 215, 266
 Hoffmann, R.W., see Beck, D.D. 286
 Hofmann, W.K. 32, 34, 38, 40
 Hohnke, D. 6–8, 49, 51
 Hoistad, L.M., see Jensen, E.A. 74, 75
 Hokkoku, S., see Onishi, Y. 359
 Holm, A.P. 19
 Holschbach, M.H., see Mennicke, E. 334
 Holtzberg, F. 60, 61
 Holub, D.P., see Enholm, E.J. 402
 Honda, Y. 399
 Horiuchi, C.A. 329, 338
 Horiuchi, C.A., see He, L. 304
 Horiuchi, C.A., see Itoh, K.I. 342
 Hou, Z. 419, 420, 446, 447, 454, 455, 457, 459, 461, 463, 465, 469
 House, H.O. 415
 Hoveyda, A.H., see Evans, D.A. 397, 399
 Hoz, S. 413
 Hsu, W.C. 355
 Huang, M.Q., see Saha, S. 21
 Huang, M.Z., see Li, Z.C. 359
 Huang, Q., see Udovic, T.J. 113, 117, 210, 222
 Huang, R.Y.M. 358
 Huang, R.Y.M., see Jin, Y. 360

- Huang, S.D., see Shan, Y. 302, 303
Huang, Y.K., see Ye, J. 48, 49
Hudson, A.G. 312, 326
Huerta, M., see Concellon, J.M. 396
Hughes, L.A., see Evans, W.J. 435, 436
Hui, S.H., see Lepoutre, P. 362
Huiberts, J.H. 88–92, 96, 98–101, 103, 104,
107–109, 112, 113, 116–118, 120–123, 133, 136,
163, 166, 167, 183, 208, 214, 224
Huiberts, J.H., see Griessen, R. 98, 103, 116, 117,
120, 224
Huiberts, J.N., see Dekker, J.P. 208, 221
Huiberts, J.N., see den Broeder, F.J.A. 103, 120,
141, 167, 197–199, 215, 266
Huisman, M.C. 98, 100–103, 116, 117
Huisman, W.H., see den Broeder, F.J.A. 103, 120,
141, 167, 197–199, 215, 266
Huisman, W.H., see van der Molen, S.J. 103, 167,
197–199, 201, 202, 215, 266
Hulliger, F. 3, 5, 6, 9, 59, 72, 73
Hulliger, F., see Fisher, P. 9
Hundley, M.F. 43, 44, 48
Hundley, M.F., see Canfield, P.C. 43, 44, 46, 47
Hundley, M.F., see Fisk, Z. 47
Hundley, M.F., see Pagliuso, P.G. 46
Hundley, M.F., see Thompson, J.D. 47
Hung, Q., see Udovic, T.J. 113
Hungria, A.B., see Hernandez-Alonso, M.D. 312
Hunter, W.E., see Evans, W.J. 432–435, 437, 445,
455
Huntley, D.R., see Overbury, S.H. 286
Hurdis, E.C. 290
Hurng, W.-M. 11, 75
Hurng, W.-M., see Leon-Escamilla, E.A. 4, 8, 10
Hursthouse, M.B., see Baxter, I. 314
Hushagen, R.W., see Ferguson, M.J. 18
Hussain, N., see Balanikas, G. 314
Hutton, T.K. 413
Hwu, J.R. 283, 313, 343
Hynne, F., see Wang, J.C. 297

Ibl, N. 351
Ibl, N., see Kramer, K. 351
Idehen, K.I., see Okieimen, E.F. 359
Iga, F., see Kim, M.-S. 43, 45, 47
Igawa, T. 369
Igawa, T., see Sumaoka, J. 369
Ignaczak, M. 321
Ii'inskii, A.L., see Kiselev, Yu.M. 312
Iitaka, Y. 67
Ijima, Y., see Shigekawa, H. 368
Ikawa, H., see Shigekawa, H. 368
Il'yasov, T.M., see Sadygov, F.M. 71, 72
Imai, N., see Kawasaki, Y. 30
Imai, T., see Sumaoka, J. 369
Imai, T., see Tikeda, N. 369
Imai, Y. 360
Imamoto, T. 283, 307, 317, 402
Imamoto, T., see Hatanaka, Y. 314, 348
Inanaga, J. 396, 398, 403, 410, 417–419
Inanaga, J., see Honda, Y. 399
Inanaga, J., see Kusuda, K. 399
Inanaga, J., see Matsukawa, M. 399
Inanaga, J., see Otsubo, K. 399, 401
Inanaga, J., see Tabuchi, T. 402
Inanaga, J., see Yoshida, A. 411
Indrayan, A.K. 365
Inokuchi, S., see Saiki, K. 28
Inokuchi, T., see Torii, S. 351
Inoue, H., see Korematsu, A. 360
Inoue, M., see Kurita, K. 360
Iranpoor, N. 308, 309, 311, 325, 340
Iranpoor, N., see Firouzabadi, H. 309–311, 326,
332
Iranpoor, N., see Tamani, B. 314
Irisawa, M., see Tikeda, N. 369
Irish, D.E., see Miller, J.T. 300
Isber, S., see Gratens, X. 71
Ishida, M., see Shigekawa, H. 368
Ishigaki, T., see Robinson, R.A. 43, 45, 47
Ishii, T., see Oh, S.-J. 74
Ishii, Y., see Akane, N. 424
Ishikawa, M., see Inanaga, J. 398, 418, 419
Isidorsson, J. 90, 91, 233, 235, 237–239
Isidorsson, J., see Giebels, I.A.M.E. 90, 91, 98,
234, 235, 243, 250–253
Isobe, A., see Oyamada, A. 14
Ito, H., see Murakami, M. 404
Ito, Y., see Murakami, M. 404
Itoh, K.I. 342
Iwahara, Y., see Yamada, T. 348
Iwakura, Y., see Imai, Y. 360

Jacob, A. 91, 147
Jacob, A., see Borgschulze, A. 92, 103, 168,
170–173, 176, 177, 179
Jacob, A., see Kiersey, H. 211
Jacob, A., see Rode, M. 116, 206–209, 215, 247
Jacob III, P. 325
Jacobs, S.S. 293, 296
Jacoby, R., see Meyer, R.J. 301
Jahnke, W. 298, 299

- Jain, M.L., see Hwu, J.R. 313, 343
 Jain, M.T., see Hwu, J.R. 313
 James, C., see Abbott, T.P. 361
 James, C., see Grant, A.J. 309
 Jana, S.C. 360
 Janarthanan, J. 361
 Janjic, D. 296
 Jankowski, P., see Menzinger, M. 297
 Janner, A.-M. 197, 246
 Janner, A.-M., see Di Vece, M. 91
 Jansen, A.G.M., see Goll, G. 45, 46
 Jarosz, J. 57
 Jayaraman, A. 283
 Jayaraman, K. 353
 Jayaraman, K., see Devadoss, V. 353
 Jayaraman, K.S., see Rao, K.P. 363
 Jeffery, G.H., see Bassett, J. 286, 288
 Jeitschko, W., see Haase, M.G. 28–30, 32, 36, 38–40, 43, 44
 Jeitschko, W., see Hofmann, W.K. 32, 34, 38, 40
 Jeitschko, W., see Prill, M. 10, 13
 Jeitschko, W., see Schmidt, T. 54
 Jemetio, J.-P. 35
 Jensen, E.A. 74, 75
 Jetten, S., see Huiberts, J.H. 88, 90–92, 98–100, 103, 104, 107, 112, 113, 116–118, 123, 133, 136, 163, 167, 183, 214, 224
 Jezierski, A., see Szytuła, A. 41
 Ji, L.C., see Fang, T.R. 360
 Ji, S.J., see Horiuchi, C.A. 338
 Ji, X.H. 74
 Ji, X.H., see Zhao, X.B. 74
 Jiang, L.M., see Wang, L.Q. 359
 Jiang, Y.F., see Xi, C.J. 337
 Jiang, Y.F., see Yang, X.H. 337
 Jin, Y. 360
 Job, A. 310
 Johanson, B., see Ahuja, R. 231
 Johnson, C.R. 400
 Johnson, D.C., see Hintz, H.L. 319, 321
 Jones, C.D.W., see Cho, B.K. 42
 Jones, C.D.W., see Gordon, R.A. 39, 42
 Jones, C.J., see Moss, M.A.J. 466
 Jones, C.W., see Auty, K. 346
 Jones, E.G. 304
 Jongerden, M.R., see Huisman, M.C. 98, 101, 103
 Joseph, K.T., see Kumaraswamy, M.D.K. 359
 Joseph, K.T., see Rao, K.P. 363
 Joseph, K.T., see Sudhakar, D. 360
 Joseph, K.T., see Vijayakumar, M.T. 357
 Jow, J.J. 353
 Jung, B.O. 359
 Jung, H.C., see Kim, S.S. 348
 Jung, M.H. 32, 34, 36, 43, 46
 Jungblut, R.M., see den Broeder, F.J.A. 103, 120, 141, 167, 197–199, 215, 266
 Jwo, J.J. 297
 Jwo, J.J., see Noyes, R.M. 295
 Kaczorowski, D. 32, 38, 39, 41, 49–52
 Kaczorowski, D., see Pietri, R. 41
 Kaczorowski, D., see Szytuła, A. 41
 Kadowaki, K., see Ye, J. 48, 49
 Kaeriyama, K. 355
 Kagan, H.B. 283, 396, 402, 404, 410, 430, 432
 Kagan, H.B., see Bied, C. 433
 Kagan, H.B., see Collin, J. 432, 433
 Kagan, H.B., see Girard, P. 395–398, 401, 402, 404, 434
 Kagan, H.B., see Hamann, B. 425
 Kagan, H.B., see Lebrun, A. 430
 Kagan, H.B., see Namy, J.L. 396, 402, 425, 431
 Kagan, H.B., see Soupe, J. 400, 402
 Kahn, M., see Baker, F.B. 307
 Kaiser, E.W. 312
 Kaith, B.S., see Chauhan, G.S. 360
 Kaizerman, S., see Mino, G. 319, 356
 Kajimura, A., see Sumaoka, J. 369
 Kakizaki, A., see Oh, S.-J. 74
 Kalkman, J., see van der Molen, S.J. 211, 228, 229, 231–233, 246
 Kaltsoyannis, N., see Edelman, N.M. 285, 286
 Kamiya, S., see Onishi, Y. 359
 Kamiyama, T., see Robinson, R.A. 43, 45, 47
 Kamochi, Y. 397, 417
 Kanakogi, T., see Yamato, T. 313, 345
 Kanamori, M., see He, L. 304
 Kanatzidis, M.G., see Kim, S.-J. 54, 56
 Kanatzidis, M.G., see Larson, P. 36
 Kanemoto, S. 313, 344–346
 Kanniappan, E.P., see Rao, K.P. 363
 Kantouch, A. 359, 362
 Kappel, M.J., see Raymond, K.N. 375
 Kappel, M.J., see Zhu, D.H. 375
 Kapur, S.L., see Rao, S.R. 358
 Karady, S., see Weinstock, L.M. 304
 Karimi Zarchi, M.A.K., see Tamani, B. 314
 Karmakar, G.P. 357
 Karmakar, N.C., see Tripathy, T. 361
 Karraker, D.G. 300
 Kasaya, M. 47
 Kasaya, M., see Kawasaki, Y. 30

- Kasaya, M., see Naher, S. 47
Kasaya, M., see Suzuki, H. 43, 46, 47
Kasaya, M., see Yoshii, S. 28–30
Kašpar, J. 283
Kasperek, G.J. 296
Kasuya, M. 298
Kasuya, T. 14
Kasuya, T., see Alonso, J.A. 7
Kasuya, T., see Bartholin, H. 74
Kasuya, T., see Oh, S.-J. 74
Kasuya, T., see Oyamada, A. 14
Kasuya, T., see Sera, M. 74
Katakai, R., see Kondo, T. 358
Kato, H., see Oh, S.-J. 74
Katoh, K. 44
Katz, H.M. 13
Kaur, I., see Chauhan, G.S. 360
Kaur, I., see Misra, B.N. 362
Kauzlarich, S.M., see Chan, J.Y. 17, 18, 58
Kauzlarich, S.M., see Holm, A.P. 19
Kauzlarich, S.M., see Sunstrom, J.E. 286
Kauzlarich, S.M., see Wang, M.E. 4, 8
Kawano, T., see Murakami, M. 404
Kawaoka, A.M. 440
Kawasaki, S., see Jung, M.H. 43, 46
Kawasaki, Y. 30
Kazakova, G.M., see Yakovlev, N.G. 376
Kazemian, P., see Heravi, M.M. 313
Keatch, C.J. 288
Keck, G.E. 412
Keener, J.P. 298
Kelly, J.F., see Paquette, L.A. 343
Kelly, J.J., see Di Vecce, M. 91, 97, 98, 103,
119–121, 139, 140, 142, 244–249
Kelly, P.J. 202, 203, 206, 209–211, 222, 224
Kelly, P.J., see Kremers, M. 92, 97–99, 103–105,
163, 175
Kelly, P.J., see van Gelderen, P. 193, 210, 211,
217–220, 224, 226, 231
Kende, A.S. 400
Kenny, C., see Molander, G.A. 406
Keogh, D.W., see Brady, E.K. 458
Kero, Y., see Shiozaki, R. 314, 346
Kerssemakers, J., see Dornheim, M. 103, 119
Kerssemakers, J., see Nagengast, D.G. 89, 91, 147,
148, 150, 151, 153, 154, 266
Kerssemakers, J.W.J. 147–152, 157, 160, 266
Kerssemakers, J.W.J., see Dam, B. 90, 195
Kerssemakers, J.W.J., see Kooij, B.J. 151, 154,
157–159
Kerssemakers, J.W.J., see Kooij, E.S. 154–157
Kerssemakers, J.W.J., see Remhof, A. 103, 118,
185, 186
Kerssemakers, J.W.J., see van der Molen, S.J. 91,
92, 103, 119, 163–169, 175, 177
Kerssemakers, J.W.J., see van Gogh, A.T.M. 92,
93, 103, 118, 163, 173–175, 184, 186, 189
Keutgen, C., see Bour, G. 90, 91, 255, 257–259,
266
Keutgen, C., see Gartz, M. 255
Khalafi-Nezhad, A. 308
Khalil, M.I., see Abdel-Hay, F.I. 362
Khan, S.A., see Aruna, I. 98, 255, 260–266
Khan, S.I., see Evans, W.J. 440, 443
Khandekar, K., see Gupta, K.C. 357, 358
Khatib, J.I., see Misra, G.S. 355
Khodadad, P., see Céolin, R. 63–65
Kiaeezadeh, F., see Firouzabadi, H. 311, 326
Kiatkamjornwong, S., see Chansook, N. 360
Kido, G., see Suzuki, O. 47
Kierey, H. 211
Kierey, H., see Schoenes, J. 103, 116
Kiji, S., see Horiuchi, C.A. 329
Kilbourn, T. 283
Kim, J.H. 312, 366
Kim, J.S., see Cho, B.K. 42
Kim, M. 463
Kim, M.-S. 43, 45, 47
Kim, S.-J. 54, 56
Kim, S.S. 348, 350
Kim, Y.D., see Shim, S.J. 361
Kimura, T., see Tanaka, Y. 402
Kindo, K., see Thamizhavel, A. 34, 36, 48
Kindo, T., see Kamochi, Y. 397
King, C.B., see Sherrill, M.S. 307
King, K.Y., see Hwu, J.R. 283, 343
King, N.C. 365
Kino, H., see Miyake, T. 215–217, 222, 226, 231
Kirchheim, R., see Dornheim, M. 103, 119
Kirchheim, R., see Pundt, A. 147
Kirowa Eisner, E., see Gileadi, E. 134
Kiselev, Yu.M. 312
Kiselev, Yu.M., see Spitsyn, V.I. 312
Kishimoto, Y., see Kawasaki, Y. 30
Kiss, Z. 395
Kiss, Z., see McClure, D.S. 395
Kitagawa, H., see Kobayashi, S. 307
Kitai, T., see Naher, S. 47
Kitamura, Y. 369
Kitamura, Y., see Chen, W. 370
Kitamura, Y., see Komiyama, M. 368, 370
Kitazawa, H., see Oyamada, A. 14

- Kitazawa, H., see Suzuki, O. 47
- Klavins, P., see Chan, J.Y. 18
- Kleinke, H. 19
- Knettle, B.W. 431
- Knettle, B.W., see Kim, M. 463
- Knettle, B.W., see Prasad, E. 421, 458
- Knoch, K.G., see Coey, J.M.D. 21–23
- Kobayashi, S. 307
- Kobayashi, T.C., see Thamizhavel, A. 34, 36, 48
- Kobs, R., see Urner-Wille, M. 23
- Kocevar, M., see Stefane, B. 334
- Koch, G.H. 290
- Koch, M.H.J., see Petrascu, A.M. 297
- Kochi, J.K., see Hay, N. 304
- Kochi, J.K., see Sheldon, R.A. 323
- Kodama, T., see Komiyama, M. 366, 368, 370
- Koeman, N.H., see Isidorsson, J. 90, 91, 233, 235, 237–239
- Koeman, N.J., see den Broeder, F.J.A. 103, 120, 141, 167, 197–199, 215, 266
- Koeman, N.J., see Giebels, I.A.M.E. 90, 91, 98, 250–253
- Koeman, N.J., see Griessen, R. 98, 103, 116, 117, 120, 224
- Koeman, N.J., see Hoekstra, A.F.Th. 103, 108, 110–112, 215, 266
- Koeman, N.J., see Huiberts, J.H. 88–92, 96, 98–101, 103, 104, 107, 112, 113, 116–118, 120–123, 133, 136, 163, 166, 167, 183, 208, 214, 224
- Koeman, N.J., see Kerssemakers, J.W.J. 147, 148, 151, 157, 266
- Koeman, N.J., see Kooij, E.S. 101, 103, 116–118, 126, 127, 136, 137, 148–150, 180, 182, 183, 185, 186
- Koeman, N.J., see Kremers, M. 92, 97–99, 103–105, 163, 175
- Koeman, N.J., see Lokhorst, A.C. 195, 196, 260
- Koeman, N.J., see Remhof, A. 103, 270, 271
- Koeman, N.J., see van der Molen, S.J. 91, 92, 103, 119, 163–169, 175, 177
- Koeman, N.J., see van Gogh, A.T.M. 89, 92, 93, 97, 98, 103, 116, 118, 120–122, 163, 173–175, 184–195, 217, 224, 226
- Kohgi, M., see Robinson, R.A. 43, 45, 47
- Koide, Y., see Imamoto, T. 307, 317
- Koisumi, T.-A., see Hou, Z. 455, 461, 465
- Koitzsch, C., see Hayoz, J. 201, 215
- Koizumi, T.-A., see Hou, Z. 446
- Kolos, E., see Bányai, É. 289
- Kolosov, O., see Grier, E.R. 147
- Kolthoff, I.M. 286, 289
- Kominami, H., see Shiozaki, R. 314, 346
- Komiyama, M. 283, 366–370
- Komiyama, M., see Chen, W. 370
- Komiyama, M., see Kitamura, Y. 369
- Komiyama, M., see Miyama, S. 368
- Komiyama, M., see Shigekawa, H. 368
- Komiyama, M., see Sumaoka, J. 368, 369
- Komiyama, M., see Takarada, T. 371
- Komiyama, M., see Tikeda, N. 369
- Komiyama, M., see Yamamoto, Y. 369, 370
- Komiyama, M., see Yashiro, M. 371
- Komiyama, M. 368
- Komiyama, M., see Igawa, T. 369
- Kondo, T. 358
- Koningsberger, D.C., see Di Vecce, M. 103, 120, 247–249
- Kooij, B.J. 151, 154, 157–159
- Kooij, E.S. 93–98, 101, 103, 105, 106, 111, 116–118, 126, 127, 133, 136, 137, 148–150, 154–157, 180, 182, 183, 185, 186, 204
- Kooij, E.S., see Dornheim, M. 103, 119
- Kooij, E.S., see Giebels, I.A.M.E. 90, 91, 98, 250–253
- Kooij, E.S., see Isidorsson, J. 90, 91, 233, 235, 237–239
- Kooij, E.S., see Nagengast, D.G. 228–230, 232, 246
- Kooij, E.S., see Remhof, A. 103, 118, 185, 186
- Kooij, E.S., see van der Molen, S.J. 211, 228, 229, 231–233, 246
- Kooij, E.S., see van Gogh, A.T.M. 89, 92, 97, 98, 103, 116, 120–122, 184–195, 203–206, 211, 217, 224, 226
- Korematsu, A. 360
- Kornilov, V.V., see Asovich, V.S. 312, 326
- Koroliuk, A.L., see Bolotaev, A.G. 17, 19, 20
- Körös, E. 298
- Körös, E., see Field, R.J. 292, 294
- Körös, E., see Gyenge, R. 294
- Körös, E., see Nagy, G. 298
- Körös, E., see Noyes, R.M. 292, 294
- Körös, E., see Ruoff, P. 292, 293, 295
- Körös, E., see Varga, M. 295
- Kostecki, R., see Richardson, T.J. 90
- Kosyakov, V.N., see Yakovlev, N.G. 376
- Koto, H., see Imamoto, T. 402
- Kozlova, N., see Wosnitza, J. 46
- Kramer, K. 351
- Kramer, K., see Ibl, N. 351
- Krämer, R., see Ott, R. 366

- Kreh, R.P. 307, 351, 352
 Kreh, R.P., see Spotnitz, R.M. 351, 352
 Kreibig, U., see Bour, G. 90, 91, 255, 257–259, 266
 Kreibig, U., see Gartz, M. 255
 Kreibig, U., see Stepanov, A.L. 255–257, 260
 Kremers, M. 92, 97–99, 103–105, 163, 175
 Kremers, M., see den Broeder, F.J.A. 103, 120, 141, 167, 197–199, 215, 266
 Kremers, M., see Griessen, R. 98, 103, 116, 117, 120, 224
 Kremers, M., see Huiberts, J.H. 103, 107–109, 118
 Kremers, M., see Notten, P.H.L. 93, 94, 97, 103, 104, 133
 Kresinski, R.A., see Moss, M.A.J. 466
 Krinskii, V.I., see Agladze, K.I. 298
 Krinskii, V.I., see Mikhailov, A.S. 298
 Krishnamoorthy, S., see Jayaraman, K. 353
 Krishnaveni, N.K., see Surendra, K. 325
 Krohn, K. 346
 Krypyakevich, P.I. 19
 Kuanar, M., see Mishra, B.K. 309
 Kubo, H., see Kawasaki, Y. 30
 Kubota, H., see Kondo, T. 358
 Kubota, H., see Ogiwara, Y. 358
 KÜchle, W., see Dolg, M. 285
 Kudo, T., see Kamochi, Y. 417
 Kuenneke, S., see Gartz, M. 255
 Kuhlman, M.L., see Miller, R.S. 418, 430
 Kuhn, A., see Clarke, R. 350
 Kuhn, A.T. 285
 Kuhn, A.T., see Randle, T.H. 285
 Kuhnert, L. 292
 Kuliev, A.G., see Garibov, F.A. 63, 64, 68
 Kuliev, F.I., see Sadygov, F.M. 70, 71
 Kum-Tatt, L. 289
 Kumar, P. 89, 92, 97, 98, 129–139, 163, 164, 175, 176, 266, 273, 274
 Kumar, R.N., see Han, T.L. 360
 Kumar, V., see Sharma, B.R. 357
 Kumaraswamy, M.D.K. 359
 Kundu, T., see Chowdhury, P. 359
 Kunii, S., see Naher, S. 47
 Kunii, S., see Suzuki, H. 47
 Kunishima, M. 396
 Kunz, A.H. 284
 Kuo, C.Y., see Lee, M.W. 103, 111, 113, 115
 Kuo, J.F., see Hsu, W.C. 355
 Kurita, K. 360
 Kurosawa, K., see Yamada, T. 348
 Kurz, M.R. 306, 337
 Kusuda, K. 399
 Kusui, H., see Akane, N. 424
 Kuz'ma, Y. 3
 Kuz'ma, Yu.B., see Mozharivskii, Yu.A. 30, 32, 33, 36
 Kuz'ma, Yu.B., see Mozharivsky, Yu.A. 33, 37
 Kuznetsov, N.T., see Chechernikov, V.I. 61
 Kuznetsov, V.Y., see Rogachev, D.L. 304, 305
 Kvernberg, P.O., see Treindl, L. 297
 Kwei, G.H. 44
 Kwon, Y.-U. 19
 Laali, K.K. 308
 Labarre, D., see Chauvierre, C. 355
 Labergerie, D., see Remhof, A. 117, 146, 151, 210
 Laborde, O., see Sera, M. 74
 Lacerda, A., see Canfield, P.C. 43, 44, 46, 47
 Lacerda, A., see Movshovich, R. 47
 Lacerda, A., see Thompson, J.D. 47
 Lacerda, A.H., see Jung, M.H. 32, 34, 36
 Lacher, P.R. 188
 Lai, W., see Li, Z. 21
 Laing, S.B. 316
 Lakhanpal, S., see Misra, B.N. 358
 Lam, R., see Mills, A.M. 75
 Lam, W.W.L., see Kobayashi, S. 307
 Lamprecht, I. 298
 Lance, M., see Berthet, J.C. 308
 Lane, E.I., see Fritz, J.S. 290
 Lange, L.T. 286
 Langston, S.P., see Myers, R.M. 400
 Lannou, M.I., see Hélon, F. 430
 Lannoye, G. 407
 Lanza, G. 312
 Lapunova, R.V., see Sichevich, O.M. 23
 Larsen, R.D. 300
 Larson, P. 36
 Lässer, R., see Bracconi, P. 91
 Laubschat, C., see Schneider, W. 170
 Lawrence, J.M., see Hundley, M.F. 43, 44
 Lawrence, J.M., see Kwei, G.H. 44
 Lawson, A.C., see Kwei, G.H. 44
 Le, H., see Molander, G.A. 408
 Leach, D.R., see Ali, M.H. 313
 Leard, D.C., see Pojman, J.A. 297
 Lebedev, I.A. 376
 LeBras, G. 39, 41
 Lebrun, A. 430
 Lebrun, A., see Kagan, H.B. 430, 432
 Lee, M.W. 89, 103, 111, 113–115, 139, 141, 143–145

- Lee, S.B., see Jung, B.O. 359
 Leervad Pedersen, T.P. 143
 Léger, J.M. 5, 7
 Leithe-Jasper, A., see Coey, J.M.D. 21–23
 Leithe-Jasper, A., see Flandorfer, H. 32, 34, 48, 49
 Leithe-Jasper, A., see Kaczorowski, D. 39, 41, 49–51
 Leithe-Jasper, A., see Pietri, R. 41
 Leithe-Jasper, A., see Szytuła, A. 41
 Leithe-Jasper, A., see Weitzer, F. 21, 22, 25, 26
 Lele, V., see Athawale, V.D. 360
 Leman, J.T., see Evans, W.J. 440
 Lemaux, S., see Di Vece, M. 103, 120, 247–249
 Lemoine, P. 63, 64, 66, 67
 Lenka, S. 355
 Leon-Escamilla, E. 10, 11
 Leon-Escamilla, E., see Corbett, J.D. 11
 Leon-Escamilla, E.A. 4, 8, 10
 Leong, V.S., see Evans, W.J. 451
 Lepage, M., see Bäck, S.Å.J. 373
 Lepoutre, P. 362
 Leskiv, M.S., see Rau, J.V. 312
 Letant, A., see Allemand, J. 23
 Levan, K.R., see Evans, W.J. 449
 Levason, W. 310
 Levdik, V.A., see Miron, N.F. 210
 Levy, S.V. 344
 Li, D., see Fang, R. 21
 Li, G.-R. 28, 38
 Li, J., see Li, R. 297
 Li, Q.L., see Wang, Y.P. 370
 Li, R. 297
 Li, R.K.Y., see Ge, X.C. 359
 Li, Y. 119
 Li, Y.J., see Tomita, T. 360
 Li, Y.P., see Wang, L.Q. 359
 Li, Z. 21
 Li, Z.C. 359
 Lian, N., see Li, Z.C. 359
 Liang, Y., see Lu, Y.-M. 32, 34, 35
 Libowitz, G.G. 87, 112, 139, 207, 246
 Libowitz, G.G., see Mueller, W.M. 87, 117, 133, 138, 139, 183, 186, 188
 Lichtenberg, R.R., see Schmidt, F.A. 6
 Lide, D.R. 155
 Lightner, D.A., see Bobal, P. 345
 Lightner, D.A., see Thyran, T. 308
 Lin, C.H., see Lee, M.W. 89, 139, 141, 143–145
 Lin, H.C., see Lee, M.W. 103, 111, 113, 115
 Lin, R., see Zhang, Y. 400
 Lin, S.C., see Zhang, J. 309
 Lin, S.G., see Cao, Y.M. 357
 Lin, X.F., see Zheng, S.Y. 360
 Lin, Y.-H., see Qi, G.-Z. 457
 Linde, H., see Kuhnert, L. 292
 Lindgren, O. 304, 305
 Lingane, J.J. 284
 Lipponen, M., see Bidoglio, G. 286
 Liu, G.-K., see Li, G.-R. 28, 38
 Liu, M.Z. 361
 Liu, S.-Y., see Hillier, A.C. 468
 Liu, S.Y., see Hillier, A.C. 466
 Liveri, M.L.T., see Cavasino, F.P. 297
 Lodder, A., see Dekker, J.P. 208, 221
 Loewenhaupt, M. 283
 Lohstroh, W., see Enache, S. 90
 Lohstroh, W., see van Mechelen, J.L.M. 90
 Lokhorst, A.C. 195, 196, 260
 Lokhorst, A.C., see Dam, B. 90, 195
 Lombardo, R., see Cavasino, F.P. 297
 Long, J.R. 283
 Long, P., see Dai, D. 21
 Long, P., see Fang, R. 21
 Lopez de la Torre, M.A., see Fisk, Z. 47
 Lopez de la Torre, M.A., see Thompson, J.D. 47
 Loppnow, G.R., see Zhang, X. 467
 Losada, C.P., see Molander, G.A. 408
 Louie, S.G., see Alford, J.A. 221–223
 Louie, S.G., see Chang, K.E. 220, 221
 Lu, B.H., see Ji, X.H. 74
 Lu, D.S., see Zheng, S.Y. 360
 Lu, Y.-M. 32, 34, 35
 Lu, Y.M. 48, 49
 Luche, J.L. 397
 Lundquist, J.T., see Kreh, R.P. 307, 351, 352
 Lundquist, J.T., see Spotnitz, R.M. 351, 352
 Luo, H., see Li, Z. 21
 Luo, Y., see Wang, D.F. 363
 Lutford, M.R. 360
 Lützenkirchen-Hecht, D., see Briois, V. 319
 Lynch, D.W. 283
 Lynn, J.W., see Robinson, R.A. 43, 45, 47
 Ma, C., see Liu, M.Z. 361
 Ma, J.-A. 438
 Ma, T., see Dai, D. 21
 Ma, T., see Fang, R. 21
 Macaulay, D.B., see Trahanovsky, W.S. 319
 Machrouhi, F. 400
 Mack, D.J., see Reiswig, R.D. 13
 Macland, A.G., see Libowitz, G.G. 87, 139, 246
 MacLaughlin, D.E., see Amato, A. 47

- MacLaughlin, D.E., see Canfield, P.C. 47
- Madurro, J.M., see Cho, L.Y. 353
- Maeda, S., see Yoneyama, M. 298
- Maeda, Y. 285
- Magarill, S.A., see Borisov, S.V. 69
- Magengast, D.G., see Kooij, E.S. 154–157
- Magnani, A., see Barbucci, R. 358
- Magus, P., see Anathanarayan, T.P. 399
- Mahanta, M.C., see Mohanty, N. 355
- Mahanti, S.D., see Kim, S.-J. 54, 56
- Mahanti, S.D., see Larson, P. 36
- Mahdavi, B. 353
- Maier-Komor, P. 87
- Maini, S. 309
- Maiti, G., see Roy, S.C. 328, 329
- Maiti, S., see Jana, S.C. 360
- Maiuolo, L., see Bartoli, C. 308
- Maknon'kov, D.I. 327
- Makrandi, J.K., see Dehmlow, E.V. 301, 308, 309
- Maksimov, B.N., see Asovich, V.S. 312, 326
- Maksudova, T.F. 5, 9, 10, 73
- Maksudova, T.F., see Aliev, O.M. 63, 64, 69–73
- Maldas, D., see Bhattacharyya, S.N. 356
- Maldonado, A.L. 369
- Malhotra, L.K., see Aruna, I. 90, 91, 93, 98, 175, 178, 180, 181, 255, 257, 260–266
- Malhotra, L.K., see Kumar, P. 89, 92, 97, 98, 129–139, 163, 164, 175, 176, 266, 273, 274
- Malhotra, L.K., see Mor, G.K. 89, 90, 92, 93, 122–129, 134, 136, 163, 175, 176
- Malik, K.M.A., see Baxter, I. 314
- Malik, S.K., see Morozkin, A.V. 24, 25, 49, 52
- Malikov, D.A., see Milyukova, M.S. 284, 376
- Mamedov, V.N., see Garibov, F.A. 63, 64, 68, 69
- Mamedova, S.G. 69, 71
- Mancin, F. 366, 367
- Mandal, P.K. 326
- Mandolini, L., see Baciocchi, E. 301, 302, 317
- Mandolini, L., see Della Cort, A. 317
- Mandolini, L., see Maini, S. 309
- Mannsmann, M. 210
- Mansor, A., see Lutfur, M.R. 360
- Mansour, O.Y., see Nagaty, A. 361
- Mao, J.-G., see Pan, D.-C. 10, 12, 13, 18
- Maple, M.B., see Fisk, Z. 47
- Maple, M.B., see Thompson, J.D. 47
- Mar, A., see Désévéday, F. 58
- Mar, A., see Ferguson, M.J. 18
- Mar, A., see Mills, A.M. 75
- Mar, A., see Morgan, M.G. 57
- Mar, A., see Sykora, R.E. 286
- Mar, A., see Tkachuk, A.V. 16, 18, 25, 26, 28, 37, 49–51, 53, 59
- Mar, A., see Wang, M. 34
- Marazza, R. 32, 36, 38, 40, 43, 44
- Marazza, R., see Riani, P. 38–41
- March, J., see Smith, A.B. 405
- Marchand, R. 3
- Marchiando, J., see Peterman, D.J. 105, 191, 205
- Margerum, S.L., see Fritz, J.S. 290
- Mariano, P.S., see Chen, C. 309
- Markiv, V.Ya., see Krypyakevich, P.I. 19
- Marko, I.E. 343
- Marks, T.J., see Kawaoka, A.M. 440
- Marques, N. 466, 467
- Marques, N., see Hillier, A.C. 466
- Marrocco, M. 306
- Martin, T.W. 364
- Martin, T.W., see Glass, R.W. 364
- Martinez-Arias, A., see Hernandez-Alonso, M.D. 312
- Martins, G.B. 46
- Martins, G.B., see Pagliuso, P.G. 46
- Martins, J.C.A., see Coutinho, F.M.B. 355
- Martynenko, L.I., see Spitsyn, V.I. 312
- Martynova, L.F., see Chechernikov, V.I. 61
- Maruno, S., see Onishi, Y. 359
- Masatani, T., see Morita, M. 353
- Mateos, A.M., see Riande, E. 360
- Mathai, S., see Nair, V. 328, 342
- Mathew, J., see Nair, V. 283, 338
- Mathews, J., see Nair, V. 283
- Matlak, M. 57
- Matsuda, Y., see Morita, M. 353
- Matsukawa, M. 399
- Matsukawa, S. 430
- Matsumoto, T., see Ye, J. 48, 49
- Matsumura, K., see Komiyama, M. 370
- Matsumura, M., see Navarro, R.R. 358
- Matsuno, T., see Namura, R. 470
- Matsuoka, K., see Yamamoto, Y. 397
- Matsuyama, G., see Kolthoff, I.M. 286, 289
- Mattausch, H., see Zheng, C. 74, 75
- Matthews, R.W. 372
- Matthews, R.W., see Church, V.E. 372
- Matveeva, E.S. 93, 97, 103, 267
- Matveeva, E.S., see Parkhutik, V. 93, 97, 103, 267
- Mauermann, H., see Gräfe, P.S. 312
- Mauldin III, R.L., see Wine, P.H. 364
- Maunder, G.H., see Edelstein, N.M. 285, 286
- Maunder, G.H., see Hillier, A.C. 466
- Maurino, V., see Vione, D. 364

- Mazhar-ul-Haque, 314
 Mazzone, D., see Riani, P. 38–41
 McAuley, B.J. 400
 McClure, D.S. 395
 McCormick, C.L. 359
 McDonald, R., see Hillier, A.C. 466
 McDonald, R., see Wang, M. 34
 McDonald, R., see Zhang, X. 467
 McDowall, D.J. 356
 McGuire, T.R. 23
 McGuire, T.R., see Hartmann, M. 23
 McGuire, T.R., see Holtzberg, F. 60, 61
 McKie, J.A., see Molander, G.A. 400, 402, 403, 407, 419
 McMasters, O.D., see Schmidt, F.A. 6
 McMillan, A.F., see Heidt, L.J. 365
 McMullan, G.J. 47
 Meese-Markscheffel, J.A., see Schumann, H. 431
 Mehicic, M., see Antonio, M.R. 286
 Mehrotra, B., see Reddy, M.V.K. 342
 Mehrotra, R.C., see Sharma, N.N. 290
 Mehrotra, R.N., see Nagori, R.R. 323
 Mehta, B.R., see Aruna, I. 90, 91, 93, 98, 175, 178, 180, 181, 255, 257, 260–266
 Mehta, G. 304, 323
 Mehta, I.K., see Misra, B.N. 358, 362
 Mehta, M., see Nagori, R.R. 323
 Mehta, P.C., see Hebeish, A. 358
 Meidema, A.R. 91
 Meister, J.J. 360
 Melikova, Z.D., see Rustamov, P.G. 71–73
 Mellor, J.M. 335
 Meloche, C.G. 310
 Mendham, J., see Bassett, J. 286, 288
 Mendoza, J.S., see Kende, A.S. 400
 Meng, Y.Z., see Ge, X.C. 359
 Mennicke, E. 334
 Menzinger, M. 297
 Mercier, V., see Janner, A.-M. 197, 246
 Mercier, V.M.M. 90, 197, 246, 267
 Mercier, V.M.M., see van der Sluis, P. 90, 97, 197, 246, 269
 Merlo, F. 49–51
 Methfessel, S., see Holtzberg, F. 60, 61
 Metz, M.V., see Hillier, A.C. 466
 Meyer, K. 320, 321
 Meyer, R.J. 301
 Miao, J.K., see Li, Z.C. 359
 Michalak, F., see von Rottkay, K. 90–93, 97, 128–130, 239, 241, 243, 245, 246, 250, 267
 Michalecki, T., see Drzyzga, M. 4
 Mielke, C.H., see Wosnitza, J. 46
 Miftakhudinova, I.K., see Nikitina, G.P. 285
 Mikami, K., see Yoshida, A. 411
 Mikhailov, A.S. 298
 Mikheev, N.B. 395
 Mil'chenko, A.Y., see Maknon'kov, D.I. 327
 Millar, R.W., see Mellor, J.M. 335
 Miller, F.J. 285
 Miller, J.T. 300
 Miller, R.S. 418, 430
 Mills, A. 365
 Mills, A.M. 75
 Milner, G.W.C. 15
 Milyukova, M.S. 284, 376
 Minero, C., see Vione, D. 364
 Mingos, D.M.P., see Baxter, I. 314
 Miniotas, A. 271, 273
 Mino, G. 319, 356
 Mioković, T., see Pietrus, T. 46
 Mirkhani, V. 314
 Miron, N.F. 210
 Mirzoeva, R.D., see Sadygov, F.M. 72, 73
 Mishra, A. 360
 Mishra, B.K. 309
 Mishra, S.K., see Indrayan, A.K. 365
 Mishra, S.N., see Das, N.R. 359
 Misra, B.N. 358, 362
 Misra, G.S. 355
 Misra, S.K., see Gratens, X. 71
 Mitamura, H., see Kim, M.-S. 43, 45, 47
 Mitchell, M.L., see Fuchs, J.R. 418, 430
 Mittal, R.S., see Chawla, H.M. 313, 335
 Mittoo, S., see Mellor, J.M. 335
 Miura, Y., see Ren, L. 358
 Miyahara, T., see Oh, S.-J. 74
 Miyake, K., see Shigekawa, H. 368
 Miyake, T. 215–217, 222, 226, 231
 Miyama, S. 368
 Miyama, S., see Sumaoka, J. 368, 369
 Miyami, S., see Yashiro, M. 371
 Miyano, T., see Hou, Z. 454, 457, 459, 463
 Miyazaki, T., see Suzuki, H. 43, 46
 Mizuno, M., see Naher, S. 47
 Mizuno, M., see Suzuki, H. 47
 Młochowski, J., see Skarzewski, J. 301
 Mohanta, M.C., see Mohanty, N. 355, 361
 Mohanty, N. 355, 361
 Molander, G. 283
 Molander, G.A. 395, 396, 399–403, 406–408, 417, 419
 Molodtsov, S.L., see Schneider, W. 170

- Montiel, R., see Fernández, M.J. 358
- Mor, G.K. 89, 90, 92, 93, 122–129, 134, 136, 163, 175, 176
- Mor, G.K., see Kumar, P. 89, 92, 129–131, 136, 137, 139, 163, 175, 274
- Morales-Rojas, H., see Moss, R.A. 368, 371
- Moreau, J.M., see Allemand, J. 23
- Moreea, R.G.H., see Griffith, W.P. 310, 346
- Morelli, D.T. 47
- Morey, J. 323
- Morgan, M.G. 57
- Mori, N., see Yoshii, S. 28, 30
- Morita, M. 353
- Morozkin, A.V. 17, 19–25, 49, 52
- Morozkin, A.V., see Bolotaev, A.G. 17, 19, 20
- Morss, L.R. 283, 395, 432
- Morton, S.A., see Holm, A.P. 19
- Mosel, B.D., see Prill, M. 10, 13
- Moss, M.A.J. 466
- Moss, R.A. 368, 369, 371
- Moss, R.A., see Bracken, K. 370
- Mostafa, K.M. 359
- Movshovich, R. 47
- Movshovich, R., see Canfield, P.C. 47
- Movshovich, R., see Robinson, R.A. 43, 45, 47
- Mozharivskii, Yu.A. 30, 32, 33, 36
- Mozharivsky, Yu.A. 33, 37
- Mozharivskiy, Y. 31, 33, 37, 39, 41, 43, 44, 48
- Mozharivskiy, Y., see Tkachuk, A.V. 16, 49–51
- Muathen, H.A. 309
- Mueller, W.M. 87, 117, 133, 138, 139, 183, 186, 188
- Muir, K., see Hutton, T.K. 413
- Muirhead, C.P.T., see Tkachuk, A.V. 18
- Müller, K.-H., see Wosnitza, J. 46
- Müller, P., see Grund, I. 10, 11
- Müller, S.C. 298
- Müller, S.C., see Nagy-Ungvarai, Z. 298
- Müller, S.C., see Neumann, B. 294
- Müller-Warmuth, W., see Prill, M. 10, 13
- Mullins, D.R., see Overbury, S.H. 286
- Mulvaney, A.W., see Bull, S.D. 343
- Mumbai, V., see Athawale, V.D. 361
- Murakami, M. 404
- Muranyi, S., see Försterling, H.D. 294
- Murgja, S.M., see Baciocchi, E. 364
- Murray, W.M., see Furman, N.H. 290
- Murty, K.S., see Rao, G.G. 288
- Murugan, R. 363
- Muto, A., see Horiuchi, C.A. 338
- Myasoedov, B.F., see Lebedev, I.A. 376
- Myasoedov, B.F., see Milyukova, M.S. 284, 376
- Mydlarz, T., see Talik, E. 266
- Myers, R.M. 400
- Nagaty, A. 361
- Nagengast, D.G. 89, 91, 147, 148, 150, 151, 153, 154, 228–230, 232, 246, 266
- Nagengast, D.G., see den Broeder, F.J.A. 103, 120, 141, 167, 197–199, 215, 266
- Nagengast, D.G., see Kooij, E.S. 101, 103, 116–118, 126, 127, 136, 137, 148–150, 180, 182, 183, 185, 186
- Nagengast, D.G., see van der Molen, S.J. 211, 228, 229, 231–233, 246
- Nagengast, D.G., see van Gogh, A.T.M. 89, 92, 97, 98, 116, 120–122, 184–195, 217, 224, 226
- Nagieb, Z.A. 358
- Nagori, R.R. 323
- Nagy, G. 298
- Nagy-Ungvarai, Z. 298
- Nagygyory, S. 294
- Naher, S. 47
- Naher, S., see Suzuki, H. 47
- Nair, L.G., see Nair, V. 338, 339
- Nair, V. 283, 327, 328, 338, 339, 342
- Nakamura, N., see Thamizhavel, A. 34, 36, 48
- Nakane, S., see Torii, S. 351
- Nakane, T., see Robinson, R.A. 47
- Nakanishi, A., see Fukuzawa, S. 403
- Nakaya, T., see Korematsu, A. 360
- Nakaya, T., see Tomita, T. 360
- Nakotte, H., see Robinson, R.A. 47
- Nambudripad, N., see Dhar, S.K. 39, 41
- Namura, R. 470
- Namy, J.-L., see Hélon, F. 470
- Namy, J.L. 396, 402, 425, 431
- Namy, J.L., see Collin, J. 432
- Namy, J.L., see Girard, P. 395–398, 401, 402, 404, 434
- Namy, J.L., see Hamann, B. 425
- Namy, J.L., see Hélon, F. 430
- Namy, J.L., see Kagan, H.B. 283, 396, 402, 404, 410, 430, 432
- Namy, J.L., see Lebrun, A. 430
- Namy, J.L., see Machrouhi, F. 400
- Namy, J.L., see Soupe, J. 400, 402
- Nandi, M.M., see Chowdhury, P. 359
- Nanke, T., see Ogawa, A. 398, 401
- Nash, K.L. 283, 284
- Naumović, D., see Hayoz, J. 91, 146, 151, 160, 201, 202, 215

- Navarro, R.R. 358
 Nave, P.M. 319
 Nave, P.M., see Trahanovsky, W.S. 321
 Navratil, J.D., see Paulenova, A. 304
 Nayak, B.B., see Mishra, B.K. 309
 Nayak, B.R. 359
 Nayak, N.C. 359
 Nayak, N.C., see Das, N.R. 359
 Nayak, P.L., see Lenka, S. 355
 Nayudamma, Y., see Rao, K.P. 363
 Nazy, Zs., see Körös, E. 298
 Nelson, N. 373
 Nelson, N., see Surma, J.E. 373
 Nemoto, H., see Yamamoto, Y. 397
 Nemoto, Y., see Suzuki, H. 43, 46
 Netzer, F.P. 283
 Neumann, B. 294
 Neumann, C.S. 285
 Neumann, C.S., see Dolg, M. 285
 Neumann, H., see Zwiener, G. 12
 Neumann, M., see Chełkowska, G. 57
 Neumann, M., see Talik, E. 266
 Newham, R.H., see Bond, A.M. 432
 Newton, T.W., see Baker, F.B. 307
 Ng, K.K. 107, 126, 127, 136, 191, 192, 198, 199, 202, 206, 212–214, 219, 222, 231
 Ngoviwatchai, P., see Kurz, M.R. 306, 337
 Ni, H.L., see Ji, X.H. 74
 Nicolis, G. 291
 Nielsen, K., see Wang, J.C. 297
 Nierlich, M., see Berthet, J.C. 308
 Nieuwenhuyzen, M., see McAuley, B.J. 400
 Nikiforov, V.N., see Bolotaev, A.G. 17, 19, 20
 Nikitina, G.P. 285
 Nirmala, R., see Morozkin, A.V. 24, 25, 49, 52
 Nishi, N., see Ren, L. 358
 Nishiguchi, T. 313
 Nishimura, S., see Imamoto, T. 402
 Nishino, H., see Yamada, T. 348
 Nishiura, M., see Hou, Z. 455, 461, 465
 Nishiyama, Y., see Akane, N. 424
 Niu, X.J. 60, 61
 Nkumah, J.E., see Okieimen, F.E. 361
 Noël, H., see Flandorfer, H. 32, 34, 48, 49
 Noël, H., see Weitzer, F. 21, 22, 25, 26
 Noel, M., see Devadoss, V. 353
 Noel, M., see Vijayarathi, T. 285, 353
 Nogueira, H.I.S., see Griffith, W.P. 310, 346
 Noheda, B., see van Mechelen, J.L.M. 90
 Nomura, K. 4, 6
 Noor, M.A.M., see Han, T.L. 360
 Nooshabadi, M.A., see Aghapoor, K. 313
 Norblad, P., see Miniotas, A. 271, 273
 Nordgren, J., see Hjärvarsson, B. 206
 Norman, R.O.C. 306, 317
 Norskov, J.K., see Hammer, B. 171
 Nosaka, Y., see Takashima, M. 312
 Noszticzus, Z. 294
 Noszticzus, Z., see Försterling, H.D. 294
 Noszticzus, Z., see Gao, Y. 294
 Noszticzus, Z., see Hegedus, L. 295
 Noszticzus, Z., see Nagygyory, S. 294
 Noszticzus, Z., see Oslonovitch, J. 294
 Noszticzus, Z., see Sirimungkala, A. 294
 Notten, P.H.L. 93, 94, 97, 103, 104, 133
 Notten, P.H.L., see Griessen, R. 98, 103, 116, 117, 120, 224
 Notten, P.H.L., see Kremers, M. 92, 97–99, 103–105, 163, 175
 Nowacki, W., see Iitaka, Y. 67
 Noyes, A.A. 284
 Noyes, R.M. 292, 294, 295
 Noyes, R.M., see Barkin, S. 297, 310
 Noyes, R.M., see Edelson, D. 294
 Noyes, R.M., see Field, R.J. 292, 294, 295
 Noyes, R.M., see Ganapathisubramanian, N. 297
 Noyes, R.M., see Jwo, J.J. 297
 Noyes, R.M., see Ruoff, P. 297
 Nozaki, H., see Kanemoto, S. 313, 344–346
 Nozaki, H., see Tomioka, H. 344
 Nozaki, S., see Horiuchi, C.A. 338
 Nozières, J.P., see Allemand, J. 23
 Nunn, J.H., see Milner, G.W.C. 15
 Obermyer, R.T., see Saha, S. 21
 O'Brien, N., see Armitage, R. 97, 233, 267, 268
 Ochiai, A., see Aoki, H. 60, 61
 Ochiai, A., see Oh, S.-J. 74
 Ochiai, A., see Oyamada, A. 14
 Oehr, K. 351
 Oftedal, N., see Nagy, G. 298
 Ogawa, A. 398, 401
 Ogbeifun, D.E., see Okieimen, F.E. 357
 Ogiwara, Y. 358
 Oguchi, T. 45, 46
 Oh, S.-J. 74
 Ohara, T., see Kunishima, M. 396
 Ohgo, Y. 397
 Ohno, H., see Sumaoka, J. 369
 Ohno, M., see Sumaoka, J. 369
 Ohno, T., see Kawasaki, Y. 30
 Ohya, S., see Ogawa, A. 398, 401

- Okada, M., see Yoshimura, K. 90
 Okayama, Y., see Kasuya, T. 14
 Oki, K., see Léger, J.M. 5, 7
 Okieimen, E.F. 356, 358, 359, 363
 Okieimen, E.F., see Bazuaye, A. 361
 Okieimen, F.E. 357, 359, 361, 363
 Okninski, A. 291
 Okoh, E., see Clarke, R. 350
 Okubo, T., see Thamizhavel, A. 34, 36, 48
 Olafsson, S., see Huiberts, J.H. 88, 90–92,
 98–100, 103, 104, 107, 112, 113, 116–118, 123,
 133, 136, 163, 167, 183, 214, 224
 Olah, G.A. 345
 Oldroyd, R.D., see Levason, W. 310
 Olmstead, M.M., see Chan, J.Y. 17, 18
 Olofson, J.M., see Evans, W.J. 312
 Omenetoo, N., see Bidoglio, G. 286
 Onishi, K., see Saiki, K. 28
 Onishi, Y. 359
 Ono, S., see Nomura, K. 4, 6
 Ōnuki, Y., see Thamizhavel, A. 34, 36, 48
 Oppeneer, P.M. 47
 Orban, M., see Körös, E. 298
 Orehotsky, J., see Washko, S. 28
 Ortega Ramiro, R.J., see Matveeva, E.S. 93, 97,
 103, 267
 Osakabe, T., see Kasaya, M. 47
 Osakabe, T., see Robinson, R.A. 47
 Osborne, D.W., see Flotow, H.E. 88, 117, 183
 Oseroff, S., see Martins, G.B. 46
 Oseroff, S.B., see Pagliuso, P.G. 46
 Oshima, K., see Kanemoto, S. 313, 344–346
 Oshima, K., see Tomioka, H. 344
 Osin, Yu.N., see Stepanov, A.L. 255–257
 Oskooie, H.A. 311
 Oskooie, H.A., see Heravi, M.M. 311, 313
 Oslonovitch, J. 294
 Osman, M.E., see Fares, M.M. 361
 Osterwalder, J. 206
 Otsubo, K. 399, 401
 Ott, H.-R., see Thompson, J.D. 47
 Ott, H.R., see Amato, A. 47
 Ott, H.R., see Canfield, P.C. 43, 44, 46, 47
 Ott, H.R., see Fisk, Z. 47
 Ott, H.R., see Hulliger, F. 6, 59
 Ott, R. 366
 Otto, K., see Flotow, H.E. 88, 117, 183
 Ouwerkerk, M. 97, 98, 239, 240, 242
 Ouwerkerk, M., see van der Sluis, P. 89–91, 227,
 233, 242, 244
 Overbury, S.H. 286
 Owji, J., see Iranpoor, N. 309
 Oyamada, A. 14
 Öz, N. 355
 Pack, J.G., see Libowitz, G.G. 87, 207
 Padhi, N.P. 355
 Padwaldesai, M.P., see Athawale, V.D. 357
 Pagliuso, P.G. 46
 Pal, C.M., see Chowdhury, P. 360
 Palmisano, G., see Danieli, B. 323
 Pan, D.-C. 10, 12, 13, 18
 Pan, W.B. 334
 Panda, A. 355
 Panda, J., see Reddy, G.V.R. 355
 Pandey, K. 437
 Pandey, P.N., see Mehta, G. 304, 323
 Pandey, S.N., see Thejappa, N. 359
 Pandey, S.R., see Tripathy, T. 361
 Pani, M., see Merlo, F. 49–51
 Panicker, S.B., see Nair, V. 327, 328, 342
 Paquette, L.A. 343
 Parham, H., see Firouzabadi, H. 311
 Park, L.S., see McCormick, C.L. 359
 Parkes, R., see Mellor, J.M. 335
 Parkhutik, V. 93, 97, 103, 267
 Parkhutik, V., see Matveeva, E.S. 93, 97, 103
 Parkhutik, V.P., see Matveeva, E.S. 93, 97, 103,
 267
 Parodi, N. 4
 Parodi, N., see Borzone, G. 4
 Parsons, A.F., see Bar, G. 302
 Parthé, E. 3
 Parthé, E., see Gelato, L.M. 3
 Parthé, E., see Hohnke, D. 6–8, 49, 51
 Pascual, B. 357
 Passell, L., see Turberfield, K.C. 7
 Pastor, T.J. 288
 Patel, C.P., see Patel, G.M. 361
 Patel, C.P., see Shah, S.B. 361
 Patel, C.P., see Vora, R.A. 361
 Patel, G.M. 361
 Patil, D.R. 361
 Patil, D.R., see Meister, J.J. 360
 Patra, C.M. 355, 359, 360
 Paulenova, A. 304
 Paulrajan, S. 355
 Pavlyuk, V.V., see Stetskiv, A.O. 59
 Payne, D.S., see Grant, D. 365
 Pecharsky, A.O. 15, 17
 Pecharsky, A.O., see Niu, X.J. 60, 61
 Pecharsky, V.K., see Niu, X.J. 60, 61

- Pedler, A.E., see Hudson, A.G. 312, 326
 Pei, X.W., see Wang, Y.P. 370
 Peleshanko, S.A., see Fokin, A.A. 364
 Pelizzetti, E., see Vione, D. 364
 Pen, H.F., see Eder, R. 107, 198, 199, 212–214, 216, 222, 231
 Penc, B., see Szytuła, A. 41
 Penciner, J., see Gileadi, E. 134
 Peng, C., see Fang, R. 21
 Periasamy, M. 304, 315
 Periasamy, M., see Bhat, G.A. 315
 Periasamy, M., see Bhatt, M.V. 315
 Perissinotti, L.J., see Brusa, M.A. 294
 Perlov, A.Ya., see Oppeneer, P.M. 47
 Perrier de la Bâthie, R., see Allemand, J. 23
 Pervukhina, N.V., see Borisov, S.V. 69
 Peterman, D.J. 105, 191, 205
 Peterson, D.T., see Shinar, J. 87, 207
 Peterson, D.T., see Weaver, J.H. 87, 105, 191, 205
 Peterson, E., see Canfield, P.C. 43, 44, 46
 Peterson, E., see Robinson, R.A. 43, 45, 47
 Peterson, E.S., see Leon-Escamilla, E.A. 4, 8, 10
 Peterson, T.T., see Evans, W.J. 449
 Petford-Long, A.K., see Grier, E.R. 147
 Petrascu, A.M. 297
 Petrovic, C. 4, 52, 53
 Pettit, R., see Emerson, G.F. 343
 Pettit, R., see Watts, L. 343
 Philip, R., see Kumar, P. 89, 92, 129–131, 136, 137, 139, 163, 175, 274
 Phillips, A., see Toy, S.M. 272
 Phillips, R.C., see Reyes, Z. 361
 Pick, M.A. 91
 Pickett, W.E., see Holm, A.P. 19
 Piermattei, A., see Baciocchi, E. 301, 302, 326
 Pietri, R. 41
 Pietri, R., see Kaczorowski, D. 39, 41, 49–51
 Pietrus, T. 46
 Pietrus, T., see Goll, G. 45, 46
 Pietrus, T., see Jung, M.H. 43, 46
 Pillo, Th., see Hayoz, J. 91, 146, 151, 160, 194, 201, 202
 Pinter, S., see Nagygyory, S. 294
 Pitzer, R.M., see Dolg, M. 285
 Plackowski, T., see Kaczorowski, D. 41
 Plakatouras, J.C., see Baxter, I. 314
 Plessner, T., see Müller, S.C. 298
 Pletcher, D. 285, 301, 302, 354
 Plota, S., see den Broeder, F.J.A. 103, 120, 141, 167, 197–199, 215, 266
 Po, R. 363
 Podberezskaya, N.V., see Borisov, S.V. 69
 Pojman, J.A. 297
 Polanc, S., see Stefane, B. 334
 Ponto, L., see Ibl, N. 351
 Porai-Koshits, M.A., see Rogachev, D.L. 304, 305
 Porret, D., see Weiss, J. 365
 Pörschke, E., see Bracconi, P. 91
 Pospelova, L.A., see Golovnya, V.A. 304
 Pourjavadi, A. 361
 Prabhakaran, J., see Nair, V. 283
 Pradhan, B., see Mohanty, N. 355, 361
 Pramanick, D. 355
 Prasad, E. 420, 421, 458, 462
 Prasad, E., see Chopade, P.R. 414, 428
 Prasad, R.S., see Bull, S.D. 343
 Prawicki, K. 321
 Press, P.J., see Spontitz, R.M. 351, 352
 Preuss, H., see Dolg, M. 285
 Preuss, W.H. 243
 Prewitt, C.T., see Shannon, R.D. 374
 Prigogine, I. 291
 Prigogine, I., see Nicolis, G. 291
 Prill, M. 10, 13
 Procopio, A., see Bartoli, C. 308
 Procter, D.J., see Hutton, T.K. 413
 Pundt, A. 147
 Pundt, A., see Dornheim, M. 103, 119
 Pungor, E., see Gyenge, R. 294
 Purgato, F.L.S. 353
 Purwanto, A., see Robinson, R.A. 43, 45, 47
 Qi, G.-Z. 457
 Qi, Q., see Coey, J.M.D. 21–23
 Qing, X.S., see Cao, Y.M. 357
 Qiu, K.Y., see Dong, J.H. 355
 Qiu, K.Y., see Feng, X.D. 360
 Qudsieh, I.Y.M., see Fakhru'l-Razi, A. 360
 Que Jr., L., see Branum, M.E. 370
 Quesnel, Y., see Marko, I.E. 343
 Quezel, S., see Rossat-Mignod, J. 6
 Rabe, G.W., see Evans, W.J. 441
 Rachmatov, O.I., see Abdusalyamova, M.N. 4, 9, 10
 Rademacher, O., see Jemetio, J.-P. 35
 Radkov, E., see Xu, J.D. 375, 376
 Radu, N.S. 456
 Ragunathan, K.G., see Bracken, K. 370
 Ragunathan, K.G., see Moss, R.A. 368, 369, 371
 Rahman, L. 360
 Rahman, M.K.A., see Fakhru'l-Razi, A. 360

- Rahman, M.Z.A., see Lutfor, M.R. 360
 Rahman, M.Z.A., see Rahman, L. 360
 Rahman Khan, M.S. 91
 Raines, A.J., see Zhang, Y. 309, 359
 Rajagopal, G., see Kim, S.S. 350
 Rajan, R., see Nair, V. 283, 338
 Rajani, S., see Mishra, A. 360
 Ramakrishna, S., see Murugan, R. 363
 Ramaraj, R., see Maeda, Y. 285
 Rameev, B., see Güner, S. 46
 Rammo, J. 368
 Ramussen, E., see Mino, G. 319
 Rana, K.K., see Roy, S.C. 327, 328
 Randle, T.H. 285
 Randle, T.H., see Kuhn, A.T. 285
 Rao, D., see Martins, G.B. 46
 Rao, G.G. 288
 Rao, G.V.G., see Shukla, S.R. 358
 Rao, K.P. 363
 Rao, K.P., see Kumaraswamy, M.D.K. 359
 Rao, K.R., see Surendra, K. 325
 Rao, P.V.K., see Rao, G.G. 288
 Rao, S.R. 358
 Rao, T.N., see Maeda, Y. 285
 Rao, U.N., see Sathunuru, R. 338
 Rath, S.K. 357
 Rathi, S.C., see Athawale, V.D. 361
 Rathore, M.P.S., see Misra, B.N. 358
 Rau, J.V. 312
 Ravot, D., see Rossat-Mignod, J. 6
 Ray, M.P., see McMullan, G.J. 47
 Raymond, K.N. 375
 Raymond, K.N., see Gorden, A.E.V. 375
 Raymond, K.N., see Gramer, C.J. 376
 Raymond, K.N., see Haddad, S.F. 376
 Raymond, K.N., see Sofen, S.R. 376
 Raymond, K.N., see Xu, J.D. 375, 376
 Raymond, K.N., see Zhu, D.H. 375
 Rector, J.H., see Borgschulte, A. 92, 93, 103, 163, 166, 175, 176, 178
 Rector, J.H., see Dam, B. 90, 195
 Rector, J.H., see den Broeder, F.J.A. 103, 120, 141, 167, 197–199, 215, 266
 Rector, J.H., see Giebels, I.A.M.E. 90, 91, 98, 250–253
 Rector, J.H., see Huiberts, J.H. 88–92, 96, 98–101, 103, 104, 107, 112, 113, 116–118, 120–123, 133, 136, 163, 166, 167, 183, 208, 214, 224
 Rector, J.H., see Isidorsson, J. 90, 91, 233, 235, 237–239
 Rector, J.H., see Kooij, E.S. 154–157
 Rector, J.H., see Lokhorst, A.C. 195, 196, 260
 Rector, J.H., see van der Molen, S.J. 91, 92, 103, 119, 163–169, 175, 177, 211, 228, 229, 231–233, 246
 Rector, J.H., see van Gogh, A.T.M. 89, 97, 98, 116, 120–122, 186–195, 217, 224, 226
 Rector, J.H., see van Mechelen, J.L.M. 90
 Reddy, C.R., see Vijayakumar, M.T. 357
 Reddy, G.V.R. 355
 Reddy, M.V.K. 342
 Reddy, N.S., see Thimma, R.T. 359
 Rehr, A., see Chan, J.Y. 17, 18, 58
 Reidy, R.F. 286
 Reinholdt, A., see Bour, G. 90, 91, 255, 257–259, 266
 Reinholdt, A., see Stepanov, A.L. 255–257, 260
 Reiswig, R.D. 13
 Remhof, A. 91, 103, 117, 118, 146, 151, 185, 186, 210, 270–272
 Remhof, A., see Dam, B. 90, 195
 Remhof, A., see Giebels, I.A.M.E. 90, 91, 98, 250–253
 Remhof, A., see Kooij, E.S. 154–157
 Ren, L. 358
 Rennie, R.A.C. 351
 Rettori, C., see Martins, G.B. 46
 Rettori, C., see Pagliuso, P.G. 46
 Reyes, Z. 361
 Riande, E. 360
 Riani, P. 38–41
 Rice, T.M., see Ng, K.K. 107, 126, 127, 136, 191, 192, 198, 199, 202, 206, 212–214, 219, 222, 231
 Richardson, T., see Armitage, R. 97, 233, 267, 268
 Richardson, T., see von Rottkay, K. 90–93, 97, 128–130, 239, 241, 243, 245, 246, 250, 267
 Richardson, T.J. 90
 Richter, C.G., see Haase, M.G. 28–30, 32, 36, 38–40, 43, 44
 Richter, M., see Schneider, W. 170
 Ridd, J.H., see Dinçtürk, S. 334, 335
 Riley, D.P. 350
 Rindone, B. 315, 316
 Riseborough, P., see Severing, A. 43, 44
 Rist, C.E., see Fanta, G.F. 358, 361
 Rist, C.E., see Reyes, Z. 361
 Rizkalla, E.N. 283
 Robbins, M.D., see Trahanovsky, W.S. 317, 339
 Robertson, E., see Hardwick, T.J. 304
 Robertson, P., see Ibl, N. 351
 Robertson, P.M., see Kramer, K. 351
 Robins, M.J., see Asakura, J. 329

- Robinson, R.A. 43, 45, 47
 Robinson, R.A., see Canfield, P.C. 47
 Robledo, C.B., see Evans, W.J. 451
 Robson, A., see Barkakaty, B.C. 361
 Roček, J., see Meyer, K. 320, 321
 Rode, M. 116, 206–209, 215, 247
 Rode, M., see Borgschulte, A. 92, 103, 168, 170–173, 176, 177, 179
 Rode, M., see Kierey, H. 211
 Rode, M., see Schoenes, J. 103, 116
 Rodier, N., see Céolin, R. 63–65
 Rodkin, M.A., see Maknon'kov, D.I. 327
 Rodriguez-Franco, M.I. 329
 Rodriguez-Solla, H., see Concellon, J.M. 396
 Roelofs, M.G. 298
 Roesbaum, T.F. 108, 266
 Rogachev, D.L. 304, 305
 Rogl, P., see Coey, J.M.D. 21–23
 Rogl, P., see Flandorfer, H. 32, 34, 48, 49
 Rogl, P., see Kaczorowski, D. 39, 41, 49–51
 Rogl, P., see Pietri, R. 41
 Rogl, P., see Weitzer, F. 21, 22, 25, 26
 Rohrer, C., see Furstner, A. 402
 Rohwer, H.E., see Barry, J. 309
 Rohxer, H.E., see du Preez, J.G.H. 310
 Roigk, A. 366
 Roigk, A., see Rammo, J. 368
 Rol, C., see Baciocchi, E. 301, 302, 317, 327, 335
 Rol, C., see Maini, S. 309
 Rollier, M.A., see Cunningham, B.B. 312
 Romero, J.R., see Aleixo, P.C. 353
 Romero, J.R., see Cho, L.Y. 302, 314, 323, 351, 353
 Romero, J.R., see Purgato, F.L.S. 353
 Romeyn Jr., H., see Hurdis, E.C. 290
 Roncolini, C., see Barbucci, R. 358
 Rosenbaum, T.F., see Hoekstra, A.F.Th. 103, 108, 110–112, 215, 266
 Rosenbaum, T.F., see Roy, A.S. 108, 215, 266
 Rosie, R., see Weaver, J.H. 87, 105, 205
 Rossat-Mignod, J. 6
 Rossat-Mignod, J., see Alonso, J.A. 7
 Rossat-Mignod, J., see Léger, J.M. 5, 7
 Rossi, D., see Marazza, R. 32, 36, 38, 40, 43, 44
 Rössle, M. 285, 348
 Rossmannith, K. 430
 Rout, A. 355
 Rout, S.P., see Rout, A. 355
 Rowe, J.M., see Anderson, I.S. 113
 Roy, A.S. 108, 215, 266
 Roy, A.S., see Hoekstra, A.F.Th. 103, 108, 110–112, 215, 266
 Roy, S.C. 327–329
 Roy, S.C., see Mandal, P.K. 326
 Rozman, H.D., see Han, T.L. 360
 Ruben, H., see Tilley, D.T. 434
 Rubin, M., see Armitage, R. 97, 233, 267, 268
 Rubin, M., see von Rottkay, K. 90–93, 97, 128–130, 136, 239–241, 243–246, 249, 250, 267
 Rubin, M.D., see Richardson, T.J. 90
 Ruder, S.M. 396, 423
 Rudin, A., see Hecker De Carvalho, L. 362
 Rummel, R.E., see Martin, T.W. 364
 Ruoff, P. 292, 293, 295, 297, 298
 Ruoff, P., see Nagy, G. 298
 Ruoff, P., see Treindl, L. 297
 Rush, J.J. 113
 Rush, J.J., see Anderson, I.S. 113
 Rush, J.J., see Udovic, T.J. 113, 117, 210, 222
 Rushton, P.P. 224
 Russell, C.R., see Fanta, G.F. 358, 361
 Russell, C.R., see Reyes, Z. 361
 Russo, M.R., see Edelstein, N.M. 285, 286
 Rustamov, P.G. 63, 64, 70–73
 Rustamov, P.G., see Aliev, O.M. 63, 64, 69–73
 Rustamov, P.G., see Godzhaev, E.M. 63, 70, 71, 73
 Rustamov, P.G., see Maksudova, T.F. 5, 9, 10
 Rustamov, P.G., see Sadigov, F.M. 4, 8
 Rustamov, P.G., see Sadygov, F.M. 71–73
 Ruzziconi, R., see Baciocchi, E. 301, 302, 326, 343
 Saá, J.M., see Morey, J. 323
 Saccone, A., see Borzone, G. 4
 Sadigov, F.M. 4, 8
 Sadygov, F.M. 63, 64, 68–73
 Sadygov, F.M., see Dzhaifarova, E.K. 70, 71
 Sadygov, F.M., see Mamedova, S.G. 69, 71
 Sadygov, F.M., see Rustamov, P.G. 71–73
 Safarov, M.G., see Rustamov, P.G. 71, 72
 Safavi, A., see Iranpoor, N. 308
 Saforov, M.G., see Rustamov, P.G. 71, 72
 Saha, S. 21
 Sahoo, S., see Gupta, K.C. 358
 Said, O.B., see Bazuaye, A. 361
 Saiki, K. 28
 Saikia, C.N. 357
 Saimoto, H., see Kanemoto, S. 313, 345, 346
 Saito, E., see Hayon, E. 364
 Saito, N., see Torii, S. 351
 Saito, Y., see Horiuchi, C.A. 338
 Saito, Y., see Oh, S.-J. 74

- Sakai, S., see Fukuzawa, S. 403
 Sakata, Y., see Horiuchi, C.A. 338
 Sakurai, H., see Takahashi, T. 290
 Sakurai, Y., see Saiki, K. 28
 Salamakha, P. 28, 29
 Salamakha, P.S., see Sologub, O.L. 3
 Salch, J.H., see Fanta, G.F. 359, 361
 Salehi, P., see Iranpoor, N. 325
 Salinga, C., see Leervad Pedersen, T.P. 143
 Salvador, J., see Kim, S.-J. 54, 56
 Samal, R.K. 360
 Sambasivarao, K.W.S., see Lannoye, G. 407
 Sambri, L., see Bartoli, C. 308
 Samsonova, N.D., see Aliev, O.M. 63, 64, 69–73
 Samui, S., see Chowdhury, P. 359
 Sanchez Bolinchez, A., see Matveeva, E.S. 93, 97, 103, 267
 Sander, I., see Heitmann, H. 23
 Sanderson, W.R. 345
 Sanderson, W.R., see Auty, K. 346
 Sankar, S.G., see Saha, S. 21
 Santappa, M., see Rout, A. 355
 Santappa, M., see Sudhakar, D. 360
 Saraç, A.S., see Dinger, B. 355
 Sarac, S.A., see Hanna, S.B. 323
 Sarbach, S., see Hayoz, J. 91, 146, 151, 160, 202
 Sardarian, A., see Firouzabadi, H. 311
 Sarkar, S.K., see Pramanick, D. 355
 Sarrao, J., see Martins, G.B. 46
 Sarrao, J.L., see Pagliuso, P.G. 46
 Sasakawa, T., see Kim, M.-S. 43, 45, 47
 Sâthe, C., see Hjörvarsson, B. 206
 Sathunuru, R. 338
 Sato, K., see Maeda, Y. 285
 Savall, A., see Tzedakis, T. 285
 Savall, A.J., see Tzedakis, T. 316, 354
 Sawada, A., see Kasaya, M. 47
 Sawatsky, G.A., see Eder, R. 107, 198, 199, 212–214, 216, 222, 231
 Sayama, K., see Bamwenda, G.R. 365
 Schaafsma, S.E. 320
 Schäfer, H., see Brechtel, E. 54
 Schäfer, H., see Cordier, B. 59
 Schelly, Z., see Noszticzus, Z. 294
 Schenck, A., see Amato, A. 47
 Scheones, J., see Rode, M. 116, 206–209, 215, 247
 Schlapbach, L. 87
 Schlapbach, L., see Hayoz, J. 91, 146, 151, 160, 161, 194, 201–204, 215
 Schmerber, G., see LeBras, G. 39, 41
 Schmidt, F.A. 6
 Schmidt, T. 54
 Schmidt, T., see Haase, M.G. 28–30, 32, 36, 38–40, 43, 44
 Schmitz, C.E., see Ali, M.H. 313
 Schneider, F.W., see Field, R.J. 292, 295
 Schneider, H.J., see Rammo, J. 368
 Schneider, H.J., see Roigk, A. 366
 Schneider, W. 170
 Schoenes, J. 103, 116
 Schoenes, J., see Borgschulte, A. 91–93, 103, 151, 161–163, 166, 168, 170–173, 175–179
 Schoenes, J., see Hayoz, J. 160, 161, 203, 204
 Schoenes, J., see Jacob, A. 91, 147
 Schoenes, J., see Kierey, H. 211
 Schoonover, C., see Furman, N.H. 290
 Schreiber, F.G., see Gradef, P.S. 312
 Schreiner, P.R., see Fokin, A.A. 364
 Schreyer, A., see Remhof, A. 117, 146, 151, 210
 Schröder, A., see Pietrus, T. 46
 Schumann, H. 431
 Schumann, H., see Bochkarev, M.N. 395
 Schuster, H.-U., see Grund, I. 10, 11, 13
 Schuster, H.-U., see Steinberg, G. 13
 Schuster, H.-U., see Tomuschat, C. 49–51
 Schuster, H.-U., see Zwiener, G. 12
 Schweizer, J., see Alonso, J.A. 7
 Scolastico, C., see Rindone, B. 315, 316
 Scott, B., see Radu, N.S. 456
 Scott, B.L., see Brady, E.K. 458
 Scott, K. 350
 Scrimin, P., see Mancin, F. 366, 367
 Sealy, J.M., see Miller, R.S. 418, 430
 Sealy, J.M., see Shotwell, J.B. 420
 Seaman, C.L., see Fisk, Z. 47
 Seaman, C.L., see Thompson, J.D. 47
 Sebastiani, G.V., see Baciocchi, E. 317, 327, 335, 364
 Seibel, C.A., see Evans, W.J. 395, 444
 Sell, T., see Keck, G.E. 412
 Sella, A., see Edelstein, N.M. 285, 286
 Sella, A., see Hillier, A.C. 466, 468
 Sella, A., see Marques, N. 466, 467
 Selvakumar, S., see Reddy, G.V.R. 355
 Sen, A., see Chebolu, V. 427
 Senanayake, C.H., see Johnson, C.R. 400
 Sera, M. 74
 Sera, M., see Bartholin, H. 74
 Sera, M., see Jung, M.H. 43, 46
 Sera, M., see Kasuya, T. 14
 Serebrennikov, V.V., see Degtyar, V.A. 57
 Serena, B., see Baciocchi, E. 317, 327, 335

- Sereni, J.G. 283
 Serhatli, I.E., see Erim, M. 355
 Serhatli, I.E., see Tunca, U. 355
 Settai, R., see Thamizhavel, A. 34, 36, 48
 Sevcik, P. 297
 Sevcikova, H., see Kasuya, M. 298
 Severing, A. 43, 44
 Sevov, S.C., see Kwon, Y.-U. 19
 Shabangi, M., see Fuchs, J.R. 418, 430
 Shabangi, M., see Miller, R.S. 418, 430
 Shah, S.B. 361
 Shakhshiri, B.Z. 296, 299
 Sham, T.K. 286
 Shan, Y. 302, 303
 Shannon, R.D. 374, 427
 Sharma, A., see Mishra, B.K. 309
 Sharma, B.R. 357
 Sharma, G.K., see Shukla, J.S. 362
 Sharma, N.N. 290
 Sharma, R.K., see Misra, B.N. 362
 Sharma, S.K., see Chawla, H.M. 346
 Shcherbak, V.I., see Miron, N.F. 210
 Sheeba, V., see Nair, V. 339
 Shekarize, M., see Iranpoor, N. 308
 Shekarriz, M., see Iranpoor, N. 308, 340
 Sheldon, R.A. 323
 Sheldrake, G.N., see McAuley, B.J. 400
 Shelton, R.N., see Chan, J.Y. 18
 Shen, J., see Zhang, J. 309
 Shen, Q., see Qi, G.-Z. 457
 Sherrill, M.S. 307
 Sherrington, D.C. 346
 Shi, Q.Z. 345
 Shigekawa, H. 368
 Shigekawa, H., see Komiyama, M. 366–369
 Shigekawa, H., see Tikedu, N. 369
 Shiiba, T., see Komiyama, M. 366, 368, 370
 Shim, S.J. 361
 Shin, W.P., see Lee, M.W. 103, 111, 113–115
 Shinar, J. 87, 207, 214
 Shinoda, N., see Yamato, T. 313, 345
 Shiozaki, R. 314, 346
 Shirakawa, M., see Kasaya, M. 47
 Shiriny, F., see Firouzabadi, H. 311
 Shiriny, F., see Iranpoor, N. 308
 Shishkin, E.I., see Abdusalyamova, M.N. 4, 10
 Shivaprasad, S.M., see Aruna, I. 90, 91, 175, 255, 257, 260, 261, 263–266
 Shotwell, J.B. 420
 Shuh, D.K., see Edelstein, N.M. 285, 286
 Shukla, J.S. 362
 Shukla, S.R. 358
 Shulglin, A.T., see Jacob III, P. 325
 Sibel, C.A., see Evans, W.J. 395, 437
 Sichevich, O.M. 23
 Sichevich, O.M., see Mozharivskii, Yu.A. 30, 32, 33, 36
 Sidik, S., see Lutfur, M.R. 360
 Sidorov, L.N., see Rau, J.V. 312
 Sievers, R.E., see Gradeff, P.S. 312
 Silong, S., see Rahman, L. 360
 Simizu, S., see Saha, S. 21
 Simon, A., see Zheng, C. 74, 75
 Simoyi, R.H., see Neumann, B. 294
 Simpson, R.E., see Feldman, K.S. 400
 Singh, A.K. 410
 Singh, B.C., see Das, N.R. 359
 Singh, B.C., see Nayak, N.C. 359
 Singh, B.C., see Padhi, N.P. 355
 Singh, B.C., see Panda, A. 355
 Singh, B.C., see Patra, C.M. 355, 359, 360
 Singh, B.C., see Rout, A. 355
 Singh, H.S., see Singh, M.P. 323
 Singh, M.P. 323
 Singh, N.J., see Wu, Z. 224, 226, 227
 Singh, O., see Curzon, A.E. 90, 91
 Singh, R.P., see Biswal, D.R. 357
 Singh, R.P., see Deshmukh, S.R. 356
 Singh, R.P., see Karmakar, G.P. 357
 Singh, R.P., see Nayak, B.R. 359
 Singh, R.P., see Rath, S.K. 357
 Singh, R.P., see Tripathy, T. 361
 Singha, A.S., see Chauhan, G.S. 360
 Sirakawa, T., see Torii, S. 351
 Sirimungkala, A. 294, 295
 Sirimungkala, A., see Hegedus, L. 295
 Skaggs, W.E., see Jahnke, W. 298
 Skanthakumar, S. 286
 Skanthakumar, S., see Sykora, R.E. 286
 Skarzewski, J. 284, 301, 302, 304
 Skrydstrup, T., see Enemark, R.J. 420, 421
 Slack, J., see von Rottkay, K. 90–93, 97, 128–130, 239, 241, 243, 245, 246, 250, 267
 Slack, J.L., see Richardson, T.J. 90
 Ślebarnski, A., see Jarosz, J. 57
 Slovyanskikh, V.K., see Chechernikov, V.I. 61
 Smeets, R.J.J.G.A.M., see van Gogh, A.T.M. 89, 97, 98, 116, 120–122, 186–195, 217, 224, 226
 Smirnova, E.M., see Zhuravlev, N.N. 6
 Smith, A.B. 405
 Smith, A.D., see Bull, S.D. 343
 Smith, F.J. 32, 38

- Smith, G.F. 284, 287, 289, 299, 300, 306
 Smith, G.F., see Brandt, W.W. 289
 Smith, G.F., see Duke, F.R. 372
 Smith, L.M., see Trahanovsky, W.S. 321
 Smith, M.E., see Heidt, L.J. 307, 365
 Smith, W.L., see Raymond, K.N. 375
 Smith III, A.B. 399
 Sobolev, A.N., see Sichevich, O.M. 23
 Soderholm, L., see Antonio, M.R. 286
 Soderholm, L., see Skanthakumar, S. 286
 Soderholm, L., see Sykora, R.E. 286
 Sofen, S.R. 376
 Sofield, C.D., see Edelstein, N.M. 285, 286
 Sologub, O., see Flandorfer, H. 32, 34, 48, 49
 Sologub, O., see Salamakha, P. 28, 29
 Sologub, O.L. 3
 Sonada, N., see Ogawa, A. 398, 401
 Song, G., see Remhof, A. 91, 117, 146, 151, 210
 Soni, P.L., see Sharma, B.R. 357
 Soper, F.G., see Jones, E.G. 304
 Sørensen, P.G., see Wang, J.C. 297
 Soria, J., see Hernandez-Alonso, M.D. 312
 Soucy, P. 321, 323
 Soupe, J. 400, 402
 Soupe, J., see Namy, J.L. 402
 Speirs, J.L., see Katz, H.M. 13
 Spender, B., see Tilley, D.T. 434
 Spitsyn, V.I. 312
 Spooner, R.C., see Sherrill, M.S. 307
 Sportouch, S., see Larson, P. 36
 Spotnitz, R.M. 351, 352
 Spotnitz, R.M., see Kreh, R.P. 307, 351, 352
 Sreedhara, A. 366
 Srinivasan, K.S.V., see Sudhakar, D. 360
 Srinivasan, R., see Mishra, A. 360
 Srinivasan, R.K., see Jayaraman, K. 353
 Srinivasan, R.K., see Vijayarathi, T. 353
 Stahel, E.P., see Vitta, S.B. 358
 Stahl, E. 371
 Stannett, V.T., see McDowall, D.J. 356
 Stannett, V.T., see Vitta, S.B. 358
 Staub, U., see Antonio, M.R. 286
 Steel, P.G. 396
 Steenken, S., see Del Giacco, T. 364
 Stefane, B. 334
 Stefanescu, V., see Atanasiu, J.A. 286
 Steglińska, V., see Domagała, S. 321
 Steigman, J. 289
 Stein, G., see Ardon, M. 346
 Stein, G., see Baer, S. 345, 346
 Steinberg, G. 13
 Steinberg, H., see Schaafsma, S.E. 320
 Steinbock, O., see Neumann, B. 294
 Steiner, W., see Weitzer, F. 21, 22, 25, 26
 Stellmach, C., see Rode, M. 116, 206–209, 215, 247
 Stengel, P.J., see Molander, G.A. 400
 Stenger, V.A., see Kolthoff, I.M. 286, 289
 Stepanov, A.L. 255–257, 260
 Stepanov, A.L., see Bour, G. 90, 91, 255, 257–259, 266
 Stepien-Damm, J., see Bodak, O. 21, 22
 Stetskiy, A.O. 59
 Steward, G.A. 373
 Steward, G.A., see Surma, J.E. 373
 Stewart, G.R., see Cho, B.K. 42
 Stiepin, V.V., see Syrokoskii, V.S. 289
 Stoll, H., see Dolg, M. 285
 Stone, K.G., see Hinsvark, O.N. 288
 Storch, D.G., see Molander, G.A. 408
 Strand, J.D., see Petrovic, C. 52, 53
 Strong, F.M., see Koch, G.H. 290
 Strongin, M., see Pick, M.A. 91
 Stroot, P., see Janjic, D. 296
 Stucki, F., see Hulliger, F. 5
 Studer, A. 400
 Stumpf, L.F., see Bassett, L.G. 289
 Stumpf, R., see Kelly, P.J. 202, 203, 206, 209–211, 222, 224
 Subbaratnam, N.R., see Paulrajan, S. 355
 Sudhakar, D. 360
 Suemitsu, T., see Jung, M.H. 43, 46
 Suemitsu, T., see Kim, M.-S. 43, 45, 47
 Suemitsu, T., see Salamakha, P. 28, 29
 Suga, S., see Oh, S.-J. 74
 Sugiura, M., see Kobayashi, S. 307
 Sugiyama, K., see Thamizhavel, A. 34, 36, 48
 Sugiyama, T. 329
 Sugiyama, T., see Horiuchi, C.A. 338
 Sugiyama, T., see Itoh, K.I. 342
 Suits, J.C., see Holtzberg, F. 60, 61
 Suja, T.D., see Nair, V. 328
 Sukhoverkhov, V.F., see Rau, J.V. 312
 Sulikowski, G.A., see Smith III, A.B. 399
 Sullivan, J.C., see Nash, K.L. 283, 284
 Sullivan, V.R., see Smith, G.F. 287, 299, 300
 Sumaoka, J. 368, 369
 Sumaoka, J., see Chen, W. 370
 Sumaoka, J., see Igawa, T. 369
 Sumaoka, J., see Kitamura, Y. 369
 Sumaoka, J., see Komiyama, M. 366–368
 Sumaoka, J., see Shigekawa, H. 368

- Sumaoka, J., see Takeda, N. 369
 Sumi, K., see Navarro, R.R. 358
 Sumino, Y., see Ogawa, A. 398, 401
 Sun, J., see Cao, Y.M. 357
 Sun, J.P., see Wang, D.F. 363
 Sun, Y.H., see Feng, X.D. 360
 Sun, Z.-M., see Pan, D.-C. 10, 12, 13, 18
 Sunder, W.A., see Kaiser, E.W. 312
 Sunstrom, J.E. 286
 Surendra, K. 325
 Suresh, V.V., see Chakrabarty, K. 346
 Surma, J.E. 373
 Sutin, N., see Dulz, G. 289
 Sutter, Ch., see Remhof, A. 117, 146, 151, 210
 Suzuki, H. 43, 46, 47
 Suzuki, H., see Kasaya, M. 47
 Suzuki, H., see Naher, S. 47
 Suzuki, H., see Suzuki, O. 47
 Suzuki, O. 47
 Suzuki, T., see Alonso, J.A. 7
 Suzuki, T., see Aoki, H. 60, 61
 Suzuki, T., see Kasuya, T. 14
 Suzuki, T., see Oh, S.-J. 74
 Suzuki, T., see Oyamada, A. 14
 Svehla, G. 284
 Swamy, S.J. 431
 Swart, I., see Di Vece, M. 97, 103, 120, 139, 140, 142
 Swider, K.E., see Reidy, R.F. 286
 Switendick, A.C. 207
 Sworski, T.J. 365
 Sydnes, L.K. 317
 Sykora, R.E. 286
 Syper, L. 316
 Syrokonskii, V.S. 289
 Szade, J., see Drzyzga, M. 4, 8, 9
 Szytuła, A. 41

 Tabata, K., see Thamizhavel, A. 34, 36, 48
 Tabuchi, T. 402
 Tabuchi, T., see Matsukawa, M. 399
 Tagarelli, A., see Bartoli, C. 308
 Takabatake, T., see Goll, G. 45, 46
 Takabatake, T., see Jung, M.H. 32, 34, 36, 43, 46
 Takabatake, T., see Katoh, K. 44
 Takabatake, T., see Kim, M.-S. 43, 45, 47
 Takabatake, T., see Pietrus, T. 46
 Takabatake, T., see Salamakha, P. 28, 29
 Takabatake, T., see Wosnitza, J. 46
 Takagi, K., see Pietrus, T. 46
 Takahashi, H., see Yoshii, S. 28, 30
 Takahashi, S., see Itoh, K.I. 342
 Takahashi, T. 290
 Takahashi, T.T., see Horiuchi, C.A. 338
 Takahashi, T.T., see Itoh, K.I. 342
 Takahashi, Y., see Komiyama, M. 366, 368, 370
 Takamasu, T., see Suzuki, O. 47
 Takarada, T. 371
 Takarada, T., see Yashiro, M. 371
 Takasaki, B., see Williams, N.H. 366
 Takasaki, B.K. 366
 Takashima, M. 312
 Takashima, M., see Kim, J.H. 312
 Takats, J., see Hillier, A.C. 466
 Takats, J., see Hou, Z. 455, 461, 465
 Takats, J., see Marques, N. 466, 467
 Takats, J., see Zhang, X. 467
 Takeda, N., see Komiyama, M. 366–370
 Takemoto, Y., see Korematsu, A. 360
 Takeuchi, T., see Thamizhavel, A. 34, 36, 48
 Takeyama, T., see Imamoto, T. 402
 Talik, E. 266
 Tam, T., see Tkachuk, A.V. 53
 Tamani, B. 314
 Tammishetti, S., see Thimma, R.T. 359
 Tanaka, H., see Torii, S. 351
 Tanaka, Y. 402
 Tangestaninejad, S., see Mirkhani, V. 314
 Tani, S., see Kunishima, M. 396
 Taniguchi, M., see Oh, S.-J. 74
 Taniguchi, N., see Tanaka, Y. 402
 Tanko, J.M., see Wang, Y.H. 317
 Tanryverdiev, V.S. 63, 64, 68
 Tardif, O., see Hou, Z. 446, 447
 Tatlow, J.C., see Hudson, A.G. 312, 326
 Taya, H., see Nishiguchi, T. 313
 Taylor, J.B., see Wang, Y. 4, 6, 24
 Taylor, J.B., see Yoshihara, K. 3, 4, 6–9
 Taylor, R.L., see Daugherty, N.A. 307
 Tazawa, D., see Kasaya, M. 47
 Tazawa, D., see Yoshii, S. 28–30
 Tecilla, P., see Mancin, F. 366, 367
 Tedenac, J.C., see Graten, X. 71
 Teller, R.G., see Antonio, M.R. 286
 Templeton, D.H., see Tilley, D.T. 434
 Terakura, K., see Miyake, T. 215–217, 222, 226, 231
 Termini, D.J., see Brauer, G.M. 359
 Terrano, D., see Laali, K.K. 308
 Teukolsky, S.A., see Preuss, W.H. 243
 Tezuka, H., see Hou, Z. 446
 Thamizhavel, A. 34, 36, 48

- Than, M.M. 296
 Thaper, C.L., see Rush, J.J. 113
 Theis-Bröhl, K., see Remhof, A. 91, 146, 151, 210
 Thejappa, N. 359
 Théorêt, A., see Harrison, S. 353
 Thimma, R.T. 359
 Thomas, C.B., see Auty, K. 346
 Thomas, C.B., see Norman, R.O.C. 306, 317
 Thomas, H.C., see Yates, J.S. 290
 Thomas, S., see Nair, V. 327
 Thompson, J.D. 47
 Thompson, J.D., see Amato, A. 47
 Thompson, J.D., see Canfield, P.C. 43, 44, 46, 47
 Thompson, J.D., see Fisk, Z. 47
 Thompson, J.D., see Hundley, M.F. 43, 44, 48
 Thompson, J.D., see Kwei, G.H. 44
 Thompson, J.D., see Martins, G.B. 46
 Thompson, J.D., see Movshovich, R. 47
 Thompson, J.D., see Robinson, R.A. 47
 Thompson, J.D., see Severing, A. 43, 44
 Thong, C.J., see Saha, S. 21
 Thorn, R.P., see Wine, P.H. 364
 Thuy, N.B., see Nagygyory, S. 294
 Thyrann, T. 308
 Tian, J.Z., see Moss, R.A. 371
 Tikeda, N. 369
 Tilley, D.T. 434
 Tilley, T.D., see Castillo, I. 445
 Tipton, A.K., see Branum, M.E. 370
 Tjelflaat, K., see Nagy, G. 298
 Tkachuk, A.V. 16, 18, 25, 26, 28, 37, 49–51, 53, 59
 Tkachuk, A.V., see Désévéday, F. 58
 Tobin, J.G., see Holm, A.P. 19
 Toffoli, P., see Céolin, R. 63–65
 Tokura, S., see Ren, L. 358
 Tolboom, R., see Kremers, M. 92, 97–99, 103–105, 163, 175
 Tolboom, R., see van Gelderen, P. 217–220
 Tomioka, H. 344
 Tomioka, H., see Kanemoto, S. 344
 Tomita, T. 360
 Tomita, T., see Yamamoto, Y. 370
 Tomuschat, C. 49–51
 Tonellato, U., see Mancin, F. 366, 367
 Tong, H.K., see Kum-Tatt, L. 289
 Tong, Y.-X., see Li, G.-R. 28, 38
 Toofan, J., see Firouzabadi, H. 310, 311, 326
 Tootan, J., see Firouzabadi, H. 311
 Torelli, M.E., see Pagliuso, P.G. 46
 Torii, S. 351
 Toth, K., see Gyenge, R. 294
 Totleben, M.J. 396
 Totleben, M.J., see Curran, D.P. 406, 420
 Touchstone, J. 371
 Toy, S.M. 272
 Tozer, D.J., see Rushton, P.P. 224
 Trahanovsky, W.S. 317, 319–321, 323, 339
 Trahanovsky, W.S., see Nave, P.M. 319
 Trahanovsky, W.S., see Young, L.B. 316, 319, 372
 Treindl, L. 297
 Tripathy, T. 361
 Trivedi, H.C., see Patel, G.M. 361
 Trivedi, H.C., see Shah, S.B. 361
 Trivedi, H.C., see Vora, R.A. 361
 Trivedi, M.C., see Vora, R.A. 361
 Troć, R. 61
 Troć, R., see Żolnierek, Z. 61, 62
 Trouw, F., see Canfield, P.C. 47
 Trouw, F., see Robinson, R.A. 47
 Trovarelli, A. 283, 312
 Tryk, D.A., see Maeda, Y. 285
 Tsai, F.Y., see Hwu, J.R. 313
 Tsay, S.C., see Hwu, J.R. 313, 343
 Tsuboi, W., see Yamamoto, Y. 369
 Tu, K.H., see Wang, L.Q. 359
 Tunca, U. 355
 Turberfield, K.C. 7
 Turet, L., see Marko, I.E. 343
 Tyson, J.J., see Keener, J.P. 298
 Tyson, J.J., see Nagy-Ungvarai, Z. 298
 Tzedakis, T. 285, 316, 354
 Uchida, H., see Komiyama, M. 366, 368
 Udovic, T., see Anderson, I.S. 113
 Udovic, T.J. 113, 117, 210, 222
 Uehara, A., see Yamamoto, Y. 370
 Ueki, T., see Itoh, K.I. 342
 Uemura, M., see Tanaka, Y. 402
 Uesigi, T., see Bamwenda, G.R. 365
 Ufer, H. 57
 Ujikawa, O., see Inanaga, J. 403
 Ulibarri, T.A., see Evans, W.J. 434, 435, 439, 444, 448–450
 Ullah, N., see Antonio, M.R. 286
 Umeo, K., see Kim, M.-S. 43, 45, 47
 Umeo, K., see Pietrus, T. 46
 Unger, S., see Christoffers, J. 285, 346
 Unishi, T., see Takashima, M. 312
 Urner-Wille, M. 23
 Urner-Wille, M., see Hansen, P. 23
 Urner-Wille, M., see Heitmann, H. 23
 Utimoto, K., see Kanemoto, S. 345, 346

- Vairamani, M., see Nair, V. 327
- Vajda, P. 87, 117, 207
- Vajgand, V.J., see Pastor, T.J. 288
- Valdes, E.M., see Pletcher, D. 285, 301, 302, 354
- Valero, M., see Goñi, I. 357
- Valero, M., see Gurruchaga, M. 357
- Valero, M., see Vázquez, M.B. 357
- Valla, C., see Aspinall, H.C. 470
- van Bokhoven, J.A., see Di Vece, M. 103, 120, 247–249
- van der Eerden, A.M.J., see Di Vece, M. 103, 120, 247–249
- van der Molen, S.J. 91, 92, 103, 119, 163–169, 175, 177, 197–202, 211, 215, 228, 229, 231–233, 246, 266
- van der Molen, S.J., see den Broeder, F.J.A. 103, 120, 141, 167, 197–199, 215, 266
- van der Molen, S.J., see Dornheim, M. 103, 119
- van der Molen, S.J., see Giebels, I.A.M.E. 90, 91, 98, 103, 235, 236
- van der Molen, S.J., see Huisman, M.C. 98, 100–103, 116, 117
- van der Molen, S.J., see Kerssemakers, J.W.J. 147–152, 157, 160, 266
- van der Molen, S.J., see Remhof, A. 103, 118, 185, 186, 270, 271
- van der Molen, S.J., see van Gogh, A.T.M. 92, 93, 103, 118, 163, 173–175, 184, 186, 189
- van der Sluis, P. 89–91, 97, 103, 197, 227, 233, 241, 242, 244, 246, 247, 251–255, 269
- van der Sluis, P., see Di Vece, M. 91
- van der Sluis, P., see Janner, A.-M. 197, 246
- van der Sluis, P., see Mercier, V.M.M. 90, 197, 246, 267
- van Ek, J., see Dekker, J.P. 208, 221
- van Gelderen, P. 193, 210, 211, 217–220, 224, 226, 231
- van Gogh, A.T.M. 89, 92, 93, 97, 98, 103, 116, 118, 120–122, 163, 173–175, 184–195, 203–206, 211, 217, 224, 226
- van Gogh, A.T.M., see den Broeder, F.J.A. 103, 120, 141, 167, 197–199, 215, 266
- van Gogh, A.T.M., see Giebels, I.A.M.E. 90, 91, 98, 250–253
- van Gogh, A.T.M., see Griessen, R. 98, 103, 116, 117, 120, 224
- van Gogh, A.T.M., see Isidorsson, J. 90, 91, 233, 235, 237–239
- van Gogh, A.T.M., see Kooij, E.S. 93–98, 101, 103, 105, 106, 111, 116–118, 126, 127, 133, 136, 137, 148–150, 180, 182, 183, 185, 186, 204
- van Gogh, A.T.M., see Nagengast, D.G. 89, 91, 147, 148, 150, 151, 153, 154, 228–230, 232, 246, 266
- van Gogh, A.T.M., see van der Molen, S.J. 211, 228, 229, 231–233, 246
- van Mechelen, J.L.M. 90
- Vankar, Y.D., see Reddy, M.V.K. 342
- VanNice, R., see Mazhar-ul-Haque, 314
- Varga, M. 295
- Varga, M., see Ruoff, P. 292, 293, 295
- Vauthier, C., see Chauvierre, C. 355
- Vázquez, B. 359
- Vazquez, B., see Goñi, I. 357
- Vazquez, B., see Pascual, B. 357
- Vázquez, M.B. 357
- Vázquez-Torres, H., see Vera-Pacheco, M. 357
- Velayutham, D., see Vijayarathai, T. 285
- Venkatarao, K., see Paulrajan, S. 355
- Vera-Pacheco, M. 357
- Verma, M.K., see Singh, M.P. 323
- Vetterling, W.T., see Preuss, W.H. 243
- Vijayarathai, T. 285, 353
- Vijayakumar, M.T. 357
- Vijayaraghavan, R., see Dhar, S.K. 39, 41
- Vijayaraghavan, S., see Moss, R.A. 371
- Villain, F., see Briois, V. 319
- Vincenti, M., see Vione, D. 364
- Vione, D. 364
- Vis, R.D., see Huisman, M.C. 98, 100–103, 116, 117
- Visani, P., see Fisk, Z. 47
- Visani, P., see Thompson, J.D. 47
- Visegrady, A., see Nagygyory, S. 294
- Visokay, M., see Basceri, C. 372
- Visser, J., see Claassen, A. 290
- Vitta, S.B. 358
- Vitz, J., see Krohn, K. 346
- Vnuchkova, L.A., see Degtyar, V.A. 57
- Vogt, O., see Léger, J.M. 5, 7
- Vogt, O., see Rossat-Mignod, J. 6
- von Löhneysen, H., see Goll, G. 45, 46
- von Löhneysen, H., see Pietrus, T. 46
- von Rottkay, K. 90–93, 97, 128–130, 136, 239–241, 243–246, 249, 250, 267
- Vora, R.A. 361
- Voss, D. 108, 266
- Waddill, G.D., see Holm, A.P. 19
- Wadsworth, E. 284, 306
- Wager, C.A., see Keck, G.E. 412
- Wager, T.T., see Keck, G.E. 412

- Wahlbeck, P.G., see Yannopoulos, L.N. 88, 116, 117, 183
- Wakatsuki, Y., see Hou, Z. 419, 420, 446, 447, 454, 455, 457, 459, 461, 463, 465, 469
- Walden, G.H. 289
- Wall, M., see Williams, N.H. 366
- Wallace, W.E., see Mannsman, M. 210
- Wallace Jr., J.M., see Furman, N.H. 286
- Wang, C.H., see Wang, D.F. 363
- Wang, D.F. 363
- Wang, H.C., see Lee, M.W. 103, 111, 113, 115
- Wang, J.C. 297
- Wang, J.G., see Shi, Q.Z. 345
- Wang, L.P., see Wang, Y.P. 370
- Wang, L.Q. 359
- Wang, L.Y., see Fang, T.R. 360
- Wang, M. 34
- Wang, M., see Morgan, M.G. 57
- Wang, M.E. 4, 8
- Wang, M.E., see Chan, J.Y. 17, 18, 58
- Wang, Y. 4, 6, 24, 208, 224, 226
- Wang, Y.H. 317
- Wang, Y.P. 370
- Wanka, S., see Goll, G. 45, 46
- Ward, P.J., see Norman, R.O.C. 306, 317
- Ward, R.C.C., see Grier, E.R. 147
- Ward, R.C.C., see Hjärvarsson, B. 206
- Ward, R.C.C., see Kooi, B.J. 151, 154, 157–159
- Ward, R.C.C., see Udovic, T.J. 222
- Ward, R.C.C., see Wildes, A.R. 90, 91, 146
- Wardlaw, W., see Bradley, D.C. 309–312
- Warren, C.G. 310
- Wartenburg, H. 312
- Washko, S. 28
- Watkin, J.G., see Brady, E.K. 458
- Watson, L.T., see Nagy-Ungvarai, Z. 298
- Watt, G.W. 431
- Watts, L. 343
- Watts, L., see Emerson, G.F. 343
- Weaver, J.H. 87, 105, 191, 205
- Weaver, J.H., see Lynch, D.W. 283
- Weaver, J.H., see Peterman, D.J. 105, 191, 205
- Webb, D.J., see Chan, J.Y. 17, 18, 58
- Weber, S., see Borgschulte, A. 91, 151, 161–163
- Wei, L.M., see Pan, W.B. 334
- Wei, Y., see Paulenova, A. 304
- Weidmann, H., see Furstner, A. 402
- Weinstock, L.M. 304
- Weis, H., see Leervad Pedersen, T.P. 143
- Weiss, J. 365
- Weitzer, F. 21, 22, 25, 26
- Welling, M.S., see van der Molen, S.J. 103, 167, 197, 198, 200, 215, 266
- Wells, A.F. 26
- Wells, M.R., see Grier, E.R. 147
- Wells, M.R., see Hjärvarsson, B. 206
- Wells, M.R., see Wildes, A.R. 90, 91, 146
- Werner, T., see Christoffers, J. 285, 346, 348
- Werner, T., see Rössle, M. 285, 348
- West, W., see Pojman, J.A. 297
- Westerwaal, R.J., see Borgschulte, A. 92, 93, 103, 163, 166, 175, 176, 178
- Westerwaal, R.J., see van Mechelen, J.L.M. 90
- Whittle, R.R., see Chebolu, V. 427
- Wiaux, M., see Marko, I.E. 343
- Wiesendanger, R., see Pundt, A. 147
- Wiesinger, G. 87
- Wiesinger, G., see Weitzer, F. 21, 22, 25, 26
- Wijngaarden, R.J., see Hoekstra, A.F.Th. 103, 108, 110–112, 215, 266
- Wijngaarden, R.J., see Huiberts, J.H. 88–92, 96, 98–101, 103, 104, 107–109, 112, 113, 116–118, 120–123, 133, 136, 163, 166, 167, 183, 208, 214, 224
- Wijngaarden, R.J., see Remhof, A. 103, 271, 272
- Wildes, A.R. 90, 91, 146
- Willard, H.H. 286, 289, 290
- Willett, J.L. 361
- Williams, C.W., see Antonio, M.R. 286
- Williams, N.H. 366
- Willich, P., see Hartmann, M. 23
- Willis, J.M., see Ahuja, R. 231
- Wills, J.M., see Eriksson, O. 47
- Wilson, M., see Ewing, D.T. 290
- Win, D.T., see Than, M.M. 296
- Windgasse, J., see Remhof, A. 117, 146, 151, 210
- Wine, P.H. 364
- Winfree, A.T. 291, 298
- Winfree, A.T., see Jahnke, W. 298, 299
- Winiarski, A., see Szytuła, A. 41
- Winkler, C. 87
- Wipf, P., see Totleben, M.J. 396
- Witter, K., see Hartmann, M. 23
- Witter, K., see Heitmann, H. 23
- Witter, K., see Urner-Wille, M. 23
- Wittmann, M., see Hegedus, L. 295
- Wittmann, M., see Nagygyory, S. 294
- Wittmann, M., see Oslovovitch, J. 294
- Wolf, W. 222, 224, 225
- Wong, C.M., see Ho, T.L. 314, 322, 325
- Wosnitza, J. 46
- Wosnitza, J., see Goll, G. 45, 46

- Wrigge, F.W., see Geilmann, W. 289
 Wright, P.J., see Barry, J. 309
 Wu, J.J., see Liu, M.Z. 361
 Wu, M.J., see Pan, W.B. 334
 Wu, Q., see Zheng, S.Y. 360
 Wu, Y.C., see Pan, W.B. 334
 Wu, Z. 224, 226, 227
 Wutting, M., see Leervad Pedersen, T.P. 143
- Xavier, B., see Chang, K.E. 220, 221
 Xi, C.J. 337
 Xi, C.J., see Yang, X.H. 337
 Xie, P., see Hou, Z. 446
 Xu, J.D. 375, 376
 Xu, J.D., see Gorden, A.E.V. 375
 Xu, S.X., see Fang, T.R. 360
 Xu, Y., see Ge, X.C. 359
 Xue, C.H., see Wang, D.F. 363
 Xue, J.S., see Antonio, M.R. 286
 Xue, Y., see Naher, S. 47
 Xue, Y., see Suzuki, H. 47
- Yacovan, A., see Hoz, S. 413
 Yağci, Y., see Tunca, U. 355
 Yagi, T., see Sumaoka, J. 369
 Yakovlev, N.G. 376
 Yamada, M., see Thamizhavel, A. 34, 36, 48
 Yamada, T. 348
 Yamada, Y., see Yoshimura, K. 90
 Yamaguchi, M., see Honda, Y. 399
 Yamaguchi, M., see Inanaga, J. 398, 403, 417–419
 Yamaguchi, M., see Kusuda, K. 399
 Yamaguchi, M., see Matsukawa, M. 399
 Yamaguchi, M., see Otsubo, K. 399, 401
 Yamaguchi, M., see Tabuchi, T. 402
 Yamamoto, E., see Thamizhavel, A. 34, 36, 48
 Yamamoto, Y. 369, 370, 397
 Yamamoto, Y., see Komiyama, M. 368, 370
 Yamato, T. 313, 345
 Yamauchi, R., see Suzuki, H. 47
 Yamazaki, H., see Hou, Z. 446, 454, 457, 459, 463
 Yan, J.M. 369
 Yan, S.H., see Hegedus, L. 295
 Yang, X.-X., see Lu, Y.-M. 32, 34, 35
 Yang, X.H. 337
 Yang, X.H., see Xi, C.J. 337
 Yang, X.X., see Lu, Y.M. 48, 49
 Yannopoulos, L.N. 88, 116, 117, 183
 Yaresko, A.N., see Oppeneer, P.M. 47
 Yarmolyuk, Ya.P., see Sichevich, O.M. 23
 Yashiro, M. 371
 Yashiro, M., see Komiyama, M. 366, 368
 Yashiro, M., see Takarada, T. 371
 Yashiro, M., see Tikedá, N. 369
 Yates, J.S. 290
 Yatsimirsky, A.K., see Maldonado, A.L. 369
 Ye, J. 48, 49
 Yilmaz, E. 359
 Yilmaz, O., see Yilmaz, E. 359
 Yocum, P.N., see Kiss, Z. 395
 Yoda, C., see Hou, Z. 455, 461, 465
 Yokoyama, M., see Hatanaka, Y. 314, 348
 Yokoyama, M., see Komiyama, M. 368, 370
 Yokoyama, Y., see Inanaga, J. 417
 Yoneyama, M. 298
 Yonezawa, S., see Kim, J.H. 312
 Yoshida, A. 411
 Yoshihara, K. 3, 4, 6–9
 Yoshii, S. 28–30
 Yoshii, S., see Kawasaki, Y. 30
 Yoshimura, K. 90
 Yoshino, T., see Goll, G. 45, 46
 Yoshino, T., see Jung, M.H. 43, 46
 Yoshino, T., see Pietrus, T. 46
 Yoshino, T., see Wosnitzá, J. 46
 Yoshizaki, R., see Shigekawa, H. 368
 Young, L.B. 316, 317, 319, 372
 Young, L.B., see Trahanovsky, W.S. 317, 319
 Young, L.H., see Trahanovsky, W.S. 319
 Young, M.G., see Trahanovsky, W.S. 321
 Young, P. 286
 Young, P., see Willard, H.H. 286, 289, 290
 Yu, J.G., see Fang, T.R. 360
 Yuan, D.Q., see Yan, J.M. 369
 Yuan, K., see Wang, Y.P. 370
 Yuan, Y.L., see Zhang, J. 309
 Yunus, W.M.Z.W., see Fakhru'l-Razi, A. 360
 Yunus, W.M.Z.W., see Janarthanan, J. 361
 Yunus, W.M.Z.W., see Lutfor, M.R. 360
- Zabel, H., see Kooij, E.S. 154–157
 Zabel, H., see Remhof, A. 91, 117, 146, 151, 210
 Zachariassen, W.H., see Benz, R. 61, 62
 Zaikin, A.N. 291
 Zalkin, A., see Tilley, D.T. 434
 Zamani, F.F., see Oskooie, H.A. 311
 Zameni, F.F., see Heravi, M.M. 311, 313
 Zande, B.J., see Saha, S. 21
 Zanichi, G., see Riani, P. 38–41
 Zanna, H.K., see Eromosele, I.C. 360
 Zardaloo, F.S., see Iranpoor, N. 325
 Zardaloo, F.Z., see Iranpoor, N. 311

- Zellner, R., see Herrmann, H. 364
Zeng, L. 32, 34, 35
Zeng, Z., see Li, Z. 21
Zevenhuizen, S.J.M., see Di Vece, M. 97, 98, 139, 140, 244–246
Zhabotinsky, A.M. 291, 293, 295, 296
Zhabotinsky, A.M., see Zaikin, A.N. 291
Zhang, F.C., see Ng, K.K. 107, 126, 127, 136, 191, 192, 198, 199, 202, 206, 212–214, 219, 222, 231
Zhang, H., see Evans, W.J. 436, 449, 456, 458
Zhang, J. 309
Zhang, J., see Wang, L.Q. 359
Zhang, S., see Dai, D. 21
Zhang, S., see Fang, Q. 21
Zhang, S., see Fang, R. 21
Zhang, W., see Fujieda, S. 298
Zhang, X. 467
Zhang, X., see Dai, D. 21
Zhang, X., see Fang, R. 21
Zhang, X.W., see Hillier, A.C. 466
Zhang, Y. 309, 359, 400
Zhang, Y., see Hou, Z. 419, 420, 446, 447, 454, 457, 459, 463
Zhang, Y.H., see Ji, X.H. 74
Zhang, Y.H., see Zhao, X.B. 74
Zhang, Z.H., see Wang, L.Q. 359
Zhao, J.-T., see Lu, Y.-M. 32, 34, 35
Zhao, J.T., see Lu, Y.M. 48, 49
Zhao, X.B. 74
Zhao, X.B., see Ji, X.H. 74
Zheng, C. 74, 75
Zheng, Q., see Li, Z. 21
Zheng, S.Y. 360
Zhou, F.M., see Cao, Y.M. 357
Zhou, J.M., see Chen, W. 370
Zhou, W.Z., see King, N.C. 365
Zhou, X.L., see Wang, D.F. 363
Zhu, D.H. 375
Zhu, S., see Branum, M.E. 370
Zhuravlev, N.N. 6
Ziegler, M., see Xu, J.D. 375, 376
Zielen, A.J. 288
Zieliński, J., see Matlak, M. 57
Ziller, J.W., see Evans, W.J. 286, 312, 395, 396, 420, 427, 434, 435, 437–441, 443, 444, 449–451, 457
Zin, W., see Rahman, L. 360
Zinke, P.W., see Molander, G.A. 401
Zittel, H.E., see Miller, F.J. 285
Zoestbergen, E., see Kooi, B.J. 151, 154, 157–159
Zohuriaan-Mehr, M.J., see Pourjavadi, A. 361
Żolnierek, Z. 61, 62
Żolnierek, Z., see Troć, R. 61
Zuidema, L.J., see Doyle, M.P. 321
Züttel, A., see Hayoz, J. 194, 201
Zwicknagl, G., see Goll, G. 45, 46
Zwiener, G. 12
Zwiener, G., see Grund, I. 10, 13

SUBJECT INDEX

- ^{15}N technique 99, 100
- 360° in-plane rocking scans 155
- α phase 117
- α phase of $\text{LaH}_{2-\delta}$ (111) 237
- α phase of Y 117
- α phase of YH_δ 96
- α phase of YH_x 96
- β phase 114, 117
- β phase of La fcc 239
- β phase of La (111) 237
- β phase of $\text{LaH}_{2-\delta}$ (111) 237
- β phase of YH_2 104, 105, 117, 197
- β phase of $\text{YH}_{2\pm\delta}$ 96
- $\beta \rightarrow \gamma$ transition 114
- $\Delta\chi$ 132, 133
- γ phase 114, 117
- γ phase of GdH_3 141, 249
- γ phase of $\text{LaH}_{3-\delta}$ (111) 237
- γ phase of $\text{Y}_{0.5}\text{Mg}_{0.5}\text{H}_x$ 228
- γ phase of $\text{YH}_{3-\delta}$ 96, 104, 105, 111, 117, 197, 198
- γ phase of YH_x 111, 127
- ψ spectra 126
- Δ spectra 126

- ab initio band structure calculations 215
- absorber-backscatterer combinations 248
- absorption coefficient 114, 144
- activated hopping 111
- adjustable shift to account for uncertainties in
 - chemical bonding and core relaxation effects 249
- AFM images of Gd films capped with Pd nanoparticles 180
- alloy
 - Ce-Mg-Bi 13
 - Sm-Mg-Bi 13
 - U-(Th,Nd,Pr)-Bi 15
- AlO_x buffer 93
- AlO_x buffer layer 92, 173, 237
- ammonium cerium(IV) sulfate 302
- ammonium hexanitratocerate(IV) 299
 - crystal structure 300
 - hydrophobic analogues 301
 - preparation 299, 300
 - solubility 301
 - solvents for reactions 302
 - structure in solution 300, 301
- angular resolved photoemission spectra 172
- angular yield profile 157
- Arrhenius plot 142
- artificial restriction enzymes 370
- assignment of oxidation states 285
- Au and Pt over layers 91
- Auger
 - electron spectra 162
 - spectra of Y films 171
 - spectra of Y films capped with Pd overlayer 173
- average island diameter 167

- backbone polymer 356
- Baeyer-Villiger oxidation 323
- band structure
 - broken symmetry structure 211
 - $\text{Gd}(\text{Al}_{1-x}\text{Bi}_x)_2$ 57
 - HoD_3 -type structure 211
 - La_3MgBi_5 13
 - LaH_2 and LaH_3 192
 - LaH_3 213
 - LaLiBi_2 13
 - LaPtBi 46
 - $\text{MnBi}_{1-x}\text{R}_x$ 21
 - $\text{Sc}_6\text{Bi}_{1.68}\text{Te}_{0.80}$ 74
 - $\text{Y}_{12}\text{Co}_5\text{Bi}$ 28
 - $\text{Yb}_9\text{Zn}_4\text{Bi}_9$ 56
 - YbPdBi 41
 - YbPtBi 47
 - YH_3 211, 220
 - YH_3 and LaH_3 223
 - YNiBi 36
- Belousov-Zhabotinsky reaction
 - demonstration experiments 298
 - effect of molecular oxygen 297
 - effect of surfactants 297
 - effect of temperature 298

- formation of spatial patterns 298
- history 291
- induction period 296
- inhibition by chloride ions 296, 297
- mechanism 292
- oscillating electrical potential 299
- oscillating polymerization reactions 297, 298
- oscillation period 296
- oscillations characteristics 296
- reactants 295, 296
- study by calorimetry 298
- study by magnetic resonance imaging 298
- study by photoluminescence 298
- trigger waves 298
- Bi flux 3
 - $\text{CeCu}_{1-x}\text{Bi}_2$ 48
 - CeNiBi_2 34, 36
 - $\text{R}_3\text{Pt}_3\text{Bi}_4$ 44
 - RAgBi_2 52
 - RPtBi 44
- BiF_3 -type structure 215, 217
- binary rare earth bismuthides 3, 5
 - electrical and magnetic properties 4
 - structure 3, 6
- biopolymers 356
- bis[trinitratocerium(IV)] chromate 311
- black state in RMgH_x alloys 232
- Blue stain 372
- bonding
 - homoatomic Bi–Bi 3, 12, 13, 18, 54, 75
 - LaGaBi_2 57
 - $\text{R}_{12}\text{Co}_5\text{Bi}$ 28
 - RNiBi , RPdBi , and RPtBi 46
- Born and Szigeti effective charges 207
- bounding domain 148
- broken symmetry structure 203, 209, 210, 220
- bromate-driven oscillators 292
- bromination 327, 329
- bulk Y–H phase diagram 119

- CaF_2 155
- Car–Parrinello method 210
- carrier concentration 109
- catalyst for cerium(IV)-mediated oxidations 323
- catastrophe theory 291
- $\text{Ce}_{1.25}\text{Bi}_{3.78}\text{S}_8$ 63–65
- $\text{Ce}_2\text{Bi}_2\text{Se}_5$ 69
- Ce_3GeBi 59
- Ce_3MnBi_5 15, 17
- $\text{Ce}_3\text{Pt}_3\text{Bi}_4$ 43, 44
- Ce_5SiBi_2 58
- $\text{Ce}_6\text{ZnBi}_{14}$ 53–55
- $\text{Ce}_8\text{Pd}_{24}\text{Bi}$ 39, 42
- $\text{Ce}^{4+}/\text{Ce}^{3+}$ couple 284
- CeGeBi_2 59, 60
- CeH_2 107
- $\text{CeH}_{2+\xi}$ 87
- $\text{CeH}_{3-\delta}$ 112
- CeNiBi_2 32, 34
- CePtBi 43, 46
- cerate oxidimetry 286
- ceria 312
- ceric-cerous sulfate dosimeter 372
- cerimetry
 - advantages 286, 287
 - applications 289
 - catalysts 290
 - determination of hydrogen peroxide 290
 - determination of inorganic ions 289, 290
 - determination of organic compounds 290
 - end-point determination 288
 - redox indicators 288
 - standard solutions 286, 287
 - standardization of cerium(IV) solutions 288
- cerium-catalyzed Belousov–Zhabotinsky reactions 291
- cerium-mediated electrosynthesis 350
- cerium(IV)
 - acetate 304
 - alkoxides 311
 - dioxide 312
 - fluoride 284, 312
 - – oxidation of cerium(III) 284, 285
 - – oxidizing agents for cerium(III) 284, 285
 - – strong oxidizing agents 284, 285
 - methanesulfonate 307
 - perchlorate 306
 - periodate 310
 - polyoxometalates 314
 - reagents 299
 - sulfate tetrahydrate 304
 - triflate 307
 - trifluoroacetate 306
 - trihydroxy hydroperoxide 310
- cerocene 285
- CerOx^{TM} process 373
 - waste treatment 373
- changes in electrical resistance during hydrogen loading–deloading cycles 181
- charcoal-supported reagents 314, 348
- chemical loading 103
- chi potential difference 132

- chlorination 327
 Clay-supported reagents 313
 coherence length 154, 237
 color neutral switchable mirrors 226
 colored trihydride state 226
 compositional disproportionation 228
 contour plots of the X-ray intensity as a function of time 252
 coordination number 249
 cosolvent 398–401, 405, 409, 410, 416–419, 423, 429
 Coulomb gap 111
 cross-sectional HRTEM images 159
 cubic SmH_2 130
 CV curve 242
 cyclic
 – durability 246
 – structural changes 149
 – variation in resistance 260
 cyclopentadienyl 395, 431, 456

 decomposition of water
 – catalysts for water decomposition 365
 – oxidation of water 365
 defects
 – $\text{CeCu}_{1-x}\text{Bi}_2$ 48
 – DyRhBi 30
 – $\text{R}_5\text{Ni}_2\text{Bi}$ 37
 – $\text{RNi}_{1-x}\text{Bi}_2$ 34, 35
 deloaded PrH_x films 126
 deloaded $\text{SmH}_{2\pm\xi}$ 139
 density functional theory (DFT) 208
 dependence of optical switching time on Pd thickness 174
 DFT-LDA 208
 dhcp structure 121
 dielectric function 113
 – $\text{YH}_{3-\delta}$ 208
 diffusion 197
 – coefficient 121, 141, 142
 – sample 102
 dihydride state 87
 dihydride transmittance window for $\text{La}_{1-y}\text{Y}_y\text{H}_2$ films 192
 dinitratocerium(IV) chromate dihydrate 311
 disproportionation 187
 distance between the hexagonal planes 118
 domain switching 150, 163
 doping
 – Bi in rare earth cobalt alloys 28
 – Gd in Bi_2Se_3 71
 – R in Bi_2Te_3 74
 – R in MnBi 21
 Drude oscillator 125, 189
 Drude-like dielectric function 114
 Dy 146
 dysprosium films 145

 effective optical bandgap 230, 250
 elastic recoil detection analysis (ERDA) 98
 electrical resistivity 103
 – $\text{Ce}_3\text{Pt}_3\text{Bi}_4$ 44
 – $\text{Ce}_8\text{Pd}_{24}\text{Bi}$ 42
 – $\text{CeCu}_{1-x}\text{Bi}_2$ 49
 – CeNiBi_2 36
 – CePtBi 46
 – CeRhBi 30
 – ErPdBi and ErPd_2Bi 41
 – EuBi_4S_7 and $\text{Eu}_3\text{Bi}_4\text{S}_9$ 69
 – $\text{Gd}(\text{Al}_{1-x}\text{Bi}_x)_2$ 57
 – LaGaBi_2 57
 – LaPtBi 46
 – NdPtBi 47
 – PrPtBi 46
 – $\text{R}_{12}\text{Co}_5\text{Bi}$ 26
 – RAgBi_2 52
 – RBi_2Te_4 and RBi_4Te_7 73
 – RBiTe_3 73
 – SmPtBi 47
 – $\text{Yb}_9\text{Zn}_4\text{Bi}_9$ 56
 – YbCuBi 51
 – YbPdBi 41
 electrochemical
 – hydrogenation 97
 – loading 93, 99, 103, 104, 129
 – potential 94
 – synthesis 350
 electrochromic devices 266
 electrode
 – bubbling platinum electrode 285
 – conductive diamond electrode 285
 – dropping mercury electrodes 285
 – glassy carbon electrode 285
 – gold electrode 285
 – platinized titanium electrode 285
 – potential 95, 132, 135
 – pyrolytic graphite electrode 285
 – rotating platinum disc electrode 285
 – stationary platinum disc electrode 285
 electromigration 167, 197, 198
 electron bands
 – cubic LaH_3 227
 – cubic YH_3 227

- hexagonal YH_3 227
- YH_3 218
- electron correlation theories 199
- electron spin resonance
 - Gd-doped Bi_2Se_3 71
 - Gd-doped Bi_2Te_3 74
 - YPtBi 46
- electron–electron correlations 111
- electronic band structure for YH_3 225
- electronic structure of $\text{YH}_{3-\delta}$ 201
- electrosynthesis 350
- ellipsometric measurements 125
- enthalpy of formation 183
- epitaxial MBE 196
- epitaxial PLD 196
- epitaxial films 89
 - Y (0001) 170
 - Y (10–400 nm) 154
 - Y (300 nm) 153
 - YH_2 194
 - YH_x 148
- epitaxial switchable mirrors 146
- equilibrium potential 96
- Er–Mg alloy 249
- $\text{Er}_{0.42}\text{Mg}_{0.58}$ 243, 249
- ERDA 98, 100, 116
- $\text{ErH}_{2+\xi}$ 87
- esterification reactions 334
- etchant 372
- $\text{Eu}_{1.1}\text{Bi}_2\text{S}_4$ 63, 67, 68
- $\text{Eu}_{14}\text{InBi}_{11}$ 58
- $\text{Eu}_{16}\text{Bi}_{11}$ 4
- Eu_2BiS_4 63, 64, 66
- $\text{Eu}_3\text{Bi}_4\text{S}_9$ 63, 69
- $\text{Eu}_3\text{Bi}_4\text{Se}_9$ 70, 71
- Eu_3GdBi_3 14
- Eu_4Bi_3 4
- $\text{Eu}_5\text{Bi}_3\text{H}$ 10, 11
- EuBi_2S_4 63, 64
- EuBi_2Se_4 70, 71
- EuBi_4S_7 69
- EuBi_4Se_7 70, 71
- EuCuBi 49, 50
- EuLiBi 10, 13
- EuPd_2Bi_2 38, 40
- ex-cell method 350
- EXAFS 249
 - normalized EXAFS data 248
- expansion-induced stress potential 150
- extended constant transmittance 262
- extinction coefficient 113, 115, 145
- F 1s singlet 161
- fcc $\text{LaH}_{3-\delta}$ 236
- fcc $\text{YH}_{3-\delta}$ 230
- fcc $\text{YH}_{3-\delta}$ clusters 232
- fcc- YH_2 film 157
- ferriin 289
- ferroin 289
- Field, Körös, Noyes model 292
- FKN model 292
- flash photolysis 364
- fluorinating agent 312
- fluorination 326
- Fourier transform 248
- frequency dependent conductivity 209
- functionalization of alkenes 338
- gadolinium films 139
- galvanostatic
 - configuration 94
 - hydriding 95
 - hydrogen loading 135
 - intermittent titration technique (GITT) 96, 105, 140, 182
 - loading 96, 106, 129, 182
- gas phase loading 93, 103
- gasochromic applications 143
- Gd nanoparticles 257, 260
- Gd–Gd 249
- Gd–H 249
- Gd–Mg 249
- Gd–Mg alloy 241
- Gd–Mg multilayers 251, 252
- Gd–O 249
- $\text{Gd}_{0.38}\text{Mg}_{0.62}$ 246
- $\text{Gd}_{0.40}\text{Mg}_{0.60}$ 249, 254
- $\text{Gd}_{0.42}\text{Mg}_{0.58}$ 243, 249
- $\text{Gd}_{0.4}\text{Mg}_{0.6}$ 246, 248
- $\text{Gd}_{0.5}\text{Mg}_{0.5}$ 243, 246
- $\text{Gd}_{0.6}\text{Mg}_{0.4}$ 246, 252
- $\text{Gd}_{0.7}\text{Mg}_{0.3}$ 246
- $\text{Gd}_{0.80}\text{Mg}_{0.20}$ 254
- $\text{Gd}_{1-z}\text{Mg}_z$ 241
- $\text{Gd}_{1-z}\text{Mg}_z\text{H}_x$ 233, 246, 247
- Gd_3DyBi_3 14
- Gd_3Pd 266
- Gd_xT_y 264
- GdH_2 246
- GdH_3 142, 246
- $\text{GdH}_{3-\delta}$ 139, 143–145
- GdMg 197
- GdMg switchable mirrors 247

- GdMgH_x 197
 generalized gradient approximation 226
 graft copolymer 356
 grafting yield 356
 grain size 237
 Grob fragmentation 408
 GW
 – approximation 215
 – calculations 193

 H recoil spectra of various films 265
 half-Heusler alloy
 – RNiBi 36
 – RPdBi 41
 halide–olefin coupling reactions 403, 405
 Hall
 – coefficient 107, 109
 – measurements 107
 – voltage 109, 111
 halogenation reactions 326
 Hanessian's stain 372
 hcp MgH₂ 236
 hcp YH_{3–δ} 230
 heavy fermion
 – CeNiBi₂ 36
 – CeRhBi 30
 – YbPdBi 41
 – YbPtBi 47
 height histogram 152
 Heusler alloy, RPd₂Bi 41
 hexagonal SmH₃ 130
 Hg/HgO 104
 HMPA 397–401, 405, 409, 410, 417–423, 426,
 427, 431, 447, 455, 457, 460, 462, 464
 Ho₁₂Co₅Bi 27
 Ho₅Cu_{0.7}Bi_{2.3} 49, 52
 HoD₃ (*P3c1*) 117
 HoD₃-type structure 201–203, 208, 210, 220
 HoH_{2+ξ} 87
 homogeneous switching 101
 homopolymer 356
 HoNiBi 32, 36
 HRTEM micrograph of Y nanoparticles 257
 hybridization of 4f orbitals 368, 369
 hydride
 – R₅Bi₃H 10
 – R₆Fe₁₃BiH_x 22, 23
 hydrogen
 – bonds 300
 – concentration determination 95, 98
 – depth profiles 100
 – diffusion coefficient 119
 – interaction in metal hydrides 88
 – loading 103
 – local modes 114
 – permeable oxide shell 257
 – sensors 272
 – traffic jam 199
 – vibration modes 113
 – visualization of hydrogen migration 197
 hydrogenation techniques 93
 hydrolysis
 – DNA 366
 – peptides 371
 – phosphodiester 366
 hydrophobic cerium(IV) reagents 308
 hysteresis 107, 180, 182–184, 188

in situ electrochemical hydrogenation 94
 in-cell method 350
 in-plane
 – expansion 128
 – lattice parameter 163
 indicator layers 269
 inelastic neutron scattering experiments 113
 inert gas evaporation 91, 257
 infrared transmittance spectra 115
 initiation of radical polymerization reactions 354
 inorganic–organic hybrid materials 363
 interatomic distance 249
 interband 105
 intermetallic LaMg 237
 intraband transitions 105
 iodination 329
 ionic bonding in YH_{3–δ} 206
 isotope effect 197, 203

 ketone–olefin coupling reactions 403
 kinetic barrier 285
 Kohn–Sham eigenvalues 209
 Kondo insulator
 – Ce₃Pt₃Bi₄ 44
 Kondo lattice
 – CeNiBi₂ 36
 Kondo scattering 108
 – CeRhBi 30

 La–H system 120
 La–Mg alloy 235
 La–Y alloy films 186
 La_{0.51}Mg_{0.49} 237
 La_{0.54}Y_{0.46}H_x 188, 192
 La_{0.55}Mg_{0.45} 237

- $\text{La}_{0.55}\text{Mg}_{0.45}\text{H}_2$ 236, 237
 $\text{La}_{0.55}\text{Mg}_{0.45}\text{H}_{2.55}$ 236, 237
 $\text{La}_{0.55}\text{Y}_{0.45}\text{H}_x$ 188
 $\text{La}_{0.5}\text{Mg}_{0.5}\text{H}_x$ 232
 $\text{La}_{1-y}\text{Y}_y$ 189, 190
 $\text{La}_{1-y}\text{Y}_y\text{H}_2$ 190
 $\text{La}_{1-y}\text{Y}_y\text{H}_{3-\delta}$ 193
 $\text{La}_{1-y}\text{Y}_y\text{H}_x$ 186
 $\text{La}_{1-y}\text{Y}_y\text{H}_x$ films 193
 La_3MgBi_5 10, 13
 $\text{La}_3\text{Pt}_3\text{Bi}_4$ 43, 44
 La_4SnBi_2 59
 $\text{La}_6\text{Co}_{13}\text{Bi}$ 24–26
 LaCeBi 14
 Lacher's equation 188
 LaF_3 -type structure 215, 217
 LaGaBi_2 57, 58
 LaH_2 236
 $\text{LaH}_{2+\xi}$ 87
 LaH_3 208, 209
 $\text{LaH}_{3-\delta}$ 238, 239
 LaH_x 121, 122, 127, 209, 239
 LaLi_3Bi_2 10–12
 LaLiBi_2 10, 12
 LaMg 239
 LaMg (110) 237
 LaMg alloy film 239
 $\text{LaMgH}_{2.5}$ 238
 lanthanum films 120
 LaPtBi 43, 46
 laser ablation 91
 lateral
 – diffusion geometry 168
 – hydrogen concentration 102
 – hydrogen diffusion 199
 – hydrogen transport 141
 lattice constants 118
 LDA 209
 – approximation 210
 – based band structure calculation for the
 HoD_3 -type structure 204
 LEED 161
 lifetime 119
 light R metal 89
 linear–muffin–tin–orbital (LMTO) 215
 local hydrogen concentration 200
 localized states 126
 Lorentz oscillators 125, 190

 magnetic properties
 – Ce_3MnBi_5 15
 – $\text{Ce}_8\text{Pd}_{24}\text{Bi}$ 42
 – $\text{CeBi}_{1-x}\text{Te}_x$ 74
 – $\text{CeCu}_{1-x}\text{Bi}_2$ 48
 – CeNiBi_2 36
 – CePtBi 46
 – CeRhBi 30
 – $\text{Er}_5\text{Pt}_2\text{Bi}$ 48
 – Er_6MnBi_2 20
 – ErPdBi and ErPd_2Bi 41
 – $\text{Eu}_{14}\text{InBi}_{11}$ 58
 – $\text{Eu}_{14}\text{MnBi}_{11}$ 18
 – EuCuBi 51
 – EuLiBi 13
 – Gd–Fe–Bi 23
 – $\text{Gd-doped Bi}_2\text{Te}_3$ 74
 – $\text{Gd}_4(\text{Sb}_x\text{Bi}_{1-x})_3$ 61
 – $\text{Gd}(\text{Al}_{1-x}\text{Bi}_x)_2$ 57
 – LaCeBi 14
 – NdPtBi 47
 – PrPtBi 46
 – $R_{12}\text{Co}_5\text{Bi}$ 26
 – $R_4\text{Bi}_2\text{Te}$ 73
 – $R_5\text{CoBi}_2$ 24
 – $R_6\text{Fe}_{13}\text{Bi}$ 23
 – $R_6\text{Fe}_{13}\text{BiH}_x$ 23
 – RAgBi_2 52
 – RLi_2Bi_2 12
 – $\text{Sm}_5\text{Bi}_3\text{H}$ 11
 – SmPtBi 47
 – ThNiBi_2 38
 – $\text{U}_2\text{N}_2\text{Bi}$ 62
 – UCuBi_2 52
 – USbBi 61
 – $\text{Yb}_9\text{Zn}_4\text{Bi}_9$ 54
 – YbLiBi 13
 – YbPdBi 41
 – YbPtBi 47
 magnetoresistance 107, 109
 – CeNiBi_2 36
 – CePtBi 46
 – $\text{Eu}_{14}\text{MnBi}_{11}$ 18
 – YbPdBi 41
 magnetotransport properties 108
 Manhattan
 – effect 147, 149
 – skyline 147, 163
 – switching 147
 many-body effects 215
 melts
 – La–Al–Bi 57
 metal insulator transitions 109, 111

- metal to semiconductor (M-S) transition 87
- Mg clusters 228
- MgH₂ 228, 236, 237, 239
- micrometer-sized domains 147
- Mie theory 257
- miscibility gap 185
- mixed valence
 - Eu₂BiS₄ 67
 - Yb₉Zn₄Bi₉ 56
 - YbPdBi 41
- MMTr 343
- model for tetravalent plutonium 374
- molar volume 118
- molecular beam deposition 90
- monomethoxytrityl 343
- Mössbauer spectroscopy
 - EuLiBi 13
- NaBH₄ 97
- Nafion[®] 117 membrane 97
- nanocrystalline
 - PLD films 195
 - PLD Y films 196
 - PrH_{3-δ} films 127
 - YH₂ 195
- nanoparticle based switchable mirrors 255
- Nd₆Fe₁₃Bi 22
- NdPtBi 43, 47
- nearest neighbor distances 118
- Nernst equation 96, 183
- nitrate free radicals, generation 364
- nitration reactions 334
- nitroferroin 289
- normalized oxygen concentration 102
- nuclear reaction analysis (NRA) 98
- octahedral sites 113, 117
- optical contrast 119, 180
- optical microscope images 168
- optical transmittance 89, 95, 103, 135, 140, 143
 - vs. photon energy 113
- Oregonator model 295
- organometallic compounds, splitting 343
- organosamarium 401, 402, 404, 406-408, 413, 420, 421, 434, 437, 445, 459
- oscillating reactions 291
- out-of-plane
 - expansion 128
 - lattice parameter 154
- oxidation
 - by bromate ions 344
 - by molecular oxygen 346
 - by peroxides 345
 - of alcohols 319
 - of carbonyl compounds 323
 - of catechols 322
 - of cerium(III)
 - by lead(IV) oxide, 284
 - by molecular oxygen 285
 - by ozone 285
 - by persulfate 284, 285
 - by silver(II) oxide 284
 - of epoxides 325
 - of ethers 325
 - of hydrocarbons 314
 - of hydroquinones 322
 - of phenols 319
 - of sulfur-containing compounds 325
- oxidimetry (cerimetry) 286
- parameter-free quasi-particle calculations 217
- partial molar enthalpy 183
- Pd (111) 237
- Pd clusters 178
- Pd d-band centroid 178
- Pd dots 92, 123
- Pd MNN peak 171
- Pd nanoparticle 93, 178
- Pd stair 165
- Pd-Gd interfacial alloy 175
- Pd-Y interdiffusion 168
- Pd/AlO_x composite cap layer 174
- Pd/AlO_x/Y 173
- Pd/Y matrix sample 164, 166
- Pd/Y₂O₃/Y 167
- Pd/YO_x layer 174
- Peierls distortion 208
- pentamethylcyclopentadienyl 395
- persistent photoconductivity 108, 111
- phase boundaries 102
- phase diagram
 - Ce-Ge-Bi 59
 - Ho-Ni-Bi 30
 - La-In-Bi 58
 - polycrystalline thin YH_x 185
 - Pr-Fe-Bi 22
 - R-Bi 4
 - R-Bi-Se 69
 - R-Bi-Te 71
 - R₂S₃-Bi₂S₃ 64
 - Sm-Fe-Bi 22
 - Y-Ni-Bi 30
- phase transition

- ErPd₂Bi 41
- YbCuBi 50
- photocatalyst 365
- photochemical reduction 365
- photoconductivity 110
- photodoping 108
- photoemission spectra 177
- photoreduction of water 365
- pinacol coupling reactions 402, 430, 431
- pixel switching 146, 147, 163
- plaquette 165
- polycrystalline
 - rare earth films 101
 - switchable mirrors 89
 - YH_x epitaxial YH_x films 184
- potential landscape 150
- potentiostatic configuration 94
- potentiostatic electrolytic measurement 116
- power-law quantum fluctuations 111
- Pr₅FeBi₂ 21, 22
- Pr₆Fe₁₃Bi 21, 22
- praseodymium films 122, 176
- pressure composition isotherm 94, 98, 116, 139, 140, 182
 - La_{0.55}Y_{0.45}H_x 189
- PrH_{2±ξ} 128
- PrH_{3-δ} 125, 128
- PrH_x 125-127
- PrH_x films 176
- proton donor 396, 400, 402, 404, 405, 408-416, 422, 429
- proton induced X-ray emission (PIXE) 100
- PrPtBi 43, 46
- pulsed laser deposition 90
- Pummerer-type rearrangement 326
- pyridinium hexachloroacetate(IV) 309

- QCM 98, 116
- quantum confinement effects 231
- quantum critical point 109, 111, 112
- quartz crystal
 - microbalance 98
 - monitor (QCM) 98
- quasiparticle
 - band structure for YH₃ 217
 - band structures 221
 - calculations 220
 - correction 209
- quenched hysteresis 195

- R-Bi-S 62
- R-Bi-Se 69
- R-Bi-Te 71
- R-Co-Bi 24
- R-Cu-Bi 48
- R-d-element-Bi 15, 16
- R-f-element-Bi 14
- R-Fe-Bi 21
- R-Li-Bi 11
- R-Mg
 - alloy 90, 92
 - alloy film 91, 227
 - multilayer films 249
 - multilayers 91
- R-Mn-Bi 15
- R-Ni-Bi 30
- R-p-element-Bi 56
- R-Pd-Bi 38
- R-Pt-Bi 42
- R-R alloy 89
- R-R alloy films 186
- R-s-element-Bi 10
- R₁₂Co₅Bi 25, 26, 28
- R₁₄MnBi₁₁ 17-19
- R₄Bi₂S₉ 63, 68-70
- R₄Bi₂Te 72, 73
- R₅Bi₃ 4
- R₅Bi₃Br 74
- R₅CoBi₂ 24, 25
- R₅CuBi₃ 49, 51
- R₅Ni₂Bi 33, 37
- R₅Pd₂Bi 37, 39, 41
- R₅Pt₂Bi 37, 43, 48
- R₆CoBi₂ 25
- R₆Fe₁₃Bi 22
- R₆Fe₁₃Si 24
- R₆FeBi₂ 21-23
- R₆MBi₂ 20
- R₆MnBi₂ 17, 19, 20
- radial hydrogen diffusion 198
- radiolabeling 334
- RAgBi₂ 52, 53
- rare earth hydrides 87
- RBi₂ 4
- RBi₂S₄ 63, 64
- RBi₂Te₄ 72, 73
- RBi₄Te₇ 72, 73
- RBiS₃ 63, 68
- RBiTe₃ 72, 73
- RBS spectra 169
- RCu_{1-x}Bi₂ 48, 49
- real and imaginary dielectric constant 115, 190, 193

- La_{1-y}Y_yH₂ 191
- redox 289
- indicator 289
- mediator 350, 351
- potential 284
- potential dependence on acidity 284
- properties of cerium(IV) 284
- reduction of cerium(IV)
- by water 285
- reflectance spectra 124
- refractive index 113, 115, 145
- resistivity of Pr films 123
- response (τ_s) and recovery times (τ_R) 181
- Reststrahlen 207
- RH₂ films 194
- RHEED pattern 162, 170
- rib polymer 356
- ridge switching 150
- RLi₂Bi₂ 12
- rms roughness 167
- RNiBi 32, 36, 40, 45
- RNiBi₂ 32, 34, 35
- role of additives 409, 416
- RPd₂Bi 39-41
- RPdBi 38, 40, 45
- RPtBi 40, 43-45
- RRhBi 28, 29, 31
- Rutherford backscattering 100, 156

- SAED pattern 159
- samarium
- (II) iodide 395-397, 399, 429
- (II) bromide 429
- (II) chloride 429
- films 128
- Sc₆Bi_{1.68}Te_{0.80} 72, 73
- screened exchange LDA (sX-LDA) 222
- self-consistent
- band structure calculations 105
- local density approximation (LDA) 208
- 'sequential' (or 'tandem') reactions 405
- Shockley partial dislocations 158
- side-chain polymer 356
- silica-supported reagents 313
- single electron reducing agent 395, 396
- single-crystalline films 146
- size-induced structural transitions 261
- Sm 139
- Sm-Mg alloy 239
- Sm_{0.30}Mg_{0.70} 240
- Sm_{0.30}Mg_{0.70}H_x 240, 241
- Sm_{0.32}Mg_{0.68} 239
- Sm_{0.34}Mg_{0.66} 239, 240
- Sm_{0.34}Mg_{0.66}H_x 241
- Sm_{0.48}Mg_{0.52} 240, 243, 249
- Sm₃GdBi₃ 14
- Sm₅Bi₃H 10, 11
- Sm₅FeBi₂ 21, 22
- Sm₆Fe₁₃Bi 22
- SmBi₂Se₄ 70, 71
- SmBi₄S₇ 69
- SmBi₄Se₇ 70, 71
- SmBiSe₃ 70, 71
- SmH_{3- δ} 130, 134, 138, 139
- SmH_x 136-138
- Sm(II) alkoxide and amide reductants 456
- Sm(II) pyrazolylborate 466
- SmPtBi 43, 47
- solar energy conversion 366
- solid solution
- CeBi_{1-x}Te_x 74
- Gd(Al_{1-x}Bi_x)₂ 57
- La₄(Pb_xBi_{1-x})₃ 59
- La_xCe_{1-x}Bi 14
- (R_{1-x}Bi_x)₂S₃ 64
- Sm₄(Sb_xBi_{1-x})₃ and Gd₄(Sb_xBi_{1-x})₃ 60, 61
- solubility
- Pd in RBi 40
- rare earth bismuth chalcogenides 56
- Th in Bi, effect of adding Ni 38
- specific heat
- Ce₈Pd₂₄Bi 42
- CeCu_{1-x}Bi₂ 49
- CePtBi 46
- CeRhBi 30
- Gd₄(Sb_xBi_{1-x})₃ 61
- PrPtBi 46
- YbPdBi 41
- YbPtBi 47
- sputter deposition 90
- strong correlation model 212
- strong metal-support interaction (SMSI) state 178
- structural and optical switching 151
- structural relationship
- antimonides and bismuthides 75
- DyRhBi and R₆MBi₂ 30
- Gd₅CuBi₃ and Gd₅Bi₃ 51
- Ho₁₂Co₅Bi and Ho₆Co₂Ga 26
- La₄Bi₂S₉ and other chalcogenides 68
- RBi and RNiBi 36
- RBiS₃ and Sb₂S₃ 68
- RPd₂Bi and RPdBi 41

- RPtBi and RBi 45
- SmRhBi and DyRhBi 28
- substrate polymer 356
- Super Slurper 363
- superabsorbent polymers 363
- superconductor
 - $\text{La}_4(\text{Pb}_x\text{Bi}_{1-x})_3$ 59
 - LaRhBi 30
- superstructure peaks 170
- supported cerium(IV) reagents 313
- surface potential difference 132
- switchable mirror effect 87, 88, 90, 97, 226
- switchable mirrors, first generation 89, 97, 101
- switching time 92, 119, 122, 141, 142, 165, 166, 169, 177, 254
- synthesis
 - bismuthides 3
- Szigeti effect charge 116

- Tauc's plot 123, 126, 128
- Tb_4Bi_3 4
- TBDMS 343
- TEM micrograph
 - Gd film nanoparticle film 261
 - Y nanoparticles prepared by PLA 256
- tert*-butoxycarbonyl group 343
- tert*-butyldimethylsilyl 343
- test reagents for alcohols 372
- tetrahedral sites 113, 117
- $\text{Th}_2\text{N}_2\text{Bi}$ 61, 62
- theoretical models 207
- thermal evaporation 90
- thermochromic effect 235
- thin film
 - Gd–Fe–Bi 23
 - Gd($\text{Fe}_{1-x}\text{Co}_x$) 28
 - Lu–Co–Bi 28
 - Lu–Ni–Bi 38
 - $\text{MnBi}_{1-x}\text{R}_x$ 21
- thioacetalization 326
- ThNiBi_2 32, 38
- TLC stains 371
- TmBi_2Se_4 70, 71
- TmBi_4Se_7 70, 71
- TmBiSe_3 70, 71
- Tomlin's algorithm 123
- topographical histograms 152
- topography 179
- transient of current 120, 121, 140
- transmittance 124, 132
 - histograms 152
 - spectra of 500 nm $\text{YH}_{3-\delta}$ films capped with Pd 175
 - window 139
- transparency window 105
- triangular domains 89
- triangular network of dark ridges 148
- triangular ridge network 147, 148
- trihydride state 87, 90
- triphenylmethyl 343
- tris[trinitratocerium(IV)] paraperiodate 310
- trityl 343
- tunable constant transmittance 226
- tunable magnetic layers 271
- twinning 158
- two-dimensional weak localization 108

- $\text{U}_2\text{N}_2\text{Bi}$ 61, 62
- UCuBi_2 52
- uncapped Pr film 124
- UNiBi_2 32, 38
- USbBi 61

- vacancy states 126
- valance band spectra of Pd capped Gd films 265
- variation in electrical resistivity 89
- Volmer–Weber growth 162

- weak correlation model 209
- weighted density approximation (WDA) 224
- wind force 197, 199
- WO_x 144

- X-ray
 - absorption spectra of $\text{Gd}_{0.40}\text{Mg}_{0.60}$ 247
 - coherence length 233
 - diffractograms of $\text{La}_{1-y}\text{Y}_y\text{H}_x$ 187
 - diffractograms of the Pd capped Pr films 129
- XANES 286
- XPD 161
- XPS 161
- XPS spectra 161
- XRD peaks, time evolution 229

- yttrium 162
 - 3d doublet 161
 - channel spectra 156
 - concentration dependence of optical band gap 195
 - core clusters with Y_2O_3 shell 256
 - dihydride 105
 - domains 159
 - films 103

- hydroxide 178
- nanoparticles 255
- on Nb coated Al₂O₃ 146
- on W 146
- ridges 159
- stair 165
- thin film (200 nm) 176
- Y-Mg alloy 228
- Y-Mg multilayers 250
- Y-Pd alloy 92, 168
- Y_{0.40}Mg_{0.60} 250
- Y_{0.40}Mg_{0.60}H_{0.8} 251
- Y_{0.40}Mg_{0.60}H_{2.4} 251
- Y_{0.4}Mg_{0.6}H_{2.4} 250
- Y_{0.5}M_{0.5}H_x 228
- Y_{0.5}Mg_{0.5} 228, 229
- Y_{0.5}Mg_{0.5} alloy film 228
- Y_{0.9}Mg_{0.1}H_{2.9-δ} 235
- Y_{0.9}Mg_{0.1}H_x 235
- Y_{1-z}Mg_z 229-231
- Y_{1-z}Mg_zH_x alloys 232
- Y₁₅Pd₈₅ 170
- Y₂₅Pd₇₅ 170
- Y₂O₃ 167, 197
- Y/Mg-H_{2.4} multilayers 250
- Yb₁₆Bi₁₁ 4
- Yb₅Bi₃H 10, 11
- Yb₉Zn₄Bi₉ 54-56
- YbCuBi 49, 50
- YbLiBi 10, 13
- YbPdBi 41
- YbPtBi 43, 47
- YD₃ 204
- YD_{3-δ} 206, 207
- YD_x 204, 206
- YH_{0.19} 118
- YH_{1.73} 105
- YH₂ 118, 148, 155, 158, 205, 251
- YH₂ domains 159
- YH₂ films 194
- YH₂ ridges 159
- YH_{2+ξ} 87
- YH_{2.3} 160
- YH_{2.86±0.02} 88
- YH_{2.87} 112
- YH_{2.9} 107
- YH_{2.99} 109
- YH_{2±ξ} 88, 118
- YH₃ 88, 108, 118, 158, 204, 208, 250
- volume of YH₃ per formula unit 231
- YH_{3-δ} 88, 105-109, 112-115, 118, 141, 147, 148, 175, 206, 207, 228-230, 235
- YH_{3-δ} clusters 231
- YH_x 110, 114, 115, 126, 149, 204, 206, 209
- YH_x films 105
- YH_x (LaH_x) 87
- YLi₃Bi₂ 10-12
- YMG intermetallic 251
- YMGH_{0.8} 251
- YMGH_{2.4} 251
- YO_x 177
- YO_x layer 92, 93
- Y(OH)₃ 195
- YPtBi 43, 46
- zero-value band gap 209
- Zhang-Rice singlet 192, 199
- Zintl phase 3
- Ce₃MnBi₅ 18
- Eu₁₄InBi₁₁ 58
- R₁₄MnBi₁₁ 18
- RCuBi 51
- ZrO₂H_x 97